

平成 28 (2016) 年度 研究成果
著書・総説・発表論文等

著書・総説・発表論文等リスト

著書・総説・解説

1. 井上和仁
「人工光合成への道筋（1）— 生物学からのアプローチ」
夢の新エネルギー「人工光合成」とは何か、光生物学協会編、井上晴夫監修 2016、第4章 pp. 105-120 講談社ブルーバック
2. 北島正治、櫻井英博、井上和仁、増川一
「シアノバクテリアからの高効率水素生産」
再生可能エネルギーによる水素製造、2016
第4節 pp. 143-151 S&T出版
3. 井上和仁
「ヘテロシスト形成型シアノバクテリアを利用した光生物学的水素生産法」
光触媒／光半導体を利用した人工光合成、堂免一成、瀬戸山亨監修 2017
第2編、第2章 pp. 84-91 NTS
4. 石川理史、村山 徹、上田 渉
ゼオライト、**2016**, 33,110-120
5. Sun, S. Sato, W. Ueda
Glycerol hydrogenolysis into useful C3 chemicals
Applied Catalysis B: Environmental, **2016**, 193, 75-92
6. D. Sun, S. Sato, W. Ueda, A. Primo, H. Garcia, A. Corma
Production of C4 and C5 alcohols from biomass-derived materials
Green Chemistry, **2016**, 18(9), 2597-2016
7. 上田 渉
複雑構造がもたらす複合酸化物の酸化触媒機
CSJカレントレビュー（活性酸素・フリーラジカルの科学）, **2016**, 21, 74-80
8. S. Ishikawa, T. Murayama, W. Ueda

Microporous Crystalline Mo-V Mixed Oxides for Selective Oxidations
Catal. Sci. & Tech., **2016**, 6, 617-629

9. 上村大輔
植物化学研究の動向について
常磐植物化学研究所 寄稿 (2016)
10. 上村大輔編
天然物の化学 - 魅力と展望-
科学のとびら 60、1-6、東京化学同人 (2016)
11. 上村大輔
化学の要点シリーズ 18 基礎から学ぶケミカルバイオロジー (2017)
「まえがき」「第1章ケミカルバイオロジーとは」「第2章ケミカルバイオロジー理解のために」、
12. 坪村太郎、川本達也、佃俊明
「無機化学の基礎」化学同人
2017年3月1日
13. K. Nomiya, T. Yoshida, and S. Matsunaga
Nova book, Capter 7, 213-242 (2016) in Polyoxometalates: Properties, Structure and Synthesis, Ed by A. P. Roberts;
Formation of Phosphanegold(I) Cluster Cations Mediated by Polyoxometalates, Molecular Structures and Catalysis for Organic Transformation
[2016 *Nova Science Publishers, Inc.*]
14. 引地 史郎
金属酵素モデルの構造と特性
「活性酸素・フリーラジカルの科学: 計測技術の新展開と広がる応用 (CSJ Current Review 21 ; 日本化学会編)」, Part I, 2章, Basic concept-5, pp. 42-50, 化学同人 (2016).
15. 田邊豊和, 伊藤拳人, 金子信悟, 郡司貴雄, 大坂 武男, 松本 太
多重定電流パルスによって作製した Ni/Cu 電気めっき多層膜 におけるナノ周期構造と耐摩耗性
まてりあ 第 55 巻 第 12 号特集 601 (2016).

16. 大平剛

「甲殻類の脱皮・変態とホルモン」

天野勝文・田川正朋編集、ホルモンから見た生命現象と進化シリーズ II 発生・変態・リズム 一時一、第三章、2016年、26-43

発表論文

1. Daisuke Seo, Masaharu Kitashima, Takeshi Sakurai, Kazuhito Inoue
Kinetics of NADP⁺/NADPH reduction-oxidation catalyzed by the ferredoxin-NAD(P)⁺ reductase from the green sulfur bacterium *Chlorobaculum tepidum*
Photosynth. Res. **2016**, 130:479-489
2. Tatyana Laurinavichene, Masaharu Kitashima, Kenji V. P. Nagashima, Takeshi Sato, Hidehiro Sakurai, Kazuhito Inoue, Anatoly Tsygankov
Effect of growth conditions on advantages of hup⁻ strain for H₂ photoproduction by *Rubrivivax gelatinosus*
Int. J. Hydrogen Energy. in press
3. Hajime Masukawa, Hidehiro Sakurai, Robert P. Hausinger, Kazuhito Inoue
Increased heterocyst frequency by patN disruption in *Anabaena* leads to enhanced photobiological hydrogen production at high light intensity and high cell density
Appl. Microbiol. Biotechnol., in press.
4. Takeshi Sato, Kazuhito Inoue, Hidehiro Sakurai, Kenji V. P. Nagashima
Effects of the deletion of hup genes encoding the uptake hydrogenase on the activity of hydrogen production in the purple photosynthetic bacterium *Rubrivivax gelatinosus* IL144
J. Gen. Appl. Microbiol. in press
5. T. Igarashi, Z-X. Zhang, T. Haioka, N. Iseki, N. Hiyoshi, N. Sakaguchi, C. Kato, S. Nishihara, K. Inoue, A. Yamamoto, H. Yoshida, N. Tsunoji, W. Ueda, T. Sano, M. Sadakane
Synthesis of ε-Keggin-type Cobaltomolybdate-based 3D Framework Material and

Characterization Using Atomic-scale HAADF-STEM and XANES
Inorg. Chem., **2017**, *56*, 2042-2049

6. Z. Zhang, Sadakane, S-I. Noro, N. Hiyoshi, A. Yoshida, M. Hara, W. Ueda
All-inorganic porous soft-framework by assembly of metal oxide molecular wires
Chem. Eur. J., **2017**, *23*, 1972-1980.
7. T. Murayama, J. Hirata, K. Nakajima, K. Omata, E. Hensen, W. Ueda
Hydrothermal Synthesis of a Layered-type W-Ti-O Mixed Metal Oxide and its
Solid Acid Activity
Catal. Sci. Technol., **2017**, *7*, 243-250
8. S. Ishikawa, D. Jones, S. Iqbal, R. Christian, D. Morgan, D. Willock, P. Miedziak,
J. Bartley, J. Edwards, T. Murayama, W. Ueda, G. Hutchings
Identification of the catalytically active component of Cu-Zr-O catalyst for the
hydrogenation of levulinic acid to γ -valerolactone
Green Chemistry, **2017**, *19*, 225-236.
9. Y. Goto; K.-I. Shimizu, K. Kon, T. Toyao, T. Murayama, W. Ueda
NH₃-efficient ammoxidation of toluene by hydrothermally synthesized layered
tungsten-vanadium complex metal oxides
J. Catal., **2016**, *344*, 346-353
10. T. Murayama, W. Ueda, M. Haruta
Deposition of Gold nanoparticles on Niobium Pentoxide with Different Crystal
Structures for Room-Temperature Carbo Monoxide Oxidation
ChemCatChem, **2016**, *8*, 2620-2624
11. N. Napan, T. Takeguchi, T. Mori, S. Iwamura, I. Ogino, S.R. Mukai, W. Ueda
Effect of the mesopores of carbon supports on the CO tolerance of Pt₂Ru₃ polymer
electrolyte fuel cell anode catalyst
International J. Hydrogen Energy, **2016**, *41*, 13697-13704
12. Z. Zhang, M. Sadakane, N. Hiyoshi, A. Yoshida, M. Hara, W. Ueda
Acidic Ultrafine Tungsten Oxide Molecular Wires for Cellulosic Biomass
Conversion
Angew. Chem. Int. Ed., **2016**, *55*, 10234-10238
13. T. Murayama, B. Katrynick, S. Heyte, M. Araque, S. Ishikawa, F. Dumeignil, S.
Paul, W. Ueda
Role of crystalline structure in allyl alcohol selective oxidation over Mo₃VO_x

complex metal oxide catalysts
ChemCatChem, **2016**, 8, 2415-2420

14. T. Murayama, N. Kuramata, W. Ueda
Hydrothermal Synthesis of W-Ta-O Complex Metal Oxides by Assembling MO₆ (M = W or Ta) Octahedra and Creation of Solid Acid
J. Catal., **2016**, 339, 143-152
15. Z. Zhang, S. Ishikawa, Y. Tsuboi, M. Sadakane, T. Murayama, W. Ueda
New crystalline complex metal oxides created by unit-synthesis and their catalysis based on porous and redox properties
Faraday Discussions, **2016**, 188, 81-98
16. S. Ishikawa, T. Murayama, M. Kumaki, Z. Zhang, A. Yoshida, W. Ueda
Synthesis of trigonal Mo-V-M^{3rd}-O (M^{3rd} = Fe, W) catalysts by using structure-directing agent and catalytic performances for selective oxidation of ethane
Topics in Catal., **2016**, 59, 1477-1488
17. Z.X. Zhang, H. Yoshikawa, Z.Y. Zhang, T. Murayama, M. Sadakane, Y. Inoue, W. Ueda, K. Awaga, M. Hara
Synthesis of Vanadium-incorporated, polyoxometalate-based open frameworks and their applications for cathode-active materials
Eur. J. Inorg. Chem., **2016**, 8, 1242-1250
18. Y. Goto, K.-I. Shimizu, T. Murayama, W. Ueda
Hydrothermal synthesis of microporous W-V-O as an efficient catalyst for ammoxidation of 3-picoline
Appl. Catal., General A, **2016**, 509, 118-122
19. K. Omata, K. Matsumoto, T. Murayama, W. Ueda
Direct Oxidative Transformation of Glycerol to Acrylic Acid over Nb-based Complex Metal Oxide Catalysts
Catal. Today, **2016**, 259, 205-212
20. Hisao Saneyoshi, Yuta Yamamoto, Kazuhiko Kondo, Yuki Hiyoshi, Akira Ono
"Conjugatable/Bioreduction Cleavable Linker for the 5'-Functionalization of Oligonucleotides"
J. Org. Chem., **2017**, 82, 1796-1802. (DOI:10.1021/acs.joc.6b02527)
21. Hisao Saneyoshi, Koichi Iketani, Kazuhiko Kondo, Takeo Saneyoshi, Itaru

- Okamoto, and Akira Ono
“Synthesis and Characterization of Cell-Permeable Oligonucleotides Bearing Reduction-Activated Protecting Groups on the Internucleotide Linkages”
Bioconjugate Chem., **2016**, *27*, 2149–2156.
(DOI:10.1021/acs.bioconjchem.6b00368)
22. Takenori Dairaku, Kyoko Furuita, Hajime Sato, Jakub Šebera, Katsuyuki Nakashima, Jiro Kondo, Daichi Yamanaka, Yoshinori Kondo, Itaru Okamoto, Akira Ono, Vladimír Sychrovský, Chojiro Kojima, and Yoshiyuki Tanaka
“Structure Determination of an Ag^I-Mediated Cytosine–Cytosine Base Pair within DNA Duplex in Solution with ¹H/¹⁵N/¹⁰⁹Ag NMR Spectroscopy”
Chem. Eur. J. **2016**, *22*, 13028-13031. (DOI: 10.1002/chem.201603048)
23. Takenori Dairaku, Kyoko Furuita, Hajime Sato, Jakub Šebera, Katsuyuki Nakashima, Akira Ono, Vladimír Sychrovský, Chojiro Kojima, and Yoshiyuki Tanaka
“Hg^{II}/Ag^I-mediated base pairs and their NMR spectroscopic studies”
Inorg. Chim. Acta, **2016**, *452*, 34-42. (DOI: 10.1016/j.ica.2016.03.018)
24. Yusuke Kataoka, Konomi S. Kataoka, Hidenobu Murata, Makoto Handa, Wasuke Mori, Tatsuya Kawamoto
Synthesis and characterizations of a paddlewheel-type dirhodium-based photoactive porous metal-organic framework
Inorg. Chem. Commun. **2016**, *68*, 37-41.
25. Yusuke Kataoka, Natsumi Yano, Takashi Shimodaira, Yin-Nan Yan, Mikio Yamasaki, Hidekazu Tanaka, Kohji Omata, Tatsuya Kawamoto, Makoto Handa
Paddlewheel-Type Dirhodium Tetrapivalate Based Coordination Polymer: Synthesis, Characterization, and Self-Assembly and Disassembly Transformation Properties
Eur. J. Inorg. Chem. **2016**, 2810-2815.
26. Tomoyo Suzuki, Yutaka Suzuki, Tatsuya Kawamoto, Ryo Miyamoto, Shinkoh Nanbu, Hirotaka Nagao
Dinuclear Ruthenium(III)-Ruthenium(IV) Complexes, Having a Doubly Oxido-Bridged and Acetato- or Nitrate-Capped Framework
Inorg. Chem. **2016**, *55*, 6830-6832.

27. Natsumi Yano, Yusuke Kataoka, Hidekazu Tanaka, Tatsuya Kawamoto, Makoto Handa
A New Paddlewheel-Type Dirhodium-Based Metal-Organic Framework with Deprotonated 2,6-Bis(2-benzimidazolyl) pyridine
ChemistrySelect **2016**, *1*, 2571-2575.
28. Yusuke Kataoka, Saki Mikami, Hiroshi Sakiyama, Minoru Mitsumi, Tatsuya Kawamoto, Makoto Handa
A neutral paddlewheel-type diruthenium(III) complex with benzamidinato ligands: Synthesis, crystal structure, magnetism, and electrochemical and absorption properties
Polyhedron in press.
29. R. Sakamoto, S. Morozumi, Y. Yanagawa, M. Toyama, A. Takahayama, N. C. Kasuga, and K. Nomiya
Synthesis, structure-activity relationship of the antimicrobial activities of dinuclear *N*-heterocyclic carbene (NHC)-silver(I) complexes
J. Inorg. Biochem., **163**, 110-117 (2016).
30. Y. Takagi, Y. Okamoto, C. Inoue, N. C. Kasuga and K. Nomiya
Crystal structure of poly[(L-valinato-*N,O*)silver(I)]
Acta Cryst. Section E73, 354-357 (2017).
31. S. Matsunaga, T. Otaki, Y. Inoue, H. Osada, and K. Nomiya
Aluminum- and gallium-containing open-Dawson polyoxometalates
Z. Anorg. Allgem. Chem., **642**, (7), 539-545 (2016).
32. S. Matsunaga, E. Miyamae, Y. Inoue, and K. Nomiya
 β,β -Isomer of Open-Wells-Dawson Polyoxometalate Containing Tetra-Iron(III) Hydroxide Cluster: $[\{\text{Fe}_4(\text{H}_2\text{O})(\text{OH})_5\}(\beta,\beta\text{-Si}_2\text{W}_{18}\text{O}_{66})]^{9-}$
Inorganics **4** (2), article number 15 (2016). doi:10.3390/inorganics4020015
33. S. Matsunaga, T. Otaki, Y. Inoue, K. Mihara, and K. Nomiya
Synthesis, Structure, and Characterization of In_{10} -Containing Open-Dawson Polyoxometalate
Inorganics **4** (2), article number 16 (2016). doi:10.3390/inorganics4020016

34. H. Arai, T. Yoshida, E. Nagashima, A. Hatayama, S. Horie, S. Matsunaga, and K. Nomiya
Silver- and Acid-free Catalysis by POM-Assisted Phosphanegold(I) Species for Hydration of Diphenylacetylene
Organometallics, **35**, 1658-1666 (2016).
35. E. Nagashima, T. Yoshida, S. Matsunaga and K. Nomiya
Effects of counteranions on the molecular structures of phosphanegold(I) cluster cations formed by polyoxometalate (POM)-mediated clusterization
Dalton Trans., **45**, 13565-13575 (2016).
36. A. Nakamizu, T. Kasai, J. Nakazawa, and S. Hikichi
Immobilization of a Boron Center-Functionalized Scorpionate Ligand on Mesoporous Silica Supports for Heterogeneous Tp-Based Catalysts
ACS Omega, **2017**, 2, 1025-1030.
37. T. Nozawa, Y. Mizukoshi, A. Yoshida, S. Hikichi and S. Naito
Formation of Ru active species by ion-exchange method for aqueous phase reforming of acetic acid
Int. J. Hyd. Energy, **2017**, 42, 168-176.
38. T. Takayama, J. Nakazawa and S. Hikichi
A pseudotetrahedral nickel(II) complex with a tridentate oxazoline-based scorpionate ligand: chloride[tris(4,4-dimethyloxazolin-2-yl)phenylborato]nickel(II)
Acta Cryst., **2016**, C72, 842-845.
39. K. Ando, J. Nakazawa and S. Hikichi
Synthesis, Characterization and Aerobic Alcohol Oxidation Catalysis of Palladium(II) Complexes with a Bis(imidazolyl)borate Ligand
Eur. J. Inorg. Chem., **2016**, 2603-2608.
40. A. J. Jeevagan, T. Gunji, F. Ando, T. Tanabe, S. Kaneko, F. Matsumoto
Enhancement of the Electrocatalytic Oxygen Reduction Reaction on Pd₃Pb Ordered Intermetallic Catalyst in Alkaline Aqueous Solutions
J. Appl. Electrochem., **46**, 745-753 (2016).

41. T. Tanabe, W. Miyazawa, T. Gunji, M. Hashimoto, S. Kaneko, T. Nozawa, M. Miyauchi, F. Matsumoto
Site-selective deposition of binary Pt-Pb alloy nanoparticles on TiO₂ nanorod for acetic acid oxidative decomposition
J. Catal., **340**, 276-286 (2016).
42. Kazuma Uehara, Keitaro Yamazaki, Takao Gunji, Shingo Kaneko, Toyokazu Tanabe, Takeo Ohsaka, Futoshi Matsumoto
Evaluation of Key Factors for Preparing High Brightness Surfaces of Aluminum Films Electrodeposited from AlCl₃-1-Ethyl-3-Methylimidazolium Chloride-Organic Additive Baths
Electrochimica Acta, **215**, 556–565 (2016).
43. Toyokazu Tanabe, Takao Gunji, Youhei Honma, Koki Miyamoto, Takashi Tsuda, Yasumasa Mochizuki, Shingo Kaneko, Shinsaku Ugawa, Hojin Lee, Takeo Ohsaka, Futoshi Matsumoto
Preparation of Water-Resistant Surface Coated High-Voltage LiNi_{0.5}Mn_{1.5}O₄ Cathode and Its Cathode Performance to Apply a Water-Based Hybrid Polymer Binder to Li-Ion Batteries
Electrochimica Acta, **224**, 429-438 (2017).
44. Toshiaki Matsubara and Tomoyoshi Ito
Theoretical Study of the Heterolytic σ Bond Cleavage on the Ge=O Bond of Germanone. An Insight into the Driving Force from both Electronic and Dynamical Aspects.
J. Phys. Chem. A, **121**, 1768-1778 (2017).
45. N. Watanabe, H. Takatsuka, H. K. Ijuin, A. Wakatsuki and M. Matsumoto
Hydrogen bonding network-assisted chemiluminescent thermal decomposition of 3-hydroxyphenyl-substituted dioxetanes in crystal
Tetrahedron Letters, **2017**, 57, 2558-2562.
46. N. Watanabe, K. Hiragaki, K. Tsurumi, H. K. Ijuin, and M. Matsumoto
Solvent- and temperature-controlled inversion of π -facial selectivity in the 1,2-cycloaddition of singlet oxygen to hydroxyphenyl-substituted cyclohexadihydrofurans
Tetrahedron, **2017**, 73, 1845-1853.

47. N. Watanabe, Y. Mizuno, Y. Maeda, H. K. Ijuin and M. Matsumoto
Synthesis of tricyclic dioxetanes that exhibit intramolecular charge-transfer-induced decomposition: relationship between structure and chemiluminescence efficiency
Heterocycles, in press.

プロシーディング

1. Arockiam John Jeevagan, Takao Gunji, Toyokazu Tanabe, Shingo Kaneko, Futoshi Matsumoto
Synthesis of Reduced Graphene Oxide-Supported PtAu Catalysts and Their Electrochemical Activity for Formic Acid Oxidation
ECS Transactions, Electrochemical Society, **72(29)**, 15-21 (2016).
2. Fuma Ando, Takao Gunji, Toyokazu Tanabe, Shingo Kaneko, Tsuyoshi Takeda, Takeo Ohsaka, Futoshi Matsumoto
Enhancement of the Oxygen Reduction Reaction (ORR) on a PtPb Nanoparticle /TiO₂/Cup-stacked Carbon Nanotube Composite in Acidic Aqueous Solutions based on the Electronic Interaction between PtPb and TiO₂
ECS Transactions, Electrochemical Society, Inc., **72(33)**, 53-62 (2016).

報告書・紀要

1. 村山徹, Z. Zhang, 定金正洋、上田 渉、坂口紀史
複合酸化物ナノワイヤの合成と構造解析
Nanotech Japan Bulletin, **2016**, 9(3)
2. Z. Zhang, T. Murayama, N. Yasuda, W. Ueda
Ultrathin inorganic molecular wires based on transition metal oxide
SPRING-8 Research Frontiers 2015, **2016**, 70-71.
3. 松永諭、井上雄介、長田宏紀、大滝卓也、三原航平、力石紀子、

野宮健司

2015 年度神奈川大学総合理学研究所共同研究助成論文「 Al^{3+} および Ga^{3+} イオンを開口部に導入した open-Dawson 型ポリ酸塩の合成と構造解析」
Science J. of Kanagawa University, **27**, 39-43 (2016)

「人工光合成への道筋（1）－生物学からのアプローチ」
 夢の新エネルギー「人工光合成」とは何か、光生物学協会編、井上晴夫監修 2016、
 第4章 pp105-120。講談社ブルーバックス



光化学協会 編
 井上 晴夫 監修

〈執筆一覧〉 (五十音順)

- | | |
|------|---------|
| 石谷 治 | 東京工業大学 |
| 伊藤 繁 | 名古屋大学 |
| 井上和仁 | 神奈川大学 |
| 井上晴夫 | 首都大学東京 |
| 神谷信夫 | 大阪市立大学 |
| 工藤昭彦 | 東京理科大学 |
| 瀬戸山亨 | 三菱化学 |
| 民秋 均 | 立命館大学 |
| 堂免一成 | 東京大学 |
| 久富隆史 | 東京大学 |
| 藤井律子 | 大阪市立大学 |
| 正岡重行 | 分子科学研究所 |
| 三澤弘明 | 北海道大学 |

〈執筆協力・資料提供〉

- | | |
|------|---------|
| 荒井健男 | 豊田中央研究所 |
| 稲垣伸二 | 豊田中央研究所 |
| 定金正洋 | 広島大学 |
| 佐藤俊介 | 豊田中央研究所 |
| 高木慎介 | 首都大学東京 |
| 森川健志 | 豊田中央研究所 |

再生可能エネルギーによる 水素製造

 S&T 出版

ISBN978-4-907002-58-9
C3058 ¥60,000E
定価(本体 60,000 円 + 税)



再生可能エネルギーによる 水素製造

 S&T 出版

執筆 者 (執筆順)

柴田 善朗	(一財)日本エネルギー経済研究所 新エネルギーグループ マネージャー
石原 顕光	横浜国立大学 先端科学高等研究院 グリーン水素研究センター 特任教員(教授)
太田 健一郎	横浜国立大学名誉教授
児玉 竜也	新潟大学 工学部 化学システム工学科 教授
木村 元昭	日本大学 理工学部 機械工学科 教授
加納 純也	東北大学 多元物質科学研究所 教授
堂脇 清志	東京理科大学 理工学部 経営工学科 教授
平田 好洋	鹿児島大学 大学院理工学研究科 化学生命・化学工学専攻 教授
鮫島 宗一郎	鹿児島大学 大学院理工学研究科 化学生命・化学工学専攻 准教授
下之菌 太郎	鹿児島大学 大学院理工学研究科 化学生命・化学工学専攻 助教
中島田 豊	広島大学 大学院先端物質科学研究科 分子生命機能科学専攻 教授
石原 達己	九州大学 カーボンニュートラル・エネルギー国際研究所 教授
松本 広重	九州大学 カーボンニュートラル・エネルギー国際研究所 教授
曾根 理嗣	宇宙航空研究開発機構 宇宙科学研究所 准教授
杉山 正和	東京大学 大学院工学系研究科 電気系工学専攻 准教授
泉 康雄	千葉大学 大学院理学研究科 准教授
佐山 和弘	産業技術総合研究所 太陽光発電研究センター 首席研究員
野地 智康	大阪市立大学 複合先端研究機構 特任講師
近藤 政晴	名古屋工業大学 生命・応用化学専攻 助教
神 哲郎	産業技術総合研究所 材料・化学領域 無機機能材料研究部門 機能調和材料グループ 研究グループ長
丹後 佑斗	岡山大学 大学院環境生命科学研究科
村上 範武	岡山大学 大学院環境生命科学研究科
石本 寛伍	岡山大学 大学院環境生命科学研究科
田嶋 智之	岡山大学 大学院環境生命科学研究科 講師
高口 豊	岡山大学 大学院環境生命科学研究科 准教授
北島 正治	神奈川大学 総合理学研究所 研究員
櫻井 英博	神奈川大学 光合成水素生産研究所 プロジェクト研究員・早稲田大学名誉教授
井上 和仁	神奈川大学 理学部 教授
増川 一	大阪市立大学 複合先端研究機構 特任准教授
三宅 淳	大阪大学 大学院基礎工学研究科 機能創成専攻 教授
比護 拓馬	早稲田大学 先進理工学研究科 助手
小河 脩平	早稲田大学 先進理工学研究科 助教
関根 泰	早稲田大学 先進理工学研究科 教授
井口 昌幸	産業技術総合研究所 化学プロセス研究部門 産総研特別研究員
姫田 雄一郎	産業技術総合研究所 再生可能エネルギー研究センター 上級主任研究員
川波 肇	産業技術総合研究所 化学プロセス研究部門 グループ長
花田 信子	筑波大学 大学院システム情報工学研究科 構造エネルギー工学専攻 助教

※大学法人、国立研究開発法人格は省略しております。

第4節 シアノバクテリアからの高効率水素生産

神奈川大学 北島 正治 櫻井 英博 井上 和仁
大阪市立大学 増川 一

1. はじめに

今日の人類社会が消費するエネルギーは、全世界ではその約80%が化石燃料の燃焼から得られている。しかしながら、化石燃料消費によって二酸化炭素ガスが放出された結果、大気中の二酸化炭素濃度は産業革命前には約280 ppmであったものが400 ppmに上昇し、気候への影響が懸念されており、化石燃料に代わる代替エネルギー資源の開発が期待されている。地球に降り注ぐ太陽光エネルギーは、化石燃料消費のおよそ6,000倍(表1)と膨大であるが、エネルギー密度は平均約1,500 kWh/m²/年と低いことから、大規模に活用するためには広大な面積を利用する必要がある。光合成生物は、光合成によって太陽光エネルギーを利用し、炭素同化や窒素同化などの生命活動を行う。筆者らは、光合成微生物であるシアノバクテリアによる水素生産を、将来的には海洋上で大規模に行うことを構想し、研究を行っている^{1,5)}。

表1 太陽光エネルギーと社会的エネルギー消費

	エネルギー 10 ¹⁸ MJ/年	比 対化石燃料消費
太陽光エネルギー	2,660,000	5800
化石燃料消費	460	1
人類の食物摂取エネルギー	22	0.05

(IEA Energy Outlook 2014より)

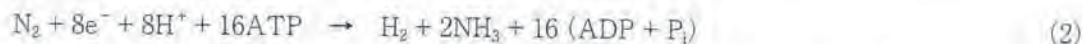
2. 水素生産に関与する酵素

様々な光合成微生物が水素発生活性を持つことが知られており、これらの水素発生には酵素ヒドロゲナーゼあるいはニトロゲナーゼが関与している。ヒドロゲナーゼは一般的に、Feのみ、あるいはFeおよびNiからなる金属クラスターを含む酵素で、[FeFe]ヒドロゲナーゼあるいは[NiFe]ヒドロゲナーゼが知られている。これらが触媒する反応を式(1)に示す。



生理学的に、ヒドロゲナーゼは、式(1)の両方向の反応を行う双方向性ヒドロゲナーゼと、左方向の反応(水素吸収)のみを行う取り込み型ヒドロゲナーゼの二種類に大別できる。双方向性ヒドロゲナーゼは、細胞内の酸化還元状態によって反応の方向が決まるため、一般に、酸素が存在すると水素吸収が起こる。

ニトロゲナーゼは、分子状窒素をアンモニアへと固定する酵素であるが、その反応の過程で必然的な副産物として水素を発生する。この酵素の活性部位にはFeを足場として中心にMo、VあるいはFeを持つ金属クラスターが結合しており、それぞれMo型ニトロゲナーゼ、V型ニトロゲナーゼおよびFe-only型ニトロゲナーゼと呼ばれている。代表的なMo型の反応式を式(2)に示す。



大気下では1分子のN₂を固定する際に、8個の電子と16分子のATPを使って、2分子のアンモニアの他に副産物として1分子のH₂が発生する。一方で、反応気相中にN₂が存在しない場合でも、e⁻、H⁺、ATPが供

給されるとニトロゲナーゼ反応が駆動され水素が発生するが、その場合の反応式を式(3)に示す。



ニトロゲナーゼによる水素発生は、ATPを必要とすることからヒドロゲナーゼよりもエネルギー変換効率の点で劣るが、一方向的な反応であることから水素の再吸収を防ぐためのコストを必要としない点が有利といえる。

なお、ヒドロゲナーゼもニトロゲナーゼも一般に、酸素感受性の高い酵素であり、高効率な水素生産を長期間維持するためには、酵素が存在する細胞部位を低酸素濃度に維持することが必要であるという点は共通している。

3. シアノバクテリアによる水素生産

シアノバクテリアは、単細胞性のものや糸状性のものなどがあり形態は多様であるが、細菌でありながら高等植物などと同様の酸素発生を伴う光合成を行う。酸素発生型の光合成では光エネルギーを利用して水を分解し電子を得て、細胞内での炭素同化や窒素固定に利用する。

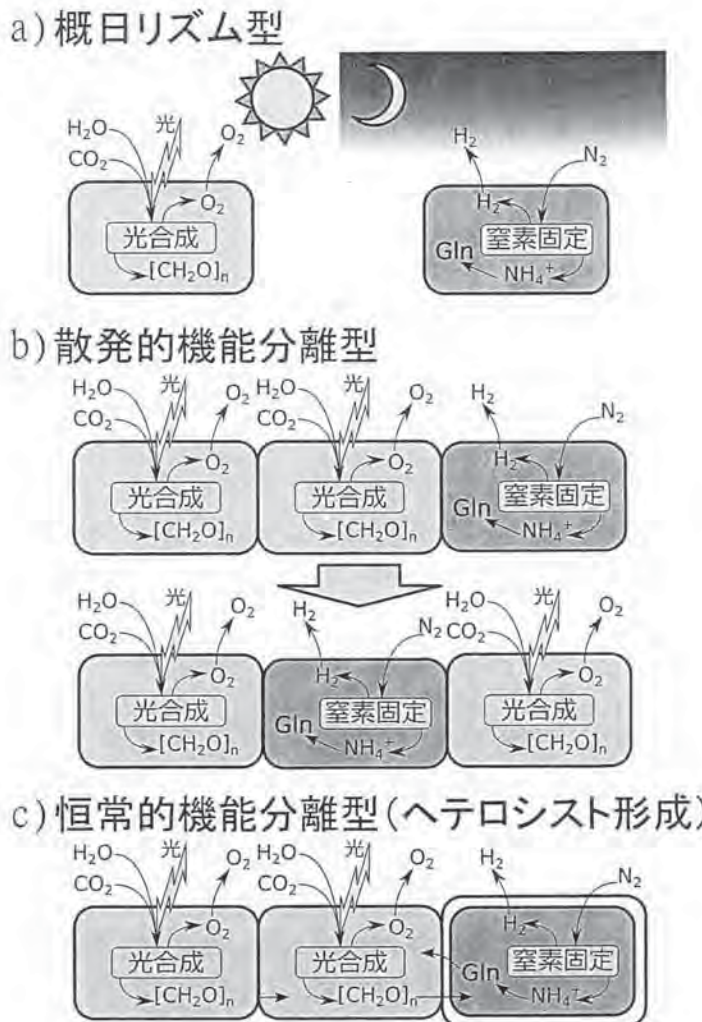


図1 シアノバクテリアの窒素固定

a) 単細胞性のシアノバクテリア。昼に光合成を行い夜に窒素固定を行う(時間的分離)。b) 糸状性シアノバクテリア。糸状体の細胞が、かわるがわる光合成と窒素固定を行う(同一細胞が時間的に交代)。c) ヘテロシスト形成型シアノバクテリア。栄養細胞(左側の2つ)で光合成を行い、ヘテロシスト(右端)で窒素固定を行う(空間的分離)。

シアノバクテリアは、いくつかの種が窒素固定活性を持つことが知られているが、細胞の形態は様々である。窒素固定を行う種の多くは、一般に取り込み型ヒドロゲナーゼを持つが、さらに双方向性ヒドロゲナーゼ活性を持つものも知られている。単細胞性のシアノバクテリアでは、一つの細胞内で酸素を発生する光合成と、酸素感受性であるニトロゲナーゼによる窒素固定を行うことになる(図1a)。これらの生物では、2つの活性は時間的に分離されており、昼間に光合成による炭素同化を行い、夜間に活発な酸素呼吸を行ってATP合成を行いつつ細胞内酸素濃度を下げ、ニトロゲナーゼによる窒素固定とそれに伴う水素生産が行われる。

窒素固定能を持つ糸状性のシアノバクテリアには、細胞分化を伴わずに窒素固定を行うものと、窒素固定に特化した異型細胞(ヘテロシスト)を分化して窒素固定を行うものが知られている。前者では、一つの細胞内で酸素発生型光合成と酸素感受性のニトロゲナーゼによる窒素固定を両立させなければならないが、糸状体の一部の細胞は酸素発生型光合成を行って糖質を蓄積し、他の細胞は一時的に光合成を止めて自身の細胞内に蓄積した糖質を分解しつつ窒素固定と水素生産を行っているが、その役割を時間的に次々と順次別の細胞が担うことで解決している(図1b)。糸状体全体で見ると、酸素発生型光合成と同時に窒素固定も行っているように見える。一方、ヘテロシスト形成型シアノバクテリアでは、窒素欠乏になると糸状体の一部の細胞が、10-20細胞に1細胞の割合で、窒素固定に特化したヘテロシストと呼ばれる異型細胞を分化する。ヘテロシストでは酸素発生型光合成は行われず、厚い細胞壁を形成して外部からの酸素の透過を防ぎ、呼吸活性を高めることで酸素濃度を下げ、安定してニトロゲナーゼによる窒素固定と水素生産を行うことができる(図1c)。一方、ヘテロシスト以外の栄養細胞は酸素発生型光合成を行い、合成した糖質をヘテロシストへ輸送し、その糖質はニトロゲナーゼ反応の還元力源として使われる。ヘテロシストからは、窒素固定産物であるアンモニアがグルタミンに変換され、栄養細胞へと輸送される。このようにヘテロシスト形成型シアノバクテリアでは、糸状体を構成する細胞が分化し役割分担することで、全体として酸素発生型光合成とニトロゲナーゼ反応(窒素固定および水素生産)を両立させている。筆者らは、ヘテロシスト形成型シアノバクテリアを光生物学的水素生産に利用し、研究・開発を行っている。

4. 水素生産性向上

地表に降り注ぐ太陽光エネルギーを用いて、光生物学的に水から水素を生産するという点で、シアノバクテリアのニトロゲナーゼに基づく水素生産はクリーンな再生可能エネルギー資源生産方法として期待できるが、実用化にはいくつかの課題がある。

4.1 ヒドロゲナーゼ活性による水素の再吸収

窒素固定を行う多くのシアノバクテリアは、ヒドロゲナーゼを有しており、ヒドロゲナーゼは、水素を吸収すると考えられるので、高効率な水素生産を目指すためにはヒドロゲナーゼ活性を抑えることが必要となる。天然の株からニトロゲナーゼ活性が高くかつヒドロゲナーゼ活性を持たないものを単離することも考えられるが、その選抜は一般に困難である。一方で、遺伝子工学的にヒドロゲナーゼ活性を抑えることは容易であり、筆者らもいくつかのヒドロゲナーゼに関する変異株を作出している。ヘテロシスト形成型シアノバクテリアのモデル生物である *Anabaena/Nostoc* sp. PCC 7120株(以降PCC 7120株)からは、取り込み型ヒドロゲナーゼの構造遺伝子 *hupL*、ヒドロゲナーゼ成熟化酵素遺伝子 *hypF*の挿入破壊株を作成している。*hupL*または *hypF*の破壊株では水素生産活性の最大値は、親株と比較して4-10倍へと増大した。

Nostoc sp. PCC 7422株(以降PCC 7422株)は、実験室条件下でのスクリーニングで、ニトロゲナーゼ活性がPCC 7120株よりも高く双方向性ヒドロゲナーゼの活性が非常に低い株として選抜され⁶⁷⁾、この株からの *hupL*破壊株は、PCC 7120 *hupL*破壊株よりも高い水素生産速度の変異株が得られた。筆者らは、主としてPCC 7120株の *hupL*破壊株、*hypF*破壊株およびPCC 7422 *hupL*破壊株を用いて水素生産の更なる効率化へ向けて研究を続けている。

4.2 窒素栄養充足によるニトロゲナーゼ活性の低下

水素生産活性はニトロゲナーゼ活性に依存しているため、窒素固定が十分に行われて窒素栄養が充足されると水素生産活性が低下してしまう。例えば、経時的に水素生産活性を測定すると、空気を培養気相とした場合では高い水素生産活性は1-2日程度しか継続しないが、培養気相をArで置換した場合は5-6日間高い水素生産活性が持続する。大規模に水素生産を行う場合、経済的観点からは、培養気相として高価なArを用いる代わりに安価なN₂を利用しても高活性が維持できることが望ましい。筆者らはニトロゲナーゼ反応で窒素固定よりも水素生産に向かう電子の割合を高めることを目的に、以下のような遺伝子改変を導入した。

4.2.1 金属クラスター周辺配位子の改変

ニトロゲナーゼの活性中心にはFeを足場とした金属クラスターが結合しており、生物界では中心金属としてMoが結合したFeMo-cofactorを持つMo型ニトロゲナーゼが主に利用されている。このMo原子にはホモクエン酸が結合しており(図2)、従属栄養細菌*Klebsiella pneumoniae*では、ホモクエン酸合成酵素を破壊することで水素生産活性を維持したまま窒素固定能が大幅に低下することが知られている⁸⁾。シアノバクテリアPCC 7120株の*hupL*破壊株から、ホモクエン酸合成酵素遺伝子*nifV1*の破壊株を作成したところ、N₂存在下で培養液当たりの水素生産性が2倍程度に増加した⁹⁾。

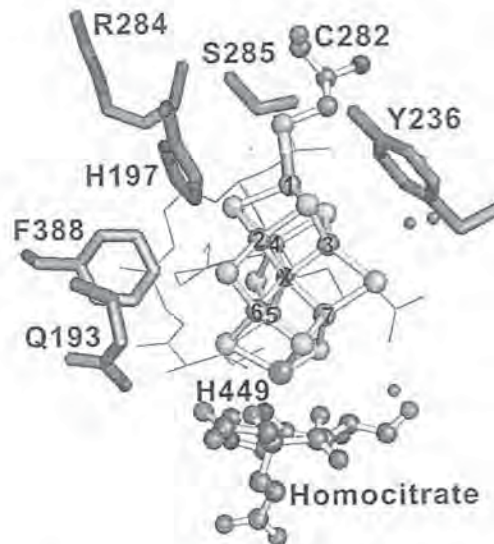


図2 FeMo-cofactorと周辺構造
Mo型ニトロゲナーゼのFeMo-cofactorと結合に関与するアミノ酸残基およびホモクエン酸
(文献10, H. Masukawa et al., *Appl. Environ. Microbiol.*, 76, 6741-6750 (2010) より改変)

4.2.2 金属クラスター周辺環境の改変

Mo型ニトロゲナーゼのアミノ酸一次配列情報は、多くの窒素固定生物から得られており、また*Azotobacter vinelandii*などの生物からは単離精製され、立体構造が解かれている。これらの情報から、金属クラスター近傍の非常によく保存されているアミノ酸残基のうち6残基を選び、49株のアミノ酸残基置換変異株を作成した¹⁰⁾。これらの株の多くが窒素固定能の大幅な低下を示し、そのうちのいくつかの株では培養気相中にN₂が存在しても水素生産性が低下することなく、空気下で親株と比較して3-4倍の水素生産活性を示すものが得られた。また、親株では高濃度の窒素ガスを含む培養気相では、水素生産活性が急速に低下するが、変異株の一部では、同じ気相条件下でも、3週間程度にわたって水素生産活性が維持可能であった¹¹⁾。すなわち一部のアミノ酸残基置換変異株では、ニトロゲナーゼの窒素固定および水素生産活性のう

ち前者の活性は大幅に低下しており、窒素栄養が充足されないため高い酵素活性レベルが持続するが、変異酵素の水素生産活性は低下していないため高い水素生産活性が持続すると考えられる。

これらの変異株を利用すれば、水素生産の実用化に当たって、培養気相をArに置換する必要がなく、安価なN₂で済むため、気体コストの削減が可能である。

4.3 強光下での光阻害

シアノバクテリアは一般に、アンテナ色素蛋白質複合体としてフィコビリ色素を結合したタンパク質であるフィコシアニンやフィコエリスリンなどからなるフィコビリソームと呼ばれる巨大な分子集合体を高濃度に形成している。高濃度のアンテナ色素系を持つことにより、陰性植物が林の木陰のような薄暗い環境でも光合成成長を行い成長できるのと同じように、水系の光が弱い環境下でも生育できる。しかし、夏の直達光のような非常に強い光条件下では、シアノバクテリアは捕集した光エネルギーの大部分を光合成に利用できず、過剰に捕集したエネルギーによって光化学反応系が障害を受ける。また、培養液全体を考えれば、表層の細胞だけが光をほとんど吸収するので、深層の細胞は光を利用できなくなり、全体としての水素生産性が低下すると考えられる。筆者らの将来的な構想である洋上での大規模生産においては、光が培養液の深層にも行き渡ることによって、全体として効率的に水素生産できることが望ましい。フィコビリソーム削減株が、強光下でも生育が可能であれば、大規模化実用化において、培養液全体としての水素生産の効率化に貢献することが期待される。

5. バイオリアクターの検討

太陽光エネルギーを利用する場合、前述のように広大な面積で利用することが重要である。陸上では、新たなエネルギー作物の栽培は、食物生産の場との競合が懸念されるので、筆者らは海洋表面を利用することを提案している。しかし、洋上で水素生産工場のようなものを建設する場合そのコストは莫大なものとなり、経済的に立ち行かないと考えられる。Amos¹²⁾は緑藻の光合成を利用した水素生産コストに関する試算を行っており、経済性の確保には、バイオリアクターのコストについて、受光面1 m²あたり数10 USドルを超えないことが必要だと結論している。筆者らは、低コストで生産可能なバイオリアクターとして、水素バリアー性のプラスチックフィルムを加工したバッグを利用することを提案している。海洋上での使用を想定した場合、波による物理的な障害、紫外線などによる光化学的な障害、付着生物などによる障害などによって引き起こされる水素バリアー性の低下が考えられるため、外層として上記障害に耐性のあるものを付加し、さらに培養液の接触による水素バリアー性の低下も考えられるため、内層として培養液保持バッグを用いる、三層構造のバイオリアクターが再利用性などの観点から有用であると考えている(図3)。筆者らは、水素バリアー性プラスチックフィルムバッグの内部気相組成の経時変化を測定するためのガスサンプリングポートを開発した¹³⁾。内部ガスのサンプリング時に針が貫通するフィルム部分は、内側・外側からブチルゴムセプタムに挟まれ、パイスのプッシュロッドを繰り出すことによりインナーパッドおよびニードルポートを介して支持される(図4)。水素バリアー性プラスチックフィルムは、高温水蒸気滅菌に耐え透明度の高い柔軟プラスチックフィルムである市販品のGLフィルムおよびベセーラフィルム(共に凸版印刷)を用いた。どちらもPET樹脂をベースとした積層膜で、水素バリアー層は前者が酸化アルミニウムコート後者がアクリル酸樹脂系高分子コートとなっており、その上に二軸延伸ナイロン層が積層されている。各々にさらに無延伸ポリプロピレン(CPP)層あるいは直鎖状低密度ポリエチレン(LLDPE)層が積層されたものを選択し、これら4種のプラスチックフィルムを用いたバッグに、ガスサンプリングポートを装着して内部気相の経時変化について測定を行った。CPPを積層されたものの耐熱温度が120℃と高圧蒸気滅菌に耐えられるが透明度がやや低く、LLDPEを積層されたものの耐熱温度は100℃と高圧蒸気滅菌には耐えられないが透明度が高く、前者はオートクレーブ滅菌(120℃, 20分)処理を、後者は間歇滅菌(100℃, 20分, 3回)処理したものを測定に使用した。これらのバッグの水素透過性は20-90 cm³ m⁻² day⁻¹ atm⁻¹であり、将来の

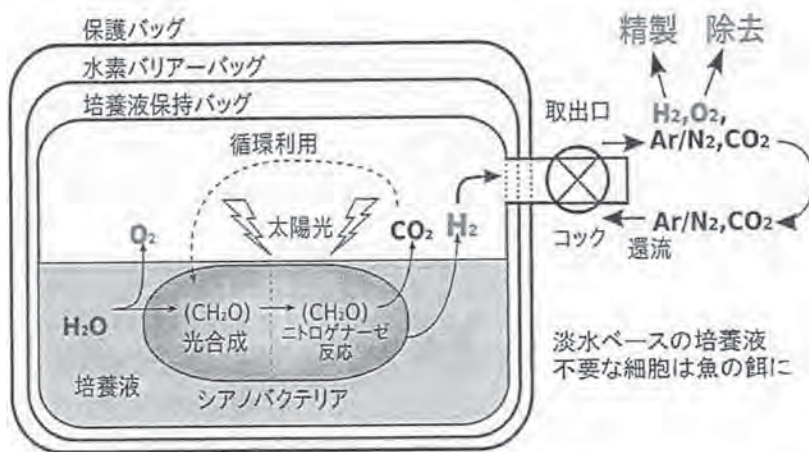


図3 バイオリアクターの構想図
培養液保持バッグ、水素バリアーバッグ、保護バッグの三層構造。

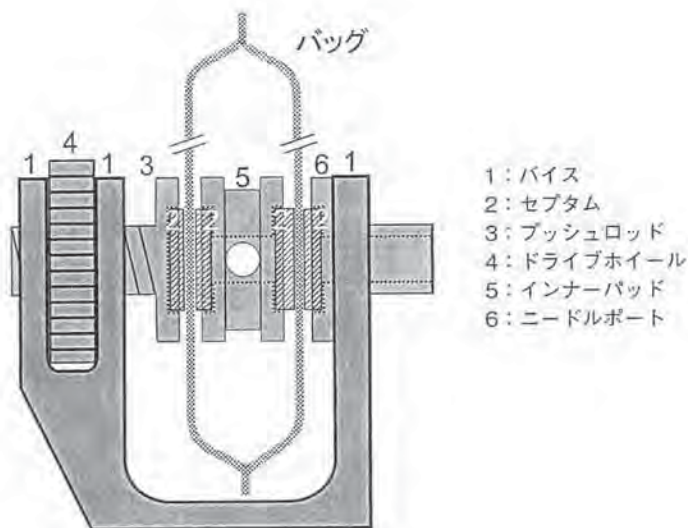


図4 ガスサンプリングポート
(文献13, M. Kitashima et al., *Biosci. Biotech. Bioch.*, 76, 831-833 (2012) より)

実用に期待が持てる水素ガスバリアー性を持つことが示された(表2)。なお、ガスサンプリングポート、水素バリアー製バッグは(株)Wakhy研究所が製作し、GLサイエンスから入手可能である。

5.1 密閉ガラス容器とバッグでの水素生産性比較

実験室条件下での水素生産性の測定には、多くの場合、密閉ガラス容器が用いられている。前述のとおり、シアノバクテリアのニトロゲナーゼに基づく水素生産では、光合成による酸素発生条件下で酸素感受性のあるニトロゲナーゼを利用するが、酸素に対する防御は必ずしも完全でないため、酸素濃度の上昇によりニトロゲナーゼ活性の低下が引き起こされる。固定容量の密閉ガラス容器と、新規考案したプラスチックバッグとで水素蓄積を比較(図5)したところ、後者の方が30%程度水素の生産量が多くなることが明らかとなった。これは、気体発生に伴う酸素分圧上昇の程度が、柔軟プラスチックバッグでは体積固定容器よりも低く、ニトロゲナーゼの酸素による阻害が軽減されたためだと考えられる。

表2 フィルムの水素透過性

処理方法	フィルム素材	水素透過性 ($\text{cm}^3 \cdot \text{m}^{-2} \cdot \text{day}^{-1} \cdot \text{atm}^{-1}$)
処理なし	Be-E	87
	Be-P	44
	Gl-E	49
	Gl-P	44
間歇減菌 (3回) 100℃ × 20 min	Be-E	22
	Be-P	53
	Gl-E	29
	Gl-P	48
オートクレーブ減菌 120℃ × 20 min	Be-E	89
	Be-P	67
	Gl-E	n.d.*
	Gl-P	41

*オートクレーブ減菌したGl-Eは変形が激しく測定不能だった。Be: Beselaフィルム。Gl: GLフィルム。E: 直鎖状低密度ポリエチレン。P: 無延伸ポリプロピレン。(文献13 M. Kitashima *et al.*, *Biosci. Biotech. Bioch.*, 76, 831-833 (2012) より)



図5 密閉ガラス容器とプラスチックバッグでの水素生産の比較
左: プチルゴム中栓を付けた密閉ガラス容器。右: ガスサンプリングポートを付けたプラスチックバッグ。実験開始時の気相体積は等しい。

6. 模擬太陽光照射装置による条件検討

自然光の光強度変化のように日周性のある強光下での水素生産活性を評価するため、模擬太陽光照射装置(ソーラーシミュレーター, コイト電工社)を神奈川大学湘南ひらつかキャンパスに設置した(図6)。この模擬太陽光照射装置は、横2メートル縦1メートルの調温可能な水槽の上方に、20灯のグローセラランプと6灯の赤色LEDと、無段階に角度調節可能な52枚のシャッターブレードが設置されており、水槽に浮かべた培養試料への照射光強度および範囲は、光源の点灯数および点灯位置とシャッターブレードの角度とを調節

参 考 文 献

- 1) H. Masukawa *et al.*, *Ambio*, 41, 169-173 (2012).
- 2) H. Sakurai *et al.*, *J. Photochem. Photobiol., C. Photochem. Rev.*, 17, 1-25 (2013).
- 3) H. Sakurai *et al.*, *Mar. Biotechnol.*, 9, 128-145 (2007).
- 4) H. Sakurai *et al.*, *Life*, 5, 997-1018 (2015).
- 5) 増川一他, *BIOINDUSTRY*, 33, 36-42 (2016).
- 6) H. Masukawa *et al.*, *Mar. Biotechnol.*, 11, 397-409 (2009).
- 7) F. Yoshino *et al.*, *Mar. Biotechnol.*, 9, 101-112 (2007).
- 8) P. A. McLean *et al.*, *Nature*, 292, 655-656 (1981).
- 9) H. Masukawa *et al.*, *Appl. Environ. Microbiol.*, 73, 7562-7570 (2007).
- 10) H. Masukawa *et al.*, *Appl. Environ. Microbiol.*, 76, 6741-6750 (2010).
- 11) H. Masukawa *et al.*, *Int. J. Hydrogen Energ.*, 39, 19444-19451 (2014).
- 12) W. A. Amos, <http://www.nrel.gov/docs/fy04osti/35593.pdf> : Milestone Completion Report NREL, Golden, CO, 2004, Jan.
- 13) M. Kitashima *et al.*, *Biosci. Biotech. Bioch.*, 76, 831-833 (2012).

光触媒/光半導体を利用した 人工光合成

— 最先端科学から実装技術への発展を目指して —

第2編 材料・システム創製

第2章 ヘテロシスト形成型シアノバクテリアを利用した
光生物学的水素生産法

神奈川大学 井上 和仁

第2章 ヘテロシスト形成型シアノバクテリアを利用した 光生物学的水素生産法



神奈川大学 井上 和仁

1. はじめに

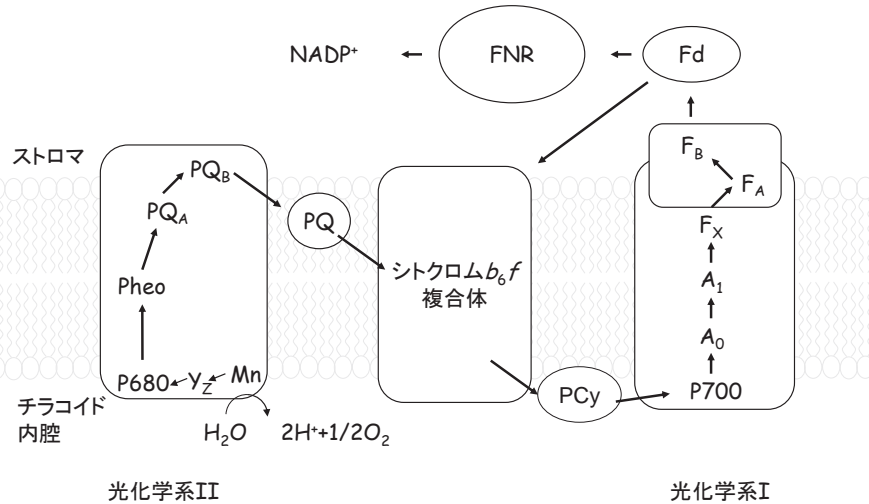
地表に到達する太陽光エネルギーは、人類が消費する化石燃料エネルギーの6,000倍以上と膨大であり、量的に再生可能エネルギー源として有望であるが、その平均エネルギー密度は約 $1,500 \text{ kWhm}^{-2}\text{yr}^{-1}$ と低く、いかにして経済性を確保しつつこれを利用するかが課題となる。植物や藻類などの光合成生物を利用したバイオ燃料の研究はさまざまに行われているが、エネルギー変換効率、経済性、大規模化、食料生産との競合など克服すべき課題は多い。本稿では、ヘテロシスト形成型シアノバクテリアを利用した光生物学的水素生産に関する研究の現状について、筆者らがやっている研究を中心に紹介する。

2. 光合成の電子伝達系

光合成での光エネルギーの化学エネルギーへの変換は光化学系と呼ばれる反応系で行われ、シアノバクテリアや植物の葉緑体には光化学系IIと光化学系Iの2種類の光化学系が存在する。光化学系IIは強い酸化力を形成して H_2O を分解し、光化学系Iは強い還元力を形成して NADP^+ を還元する(図1)。光化学系IIもIもチラコイド膜内で大きな色素タンパク質複合体として存在するが、これはそれぞれ複合体のコアをなす反応中心とその周辺を取り巻くアンテナ複合体から構成される。

光合成の最初の反応は光合成色素による光吸収で、そのエネルギーは励起エネルギーとして反応中心に存在する反応中心クロロフィルに移動する。反応中心クロロフィルは特殊な環境に置かれたクロロフィルの二量体(スペシャルペア)で、光化学系IIではP680、光化学系IではP700と呼ばれる。光合成色素の種類は生物種により多様性がみられ、多くのシアノバクテリアはクロロフィル a 、カロテノイド、フィコビリリンを持つ。

励起状態の反応中心クロロフィルから電子が一次電子受容体、さらに、二次、三次の電子受容体へと次々と受け渡される。光化学系IIでは P680^* (*は励起状態を示す)から電子がフェオフィチン(Pheo)、 PQ_A を経て PQ_B に渡る。 PQ_A と PQ_B はキノンの1種であるプラストキノンである。 PQ_B は2個の電子を受け取るとストロマ側で H^+ を2個結合して還元型の PQH_2 となって反応中心からチラコイドの膜中に遊離する。一方、光化学系Iでは P700^* から放出された電子は5種類の電子受容体 A_0 、 A_1 、 F_X 、 F_A 、 F_B を経てストロマにある可溶性のタンパク質であるフェレドキシン(Fd)に渡り NADP^+ を還元して NADPH を生産する。 F_X 、 F_A 、 F_B はいずれも4個の鉄と4個の硫黄が作る $4\text{Fe}-4\text{S}$ 型の鉄硫黄クラスターである。反応中心に多く



Mn：光化学系II複合体に結合したマンガンクラスター，Y_z：光化学系II複合体のチロシン残基，Pheo：フェオフィチン，PQ：プラストキノン，PCy：プラストシアニン，A₀：初発電子受容体，A₁：二次電子受容体，F_x：鉄硫黄クラスターX，F_B：鉄硫黄クラスターB，F_A：鉄硫黄クラスターA，Fd：フェレドキシン，FNR：Fd-NADP⁺レダクターゼ

図1 光合成の電子伝達系

の電子受容体が存在するのは、電子を放出して正電荷を持った反応中心クロロフィルから電子を引き離して電荷の再結合を防ぐことにあると考えられる。酸化された反応中心クロロフィルは、外部の電子源から電子を得て還元される。光化学系II反応中心のチラコイドの内腔側にはマンガンクラスターを触媒中心に持つ酸素発生系（水分解系）があり、水の酸化によって放出された電子によってP680⁺が還元される。P700⁺は光化学系IIで還元されたPQH₂からシトクロム b₆f複合体を経て、最終的にはチラコイドの内腔に存在する銅タンパク質であるプラストシアニン（PCy）に渡った電子により還元される（図1）。キノンは脂溶性の物質で、チラコイド膜内部にキノンプールとして大量の分子が存在している。光化学系IIとシトクロム b₆f複合体の間でのキノンを介したH⁺の移動と電子伝達はキノンサイクルと呼ばれ、チラコイド膜を隔て内腔とストロマとの間に大きなH⁺の濃度勾配、すなわち電気化学ポテンシャルを形成する。この電気化学ポテンシャルを利用して、F型ATPアーゼCF₀-CF₁複合体がADPと無機リン酸を結合してATPを合成する。二酸化炭素固定反応（カルビン回路）は、光合成電子伝達系で合成されたATPとNADPHにより駆動される。

上述した水からNADP⁺に至る電子伝達系はZ-スキームまたは直線的な電子伝達系と呼ばれるが、条件により、光化学系Iだけを使った循環的な電子伝達系も働く。この場合は、光化学系Iからの電子がFdを経由してシトクロム b₆f複合体に渡り酸化型のPQを還元しストロマ側のH⁺を利用してPQH₂となる。チラコイド膜中に遊離したPQH₂はシトクロム b₆f複合体の還元型キノンの結合部位に到達するとルーメン側へH⁺を放出し、チラコイド膜を隔てたH⁺の濃度勾配を形成しCF₀-CF₁複合体でのATP合成に利用される。循環的な電子伝達系では光化学系IIは駆動しないので、水の分解は起こらない。また、緑色硫黄細菌や紅色細菌などの、いわゆる光合成細菌は光化学系を1種類しか持っておらず、循環的な電子伝達系でH⁺の濃度勾配を形成する。

3. ヘテロシスト形成型シアノバクテリア

シアノバクテリアは形態学的にも、生態学的にも非常に大きな多様性を持つ細菌群である。このなかで一部の糸状性シアノバクテリア (*Anabaena* や *Nostoc* 属など) は、硝酸塩類などの窒素栄養源が欠乏した条件下では、通常の酸素発生型光合成を行う栄養細胞の一部が、約10~20細胞の間隔で異型細胞 (ヘテロシスト) へと分化する。ヘテロシストは窒素固定に特化した細胞で、内部でニトロゲナーゼを発現し大気中の N_2 を還元しアンモニアを生産する。

ヘテロシスト内部は、酸素発生を行う光化学系IIの活性を欠いており、加えて細胞壁を肥厚させて外部から細胞内への酸素透過を防ぎ、呼吸活性を増加させて酸素を除去しており、細胞内部の酸素濃度は低い状態に保たれている。ニトロゲナーゼは酸素により失活しやすいが、上記のように、ヘテロシスト内部は酸素濃度が低いため活性を維持することができる。糸状体全体としては通常の光合成を行う栄養細胞と窒素固定を行うヘテロシストで役割を分業させており、糸状体はあたかも多細胞生物のような細胞共同体として存在している。糸状体の細胞間には細胞間連絡が存在し、栄養細胞で酸素発生型光合成による糖質合成が行われ、その糖質がヘテロシストへ運ばれ、ニトロゲナーゼ反応を駆動する還元力の源となる。ヘテロシストには光化学系Iが存在するので循環的な電子伝達系によって光エネルギーを利用してニトロゲナーゼ反応に必要なATPを生産でき、合成されたアンモニアはグルタミンに変換されて栄養細胞へと輸送される。このように酸素発生を伴う光合成と嫌気条件を必要とする窒素固定が空間的に分離されることにより、糸状体全体として酸素発生型光合成とニトロゲナーゼ反応の両立が可能となる (図2)。

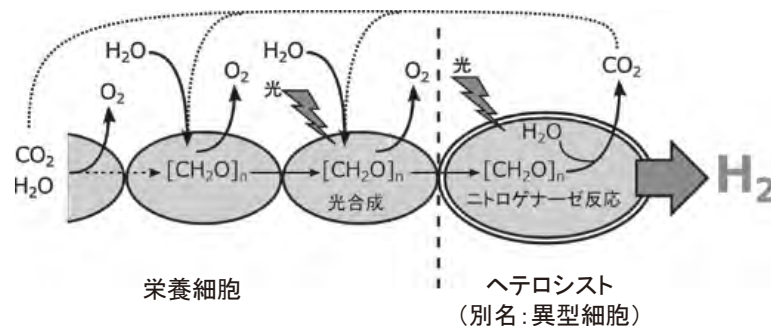


図2 糸状性シアノバクテリアにおけるヘテロシストと栄養細胞の分業

4. ヒドロゲナーゼとニトロゲナーゼ

シアノバクテリアの水素生産に利用できる酵素はヒドロゲナーゼとニトロゲナーゼであり、後者は一部のものだけが持つ。ニトロゲナーゼは、空気中の窒素ガスをアンモニアへと固定する酵素で、マメ科植物の根に共生する根粒菌など、一部の原核生物のみが活性を持つ。水を電子供与体として利用できる光合成生物のうち、ニトロゲナーゼを持つのは、一部のシアノバクテリアに限られ、クロレラ、クラミドモナス、ユーグレナなどの真核光合成生物は持たない。ニトロゲナーゼは、多くの場合、モリブデン (Mo)、鉄 (Fe)、硫黄 (S) からなる金属クラスターを結合している (Mo型ニトロゲナーゼ) が、Moの代わりにバナジウム (V) (V型ニトロ

ゲナーゼ) やFeのみ (Fe-only型ニトロゲナーゼ) を持つものもある。窒素固定の効率が最も高いとき (N₂濃度が十分高いとき), Mo型酵素の反応は, 式(1)のように表され, 電子の1/4が水素生産に向けられるニトロゲナーゼによる窒素 (N₂) 固定反応では, アンモニア生成に伴う必然的な副産物として水素が発生する。



式(1)では, 電子の約3/4が窒素固定 (N₂還元) に, 残りの約1/4が水素発生 (H⁺還元) に使われる。窒素ガスが存在しないアルゴン (Ar) 気相下などでは, 投入された全ての電子が水素生産に向かう。



反応に必要な電子は, 直接的にはFdまたはフラボドキシシン (フラビントタンパク質) から供給される。ニトロゲナーゼは, 式(1)に示されるように大量のATP (生体内の高エネルギー物質) を消費するので, 理論的な最大エネルギー変換効率は低いが, ヒドロゲナーゼと異なり酸素存在下でも不可逆的に水素を生産できる点が, 大規模生産時の省力化にとっての利点となる (表1)。

ヒドロゲナーゼは, 水素の発生または吸収を触媒する酵素で, 次の反応を触媒する。



生理的条件下で, 上記のように可逆的に反応を触媒できるものは, 双方向性 (可逆的) ヒドロゲナーゼ (シアノバクテリアのものはNiFe型ヒドロゲナーゼHox, 緑藻のものはFe型ヒドロゲナーゼ) と呼ばれ, 水素生産への利用が可能である。この反応の電子供与体はFdまたはNADPHである。これに対し, 水素の吸収だけを触媒するものは, 取込み型ヒドロゲナーゼ (Hup) と呼ばれ, ヘテロシスト内部で発現している。Hupはニトロゲナーゼにより発生するH₂を再吸収し, エネルギーの損失を防いでいると考えられる。

光合成微生物では, 各種光合成細菌, シアノバクテリア, 緑藻など多くのものがヒドロゲナーゼを持つ。ニトロゲナーゼと比較して, ヒドロゲナーゼは反応にATPを必要としないので理論的最大エネルギー変換効率高い。しかし, 酸素発生型光合成生物のヒドロゲナーゼを利用して水素生産を行わせる場合は, 酵素が正逆両方向の反応を触媒するため (式(3)), 夜間や曇天下では水素の再吸収が起こり, 水素の生産効率は著しく低下する。窒素ガスを常にフローさせながら水素を収穫する方法もあるが, 低濃度の水素しか得られない。緑藻クラミドモナスでは,

表1 水素生産に利用されるヒドロゲナーゼとニトロゲナーゼ

	反応式	長所	短所
ヒドロゲナーゼ	$2\text{e}^- + 2\text{H}^+ \rightleftharpoons \text{H}_2$	理論的エネルギー効率が 高い	可逆反応であり, 水素の再吸収 (夜間、曇天下) の抑制が必要
ニトロゲナーゼ	$8\text{e}^- + 8\text{H}^+ + 16\text{ATP} \rightarrow 2\text{NH}_3 + \text{H}_2 + 16 (\text{ADP} + \text{P}_i)$	不可逆反応であり、酸素存在下でも水素の吸収を抑制可能	理論的エネルギー変換効率が低い

第1段階で通常の光合成を行わせて細胞内に光合成産物を蓄積させたのち、第2段階で細胞を嫌氣的気相下で硫黄欠乏培地に移して光照射を続けると、酸素発生を伴う通常の光合成活性が低下し、次いで、前段階で蓄積した糖質を分解して水素を連続光下で3~5日程度生産できる。硫黄欠乏下ではタンパク質の合成が阻害され、光化学系Ⅱの光失活からの修復が行えず酸素発生が停止すると考えられる。このようにして、酸素発生期から嫌氣的水素生産期へと培養条件を変えることで時間的に分離できるので、ヒドロゲナーゼを利用して水素生産を行うことは可能である¹⁾。

水素生産におけるヒドロゲナーゼとニトロゲナーゼの長所および短所を表1に示す。ニトロゲナーゼを利用した水素生産は、理論的最大エネルギー変換効率の点ではヒドロゲナーゼ利用系より低いですが、遺伝子工学的的手法による改良を積み重ね、エネルギー変換効率を高めていけば、その長所(表1)から水素生産の省力化、低コスト化、大規模化の可能性が開けると期待される。

筆者らは、このような総合的判断から、ニトロゲナーゼを基礎とする水素生産方式を採用し、その研究開発に取り組んでいる^{2)~5)}。

5. 遺伝子工学によるシアノバクテリアの改良

5.1 形質転換法

光合成の研究によく用いられる *Synechocystis* sp. PCC6803 は自然形質転換が可能であり、単に DNA と細胞を混合するだけで DNA は細胞内に取り込まれて、相同組み換えでゲノムに取り込ませることが可能である。一方、多くのシアノバクテリア (*Nostoc*, *Anabaena* など) は、独自の制限酵素系を持っているため、その認識部位をあらかじめ DNA メチラーゼ遺伝子を組み込んだ大腸菌内でメチル化する必要がある。著者らは、Wolk らの開発した triparental mating⁶⁾ を用いて、*Nostoc* や *Anabaena* の形質転換を行っている。この方法は、形質転換させたいシアノバクテリア株と、その株が持つ制限酵素の認識部位をメチル化するメチラーゼ遺伝子と導入したい遺伝子の両方を持つ大腸菌株、さらに接合性プラスミドを持つ大腸菌の3種の細菌細胞を混合後、形質転換できたシアノバクテリア株を薬剤スクリーニングする。*Nostoc* や *Anabaena* では、ほとんどの場合、相同組換えは1点(1カ所)でしか起こらない。2点(2カ所)での相同組換えによる遺伝子置換を行う場合、1点での相同組換え株を単離後、この株を用いて、もう一度接合による形質転換、薬剤耐性および *sacB* 遺伝子(スクロース致死遺伝子)を用いたスクロース耐性によるスクリーニングを行うので、自然形質転換法に比べて時間と労力が必要となる。

5.2 取込み型ヒドロゲナーゼ HupL の遺伝子破壊

Anabaena sp. PCC 7210 株は、窒素固定シアノバクテリアとして初めて全ゲノム塩基配列が明らかにされた株である⁷⁾。この株は、取込み型(Hup)および双方向型(Hox)の2種類のヒドロゲナーゼ遺伝子を持つ^{3) 8)}。また、*Nostoc* sp. PCC 7422 株は、シアノバクテリア株のなかから光合成に基づくニトロゲナーゼ活性が最も高い野生株として選抜された株である⁹⁾。この株は Hox 活性がほとんどなく、Hup 活性のみが高い。筆者らは、この2株を主に用いて遺伝子工

学的な改良を進めている。

Nostoc sp. PCC 7422 の Hup 活性を遺伝子工学的に不活性化した変異株 Δ Hup 株では、水素生産活性が野生株に比べて3倍程度増加し、光合成による酸素発生を行いながら水素を約30% (v/v) まで蓄積できた⁹⁾。

5.3 ホモクエン酸合成酵素 NifV の破壊

Mo型ニトロゲナーゼは N_2 還元触媒活性部位であるFeMo-cofactorと呼ばれる金属クラスターを結合するモリブデン・鉄タンパク質（ジニトロゲナーゼ）とこれに電子を供給する鉄タンパク質（ジニトロゲナーゼレダクターゼ）から構成される¹⁰⁾。モリブデン・鉄タンパク質は *nifD* 遺伝子がコードする α サブユニット2個と *nifK* 遺伝子がコードする β サブユニット2個からなるヘテロ四量体から構成されるが、結晶構造解析によるとFeMo-cofactorはシステイン残基とヒスチジン残基を介して α サブユニットに結合している（図3）。FeMo-cofactorのMo原子に結合するホモクエン酸は、効率的な窒素固定反応を行うためには必須であり、従属栄養細菌 *Klebsiella pneumoniae* では、ホモクエン酸の合成酵素遺伝子 *nifV* を破壊すると、ホモクエン酸の代わりに炭素鎖が1つ短いクエン酸がFeMo-cofactorに結合するようになり¹¹⁾、 N_2 還元はほとんどできなくなるが、水素生産は野生株と同程度の活性を持つ¹²⁾。Masukawaら¹³⁾は *Anabaena* PCC7120の Δ Hup株を親株としてヘテロシスト内で発現するホモクエン酸合成酵素の遺伝子 *nifV1* の破壊株を作成した。この株は親株である Δ Hup株に比べて培養液あたり水素生産性が2倍程度増加した。

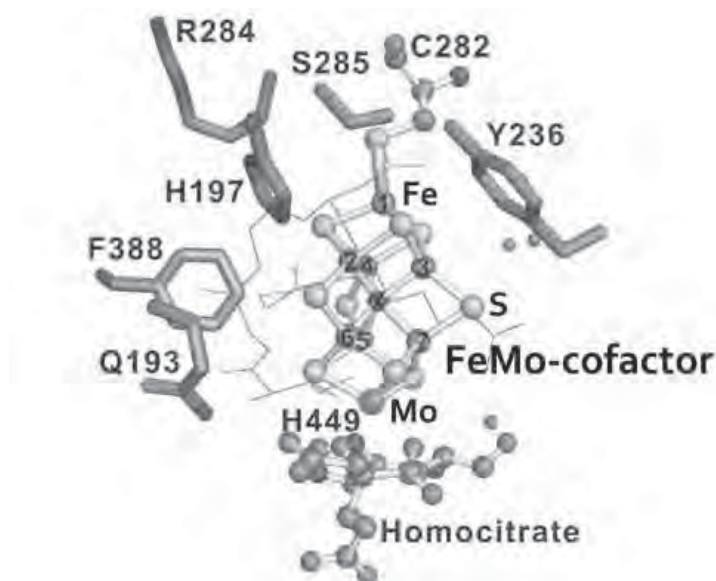


図3 Mo型ニトロゲナーゼのFeMo-cofactor周辺の立体構造¹⁴⁾

5.4 FeMo-Co 周辺を取り巻くアミノ酸残基の部位特異的置換株

続いて, Masukawaら¹⁴⁾は, N_2 ガス存在下のニトロゲナーゼ反応(式(1))における電子の大部分(約3/4)が窒素固定に使われ, 水素生産に使われる電子がわずか(約1/4)であるため, この電子配分比率を遺伝子工学的手法により変更し, N_2 存在下の窒素固定活性が低く, 水素生産活性が上昇する変異株を作成した。ニトロゲナーゼは, その活性部位にモリブデン(Mo)と鉄(Fe)からなる金属クラスターを持ち, その近傍には高度に保存されたアミノ酸残基が位置している。この立体構造情報をもとに, 活性中心近傍アミノ酸残基のなかから6つの残基を選び(図3), 別の残基への置換株を合計49株作成した。ほとんど変異株で窒素固定活性が大幅に低下したが, そのうちのいくつかの株は, N_2 ガス存在下でも水素生産の低下が見られず, 親株 Δ Hup株と比較して, 約3~4倍高い水素生産活性を示し向上した。これらのなかから最も優れた置換株を選び, 長期間にわたる水素生産性について評価した¹⁵⁾。親株は窒素固定活性が高いので窒素栄養充足になりニトロゲナーゼ活性が低下する結果, 水素生産の活性レベルは低く持続しない。一方, 置換株では, 窒素固定活性が大幅に低下しているため, N_2 存在下でも窒素栄養充足になりやすく, 比較的高い水素生産活性が約3週間にわたり持続するようになった。これまでは, 気相中の N_2 ガスをArガスで置換することで, 窒素栄養飢餓状態にして高活性を持続させることができたが, このような改変株の利用により, コストのかかるArガスは必要なくなり, 水素生産のための培養ガスのコストの削減が可能となった。

6. 水素バリア性プラスチック素材を利用したバイオリアクター

大規模にシアノバクテリアを培養し水素生産を行わせる場合, バイオリアクターのコスト低減が大きな課題となる。ガラスやアクリルを素材としたバイオリアクターは大型化が困難であり, 大きなコストもかかる。筆者らは水素バリア性プラスチック膜を含む3層のプラスチックバッグを用いることで, 安価なバイオリアクターの作成が可能であると提案している¹⁶⁾。水素バリア性プラスチック膜として, 市販品のBeselaフィルム(株クレハ)およびGLフィルム(凸版印刷株)を選択し, 水素のバリア性について検討した。両者ともPET樹脂フィルムをベースとしたラミネート膜で, 水素ガスバリア層は前者がアクリル酸樹脂系高分子コート, 後者が酸化アルミニウムコートとなっている。どちらも水素ガスバリア層の上に, 二軸延伸ナイロン層, さらに無延伸ポリプロピレン(CPP)または直鎖状低密度ポリエチレン(LLDPE)層がラミネートされている。これら4種類のバッグ, Besela-CPP(Be-P), Besela-LLDPE(Be-E), GL-CPP(GI-P), GL-LLDPE(GI-E)をオートクレーブ滅菌処理(120℃, 20 min), 間欠滅菌処理(100℃, 20 min, 3回)したもの, および未加熱処理のものを, 熱融着によって密閉バッグを作り, 内部に封入した水素ガスの透過性を測定した。一例を挙げると, ガスサンプリングデバイスを付けたGI-Eバッグに17%(v/v)となるように水素ガスを注入し, 内部水素ガス濃度の測定を行ったところ, 15日目でも15%程度保持された。同様の測定を4種類の未加熱および加熱処理済みフィルムで行い, 水素透過性を算出した。これらプラスチックバッグの水素透過性は $20\sim 90\text{ cm}^3\text{m}^{-2}\text{day}^{-1}\text{atm}^{-1}$ 程度であり, 将来の実用化の材料として候補となり得ることが示された。

また、加熱処理の GI-E を用いて、密閉容器内での水素生産量とプラスチックバッグ内での水素生産量を比較した。窒素栄養充足培地 (BG11) から窒素欠乏培地 (BG11₀) へと移した *Nostoc* sp. PCC 7422 ΔHupL 株の細胞培養液を、同じ直径の、容量のガラス容器に等量ずつ分注し、一方の容器はブチルゴム栓で密封、もう一方の容器はプラスチックバッグに入れた。初期気相を 1% N₂/5% CO₂/94% Ar にして、12 時間ごとの明暗周期光照射を行いながら生産された水素の蓄積量を測定した。その結果、3 日目まではどちらの水素蓄積量もほぼ同等であったが、光照射後 9 日目ではプラスチックバッグの水素蓄積量が密閉容器に比べて約 30% 程度多かった。密閉内部では水素と酸素の混合ガスが蓄積し、酸素の分圧が高まることでニトロゲナーゼの活性が低下することが予想される。しかし、柔軟性のあるプラスチック素材によるバッグでは、この活性の低下が緩和されたことが考えられる。

7. 今後の課題

今後さらにエネルギー変換効率と長期の生産性を向上させコストを削減するためには、ヘテロシスト形成頻度の改変、V 型、Fe-only 型などの代替ニトロゲナーゼの利用、電子伝達系や色素系などの改変、バイオリアクターの大型化、多層化も今後必要である。

これらの改良を積み重ねることで、水素生産が強光下で数週間持続するようにし、光から水素へのエネルギー変換効率を屋外の条件下で 1% 以上に高めることが今後の目標である。

文 献

- 1) M. L. Ghirardi et al. : *Annu. Rev. Plant Biol.*, **58**, 71 (2007).
- 2) H. Masukawa et al. : *Ambio*, **41**, 169-173 (2012).
- 3) H. Sakurai et al. : *J. Photochem. Photobiol., C. Photochem. Rev.*, **17**, 1-25 (2013).
- 4) H. Sakurai et al. : *Mar. Biotechnol.*, **9**, 128-145 (2007).
- 5) H. Sakurai et al. : *Life*, **5**, 997-1018 (2015).
- 6) T. Thiel et al. : *Methods Enzymol.*, **153**, 232-243 (1987).
- 7) T. Kaneko et al. : *DNA Res.*, **8**, 205-213 (2001).
- 8) P. Tamagnini et al. : *Microbiol. Mol. Biol. Rev.*, **66**, 1-20 (2002).
- 9) F. Yoshino et al. : *Mar. Biotechnol.*, **9**, 101-112 (2007).
- 10) L. C. Seefeldt et al. : *Annu. Rev. Biochem.*, **78**, 701-722 (2009).
- 11) S. M. Mayer et al. : *J. Biol. Chem.*, **277**, 35263-35266 (2002).
- 12) P. A. McLean et al. : *Nature*, **292**, 655-656 (1981).
- 13) H. Masukawa et al. : *Appl. Environ. Microbiol.*, **73**, 7562-7570 (2007).
- 14) H. Masukawa et al. : *Appl. Environ. Microbiol.*, **76**, 6741-6750 (2010).
- 15) H. Masukawa et al. : *Int. J. Hydrogen Energ.*, **39**, 19444-19451 (2014).
- 16) M. Kitashima et al. : *Biosci. Biotech. Bioch.*, **76**, 831-833 (2012).
- 17) 桜井英博, 柴岡弘郎, 芦原坦, 高橋陽介著: 植物生理学概論 培風館, 49-98 (2008).
- 18) L. Taiz and E. Zaiger 編, 西谷和彦, 島崎件一郎 監訳: 植物生理学 第3版, 培風館, 109-141 (2004).



《 解 説 》

マイクロポーラス Mo-V-O 複合酸化物の調製と
選択酸化反応への応用

石川理史*・村山 徹**・上田 渉***

* 豊田中央研究所 稲垣特別研究室

** 首都大学東京 都市環境学部分子応用化学コース

*** 神奈川大学 工学部 物質生命化学科

水熱合成法により結晶性 Mo_3VO_x 複合酸化物 (MoVO) を合成した。合成の前駆体溶液中には $[\text{Mo}_{72}\text{V}_{30}\text{O}_{282}(\text{H}_2\text{O})_{56}(\text{SO}_4)_{12}]^{36-}$ ($|\text{Mo}_{72}\text{V}_{30}|$) ボール型ポリオキシメタレートが形成しており、これが MoVO 形成に必要なビルディングユニットを供給することで結晶形成が進行した。この合成において種結晶を用いると、種結晶が結晶核として機能し、 $|\text{Mo}_{72}\text{V}_{30}|$ から供給されるビルディングユニットが種結晶上に集積しながら結晶形成が進行することが分かった。MoVO はエタンおよびアクロレインの選択酸化反応に極めて高い触媒活性を示した。これらの反応には構造の 7 員環が深く関与しており、エタン酸化反応では 7 員環内部が、アクロレイン酸化反応では 7 員環表面が反応場として機能することが明らかとなった。エタン酸化反応においては 7 員環近傍の局所構造が触媒活性に大きく影響することが明らかとなり、酸化活性が触媒の部分構造で発現している様子が分子レベルで表現できるようになった。

キーワード：選択酸化反応, 結晶性 Mo_3VO_x 複合酸化物, ミクロ細孔, 構造依存性, 酸化還元

1. 緒言

結晶性 Mo_3VO_x 複合酸化物 (MoVO) は $|\text{Mo}_6\text{O}_2|^{6-}$ 5 員環ユニットと $|\text{MO}_6|$ ($M = \text{Mo}, \text{V}$) 金属酸素八面体が複雑に配列した板 (a - b 面) が c 軸方向に積層して形成する棒状の結晶である¹⁻³⁾。 a - b 面ではこれらのユニットの縮合により構造内に 5, 6, および 7 員環が形成し、このうち 7 員環は直径 0.40 nm のミクロ細孔として機能する⁴⁾。7 員環細孔径は酸化還元により制御可能である⁵⁻⁶⁾。これはレドックス能に優れた Mo, V を構成元素とすることに由来し、レ

ドックス能の低い Si や Al で構成されるゼオライトや有機物をリンカーとする MOF には見られない興味深い現象である。また、MoVO はアルコール、アルデヒド、低級アルカンの選択酸化反応について、その洗練された触媒構造を反映した極めて高い触媒活性を示す⁷⁻¹¹⁾。このような性質から、MoVO は高い酸化活性を示す八面体モレキュラーシーブとして大きく注目されている。

さらに近年では $|\text{Mo}_6\text{O}_2|^{6-}$ 5 員環ユニットと $|\text{MO}_6|$ ($M = \text{Mo}, \text{V}$) 金属酸素八面体で構成される同様の組成の棒状結晶で、断面部の構造のみが異なる斜方晶 MoVO, 三方晶 MoVO, 正方晶 MoVO, および積層方向の配列は規則的であるが断面部がディスオーダーであるアモルファス MoVO の作りわけに成功した¹⁰⁻¹²⁾ (Fig. 1)。これらの結晶相の比較から、触媒反応における結晶面の強い依存性が見て取れた。さらに斜方晶 MoVO についてはエタン選択酸化反応をモデル反応として、その触媒構造と触媒機能に強い関係を見出すことができた¹³⁻¹⁶⁾。本稿で

受理日：2016年5月10日

*〒480-1192 愛知県長久手市横道41番地の1

E-mail: s-ishikawa@mosk.tytlabs.co.jp

**〒192-0397 東京都八王子市南大沢1-1

E-mail: murayama@tmu.ac.jp

***〒221-8686 神奈川県横浜市神奈川区六角橋3-27-1

E-mail: uedaw@kanagawa-u.ac.jp

Copyright © 2016 Japan Association of Zeolite All Rights

Reserved.

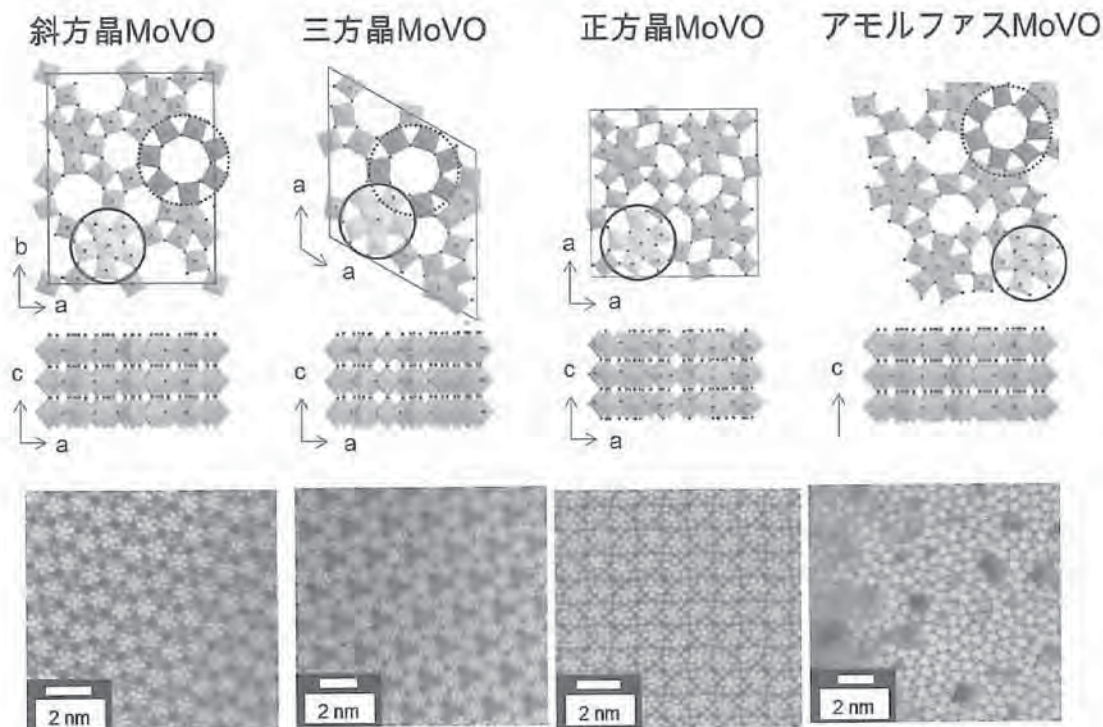


Fig. 1. Structural model and HAADF-STEM images of crystalline Mo_3VO_x oxides. Structural units enclosed by solid and dot circles are a pentagonal $[\text{Mo}_6\text{O}_{21}]^{6-}$ unit and a 7-membered ring, respectively.

はMoVOの結晶形成プロセスから触媒機能評価に至るまで、最新の展開も含めて概説する。

2. MoVOの結晶形成プロセス

MoVOは $(\text{NH}_4)_6\text{Mo}_7\text{O}_{24} \cdot 4\text{H}_2\text{O}$ (AHM)と $\text{VOSO}_4 \cdot 5.4\text{H}_2\text{O}$ の混合溶液を水熱合成することで得られる。この合成において、透明なAHM溶液と青色の VOSO_4 溶液を混ぜ合わせると深い紫色の溶液が得られる。この溶液を溶液Ramanや溶液UVにより検討したところ、溶液内には $[\text{Mo}_{72}\text{V}_{30}\text{O}_{282}(\text{H}_2\text{O})_{56}(\text{SO}_4)_{12}]^{36-}$ ($[\text{Mo}_{72}\text{V}_{30}]$)が形成しており、 $[\text{Mo}_{72}\text{V}_{30}]$ 中の Mo^{6+} と V^{4+} 間の原子価間電荷移動により紫色に呈色していることが分かった^{11), 16-19)}。前駆体溶液のpHを変えて水熱合成を行ったところ、MoVOの形成はpHに敏感であった。Table 1に溶液UVにより測定した種々pHにおけるMoVO前駆体溶液中の $[\text{Mo}_{72}\text{V}_{30}]$ 量と形成した結晶の結晶相および収量を示す。

種結晶なしでは前駆体溶液のpHが3.4~4.0のときにはほとんど結晶は得られなかったが(Entry 1, 2), pHを3.2まで低下させると斜方晶MoVO(Ortho-MoVO)が形成した(Entry 3)。pHを2.2までさらに低下させると、斜方晶MoVOと同様な組成、構

造ユニットで構成されるがユニットの配列が異なる三方晶MoVO(Tri-MoVO)が形成した(Entry 5)。pHをさらに下げ、1.7とすると、金属酸素八面体のみから成り、構造内に $[\text{Mo}_6\text{O}_{21}]^{6-}$ 5員環ユニットを含まない擬六方晶系の $\text{Mo}_{0.87}\text{V}_{0.13}\text{O}_{2.94}$ 酸化物(Hex- $\text{Mo}_{0.87}\text{V}_{0.13}\text{O}_{2.94}$)が三方晶MoVOとともに副生した(Entry 6)。pHを1.2とすると擬六方晶 $\text{Mo}_{0.87}\text{V}_{0.13}\text{O}_{2.94}$ のみが得られた(Entry 7)。溶液UVにより前駆体溶液中の $[\text{Mo}_{72}\text{V}_{30}]$ 量を測定したところ、pH=2.7~4.0における $[\text{Mo}_{72}\text{V}_{30}]$ 量は0.9~1.1 mMほどであった。これは加えたVの51~63%が $[\text{Mo}_{72}\text{V}_{30}]$ 形成に関与していることを示している。pHを2.2まで下げると $[\text{Mo}_{72}\text{V}_{30}]$ 量は0.6 mMまで減少し、pHを1.2までさらに下げると同量はほとんど0となった。このとき、溶液中のポリ酸種としては $[\text{Mo}_{72}\text{V}_{30}]$ ではなく、より縮合が進行した $[\text{Mo}_{36}\text{O}_{112}]^{8-}$ ($[\text{Mo}_{36}]$)ユニットが形成していた。ここまでの結果を総合すると、 $[\text{Mo}_{72}\text{V}_{30}]$ 存在下では $[\text{Mo}_6\text{O}_{21}]^{6-}$ 5員環ユニットを構造内に含む斜方晶および三方晶MoVOが形成し、 $[\text{Mo}_{72}\text{V}_{30}]$ 非存在下では擬六方晶 $\text{Mo}_{0.87}\text{V}_{0.13}\text{O}_{2.94}$ のみが得られた。 $[\text{Mo}_{72}\text{V}_{30}]$ と斜方晶MoVO、および三方晶MoVOはそれぞれ共通の構造パーツを有

Table 1. pH and concentration of $\{\text{Mo}_{72}\text{V}_{30}\}$ in the precursor solution, and the product amount and their crystal phases after hydrothermal synthesis with or without the seed at 175 °C for 20 h^a.

Entry	pH ^b	Concentration of $\{\text{Mo}_{72}\text{V}_{30}\}$ ^c	$\{\text{Mo}_{72}\text{V}_{30}\}$ yield ^d	Seed ^e	Crystal structure of the obtained solid	Amount of solid
1	4.0	0.9 mM	51%	— ^f	— ^g	0.0 g
2	3.4	1.0 mM	57%	— ^f	Orth-MoVO	0.3 g
3	3.2	1.1 mM	63%	— ^f	Orth-MoVO	1.4 g
4	2.7	1.0 mM	57%	— ^f	Orth-MoVO	—
5	2.2	0.6 mM	35%	— ^f	Tri-MoVO	5.0 g
6	1.7	0.4 mM	23%	— ^f	Hex-Mo _{0.87} V _{0.13} O _{2.94} ^h + Tri-MoVO	—
7	1.2	0.0 mM	0%	— ^f	Hex-Mo _{0.87} V _{0.13} O _{2.94} ^h	6.7 g
8	4.0	0.9 mM	51%	Orth-MoVO	Orth-MoVO	1.3 g
9	4.0	0.9 mM	51%	Tri-MoVO	Tri-MoVO	1.7 g
10 ⁱ	4.0	0.9 mM	51%	Orth-MoVO	Orth-MoVO	0.7 g
11 ^j	4.0	0.9 mM	51%	Tri-MoVVO	Tri-MoVO	1.8 g
12 ^k	4.0	0.0 mM	0%	Orth-MoVO	— ^g	0.0 g
13	1.2	0.0 mM	0%	Orth-MoVO	Hex-Mo _{0.87} V _{0.13} O _{2.94} ^h	6.9 g

^a Hydrothermal synthesis was carried out using the precursor solution prepared by $(\text{NH}_4)_2\text{Mo}_7\text{O}_{24} \cdot 4\text{H}_2\text{O}$ (Mo: 50 mmol) and $\text{VOSO}_4 \cdot 5\text{H}_2\text{O}$ (V: 12.5 mmol).

^b pH of the reaction mixture was changed from 1.0 to 4.0 by adding 2 M H_2SO_4 or 10 wt% ammonia.

^c Estimated by UV-Vis.

^d Based on V.

^e Seed amount was 0.3 g.

^f No seed was added.

^g No solid was formed.

^h JCPDF: 00-048-0766.

ⁱ Unground Orth-MoVO seed was added.

^j Tri-MoVVO was used as a seed.

^k V_2O_5 was used as a V source.

している。斜方晶 MoVO では2つの $\{\text{Mo}_6\text{O}_{21}\}^{6-}$ 5員環ユニットが一つの $\{\text{VO}_6\}$ リンカーで架橋した直線型のユニットであり、三方晶 MoVO では3つの $\{\text{Mo}_6\text{O}_{21}\}^{6-}$ 5員環ユニットが3つの $\{\text{VO}_6\}$ リンカーで架橋した三角形型のユニットである。この事実を鑑み、 $\{\text{Mo}_{72}\text{V}_{30}\}$ から供給されるビルディングユニットがそれぞれ縮合し結晶形成が進行するというユニット式結晶形成プロセスを提案した (Fig. 2(a))。高 pH 領域で $\{\text{Mo}_{72}\text{V}_{30}\}$ が存在していても MoVO が形成しなかった事実については、以降に概説する。

続いて、MoVO 前駆体溶液中に粉碎した斜方晶 MoVO や三方晶 MoVO を種結晶として加えて水熱合成を行った²⁰⁾。すると、本来 MoVO が形成しない pH=4.0 においても、種結晶と同様の結晶構造の MoVO が形成した (Entry 8, 9)。種結晶を粉碎せず、長い棒状結晶のまま用いると結晶収率は大きく低下したことから、棒状結晶を粉碎することで露出する結晶断面 (*a-b* 面) が結晶形成に強く関与している

ことが示唆された (Entry 10)。W を含んだ三方晶 MoVVO を種結晶として用いた場合、三方晶 MoVO を種結晶とした場合とほぼ同収率で三方晶 MoVO が得られた (Entry 11)。Fig. 2(b) に三方晶 MoVVO を種結晶として合成した MoVO の STEM-mapping 像を示す。Mo, V は棒状結晶に均一に分布していたが、W は棒状結晶の真ん中までしか含まれていなかった。この時に合成した MoVO では種結晶のみが W を含んでいることから、MoVO は MoVVO 棒状結晶の断面から形成していることが分かった。以上より、MoVO を種結晶として用いると、MoVO 結晶断面 (*a-b* 面) から新たな MoVO が形成すると結論した。一方、種結晶を用いた合成においても、 $\{\text{Mo}_{72}\text{V}_{30}\}$ は必須であった。同 pH (pH=4)、同 Mo, V 量で、V 源に NH_4VO_3 を用いて水熱合成を行ったところ (この時 $\{\text{Mo}_{72}\text{V}_{30}\}$ は形成していない)、MoVO の結晶形成は観測されなかった (Entry 12)。また、 $\{\text{Mo}_{72}\text{V}_{30}\}$ の存在しない pH=1.2 で水熱合成を行った場合、種

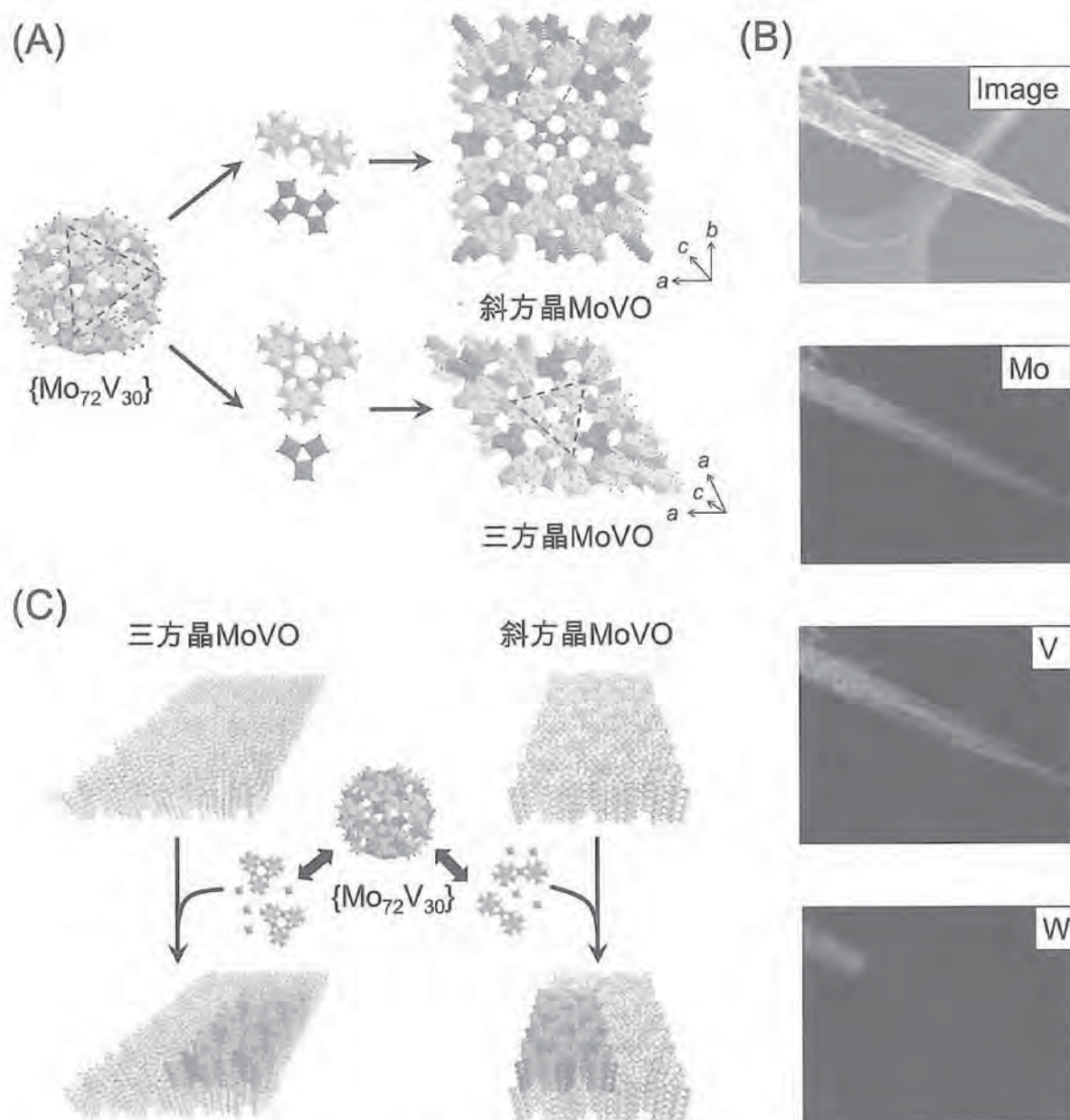


Fig. 2. (A) Crystal formation scheme of orthorhombic MoVO and trigonal MoVO. (B) STEM-mapping image of trigonal MoVO prepared by using trigonal MoVWO as a seed. Formed crystal didn't contain W. (C) Crystal formation scheme of MoVO in the presence of the seeds.

結晶の添加の有無にかかわらず、 $[\text{Mo}_6\text{O}_{21}]^{6-}$ 5員環ユニットを含まない擬六方晶系の $\text{Mo}_{0.87}\text{V}_{0.13}\text{O}_{2.94}$ 酸化物しか得られなかった (Entry 13)。以上の結果を総合すると、種結晶を用いた MoVO 合成においては、種結晶の結晶断面 (a - b 面) が結晶核として機能し、 $[\text{Mo}_{72}\text{V}_{30}]$ が構造ユニット供給を担っていることが理解できる (Fig. 2(c))。pH=4.0 で種結晶を用いない場合に MoVO が形成しなかった結果は、この pH において $[\text{Mo}_{72}\text{V}_{30}]$ が結晶核を形成できなかったことに起因すると考えられる。ゼオライト合成にお

ける種結晶添加法では、ゼオライト合成の前駆体溶液中に種結晶が有する構造ユニットが含まれているときに、新たなゼオライトが形成する²¹⁻²³)。MoVO と $[\text{Mo}_{72}\text{V}_{30}]$ が共通の構造ユニットを有していることを考えると、種結晶を用いた MoVO 結晶形成プロセスはゼオライトのそれと類似している。金属酸素八面体をベースとした MoVO と TO_4 四面体 (T = Si, Al などの元素) をベースとしたゼオライトが類似した機構で結晶形成する事実は大変興味深い。

以上、MoVO は前駆体溶液中に存在する $[\text{Mo}_{72}\text{V}_{30}]$

から供給されるビルディングユニットを基盤としたユニット式の結晶形成プロセスにより形成することが明らかとなった。MoVO種結晶が存在すると、 $[\text{Mo}_{72}\text{V}_{30}]$ と共通の構造ユニットを有する種結晶断面にビルディングユニットが集積し、新たなMoVOが形成していくことが分かった。

3. 7員環と触媒活性の関係¹⁰⁻¹¹⁾

我々はこれまでに、水熱合成条件の制御、適切な熱処理により、同様の組成で構造ユニットの配列のみが異なる、斜方晶、三方晶、正方晶、および積層方向の配列は規則的であるが面方向が不規則な配列をしているアモルファスMoVOの合成に成功している (Fig. 1)。これらはいずれも、Mo, V金属を中心とした酸素八面体の複雑な配列により形成した $a-b$ 面が、 c 軸方向に頂点共有して積み重なった層状構造体である。 $a-b$ 面は、 $[\text{Mo}_6\text{O}_{21}]^{6-}$ 5員環ユニットが酸素八面体を介してネットワーク状に連結し、斜方晶、三方晶、およびアモルファスでは6, 7員環が形成され、正方晶では5, 6員環が形成する。Fig. 1に示したこれらの結晶構造の妥当性は、HAADF-STEM像から明らかである。Table 2にこれら4つの結晶の N_2 吸着測定および触媒反応結果を示す。4つの結晶について、 100 nm^2 当たりの7員環数を結晶構造モデルやHAADF-STEM像から見積もったところ、斜方晶MoVOでは73個、三方晶MoVOでは68個、アモルファスMoVOでは10~30個、正方晶では0個であった。これらを用いて窒素吸着測定を行ったところ、7員環を有する斜方晶、三方晶、アモルファスはマイクロ細孔吸着を示したが、正方晶で

は示さなかった。このことから構造中の7員環がマイクロ細孔として機能していることは明らかである。

これらを用いてエタンおよびアクロレイン選択酸化反応を行った。斜方晶、三方晶、アモルファスはエタンおよびアクロレインの転化に活性を示したが、正方晶では活性を示さなかった (Table 2)。エタン、アクロレイン選択酸化反応において触媒活性の強い構造依存性が見て取れた。これらの触媒の違いは構造中の7員環の有無のみであったことから、7員環がエタン、アクロレインの転化に関与していることは明らかであろう。

エタン選択酸化活性は斜方晶MoVO > 三方晶MoVO > アモルファスMoVO > 正方晶MoVOであった。この序列は触媒の表面積 (斜方晶: $7.2 \text{ m}^2 \text{ g}^{-1}$, 三方晶: $18.0 \text{ m}^2 \text{ g}^{-1}$, 正方晶: $2.7 \text{ m}^2 \text{ g}^{-1}$, アモルファス: $5.7 \text{ m}^2 \text{ g}^{-1}$) や 100 nm^2 当たりの7員環数 (斜方晶: 73個, 三方晶: 68個, 正方晶: 0個, アモルファス: 10~30個) と関係せず、 N_2 吸着測定から求めた7員環に由来するマイクロ孔容積 (斜方晶: $14.0 \text{ cm}^3 \text{ g}^{-1}$, 三方晶: $4.0 \text{ cm}^3 \text{ g}^{-1}$, 正方晶: $0 \text{ cm}^3 \text{ g}^{-1}$, アモルファス: $2.8 \text{ cm}^3 \text{ g}^{-1}$) の序列と一致していた。これはエタンが7員環表面でなく7員環細孔内で転化していることを示唆している。一方でアクロレイン選択酸化活性は三方晶MoVO > 斜方晶MoVO > アモルファスMoVO > 正方晶MoVOであり、エタン酸化活性とは異なる序列となった。この活性の序列は触媒の表面積と 100 nm^2 当たりの7員環の数を考えるとよく理解できる。この事実はアクロレインが7員環の表面で転化していることを示唆している。これらの詳細については次項で詳しく解説する。

Table 2. Relationship between micropore and catalytic activity.

Catalyst	Elemental composition ^a (V/Mo)	Number of 7-membered ring/ 100 nm^2	External surface area ^b / $\text{m}^2 \text{ g}^{-1}$	Micropore volume ^b / $\text{cm}^3 \text{ g}^{-1}$	Ethane conv. ^c /%	ACR conv. ^d /%
Orth-MoVO	0.38	73	7.2	14.0	42.2	53.8
Tri-MoVO	0.32	68	18.0	4.0	25.2	99.8
Tet-MoVO	0.38	0	2.7	0	<1	<1
Amor-MoVO	0.38	10~30	5.7	2.8	5.9	9.7

^a Determined by ICP.

^b Measured by N_2 adsorption at liquid N_2 temperature and estimated by t-plot method.

^c Reaction condition: catalyst amount, 0.5 g; reaction gas feed, $\text{C}_2\text{H}_6/\text{O}_2/\text{N}_2 = 5/5/40 \text{ ml min}^{-1}$; reaction temperature, 313~319 °C.

^d Reaction condition: catalyst amount, 0.25 g, reaction gas feed, $\text{ACR}/\text{O}_2/\text{H}_2\text{O}/\text{N}_2/\text{He} = 2.5/8.0/27.1/39.5/30.5 \text{ ml min}^{-1}$; reaction temperature, 217~218 °C. ACR represents acrolein.

4. 7員環の選択酸化活性への関与¹³⁻¹⁴⁾

4つの異なる結晶相のMoVOの触媒活性を比較することで、エタンとアクロレインはMoVOの7員環部位で転化することは明らかである。一方、エタンとアクロレインでは基質活性化部位が異なることが示唆されている。エタン、アクロレイン選択酸化反応における基質活性化部位を明らかにするため、マイクロ細孔容積が同じで外表面積の異なる種々のMoVOを合成し、触媒活性の外表面積依存性を検討した。もし基質が7員環表面で転化してれば、触媒活性は外表面積の変化に依存するはずである。一方、基質がマイクロ細孔内で転化しているとすれば、活性は外表面積に依存しないはずである。MoVOの外表面積を制御するため、界面活性剤 (Sodium dodecyl sulfonate, SDS) の添加や水熱合成温度の制御を行うことで、結晶核形成速度および結晶成長速度を変化させ、MoVOの結晶サイズ制御を試みた。SDSの添加量は仕込み比で $\text{SDS} [\text{mol}]/(\text{Mo} + \text{V}) [\text{mol}] = x$

($x=0, 0.15, 0.30, 0.60$) とし、合成温度は175℃または230℃とした。以下、合成した触媒をMoVO-SDS_x (175 or 230) で表す。合成した試料はいずれも同様の組成のMoVOであった。これらの触媒の諸物性 (組成, 結晶構造, 外表面積等) は反応前後でほとんど変化しなかったため、以下のキャラクターゼーションは触媒反応の影響を受けた後の、反応後の試料について行った。Fig. 3にエタン反応後の代表的な試料のSEM像および各棒状結晶の軸径、軸長の平均値を示す。

Fig. 3に示すように、SDSの添加や水熱合成温度の制御によって、MoVOの結晶サイズを大きく変化させることができた。175℃で合成した試料では、SDSを過剰に転化したとき (MoVO-SDS_{0.60}(175)), 棒状結晶の軸径平均 (100個の結晶を測定) はSDSを添加していない場合の0.40 μmから0.21 μmまで減少した。230℃で合成した試料は、軸径平均が0.76 μmへと大きく増大した (MoVO-SDS₀(230))。

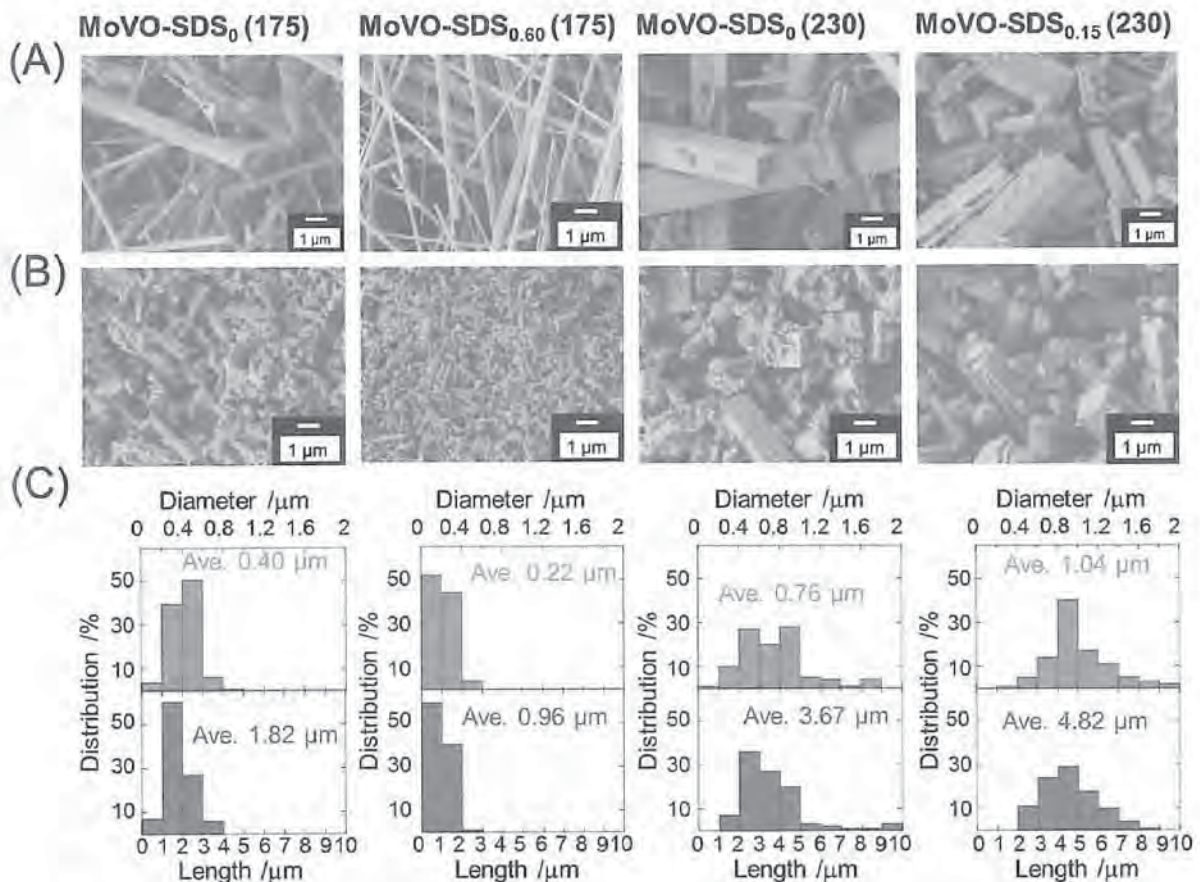


Fig. 3. SEM image of MoVO crystals. (A) Before the grind treatment. (B) After the ethane oxidation (after the grinding). (C) Histogram of the diameter (top) and length (bottom) of rod-shaped crystal measured after the ethane oxidation. Values shown on the histogram represent the average of 100 crystallites.

この温度で $x=0.15$ となるようにSDSを添加すると(MoVO-SDS_{0.15}(230)), 軸径平均は $1.04\ \mu\text{m}$ へとさらに大きく増大した。一方, これらの結晶の軸長に対する軸径の比(アスペクト比)は結晶サイズに関係なく, ほとんど同様であった。この事実は, 合成した試料が相似形であることを示している。以上, SDSの添加や合成温度の制御により, 結晶核生成速度や結晶成長速度が変化し, 相似形で異なるサイズの結晶が得られたと結論した。結晶サイズの変化による外表面積の変化は N_2 吸着測定の結果からも明らかであり, $1.2\sim 14.0\ \text{m}^2\ \text{g}^{-1}$ の範囲で触媒の外表面積を制御することができた。続いて, エタン酸化反応後の各MoVOに対しエタン吸着測定を行ったところ, 結晶サイズに関係なく, これらはいずれもほぼ同様のエタン吸着量を示した($16.1\sim 18.8\times 10^{-3}\ \text{cm}^3\ \text{g}^{-1}$)。結晶構造から見積もられるマイクロ細孔容積の理論値は $22.4\times 10^{-3}\ \text{cm}^3\ \text{g}^{-1}$ である。観測されたエタン吸着量は理論値と比べて若干小さい値となったが, それでも合成した試料がエタンを吸着できる7員環を有することは明らかである。以上の実験から, 合成した試料は結晶構造, 組成, 結晶形状, およびマイクロ細孔容積がほぼ同様で外表面積のみが異なるMoVOであると結論した。Fig. 4にこれらが示したエタンおよびアクロレイン転化率と触媒の外表面積との関係を示す。触媒反応条件はFig. 4の脚注に示した。生成物選択性は各MoVOで変化はなく, エタン選択酸化反応では, エチレンが90%程度の選択率で生成し, 残りは酢酸, CO_x であった。アクロレイン選択酸化反応では95%程度の選択率でアクリル酸が生成し, 残りは酢酸, CO_x であった。

アクロレインを基質に用いた場合, アクロレイン転化率は触媒の外表面積に大きく依存した。この事実は, アクロレインが触媒表面で転化していることを示している。MoVO-SDS₀(175)に粉碎処理を行わなかった場合(MoVO-SDS₀(175, ng)), アクロレイン転化率は大きく減少した。この事実は粉碎処理によって露出した結晶断面(α - b 面)がアクロレインの転化に寄与していることを示している。前述した4つの結晶相におけるアクロレイン選択酸化活性の比較も考慮し, アクロレインは触媒表面に位置する7員環で転化していると結論した。反応性の高いアルデヒド基が7員環表面に効率的にトラップされ, 活性化されたと考えられる。一方, エタンを基

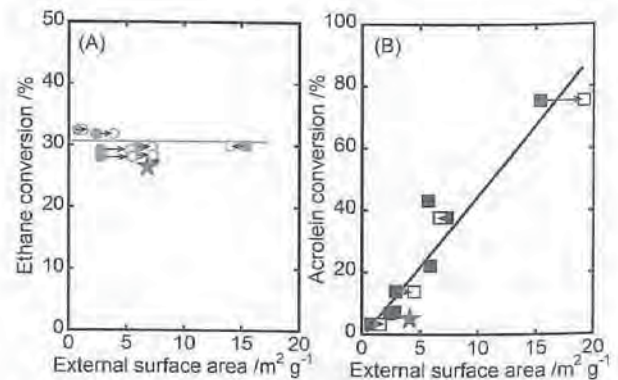


Fig. 4. Ethane (A) and acrolein (B) conversion as a function of the external surface area of MoVO catalysts. External surface area before (closed symbols) and after (open symbols) the reactions are plotted. Reaction condition of ethane oxidation: reaction temperature, $300\ ^\circ\text{C}$; catalyst amount, $0.50\ \text{g}$; reaction gas, $\text{C}_2\text{H}_6/\text{O}_2/\text{N}_2 = 5/5/40\ \text{ml}\ \text{min}^{-1}$. Reaction condition of acrolein oxidation: reaction temperature, $220\ ^\circ\text{C}$; catalyst amount, $0.13\ \text{g}$; reaction gas, $\text{C}_3\text{H}_4\text{O}/\text{O}_2/(\text{N}_2 + \text{He})/\text{H}_2\text{O} = 2.5/8.0/71.0/18.5\ \text{ml}\ \text{min}^{-1}$. Star represents the catalytic activity of MoVO-SDS₀(175, ng). External surface area of MoVO-SDS₀(175, ng) after the reaction was plotted.

質に用いた場合, エタンの転化率は触媒の外表面積と関係なく, ほとんど同様であった。これはエタンが触媒表面で転化していないことを意味している。前述した4つの結晶相におけるエタン選択酸化活性の比較から, エタンの転化に7員環が必須であることは明らかである。一方, MoVO-SDS₀(175, ng)がMoVO-SDS₀(175)とほぼ同様の活性を示したことから, 粉碎処理により露出した α - b 面はほぼ反応に関与しないことが分かる。さらに, 本実験で用いた反応条件において, 7員環が異元素で占有されている触媒がほとんど活性を示さないことも別途実験により明らかにしている²⁴⁾。また, 拡散の影響を評価するために, 結晶サイズの大きく異なる3つの触媒(軸径平均: $0.21\ \mu\text{m}$, $0.40\ \mu\text{m}$, $1.04\ \mu\text{m}$)を用いて触媒活性の接触時間依存性を評価した。その結果, これらの触媒の活性はいずれの接触時間においてもほとんど同様であった。以上の結果から, MoVOは7員環マイクロ細孔内で拡散の影響なくエタンを活性化し, エチレンを与えることが明らかになった。ここまでで得られた結果は, エタン選択酸化反応において, 7員環マイクロ細孔内が7員環表面に比べて明

らかに優位な触媒反応場として機能していることを示している。これにはマイクロ細孔中の電場の勾配による基質のC-H結合分極や、基質濃度の部分的な増大が関与していると思われる²⁵⁻²⁶⁾。

5. 7員環周りの局所構造とエタン選択酸化活性の関係¹⁵⁻¹⁶⁾

これまでの研究から、MoVOの7員環マイクロ細孔径が酸化還元処理により、連続的に、かつ可逆的に制御可能であることが明らかになっている。ここまですべて7員環はエタンを内部に取り込み活性化していることは明らかなので、7員環細孔径はエタン酸化活性に大きく影響することが考えられる。そこで、MoVOに酸化還元処理を行うことによってマイクロ細孔性質を変化させ、マイクロ細孔性質がエタン選択酸化活性に及ぼす影響を検討した。この目的のため、構造ユニット内からの格子酸素脱離量が異なる種々MoVOを調製し、キャラクタリゼーションを行った。格子酸素脱離量の測定にはTPR, TGを用いた。以下、調製した試料をMoVO(δ) (δ は $\text{Mo}_{29}\text{V}_{11}\text{O}_{112}$ からの酸素脱離量)とする。MoVO(0)は水熱合成後のMoVOを400℃で2h空気焼成を行うことで得た。還元処理後に同じ条件で空気焼成を行うことで得た試料は、試料名の末尾にACを付けて表記している。酸化還元処理による不純物の生成は、XRD, IR, およびRaman測定では観測されなかった。種々解析の結果、還元によって優先的に構造から脱離し、再酸化しても構造内に戻らない格子酸素と、還元によって連続的に脱離し、可逆的に構造内に戻る格子酸素が存在することが分かった。以下、前者を α 酸素、後者を β 酸素とする。TPRスペクトルから、MoVO(4.2)までの還元で α 酸素は構造から脱離し終えることが示されている。Fig. 5にMoVOの構造モデル、Rietveld解析によって得られた構造モデルから算出した7員環マイクロ細孔の長軸径、短軸径、および種々還元度の異なるMoVOのエタン吸着量を示す。種々解析の結果、 α 酸素は7員環に面したペンタマーユニット内の架橋酸素、 β 酸素は c 軸に結合したアキシャル酸素であることが分かった。エタン吸着量はMoVO(0)~MoVO(4.2)では $15.8\sim 22.1\times 10^{-3}\text{ cm}^3\text{ g}^{-1}$ であり、有意な差は観測されなかった。一方、MoVO(5.4)以上に還元した試料では、エタン吸着がほとんど観測されなかった。Riet-

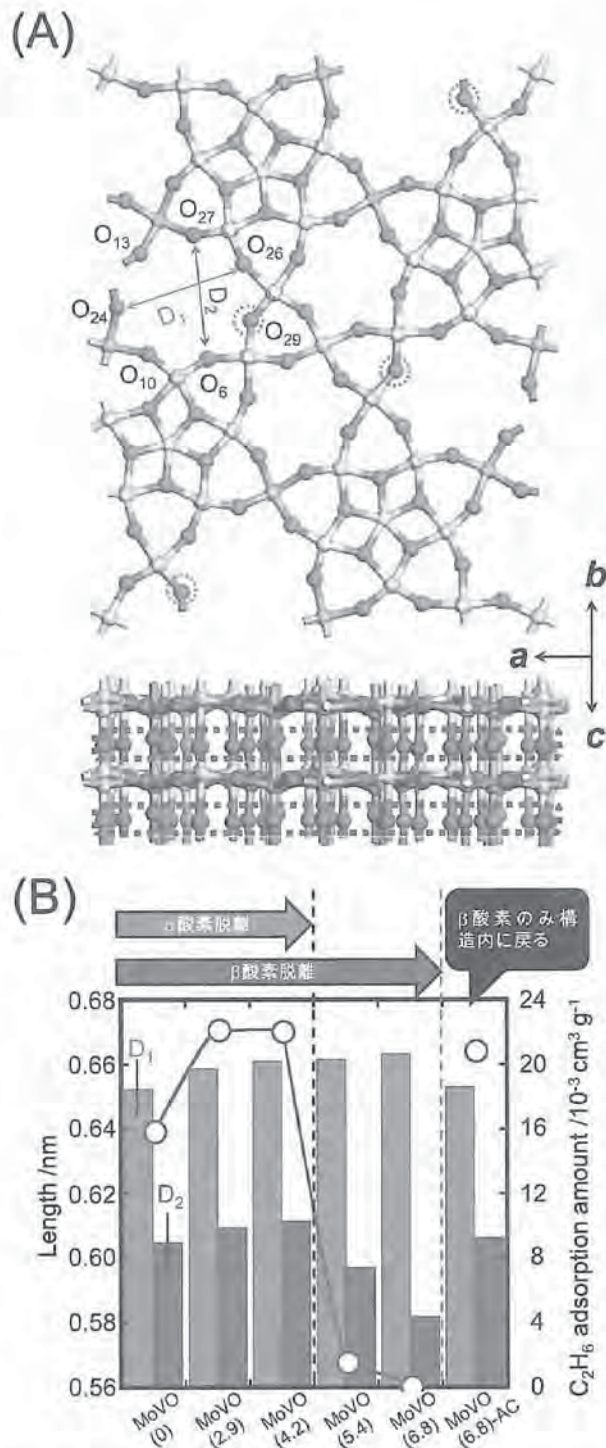


Fig. 5. (A) Crystal structure of MoVO. α oxygen (O_{29}) is marked with dot circle. β oxygen is marked with dot rectangle. (B) Left side: diameters of the heptagonal channel. Diameters were determined on the basis of the atomic positions of oxygen. Left bar, long axis ($\text{O}_{24}\text{--}\text{O}_{26}$, D_1); Right bar, short axis ($\text{O}_6\text{--}\text{O}_{27}$, D_2). Right side: ethane adsorption amount of MoVO with each reduction state measured by C_2H_6 adsorption and estimated by the Dubinin–Astakhov (DA) method (open circle).

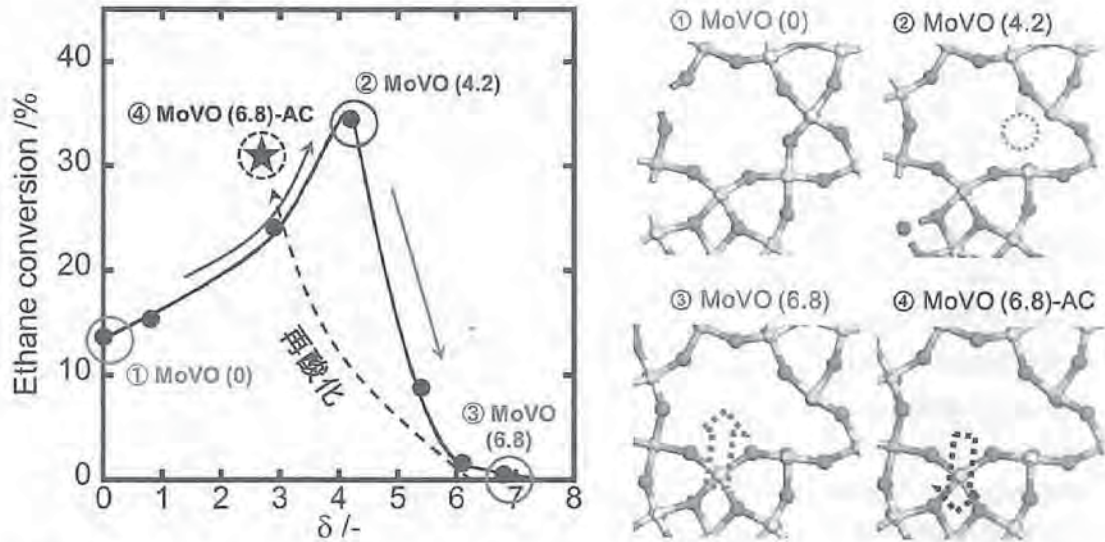


Fig. 6. Relationship between the crystal structure and ethane conversion measured at 10 min from the start of the reaction.

veld解析後の構造モデルから算出した7員環マイクロ細孔径について、7員環長軸径は還元に伴って連続的に増大した。一方、7員環短軸径はMoVO (4.2)までの還元では連続的に増大したにもかかわらず、以降の還元で大きく減少した。

XRD, IR, Raman測定により、MoVO (5.4)以上の還元で、 $[\text{Mo}_6\text{O}_{21}]^{6-}$ 5員環ユニットの膨張に伴う a - b 面の局所構造変化が観測された。このことから、MoVO (5.4)以上の還元によって観測されるエタン吸着量の減少は、 $[\text{Mo}_6\text{O}_{21}]^{6-}$ 5員環ユニットが膨張することで7員環が圧迫され、エタンが7員環細孔内にアクセスできなくなったことによると結論した。再酸化処理を行ったMoVO (6.8)-ACでは、7員環細孔径は還元前のMoVO (0)とほぼ同様となった。実際、IR, Raman測定でも、再酸化処理によって $[\text{Mo}_6\text{O}_{21}]^{6-}$ 5員環ユニットが収縮することが示されている。再酸化処理を行うと α 酸素は構造内に戻らないまま、 $[\text{Mo}_6\text{O}_{21}]^{6-}$ 5員環ユニットが収縮することで7員環径が増大すると結論した。以上の実験により、還元度の異なる種々MoVOの構造モデルが得られた。Fig. 6に還元度の異なるMoVOを用いた反応開始10 min時点でのエタン転化率と δ の関係を示す。

MoVO (0)のエタン転化率は13%程度であった。還元処理を行ったMoVO (2.9)では、エタン転化率は24%程度に増大した。さらに還元が進行したMoVO (4.2)ではエタン転化率は35%程度へと大きく増大した。しかし、これ以上の還元により、MoVO

(5.4)では9%程度、MoVO (6.1), MoVO (6.8)ではほとんど0%と、エタン転化率は大きく減少した。エタン吸着実験から、MoVO (5.4)以上の還元によって7員環細孔径が収縮し、エタンが細孔内にアクセスできなくなることが分かっている。エタンは7員環細孔内で転化することから、MoVO (5.4)以上の還元で観測されたエタン酸化活性の減少は、エタンが細孔内にアクセスできなくなったことに起因する。MoVO (6.8)-ACのエタン転化率はMoVO (0)よりもはるかに高く、31%程度であった。MoVO (0)とMoVO (6.8)-ACでは結晶構造、組成、および酸化状態がほぼ同じであり、両者の違いは α 酸素の有無のみである。このことから、 α 酸素が脱離することでエタン酸化活性が大きく増大することが明らかであろう。MoVO (0)とMoVO (6.8)-ACを用いてアレニウスプロットを取ったところ、 α 酸素の脱離は活性化エネルギーに影響せず、反応頻度因子のみを増大させることが分かった。この結果は α 酸素が脱離した構造がエタン転化における活性点構造であることを示している。以上の結果を総合し、MoVOを用いたエタンの酸化に関してFig. 7に示す反応スキームを提案した。

エタンと酸素は反応中、同時にマイクロ細孔に取り込まれる。この時、 α 酸素欠損部位が存在するとエタンからのC-H引き抜きに活性な酸素種が形成し、効率的にエタンがエチレンへ転化する。以上より、7員環近傍の局所構造変化とエタン選択酸化反応における触媒活性の関係が明らかになった。

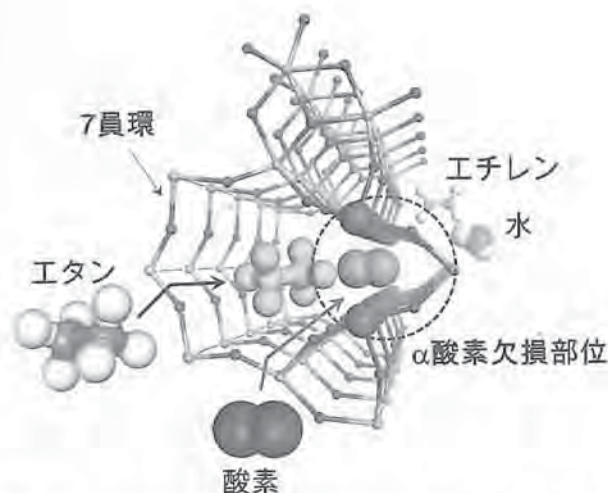


Fig. 7. Reaction image of ethane to ethene inside the heptagonal channel. Oxygen is activated at the α oxygen defect.

6. おわりに

結晶性 Mo_3VO_x 複合酸化物 (MoVO) の触媒調製から触媒反応に至るまで、最近の進歩を概説した。MoVOは水熱条件下、巨大ボール型ポリオキシメタレートから供給されるビルディングユニットの自己組織化によって洗練された結晶構造を形成する。その結晶構造中には低級アルカンがちょうど取り込めるほどの大きさのマイクロ細孔が形成し、5つの金属酸素八面体で構成されるペンタマーユニットがこれに隣接する。エタン選択酸化反応においては、エタンはマイクロ細孔中に取り込まれ、細孔中の電場勾配によりC-H結合が分極する。同時に、マイクロ細孔に隣接したペンタマーユニット内に形成している酸素欠陥が分子酸素を適度に活性化し、活性化されたエタンから水素原子を引き抜く。このように、MoVOの極めて高い触媒機能はマイクロ細孔に隣接した触媒活性点が高密度に周期的に配列していることに由来し、これは見事なまでに緻密に制御された結晶構造によってはじめて成し遂げられる。ナノスケールな視点で触媒反応を俯瞰すると、高活性な触媒創出のためには触媒活性点の構造設計が決定的に重要と思われる。触媒設計論は議論百出であろうが、結晶構造をベースとした議論は常に心に留めておくべきであろう。

文献

- 1) T. Katou, D. Vitry, W. Ueda, *Chem. Lett.*, **32**, 1028 (2003).
- 2) W. D. Pyrz, D. A. Blom, M. Sadakane, K. Kodato, W. Ueda, T. Vogt, D. J. Buttrey, *Chem. Mater.*, **22**, 2033 (2010).
- 3) T. Lunkenbein, F. Girgsdies, A. Wernbacher, J. Noack, G. Auffermann, A. Yasuhara, A. K. Hoffmann, W. Ueda, M. Eichelbaum, A. Trunschke, R. Schlögl, M. G. Willinger, *Angew. Chem. Int. Ed.*, **54**, 6828 (2015).
- 4) M. Sadakane, K. Kodato, T. Kuranishi, Y. Nodasaka, K. Sugawara, N. Sakaguchi, T. Nagai, Y. Matsui, W. Ueda, *Angew. Chem. Int. Ed.*, **47**, 2493 (2008).
- 5) M. Sadakane, S. Ohmura, K. Kodato, T. Fujisawa, K. Kato, K. Shimidzu, T. Murayama, W. Ueda, *Chem. Commun.*, **47**, 10821 (2011).
- 6) W. Ueda, *Jpn. Petrol. Inst.*, **56**, 122 (2013).
- 7) F. Wang, W. Ueda, *Appl. Catal., A*, **346**, 155 (2008).
- 8) N. Watanabe, W. Ueda, *Ind. Eng. Chem. Res.*, **45**, 607 (2006).
- 9) C. Qiu, C. Chen, S. Ishikawa, T. Murayama, W. Ueda, *Top. Catal.*, **57**, 1163 (2014).
- 10) C. Chen, K. Nakatani, T. Murayama, W. Ueda, *ChemCatChem*, **5**, 2869 (2013).
- 11) T. Konya, T. Katou, T. Murayama, S. Ishikawa, M. Sadakane, D. Buttrey, W. Ueda, *Catal. Sci. Technol.*, **3**, 380 (2013).
- 12) M. Sadakane, N. Watanabe, T. Katou, Y. Nodasaka, W. Ueda, *Angew. Chem., Int. Ed.*, **46**, 1493 (2007).
- 13) S. Ishikawa, X. Yi, T. Murayama, W. Ueda, *Appl. Catal., A*, **474**, 10 (2014).
- 14) S. Ishikawa, X. Yi, T. Murayama, W. Ueda, *Catal. Today*, **238**, 35 (2014).
- 15) S. Ishikawa, D. Kobayashi, T. Konya, S. Ohmura, T. Murayama, N. Yasuda, M. Sadakane, W. Ueda, *J. Phys. Chem. C*, **119**, 7195 (2015).
- 16) S. Ishikawa, W. Ueda, *Catal. Sci. Technol.*, **6**, 617 (2016).
- 17) M. Sadakane, K. Endo, K. Kodato, S. Ishikawa, T. Murayama, W. Ueda, *Eur. J. Inorg. Chem.*, **10-11**, 1731 (2013).
- 18) R. Canioni, M. Roch, L. Laronze, M. Haouas, F. Tauléille, J. Marrot, S. Paul, C. Lamonier, F. Paul, S. Lorient, M. M. J. Millet, E. Cadot, *Chem. Commun.*, **47**, 6413 (2011).
- 19) M. S. Sanchez, F. Girgsdies, M. Jastak, P. Kube, R. Schlögl, A. Trunschke, *Angew. Chem., Int. Ed.*, **51**, 7196 (2012).
- 20) S. Ishikawa, M. Tashiro, T. Murayama, W. Ueda, *Cryst. Growth Des.*, **14**, 4553 (2014).
- 21) K. Itabashi, Y. Kamimura, K. Iyoki, A. Shimojima, T. Okubo, *J. Am. Chem. Soc.*, **134**, 11542 (2012).
- 22) K. Iyoki, K. Itabashi, W. Chaikittisilp, S. P. Elangovan, T. Wakihara, S. Kohara, T. Okubo, *Chem. Mater.*, **26**, 1957 (2014).
- 23) S. Goel, S. I. Zones, E. Iglesia, *Chem. Mater.*, **27**, 2056 (2015).
- 24) S. Ishikawa, T. Murayama, M. Kumaki, M. Tashiro, Z. Zhang, A. Yoshida, W. Ueda, *Submitted*.
- 25) G. Sastre, A. Corma, *J. Mol. Catal. A - Chem.*, **305**, 3 (2009).
- 26) C. M. Z. Wilson, A. Corma, P. Viruela, *J. Phys. Chem.*, **98**, 10863 (1994).

Synthesis of microporous crystalline Mo-V-Oxide and its application for selective oxidations

Satoshi ISHIKAWA*, Toru MURAYAMA** and Wataru UEDA***

*Toyota Central R&D Labs., Inc., Nagakute, Aichi 480-1192, Japan

**Department of Applied Chemistry, Graduate School of Urban Environmental Sciences,
Tokyo Metropolitan University, 1-1 Minami-osawa, Hachioji, Tokyo, 192-0397, Japan

***Department of Material and Life Chemistry, Faculty of Engineering, Kanagawa University, 3-27,
Rokkakubashi, Kanagawa-ku, Yokohama, 221-8686, Japan

Recent development of microporous crystalline Mo-V mixed oxides (MoVO) are reviewed. MoVO is formed by a self-assembly of structural units supplied by the ball-shaped large polyoxometalate, $[\text{Mo}_{72}\text{V}_{30}\text{O}_{282}(\text{H}_2\text{O})_{56}(\text{SO}_4)_{12}]^{36-}$ ($|\text{Mo}_{72}\text{V}_{30}|$), resulting in the formation of a sophisticated crystal structure. Addition of MoVO seed crystal into the precursor solution of MoVO induced the crystal formation of MoVO having the same crystal structure with the seed crystal. Comparison of catalytic activities of 4 distinct MoVO catalysts with the same elemental composition and with different crystal structure clearly demonstrated a strong dependence of the crystal structure on the catalytic activity for the selective oxidation of ethane and acrolein. Then, catalysis field of MoVO for selective oxidations were investigated by using MoVO catalysts with the same microporosity and with the difference external surface area. It was proved that ethane, accessible into the micropore, is converted to ethene inside the micropore without diffusion effect. On the other hand, acrolein which is inaccessible into the micropore is converted to acrylic acid at the mouth of the micropore. Proper redox treatment for MoVO led a partial structural change around the micropore which strongly affected its microporosity and the catalytic performance of the ethane oxidation. The significant role of the micropore for the selective oxidation of ethane was observed. On the basis of the comprehensive studies, molecular-level insight of the selective oxidation by using MoVO could be obtained.

Key words: Selective oxidation, Crystalline Mo_3VO_8 , Micropore, Structure-activity relationship, redox



Contents lists available at ScienceDirect

Applied Catalysis B: Environmental

journal homepage: www.elsevier.com/locate/apcatb

Review

Glycerol hydrogenolysis into useful C3 chemicals

Daolai Sun^a, Yasuhiro Yamada^a, Satoshi Sato^{a,*}, Wataru Ueda^b^a Graduate School of Engineering, Chiba University, Chiba 263-8522, Japan^b Department of Material and Life Chemistry, Faculty of Engineering, Kanagawa University, Kanagawa 221-8686, Japan

ARTICLE INFO

Article history:

Received 1 March 2016
 Received in revised form 5 April 2016
 Accepted 7 April 2016
 Available online 9 April 2016

Keywords:

Glycerol
 Hydrogenolysis
 1,2-Propanediol
 1,3-Propanediol
 Allyl alcohol
 1-Propanol
 Propylene

ABSTRACT

Applications of renewable biomass provide facile routes to alleviate the shortage of fossil fuels as well as to reduce the emission of CO₂. Glycerol, which is currently produced as a waste in the biodiesel production, is one of the most attractive biomass resources. In the past decade, the conversion of glycerol into useful chemicals has attracted much attention, and glycerol is mainly converted by steam reforming, hydrogenolysis, oxidation, dehydration, esterification, carboxylation, acetalization, and chlorination. In this review, we focused on the catalytic hydrogenolysis of glycerol into C3 chemicals, which contain many industrially important products such as 1,2-propanediol, 1,3-propanediol, allyl alcohol, 1-propanol and propylene. In the hydrogenolysis of glycerol into propanediols, advantages and disadvantages of liquid- and vapor-phase reactions are compared. In addition, recent studies on catalysts, reaction conditions, and proposed pathways are primarily summarized and discussed. Furthermore, new research trends are introduced in connection with the hydrogenolysis of glycerol into allyl alcohol, propanols and propylene.

© 2016 Elsevier B.V. All rights reserved.

Contents

1. Introduction	76
2. 1,2-Propanediol	76
2.1. Reaction route of glycerol hydrogenolysis into 1,2-propanediol	77
2.2. Liquid-phase glycerol hydrogenolysis into 1,2-PDO over precious metal catalysts	79
2.3. Liquid-phase glycerol hydrogenolysis into 1,2-PDO over base metal catalysts	80
2.4. Liquid-phase glycerol hydrogenolysis into 1,2-PDO over bimetallic catalysts	80
2.5. Liquid-phase glycerol hydrogenolysis into 1,2-PDO using hydrogen generated <i>in situ</i>	82
2.6. Vapor-phase glycerol hydrogenolysis into 1,2-PDO	83
3. 1,3-Propanediol	85
3.1. Hydrogenolysis of glycerol into 1,3-propanediol using a batch-type reactor	85
3.2. Hydrogenolysis of glycerol into 1,3-propanediol using a flow-type reactor	85
3.3. General summary of glycerol hydrogenolysis into 1,3-propanediol	87
4. Monoalcohols and propylene	87
4.1. Allyl alcohol	87
4.2. Propanols	88
4.3. Propylene	89
5. Concluding remarks and prospects	90
Acknowledgement	91
References	91

* Corresponding author.

E-mail address: satoshi@faculty.chiba-u.jp (S. Sato).

1. Introduction

Biomass is biological material derived from living organisms, and it represents abundant carbon-neutral renewable resources for the production of bioenergy and biochemicals, which can replace the energy and the materials produced from fossil resources. In recent years, applications of the biomass resources have attracted much attention from the view point of CO₂ emission. Shifting society's dependence away from petroleum to renewable biomass resources is essential for the development of sustainable industrial societies and efficient management of greenhouse gas emissions [1]. The bio-derived chemicals are mainly produced by two types of main components of sugars: hexoses and pentoses, which can be obtained from starch, cellulose and hemicellulose [2]. Bioenergy usually means biofuels, which mainly consist of bioethanol and biodiesel, and the production of those fuels has been increasing rapidly in the last decade [3]. The bioethanol production depends heavily on the fermentation of starch obtained from corn and sugar cane [4].

Glycerol is the smallest polyol available from triglycerides, vegetable oil and animal fat, which constitute approximately 10 wt.% of total biomass [5]. Biodiesel is produced from triglycerides by transesterification with short chain alcohols through catalysis by alkali, and a huge amount of glycerol, ca. 10 wt.% of the overall biodiesel production, is generated as the by-product in the process [6]. Consequently, glycerol constitutes ca. 1 wt.% of total biomass. The production of biodiesel is 22.7 million metric tons in 2012, and it increases rapidly and is even forecasted to increase to 36.9 million metric tons in 2020 [7]. Glycerol is also produced as a by-product of ethanol production by fermentation of sugars. Although the extraction of glycerol from this residue is not economically feasible, the fermentation of sugar into ethanol is also a potential additional resource of glycerol [8]. In the cleavage processes of fatty acids, the purity of the crude glycerol is high and ca. 80 wt.% glycerol aqueous solutions can be obtained from most of the conventional processes of biodiesel production, but it also contains water, methanol, traces of fatty acids as well as various inorganic and organic impurities [9,10]. Crude glycerol has to be purified by distillation prior to further use in most cases, whereas the cost of the distillation is high. Furthermore, although glycerol has been produced at a large quantity with a rapid growth, the market of glycerol is small and the price of glycerol is low [9]. As a consequence, the proportion of refined glycerol is actually steadily decreasing and the unrefined crude glycerol is generally disposed by burning, which must be considered as a waste of a potentially useful organic raw material [10]. Thus, new economical ways of using glycerol must be developed in order to substantially increase the demand and the price of crude glycerol, and also to ensure the sustainability of the biodiesel production. Glycerol can be a starting material for further chemical derivatization, and many useful intermediates and specialty chemicals can be produced by catalytic reactions [11–13].

The catalytic conversion of glycerol into useful chemicals are mainly performed through steam reforming, oxidation, dehydration, acetalization, esterification, etherification, carboxylation, and chlorination, which have been summarized in many review papers at different periods [2,11,14–17]. Among the various ways for glycerol derivatization, the dehydration of glycerol into acrolein, the oxidation of glycerol into dihydroxyacetone and glyceric acid, and the hydrogenolysis of glycerol into 1,2-propanediol (1,2-PDO) and 1,3-propanediol (1,3-PDO) have been intensively investigated because of the wide and important use of the corresponding chemicals (Scheme 1). Dehydration of glycerol into acrolein has been well summarized in some review papers [7,10,18–21]. Although high acrolein selectivity has been obtained over some solid acid catalysts in many reports, the catalysts are deactivated rapidly in most cases and the development of solid catalysts for a stable acrolein

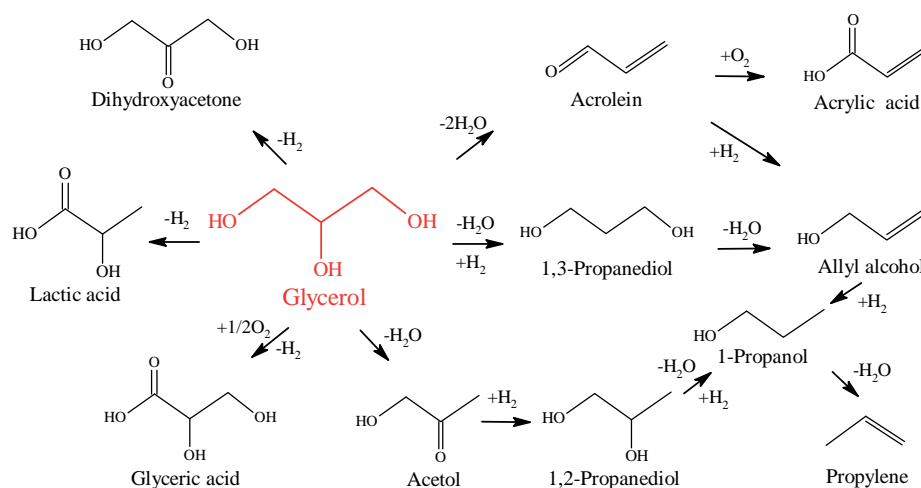
formation from glycerol is still required. Because acrolein is mainly used for acrylic acid formation, the direct production of acrylic acid from glycerol is also attractive. In recent 5 years, direct synthesis of acrylic acid from glycerol has been extensively reported [22–37]. In the processes, acrolein is generated as an intermediate and it is further oxidized into acrylic acid under either O₂ or air flow conditions.

The oxidation of glycerol into dihydroxyacetone and glyceric acid has been reviewed [38,39]. Supported precious metals, such as Pt, Pd and Au, are generally used as catalysts for glycerol oxidation into both dihydroxyacetone and glyceric acid. The features of the supported precious metals, such as the particle size and the acid-base conditions, significantly affect the selectivity to the oxidized products. In the latest review paper [39], a detailed summary has been reported on the glycerol oxidation into glyceric acid over Au-based catalysts, which show more advantages than the traditional Pt- and Pd-based catalysts. Lactic acid is another attractive chemical which can be derived via oxidation [40–55]. The catalyst system for glycerol oxidation into lactic acid is similar to that into glyceric acid, whereas the reaction conditions are much different: the formation of lactic acid requires much higher reaction temperatures and a basic media is indispensable in most cases. The glycerol oxidation is expected to be applied for further studies and even industrial applications.

In this review, we focused on the glycerol hydrogenolysis into useful chemicals, which contain 1,2-PDO, 1,3-PDO, allyl alcohol, 1-propanol, and propylene. All these chemicals in the glycerol hydrogenolysis are commercially produced from fossil resources now, and the technologies of catalytic transformation make it possible to produce these chemicals from a renewable resource such as glycerol. It is generally accepted that both 1,2-PDO and 1,3-PDO are produced via the dehydration of glycerol followed by hydrogenation, whereas different catalysts are reported to work effectively under different reaction conditions. In 2011, Dam and Hanefeld published a detailed review on glycerol dehydroxylation [5], and Nakagawa and Tomishige also published a review paper summarizing their works on glycerol hydrogenolysis into propanediols [6]. However, the reviews have focused mainly on the liquid-phase reactions, while vapor-phase reactions are less discussed. Although new achievements are summarized in review papers for the recent 5 years [56–65], the advantages and disadvantages of vapor- and liquid-phase reactions are less discussed. In addition, some important achievements have been reported in the past 5 years. Allyl alcohol is an attractive target chemical, which is also an intermediate in glycerol hydrogenolysis, but it is difficult to be produced selectively because it is easy to be further hydrogenated into 1-propanol under H₂ flow conditions. Consequently, efforts have been made to produce allyl alcohol from glycerol by hydrogen-transfer reactions using either monoalcohols or formic acid as the H-donor molecule. Recently, glycerol multi-step hydrogenolysis into propanols and propylene has also attracted much attention. In this review, the new trends in the glycerol hydrogenolysis are also summarized and discussed.

2. 1,2-Propanediol

1,2-PDO is a valuable chemical used widely in the synthesis of pharmaceuticals, polymers, agricultural adjuvants, plastics, and transportation fuel [66–68]. Depending on its purity, 1,2-PDO can be used as an antifreeze agent, a hydraulic fluid, and a solvent, and it has also usages for cosmetics and food applications [69]. 1,2-PDO is currently produced by the hydration of propylene oxide, which is produced through the selective oxidation of propylene [62]. Because propylene is produced from fossil resources, the production of 1,2-PDO from bio-derived glycerol is attractive. Glycerol



Scheme 1. Glycerol conversion into useful chemicals.

hydrogenolysis into 1,2-PDO is extensively investigated in a liquid-phase reaction under high H_2 pressure conditions, and several studies focused on vapor-phase reactions has also been reported. Many kinds of transition metals, such as Pt, Pd, Ru, Ir, Cu, and Ni, are effective for 1,2-PDO formation. In the following sections, we divide and summarize the previous studies by the catalyst systems as well as by the reaction conditions.

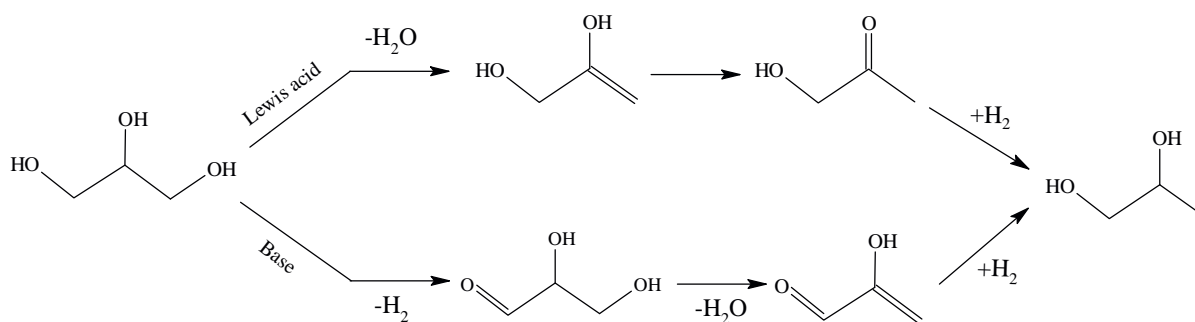
2.1. Reaction route of glycerol hydrogenolysis into 1,2-propanediol

The reported formation route of glycerol hydrogenolysis into 1,2-PDO is different according to the catalyst system and the reaction phase. Generally, a catalyst system with both dehydration and hydrogenation ability is required for the reaction. In the liquid-phase reactions, it is generally accepted that acid sites catalyze the dehydration of glycerol into acetol, which is further hydrogenated into 1,2-PDO over transition metal catalysts, such as Pt, Ru, and Cu (Scheme 2) [5,6,70,71]. Alhanash et al. performed the glycerol dehydration over Zn-Cr mixed oxide catalysts at a Zn/Cr ratio of 1:1, which gives 40% selectivity to acetol at 18% conversion, and proposed a reaction mechanism of glycerol dehydration into acetol over Lewis acid sites, as shown in Scheme 3, in which M represents the Lewis acid sites [72]. It is proposed that the terminal OH group of glycerol rather than the internal one interact more likely with a Lewis acid site. Both the transfer of the terminal OH group to the Lewis acid site and the migration of the H^+ from the internal carbon atom to the bridging O atom of the oxide gave 2,3-dihydroxypropene, which is further tautomerized to yield acetol. In contrast, Brønsted acid sites are also proposed to catalyze glycerol dehydration into acetol, as shown in Scheme 4 [5], in which acetol is formed via direct dehydration of glycerol and the subsequent keto-enol tautomerization. Scheme 2 also shows a generally accepted formation route of 1,2-PDO under alkaline conditions. Dehydrogenation of glycerol firstly proceeds over metal sites assisted by the base to form glyceraldehyde, which dehydrates to 2-hydroxy-2-propenal over base sites, and finally 1,2-PDO is produced from 2-hydroxy-2-propenal via a two-step hydrogenation process [5,6]. Tomishige's group has performed a series of works on liquid-phase glycerol hydrogenolysis into 1,2-PDO and 1,3-PDO over Ir and Ru catalysts modified with ReO_x [6], and proposed a direct glycerol hydrogenolysis route with different coordination (Fig. 1). It is suggested that glycerol is firstly adsorbed on the surface of ReO_x clusters to form alkoxide species of 2,3-dihydroxypropoxide. Then, the hydride attacking the 2-position of the hydroxyl group of 2,3-

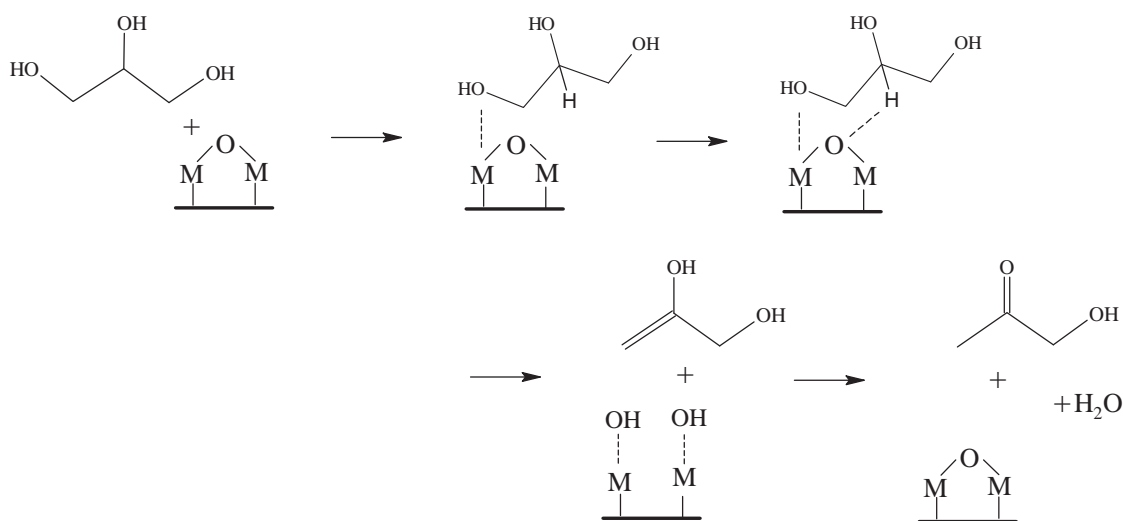
dihydroxypropoxide gives 1,3-PDO, while the hydride attacking the 3-position of the hydroxyl group of 2,3-dihydroxyisopropoxide gives 1,2-PDO [73].

Sato's group has continued a series of works on vapor-phase glycerol hydrogenolysis into 1,2-PDO [74–77]. Al_2O_3 - and Cr_2O_3 -supported Cu catalysts show high activity for the formation of 1,2-PDO from glycerol, and it is confirmed that acetol is generated as the intermediate. In order to determine the active sites for acetol formation from glycerol, vapor-phase reactions of glycerol is performed under N_2 atmosphere [78]: Cu supported on Al_2O_3 gives 82.9% selectivity to acetol at a complete conversion, whereas Al_2O_3 gives 26.5% selectivity to acetol at 11.5% conversion at 250 °C. Furthermore, 84.6% acetol selectivity can be achieved at 74.9% glycerol conversion over Raney Cu without acid sites. Schmidt et al. have also reported that higher than 94% 1,2-PDO yield is obtained from glycerol over Raney Cu under H_2 flow conditions [79,80]. These results indicate that Cu metal provides the active sites for the dehydration of glycerol into acetol, and the supports such as Al_2O_3 work as a mere support not as an acid catalyst. In other words, Cu metal catalyzes the glycerol dehydration into acetol as well as the following hydrogenation of acetol into 1,2-PDO. For 1,2-PDO used as a reactant, on the other hand, Cu metal catalyzes the dehydrogenation of 1,2-PDO to acetol but never acts as a dehydration catalyst to produce propanal and allyl alcohol. That is why Cu metal selectively works as a catalyst for the formation of 1,2-PDO from glycerol. It is probable that Cu metal surface provides the active sites for the catalytic glycerol hydrogenolysis in a vapor phase. A radical mechanism in the glycerol dehydration catalyzed by Cu metal is proposed in Scheme 5 [78]. There are two possible reaction routes, the elimination of one hydrogen atom from a primary and secondary OH group of glycerol initiates the dehydration. In both routes, a hydroxy radical is eliminated after the elimination of the hydrogen atom. In addition, supported Ag catalysts are tested for glycerol dehydration under N_2 atmosphere, and SiO_2 -supported Ag metal catalyst gives the acetol selectivity of 91.1% with 46.1% glycerol conversion at 240 °C [76]. Furthermore, an Ag powder can give 84.6% selectivity to acetol at 30.8% conversion even in H_2 atmosphere. Therefore, it is proved that transition metals, such as Cu and Ag, can provide active sites for the dehydration of glycerol into acetol.

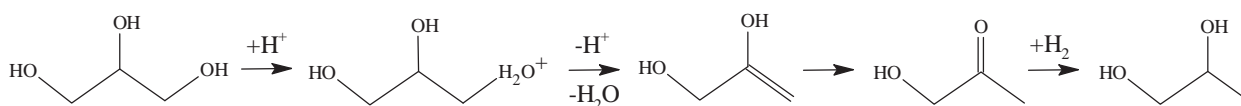
In liquid-phase reactions, although the glycerol dehydration step is generally accepted to be catalyzed by either an acid or a base (Scheme 2), we have different opinions. We are afraid that the transition metals, such as Pt, Ru, and Cu, do not only work as



Scheme 2. Reaction routes of glycerol hydrogenolysis into 1,2-PDO [5].



Scheme 3. Reaction mechanism of glycerol dehydration into acetol over Lewis acid sites proposed by Alhanash et al. [72].



Scheme 4. Reaction mechanism of glycerol dehydration into acetol over Brønsted acid sites [5,62].

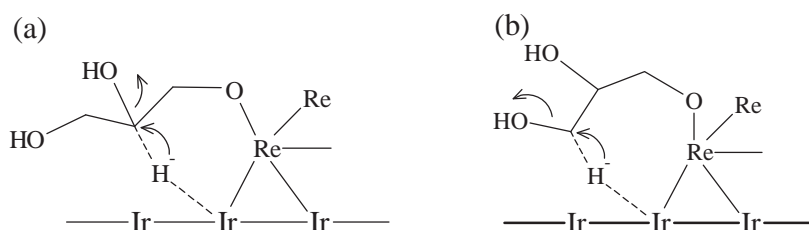
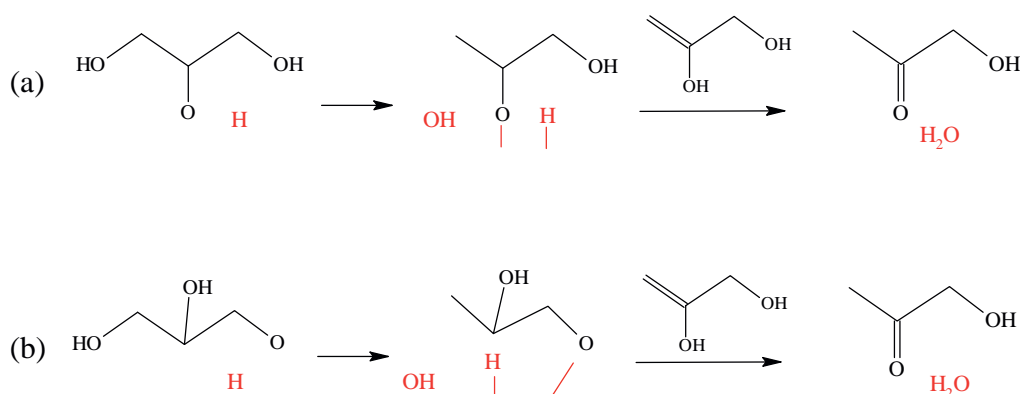


Fig. 1. Direct glycerol hydrogenolysis mechanism proposed by Tomishige et al. [73]. (a) Glycerol hydrogenolysis to 1,3-PDO. (b) Glycerol hydrogenolysis to 1,2-PDO.

a hydrogenation catalyst, but also involve the glycerol dehydration into acetol, which is further hydrogenated into 1,2-PDO. Based on the abundant reports performed in liquid phase [81–115], we found that the species of the loaded metals significantly affect the selectivity to 1,2-PDO rather than the acid-base properties of the supports. For example, higher than 90% 1,2-PDO selectivity can be obtained over Cu catalyst supported on chromite [90], ZrO₂ [91], ZnO [92], boehmite [93], Al₂O₃ [94], SiO₂ [95], MgO [96] and MgAlO [97]. These metal oxides seem to work only as inert supports for dispersing Cu but do not seem to catalyze the first-step dehydra-

tion of glycerol into acetol in the formation of 1,2-PDO. Indeed, in the vapor-phase glycerol dehydration, acetol is difficult to be selectively obtained over metal oxides catalysts, such as Al₂O₃ [78], ZrO₂, and TiO₂ [105]. In the liquid-phase glycerol hydrogenolysis into 1,2-PDO, an acidic support catalyzed selective dehydration of glycerol into acetol has never been proved by experiments. On the contrary, Cu/Al₂O₃ shows high activity for 1,2-PDO formation, while Al₂O₃ gives 0% selectivity to acetol at a low conversion of 7% under the same reaction conditions [94]. Hirunsit et al. [94] performed DFT calculations, which demonstrate that the Al₂O₃ support facilitates



Scheme 5. Reaction mechanism of glycerol dehydration into acetol over Cu metal proposed by Sato et al. [78].

Cu to be more active toward interacting with glycerol and acetol intermediate species. Mane et al. firstly reported a detailed study focusing on the mechanism of liquid-phase glycerol dehydration into acetol over Cu-supported catalysts [106]. Ba-, Mg-, Zr-, Zn-, Al-, and Cr-modified Cu catalysts were studied to understand the role of active species in selective glycerol dehydration to acetol. Cu-Al, Cu-Zr, and Cu-Mg showed relatively high activity and gave acetol selectivities of 92, 87, and 79% at conversions of 24, 21 and 24%, respectively, at 220 °C under an N₂ ambient pressure. In contrast, metallic Cu and acidic catalysts such as Al₂O₃ and ZrO₂ showed extremely low activity with low glycerol conversions less than 2%. They concluded that glycerol dehydration to acetol is not only catalyzed by acid sites but also by the metallic Cu. Raney catalysts were also investigated for the liquid-phase glycerol hydrogenolysis to 1,2-PDO [90,99,116]. Montassier et al. firstly reported that Raney Cu gave 86% selectivity to 1,2-PDO with a conversion higher than 80% at 240 °C and an H₂ pressure of 30 atm [116]. Raney Ni is reported to give 77% 1,2-PDO selectivity with 63% conversion at 190 °C and an H₂ pressure of 10 atm [99], and Raney Cu is also reported to give 69% 1,2-PDO selectivity with 49% conversion at 200 °C and an H₂ pressure of 14 atm [90], respectively. These results indicate that transition metals, such as Cu and Ni, can also effectively catalyze the first-step dehydration of glycerol to acetol even in a liquid phase.

Comparing to the reaction mechanisms initiated by either an acid or a base (Schemes 2–4), we suppose that metal-oxide concerted mechanism (Fig. 1) is acceptable in a liquid-phase reaction. On the other hand, it is also possible that the supported metal solely provides the active sites to catalyze the liquid-phase dehydration of glycerol into acetol at temperatures as high as those at which the dehydrogenation could proceed.

2.2. Liquid-phase glycerol hydrogenolysis into 1,2-PDO over precious metal catalysts

Table 1 summarizes some representative reports of glycerol hydrogenolysis to 1,2-PDO in liquid phase over supported precious metal catalysts [81–88]. Feng et al. have investigated glycerol hydrogenolysis over basic oxide-supported Ru catalysts, such as Ru/CeO₂, Ru/La₂O₃, and Ru/MgO [84]. Among the tested catalysts, Ru/CeO₂ has the smallest Ru particle size and the weakest surface basicity feature, and it is effective to promote 1,2-PDO formation from glycerol: 62.7% selectivity to 1,2-PDO at 85.2% conversion is obtained over Ru/CeO₂ at 180 °C and an H₂ pressure of 50 atm, and the by-products contain propanols, which are generated via 1,2-PDO further hydrogenolysis, and glycerol decomposition products such as methanol, ethanol, and ethylene glycol. Lee et al.

prepared a series of Ru-supported hydrotalcite-like and Ca-Zn-modified hydrotalcite-like catalysts for 1,2-PDO formation from glycerol [87]. They indicated that the support with strong acidity is effective for Ru dispersion and highly dispersed Ru can promote both the conversion and the 1,2-PDO selectivity. Hamzah et al. also reported that small Ru particles are effective for 1,2-PDO formation [86]. They have found that a mixed support of bentonite and TiO₂ at a weight ratio of 1:2 improves the dispersion of Ru and the catalytic activity. An 80.6% 1,2-PDO selectivity is achieved at a low temperature of 150 °C and an H₂ pressure of 20 atm, and ethylene glycerol is generated as the main by-product with a selectivity of ca. 10%. Gandarias et al. studied glycerol hydrogenolysis over SiO₂-Al₂O₃-supported Pt catalyst, and they indicate that the acid sites of SiO₂-Al₂O₃ are responsible for glycerol dehydration to acetol while Pt metal sites catalyze the acetol hydrogenation to 1,2-PDO [81]. Pt also catalyzes C–C bond cleavage reactions, whereas it inhibits the formation of coke. The maximum selectivity to 1,2-PDO is 31.9%: further hydrogenolysis products, such as 1-propanol and 2-propanol, are produced with high total selectivity.

Furikado et al. have studied glycerol hydrogenolysis over supported precious metal, such as Rh, Ru, Pt, and Pd [82]. Rh/SiO₂ exhibits a high activity to form glycerol hydrogenolysis products such as propanediols and propanols, while the maximum selectivity to 1,2-PDO was 34.6% because of the further hydrogenation of 1,2-PDO into 1-propanol. The catalytic activity is further promoted by the loading of Re onto Rh/SiO₂, whereas the selectivity to 1,2-PDO is maximized at 46.9% because of competitive formation of 1,3-PDO and propanols [83]. Auneau et al. studied supported Ir catalysts for glycerol transformation in the presence of NaOH in an H₂ atmosphere [85]. Ir/C gives a 76% selectivity to 1,2-PDO with 85.0% conversion at 180 °C and an H₂ pressure of 50 atm. Zhou et al. reported that Al₂O₃-supported Ag catalyst affords high 1,2-PDO selectivity of 96.0% with 46% conversion at 220 °C and 15 atm [88]. Although high 1,2-PDO selectivity is achieved, the catalytic activity of Ag/Al₂O₃ is not so high because of the low hydrogenation ability of Ag.

In the above-mentioned studies, we know that almost all the precious metals can be used for glycerol hydrogenation into 1,2-PDO, while the supports play an important role on the catalytic activity of the precious metals. The studies similarly indicate that the acid-base property of the support affects the dispersion of the precious metals, and highly dispersed precious metal catalysts show high catalytic activity for 1,2-PDO formation from glycerol. Although the liquid-phase reactions are performed at relatively low temperatures, the C–C bond cleavage products of glycerol, such as methanol, ethanol, and ethylene glycol, are still by-produced

Table 1
Liquid-phase 1,2-propanediol formation from glycerol over precious metal catalysts.

Catalyst	Temp. (°C)	H ₂ pressure (atm)	Glycerol/Catalyst (g/g)	Time (h)	Conversion of glycerol (%)	Selectivity to 1,2-PDO (%)	Ref.
Pt/SiO ₂ -Al ₂ O ₃	220	45	6.0	24	19.8	31.9	[81]
Rh/SiO ₂	120	80	27.8	10	19.6	34.6	[82]
Rh/Re-SiO ₂	120	80	27.8	2	38.4	46.9	[83]
Ru/CeO ₂	180	50	12.5	10	85.2	62.7	[84]
Ir/C	180	50	10.1	24	85.0	76.0	[85]
Ru/bentonite-TiO ₂	150	20	4.8	7	69.8	80.6	[86]
Ru/CaZnMgAlO	180	25	34.8	18	58.5	85.5	[87]
Ag/Al ₂ O ₃	220	15	7.6	10	46.0	96.0	[88]

at a certain amount over the precious metal catalysts, except Ag [81–87]. In some reports [81–83], it is described that a high yield of 1,2-PDO is difficult to be achieved because 1,2-PDO further converts into propanols. However, this could be a common problem in the liquid-phase glycerol hydrogenolysis, especially when an acidic metal oxide is used as the support because it catalyzes the further dehydration of 1,2-PDO into propanal [89]. As shown in Table 1, both the high conversion and the high selectivity are difficult to be achieved at the same time, which indicates that 1,2-PDO is usually unstable in liquid-phase catalytic conditions and that consecutive reactions occur. In another word, a long reaction time is usually required for achieving high conversions of glycerol in a liquid phase, whereas the resulting 1,2-PDO is easier to be further converted into propanols and even propylene for a long reaction time.

2.3. Liquid-phase glycerol hydrogenolysis into 1,2-PDO over base metal catalysts

Table 2 summarizes base metals such as Cu, Ni, and Co which have been also extensively studied for liquid-phase hydrogenolysis of glycerol into 1,2-PDO [90–99]. In an early report, Suppes et al. studied glycerol hydrogenolysis using various commercial catalysts, and copper-chromite was found to show a high activity for 1,2-PDO formation [90]: an 89.6% 1,2-PDO selectivity with 65.3% conversion was obtained. Balaraju et al. prepared a series of Cu/ZnO catalysts with different Cu/Zn ratios for glycerol hydrogenolysis [92]. Cu/ZnO catalyst with a Cu/Zn weight ratio of 50/50 shows a 1,2-PDO selectivity of 92% at 37% conversion. The 1,2-PDO selectivity is maximized at 92% because it decreases with increasing the conversion at a longer reaction time. Based on the physicochemical properties of Cu/ZnO catalysts measured by XRD and the reaction results, they indicate that the sufficient amount of ZnO and Cu with small particle size are required for achieving high glycerol conversion and high 1,2-PDO selectivity. Vasilidou et al. prepared various SiO₂-supported Cu catalysts with large crystals, small monodispersed crystallites and a highly dispersed XRD amorphous Cu phase [95]. Their results show that different dispersion characteristics result in different conversion of glycerol at a range of 20–50%, while all the catalysts give high selectivity to 1,2-PDO at a range of 92–97%. Wu et al. have prepared highly dispersed Cu clusters (<1 nm) over boehmite via an aqueous chemical reduction method and compared the catalytic activity with that of Cu/Al₂O₃, Cu/SiO₂ and Ru/C [93]. Cu/boehmite shows the highest activity for 1,2-PDO formation among the tested catalysts, which is illustrated to assign to the small particle size of Cu and the Lewis acid sites of boehmite. A complete conversion of glycerol is achieved at a reaction time of 12 h, whereas the selectivity to 1,2-PDO decreases to ca. 85% and the selectivity to propanols increases to ca. 13%.

Basic metal oxides-supported Cu is also effective for 1,2-PDO formation from glycerol. In a report of Yuan's group, a 97.6% 1,2-PDO selectivity with a glycerol conversion of 72% is achieved over Cu/MgO [96]. The activity of the Cu/MgO depends strongly on the particle sizes of both Cu and MgO: the catalysts with smaller sized Cu and MgO particles are more active. The same group also prepared

a Cu/MgAlO catalyst, which is synthesized via thermal decomposition of the as-synthesized Cu_{0.4}Mg_{5.6}Al₂(OH)₁₆CO₃ with layered double hydroxides. Comparing with the catalysts prepared by an impregnation and an ion-exchange method, Cu prepared by thermal decomposition is highly dispersed on MgAlO support and 98.2% 1,2-PDO selectivity with 80.0% conversion is obtained at 180 °C and an H₂ pressure of 30 atm [97]. Furthermore, the 1,2-PDO selectivity slightly decreases to ca. 97% when the conversion increases to ca. 95%.

Co and Ni also show catalytic activity for 1,2-PDO formation from glycerol, whereas the selectivity to 1,2-PDO is lower than that of Cu because Co and Ni promote the C–C cleavage and increase ethylene glycol and/or ethanol selectivity [98,99]. In the glycerol hydrogenolysis over Co/ZnAlO catalyst prepared by a coprecipitation method followed by reduction at 600 °C [98], the selectivity to 1,2-PDO is maximized at 57.8% at 200 °C, and the selectivities to ethylene glycol and ethanol are 21.0 and 4.5%, respectively. Perosa et al. studied the glycerol hydrogenolysis over Raney-Ni catalyst: the selectivities to 1,2-PDO and ethanol are 77 and 15%, respectively, even at a low temperature of 190 °C and an H₂ pressure of 10 atm [99].

Among the three base metals, Cu shows the highest activity for 1,2-PDO formation. Because of the competitive formation of glycerol C–C cleavage products, such as methanol, ethanol and ethylene glycol, 1,2-PDO cannot be selectively produced over Co- and Ni-based catalysts [98,99]. The 1,2-PDO selectivities higher than 90% can be achieved over most of the Cu-supported catalysts [90–97], and Cu with small particle sizes is preferable for 1,2-PDO formation [91–93,95–97]. Comparing with precious metals, Cu has low C–C cleavage ability and provides high 1,2-PDO selectivities. The selectivity to C–C bond-cleavage products over Cu-based catalysts is at most 3% [90–97]. However, in most of the liquid-phase reactions using acidic supports, 1,2-PDO selectivity decreases at high conversion levels because further hydrogenolysis of 1,2-PDO proceeds for a long reaction time. On the other hand, high 1,2-PDO selectivity can be maintained at high conversion levels over Cu supported on basic supports [96,97], although hydrogenolysis of 1,2-PDO still proceeds slowly with increasing the reaction time.

2.4. Liquid-phase glycerol hydrogenolysis into 1,2-PDO over bimetallic catalysts

Bimetallic catalysts are prepared in some studies to promote the catalytic activity toward 1,2-PDO formation from glycerol, as shown in Table 3 [100–104]. Li et al. prepared supported Pd-Re bimetallic catalysts by an impregnation method for glycerol hydrogenolysis [100]. They indicate that the added Re might have an interaction with Pd and can increase the ability of the catalysts for the activation of a C–O bond. The proposed reaction mechanism is shown in Fig. 2. The addition of Re also increases the acidity of the Pd-Re catalysts, whereas it decreases the selectivity to 1,2-PDO due to the further hydrogenolysis of 1,2-PDO into lower alcohols under acidic conditions. However, basic oxides-supported Pd-Re catalysts can promote the conversion of glycerol, and also maintain the selec-

Table 2
Liquid-phase 1,2-propanediol formation from glycerol over base metal catalysts.

Catalyst	Temp. (°C)	H ₂ pressure (atm)	Glycerol/Catalyst (g/ g)	Time (h)	Conversion of glycerol (%)	Selectivity to 1,2-PDO (%)	Ref.
Copper-chromite	200	21	Unclear	24	65.3	89.6	[90]
Cu/ZrO ₂	200	40	16.7	8	10.0	90.0	[91]
Cu/ZnO	200	20	17.4	16	37	92	[92]
Cu/boehmite	200	40	20	6	77.5	92.5	[93]
Cu/Al ₂ O ₃	220	50	10	6	61	93.3	[94]
Cu/SiO ₂	240	80	166.7	5	51.9	96.6	[95]
Cu/MgO	180	30	7.1	20	72.0	97.6	[96]
Cu/MgAlO	180	30	7.1	20	80	98.2	[97]
Co/ZnAlO	200	20	13.3	12	70.6	57.8	[98]
Raney Ni	190	10	4	20	63	77	[99]

Table 3
Liquid-phase 1,2-propanediol formation from glycerol over bimetallic metal catalysts.

Catalyst	Temp. (°C)	H ₂ pressure (atm)	Glycerol/Catalyst (g/ g)	Time (h)	Conversion of glycerol (%)	Selectivity to 1,2-PDO (%)	Ref.
Pd-Re/La ₂ O ₃	200	80	29.1	18	52.9	89.3	[100]
Cu-Ru/TiO ₂	200	25	46.2	12	39	90	[101]
Cu-Ru/bentonite	230	100	5.5	18	100	86.4	[102]
Cu-Ag/Al ₂ O ₃	200	15	Unclear	10	27	96.0	[103]
Cu-Pd/MgAlO	180	20	7.1	10	76.9	97.2	[104]

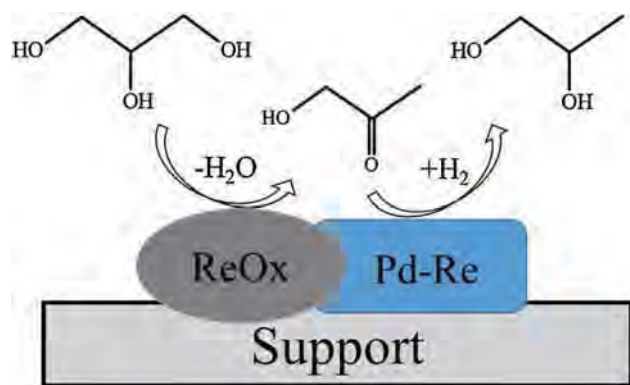


Fig. 2. Proposed mechanism of glycerol hydrogenolysis over supported Pd-Re bimetallic catalysts [100].

tivity to 1,2-PDO. 89.3% selectivity to 1,2-PDO at 52.9% conversion is achieved over Pd-Re/La₂O₃.

Because Cu shows low C–C cleavage ability and gives high 1,2-PDO selectivity as described in Section 2.3, Cu in bimetallic catalysts of precious metals, such as Ru and Pd, improves the catalytic activity. Salazar et al. have studied TiO₂ supported Cu-Ru bimetallic catalysts for glycerol hydrogenolysis into 1,2-PDO: the addition of Cu metal to a Ru-based catalyst significantly enhances the selectivity toward 1,2-PDO and the appropriate mass ratio of Cu/Ru is 1:1 [101]. The selectivity to 1,2-PDO is 90% at 39% conversion over Cu-Ru/TiO₂ whereas the 1,2-PDO selectivity is only 57% at 31% conversion over Ru/TiO₂ at the same reaction conditions. The role of Cu is illustrated to disperse large Ru agglomerates which are responsible for C–C bond cleavage to form ethylene glycol. Bentonite-supported Cu-Ru bimetallic catalysts are also effective for 1,2-PDO formation from glycerol, and the selectivity to 1,2-PDO and ethylene glycol is 86.4 and 9.4%, respectively, at 100% conversion at 230 °C and an H₂ pressure of 100 atm at a Ru/Cu molar ratio of 3:1 [102].

Zhou et al. have prepared a series of Ag-modified Cu/Al₂O₃ catalysts and studied the effect of Ag loading on the catalytic activity [103]. The reactions are performed at 200 °C and an H₂ pressure of 15 atm over Cu-Ag/Al₂O₃ without pre-reduction, and a 96% selectivity to 1,2-PDO is achieved at 27% conversion over Cu-Ag/Al₂O₃

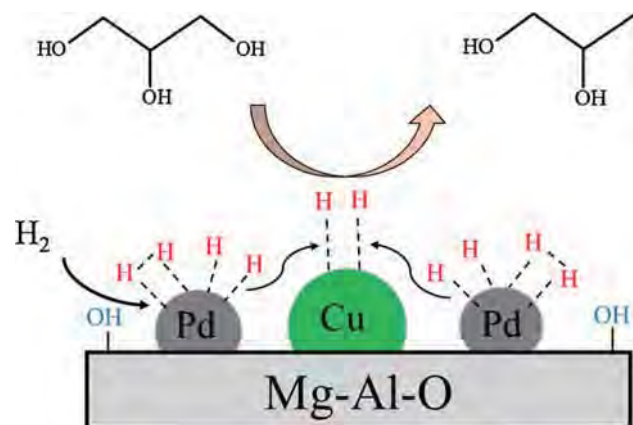


Fig. 3. Proposed mechanism of glycerol hydrogenolysis over Cu-Pd/MgAlO catalyst [104].

with a Cu/Ag molar ratio of 7:3. Based on the characterization results of TPR and XPS, it is indicated that the formation of low valence Cu species (Cu⁰ or Cu⁺) is the key for high activity and the addition of Ag promotes the reduction of the Cu species, which results in the generation of low valence Cu species. The addition of Ag is also illustrated to improve the dispersion of the Cu species, which increases the catalytic activity. Pd_{0.04}Cu_{0.4}/Mg_{5.56}Al₂O_{8.56} (Cu-Pd/MgAlO) catalysts are prepared via thermal decomposition of Pd_xCu_{0.4}Mg_{5.6-x}Al₂(OH)₁₆CO₃ precursors with layered double hydroxides for glycerol hydrogenolysis by Xia et al. [104]. Cu-Pd/MgAlO with highly dispersed Pd and Cu shows higher catalytic activity than mono-metallic Pd- and Cu-supported catalysts. A high 1,2-PDO selectivity of 97.2% with a glycerol conversion of 76.9% is achieved over Cu-Pd/MgAlO at 180 °C and an H₂ pressure of 20 atm. They conclude that the high catalytic performance of Cu-Pd/MgAlO is attributed to the H₂ spillover from Pd to Cu as shown in Fig. 3. Although the results of the reaction of Cu-Pd/MgAlO is similar with that of the Cu/MgAlO catalyst [97], which is reported by the same group [104], the reaction using bimetallic catalyst is performed at a lower H₂ pressure condition with a shorter reaction time.

We summarize the catalytic activity of various catalysts mentioned in Sections 2.2–2.4 in Fig. 4. The conversion-selectivity plots in the hydrogenolysis indicate that Cu and Cu-containing bimetallic

Table 4
Liquid-phase 1,2-propanediol formation from glycerol using *in-situ* generated hydrogen.

Catalyst	Temp. (°C)	Pressure (atm)	Solvent (H donor)	Glycerol/Catalyst (g/g)	Time (h)	Conversion of glycerol (%)	Selectivity to 1,2-PDO (%)	Ref.
Pt/NaY zeolite	230	1 (air)	Glycerol	5.3	15	85.4	64	[107]
Pt-Sn/SiO ₂	200	4 (N ₂)	Glycerol	4.1	2	54	59	[108]
Pd/Fe ₂ O ₃	180	5 (inert gas)	2-propanol	5.1	24	100	94	[109]
Cu/MgAlO	200	30 (N ₂)	Ethanol	8.1	10	93.9	93.1	[110]
Ni-Cu/Al ₂ O ₃	220	45 (N ₂)	formic acid	10.9	24	89.9	81.6	[111]
Pd/Co ₃ O ₄	180	5 (N ₂)	2-propanol	6.1	24	100	64	[114]
Cu/ZnAlO	220	35 (N ₂)	Methanol	1.7	4	86.6	51.9	[115]

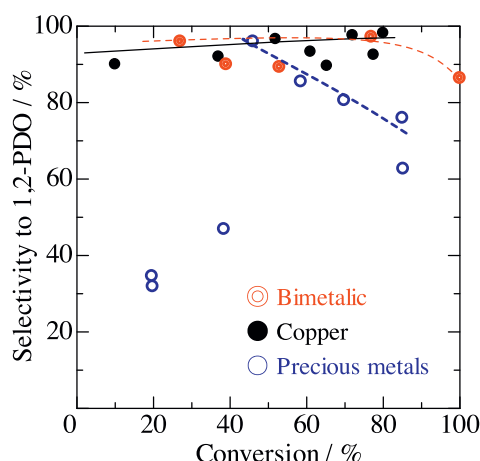


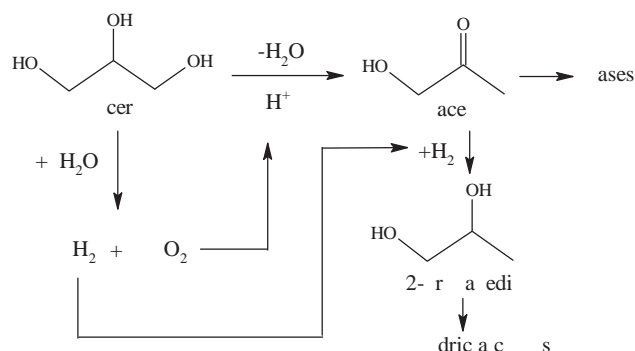
Fig. 4. Conversion-selectivity plots in the glycerol hydrogenolysis in liquid phase. Open, closed, and double circles represent the data listed in Tables 2–4, respectively, while the data for Co/ZnO/AlO and Raney Ni catalysts in Table 3 are not addressed.

catalysts are efficient and selective to form 1,2-PDO from glycerol in a liquid phase.

2.5. Liquid-phase glycerol hydrogenolysis into 1,2-PDO using hydrogen generated *in situ*

External supply of hydrogen is necessary for all the above-mentioned hydrogenolysis processes for producing 1,2-PDO from glycerol. The use of hydrogen gas as an H donor is common in a hydrogenolysis process, whereas a high H₂ pressure is always necessary and a pressure tight reaction equipment is required, which increases the production cost. One interesting alternative is to produce 1,2-PDO from glycerol hydrogenolysis using the hydrogen generated *in situ* from H-containing molecules via hydrogen transfer. Martin et al. have summarized glycerol hydrogenolysis into propanediols using hydrogen generated *in situ* [60]. The *in situ*-generated hydrogen can be supplied by glycerol itself via aqueous phase reforming as well as by the additive H-containing molecules, such as monoalcohols and formic acid, via catalytic transfer hydrogenation. A hydrogen molecule is produced together with CO₂ in the aqueous phase reforming of glycerol, while hydrogen atoms transfer from the H donor to glycerol in a catalytic transfer hydrogenation reaction [60].

Table 4 summarizes new significant reports of glycerol hydrogenolysis into 1,2-PDO using hydrogen generated *in situ* [107–115]. D'Hondt et al. firstly reported glycerol hydrogenolysis into 1,2-PDO using H₂ produced via *in-situ* reforming of glycerol [107]. NaY zeolite-supported Pt catalyst gives 64% selectivity to 1,2-PDO with a glycerol conversion of 85.4% at 230 °C under atmospheric conditions. The proposed reaction pathways are shown in Scheme 6. The reforming of glycerol over Pt generates H₂ and CO₂. The formed CO₂ works as an acid, which is proposed to catalyze glycerol dehydration into acetol and the formed H₂ is consumed for



Scheme 6. Reaction routes of glycerol hydrogenolysis into 1,2-PDO in the absence of H₂ proposed by D'Hondt et al. [107].

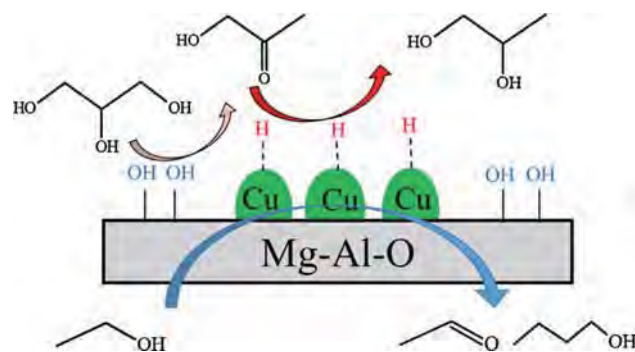


Fig. 5. Proposed mechanism of glycerol hydrogenolysis over Cu/MgAlO catalyst using ethanol as the H donor [110].

the later hydrogenation of acetol into 1,2-PDO over Pt. Maria et al. studied glycerol hydrogenolysis over SiO₂-supported Pt-Sn catalysts under pressured N₂ atmosphere [108]. The suitable amount of additive Sn into Pt/SiO₂ is 0.2 wt.%, and the maximum 1,2-PDO selectivity is 59% at 54% conversion at 200 °C. In the studies [107,108], because a part of glycerol is used for reforming to produce H₂, the selectivity to 1,2-PDO is low.

Musolino et al. firstly reported glycerol hydrogenolysis via catalytic transfer hydrogenation, in which they used 2-propanol as the H-donor molecule [109]: PdO/Fe₂O₃ is used as the catalyst and PdO is reduced to Pd by hydrogen generated from 2-propanol. 94% selectivity to 1,2-PDO with a complete conversion is achieved at 180 °C under 5 atm inert gas atmosphere, and acetone is described to be the only product formed by the oxidation of 2-propanol. Under such a reaction condition, gas products such as CO₂ are reasonable to be formed via glycerol reforming over Pd metal, and propylene is also possible to be formed via 1,2-PDO further hydrogenolysis. However, there is no description about the carbon balance and the analysis of the gaseous products in the paper. Xia et al. performed glycerol hydrogenolysis over Cu/MgAlO catalyst in the presence of an H-donor molecule, such as methanol, ethanol and 2-propanol,

under pressured N_2 conditions [110]. Among the tested H donors, ethanol is proved to be the best hydrogen source. The proposed mechanism is shown in Fig. 5. The dehydrogenation of ethanol yields acetaldehyde, which further converts to ethyl acetate, 1-butanol and 1,1-diethoxyethane. Considering that no dihydrogen molecule was detected in the gas phase, it is supposed that hydrogen dehydrogenated from ethanol exists mainly in the form of active hydrogen atom which adsorbed on the surface of the Cu, and then it reacts with acetol quickly. The Cu/MgAlO catalyst with a Cu:Mg:Al:O molar ratio of 0.4:5.6:2:9 shows the largest amount of basic sites and the highest Cu dispersion degree, and also gives the highest 1,2-PDO selectivity of 93.1% at a conversion of 93.9% at 200 °C and an N_2 pressure of 30 atm. Gandarias et al. have conducted a series of works dealing with hydrogen-free glycerol hydrogenolysis over Ni-Cu/Al₂O₃ in the presence of formic acid, which is used as the H-donor molecule [111–113]. Large loading of Ni promotes acetol hydrogenation into 1,2-PDO, whereas it also increases the selectivities to glycerol decomposition products. A 1,2-PDO selectivity of 81.6% at 89.9% conversion is obtained over Ni-Cu/Al₂O₃ with a Ni/Cu weight ratio of 20:15 at 220 °C and 45 atm N_2 . In a recent study, Mauriello et al. reported a 64% selectivity to 1,2-PDO with a complete conversion of glycerol over Pd/Co₃O₄ at 180 °C and 5 atm N_2 using 2-propanol as the H donor [114]. The preparation method of the catalysts significantly affects the activity, and the catalysts prepared by a co-precipitated method show the highest catalytic performance toward 1,2-PDO formation. They conclude that the co-precipitation method ensures a strong interaction between Pd and the support, and leads to the formation of bimetallic ensembles which positively promote the glycerol catalytic transfer hydrogenolysis reaction. Considering that unreacted methanol remains in the crude glycerol solution in biodiesel production process, Vasiliadou et al. studied hydrogen-free glycerol hydrogenolysis using methanol as the H donor [115]. The reactions are performed over Pt- or Cu-based catalysts using 7.2 wt.% methanol and 11.4% glycerol mixed aqueous solution as the reactant. Cu/ZnAlO catalyst prepared by the co-precipitation method shows a relatively high activity and gives a 51.9% selectivity to 1,2-PDO with a glycerol conversion of 86.6%. In the experiments using labeled ¹³CH₃OH, it is concluded that methanol reformation with water mainly contributes to hydrogen production, and ca. 70% of the total hydrogen is produced from the reformation of methanol, while the extent of glycerol aqueous phase reforming is limited in the presence of methanol.

Glycerol hydrogenolysis into 1,2-PDO using hydrogen generated *in situ* have some advantages such as the use of renewable H-donor resources of methanol, ethanol, and formic acid, while the most attractive advantage is that the hydrogen generated *in situ* can be performed at low or even ambient pressure. On the other hand, the use of additional substances will result in additional by-products and requires the additional separating processes. From this view point, catalytic transfer hydrogenation using H-donor molecules is more preferable than using glycerol aqueous phase reforming because the latter generally produces more kinds of by-products. Among the well-used H-donor molecules, such as formic acid, methanol, ethanol, and 2-propanol, formic acid can be considered to be the most preferable one because only CO₂ is generated after dehydrogenation and CO₂ is easily separated from the liquid products.

2.6. Vapor-phase glycerol hydrogenolysis into 1,2-PDO

Vapor-phase glycerol hydrogenolysis into 1,2-PDO is preferable for industrial applications, whereas there are not so many studies dealing with vapor-phase reactions. Table 5 summarizes glycerol hydrogenolysis to 1,2-PDO in a vapor phase. Suppes et al. firstly reported vapor-phase hydrogenolysis of glycerol to 1,2-PDO using

copper-chromite catalyst [117]. They perform the reaction under atmospheric H₂ pressure: 55.5% selectivity to 1,2-PDO and 44.5% selectivity to acetol at complete glycerol conversion are obtained at 200 °C at a glycerol aqueous concentration of 2.5 wt.%. In their further report [118], the effects of reaction conditions are investigated: lower temperatures and higher hydrogen pressures shift the equilibrium from acetol to 1,2-PDO. Lower reaction temperatures also inhibit the formation of glycerol cracking products such as ethylene glycol, and higher than 90% 1,2-PDO selectivity is achieved at 230 °C under H₂ pressures at a range of 5–15 atm.

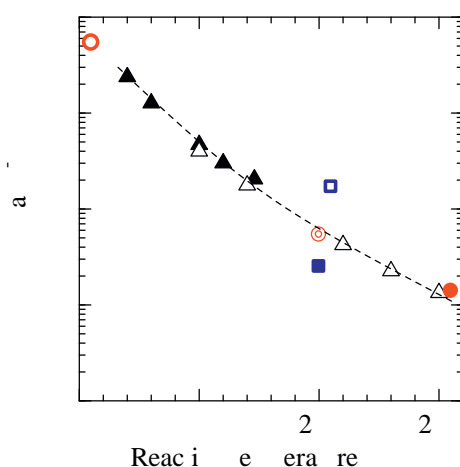
Since the dehydration of glycerol needs relatively high reaction temperatures and the hydrogenation of acetol into 1,2-PDO favors low temperatures, Sato et al. developed an efficient direct process which is performed over Cu/Al₂O₃ catalyst at an atmospheric H₂ pressure and gradient temperatures: the dehydration of glycerol into acetol is catalyzed by the upper-layer catalyst at high temperature, and the following hydrogenation of acetol into 1,2-PDO is catalyzed by the lower-layer catalyst at low temperature [74,75]. In the system, glycerol can be dehydrated to acetol completely and acetol can be hydrogenated into 1,2-PDO efficiently: a 96.1% yield of 1,2-PDO is achieved at a gradient temperature from 200 to 130 °C under ambient H₂ pressure. However, even higher 1,2-PDO yield cannot be achieved because the by-production of ethylene glycol, which is generated by glycerol decomposition over Cu metal. In our further study, Ag-modified Cu/Al₂O₃ is prepared and found to be effective for reducing the cracking ability of Cu and inhibiting ethylene glycol formation [77]. Although the formation of ethylene glycol can be inhibited by the loading of Ag onto Cu/Al₂O₃, it also decreases the hydrogenation ability of the catalyst and inhibits the further hydrogenation of acetol into 1,2-PDO. In a reactor with double-layered catalysts, Ag-modified Cu/Al₂O₃ is loaded on the upper layer of the catalyst bed to inhibit ethylene glycol formation and Cu/Al₂O₃ without Ag is loaded on the lower layer to complete the acetol hydrogenation into 1,2-PDO: a 98.3% yield of 1,2-PDO is achieved over the double-layered catalysts at gradient temperatures from 170 to 105 °C.

In the vapor-phase hydrogenolysis of glycerol over Cu/SiO₂ prepared by an incipient wetness method, 87.0% selectivity to 1,2-PDO is achieved with a complete glycerol conversion at 255 °C and an H₂ pressure of 15 atm [119]. Zhu et al. modified Cu/SiO₂ with B₂O₃ and found that the addition of B₂O₃ into Cu/SiO₂ could greatly restrain the growth of copper particles and maintain the dispersion of copper species upon calcination, reduction and reaction during the vapor-phase glycerol hydrogenolysis [120]. The addition of suitable B₂O₃ to Cu/SiO₂ significantly enhances the catalytic activity, catalytic stability and 1,2-PDO selectivity: a 98.0% selectivity to 1,2-PDO with a complete glycerol conversion is obtained over Cu-B₂O₃/SiO₂ catalyst at 200 °C and an H₂ pressure of 50 atm. Besides Cu-based catalysts, Ag- and Ru-based catalysts are also applied for the vapor-phase glycerol hydrogenolysis, whereas these catalysts do not show better catalytic performance than Cu-based catalysts. In their further study, a Cu/SiO₂ catalyst is prepared by an ammonia evaporation hydrothermal method, and 1,2-PDO yield could be maintained at ca. 98% for 300 h at an H₂ pressure of 50 atm [121]. Recently, they also reported a Cu/CeO₂ catalyst prepared by a solidstate grinding-assisted nanocasting method, which provides a stable yield of ca. 97% [122]. The high performance of the Cu/SiO₂ and Cu/CeO₂ catalysts is explained to attribute the well dispersed Cu nanoparticles and the strong interaction between Cu and the supports. Cu-ZnO/Al₂O₃ catalysts are studied by several groups: the loading of ZnO promotes the formation of 1,2-PDO from glycerol, and 1,2-PDO selectivity higher than 90% can be achieved under H₂ pressured conditions [124–126]. In a recent study, Harisekhar et al. studied Cu/SBA-15 catalyst, which gives a 84% selectivity to 1,2-PDO at 90% conversion at 200 °C under atmospheric H₂ pressure [127]. Tanielyan et al. performed the reaction over various Raney

Table 5

Vapor-phase glycerol hydrogenolysis into 1,2-PDO.

Catalyst	Temp. (°C)	Pressure (atm)	WHSV (h ⁻¹)	TOS (h)	Conversion (%)	Selectivity to 1,2-PDO (%)	Ref.
Cu/Al ₂ O ₃	200–130 ^a	1	0.06	1–5 ^b	100	96.1	[74]
Ag-Cu/Al ₂ O ₃	170–105 ^a	1	0.03	1–5 ^b	100	98.3	[77]
Raney Cu	205	14	0.18	6.2 ^d	100	95	[80]
Cu/SiO ₂	255	15	2.2	unclear	100	87	[119]
Copper-Chromite	200	1	0.04	0.5	100	55.5	[117]
Cu-B ₂ O ₃ /SiO ₂	200	50	0.08	56	100	98	[120]
Cu/SiO ₂	200	50	0.08	300	100	98.3	[121]
Cu/CeO ₂	180	50	0.15	300	100	96.9	[122]
Cu-ZnO/Al ₂ O ₃	190	6.4	0.08	unclear	96.2	92.2	[124]
Cu-ZnO/Al ₂ O ₃	250	32	2.8	12	100	>90	[125]
Cu-ZnO/Al ₂ O ₃	250	1	0.05	48.5	85.5	83.7	[126]
Cu/SBA-15	220	1	1.03	10	90	84	[127]
Ag/OMS-2 ^c	200	50	unclear	92	ca. 30	ca. 65	[128]
Ru/MCM-41	230	1	2.09	10	62	38	[129]

^a Gradient temperature.^b Averaged activity between 1 and 5 h.^c OMS-2, octahedral molecular sieve.^d Time on stream of 6.2 days.**Fig. 6.** Changes in equilibrium constants of acetol hydrogenation with temperature.

catalysts such as Raney Cu, Cu–Cr, and Cu–Cr–Ni [79,80]. Among the tested catalysts, Raney Cu shows the highest stability and gives the highest selectivity to 1,2-PDO. In a long run, higher than 95% yield of 1,2-PDO can be kept in 6.2 days. Ag catalyst supported on octahedral molecular sieve (OMS-2) gives an initial glycerol conversion of ca. 65% and 1,2-PDO selectivity of ca. 90% at 200 °C and an H₂ pressure of 50 atm [128]. However, the catalyst gradually deactivates with time on stream (TOS): after 92 h, the conversion and 1,2-PDO selectivity decreases to ca. 30 and 65%, respectively. The decrease in the 1,2-PDO selectivity is caused by the decrease of hydrogenation ability of the catalyst: the selectivity to acetol increases up to 30% at a TOS of 92 h. Vanama et al. studied vapor-phase glycerol hydrogenolysis over Ru/MCM-41 catalyst [129]. Because of the high hydrogenolysis ability of Ru, 1,2-PDO further hydrogenates into lower alcohols such as 1-propanol and 2-propanol, and the maximum 1,2-PDO selectivity is only 38% at 230 °C under atmospheric H₂ pressure. The low 1,2-PDO selectivity also ascribes to the competitive formation of 1,3-PDO and the by-production of ethylene glycol.

Fig. 6 depicts equilibrium constants, K_p , in the hydrogenation of acetol at different temperatures. The closed and open triangles present the equilibrium constants of acetol hydrogenation in the reaction of glycerol hydrogenolysis and acetol hydrogenation, respectively, calculated from the data in our previous study [74]. The K_p values are fitted to a master curve, as shown in Fig. 6. The K_p

values decreases with increasing the temperature, which indicates that the reaction is exothermic. Under gradient temperature conditions [74,77], after the dehydration of glycerol has proceeded at higher temperatures of the upper layer of the catalyst bed, low bottom temperatures would work to shift the equilibrium to the right side. Sato et al. have discussed chemical equilibrium in the dehydrogenation of 1,2-PDO to acetol, in which the equipment constant is estimated to be 0.15 atm at 210 °C [123]. Because the K_p in the hydrogenation of acetol is equal to the reciprocal of the equilibrium constant in the dehydrogenation of 1,2-PDO, the equilibrium constant in the hydrogenation of acetol is 6.7 atm⁻¹ at 210 °C. The estimated K_p value of acetol hydrogenation is close to the master curve in Fig. 6, which strongly supports that the hydrogenation of acetol achieves equilibrium at gradient temperatures [74]. K_p values are calculated from several reference data at 100% glycerol conversion, and plotted in Fig. 6 (circles). The K_p values calculated from the data in Refs. [77,119,120] are close to the master curve, which indicates that the hydrogenation of acetol formed from glycerol achieves equilibrium in these studies. Because the selectivities to acetol are not shown in Refs. [121,122], K_p values are not calculated for the reports. A K_p value calculated from Ref. [80], however, is located above the master curve (open square). Because the large amount, 16.5 g, of catalyst is used in the study, it is plausible that the bottom temperature of the catalyst bed could be lower than the monitored temperature. On the other hand, the K_p value calculated from Ref. [117] is located below the master curve (closed square), which indicates that equilibrium is not achieved possibly.

Closed triangles present the equilibrium constants of acetol hydrogenation in the reaction of glycerol hydrogenolysis from Ref. [74]. Open triangles represent the equilibrium constants of acetol hydrogenation in the reaction of acetol hydrogenation from Ref. [74]. Open, closed, and double circles represent the equilibrium constants of acetol hydrogenation in glycerol hydrogenolysis calculated from the data in Table 5 cited from Refs. [77,119,120], respectively. Open and closed squares are from those in Refs. [80,117], respectively.

Cu-based catalysts show stable high activity toward 1,2-PDO formation in vapor-phase glycerol hydrogenolysis, and yields of 1,2-PDO over 96% have been achieved in some studies [74,77,117]. Although a high H₂ pressure is generally used for shifting the equilibrium from acetol to 1,2-PDO, acetol can be efficiently hydrogenated into 1,2-PDO even at an ambient H₂ pressure and gradient temperatures in a vapor-phase reaction [74,77]. Comparing with liquid-phase reactions, vapor-phase reactions can achieve both high conversion and high 1,2-PDO selectivity. As mentioned in Sections 2.2–2.4, the consecutive reactions of dehydration and

hydrogenation proceed in liquid-phase reactions to decrease the 1,2-PDO selectivity, especially when using acidic supports. However, 1,2-PDO is not further dehydrated over acidic supports even in vapor-phase reactions at relatively low temperatures as 200 °C. Furthermore, the catalytic activity of Cu-based catalysts is stable in a vapor phase [74,77,117]. Thus, from a view point of achieving high 1,2-PDO yield and inhibiting the formation of by-products, the vapor-phase reactions would be preferable in the selective glycerol hydrogenolysis into 1,2-PDO.

3. 1,3-Propanediol

1,3-Propanediol (1,3-PDO) is commercially the most valuable product in the hydrogenolysis of glycerol. It is used in resins, engine coolants, dry-set mortars, water-based inks, but most of 1,3-PDO is used in the production of polypropylene terephthalate, which is a polyester synthesized from 1,3-PDO and terephthalic acid [5]. The market for 1,3-PDO is currently over 10⁵ tons per year, and the methods for producing 1,3-PDO are hydroformylation of ethylene oxide followed by hydrogenation, hydration of acrolein followed by hydrogenation, and fermentation of either glycerol or glucose [130]. The petroleum-based methods have a problem in selectivity, while the fermentation processes have a problem in production efficiency. Hydrogenolysis of glycerol to 1,3-PDO is an alternative process that could replace the current processes if efficient catalysts are developed. Although many attempts have been made to produce 1,3-PDO by hydrogenolysis of glycerol, the selectivity to 1,3-PDO is still unsatisfied for the industrial application.

Scheme 7 is the generally accepted reaction route of glycerol hydrogenolysis into 1,3-PDO. 1,3-PDO is produced by the hydrogenation of 3-hydroxypropanal [5,6], which is the dehydration product of glycerol. Thus, an acid catalyst is necessary in the first step of glycerol dehydration. In particular, Brønsted acid sites are necessary for the formation of 3-hydroxypropanal from glycerol [5]. Another possible route of 1,3-PDO is proposed by Tomishige et al. [73] as mentioned in Section 2.1 (Fig. 1).

3.1. Hydrogenolysis of glycerol into 1,3-propanediol using a batch-type reactor

Table 6 summarizes glycerol hydrogenolysis into 1,3-PDO performed in a batch-type reactor. Tomishige's group has performed a series of works dealing with glycerol hydrogenolysis into 1,3-PDO [6,73,131–134]. SiO₂-supported precious metals with ReO_x are found to be efficient for 1,3-PDO formation from glycerol, and Ir shows the highest catalytic activity among the precious metals such as Rh, Ru, Pt, and Pd. The yield of 1,3-PDO is maximized at 38% over Ir-ReO_x/SiO₂ catalyst at 120 °C and an H₂ pressure of 80 atm in the presence of H₂SO₄. The conversion of glycerol increases with increasing the reaction time, whereas the selectivity to 1,3-PDO decreases with increasing the reaction time because 1,3-PDO further converts into 1-propanol and propane. The maximum yield of 1,3-PDO is obtained at a reaction time of 36 h: the conversion of glycerol and the selectivity to 1,3-PDO are 81% and 46%, respectively. The relatively low reaction temperature is indicated to be significant for inhibiting the side reactions and increasing the 1,3-PDO selectivity. The H₂ pressure affects the reaction rate, while the H₂ pressure rarely affects the selectivity to 1,3-PDO. Recently, mesoporous silica (KIT-6) supported Ir-Re alloy catalysts are applied for the glycerol hydrogenolysis in the presence of amberlyst-15 as an acidic promoter at the same reaction conditions [135].

Pt and tungsten oxide as an acidic modifier are reported to accelerate the formation of 1,3-PDO from glycerol. Kurosaka et al. have studied glycerol hydrogenolysis into 1,3-PDO in the pioneer-

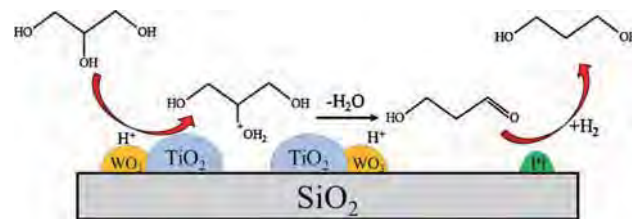


Fig. 7. Proposed mechanism of glycerol hydrogenolysis to 1,3-PDO over Pt/WO₃-TiO₂/SiO₂ catalyst [137].

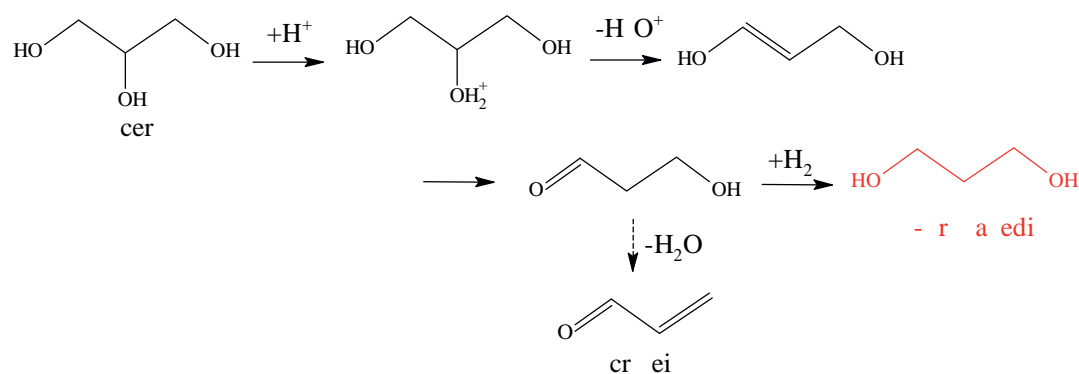
ing report [136]. A 24% yield of 1,3-PDO is obtained from glycerol at 170 °C and an H₂ pressure of 80 atm over Pt-WO₃/ZrO₂ catalyst, in which ZrO₂-supported WO₃ is well known as a super acid. Besides Pt, other precious metals such as Pd, Ru, Rh, and Ir are not active for 1,3-PDO formation and give 1,3-PDO yields lower than 5%. Gong et al. have investigated the glycerol hydrogenolysis over Pt/WO₃-TiO₂/SiO₂ catalyst [137]. WO₃ species are concluded to regulate the acidity of the Pt/WO₃-TiO₂/SiO₂ catalyst by producing Brønsted acid sites, which play a key role during 1,3-PDO formation, and the existence of TiO₂ species improves the dispersion of Pt metal. It is supposed that the Brønsted acid sites on WO₃ surface catalyze the dehydration of glycerol to 3-hydroxypropanal, and the highly dispersed Pt particles catalyze the further hydrogenation of 3-hydroxypropanal to 1,3-PDO as shown in Fig. 7. The selectivity to 1,3-PDO is maximized at 50.5% at 180 °C and an H₂ pressure of 55 atm, whereas the conversion of glycerol is as low as 15.3%. In a recent report, Pt supported on mesoporous WO_x-TiO_x shows similar results of reactions using Pt/WO₃-TiO₂/SiO₂ [138].

Kaneda's group has studied the glycerol hydrogenolysis using WO_x-supported Pt-AlO_x catalyst, and 44% 1,3-PDO selectivity with a high glycerol conversion of 90% is achieved at 180 °C under a relatively low H₂ pressure of 30 atm without any acidic additives [139]. In their study, boehmite-supported Pt/WO_x shows much better catalytic performance and gives a 1,3-PDO yield of 66%, which is the highest value reported ever before, at 180 °C and an H₂ pressure of 50 atm [140]. They have also performed the hydrogenolysis of some diols, such as 1,3-PDO, 1,2-PDO, 1,2-butanediol, and 2,3-butanediol, over Pt/WO_x/AlOOH, and found that 1,2-PDO and 1,2-butanediol are much more reactive than 1,3-PDO and 2,3-butanediol. They conclude that Pt-WO_x/AlOOH has high activity for the secondary OH group adjacent to a primary OH group. Consequently, both high glycerol conversion and high 1,3-PDO selectivity are obtained because 1,3-PDO is less reactive over Pt/WO_x/AlOOH. The catalyst is also stable and can be reused for 3 times without deactivation. Comparing with AlOOH-supported Pt-WO_x, Al₂O₃-support Pt-WO_x catalyst shows both low glycerol conversion and low 1,3-PDO selectivity [140–142], and they propose that the large quantity of Al-OH groups on the surface of the Al₂O₃ enhances its catalytic activity.

Oh et al. reported selective formation of 1,3-PDO from glycerol using Pt/sulfated ZrO₂ catalyst, in which sulfated zirconia is a well-known super acid [143]. An extremely high 1,3-PDO selectivity of 83.6% at a glycerol conversion of 66.5% is achieved in 1,3-dimethyl-2-imidazolidinone (DMI) solvent at 170 °C and an H₂ pressure of 73 atm. It is interesting that when DMI is replaced by water, the selectivity to 1,3-PDO is only 19.6%. Thus, DMI probably plays an essential role on the 1,3-PDO formation.

3.2. Hydrogenolysis of glycerol into 1,3-propanediol using a flow-type reactor

Table 7 summarizes vapor-phase hydrogenolysis of glycerol into 1,3-PDO using a flow-type reactor [144–150]. Huang et al. firstly reported glycerol hydrogenolysis into 1,3-PDO over non-precious metal catalysts in a flow-type reactor [144]. SiO₂-supported Cu-



Scheme 7. Reaction routes of glycerol hydrogenolysis into 1,3-PDO [5].

Table 6
Hydrogenolysis of glycerol into 1,3-propanediol using a batch-type reactor.

Catalyst	Temp. (°C)	H ₂ pressure (atm)	Solvent	Glycerol/Catalyst (g/g)	Time (h)	Conversion of glycerol (%)	Selectivity to 1,3-PDO (%)	Ref.
Ir-ReO _x /SiO ₂	120	80	H ₂ O	26.7	36	81	46	[131]
Rh-ReO _x /SiO ₂	120	80	H ₂ O	26.7	5	ca. 42	ca. 20	[132]
Ir-Re alloy/KIT-6 ^a	120	80	H ₂ O	26.7	12	63.3	34.7	[135]
Pt-WO ₃ /ZrO ₂	170	80	DMI ^c	2.8	18	85.8	28.2	[136]
Pt/WO ₃ -TiO ₂ /SiO ₂	180	55	H ₂ O	2 ^b	12	15.3	50.5	[137]
Pt/WO _x -TiO _x	180	55	H ₂ O	4	12	18.4	40.3	[138]
Pt-AlO _x /WO _x	180	30	H ₂ O	0.9	10	90	44	[139]
Pt-WO _x /AlOOH	180	50	H ₂ O	0.9	12	100	66	[140]
Pt-WO _x /Al ₂ O ₃	180	50	H ₂ O	0.9	12	89	35	[140]
Pt-WO _x /Al ₂ O ₃	200	40	H ₂ O	4.7	18	49	28	[141]
Pt-WO _x /Al ₂ O ₃	200	45	H ₂ O	6.1	24	51.9	53.1	[142]
Pt/Sulfated ZrO ₂	170	73	DMI ^c	2.8	24	66.5	83.6	[143]

^a KIT-6, mesoporous silica.

^b Volume ratio of glycerol/catalyst.

^c DMI: 1,3-dimethyl-2-imidazolidinone.

Table 7
Hydrogenolysis of glycerol into 1,3-propanediol using a flow-type reactor.

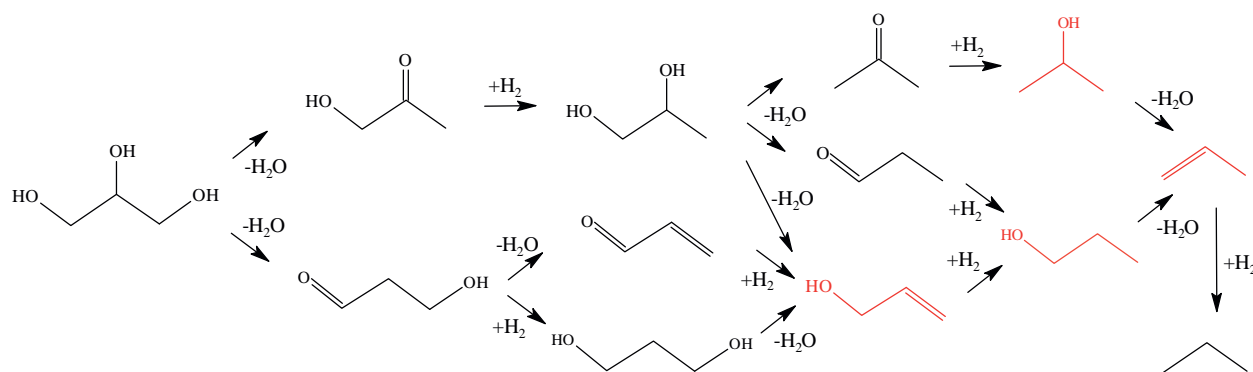
Catalyst	Temp. (°C)	H ₂ pressure (atm)	WHSV (h ⁻¹)	TOS (h)	Conversion of glycerol (%)	Selectivity to 1,3-PDO (%)	Ref.
Cu-H ₄ SiW ₁₂ O ₄₀ /SiO ₂	210	5.4	0.1	unclear	83.4	32.1	[144]
Pt-WO ₃ /ZrO ₂	130	40	0.25 ^a	24	70.2	45.6	[145]
Pt-WO _x -SiO ₂ /ZrO ₂	180	50	0.1	unclear	54.3	52	[146]
Cu-H ₄ SiW ₁₂ O ₄₀ /ZrO ₂	180	50	0.1	unclear	24.1	48.1	[147]
Pt-Li ₂ H ₂ SiW ₁₂ O ₄₀ /ZrO ₂	180	50	0.1	120	43.5	53.6	[148]
Pt-WO _x /Al ₂ O ₃	160	50	0.1	unclear	64.2	66.1	[149]
Pt/AlPO ₄	260	1	2.1	4	100	35.4	[150]

^a LHSV value.

H₄SiW₁₂O₄₀ catalyst gives a maximum 1,3-PDO selectivity of 32.1% at 83.4% conversion. The effects of reaction temperatures, H₂ pressures, and WHSV are investigated in detail: high reaction temperatures promote the conversion of glycerol, but decrease the selectivity to 1,3-PDO because of the competitive formation of decomposed products at high temperatures; high H₂ pressures are efficient for achieving both high glycerol conversion and 1,3-PDO selectivity; the conversion of glycerol increases with decreasing the WHSV, whereas the selectivity to both 1,3-PDO and 1,2-PDO decreases because the produced diols are further converted into cyclic acetals for a long residence time. Qin et al. studied glycerol hydrogenolysis into 1,3-PDO using Pt-WO₃/ZrO₂ catalyst which gives 45.6% 1,3-PDO selectivity at 70.2% conversion at 130 °C and an H₂ pressure of 40 atm [145]. The effects of reaction temperatures and H₂ pressures are studied and the conclusions agree with those in the reports of Huang et al. mentioned above [144].

In a recent study, Zhu et al. have prepared SiO₂-modified Pt-WO_x/ZrO₂ catalyst which gives an improved 1,3-PDO selectivity of 52% [146]: the addition of SiO₂ enhances Pt dispersion and acid-

ity, which leads to the improved activity and 1,3-PDO selectivity. Zhu's group has also performed the glycerol hydrogenolysis using Cu-H₄SiW₁₂O₄₀/ZrO₂ [147], Pt-Li₂H₂SiW₁₂O₄₀/ZrO₂ [148] and Pt-WO_x/Al₂O₃ catalysts [149], and study the effect of the acid property on the 1,3-PDO formation. It is found that the yield of 1,3-PDO is proportional to the concentration of the Brønsted acid sites, while the yield of 1,2-PDO is proportional to the concentration of Lewis acid sites [149]. Thus, the existence of the large amount of Brønsted acid sites on the support are significant for the selective hydrogenolysis of glycerol to 1,3-PDO. The highest 1,3-PDO yield of 42% is achieved over Pt-WO_x/Al₂O₃ catalyst at 160 °C and an H₂ pressure of 50 atm. Priya et al. have studied the glycerol hydrogenolysis over Pt/AlPO₄ catalyst at atmospheric H₂ pressure [150,151]. The selectivity to 1,3-PDO is maximized at 35.4% at 260 °C with a complete glycerol conversion. However, the analysis of gaseous products and the information of recovery are not mentioned although it is reasonable that decomposition of products is possible at high reaction temperatures.



Scheme 8. Reaction routes of glycerol hydrogenolysis into allyl alcohol, propanols, and propylene.

3.3. General summary of glycerol hydrogenolysis into 1,3-propanediol

The property of acid promoter is a key for the 1,3-PDO formation from glycerol. As summarized in Tables 6 and 7, high 1,3-PDO selectivity can be obtained in the presence of strong Brønsted acid sites, and the reaction temperature is generally lower than that for 1,2-PDO formation. Acetol, which can be further hydrogenated into 1,2-PDO (Scheme 4), and 3-hydroxypropanal that can be further hydrogenated into 1,3-PDO (Scheme 7) are two determinate intermediates in the glycerol hydrogenolysis. In another word, the formation of 1,2-PDO and 1,3-PDO is competitive and thus the selectivity to 1,2-PDO and 1,3-PDO is determined by which intermediate, acetol or 3-hydroxypropanal, is preferentially produced from glycerol. Glycerol dehydration into acetol generally prefers either metal active sites [74–78] or Lewis acid sites [149] at high reaction temperatures. On the other hand, glycerol dehydration into 3-hydroxypropanal prefers Brønsted acid sites [149]. Although high reaction temperatures accelerate the glycerol dehydration into 3-hydroxypropanal, they also promote the further dehydration of 3-hydroxypropanal into acrolein. Thus, relatively low reaction temperatures are efficient for inhibiting the further dehydration of 3-hydroxypropanal into acrolein, and 1,3-PDO can be produced via the hydrogenation of 3-hydroxypropanal. Additionally, strong Brønsted acid sites are necessary for the hydrogenolysis of glycerol into 1,3-PDO because they can catalyze the hydrogenolysis of glycerol into 3-hydroxypropanal at lower reaction temperatures than weak and medium Brønsted acid sites. Therefore, a successful catalyst system for the selective transformation of glycerol into 1,3-PDO requires to minimize the side reaction of 3-hydroxypropanal dehydration into acrolein as well as to promote the coupled dehydration-hydrogenation reactions.

It is reasonable that it is difficult to produce 1,3-PDO selectively because 1,3-PDO is easily further converted into 1-propanol in addition to the unstable intermediate such as 3-hydroxypropanal [5,6]. The reactivity of 1,3-PDO is higher than 1,2-PDO in most catalyst systems for glycerol hydrogenolysis [5,6] except the Pt-WO_x/AlOOH catalyst reported by Kaneda et al. [140]. Glycerol hydrogenolysis into 1,3-PDO requires low reaction temperatures and high H₂ pressures to promote the hydrogenation of 3-hydroxypropanal. In a flow-type reactor under the conditions at a low temperature and a high H₂ pressure, it is difficult to vaporize a less volatile glycerol [144–149]. In a liquid-phase reaction using a batch-type reactor at a low temperature, on the other hand, a high H₂ pressure condition can be readily realized. In future studies, the development of a catalyst system, which is extremely active for 1,3-PDO formation from glycerol but inactive for the further conversion of 1,3-PDO, is considered as a big challenge.

4. Monoalcohols and propylene

As described in the previous sections, a large number of efforts have been conducted for producing 1,2-PDO and 1,3-PDO through glycerol hydrogenolysis. On the other hand, the further hydrogenolysis products from 1,2-PDO and 1,3-PDO, such as allyl alcohol, propanols, and propylene, are also attractive and valuable. In the last 5 years, many studies dealing with glycerol hydrogenolysis into these chemicals have been reported. Scheme 8 summarizes the reaction routes of multi-step hydrogenolysis of glycerol. Allyl alcohol is an important chemical intermediate due to the bifunctionality, such as a hydroxyl group and a C=C double bond in the molecule, and it has wide uses for producing resins, paints, coatings, silane coupling agents, and polymers [152]. Propanols, such as 1-propanol and 2-propanol, have lower value than 1,3-PDO and 1,2-PDO, while they are also attractive chemicals available to be produced from glycerol. Both 1-propanol and 2-propanol have a wide array of solvent uses. In glycerol hydrogenolysis, 1-propanol can be produced via either 1,2-PDO, 1,3-PDO, or acrolein, while 2-propanol can be only produced via 1,2-PDO. Propylene, which is also an important starting resource in the petrochemical industry, can be produced from glycerol via both 1-propanol and 2-propanol dehydration. In this section, glycerol hydrogenolysis into allyl alcohol, propanols, and propylene are summarized and discussed.

4.1. Allyl alcohol

In Scheme 8, it is reasonable that allyl alcohol can be generated from glycerol via both 1,2-PDO and 1,3-PDO dehydration. However, selective synthesis of allyl alcohol from glycerol under H₂ pressure conditions has not been reported. 1,2-PDO dehydration gives three kinds of products, such as acetone, propanal, and allyl alcohol (Scheme 8), whereas selective dehydration of 1,2-PDO into allyl alcohol is very difficult and has not been reported. Propanal is the main product in 1,2-PDO dehydration over acid catalysts, such as H₄SiW₁₂O₄₀/SiO₂ [153], SiO₂-Al₂O₃ [154], and WO₃/SiO₂ [89], and the selectivity to allyl alcohol is lower than 5% [89,153,154]. Allyl alcohol can be also generated from glycerol via 1,3-PDO dehydration and acrolein hydrogenation, whereas it is difficult to be selectively produced because it is easy to be further hydrogenated into 1-propanol under H₂ pressure conditions. As a consequence, all the successful reports aimed to produce allyl alcohol from glycerol are performed through a hydrogen transfer reaction in which either monoalcohols or acids are used as the H donor instead of H₂.

Table 8 summarizes liquid-phase glycerol hydrogenolysis into allyl alcohol through a hydrogen transfer reaction. Arceo et al. have performed glycerol hydrogenolysis by heating a mixture of glycerol and formic acid without other additives under reflux conditions [155,156]. Formic acid works as the H donor and also as the cata-

Table 8
Liquid-phase glycerol hydrogenolysis into allyl alcohol through a hydrogen transfer reaction.

Catalyst	Temp. (°C)	Pressure (atm)	Solvent (H donor)	Glycerol/Catalyst (g/ g)	Time (h)	Yield of AA ^a (%)	Ref.
–	230–240	1	formic acid	–	3	89	[155]
MTO ^b	170	1	3-octanol	unclear	2.5	90	[157]
NaReO ₄	165	1	Glycerol	18.6	1	38	[158]

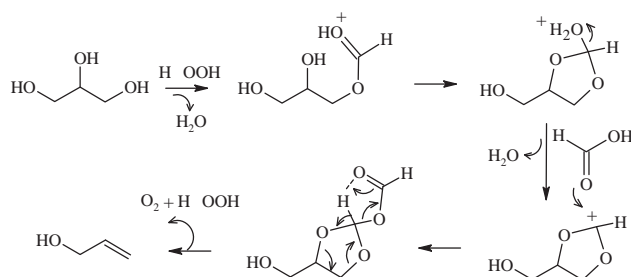
^a AA, allyl alcohol.

^b MTO, methyltrioxorhenium.

Table 9
Vapor-phase glycerol hydrogenolysis into allyl alcohol using glycerol itself as the H donor.

Catalyst	Temp. (°C)	Pressure (N ₂) (atm)	H donor	TOS (h)	WHSV (h ⁻¹)	Conversion of glycerol (%)	Selectivity to AA ^a (%)	Ref.
Fe ₂ O ₃	320	1	glycerol	6	2.5	100	23	[159]
ZrO ₂ -FeO _x	350	1	glycerol	6	1.0	100	20	[160]
K/ZrO ₂ -FeO _x	350	1	glycerol	6	0.2	100	27	[162]
Rb/FeO _x -Al ₂ O ₃	340	1	glycerol	3	0.3	89.8	13	[163]

^a AA, allyl alcohol.



Scheme 9. Mechanism for the formic acid-mediated double dehydroxylation of glycerol into allyl alcohol proposed by Arceo et al. [155].

lyst, and the proposed reaction mechanism is shown in Scheme 9. The maximum yield of allyl alcohol is 89%, which is achieved at a heating temperature of 230–240 °C. Oxorhenium-catalyzed deoxydehydration of sugars and sugar alcohols into olefins is investigated by Shiramizu et al. [157]. 3-Octanol is used as the H donor for glycerol hydrogenolysis and a 90% yield of allyl alcohol is achieved over the methyltrioxorhenium (MTO) catalyst at 170 °C. Yi et al. have also studied deoxydehydration of glycerol using oxorhenium-based catalysts, in which the reactions are performed using neat glycerol without any other additives [158]. Because a half of glycerol is consumed as the H donor and the maximum yield of allyl alcohol cannot exceed 50%. The maximum yield of allyl alcohol is 38%, which is achieved over NaReO₄ catalyst at 165 °C in the presence of NH₄Cl, and the main by-product is 1,3-dihydroxyacetone, which is formed by glycerol dehydrogenation.

Table 9 summarizes vapor-phase glycerol hydrogenolysis into allyl alcohol in N₂ atmosphere using glycerol itself as the H donor. Liu et al. have performed the reaction over Fe₂O₃ catalyst using 35 wt.% glycerol aqueous solution under N₂ flow conditions [159]. Allyl alcohol is mainly produced at a selectivity of 20–25% at 320 °C, and the selectivity to acrolein and acetol is 6–9% and 18–20%, respectively. Allyl alcohol is supposed to be produced via acrolein partial hydrogenation though a catalytic hydrogen transfer mechanism, and the intermediates with hydroxy groups together with glycerol are supposed to be the H donors. However, because the selectivity to the undetectable products is as high as ca. 40%, it is also possible that an H₂ molecule is generated *in-situ* by the catalytic reforming of glycerol. Masuda's group has conducted a series of works on glycerol conversion into useful chemicals containing allyl alcohol and propylene [152,160–162]. ZrO₂-FeO_x is firstly prepared and gives ca. 20% selectivity to allyl alcohol at 350 °C using 50% glycerol aqueous solution as a reactant [160]. Besides allyl alcohol,

many kinds of products are formed during the reaction: the selectivity to carboxylic acids (acetic acid and propionic acid), ketones (acetone and 2-butanone), and aldehydes (acrolein and acetaldehyde) is ca. 20, 10, and 10%, respectively. In a recent study, 10 wt.% crude glycerol aqueous solution is used as the reactant, and 27% yield of allyl alcohol is achieved over K-modified ZrO₂-FeO_x catalyst [152]. Because the modification of K decreases the acidic property but increases allyl alcohol yield, it is proposed that allyl alcohol is produced over non-acidic sites through a hydrogen transfer mechanism. It is also proposed that the hydrogen atoms are derived from formic acid which is formed by glycerol decomposition during the reaction. Sánchez et al. have studied glycerol conversion into allyl alcohol using alkali metal-modified FeO_x-Al₂O₃ catalysts, and 12% yield of allyl alcohol is obtained over Rb/FeO_x-Al₂O₃ at 340 °C [163]. FeO_x plays an important role for allyl alcohol formation from glycerol. Nevertheless, vapor-phase reaction over FeO_x-based catalyst systems requires a high reaction temperature, which results in many kinds of by-products. Therefore, in such a process, it is difficult to selectively produce allyl alcohol. The improvement of the catalyst system is considerable to be necessary for selective production of allyl alcohol in future studies.

Generally, the selective hydrogenation of acrolein to allyl alcohol in an H₂ atmosphere is difficult. However, some achievements have been obtained using Au- [164] and Ag-based catalysts [165–167]. An Ag-In/SiO₂ catalyst can give 61% selectivity to allyl alcohol at 97% conversion of acrolein at 240 °C under 20 atm H₂ pressure [167]. Thus, the development of combined catalysts, which contain both the proper acidity for glycerol dehydration to acrolein and the suitable hydrogenation activity for the partial hydrogenation of acrolein to allyl alcohol, is worthy to be attempted in a direct conversion of glycerol to allyl alcohol in an H₂ atmosphere instead of using H-donor molecules.

4.2. Propanols

Comparing with 2-propanol, it is easy to produce 1-propanol selectively from glycerol because 1,2-PDO, which is readily formed from glycerol, prefers to convert to 1-propanol rather than 2-propanol [168,169]. Table 10 summarizes the liquid-phase hydrogenolysis of glycerol into propanols. Xiao et al. have performed glycerol hydrogenolysis over copper chromite catalyst and studied the pathway of glycerol hydrogenolysis [170]. 1,2-PDO is the main product over copper chromite catalyst, and it is further converted into 1-propanol and 2-propanol especially at high reaction temperatures and high H₂ pressures for long reaction time. The selectivity to 1-propanol and 2-propanol is 34.9 and 0.7%,

Table 10
Hydrogenolysis of glycerol into propanols using a batch-type reactor.

Catalyst	Temp. (°C)	H ₂ pressure (atm)	Solvent	Glycerol/Catalyst (g/g)	Time (h)	Conversion of glycerol (%)	Selectivity to 1-propanol (%)	Selectivity to 2-propanol (%)	Ref.
Rh-ReO _x /SiO ₂	120	80	neat	26.7	24	100	76	15	[168]
Ru-Ir-ReO _x /SiO ₂	120	80	H ₂ O	26.7	19	100	71	15	[169]
Copper chromite	210	41	H ₂ O	20	10	49.2	34.9	0.7	[170]
Pd/C	230	80	H ₂ O	20	24	20.3	72.6	0.0	[171]
Ir/ZrO ₂	250	50	H ₂ O	Unclear	4	100	94	–	[172]

Table 11
Vapor-phase glycerol hydrogenolysis into propanols.

Catalyst	Temp. (°C)	Pressure (atm)	TOS (h)	WHSV (h ⁻¹)	Conversion of glycerol (%)	Selectivity to 1-propanol (%)	Selectivity to 2-propanol (%)	Ref.
Ni/SiO ₂	320	60	unclear	2.2	99.9	42.8	–	[173]
Pt-H ₄ SiW ₁₂ O ₄₀ /ZrO ₂	200	50	160	0.05	99.7	80.0	10.9	[175]
Zeolite + Ni/Al ₂ O ₃	220	20	0.5	1.9	100	69	–	[176]

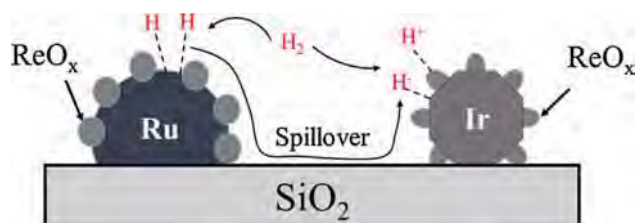


Fig. 8. Proposed catalyst and reaction model in Ref. [169].

respectively, at 210 °C and an H₂ pressure of 41 atm. Ryneveld et al. have studied supported Ru, Pd, and Pt catalysts for glycerol hydrogenolysis [171]. Pd/C shows the best catalytic performance for 1-propanol formation via 1,2-PDO as an intermediate: the selectivity to 1-propanol is 72.6% at 20.3% conversion at 230 °C. Although 1-propanol is readily dehydrated into propylene at a high temperature of 230 °C, there is no description about the analysis of gaseous products. Tomishige's group has investigated a Rh-ReO_x/SiO₂ catalyst, which is efficient for propanols formation from glycerol [168]. The selectivities to 1,2-PDO and 1,3-PDO are 30 and 15%, respectively, at 120 °C and an H₂ pressure of 8 atm at a reaction time of 5 h, and they decrease with increasing the reaction time. 1,2-PDO and 1,3-PDO are completely converted into propanols at a reaction time of 24 h, and a 76% yield of 1-propanol and a 15% yield of 2-propanol are achieved. In their recent study, Ru promoted Ir-ReO_x/SiO₂ catalyst also shows activity for propanols formation, and the maximum total yield of propanols is 86% at 120 °C and an H₂ pressure of 80 atm [169]. It is supposed that Ru can dissociate an H₂ molecule into two H species such as two H radicals, and they can spill over onto Ir-ReO_x species as shown in Fig. 8. The high activity of Ru-Ir-ReO_x/SiO₂ was proposed to attribute to the increase of the active H species on Ir-ReO_x species. Yu et al. have reported a high 1-propanol yield of 94% over Ir/ZrO₂ [172]. Ir shows the highest activity to produce 1-propanol among other metals such as Pt, Pd, Rh, and Ru, where ZrO₂ support shows better performance than other supports such as Al₂O₃, TiO₂, C, and SiO₂. The yield of 1-propanol is significantly affected by the reaction temperature, and is maximized at 250 °C over Ir/ZrO₂. Over the ZrO₂ support, the selectivity to further hydrogenolysis products such as propylene is lower than 5% even at 250 °C.

Table 11 summarizes the vapor-phase glycerol hydrogenolysis into propanols. SiO₂-supported Ni catalyst gives 42.8% yield of 1-propanol at a high temperature of 320 °C and an H₂ pressure of 60 atm, whereas even higher selectivity is difficult to be obtained because of the competitive formation of cracking products, such as

methanol and ethanol [173,174]. Pt-H₄SiW₁₂O₄₀/ZrO₂ is reported to be very efficient for the formation of propanols from glycerol: the total yield of propanols of 91% is achieved at 200 °C and an H₂ pressure of 50 atm [175]. Crude glycerol can be also used as the reactant in the catalyst system: ca. 90% yield of propanols is achieved at the same reaction conditions. The catalyst is stable and catalytic deactivation is not observed during 160 h at a relatively low WHSV of 0.05 h⁻¹. Lin et al. performed glycerol hydrogenolysis over double-layered catalysts, in which H-β zeolite is loaded at the upper layer to catalyze glycerol dehydration into acrolein and Ni/Al₂O₃ is loaded at the bottom layer to hydrogenate acrolein into 1-propanol [176]: a 69% yield of 1-propanol is obtained at 220 °C and an H₂ pressure of 20 atm at an initial TOS of 0.5 h, whereas the upper-layer catalyst is deactivated rapidly because of the coke formation caused by acrolein.

Glycerol hydrogenolysis into propanols requires an acidity in the catalyst, which must be active for dehydration of either 1,2-PDO or 1,3-PDO but inactive for further dehydration of propanols. Catalysts, such as Ir/ZrO₂ [172] and Pt-H₄SiW₁₂O₄₀/ZrO₂ [175], which give higher than 90% yields of propanols, possibly have the suitable acidity. Two-step production of 1-propanol from glycerol via acrolein has no problem in the further dehydration of propanols [176]. However, inhibition of catalyst deactivation is a difficult problem in the process.

4.3. Propylene

Propylene can be produced from glycerol multi-step hydrogenolysis via 1-propanol dehydration. Since propylene has lower market value than other products, such as propanediols and propanols, high level of propylene selectivity is required in such a process. Table 12 summarizes vapor-phase glycerol hydrogenolysis into propylene. Yu et al. firstly reported the selective production of propylene from glycerol over double-layered catalysts, in which Ir/ZrO₂ is loaded at the upper layer and HZSM-5 is loaded at the lower layer [172]. Ir/ZrO₂ is introduced to be an efficient catalyst for 1-propanol formation from glycerol in Section 4.2, and HZSM-5 is used for the further conversion of 1-propanol into propylene. High H₂ pressures are required to promote glycerol conversion in the catalyst system, while high H₂ pressures decrease the selectivity to propylene which is hydrogenated into propane. As a consequence, the maximum yield of propylene is achieved at 85% under a moderate H₂ pressure of 10 atm.

Sato's group recently reported the efficient glycerol conversion into propylene at an atmospheric H₂ pressure [177]. WO₃-modified Cu/Al₂O₃ catalyst was investigated and it gave 38.2 and 47.4% selec-

Table 12
Vapor-phase glycerol hydrogenolysis into propylene.

Catalyst	Temp. (°C)	Pressure (atm)	TOS (h)	WHSV (h ⁻¹)	Conversion of glycerol (%)	Selectivity to propylene (%)	Ref.
Ir/ZrO ₂ + HZSM-5	250	10	2	1	100	85	[172]
WO ₃ -Cu/Al ₂ O ₃ (upper) + SiO ₂ -Al ₂ O ₃ (bottom)	250	1	2–5 ^a	0.2	100	84.8	[177]

^a Averaged value in 2–5 h.

tivity to 1-propanol and propylene, respectively, with a complete conversion of glycerol at 250 °C. Although WO₃-Cu/Al₂O₃ is efficient for glycerol hydrogenolysis into 1-propanol, the ability to further convert 1-propanol into propylene as an acid catalyst is low. Thus, the reaction using double-layered catalysts, in which WO₃-Cu/Al₂O₃ is loaded at the upper layer and SiO₂-Al₂O₃ is loaded at the bottom layer to convert 1-propanol into propylene completely, is performed: an 84.8% yield of propylene is achieved over the double-layered catalysts at 250 °C at an ambient H₂ pressure. In addition, in such a multi-step dehydration-hydrogenation process, although acetol and propanal can be completely hydrogenated to 1,2-PDO and 1-propanol, respectively, no hydrogenation of propylene proceeds and the selectivity to propane is at most 1%. It is supposed that the carbonyl group in acetol and propanal is readily absorbed on the Cu surface comparing with the double bond in propylene, which results in the selective production of propylene. Zacharopoulou et al. reported a liquid-phase glycerol hydrogenolysis into propylene using Fe-Mo/C catalyst [178]. The maximum conversion and propylene selectivity are 88 and 76%, respectively, which are achieved at 300 °C and an H₂ pressure of 80 atm at a reaction time of 6 h. It is found that high reaction temperatures and H₂ pressures promote glycerol conversion toward propylene, and suppress the formation of by-products such as acetol, propanols, 1,2-PDO, and 1,3-PDO. In the reaction route of propylene formation over Fe-Mo/C, it is interesting that allyl alcohol is proved to be an intermediate of propylene, which is different from propanal reported in the vapor-phase reaction [177].

5. Concluding remarks and prospects

Glycerol is the smallest polyol readily available from biomass, and it is now produced as a large amount of waste in the biodiesel production process. Glycerol can be converted to various useful chemicals, and glycerol hydrogenolysis into C3 useful chemicals, such as 1,2-PDO, 1,3-PDO, allyl alcohol, propanols, and propylene, is particularly summarized and discussed in this review.

Glycerol conversion into 1,2-PDO is mostly investigated among the glycerol hydrogenolysis processes, and most of the studies are performed in batch-type reactors at a high H₂ pressure. Liquid-phase glycerol hydrogenolysis into 1,2-PDO can be catalyzed over various precious metal catalysts, whereas only Cu shows high selectivity toward 1,2-PDO in a vapor-phase reaction because most of the precious metals enhance the formation of the C–C cleavage products. Cu also shows the best catalyst performance in liquid-phase reactions. In the vapor phase, on the other hand, Cu metal species work as catalysts both for the dehydration of glycerol and for the hydrogenation of acetol. It is summarized that vapor-phase processes over Cu catalysts are more preferable than liquid-phase reactions in the selective formation of 1,2-PDO in glycerol hydrogenolysis. 1,2-PDO is produced with the highest yield of 98.3% in the vapor-phase reaction over Ag-Cu/Al₂O₃ catalyst under ambient H₂ pressure [77]. Because the particle size of metal significantly affects the catalytic activity, further developments of the catalyst preparation techniques for controlling the catalyst structure would be highly required. On the other hand, theoretical studies such as quantum-chemical calculations have rarely been reported to support speculative reaction mechanisms

whereas some possible reaction mechanisms have been proposed. In further studies, quantum-chemical calculations are essential to understand the exact surface reaction mechanism.

1,3-PDO is the most attractive chemical which can be derived from glycerol. Recently, research interest has been alerted from 1,2-PDO to 1,3-PDO while 1,3-PDO is much more difficult to be selectively produced. Because 3-hydroxypropanal, the intermediate of 1,3-PDO, is ready to be dehydrated into acrolein under acidic conditions before the hydrogenation of 3-hydroxypropanal proceeds to form 1,3-PDO, successful glycerol hydrogenolysis into 1,3-PDO requires a catalyst system with the ability to promote the coupled dehydration-hydrogenation reactions as well as to minimize the side reactions. The stability of 1,3-PDO under catalytic conditions is another problem limiting the selective production of 1,3-PDO from glycerol. The maximum yield of 1,3-PDO achieved from glycerol is 66% over Pt-WO_x/AlOOH catalyst [140], and how to increase the 1,3-PDO selectivity is a key of challenge in future studies.

Allyl alcohol can be generated from glycerol via 1,3-PDO dehydration and acrolein hydrogenation, whereas it is difficult to be produced selectively because it is easy to be further hydrogenated into 1-propanol under H₂ pressured conditions. As a consequence, the studies aimed to produce allyl alcohol from glycerol are performed in the absence of H₂, in which either monoalcohol or acid is used as the H donor instead of H₂. Allyl alcohol can be achieved from glycerol at ca. 90% yield in the presence of methyltrioxorhenium catalyst [157] and formic acid [155] in a liquid phase.

Propanols and propylene can also be selectively produced from glycerol via multi dehydration-hydrogenation steps. The formation of propanols from glycerol requires an acid catalyst component, which is active for the dehydration of glycerol, 1,2-PDO, and 1,3-PDO but it must be inactive for the further dehydration of propanols. Higher than 90% yields of propanols have been achieved in several reports [168,169,172,175]. A propylene yield of 84.8% is achieved in vapor-phase glycerol hydrogenolysis over WO₃-modified Cu/Al₂O₃ and SiO₂-Al₂O₃ double-layered catalysts at an ambient H₂ pressure [177].

The above-mentioned C3 chemicals are all bulk chemicals, which are commercially produced from fossil resources at present. Therefore, in glycerol hydrogenolysis processes, the atom efficiency and the productivity are very important. From this point of view, a vapor-phase continuous system using flow type reactors is preferable comparing with a batch system. Recent progress in the technologies of catalytic transformation of glycerol makes it possible to produce these chemicals from renewable resources. However, there is still an opportunity for the development of more efficient catalysts without containing precious metals. In the research of glycerol hydrogenolysis, although noble metals have been widely used as the hydrogenation catalysts, it would be unrealistic to use the noble metal-containing catalysts in industrial processes, particularly because indefinite reusability of these catalysts is not possible. Therefore, replacement of noble metals by abundant base metals is necessary for the practical usage. In the early 2016, it is a hard time for biomass-based industrial processes during the drops in the price of fossil resources. However, it is probably just a question of time until we see more processes on glycerol conversion technology in the future.

Acknowledgement

This research was partly supported by JST, Strategic International Collaborative Research Program, SICORP.

References

- [1] J.E. Rekoske, M.A. Barreau, *Ind. Eng. Chem. Res.* 50 (2011) 41–51.
- [2] A. Corma, S. Iborra, A. Velty, *Chem. Rev.* 107 (2007) 2411–2502.
- [3] C.A.G. Quispe, C.J.R. Coronado, J.A. Carvalho Jr., *Renew. Sustain. Energy Rev.* 27 (2013) 475–493.
- [4] M. Parikka, *Biomass Bioenergy* 27 (2004) 613–620.
- [5] J. ten Dam, U. Hanefeld, *ChemSusChem* 4 (2011) 1017–1034.
- [6] Y. Nakagawa, K. Tomishige, *Catal. Sci. Technol.* 1 (2011) 179–190.
- [7] B. Katryniok, S. Paul, F. Dumeignil, *ACS Catal.* 3 (2013) 1819–1834.
- [8] F. Bauer, C. Hulteberg, *Biofuels Bioprod. Biorefin.* 7 (2013) 43–51.
- [9] C.S. Callam, S.J. Singer, T.L. Lowary, C.M. Hadad, *J. Am. Chem. Soc.* 123 (2001) 11743–11754.
- [10] B. Katryniok, S. Paul, V. Belliere-Baca, P. Rey, F. Dumeignil, *Green Chem.* 12 (2010) 2079–2098.
- [11] C.H. Zhou, J.N. Beltrami, Y.X. Fan, G.Q. Lu, *Chem. Soc. Rev.* 37 (2008) 527–549.
- [12] A. Behr, J. Eilting, K. Irawadi, J. Leschinski, F. Lindner, *Green Chem.* 10 (2008) 13–30.
- [13] J. Barrault, F. Jérôme, *Eur. J. Lipid Sci. Technol.* 110 (2008) 825–830.
- [14] M. Pagliaro, R. Ciriminna, H. Kimura, M. Rossi, C.D. Pina, *Angew. Chem. Int. Ed.* 46 (2007) 4434–4440.
- [15] M. Pagliaro, M. Rossi, *The Future of Glycerol: New Uses of a Versatile Raw Material*. Royal Society of Chemistry, UK, 2008.
- [16] C.H. Zhou, H. Zhao, D.S. Tong, L.M. Wu, W.H. Yu, *Catal. Rev.* 55 (2013) 369–453.
- [17] S. Bagheri, N.M. Julkapli, W.A. Yehye, *Renew. Sustain. Energy Rev.* 41 (2015) 113–127.
- [18] B. Katryniok, S. Paul, M. Capron, F. Dumeignil, *ChemSusChem* 2 (2009) 719–730.
- [19] A. Martin, U. Armbruster, H. Atia, *Eur. J. Lipid Sci. Technol.* 114 (2012) 10–23.
- [20] L. Liu, X.P. Ye, J.J. Bozell, *ChemSusChem* 5 (2012) 1162–1180.
- [21] A. Talebian-Kiakalaie, N.A.S. Amin, H. Hezaveh, *Renew. Sustain. Energy Rev.* 40 (2014) 28–59.
- [22] J. Deleplanque, J.-L. Dubois, J.-F. Devaux, W. Ueda, *Catal. Today* 157 (2010) 351–358.
- [23] K. Omata, K. Matsumoto, T. Murayama, W. Ueda, *Chem. Lett.* 43 (2014) 435–437.
- [24] T. Katou, D. Vitry, W. Ueda, *Catal. Today* 91–92 (2004) 237–240.
- [25] W. Ueda, D. Vitry, T. Katou, *Catal. Today* 96 (2004) 205–209.
- [26] W. Ueda, D. Vitry, T. Katou, *Catal. Today* 99 (2005) 43–49.
- [27] M.D. Soriano, P. Concepción, J.M.L. Nieto, F. Cavani, S. Guidetti, C. Trevisanut, *Green Chem.* 13 (2011) 2954–2962.
- [28] A. Chieregato, F. Basile, P. Concepción, S. Guidetti, G. Liosi, M.D. Soriano, C. Trevisanut, F. Cavani, J.M.L. Nieto, *Catal. Today* 197 (2012) 58–65.
- [29] A. Chieregato, M.D. Soriano, F. Basile, G. Liosi, S. Zamora, P. Concepción, F. Cavani, J.M.L. Nieto, *Appl. Catal. B: Environ.* 150–151 (2014) 37–46.
- [30] A. Chieregato, M.D. Soriano, E. García-González, G. Puglia, F. Basile, P. Concepción, C. Bandinelli, J.M.L. Nieto, F. Cavani, *ChemSusChem* 8 (2015) 398–406.
- [31] L.G. Possato, W.H. Cassinelli, T. Garetto, S.H. Pulcinelli, C.V. Santilli, L. Martins, *Appl. Catal. A: Gen.* 492 (2015) 243–251.
- [32] C.F.M. Pestana, A.C.O. Guerra, G.B. Ferreira, C.C. Turcia, C.J.A. Mota, J. Braz, *Chem. Soc.* 24 (2013) 100–105.
- [33] L. Liu, B. Wang, Y. Du, Z. Zhong, A. Borgna, *Appl. Catal. B: Environ.* 174–175 (2015) 1–12.
- [34] A. Witsuthammakul, T. Sooknoi, *Appl. Catal. A: Gen.* 413–414 (2012) 109–116.
- [35] R. Liu, T. Wang, D. Cai, Y. Jin, *Ind. Eng. Chem. Res.* 53 (2014) 8667–8674.
- [36] S. Thanasilp, J.W. Schwank, V. Meeyoo, S. Pengpanich, M. Hunsom, *J. Mol. Catal. A: Chem.* 380 (2013) 49–56.
- [37] B. Sarkar, C. Pendem, L.N.S. Konathala, R. Tiwari, T. Sasaki, R. Bal, *Chem. Commun.* 50 (2014) 9707–9710.
- [38] B. Katryniok, H. Kimura, E. Skrzyńska, J. Girardon, P. Fongarland, M. Capron, R. Ducoulombier, N. Mimura, S. Paul, F. Dumeignil, *Green Chem.* 13 (2011) 1960–1979.
- [39] A. Villa, N. Dimitratos, C.E. Chan-Thaw, C. Hammond, L. Prati, G.J. Hutchings, *Acc. Chem. Res.* 48 (2015) 1403–1412.
- [40] Y. Shen, S. Zhang, H. Li, Y. Ren, H. Liu, *Chem. Eur. J.* 16 (2010) 7368–7371.
- [41] D. Roy, B. Subramaniam, R.V. Chaudhari, *ACS Catal.* 1 (2011) 548–551.
- [42] F. Auneau, L.S. Arani, M. Besson, L. Djakovitch, C. Michel, F. Delbecq, P. Sautet, C. Pinel, *Top. Catal.* 55 (2012) 474–479.
- [43] P. Lakshmanan, P.P. Upare, N. Le, Y.K. Hwang, D.W. Hwang, U. Lee, H.R. Kim, J. Chang, *Appl. Catal. A: Gen.* 468 (2013) 260–268.
- [44] J. Xu, H. Zhang, Y. Zhao, B. Yu, S. Chen, Y. Li, L. Hao, Z. Liu, *Green Chem.* 15 (2013) 1520–1525.
- [45] R.K.P. Purushothaman, J. van Haveren, A. Mayoral, I. Melián-Cabrera, H.J. Heeres, *Top. Catal.* 57 (2014) 1445–1453.
- [46] H.J. Cho, C. Chang, W. Fan, *Green Chem.* 16 (2014) 3428–3433.
- [47] Y. Zhang, Z. Shen, X. Zhou, M. Zhang, F. Jin, *Green Chem.* 14 (2012) 3285–3288.
- [48] H. Kishida, F. Jin, Z. Zhou, T. Moriya, H. Enomoto, *Chem. Lett.* 34 (2005) 1560–1561.
- [49] Z. Shen, F. Jin, Y. Zhang, B. Wu, A. Kishita, K. Tohji, H. Kishida, *Ind. Eng. Chem. Res.* 48 (2009) 8920–8925.
- [50] C.A. Ramírez-López, J.R. Ochoa-Gómez, M. Fernández-Santos, O. Gómez-Jiménez-Aberasturi, A. Alonso-Vicario, J. Torrecilla-Soria, *Ind. Eng. Chem. Res.* 49 (2010) 6270–6278.
- [51] T. Shimanouchi, S. Ueno, K. Shidahara, Y. Kimura, *Chem. Lett.* 43 (2014) 535–537.
- [52] L. Chen, S. Ren, X.P. Ye, *React. Kinet. Mech. Catal.* 114 (2015) 93–108.
- [53] R.K.P. Purushothaman, J. van Haveren, D.S. van Es, I. Melián-Cabrera, J.D. Meeldijk, H.J. Heeres, *Appl. Catal. B: Environ.* 147 (2014) 92–100.
- [54] Y. Li, M. Nielsen, B. Li, P.H. Dixneuf, H. Junge, M. Beller, *Green Chem.* 17 (2015) 193–198.
- [55] T. van Haasterech, T.W. van Deelen, K.P. de Jong, J.H. Bitter, *Catal. Sci. Technol.* 4 (2014) 2353–2366.
- [56] D.M. Alonso, S.G. Wettstein, J.A. Dumesic, *Chem. Soc. Rev.* 41 (2012) 8075–8098.
- [57] A.M. Ruppert, K. Weinberg, R. Palkovits, *Angew. Chem. Int. Ed.* 51 (2012) 2564–2601.
- [58] J. Ma, W. Yu, M. Wang, X. Jia, F. Lu, J. Xu, *Chin. J. Catal.* 34 (2013) 492–507.
- [59] R.V. Chaudhari, A. Torres, X. Jin, B. Subramaniam, *Ind. Eng. Chem. Res.* 52 (2013) 15226–15243.
- [60] A. Martin, U. Armbruster, I. Gandarias, P.L. Arias, *Eur. J. Lipid Sci. Technol.* 115 (2013) 9–27.
- [61] K. Tomishige, Y. Nakagawa, M. Tamura, *Top. Curr. Chem.* 353 (2014) 127–162.
- [62] M. Besson, P. Gallezot, C. Pinel, *Chem. Rev.* 114 (2014) 1827–1870.
- [63] J. Feng, B. Xu, *Prog. React. Kinet. Mech.* 39 (2014) 1–15.
- [64] C.S. Lee, M.K. Aroua, W.M.A.W. Daud, P. Cognet, Y. Pérès-Lucchese, P.-L. Fabre, O. Reynes, L. Latapie, *Renew. Sustain. Energy Rev.* 42 (2015) 963–972.
- [65] Y. Wang, J. Zhou, X. Guo, *RSC Adv.* 5 (2015) 74611–74628.
- [66] T. Miyazawa, Y. Kusunoki, K. Kunimori, K. Tomishige, *J. Catal.* 240 (2006) 213–221.
- [67] E.P. Maris, R.J. Davis, *J. Catal.* 249 (2007) 328–337.
- [68] T. Miyazawa, S. Koso, K. Kunimori, K. Tomishige, *Appl. Catal. A: Gen.* 318 (2007) 244–251.
- [69] J. Chaminand, L. Djakovitch, P. Gallezot, P. Marion, C. Pinel, C. Rosier, *Green Chem.* 6 (2004) 359–361.
- [70] C. Montassier, J.C. Menezes, L.C. Hoang, C. Renaud, J. Barbier, *J. Mol. Catal. A: Chem.* 70 (1991) 99–110.
- [71] J. Feng, J. Wang, Y. Zhou, H. Fu, H. Chen, X. Li, *Chem. Lett.* 36 (2007) 1274–1275.
- [72] A. Alhanash, E.F. Kozhevnikova, I.V. Kozhevnikov, *Appl. Catal. A: Gen.* 378 (2010) 11–18.
- [73] Y. Amada, Y. Shinmi, S. Koso, T. Kubota, Y. Nakagawa, K. Tomishige, *Appl. Catal. B: Environ.* 105 (2011) 117–127.
- [74] M. Akiyama, S. Sato, R. Takahashi, K. Inui, M. Yokota, *Appl. Catal. A: Gen.* 371 (2009) 60–66.
- [75] S. Sato, M. Akiyama, K. Inui, M. Yokota, *Chem. Lett.* 38 (2009) 560–561.
- [76] S. Sato, D. Sakai, F. Sato, Y. Yamada, *Chem. Lett.* 41 (2012) 965–966.
- [77] D. Sun, Y. Yamada, S. Sato, *Appl. Catal. A: Gen.* 475 (2014) 63–68.
- [78] S. Sato, M. Akiyama, R. Takahashi, T. Hara, K. Inui, M. Yokota, *Appl. Catal. A: Gen.* 347 (2008) 186–191.
- [79] S.R. Schmidt, S.K. Tanielyan, N. Marin, G. Alvez, R.L. Augustine, *Top. Catal.* 53 (2010) 1214–1216.
- [80] S.K. Tanielyan, N. Marin, G. Alvez, R. Bhagat, B. Miryala, R.L. Augustine, S.R. Schmidt, *Org. Process Res. Dev.* 18 (2014) 1419–1426.
- [81] I. Gandarias, P.L. Arias, J. Requies, M.B. Güemez, J.L.G. Fierro, *Appl. Catal. B: Environ.* 97 (2010) 248–256.
- [82] I. Furikado, T. Miyazawa, S. Koso, A. Shima, K. Kunimori, K. Tomishige, *Green Chem.* 9 (2007) 582–588.
- [83] A. Shima, S. Koso, N. Ueda, Y. Shinmi, I. Furikado, K. Tomishige, *Chem. Lett.* 38 (2009) 540–541.
- [84] J. Feng, W. Xiong, B. Xu, W. Jiang, J. Wang, H. Chen, *Catal. Commun.* 46 (2014) 98–102.
- [85] F. Auneau, S. Noël, G. Aubert, M. Besson, L. Djakovitch, C. Pinel, *Catal. Commun.* 16 (2011) 144–149.
- [86] N. Hamzah, N.M. Nordin, A.H.A. Nadzri, Y.A. Nik, M.B. Kassim, M.A. Yarmo, *Appl. Catal. A: Gen.* 419–420 (2012) 133–141.
- [87] S. Lee, D.J. Moon, *Catal. Today* 174 (2011) 10–16.
- [88] J. Zhou, J. Zhang, X. Guo, J. Mao, S. Zhang, *Green Chem.* 14 (2012) 156–163.
- [89] D. Sun, Y. Yamada, S. Sato, *Appl. Catal. A: Gen.* 487 (2014) 234–241.
- [90] M.A. Dasari, P. Kiatsimkul, W.R. Sutterlin, G.J. Suppes, *Appl. Catal. A: Gen.* 281 (2005) 225–231.
- [91] D. Durán-Martín, M. Ojeda, M. López Granados, J.L.G. Fierro, R. Mariscal, *Catal. Today* 210 (2013) 98–105.
- [92] M. Balaraju, V. Rekha, P.S.S. Prasad, R.B.N. Prasad, N. Lingaiah, *Catal. Lett.* 126 (2008) 119–124.
- [93] Z. Wu, Y. Mao, M. Song, X. Yin, M. Zhang, *Catal. Commun.* 32 (2013) 52–57.
- [94] P. Hirunsit, C. Luadthong, K. Faungnawakij, *RSC Adv.* 5 (2015) 11188–11197.
- [95] E.S. Vasiliadou, T.M. Eggenhuisen, P. Munnik, P.E. de Jongh, K.P. de Jong, A.A. Lemonidou, *Appl. Catal. B: Environ.* 145 (2014) 108–119.

- [96] Z. Yuan, J. Wang, L. Wang, W. Xie, P. Chen, Z. Hou, X. Zheng, *Bioresour. Technol.* 101 (2010) 7088–7092.
- [97] Z. Yuan, L. Wang, J. Wang, S. Xia, P. Chen, Z. Hou, X. Zheng, *Appl. Catal. B: Environ.* 101 (2011) 431–440.
- [98] X. Guo, Y. Li, W. Song, W. Shen, *Catal. Lett.* 141 (2011) 1458–1463.
- [99] A. Perosa, P. Tundo, *Ind. Eng. Chem. Res.* 44 (2005) 8535–8537.
- [100] Y. Li, H. Liu, L. Ma, D. He, *RSC Adv.* 4 (2014) 5503–5512.
- [101] J.B. Salazar, D.D. Falcone, H.N. Pham, A.K. Datye, F.B. Passos, R.J. Davis, *Appl. Catal. A: Gen.* 482 (2014) 137–144.
- [102] T. Jiang, Y. Zhou, S. Liang, H. Liu, B. Han, *Green Chem.* 11 (2009) 1000–1006.
- [103] J. Zhou, L. Guo, X. Guo, J. Mao, S. Zhang, *Green Chem.* 12 (2010) 1835–1843.
- [104] S. Xia, Z. Yuan, L. Wang, P. Chen, Z. Hou, *Appl. Catal. A: Gen.* 403 (2011) 173–182.
- [105] D. Stošić, S. Bennici, S. Sirotni, P. Stelmachowski, J. Couturier, J. Dubois, A. Travert, A. Auroux, *Catal. Today* 226 (2014) 167–175.
- [106] R.B. Mane, A. Yamaguchi, A. Malawadkar, M. Shirai, C.V. Rode, *RSC Adv.* 3 (2013) 16499–16508.
- [107] E. D'Hondt, S.V. de Vyver, B.F. Sels, P.A. Jacobs, *Chem. Commun.* (2008) 6011–6012.
- [108] M.L. Barbelli, G.F. Santori, N.N. Nichio, *Bioresour. Technol.* 111 (2012) 500–503.
- [109] M.G. Musolino, L.A. Scarpino, F. Mauriello, R. Pietropaolo, *Green Chem.* 11 (2009) 1511–1513.
- [110] S. Xia, L. Zheng, L. Wang, P. Chen, Z. Hou, *RSC Adv.* 3 (2013) 16569–16576.
- [111] I. Gandarias, J. Requies, P.L. Arias, U. Armbruster, A. Martin, *J. Catal.* 290 (2012) 79–89.
- [112] I. Gandarias, P.L. Arias, S.G. Fernández, J. Requies, M.E. Doukkali, M.B. Güemez, *Catal. Today* 195 (2012) 22–31.
- [113] I. Gandarias, S.G. Fernandez, M.E. Doukkali, J. Requies, P.L. Arias, *Top. Catal.* 56 (2013) 995–1007.
- [114] F. Mauriello, H. Ariga, M.G. Musolino, R. Pietropaolo, S. Takakusagi, K. Asakura, *Appl. Catal. B: Environ.* 166–167 (2015) 121–131.
- [115] E.S. Vasiliadou, V.-L. Yfanti, A.A. Lemonidou, *Appl. Catal. B: Environ.* 163 (2015) 258–266.
- [116] C. Montassier, D. Giraud, J. Barbier, *J. Stud. Surf. Sci. Catal.* 41 (1988) 165–170.
- [117] C.W. Chiu, A. Tekeei, W.R. Sutterlin, J.M. Ronco, G.J. Suppes, *AIChE J.* 54 (2008) 2456–2463.
- [118] C.W. Chiu, A. Tekeei, J.M. Ronco, M.L. Banks, G.J. Suppes, *Ind. Eng. Chem. Res.* 47 (2008) 6878–6884.
- [119] A. Bienholz, H. Hofmann, P. Claus, *Appl. Catal. A: Gen.* 391 (2011) 153–157.
- [120] S. Zhu, X. Gao, Y. Zhu, Y. Zhu, H. Zheng, Y. Li, *J. Catal.* 303 (2013) 70–79.
- [121] S. Zhu, X. Gao, Y. Zhu, W. Fan, J. Wang, Y. Li, *Catal. Sci. Technol.* 5 (2015) 1169–1180.
- [122] S. Zhu, X. Gao, Y. Zhu, Y. Li, *Green Chem.* 18 (2016) 782–791.
- [123] S. Sato, R. Takahashi, T. Sodesawa, H. Fukuda, T. Sekine, E. Tsukuda, *Catal. Commun.* 6 (2005) 607–610.
- [124] L. Huang, Y. Zhu, H. Zheng, Y. Li, Z. Zeng, *J. Chem. Technol. Biotechnol.* 83 (2008) 1670–1675.
- [125] S. Panyad, S. Jongpatiwut, T. Sreethawong, T. Rirksomboon, S. Osuwan, *Catal. Today* 174 (2011) 59–64.
- [126] T. Li, C. Fu, J. Qi, J. Pan, S. Chen, J. Lin, *React. Kinet. Mech. Catal.* 109 (2013) 117–131.
- [127] M. Harisekhar, V.P. Kumar, S.S. Priya, K.V.R. Chary, *Chem. Technol. Biotechnol.* 90 (2015) 1906–1917.
- [128] G.D. Yadav, P.A. Chandan, D.P. Tekale, *Ind. Eng. Chem. Res.* 51 (2012) 1549–1562.
- [129] P.K. Vanama, A. Kumar, S.R. Ginjupalli, V.R.C. Komandur, *Catal. Today* 250 (2015) 226–238.
- [130] G.A. Kraus, *Clean* 36 (2008) 648–651.
- [131] Y. Nakagawa, Y. Shinmi, S. Koso, K. Tomishige, *J. Catal.* 272 (2010) 191–194.
- [132] Y. Shinmi, S. Koso, T. Kubota, Y. Nakagawa, K. Tomishige, *Appl. Catal. B: Environ.* 94 (2010) 318–326.
- [133] Y. Nakagawa, X. Ning, Y. Amada, K. Tomishige, *Appl. Catal. A: Gen.* 433–434 (2012) 128–134.
- [134] Y. Nakagawa, M. Tamura, K. Tomishige, *J. Mater. Chem. A* 2 (2014) 6688–6702.
- [135] C. Deng, X. Duan, J. Zhou, X. Zhou, W. Yuan, S.L. Scott, *Catal. Sci. Technol.* 5 (2015) 1540–1547.
- [136] T. Kurosaka, H. Maruyama, I. Naribayashi, Y. Sasaki, *Catal. Commun.* 9 (2008) 1360–1363.
- [137] L. Gong, Y. Lu, Y. Ding, R. Lin, J. Li, W. Dong, T. Wang, W. Chen, *Appl. Catal. A: Gen.* 390 (2010) 119–126.
- [138] Y. Zhang, X. Zhao, Y. Wang, L. Zhou, J. Zhang, J. Wang, A. Wang, T. Zhang, *J. Mater. Chem. A* 1 (2013) 3724–3732.
- [139] T. Mizugaki, T. Yamakawa, R. Arundhathi, T. Mitsudome, K. Jitsukawa, K. Kaneda, *Chem. Lett.* 41 (2012) 1720–1722.
- [140] R. Arundhathi, T. Mizugaki, T. Mitsudome, K. Jitsukawa, K. Kaneda, *ChemSusChem* 6 (2013) 1345–1347.
- [141] J. ten Dam, K. Djanashvili, F. Kaptejin, U. Hanefeld, *ChemCatChem* 5 (2013) 497–505.
- [142] S. García-Fernández, I. Gandarias, J. Requies, M.B. Güemez, S. Bennici, A. Auroux, P.L. Arias, *J. Catal.* 323 (2015) 65–75.
- [143] J. Oh, S. Dash, H. Lee, *Green Chem.* 13 (2011) 2004–2007.
- [144] L. Huang, Y. Zhu, H. Zheng, G. Ding, Y. Li, *Catal. Lett.* 131 (2009) 312–320.
- [145] L. Qin, M. Song, C. Chen, *Green Chem.* 12 (2010) 1466–1472.
- [146] S. Zhu, X. Gao, Y. Zhu, J. Cui, H. Zheng, Y. Li, *Appl. Catal. B: Environ.* 158–159 (2014) 391–399.
- [147] S. Zhu, Y. Qiu, Y. Zhu, S. Hao, H. Zheng, Y. Li, *Catal. Today* 212 (2013) 120–126.
- [148] S. Zhu, X. Gao, Y. Zhu, X. Xiang, C. Hu, Y. Lia, *Appl. Catal. B: Environ.* 140–141 (2013) 60–67.
- [149] S. Zhu, X. Gao, Y. Zhu, Y. Li, *J. Mol. Catal. A: Chem.* 398 (2015) 391–398.
- [150] S.S. Priya, V.P. Kumar, M.L. Kantam, S.K. Bhargava, K.V.R. Chary, *RSC Adv.* 4 (2014) 51893–51903.
- [151] S.S. Priya, V.P. Kumar, M.L. Kantam, S.K. Bhargava, K.V.R. Chary, *Catal. Lett.* 144 (2014) 2129–2143.
- [152] A. Konaka, T. Tago, T. Yoshikawa, A. Nakamura, T. Masuda, *Appl. Catal. B: Environ.* 146 (2014) 267–273.
- [153] K. Mori, Y. Yamada, S. Sato, *Appl. Catal. A: Gen.* 366 (2009) 304–308.
- [154] D. Sun, R. Narita, F. Sato, Y. Yamada, S. Sato, *Chem. Lett.* 43 (2014) 450–452.
- [155] E. Arceo, P. Marsden, R.G. Bergman, J.A. Ellman, *Chem. Commun.* (2009) 3357–3359.
- [156] E. Arceo, J.A. Ellman, R.G. Bergman, *ChemSusChem* 3 (2010) 811–813.
- [157] M. Shiramizu, F.D. Toste, *Angew. Chem. Int. Ed.* 51 (2012) 8082–8086.
- [158] J. Yi, S. Liu, M.M. Abu-Omar, *ChemSusChem* 5 (2012) 1401–1404.
- [159] Y. Liu, H. Tüysüz, C. Jia, M. Schwickardi, R. Rinaldi, A. Lu, W. Schmidt, F. Schüh, *Chem. Commun.* 46 (2010) 1238–1240.
- [160] T. Yoshikawa, T. Tago, A. Nakamura, A. Konaka, M. Mukaida, T. Masuda, *Res. Chem. Intermed.* 37 (2011) 1247–1256.
- [161] A. Konaka, T. Tago, T. Yoshikawa, H. Shitara, Y. Nakasaka, T. Masuda, *Ind. Eng. Chem. Res.* 52 (2013) 15509–15515.
- [162] T. Tago, Y. Nakasaka, T. Masuda, *J. Jpn. Pet. Inst.* 57 (2014) 197–207.
- [163] G. Sánchez, J. Friggieri, C. Keast, M. Drewery, B.Z. Dlugogorski, E. Kennedy, M. Stockenhuber, *Appl. Catal. B: Environ.* 152–153 (2014) 117–128.
- [164] C. Mohr, H. Hofmeister, J. Radnik, P. Claus, *J. Am. Chem. Soc.* 125 (2003) 1905–1911.
- [165] C.E. Volckmar, M. Brona, U. Bentrup, A. Martin, P. Claus, *J. Catal.* 261 (2009) 1–8.
- [166] H. Wei, C. Gomez, J. Liu, N. Guo, T. Wu, R. Lobo-Lapidus, C.L. Marshall, J.T. Miller, R.J. Meyer, *J. Catal.* 298 (2013) 18–26.
- [167] M. Lucas, P. Claus, *Chem. Eng. Technol.* 28 (2005) 867–870.
- [168] Y. Amada, S. Koso, Y. Nakagawa, K. Tomishige, *ChemSusChem* 3 (2010) 728–736.
- [169] M. Tamura, Y. Amada, S. Liu, Z. Yuan, Y. Nakagawa, K. Tomishige, *J. Mol. Catal. A: Chem.* 388–389 (2014) 177–187.
- [170] Z. Xiao, C. Li, J. Xiu, X. Wang, C.T. Williams, C. Liang, *J. Mol. Catal. A: Chem.* 365 (2012) 24–31.
- [171] E. van Ryneveld, A.S. Mahomed, P.S. van Heerden, H.B. Friedrich, *Catal. Lett.* 141 (2011) 958–967.
- [172] L. Yu, J. Yuan, Q. Zhang, Y. Liu, H. He, K. Fan, Y. Cao, *ChemSusChem* 7 (2014) 743–747.
- [173] E. van Ryneveld, A.S. Mahomed, P.S. van Heerden, M.J. Green, H.B. Friedrich, *Green Chem.* 13 (2011) 1819–1827.
- [174] E. van Ryneveld, A.S. Mahomed, P.S. van Heerden, M.J. Green, C. Holzapfel, H.B. Friedrich, *Catal. Sci. Technol.* 4 (2014) 832–837.
- [175] S. Zhu, Y. Zhu, S. Hao, H. Zheng, T. Mo, Y. Li, *Green Chem.* 14 (2012) 2607–2616.
- [176] X. Lin, Y. Lv, Y. Xi, Y. Qu, D.L. Phillips, C. Liu, *Energy Fuels* 28 (2014) 3345–3351.
- [177] D. Sun, Y. Yamada, S. Sato, *Appl. Catal. B: Environ.* 174 (2015) 13–20.
- [178] Y. Zacharopoulou, E.S. Vasiliadou, A.A. Lemonidou, *Green Chem.* 17 (2015) 903–912.



Cite this: *Green Chem.*, 2016, **18**, 2579

Production of C4 and C5 alcohols from biomass-derived materials

Daolai Sun,^a Satoshi Sato,^{*a} Wataru Ueda,^b Ana Primo,^c Hermenegildo Garcia^c and Avelino Corma^{*c}

C4 and C5 diols and alcohols are important commodity chemicals mainly used as monomers in the production of polyesters, polyurethanes and polyethers. C4 and C5, on the other hand, can be used in the fuel industry for the preparation of additives to boost the gasoline octane number. The present critical review covers those reports describing the obtainment of these diols and alcohols from precursors derived from biomass. Emphasis is made on the description of the catalysts required for these transformations and on common traits referring to the bifunctionality combining hydrogenation activity and acidity and on the mechanistic proposals. The need for finding a suitable replacement for noble metals on the composition of these catalysts has been remarked throughout the review.

Received 8th February 2016,
Accepted 22nd March 2016

DOI: 10.1039/c6gc00377j

www.rsc.org/greenchem

1. Introduction

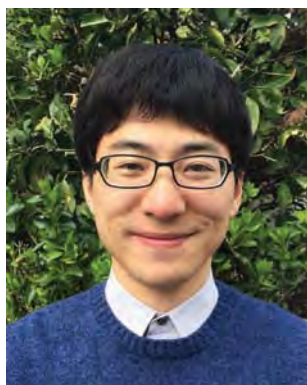
Biomass is an important renewable resource that is increasingly contributing to satisfy the total demand on materials, energy and chemicals. Particularly in the field of energy, the percentage of transportation fuel derived from biomass, replacing in part fossil fuels, is growing in developed countries.¹

The use of biomass as fuel is, however, an application of low added value compared to the potential of biomass as a provider of chemicals for industry.² The variety and complexity of the chemical structures found in biomass components allow the development of novel processes aimed at supplying the necessary raw materials to the chemical industry. The shift from oil and natural gas to biomass as feedstock for chemicals should contribute to sustainability, while at the same time should reduce the CO₂ footprint of some processes. In this revolutionary change from an oil- to biomass-based chemical industry, one of the most attractive strategies is to obtain from biomass some of the bulk and commodity chemicals that are currently obtained from oil and natural gas and that play key

^aGraduate School of Engineering, Chiba University, Chiba, 263-8522, Japan. Fax: +81 43 290 3401; Tel: +81 43 290 3376

^bInstitute of Chemical Technology, Technical University of Valencia, Av. De los Naranjos s/n, 46022 Valencia, Spain. E-mail: acorma@itq.upv.es

^cEngineering Department of Material and Life Chemistry, Kanagawa University, Japan



Daolai Sun

Daolai Sun is now a research associate in the Department of Applied Chemistry and Biotechnology in Chiba University, Japan. He received his B.Eng. from Nanjing University of Science and Technology (2004–2008) and M.Eng. from Chiba University (2010–2012). He also received his PhD from Chiba University in September 2014. Currently, his researches focus on the catalytic transformation of biomass resources into valuable

chemicals, such as conversion of levulinic acid to lactones and 1,4-pentanediol.



Satoshi Sato

Satoshi Sato studied synthetic chemistry at Nagoya University (1979–1986) and received his Dr. Eng. in 1992. He joined Industrial Chemistry Department of Chiba University as Research Associate in 1986, becoming Lecturer in 1992, Associate Professor in 1997, and Professor in 2006 in the same university. Currently, he is the vice president of Chiba University. His research interests include application of heterogeneous catalysts and inhibition

of catalyst deactivation for catalytic conversion of chemicals, especially in the vapor phase.

roles as synthetic intermediates for the preparation of a variety of commodity compounds, fine chemicals or polymers. This strategy will allow maintaining most of the current processes in the chemical industry, by just replacing the origin of the precursors.

In this context of preparation from biomass of currently important chemicals, alcohols and diols of short alkyl chain are of increasing importance due to their use as monomers in polyesters and the potential use of C4 and C5 alcohols as gasoline additives, as potential fuels, as solvents and for a variety of other uses. The present review is focused on the preparation of C4 and C5 diols and mono alcohols from biomass. Although there are several reviews summarizing the state of the art in the preparation of chemicals from biomass in the literature,^{2–4} the field is developing at a fast pace and is sufficiently broad to focus on a review in specific types of compounds and provide an overview of the existing production processes and precursors, making special emphasis on the recent developments and the gaps to be filled.

2. Aim and scope of the review

This review describes the current state of the art in the production of C4 and C5 alcohols, both mono and diols, from biomass-derived feedstocks and covers the literature up to the end of 2015. It has been organized by presenting, separately, the preparation of C4 and C5 diols and monoalcohols, grouped in each case according the starting material. The emphasis of the review is on the characterization and performance of the catalysts. As shown below, all the preparation methods are based on hydrogenation or hydrogenolysis of biomass precursors and, therefore, the processes employ catalysts with hydrogenation activity, frequently combined with components that introduce some acidity and result in a synergistic effect. A clear distinction of those processes that have been performed under batch conditions from those that have

been conducted under a continuous flow has been made throughout the review.

The final section of this review summarizes the main achievements, indicating the existing gaps with respect to catalyst development and providing our view on future targets in this regard.

3. Conversion of succinic acid and its derivatives

Succinic acid is a precursor of some specialized polyesters and a component of some alkyl resins, and it is also widely used in the food and beverage industry, primarily as an acidity regulator.⁵ Succinic acid, its anhydride, and its esters are primary products by hydrogenation of maleate obtained from maleic anhydride that is currently mostly produced from butane.² In recent years, the efficient production of succinic acid from biomass has attracted considerable attention. Succinic acid can be produced through the fermentation of glucose,^{2,6} and also can be obtained by catalytic transformation from furfural, which can be produced from agricultural raw materials rich in pentose polymers by acid degradation.^{2,4} Many important chemicals, such as γ -butyrolactone, tetrahydrofuran (THF), 1,4-butanediol, *N*-methyl-2-pyrrolidone, and 2-pyrrolidone, can be derived from succinic acid.^{5,7} The economic and environmental analyses of a biorefinery producing succinic acid indicate that bio-derived succinic acid would become a promising intermediate, particularly for the synthesis of C4 alcohols.

3.1 Production of C4 alcohols from succinic acid

Useful C4 alcohols, such as 1,4-butanediol and 1-butanol, can be derived through succinic acid hydrogenation and hydrogenolysis. 1,4-Butanediol is the most attractive chemical in the series of succinic acid derivatives because of its global use in the polymer industry. As shown below, the current state of the



Wataru Ueda

Professor Wataru Ueda is a solid-state catalyst chemist. His main research interests are in catalytic selective oxidation of light alkanes over solid catalysts having controlled structures and developments of new solid-state catalysts for conversion of biomass-derived materials into chemicals. He is currently the representative of the EU(ERC)-Japan(JST) joint project on Novel cheap and Abundant materials for Catalytic bio-Mass conversion (NOVACAM).



Ana Primo

Ana Primo obtained her PhD from the Institute of Chemical Technology (ITQ) in Valencia, Spain, under the guidance of Avelino Corma and Hermenegildo García. She was a postdoctoral researcher in the Institut Charles Gerhardt of Montpellier (France, 2007–2009). She is currently a Ramón y Cajal researcher at the ITQ, where she works on the synthesis of heterogeneous catalysts based on metal nanoparticles supported on

porous polysaccharides, graphenes and metal oxides for their application in biomass and photochemistry. She has co-authored 50 publications.

art is based on the use of noble or critical metals to promote hydrogenation of succinic acid and, therefore, the finding of alternative catalysts based on abundant and affordable metals will be very important. It should be noted that one of the main prerequisites of the catalyst is to be water tolerant, since water is the most convenient solvent for this reaction considering succinic acid solubility.

1,4-Butanediol is a starting material for the production of important polymers such as polyesters, polyurethanes, and polyethers. A major 1,4-butanediol-based polymer is polybutylene terephthalate, which is mainly used for engineering plastics, fibers, and films. Furthermore, 1,4-butanediol is also the feedstock of THF production.

In an early report, Carnahan *et al.* studied hydrogenation of acids to alcohols over Ru-based catalysts.⁸ The total yield of 1,4-butanediol, 1-propanol and 1-butanol was 59% in the hydrogenation of succinic acid over the RuO₂ catalyst at a temperature of 152–192 °C under an H₂ pressure of 72–95 MPa. In US patents, Schwartz prepared Pd–Re/C catalysts for hydrogenolysis of succinic acid into useful chemicals such as γ -butyrolactone, 1,4-butanediol, and THF.^{9,10} 1 wt% Pd–4 wt% Re/C catalysts show the best catalytic performance for the formation of alcohols, and the selectivities to 1,4-butanediol, 1-propanol and 1-butanol are 34, 8 and 13%, respectively, with a succinic acid conversion of 92% at 250 °C under 8.3 MPa H₂ pressure. It is clear that to be useful, selectivity to a single alcohol should be notably increased. Deshpande *et al.* studied the hydrogenolysis of succinic acid using Ru–Co catalysts, in which the existence of Ru metal, Co metal, carbonates, CoO and Ru₂O₃ is confirmed by XRD analysis.¹¹ The presence of all these species on the catalyst makes it difficult to determine

the nature of the active sites, being convenient to evaluate the catalytic activity of better defined samples. They investigated the changes of the concentration of each product with the reaction time using the Ru–Co catalyst at 250 °C under a H₂ pressure of 10.35 MPa. γ -Butyrolactone is the only product in the initial 1 h of reaction and after that the concentration of γ -butyrolactone decreases steeply with increasing reaction time together with the formation of THF. The maximum selectivity to 1,4-butanediol and THF is *ca.* 50% and 60%, respectively. The concentration of 1-butanol and 1-propanol slightly increases with increasing reaction time, and the selectivity is *ca.* 25% and 12% at 6 h, respectively. They proposed a reaction route as shown in Scheme 1. Although the mechanistic proposal is in general terms reasonable and γ -butyrolactone is the most likely primary product, another possibility that was not considered is THF formation by cyclodehydration of 1,4-butanediol. In addition, 1-propanol may result directly from 1,4-butanediol, besides through 1-butanol.

Table 1 summarizes recent studies on the synthesis of 1,4-butanediol from succinic acid, where all the reactions are performed in the liquid phase under H₂ pressure. Luque *et al.* studied the hydrogenation of succinic acid over various Starbon®-supported precious metal catalysts. Starbon® is a commercial porous carbon material obtained by pyrolysis of expanded starch.¹² Among the tested metal/C catalysts, Rh/C and Pt/C showed high activity for the formation of 1,4-butanediol, whereas Ru/C prefers the formation of THF. The maximum 1,4-butanediol selectivity was 90% over Rh/C at a succinic acid conversion of 60%. Chung *et al.* prepared MCM-41- and SBA-15-supported Pd catalysts for the hydrogenation of succinic acid.¹³ Pd particles are located on the exterior



Hermenegildo García

Hermenegildo García is full Professor at the Instituto de Tecnología química of the Technical University of Valencia, a joint center of the Technical University of Valencia and the Spanish National Research Council and Honorary Adjunct Professor at the Center of Excellence in Advanced Materials Research of King Abdullah University. Prof. García has been active in the field of heterogeneous catalysis working with porous catalysts

and nanoparticles, has published over 600 papers and has filed over 25 patents. Prof. García is Doctor Honoris Causa from the University of Bucharest and the recipient of the 2011 Janssen-Cilag award given by the Spanish Royal Society of Chemistry and the 2008 Alpha Gold of the Spanish Society of Glass and Ceramics.



Avelino Corma

Avelino Corma, Professor at the Instituto de Tecnología Química (CSIC-UPV), has been carrying out research on heterogeneous catalysis in academia and in collaboration with companies for nearly 30 years. He has published more than 900 research papers, and is an inventor on more than 130 patents. He has received the M. Boudart Award on Catalysis from the North American and European Catalysis Societies, the G. J. Somorjai ACS Award on

Creative Catalysis, the Breck Award of the International Zeolite Association, the National Award of Science and Technology of Spain, "Rey Jaume I" Prize for New Technologies (2000), the ENI Award on Hydrocarbon Chemistry, the Royal Society of Chemistry Centenary Prize, Solvay Pierre-Gilles de Gennes Prize for Science and Industry and Gold Medal for the Chemistry Research Career 2001–2010 in Spain, La Grande Médaille de l'Académie des sciences de France 2011 and Prince of Asturias Award for Science & Technology 2014.

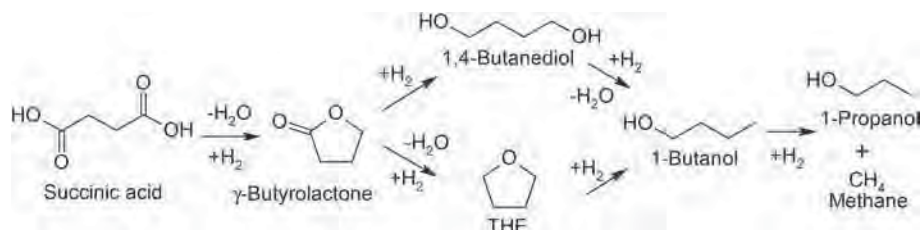
Scheme 1 Reaction routes of succinic acid hydrogenolysis.¹¹

Table 1 Liquid-phase synthesis of 1,4-butanediol (BDO) from succinic acid (SA)

Catalyst	Temp. (°C)	H ₂ pres. (MPa)	Time (h)	Solvent	SA/catalyst (g/g)	SA conv. (%)	BDO select. (%)	Ref.
Rh/Starbon®	100	1	24	H ₂ O + ethanol	11.8	60	90	12
Pt/Starbon®	100	1	24	H ₂ O + ethanol	11.8	78	85	12
Pd/MCM-41	250	10	8	H ₂ O + ethanol	1.8	60	53	13
Pd-FeO _x /C	200	5	50	H ₂ O	2.2	100	70	14
Re-Pd/C	160	15	77	H ₂ O	15	100	66	15
Re-Ru/C	160	15	51	H ₂ O	15	100	62	15
Re-Pd/TiO ₂	160	15	48	H ₂ O	5	100	83	16
Re-Ru/C	200	8	7	1,4-Dioxane	2.5	100	71.2	20

of the pore channels of MCM-41, while due to its larger pore size, they are encapsulated inside of the channels of SBA-15. Pd/MCM-41 with a large Pd particle size of 9.4 nm shows relatively low succinic acid conversion, but high 1,4-butanediol selectivity, whereas Pd/SBA-15 with a small Pd size prefers the production of γ -butyrolactone and THF from succinic acid. Thus, a maximum selectivity to 1,4-butanediol of 53% at a succinic acid conversion of 60% was achieved over Pd/MCM-41 at 250 °C and 10 MPa H₂ pressure. A series of Pd-FeO_x/C catalysts were prepared by Liu *et al.* for succinic acid hydrogenation to 1,4-butanediol. The introduction of Fe was proposed to increase the Lewis acid sites of the catalysts, which was beneficial due to a better dehydration activity, and enhanced the dispersion of Pd particles on the support. In this way a 70% yield of 1,4-butanediol was obtained over Pd-FeO_x/C at 200 °C under 5 MPa H₂ pressure.¹⁴

The group of Besson and Pinel performed a series of studies on the hydrogenation of succinic acid into 1,4-butanediol over Re-modified precious metal catalysts.^{15–19} They found that carbon-supported monometallic catalysts are effective for the conversion of succinic acid into γ -butyrolactone, but not for further hydrogenation into 1,4-butanediol. In contrast, Re as an additive promotes the formation of 1,4-butanediol from γ -butyrolactone, achieving *ca.* 65% selectivity to 1,4-butanediol over bimetallic catalysts such as Re-Pd/C and Re-Ru/C.¹⁵ They also compared the reactivity of succinic acid with that of levulinic acid over the Re-Pd/C and Re-Ru/C catalysts.¹⁷ The reactivity of succinic acid is much lower than that of levulinic acid, and a longer reaction time is required to achieve high 1,4-butanediol yields from succinic acid. Among the Re-modified bimetallic catalysts, the highest selectivity to 1,4-butanediol was 83% over Re-Pd/TiO₂.¹⁶ The ReO_x species, which interact with

Pd in this bimetallic catalyst, were deposited following different methods that lead to different spatial Re locations in the material.¹⁹ The catalytic reduction method induced a selective Re deposition on the Pd interface as compared to a random Re distribution obtained by successive impregnation. It was found that random Re distribution results in a higher activity for 1,4-butanediol formation.¹⁸ In a recent report, Song *et al.* studied the activity of the Re-Ru/C bimetallic catalyst for succinic acid hydrogenation. Re-Ru/C was prepared by a single-step surfactant-templating method and subsequent incipient wetness impregnation varying the Ru loading. The Ru and Re content in the catalyst significantly affects the catalytic activity of the material. The catalyst with both Ru and Re loading of 0.3% mol showed the best catalytic performance for 1,4-butanediol formation, achieving a selectivity to 1,4-butanediol of 71.2% at complete conversion working at 200 °C and 8 MPa H₂ pressure.²⁰

As described above, a precious metal is indispensable for the hydrogenation of succinic acid into 1,4-butanediol. The addition of Re into a supported mono-metallic catalyst seems to be effective for promoting the further formation of 1,4-butanediol from an intermediate of γ -butyrolactone. As far as we know, the effects of the reaction conditions on the hydrogenation of succinic acid into 1,4-butanediol are not deeply studied. In the hydrogenation of levulinic acid into 1,4-pentanediol,¹⁷ the successive formation of 2-methyltetrahydrofuran, 1-pentanol, and 2-pentanol has been, however, determined to occur at a high temperature. Therefore, it is reasonable to assume that the selective formation of 1,4-butanediol from succinic acid would also prefer a low reaction temperature and high H₂ pressure, although this assumption is still to be confirmed experimentally.

3.2 Production of C4 alcohols from dialkyl succinates

Because succinic acid reacts with alcohols in the presence of acid catalysts to form dialkyl succinates,² succinic esters can also be starting materials of C4 alcohols. The use of succinic esters as substrates overcomes the low solubility of succinic acid in many solvents other than water and enables amenable gas phase hydrogenation. The use of organic solvents can influence catalyst stability positively and decrease the extent of metal leaching that is a common deactivation mechanism. Therefore, it is not totally unexpected that the most common catalysts for hydrogenation of dialkyl succinates contain copper. The production of 1,4-butanediol has been mainly studied starting from dimethyl and diethyl succinates as a feedstock. The investigations of dialkyl succinate hydrogenolysis are summarized in Tables 2 and 3. In an early patent, vapor-phase hydrogenolysis of diethyl succinate was performed over the Cu/CrBaMnO catalyst, in which the weight percentage of Cu, Cr, Ba and Mn was 27.7, 29.7, 2.0 and 4.4%, respectively. The selectivity to 1,4-butanediol achieved *ca.* 85% at a conversion higher than 95% at 180 °C under 6.4 MPa H₂ pressure.²¹ Ding *et al.* reported vapor-phase hydrogenolysis of diethyl succinate into useful chemicals using Cu/ZnO catalysts.^{22,23} It was observed that the selectivity to γ -butyrolactone is as high as 49.2% at a low residence time of 0.5 s, and it decreases upon increasing the residence time because γ -butyrolactone is further hydrogenated into 1,4-butanediol at long residence times. In this way, the selectivity to 1,4-butanediol is maximized at 86.1% at a residence time of 1.8 s at 170 °C under 4 MPa H₂ pressure (Table 2). At temperatures lower than 170 °C, the product 1,4-butanediol reacts with diethyl succinate to form ethyl 4-hydroxybutyl succinate, causing an apparent decrease of 1,4-butanediol selectivity. Monoalcohols such as 1-butanol and 1-propanol are also generated *via* 1,4-butanediol, but with a total selectivity lower than 2%. In addition, over the Cu/ZnO catalyst mixed with zeolite, the presence of

strong acid sites promotes further dehydration of 1,4-butanediol into THF, making it possible to achieve a THF yield higher than 98% at 260 °C and 4 MPa H₂ pressure.

Liquid-phase hydrogenolysis of dimethyl succinate using a commercial copper chromite catalyst was reported in an early patent. Using this catalyst the reaction is performed at a dimethyl succinate/catalyst weight ratio of 10 in methanol as the solvent, attaining 57.4% selectivity to 1,4-butanediol at a conversion of 38.7% at 200 °C under 12.4 MPa H₂ pressure for 6.5 h.²⁴ The use of copper chromite as a solid hydrogenation catalyst has several advantages with respect to other alternatives including a lower sensitivity to the presence of sulfur or halogen in the feed, the need for lower quantities, the catalyst does not need to be freshly prepared and can be used repeatedly due to its low tendency to deactivate. The major drawbacks of copper chromite are the toxicity of Cr species, the need for high hydrogen pressures and, frequently, the low product selectivity. Although, as reported in the previous section, precious metals catalyze the direct hydrogenolysis of succinic acid into 1,4-butanediol; Cu-based catalysts are efficient for the hydrogenolysis of dialkyl succinates into 1,4-butanediol. Song *et al.* developed a liquid-phase process for hydrogenolysis of succinic acid into 1,4-butanediol using Cu-based catalysts, in which methanol is used as the solvent, reacting first with succinic acid to produce dimethyl succinate that is subsequently hydrogenated slowly into 1,4-butanediol over Cu catalysts.^{25–27} They focused on mesoporous carbon-supported Cu and Re–Cu bimetallic catalysts prepared by different methods. Thus, one of the catalysts, Re/15.9% Cu–C (Table 3), was prepared through two steps: the first one was the preparation of the Cu–C catalyst by a surfactant-templating method, and the second step was the addition of Re into Cu–C through an impregnation method.²⁶ Other catalyst, Re–20% Cu/C (Table 3), was prepared by a single-step surfactant-templating method. The latter gives a relatively higher 1,4-butanediol selectivity of 22.5% than the former at 200 °C under 8 MPa H₂ pressure. The Cu metal was found to be highly dispersed on the surface of carbon in Re–20%Cu/C, this fine dispersion being one important factor to reach high selectivity in the formation of γ -butyrolactone and 1,4-butanediol.²⁷ Succinic acid is converted completely to dimethyl succinate that remains as such in *ca.* 50–60 mol% of the final reaction mixture. Apparently the Cu catalyst is not able to convert dimethyl succinate completely into 1,4-butanediol. Thus, a catalytic system active for both succinic acid conversion into dialkyl succinate and the subsequent complete hydrogenolysis into 1,4-butanediol, is still to be developed.

Hydrogenolysis of dimethyl succinate was also performed using a homogeneous catalyst by Li *et al.*²⁸ Ru complexes of tetradentate bipyridine ligands (see structure in Scheme 2) are extremely effective for the hydrogenolysis of carboxylic esters and lactones into the corresponding diols. A 99% yield of 1,4-butanediol is achieved in 6 h from dimethyl succinate at a temperature as low as 25 °C, and H₂ pressure of 5 MPa, and a dimethyl succinate/catalyst molar ratio of 1000. Considering the high activity of this Ru bipyridyl complex it could be con-

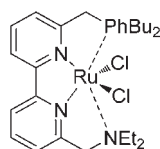
Table 2 Vapor-phase synthesis of 1,4-butanediol (BDO) from pure diethyl succinate (DES) as the reactant

Catalyst	Temp. (°C)	H ₂ pres. (MPa)	WHSV (h ⁻¹)	DES conv. (%)	BDO select. (%)	Ref.
Cu/CrBaMnO	180	6.4	0.3	98.1	84.9	21
Cu/ZnO	170	4	1.8 ^a	100	86.1	22

^aThe value corresponds to the residence time.

Table 3 Liquid-phase synthesis of 1,4-butanediol (BDO) from succinic acid (SA) and methanol. Reaction conditions: SA/catalyst wt ratio 2.5, solvent 1,4-dioxane; temperature 200 °C, H₂ pressure 8 MPa, reaction time 20 h

Catalyst	SA conversion (%)	BDO selectivity (%)	Ref.
Re/15.9%Cu–C	100	11.3	26
Re–20%Cu/C	100	22.5	27



Scheme 2 Chemical structure of a tetradentate Ru bipyridyl complex used as a homogeneous catalyst for the hydrogenolysis of dimethyl succinate.

venient to determine if its immobilization on a solid support could convert the system from a homogeneous to heterogeneous and reusable catalyst.

3.3 Production of C4 alcohols from γ -butyrolactone

γ -Butyrolactone is an important solvent consumed in large amounts that can also be used as an intermediate for the synthesis of agrochemicals and pharmaceuticals. γ -Butyrolactone can be produced from the hydrogenation of maleic anhydride and succinic anhydride. γ -Butyrolactone yields higher than 90% from maleic anhydride and succinic acid have been achieved according to several reports.^{29–32} Because succinic acid can be readily produced from renewable resources, hydrogenolysis of succinic acid into γ -butyrolactone has also attracted much attention in recent years. In a recent report, yields of γ -butyrolactone from succinic acid exceeding 95% have been attained over the Pt/TiO₂ catalyst at 160 °C under 15 MPa H₂ pressure.³³ Thus, it is considered that γ -butyrolactone can be a potential renewable resource for C4 alcohols, although it should be noted that an alternative efficient cata-

lyst not containing a noble metal would be of much interest for this process.

Several patents dealing with the hydrogenation of γ -butyrolactone into 1,4-butanediol have been reported for the past 30 years. Cu-based catalysts show high catalytic performance for this process. Table 4 summarizes the hydrogenation of γ -butyrolactone into 1,4-butanediol performed in a flow type reactor. Copper chromite as the catalyst yields a 92.3% selectivity to 1,4-butanediol at a γ -butyrolactone conversion of 68.4% at 211 °C under 4.1 MPa H₂ pressure, and 1-butanol is barely detectable with a selectivity of *ca.* 1%.³⁴ Related to copper chromite, a Cu/CrBaMnO catalyst, in which the weight percentage of Cu, Cr, Mn, and Ba is 27.6, 31.2, 2.5 and 0.6%, respectively, yields an 83.5% selectivity to 1,4-butanediol at a γ -butyrolactone conversion of 73% at 210 °C under 6 MPa H₂ pressure, and the selectivity to 1-butanol is *ca.* 5%.³⁵ A high 1,4-butanediol yield of *ca.* 96% obtained from γ -butyrolactone has been reported in a US patent, in which the reactions were performed over a magnesium silicate-supported Cu–Pd–KOH catalyst with a Cu, Pd, and KOH weight percentage of 12, 0.5 and 2%, respectively.³⁶ In a world patent, hydrogenolysis of a mixture of γ -butyrolactone and dimethyl succinate was performed over the Cu/ZnO catalyst at 180–220 °C under 8 MPa H₂ pressure, achieving a 1,4-butanediol selectivity of 90.5% at a γ -butyrolactone conversion of 90%.³⁷

Table 5 summarizes the hydrogenation of γ -butyrolactone into 1,4-butanediol performed under batch conditions using a water–ethanol mixture or organic solvents. In a Japanese patent, an 88.6% selectivity to 1,4-butanediol was obtained at a γ -butyrolactone conversion of 98% over the Pd/C catalyst at 180 °C under 10 MPa H₂ pressure in the presence of tetrabutylammonium rhenium oxide.³⁸ Pd/C is the only heterogeneous catalyst reported under batch conditions. Homogeneous catalysts have also been used for hydrogenation of γ -butyrolactone into 1,4-butanediol. In one of these reports a 94% selectivity to 1,4-butanediol was obtained at a γ -butyrolactone conversion of 53% over ruthenium acetylacetonate (Ru(acac)₃) as the catalyst at 200 °C in the presence of trioctylphosphine ligand and ammonium hexafluorophosphate.³⁹ The Ru complexes of tetradentate bipyridine ligands, which have been previously mentioned to be effective for dimethyl succinate hydrogenolysis into 1,4-butanediol in section 2.1.2 (Scheme 2), are also effective for hydrogenation of γ -butyrolactone into 1,4-butanediol, attaining a 99% yield of 1,4-butanediol from γ -butyrolactone at a low temperature of 25 °C in the presence of sodium methoxide.⁴⁰ As commented earlier, given the high activity of this Ru(II) bipyridyl

Table 4 Synthesis of 1,4-butanediol (BDO) from γ -butyrolactone (GBL) under continuous flow

Catalyst	Temp. (°C)	H ₂ pres. (MPa)	GHSV (h ⁻¹)	GBL conv. (%)	BDO select. (%)	Ref.
Copper chromite	211	4.1	9018 ^a	68.4	92.3	34
Cu/CrBaMnO	210	6	36 000	73	83.5	35
Cu–Pd–KOH/MgSiO ₃	160	6.2	0.12 ^b	99.5	96	36
Cu/ZnO	180–220	8	0.35 ^b	90	90.5	37 ^c

^a The mass velocity of the γ -butyrolactone stream through the catalyst bed was 9018 kg h⁻¹ m⁻². ^b The LHSV value. ^c A mixed γ -butyrolactone and dimethyl succinate solution with a ratio of 70 : 30 was used as the reactant.

Table 5 Synthesis of 1,4-butanediol (BDO) from γ -butyrolactone (GBL) under batch conditions

Catalyst	Temp. (°C)	H ₂ pres. (MPa)	Time (h)	Solvent	GBL/catalyst (g/g)	GBL conv. (%)	BDO select. (%)	Ref.
Pd/C	180	10	16	H ₂ O + ethanol	4.1	98	88.6	38
Ru(acac) ₃ ^a	200	10	3	Tetraglyme	1570 ^c	53	94	39
Ru(TBL) ^b	25	5	6	2-Propanol	1000 ^c	—	99 ^d	40

^a Ru(acac)₃, ruthenium acetylacetonate. ^b Ru(TBL), Ru complexes of tetradentate bipyridine ligands (Scheme 2). ^c The value of GBL/catalyst molar ratio. ^d The conversion and the selectivity to 1,4-butanediol were not shown separately and the yield of 1,4-butanediol was 99%.

complex, it would be of interest to attach a suitable derivative to a solid support to develop a heterogeneous version of this complex, assessing its stability under the apparently mild reaction conditions required for the process.

4 Production of C5 alcohols

4.1 Production of C5 alcohols from levulinic acid

Levulinic acid is a useful chemical employed as a food flavoring agent and as a starting material for the preparation of a variety of industrial and pharmaceutical compounds.^{41,42} Levulinic acid can be produced at the industrial scale from renewable resources, such as cellulose and hemicellulose which are present in agricultural or forest residues.⁴³ Levulinic acid is a potential raw material of some C5 alcohols, such as 1,4-pentanediol and 1-pentanol. The conversion of levulinic acid into 1,4-pentanediol is an interesting target in view of the potential use of this diol for the production of polyesters³ that can be carried out in water or under solventless conditions. Considering that in the current state of the art only catalysts containing noble or critical metals have been used, it would be important to develop novel heterogeneous catalysts based on abundant metals for levulinic acid hydrogenation.

It has been reported that homogeneous Ru-based catalysts are effective for hydrogenation of levulinic acid into 1,4-pentanediol (Table 6).^{44–46} Mehdi *et al.* performed the hydrogenation of levulinic acid in a pressurized NMR tube using the Ru(acac)₃ catalyst with different ligands, reaching a 63% selectivity to 1,4-pentanediol at 200 °C under 8.3 MPa H₂ pressure with a complete conversion of levulinic acid in the presence of a tributylphosphine ligand.⁴⁴ Similarly, a 95% yield of 1,4-pentanediol was achieved at a low levulinic acid/Ru(acac)₃ catalyst

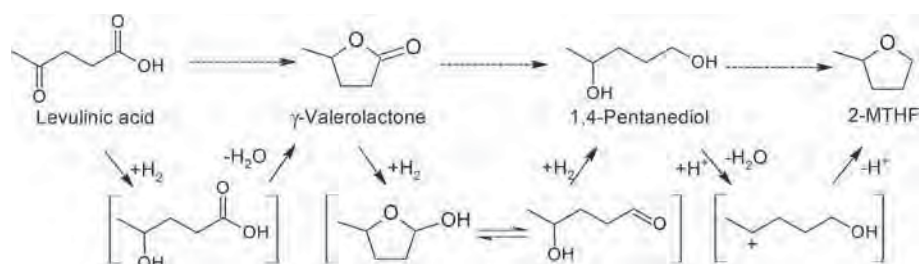
ratio in the presence of a triphos ligand in the reports of Geilen *et al.*^{45,46} They proposed that the hydrogenation of levulinic acid follows the route shown in Scheme 3. Following a similar reaction route as that proposed for succinic acid hydrogenation into 1,4-butanediol *via* γ -butyrolactone, 1,4-pentanediol would be produced from levulinic acid *via* γ -valerolactone as the intermediate. γ -Valerolactone is proposed to be produced from levulinic acid *via* hydrogenation followed by cyclodehydration. An alternative that could also be possible is the cyclodehydration of levulinic acid followed by hydrogenation. Because addition of acidic ionic liquids of NH₄PF₆ and 1-butyl-2-(4-sulfobutyl)imidazolium-*p*-toluenesulfonate shifts the reaction to the selective formation of 2-methyltetrahydrofuran (2-MTHF) (92% yield) under identical reaction conditions, it was proposed that the formation of 2-MTHF from 1,4-pentanediol is an acid catalyzed reaction.⁴⁵ Thus, it is reasonable that the catalysts without or with weak acidity exhibit high selectivity toward the formation of 1,4-pentanediol.

Corbel-Demilly *et al.* reported hydrogenation of levulinic acid into 1,4-pentanediol using heterogeneous catalysts.¹⁷ It was found that Ru/C was the most efficient catalyst compared to Pd/C and Pt/C. While the presence of Re increased the catalytic activity of Pd/C and Pt/C considerably, it almost does not affect the performance of Ru. The reaction temperature significantly affects product selectivity; formation of 1,4-pentanediol occurs with higher selectivity at low reaction temperatures because at higher temperatures further conversion of 1,4-pentanediol into 2-MTHF and alcohols, such as 1-pentanol, 2-pentanol and 1-butanol, can take place. An 82% yield of 1,4-pentanediol is achieved over the Ru–Re/C catalyst at 140 °C under 15 MPa H₂ pressure. Comparing the relative activity of Ru–Re/C and Pd–Re/C for hydrogenation of levulinic and succi-

Table 6 Synthesis of 1,4-pentanediol (PDO) from levulinic acid (LA) under batch conditions

Catalyst	Temp. (°C)	H ₂ pres. (MPa)	Time (h)	Solvent	LA/catalyst (mol/mol)	LA conv. (%)	PDO select. (%)	Ref.
Ru(acac) ₃ ^a	200	8.3	6	Neat	417	100	63	44
Ru(acac) ₃ ^a	160	10	18	Neat	1000	100	95	45
Ru–Re/C	140	15	28	Water	7.5 ^b	100	82	17
Pt–Mo/HAP ^c	130	5	12	Water	1.2 ^b	>99	93	47

^a Ru(acac)₃, ruthenium acetylacetonate. ^b The value of LA/catalyst weight ratio. ^c HPA, hydroxyapatite.



Scheme 3 Proposed reaction route of levulinic acid hydrogenation.⁴⁵

nic acids, it was observed that at 160 °C full conversion of levulinic acid required only 10 min, whereas succinic acid was completely converted after more than 40 h of reaction time.¹⁷ Recently, Mizugaki *et al.* reported that a hydroxyapatite-supported Pt–Mo bimetallic catalyst affords a high 1,4-pentanediol yield of 93% at 130 °C under 5 MPa H₂ pressure at a levulinic acid/catalyst weight ratio of 1.2.⁴⁷ Li *et al.* performed the hydrogenation of levulinic acid under continuous flow over SiO₂-supported precious metal catalysts modified by MoO_x.⁴⁸ The Rh–MoO_x/SiO₂ catalyst shows the best catalytic performance for 1,4-pentanediol formation, attaining a 70% selectivity at complete conversion at a WHSV of 0.24 h⁻¹ at a low reaction temperature of 70 °C under 6 MPa H₂ pressure using 10 wt% levulinic acid aqueous solution. 2-Pentanol and 1-pentanol are also produced with relatively high selectivities of 13.2 and 2.6%, respectively. It was proposed that the close contact between Rh and MoO_x (physical mixtures of Rh/SiO₂ and MoO_x/SiO₂ behave like Rh/SiO₂) leads to a synergy derived from adsorption of carboxylic acids on MoO_x. In fact, beyond levulinic acid, Rh–MoO_x/SiO₂ is an efficient catalyst for the aqueous phase hydrogenation of a wide range of carboxylic acids.

4.2 Production of C5 alcohols from levulinate and γ -valerolactone

Esters of levulinic acid are important compounds for producing flavors and plasticizers, and can be synthesized by esterification of levulinic acid with the respective alcohols even at room temperature.⁴⁹ γ -Valerolactone is widely used as a solvent as well as a synthetic intermediate in the chemical industry and even as a compound for energy storage. Production of γ -valerolactone from levulinic acid or its esters has attracted great attention in the past few years and almost quantitative yields of γ -valerolactone are achieved in some reports.^{50,51} Esters of levulinic acid and γ -valerolactone can be biomass-derived renewable raw materials for producing C5 alcohols.

Table 7 summarizes the synthesis of 1,4-pentanediol from γ -valerolactone and methyl levulinate in a batch-type reactor. It should be noted that according to current reports, reactions were performed in organic solvents and some of the copper-based heterogeneous catalysts could undergo leaching and deactivation if water was used as the solvent. Ru complexes of tetradentate bipyridine ligands (Scheme 2), which have been mentioned to be effective for dimethyl succinate and γ -butyrolactone hydrogenation into 1,4-butanediol, also exhibit extre-

mely high catalytic activity for the hydrogenation of methyl levulinate and γ -valerolactone to produce 1,4-pentanediol.⁴⁰ A 99 and 95% yield of 1,4-pentanediol is achieved from γ -valerolactone and methyl levulinate, respectively, at 25 °C under 5 MPa H₂ pressure. Du *et al.* studied the hydrogenation of γ -valerolactone using ethanol as the solvent, attaining 99% 1,4-pentanediol selectivity at a γ -valerolactone conversion of 97% at a reaction temperature of 200 °C under 6 MPa H₂ pressure over Cu/ZrO₂ calcined at 600 °C.⁵² The fact that the calcination temperature of Cu/ZrO₂ affected such drastically the product selectivity from 1,4-pentanediol to 2-MTHF has led to propose Cu/ZrO₂ as a tunable catalyst.⁵² Thus, Cu/ZrO₂ calcined at a low temperature of 400 °C yields a high 2-MTHF selectivity of 93% at 240 °C under 6 MPa H₂ pressure. Cu/ZrO₂ calcined at 400 °C has a large amount of weak acid sites that are not present in the Cu/ZrO₂ sample calcined at 600 °C.⁵² These mild acid sites can catalyze the further dehydration of 1,4-pentanediol into 2-MTHF. The effect of reaction temperature and H₂ pressure was also investigated. It was observed that the conversion of γ -valerolactone increased along the reaction temperature and H₂ pressure, whereas 1,4-pentanediol formation occurs with higher selectivity at low reaction temperatures because 1,4-pentanediol can undergo further transformation to 2-MTHF and 1-pentanol at high reaction temperatures.⁵² From the catalyst viewpoint, the available data suggest that the synergistic cooperation of dispersed Cu nanoparticles and active sites is essential to promote the hydrogenation of the carbonyl group of γ -valerolactone.⁵²

A Cu–TiO₂/ZrO₂ catalyst, which was prepared by co-precipitation and calcined at 600 °C gave a 96% selectivity to 1,4-pentanediol at 27% conversion in a later report of Xu *et al.*⁵³ The Rh–MoO_x/SiO₂ catalyst, which has been mentioned to be effective for 1,4-pentanediol formation from levulinic acid under a continuous flow, has also been applied for γ -valerolactone hydrogenation into 1,4-pentanediol.⁴⁸ A selectivity to 1,4-pentanediol of 61.8% was attained at a γ -valerolactone conversion of 68.2% at 70 °C under 6 MPa H₂ pressure at a WHSV of 0.24 h⁻¹.

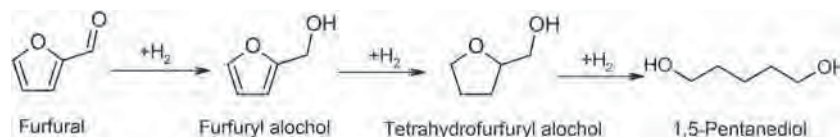
5 Conversion of furfural and its derivatives.

Furfural is one of the key chemicals derived from biomass.⁵⁴ It is produced industrially by hydrolysis of agricultural and for-

Table 7 Synthesis of 1,4-pentanediol (PDO) from γ -valerolactone (GVL) and methyl levulinate (ML) under batch conditions

Catalyst	Temp. (°C)	H ₂ pres. (MPa)	Time (h)	Solvent	GVL/catalyst (mol/mol)	GVL conv. (%)	PDO select. (%)	Ref.
Ru(TBL) ^a	25	5	4	2-Propanol	1000	—	99 ^b	40
Ru(TBL) ^a	25	5	16	2-Propanol	1000 ^c	—	95 ^b	40
Cu/ZrO ₂	200	6	6	Ethanol	5 ^d	97	99	52
Cu–TiO ₂ /ZrO ₂	200	5	6	Ethanol	2.5 ^d	27	96	53

^a Ru(TBL), Ru complexes of tetradentate bipyridine ligands (Scheme 2). ^b Yield of 1,4-pentanediol (PDO). ^c Methyl levulinate was used as the reactant, and the ML/catalyst molar ratio was 1000. ^d Value of GVL/catalyst weight ratio.



Scheme 4 Furfural hydrogenation into useful alcohols.^{57,58}

estry wastes with concentrated sulfuric acid,⁵⁵ or by the cyclodehydration of xylose on acid catalysts.⁵⁶ Recently, reviews on the furfural conversion have been published.^{57,58} Some useful C5 alcohols, such as furfuryl alcohol (FA), tetrahydrofurfuryl alcohol, and 1,5-pentanediol, can be derived from furfural and its derivatives, as shown in Scheme 4. 1,4-Butanediol can be also derived from furfural *via* decarbonylation.

5.1 Production of FA from furfural

FA is an important chemical, which is mainly used in the manufacture of resins, and it is also used as an intermediate for the synthesis of fragrances, vitamin C, and lysine.² FA is currently manufactured by hydrogenation of furfural in the liquid or vapor phase over copper chromite as the catalyst.³ Water and alcohols are the preferred solvents for this transformation. Although, noble metal catalysts have also been used for FA formation from furfural, there is abundant literature showing that base transition metal catalysts are also able to promote the reaction. Thus, a selectivity to FA over 98% is achieved from furfural over copper chromite.⁵⁶ However, in spite of the high selectivity of copper chromite, its use is not environmentally benign due to the high toxicity associated with chromium. Thus, many studies have focused on finding environmentally more acceptable catalysts able to selectively hydrogenate the carbonyl group without affecting the C=C bonds.

Table 8 summarizes the hydrogenation of furfural into FA in a batch type reactor. Not only precious metals, such as Rh, Pt and Ir, but also base metals, such as Cu, Ni and Co, showed catalytic activity for the hydrogenation of the unsaturated aldehyde, furfural, into unsaturated alcohol, FA. Vetere *et al.* studied furfural hydrogenation over SiO₂-supported Pt, Rh and Ni catalysts.^{59,75} FA is the major product over these catalysts, Pt/SiO₂ showing a relatively high furfural conversion of 46%. The addition of Sn into Pt/SiO₂ significantly increases the conversion of furfural, and a full conversion with an FA selectivity of 96% was obtained at 100 °C under 10 MPa H₂ pressure in the presence of 2-propanol as the solvent. The effect of the solvent was also investigated,⁷⁵ reaching the conclusion that alcoholic and polar solvents lead to the preferential FA formation from furfural. Bhogeswararao *et al.* studied furfural hydrogenation into useful chemicals over Al₂O₃-supported Pt and Pd catalysts.⁶⁰ Pt/Al₂O₃ and Pd/Al₂O₃ catalyze the formation of FA and tetrahydrofurfuryl alcohol, respectively. 95% FA selectivity is obtained at 95.5% furfural conversion over 5% Pt-loaded Al₂O₃ at 120 °C under 2 MPa H₂ pressure. Taylor *et al.* prepared various supported Pt catalysts for furfural hydrogenation to FA, and concluded that the selectivity to FA is strongly dependent on the supports and solvents.⁶¹ 97–99% selectivity to FA at 77–80% conversion was obtained over Pt/Al₂O₃, Pt/MgO and Pt/CeO₂ catalysts in the presence of a polar solvent such as methanol. The Tomishige group develo-

Table 8 Synthesis of FA from furfural under batch conditions

Catalyst	Temp. (°C)	H ₂ pres. (MPa)	Time (h)	Solvent	Furfural/catalyst (g/g)	Furfural conv. (%)	FA select. (%)	Ref.
Rh/SiO ₂	100	1	8	2-Propanol	9.3	15	97	59
Pt/SiO ₂	100	1	8	2-Propanol	9.3	46	99	59
Pt-Sn/SiO ₂	100	1	8	2-Propanol	9.3	100	96	59
Pt/Al ₂ O ₃	120	2	10	2-Propanol	20	95.5	95	60
Pt/Al ₂ O ₃	50	0.1	7	Methanol	1.0	80	99	61
Ir-ReO _x /SiO ₂	30	0.8	6	Water	5.8	>99	>99	62
Ru/Zr-MOFs ^d	20	0.5	4	Water	1.2	94.9	100	63
Ni-Sn	110	3	1.25	2-Propanol	2.1	72	70	64
Ni-Sn/TiO ₂	110	3	1.25	2-Propanol	2.1	>99	100	64
Ni-B-Fe	100	1	4	Ethanol	11.6	100	100	65
Co-B-Mo	100	1	3	Ethanol	5.8	100	100	66
Ni-B-Mo/Al ₂ O ₃	80	5	3	Methanol	5	99	91	67
Co/SBA-15	150	2	1.5	Ethanol	20	92	96	68
CuPMo/RANEY® Ni ^b	80	2	1	Ethanol	23.2	98.1	98.5	69
Cu/MgAlO	110	1	4	2-Propanol	6.2	100	100	70
Cu/MgAlO	150	0.1 (N ₂)	6	2-Propanol	5.8	100	100	71
Ni-Cu/MgAlO	200	1	2	Ethanol	34.8	93.2	89.2	72
Pd-Cu/MgO	130	0.8	30	Water	6	100	98.7	73
Cu/ZnCrZrO	170	2	3	2-Propanol	9.6	100	96	74

^a Zr-MOFs, zirconium based metal organic frameworks. ^b CuPMo, Cu_{3/2}PMo₁₂O₄₀.

ped an Ir–ReO_x/SiO₂ catalyst.⁶² A quantitative yield of FA was achieved from furfural over Ir–ReO_x/SiO₂ at a low reaction temperature of 30 °C under 0.8 MPa H₂ pressure. Selective hydrogenation of furfural to FA has also been investigated over Ru nanoparticles supported on a series of zirconium based metal organic frameworks, achieving 94.9% yield of FA at a temperature as low as 20 °C.⁶³

Ni- and Cu-based catalysts have been widely studied for furfural hydrogenation into FA. Liu *et al.* studied furfural hydrogenation over RANEY® Ni modified with a heteropolyacid salt of Cu_{3/2}PMo₁₂O₄₀, attaining 98.5% selectivity to FA at a conversion of 98.1% at 80 °C under 2 MPa H₂ pressure.⁶⁹ The Shimazu group prepared Ni–Sn alloy catalysts.⁶⁴ The loading of the Ni–Sn alloy on a TiO₂ support was found to promote the catalytic activity toward unsaturated alcohol formation, obtaining a FA yield higher than 99% from furfural over Ni–Sn/TiO₂ at 110 °C under 3 MPa H₂ pressure. The Fe-promoted Ni–B alloy, Mo-modified Co–B alloy, and Al₂O₃-supported Mo-modified Ni–B alloy have also been reported to be effective catalysts for furfural hydrogenation into FA,^{65–67} achieving 100% yield of FA.^{65,66} Co/SBA-15 is effective for furfural hydrogenation into FA, and 96% selectivity to FA is achieved at 92% conversion under the optimal conditions of 150 °C under 2.0 MPa of H₂.⁶⁸

Villaverde prepared by co-precipitation, a series of Cu-based catalysts such as CuMgAlO, CuZnAlO and Cu/SiO₂.⁷⁰ The selectivity in furfural hydrogenation to FA over these catalysts was 100%, whereas the conversion rate of furfural was different: CuMgAlO shows the highest furfural conversion rate of 5.09 mmol g_{Cu}⁻¹ min⁻¹ at 110 °C and 1 MPa H₂. In this case, furfural hydrogenation proceeds even under an N₂ atmosphere, proving that the solvent 2-propanol can act as a hydrogen donor reagent.⁷¹ Xu *et al.* performed furfural hydrogenation over Ni-promoted Cu/MgAlO catalysts, which were prepared from hydrotalcite-like precursors following a co-precipitation method.⁷² 89.2% selectivity to FA was obtained at a furfural conversion of 93.2% at a relatively high reaction temperature of 200 °C, furfural/catalyst weight ratio of 34.8, and H₂ pressure of 1 MPa for 2 h. It was found that Ni as a promoter increases both the selectivity to FA and the conversion of furfural. MgO-supported Pd–Cu bimetallic catalyst also gave high FA selectivity of 98.7% at 100% conversion at 130 °C, although a long reaction time of 30 h was required.⁷³ Sharma *et al.* prepared a series of Cu/ZnCrZrO catalysts with different Cu : Zn : Cr : Zr atomic ratios for furfural hydrogenation.⁷⁴ The selectivity to FA increases with the decreasing particle size of Cu, and it is interesting that the Cu particle size decreases upon increasing the Zr. The average particle size of Cu is minimized at 16.6 nm in a Cu/ZnCrZrO catalyst with a Cu : Zn : Cr : Zr atomic ratio of 3 : 2 : 1 : 4 that reaches 96% FA yield at 170 °C and H₂ pressure of 2 MPa.

Table 9 summarizes the hydrogenation of furfural into FA in a flow-type reactor. In an early report, the Pt/TiO₂–V₂O₅/SiO₂ catalyst was reported to be effective for furfural hydrogenation in the vapor-phase under atmospheric H₂ pressure.⁷⁶ 91.1% selectivity to FA was obtained at a furfural conversion of 87.3%

Table 9 Synthesis of FA from furfural under flow conditions^a

Catalyst	Temp. (°C)	TOS (h)	WHSV (h ⁻¹)	Furfural conv. (%)	FA select. (%)	Ref.
Pt/TiO ₂ –V ₂ O ₅ /SiO ₂	150	0.5	2	87.3	91.1	76
Cu/SiO ₂	230	0.08	2.3	69	98	77
Cu/SBA-15	170	5	1.5	54.1	95.8	78
Cu–Ca/SiO ₂	130	80	0.33 ^b	100	98.5	79
Cu–La/MCM41	180	n.c.	8.4	98.6	>99	80
Cu/MgO	180	n.c.	4.8	98	98	81
Au/Al ₂ O ₃	140	0.5	—	ca. 30	100	82

^a H₂ pressure 0.1 MPa. ^b LHSV value.

at 200 °C. Sitthisa *et al.* prepared SiO₂-supported Cu, Ni and Pd catalysts for furfural hydrogenation under atmospheric H₂ pressure.⁷⁷ It is found that different metals give different products: Cu/SiO₂ prefers FA formation and 98% selectivity is achieved at 69% furfural conversion at 230 °C, whereas Pd/SiO₂ and Ni/SiO₂ prefer 2-methylfuran and ring opening product formation, respectively. There is a similar influence for the three SiO₂-supported catalysts on the effect of the reaction temperature: the selectivity to FA decreases with increasing reaction temperature, while the selectivity to 2-methylfuran follows the opposite trend.^{76,77}

In a recent report, Cu supported on SBA-15 was also applied for furfural hydrogenation, and the selectivity to FA and the conversions of furfural were 95.8 and 54.1%, respectively at 170 °C.⁷⁸ Besides composition it is well-known that the preparation procedure has a strong influence on the activity of supported metal nanoparticles as the catalyst, due to variations in parameters such as dispersion and particle size distribution, among others. Wu *et al.* prepared Cu–Ca/SiO₂ catalysts for furfural hydrogenation using two different preparation methods.⁷⁹ Compared with the Cu–Ca/SiO₂ catalyst prepared by impregnation, the Cu–Ca/SiO₂ catalyst prepared by sol-gel shows higher copper dispersion and higher activity, giving 98.5% FA yield at 130 °C. It is proposed that Ca is acting as a promoter of Cu activity. In a similar way to the effect of Ca loading in Cu–Ca/SiO₂, modification of a Cu/MCM41 catalyst by La was found to promote copper dispersion and, therefore, its catalytic activity, achieving a FA yield ca. 99% over Cu–La/MCM41 at 180 °C.⁸⁰ The effect of the support was also studied: acidic supports such as zeolites favor the formation of 2-methylfuran. Nagaraja *et al.* performed furfural hydrogenation over MgO-supported Cu catalysts prepared by different methods.^{81,83} Cu/MgO prepared by co-precipitation shows the smallest average Cu size and the largest number of surface Cu and Cu⁺ sites, which were proposed to be important for FA formation. 98% selectivity to FA was achieved at a furfural conversion of 98% over Cu/MgO at 180 °C. Au/Al₂O₃ has also been reported to give an initial FA selectivity of 100% at ca. 30% conversion at 140 °C, whereas it is deactivated with time on stream.⁸²

5.2 Production of tetrahydrofurfuryl alcohol from furfural

Tetrahydrofurfuryl alcohol (THFA) is a high-boiling point transparent liquid that is completely miscible with water.

Table 10 Synthesis of THFA from furfural under batch conditions

Catalyst	Temp. (°C)	H ₂ pres. (MPa)	Time (h)	Solvent	Furfural/catalyst (g/g)	Furfural conv. (%)	THFA select. (%)	Ref.
Ni/SiO ₂ -Al ₂ O ₃	120	4	2	Methanol	29	99	97	85
RANEY® Ni/AlOH	130	3	1.25	2-Propanol	2.1	>99	100	64
Pd/Al ₂ O ₃	25	6	8	2-Propanol	20	65.6	99.7	60
Ni-Pd alloy/SiO ₂	40	8	2	Water	4.8	99	97	87
Pd-Ir-ReO _x /SiO ₂	50	6	2	Water	10	>99	78	88
Ni-Pd/TiO ₂ -ZrO ₂	130	5	8	Ethanol	8.7	100	93.4	89

THFA is considered a green and sustainable solvent used in agricultural applications, printing inks, industrial and electronics cleaners.⁵⁸ THFA is also a potential raw material for producing 1,5-pentanediol, which can be used for polyester production.

The most important route for THFA is a two-step catalytic hydrogenation of furfural *via* FA as an intermediate.⁵⁸ Copper chromite and Pd/C are used for furfural hydrogenation into FA and the following FA hydrogenation into THFA separately at 120 °C and 200 °C, respectively, in a continuous process under 15 MPa H₂ pressure, achieving 96% yield of THFA.⁸⁴ Although Cu-based catalysts show high activity on hydrogenation of the C=O bond in furfural as previously mentioned in section 5.1, they are less active for the hydrogenation of the C=C bond in furfural. Thus, the combination of the two materials is an obvious possible catalyst for the direct conversion of furfural into THFA. Table 10 summarizes the production of THFA from furfural in a batch-type reactor. As can be seen, the reaction has been performed using alcohols or water as solvents, but in the later case, only catalysts containing Pd have been reported. In a pioneering paper, various commercial supported Cu, Pd, Ru, Rh, and Ni catalysts were tested for furfural hydrogenation.⁸⁵ Among these catalysts, Ni/SiO₂-Al₂O₃ shows the highest activity for THFA formation and THFA yield higher than 98% at 120 °C under 4 MPa H₂ pressure. RANEY® Ni loaded on AlOH is active for hydrogenation of both C=C and C=O in furfural. Accordingly, RANEY® Ni/AlOH catalyst shows THFA yield higher than 99% at 130 °C under 3 MPa H₂ pressure.⁶⁴ As mentioned in section 5.1, the Al₂O₃-supported Pd catalyst is effective for THFA formation from furfural, exhibiting the catalyst at a Pd loading of 10 wt%, 99.7% selectivity to THFA at 65.6% conversion at 25 °C under 6 MPa H₂ pressure.⁶⁰

Tomishige *et al.* performed a series of studies on furfural hydrogenation. In one of these studies they performed vapor-phase furfural hydrogenation using the Ni/SiO₂ catalyst, which was prepared by reduction of nickel nitrate supported on SiO₂.⁸⁶ The maximum yield of THFA was 94% over Ni/SiO₂ calcined at 500 °C at a reaction temperature of 140 °C. They indicate that THFA is produced from FA as the intermediate, observing that while the conversion of furfural to FA is less structure-sensitive, FA hydrogenation into THFA is promoted preferentially by Ni particles with a smaller size. In aqueous media, Ni-Pd alloy/SiO₂ and Pd-Ir-ReO_x/SiO₂ showed 97 and 78% selectivity to THFA, respectively, at low reaction temperature and high H₂ pressure.^{87,88} In a recent report, Chen *et al.*

studied the TiO₂-ZrO₂-supported Ni-Pd catalyst, observing that the catalyst with a Ni/Pd atomic ratio of 5 gives a 93.4% yield of THFA at 130 °C under 6 MPa H₂ pressure in ethanol.⁸⁹ Vapor-phase hydrogenation of furfural has been studied over Pd supported on MFI zeolite (Pd/MFI), attaining a 95% yield of THFA over Pd/MFI with a Pd loading of 3 wt% at 220 °C under 3.4 MPa H₂ pressure.⁹⁰

5.3 Production of C4 and C5 diols from furfural and its derivatives

As reported in the introduction, 1,5-pentanediol, 1,2-pentanediol and 1,4-butanediol are important chemicals mainly used for polyester production, and for producing unsaturated alcohols and lactones. Recently, catalytic transformation of furfural and its derivatives, such as THFA and FA, into these diols has attracted much attention. Pentanediols and pentanols could be conveniently obtained by furfural and THFA hydrogenolysis provided that efficient catalysts for these processes are developed. Particularly interesting from the fundamental and practical viewpoints is the use of THFA as a starting material for the preparation of these alcohols (Scheme 5). This process is promoted in general by bifunctional (hydrogenating and Lewis acid) catalysts that require the combination in the appropriate proportion of two different metals having different roles.

As shown in Scheme 5, 1,2- and 1,5-pentanediols can be generated from THFA by hydrogenolysis of C-O bonds of the five-member ring heterocycle, the dissociation of different side C-O bonds leading to different diols. In most of the reports, 1-pentanol and 2-pentanol are produced in small amounts as secondary products through the subsequent hydrogenolysis of diols. Table 11 summarizes the production of 1,5- and 1,2-pentanediols from THFA in batch reactions. The Tomishige group has made several contributions studying the hydrogenolysis of THFA into 1,5-pentanediol,⁹¹⁻⁹⁷ and has published a review paper of the catalytic furfural conversion to pentanediols.⁹⁸ Rh-MoO_x/SiO₂, Rh-ReO_x/SiO₂, Rh-ReO_x/C, Ir-ReO_x/SiO₂ have

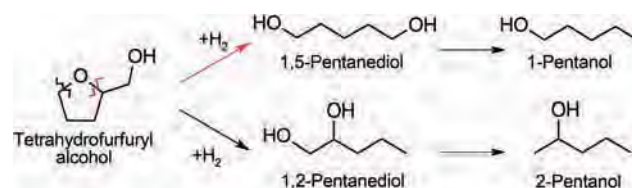
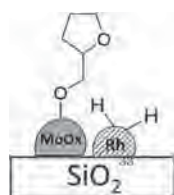
**Scheme 5** Alcohols derived from THFA hydrogenation.⁵⁷

Table 11 Synthesis of 1,5-pentanediol and 1,2-pentanediol (PDO) from THFA under batch conditions

Catalyst	Temp. (°C)	H ₂ pres. (MPa)	Time (h)	Solvent	THFA/catalyst (g/g)	THFA conv. (%)	PDO select. (%)	Ref.
Rh/MCM-41	80	4	24	CO ₂ (14 MPa)	4	80.5	91.2 ^a	100
Pt/MCM-41	80	4	24	CO ₂ (14 MPa)	4	50.5	77.4 ^b	100
Rh-MoO _x /SiO ₂	120	8	12	Water	60	53.5	93.7 ^a	91
Rh-ReO _x /SiO ₂	120	8	4	Water	20	56.9	94.2 ^a	92
Rh-ReO _x /C	100	8	24	Water	10	100	94 ^a	93
Ir-ReO _x /SiO ₂	100	8	2	Water	6.7	58.2	95.8 ^a	94

^a The selectivity to 1,5-pentanediol. ^b The selectivity to 1,2-pentanediol.

been reported to be active catalysts for THFA hydrogenation into 1,5-pentanediol, and selectivity to 1,5-pentanediol higher than 94% is obtained over the catalysts. One of the key factors for achieving high selectivity for 1,5-pentanediol is optimization of the promoter-to-Rh atomic ratio. The occurrence of the metal-metal bond between metal particles and partially reduced modifiers is considered to be a key factor for reaching a high selectivity.⁹⁷ Among the catalysts, Ir-ReO_x/SiO₂ was the most active material for THFA conversion,^{91,94} while, on the other hand, Rh-ReO_x/SiO₂ was more active but less stable than Rh-MoO_x/SiO₂.⁹¹ The presence of MoO_x at a low Mo/Rh ratio of 0.13 was found to increase activity, but, more importantly, also selectivity towards 1,5-pentanediol.⁹¹ In the absence of Mo, Rh/SiO₂ gives a mixture of products, in which 1,5-pentanediol was present (18% selectivity), but in which the major product was 1,2-pentanediol (61.7% selectivity). Using Rh-ReO_x/SiO₂ the selectivity to 1,5-pentanediol was 93.7%. In addition the performance of Rh-ReO_x/SiO₂ is less dependent on THFA concentration than analogous catalysts with Re or W. To understand the interaction between Rh and the promoter, CO adsorption studies monitored by IR spectroscopy were carried out. It was observed that the amount of CO adsorbed decreases stoichiometrically with the amount of incorporated Mo, suggesting that Mo interacts strongly with Rh metal NPs (3.2 ± 0.3 nm) blocking the CO adsorption sites. Based on these quantitative CO adsorption measurements, a mechanism of the promotional effect of MoO_x was proposed (Scheme 6) in which THFA would be adsorbed on MoO_x species *via* the OH group while hydrogen would be split by Rh NPs in close proximity to MoO_x causing a synergy in the efficiency of THFA hydrogenolysis.⁹⁶ Similar decrease in CO adsorption was also observed after deposition of ReO_x on Rh/SiO₂. It is worth commenting that besides THFA, tetrahydropyran-2-methanol also undergoes selective hydrogenolysis to the corresponding 1,6-

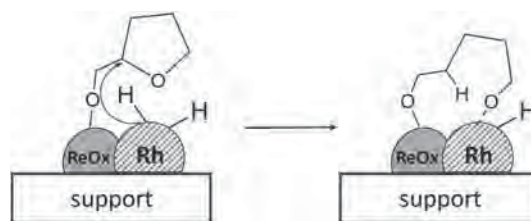


Scheme 6 Synergism between MoO_x and Rh in the hydrogenolysis of THFA.

hexanediol by Rh-ReO_x/SiO₂, while again Rh/SiO₂ is unselective or promotes the formation of less wanted 1,2-hexanediol.⁹⁶

Preferential leaching of Mo species may occur and contribute to the reaction mechanism. In one study regarding the promotion of Rh activity for THFA hydrogenolysis to 1,5-pentanediol by supported MoO₃, it was found that this metal oxide leaches to the aqueous phase, presumably as H_{0.9}MoO₃, and calculations suggest that there should be a cooperation between the dissolved H_{0.9}MoO₃ and heterogeneous Rh catalyst, the acidic Mo-OH group being responsible for the C-O bond cleavage of THFA.⁹⁹

In the hydrogenolysis of cyclic ethers, such as tetrahydro-5-methyl-2-furfuryl alcohol and 2-methyltetrahydrofuran, the C-O bond closest to the -CH₂OH group was the one which preferentially dissociated over Rh-ReO_x/SiO₂.⁹⁵ Mechanistic studies have found that THFA hydrogenolysis to 1,5-pentanediol using Rh-ReO_x/SiO₂ follows a different pathway compared to the hydrogenolysis of dihydropyran and δ-hydroxyvaleraldehyde, since in contrast to the last two processes in the former reaction the presence of H₂SO₄ does not increase the efficiency of the Rh-ReO_x/SiO₂ catalyst. This mechanistic study has also led to the conclusion that hydrogenolysis occurs by a heterolytic activation of H₂ forming hydride and proton on the Rh-ReO_x/SiO₂ catalyst that are subsequently transferred to the substrate. It is suggested that the hydride is located at the interface between the Rh metal and ReO_x cluster and is the species that attacks the C-O single bond of the heterocycle next to the primary CH₂OH group through which the molecule is adsorbed on ReO_x clusters (Scheme 7). Accordingly, the presence of 1,5-pentanediol decreases the activity of the catalyst for hydrogenolysis by competing with THFA for the sites where primary OH groups are adsorbed. Kinetic analyses



Scheme 7 Proposal to rationalize the regioselectivity of the 5-member ring opening leading to the observed 1,ω-regioselectivity for the resulting pentanediol.

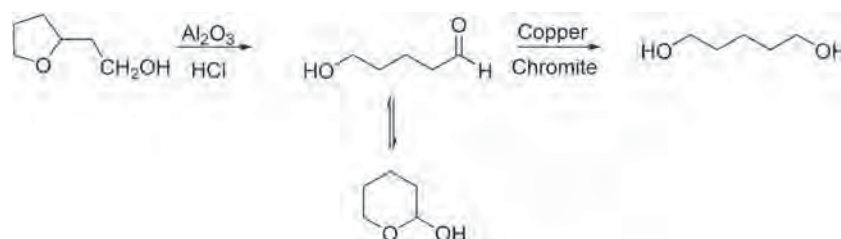
have also revealed that THFA hydrogenolysis on Rh–ReO_x/SiO₂ is of the first order with respect to hydrogen pressure and zero order with respect to THFA concentration, following a Langmuir–Hinshelwood type model in which both substrates are adsorbed on the catalyst surface before undergoing the reaction. Further studies by Tomishige and coworkers have shown that the presence of a terminal CH₂OH group is a structural prerequisite for the selective ring aperture hydrogenolysis catalyzed by Rh/ReO_x/SiO₂.⁹⁶ Accordingly when a terminal CH₂OH group is located next to an acyclic glycol ether, hydrogenolysis also occurs in a selective way similarly to the case of THFA of FA, thus, proving that the presence of a cycle is not necessary for the hydrogenolysis.⁹⁶

Chatterjee *et al.* performed THFA hydrogenation over Rh and Pd supported on MCM-41 in supercritical carbon dioxide without any other co-solvent, overcoming in this way the low solubility of hydrogen in aqueous media.¹⁰⁰ It was observed that Rh/MCM-41 and Pd/MCM-41 prefer 1,5-pentanediol and 1,2-pentanediol formation, respectively. The conversion of THFA increases along the reaction temperature and H₂ pressure, whereas the selectivity to diols decreases in the same order, because of the consecutive hydrogenolysis of diols into monoalcohols. The conversion of THFA is found to increase with increasing CO₂ pressure due to the enhanced solubility of THFA in CO₂. The maximum selectivities to 1,5-pentanediol and 1,2-pentanediol were 91.2% and 77.4% over Rh/MCM-41 and Pd/MCM-41, respectively, at 80 °C under 14 MPa CO₂ and 4 MPa H₂ pressure. In the case of Rh/MCM-41, it was proposed that its catalytic activity arises from the simultaneous presence of Rh₂O₃ and Rh(0), both species being necessary for achieving high selectivity towards 1,5-pentanediol. Accordingly, the induction period observed for THFA conversion was interpreted as the time required to reduce some Rh₂O₃ to Rh(0) reaching the optimal Rh₂O₃–Rh(0) composition to become an efficient catalyst. An interesting feature is that the presence of water is unfavorable for the catalytic activity and selectivity of the process, something that is a drawback for the possible implementation of THFA hydrogenolysis in supercritical CO₂, THFA samples usually should contain water.

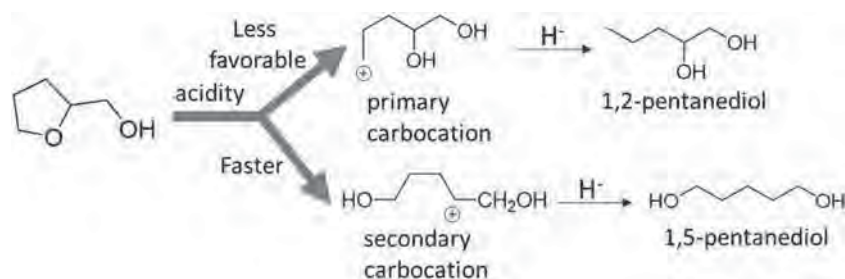
In the context of conversion of THFA into 1,5-pentanediol, one possibility could be a two-step process in which at first THFA is converted to δ-hydroxyvaleraldehyde that subsequently is hydrogenated into 1,5-pentanediol (Scheme 8). It has been found that copper chromite can be used for the hydrogenation

of ω-hydroxyvaleraldehyde to 1,5-pentanediol reaching 70% yield under high hydrogen pressure at 150 °C.¹⁰¹ Conversion of THFA into the hemiacetal of δ-hydroxyvaleraldehyde can be catalysed by Al₂O₃ and HCl.¹⁰¹ Since the tendency in process intensification is to combine several independent reactions in a one-step cascade process, it seems that a direct conversion of THFA into 1,5-pentanediol is more appealing than a multi-step process, even though some individual reactions could be performed separately with higher yields. In this regard, it should be commented that attempts to perform the direct hydrogenation of cyclic δ-hemiacetal of ω-hydroxyvaleraldehyde with copper chromite without prior isolation of ω-hydroxyvaleraldehyde have failed so far in giving the wanted pentanediol.¹⁰¹

In a fairly complete study combining activity data, catalyst characterization, kinetics study and theoretical calculations, Dumesic and co-workers have shown that C supported Rh–Re catalyst is a bifunctional, highly selective and stable catalyst for hydrogenolysis of cyclic ethers and polyols to α,ω-diols.¹⁰² Rh/C exhibits no hydrogenolysis activity. Apparently, the activity of the ReO_x–Rh/C arises from the coupling of a highly reducible metal (Rh) with another strongly oxophilic one (Re or Mo).¹⁰² The strong interaction between the two types of metals was convincingly proved in a simple way by determining that the reduction temperature of the oxophilic metal in TPR diminishes significantly due to the influence of Rh. It was found that the Rh/Re or Rh/Mo atomic ratio is an important parameter controlling the catalytic activity of the resulting bimetallic catalyst.¹⁰² In this way, the hydrogenolysis rate of THFA for Rh–ReO_x/C (Rh/Re atomic ratio: 0.5) increases about 15 times compared to the activity of analogous monometallic Rh/C.¹⁰² In the case of Rh–MoO_x/C (Rh/Mo atomic ratio 1 : 0.1) the increase in rate was by a factor of 6.¹⁰² It was observed that catalyst pretreatment by aniline at 150 °C increases catalyst stability, reducing the amount of metal leaching to less than 0.5%, a significant improvement compared with 2% Re leaching observed for the untreated Rh–ReO_x/C catalyst.¹⁰² The ring aperture was selective to the α,ω-diols, indicating that the C–O bond cleavage occurs at the sterically more hindered secondary C–O bond. Comparison of the reactivity for various six and five member cyclic ethers indicates that the presence of primary hydroxyl groups significantly increases the catalytic activity for C–O hydrogenolysis.¹⁰² With regard to the reaction mechanism, an important data determined by NH₃ desorption shows that Rh–ReO_x/C has a significant density of acid sites (40 μmol g⁻¹)



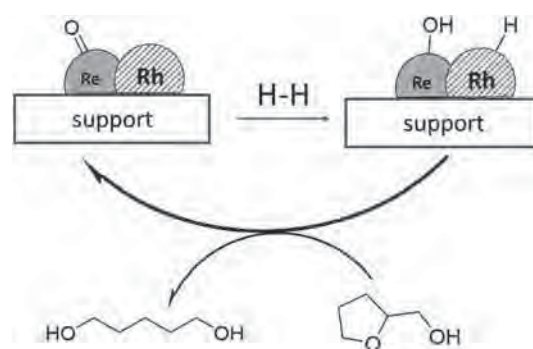
Scheme 8 Route for 1,5-pentanediol formation based on a two-step process starting from THFA and involving δ-hydroxyvaleraldehyde as the synthetic intermediate.



Scheme 9 Rationalization of the preferential formation of 1,5-pentanediol over 1,2-pentanediol based on the relative stability of the corresponding carbocations.

corresponding to 0.28 acid sites/metal atom.¹⁰² In contrast, analogous Rh/C or Re/C samples did not exhibit measurable acidity against NH_3 . Overall these characterization data showing the bifunctionality (hydrogen activation and acidity) of the Rh– ReO_x/C catalyst suggest a mechanism in which acidity promotes the initial ring opening to the more stable secondary carbocation that subsequently would undergo hydrogenation (Scheme 9).¹⁰² According to this mechanism, supported by DFT calculations, the origin of product selectivity is the higher stability of intermediates with a secondary carbenium ion formed in the acid catalyzed ring aperture.¹⁰² This carbenium intermediate is, in addition, stabilized by an α -hydroxy substituent when this group is present. The role of hydrogen would be hydrogenation of the unsaturated organic intermediate after the acid catalyzed ring opening and recovery of the ReOH groups by hydrogenation of Re=O species closing the reaction cycle. Scheme 10 summarizes the proposed mechanism and the key factor responsible for the observed product selectivity.

The Li group recently performed THFA hydrogenation into 1,5-pentanediol in a continuous flow type reactor.^{103,104} A 65% selectivity to 1,5-pentanediol was obtained at a THFA conversion of 75% over the MoO_x -promoted Ir/SiO₂ catalyst at 120 °C under 6 MPa H₂ pressure at a WHSV of 0.24 h⁻¹ and a time on stream (TOS) of 6 h.¹⁰³ The catalyst system is similar to that reported by the Tomishige group.^{91,94} High H₂ pressure increases the conversion of THFA, whereas it slightly decreases the selectivity to 1,5-pentanediol. Catalytic deactivation was observed, decreasing the conversion from 75% at a TOS of 6 h to 46% at 30 h. This deactivation is attributed to the leaching of Mo species during the reaction. In contrast to MoO_x -promoted Ir/SiO₂, VO_x -modified Ir/SiO₂ yields even higher 1,5-pentanediol



Scheme 10 Heterolytic hydrogen activation of the supported ReO_x –Rh catalyst that results in the conversion of THFA into 1,5-pentanediol.

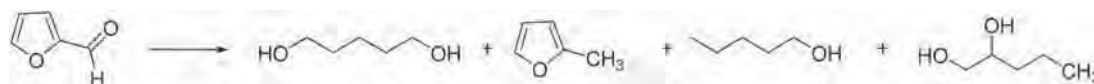
selectivity of ca. 90%, but at a lower THFA conversion of ca. 58% under the same reaction conditions except for the reaction temperature of 80 °C.¹⁰⁴ Ir– VO_x/SiO_2 becomes also deactivated, decreasing THFA conversion to ca. 20% at a TOS of 30 h.

Considering the various possible routes to obtain 1,5-pentanediol from biomass, it is clear that in principle the most advantageous ones are those with the lower number of independent reactions, coupling several individual processes in one single step. Accordingly, the conversion of furfural directly to 1,5-pentanediol would make THFA unnecessary as the synthetic intermediate. Table 12 summarizes the production of diols using furfural and FA as starting materials. In one of the studies aimed at converting FA into 1,5-pentanediol, Xu *et al.* have reported one-pot hydrogenation of furfural into 1,5-pentanediol, accompanied by methylfuran, pentanols and pentanediols (Scheme 11).¹⁰⁵

Table 12 Synthesis of diols (DO) from furfural and FA under batch conditions

Catalyst	Temp. (°C)	H ₂ pres. (MPa)	Time (h)	Solvent	Furfural/catalyst (g/g)	Furfural conv. (%)	DO select. (%)	Ref.
Li–Pt/Co ₂ AlO ₄	140	1.5	24	Ethanol	2	99.9	34.9 ^c	105
Pd–Ir–ReO _x /SiO ₂	40 ^a –100 ^b	6	8 ^a –72 ^b	Water	10	>99.9	71.4 ^c	88
Rh–Ir–ReO _x /SiO ₂	40 ^a –100 ^b	6	8 ^a –32 ^b	Water	10	>99.9	78.2 ^c	106
Ru/MnO _x	150	1.5	4	Water	20	100 ^e	42.1 ^d	107
Pt/Hydrotalcite	150	3	4	2-Propanol	1	>99	73 ^d	108

^a First reaction step. ^b Second reaction step. ^c Selectivity to 1,5-pentanediol. ^d Selectivity to 1,2-pentanediol. ^e FA was used as the reactant and its conversion was 100%.



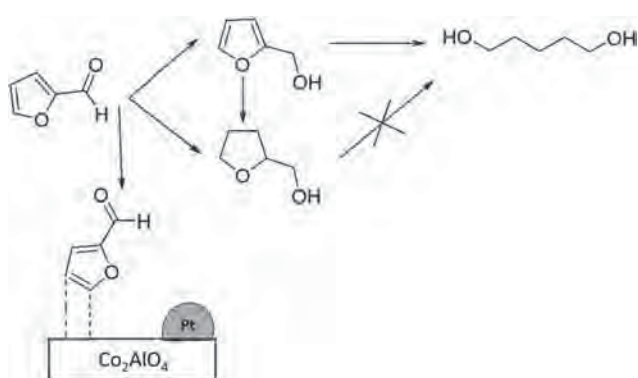
Scheme 11 Products observed in the hydrogenolysis of furfural.

The maximum yield of 1,5-pentanediol was 34.9%, attained at 140 °C under 1.5 MPa H₂ pressure over Li-promoted Pt/Co₂AlO₄ prepared by co-precipitation. The time course of furfural conversion over Pt/Co₂AlO₄ showed that the reaction sequence proceeds stepwise *via* FA as the intermediate. FA is the only product for the initial period, and, then, the selectivity to FA almost linearly decreases after the initial period. In contrast, the selectivity to 1,5-pentanediol, 2-methylfuran, THFA and monoalcohols increases after the initial period upon increasing the reaction time, and the order of the selectivity to the main products at 24 h was 1,5-pentanediol > 2-methylfuran > THFA. In the case of the reaction using THFA as the reactant, no formation of 1,5-pentanediol was observed. Based on this kinetics, it was proposed that 1,5-pentanediol is produced *via* FA and not *via* THFA. They also studied the effects of the reaction conditions, reaching the conclusion that low temperature and high H₂ pressure are preferable for the formation of 1,5-pentanediol. Concerning the reaction mechanism, comparison of the catalytic activity of Pt/Co₂AlO₄ with those of Pt/Al₂O₃ and Co/Al₂O₃ separately led to the conclusion that FA should be adsorbed on the surface of Co₂AlO₄ through C=C bonds and the furan ring should be open and finally hydrogenated by Pt (Scheme 12).

The Tomishige group also performed hydrogenolysis of furfural into 1,5-pentanediol using the Pd-promoted Ir-ReO_x/SiO₂ catalyst. They suggest that 1,5-pentanediol could not be selectively produced at high reaction temperatures because THFA formation prefers low temperatures, high reaction temperatures yielding a large amount of unidentified products.⁸⁸ This information was used to devise a two-step furfural hydrogenation over Pd-promoted Ir-ReO_x/SiO₂, performing each step at a different reaction temperature aimed to produce firstly THFA at a low temperature and subsequently to convert THFA to 1,5-

pentanediol at higher temperature. The maximum yield of 1,5-pentanediol achieved 71.4% under the conditions of the first step at 40 °C for 8 h and the second step at 100 °C for 72 h at 6 MPa H₂ pressure using 10 wt% aqueous furfural solution. Furthermore, the Re-modified SiO₂-supported Rh-Ir alloy was reported to be a more active catalyst than Ir-ReO_x/SiO₂, achieving 78.2% yield of 1,5-pentanediol.¹⁰⁶ They also performed the hydrogenation of furfural and THFA individually over Rh-Ir-ReO_x/SiO₂, observing THFA and 1,5-pentanediol as the main products, respectively. It was confirmed that 1,5-pentanediol is generated *via* THFA as the intermediate.

The production of 1,2-pentanediol from FA hydrogenation has been reported by Zhang *et al.* Among the tested MnO_x-supported precious metal catalysts the MnO_x-supported Ru catalyst shows the best catalytic performance for 1,2-pentanediol formation.¹⁰⁷ The maximum yield of 1,2-pentanediol over Ru/MnO_x was 42.1% at 150 °C under 1.5 MPa H₂ pressure. A high temperature and a low pressure are favorable for the formation of 1,2-pentanediol, water increasing the reaction rate. Ru/MnO_x is less active for THFA conversion than for FA conversion. This relative reactivity order is compatible with a reaction pathway in which 1,2-pentanediol is generated from furfural *via* 1-hydroxy-2-pentanone as the intermediate. Mizugaki *et al.* performed furfural hydrogenation to 1,2-pentanediol over hydrotalcite-supported Pt catalysts, attaining 73% yield of 1,2-pentanediol at 150 °C under 3 MPa H₂ pressure.¹⁰⁸ Li *et al.* reported that 1,4-butanediol can be selectively formed from furfural over Pt/TiO₂-ZrO₂. It was proposed that the process comprises two steps consisting of the oxidation of furfural to produce 2-furanone isomers *via* decarbonylation and the subsequent hydrogenation of the 2-furanone mixture to 1,4-butanediol.¹⁰⁹ The first step is performed over Pt/TiO₂-ZrO₂ at 20 °C under atmospheric pressure in the presence of formic acid, water, methanol and hydrogen peroxide. The conversion of furfural and the selectivity to 2-furanone were 95.8 and 93.6%, respectively. After decomposition of the residual peroxide, the second step reaction was performed at 120 °C under 3.5 MPa H₂ pressure, converting 2-furanone into 1,4-butanediol with 98.2% selectivity at 96.8% conversion. The total yield of 1,4-butanediol achieved through the two-stage reaction was 85.2%.



Scheme 12 Mechanistic proposal for the hydrogenolysis of furfural to 1,5-pentanediol.

6. Hydrogenation and hydrogenolysis of other biomass oxygenates to alcohols

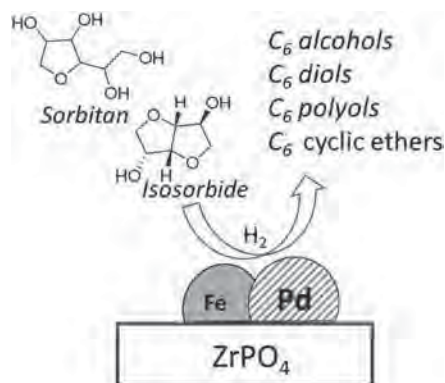
In one of the studies aimed at showing the superior performance of bimetallic over monometallic catalysts, the relationship between the reaction rate for hydrogenation of different

feed molecules containing a carbonyl group and different $\gamma\text{-Al}_2\text{O}_3$ - or zirconium phosphate-supported bimetallic catalysts was determined.¹¹⁰ This catalytic data should provide valuable information about general catalysts for aqueous-phase conversion of complex biomass mixtures. A preliminary high-throughput screening allowed determining the most promising bimetallic catalysts containing Pd, Pt or Ru and Ni, Co or Fe that were, then, tested for the hydrodeoxygenation of sorbitol. It was observed that the addition of Ni, Co, or Fe to the monometallic Pd and Pt catalysts usually increased the activity for aqueous-phase hydrogenation of propanal and furfural, the Pd_1Fe_3 catalyst being the most active of the series. Addition of Fe to the monometallic Pd catalyst increased the reaction rate for aqueous phase hydrogenation of xylose by a factor of 51. In contrast, all bimetallic catalysts tested in this study had a lower activity than the monometallic Ru catalyst for aqueous phase hydrogenation of xylose.

In the case of furfural hydrogenation in water, Pd-based bimetallic catalysts produced not only FA but also THFA, meaning that the Pd-based bimetallic catalysts are active not only for C=O bond hydrogenation, but also for C=C bond hydrogenation. The Pd_1Fe_3 bimetallic catalyst, supported in this case on zirconium phosphate, was the most active catalyst of the series for sorbitol hydrodeoxygenation in water.¹¹⁰ It was observed that addition of Fe to Pd enhanced the activity of the resulting material by both C–C bond cleavage and C–O hydrogenolysis reactions. Moreover, Fe addition to Pd increased the conversion of sorbitan and isosorbide to C₆ alcohols, C₆ diols, C₆ polyols, and C₆ cyclic ethers (Scheme 13). The Pd_1Fe_3 supported on zirconium phosphate was also more selective to gasoline-range products than the analogous monometallic Pd catalyst.

7. Concluding remarks and future prospects

Considering the general trend in applying biomass-derived feedstocks as platforms for the production of chemicals as



Scheme 13 Conversion of sorbitan and isosorbide into a mixture of C₆ alcohols and ether by hydrogenolysis promoted by Fe–Pd/ZrPO₄.

well as the importance of diols as monomers in the synthesis of polyesters, it can be anticipated that industrial processes based on biomass transformation will be implemented in the near future for the production of butanediol and pentanediol, particularly the 1,ω-isomers, but also for the corresponding glycols. These C₄ and C₅ diols, together with ethylene glycol and propanediols, form part of the pool of available diols that can be derived from biomass. It can be anticipated that the contribution of biomass-derived diols to the total market of these monomers will increase steadily in percentage in the next years, contributing to the sustainability of the chemical industry. Also, the production of C₄ and C₅ monoalcohols from biomass will gain importance, particularly for their use in the transportation fuel industry, for preparation of gasoline octane boosters and maybe also directly as fuels.

In the corresponding sections, the major biomass-derived precursors for C₄ and C₅ alcohols including (di)carboxylic acids, their alkyl esters and furan derivatives have been described, there still being an opportunity for the development of more efficient and durable catalysts without containing precious or critical metals. It appears that the field has been dominated so far by the use of hydrogenation catalysts containing noble or critical metals. Although these catalysts exhibit the highest activity, it seems unrealistic to think in industrial processes based on the use of catalysts containing these costly and critical metals, particularly because indefinite reusability of these catalysts is not possible.

Thus, replacement of noble metals and ruthenium by abundant transition metals is mandatory. These catalysts should also be able to act in water without undergoing metal leaching or at least to be water-tolerant. It seems that, using certain supports and avoiding chromium in the composition, copper catalysts could be an alternative to noble metals. However, the use of copper catalysts requires harsh reaction conditions in terms of hydrogen pressure and reaction temperatures. In addition, Cu-based catalysts are prone to undergo leaching when in contact with water. Thus, effort in developing more efficient copper catalysts is necessary.

Perusal of the current state of the art seems to indicate that the combination of acid sites and hydrogenation centers creates a synergy, particularly for hydrogenolysis where cyclic lactones can be formed in the route to diols. Rhenium has so far been the favorite metal to combine with hydrogenation centers and it has been frequently shown that the presence of an optimal amount of rhenium increases the activity of hydrogenation catalysts for certain processes. Also in this regard and considering the scarcity of rhenium, the development of other metal oxides based on abundant alternatives is necessary. Molybdenum and tungsten can be more convenient metals compared to rhenium as a promoter of hydrogenolysis catalysts.

The final goal in the area is the development of competitive industrial processes based on biomass feedstocks that can be economically attractive and competitive with respect to analogous processes based on fossil fuels.

Acknowledgements

This research is partly funded by the EU-JSPS joint initiative through the NOVACAM project, by JST, Strategic International Collaborative Research Program, SICORP and by the Spanish Ministry of Economy and Competitiveness (Severo Ochoa and CTQ2012-32315). AP also thanks the Spanish Ministry for a Ramon y Cajal research contract.

References

- G. W. Huber, S. Iborra and A. Corma, *Chem. Rev.*, 2006, **106**, 4044–4098.
- A. Corma, S. Iborra and A. Velty, *Chem. Rev.*, 2007, **107**, 2411–2502.
- P. Gallezot, *Chem. Soc. Rev.*, 2012, **41**, 1538–1558.
- M. Besson, P. Gallezot and C. Pinel, *Chem. Rev.*, 2014, **114**, 1827–1870.
- J. G. Zeikus, M. K. Jain and P. Elankovan, *Appl. Microbiol. Biotechnol.*, 1999, **51**, 545–552.
- C. Delhomme, D. Weuster-Botz and F. E. Kuehn, *Green Chem.*, 2009, **11**, 13–26.
- I. Bechthold, K. Bretz, S. Kabasci, R. Kopitzky and A. Springer, *Chem. Eng. Technol.*, 2008, **31**, 647–654.
- J. E. Carnahan, T. A. Ford, W. F. Gresham, W. E. Grigsby and G. F. Hager, *J. Am. Chem. Soc.*, 1955, **77**, 3766–3767.
- J. T. Schwartz, *United States Pat*, US1995/5478952A1, 1995.
- J. T. Schwartz, *United States Pat*, US1996/9627436, 1996.
- R. M. Deshpande, V. V. Buwa, C. V. Rode, R. V. Chaudhari and P. L. Mills, *Catal. Commun.*, 2002, **3**, 269–274.
- R. Luque, J. H. Clark, K. Yoshida and P. L. Gai, *Chem. Commun.*, 2009, **35**, 5305–5307.
- S. H. Chung, Y. M. Park, M. S. Kim and K. Y. Lee, *Catal. Today*, 2012, **185**, 205–210.
- X. Liu, X. Wang, G. Xu, Q. Liu, X. Mu and H. Liu, *J. Mater. Chem. A*, 2015, **3**, 23560–23569.
- D. P. Minh, M. Besson, C. Pinel, P. Fuertes and C. Petitjean, *Top. Catal.*, 2010, **53**, 1270–1273.
- B. K. Ly, D. P. Minh, C. Pinel, M. Besson, B. Tapin, F. Epron and C. Especel, *Top. Catal.*, 2012, **55**, 466–473.
- L. Corbel-Demilly, B. K. Ly, D. P. Minh, B. Tapin, C. Especel, F. Epron, A. Cabiach, E. Guillon, M. Besson and C. Pinel, *ChemSusChem*, 2013, **6**, 2388–2395.
- B. Tapin, F. Epron, C. Especel, B. K. Ly, C. Pinel and M. Besson, *Catal. Today*, 2014, **235**, 127–133.
- B. K. Ly, B. Tapin, M. Aouine, P. Delichere, F. Epron, C. Pinel, C. Especel and M. Besson, *ChemCatChem*, 2015, **7**, 2161–2178.
- K. H. Kang, U. G. Hong, Y. Bang, J. H. Choi, J. K. Kim, J. K. Lee, S. J. Han and I. K. Song, *Appl. Catal., A*, 2015, **490**, 153–162.
- K. Kobayashi, T. Ichiki, S. Suzuki and H. Ueno, *Japan Pat*, JP1995/07285898A1, 1995.
- G. Ding, Y. Zhu, H. Zheng, W. Zhang and Y. Li, *Catal. Commun.*, 2010, **11**, 1120–1124.
- G. Ding, Y. Zhu, H. Zheng, H. Chen and Y. Li, *J. Chem. Technol. Biotechnol.*, 2011, **86**, 231–237.
- J. K. Kouba and A. Zletz, *United States Pat*, US1986/4613707A1, 1986.
- U. G. Hong, H. W. Park, J. Lee, S. Hwang, J. Kwak, J. Yi and I. K. Song, *J. Nanosci. Nanotechnol.*, 2013, **13**, 7448–7453.
- U. G. Hong, J. K. Kim, J. Lee, J. K. Lee, J. Yi and I. K. Song, *J. Nanosci. Nanotechnol.*, 2014, **14**, 8867–8872.
- K. H. Kang, U. G. Hong, J. O. Jun, J. H. Song, Y. Bang, J. H. Choi, S. J. Han and I. K. Song, *J. Mol. Catal. A: Chem.*, 2014, **395**, 234–242.
- W. Li, J.-H. Xie, M.-L. Yuan and Q.-L. Zhou, *Green Chem.*, 2014, **16**, 4081–4085.
- U. Hermann and G. Emig, *Ind. Eng. Chem. Res.*, 1997, **36**, 2885–2896.
- W. De Thomas, P. D. Taylor and H. F. Tomfohrde, *United States Pat*, US1992/5149836A1, 1992.
- M. Roesch, R. Pinkos, M. Hesse, S. Schlitter, H. Junicke, O. Schubert, A. Weck and G. Windecker, *PCT Int. Appl.*, WO2005/058853A2, 2005.
- G. Budroni and A. Corma, *J. Catal.*, 2008, **257**, 403–408.
- B. Tapin, F. Epron, C. Especel, B. K. Ly, C. Pinel and M. Besson, *ACS Catal.*, 2013, **3**, 2327–2335.
- J. N. Cawse, N. E. Johnson and M. T. Whitaker, *United States Pat*, US1987/4652685A1, 1987.
- H. Ueno, *Japan Pat*, JP1991/03178943, 1991.
- W. De Thomas and P. D. Taylor, *United States Pat*, US1989/4797382A1, 1989.
- B. Aldo and V. L. Illica, *United States Pat*, US1999/9935114, 1999.
- T. Fuchigami, N. Wakasa and N. Iwai, *Japan Pat*, JP1995/07082189A1, 1995.
- K. Wada and Z. Hara, *Japan Pat*, JP1989/01290640, 1989.
- W. Li, J. H. Xie, M. L. Yuan and Q. L. Zhou, *Green Chem.*, 2014, **16**, 4081–4085.
- D. C. Elliott, S. W. Fitzpatrick, J. J. Bozell, J. L. Jarnefeld, R. J. Bilski, L. Moens, Y. Wang and G. G. Neuenschwander, *Resour., Conserv. Recycl.*, 2000, **28**, 227–239.
- L. E. Manzer, *ACS Symp. Ser.*, 2006, **921**, 40–51.
- S. W. Fitzpatrick, *ACS Symp. Ser.*, 2006, **921**, 271–287.
- H. Mehdi, V. Fabos, R. Tuba, A. Bodor, L. T. Mika and I. T. Horvath, *Top. Catal.*, 2008, **48**, 49–54.
- F. M. A. Geilen, B. Engendahl, A. Harwardt, W. Marquardt, J. Klankermayer and W. Leitner, *Angew. Chem., Int. Ed.*, 2010, **49**, 5510–5514.
- F. M. A. Geilen, B. Engendahl, M. Holscher, J. Klankermayer and W. Leitner, *J. Am. Chem. Soc.*, 2011, **133**, 14349–14358.
- T. Mizugaki, Y. Nagatsu, K. Togo, Z. Maeno, T. Mitsudome, K. Jitsukawa and K. Kaneda, *Green Chem.*, 2015, **17**, 5136–5139.
- M. Li, G. Li, N. Li, A. Wang, W. Dong, X. Wang and Y. Cong, *Chem. Commun.*, 2014, **50**, 1414–1416.

- 49 C. K. Shu and B. M. Lawrence, *J. Agric. Food Chem.*, 1995, **43**, 782–784.
- 50 P. P. Upare, J. M. Lee, Y. K. Hwang, D. W. Hwang, J. H. Lee, S. B. Halligudi, J. S. Hwang and J. S. Chang, *ChemSusChem*, 2011, **4**, 1749–1752.
- 51 P. P. Upare, J. M. Lee, D. W. Hwang, S. B. Halligudi, Y. K. Hwang and J. S. Chang, *J. Ind. Eng. Chem.*, 2011, **17**, 287–292.
- 52 X.-L. Du, Q.-Y. Bi, Y.-M. Liu, Y. Cao, H.-Y. He and K.-N. Fan, *Green Chem.*, 2012, **14**, 935–939.
- 53 Q. Xu, X. Li, T. Pan, C. Yu, J. Deng, Q. Guo and Y. Fu, *Green Chem.*, 2016, **18**, 1287–1294.
- 54 A. S. Mamman, J. M. Lee, Y. C. Kim, I. T. Hwang, N. J. Park, Y. K. Hwang, J. S. Chang and J. S. Hwang, *Biofuels, Bioprod. Biorefin.*, 2008, **2**, 438–454.
- 55 S. Lima, M. M. Antunes, A. Fernandes, M. Pillinger, M. F. Ribeiro and A. A. Valente, *Appl. Catal., A*, 2010, **388**, 141–148.
- 56 G. Seo and H. Chon, *J. Catal.*, 1981, **67**, 424–429.
- 57 Y. Nakagawa, M. Tamura and K. Tomishige, *ACS Catal.*, 2013, **3**, 2655–2668.
- 58 K. Yan, G. Wu, T. Lafleur and C. Jarvis, *Renewable Sustainable Energy Rev.*, 2014, **38**, 663–676.
- 59 V. Vetere, A. B. Merlo, J. F. Ruggera and M. L. Casella, *J. Braz. Chem. Soc.*, 2010, **21**, 914–920.
- 60 S. Bhogeswararao and D. Srinivas, *J. Catal.*, 2015, **327**, 65–77.
- 61 M. J. Taylor, L. J. Durndell, M. A. Isaacs, C. M. A. Parlett, K. Wilson, A. F. Lee and G. Kyriakou, *Appl. Catal., B*, 2016, **180**, 580–585.
- 62 M. Tamura, K. Tokonami, Y. Nakagawa and K. Tomishige, *Chem. Commun.*, 2013, **49**, 7034–7036.
- 63 Q. Yuan, D. Zhang, L. Haandel, F. Ye, T. Xue, E. J. M. Hensen and Y. Guan, *J. Mol. Catal. A: Chem.*, 2015, **406**, 58–64.
- 64 Rodiansono, S. Khairi, T. Hara, N. Ichikuni and S. Shimazu, *Catal. Sci. Technol.*, 2012, **2**, 2139–2145.
- 65 H. Li, H. Luo, L. Zhuang, W. Dai and M. Qiao, *J. Mol. Catal. A: Chem.*, 2003, **203**, 267–275.
- 66 X. Chen, H. Li, H. Luo and M. Qiao, *Appl. Catal., A*, 2002, **233**, 13–20.
- 67 S. Wei, H. Cui, J. Wang, S. Zhuo, W. Yi, L. Wang and Z. Li, *Particuology*, 2011, **9**, 69–74.
- 68 M. Audemar, C. Ciotonea, K. Vigier, S. Royer, A. Ungureanu, B. Dragoi, E. Dumitriu and F. Jerome, *ChemSusChem*, 2015, **8**, 1885–1891.
- 69 B. Liu, L. Lu, B. Wang, T. Cai and K. Iwatani, *Appl. Catal., A*, 1998, **171**, 117–122.
- 70 M. M. Villaverde, N. M. Bertero, T. F. Garetto and A. J. Marchi, *Catal. Today*, 2013, **213**, 87–92.
- 71 M. M. Villaverde, T. F. Garetto and A. J. Marchi, *Catal. Commun.*, 2015, **58**, 6–10.
- 72 C. Xu, L. Zheng, J. Liu and Z. Huang, *Chin. J. Chem.*, 2011, **29**, 691–697.
- 73 K. Fulajtarova, T. Sotak, M. Hronec, I. Vavra, E. Dobrocka and M. Omastova, *Appl. Catal., A*, 2015, **502**, 78–85.
- 74 R. V. Sharma, U. Das, R. Sammynaiken and A. K. Dalai, *Appl. Catal., A*, 2013, **454**, 127–136.
- 75 A. B. Merlo, V. Vetere, J. F. Ruggera and M. L. Casella, *Catal. Commun.*, 2009, **10**, 1665–1669.
- 76 J. Kijenski, P. Winiarek, T. Paryjczak, A. Lewicki and A. Mikolajska, *Appl. Catal., A*, 2002, **233**, 171–182.
- 77 S. Sithisa and D. E. Resasco, *Catal. Lett.*, 2011, **141**, 784–791.
- 78 D. Vargas-Hernandez, J. M. Rubio-Caballero, J. Santamaria-Gonzalez, R. Moreno-Tost, J. M. Merida-Robles, M. A. Perez-Cruz, A. Jimenez-Lopez, R. Hernandez-Huesca and P. Maireles-Torres, *J. Mol. Catal. A: Chem.*, 2014, **383–384**, 106–113.
- 79 J. Wu, Y. Shen, C. Liu, H. Wang, C. Geng and Z. Zhang, *Catal. Commun.*, 2005, **6**, 633–637.
- 80 X. Y. Hao, W. Zhou, J. W. Wang, Y. Q. Zhang and S. Liu, *Chem. Lett.*, 2005, **34**, 1000–1001.
- 81 B. M. Nagaraja, V. Siva Kumar, V. Shasikala, A. H. Padmasri, B. Sreedhar, B. David Raju and K. S. Rama Rao, *Catal. Commun.*, 2003, **4**, 287–293.
- 82 M. Li, Y. Hao, F. Cardenas-Lizana and M. A. Keane, *Catal. Commun.*, 2015, **69**, 119–122.
- 83 B. M. Nagaraja, A. H. Padmasri, B. D. Raju and K. S. R. Rao, *J. Mol. Catal. A: Chem.*, 2007, **265**, 90–97.
- 84 J. G. Stevens, R. A. Bourne, M. V. Twigg and M. Poliakoff, *Angew. Chem., Int. Ed.*, 2010, **49**, 8856–8859.
- 85 N. Merat, C. Godawa and A. Gaset, *J. Chem. Technol. Biotechnol.*, 1990, **48**, 145–159.
- 86 Y. Nakagawa, H. Nakazawa, H. Watanabe and K. Tomishige, *ChemCatChem*, 2012, **4**, 1791–1797.
- 87 Y. Nakagawa and K. Tomishige, *Catal. Commun.*, 2010, **12**, 154–156.
- 88 S. Liu, Y. Amada, M. Tamura, Y. Nakagawa and K. Tomishige, *Green Chem.*, 2014, **16**, 617–626.
- 89 B. Chen, F. Li, Z. Huang and G. Yuan, *Appl. Catal., A*, 2015, **500**, 23–29.
- 90 N. S. Biradar, A. M. Hengne, S. N. Birajdar, P. S. Niphadkar, P. N. Joshi and C. V. Rode, *ACS Sustainable Chem. Eng.*, 2014, **2**, 272–281.
- 91 S. Koso, N. Ueda, Y. Shinmi, K. Okumura, T. Kizuka and K. Tomishige, *J. Catal.*, 2009, **267**, 89–92.
- 92 S. Koso, I. Furikado, A. Shima, T. Miyazawa, K. Kunimori and K. Tomishige, *Chem. Commun.*, 2009, 2035–2037.
- 93 K. Chen, S. Koso, T. Kubota, Y. Nakagawa and K. Tomishige, *ChemCatChem*, 2010, **2**, 547–555.
- 94 K. Chen, K. Mori, H. Watanabe, Y. Nakagawa and K. Tomishige, *J. Catal.*, 2012, **294**, 171–183.
- 95 S. I. Koso, Y. Nakagawa and K. I. Tomishige, *J. Catal.*, 2011, **280**, 221–229.
- 96 S. Koso, H. Watanabe, K. Okumura, Y. Nakagawa and K. Tomishige, *Appl. Catal., B*, 2012, **111–112**, 27–37.
- 97 Y. Nakagawa and K. Tomishige, *Catal. Today*, 2012, **195**, 136–143.
- 98 Y. Nakagawa, M. Tamura and K. Tomishige, *Catal. Surv. Asia*, 2015, **19**, 249–256.
- 99 J. Guan, G. Peng, Q. Cao and X. Mu, *J. Phys. Chem. C*, 2014, **118**, 25555–25566.

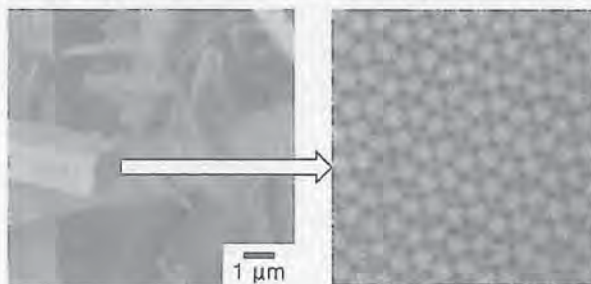
- 100 M. Chatterjee, H. Kawanami, T. Ishizaka, M. Sato, T. Suzuki and A. Suzuki, *Catal. Sci. Technol.*, 2011, **1**, 1466–1471.
- 101 L. E. Schniepp and H. H. Geller, *J. Am. Chem. Soc.*, 1946, **68**, 1646–1648.
- 102 M. Chia, Y. J. Pagán-Torres, D. Hibbitts, Q. Tan, H. N. Pham, A. K. Datye, M. Neurock, R. J. Davis and J. A. Dumesic, *J. Am. Chem. Soc.*, 2011, **133**, 12675–12689.
- 103 W. Dong, N. Li, A. Wang, X. Wang, Y. Wang, T. Cong and J. Zhang, *J. Energy Chem.*, 2014, **23**, 427–434.
- 104 B. Pholjaroen, N. Li, Y. Huang, L. Li, A. Wang and T. Zhang, *Catal. Today*, 2015, **245**, 93–99.
- 105 W. Xu, H. Wang, X. Liu, J. Ren, Y. Wang and G. Lu, *Chem. Commun.*, 2011, **47**, 3924–3926.
- 106 S. Liu, Y. Amada, M. Tamura, Y. Nakagawa and K. Tomishige, *Catal. Sci. Technol.*, 2014, **4**, 2535–2549.
- 107 B. Zhang, Y. Zhu, G. Ding, H. Zheng and Y. Li, *Green Chem.*, 2012, **14**, 3402–3409.
- 108 T. Mizugaki, T. Yamakawa, Y. Nagatsu, Z. Maeno, T. Mitsudome, K. Jitsukawa and K. Kaneda, *ACS Sustainable Chem. Eng.*, 2014, **2**, 2243–2247.
- 109 F. Li, T. Lu, B. Chen, Z. Huang and G. Yuan, *Appl. Catal., A*, 2014, **478**, 252–258.
- 110 J. Lee, Y. T. Kim and G. W. Huber, *Green Chem.*, 2014, **16**, 708–718.

複雑構造がもたらす複合酸化物の選択酸化触媒能

上田 渉
(神奈川大学工学部)

Overview

固 体触媒物質はただ複雑なものと考えてしまいがちである。しかし、その複雑性の中身がわかるにつれ、実はその複雑な状態は密接に触媒機能と関連していたのである。その一例が気相選択酸化の触媒となる複合酸化物である。最近合成された結晶性 MoVO 触媒は、元素構成は単純でありながら、その高次元な結晶構造は複数の酸素八面体からなるユニット単位で組織化され、さまざまな状態の酸素八面体からなっていて、酸化物触媒の従来の元素単位の視点を超えていたのである(オーバービュー図)。このような構造組織を形成したときのみアルカンの選択酸化に活性を示し、アルカン酸化触媒の研究に新展開をもたらした。同時にこの触媒は工業的なプロセスであるアクロレイン酸化によるアクリル酸合成にきわめて高い活性を有していた。このように、触媒の状態に見られる複雑性は高機能性触媒の本質的な姿であることがわかってきた。構造的な複雑性が触媒の機能性を左右する系は、固体触媒には多く存在していると考えられる。



▲ Mo_3VO_x 触媒の SEM と HAADF-STEM 像
明るい点は Mo 原子で、五角形の集積によりできる網目状の構造が触媒作用の根源。

■ KEYWORD □マークは用語解説参照

- 複合酸化物触媒 (complex metal oxide catalysts)
- 高次元な結晶構造 (high dimensional crystal structure)
- ユニット合成 (unit synthesis)
- ポリオキシメタレート (polyoxometalates) □
- 水熱合成 (hydrothermal synthesis) □
- Mo_3VO_x 触媒 (Mo_3VO_x catalysts)
- アルカン選択酸化 (selective oxidation of alkanes) □
- アクロレイン選択酸化 (selective oxidation of acrolein)
- 細孔構造 (pore structure)
- 酸素分子活性化 (activation of molecular oxygen)

はじめに

固体触媒は、触媒反応が必然とする動的な変化をしっかりと担保した固体物質でなくてはならない。とくに触媒酸化反応のように有機反応物と酸素分子の活性化を同時に成し遂げるうえで動的な変化の成立は欠かせない。その意味で単純な二次元的固体表面の触媒作用の理解といった旧来の視点では到底触媒反応を成立させることはできない。実際、触媒開発、とくに選択酸化触媒開発の歴史からわかるように、固体表面の機能だけを基本として触媒作用を理解するような学術的取り組みとは大きくかけ離れて、触媒自体は構成元素種的にも構造的にもはるかに複雑化させ、見事に工業触媒を成立させてきた。三次元的固体表面反応場が多くの元素の構造的秩序と協調で成立していることが伺える。これは固体触媒研究者であれば誰もが思うことであるが、その具体を示すことはこれまでほとんどなかった。また、固体触媒のさらなる進化への要望は年々強くなるなか、ただただ複雑化をきわめ、そのことは結果として触媒活性部位の真の姿を見えなくさせ、かえって進化の速度を弱めた部分もあった。

そのようななか、最近、アルカン酸化やアクロレイン酸化にきわめて高活性な結晶性 Mo_3VO_x 触媒物質が登場し、工業触媒の根源をなす物質として注目を集めた。その物質は決して単に複雑なのではなく、美しい秩序ある複雑物質となっていた。この物質は、筆者とそのグループが秩序ある複雑物質をはじめから設計的につくることを目的に、構造ユニットの考え方すなわち二次元性連続ユニット(層構造)や二次元性ポリ酸ユニット(平面性ポリ酸)、三次元性ポリ酸ユニット(球状ポリ酸)などをビルディングユニットとして三次元固体と導くことでユニットの構造性が保たれたまま、高次構造形成が可能となる方法論の展開のなかで生まれた。このことは逆に、触媒開発のなかでさまざまに検討され、最適化された触媒調製方法自体が、結果として秩序ある複雑構造形が生まれるようにしていた、との理解につながった。

本章は以上の流れの一端をまとめる。

⑦ 選択酸化とその複合酸化物触媒の複雑化

有機物の酸化はエネルギーを生み、あるいは化学品を生む反応である。その重要性は次の簡単な説明から理解できる。すなわち、生命は生体内酸素酸化を利用して生命体を維持、構築している。そして自然界では酸化と逆の反応すなわち光合成が同時に進行し、バランスが成立している。一方、人工的な酸化プロセスにおいては、化石資源を使うかぎりバランスを取る逆の反応はいまのところ成立していない。当然のことながら光触媒など人工光合成の進歩はこれから進むであろうが、当面は人工的な有機物の酸化は触媒を使ってより効率よく、環境に適合した反応にしていくことが求められる。触媒を使わない内燃機関から触媒を駆使した燃料電池への効率化のシフトが起ころうしているのはこのことの現れである。

化学工業では酸化触媒は著しく発展し、実に多くの酸化触媒プロセスが工業化した。代表例はプロピレンからアクリル酸を製造する気相酸化反応で、きわめて完成度が高い。この反応は中間にアクロレインを経由する二段プロセスであるにもかかわらず、一段目で95%、後段で98%の驚異的な収率を達成し、全体で93%の収率でアクリル酸が得られる^[1]。ここで使われる触媒は5種以上の元素から構成されるのが普通で、複雑化した触媒の代表である^[2]。それでもなお、より効率の高みを目指して開発の努力がなされている。しかし、はじめに記したように、酸化触媒が早い時期に複雑化の方法論を取り入れ、成功したため、その後の開発に難度が高くなっている。これまでの延長ではない、複雑の本質をもとにした触媒改良が必要な時機にきている。

複雑になる原因は酸化反応の本質にある。すなわち、酸素分子の複雑な活性化プロセスと活性化された有機物と活性酸素との反応の多様性にある。したがって、目的どおりに反応を起こさせるためには、いうまでもなく触媒による酸化反応の制御が不可欠である。また、多くの反応ステップの制御を完全に行わせるには、単一元素の触媒で行わせるのはほとんど無理で、複数の触媒元素でつくる複数の触媒機能が協働する構造環境を整えることが必要になる^[3]。多くの金属元素から構成できる複合酸化物が選択酸

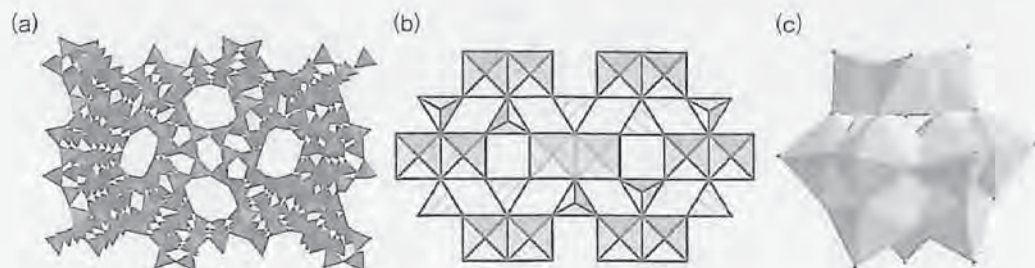


図 4-1 単核活性サイトのチタノシリケート(a)、二核活性サイトのピロリン酸バナジル (b)、複核活性サイトのケギン型ポリオキソメタレート(c)

化触媒として最も適し、実際に多くの気相選択酸化反応で使われているのは当然の帰結と思われる。

酸化物触媒の複雑性を理解するため、触媒の構造に基づく活性サイト広がり大きさとの関係を以下比較する(図 4-1)。単核的な酸化活性サイトを構成する例がチタノシリケート[図 4-1(a)]である。これは有機物を過酸化水素酸化する触媒である。多孔性であり、酸化活性元素である Ti サイトがゼオライト格子中に孤立した状態にあることを特徴とする。触媒作用点自体は Ti サイトであるので複雑さはないが、厳密に触媒作用する Ti の構造環境をゼオライトが規定していることや、ゼオライトの細孔環境が反応する有機分子を規制している点など、単なる 1 個の活性点で触媒が成立していない意味で複雑さがある。ゼオライト構造が生み出した触媒作用場といえる。

次がピロリン酸ジバナジル触媒[図 4-1(b)]で、ブタンの気相酸化による無水マレイン酸合成に活性を示すものである^[1]。活性サイトはバナジウム酸素多面体の二核がペアになっているところで、二核ペアが四面体配位の P によって取り囲まれ孤立している。同じ V と P の構成でありながら非晶質の複合酸化物では触媒機能が低く、このような構造が生じてはじめて触媒機能が発現した。この発見は、結晶で形成される局所構造のもつ重要性が認識されるきっかけとなった。しかしながら、ブタンを活性化する活性酸素を発生させるために二核ペアの形成を必要とした、とのレベルで理解は止まっていて、真の理解になっているか判断はつかない。実際のところ、この事実をもとにしたさらなる触媒の発展が見られていないことから、より深い、複雑な触媒作用

構造を導き出す必要性が残っているのではないだろうか。また一面、一定の結晶構造形成が必然となるため、触媒のさらなる複雑化を阻んでいることも、発展が進まない要因であろう。

核数をさらに大きくし、その数が複核(多くの場合は 12 個)で単一な物質、すなわちポリオキソメタレート(あるいはケギン型のヘテロポリ酸)触媒も酸化物触媒の一群に加えられる[図 4-1(c)]^[2]。この物質は前述の酸化物触媒の例とは大きく異なり、三次元的に広がりをもった分子性の複核酸化物クラスターが孤立活性サイトを構成していて、それがさらに三次元的に結晶を形成し、固体となったものである。孤立した複核酸化物クラスター自身が触媒となるため、触媒物質の電子状態や構造環境が厳密に規定でき、さらにはカウンターカチオンにプロトンがなることが可能で、酸性質も加味することができる特徴ある物質である。活性構造がより均質である点が有利に作用し、反応性に富む有機物の選択酸素酸化や過酸化水素酸化に活性を示す。すでにこのような構造的意味において複雑さは生まれているが、実際の工業触媒はさらに構成元素が複雑であり、実態ではまだ未知の複雑構造状態が成立している可能性は高い。

2 複雑さを導くユニット合成の考えと結晶性 Mo_3VO_x 酸化物の創出

前述の孤立活性サイト形成とその環境の複雑化の方向性を考えてみれば、複数の触媒元素を結晶構造的に高次に配列することが可能になれば、従来の触媒合成の限界を超え、より高度な触媒機能が生まれと考えるのは当然であろう。そうすれば、酸化物触

媒で金属-酸素結合サイトの局所的視点から広がりをもった高次な金属-酸素結合ネットワークの触媒場が生まれよう。問題はその方法論である。一つの有効な方法として構造ユニットの考え方がある。構造ユニットの考え方は、ポリオキソメタレート物質合成^[6]や有機固体の合成^[7]の分野で大きく進展してきたものである。ポリオキソメタレートはさまざまな物質群からなる。これを合成するうえで、ポリオキソメタレートの構成ユニットを切りだし、これを新しい方向性で組み立てて、新しいポリオキソメタレートを合成しようとするものである。また、ポリオキソメタレート自体を構造ユニットとし、有機物質と介在させて共有結合を成立させるなどの方法でポリオキソメタレート自体を高次構造物質へと導く取り組みもある。有機物をリンカーとしたポリオキソメタレートユニットが連結したフレームワークの物質が合成されるようになり、反応物を取り込むことができる細孔空間をもち、安定したポリ酸物質が達成されている。

固体触媒合成での構造ユニットの取り組みは少ないが、金属酸化物触媒を対象とした場合でも、分子性構造が明確なポリオキソメタレートが有効と考えられる。そこで、筆者らは二次元性ポリ酸ユニット、すなわち平面性ポリ酸ユニットに着目した。三次元性ポリ酸ユニットの複雑性を低減する考えである。すなわち、平面性ポリ酸ユニットを無機のリンカーで結合展開し、板状構造体を形成させ、その後板状構造体を積層させ、三次元固体とするものである。二次元性ポリ酸ユニットとしてアンダーソン型のヘテロポリモリブデン酸を、無機のリンカーとしてカチオン性のバナジルイオンを選んだ。さらに、ポリ酸ユニットを無機のリンカーで結合展開が高次な構造で進むためにはソフトな合成条件が必要と考え、水熱合成を採用した。

合成手順はきわめて単純である。アンダーソン型ヘテロポリモリブデン酸を別途合成し、これにバナジルイオンを加えて水熱合成するだけである。きわめて容易に固体物質が得られた。しかし、水熱合成のようなソフトな方法だけでは、完全な形で構造ユニットを保持したまま三次元結晶にすることはでき

なかった。そこで想定する構造ユニットの別途合成はひとまず別にし、酸性条件であれば単純なモリブデンの原料もポリ酸イオンとして存在できるうえ、リンカーとして硫酸バナジルを用いると pH 調整する必要もなく混合溶液は酸性を示すことから、まったく工夫のない直接的な合成法を検討した。水熱合成したところ、思いがけず結晶の物質が得られ、これが Mo_3VO_x 酸化物結晶であった^[8]。この段階では一見ユニット合成らしきものが成功したかに見えたが、得られた物質はまったく想定を超えていた。しかし、後述するように、結果としてユニット合成がまったく別の物質で成立していたのは幸いであった。

得られた Mo_3VO_x 酸化物は予想を超えた美しい複雑物質であった。それはこの物質の高角度環状暗視野走査透過型電子顕微鏡 (high-angle annular dark-field scanning transmission electron microscopy: HAADF-STEM) 像^[9,10]がはっきり示している。pH = 3.2 の条件で斜方晶 [図 4-2(a)] が生成し、pH = 2.2 の条件で三方晶 [図 4-2(b)] が生成する。これらは五員環状ユニットの配置が異なる構造変態である。これらは層状構造をとり、強い異方性を示し、c 軸方向の元素配列様式はまったく同じであるが、a-b 面の図 4-2 の像をよく見ると、5 個の酸素八面体が五角両錐を中心に稜共有した 6 金属からなる五員環ユニット $\{\text{Mo}_5\text{O}_{21}\}$ が全体に見える。これらは酸素八面体 (リンカー) を介して一面につながっていることがわかる。すなわち、五員環ユニットが連結したユニットネットワークが形成されている。

さらに、リンカー酸素八面体と五員環ユニット $\{\text{Mo}_5\text{O}_{21}\}$ とは HAADF-STEM 像コントラストが異なることがわかる。すなわち、五員環ユニット部位には原子量の重い Mo がもっぱらここに位置し、一方リンカー酸素八面体部位は原子量の軽い V が多く占有していることを示している。このことは三方晶でも確認され、また斜方晶の加熱処理によって得られる正方晶 [図 4-2(c)] でも確認される。まさに五員環ユニットが連結酸素八面体 (バナジルリンカー) とつながって、ユニットが一面に広がったユニットネットワークが形成し、これが積層して三次

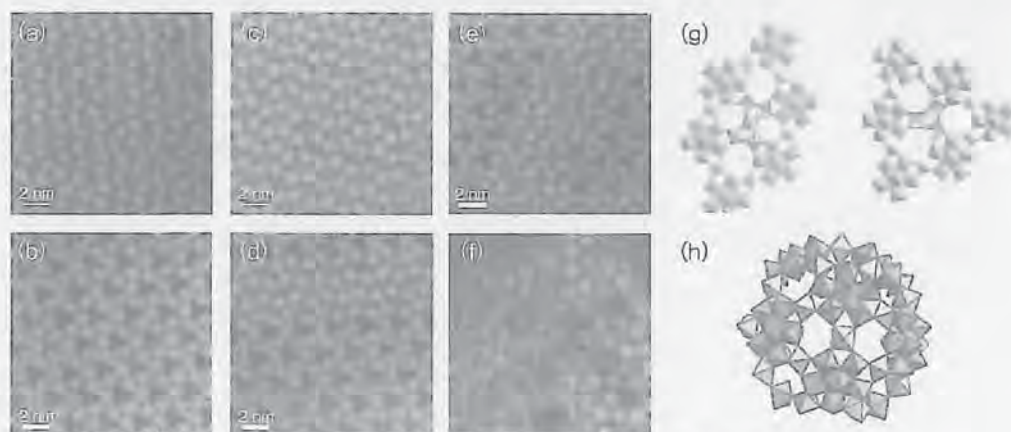


図 4-2 結晶性 Mo_3VO_x 酸化物の HAADF-STEM 像 (a - b 面)

(a) 斜方晶, (b) 三方晶, (c) 正方晶, (d) 結晶不整, (e) 結晶不整, (f) アモルファス相, (g) 酸化物局所構造(斜方晶:左, 三方晶:右), (h) ポリ酸型前駆体 $\text{Mo}_{72}\text{V}_{30}$.

元固体へと結晶化することを示している。すなわち、結晶構造が五員環ユニットの配列で決定されていることを意味する。また、このことにより五員環ユニットの連結が異なった方向に進むと三方晶になることが説明できる。このことは三方晶の一部で見られた結晶不整の存在[図 4-2(d), (e)]からも支持される。すなわち、単純な金属酸化物の結晶不整は元素の単位で生じるが、結晶性 Mo_3VO_x 酸化物ではユニット単位で結晶不整が起こっていることがわかる。アモルファス状態の Mo_3VO_x 酸化物でも五員環ユニットが構造形成基本ユニットになっている。ただそれが不規則になっているだけである[図 4-2(f)]。

さらに構造を詳しく見ると、五員環ユニットネットワークによって隙間空間が形成され[図 4-2(g)]、その部位に斜方晶では 5 個の酸素八面体が、三方晶では 3 個の酸素八面体を取り込まれていることがわかる。隙間空間の大きさは五員環ユニットネットワークによって決定され、斜方晶では 5 個の酸素八面体が位置するうえでぴったりの空間をもつが、三方晶ではその空間が 3 個の酸素八面体を取り込む以上の広さをもつため、安定的に占有することができず(占有率が低い)、HAADF-STEM 像[図 4-2(b)]からわかるように、暗いコントラストになっている。

さらに加えて、五員環ユニットネットワークによって形成された隙間空間に斜方晶では 5 個の酸素八面体クラスターが、三方晶では 3 個の酸素八面体

クラスターが取り込まれると同時に、その近辺に六員環チャンネル構造と七員環チャンネル構造が形成される。これは HAADF-STEM 像から容易に確認でき、さらにはこれらのチャンネルの中心部には元素は存在しないことがわかる。後述するように七員環チャンネル構造部位は細孔として機能できる構造である。以上のように、結晶性 Mo_3VO_x 酸化物の a - b 面は平面構造でありながら、五員環ユニットネットワーク、酸素八面体クラスター、六員環チャンネル構造、そして七員環チャンネルポア構造が組織的に複雑に集積している。

このような複雑な構造がユニット単位で生じていることは大変興味深い⁸、同時に構成元素の構造中に位置が限定されていることも重要な意味をもっている。すなわち通常 Mo と V は酸化物中では互いの位置を共有できるので、何らかの規制が合成段階で働いていることを意味している。このことを詳しく調べたところ、原料調製過程でまさに当初意図していたユニット合成が働いていたのである。まず水熱合成前の溶液中には、六価モリブデンと四価バナジウムが反応して Mo 酸素八面体が縮合した五員環状ユニットからなるボール状のポリ酸型前駆体^[11] $\text{Mo}_{72}\text{V}_{30}$ [図 4-2(h)]が最初に生成していることが、ラマン分光、UV-vis 分光で判明した^[8]。このポリ酸は、結晶性 Mo_3VO_x 酸化物固体で見られた五員環ユニット $\{\text{Mo}_6\text{O}_{21}\}$ をすでに備え、同時にこれらのユニットはバナジウムイオンリンカーで連結されてい

ることから、この構造様式をそのままに水熱条件下で三次元固体に変化したことになる。これなら、構成元素の構造位置が限定されていたことも説明できる。また、ボール状のポリ酸型前駆体 $\text{Mo}_{72}\text{V}_{30}$ が生成しない条件ではまったく結晶が生成しないことも符合する。したがって、結果的にユニット合成が成立していたことになった。

結晶生成過程を要約すると次のようになる。ポリ酸型前駆体 $\text{Mo}_{72}\text{V}_{30}$ が第一段階である。これにはすでに五員環ユニットが形成されている。水熱合成条件下で $\text{Mo}_{72}\text{V}_{30}$ 中の五員環状ユニットは遊離し、平面性五員環状ポリ酸ユニット $\{\text{Mo}_6\text{O}_{21}\}$ を生じる。これが再度バナジウムリンカーで縮合することで板状組織が形成される。これが積層することで三次元固体となる。平面性ポリ酸ユニット $\{\text{Mo}_6\text{O}_{21}\}$ は pH が 3.2 では 1 個のバナジウムリンカーが介したペアで存在し、その構造を反映して斜方晶に見られるユニットネットワーク(リンカーを介した $\{\text{Mo}_6\text{O}_{21}\}$ の無限つながり)が形成される。酸性度が上がると平面性ポリ酸ユニット $\{\text{Mo}_6\text{O}_{21}\}$ の縮合が進み、3 個の平面性ポリ酸ユニット $\{\text{Mo}_6\text{O}_{21}\}$ が連なった縮合体が形成され、この縮合ユニット構造を保持したまま三方晶結晶にみられるユニットネットワークを形成する。このようにしてできたユニットネットワークの間隙に斜方晶では 5 個の酸素八面体 (Mo と V) が、三方晶では 3 個の酸素八面体が位置して結晶化を完了する^[12, 13]。

③ 結晶性 Mo_3VO_x の選択酸化触媒能

以上のようにして得られた結晶性 Mo_3VO_x 触媒はほかの複合酸化物触媒に比べ特異的にアルカン酸化に高活性で、とくに低温領域で十分な活性を示した。たとえば、この触媒は 200℃ 以下の条件でもエタンを選択酸化し、エチレンを 90% 程度の選択性で与える。この触媒はまた、アクロレインを気相酸化してアクリル酸を合成する工業触媒とも基盤元素を同一にし、実際この反応にもきわめて高い活性を示した。成績は工業触媒を凌駕するほどであった。工業的なアクロレイン酸化触媒の根源的な姿が現れた瞬間である。

結晶性 Mo_3VO_x 触媒がきわめて優れたエタン酸化触媒活性、アクロレイン酸化触媒活性を示すことから、複雑構造をもとに酸化活性発現の本質を理解することが可能となる。幸いなことにユニット合成法では元素組成や粒子形態を同一に、前出の結晶の a - b 面の構造配列が異なる複数の触媒、すなわち斜方晶 Mo_3VO_x 、三方晶 Mo_3VO_x 、正方晶 Mo_3VO_x 、およびアモルファス Mo_3VO_x 触媒を合成できるので、複雑構造の視点で触媒活性を比較できた。そうすると、エタン酸化の活性序列は斜方晶 $\text{Mo}_3\text{VO}_x >$ 三方晶 $\text{Mo}_3\text{VO}_x =$ アモルファス $\text{Mo}_3\text{VO}_x \gg$ 正方晶 Mo_3VO_x であった。エチレンへの選択性は触媒間で大きな差はなく、低転化率では 90% 以上である。また反応の活性化エネルギーにも差はなく、活性部位の数に差があることを示している。唯一これらの触媒で異なった物性はマイクロ細孔吸着能であった。前述のとおりマイクロ細孔吸着能は七員環チャンネルで発現する。七員環チャンネルは 0.4 nm の細孔径をもち、エタン分子は容易にチャンネル内全体に吸着できる。結晶構造からは七員環チャンネル密度が一番高いのは斜方晶であり、それに三方晶が続く。しかし、構造の説明でしたとおり、三方晶では五員環ユニットネットワークがつくる隙間空間は 3 個以上の酸素八面体からなるクラスターを保持することが可能で、七員環チャンネルは部分的に酸素八面体が侵入し、マイクロ細孔吸着能は十分に現れない。アモルファス Mo_3VO_x は七員環チャンネルをもつが、その密度は低く、正方晶 Mo_3VO_x ではまったくない。明らかに構造因子とマイクロ細孔吸着能は関連し、ひいてはエタン酸化活性と関係したことから、エタン酸化活性は七員環チャンネルのマイクロ細孔能で決定されると結論できる。さらには触媒粒子の大小に関係なく、すなわち外表面積の大小に関係なく単位重量当たりの斜方晶 Mo_3VO_x 触媒活性は一定であることがわかり、エタン分子は七員環チャンネルマイクロ細孔内全体で反応していることが明らかとなった^[14]。

結晶性 Mo_3VO_x 触媒の酸化活性の発現は以下のように考える。酸化触媒活性は第一義的には活性な酸素の生成によるところが大きい。触媒を還元すると最初に取り除かれる格子酸素は七員環チャンネル

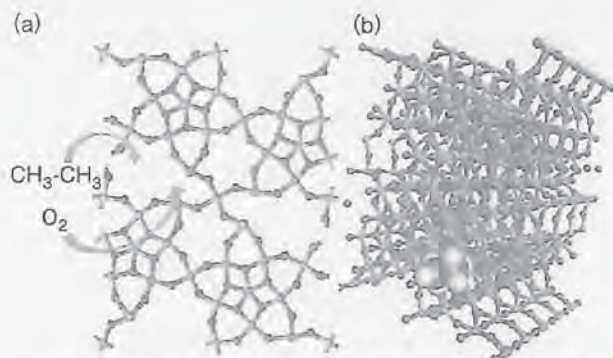


図 4-3 斜方晶 Mo_3VO_x 酸化物の七員環チャンネル内の酸素分子の活性化(a)とエタン酸化モデル(b)

に面した5個の酸素八面体クラスターの結合角をもったM-O-M(M = Mo, V)の酸素であった。また、格子酸素が取り除かれた部位に酸素分子が入り、架橋型のペルオキシ酸素種が生成する[図4-3(a)]。一方、エタン分子は容易に七員環チャンネルに侵入し、活性な酸素種と強く相互作用できる。このようにしてエタンは酸化されエチレンとなってマイクロ細孔から放出される[図4-3(b)]。結晶性 Mo_3VO_x 触媒がほかの触媒に比して低温活性であるのは、エタン分子が七員環チャンネル内の活性な触媒酸素近傍に捕捉され、分子運動が制限されて活性酸素との反応確率が上がったためと説明できる。さらに、触媒反応による格子内活性酸素のやり取りのなかで酸素八面体クラスターの構造ダイナミズムが成立する必要があるが、酸素八面体クラスターを保持している周りの五員環ユニットネットワークがこれを定常的に支えている構図が見える。このように固体酸化触媒の作用がかなり分子論的に表現できるようになった^[15]。

4 まとめと今後の展望

本章によりユニット合成による触媒機能の複雑集積の考え方は理解していただけたかと思う。しかし、同時にその難しさも感じられたかと思う。現実的にはまだ実際例が少ないからである。ただ冒頭に記したとおり、まだまだ多くの複雑な触媒物質の本質が理解されないまま現実のものとして触媒が調製され、利用されていることを考えるとユニット合成の展開を強力に押し進めないといけないであろう。あるい

は、ユニット合成に比類する新しい触媒物質合成の方法論を積極的に展開すべきであろう。高度にして秩序たる状態で固体触媒機能が生じていると考えれば、自ずとなすべき方向が見えてくるのではないだろうか。

◆ 文献 ◆

- [1] N. Nojiri, Y. Sakai, Y. Watanabe, *Catal. Rev-Sci. Eng.*, **37**, 145 (1995).
- [2] T. V. Andrushkevich, *Catal. Rev-Sci. Eng.*, **35**, 213 (1993).
- [3] Y. Moro-oka, W. Ueda, *Adv. Catal.*, **40**, 233 (1994).
- [4] M. Havecker, R. W. Mayer, A. K.-Gericke, H. Bluhm, E. Kleimenov, A. Liskowski, D. Su, R. Folloath, F. G. Requejo, D. F. Ogletree, M. Salmeron, J. A. L. Sanchez, J. K. Bartly, G. H. Hutchings, R. Schlogl, *J. Phys. Chem. B*, **107**, 4587 (2003).
- [5] T. Okuhara, N. Mizuno, M. Misono, *Adv. Catal.*, **41**, 113 (1996).
- [6] D.-L. Long, R. Tsunashima, L. Cronin, *Angew. Chem., Int. Ed.*, **49**, 1736 (2010).
- [7] S. Kitagawa, R. Kitamura, S. Noro, *Angew. Chem., Int. Ed.*, **43**, 2334 (2004).
- [8] M. Sadakane, N. Watanabe, T. Katou, Y. Nodasaka, W. Ueda, *Angew. Chem., Int. Ed.*, **46**, 1493 (2007).
- [9] W. D. Pyrz, D. A. Blom, M. Sadakane, K. Kodato, W. Ueda, T. Vogt, D. J. Buttrey, *Proc. Natl. Acad. Sci. USA*, **107**, 6152 (2010).
- [10] W. D. Pyrz, D. A. Blom, M. Sadakane, K. Kodato, W. Ueda, T. Vogt, D. J. Buttrey, *Chem. Mater.*, **22**, 2033 (2010).
- [11] A. Muller, A. M. Todea, J. van Slageren, M. Dressel, H. Bogge, M. Schmidtman, M. Luban, L. Engelhardt, M. Rusu, *Angew. Chem., Int. Ed.*, **44**, 3857 (2005).
- [12] M. Sadakane, K. Yamagata, K. Kodato, K. Endo, K. Toriumi, Y. Ozawa, T. Ozeki, T. Nagai, Y. Matsui, N. Sakaguchi, W. D. Pyrz, D. J. Buttrey, D. A. Bolm, T. Vogt, W. Ueda, *Angew. Chem., Int. Ed.*, **48**, 3782 (2009).
- [13] H. Sadakane, T. Murayama, K. Endo, W. Ueda, *Eur. J. Inorg. Chem.*, **10-11**, 173 (2013).
- [14] S. Ishikawa, X. D. Yi, T. Murayama, W. Ueda, *Appl. Catal., General A*, **474**, 10 (2014).
- [15] S. Ishikawa, D. Kobayashi, T. Konya, S. Ohmura, T. Murayama, N. Yasuda, M. Sadakane, W. Ueda, *J. Phys. Chem., C*, **119**, 7195 (2015).

Cite this: *Catal. Sci. Technol.*, 2016,
6, 617

Microporous crystalline Mo–V mixed oxides for selective oxidations

Satoshi Ishikawa^{ab} and Wataru Ueda^{*ac}

Recent developments of crystalline Mo_3VO_x catalysts (MoVO), a new type of oxidation catalysts for selective oxidations of ethane to ethene and of acrolein to acrylic acid, are reviewed. MoVO are formed by the building unit assembly of polyoxomolybdates under hydrothermal conditions. These catalysts are composed of a network arrangement based on a $\{\text{Mo}_6\text{O}_{21}\}^{6-}$ pentagonal unit and a $\{\text{MO}_6\}$ ($M = \text{Mo}, \text{V}$) octahedral unit to form a hexagonal channel and a heptagonal channel. Between these channels, the heptagonal channel acts as a micropore of 0.40 nm in diameter which can adsorb small molecules such as CO_2 , N_2 , methane, ethane, etc. The size of the heptagonal channel micropore is reversibly and continuously tunable by redox treatment. Interestingly, the heptagonal channel activates ethane inside and acrolein on the channel located over the external surface. Tuning of the heptagonal channel size significantly modifies the catalytic performance for the selective oxidation of ethane. Strong relationships among crystal structure, microporosity, and catalytic performance were observed here.

Received 28th August 2015,
Accepted 4th November 2015

DOI: 10.1039/c5cy01435b

www.rsc.org/catalysis

1. Introduction

1.1. Selective oxidation of light alkanes

Transformation of light alkanes into olefins and valuable oxygenated compounds by catalytic selective oxidations has been attracting much attention since this reaction produces important industrial organic chemicals and intermediates, such as alcohols, aldehydes, ketones, acids, and their anhydrides. Recently, interest in the catalytic selective oxidations has been expanding because of the shale gas revolution in the USA. Therefore, utilization of light alkanes as a cheap and an abundant feedstock for the catalytic selective oxidations has been attracting further attention. However, in spite of tremendous efforts, only a limited number of processes for selective oxidations of light alkanes are used in industry due to the difficulty in obtaining a particular product.^{1–3}

The difficulty in obtaining desired products by the selective oxidation of light alkanes is largely derived from the chemical properties of alkanes, such as (i) no lone pairs of electrons, (ii) no empty orbital, and (iii) little polarity of the C–H bonds.^{1–5} For these reasons, light alkanes are poorly reactive, thus severe reaction conditions to activate light alkanes are required. This situation makes it difficult to achieve high selectivity toward the desired products because

of many undesirable side-reactions and unavoidable further oxidations of the desired products.^{4,5} In order to overcome these problems, Grasselli *et al.* introduced an important principle, which is now recognized as the site-isolation concept.^{6–8} This concept points out that active sites must be spatially isolated from each other in order to prevent overoxidation and that the active sites must be composed of the appropriate number of hydrocarbon activating elements and the appropriate number of lattice oxygens available for directing the reaction toward the desired products. This idea emphasizes the importance of the crystal structure of catalysts, more specifically, the rational design of the catalyst structure. After the proposal of this idea, the importance of catalyst synthesis to construct a well-organized crystal structure has been widely recognized in the research area of the catalytic selective oxidation of light alkanes.^{9–15}

1.2. Crystalline Mo–V based catalysts

One of the most promising catalysts for the selective oxidation of light alkanes is the Mo–V–Te–Nb oxide catalyst (MoVTeNbO) discovered by Mitsubishi Chemicals.^{16–19} This catalyst showed extremely high catalytic activity for selective (amm)oxidation of propane to acrylonitrile or to acrylic acid and selective oxidation of ethane to ethene.^{16–21} Especially, for the ammoxidation of propane, this catalyst has already been commercialized by PTT Asahi Chemical Company Limited with the production of acrylonitrile about 200 000 t per year.

There are two main crystalline phases in the active and selective MoVTeNbO catalyst: (i) an orthorhombic structure

^a Catalysis Research Center, Hokkaido University, N-21, W-10, Sapporo 001-0021, Japan

^b Research Fellow of the Japan Society for the Promotion of Science, Japan

^c Department of Material and Life Chemistry, Faculty of Engineering, Kanagawa University, 3-27, Rokkakubashi, Kanagawa-ku, Yokohama, 221-8686, Japan.
E-mail: uedaw@kanagawa-u.ac.jp; Tel: +81 45 481 5661

(space group: *Pba2*) with a composition of $(\text{Te}_2\text{O})_2\text{M}_{40}\text{O}_{112}$ ($\text{M} = \text{Mo}, \text{V}, \text{Nb}$), called the M1 phase and (ii) a pseudohexagonal structure (space group: *Pmm2*) with a composition of $(\text{TeO})\text{M}_3\text{O}_9$ ($\text{M} = \text{Mo}, \text{V}, \text{Nb}$), called the M2 phase. For these phases, the M1 phase contains all of the elements needed to complete every elementary step for the selective (amm)oxidation of propane to acrylonitrile or to acrylic acid, and actually, only the M1 phase of MoVTenbO itself can show a quite high catalytic activity for this reaction.^{8,22,23} M2 phase is reported as a co-catalyst to complete the reaction by helping the sequential oxidation of propylene, formed from propane, to acrylonitrile.^{23,24} Accordingly, the M1 phase is far more important than the M2 phase in the sense of the catalytic oxidation. The basic crystal structure of the M1 phase of MoVTenbO is the same as Orth-MoVO in Fig. 1 (as shown later). The M1 phase of MoVTenbO is composed of the network arrangement of a pentagonal $\{(\text{Nb})\text{Mo}_5\}$ unit with a MO_6 ($\text{M} = \text{Mo}, \text{V}$) octahedral unit. Due to the arrangement of these units, a hexagonal channel and a heptagonal channel are formed in the *a*-*b* plane which are stacked with each other along the *c*-direction, resulting in the formation of a rod-shaped crystal.²⁵ The center of the $\{(\text{Nb})\text{Mo}_5\}$ pentagonal unit is occupied by Nb and is surrounded by five Mo octahedra. A MO_6 ($\text{M} = \text{Mo}, \text{V}$) octahedron connects two pentagonal units as a linker. Te is located preferentially in the hexagonal channel and partly in the heptagonal channel.^{25,26} The detailed elemental composition of this phase determined by ICP, XANES and Rietveld refinement was $\text{Mo}_{0.55}^{5+}\text{Mo}_{6.76}^{6+}\text{V}_{1.52}^{4+}\text{V}_{0.17}^{5+}\text{Te}_{0.69}^{4+}\text{Nb}_{1.0}^{5+}\text{O}_x^{2-}$ ($28.34 < x < 28.69$).²⁷ For the catalytic reactions, the *a*-*b* plane is responsible for the catalysis. Actually, a grinding treatment to expose the cross-section of the rod, where the *a*-*b* plane is present, significantly enhanced the catalytic performance.²⁸ It is suggested for MoVTenbO that the combination of various elements having different roles in the catalysis

(e.g. hydrogen abstraction, oxygen insertion, product desorption) makes it possible to complete all the elementary steps smoothly which results in the high selectivity toward the desired product. The important point is that each constituting element is spatially located near to the others which allows reaction intermediates to interact with the element needed for the next reaction step. The quite high catalytic activity of MoVTenbO is now recognized due to the appropriate structural arrangement of the appropriate elements which are active for each elementary step in the selective (amm)oxidation of propane.

There are several examples of the crystalline Mo-V based catalysts besides MoVTenbO. From the late 1990s, our group has been developing the synthesis of Mo-V based materials by hydrothermal methods and successfully obtained several Mo-V based catalysts in a pure manner.^{29,30} In the early stage of the research, we successfully obtained ternary Mo-V-Te oxide (MoVTeO) and Mo-V-Sb oxide (MoVSbO) with M1 structure by a hydrothermal method.³⁰ For these materials, Te and Sb were located mainly at the hexagonal channel and partly at the heptagonal channel and the structural framework of these channels was composed only of Mo and V. This fact suggested us that the binary Mo-V oxide should be obtainable since only Mo and V can constitute the structural framework of the M1 structure. By the careful control of the synthesis temperature, synthesis time, precursor, volume, and metal concentrations, we successfully obtained a crystalline Mo_3VO_x mixed oxide with M1 structure (Orth-MoVO) for the first time in 2003 (ref. 31 and 32) (Fig. 1).

Table 1 summarizes how the Mo-V based oxides with M1 structure were developed during the past two decades. In the early 1990s, Mitsubishi Chemicals first discovered the MoVTenbO catalyst and demonstrated that this catalyst is active for the selective (amm)oxidation of propane.¹⁶⁻¹⁹ This

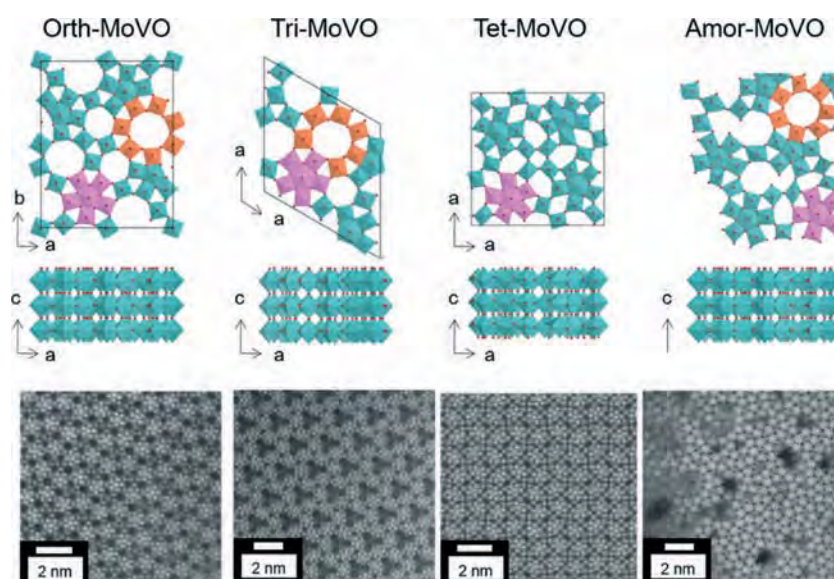


Fig. 1 Structural images and HAADF-STEM images of orthorhombic, trigonal, tetragonal, and amorphous Mo_3VO_x . Pink, pentagonal $\{\text{Mo}_6\text{O}_{21}\}^{6-}$ unit; orange, heptagonal channel. For the HAADF-STEM images, a white spot represents an element and a black spot represents a void space.

Table 1 Development of Mo–V based materials

Year	Development	Ref.
~1995	Discovery of MoVTeNbO	16–19
~1998	Application of a hydrothermal method to produce Mo–V based materials	29, 30, 33
2000	Discovery of MoVTeO and MoVSbO with M1 structure	30
~2000	Role of crystal plane in selective oxidations	28, 30
~2003	Identification of the crystal structure of MoVTeNbO	25–27
2003	Discovery of Orth-MoVO	31, 32
~2003	Identification of the constituent elements of Mo–V based materials for selective oxidations	34–39
~2008	Electron microscopy	24, 40–43
~2009	Computational calculation	22, 44–46
~2009	Investigation of the crystal formation mechanism of Mo–V based materials	47–51
~2012	<i>In situ</i> XPS analysis of Mo–V based materials during selective oxidations	52, 53
~2014	<i>In situ</i> measurement of electron conductivity during selective oxidations	54–56
~2014	Incorporation of additional elements	57, 58
~2014	Role of the micropores of Orth-MoVO in selective oxidations	59, 60
~2015	Discovery of a relationship between the crystal structure around the micropore and the catalytic activity for the selective oxidation of ethane	61

catalyst had been synthesized by a slurry method, in which a mixed solution of stoichiometric Mo, V, Te, and Nb sources is mixed and evaporated, followed by heat-treatment around 600 °C under an inert gas atmosphere. This synthesis method is simple and a large amount of the catalyst can be easily obtained. However, the reproducibility was poor and impurities were easily formed simultaneously which caused undesirable catalytic reactions. Thus, the efforts to obtain the pure MoVTeNbO catalyst with the M1 phase continued. In the late 1990s, since we thought that the formation of Mo–V based mixed oxides was a result of a self-organization of polyoxometalates, we applied a soft synthesis method, the hydrothermal method, for the synthesis of Mo–V based materials which was a less common method for the synthesis of mixed oxides at that time. As a consequence, we successfully obtained various Mo–V based mixed materials in a pure manner.^{29,30} By applying this method, synthesis of pure M1 MoVTeNbO has been achieved and high reproducibility of this synthesis has been confirmed.^{20,33} After the discovery of the synthesis method of the pure M1 MoVTeNbO, the role of the constituent elements in catalytic reactions was revealed.^{34–39} In addition, computer calculation and electron microscopy have been developed by using the highly pure and crystalline M1 MoVTeNbO as the model.^{22,24,40–46} The crystal formation mechanism has also attracted much attention since the understanding of this formation mechanism may lead to the development of synthesizing an active catalyst.^{47–51} In our view point, the recent research topics in these materials are (i) *in situ* XPS analysis of Mo–V based materials during selective oxidations,^{52,53} (ii) *in situ* measurement of the electron conductivity during selective oxidations^{54–56} as Schlögl *et al.* are focusing on, and (iii) incorporation of additional elements to enhance the catalytic activity.^{57,58}

For the synthesis of Mo–V based materials, we obtained Orth-MoVO, MoVTeO, MoVSbO, MoVsbNbO with the M1

phase. For the development of the oxidation catalysts, an understanding of their structure–activity relationships has been strongly desired. Therefore, we focused on a ternary MoVO system as a simple system. By using this simple MoVO system, we found that a micropore in the MoVO structure worked to activate ethane and acrolein, and recently, the relationship between the structure around the micropore and the catalytic performance for the selective oxidation of ethane has been determined. The obtained results provided a molecular level understanding on the catalytic selective oxidation.

1.3. Crystalline Mo₃VO_x catalysts

We have successfully synthesized Orth-MoVO with M1 structure for the first time by a hydrothermal synthesis. Orth-MoVO has a layered structure. *a*–*b* planes form slabs which stack with each other to form a rod-shaped material. The *a*–*b* plane of Orth-MoVO is constructed from a network arrangement based on the pentagonal {Mo₆O₂₁}^{6–} unit and the {Mo₆} (M = Mo, V) octahedron and forms an empty hexagonal channel and an empty heptagonal channel. The structural model and the HAADF-STEM image of Orth-MoVO are shown in Fig. 1.

Orth-MoVO is produced by the hydrothermal synthesis. Interestingly, the control of the precursor solution for the hydrothermal synthesis produced various crystal analogues of Orth-MoVO. For example, a trigonal Mo₃VO_x material (Tri-MoVO) was obtained when the pH of the precursor solution was decreased.⁶² An amorphous Mo₃VO_x material (Amor-MoVO), which has an ordered structure in the *c*-direction and has a disordered structure in the *a*–*b* plane, was obtained by increasing the concentration of the precursor solution.⁶³ Apart from the hydrothermal synthesis, it was found that a suitable heat-treatment of Orth-MoVO produced a tetragonal Mo₃VO_x material (Tet-MoVO).⁶³ These are all rod-shaped crystals with the elemental composition of Mo₃VO_x (*x* = 11.2) and

are composed of the same structural parts, a pentagonal $\{\text{Mo}_6\text{O}_{21}\}^{6-}$ unit and a MO_6 ($\text{M} = \text{Mo}, \text{V}$) octahedron. We, therefore, describe these catalysts as 'crystalline Mo_3VO_x catalysts'. The difference in these materials is only the structural arrangement of the pentagonal $\{\text{Mo}_6\text{O}_{21}\}^{6-}$ unit and the MO_6 ($\text{M} = \text{Mo}, \text{V}$) octahedron into the slab where the a - b plane is present. Depending on the structural arrangement, Orth-MoVO, Tri-MoVO, and Amor-MoVO form the pentagonal, the hexagonal, and the heptagonal channels in their crystal structure, while Tet-MoVO forms the pentagonal channel and the hexagonal channel. Structure dependence of the catalytic activity will be discussed in chapter 3.

Orth-MoVO showed interesting features derived from an empty heptagonal channel. First, we found that the empty heptagonal channel of Orth-MoVO can work as a micropore of 0.40 nm in diameter which adsorbs small molecules like light alkanes.⁶⁴⁻⁶⁶ This microporous property was, surprisingly, controlled by tuning the reduced state of Orth-MoVO.^{65,66} This is the first example showing that the sorption behavior of an ordered porous crystalline material is continually and reversibly controlled by tuning the reduced state of the material. Second, Orth-MoVO was found to show an outstanding catalytic activity for the selective oxidation of ethane.⁶³ Because of the fact that the catalytic activity of Orth-MoVO was far superior to MoVTeNbO, an involvement of the empty heptagonal channel for the reaction has been implied for the selective oxidation of ethane.^{63,66} In addition, Orth-MoVO showed extremely high catalytic activity for the selective oxidation of acrolein to acrylic acid and was superior to industrial catalysts.^{67,68} In this case also, the catalytic activity of Orth-MoVO for the selective oxidation of acrolein was far superior to MoVTeO and MoVTeNbO.⁶⁹ Therefore, the participation of the empty heptagonal channel in the catalysis has been suggested. The role of the empty heptagonal channel in the catalytic reactions will be discussed in chapters 4 and 5.

The present review provides comprehensive information including the crystal formation mechanism (chapter 2) and the structure-activity relationship of the crystalline Mo_3VO_x catalysts (chapters 3 to 5). We believe that the present review provides not only a deep understanding of the catalytic reactions but also an idea to design structurally well-organized catalysts which are active for selective oxidations.

2. Formation mechanism of crystalline Mo_3VO_x catalysts

Orth-MoVO and Tri-MoVO are produced by the hydrothermal reaction of a precursor solution prepared from $(\text{NH}_4)_6\text{Mo}_7\text{O}_{24} \cdot 4\text{H}_2\text{O}$ (AHM) and $\text{VOSO}_4 \cdot n\text{H}_2\text{O}$. Once the two compounds are mixed in water, the color of the solution immediately changes to dark-violet due to the formation of the giant polyoxomolybdate, $[\text{Mo}_{72}\text{V}_{30}\text{O}_{282}(\text{H}_2\text{O})^{56-}(\text{SO}_4)_{12}]^{36-}$ ($\{\text{Mo}_{72}\text{V}_{30}\}$), which consists of 12 pentagonal $\{\text{Mo}_6\text{O}_{21}\}^{6-}$ polyoxomolybdate units and 30 $[\text{V}=\text{O}]^{2+}$ units. The formation of $\{\text{Mo}_{72}\text{V}_{30}\}$ can be confirmed by IR, Raman, and UV spectroscopy as

we have shown previously.⁵¹ Since both Orth-MoVO and Tri-MoVO are produced from the precursor solution containing $\{\text{Mo}_{72}\text{V}_{30}\}$, we assumed that Orth-MoVO and Tri-MoVO are formed by an assembly of building units provided by $\{\text{Mo}_{72}\text{V}_{30}\}$ under the hydrothermal conditions. Table 2 shows the relationship between the concentration of $\{\text{Mo}_{72}\text{V}_{30}\}$ in the precursor solution and the crystal phase produced from the solution. The concentration of $\{\text{Mo}_{72}\text{V}_{30}\}$ was controlled by changing the pH of the precursor solution. When no pH control was done ($\text{pH} = 3.2$), 63% of V in the precursor solution took part in the formation of $\{\text{Mo}_{72}\text{V}_{30}\}$. The increase of pH caused a slight decrease in the $\{\text{Mo}_{72}\text{V}_{30}\}$ amount. However, the decrease of pH led to a severe decrease in the amount of $\{\text{Mo}_{72}\text{V}_{30}\}$ due to the transformation of $\{\text{Mo}_{72}\text{V}_{30}\}$ into more condensed $\{\text{Mo}_{36}\text{O}_{112}\}$ ($\{\text{Mo}_{36}\}$), as confirmed by Raman spectroscopy. After the hydrothermal synthesis, Orth-MoVO can be obtained when no pH control was applied (entry 5). The decrease in pH to 2.2 led to the formation of Tri-MoVO (entry 3). Further decrease in pH led to the formation of hexagonal $\text{Mo}_{0.87}\text{V}_{0.13}\text{O}_{2.94}$ which does not contain a pentagonal $\{\text{Mo}_6\text{O}_{21}\}^{6-}$ unit in the structure (entries 1 and 2). When the pH of the precursor solution was increased, only a tiny amount of solid could be obtained (entry 6) even though enough $\{\text{Mo}_{72}\text{V}_{30}\}$ was present in the solution. Further increase of the pH to 4.0 produced no solids (entry 7). Based on these experimental facts, we have proposed a crystal formation process of Orth-MoVO and Tri-MoVO as shown in Scheme 1(A).⁵¹ For the formation of Orth-MoVO, a dimer of the pentagonal $\{\text{Mo}_6\text{O}_{21}\}^{6-}$ unit provided by $\{\text{Mo}_{72}\text{V}_{30}\}$ assembles together with a pentamer unit which consists of five $\{\text{MO}_6\}$ ($\text{M} = \text{Mo}, \text{V}$) octahedra to form Orth-MoVO. For the formation of Tri-MoVO, in reflection of the low pH condition in which Tri-MoVO forms, a trimer of the pentagonal $\{\text{Mo}_6\text{O}_{21}\}^{6-}$ unit which is a more condensed unit than the dimer unit used for Orth-MoVO formation takes part in the formation of Tri-MoVO, with the trimer unit consisting of three $\{\text{MO}_6\}$ ($\text{M} = \text{Mo}, \text{V}$) octahedra. When the pH of the precursor solution was increased, possibly, the pentagonal $\{\text{Mo}_6\text{O}_{21}\}^{6-}$ unit cannot condense to form the dimer or the trimer, the building units for the formation of Orth-MoVO or Tri-MoVO, which inhibits the formation of these materials.

Recently, we found that the seed of Orth-MoVO and Tri-MoVO can work as a crystallization nucleus for the formation of Orth-MoVO and Tri-MoVO.⁷⁰ Addition of Orth-MoVO or Tri-MoVO seed crystals resulted in the formation of Orth-MoVO or Tri-MoVO even when the pH of the precursor solution was 4.0 (entries 8 and 9). Since the yield of the solid decreased when an unground seed (long rod-shaped crystal) was used, the crystal formation was found to occur from the cross-section of the rods where the a - a or the a - b planes are present (entry 10). Since no formation of Orth-MoVO or Tri-MoVO occurred without $\{\text{Mo}_{72}\text{V}_{30}\}$, even though the same Mo and V concentrations were used, we concluded that the building units provided by $\{\text{Mo}_{72}\text{V}_{30}\}$ assembled on the a - b or the a - a planes of Orth-MoVO and Tri-MoVO to form the rod-shaped crystals (entries 11 and 12). $\{\text{Mo}_{72}\text{V}_{30}\}$, Orth-MoVO,

Table 2 pH and concentration of $\{\text{Mo}_{72}\text{V}_{30}\}$ in the precursor solution, and the product amount and their crystal phases after hydrothermal synthesis with or without the seed at 175 °C for 20 h

Entry	pH ^a	Concentration of $\{\text{Mo}_{72}\text{V}_{30}\}$ ^b	$\{\text{Mo}_{72}\text{V}_{30}\}$ yield ^c	Seed ^d	Crystal of the obtained solid	Amount of solid
1	1.2	0.0 mM	0%	— ^e	Hex- $\text{Mo}_{0.87}\text{V}_{0.13}\text{O}_{2.94}$ ^f	6.7 g
2	1.7	0.4 mM	23%	— ^e	Hex- $\text{Mo}_{0.87}\text{V}_{0.13}\text{O}_{2.94}$ ^f + Tri-MoVO	—
3	2.2	0.6 mM	35%	— ^e	Tri-MoVO	5.0 g
4	2.7	1.0 mM	57%	— ^e	Orth-MoVO	—
5	3.2	1.1 mM	63%	— ^e	Orth-MoVO	1.4 g
6	3.4	1.0 mM	57%	— ^e	Orth-MoVO	0.3 g
7	4.0	0.9 mM	51%	— ^e	— ^g	0.0 g
8	4.0	0.9 mM	51%	Orth-MoVO	Orth-MoVO	1.3 g
9	4.0	0.9 mM	51%	Tri-MoVO	Tri-MoVO	1.7 g
10 ^h	4.0	0.9 mM	51%	Orth-MoVO	Orth-MoVO	0.7 g
11 ⁱ	4.0	0.0 mM	0%	Orth-MoVO	— ^g	0.0 g
12	1.2	0.0 mM	0%	Orth-MoVO	Hex- $\text{Mo}_{0.87}\text{V}_{0.13}\text{O}_{2.94}$ ^f	6.9 g

^a pH of the reaction mixture was changed from 1.0 to 4.0 by adding 2 M H_2SO_4 or 10 wt% ammonia. ^b Estimated by UV-vis spectroscopy.

^c Based on V. ^d Seed amount was 0.3 g. ^e No seed was added. ^f JCPDF: 00-048-0766. ^g No solid was obtained. ^h Unground Orth-MoVO seed was added. ⁱ V_2O_5 was used as the V source.

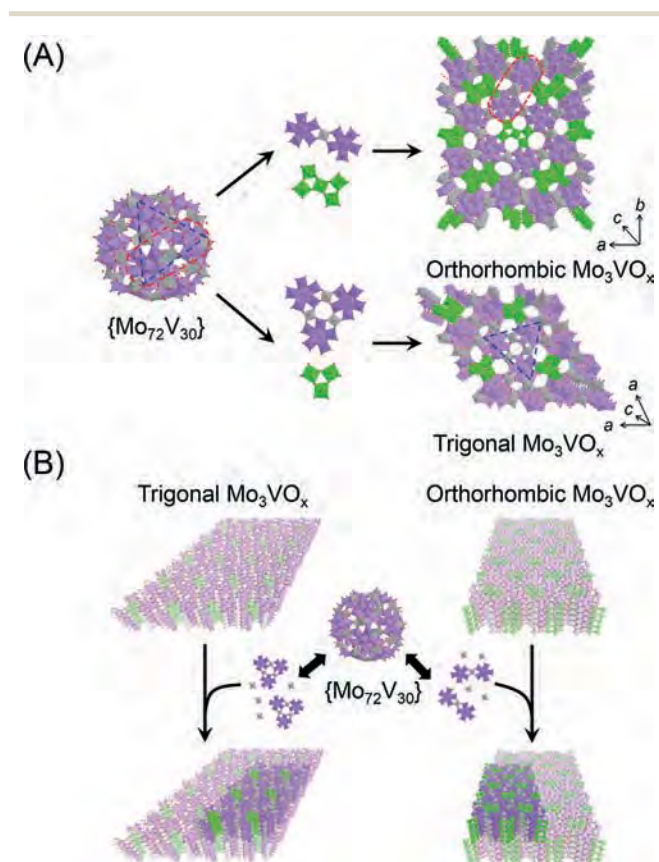
and Tri-MoVO contain common structural parts, a pentagonal $\{\text{Mo}_6\text{O}_{21}\}^{6-}$ unit linked with a V octahedron, so that the structural parts are thought to preferentially assemble on the a - b or the a - a planes of Orth-MoVO or Tri-MoVO. In zeolite synthesis, the hydrothermal synthesis of zeolites in the presence of zeolite seeds has widely been studied.^{71–75} In this

case, the seed zeolites and the reactant gel need to have the same structural units. When the zeolite seeds and the reactant gel contain the same structural units, the structural units in the gel stack on the surface of the seed crystal, and the zeolite having the same crystal phase as the seed can be formed. Our seed-assisted synthesis of Orth-MoVO and Tri-MoVO seems to be very similar to the seed-assisted synthesis of zeolites. On the basis of these facts, we proposed the crystal formation scheme of Orth-MoVO and Tri-MoVO in the presence of a seed (Scheme 1(B)).⁷⁰ When the seed is present in the precursor solution, the building units provided by $\{\text{Mo}_{72}\text{V}_{30}\}$ stack on the cross-section of the seeds to form the rod-shaped material having the same crystal structure as the seed. In this case, $\{\text{Mo}_{72}\text{V}_{30}\}$ only contributes to the crystal growth for the formation of Orth-MoVO and Tri-MoVO.

On the basis of these experiments, we concluded that Orth-MoVO and Tri-MoVO are produced by the building unit assembly *via* a giant polyoxometalate, $\{\text{Mo}_{72}\text{V}_{30}\}$.^{51,70} Building block assembly using a giant polyoxometalate will be an effective way to create structurally well-organized materials like Orth-MoVO and Tri-MoVO.

3. Structure–activity relationship for the selective oxidation of ethane and acrolein

We demonstrated the structure–activity relationship using the synthesized crystalline Mo_3VO_x catalysts in the selective oxidation of ethane and acrolein. As we have shown in the Introduction, we have successfully obtained 4 distinct crystalline Mo_3VO_x materials (Fig. 1); orthorhombic MoVO (Orth-MoVO), trigonal MoVO (Tri-MoVO), tetragonal MoVO (Tet-MoVO), and amorphous MoVO (Amor-MoVO). These materials are all rod-shaped crystals with almost the same elemental composition and are composed of the structural arrangement based on the pentagonal $\{\text{Mo}_6\text{O}_{21}\}^{6-}$ unit and the $\{\text{Mo}_6\}$ (M = Mo, V) octahedron, while the arrangement of



Scheme 1 (A) Proposed schemes of structure formation of orthorhombic Mo_3VO_x and trigonal Mo_3VO_x . (B) Proposed schemes of structure formation in the seed-assisted synthesis. Purple; Mo, gray; V, green; mixture of Mo and V.

these units varies for each catalyst. Among the obtained materials, Orth-MoVO, Tri-MoVO, and Amor-MoVO possessed the heptagonal channel (shown as orange in Fig. 1) in their structure, while Tet-MoVO had no heptagonal channel. Table 3 shows the numbers of heptagonal channels in 100 nm². The numbers of heptagonal channels of Orth-MoVO and Tri-MoVO were almost the same and were 73 for Orth-MoVO and 68 for Tri-MoVO. The number of heptagonal channels of Amor-MoVO was considerably lower than those of Orth-MoVO and Tri-MoVO (10–30 in 100 nm²) because of the nonuniform structural arrangement as observed in the HAADF-STEM image. Table 3 shows the micropore volume of these materials measured by N₂ adsorption. Orth-MoVO, Tri-MoVO, and Amor-MoVO showed microporosity. On the other hand, Tet-MoVO showed no microporosity. The difference between Tet-MoVO and the other crystalline Mo₃VO_x materials is whether the heptagonal channel is present in the structure or not. Therefore, the heptagonal channel was found to work as a micropore. According to the adsorption experiments using various molecules, the size of the heptagonal channel was determined to be 0.40 nm.^{61,64–66} The micropore volume observed in Orth-MoVO was apparently higher than those of Tri-MoVO and Amor-MoVO (Orth-MoVO, 14.0 cm³ g⁻¹; Tri-MoVO, 4.0 cm³ g⁻¹; Amor-MoVO, 2.8 cm³ g⁻¹). The small micropore volume of Amor-MoVO can be explained by the low number of heptagonal channels in the structure. However, Tri-MoVO showed an obviously lower micropore volume than that of Orth-MoVO despite the similar number of heptagonal channels in 100 nm² (Table 3). As we have observed from the HAADF-STEM analysis that Tri-MoVO contained some additional elements inside the heptagonal channel, this situation may decrease the number of micropores.^{76,77}

Then, we evaluated the effect of the heptagonal channel on the catalytic reaction. Table 3 shows the substrate conversion for the selective oxidation of ethane and acrolein. For both reactions, Orth-MoVO, Tri-MoVO, and Amor-MoVO showed catalytic activity, while Tet-MoVO was inactive. These astonishing results indicate that the heptagonal channel is responsible for these catalytic reactions. For the ethane oxidation at 313–319 °C, Orth-MoVO showed higher catalytic activity (42.2%) than those of Tri-MoVO (25.2%) and Amor-MoVO (5.9%). The order of the micropore volume was well-matched with the order of the catalytic activity. The

participation of the heptagonal inner channel in the oxidation of ethane is implied. In contrast, Tri-MoVO showed the best catalytic activity for the oxidation of acrolein, followed by Orth-MoVO, Amor-MoVO, and Tet-MoVO (almost inactive). Taking into consideration the higher external surface area of Tri-MoVO (18.0 m² g⁻¹) than that of Orth-MoVO (7.2 m² g⁻¹), the order of the catalytic activity for the selective oxidation of acrolein can be described as Tri-MoVO ≅ Orth-MoVO > Amor-MoVO > Tet-MoVO (inactive). This order was well-matched with the order of the number of heptagonal channels in 100 nm² (Table 3). This result implied that the heptagonal channel located in the external surface takes part in the catalytic oxidation of acrolein. Although the heptagonal channel is essential for both reactions, the catalysis field may be different depending on the nature of the substrate.

In this section, we demonstrated the clear structure–catalytic activity relationship for the selective oxidation of ethane and acrolein using the 4 distinct crystalline Mo₃VO_x catalysts. It is obvious that the empty heptagonal channel is involved in both reactions. In the next section, we show the role of the heptagonal channel in both reactions.

4. Role of micropores in the selective oxidation of ethane and acrolein

4.1. Synthesis of various sizes of orthorhombic Mo₃VO_x with the same microporosity

In this section, we demonstrate the role of the heptagonal channel in the selective oxidation of ethane and acrolein. In order to understand the role of the heptagonal channel, we synthesized a number of Orth-MoVO catalysts with different external surface areas but with the same micropore volumes by controlling the crystal size. We used an anionic surfactant, sodium dodecyl sulphonate (SDS, C₁₂H₂₅SO₃Na), to control both the nucleation rate and the crystal growth rate.^{78,79} The amount of added SDS was set as SDS/(Mo + V) = *x* (*x* = 0, 0.15, 0.30, and 0.60), where *x* shows the molar ratio between SDS and (Mo + V). The synthesized materials are abbreviated as MoVO-SDS_{*x*}. Besides the SDS addition, the temperature in the hydrothermal synthesis was controlled since the hydrothermal temperature affects both the nucleation rate and the crystal growth rate.^{80,81} The synthesis temperature *y* (*y* = 175 °C or 230 °C) is described at the end of the material name, for example MoVO-SDS_{*x*} (*y*). All the synthesized catalysts were

Table 3 Relationship between micropore and catalytic activity

Catalyst	Elemental composition ^a (V/Mo)	Number of 7-membered ring/100 nm ²	External surface area ^b /m ² g ⁻¹	Micropore volume ^b /cm ³ g ⁻¹	Ethane conv. ^c /%	ACR conv. ^d /%
Orth-MoVO	0.38	73	7.2	14.0	42.2	53.8
Tri-MoVO	0.32	68	18.0	4.0	25.2	99.8
Tet-MoVO	0.38	0	2.7	0	<1	<1
Amor-MoVO	0.38	10–30	5.7	2.8	5.9	9.7

^a Determined by ICP. ^b Measured by N₂ adsorption at liquid N₂ temperature and estimated by the *t*-plot method. ^c Reaction conditions: catalyst amount, 0.5 g; reaction gas feed, C₂H₆/O₂/N₂ = 5/5/40 ml min⁻¹; reaction temperature, 313–319 °C. ^d Reaction conditions: catalyst amount, 0.25 g, reaction gas feed, ACR/O₂/H₂O/N₂/He = 2.5/8.0/27.1/39.5/30.5 ml min⁻¹; reaction temperature, 217–218 °C. ACR represents acrolein.

ground with a mortar prior to the reaction in order to expose the cross-section of the rod. We also used Orth-MoVO without the grinding treatment (Orth-MoVO (ng)). All the synthesized materials showed the XRD patterns attributable to Orth-MoVO and no peaks related to impurities were observed. The elemental composition of these materials determined by ICP-AES was identical. Table 4 summarizes the size of the rod-shaped materials measured by using SEM images and its external surface area and microporosity measured by N_2 or ethane adsorption. All the characterization methods were carried out for the catalysts after the selective oxidation of ethane. The crystal size of the Orth-MoVO catalysts was clearly changed by the introduction of SDS or by the control of the synthesis temperature due to the change in the nucleation rate and crystal growth rate. The most intense difference in the crystal size could be seen among Orth-MoVO, MoVO-SDS_{0.60} (175), and MoVO-SDS_{0.15} (230) and is shown in Fig. 2 (inlet images) and Table 4. It is interesting to note that the aspect ratio, the ratio between the length and the diameter of the rods, was almost the same for the materials, indicating that the shape of the rods was the same regardless of the addition of SDS or of the synthesis temperature. Based on these facts, we successfully obtained Orth-MoVO catalysts with different crystal sizes and the same crystal shape by adding SDS or by controlling the synthesis temperature.

N_2 adsorption experiment was carried out in order to determine their external surface areas. Depending on the crystal size of the catalysts, the estimated external surface areas were drastically changed (Table 4). On the other hand, the micropore volume of the materials estimated by the ethane adsorption experiment was almost the same in the studied materials and was in the range of $16.1\text{--}22.3 \times 10^{-3} \text{ cm}^3 \text{ g}^{-1}$ (Table 4). The theoretical micropore volume calculated by assuming that ethane is adsorbed in the heptagonal channel was $22.4 \times 10^{-3} \text{ cm}^3 \text{ g}^{-1}$. The observed micropore volumes were slightly lower than the theoretically obtained value except Orth-MoVO (ng). The grinding treatment may cause dislocation in the a - b plane which decreases the number of

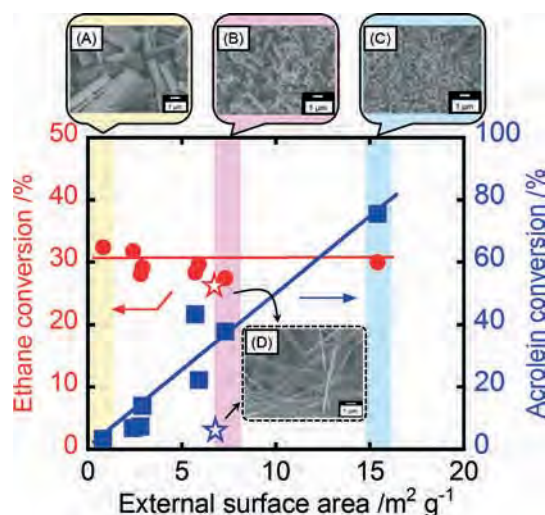


Fig. 2 Ethane conversion as a function of the external surface area of the catalysts (red circle). Reaction conditions of ethane oxidation: catalyst amount, 0.50 g; reaction gas feed, $C_2H_6/O_2/N_2 = 5/5/40 \text{ ml min}^{-1}$; reaction temperature, 300 °C. Acrolein conversion as a function of the external surface area of the catalysts (blue square). Reaction conditions of acrolein oxidation: catalyst amount, 0.125 g; reaction gas feed, $acrolein/O_2/H_2O/N_2/He = 2.5/8.0/27.1/39.5/30.5 \text{ ml min}^{-1}$; reaction temperature, 220 °C. The red star and the blue star represent the ethane conversion and acrolein conversion of Orth-MoVO (ng), respectively. SEM images of (A) MoVO-SDS_{0.15} (230), (B) Orth-MoVO, (C) MoVO-SDS_{0.60} (175), and (D) Orth-MoVO (ng) after the ethane oxidation are represented.

micropores being capable of adsorbing ethane. Nevertheless, the ethane adsorption results evidently confirm the existence of the heptagonal channel micropore where ethane molecules can freely have access. We concluded that the studied materials have different external surface areas but with the same micropore volume.

4.2. Crystal size dependence on the catalytic activity

The selective oxidations of ethane to ethene and of acrolein to acrylic acid were carried out by using the Orth-MoVO

Table 4 Rod size, external surface area, and micropore properties of the catalysts

Catalyst	Rod-shaped crystal			Surface area/ $\text{m}^2 \text{ g}^{-1}$			Micropore volume ^d / $10^{-3} \text{ cm}^3 \text{ g}^{-1}$
	Average diameter ^a / μm	Average length ^a / μm	Aspect ratio ^b /—	External surface area ^c	Side area	Section area	
Orth-MoVO	0.40	1.8	4.5	7.2	6.5	0.7	17.7
Orth-MoVO (ng) ^e	0.39	7.9	22.3	6.8	6.6	0.2	22.3
MoVO-SDS _{0.15} (175)	0.44	2.0	4.5	7.2	6.5	0.7	16.6
MoVO-SDS _{0.30} (175)	0.45	1.5	3.3	7.3	6.3	1.0	18.8
MoVO-SDS _{0.60} (175)	0.21	0.7	3.5	14.0	12.1	1.9	17.3
MoVO (230)	0.76	3.7	4.9	5.3	4.8	0.5	16.7
MoVO-SDS _{0.15} (230)	1.04	4.8	4.6	1.2	1.1	0.1	16.6
MoVO-SDS _{0.30} (230)	0.99	3.4	3.4	3.9	3.4	0.5	18.5
MoVO-SDS _{0.60} (230)	0.95	3.5	3.7	5.5	4.8	0.7	16.1

^a Average of 100 crystallites in the SEM images. ^b Ratio of the average length to the average diameter of the rod. ^c Measured by N_2 adsorption at liq. N_2 temperature and determined by the t -plot method. ^d Measured by ethane adsorption at room temperature and determined by the DA method. ^e Orth-MoVO without grinding treatment.

catalysts with different external surface areas and the same micropore volume. For both reactions, the participation of the heptagonal channel was evidenced as has been shown in chapter 3. Here, a catalytically active part related to the heptagonal channel is elucidated by evaluating the dependence of the catalytic activity on the external surface area. Fig. 2 shows the substrate conversion as a function of the external surface area of the Orth-MoVO catalysts. The ethane oxidation was carried out at 300 °C and the acrolein oxidation was carried out at 220 °C. The external surface area was almost maintained even after the reactions were carried out. Stars represent the substrate conversion over Orth-MoVO (ng). The obtained products by the ethane oxidation were ethene, CO_x, and acetic acid. Almost the same selectivity was observed in the studied catalysts and the selectivity to ethene was around 90%. In the case of the acrolein oxidation, the obtained products were acrylic acid, CO_x, and acetic acid. In this case also, product selectivity was almost the same in the studied catalysts and the selectivity to acrylic acid was around 95%. For the ethane oxidation, the ethane conversion over the catalysts was *ca.* 30% and was almost the same regardless of the change of the external surface area (Fig. 2, circle). This result indicates that the external surface of Orth-MoVO contributes less to the catalytic activity for the selective oxidation of ethane. It can be concluded that ethane is converted mainly in the micropore channel. Actually, the molecular size of ethane (0.40 nm) is almost the same as that of the heptagonal channel micropore (0.40 nm) and the fact that the micropore can adsorb ethane (Table 4) has already been confirmed. In addition, according to Monte Carlo simulation, the highest ethane adsorption energy was obtained when an ethane molecule is confined inside the heptagonal channel. Diffusion effects were studied in this catalyst by evaluating the dependence of the catalytic activity on the contact time using MoVO-SDS_{0.60} (175), Orth-MoVO, and MoVO-SDS_{0.15} (230), in which the average crystal size was apparently different for each other. As a result, almost no difference in the dependence of the catalytic activity on the contact time was observed in these catalysts, indicating that Orth-MoVO oxidizes ethane catalytically without diffusion effects. The unground catalyst, Orth-MoVO (ng), showed a comparable catalytic activity with the ground catalyst for this reaction (Fig. 2, red star). Since the external surface of Orth-MoVO contributes less to the catalytic reaction, the micropore in the whole particle should be involved in the ethane oxidation. Based on the above results and discussion, we concluded that an ethane molecule enters the heptagonal channel micropore and goes through without diffusion barriers under the reaction conditions. During ethane diffusion in the heptagonal channel, the ethane oxidation takes place and ethene is formed inside the heptagonal channel.

In contrast, the acrolein conversion clearly depended on the external surface area of the catalysts (Fig. 2, square). The linear relationship between the acrolein conversion and the external surface area unambiguously indicates that acrolein is converted on the external surface. Since the participation

of the heptagonal channel micropore in the selective oxidation of acrolein has been implied by the comparison of 4 distinct crystalline Mo₃VO_x catalysts, it is apparent that the heptagonal channel which is present over the external surface of the catalyst should catalyze acrolein. In this case, the contribution of the side surface of the rods can be easily excluded because of the fact that Orth-MoVO (ng), having almost the same side surface area and far less section surface area compared with Orth-MoVO, showed far less catalytic activity. Based on these experimental facts, we concluded that acrolein is activated over the heptagonal channel present in the external surface of the cross-section of the rod-shaped crystals (*a-b* plane). The mouth of the heptagonal channel on the cross-section of the rod might effectively trap the aldehyde group in acrolein and convert it to form acrylic acid.

We concluded, on the basis of the above results, that both ethane and acrolein are activated at the heptagonal channel micropore. However, ethane is activated inside the channel and acrolein is activated on the mouth of the heptagonal channel. The catalysis field of the heptagonal channel was found to be strongly dependent on the nature of the substrates.

5. Relationships between crystal structure, microporosity, and catalytic performance

5.1. Relationship between crystal structure and microporosity

In this chapter, we introduce the relationships between the crystal structure around the heptagonal channel, microporosity, and catalytic activity for the selective oxidation of ethane. Since it was found that the oxidation of ethane takes place inside the heptagonal channel micropore, we thought that the bulk properties of Orth-MoVO should strongly affect the catalytic activity for the selective oxidation of ethane. Orth-MoVO is amenable to the characterization methods in reflection of its high crystallinity. Therefore, the use of this catalyst for the catalytic reaction allows us to understand the structure–activity relationship, unambiguously, and enables us to understand the catalytic reaction at the molecular level. Such knowledge is surely helpful for developing new oxidation catalysts. We have reported that the size of the heptagonal channel is reversibly and continuously controlled by a redox treatment. Since ethane is converted to ethene in the heptagonal channel, the tuning of the heptagonal channel size should affect the catalytic activity. Based on this perspective, we prepared Orth-MoVO with various reduced states by reduction treatment.

First, Orth-MoVO was calcined at 400 °C for 2 h and then, the calcined Orth-MoVO was reduced under 5% H₂/Ar flow at 400 °C by varying the temperature holding time. The catalysts obtained were abbreviated as MoVO (δ), where δ is the amount of lattice oxygen evolved from the unit cell (represented as Mo₂₉V₁₁O_{112- δ}) by the reduction and was measured

by TPR and TG. MoVO (0) represents the Orth-MoVO after the air calcination at 400 °C for 2 h. The catalyst oxidized at 400 °C for 2 h under air atmosphere after the reduction treatment was abbreviated as MoVO (δ)-AC. All the catalysts showed the XRD pattern attributable to Orth-MoVO and no impurities were observed by XRD regardless of the redox treatment. No morphological changes were observed by SEM. These results indicate that the Orth-MoVO is stable under the redox treatments and oxidation–reduction of the solid proceeds uniformly.

Fig. 3 shows the structural model of Orth-MoVO (A) and the heptagonal channel size change and the microporosity change by the redox treatment (B). Orth-MoVO had two types of lattice oxygen in the unit cell. One is the oxygen evolved in the early stage of the reduction that hardly comes back to the structure during the re-oxidation. The other is the oxygen evolved continuously with the reduction that reversibly comes back to the structure during the re-oxidation. We abbreviated the former oxygen as ' α -oxygen' and the latter oxygen as ' β -oxygen'. Detailed characterization revealed that α -oxygen is the oxygen in the pentamer unit which faces the heptagonal channel (O_{29} in Fig. 3(A)) and β -oxygen is the axial oxygen which connects the metals to the c -axis (blue enclosure in Fig. 3(A)). It was found that the occupancy of α -oxygen rapidly decreased with the reduction and the occupancy reached almost 0 with the reduction from MoVO (0) to MoVO (4.2), although β -oxygen can be continuously evolved by further reduction. In the case of MoVO (6.8)-AC, since α -oxygen can hardly come back to the structure during the re-oxidation, this catalyst contained almost no α -oxygen, although β -oxygen returned to the structure during the re-oxidation treatment. Fig. 3(B) shows the size of the heptagonal channel for the samples with various reduced states and the micropore volumes measured by ethane or propane adsorption. The size of the heptagonal channel was estimated using the structural model obtained from the single crystal analysis and the Rietveld analysis. The lengths of the heptagonal channel in the long axis (D_1 : O_{24} – O_{26}) and the short axis (D_2 : O_6 – O_{27}) are shown by the red bar and the blue bar, respectively. For D_1 , the length increased with the increase of the reduction degree due to the lattice expansion. For D_2 , the length increased until the reduction of MoVO (4.2). However, the length significantly decreased by further reduction. From the Rietveld analysis, an expansion of the pentagonal $\{Mo_6O_{21}\}^{6-}$ unit was indicated. Therefore, the decrease in D_2 should be derived from the movement of the atoms in the pentagonal unit toward the heptagonal channel. The adsorption experiments using ethane and propane were carried out for the samples with various reduced states. Interestingly, the decreases in the micropore volumes were observed for the reduction using catalysts after MoVO (4.2) (Fig. 3(B)). Since the heptagonal channel works as the micropore to adsorb small molecules, the decrease in D_2 might be related to the decline in the microporosity. Re-oxidation of MoVO (6.8) restored D_2 , which resulted in the restoration of the microporosity (Fig. 3(B)).

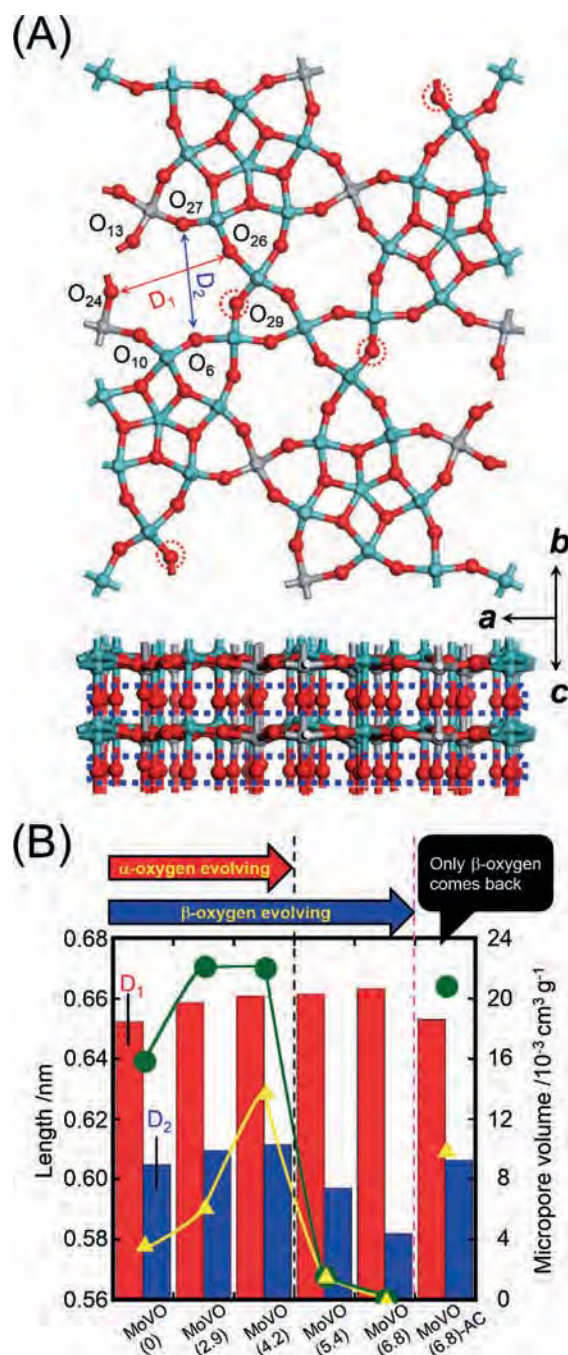


Fig. 3 (A) Structural model of Orth-MoVO (Mo, light green; V, gray; O, red). A red circle (top image, O_{29}) represents α -oxygen and a blue circle (bottom image) represents β -oxygen. (B) Left side: diameters of the heptagonal channel. Diameters were determined on the basis of the atomic positions of oxygen. Red bar, D_1 (O_{24} – O_{26} , long axis); blue bar, D_2 (O_6 – O_{27} , short axis). Right side: micropore volumes of Orth-MoVO with each reduction state measured by C_2H_6 adsorption (green circle) and C_3H_8 adsorption (yellow triangle) and estimated by the Dubinin–Astakhov (DA) method.

The propane adsorption experiment showed an interesting profile against the reduction degree (Fig. 3, yellow triangle). With the increase of the reduction degree up to MoVO (4.2), the propane adsorption capacity increased. Such increase

could not be seen in the ethane adsorption. Further increase in the reduction degree significantly decreased the propane adsorption capacity in the same manner as the ethane adsorption capacity due to the decrease in the length of the heptagonal channel in the short axis (D_2). The molecular sizes of ethane and propane are 0.40 nm and 0.43 nm, respectively. Taking into consideration the heptagonal channel size (0.40 nm), ethane can freely access the heptagonal channel. On the other hand, propane has some difficulty in accessing the heptagonal channel. An increase of the heptagonal channel size is essential to adsorb propane. Desorption of α -oxygen is a presumable reason for the increase in the propane adsorption capacity since α -oxygen is facing the heptagonal channel so that the desorption of α -oxygen can expand the heptagonal channel size. In the same reason, the propane adsorption capacity of MoVO (6.8)-AC was much higher than that of MoVO (0) which was treated under the same oxidative conditions and had almost the same physicochemical properties except the residence of α -oxygen. The partial structural changes including the evolution of α -oxygen and the expansion of the pentagonal $\{\text{Mo}_6\text{O}_{21}\}^{6-}$ unit were found to affect the size of the heptagonal channel which resulted in a significant change in their microporosity.

5.2. Relationship between microporosity and catalytic performance

Since Orth-MoVO activates ethane inside the heptagonal channel, the microporosity derived from the heptagonal channel is expected to affect the catalytic activity. Fig. 4 shows the ethane conversion of the catalyst as a function of δ . When δ was in the range of 0–4.2, ethane conversion increased with the increase of δ (from 14% to 33%). However, the ethane conversion dropped drastically when δ was increased to 5.4 (9%) and became almost 0 when $\delta = 6.8$. The ethane conversion of MoVO (6.8)-AC was 31% and was almost the same as that of MoVO (4.2). Selectivity to ethene decreased in the δ range of 0–4.2 from 88.5% to 76.8% due to the increase of the selectivity to CO_x . Further reduction

increased the selectivity to ethene to 93.3%. Ethene selectivity of MoVO (6.8)-AC was 84.4%. Taking into consideration the physicochemical properties of MoVO (0) and MoVO (6.8)-AC, the major difference is only the occupancy of α -oxygen. Therefore, it is obvious that the occupancy of α -oxygen is the critical factor for the ethane oxidation. This explanation has no conflict for the increase of the catalytic activity from MoVO (0) to MoVO (4.2) because the occupancy of α -oxygen rapidly decreases against δ and reaches almost 0 when δ reached 4.2. For the decrease in the catalytic activity by the reduction using the catalysts after MoVO (4.2), we showed that the reduction using the catalysts after MoVO (4.2) caused the expansion of the pentagonal $\{\text{Mo}_6\text{O}_{21}\}^{6-}$ unit which resulted in the decrease in the microporosity. Since Orth-MoVO activates ethane inside the heptagonal channel, no conversion should occur if ethane cannot get inside the channel. Therefore, the decrease in the catalytic activity by the reduction using the catalysts after MoVO (4.2) is derived from the decrease in the length of the heptagonal channel, which prohibits ethane from going through the heptagonal channel. The microporosity changes caused by the partial structural changes around the heptagonal channel were found to strongly affect the catalytic activity for the selective oxidation of ethane.

Then, we discuss how the catalytic activity increased with the decrease of the α -oxygen occupancy. For this purpose, we generated Arrhenius plots for MoVO (0) and MoVO (6.8)-AC. The obtained results are shown in Fig. 5. No change in the slope of the line was observed between them, and the calculated activation energy was 81–82 kJ mol^{-1} . The frequency factor, however, was much different and the frequency factor of MoVO (6.8)-AC was 3 times higher than that of MoVO (0) (frequency factor: MoVO (0), $0.87 \times 10^9 \text{ mmol s}^{-1} \text{ g}_{\text{cat}}^{-1}$; MoVO (6.8)-AC, $2.20 \times 10^9 \text{ mmol s}^{-1} \text{ g}_{\text{cat}}^{-1}$). These results clearly indicate that the increase of the catalytic activity by the evolution of α -oxygen was due to the increase of the number of active sites in the structure. Taking into consideration the structural model of Orth-MoVO, the heptagonal channel with α -oxygen defects should be

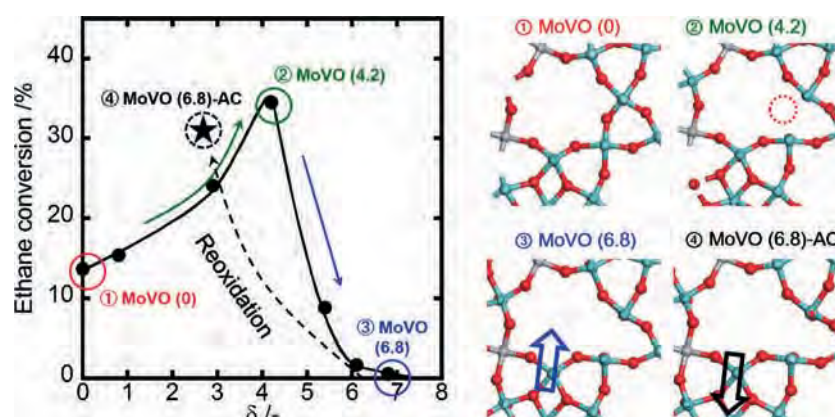


Fig. 4 Explanation of the catalytic activity change on the basis of the catalyst structure.

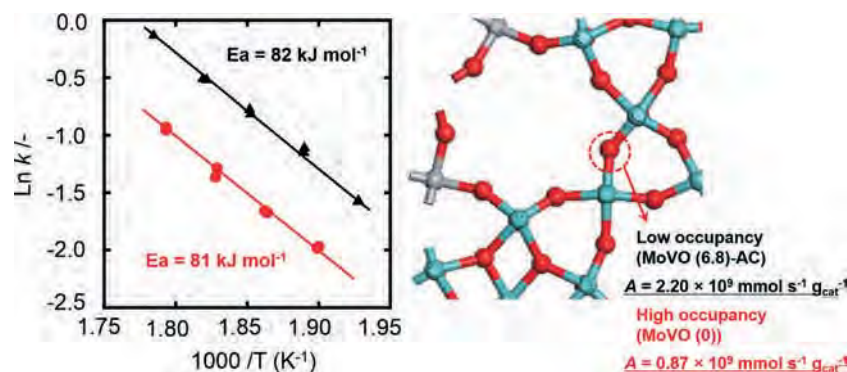
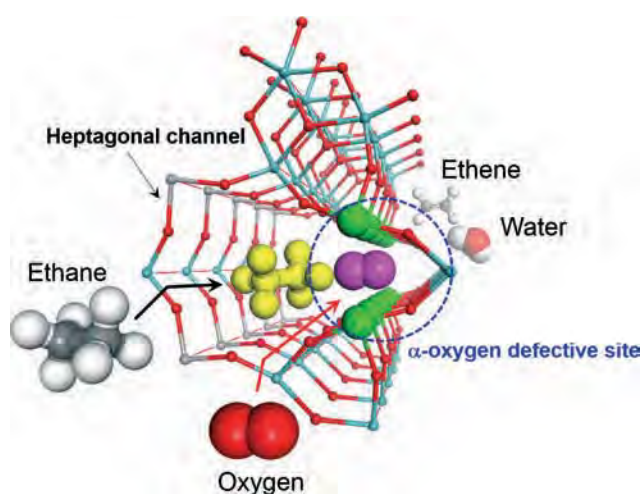


Fig. 5 Arrhenius plot for ethane conversion over MoVO (0) (circle) and MoVO (6.8)-AC (triangle). k represents the reaction rate constant. Although no change was observed in the activation energy between them, the occupancy of α -oxygen affected the frequency factor (A) for the selective oxidation of ethane.

related to the catalysis field where ethane oxidation can take place.

We propose a reaction scheme for the selective oxidation of ethane with Orth-MoVO (Scheme 2). There are two important points in this reaction. The first point is the existence of the micropore where ethane can freely have access. The existence of the micropore not only enhances the contact of ethane with activated oxygen, but also weakens the strong C–H bond of ethane due to a possible electric field in the channel. The second point is the α -oxygen defective site which may produce a special oxygen species, like the μ - η^2 : η^2 -peroxo species as reported to be produced by a V dimer in the Keggin structure.^{82,83} Such molecular level insight for the selective oxidation of ethane could be expressed by the use of the simple but highly multifunctional crystalline oxide catalyst and it can be seen that the sophisticated catalyst structure has a crucial role in the selective oxidation. This insight may help in the development of the catalyst design for the selective oxidation of light alkanes.



Scheme 2 Conversion of ethane to ethene in the heptagonal channel. Ethane and oxygen marked with yellow and purple, respectively, represent the ethane and oxygen that are activated inside the heptagonal channel.

6. Conclusions

The assembly of the building unit provided from the giant sized and ball shaped polyoxometalate ($[\text{Mo}_{72}\text{V}_{30}\text{O}_{282}(\text{H}_2\text{O})^{56-}(\text{SO}_4)_{12}]^{36-}$ ($\{\text{Mo}_{72}\text{V}_{30}\}$)) produced crystalline Mo_3VO_x oxides with a highly organized crystal structure at the nano-scale level. The comparison of these crystalline catalysts showed that a heptagonal channel in the structure takes part in the catalysis for the selective oxidation of ethane to ethene and of acrolein to acrylic acid. The comparison of the orthorhombic Mo_3VO_x catalysts with tailored crystal sizes unambiguously showed that the heptagonal channel activates ethane inside. On the other hand, acrolein is activated over the channel located on the external surface in the cross-section of the rod-shaped crystal (a - b plane). The change in the size of the heptagonal channel strongly affected the catalytic activity for the selective oxidation of ethane. Especially, the evolution of the oxygen which faces the heptagonal channel increased the number of the active sites for the ethane oxidation which resulted in the enhancement of the catalytic activity.

In this review, we demonstrated the molecular level insight for the catalytic selective oxidations using the structurally well-organized catalyst. Deep understanding of the catalytic reaction may enable us to design the catalytically active site more rationally. We believe that the rational catalyst design based on the understanding of the catalytic reaction at the molecular level finally produces the evolutionary catalyst which can achieve dream reactions like as the selective oxidation of methane to methanol or benzene to phenol.

Acknowledgements

This work was supported by JSPS KAKENHI Grant No. 2324-6135.

References

- 1 A. Chiericato, J. M. L. Nieto and F. Cavani, *Coord. Chem. Rev.*, 2015, 301–302, 3.
- 2 M. Sun, J. Zhang, P. Putaj, V. Caps, F. Lefebvre, J. Pelletier and J. M. Basset, *Chem. Rev.*, 2014, 114, 981.

- 3 F. Cavani, *Catal. Today*, 2010, **157**, 8.
- 4 W. Ueda, K. Oshihara, D. Vitry, T. Hisano and Y. Kayashima, *Catal. Surv. Asia*, 2002, **6**, 33.
- 5 C. Batiot and B. K. Hodnett, *Appl. Catal., A*, 1996, **137**, 179.
- 6 R. K. Grasselli, *Top. Catal.*, 2001, **15**, 93.
- 7 R. K. Grasselli, *Top. Catal.*, 2002, **21**, 79.
- 8 R. K. Grasselli, *Catal. Today*, 2014, **238**, 10.
- 9 N. Mizuno and M. Misono, *Chem. Rev.*, 1998, **98**, 199.
- 10 G. Koyano, T. Okuhara and M. Misono, *J. Am. Chem. Soc.*, 1998, **120**, 767.
- 11 J. M. Thomas, R. Raja, G. Sankar and R. G. Bell, *Nature*, 1999, **398**, 227.
- 12 J. M. Thomas, R. Raja, G. Sankar and R. G. Bell, *Acc. Chem. Res.*, 2001, **34**, 191.
- 13 J. M. Thomas and R. Raja, *Proc. Natl. Acad. Sci. U. S. A.*, 2005, **102**, 13732.
- 14 A. B. Getsoian, V. Shapovalov and A. T. Bell, *J. Phys. Chem. C*, 2013, **117**, 7123.
- 15 A. B. Getsoian, Z. Zhai and A. T. Bell, *J. Am. Chem. Soc.*, 2014, **136**, 13684.
- 16 T. Ushikubo, K. Oshima, A. Kayo, T. Umezawa, K. Kiyono and I. Sawaki, *Eur. Pat.*, 529852, 1992.
- 17 T. Ushikubo, K. Oshima, A. Kayo, T. Umezawa, K. Kiyono and I. Sawaki, *US Pat.*, 5281745, 1994.
- 18 T. Ushikubo, H. Nakamura, Y. Koyasu and S. Wagiki, *US Pat.*, 5380933, 1995.
- 19 T. Ushikubo, K. Oshima, A. Kayo, M. Vaarkamp and M. Hatano, *J. Catal.*, 1997, **169**, 394.
- 20 P. Botella, E. G. Gonzalez, A. Dejoz, J. M. L. Nieto, M. I. Vazquez and J. G. Calbet, *J. Catal.*, 2004, **225**, 428.
- 21 T. T. Nguyen, B. Deniau, P. Delichere and J. M. M. Millet, *Top. Catal.*, 2014, **57**, 1152.
- 22 C. Chiu, T. Vogt, L. Zhao, A. Geneste and N. Rösch, *Dalton Trans.*, 2015, **44**, 13778.
- 23 R. K. Grasselli, D. J. Buttrey, J. D. Burrington, A. Andersson, J. Holmberg, W. Ueda, J. Kubo, C. G. Lugmair and A. F. Volpe, *Top. Catal.*, 2006, **38**, 7.
- 24 Q. He, J. Woo, A. Belianinov, V. V. Gulians and A. Y. Borisevich, *ACS Nano*, 2015, **9**, 3470.
- 25 P. DeSanto, D. J. Buttrey, R. K. Grasselli, C. G. Lugmair, A. F. Volpe, B. H. Toby and T. Vogt, *Top. Catal.*, 2003, **23**, 23.
- 26 J. M. M. Millet, H. Roussel, A. Pigamo, J. L. Dubois and J. C. Jumas, *Appl. Catal., A*, 2002, **232**, 77.
- 27 H. Murayama, D. Vitry, W. Ueda, G. Fuchs, M. Anne and J. L. Dubois, *Appl. Catal., A*, 2007, **318**, 137.
- 28 N. R. Shiju, X. Liang, A. W. Weimer, C. Liang, S. Dai and V. V. Gulians, *J. Am. Chem. Soc.*, 2008, **130**, 5850.
- 29 W. Ueda, N. F. Chen and K. Oshihara, *Chem. Commun.*, 1999, 517.
- 30 W. Ueda and K. Oshima, *Appl. Catal., A*, 2000, **200**, 135.
- 31 T. Katou, D. Vitry and W. Ueda, *Chem. Lett.*, 2003, **32**, 1028.
- 32 T. Katou, D. Vitry and W. Ueda, *Catal. Today*, 2004, **91–92**, 237.
- 33 H. Watanabe and Y. Koyasu, *Appl. Catal., A*, 2000, **194–195**, 479.
- 34 R. K. Grasselli, J. D. Burrington, D. J. Buttrey, P. DeSanto, C. G. Lugmair, A. F. Volpe and T. Weingand, *Top. Catal.*, 2003, **23**, 5.
- 35 R. K. Grasselli, *Catal. Today*, 2005, **99**, 23.
- 36 R. K. Grasselli, C. G. Lugmair and A. F. Volpe, *Top. Catal.*, 2008, **50**, 66.
- 37 W. Ueda, D. Vitry and T. Katou, *Catal. Today*, 2004, **96**, 235.
- 38 W. Ueda, D. Vitry and T. Katou, *Catal. Today*, 2005, **99**, 43.
- 39 N. Watanabe and W. Ueda, *Ind. Eng. Chem. Res.*, 2006, **45**, 607.
- 40 W. D. Pyrz, D. A. Blom, N. R. Shiju, V. V. Gulians, T. Vogt and D. J. Buttrey, *J. Phys. Chem. C*, 2008, **112**, 10043.
- 41 W. D. Pyrz, D. A. Blom, T. Vogt and D. J. Buttrey, *Angew. Chem., Int. Ed.*, 2008, **47**, 2788.
- 42 X. Li, D. J. Buttrey, D. A. Blom and T. Vogt, *Top. Catal.*, 2011, **54**, 614.
- 43 T. Lunkenbein, F. Girgsdies, A. Wernbacher, J. Noack, G. Auffermann, A. Yasuhara, A. K. Hoffmann, W. Ueda, M. Eichelbaum, A. Trunschke, R. Schlögl and M. G. Willinger, *Angew. Chem., Int. Ed.*, 2015, **54**, 6828.
- 44 K. Chenoweth, A. C. T. Duin and W. A. Goddard, *Angew. Chem., Int. Ed.*, 2009, **48**, 7630.
- 45 W. A. Goddard III, J. E. Mueller, K. Chenoweth and A. C. T. Duin, *Catal. Today*, 2010, **157**, 71.
- 46 L. Zhao, C. C. Chiu, A. Genest and N. Rösch, *Comput. Theor. Chem.*, 2014, **1045**, 57.
- 47 H. Tsuji and A. Kayo, *J. Am. Chem. Soc.*, 2002, **124**, 5608.
- 48 M. Sadakane, K. Yamagata, K. Kodato, K. Endo, K. Toriumi, Y. Ozawa, T. Ozeki, T. Nagai, Y. Matsui, N. Sakaguchi, W. D. Pyrz, D. J. Buttrey, D. A. Blom, T. Vogt and W. Ueda, *Angew. Chem., Int. Ed.*, 2009, **48**, 3782.
- 49 R. Canioni, C. M. Roch, N. L. Laronze, M. Haouas, F. Taulèlle, J. Marrot, S. Paul, C. Lamonier, J. F. Paul, S. Loridant, J. M. M. Millet and E. Cadot, *Chem. Commun.*, 2011, **47**, 6413.
- 50 M. S. Sanchez, F. Girgsdies, M. Jastak, P. Kube, R. Schlögl and A. Trunschke, *Angew. Chem., Int. Ed.*, 2012, **51**, 7194.
- 51 M. Sadakane, K. Endo, K. Kodato, S. Ishikawa, T. Murayama and W. Ueda, *Eur. J. Inorg. Chem.*, 1731, 2013, 10–11.
- 52 M. Hävecker, S. Wrabetz, J. Kröhnert, L. I. Csepei, R. N. Alnoncourt, Y. V. Kolen'ko, F. Girgsdies, R. Schlögl and A. Trunschke, *J. Catal.*, 2012, **285**, 48.
- 53 R. N. d'Alnoncourt, L. I. Csepei, M. Hävecker, F. Girgsdies, M. E. Schuster, R. Schlögl and A. Trunschke, *J. Catal.*, 2014, **311**, 369.
- 54 C. Heine, M. Hävecker, M. S. Sanchez, A. Trunschke, R. Schlögl and M. Eichelbaum, *J. Phys. Chem. C*, 2013, **117**, 26988–26997.
- 55 M. Eichelbaum, M. Hävecker, C. Heine, A. M. Wernbacher, F. Rosowski, A. Trunschke and R. Schlögl, *Angew. Chem., Int. Ed.*, 2015, **54**, 2922.
- 56 C. Heine, M. Hävecker, A. Trunschke, R. Schlögl and M. Eichelbaum, *Phys. Chem. Chem. Phys.*, 2015, **17**, 8983.
- 57 G. Mestl, J. L. Margitfalvi, L. Végvári, G. P. Szijjártó and A. Tompos, *Appl. Catal., A*, 2014, **474**, 3.
- 58 S. H. Morejudo, A. Massó, E. G. González, P. Concepción and J. M. L. Nieto, *Appl. Catal., A*, 2015, **504**, 51.

- 59 S. Ishikawa, X. Yi, T. Murayama and W. Ueda, *Appl. Catal., A*, 2014, **474**, 10.
- 60 S. Ishikawa, X. Yi, T. Murayama and W. Ueda, *Catal. Today*, 2014, **238**, 35.
- 61 S. Ishikawa, D. Kobayashi, T. Konya, S. Ohmura, T. Murayama, N. Yasuda, M. Sadakane and W. Ueda, *J. Phys. Chem. C*, 2015, **119**, 7195.
- 62 M. Sadakane, N. Watanabe, T. Katou, Y. Nodasaka and W. Ueda, *Angew. Chem., Int. Ed.*, 2007, **46**, 1493.
- 63 T. Konya, T. Katou, T. Murayama, S. Ishikawa, M. Sadakane, D. J. Buttrey and W. Ueda, *Catal. Sci. Technol.*, 2013, **3**, 380.
- 64 M. Sadakane, K. Kodato, T. Kuranishi, Y. Nodasaka, K. Sugawara, N. Sakaguchi, T. Nagai, Y. Matsui and W. Ueda, *Angew. Chem., Int. Ed.*, 2008, **47**, 2493.
- 65 M. Sadakane, S. Ohmura, K. Kodato, T. Fujisawa, K. Kato, K. Shimizu, T. Murayama and W. Ueda, *Chem. Commun.*, 2011, **47**, 10812.
- 66 W. Ueda, *J. Jpn. Pet. Inst.*, 2013, **56**, 122.
- 67 C. Chen, K. Nakatani, T. Murayama and W. Ueda, *ChemCatChem*, 2013, **5**, 2869.
- 68 C. Qiu, C. Chen, S. Ishikawa, T. Murayama and W. Ueda, *Top. Catal.*, 2014, **57**, 1163.
- 69 W. Ueda, D. Vitry, T. Katou, N. Watanabe and Y. Endo, *Res. Chem. Intermed.*, 2006, **32**, 217.
- 70 S. Ishikawa, M. Tashiro, T. Murayama and W. Ueda, *Cryst. Growth Des.*, 2014, **14**, 4553.
- 71 K. Itabashi, Y. Kamimura, K. Iyoki, A. Shimojima and T. Okubo, *J. Am. Chem. Soc.*, 2012, **134**, 11542.
- 72 K. Iyoki, K. Itabashi and T. Okubo, *Microporous Mesoporous Mater.*, 2014, **189**, 22.
- 73 Y. Kamimura, S. Tanahashi, K. Itabashi, A. Sugawara, T. Wakihara, A. Shimojima and T. Okubo, *J. Phys. Chem. C*, 2011, **115**, 744.
- 74 K. Iyoki, K. Itabashi, W. Chaikittisilp, S. P. Elangovan, T. Wakihara, S. Kohara and T. Okubo, *Chem. Mater.*, 2014, **26**, 1957.
- 75 S. Goel, S. I. Zones and E. Iglesia, *Chem. Mater.*, 2015, **27**, 2056.
- 76 W. D. Pysz, D. A. Blom, M. Sadakane, K. Kodato, W. Ueda, T. Vogt and D. J. Buttrey, *Chem. Mater.*, 2010, **22**, 2033.
- 77 W. D. Pysz, D. A. Blom, M. Sadakane, K. Kodato, W. Ueda, T. Vogt and D. J. Buttrey, *Proc. Natl. Acad. Sci. U. S. A.*, 2010, **107**, 6152.
- 78 C. Liu, S. Zhao, X. Ji, B. Wang and D. Ma, *Mater. Chem. Phys.*, 2012, **133**, 579.
- 79 C. Liu, D. Ma, X. Ji, B. Wang and S. Zhao, *J. Am. Ceram. Soc.*, 2011, **94**, 2266.
- 80 V. P. Valtchev, L. Tosheva and K. N. Bozhilov, *Langmuir*, 2005, **21**, 10724.
- 81 S. Lee, D. Song, D. Kim, L. Lee, S. Kim, I. Y. Park and Y. D. Choi, *Mater. Lett.*, 2004, **58**, 342.
- 82 K. Kamata, K. Yonehara, Y. Nakagawa, K. Uehara and N. Mizuno, *Nat. Chem.*, 2010, **2**, 478.
- 83 N. Mizuno and K. Kamata, *Coord. Chem. Rev.*, 2011, **255**, 2358.

60

科学的なびら

上村大輔 編

天然物の化学

魅力と展望

SCIENCE IN ACTION SERIES 60



東京化学同人

化学の要点
シリーズ

18

基礎から学ぶ ケミカルバイオロジー

日本化学会 [編]

上村大輔

袖岡幹子

阿部孝宏

関関孝介 [著]

中村和彦

宮本憲二

共立出版

In: Polyoxometalates
Editor: Aaron P. Roberts

ISBN: 978-1-53610-007-5
© 2016 Nova Science Publishers, Inc.

The license for this PDF is unlimited except that no part of this digital document may be reproduced, stored in a retrieval system or transmitted commercially in any form or by any means. The publisher has taken reasonable care in the preparation of this digital document, but makes no expressed or implied warranty of any kind and assumes no responsibility for any errors or omissions. No liability is assumed for incidental or consequential damages in connection with or arising out of information contained herein. This digital document is sold with the clear understanding that the publisher is not engaged in rendering legal, medical or any other professional services.

Chapter 7

**FORMATION OF PHOSPHANEGOLD(I)
CLUSTER CATIONS MEDIATED
BY POLYOXOMETALATES,
MOLECULAR STRUCTURES AND CATALYSIS
FOR ORGANIC TRANSFORMATION**

Kenji Nomiya^{1,}, Takuya Yoshida^{1,2}
and Satoshi Matsunaga¹*

¹Department of Chemistry, Faculty of Science, Kanagawa University,
Tsuchiya, Hiratsuka, Kanagawa, Japan

²Research Center for Gold Chemistry, Graduate School
of Urban Environmental Sciences, Tokyo Metropolitan University,
Minami-osawa, Hachioji, Tokyo, Japan

ABSTRACT

Recently, we unexpectedly discovered a clusterization of monomeric phosphanegold(I) units, $[\text{Au}(\text{PR}_3)]^+$ during the course of carboxylate elimination from a monomeric phosphanegold(I) carboxylate, $[\text{Au}(\text{RS-pyrrld})(\text{PPh}_3)]$ ($\text{RS-Hpyrrld} = \text{RS-2-pyrrolidone-5-carboxylic acid}$) in the

* Corresponding author: Kenji Nomiya. Department of Chemistry, Faculty of Science, Kanagawa University, Tsuchiya 2946, Hiratsuka, Kanagawa 259-1293, Japan. Email: nomiya@kanagawa-u.ac.jp.

presence of free-acid form of Keggin polyoxometalate (POM), $H_3[\alpha-PW_{12}O_{40}] \cdot 7H_2O$. This reaction resulted in the formation of tetrakis {triphenylphosphanegold(I)}oxonium cations, $[\{Au(PPh_3)\}_4(\mu_4-O)]^{2+}$ as a counteranion of POM anion. In the formation of the tetragold(I) cluster cations, the POM surface oxygen atoms act as a template in the clusterization of phosphanegold(I) cations. In addition, formation of various phosphanegold(I) cluster cations was strongly dependent on the bulkiness, acidity and charge density of the POMs, and substituents on the aryl group of the phosphane ligands; for example, $[\{Au(PPh_3)\}_4(\mu_4-O)]\{[Au(PPh_3)\}_3(\mu_3-O)]\}[\alpha-PW_{12}O_{40}]$, $[\{(Au\{P(p-RPh)_3\})_2(\mu-OH)\}_2]_3[\alpha-PM_{12}O_{40}]_2$ (R = Me, M = W; R = Me, M = Mo; R = F, M = Mo), $[(Au\{P(m-FPh)_3\})_4(\mu_4-O)]_2[\{(Au\{P(m-FPh)_3\})_2(\mu-OH)\}_2][\alpha-PM_{12}O_{40}]_2$, and so on have been prepared. The POM-mediated clusterization of phosphanegold(I) cations provides effective synthetic routes for novel phosphanegold(I) cluster cations by a combination of the phosphanegold(I) carboxylates and different POMs, e.g., $[Au(RS-pyrrld)(PR_3)]$ (R = Ph, *p*-FPh, *p*-ClPh, *p*-MePh, *m*-FPh, *m*-MePh) and $[\alpha-XM_{12}O_{40}]^{n-}$ (X = P, Si, B, Al; M = W, Mo; $n = 3-5$). In fact, the heptagold(I) cluster cation, $[\{Au(PPh_3)\}_4(\mu_4-O)]\{[Au(PPh_3)\}_3(\mu_3-O)]\}^{3+}$, has been synthesized only by the POM-mediated clusterization method. Also, the POM anions as a counterion can be exchanged with the other anions, such as BF_4^- , PF_6^- , and OTf^- , resulting in a formation of the various gold(I) clusters depending upon the anions. In addition, several phosphanegold(I) complexes show effective homogeneous catalysis for organic synthesis. In this context, the POM-mediated clusterization of phosphanegold(I) cations would also provide the new insights for the catalytic applications of phosphanegold(I) complexes. In this chapter, we describe the recent progress of POM-mediated clusterization of phosphanegold(I) cations, and catalytic hydration of alkynes by the intercluster compounds of phosphanegold(I) cluster species with POMs.

Keywords: phosphanegold(I) cluster, Keggin-type polyoxometalate, intercluster compound, catalysis, hydration of alkynes

1. INTRODUCTION

Polyoxometalates (POMs) are discrete metal oxide clusters that are of current interest to their applications in catalysis and materials science [1]. The preparation of POM-based materials is therefore an active field of research. Some of the intriguing aspects are that a combination of POMs with metal cluster cations or macrocations by some intermolecular interactions has resulted in the formation of various hybrid compounds (so-called

supramolecular intercluster compounds, SICCs) from the viewpoints of crystal structure, sorption, electrochemical, photochemical properties and so on [2, 3]. In many SICCs, POMs have been combined with separately prepared metal cluster cations [4].

The field of element-centered gold clusters $[E(\text{AuL})_n]^{m+}$ ($E =$ group 13-17 elements; $L =$ electron-pair donor ligand, most frequently a tertiary phosphane) has been extensively studied by the Schmidbaur [5] and Laguna [6] groups. In many gold(I) clusters, the aurophilic interaction is the driving force for the oligomerization and stabilization in the solid state. For example, oxygen-centered tri(phosphanegold(I)) cluster cations $[\{\text{Au}(\text{PR}_3)\}_3(\mu_3\text{-O})]^+$ have been reported to exhibit different forms of structural dimerization by inter-aurophilic interactions depending upon the bulkiness of the phosphane ligands, i.e., the gold(I) atoms containing inter-aurophilic interactions form a tetrahedron ($R = \text{Me}$) or a square ($R = \text{Ph}$, etc.) [5]. In addition, several phosphanegold(I) complexes have been known to serve as effective homogeneous catalysts for organic reactions [7-9]. For example, $[\{\text{Au}(\text{PPh}_3)\}_3(\mu_3\text{-O})]\text{BF}_4$ has been used as a highly active and stereoselective catalyst for a Claisen rearrangement of propargyl vinyl ethers [10].

In 2010, we unexpectedly discovered the clusterization of monomeric phosphanegold(I) cation $[\text{Au}(\text{PPh}_3)]^+$ during the course of carboxylate elimination of a monomeric phosphanegold(I) carboxylate $[\text{Au}(\text{RS-pyrrld})(\text{PPh}_3)]$ ($\text{RS-Hpyrrld} = \text{RS-2-pyrrolidone-5-carboxylic acid}$) in the presence of the free-acid form of the Keggin POM $\text{H}_3[\alpha\text{-PW}_{12}\text{O}_{40}] \cdot 7\text{H}_2\text{O}$ [11]. This reaction resulted in the formation of SICC composed of tetrakis (triphenylphosphanegold(I))oxonium cluster cation $[\{\text{Au}(\text{PPh}_3)\}_4(\mu_4\text{-O})]^{2+}$ and POM anion. In addition, we have demonstrated the structure of various phosphanegold(I) clusters formed by a combination of monomeric phosphanegold(I) carboxylates and POMs [12-17]. Here, we describe the synthesis, structures and catalytic application of SICCs composed of phosphanegold(I) cluster cations and Keggin POMs, based on several our papers published so far [11-18].

2. FORMATION OF TETRA(PHOSPHANEGOLD(I))OXONIUM CLUSTER CATIONS

The reaction by liquid-liquid diffusion method between a monomeric phosphanegold(I) carboxylate $[\text{Au}(\text{RS-pyrrld})(\text{PPh}_3)]$ and the free-acid form of

the α -Keggin POM $H_3[\alpha-PW_{12}O_{40}] \cdot 7H_2O$ resulted in the formation of a tetra(phosphanegold(I))oxonium cluster cation as a counterion of POM anion [$\{Au(PPh_3)\}_4(\mu_4-O)_3[\alpha-PW_{12}O_{40}]_2 \cdot 4EtOH$ (Au_4-PW , Figure 1a) [11]. This reaction occurs by the clusterization of monomeric phosphanegold(I) cation $[Au(PPh_3)]^+$ during the course of carboxylate elimination in the presence of POM.

The tetra(phosphanegold(I))oxonium cluster cation as a counterion of POM anion has a trigonal-pyramidal structure (C_{3v} symmetry, Figure 1b) with three intra-aurophilic interactions ($Au-Au$: 2.9728, 2.9302, 2.9836 Å), while that with BF_4^- anion in a reported compound [19] has a tetrahedral structure (T_d symmetry). The tetra(phosphanegold(I))oxonium cluster cation as a counterion of POM anion is somewhat distorted by the interactions between gold(I) and oxygen atoms of POM. Thus, the tetra(phosphanegold(I))oxonium cluster cation has a different geometry depending upon the counterions. The encapsulated μ_4-O atom is placed within the basal plane composed of three basal gold(I) atoms.

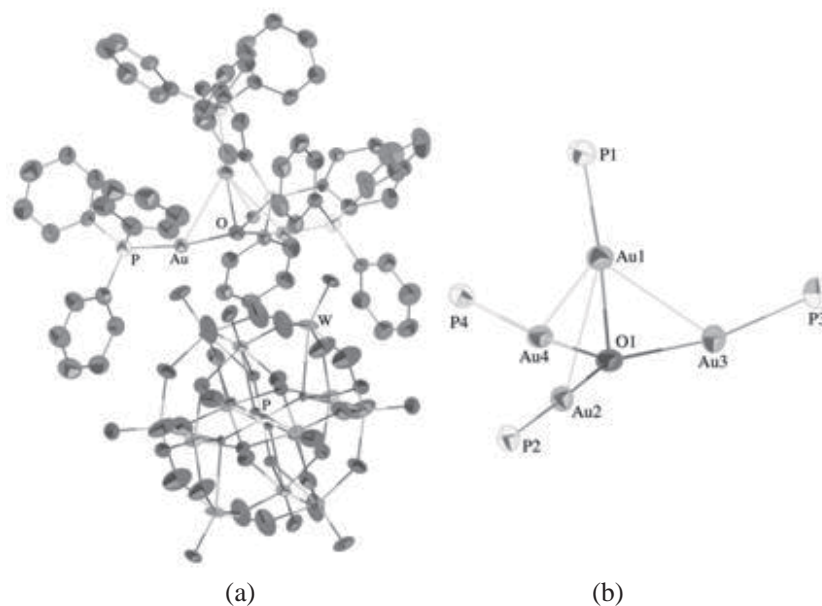


Figure 1. (a) Molecular structure of Au_4-PW and (b) core structure of $[\{Au(PPh_3)\}_4(\mu_4-O)]^{2+}$. Reprinted with permission from ref. [11]. Copyright 2010 American Chemical Society.

The solid-state CPMAS ^{31}P NMR showed three broad signals at -14.6 , 15.3 and 25.8 ppm. These signals are assignable to the heteroatom phosphorus in the POM and two inequivalent phosphorus atoms due to PPh_3 groups in the trigonal-pyramidal structure of the tetra(phosphanegold(I))oxonium cluster cation. On the other hand, the solution $^{31}\text{P}\{^1\text{H}\}$ NMR in $\text{DMSO-}d_6$ showed two sharp signals at -14.79 and 24.87 ppm due to the POM and PPh_3 groups. The peak at 24.87 ppm is an averaged signal due to motion in the solution while keeping the formula of tetra(phosphanegold(I))oxonium cluster cation, which can be compared with the peak at 25.4 ppm in CD_2Cl_2 of $[\{\text{Au}(\text{PPh}_3)_4(\mu_4\text{-O})\}(\text{BF}_4)_2]$ reported by Schmidbaur et al. [19].

Similar tetra(phosphanegold(I))oxonium cluster cations are formed when the combination of $[\text{Au}(\text{RS-pyrrld})(\text{PR}_3)]$ and $\text{H}_n[\alpha\text{-XM}_{12}\text{O}_{40}] \cdot m\text{H}_2\text{O}$ ($\text{R} = \text{Ph}$, $\text{X} = \text{P}$, $\text{M} = \text{Mo}$; $\text{R} = \text{Ph}$, $\text{X} = \text{Si}$, $\text{M} = \text{W}$; $\text{R} = m\text{-MePh}$, $\text{X} = \text{Si}$, $\text{M} = \text{W}$ or Mo ; $\text{R} = m\text{-FPh}$, $\text{X} = \text{Si}$, $\text{M} = \text{Mo}$) were used [11, 12]. All of tetra(phosphanegold(I))oxonium cluster cations as a counterion of POMs adopt trigonal-pyramidal structures (C_{3v} symmetry) due to interactions with the surface oxygen atoms of POMs.

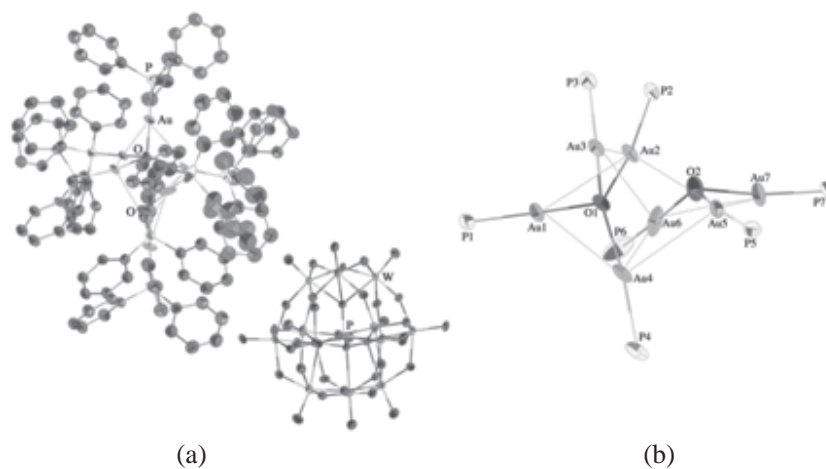


Figure 2. (a) Molecular structure of $\text{Au}_7\text{-PW}$ and (b) core structure of $[\{\{\text{Au}(\text{PPh}_3)_4(\mu_4\text{-O})\}\{\{\text{Au}(\text{PPh}_3)_3(\mu_3\text{-O})\}\}]^{3+}$. Reproduced from ref. [13] with permission from the Royal Society of Chemistry.

3. FORMATION OF HEPTA(PHOSPHANEGOLD(I))DIOXONIUM CLUSTER CATIONS

In the reaction of [Au(*RS*-pyrrld)(PPh₃)] with the sodium salt of the Keggin POM, Na₃[α -PW₁₂O₄₀] \cdot 9H₂O having lower acidity than the free-acid form, hepta(phosphanegold(I))dioxonium cluster cation as a counterion of POM anion [{{Au(PPh₃)₄(μ ₄-O)}}{{Au(PPh₃)₃(μ ₃-O)}}][α -PW₁₂O₄₀] \cdot EtOH (*Au*₇-*PW*, Figure 2a) was formed [13]. The tetra- and heptaphosphanegold(I) clusters were synthesized under the same conditions except counterions (H⁺ or Na⁺) of POMs. Thus, the acidity of the POMs plays an important role for the clusterization of [Au(PR₃)⁺].

The hepta(phosphanegold(I))dioxonium cluster cation is formed by four inter-aurophilic interactions (Au–Au: 3.1028, 3.0936, 3.2428, 3.2732 Å) between tetra(phosphanegold(I))oxonium unit {{Au(PPh₃)₄(μ ₄-O)}}²⁺ and tri(phosphanegold(I))oxonium unit {{Au(PPh₃)₃(μ ₃-O)}}⁺ (Figure 2b). The tetra(phosphanegold(I))oxonium unit has a distorted tetrahedron structure composed of three intra-aurophilic interactions. The encapsulated μ ₄-O atom is placed within the distorted tetrahedron. One of the phenyl groups in the tetra(phosphanegold(I))oxonium unit is disordered. The tri(phosphane gold(I))oxonium unit has a triangular plane by three gold(I) atoms with two intra-aurophilic interactions. The bridged μ ₃-O atom is placed out-of-plane consisting of three gold(I) atoms.

As the other hepta(phosphanegold(I))dioxonium cluster cation, only one structural analysis for [{{Au{P(*p*-MePh)₃}₄(μ ₄-O)}}{{Au{P(*p*-MePh)₃}₃(μ ₃-O)}}}]³⁺ has been reported [12]. This structure is similar to the [{{Au(PPh₃)₄(μ ₄-O)}}{{Au(PPh₃)₃(μ ₃-O)}}}]³⁺, but the number of inter-aurophilic interaction is decreased.

The hepta(phosphanegold(I))dioxonium cluster cations are only formed in the presence of POM anion. The POM-mediated clusterization for the formation of phosphanegold(I) cluster cations provides effective synthetic routes for novel phosphanegold(I) cluster cations.

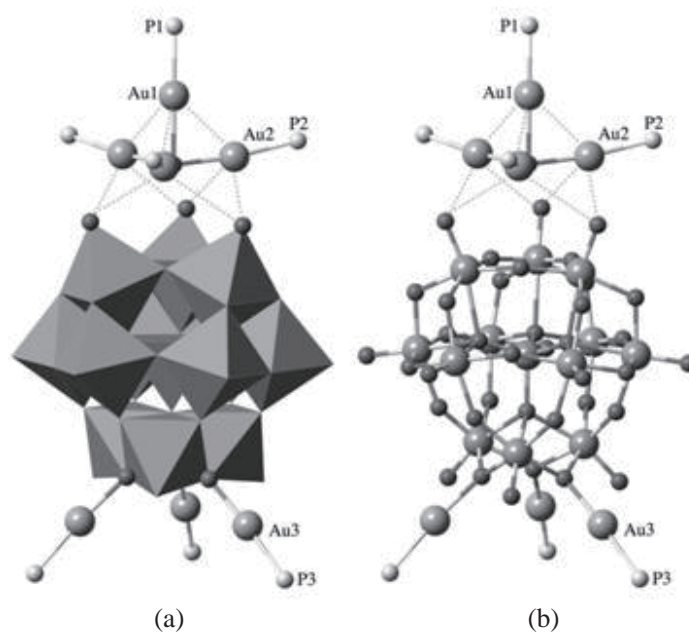


Figure 3. Partial structures of Au_4-AlW , (a) polyhedral representation and (b) ball-and-stick model. Reprinted with permission from ref. [14]. copyright 2013, The Chemical Society of Japan.

4. FORMATION OF PHOSPHANEGOLD(I) CLUSTER CATIONS AND MONOMERIC PHOSPHANEGOLD(I) CATIONS LINKED TO THE POMs

Clusterization of $[Au(PR_3)]^+$ in the presence of the POMs was strongly dependent on the bulkiness and acidity of the POMs, but a role of POMs was unclear. The reaction of $[Au(RS-pyrrld)(PPh_3)]$ with highly negative charged Keggin POMs $H_5[\alpha-XW_{12}O_{40}] \cdot nH_2O$ ($X = Al, B$) by liquid-liquid diffusion method resulted in formation of the tetra(phosphanegold(I))oxonium cluster cation and the three monomeric phosphanegold(I) cations linked to the POMs $[\{ Au(PPh_3) \}_4(\mu_4-O)] [\alpha-XW_{12}O_{40} \{ Au(PPh_3) \}_3] \cdot 3EtOH$ (Au_4-XW ; Figure 3, $X = Al$) [14]. The tetra(phosphanegold(I))oxonium cluster cation adopts a trigonal-pyramidal structure (C_{3v} symmetry) composed of three short edges associated

with the apical gold atom (Au–Au: 2.8929 Å) and a triangular plane of the three basal gold(I) atoms. Three monomeric phosphanegold(I) cations link to the OW_2 oxygen atoms of edge-shared WO_6 octahedra of the POM opposite the tetra(phosphanegold(I))oxonium cluster cation.

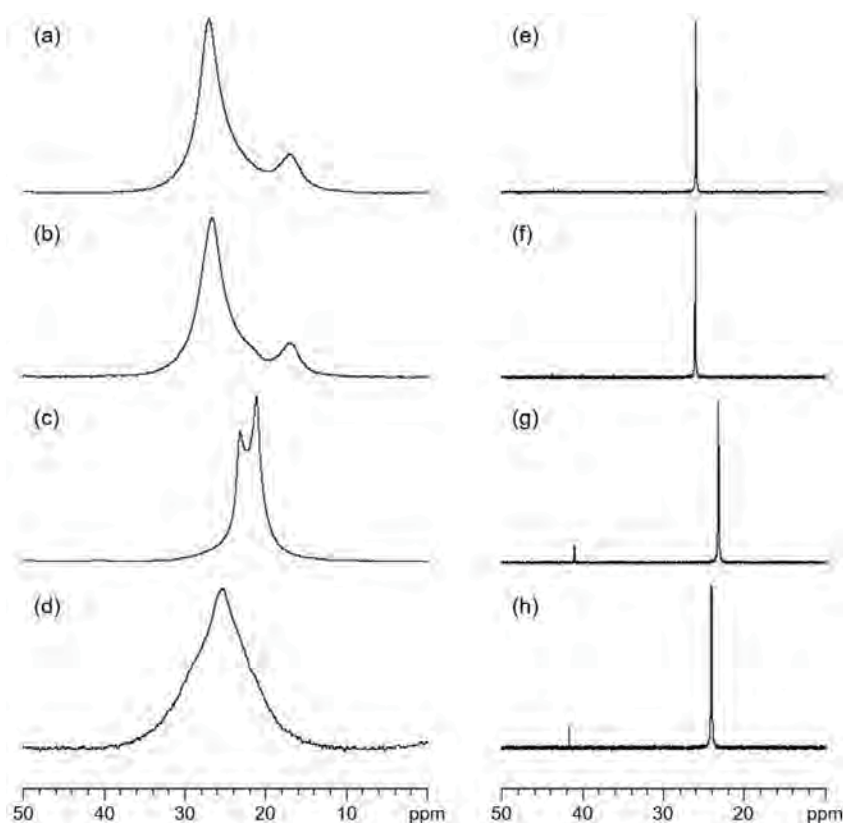


Figure 4. Solid-state CPMAS ^{31}P NMR spectra of (a) $\text{Au}_4\text{-AIW}$, (b) $\text{Au}_4\text{-BW}$, (c) $\text{Au}_4\text{-p-F-SiMo}$ and (d) $\text{Au}_4\text{-p-Cl-SiMo}$, and solution $^{31}\text{P}\{^1\text{H}\}$ NMR spectra in $\text{DMSO-}d_6$ of (e) $\text{Au}_4\text{-AIW}$, (f) $\text{Au}_4\text{-BW}$, (g) $\text{Au}_4\text{-p-F-SiMo}$ and (h) $\text{Au}_4\text{-p-Cl-SiMo}$.

Solid-state CPMAS ^{31}P NMR of $\text{Au}_4\text{-AIW}$ showed two broad signals at 17.0 and 27.1 ppm with relative intensities of 1:6 originating from the inequivalent PPh_3 groups (Figure 4a). The peak at 17.0 ppm is assignable to one apical phosphorus atom in the tetra(phosphanegold(I))oxonium cluster cation, and the peak at 27.1 ppm is assignable to the three basal phosphorus

atoms in the tetra(phosphanegold(I))oxonium cluster cation and three monomeric phosphanegold(I) cations linked to the POM. In contrast, the solution $^{31}\text{P}\{^1\text{H}\}$ NMR of $Au_4\text{-AlW}$ in $\text{DMSO-}d_6$ displayed only one sharp signal at 26.00 ppm (Figure 4e). The singlet in the solution can be explained by the rapid exchange of phosphanegold(I) cations among the tetra (phosphanegold(I))oxonium cluster cation, the three monomeric phosphanegold(I) cations linked to the POM and the monomeric $[\text{Au}(\text{dmsO})(\text{PPh}_3)]^+$ presence in solution. The same behavior was observed for $Au_4\text{-BW}$ (Figures 4b,f). Thus, the monomeric phosphanegold(I) cations linked to the POM indicate a transient state in the formation of the tetra(phosphanegold(I))oxonium cluster cation. In other words, the OW_2 oxygen atoms of edge-shared WO_6 octahedra of the Keggin POM act as multi-centered active binding sites for the monomeric phosphanegold(I) cations generated from elimination of the carboxylate ligands in the presence of the POM.

5. FORMATION OF DIMER OF DI(PHOSPHANEGOLD(I)) HYDROXIDE CATIONS

Formation of phosphanegold(I) cluster cations by POM-mediated clusterization also depends on the substituent of aryl group in the phosphane ligands. In the reaction between $[\text{Au}(\text{RS-pyrrld})\{\text{P}(p\text{-MePh})_3\}]$ and $\text{H}_3[\alpha\text{-PM}_{12}\text{O}_{40}] \cdot n\text{H}_2\text{O}$ ($\text{M} = \text{W}, \text{Mo}$), dimers of di(phosphanegold(I)) hydroxide cations with POM anions $[\{(\text{Au}\{\text{P}(p\text{-MePh})_3\})_2(\mu\text{-OH})\}_2]_3[\alpha\text{-PM}_{12}\text{O}_{40}]_2$ ($Au_4\text{-}p\text{-Me-PM}$; Figure 5a, $\text{M} = \text{W}$) were formed [15]. The dimer of di(phosphanegold(I)) hydroxide cation $[\{(\text{Au}\{\text{P}(p\text{-MePh})_3\})_2(\mu\text{-OH})\}_2]^{2+}$ can be regarded as the dimerization of di(phosphanegold(I)) hydroxide cations $\{(\text{Au}\{\text{P}(p\text{-MePh})_3\})_2(\mu\text{-OH})\}^+$. The di(phosphanegold(I)) hydroxide cation consists of two $(\text{Au}\{\text{P}(p\text{-MePh})_3\})^+$ units linked by a $\mu\text{-OH}$ group and is triangular in shape. Two di (phosphanegold(I)) hydroxide cations dimerize by four inter-aurophilic interactions (Au-Au : 2.991 Å) in a crossed-edge arrangement leading to a tetrahedral array of the four gold(I) atoms (Figure 5b). The hydrogen bonding between the peripheral phosphane ligands and the oxygen atoms of POMs was formed (Figure 5c).

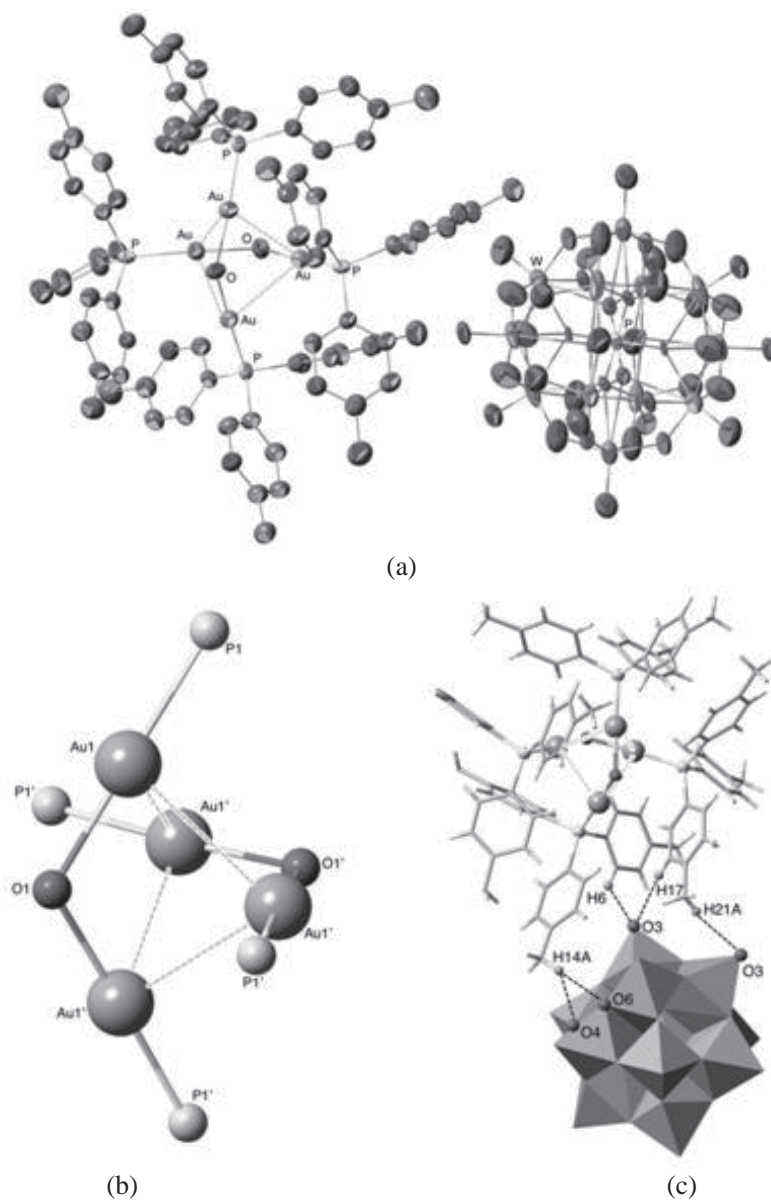
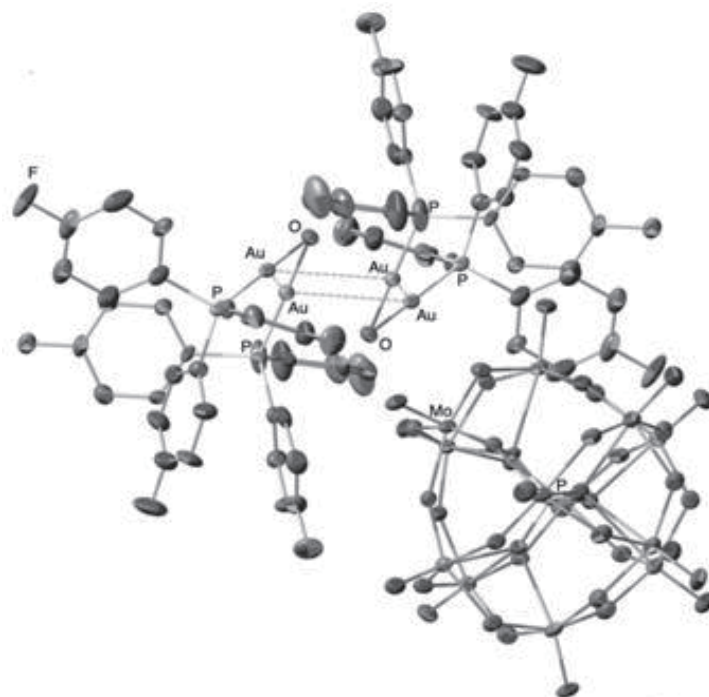


Figure 5. (a) Partial structure of Au_4 -*p*-Me-PW, (b) core structure of $[(Au\{P(p\text{-MePh})_3\})_2(\mu\text{-OH})]_2^{2+}$ in a crossed-edge arrangement and (c) hydrogen bonding between the phosphane ligands and POM anion. Reproduced from ref. [15] with permission from the Royal Society of Chemistry.

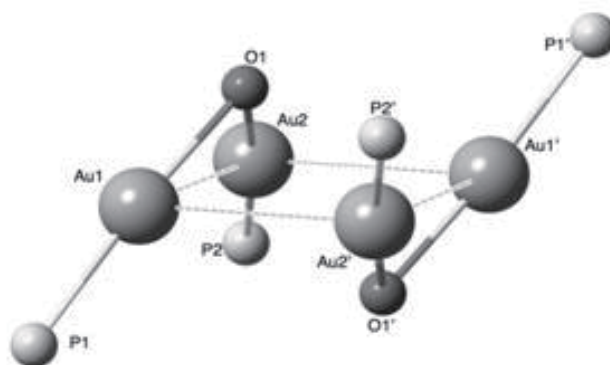
As for other substituents, the reaction of $[\text{Au}(\text{RS-pyrrld})\{\text{P}(p\text{-XPh})_3\}]$ ($X = \text{F}, \text{Cl}$) and $\text{H}_3[\alpha\text{-PMo}_{12}\text{O}_{40}] \cdot 14\text{H}_2\text{O}$ provided a dimer of di(phosphanegold(I)) hydroxide cations with POM anions $[\{(\text{Au}\{\text{P}(p\text{-XPh})_3\})_2(\mu\text{-OH})\}_2]_3[\alpha\text{-PMo}_{12}\text{O}_{40}]_2 \cdot n\text{EtOH}$ ($Au_4\text{-}p\text{-}X\text{-}PMo$; Figure 6a, $X = \text{F}$) [15, 16]. The two dimers of di(phosphanegold(I)) hydroxide cations $[\{(\text{Au}\{\text{P}(p\text{-XPh})_3\})_2(\mu\text{-OH})\}_2]^{2+}$ in $Au_4\text{-}p\text{-}X\text{-}PMo$ ($X = \text{F}, \text{Cl}$) were similar with each other. Two di(phosphanegold(I)) hydroxide cations dimerize by four inter-aurophilic interactions (Au–Au: 3.280, 3.197, 3.192 Å for $Au_4\text{-}p\text{-}F\text{-}PMo$) in a parallel-edge arrangement leading to a rectangular array of the four gold(I) atoms (Figure 6b). The interactions between di(phosphanegold(I)) hydroxide cations and the oxygen atoms of the POM were observed.

A parallel-edge phosphanegold(I) cation has been reported for the thiolate-bridged phosphanegold(I) cations $[\{(\text{Au}(\text{PR}^1_3))_2(\mu\text{-SR}^2)\}_2]^{2+}$ [5, 6]. The $[\{(\text{Au}\{\text{P}(p\text{-XPh})_3\})_2(\mu\text{-OH})\}_2]^{2+}$ is the first example of a hydroxide-bridged phosphanegold(I) cation dimerized in a parallel-edge arrangement.

A substituent position on the aryl groups in phosphane ligands also influences the clusterization. The reaction between $[\text{Au}(\text{RS-pyrrld})\{\text{P}(m\text{-FPh})_3\}]$ and $\text{H}_3[\alpha\text{-PMo}_{12}\text{O}_{40}] \cdot 14\text{H}_2\text{O}$ formed the two types of cations, i.e., tetra(phosphanegold(I))oxonium cluster cations and dimer of di(phosphanegold(I)) hydroxide cation, with POM anions $[(\text{Au}\{\text{P}(m\text{-FPh})_3\})_4(\mu_4\text{-O})]_2[\{(\text{Au}\{\text{P}(m\text{-FPh})_3\})_2(\mu\text{-OH})\}_2][\alpha\text{-PMo}_{12}\text{O}_{40}]_2 \cdot \text{EtOH}$ ($Au_4\text{-}m\text{-}F\text{-}PMo$, Figure 7a) [12]. The two tetra(phosphanegold(I))oxonium cluster cations adopt trigonal-pyramidal structures which are corresponding geometry of $Au_4\text{-}PW$ (Figure 7b). The dimer of di(phosphanegold(I)) hydroxide cation is in a parallel-edge arrangement by inter-aurophilic interactions (Au–Au: 3.2921, 3.3454 Å) (Figure 7c). This structure is similar to that of $Au_4\text{-}p\text{-}F\text{-}PMo$. The five gold(I) atoms in the tetra(phosphanegold(I))oxonium cluster cations interact with the terminal oxygen atoms and OMo_2 oxygen atoms of edge-shared MoO_6 octahedra of the Keggin POMs. The two gold(I) atoms in the dimer of di(phosphanegold(I)) hydroxide cation interact with the OMo_2 oxygen atoms of edge-shared MoO_6 octahedra of the Keggin POMs, and the short distances between $\mu\text{-OH}$ groups and Keggin POMs indicate the existence of hydrogen bonding (Figure 7d). Thus, the meta-substituted triarylphosphane ligand also significantly influences for the clusterization in presence of POM.



(a)



(b)

Figure 6. (a) Partial structure of $Au_4-p-F-PMo$ and (b) core structure of $[(Au\{P(p-FPh)_3\})_2(\mu-OH)_2]^{2+}$ in a parallel-edge arrangement. Reproduced from ref. [15] with permission from the Royal Society of Chemistry.

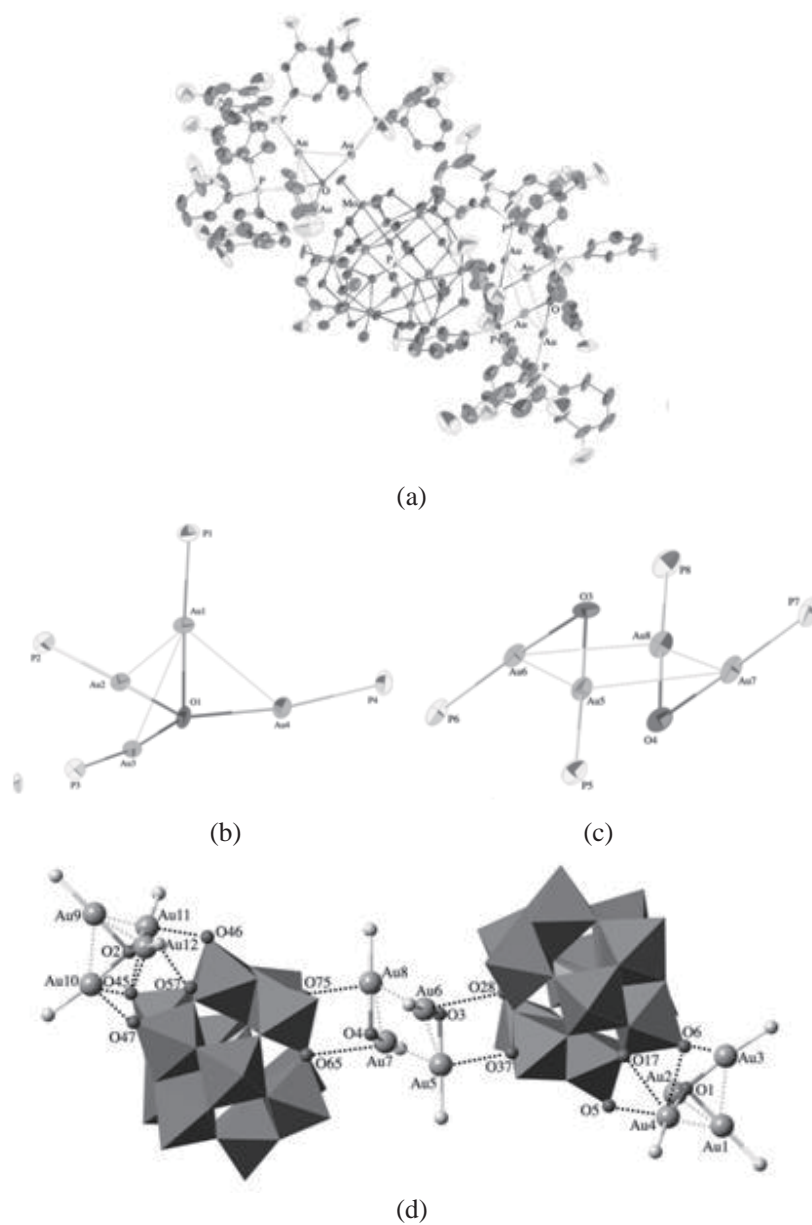


Figure 7. (a) Partial structure of $Au_4\text{-}m\text{-}F\text{-}PMo$, core structures of (b) $[(Au\{P(m\text{-}FPh)_3\})_4(\mu_4\text{-}O)]^{2+}$ and (c) $[(Au\{P(m\text{-}FPh)_3\})_2(\mu\text{-}OH)_2]^{2+}$ in a parallel-edge arrangement, and (d) the Au–O and OH–O interactions. Reproduced from ref. [12].

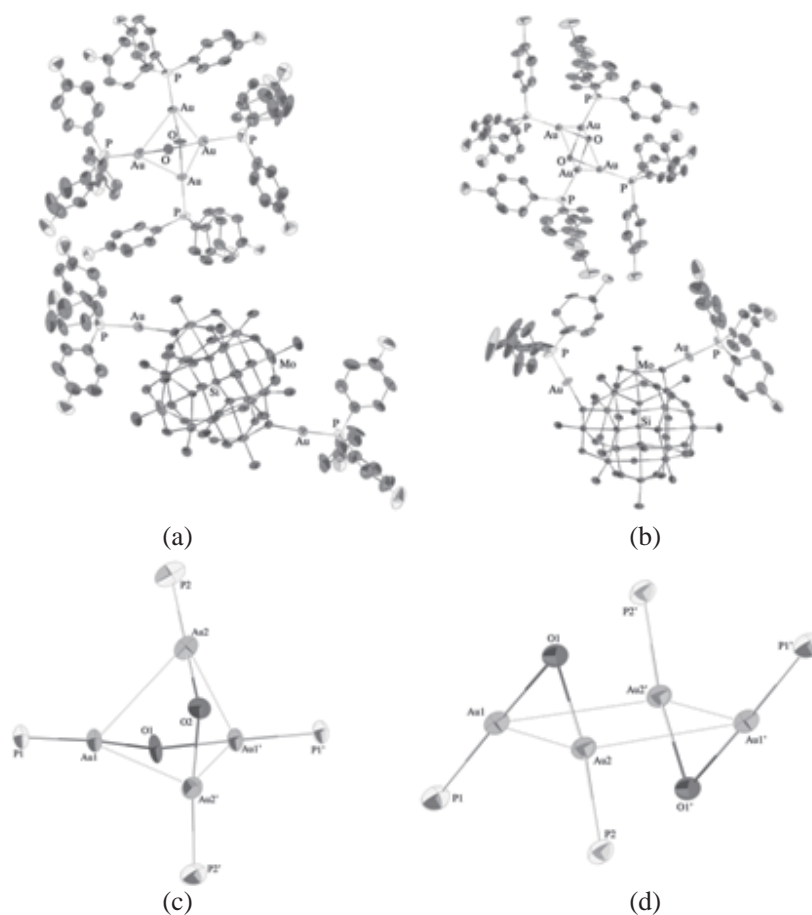


Figure 8. Molecular structures of (a) $Au_4-p-F-SiMo$ and (b) $Au_4-p-Cl-SiMo$, and core structures of (c) $[(Au\{P(p-FPh)_3\})_2(\mu-OH)]_2^{2+}$ and (d) $[(Au\{P(p-ClPh)_3\})_2(\mu-OH)]_2^{2+}$. Reproduced from ref. [17] with permission from John Wiley and Sons[©] 2015.

The surface oxygen atoms of the POM also influence the formation of dimer of di(phosphanegold(I)) hydroxide cations. The dimer of di(phosphanegold(I)) hydroxide cations and the two monomeric phosphanegold(I) cations linked to the POM $[(Au\{P(p-XPh)_3\})_2(\mu-OH)]_2[\alpha-SiMo_{12}O_{40}(Au\{P(p-XPh)_3\})_2] \cdot nEtOH$ ($X = F, Cl$; $Au_4-p-X-SiMo$, Figures 8a,b) were synthesized by reaction of $[Au(RS-pyrrld)\{P(p-XPh)_3\}]$ with $H_4[\alpha-SiMo_{12}O_{40}] \cdot 12H_2O$ [17]. In the $Au_4-p-F-SiMo$, two di(phosphanegold(I))

hydroxide cations dimerized to form a dimer of di(phosphanegold(I)) hydroxide cation $[(\text{Au}\{\text{P}(p\text{-FPh})_3\})_2(\mu\text{-OH})]^{2+}$ by four inter-aurophilic interactions in a crossed-edge arrangement leading to a tetrahedral array of the four gold(I) atoms (Figure 8c). On the other hand, in the *Au₄-p-Cl-SiMo*, two di(phosphanegold(I)) hydroxide cations dimerized to form the $[(\text{Au}\{\text{P}(p\text{-ClPh})_3\})_2(\mu\text{-OH})]^{2+}$ in a parallel-edge arrangement leading to a rectangular array of the four gold(I) atoms (Figure 8d). Two monomeric phosphanegold(I) cations in *Au₄-p-X-SiMo* (X = F, Cl) link to the OMo₂ oxygen atoms of edge-shared MoO₆ octahedra of the POMs, but coordination sites in the POMs are different. It should be noted that the OM₂ oxygen atoms of the edge-shared MO₆ octahedra in the Keggin POM also act as a multi-centered active binding site for the formation of dimer of di(phosphanegold(I)) hydroxide cations.

Solid-state CPMAS ³¹P NMR of *Au₄-p-F-SiMo* showed two signals at 21.1 and 23.1 ppm originating from the inequivalent phosphane groups (Figure 4c). The signal at 21.1 ppm is assignable to dimer of di(phosphanegold(I)) hydroxide cation, and the signal at 23.1 ppm is assignable to the two monomeric phosphanegold(I) cations linked to the POM. On the other hand, *Au₄-p-Cl-SiMo* showed one broad signal at 25.5 ppm, which will be due to the overlap of the signals based on dimer of di(phosphanegold(I)) hydroxide cation and the two monomeric phosphanegold(I) cations linked to the POM (Figure 4d). In contrast, solution ³¹P{¹H} NMR in DMSO-*d*₆ showed single sharp signals at 23.23 ppm for *Au₄-p-F-SiMo* (Figure 4g) and 24.07 ppm for *Au₄-p-Cl-SiMo* (Figure 4h). The single signals have been explained by the rapid exchange among dimer of di(phosphanegold(I)) hydroxide cations, the monomeric phosphanegold(I) cations linked to the POM and the monomeric phosphanegold(I) cations $[\text{Au}(\text{dmsO})(\text{PR}_3)]^+$ presence in solution. Because Keggin molybdo-POMs are unstable in DMSO, minor peaks at 41.06 and 41.71 ppm assignable to $[\text{Au}(\text{PR}_3)_2]^+$ were also observed (Figures 4g,h), resulting from decomposition of *Au₄-p-X-SiMo* in the DMSO-*d*₆ solution.

6. ANION-EXCHANGE FROM POMs TO OTHER ANIONS

We have been interested in the effect of POM anion on the structure of phosphanegold(I) cluster cation in the solid state SICCs. In order to explicitly clarify the effect of the POM anion, anions of the phosphanegold(I) cluster cations (*Au₇-PW*, *Au₄-p-Cl-PMo*, *Au₄-p-F-PMo*) were exchanged from the polyoxoanions to other small anions, such as BF₄⁻, PF₆⁻, OTf⁻, using anion-exchange resin, and their molecular structures were determined.

An anion of the hepta(phosphanegold(I))dioxonium cluster cation, $[\{\{\text{Au}(\text{PPh}_3)\}_4(\mu_4\text{-O})\}\{\{\text{Au}(\text{PPh}_3)\}_3(\mu_3\text{-O})\}][\alpha\text{-PW}_{12}\text{O}_{40}]\cdot\text{EtOH}$ ($\text{Au}_7\text{-PW}$), was exchanged from the polyoxoanion to BF_4^- using anion-exchange resin [13]. In the solution $^{31}\text{P}\{^1\text{H}\}$ NMR spectrum of the POM-free phosphanegold(I) cation, the peak due to the heptagold(I) cluster cation was not observed, but only tetragold(I) cluster was observed in solution. Therefore, the heptagold(I) cluster can be isolated only by the POM-mediated clusterization method.

When an anion of the dimer of di(phosphanegold(I)) cation in the parallel-edge arrangement with POM ($\text{Au}_4\text{-}p\text{-Cl-PMo}$) was exchanged from the POM to PF_6^- using anion-exchange resin, $[\{\{\text{Au}\{\text{P}(p\text{-ClPh})_3\}\}_3(\mu_3\text{-O})\}_2](\text{PF}_6)_2\cdot 4\text{CH}_2\text{Cl}_2$ ($\text{Au}_6\text{-PF}_6$) and $[(\text{Au}\{\text{P}(p\text{-ClPh})_3\})_4(\mu_4\text{-O})]_2[\alpha\text{-PMo}_{12}\text{O}_{40}]\text{PF}_6$ ($\text{Au}_4\text{-PMo}_{12}\text{-PF}_6$) were obtained [16].

X-ray crystallography revealed that the counteranion in $\text{Au}_6\text{-PF}_6$ was the dimeric cation of the $\mu_3\text{-O}$ bridged tris{phosphanegold(I)} species, $[\{(\mu_3\text{-O})(\text{Au}\{\text{P}(p\text{-ClPh})_3\})_3\}_2]^{2+}$. The fragment $\{(\mu_3\text{-O})(\text{Au}\{\text{P}(p\text{-ClPh})_3\})_3\}^+$ has a pyramidal structure and the $\mu_3\text{-O}$ atom is outside the Au_3 plane (Figures 9a,c).

On the other hand, $\text{Au}_4\text{-PMo}_{12}\text{-PF}_6$ was prepared from $\text{Au}_4\text{-}p\text{-Cl-PMo}$ using a small amount of an anion-exchange resin in the form of PF_6^- , and it was the compound with mixed counteranions of one POM and one PF_6^- anions. X-ray crystallography of $\text{Au}_4\text{-PMo}_{12}\text{-PF}_6$ showed a discrete intercluster compound containing two $[(\text{Au}\{\text{P}(p\text{-ClPh})_3\})_4(\mu_4\text{-O})]^{2+}$ cations, one $[\alpha\text{-PMo}_{12}\text{O}_{40}]^{3-}$ and one PF_6^- . The structure of $[(\text{Au}\{\text{P}(p\text{-ClPh})_3\})_4(\mu_4\text{-O})]^{2+}$ in $\text{Au}_4\text{-PMo}_{12}\text{-PF}_6$ was found to be a unusual, $\mu_4\text{-O}$ -bridged tetragonal-pyramid with C_{4v} symmetry (Figures 9b,d), which was a first class of the electron-deficient species of the oxygen-bridged gold(I) clusters.

The bonding mode of $\mu_4\text{-O}$ atom and the gold(I) centers in the $[(\mu_4\text{-O})(\text{AuPR}_3)_4]^{2+}$ ($\text{R} = p\text{-ClPh}$) cation can be described by a simple MO diagram, just like that of the S-analogous $[(\mu_4\text{-S})(\text{AuPPh}_3)_4]^{2+}$ with C_{4v} symmetry [20]. Three bonding orbitals are filled by six valence electrons available, and the non-bonding orbital a_1 as the HOMO is occupied by two electrons. Thus, the four O-AuPR₃ bonds in $\text{Au}_4\text{-PMo}_{12}\text{-PF}_6$ can be seen as electron-deficient with a bond order of 3/4, and the $\mu_4\text{-O}$ atom has a lone pair. This is contrasted to the previously reported, C_{3v} symmetry compound, i.e., $[(\mu_4\text{-O})\{\text{Au}(\text{PR}_3)_4\}]^{2+}$ ($\text{R} = \text{Ph}$ [11], $m\text{-FPh}$, $m\text{-MePh}$ [12]), in which the four O-AuPR₃ bonds can be seen as a single bond with a bond order 1. The present cation in $\text{Au}_4\text{-PMo}_{12}\text{-PF}_6$ is in a class of hypercoordinated species, together with $[(\mu_4\text{-S})(\text{AuPPh}_3)_4]^{2+}$ [20, 21] and $[(\mu_3\text{-S})(\text{AuPPh}_3)_3]^+$ [22, 23].

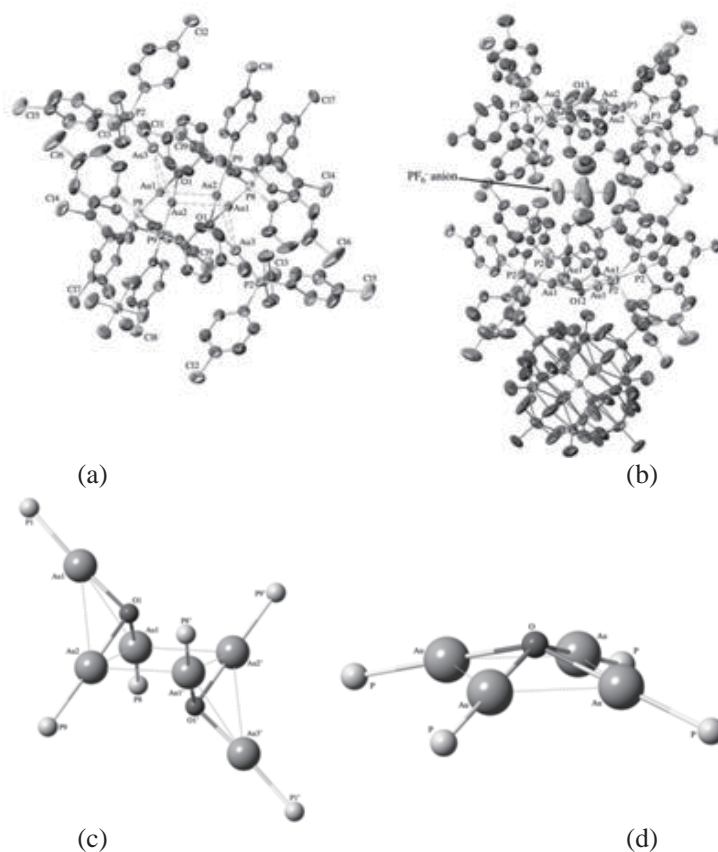


Figure 9. Molecular structures of (a) Au_6-PF_6 and (b) $Au_4-PMO_{12}-PF_6$, and core structures of (c) $[(Au\{P(p-ClPh)_3\})_3(\mu_3-O)]^{2+}$ and (d) $[(Au\{P(p-ClPh)_3\})_4(\mu_4-O)]^{2+}$.

The dimer of di(phosphanegold(I)) cation in the parallel-edge arrangement with POM, $[(Au\{P(p-FPh)_3\})_2(\mu-OH)]_2[\alpha-PMO_{12}O_{40}]_2 \cdot 3EtOH$ ($Au_4-p-F-PMO$) can be converted to the POM-free, OTf^- salt, $[(Au\{P(p-FPh)_3\})_2(\mu-OH)]_2(OTf)_2$ (Au_4-OTf) by anion-exchange resin in the form of OTf^- [16]. The digold(I) unit consists of two $\{(Au\{P(p-FPh)_3\})_2(\mu-OH)\}^+$ monomers linked by a μ -OH ligand, and the two digold(I) units dimerize in a crossed-edge arrangement by aurophilic interactions (Au-Au: 3.2530(4) Å) to form the tetragold(I) cluster cation $[(Au\{P(p-FPh)_3\})_2(\mu-OH)]_2^{2+}$. The crossed-edge cluster cation $[(Au\{P(p-FPh)_3\})_2(\mu-OH)]_2^{2+}$ in Au_4-OTf has been changed from the original parallel-edge cluster in $Au_4-p-F-PMO$ during the anion-exchange.

7. DIPHENYLACETYLENE HYDRATION AS A CATALYTIC APPLICATION

One of the most straightforward ways of synthesizing compounds with carbon–oxygen bonds is the hydration of unsaturated organic compounds. In particular, the synthesis of carbonyl compounds by the addition of water to alkynes is not only environmentally benign, but also economically attractive. For alkynes hydration, active catalytic systems composed of a highly toxic mercury salt and either Lewis or Brønsted acid have traditionally been used. Therefore, the development of less toxic methods has attracted considerable interest.

The *Au₄-PW* showed acid- and silver-free effective catalysis for the hydration of diphenylacetylene, in which its conversion to deoxybenzoin was 93.7% after a 24 h reaction in the suspended system in 1,4-dioxane/water (4/1) at 80°C [18]. The *Au₄-PW* itself is not a catalyst, but dissolved species generated in the dynamic process of *Au₄-PW*, i.e., [Au(PPh₃)]⁺ or [Au(solvent)(PPh₃)]⁺ species, will be the catalyst precursor. The *Au₇-PW* also showed effective catalytic activity (conversion to deoxybenzoin: 89.0% after a 24 h reaction). In contrast with *Au₄-PW*, an induction period was observed in the early stages of the reaction by *Au₇-PW*. In catalytic processes by *Au₄-PW* and *Au₇-PW*, the catalyst precursor will actually be the same, and the active species is the [Au(alkyne)(PPh₃)]⁺ compound derived from it. The acidic proton enhances the activity by *Au₄-PW*, suggesting that generation of the catalyst precursor is accelerated by an acidic proton.

In the catalysis by *Au₄-PW* and *Au₇-PW*, the catalyst precursor will originate from a dynamic process (or including fluxional or scrambling of [Au(PPh₃)]⁺ species in solution). ³¹P{¹H} NMR spectrum of a CD₂Cl₂ solution of the residue obtained from the reaction solution after a 6 h reaction at 80°C using *Au₄-PW* revealed a broad signal that was assigned to the [Au(diphenylacetylene)(PPh₃)]⁺ species at 36.1 ppm.

Catalysis by *Au₄-PW* for hydration of other alkynes was also examined. The hydration of phenylacetylene by *Au₄-PW* resulted in the formation of acetophenone with conversion 94.3% after a 24 h reaction at 80°C, and that of 1-phenyl-1-butyne by *Au₄-PW* resulted in the formation of butyrophenone with conversion 38.8% and 1-phenyl-2-butanone with conversion 57.0% after a 24 h reaction at 80°C.

The component species constituting *Au₄-PW* and *Au₇-PW*, i.e., tetra- and tri(phosphane-gold(I))oxonium cluster cations (conversions: 1.8 and 1.7% after

24 h reactions, respectively), and $Y_3[\alpha\text{-PW}_{12}\text{O}_{40}] \cdot n\text{H}_2\text{O}$ ($Y = \text{H}$, $n = 7$; $Y = \text{Na}$, $n = 8$) (conversions: both 0% after 24 h reactions) showed poor activities. In other words, the phosphanegold(I) cluster cations without POM showed no activity. The activities of $Au_4\text{-PW}$ and $Au_7\text{-PW}$ suggest that the phosphane gold(I) species exhibit catalytic activities only in the presence of POM.

The reaction scheme of diphenylacetylene hydration catalyzed by $Au_4\text{-PW}$ is depicted in Figure 10. In this catalytic cycle, the catalytically active, monomeric phosphanegold(I) species $[\text{Au}(\text{alkyne})(\text{PPh}_3)]^+$ would be accompanied by the POM anion throughout the process. The induction period would also be related to the process of generating the catalyst precursor $[\text{Au}(\text{solvent})(\text{PPh}_3)]^+$ from the $Au_7\text{-PW}$.

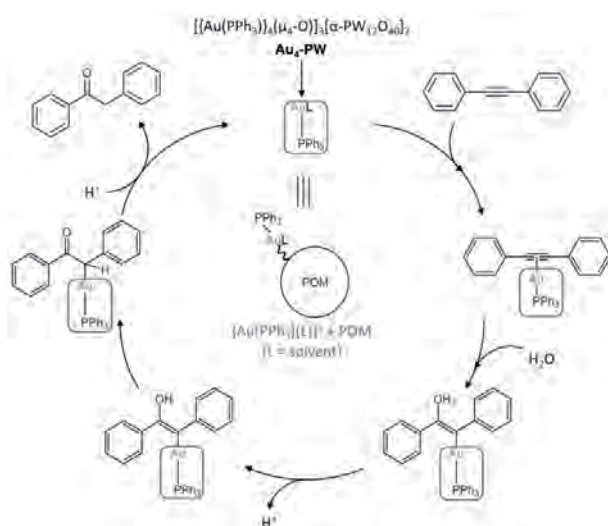


Figure 10. Catalytic cycle for diphenylacetylene hydration catalyzed by $Au_4\text{-PW}$. Reproduced from ref. [18] with permission. Copyright 2016 American Chemical Society.

CONCLUSION

In this chapter, in order to provide the readers with a sharply focused review introducing an aspect of our own research and tracing its development, we have described the syntheses and structures of several phosphanegold(I) clusters formed by polyoxometalate (POM)-mediated clusterization, and their

catalytic application such as hydration of alkynes, based on several our papers published so far [11-18].

It has been discovered that the reactions of the free-acid forms of saturated Keggin POMs, such as $H_n[\alpha\text{-XM}_{12}\text{O}_{40}] \cdot n\text{H}_2\text{O}$ ($n = 3, 4$; $X = \text{P, Si}$; $M = \text{W, Mo}$), with the monomeric phosphanegold(I) complexes, $[\text{Au}(\text{RS-pyrrld})(\text{PR}_3)]$ ($\text{RS-Hpyrrld} = \text{RS-2-pyrrolidone-5-carboxylic acid}$; $R = \text{Ph, } o\text{-MePh}$) directly give the tetra{phosphanegold(I)}oxonium cluster cations, $[\{\text{Au}(\text{PR}_3)\}_4(\mu_4\text{-O})]^{2+}$ (Au_4), as counteranions of the Keggin POM anions (XM) [11]. The intercluster compounds ($Au_4\text{-XM}$), composed of cluster cations and cluster anions, have been obtained as pure crystalline samples in good yields by liquid-liquid diffusion method. Formation of such compounds depended upon the Keggin POMs, and the bulkiness and anionic charge of the POMs contributed to clusterization of the *in situ*-generated, mononuclear $[\text{Au}(\text{PR}_3)]^+$ species after the removal of RS-pyrrld^- ligand. The bridged oxide ion ($\mu_4\text{-O}^{2-}$) encapsulated in the cluster comes from water molecules contained in the reaction system and/or the solvated water molecules in the POMs. The structure of Au_4 was stabilized by the intra-cluster aurophilic interactions and also by interactions between the gold(I) cluster cations and POM anions.

An example that the acidity of Keggin POM significantly contributes to the clusterization of the $[\text{Au}(\text{PR}_3)]^+$ species is seen in the reaction of $\text{Na}_3[\alpha\text{-PW}_{12}\text{O}_{40}] \cdot n\text{H}_2\text{O}$ and $[\text{Au}(\text{RS-pyrrld})(\text{PPh}_3)]$ [13], resulting in formation of a novel intercluster compound, $[\{\{\text{Au}(\text{PPh}_3)\}_4(\mu_4\text{-O})\}\{\{\text{Au}(\text{PPh}_3)\}_3(\mu_3\text{-O})\}][\alpha\text{-PW}_{12}\text{O}_{40}] \cdot \text{EtOH}$ ($Au_7\text{-PW}$). The heptaphosphanegold(I) cluster unit (Au_7) is composed of the tetragold(I) cluster unit (Au_4) and the trigold(I) cluster unit (Au_3), with the bridged oxygen atoms, $\mu_4\text{-O}$ and $\mu_3\text{-O}$, respectively.

Not only the POM acidity (proton vs. sodium), but also the high negative charge of the POM (5^- vs. 3^- or 4^-) plays an important role in the clusterization of the $[\text{Au}(\text{PR}_3)]^+$ unit [14]. Such an example is seen in the reactions of $[\text{Au}(\text{RS-pyrrld})(\text{PPh}_3)]$ and $\text{H}_3[\alpha\text{-XW}_{12}\text{O}_{40}] \cdot n\text{H}_2\text{O}$ ($X = \text{Al, B}$), resulting in formation of novel intercluster compounds, $[\{\{\text{Au}(\text{PPh}_3)\}_4(\mu_4\text{-O})\}][\alpha\text{-XW}_{12}\text{O}_{40}\{\text{Au}(\text{PPh}_3)\}_3] \cdot 3\text{EtOH}$ ($X = \text{Al}$ ($Au_4\text{-AlW}$) and $X = \text{B}$ ($Au_4\text{-BW}$)). These compounds appear to be intermediates in the formation of Au_4 . In these reactions, the OW_2 oxygen atoms of edge-shared WO_6 octahedra of the POM act as multi-centered active binding sites for the $[\text{Au}(\text{PR}_3)]^+$ unit.

An example that the para-substituent of aryl groups in the phosphane ligands significantly contributes to the clusterization of the $[\text{Au}(\text{PR}_3)]^+$ unit is seen in the reactions between $[\text{Au}(\text{RS-pyrrld})\{\text{P}(p\text{-MePh})_3\}]$ and $\text{H}_3[\alpha\text{-PM}_{12}\text{O}_{40}] \cdot n\text{H}_2\text{O}$ ($M = \text{W, Mo}$) [15], forming a dimer of di(phosphanegold(I)) hydroxide cations with a crossed-edge arrangement ($Au_4\text{-}p\text{-Me-PM}$; $M = \text{Mo}$,

W). On the other hand, formation of that with a parallel-edge arrangement ($Au_4-p-X-PMo$) is seen in the reaction between $[Au(RS-pyrrld)\{P(p-XPh)_3\}]$ ($X = F, Cl$) and $H_3[\alpha-PMo_{12}O_{40}] \cdot 14H_2O$ [15, 16]. The dimerization of diphosphanegold(I) cations is affected by the interactions between the diphosphanegold(I) cations, and also by interactions between the phosphane ligands and the POM anions.

An example that the meta-substituent of the aryl groups in phosphane ligands influences the clusterization is seen in the reaction between $[Au(RS-pyrrld)\{P(m-FPh)_3\}]$ and $H_3[\alpha-PMo_{12}O_{40}] \cdot 14H_2O$ [12]. A novel intercluster compound was formed as $[(Au\{P(m-FPh)_3\})_4(\mu_4-O)]_2\{[(Au\{P(m-FPh)_3\})_2(\mu-OH)]_2\}[\alpha-PMo_{12}O_{40}]_2 \cdot EtOH$ ($Au_4-m-F-PMo$), which is composed of the trigonal-pyramidal $[(Au\{P(m-FPh)_3\})_4(\mu_4-O)]^{2+}$ cations, the dimer of di(phosphanegold(I)) hydroxide cation in a parallel-edge arrangement and POM anions.

Another examples contributed by the meta-substituent in the ligands are also seen in the reactions between $[Au(RS-pyrrld)(PR_3)]$ ($R = m-FPh, m-MePh$), and $H_4[\alpha-SiMo_{12}O_{40}] \cdot 12H_2O$ or $H_4[\alpha-SiW_{12}O_{40}] \cdot 10H_2O$ [12].

Another remarkable examples are seen in the reactions between $[Au(RS-pyrrld)\{P(p-XPh)_3\}]$ ($X = F, Cl$) and $H_4[\alpha-SiMo_{12}O_{40}] \cdot 12H_2O$ [17], resulting in the formation of $[(Au\{P(p-XPh)_3\})_2(\mu-OH)]_2[\alpha-SiMo_{12}O_{40}(Au\{P(p-XPh)_3\})_2]$ ($X = F$ ($Au_4-p-F-SiMo$) and $X = Cl$ ($Au_4-p-Cl-SiMo$)). Two types of $[(Au\{P(p-XPh)_3\})_2(\mu-OH)]_2^{2+}$ cations are in a crossed-edge arrangement ($Au_4-p-F-SiMo$) and in a parallel-edge arrangement ($Au_4-p-Cl-SiMo$). The mononuclear $[Au\{P(p-XPh)_3\}]^+$ units linked to the POM anion reveal that the OMo_2 oxygen atoms of edge-shared MoO_6 octahedra of the POM act as multi-centered active binding sites. These facts also show that the POM's surface oxygen atoms have significant affinity to the phosphanegold(I) cations.

During the process of the anion exchange to PF_6 of $[(Au\{P(p-ClPh)_3\})_2(\mu-OH)]_2[\alpha-PMo_{12}O_{40}]_2 \cdot 3EtOH$ ($Au_4-p-Cl-PMo$), two types of phosphanegold(I) cluster cations were formed [16], i.e., one is the monomeric tetrakis{phosphanegold(I)} species $[(\mu_4-O)(AuPR_3)_4]^{2+}$ ($R = p-ClPh$) accompanied with both POM and PF_6 anions ($Au_4-PMo_{12}-PF_6$) and the other is the dimeric, tris{phosphanegold(I)} species $[(\mu_3-O)(AuPR_3)_3]^{2+}$ with PF_6 anion (Au_6-PF_6). The cationic species containing μ_4-O atom in $Au_4-PMo_{12}-PF_6$ took an unusual, square pyramidal structure with local C_{4v} symmetry. Its bonding mode can be understood as electron-deficient species.

It should be noted that Au_4-PW exhibits silver- and acid-free, effective catalytic activity for diphenylacetylene hydration [18]. The catalytically active species is attributable to the monomeric gold(I)-alkyne species stabilized by

POM, i.e., $[\text{Au}(\text{L})(\text{PPh}_3)]^+/\text{POM}$ (L = alkyne). The reaction systems without POM exhibited poor or no activities. In the catalysis by $\text{Au}_4\text{-PW}$, the catalyst precursor $[\text{Au}(\text{L})(\text{PPh}_3)]^+$ (L = solvent) is originated from the “dynamic” process as shown in the $^{31}\text{P}\{^1\text{H}\}$ NMR spectrum of $\text{Au}_4\text{-PW}$ in $\text{DMSO-}d_6$. Addition of an acidic proton enhanced the activity of $\text{Au}_4\text{-PW}$, suggesting that the generation of the catalyst precursor is accelerated by the acidic proton. In contrast, catalysis by $\text{Au}_7\text{-PW}$ showed an induction period, suggesting that it takes a longer time to generate the catalyst precursor $[\text{Au}(\text{L})(\text{PPh}_3)]^+$.

The present work would be extended to the molecular architecture of POM-mediated element-centered phosphanegold(I) clusters by a combination of the monomeric phosphanegold(I) carboxylate and the various saturated and/or lacunary POMs. Their catalytic applications and catalytic behaviors of such POM-based phosphanegold(I) compounds will be studied as future work.

REFERENCES

- [1] Pope, M. T. *Heteropoly and Isopoly Oxometalates*; Springer-Verlag: New York, 1983.
- [2] Uchida, S.; Mizuno, N. *Coord. Chem. Rev.* 2007, 251, 2537-2546.
- [3] Santoni, M.-P.; Hanan, G. S.; Hasenknopf, B. *Coord. Chem. Rev.* 2014, 281, 64-85.
- [4] Schulz-Dobrick, M.; Jansen, M. *Eur. J. Inorg. Chem.* 2006, 4498-4502.
- [5] Schmidbaur, H.; Schier, A. *Chem. Soc. Rev.* 2008, 37, 1931-1951.
- [6] Gimeno, M. C.; Laguna, A. *Chem. Soc. Rev.* 2008, 37, 1952-1966.
- [7] Hashmi, A. S. K. *Chem. Rev.* 2007, 107, 3180-3211.
- [8] Jiménez-Núñez, E.; Echavarren, A. M. *Chem. Rev.* 2008, 108, 3326-3350.
- [9] Gorin, D. J.; Sherry, B. D.; Toste, F. D. *Chem. Rev.* 2008, 108, 3351-3378.
- [10] Sherry, B. D.; Toste, F. D. *J. Am. Chem. Soc.* 2004, 126, 15978-15979.
- [11] Nomiya, K.; Yoshida, T.; Sakai, Y.; Nanba, A.; Tsuruta, S. *Inorg. Chem.* 2010, 49, 8247-8254.
- [12] Yoshida, T.; Yasuda, Y.; Nagashima, E.; Arai, H.; Matsunaga, S.; Nomiya, K. *Inorganics* 2014, 2, 660-673.
- [13] Yoshida, T.; Nomiya, K.; Matsunaga, S. *Dalton Trans.* 2012, 41, 10085-10090.
- [14] Yoshida, T.; Matsunaga, S.; Nomiya, K. *Chem. Lett.* 2013, 42, 1487-1489.

- [15] Yoshida, T.; Matsunaga, S.; Nomiya, K. *Dalton Trans.* 2013, 42, 11418-11425.
- [16] Nagashima, E.; Yoshida, T.; Matsunaga, S.; Nomiya, K. Manuscript in preparation.
- [17] Yoshida, T.; Nagashima, E.; Arai, H.; Matsunaga, S.; Nomiya, K. *Z. Anorg. Allg. Chem.* 2015, 641, 1688-1695.
- [18] Arai, H.; Yoshida, T.; Nagashima, E.; Hatayama, A.; Horie, S.; Matsunaga, S.; Nomiya, K. *Organometallics* 2016, DOI: 10.1021/acs.organomet.6b00114..
- [19] Schmidbaur, H.; Hofreiter, S.; Paul, M. *Nature* 1995, 377, 503-504.
- [20] Canales, F.; Gimeno, C.; Laguna, A.; Villacampa, M. D. *Inorg. Chim. Acta* 1996, 244, 95-103.
- [21] Canales, F.; Gimeno, M. C.; Jones, P. G.; Laguna, A. *Angew. Chem. Int. Ed.* 1994, 33, 769-770.
- [22] Jones, P. G.; Sheldrick, G. M.; Hädicke, E. *Acta Crystallogr., Sect. B* 1980, 36, 2777-2779.
- [23] Schmidbaur, H.; Kolb, A.; Zeller, E.; Schier, A.; Beruda, H. *Z. Anorg. Allg. Chem.* 1993, 619, 1575-1579.

BIOGRAPHICAL SKETCH

Name: Kenji Nomiya

Affiliation: Department of Chemistry, Faculty of Science, Kanagawa University

Address: Tsuchiya 2946, Hiratsuka, Kanagawa 259-1293, Japan

Educational Background:

1974 Ph.D: Tokyo Institute of Technology, Graduate School, Chemistry Course

1971 M.Sc: Tokyo Institute of Technology, Graduate School, Chemistry Course

1969 B.Sc: Tokyo Institute of Technology, Department of Chemistry

Research and Professional Experience:

Full Professor (1996-) Kanagawa University, Department of Chemistry, Faculty of Science, Kanagawa, Japan

Associate Professor (1989-1995) Kanagawa University, Department of Chemistry, Faculty of Science, Kanagawa, Japan

Research Associate (1987-1989) University of Oregon, Department of Chemistry (Prof. R. G. Finke's Lab), Eugene, Oregon, US

Research Associate/Assistant Professor/Associate Professor (1977-1987)
Seikei University, Department of Industrial Chemistry, Faculty of Engineering,
Tokyo

Research Associate (1975-1977) Sagami Chemical Research Center,
Sagamihara, Kanagawa, Japan

Professional Appointments:

Full professor

Research Interests:

Research Field: Inorganic Chemistry, Coordination Chemistry,
Bioinorganic Chemistry

Interest:

Syntheses and Structures of Polyoxometalates, and Their Catalysis,
Syntheses and Structures of Coinage Metal Complexes, and Their
Antimicrobial Activities

Honors:

Awards and Fellowship:

2014: Best Teacher Awards in Kanagawa University

2000: Poster Awards in 78th Spring National Meeting of Chemical Society
of Japan

1998: Poster Awards in 74th Spring National Meeting of Chemical Society
of Japan

1974: Postdoctoral Research Fellow for Young Scientists in Japan Society
for the Promotion of Science

Membership:

Chemical Society of Japan

American Chemical Society

Royal Society of Chemistry

Japan Society of Coordination Chemistry

The Society for Antibacterial and Antifungal Agents, Japan

Catalysis Society of Japan

Publications Last 3 Years:

Books:

- [1] Nomiya, K.; Kasuga, N. C.; Takayama, A.; RSC book, Chapter 7, 156-
207 (2014) In: "Polymeric Materials with Antimicrobial Activity From
Synthesis to Application" (Ed.) by A. Muñoz-Bonilla, M. Cerrada, M.

Fernández-García. Synthesis, structure and antimicrobial activities of polymeric and non-polymeric silver and other metal complexes.

Articles in Journals:

- [1] Matsunaga, S.; Otaki, T.; Inoue, Y.; Mihara, K.; Nomiya, K. (2016). Synthesis, Structure, and Characterization of In₁₀-Containing Open-Dawson Polyoxometalate. *Inorganics*, 4, 16..
- [2] Arai, H.; Yoshida, T.; Nagashima, E.; Hatayama, A.; Horie, S.; Matsunaga, S.; Nomiya, K. (2016). Silver- and Acid-free Catalysis by Polyoxometalate-Assisted Phosphanegold(I) Species for Hydration of Diphenylacetylene. *Organometallics*, DOI: 10.1021/acs.organomet.6b00114..
- [3] Matsunaga, S.; Miyamae, E.; Inoue, Y.; Nomiya, K. (2016). β,β -Isomer of Open-Wells-Dawson Polyoxometalate Containing Tetra-Iron(III) Hydroxide Cluster: $[\{\text{Fe}_4(\text{H}_2\text{O})(\text{OH})_5\}(\beta,\beta\text{-Si}_2\text{W}_{18}\text{O}_{66})]^{9-}$. *Inorganics*, 4, 15.
- [4] Matsunaga, S.; Otaki, T.; Inoue, Y.; Osada, H.; Nomiya, K. (2016). Aluminum- and gallium-containing open-Dawson polyoxometalates. *Z. Anorg. Allgem. Chem.*, 642, (7), 539-545.
- [5] Yoshida, T.; Nagashima, E.; Arai, H.; Matsunaga, S.; Nomiya, K. (2015). Aggregation of Dinuclear Cations $[\{\text{Au}(\text{PR}_3)_2(\mu\text{-OH})\}^+$ into Dimers Induced by Polyoxometalate (POM) Template Effects. [Cover picture] *Z. Anorg. Allgem. Chem.*, 641, (10) 1688-1695.
- [6] Inoue, Y.; Matsunaga, S.; Nomiya, K. (2015). Al₁₆-hydroxide cluster-containing tetrameric polyoxometalate, $[\{\alpha\text{-Al}_3\text{SiW}_9\text{O}_{34}(\mu\text{-OH})_6\}_4\{\text{Al}_4(\mu\text{-OH})_6\}]^{22-}$. *Chem. Lett.*, 44, (12) 1649-1651.
- [7] Matsuki, Y.; Hoshino, T.; Takaku, S.; Matsunaga, S.; Nomiya, K. (2015). Synthesis and Molecular Structure of a Water-Soluble, Dimeric Tri-Titanium(IV)-Substituted Wells-Dawson Polyoxometalate Containing Two Bridging (C₅Me₅)Rh²⁺ Groups. *Inorg. Chem.*, 54, (23), 11105-11113.
- [8] Takayama, A.; Takagi, Y.; Yanagita, K.; Inoue, C.; Yoshikawa, R.; Kasuga, N.C.; Nomiya, K. (2014). Synthesis, characterization and antimicrobial activities of sodium salt of *L*-histidinatoargentate(I) derived from the pH 11 solution. *Polyhedron*, 80, 151-156.
- [9] Aoto, H.; Matsui, K.; Sakai, Y.; Kuchizi, K.; Sekiya, H.; Osada, H.; Yoshida, T.; Matsunaga, S.; Nomiya, K. (2014). Zirconium(IV)- and Hafnium(IV)-Containing Polyoxometalates as Oxidation Precatalysts:

- Homogeneous Catalytic Epoxidation of Cyclooctene with Hydrogen Peroxide [Editor's choice paper] *J. Mol. Catal. A: Chem.*, 394, 224-231.
- [10] Yoshida, T.; Yasuda, Y.; Nagashima, E.; Arai, H.A.; Matsunaga, S.; Nomiya, K. (2014). Various Oxygen-Centered Phosphanegold(I) Cluster Cations Formed by Polyoxometalate (POM)-Mediated Clusterization: Effects of POMs and Phosphanes. Special Issue "Frontiers in Gold Chemistry," *Inorganics*, 2, 660-673.
- [11] Takayama, A.; Yoshikawa, R.; Iyoku, S.; Kasuga, N. C.; Nomiya, K. (2013) Synthesis, structure and antimicrobial activity of *L*-argininesilver(1+) nitrate. *Polyhedron*, 52, 844-847.
- [12] Osada, H.; Ishikawa, A.; Saku, Y.; Sakai, Y.; Matsuki, Y.; Matsunaga, S.; Nomiya, K. (2013). 2: 2-Type complexes of zirconium(IV)/hafnium(IV) centers with mono-lacunary Keggin polyoxometalates: Syntheses and molecular structures of $[(\alpha\text{-SiW}_{11}\text{O}_{39}\text{M})_2(\mu\text{-OH})_2]^{10-}$ (M = Zr, Hf) with edge-sharing octahedral units and $[(\alpha\text{-SiW}_{11}\text{O}_{39}\text{M})_2(\mu\text{-OH})_3]^{11-}$ with face-sharing octahedral units. *Polyhedron*, 52, 389-397.
- [13] Matsuki, Y.; Mouri, Y.; Sakai, Matsunaga, S.; Nomiya, K. (2013). Monomer and Dimer of Mono-titanium(IV)-Containing α -Keggin Polyoxometalate: Synthesis, Molecular Structures and pH-Dependent Monomer-Dimer Interconversion in Solution. *Eur. J. Inorg. Chem.*, 1754-1761.
- [14] Nomiya, K.; Ohta, K.; Sakai, Y.; Hosoya, T.; Ohtake, A.; Takakura, A.; Matsunaga, S. (2013). Tetranuclear Hafnium(IV) and Zirconium(IV) Cationic Complexes Sandwiched between Two Di-Lacunary Species of α -Keggin Polyoxometalates: Lewis Acid Catalysis of the Mukaiyama-Aldol Reaction. [Selected papers] *Bull. Chem. Soc. Jpn.*, 86, 800-812.
- [15] Yoshida, T.; Matsunaga, S.; Nomiya, K. (2013). Two types of tetranuclear phosphanegold(I) cations as dimers of dinuclear units, $[(\text{Au}\{\text{P}(p\text{-RPh})_3\})_2(\mu\text{-OH})_2]^{2+}$ (R = Me, F), synthesized by polyoxometalate-mediated clusterization. *Dalton Trans.*, 42, 11418-11425.
- [16] Yoshida, T.; Matsunaga, S.; Nomiya, K. (2013). Novel Intercluster Compounds Composed of a Tetra{phosphanegold(I)}oxonium Cation and an α -Keggin Polyoxometalate Anion Linked by Three Monomeric Phosphanegold(I) Units. *Chem. Lett.*, 42, 1487-1489.

Name: Satoshi Matsunaga

Affiliation: Department of Chemistry, Faculty of Science, Kanagawa University

Education:

2007 - Ph.D. (Chemistry)

Department of Chemistry, Tokyo metropolitan university (Prof. Ken-ichi Sugiura)

2004 - M.S. (Chemistry)

Department of Chemistry, Tokyo metropolitan university (Prof. Masahiro Yamashita)

2002 - B.S. (Chemistry)

Department of Chemistry, Tokyo metropolitan university (Prof. Masahiro Yamashita)

Address:

2946 Tsuchiya, Hiratsuka, Kanagawa 259-1293, Japan

Research and Professional Experience:

2007 Sept.-Present Assistant Professor, Department of Chemistry, Kanagawa University

2007 Apr.-Sept. Postdoctoral Researcher, Department of Chemistry, Tohoku University

Professional Appointments:

Assistant professor

Honors:

2012 - BCSJ Award

2006 - Student Presentation Award, The 86th Annual Meeting of the Chemical Society of Japan

Publications Last 3 Years:

- [1] Matsunaga, S.; Otaki, T.; Inoue, Y.; Mihara, K.; Nomiya, K. (2016). Synthesis, Structure, and Characterization of In₁₀-Containing Open-Dawson Polyoxometalate. *Inorganics*, 4, 16..
- [2] Arai, H.; Yoshida, T.; Nagashima, E.; Hatayama, A.; Horie, S.; Matsunaga, S.; Nomiya, K. (2016). Silver- and Acid-free Catalysis by Polyoxometalate-Assisted Phosphanegold(I) Species for Hydration of Diphenylacetylene. *Organometallics*, DOI: 10.1021/acs.organomet.6b00114.

- [3] Matsunaga, S.; Miyamae, E.; Inoue, Y.; Nomiya, K. (2016). β,β -Isomer of Open-Wells-Dawson Polyoxometalate Containing Tetra-Iron(III) Hydroxide Cluster: $[\{\text{Fe}_4(\text{H}_2\text{O})(\text{OH})_5\}(\beta,\beta\text{-Si}_2\text{W}_{18}\text{O}_{66})]^{9-}$. *Inorganics*, 4, 15.
- [4] Matsunaga, S.; Otaki, T.; Inoue, Y.; Osada, H.; Nomiya, K. (2016). Aluminum- and gallium-containing open-Dawson polyoxometalates. *Z. Anorg. Allgem. Chem.*, 642, (7), 539-545.
- [5] Yoshida, T.; Nagashima, E.; Arai, H.; Matsunaga, S.; Nomiya, K. (2015). Aggregation of Dinuclear Cations $[\{\text{Au}(\text{PR}_3)_2(\mu\text{-OH})\}]^+$ into Dimers Induced by Polyoxometalate (POM) Template Effects [Cover picture]. *Z. Anorg. Allgem. Chem.*, 641, (10) 1688-1695.
- [6] Inoue, Y.; Matsunaga, S.; Nomiya, K. (2015). Al_{16} -hydroxide cluster-containing tetrameric polyoxometalate, $[\{\alpha\text{-Al}_3\text{SiW}_9\text{O}_{34}(\mu\text{-OH})_6\}_4\{\text{Al}_4(\mu\text{-OH})_6\}]^{22-}$. *Chem. Lett.*, 44, (12) 1649-1651.
- [7] Matsuki, Y.; Hoshino, T.; Takaku, S.; Matsunaga, S.; Nomiya, K. (2015). Synthesis and Molecular Structure of a Water-Soluble, Dimeric Tri-Titanium(IV)-Substituted Wells-Dawson Polyoxometalate Containing Two Bridging $(\text{C}_5\text{Me}_5)\text{Rh}^{2+}$ Groups. *Inorg. Chem.*, 54, (23), 11105-11113.
- [8] Aoto, H.; Matsui, K.; Sakai, Y.; Kuchizi, K.; Sekiya, H.; Osada, H.; Yoshida, T.; Matsunaga, S.; Nomiya, K. (2014). Zirconium(IV)- and Hafnium(IV)-Containing Polyoxometalates as Oxidation Precatalysts: Homogeneous Catalytic Epoxidation of Cyclooctene with Hydrogen Peroxide [Editor's choice paper] *J. Mol. Catal. A: Chem.*, 394, 224-231.
- [9] Yoshida, T.; Yasuda, Y.; Nagashima, E.; Arai, H.A; Matsunaga, S.; Nomiya, K. (2014). Various Oxygen-Centered Phosphanegold(I) Cluster Cations Formed by Polyoxometalate (POM)-Mediated Clusterization: Effects of POMs and Phosphanes. Special Issue "Frontiers in Gold Chemistry," *Inorganics*, 2, 660-673.
- [10] Osada, H.; Ishikawa, A.; Saku, Y.; Sakai, Y.; Matsuki, Y.; Matsunaga, S.; Nomiya, K. (2013). 2: 2-Type complexes of zirconium(IV)/hafnium(IV) centers with mono-lacunary Keggin polyoxometalates: Syntheses and molecular structures of $[(\alpha\text{-SiW}_{11}\text{O}_{39}\text{M})_2(\mu\text{-OH})_2]^{10-}$ (M = Zr, Hf) with edge-sharing octahedral units and $[(\alpha\text{-SiW}_{11}\text{O}_{39}\text{M})_2(\mu\text{-OH})_3]^{11-}$ with face-sharing octahedral units. *Polyhedron*, 52, 389-397.

- [11] Matsuki, Y.; Mouri, Y.; Sakai, Matsunaga, S.; Nomiya, K. (2013). Monomer and Dimer of Mono-titanium(IV)-Containing α -Keggin Polyoxometalate: Synthesis, Molecular Structures and pH-Dependent Monomer-Dimer Interconversion in Solution. *Eur. J. Inorg. Chem.*, 1754-1761.
- [12] Matsunaga, S.; Kato, S.; Endo, N.; Mori, W. (2013) Expansion of Pore Windows and Interior Spaces of Microporous Porphyrin-Based Metal Carboxylate Frameworks: Synthesis and Crystal Structure of [Cu₂(ZnBDCBPP)]. *Chem. Lett.*, 42, 298-300.
- [13] Nomiya, K.; Ohta, K.; Sakai, Y.; Hosoya, T.; Ohtake, A.; Takakura, A.; Matsunaga, S. (2013). Tetranuclear Hafnium(IV) and Zirconium(IV) Cationic Complexes Sandwiched between Two Di-Lacunary Species of α -Keggin Polyoxometalates: Lewis Acid Catalysis of the Mukaiyama-Aldol Reaction [Selected papers]. *Bull. Chem. Soc. Jpn.*, 86, 800-812.
- [14] Yoshida, T.; Matsunaga, S.; Nomiya, K. (2013). Two types of tetranuclear phosphanegold(I) cations as dimers of dinuclear units, $[(Au P(p-RPh)_3)_2(\mu-OH)]_2^{2+}$ (R = Me, F), synthesized by polyoxometalate-mediated clusterization. *Dalton Trans.*, 42, 11418-11425.
- [15] Yoshida, T.; Matsunaga, S.; Nomiya, K. (2013). Novel Intercluster Compounds Composed of a Tetra{phosphanegold(I)}oxonium Cation and an α -Keggin Polyoxometalate Anion Linked by Three Monomeric Phosphanegold(I) Units. *Chem. Lett.*, 42, 1487-1489.

Name: Takuya Yoshida

Affiliation: Research Center for Gold Chemistry, Graduate School of Urban Environmental Sciences, Tokyo Metropolitan University

Education:

2014 - Ph.D. (Chemistry)

Department of Chemistry, Kanagawa University (Prof. Kenji Nomiya)

2011 - M.S. (Chemistry)

Department of Chemistry, Kanagawa University (Prof. Kenji Nomiya)

2009 - B.S. (Chemistry)

Department of Chemistry, Kanagawa University (Prof. Kenji Nomiya)

Address:

1-1 Minami-osawa, Hachioji, Tokyo 192-0397, Japan

Research and Professional Experience:

2014 Apr.-Present - Project Assistant Professor, Research Center for Gold Chemistry, Tokyo, Metropolitan University

Professional Appointments:

Project Assistant Professor

Publications Last 3 Years:

- [1] Arai, H.; Yoshida, T.; Nagashima, E.; Hatayama, A.; Horie, S.; Matsunaga, S.; Nomiya, K. (2016). Silver- and Acid-free Catalysis by Polyoxometalate-Assisted Phosphanegold(I) Species for Hydration of Diphenylacetylene. *Organometallics*, DOI: 10.1021/acs.organomet.6b00114..
- [2] Yoshida, T.; Nagashima, E.; Arai, H.; Matsunaga, S.; Nomiya, K. (2015). Aggregation of Dinuclear Cations $[\{Au(PR_3)\}_2(\mu-OH)]^+$ into Dimers Induced by Polyoxometalate (POM) Template Effects [Cover picture]. *Z. Anorg. Allgem. Chem.*, 641, (10) 1688-1695.
- [3] Aoto, H.; Matsui, K.; Sakai, Y.; Kuchizi, K.; Sekiya, H.; Osada, H.; Yoshida, T.; Matsunaga, S.; Nomiya, K. (2014). Zirconium(IV)- and Hafnium(IV)-Containing Polyoxometalates as Oxidation Precatalysts: Homogeneous Catalytic Epoxidation of Cyclooctene with Hydrogen Peroxide [Editor's choice paper]. *J. Mol. Catal. A: Chem.*, 394, 224-231.
- [4] Yoshida, T.; Yasuda, Y.; Nagashima, E.; Arai, H.A.; Matsunaga, S.; Nomiya, K. (2014). Various Oxygen-Centered Phosphanegold(I) Cluster Cations Formed by Polyoxometalate (POM)-Mediated Clusterization: Effects of POMs and Phosphanes. Special Issue "Frontiers in Gold Chemistry," *Inorganics*, 2, 660-673.
- [5] Yoshida, T.; Matsunaga, S.; Nomiya, K. (2013). Two types of tetranuclear phosphanegold(I) cations as dimers of dinuclear units, $[\{(Au\{P(p-RPh)_3\})_2(\mu-OH)\}_2]^{2+}$ (R = Me, F), synthesized by polyoxometalate-mediated clusterization. *Dalton Trans.*, 42, 11418-11425.
- [6] Yoshida, T.; Matsunaga, S.; Nomiya, K. (2013). Novel Intercluster Compounds Composed of a Tetra{phosphanegold(I)}oxonium Cation and an α -Keggin Polyoxometalate Anion Linked by Three Monomeric Phosphanegold(I) Units. *Chem. Lett.*, 42, 1487-1489.

Chap 2

Basic Concept-5

金属酵素モデルの構造と特性

引地 史郎
(神奈川大学工学部)

酸素代謝にかかわる金属 タンパク質および酵素とモデル研究

生体内では酸素分子の運搬や筋肉組織内での酸素貯蔵にかかわるタンパク質や、呼吸における酸素から水への変換とその逆反応に相当する光合成における酸素発生、生体組織を傷つけてしまう活性酸素種の無害化、そして生命活動に必要な化学物質をつくり出すための触媒である多くの酸化酵素(表1)が酸素代謝にかかわっている。これらのタンパク質や酵素では、活性酸素種と相互作用する遷移金属イオンが、タンパク質のアミノ酸残基やヘムなどの補欠分子族とよばれる生体分子(図1)に結合した状態、すなわち金属錯体となっている。そして酸素代謝の過程で、中心金属が活性酸素種と結合体を形成する。これらの金属タンパク質および酵素は、その機能をつかさどる活性点における錯体の構造によって2種類に大別される。ポルフィリンを基本骨格とするヘムに鉄イオンが結合したヘム鉄を活性中心にもつものはヘム鉄タンパク質あるいはヘム鉄酵素とよばれ、ヘムをもたずにアミノ酸残基自体が金属イオンを支えているものは非ヘム金属タンパク質あるいは非ヘム金属酵素とよばれる^[1-3]。

金属タンパク質および酵素の活性点である金属錯体部位は、時には分子量が数十万にも及ぶ巨大分子に埋め込まれた状態にある。このためタンパク質や酵素そのものを観察する場合、研究対象である金属錯体はごく低濃度にしか存在しない。しかもタンパク質や酵素が機能する生理的条件下では、活性点での金属と活性酸素種との結合体形成過程やその後の触媒反応は高速で進行することがほとんどであり、このような反応過程を直接観測することは技術的に困

難であることが多い。一方で近年のさまざまな分析技術の進歩により、活性点で進行している反応を観測した例も報告されるようになってきた。ただし、その観測結果や機能および反応特性を合理的に解釈するためには、根拠となる化学的事例が必要である。そこで人工的に合成したモデル化合物、いわゆるモデル錯体を用いた研究が行われている。

金属タンパク質および酵素における 金属-活性酸素錯体種

金属タンパク質や酵素と相互作用している活性酸素種は、酸素の還元体である。酸素分子の1電子還元体であるスーパーオキシド(超酸化物イオン, O_2^-)や2電子還元体であるペルオキシド(過酸化物イオン, O_2^{2-})は、酸素運搬体や酸素分子を酸化剤とする酸化酵素が酸素分子を捕捉した際に生じる。ヘモグロビンのヘム鉄中心に酸素分子が付加した状態は、Fe(III)-スーパーオキシド錯体である。一方、節足動物や軟体動物の酸素運搬体であるヘモシアニンは、還元状態では2個の銅(I)イオンを活性点に含み、これが酸素分子と反応することで2個の銅(II)イオンのあいだにペルオキシドイオンが架橋配位した二核銅-架橋ペルオキシド(μ -ペルオキシド, μ は複数の金属のあいだを橋掛けしていることを表す記号)種となる。

なお、海産無脊椎動物の酸素運搬体であるヘムエリスリンの活性点はカルボキシ基とヒドロキシ基で架橋された2個の非ヘム鉄で構成されており、そのうちの1個だけに酸素が結合する。しかし生成した酸素付加体はFe(III)-ヒドロペルオキシドイオン(OOH^-)錯体であり、酸素分子は2電子還元されて、

表1 酸素代謝にかかわるおもな金属タンパク質および酵素の機能と活性点金属

機能	反応	活性点金属
酸素の運搬 / 貯蔵	$Fe^{II} + O_2 \rightleftharpoons Fe^{III}-O=O^{\cdot}$ (ヘモグロビン)	ヘム Fe
	$Cu^I \quad Cu^I + O_2 \rightleftharpoons Cu^{II} \begin{matrix} \diagup O \diagdown \\ \diagdown O \diagup \end{matrix} Cu^{II}$ (ヘモシアニン)	二核 Cu
	$Fe^{II} \begin{matrix} H \\ \\ O \end{matrix} Fe^{II} + O_2 \rightleftharpoons Fe^{III} \begin{matrix} H-O \\ \\ O \end{matrix} Fe^{III}$ (ヘムエリスリン)	非ヘム二核 Fe
エネルギー獲得	$2H_2O \xrightleftharpoons[\text{呼吸}]{\text{光合成}} O_2 + 4H^+ + 4e^-$	(光合成) Mn-Ca クラスター (呼吸) ヘム Fe-Cu
活性酸素の無害化	$O_2^{\cdot-} + 2H^+ + e^- \longrightarrow H_2O_2$	非ヘム単核 Fe
	$2O_2^{\cdot-} + 2H^+ \longrightarrow H_2O_2 + O_2$	非ヘム単核 Fe, Mn, Ni, Cu-Zn
	$2H_2O_2 \longrightarrow 2H_2O + O_2$	ヘム Fe, 二核 Mn
基質酸化	$X + O_2 + 2H^+ + 2e^- \longrightarrow X-O + H_2O$	ヘム Fe, 非ヘム二核 Fe, 単核 Cu, 二核 Cu
	$X + O_2 \longrightarrow X-2O$ あるいは $2X + O_2 \longrightarrow 2X-O$	非ヘム単核 Fe, Mn

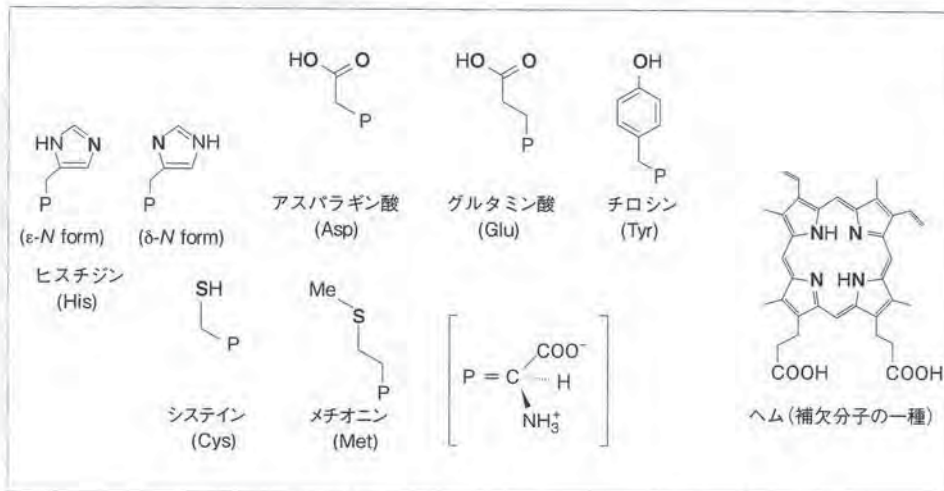


図1 金属タンパク質および酵素の活性点を構成するアミノ酸残基とヘム(太字の元素で金属に配位)

さらにプロトンが付加した状態にある。このヒドロペルオキシド錯体の生成は、酸素がFe(II)中心と結合したことにより1電子還元されたことに加え、酸素が結合しない鉄中心からも1個の電子が酸素分子に移動し、さらに架橋配位子であったヒドロキシ基からプロトンが移動するためである(表1)。

酸素分子を酸化剤とする酸化酵素においても、反応の第1段階では活性点に含まれる金属イオンの数に応じてスーパーオキシドあるいはペルオキシドが配位した中間体が生じる。代表的な酸化酵素であるシトクロムP450のヘム鉄中心では、鉄-スーパーオキシド錯体がプロトンおよび電子を受け取ることで鉄-ヒドロペルオキシド錯体に変換される。そして金属に配位しているヒドロペルオキシド(HOO)のO-O結合が開裂することで、高い酸化力をもつ高原子価金属-オキシ錯体が生じる。

オキシド(酸化物イオン, O^{2-})自体は最外電子殻(L殻)に8個の電子を保有する閉殻構造であるため、本質的には求核性を示してほかの物質から電子を奪い取る能力(酸化力)はもたない。しかし、オキシドが酸化力をもつ高原子価金属に結合した状態では、オキシルラジカルや酸素原子と電子配置が等しい閉殻構造ではない酸素種としてふるまい、ラジカル的な性質に基づくC-H結合からの水素原子引き抜き活性や、親電子的な性質に基づく酸素添加活性を示す。

高原子価金属-オキシ種は、二つの金属イオンにペルオキシドが架橋した錯体種からも生じる。メタンのヒドロキシ化反応を触媒するメタンヒドロキシ化酵素(メタンモノオキシゲナーゼ、通称MMO)のうち、複核鉄中心を活性点とするものでは、2個の鉄(II)イオンからなる還元体が酸素分子と反応することにより二核鉄(III)-架橋ペルオキシ種が生じ、この種が二核鉄(IV)-架橋ジオキシ種へと変換されることが明らかになっている。

高原子価金属-オキシ種の発生はO-O結合の開裂を経るが、結合開裂の様式には2通りある。一つは均等開裂(ホモリシス, homolysis)とよばれるもので、2個の酸素原子間の共有電子対を構成していた電子が一つずつ酸素に分配され、オキシルラジカルを与える。これに対し不均等開裂(ヘテロリシス, heterolysis)では、共有電子対を構成していた2個の電子は一つの酸素に結合してオキシドイオンとな

り、もう一方の酸素は形式的に酸素原子と等価な電子配置となる。このように開裂様式に応じて酸素の電子状態が異なり、均等開裂はラジカル的開裂、不均等開裂はイオニック開裂ともよばれる。なお金属の酸化数の変化も開裂様式に応じて異なる(図2)。

活性酸素種の無害化反応を触媒する酵素では、酵素の反応活性点で金属中心と生体内で生じた活性酸素種の一つであるスーパーオキシドや過酸化水素(あるいはヒドロペルオキシド、ペルオキシド)が直接反応することで金属-ペルオキシ種やヒドロペルオキシ種を与える。さらにペルオキシダーゼと称される酵素群は生体内で生じた過酸化水素を酸化剤として基質酸化を触媒する酵素であり、その活性点の金属中心は過酸化水素と反応してペルオキシ錯体やヒドロペルオキシ錯体を与える^[1]。

金属-活性酸素錯体種のモデル化

酸素分子と反応する金属タンパク質および酵素の性質や機能の理解を目的としたモデル研究では、人工的に合成された金属錯体と酸素分子の反応が検討される。酸素分子と反応する金属錯体は、中心金属が低原子価状態にあり、これに酸素分子が酸化的付加反応することで、金属タンパク質および酵素と同様な金属-スーパーオキシ種や金属-ペルオキシ種が生じる。生体内で酸素分子と直接反応する金属タンパク質や酵素における活性点の中心金属は3d遷移元素である銅や鉄、マンガンであり、これらの元素の場合、通常は銅(II)、鉄(II)、マンガン(II)の単核金属中心と1分子の酸素が反応してスーパーオキシド錯体となる。また錯体の構造や電子的性質によっては、いったん生成した金属-スーパーオキシド錯体に直ちにもう一分子の低原子価金属錯体と反応して二核金属- μ -ペルオキシ錯体を与える場合がある^[4,5]。

一方、超酸化カリウム(KO_2)などに由来するスーパーオキシド(O_2^-)や、過酸化水素に由来するペルオキシド(O_2^{2-})あるいはヒドロペルオキシド(HOO^-)を交換可能な適当な配位子をもつ錯体に作用させることによっても、対応する金属-活性酸素錯体が生成する^[4,5]。これにより酸素分子とは直接反応しないために取り扱いが容易な銅(II)や鉄(III)錯

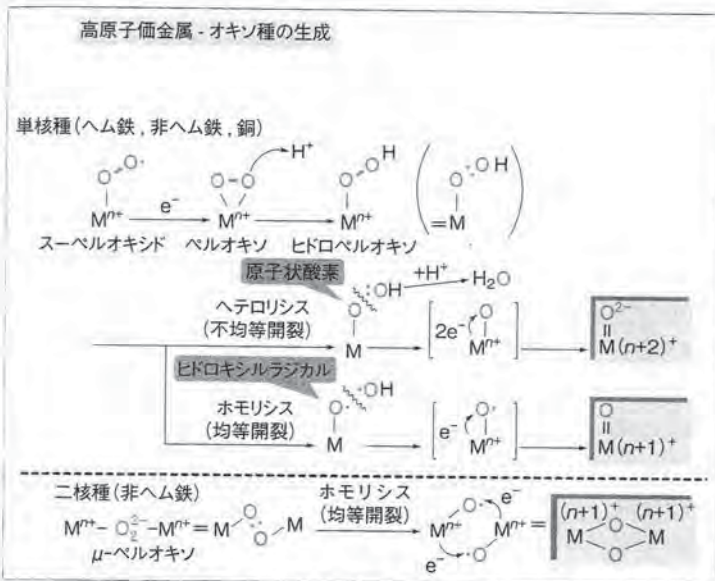


図2 高原子価金属-オキシ種の生成機構

5	6	7	8	9	10	11
V	Cr	Mn	Fe	Co	Ni	Cu
Nb	Mo	Tc	Ru	Rh	Pd	Ag

図3 研究対象となる遷移金属元素
 色の文字：酸素代謝にかかわるタンパク質・酵素に含まれる元素。
 イタリック：モデル研究の対象とされてきた元素。

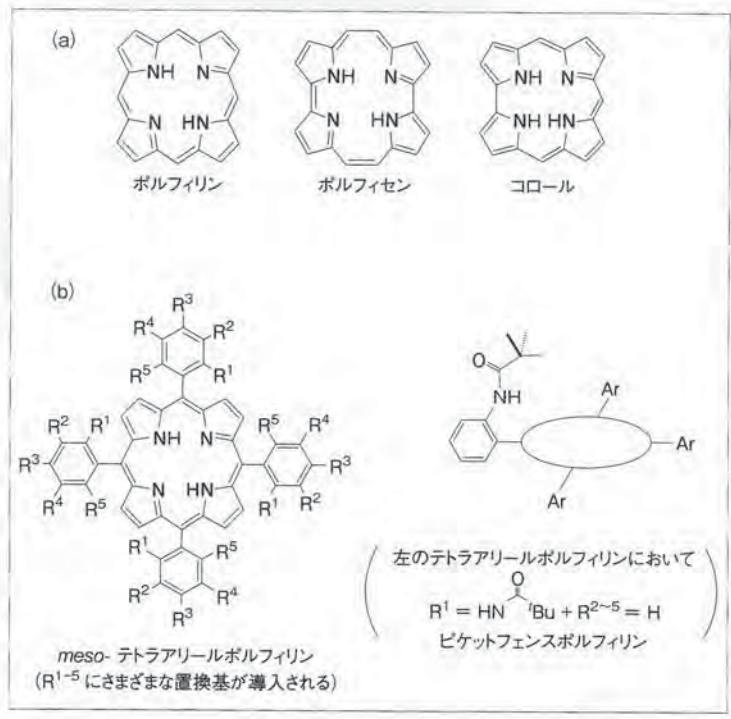


図4 ヘム鉄モデルで用いられる環状ポリピロール配位子
 (a) ヘムのモデルとなる環状ポリピロール, (b) 修飾ポルフィレンの例。

体からも同じ酸化状態の金属-スーパーオキシド、ペルオキシド、あるいはヒドロペルオキシド錯体が得られる。

なお、低原子価金属に対しスーパーオキシドを作らせると、酸化的付加反応により金属中心が1電子酸化されたペルオキシ錯体を生じることがあるが、これは活性酸素種の無害化反応の触媒過程に対応している。また過酸化水素のかわりに有機過酸化物(アルキルあるいはアシルヒドロペルオキシド、ROOH)を活性酸素源とした金属錯体も合成されている。この反応により生じるアルキルあるいはアシルペルオキシ錯体はヒドロペルオキシ錯体の類縁体とみなせるのみならず、有機物である補因子が酵素活性の発現に必須である酸化酵素における反応中間体のモデルとみなせる。

酸化酵素における活性種と同様な高原子価金属-オキシド種は、ペルオキシド、ヒドロペルオキシド、アルキルおよびアシルペルオキシド錯体のO-O結合開裂を経て発生する例が多数知られている。またこのような高原子価金属-オキシド種を直接発生させるために、次亜塩素酸ナトリウム(NaClO)やヨードシルベンゼン(PhIO)のような酸素原子供与体が酸素原子源として用いられることもある。また、水分子が配位子となっている錯体に対し、適当な条件で強力な酸化剤である硝酸セリウム(IV)アンモニウム $[(NH_4)_2[Ce(NO_3)_6]]$ を反応させても高原子価金属-オキシド錯体が合成されている⁶¹⁾。

モデル錯体の分子設計とその特性

金属タンパク質や酵素において活性点となっている金属イオンは、タンパク質のアミノ酸残基や、補欠分子族あるいは補因子とよばれる生体中に存在する有機化合物(図1)により構成される配位子場に置かれることで、その電子的および立体的な環境が制御され、それぞれに固有の機能を発揮している。モデル錯体は、タンパク質や酵素の活性点の忠実なレプリカである必要はなく、金属イオンの支持体である配位子はタンパク質や酵素と同じものでなくても構わない。重要なことは、タンパク質や酵素と同様な特性および機能を発現させるためには、金属中心がいかなる環境にあることが必須要件であるかを考察し、配位子の立体的構造や電子的性質を考慮した

分子設計を行うことである。そしてこの考え方を発展させて、触媒やセンサー、診断薬などとしての応用を見据えて、必要な機能を発揮させるための分子設計を行うことも可能である。

配位子のみならず、中心金属についてもその役割を明確にすることなどを目的として、金属タンパク質および酵素の本来の活性金属とは異なる元素の錯体もモデル研究の対象となることがある。たとえば、ヘム鉄タンパク質に関する知見としては、安定な酸素錯体を形成するコバルトを中心金属とするタンパク質の金属置換体やモデル錯体の検討の成果も含まれている。モデル化に際しては、タンパク質および酵素の中心金属元素に対して、周期表上で隣接する金属元素が選定される場合が多い(図3)。これは遷移元素の場合、同族元素のみならず左右の隣りあう元素とも似通った性質を示すことがあるためである。

ヘム鉄タンパク質およびヘム鉄酵素のモデル錯体では、ヘムの骨格をなすポルフィリンやその類縁体である環状ポリピロール類を基本骨格とした化合物(図4a)が配位子に用いられる。これらの環状ポリピロール類は分子全体に広がった π 共役系に由来する特異な電子状態をもち、その酸化還元特性が反応性に深くかかわっている。ヘム鉄の活性点では、八面体型六配位構造の鉄イオン中心に対して、環状4座配位子であるポルフィリンのピロール窒素が平面位を占めている。そしてポルフィリン環の上下に位置する軸位配位子のうちの一つとして、ヒスチジン(His)由来のイミダゾール窒素、チロシン(Tyr)由来のフェノキシド酸素、システイン(Cys)由来のチオラート硫黄といったアミノ酸残基中のヘテロ元素のいずれかが配位しており、残る一つの軸位が活性酸素種の配位部位である。

酸素代謝に関与するヘム鉄タンパク質およびヘム鉄酵素の機能、すなわち活性酸素種の反応性は、軸位のアミノ酸残基の種類と関連があると考えられている。これは酸素のトランス位に位置する配位子の電子的特性が鉄の酸化還元電位に影響を及ぼすためである。そこでヘム鉄中心をモデル化する際には、イミダゾールやピリジン類、チオラートなどさまざまなルイス塩基が軸配位子に用いられる。

ポルフィリン骨格にさまざまな官能基を導入することによって立体構造や電子的特性を制御し、これ

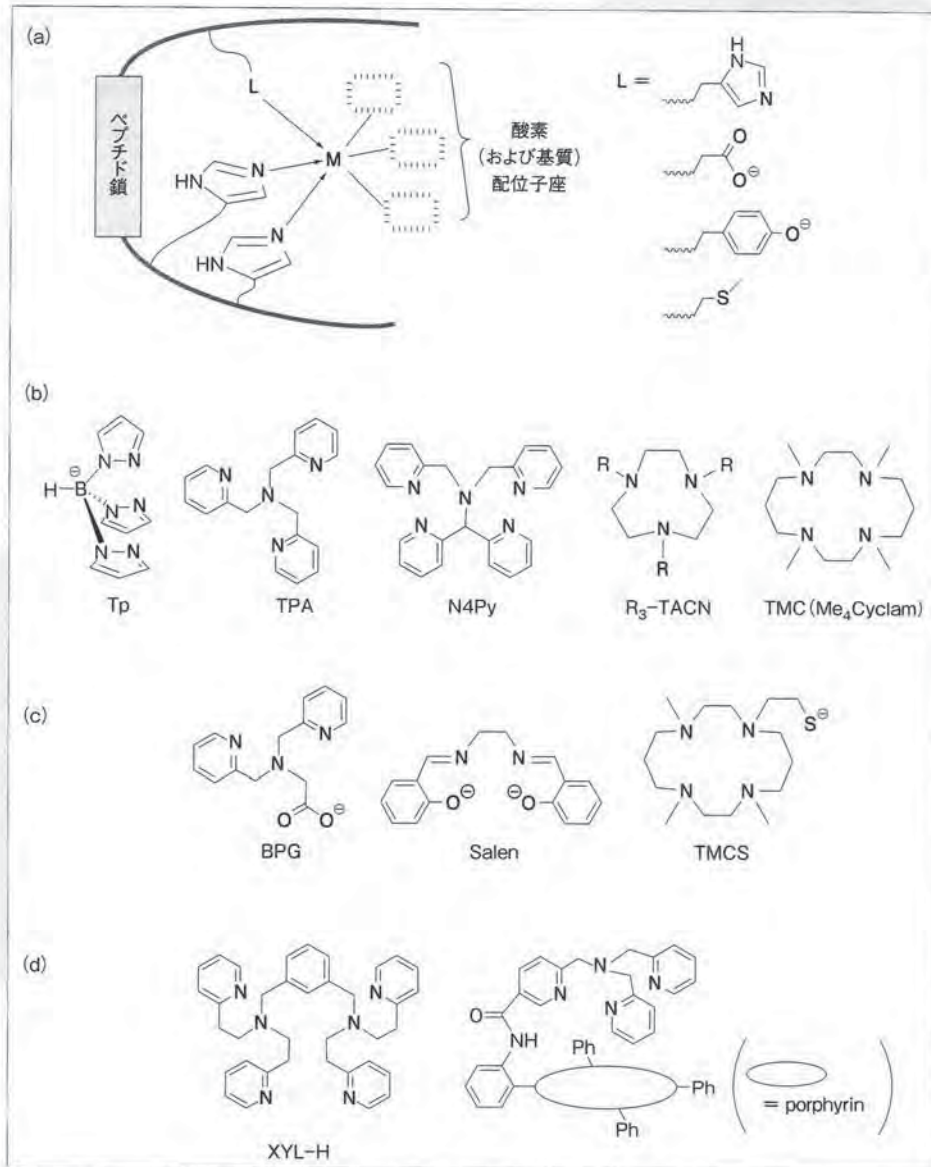


図5 非ヘム金属タンパク質・酵素の活性点とモデル化配位子
 (a) 非ヘム金属タンパク質および酵素の活性点(模式図), (b) 含窒素キレート配位子の例,
 (c) 異種元素配位基からなるキレート配位子の例, (d) 二核化配位子の例.

に基づいて生成する活性酸素錯体の反応性を変化させるといったことも行われる。たとえば、錯体分子どうしの反応によって不活性なオキソ架橋ポルフィリン錯体二量体が生成することを防ぐために、ピケットフェンスとよばれる置換基を導入した例や、電子的な特性を制御するためにポルフィリンのメソ位に電子供与性あるいは電子求引性の置換基を導入した例が知られる(図4b)。

非ヘム金属タンパク質および非ヘム金属酵素のモデル化では、分子設計の自由度は一段と増す。タンパク質や酵素の活性点と同様に、モデル錯体における中心金属上に活性酸素種を結合するための空配位座を設けるには、適当なキレート配位子を用いて金属中心の配位構造を制御するという手法がよく用いられる。生体内におけるヒスチジン(His)のイミダゾール残基が配位子となっている活性点(図5a)をモデル化する際には、イミダゾール以外にもピリジンやピラゾールなどの芳香族性窒素や、アミン窒素からなるキレート配位子が用いられることが多い(図5b)。

さらにこれらのキレート配位子中にカルボキシ基やフェノール性ヒドロキシ基といった酸素配位基、チオラートやチオエーテルなどの硫黄配位基を組み込むことで、より酵素の配位環境に近づけた分子設計も行われる(図5c)。またアスパラギン酸(Asp)やグルタミン酸(Glu)は単核非ヘム金属中心に単座あるいはキレート配位する、あるいは二核非ヘム鉄中心に架橋配位するといった具合に、多様な配位様式をとることが知られているが、このような配位環境をモデル化するために、さまざまなカルボン酸が用いられる。

金属に結合する配位基にさまざまな置換基を導入することで、金属中心の周囲を取り囲む空間のサイズや金属中心の電子状態の調節が行われる。活性酸素錯体の安定化を図るには、構造変化の要因となる錯体分子間の反応や溶媒など酸化を受ける基質となりえる物質の外部からの接近を防ぐ必要があるため、金属の周囲を覆うように立体的にかさ高い置換基が導入される。また活性酸素錯体においては、配位子の一部が基質となって酸化されてしまうこともある。これを逆手にとって、酸化酵素の機能をモデル化するため、金属に配位した活性酸素種の近傍に、あえ

て基質となりえる置換基を配置するという設計が行われる場合もある(図6)^[7]。

一方で、活性酸素錯体の安定化や、外部基質に対する反応性を担保するには、酸化に対して耐性のある置換基が導入される。また置換基の電子的特性に応じた中心金属の電子状態の制御もモデル化を行う際の重要な戦略となる。たとえば、高原子価金属種を安定化するには電子供与性が高い置換基が導入され、逆に低原子価金属種の安定化を図るには電子求引性を示す置換基が導入される。

酸素運搬体や酸化酵素には、2個以上の金属中心からなる複核および多核構造の活性点をもち、活性酸素種が結合した際には複数の金属を架橋した構造となるものもある。このような架橋活性酸素錯体を選択的に構築するため、適当な距離に複数の金属を配置するように設計された多核化配位子が用いられることもある(図5d)。そのなかでも特徴的なものとして、ポルフィリンと非ヘムキレート配位子を連結したものがある。これは呼吸における酸素から水への変換を触媒するシトクロムc酸化酵素のヘム鉄と非ヘム銅中心からなる活性点を再現するために設計されたものである。

金属に対する活性酸素種の配位様式として図7に示すようなものが知られている^[8]。スーパーオキシドやペルオキシサイドなどのO₂ユニットのうちの1個の酸素原子で金属に結合したものはend-on型(あるいは η^1 配位、 η は金属に結合している原子の数を表す記号)および2個の酸素原子がともに金属に結合したside-on型(あるいは η^2 配位)と表現される。また二つ以上の金属に対して活性酸素種が架橋配位した構造もしばしば見いだされる。そしてモデル錯体分子中における活性酸素種の種類とその配位様式は、単結晶X線構造解析により決定されるのみならず、中心金属(元素種とその酸化状態)-活性酸素種の種類-配位様式と各種分光学的特性の相関に基づき同定される。

酸素分子とその還元体であるスーパーオキシド、ペルオキシサイドでは二つの酸素原子間の結合次数が異なり、それを反映してラマンスペクトルにより観測されるO-O結合の伸縮振動値が異なる。とくにペルオキシ錯体については配位様式とO-O結合の伸縮振動値のあいだに明確な相関がみられる^[9]。た

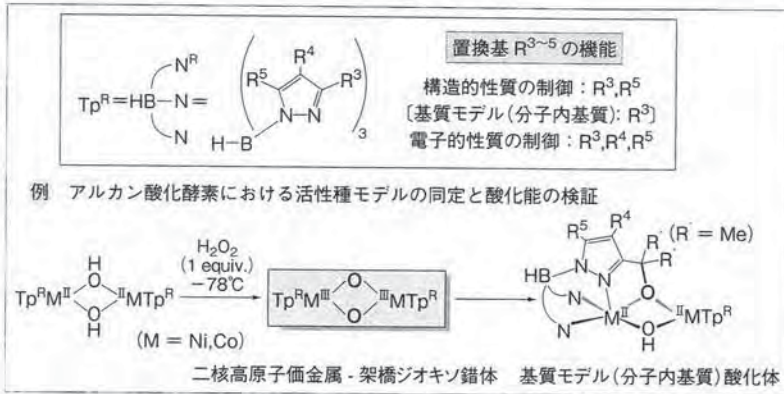


図6 配位子上の置換基に応じたモデル錯体の特性制御の例

R³ = Me(安定な第一級 C-H 結合) → オキソ錯体の安定化(単離・構造解析に成功)
 R³ = *i*Pr(反応性の高い第三級 C-H 結合) → アルキル酸化の速やかな進行

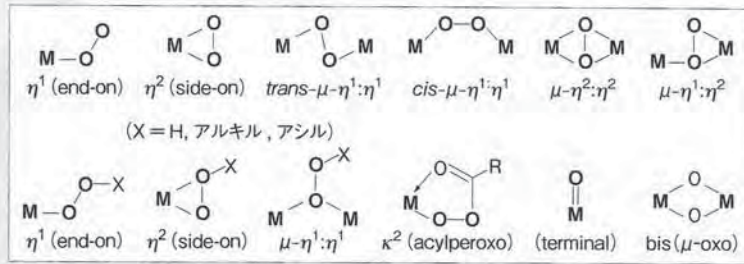


図7 活性酸素種の配位構造

たとえば、2核銅(II)-ペルオキシ種では $\mu-\eta^2:\eta^2$ 構造のものの振動値は $\mu-\eta^1:\eta^1$ 構造のものと比較して低波数であるが、これは $\mu-\eta^2:\eta^2$ 構造ではペルオキシ種のO-O結合の反結合性分子軌道と銅(II)のd軌道の相互作用の結果O-Oの結合が弱められているものと解釈されている。また紫外-可視光吸収スペクトルにおいてもペルオキシドから銅(II)への電荷移動遷移に帰属される吸収帯の波長が配位様式により異なっており、これも配位構造に応じたペルオキシドと銅(II)中心のd軌道の相互作用の違いを反映したものと考えられている^[9]。

反応性の観点から興味深い現象としては、2核銅(II)- $\mu-\eta^2:\eta^2$ -ペルオキシ種と2核銅(III)-ジ(μ -オキシ)種の相互変換がある。上に述べたように、 $\mu-\eta^2:\eta^2$ -ペルオキシ種ではO-Oの結合が弱められた状態、すなわち結合が切れかかっている状態にあるが、二つの銅(II)から1個ずつ電子がペルオキシドに移動すると、O-O結合は完全に切断されて2個のオキシドとなる。この相互変換には、配位子の立体的構造および電子的特性の両方が関与しているものと考えられる。

O-O結合開裂により生じた2核銅(III)-ジ(μ -オキシ)種は、オキシド配位子の近傍に位置するアルキル基のC-H結合から水素原子を引き抜くことが判明している。またメタンヒドロキシ化酵素においても2核鉄(IV)-ジ(μ -オキシ)中間体の存在が確認されたことや、ほかの金属[ニッケル(III)やコバルト(III)]錯体においても同様な構造のものが配位子中の炭化水素置換基に対する酸化活性を示すことが明らかになったことで、非ヘム2核高原子価金属-ジ(μ -オキシ)種が酵素による酸化触媒反応の重要な活性種であることも広く認識されるようになった^[10]。研究の歴史が深いヘム鉄酵素モデルでは、鉄(IV)-オキシ-ポルフィリンカチオンラジカル錯体[鉄(V)-オキシ種と等電子構造]が酸化活性種であることがすでに認識されていたが、これもモデル錯体の研究成果に基づくものである^[11]。また高原子価

金属-オキシ種からO-O結合形成反応が進行したことは、光合成における水の酸化による酸素発生の機構を考察するうえでも有意義な知見である。

最近になってから、単核非ヘム金属を活性点とする酸化酵素のモデルである単核銅(II)あるいは鉄(III)-スーパーオキシ種のなかにC-H結合からの水素原子引き抜き活性を示すものが発見されており、モデル研究は依然として生体機能の解明に大きな役割を果たしている^[8]。そして今後は、これまでに明らかにされた活性種の特性に基づく触媒や酸化反応プロセスの開発へと展開されていくであろう。

◆ 文 献 ◆

- [1] 増田秀樹, 福住俊一 編著, 『生物無機化学——金属元素と生命の関わり——』, 三共出版(2005)。
- [2] S. J. Lippard, J. M. Berg, 松本和子 監訳, 『生物無機化学』, 東京化学同人(1997)。
- [3] R. H. Holm, E. I. Solomon, eds, *Chem. Rev.*, **96**, 2237 (1996). (Thematic issue on "Bioinorganic Enzymology")
- [4] W. Nam, ed, *Acc. Chem. Res.*, **40**, 465 (2007) (Thematic issue on: "Dioxygen Activation by Metalloenzymes and Models")
- [5] R. H. Holm, E. I. Solomon, eds, *Chem. Rev.*, **104**, 347 (2004). (Thematic issue on "Biomimetic Inorganic Chemistry")
- [6] T. Kojima, Y. Hirai, T. Ishizuka, Y. Shiota, K. Yoshizawa, K. Ikemura, T. Ogura, S. Fukuzumi, *Angew. Chem., Int. Ed.*, **49**, 8449 (2010)。
- [7] S. Hikichi, M. Yoshizawa, Y. Sasakura, Y. Ohzu, Y. Moro-oka, M. Akita, *Chem. -Eur. J.*, **7**, 5011 (2001)。
- [8] K. Ray, F. F. Pfaff, B. Wang, W. Nam, *J. Am. Chem. Soc.*, **136**, 13942 (2014)。
- [9] K. D. Karlin, S. Itoh, eds, "Copper-Oxygen Chemistry," Wiley (2011)。
- [10] L. Que, Jr., W. B. Tolman, *Angew. Chem., Int. Ed.*, **41**, 1114 (2002)。

多重定電流パルスによって作製したNi/Cu電気めっき多層膜におけるナノ周期構造と耐摩耗性

神奈川県工学部 田邊豊和 伊藤拳人 郡司貴雄 大坂武男 松本 太
神奈川県工学研究所 金子信悟

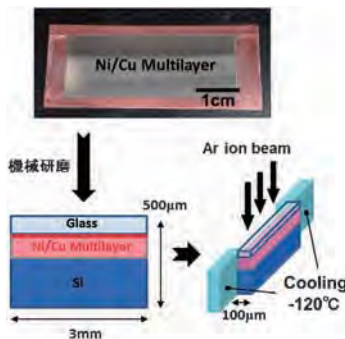


Fig. 1 Cryo-ion milling による多層膜めっきの断面薄膜化.

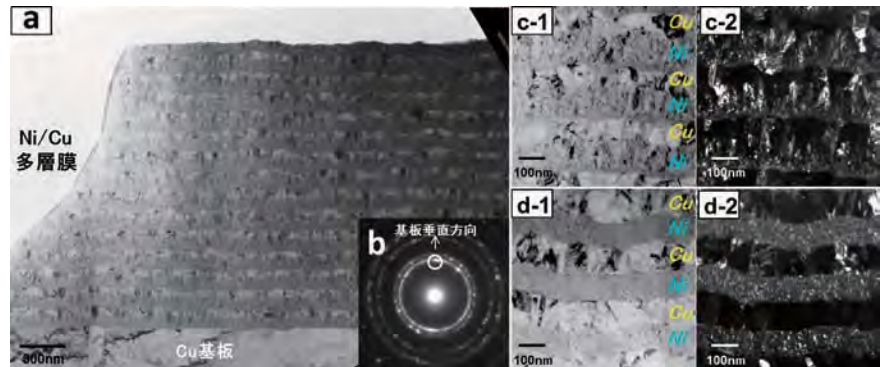


Fig. 2 Ni/Cu 多層膜めっきの断面組織 (a), 多層膜からの回折像 (b), 明視野像 (c-1, d-1), 111回折波により結像した暗視野像 (c-2, d-2) : (c)パルス1回, (d)パルス5回.

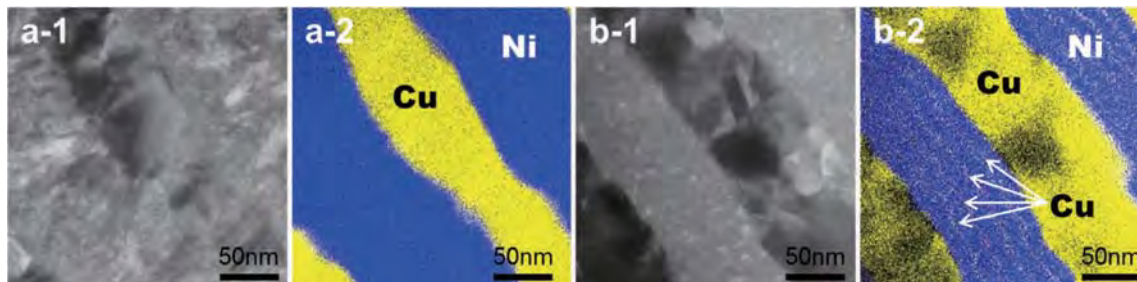


Fig. 3 Ni/Cu 多層膜の STEM-DF 像 (a-1, b-1) と EDS 元素マッピング (a-2, b-2) : (a)パルス1回, (b)パルス5回.

異なった金属めっき膜を重ね合わせる金属多層膜めっきは、単一金属膜に比べ優れた機械的強度を示すことが知られている。多層膜中の各金属層厚を数百 nm 以下に小さくするに従って引張強度や硬さが飛躍的に向上することから基材の機械的特性とナノ周期構造の関係性が示唆されている。そこで我々グループでは金属多層膜めっきの断面組織観察手法を検討し、ナノ周期構造と耐摩耗性の関係解明の検討を行なった⁽¹⁾。TEM 観察用断面試料は、Ar イオン研磨装置 (Ion slicer : 日本電子製, EM-09100IS) をベースにして液体窒素による冷却機構を増設した研磨装置⁽²⁾ を使用して多層膜を薄膜化することで作製した (Fig. 1)。冷却機構を使用することで研磨時の金属再蒸着を抑制する効果が確認され⁽³⁾、アーティファクトの少ない断面組織を得た (Fig. 2(a))。Ni 及び Cu 層を1回の印加定電流パルスで作製した Ni/Cu 多層膜では、基板垂直方向111回折波により結像した暗視野像において基板垂直方向に伸びた多数の柱状結晶が Ni 層, Cu 層ともに観察された (Fig. 2(c)-2)。それに対し、パルス5

回で各金属層を作った場合には Ni 層の結晶子は小さく、パルスの印加回数を増やすに従って、数 nm まで小さくなることを確認した (Fig. 2(d)-2)。EDS 分析により、パルス5回で単層を作った場合においては Ni 層中に数ナノ程度の Cu 層が印可パルスの回数分挿入されており (Fig. 3(b)-2)、パルス回数を増やすことにより Ni の微粒子化及び Ni 層中への極薄 Cu 層の挿入を促す効果があることが明らかになった。耐摩耗性が向上する要因としては、パルスを繰り返すことによって、Ni 層中の Ni 粒子が微細化することによる寄与と、Ni 単層中に形成した微細な Cu/Ni 多層構造の寄与の二つがあると考えられる。

文 献

- (1) T. Tanabe, K. Ito, C. Morita, S. Kaneko, T. Gunji and F. Matsumoto: *Electrochemistry*, **83** (2015), 624–629.
- (2) M. Terauchi, F. Sato, H. Sugizaki and K. Sugauma: *J. Electron Microsc.*, **60** (2011), 25.
- (3) T. Tanabe: *J. Electron Microsc.*, **60** (2011), 35.
(2016年7月20日受理) [doi:10.2320/materia.55.601]

Effect of Periodic Nanostructure in Ni/Cu Multilayers Prepared with Multi-Constant Current Pulse on Their Wear Resistance Property; Toyokazu Tanabe*, Kento Ito*, Takao Gunji*, Takeo Ohaka*, Futoshi Matsumoto* and Shingo Kaneko** (*Department of Material and Life Chemistry, Faculty of Engineering, Kanagawa University, Yokohama. **Research Institute for Engineering, Kanagawa University, Yokohama)

Keywords: Ni/Cu multilayer, electrodeposition, electroplating, cross-sectional observation, periodic nanostructure

TEM specimen preparation: Cryo-ion slicer TEM utilized: JEM-2100F (200 kV)

3. 甲殻類の脱皮・変態とホルモン

大平 剛

甲殻類は硬い殻をもつのが特徴であるが，成長するために殻を脱ぎ捨てる．また，甲殻類は成長していく過程で生活様式にあわせて形態を多様に変化させていく．これらが脱皮と変態である．同じ節足動物に属している昆虫の脱皮や変態は，小学校の理科で扱われているぐらい一般的であるが，甲殻類の脱皮や変態は，それらを解説する書籍すら非常に少ないのが現状である．本章では，甲殻類の脱皮と変態について解説するとともに，内分泌的な制御機構についても述べる．

3.1 成長のための脱皮

甲殻類は，キチン・タンパク質・炭酸カルシウムからなる硬い**外骨格**をもつ．体のサイズを大きくするためには，その硬い外骨格を脱ぎ捨てる必要がある．すなわち，甲殻類は脱皮を繰り返しながら成長していく．外骨格は外側から上クチクラ，外クチクラ，内クチクラ，上皮細胞の4つの層で構成されている（**図 3.1**）．外クチクラと内クチクラはキチン繊維の周りにタンパク質が結合したキチン・タンパク質複合体からなり，これに炭酸カルシウムが沈着し，**石灰化**することで，外骨格が硬くなる．

外骨格の石灰化は**脱皮周期**に同調している．脱皮から脱皮の間の期間である**脱皮間期（C期）**から脱皮の準備期間である**脱皮前期（D期）**に移行すると，古いクチクラが分解され，その内側に新たなクチクラ（上クチクラと外クチクラ）が形成され始める．古い外骨格中の炭酸カルシウムは，外クチクラよりも内クチクラから優先的に溶解され，上皮細胞を通じて血中に送られる．オカダンゴムシ（*Armadillidium vulgare*）の場合には，炭酸カルシウムは胸部腹面に運ばれて**胸石（sternolith）**が形成され，アメリカザリガニ（*Procambarus clarkii*）の場合には，炭酸カルシウムは胃に運ばれて**胃石**

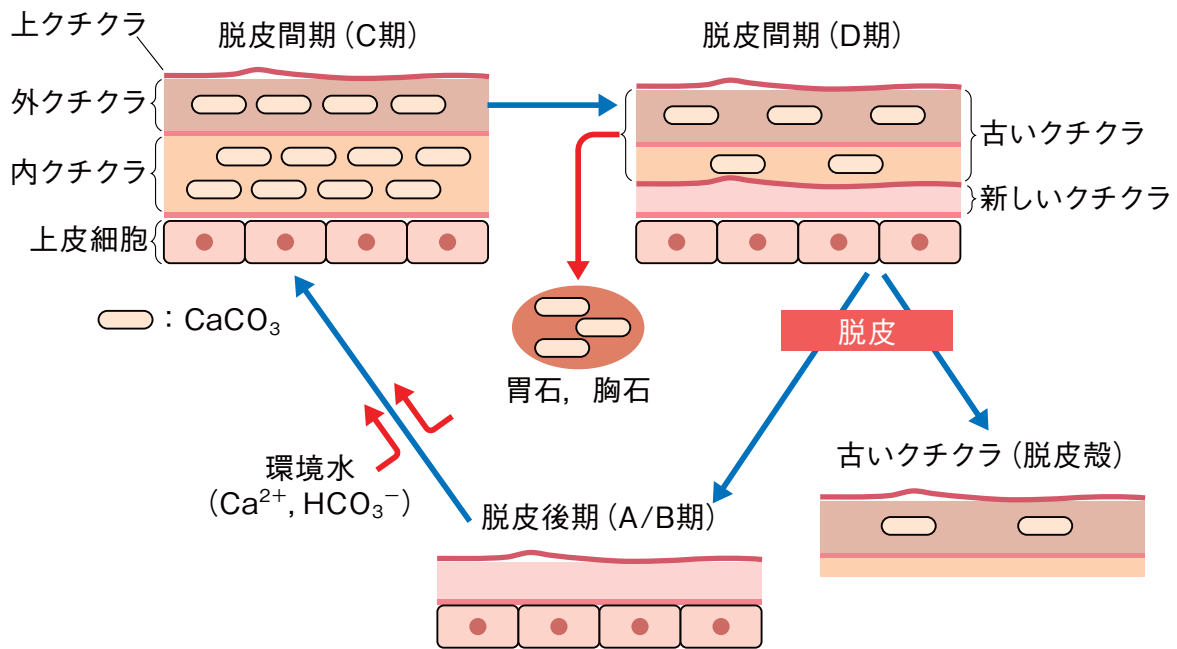


図 3.1 脱皮周期を通じた甲殻類の外骨格の石灰化と脱石灰化

(gastrolith) が形成され、それらにカルシウムを一時的に貯蔵する³⁻¹⁾。脱皮の直前には、古いクチクラ中の炭酸カルシウムの大部分は溶解、吸収される。脱皮により古いクチクラが脱ぎ捨てられ脱皮後期 (A/B 期) へと移行すると、内クチクラの形成が始まる。そして、胸石や胃石として貯蔵していたカルシウムと、環境から取り込んだカルシウムを利用して外骨格の石灰化が起こる。クチクラの形成と外骨格の石灰化が完全に終了すると、C 期へと移行していく。

一回の脱皮でどれくらい体が大きくなるのかは、成長段階に依存する。ズワイガニ (*Chionoecetes opilio*) の場合では、1 齢から 5 齢までの雌雄判別ができない幼齢の個体では、脱皮後の甲長の増加率は平均 44.4% である。6 齢から 10 齢までの若い個体では、脱皮後の甲長の増加率は雌が平均 35.4%、雄が 36.8% と値が低くなる。雌の最終脱皮にあたる 10 齢から 11 齢への脱皮では、雌個体の脱皮後の甲長の増加率はさらに下がり 17% となる。最終脱皮での成長率の低下は、10 齢で卵巣を成熟させるために多くのエネルギーを消費しているためと考えられている。

3.2 成長以外のための脱皮

甲殻類が脱皮をする目的は成長のためだけではない。たとえば、歩脚などを再生させるための脱皮がある。甲殻類は敵から逃れる目的で、歩脚などをみずから切断して身を守る『自切』を行う。自切後、体液が流出しないように傷口は薄い膜で覆われる。アメリカザリガニの場合は、ハサミを自切してから約1週間後に再生芽が観察されるようになり（図3-2, B）、約11日後にはハサミの形態へと変化して硬化する（図3-2, C）。その後、脱皮をすることで、ハサミが再生される（図3-2, D）。再生されたハサミの成長度(%)（再生中のハサミの長さ／正常なハサミの長さ×100）は、個体の大きさに依存する。体長が3 cmの若いザリガニでは一回の脱皮で再生したハサミの成長度は80%近くになる。一方、体長7 cmの成体のザリガニでは一回の脱皮でハサミはわずか40%しか再生しない。体長7 cmのザリガニは年に2回しか脱皮をしないことから、ハサミが元の大きさになるためには何年もかかることになる。

再生のための脱皮は体を成長させるための脱皮ではないため、脱皮と脱皮の間隔が短くなる^{3,2)}。平均甲長約15 mmのヒライソガニ (*Gaetice depressus*) の脱皮間隔は約65日であるが、歩脚の左右一対を除去すると脱皮間隔は約50日に短くなる。鉗脚かんきやくおよび歩脚をすべて除去すると脱皮間隔は半分以下の約27日にまで短縮される。また、脱皮による体長の増加率も歩脚の除去数に依存して減少する。鉗脚および歩脚をすべて除去したヒライソガニでは脱皮後の甲長の増加率はわずか1%である。この値からも、再生のための脱皮が成長のための脱皮とは別物であることがわかる。

脱皮は生殖とも深く関連している。クルマエビ (*Marsupenaeus japonicus*) の雌は脱皮後の殻が柔らかい状態のときに雄と交尾をする。交尾では雄から精子の入った精莢を雌が受け取り、精莢は雌の受精嚢内に入り、産卵・受精まで保存される。受精嚢内の精莢は雌が脱皮をすると古い殻とともに脱落するため、産卵・受精が終わるまでは脱皮しない。

雌が抱卵するテナガエビ科のオニテナガエビ (*Macrobrachium rosenbergii*)

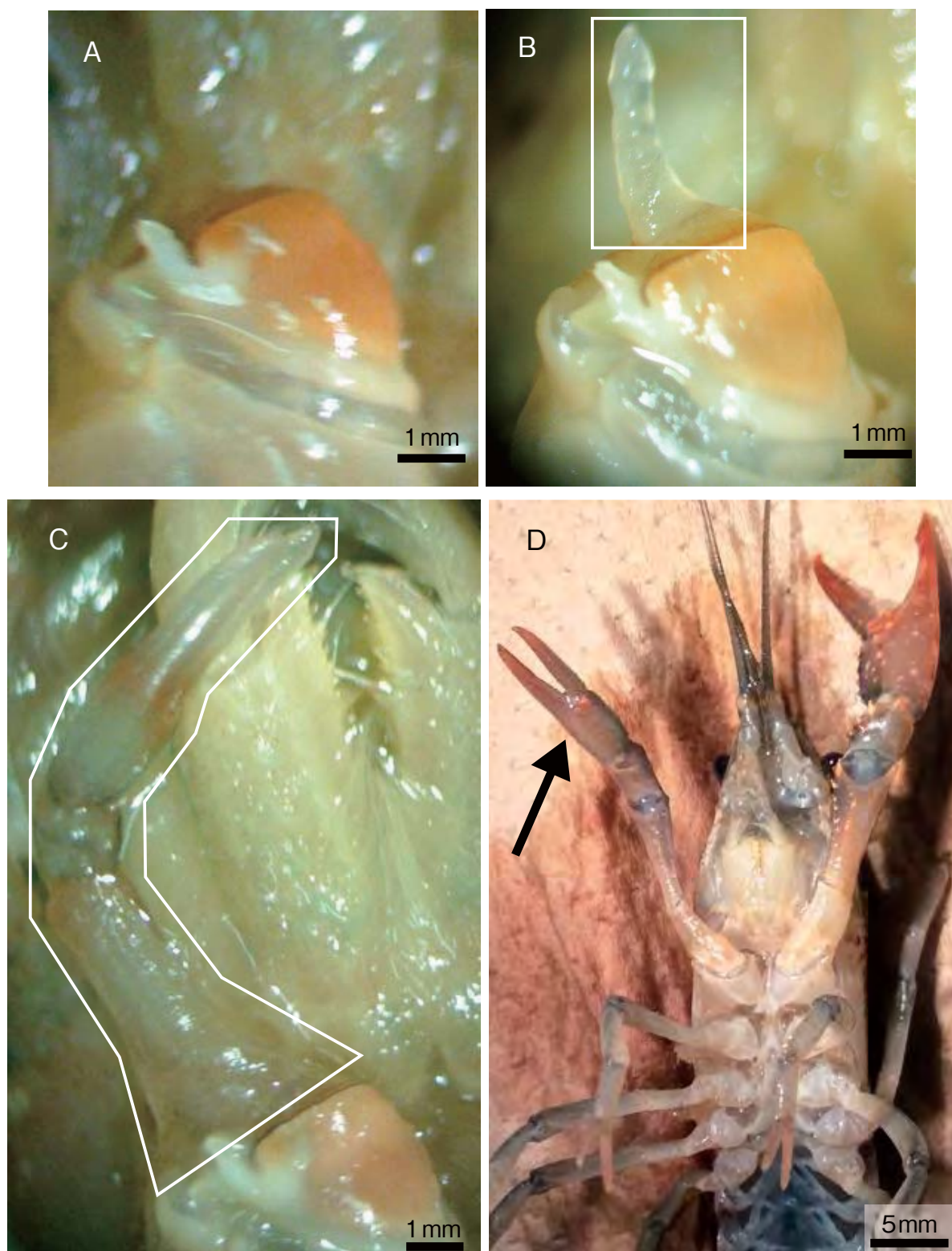


図 3.2 体長約 60 mm のアメリカザリガニ (*Procambarus clarkii*) における自切後のハサミの再生 (撮影: 神奈川大学・小暮純也)
A: 自切 4 日後, B: 自切 8 日後, C: 自切 17 日後, D: 再生脱皮 2 日後
白囲み腺 (B): 再生芽, 白囲み腺 (C): ハサミの形態に変化した再生芽, 矢印: 再生したハサミ

4 ■ ホルモンから見た生命現象と進化シリーズ

では、脱皮（通常脱皮および産卵脱皮のどちらの場合もある）をした後から卵黄形成を始め、次の産卵脱皮と呼ばれる脱皮の前には成熟した卵巣をもつ。そして、産卵直前の状態で産卵脱皮をした後に雄と交尾をし、産卵、抱卵にいたる。抱卵した雌は卵を脱落させないために脱皮しない。カニの仲間は、成熟に達するときの脱皮を成熟脱皮と呼ぶ。成熟脱皮後に交尾・産卵するが、成熟脱皮では抱卵しやすいような形態に雌の腹節が変化する³³⁾。これら生殖のために行う脱皮は、雌の生殖過程において多くのエネルギーが消費されることから、脱皮後の成長率は低い。

3.3 多様な変態の様式

同じ節足動物に属する昆虫の多くは、種が違っても共通の生活史を送る。これまでに記載されたおよそ 100 万種の昆虫のうち、約 83% が完全変態昆虫である。完全変態昆虫は、卵が孵化した後、数齢の幼虫期を経て蛹になり、そして羽化して成虫になる。一方、甲殻類の生活史は種によって大きく異なる。ここでは比較的よく調べられているクルマエビとガザミ (*Portunus trituberculatus*) について述べる。

クルマエビ科のエビ類は世界各地で盛んに養殖が行われている。そのため、幼生飼育や種苗生産が事業レベルまたは試験レベルで行われている種も多い。これまでに、クルマエビ、フトミゾエビ (*Melicertus latisulcatus*)、クマエビ (*Penaeus semisulcatus*)、ウシエビ (*Penaeus monodon*)、タイショウエビ (*Fenneropenaeus chinensis*)、モエビ (*Metapenaeus moyebi*)、ヨシエビ (*Metapenaeus ensis*) の幼生発育過程についての報告があるが、これらすべての種で幼生段階や齢数が共通していることから、ここではクルマエビについて述べる (図 3.3)。

成熟したクルマエビの雌は泳ぎながら放卵する。卵径はわずか約 0.2 mm で、産卵後 13 時間から 14 時間で孵化する。孵化直後の幼生はノウプリウスと呼ばれ、体長は約 0.3 mm である (図 3.3, A1)。ノウプリウスは 1 齢から 6 齢まであり、栄養を体内の卵黄に依存しており摂餌しない。約 36 ~ 37 時間に 6 回の脱皮を行い、体長約 0.9 mm のゾエア 1 齢へと変態する (図 3.3,

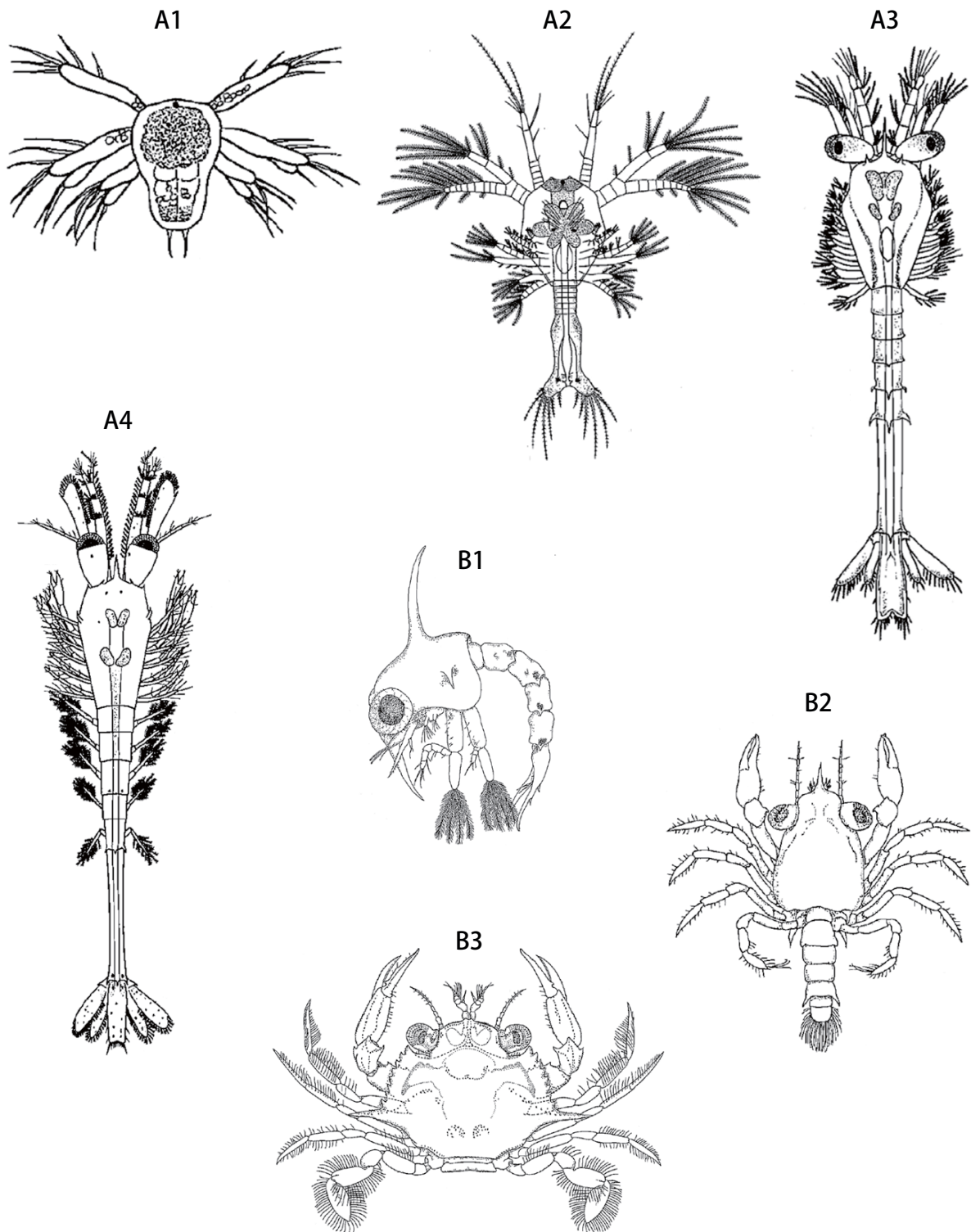


図 3.3 クルマエビ (*Marsupenaeus japonicus*) の幼生 (A1 から A4) と, ガザミ (*Portunus trituberculatus*) の幼生 (B1 から B3) (石原勝敏 編, 1996)
A1: ノウプリウス 1 齢, A2: ゾエア 1 齢, A3: ミシス 1 齢, A4: ポストラーバ 1 齢, B1: ゾエア 1 齢, B2: メガロパ, B3: 幼ガニ 1 齢

A2). ゾエアは1齢から3齢まであり、この時期から珪藻類などの微小な植物プランクトンを摂餌するようになるが、遊泳動作は緩慢である。4日間に3回の脱皮を行い、体長約2.8 mmのミシス1齢に変態する(図3.3, A3)。ミシスは1齢から3齢まであり、エビに近い形態となる。ミシスは頭を下にして活発に泳ぎ回り、動物プランクトンのような大きな餌を捕食する。3日間に3回の脱皮を行いポストラバに変態する(図3.3, A4)。ポストラバになると歩脚は摂餌および^{ほふく}匍匐器官として作用するようになり、腹部に新生した遊泳肢を用いて水平に遊泳するようになる。ポストラバの形態はほぼ成体と近いことから、ミシスからポストラバへの変態がクルマエビの最終変態であり、さらにポストラバが10回から12回の脱皮を重ねると、成体が行うような潜砂行動を示すようになる。

ワタリガニの仲間のガザミはクルマエビとは違った変態を行う(図3.3)。ガザミはクルマエビと違って産卵後に卵を抱卵する。産卵直後の卵径は約0.3 mmで、雌ガニの腹肢の毛に卵殻を付着させて、孵化するまで親ガニが保育する。抱卵中に胚発生が進み、卵内ではノウプリウスを経てプレゾエアとなる。そして、孵化とともにプレゾエアが脱皮してゾエア1齢となる。ゾエア1齢の甲長は約0.5 mmで、上下に長い棘をもつなど、クルマエビのゾエアとはまったく形態が異なる(図3.3, B1)。ゾエア1齢から2齢はワムシなどの動物プランクトンを摂餌する。ゾエア3齢になるとアルテミアなどの動物プランクトンも摂餌するようになる。ゾエア幼生は1齢から4齢まであり、約10日間に4回の脱皮を行いメガロパに変態する。メガロパの甲長は約2 mmで、カニに特徴的なハサミが観察されるようになる(図3.3, B2)。メガロパは動物プランクトンばかりでなく、アサリなどの二枚貝の肉片も食べる。メガロパになってから約5日後に脱皮をして幼ガニ1齢に変態する(図3.3, B3)。幼ガニ1齢の甲長は約2.5 mm、甲幅は約3 mmで、さらに1~2回脱皮をした後に底生生活に移行する。

ここでは詳述しないが、イセエビ(*Panulirus japonicus*)の場合はフィロソーマと呼ばれる幼生段階で約300日間の浮遊生活を送る。その間に、フィロソーマ幼生は25回前後も脱皮をする。一方、アメリカザリガニは親とほ

ば同じ形態の稚ザリガニの状態で孵化をする。このように、甲殻類の幼生の形態、幼生期の長さ、脱皮の回数など、甲殻類の変態の様式は非常に多様である。甲殻類の幼生の形態や発生過程は系統関係を反映していない場合も多いことから、甲殻類の変態の多様性は、それぞれの幼生の生息環境への適応の結果と考えられている。

3.4 脱皮・変態を制御するホルモンの役割

脱皮の研究は同じく節足動物に属する昆虫において古くから行われてきた。1940年に福田が、昆虫の脱皮を誘導するホルモンが**前胸腺**から分泌されていることを明らかにした。1954年、脱皮ホルモン活性をもつ分子として**エクジソン**が単離され、続いて1956年に、**20-ヒドロキシエクジソン**が単離された。そして、1965年にX線解析によりエクジソンの構造が決定された。翌年の1966年、甲殻類からも20-ヒドロキシエクジソンが単離された。その後、類似の構造をもつ物質が植物からも多数同定され、これらの物質は**エクジステロイド**と総称されるようになった。昆虫と同様に甲殻類においても、エクジステロイドが脱皮を引き起こす。その後、甲殻類のエクジステロイドはY器官と呼ばれる組織で合成されることが、*in vitro*の培養実験で確かめられた。

エクジステロイド以外に脱皮を制御する因子として、**眼柄内**に存在する**脱皮抑制ホルモン**（MIH：molt-inhibiting hormone）が知られている。1905年にゼレニー（Zeleny）はカニの眼柄を切除すると、脱皮の間隔が早まることを見だし、眼柄内に脱皮を抑制する因子が存在することを初めて示唆した³⁴⁾。一方、組織学的研究から、眼柄の終随と呼ばれる神経組織に神経分泌細胞群（**X器官**）が存在し、これらの神経分泌細胞群から伸びる軸索の末端は集まって神経血液器官（**サイナス腺**）を形成していることが明らかにされた（**図3.4**）。これより、脱皮を制御するホルモンはX器官で合成され、サイナス腺中に一時的に貯蔵された後、血リンパ中へ放出されると考えられるようになった。その後、眼柄切除によって血中エクジステロイド量が増加すること、およびサイナス腺抽出物がY器官からのエクジステロイドの分

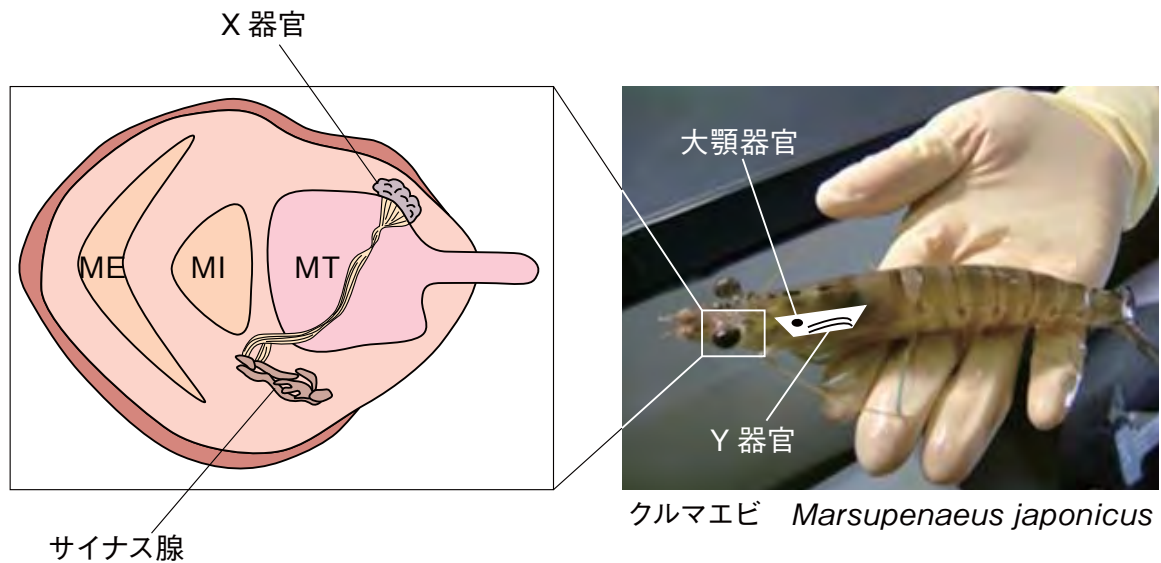


図 3.4 クルマエビ (*Marsupenaeus japonicus*) の X 器官／
サイナス腺系, Y 器官および大顎器官の分布
ME: 外髄, MI: 内髄, MT: 終髄

泌を抑制することが示された. そしてついに, 1991年に, ミドリガニ(*Carcinus maenas*) のサイナス腺から初めて MIH が単離された³⁻⁵⁾.

以上に述べた甲殻類の脱皮の主要な内分泌制御機構は, 同じ節足動物に属する昆虫と類似している. すなわち, 甲殻類も昆虫も共通の分子 (エクジステロイド) を脱皮ホルモンとして利用している. しかし, 同じエクジステロイドの合成器官であっても甲殻類の Y 器官と昆虫の前胸腺とでは制御機構はまったく異なっている. 前述したように, 甲殻類の場合は MIH が Y 器官でのエクジステロイド合成を抑制的に制御している. 一方, 昆虫の場合は, 脳で合成される前胸腺刺激ホルモン (PTTH: prothoracicotropic hormone) が前胸腺でのエクジステロイド合成を促進的に制御している. このような甲殻類と昆虫におけるエクジステロイド合成の制御機構の相違点は, 比較内分泌学的に注目されている.

3.5 脱皮ホルモン（エクジステロイド）の働き

甲殻類のエクジステロイドの産生器官である Y 器官は頭胸部の側面に左右一対存在する微小な組織である (図 3.4). Y 器官でのエクジステロイドの

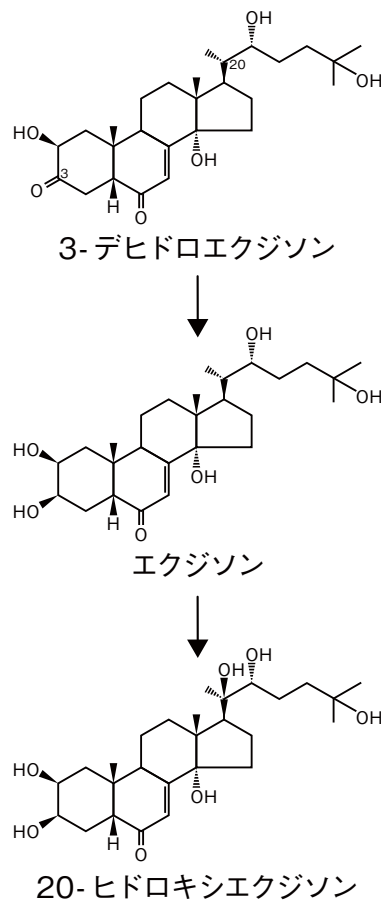


図 3.5 クルマエビ (*Marsupenaeus japonicus*) のエクジステロイド

生合成経路は、昆虫の前胸腺における生合成経路と大部分が一致していると考えられている。Y 器官から分泌されるエクジステロイドは種によって異なる。クルマエビの場合は、3-デヒドロエクジソンとエクジソンが Y 器官から分泌されている (図 3.5)。分泌された 3-デヒドロエクジソンは周辺組織で 3 位が還元されてエクジソンとなった後、20 位が水酸化されて 20-ヒドロキシエクジソンへと変換される (図 3.5)。

脱皮周期にともなう血リンパ中のエクジステロイド濃度の変化は、多くの甲殻類で調べられている。ここでは、アメリカザリガニを例として示した (図 3.6)。脱皮間期 (C 期) には血リンパ中のエクジステロイド (おもに 20-ヒドロキシエクジソン) レベルは非常に低い状態に保たれている。脱皮前期 (D 期) 前半 (D1 期) になるとエクジステロイドレベルのわずかな上昇が始まり、D 期中盤 (D2 期) には急激にエクジステロイドレベルが上昇する。脱皮直

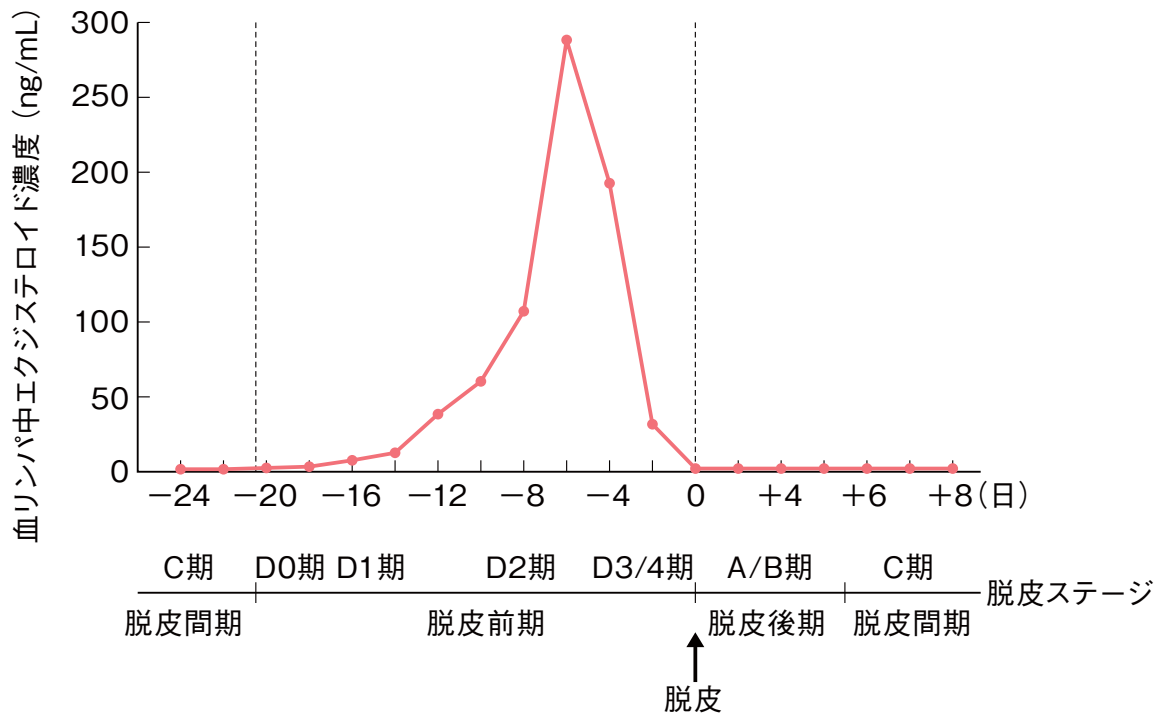


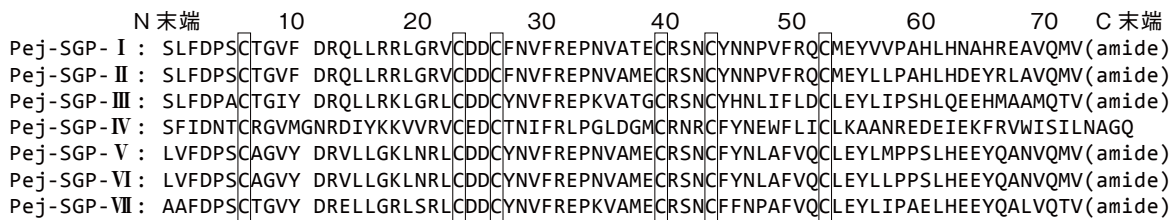
図 3.6 アメリカザリガニ (*Procambarus clarkii*) の脱皮周期にともなう血リンパ中のエクジステロイド濃度の変動 (園部治之・長澤寛道 編, 2011)

前の D 期後半 (D3/D4 期) になるとエクジステロイドレベルは一気に減少し、その後、脱皮が起こる。脱皮後期 (A/B 期) のエクジステロイドレベルは低い状態に保たれる。この血リンパ中のエクジステロイドレベルの変動パターンは、種によって脱皮周期の長さに違いはみられるものの、多くの甲殻類でよく似ており、クルマエビでも同様の結果が得られている³⁻⁶⁾。以上のことは、甲殻類においてエクジステロイドが共通して脱皮を促進することを示す。

3.6 脱皮抑制ホルモン (MIH) の働き

クルマエビを中心に MIH の働きを解説する³⁻⁷⁾。クルマエビを含む十脚目のサイナス腺には、いくつかの生理活性を有する神経ペプチドが貯蔵されている。それら神経ペプチドのうち、血糖上昇ホルモン (CHH: crustacean hyperglycemic hormone)、卵黄形成ホルモン (VIH: vitellogenesis-inhibiting hormone)、大顎器官抑制ホルモン (MOIH: mandibular organ-inhibiting

hormone) および MIH の 4 種類はお互いにアミノ酸配列が類似しており、**CHH 族**と呼ばれるペプチドファミリーを形成している。クルマエビにおいては、サイナス腺抽出物から 7 種類の CHH 族ペプチド (Pej-SGP-I ~ VII) が精製・単離され、アミノ酸配列が決定された (図 3.7)。それら 7 種類の CHH 族ペプチドをアメリカザリガニ Y 器官の *in vitro* 培養系に添加したところ、Pej-SGP-IV は Y 器官でのエクジステロイド合成を最も強く抑制する活性 (脱皮抑制活性) のみを示した (図 3.7)。残りの 6 種類はおもに血糖上昇活性や、卵巣でのビテロジェニン合成抑制活性 (卵黄形成抑制活性) を示した (図 3.7)。これらの結果より、Pej-SGP-IV がクルマエビの MIH であると推定された。アメリカザリガニが生物検定に用いられたのは、アメリカザリガニ Y 器官の *in vitro* 培養系がすでに確立されていたことと、クルマエビの Y 器官を傷つけずに摘出することが難しいためである。その後、大腸菌発現系を使って組換え Pej-SGP-IV が作製され、それをクルマエビに注射すると、脱皮の時期が有意に遅くなること、および血リンパ中のエクジステロイド濃度が低下することが確かめられた。また、放射性標識した組換え



Pej-SGP-	I	II	III	IV	V	VI	VII
脱皮抑制活性	—	—	—	+++	+	+	ND
血糖上昇活性	++	+	++	—	+++	+++	+++
卵黄形成抑制活性	++	++	++	—	++	++	++

⏟
⏟
⏟
 CHH/VIH MIH CHH/VIH

図 3.7 クルマエビの血糖上昇ホルモン (CHH) 族ペプチドのアミノ酸配列と生物活性

ボックス：保存された 6 個のシステイン残基，ND：未検定，MIH：脱皮抑制ホルモン，VIH：卵黄形成抑制ホルモン

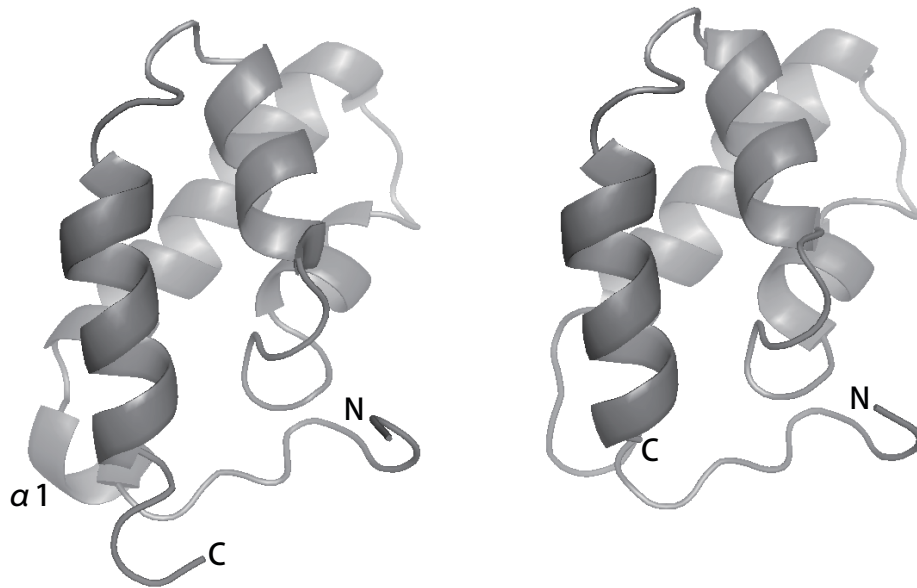


図 3.8 クルマエビ (*Marsupenaeus japonicus*) の脱皮抑制ホルモン (MIH) の立体構造 (左) と, 血糖上昇ホルモン/卵黄形成ホルモン (CHH/VIH) の 1 つ Pej-SGP-III の立体構造モデル (右)
 $\alpha 1$: MIH に特徴的な α ヘリックス, N: N 末端, C: C 末端

Pej-SGP-IV はクルマエビ Y 器官の膜画分と特異的に結合することがわかった。これらの結果より, Pej-SGP-IV はクルマエビの真の MIH と考えられるようになった。これ以降, 本稿では Pej-SGP-IV をクルマエビ MIH とする。

クルマエビの Pej-SGP-I ~ VII はともに CHH 族のメンバーであり, お互いに類似したアミノ酸配列を有している (図 3.7)。しかし, MIH と 6 種類の CHH/VIH (Pej-SGP-I ~ III および V ~ VII) のアミノ酸配列を比較すると, C 末端側のアミノ酸配列の相同性が極端に低い (図 3.7)。また, MIH の C 末端は修飾されていないが, CHH/VIH の C 末端はすべてアミド化されている。これらのことから, C 末端側の領域が MIH の生物活性に重要であると予想された。また, 核磁気共鳴による解析から, 立体構造上で N 末端に近い部位には, MIH では α ヘリックスが存在するが, CHH/VIH には存在しないことも明らかとなった (図 3.8)。そのため, MIH の機能部位は $\alpha 1$ を含んだ領域と C 末端側の領域と推定された。

MIH は眼柄内の X 器官で合成され, サイナス腺に一時貯蔵された後, 血リンパ中へ分泌される。Y 器官は脱皮前期の短期間のみ活性化されエクジス

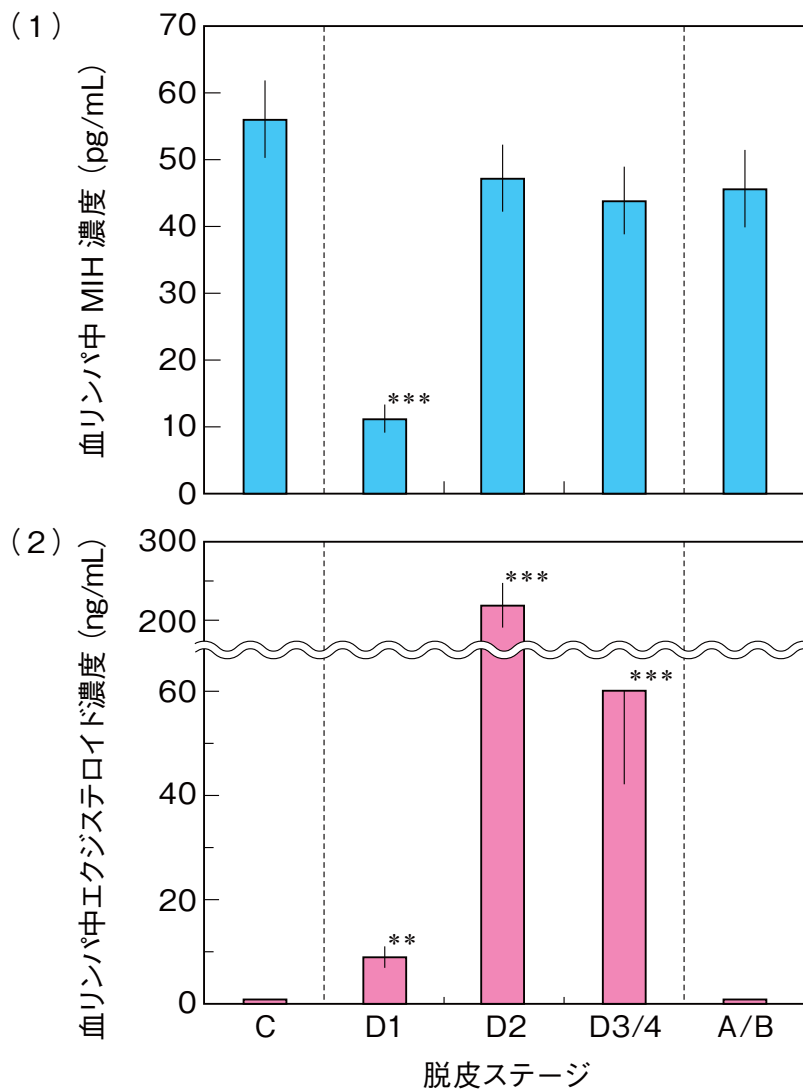


図 3.9 アメリカザリガニ (*Procambarus clarkii*) の脱皮周期にともなう血リンパ中の MIH 濃度 (1) とエクジステロイド濃度 (2) の変動 (園部治之・長澤寛道 編, 2011)

値は平均値±標準誤差で示している ($n = 13 \sim 24$).

** : $P < 0.01$, *** : $P < 0.001$ (t 検定により C 期と比較した場合)

テロイドを合成・分泌することから (図 3.6), MIH は脱皮前期にのみ血中量が減少し, Y 器官の抑制を解除していると考えられてきた. この仮説は古くから提唱されてきたが, 実際に MIH の血中動態を調べた研究は永らくなかった. 2003 年, 甲南大の中辻らは 2 抗体サンドイッチ型の時間分解蛍光免疫測定法を確立し, アメリカザリガニの脱皮周期にともなう血中 MIH の変動を明らかにした. アメリカザリガニ MIH は血リンパ中のエクジステロ

イドが最も上昇する D2 期の前の D1 期に減少しており、先に述べた仮説が正しいことが証明された (図 3.9)。また、仲辻らは Y 器官自身の MIH 感受性の変動も調べた。その結果、アメリカザリガニ Y 器官の MIH 感受性は C 期で最も高く、D1 期になると低下していき、D2 期および D3/4 期に最も低くなり、A/B 期に回復した。このように、Y 器官のエクジステロイド合成は血リンパ中の MIH 濃度の変動によって調整されているだけでなく、Y 器官自体の MIH 感受性の変動によっても調整されていることが明らかとなった。

3.7 幼若ホルモン様分子（ファルネセン酸メチル）の働き

昆虫では幼若ホルモンが幼生形質の維持に働くことで、幼虫から幼虫への脱皮をするか、変態をともなう脱皮をするかを制御している。同じ節足動物の甲殻類でも、ファルネセン酸メチル (MF: methyl farnesoate) という、昆虫の幼若ホルモンとよく似た分子が大顎器官で合成されている (図 3.4)³⁸⁾。MF は、昆虫の幼若ホルモンの 1 種 (JH III) の前駆体であることから、甲殻類の幼若ホルモンではないかと考えられてきた。MF は甲殻類において幼生形質の維持に働くとする報告も数例あるものの、その効果が JH III などの昆虫の幼若ホルモンよりも弱いことから、一般的に甲殻類の幼若ホルモンとしては受け入れられていない。一方、MF が甲殻類の脱皮の促進に関わっているという報告もいくつか存在する。アメリカイチョウガニ (*Metacarcinus magister*) の Y 器官の *in vitro* 培養系に MF を添加すると、Y 器官でのエクジステロイド合成が促進された。また、オニテナガエビでは、血中エクジステロイドレベルが上昇を始める前に MF レベルが上昇していた。これらの結果は、MF が甲殻類の脱皮を促進的に制御している可能性を示唆している。しかし、このような報告も数が少ないのが現状であり、MF と脱皮・変態との関連性については、今後のさらなる研究が必要である。本章で扱う内容ではないが、昆虫の幼若ホルモンは成虫期の卵成熟を促進的に制御している。実際に、甲殻類でも MF が生殖に関与していることを示す報告例がいくつかある。クモガニ科の 1 種 (*Libinia emarginata*) では血リンパ中の MF レベルが生殖周期を通じて変動していた。また、*L. emarginata* の大顎器官を

未熟な雌ガニに移植すると卵成熟が促進された。しかし、オニテナガエビでは成熟期と未成熟期で血リンパ中の MF レベルに有意な差は観察されなかった。甲殻類の MF の生殖調節作用は種によって異なる可能性がある。

コラム 3.1

甲殻類の眼柄切除実験

アメリカザリガニの眼柄を外科的に切除すると、MIH の合成・貯蔵器官である X 器官／サイナス腺系を体内から取り除くことができる。その結果、MIH の抑制が解除されて、Y 器官でのエクジステロイド合成が活性化される。そして、眼柄を切除したアメリカザリガニは数日後に脱皮をする。ここまでは、多くの人が想像できる結果だと思う。それでは、その後、眼柄を切除したアメリカザリガニの飼育を続けるとどうなるのか？ 実は、眼柄がないアメリカザリガニは周期的に脱皮を繰り返しながら成長する。すなわち、眼柄がないアメリカザリガニも脱皮周期を継続することが可能である。これは、眼柄がないアメリカザリガニも、通常の個体と同様に脱皮前期（D 期）に Y 器官でエクジステロイドが合成されていることを示している。実際に、オニテナガエビでは、眼柄がなくても血リンパ中のエクジステロイドの変動が続くことが明らかにされている。眼柄がないアメリカザリガニやオニテナガエビには MIH による抑制系が存在しないことから、抑制解除により Y 器官でのエクジステロイド合成を活性化することはできない。すなわち、眼柄の MIH 以外に、Y 器官を定期的に活性化する機構が備わっているはずである。眼柄を切除すると大顎器官が発達することから、大顎器官で合成される MF が脱皮促進ホルモンではないかという説もあった。しかし、今のところ MF が脱皮促進ホルモンの本命とは考えられてはいない（3.7 参照）。甲殻類に脱皮促進ホルモンは存在するのか？ それとも Y 器官自身にエクジステロイド合成のリズムが備わっているのか？ 未だに、甲殻類の脱皮にはわからないことがたくさんある。

3.8 おわりに

甲殻類の脱皮の研究の歴史は非常に古く、3.4節で述べた1905年のゼレニー（Zeleny）の実験にまでさかのぼる。それから約100年後の2003年、MIHの血中レベルが明らかにされ、MIHの立体構造も明らかにされた。近年、MIHの細胞内セカンドメッセンジャーに関する研究も行われるようになってきたが、MIH受容体やシグナル伝達経路をつなぐ分子群は未だ未同定である。今後、これらMIHの分子認識機構が解明されることを期待している。

エビやカニなどの甲殻類は水産食糧資源として重要なばかりでなく、海洋生態系において食物連鎖の維持に重要な役割を果たしている。甲殻類の脱皮・変態のメカニズムの解明は、甲殻類を食料として安定供給していくための新たな技術の確立に発展していく可能性がある。これらのことから、甲殻類の脱皮・変態に関する内分泌学的な研究は重要と思われる。しかし、この分野の研究者は国内外も含めて非常に少ないのが現状であり、日本の若手研究者に至っては数名足らずである。本稿を読んで、甲殻類の脱皮・変態に興味をもってくれる大学生が増え、その中から同分野の研究を牽引してくれる研究者が育ってくれることを願っている。

3章 参考書

朝倉 彰 編 (2003) 『甲殻類学』 東海大学出版会。

石原勝敏 編 (1996) 『動物発生段階図譜』 共立出版

奥村卓二・水藤勝喜 編 (2014) 『クルマエビ類の成熟・産卵と採卵技術』 愛知県水産業振興基金。

大澤一爽 (1984) 『ザリガニを主材とした甲殻類の実験-33章』 共立出版。

園部治之・長澤寛道 編 (2011) 『脱皮と変態の生物学』 東海大学出版会。

Justo C. C. 編 (1990) 『世界のエビ類養殖』 緑書房。

3章 引用文献

3-1) 園部治之・中辻晃明 (2002) 化学と生物, **40**: 101-108.

3-2) 加藤一夫・鈴木 博 (1985) 横浜国立大学教育学部理科教育実習施設研究報告, **2**: 1-8.

3章 甲殻類の脱皮・変態とホルモン

3-3) 渡邊精一 (1997) 水産増殖, **45**: 305-313.

3-4) Zeleny, C. (1905) J. Exp. Zool., **2**: 1-102.

3-5) Webster, S. G. (1991) Proc. R. Soc. Lond. B, **244**: 247-252.

3-6) Okumura, T. *et al.* (1989) Nippon Suisan Gakkaishi, **55**: 2091-2098.

3-7) Katayama, H. *et al.* (2013) Aqua-BioScience Monographs **6**: 49-90.

3-8) Homola, E., Chang, E. S. (1997) Comp. Biochem. Physiol., **117B**: 347-356.

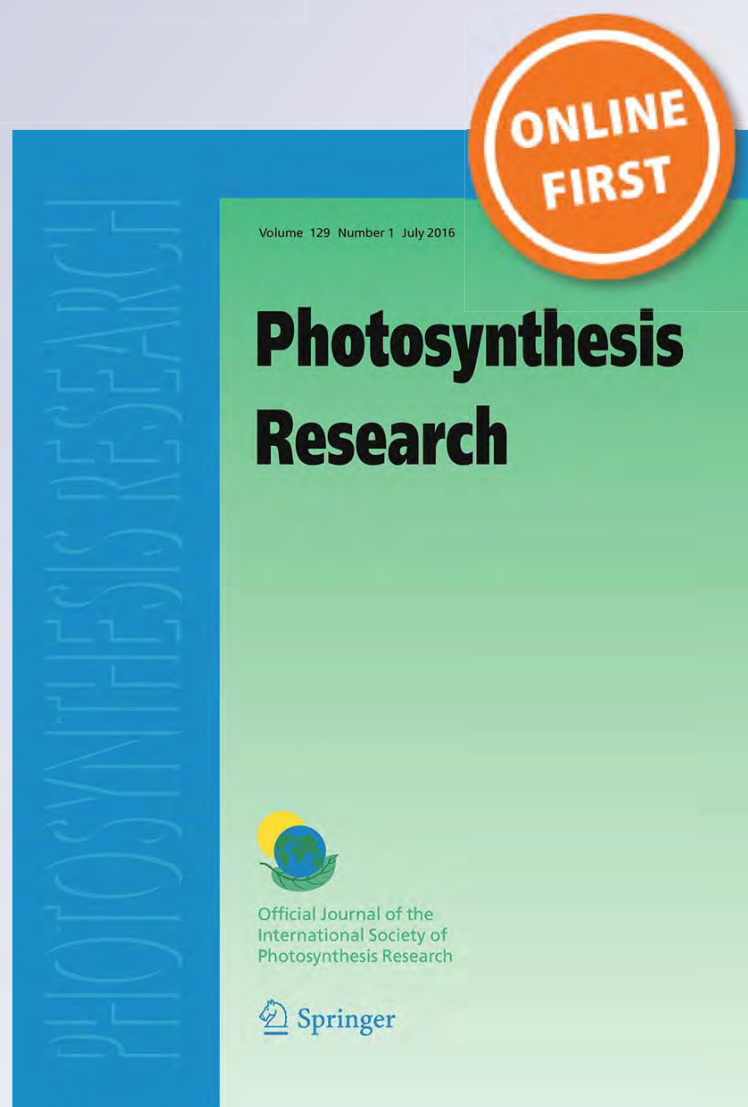
Kinetics of NADP⁺/NADPH reduction–oxidation catalyzed by the ferredoxin–NAD(P)⁺ reductase from the green sulfur bacterium Chlorobaculum tepidum

**Daisuke Seo, Masaharu Kitashima,
Takeshi Sakurai & Kazuhito Inoue**

Photosynthesis Research
Official Journal of the International
Society of Photosynthesis Research

ISSN 0166-8595

Photosynth Res
DOI 10.1007/s11120-016-0285-3



Your article is protected by copyright and all rights are held exclusively by Springer Science +Business Media Dordrecht. This e-offprint is for personal use only and shall not be self-archived in electronic repositories. If you wish to self-archive your article, please use the accepted manuscript version for posting on your own website. You may further deposit the accepted manuscript version in any repository, provided it is only made publicly available 12 months after official publication or later and provided acknowledgement is given to the original source of publication and a link is inserted to the published article on Springer's website. The link must be accompanied by the following text: "The final publication is available at link.springer.com".



Kinetics of NADP⁺/NADPH reduction–oxidation catalyzed by the ferredoxin-NAD(P)⁺ reductase from the green sulfur bacterium *Chlorobaculum tepidum*

Daisuke Seo¹ · Masaharu Kitashima^{2,3} · Takeshi Sakurai¹ · Kazuhito Inoue^{2,3}Received: 1 February 2016 / Accepted: 13 June 2016
© Springer Science+Business Media Dordrecht 2016

Abstract Ferredoxin-NAD(P)⁺ oxidoreductase (FNR, [EC 1.18.1.2], [EC 1.18.1.3]) from the green sulfur bacterium *Chlorobaculum tepidum* (CtFNR) is a homodimeric flavo-protein with significant structural homology to bacterial NADPH-thioredoxin reductases. CtFNR homologs have been found in many bacteria, but only in green sulfur bacteria among photoautotrophs. In this work, we examined the reactions of CtFNR with NADP⁺, NADPH, and (4S-²H)-NADPD by stopped-flow spectrophotometry. Mixing CtFNR_{ox} with NADPH yielded a rapid decrease of the absorbance in flavin band I centered at 460 nm within 1 ms, and then the absorbance further decreased gradually. The magnitude of the decrease increased with increasing NADPH concentration, but even with ~50-fold molar excess NADPH, the absorbance change was only ~45 % of that expected for fully reduced protein. The absorbance in the charge transfer (CT) band centered around 600 nm increased rapidly within 1 ms, then slowly decreased to about 70 % of the maximum. When CtFNR_{red} was mixed with excess NADP⁺, the absorbance in the flavin band I increased to about 70 % of that of CtFNR_{ox} with an apparent rate of ~4 s⁻¹, whereas almost no absorption changes were observed in the CT band. Obtained data suggest that the reaction between CtFNR and NADP⁺/NADPH is reversible, in accordance with its physiological function.

Keywords Flavoenzyme · Adrenodoxin · Putidaredoxin · Stopped flow · Charge transfer complex · Kinetic isotope effect

Abbreviations

A	Absorbance
Ad	Adrenodoxin
AdR	Adrenodoxin reductase
Bs	<i>Bacillus subtilis</i>
Ct	<i>Chlorobaculum tepidum</i>
CT	Charge transfer
CTC	Charge transfer complex
Ec	<i>Escherichia coli</i>
FAD	Flavin adenine dinucleotide
Fd	Ferredoxin
FNR	Ferredoxin-NAD(P) ⁺ oxidoreductase
GR	Glutathione reductase
HEPES	2-[4-(2-hydroxyethyl)-1-piperazinyl]ethanesulfonic acid
NADPD	(4S- ² H)-reduced nicotinamide adenine dinucleotide phosphate
Pd	Putidaredoxin
PdR	Putidaredoxin reductase
TrxR	Bacterial NADPH-thioredoxin reductase
Ox	Oxidized
Red	Reduced

✉ Daisuke Seo
dseo@se.kanazawa-u.ac.jp

- ¹ Division of Material Science, Graduate School of Natural Science and Technology, Kanazawa University, Kakuma, Kanazawa, Ishikawa 920-1192, Japan
- ² Department of Biological Sciences, Kanagawa University, Tsuchiya, Hiratsuka, Kanagawa 259-1293, Japan
- ³ Research Institute for Integrated Science, Kanagawa University, Tsuchiya, Hiratsuka, Kanagawa 259-1293, Japan

Introduction

Ferredoxin-NAD(P)⁺ reductase ([EC 1.18.1.2], [1.18.1.3], FNR) is a member of the NAD(P)H-dependent oxidoreductases of the flavoprotein superfamily containing a noncovalently bound flavin adenine dinucleotide (FAD) or flavin mononucleotide (FMN) as a prosthetic group. FNR

can reversibly catalyze either one- and two-redox equivalent transfer with the small iron–sulfur protein ferredoxin (Fd) and $\text{NAD(P)}^+/\text{NAD(P)H}$, respectively, using the redox properties of the flavin prosthetic group. In the final step of the electron transport chain in photosynthesis, Fd and FNR mediate electron transfer from a type I photosynthetic reaction center to NAD(P)^+ (Knaff and Hirasawa 1991; Sétif 2001; Seo and Sakurai 2002). In nonphotosynthetic processes, Fd as well as small iron–sulfur proteins, adrenodoxin (Ad), and putidaredoxin (Pd) participate in electron transfer in reactions involved in synthesis of a wide range of cellular materials such as fatty acid desaturation (cytochrome P450), nitrite reduction, sulfite reduction, and *S*-adenosylmethionine radical-dependent reactions in DNA and coenzyme synthesis (Munro et al. 2007; Knaff and Hirasawa 1991; Bianchi et al. 1993; Wan and Jarrett 2002). In the latter processes, FNR, adrenodoxin reductase (AdR, [EC 1.18.1.6]), and putidaredoxin reductase (PdR, [EC 1.18.1.5]) catalyze the reduction of Fd, Ad, and Pd by NAD(P)H . Thus, the redox coupling of Fd–FNR– $\text{NAD(P)}^+/\text{NAD(P)H}$ constitutes a key process of a widespread redox network in living organisms. The physiological direction of the process is assumed to be related to the redox midpoint potentials of the reaction partner(s).

Each of FNR, AdR, and PdR has two nucleotide-binding domains, one for FAD/FMN and the other for $\text{NAD(P)}^+/\text{H}$ (Correll et al. 1993; Ziegler et al. 1999; Sevrioukova et al. 2004; Muraki et al. 2010; Medina and Gómez-Moreno 2004; Aliverti et al. 2008). This protein topology is typical of flavin-containing NAD(P)H -dependent oxidoreductases including disulfide reductases (Dym and Eisenberg 2001; Aliverti et al. 2008). Based on structural and phylogenetic information, FNRs, PdR, and AdR are classified into two major groups of the flavoprotein superfamily, namely, the plant-type and the glutathione reductase (GR)-type FNR superfamilies and further divided into several subgroups (Aliverti et al. 2008; Ceccarelli et al. 2004; Seo et al. 2004). Among FNRs, the bacterial NADPH -thioredoxin reductase-type (TrxR-type) FNR, a subgroup of the GR-type FNR superfamily, is unique in their homodimeric form with high structural homology to *Escherichia coli* TrxR (*Ec*TrxR) (Muraki et al. 2010; Komori et al. 2010; Waksman et al. 1994). TrxR-type FNR and its homologs have been found in bacteria and archaea, including green sulfur bacteria, Firmicutes, several α -proteobacteria including Rhodospirillaceae and the archaeal genus *Sulfolobus* (Seo et al. 2002, 2004, 2009; Yan et al. 2014; Mandai et al. 2009), but it was not found in eukaryotes (Kyoto Encyclopedia of Genes and Genomes, Kanehisa et al. 2016). Among members of the TrxR-type FNR subfamily, the protein from the photoautotrophic green sulfur bacterium *Chlorobaculum tepidum* (formerly *Chlorobium tepidum*; *Ct*FNR) has been isolated as a component required for NAD(P)^+ photoreduction (Seo and Sakurai 2002). *C.*

tepidum carries out nonoxygenic photosynthesis using various sulfur compounds as the electron sources (Ogawa et al. 2008; Sakurai et al. 2010) and has a type I photosynthetic reaction center that can reduce Fds directly (Kjær and Scheller 1996; Seo et al. 2001; Tsukatani et al. 2004). In vitro, purified *Ct*FNR can catalyze the reduction of NAD(P)^+ in the presence of the photosynthetic reaction center and Fd from *C. tepidum* (Seo and Sakurai 2002). The unique features of the green sulfur bacteria among phototrophs are that they use the reductive TCA cycle as the main carbon assimilation pathway (Buchanan and Arnon 1990; Tang and Blankenship 2010), which have been found among several bacterial groups (Hügler and Sievert 2011), and that FNR and Fds are phylogenetically unrelated to their counterparts in oxygenic photosynthetic organisms/organelles but related to those from several bacterial groups described above. These would provide useful information on the origin and evolution of photosynthesis.

Although the redox reaction catalyzed by FNR is theoretically reversible, it is generally accepted that under physiological conditions, the direction of the reaction is optimized to either NAD(P)^+ reduction in many photosynthetic organisms, or NAD(P)H oxidation in nonphotosynthetic organisms and tissues. Indeed, previous studies on the TrxR-type FNR from the heterotroph *Bacillus subtilis* (*Bs*FNR) revealed that *Bs*FNR preferentially oxidizes NADPH to reduce Fd from the same organism at a high rate ($\sim 50 \text{ s}^{-1}$), rather than reducing NADP^+ with electrons from the reduced Fd (Seo et al. 2004, 2014). Pre-steady state reaction analysis of *Bs*FNR with $\text{NADP}^+/\text{NADPH}$ revealed that the hydride transfer rate for NADPH oxidation direction is much larger than that of NADP^+ reduction direction (Seo et al. 2016). Therefore, research on *Ct*FNR is important because green sulfur bacteria constitute a unique group among photoautotrophic organisms in that they contain TrxR-type FNRs that support NAD(P)^+ photoreduction at a high rate (Seo and Sakurai 2002). Some differences between *Ct*FNR and other TrxR-type FNRs have been revealed from deduced amino acid sequences and crystal structures of TrxR-type FNRs, for example, the residue stacking on the *re*-face of the isoalloxazine ring moiety of the FAD prosthetic group is Phe337, and C-terminal extension region in *Ct*FNR is longer and richer in Lys and Glu residues (Fig. 1a, b) (Muraki et al. 2010; Komori et al. 2010). It is expected that comparative studies of *Ct*FNR with other members of the TrxR-type FNR family will provide valuable information on the structure–function relationships of this family and other flavin-containing NADPH -dependent oxidoreductases. In this work, we performed pre-steady state kinetic analyses of reactions of *Ct*FNR with NADP^+ and NADPH . Our studies confirmed that the reaction between *C. tepidum* FNR and $\text{NADP}^+/\text{NADPH}$ is reversible as often been reported among plant-type FNR from photosynthetic organisms.

Materials and methods

Preparation of *C. tepidum* FNR

CtFNR was expressed in *E. coli* cells as described in Muraki et al. (2008). Purification of the CtFNR was performed basically according to the methods used for BsFNR (Seo et al. 2014), except that precipitate obtained by the addition of ammonium sulfate between 35 and 80 %

saturation was used for purification in place of that obtained from 0 to 40 % saturation.

Stopped-flow spectrophotometry

Stopped-flow spectrophotometry was performed in a glove box under a nitrogen atmosphere containing hydrogen gas (ca. 5 %) to decrease the residual O₂ (<50 ppm) with a palladium catalyst as previously described (Seo et al.

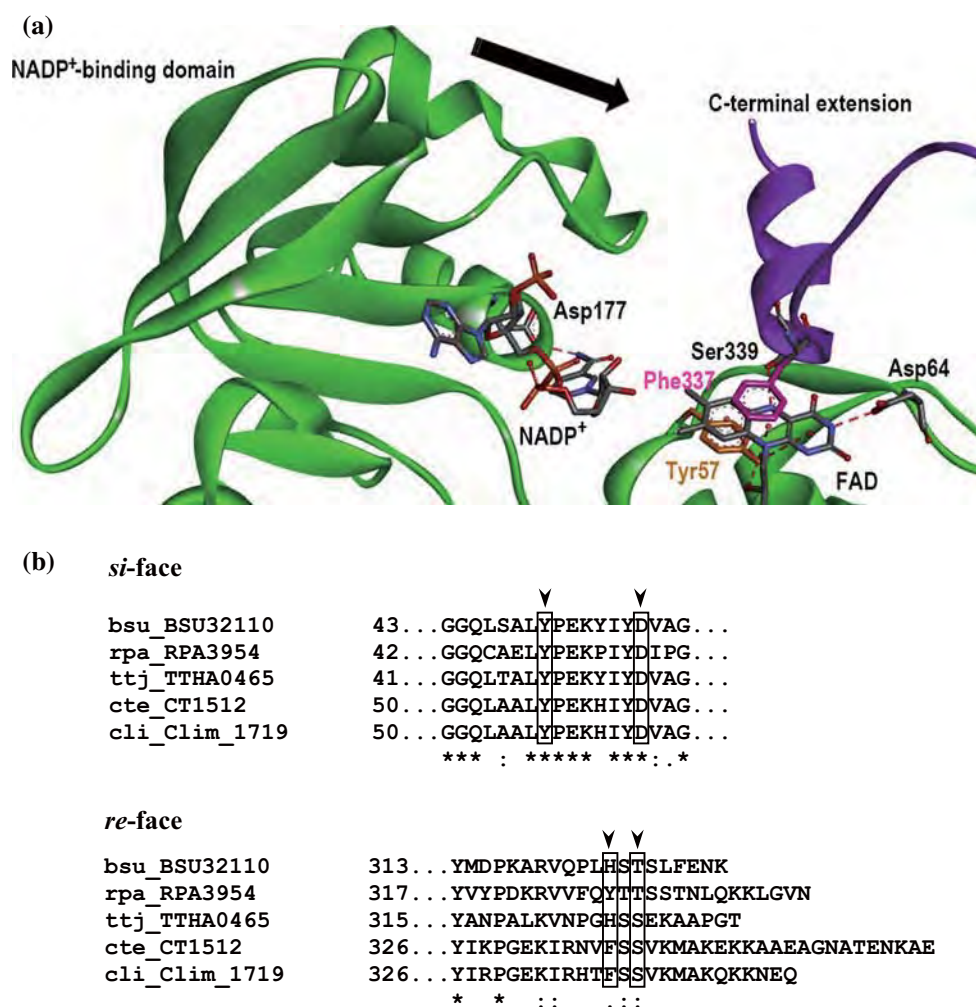


Fig. 1 **a** Close-up view around the isoalloxazine ring moiety of the FAD prosthetic group and NADP⁺-binding domain in the crystal structure of CtFNR (PDB code: 3AB1). Main chains of subunit A, which includes the FAD prosthetic group, and C-terminal region of subunit B (I327 to A348) in CtFNR are colored in green and purple, respectively. NADP⁺ is superimposed based on the superposition of NADPH-binding domain of BsFNR which binds NADP⁺ (Komori et al. 2010, PDB code 3LZW) against CtFNR on UCFS Chimera package (Pettersen et al. 2004). Side chains of Tyr57, Asp64, and Asp177 in subunit A, and Phe337 and Ser339 in subunit B are depicted as a ball and stick model. Hydrogen bondings between Tyr57 and O2' hydroxyl group of ribitol moiety of FAD, Asp64, and N3 of isoalloxazine ring portion, Asp177 and N7 of nicotinamide ring

portion of NADP⁺, and Ser339 and N5 of isoalloxazine ring portion of FAD are depicted as red dotted lines. Figure was prepared using Discovery Studio 4.0 Visualizer (Accelrys Inc., USA). **b** Partially aligned amino acid sequences around the si-face and re-face residues in TrxR-type FNRs. The number of the first amino acid residue in each row is indicated at the left. The positions of the Tyr57, Asp64, Phe337, and Ser339 residues in CtFNR sequence are indicated by arrows at upside. bsu_BSU32110: *Bacillus subtilis* subsp. *subtilis* str. 168 FNR, rpa_RPA3954: *Rhodospseudomonas palustris* CGA009 FNR, ttj_TTHA0465: *Thermus thermophilus* HB27 FNR, cte_CT1512: *Chlorobaculum tepidum* FNR, cli_Clim_1719: *Chlorobium limicola* DSM245 FNR

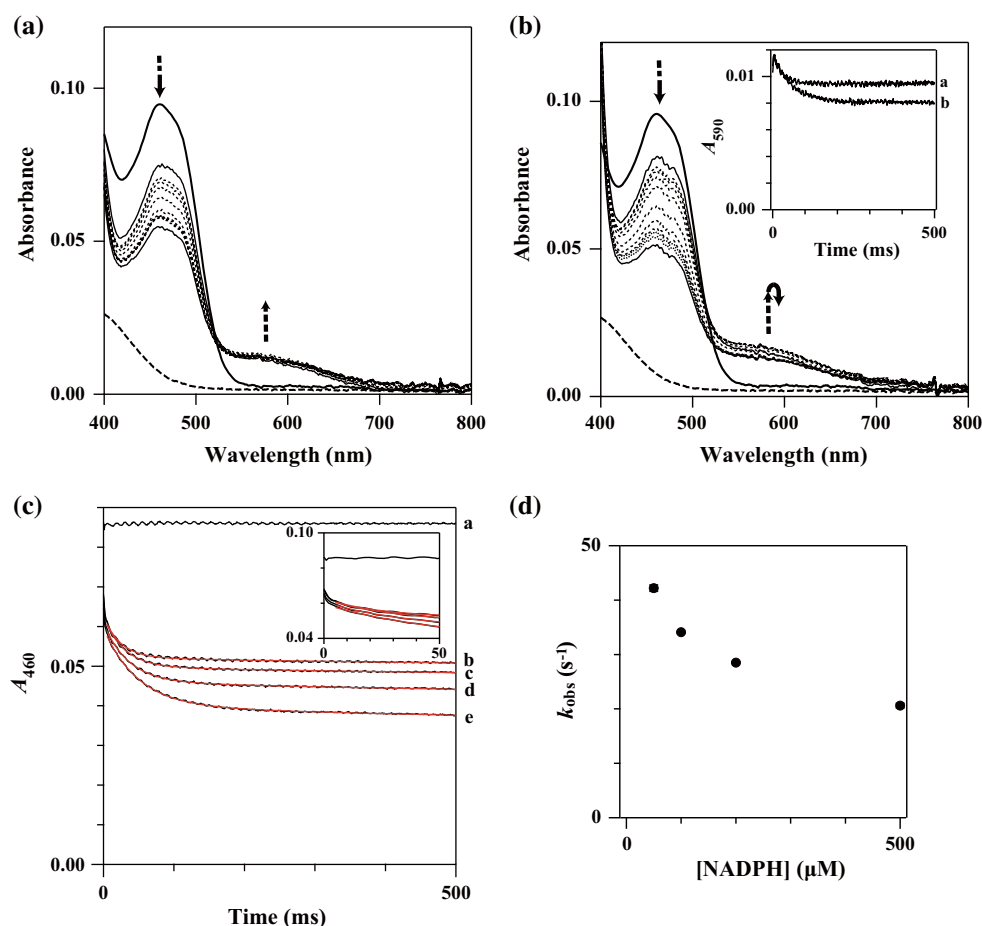


Fig. 2 **a, b** Transient spectra induced by mixing 9.0 μM CtFNR_{ox} with **a.** 100 μM or **b.** 500 μM NADPH. The reaction was performed in 20 mM HEPES–NaOH buffer (pH 7.0) at 10 $^{\circ}\text{C}$. The spectra at 0 and 2000 ms are shown as *thin continuous lines*. The spectra shown by *thin dotted lines* from the top to the bottom at 450 nm correspond to those at 2, 4, 9, 19, 49, 99, 199, and 499 ms, respectively. The spectrum of CtFNR_{ox} in the absence of NADPH is shown as a *thick continuous line* and that of $\text{CtFNR}_{\text{red}}$ (see Fig. 4) as a thick dashed line. *Arrows* indicate the directions of the absorbance change at the respective wavelengths; the *dashed parts of the arrows* indicate change that occurred within the first data acquisition period (1 ms). The inset in **b** shows the time course of A_{590} at **a.** 100 μM and

b. 500 μM NADPH. The data of the inset are the average of five measurements. **c** The time course of A_{460} after mixing CtFNR_{ox} with NADPH. The measurement conditions were the same as those in **a**, except the NADPH concentrations of **a:** 0 μM , **b:** 50 μM , **c:** 100 μM , **d:** 200 μM , and **e:** 500 μM . The data are an average of four to five measurements. The time course in the short-time range is shown in the inset. Double exponential decay curves based on the data for each NADPH concentration in the time range 5–500 ms are indicated by *continuous red lines*. **d** NADPH concentration dependency of k_{obs} of the slow phase. The observed rate constant at each NADPH concentration was obtained as shown in **c**. One standard deviation of each observed rate constant was less than 0.6 s^{-1}

2016). The reaction was initiated by mixing equal volumes of solutions in a single-mixing mode at 10 $^{\circ}\text{C}$. The dead time of the setup was estimated to be about 1 ms (Seo et al. 2016). Spectra were collected every 1 ms (Figs. 1–3, 4a–c) or 5 ms (Fig. 4e). All protein and substrate concentrations are given as the final concentrations after mixing unless otherwise stated.

Reduced CtFNR ($\text{CtFNR}_{\text{red}}$) was obtained using sodium dithionite and methyl viologen as the reductant and redox mediator, respectively, under anaerobic conditions in the glove box. Two milliliters of approximately 200 μM CtFNR solution in 20 mM HEPES–NaOH buffer (pH 7.0) were reduced by the addition of an excess of sodium

dithionite (0.4 mg/ml final concentration) in the presence of 10 μM methyl viologen. After a few minutes of incubation at 4 $^{\circ}\text{C}$, excess dithionite and methyl viologen were removed by size exclusion chromatography (Bio-Gel P-4 gel, Bio-Rad Laboratories, USA) pre-equilibrated with 20 mM HEPES–NaOH buffer (pH 7.0) containing 0.32 $\mu\text{g}/\text{ml}$ sodium dithionite in the glove box. The concentration of CtFNR in the solution was estimated from the absorbance of air-reoxidized CtFNR .

A deuterated form of NADPH, (4*S*- ^2H)-NADPD (referred to hereafter as NADPD) was prepared according to published methods (Viola et al. 1979, Ottolina et al. 1989, Pollock et al. 2001) as previously described (Seo et al.

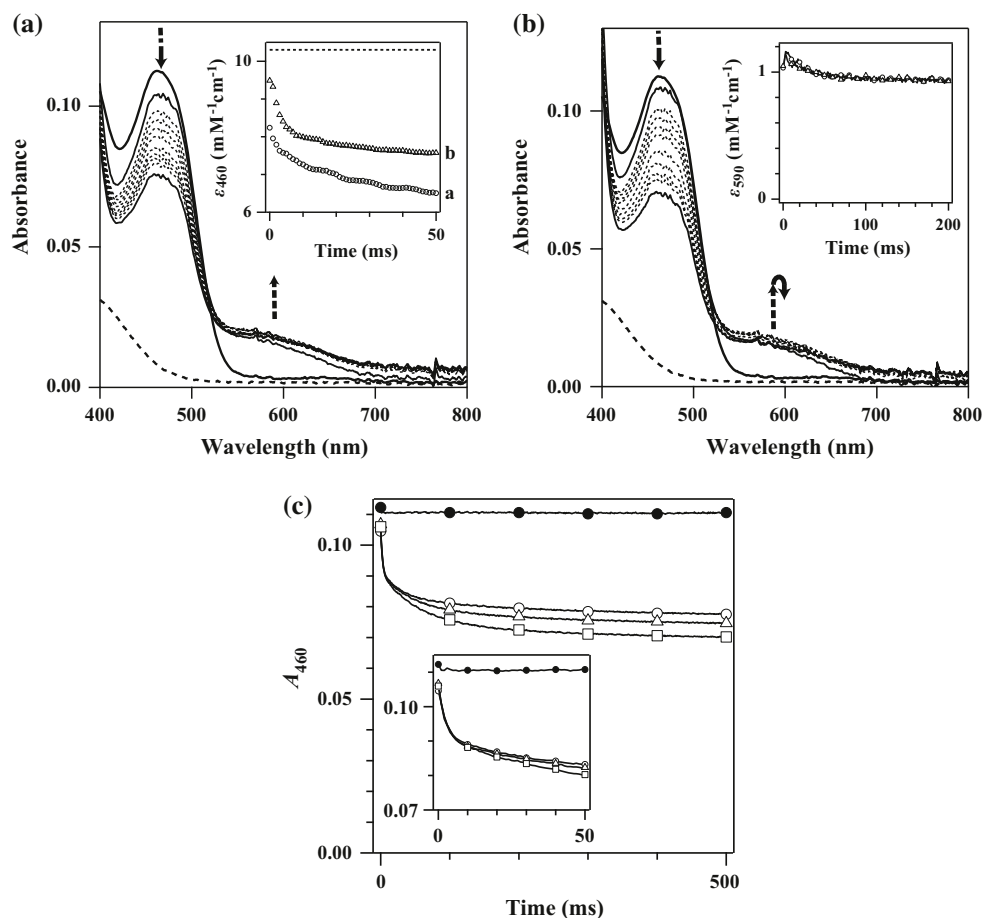
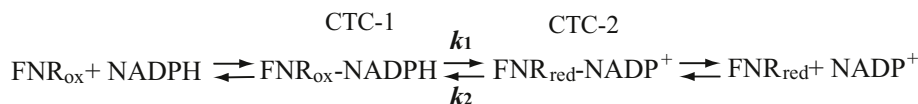


Fig. 3 **a, b** Transient spectra induced by mixing 11 μ M $CtFNR_{ox}$ with **a.** 100 μ M or **b.** 500 μ M NADPH. The reaction was performed in 20 mM HEPES–NaOH buffer (pH 7.0) at 10 °C. The spectra at 0 and 1999 ms are shown as *thin continuous lines*. The spectra shown by *thin dotted lines* from the top to the bottom at 450 nm correspond to those at 2, 4, 9, 19, 49, 99, 199, and 499 ms, respectively. The spectra of 11 μ M $CtFNR_{ox}$ in the absence of NADPH and $CtFNR_{red}$ in 20 mM HEPES–NaOH buffer (pH 7.0) are shown as a *thick continuous line* and a *thick dashed line*, respectively. *Arrows* indicate the directions of change in absorbance at the respective wavelengths; the *dashed parts of arrows* indicate change that occurred within the

first acquisition period (1 ms). The insets in **a, b** show time courses of ϵ_{460} (**a**) and ϵ_{590} (**b**) after mixing $CtFNR_{ox}$ with 100 μ M NADPH (*open circle*) and NADPH (*open triangle*) shown in Fig. 2a and **a**, respectively. The absorbance was normalized by $CtFNR$ concentration. The *dotted line* in the inset **a** represents the absorption of $CtFNR_{ox}$. **c** The time course of A_{460} after mixing $CtFNR_{ox}$ with NADPH. The measurement conditions were the same as those in **a**, except the NADPH concentrations of 0 μ M (*closed circle*), 100 μ M (*open circle*), 200 μ M (*open triangle*), and 500 μ M (*open square*). The data are an average of four to five measurements. The time course in the short-time range is shown in the *inset*

Scheme 1



2016). NADPH and NADP⁺ were purchased from Oriental Yeast Co., Ltd.

The values of A_{460} , A_{590} , ϵ_{460} , and ϵ_{590} in Figs. 2b–c, 3a–c and 4c, e were obtained by subtracting A_{800} to compensate for signal drift.

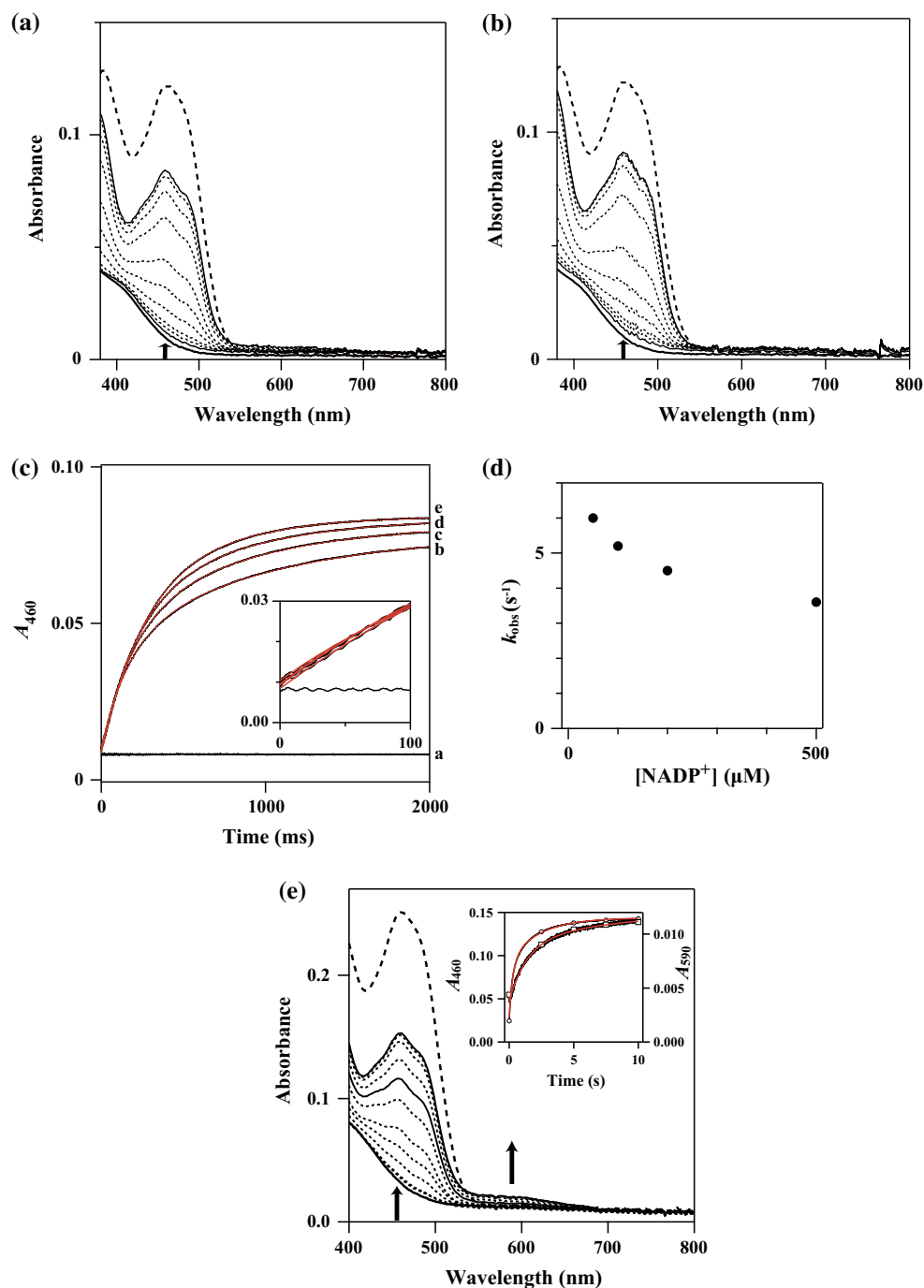
Kinetic data analysis

Data collection and basic arithmetic operations on the transient spectra obtained from stopped-flow experiments were

performed using Unispec (ver. 2.51, Unisoku Co., Ltd.) and Excel (ver. 14 and 15, Microsoft Corporation, Redmond, WA, USA) software. Curve fitting to the transient absorptions at a single wavelength was performed using Igor Pro ver. 6.3 software (Wavemetrics, Portland, OR, USA).

Miscellaneous methods

UV–Vis spectra were measured using a double beam spectrophotometer (UV-560, JASCO, Japan). Protein and



substrate concentrations were determined from the extinction coefficients: $CtFNR_{ox}$, $\epsilon_{466} = 10.3 \text{ mM}^{-1} \text{ cm}^{-1}$ (Seo and Sakurai 2002), and NADPH and NADPD, $\epsilon_{340} = 6.2 \text{ mM}^{-1} \text{ cm}^{-1}$. $NADP^+$ concentration was determined in NADPH form using glucose-6-phosphate dehydrogenase and excess amount of glucose-6-phosphate.

Results

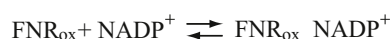
Reduction of $CtFNR_{ox}$ by NADPH

Reduction/oxidation reactions catalyzed by NAD(P)H-dependent flavoproteins are generally accompanied by the

Fig. 4 a, b Transient spectra induced by mixing chemically reduced 12 μM $CtFNR$ with *a.* 100 μM and *b.* 500 μM NADP^+ . The reaction was performed in 20 mM HEPES–NaOH buffer (pH 7.0) at 10 $^\circ\text{C}$. The spectra of 12 μM of $CtFNR_{\text{ox}}$ and chemically reduced $CtFNR_{\text{red}}$ in 20 mM HEPES–NaOH buffer (pH 7.0) are represented by *thick dashed* and *thick continuous lines*, respectively. Spectra for 0 and 3999 ms are indicated by *thin continuous lines*, and for 9, 19, 49, 99, 199, 499, 999, and 1999 ms, respectively, by *thin dotted lines* from the bottom to the top at 450 nm. *Arrows* indicate the direction of change in absorbance. **c** The time course of A_{460} after mixing $CtFNR_{\text{red}}$ with NADP^+ . The measurement conditions were the same as those in **a**, except the NADP^+ concentrations of *a:* 0 μM , *b:* 50 μM , *c:* 100 μM , *d:* 200 μM , and *e:* 500 μM . The data are an average of four to five measurements. The time course in the short-time range is shown in the inset. Double exponential decay curves based on the data for each NADP^+ concentration are indicated by *continuous red lines*. **d** NADP^+ concentration dependency of the observed rate of the faster phase. The observed rate constant at each NADP^+ concentration was obtained as shown in **c**. One standard deviation of each observed rate constant was less than 0.2 s^{-1} . **e** Transient spectra induced by mixing chemically reduced 24 μM $CtFNR$ with 25 μM NADP^+ . The reaction was performed in 20 mM HEPES–NaOH buffer (pH 7.0) at 10 $^\circ\text{C}$. The spectra of 24 μM of $CtFNR_{\text{ox}}$ and chemically reduced $CtFNR_{\text{red}}$ in 20 mM HEPES–NaOH buffer (pH 7.0) are represented by *thick dashed* and *thick continuous lines*, respectively. Spectra for 0 ms, 1, and 20 s are indicated by *thin continuous lines*, and for 9, 19, 49, 99, 199, 499 ms, 2, 5, and 10 s, respectively, by *thin dotted lines* from the bottom to the top at 450 nm. *Arrows* indicate the direction of change in absorbance. Inset of **e** represents the time course of A_{460} (*circle*) and A_{590} (*square*). The data are average of four measurements. Double exponential decay curves based on the data for both wavelengths are indicated by *continuous red lines*

formation of charge transfer complexes (CTCs), namely, $\text{FNR}_{\text{ox}}\text{-NADPH}$ (CTC-1) and $\text{FNR}_{\text{red}}\text{-NADP}^+$ (CTC-2) before the hydride transfer step, which exhibit a charge transfer (CT) absorption band in the 500–800 nm region (Scheme 1; Massey et al. 1970; Blankenhorn 1975; Batie and Kamin 1984; Lennon and Williams 1997; Tejero et al. 2007).

The reaction after mixing 9 μM $CtFNR_{\text{ox}}$ with 50–500 μM NADPH was measured by stopped-flow spectrophotometry (Fig. 2). Mixing $CtFNR$ with NADPH resulted in a decrease in flavin absorption band I with a peak around 460 nm within 1 ms (at the end of dead time), and then the absorption of this band decreased gradually with time (Fig. 2a, b). The Δ absorbance of this band region contains at least three distinctive kinetic components, namely, the fast, slow, and very slow phases (Fig. 2c). The fast phase observed as a rapid drop in 0–5 ms was too fast to estimate the rate constant. Δ absorbance of this phase was almost independent of the NADPH concentrations used (50–500 μM , inset of Fig. 2c). A_{460} in 5–500 ms time region can be approximated by a two-step reaction model (Fig. 2c, red continuous lines). Δ absorbance of the slow phase observed as a decay component in 5–200 ms time region increased with increasing NADPH concentration,



Scheme 2

and its observed rate decreased with increasing NADPH concentration (Fig. 2d). k_{obs} of the very slow phase was uncertain as the slight absorbance change seemed to continue beyond the measurement time scale. Although an increase in NADPH concentration decreased the total Δ absorbance of the flavin absorption band I (Fig. 2a, b), the absorbance change after 499 ms was only $\sim 45\%$ of that expected for fully reduced protein even with 500 μM NADPH (Fig. 2b).

The absorbance around 600 nm rapidly increased within 1 ms and reached its maximum intensity by 5 ms (Fig. 2a, b). The spectroscopic and kinetic properties of this absorption band centered at 600 nm are typical of the formation of CTCs as reported in stopped-flow works on $BsFNR$, plant-type $FNRs$, and $EcTrxR$ (Seo et al. 2016; Massey et al. 1970; Batie and Kamin 1984; Tejero et al. 2007; Lennon and Williams 1997). Subsequently, the absorption intensity of this CT absorption band decreased with time (Fig. 2a, b), but even with 500 μM NADPH , about 70 % of the maximum absorption intensity remained after 2 s (Fig. 2b). No significant peak shift of the CT absorption band was observed within 2 s during $CtFNR_{\text{ox}}$ reduction by NADPH (Fig. 2a, b). An increase in NADPH concentration did not significantly affect the maximum absorption intensity of the CT band, but Δ absorbance of the decay increased with increasing NADPH concentration (inset of Fig. 2b).

Reduction of $CtFNR_{\text{ox}}$ by NADPD

We studied the primary kinetic isotope effect by measuring the reactions mixing 11 μM $CtFNR_{\text{ox}}$ with 100 (Fig. 3a), 200, and 500 μM (Fig. 3b) NADPD . Mixing $CtFNR_{\text{ox}}$ with NADPD resulted in a rapid drop in the flavin absorption band I within 1 ms (Fig. 3a, b), but the Δ absorbance of the drop after 1 ms was much smaller than that with NADPH (Fig. 2a, b), and the subsequent absorption changes in 0–10 ms were slower than those with NADPH . These results indicated that deuterium substitution significantly affected the kinetics of the fast phase in the reduction of $CtFNR_{\text{ox}}$ (inset of Fig. 3a). The k_{obs} of the fast phase in the reaction with NADPD was nearly independent of NADPD concentration; its values were 372 ± 12 , 434 ± 11 , and $391 \pm 11 \text{ s}^{-1}$ at 100, 200, and 500 μM NADPD , respectively (inset of Fig. 3c). These values contain large errors as they are near the upper limit of the detection of the equipment. Kinetic analyses of the absorbance changes in time region 10–1000 ms provided similar rate constant

values for the slow phase in the reaction with NADPH ($36 \pm 8 \text{ s}^{-1}$, $22.3 \pm 0.4 \text{ s}^{-1}$, and $19.1 \pm 0.3 \text{ s}^{-1}$ at 100, 200, and 500 μM NADPD, respectively), which also decreased with increasing NADPD concentration.

The absorption in the CT band region increased rapidly (within 1 ms) and reached its maximum within 5 ms (Fig. 3a, b). Although the reduction of significant amount of FAD prosthetic group occurred in 1–10 ms time period (Fig. 3c), the peak wavelength and intensity of CT band were nearly stable (Fig. 3a, b). Increased NADPD concentration did not significantly affect the maximum intensity of the CT band absorption (Fig. 3a, b). Subsequently, a slight decrease in the absorbance occurred (by 100 ms) to a similar extent as was observed in the reaction with NADPH (inset of Fig. 3b). These results, almost the same as those with NADPH, indicate that the formation of CTC-1 was not affected significantly by the deuterium substitution.

Oxidation of *CtFNR*_{red} by NADP^+

*CtFNR*_{red} was prepared with dithionite in the presence of methyl viologen followed by the removal of the latter by size exclusion chromatography. The spectrum of the reduced *CtFNR* thus prepared is shown as the thick continuous line in Fig. 4a, b. Mixing *CtFNR*_{red} (12 μM) with NADP^+ resulted in a very slow increase in the flavin absorption band I (Fig. 4a, b), indicating that *CtFNR*_{red} oxidation by NADP^+ was very slow. A_{460} in 0–2 s time region can be approximated by a two-step reaction model (Fig. 4c). The k_{obs} of the faster component decreased with increasing NADP^+ concentration (Fig. 4d). The total absorption changes at near equilibrium (i.e., at 2 s) showed a significant dependency on NADP^+ concentration in the range 100–500 μM (Fig. 4a, b). From ΔA_{460} at 2 s, the oxidation level of *CtFNR* was estimated to be about 70 % (thick broken line in Fig. 4a, b).

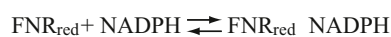
In contrast to the reduction of *CtFNR*_{ox} by NADPH/NADPD (Figs. 2 and 3), no significant absorption change was observed in the CT absorption band region (550–800 nm) during the reaction of *CtFNR*_{red} with NADP^+ in the NADP^+ concentration range 100–500 μM (Fig. 4a, b).

As the formation of *CtFNR*_{ox}- NADP^+ complex (Scheme 2) can decrease the amounts of CTCs at the equilibrium when NADP^+ is excess (Batie and Kamin 1986; Seo et al. 2016), the reaction mixing *CtFNR*_{red} (24 μM) with near equimolar NADP^+ (25 μM) was measured (Fig. 4e). Obtained transient spectra exhibited a gradual increase in the CT band absorption with time after

1000 ms following accumulation of oxidized *CtFNR* species. A_{460} predicted that the reaction was approximated by a two-step reaction model with similar k_{obs} in excess NADPH ($3.40 \pm 0.02 \text{ s}^{-1}$ and $0.426 \pm 0.001 \text{ s}^{-1}$) (inset of Fig. 4e). The change of A_{590} can be approximated by two-step reaction model with k_{obs} of $0.75 \pm 0.01 \text{ s}^{-1}$ and $0.123 \pm 0.002 \text{ s}^{-1}$ (inset of Fig. 4e).

Discussion

Previous pre-steady state kinetic studies on flavins and other types of flavin-dependent NAD(P)H oxidoreductases revealed that mixing with NADPH yielded formations of CTC-1 ($\text{FAD}_{\text{ox}}\text{-NADPH}$) and CTC-2 ($\text{FAD}_{\text{red}}\text{-NADP}^+$) with the appearance of CT absorption bands centered at 550–750 nm (Massey et al. 1970; Blankenhorn 1975; Lennon and Williams Jr 1997; Tejero et al. 2007). The pre-steady state kinetic study of TrxR-type *BsFNR* catalyzing reaction with NADP^+ /NADPH revealed that formations of both CTC-1 and CTC-2 exhibited the appearance of CT absorption bands centered at approximately 600 nm (Seo et al. 2016). In the NADPH oxidation reaction by *CtFNR*_{ox}, the CT band centered at approximately 600 nm appeared within the experimental dead time. Its maximum intensity was not significantly affected by the NADPH concentration, indicating a formation of Michaelis complex ($\text{NADPH-FNR}_{\text{ox}}$, MC-1) occurred before the formation of CTC-1 as frequently reported among flavin-containing NAD(P)H-dependent dehydrogenases (Lennon and Williams Jr 1997; Tejero et al. 2007), and 100 μM NADPH gave near saturation (Seo et al. 2016). After the rapid formation of the CTC-1, reduction of the flavin prosthetic group occurred (Figs. 2a, b and 3a, b). In the reaction, the apparent rate of the fast phase was affected by deuterium substitution (inset of Fig. 3a), indicating that the rate-limiting step in the NADPH oxidation reaction by *CtFNR*_{ox} is the hydride transfer during CTC-2 formation (Scheme 1) in the experimental conditions used. In the course of the reaction, *CtFNR*_{ox} reduction proceeded significantly, while the CT absorption band intensity (A_{590}) did not change in a corresponding amount. Based on Scheme 1, if CTC-2 has no absorption in the CT band region, a decrease in a CTC-1 amount reduces the absorbance in the CT band region. Thus obtained results could be explained by the presence of a CT absorption band centered at similar wavelength for CTC-2 as observed in *BsFNR* works (Seo et al. 2016). In the NADPH oxidation reaction by *CtFNR*_{ox}, k_{obs} and ΔA_{460} of the slower phase affected by the NADPH concentration (Fig. 2c, d). As the NADPH concentration -dependent second-order reaction step in Scheme 1 (i.e., formation of MC-1) was rapid, such the dependency could be explained by the formation of



Scheme 3 .

NADPH-*CtFNR*_{red} complex (Scheme 3) (Batie and Kamin 1986).

For NADPH oxidation by *CtFNR*_{ox}, we could not determine the rate constants of the hydride transfer step in both direction (k_1 and k_2 in Scheme 1), because the fast phase was too rapid even at 50 μM NADPH (Fig. 2c). If we assume that *CtFNR*_{ox} and CTC-1 have a similar extinction coefficient at 460 nm (inset of Fig. 2a) and that the hydride transfer step is the rate determining, Scheme 1 can be approximated by the two-component reversible reaction model $\text{CTC-1} \rightleftharpoons \text{CTC-2}$, where the rates of the forward and reverse directions corresponds to the respective hydride transfer rates in Scheme 1. According to this approximation, the ratio of CTC-1:CTC-2 at equilibrium at low NADPH concentration (Fig. 1a) corresponds to the ratio of $k_1:k_2$. From the spectrum at 4 ms in Fig. 1a, we can estimate a CTC-1: CTC-2 ratio of 3:7, suggesting that k_2 is comparable to k_1 . This result is in contrast to that of *BsFNR* where the hydride transfer rate in NADPH oxidation direction was much larger than that of NADP⁺ reduction direction ($\sim 500 \text{ s}^{-1}$ and $<10 \text{ s}^{-1}$, respectively, (Seo et al. 2016)). Similar reversibility has been reported on plant-type FNRs from photosynthetic organisms (Sánchez-Azqueta et al. 2012; Tejero et al. 2007).

Generally, formations of CTCs are considered to lead the stacking of the two-ring system, the isoalloxazine ring, and the nicotinamide ring moieties of FAD and NAD(P)⁺/NAD(P)H, respectively, which enables efficient hydride transfer between C4 of nicotinamide ring portion of NAD(P)⁺/NAD(P)H and N5 of isoalloxazine ring portion of FAD in the reaction catalyzed by flavin-dependent NAD(P)H-oxidoreductases (Blankenhorn 1975; Tejero et al. 2007; Peregrina et al. 2010; Sánchez-Azqueta et al. 2014). The pre-steady state reaction analyses of WT and mutated plant-type *Anabaena* FNRs with NADP⁺/NADPH revealed a significant correlation between the absorbance of CT bands and hydride transfer rates (Peregrina et al. 2010). In present work, NADPH oxidation by *CtFNR*_{ox} with larger k_{obs} (Fig. 2) was accompanied by an appearance of a CT absorption band, whereas NADP⁺ reduction reaction with smaller k_{obs} did no obvious CT absorption band (Fig. 4). In the NADP⁺ reduction by *CtFNR*_{red}, as the slope of the initial increasing phase in A_{460} was not affected by the NADP⁺ concentrations used (Fig. 4c), it seemed that the rate of the complex formation with NADP⁺ was saturated with respect to NADP⁺ concentration. Accordingly, the rate-limiting step in NADP⁺ reduction by *CtFNR*_{red} would be present after the formation of *CtFNR*_{red}-NADP⁺ complex. If the process of NADP⁺ reduction by *CtFNR*_{red} occurred along the same conformations in NADPH oxidation by *CtFNR*_{ox}, i.e., kinetically reversible, the hydride transfer process in NADP⁺ reduction by *CtFNR*_{red} would be rapid the same as

in the NADPH oxidation by *CtFNR*_{ox} ($k_{\text{obs}} = k_1 + k_2$). According to this scenario, the transition of *CtFNR*_{red}-NADP⁺ complex to CTC-2 would be the rate-limiting and CTC-2 would not accumulate during the reaction, but the rapid formation of CTC-1 would give an absorption in CT band region in the NADP⁺ reduction by *CtFNR*_{red}. Obtained results, however, provided almost no CT absorption bands during the NADP⁺ reduction by *CtFNR*_{red}. One can consider that rapid and strong *CtFNR*_{ox}-NADP⁺ complex formation will decrease the absorbance of CT band region (Scheme 2). But mixing *CtFNR*_{red} with near equimolar of NADP⁺ exhibited a faster formation of *CtFNR*_{ox} followed by a slower formation of CTCs (Fig. 3e). These results seem to indicate a difference in the conformation of CTCs between in the NADP⁺ reduction by *CtFNR*_{red} and in the NADPH oxidation by *CtFNR*_{ox}. In the NADPH oxidation reaction, the nicotinamide ring reacts with the oxidized isoalloxazine ring, whereas in the NADP⁺ reduction reaction, the nicotinamide ring reacts with the reduced isoalloxazine ring. The crystal structure analysis of *BsFNR* with NADP⁺ revealed that the nicotinamide ring portion of NADP⁺ attached on the surface of the NADPH-binding domain with substantial electron density and within a hydrogen bonding distance to Asp177 (Fig. 1a). In this conformation, S⁻²H at C4 of the nicotinamide moiety of NADPD can face to the N5 of isoalloxazine ring portion by the domain motion, which is consistent with the results of the primarily kinetic isotope effect (Seo et al. 2016). Similarly, structurally related *EcTrxR* also provided a substantial isotope effect in steady state assay with 4S-²H NADPD (Williams 1995). The crystal structure analyses of *EcTrxR* revealed that the isoalloxazine ring portion of the reduced FAD hydroquinone was in a bent conformation, whereas that in the oxidized FAD quinone was in a planar one (Lennon et al. 1999), suggesting that a conformational change of the isoalloxazine ring portion of FAD prosthetic group can occur during the redox transition. In the crystal structure of *BsFNR*_{ox} and *CtFNR*_{ox}, the isoalloxazine ring portion was in a planer conformation (Komori et al. 2010; Muraki et al. 2010), but we have no structural information about the conformation of isoalloxazine ring portion in the reduced TrxR-type FNR. On the UV-vis spectra, *BsFNR*_{red} had an apparent small absorption band with a peak at 430 nm, which red shifted in the presence of NADP⁺ (Seo et al. 2016), whereas in this work, *CtFNR*_{red} had only a small shoulder at 410 nm (Fig. 4a, b). According to the previous reports discussing the relation between the spectroscopic properties and the conformation of the isoalloxazine ring portion of the reduced flavin hydroquinone (Ghisla et al. 1974; Blankenhorn 1975), it is likely that the isoalloxazine ring moiety in *BsFNR*_{red} was in a more planer conformation, whereas that in *CtFNR*_{red} was in a bent one (Ghisla

et al. 1974). Actually *BsFNR* demonstrated the rapid formation of CTC-2 with an apparent CT absorption band in the NADP⁺ reduction reaction (Seo et al. 2016), indicating that the conformation of the isoalloxazine ring portion would affect the accessibility and/or distance of the nicotinamide ring portion to the isoalloxazine ring moiety. In addition, the positioning of the C-terminal extension region might play an important role during the reaction as this region hamper the stacking of the rings (Fig. 1a). Further works especially focused on the C-terminal region should be performed to reveal the mechanism of the redox reactions between TrxR-type FNRs and NADP⁺/H.

Redox equilibrium between NADP⁺/NADPH and *CtFNR* shows that *CtFNR* can catalyze NADP⁺/NADPH reduction/oxidation reversibly, which is in accordance with previous report (Seo and Sakurai 2002) and its physiological requirements. However, in our in vitro experiments in the absence of Fd, the rate of NADP⁺ reduction was rather slow compared to those by plant-type FNRs (Batie and Kamin 1984; Tejero et al. 2007) and steady state assay (Seo and Sakurai 2002). In the report by Batie and Kamin (1984), the rate of NADP⁺ reduction was enhanced by the presence of Fd, which led to the conclusion that ternary complex formation is involved in the reaction. The effects of Fd on the kinetics of *CtFNR* reactions remain to be investigated.

Acknowledgments We thank Dr. Hidehiro Sakurai for stimulating discussions. This work was supported in part by a grant-in-aid for Scientific Research on Innovative Areas (No. 24107004) and the Strategic Research Base Development Program for Private Universities from the Ministry of Education, Culture, Sports, Science and Technology (MEXT), Japan (to KI).

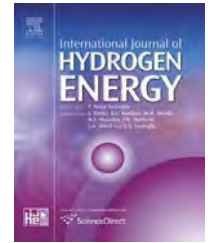
References

- Aliverti A, Pandini V, Pennati A, de Rosa M, Zanetti G (2008) Structural and functional diversity of ferredoxin-NADP⁺ reductases. *Arch Biochem Biophys* 474:283–291
- Batie CJ, Kamin H (1984) Ferredoxin:NADP⁺ oxidoreductase. Equilibria in binary and ternary complexes with NADP⁺ and ferredoxin. *J Biol Chem* 259:8832–8839
- Batie CJ, Kamin H (1986) Association of ferredoxin-NADP⁺ reductase with NADP(H) specificity and oxidation-reduction properties. *J Biol Chem* 261:11214–11223
- Bianchi V, Reichard P, Eliasson R, Pontis E, Krook M, Jornvall H, Haggard-Ljungquist E (1993) *Escherichia coli* ferredoxin NADP⁺ reductase: activation of *E. coli* anaerobic ribonucleotide reduction, cloning of the gene (*fpr*), and overexpression of the protein. *J Bacteriol* 175:1590–1595
- Blankenhorn G (1975) Flavin nicotinamide biscoenzymes: models for the interaction between NADH (NADPH) and flavin in flavoenzymes. Reaction rates and physicochemical properties of intermediate species. *Eur J Biochem* 50:351–356
- Buchanan BB, Arnon DI (1990) A reverse KREBS cycle in photosynthesis: consensus at last. *Photosyn Res* 24:47–53
- Ceccarelli EA, Arakaki AK, Cortez N, Carrillo N (2004) Functional plasticity and catalytic efficiency in plant and bacterial ferredoxin-NADP(H) reductases. *Biochim Biophys Acta* 1698:155–165
- Correll CC, Ludwig ML, Bruns CM, Karplus PA (1993) Structural prototypes for an extended family of flavoprotein reductases: comparison of phthalate dioxygenase reductase with ferredoxin reductase and ferredoxin. *Prot Sci* 2:2112–2133
- Dym O, Eisenberg D (2001) Sequence-structure analysis of FAD-containing proteins. *Prot Sci* 10:1712–1728
- Ghisla S, Massey V, Lhoste J-M, Mayhew SG (1974) Fluorescence and optical characteristics of reduced flavines and flavoproteins. *Biochemistry* 13:589–597
- Hügler M, Sievert SM (2011) Beyond the Calvin cycle: Autotrophic carbon fixation in the ocean. *Ann Rev Mar Sci* 3:261–289
- Kanehisa M, Sato Y, Kawashima M, Furumichi M, Tanabe M (2016) KEGG as a reference resource for gene and protein annotation. *Nuc Acids Res* 44(D1):D457–D462. doi:10.1093/nar/gkv1070
- Kjær B, Scheller HV (1996) An isolated reaction center complex from the green sulfur bacterium *Chlorobium vibrioforme* can photoreduce ferredoxin at high rates. *Photosyn Res* 47:33–39
- Knaff DB, Hirasawa M (1991) Ferredoxin-dependent chloroplast enzymes. *Biochim Biophys Acta* 1056:93–125
- Komori H, Seo D, Sakurai T, Higuchi Y (2010) Crystal structure analysis of *Bacillus subtilis* ferredoxin-NADP⁺ oxidoreductase and the structural basis for its substrate selectivity. *Prot Sci* 19:2279–2290
- Lennon BW, Williams CH Jr (1997) Reductive half-reaction of thioredoxin reductase from *Escherichia coli*. *Biochemistry* 36:9464–9477
- Lennon BW, Williams CH Jr, Ludwig ML (1999) Crystal structure of reduced thioredoxin reductase from *Escherichia coli*: structural flexibility in the isoalloxazine ring of the flavin adenine dinucleotide cofactor. *Prot Sci* 8:2366–2379
- Mandai T, Fujiwara S, Imaoka S (2009) A novel electron transport system for thermostable CYP175A1 from *Thermus thermophilus* HB27. *FEBS J* 276:2416–2429
- Massey V, Matthews RG, Foust GP, Howell LG, Williams CH Jr, Zanetti G, Ronchi S (1970) A new intermediate in TPNH-linked flavoproteins. In: Sund H (ed) *Pyridine Nucleotide-dependent Dehydrogenases*. Springer-Verlag, Berlin, pp 393–411
- Medina M, Gómez-Moreno C (2004) Interaction of ferredoxin-NADP⁺ reductase with its substrates: optimal interaction for efficient electron transfer. *Photosynth Res* 79:113–131
- Munro AW, Girvan HM, McLean KJ (2007) Cytochrome P450-redox partner fusion enzymes. *Biochim Biophys Acta* 1770:345–359
- Muraki N, Seo D, Shiba T, Sakurai T, Kurisu G (2008) Crystallization and preliminary X-ray studies of ferredoxin-NAD(P)⁺ reductase from *Chlorobium tepidum*. *Acta Crystallogr Sec F: Struct Biol Cryst Com* 64:186–189
- Muraki N, Seo D, Shiba T, Sakurai T, Kurisu G (2010) Asymmetric dimeric structure of ferredoxin-NAD(P)⁺ oxidoreductase from the green sulfur bacterium *Chlorobaculum tepidum*: implications for binding ferredoxin and NADP⁺. *J Mol Biol* 401:403–414
- Ogawa T, Furusawa T, Nomura R, Seo D, Hosoya-Matsuda N, Sakurai H, Inoue K (2008) SoxAX binding protein, a novel component of the thiosulfate-oxidizing multienzyme system in the green sulfur bacterium *Chlorobium tepidum*. *J Bacteriol* 190:6097–6110
- Ottolina G, Riva S, Carrea G, Danieli B, Buckmann AF (1989) Enzymatic synthesis of [4R-²H]NAD(P)H and [4S-²H]NAD(P)H and determination of the stereospecificity of 7 α - and 12 α -hydroxysteroid dehydrogenase. *Biochim Biophys Acta* 998:173–178
- Peregrina JR, Sánchez-Azqueta A, Herguedas B, Martínez-Júlvez M, Medina M (2010) Role of specific residues in coenzyme binding, charge-transfer complex formation, and catalysis in *Anabaena* ferredoxin NADP⁺-reductase. *Biochim Biophys Acta* 1797:1638–1646

- Pettersen EF, Goddard TD, Huang CC, Couch GS, Greenblatt DM, Meng EC, Ferrin TE (2004) UCSF Chimera—a visualization system for exploratory research and analysis. *J Comput Chem* 25:1605–1612
- Pollock VV, Barber MJ (2001) Kinetic and mechanistic properties of biotin sulfoxide reductase. *Biochemistry* 40:1430–1440
- Sakurai H, Ogawa T, Shiga M, Inoue K (2010) Inorganic sulfur oxidizing system in green sulfur bacteria. *Photosyn Res* 104:163–176
- Sánchez-Azqueta A, Musumeci MA, Martínez-Júlvez M, Ceccarelli EA, Medina M (2012) Structural backgrounds for the formation of a catalytically competent complex with NADP(H) during hydride transfer in ferredoxin-NADP⁺ reductases. *Biochim Biophys Acta* 1817:1063–1071
- Sánchez-Azqueta A, Catalano-Dupuy DL, López-Rivero A, Tondo ML, Orellano EG, Ceccarelli EA, Medina M (2014) Dynamics of the active site architecture in plant-type ferredoxin-NADP⁺ reductases catalytic complexes. *Biochim Biophys Acta* 1837:1730–1738
- Seo D, Sakurai H (2002) Purification and characterization of ferredoxin-NAD(P)⁺ reductase from the green sulfur bacterium *Chlorobium tepidum*. *Biochim Biophys Acta* 1597:123–132
- Seo D, Tomioka A, Kusumoto N, Kamo M, Enami I, Sakurai H (2001) Purification of ferredoxins and their reaction with purified reaction center complex from the green sulfur bacterium *Chlorobium tepidum*. *Biochim Biophys Acta* 1503:377–384
- Seo D, Kamino K, Inoue K, Sakurai H (2004) Purification and characterization of ferredoxin-NADP⁺ reductase encoded by *Bacillus subtilis yumC*. *Arch Microbiol* 182:80–89
- Seo D, Okabe S, Yanase M, Kataoka K, Sakurai T (2009) Studies of interaction of homo-dimeric ferredoxin-NAD(P)⁺ oxidoreductases of *Bacillus subtilis* and *Rhodospseudomonas palustris*, that are closely related to thioredoxin reductases in amino acid sequence, with ferredoxins and pyridine nucleotide coenzymes. *Biochim Biophys Acta* 1794:594–601
- Seo D, Asano T, Komori H, Sakurai T (2014) Role of the C-terminal extension stacked on the re-face of the isoalloxazine ring moiety of the flavin adenine dinucleotide prosthetic group in ferredoxin-NADP⁺ oxidoreductase from *Bacillus subtilis*. *Plant Physiol* 81:143–148
- Seo D, Soeta T, Sakurai H, Sétif P, Sakurai T (2016) Pre-steady-state kinetic studies of redox reactions catalysed by *Bacillus subtilis* ferredoxin-NADP⁺ oxidoreductase with NADP⁺/NADPH and ferredoxin. *Biochim Biophys Acta* 1857:678–687
- Sétif P (2001) Ferredoxin and flavodoxin reduction by photosystem I. *Biochim Biophys Acta* 1507:161–179
- Sevrioukova IF, Li H, Poulos TL (2004) Crystal structure of putidaredoxin reductase from *Pseudomonas putida*, the final structural component of the cytochrome P450cam monooxygenase. *J Mol Biol* 336:889–902
- Tang KH, Blankenship RE (2010) Both forward and reverse TCA cycles operate in green sulfur bacteria. *J Biol Chem* 285:35848–35854
- Tejero J, Peregrina JR, Martínez-Júlvez M, Gutiérrez A, Gómez-Moreno C, Scrutton NS, Medina M (2007) Catalytic mechanism of hydride transfer between NADP⁺/H and ferredoxin-NADP⁺ reductase from *Anabaena* PCC 7119. *Arch Biochem Biophys* 459:79–90
- Tsukatani Y, Miyamoto R, Itoh S, Oh-oka H (2004) Function of a PscD subunit in a homodimeric reaction center complex of the photosynthetic green sulfur bacterium *Chlorobium tepidum* studied by insertional gene inactivation: regulation of energy transfer and ferredoxin-mediated NADP⁺ reduction on the cytoplasmic side. *J Biol Chem* 279:51122–51130
- Viola RE, Cook PF, Cleland WW (1979) Stereoselective preparation of deuterated reduced nicotinamide adenine nucleotides and substrates by enzymatic synthesis. *Anal Biochem* 96:334–340
- Waksman G, Krishna TS, Williams CH Jr, Kuriyan J (1994) Crystal structure of *Escherichia coli* thioredoxin reductase refined at 2 Å resolution. Implications for a large conformational change during catalysis. *J Mol Biol* 236:800–816
- Wan JT, Jarrett JT (2002) Electron acceptor specificity of ferredoxin (flavodoxin):NADP⁺ oxidoreductase from *Escherichia coli*. *Arch Biochem Biophys* 406:116–126
- Williams CH Jr (1995) Mechanism and structure of thioredoxin reductase from *Escherichia coli*. *FASEB J* 9:1267–1276
- Yan Z, Nam YW, Fushinobu S, Wakagi T (2014) *Sulfolobus tokodaii* ST2133 is characterized as a thioredoxin reductase-like ferredoxin:NADP⁺ oxidoreductase. *Extremophiles* 18:99–110
- Ziegler GA, Vornrhein C, Hanukoglu I, Schulz GE (1999) The structure of adrenodoxin reductase of mitochondrial P450 systems: electron transfer for steroid biosynthesis. *J Mol Biol* 289:981–990

Available online at www.sciencedirect.com

ScienceDirect

journal homepage: www.elsevier.com/locate/he

Effect of growth conditions on advantages of *hup*⁻ strain for H₂ photoproduction by *Rubrivivax gelatinosus*

Tatyana Laurinavichene^a, Masaharu Kitashima^b,
Kenji V.P. Nagashima^b, Takeshi Sato^b, Hidehiro Sakurai^b,
Kazuhito Inoue^b, Anatoly Tsygankov^{a,*}

^a Institute of Basic Biological Problems, RAS, Pushchino, Moscow Region, 142290, Russia

^b Research Institute for Photobiological Hydrogen Production, Kanagawa University, Hiratsuka, Japan

ARTICLE INFO

Article history:

Received 8 November 2016

Received in revised form

15 December 2016

Accepted 18 December 2016

Available online xxx

Keywords:

H₂ production

Purple bacteria

hup⁻

Microaerobic conditions

ABSTRACT

H₂ photoproduction by growing cultures of *hup*⁻ mutant and parental strain RL2 of *Rubrivivax gelatinosus* was compared. We checked the influence of different substrates, presence of air and N₂, culture shaking, inoculum concentrations. At low inoculum concentration, *hup*⁻ strain demonstrated significant advantage over the parental strain in microaerobic conditions, while under N₂-Ar atmosphere it was lower and vanished in anaerobic conditions (Ar only). This advantage was evident when using substrates with low degree of reduction (malate and succinate). Culture shaking under microaerobic conditions and in presence of N₂ completely prevented H₂ production by both strains. The high inoculum concentration inhibited H₂ production under microaerobic conditions and in presence of N₂, unlike to anaerobic conditions. With inoculum concentration increase, H₂ production decreased not gradually but stepwise which means some metabolic shift. H₂ production by *hup*⁻ strain seems to be more tolerant to air traces than by parental strain.

© 2016 Published by Elsevier Ltd on behalf of Hydrogen Energy Publications LLC.

Introduction

Molecular hydrogen is a valuable alternative source of energy since it can be generated from water, and water is the end product of its practical utilization. Several technologies for H₂ production including photobiological ones are under consideration. Purple nonsulfur bacteria (PNSB) can photoproduce H₂ at high rates via nitrogenase reaction. However, these rates are still insufficient for practical application [1,2]. There are several ways to address this problem based mainly on genetic

modification of bacteria: using strains with reduced pigment content, strains incapable of Calvin cycle flux, insensitive to ammonium, incapable of storage compound synthesis [3–8]. One of the ways explored is using mutants with deletion of uptake hydrogenases (Hup) or even double mutants that lack both uptake hydrogenase and poly-hydroxybutyrate (PHB) synthase. Hup hydrogenase re-directs electrons from H₂ to bacterial metabolism while PHB synthesis is a process competing with H₂ production for electrons. In *hup*⁻ strains of *Rhodobacter capsulatus*, *Rhodobacter sphaeroides*, *Rhodospseudomonas palustris* an increase in total H₂ production varied

* Corresponding author. Fax +7 4967 330532.

E-mail address: ttt-00@mail.ru (A. Tsygankov).

<http://dx.doi.org/10.1016/j.ijhydene.2016.12.074>

0360-3199/© 2016 Published by Elsevier Ltd on behalf of Hydrogen Energy Publications LLC.

from 0 to above 100% [5,9–15]. The reasons of variability are not clear. The *hup*[−] mutant of *R. capsulatus* was successfully applied in large-scale photobioreactors in outdoor conditions [16].

On the basis of general consideration one can suggest that the difference in H₂ production rate, yield and total accumulation between parental and *hup*[−] strains might depend on a number of factors. For example, the degree of reduction of substrate can define the need to recycle H₂. Actually, the demonstration of *hup*[−] strain advantages was mainly done using more oxidized substrate, malate [5,10,11]. The comparison of different substrates for H₂ production by both strains was reported by Wu [15], but no correlation could be found between reduction degree and H₂ production rate. On the contrary, Rey [10] showed that the difference between H₂ production by *hup*[−] and *hup*⁺ strains was huge when using substrates with higher O/H ratio (malate and succinate vs acetate).

Another factor to take into account is the substrate concentration at given N-source concentration. The lower the substrate concentration, the higher the relative substrate portion appears in biomass and lower relative portion goes to H₂ production. As far as H₂ recycling resulted in somewhat increase in biomass production [5,11,17,18], it can be reasonably expected that H₂ production in *hup*[−] strain would increase substantially as compared to minute H₂ production in parental strain. To illustrate this, the impressive improvement of H₂ production in *hup*[−] strain of *R. palustris* was achieved by Rey [10]. In this work, the increase amounted to even 5–100-fold when using succinate or malate. However, it should be noted that substrate concentrations were as low as 10 mM. Unfortunately, this concentration is too low if we take into consideration the large-scale process of intensive H₂ production. H₂ production by two strains at different substrate concentrations was not compared yet.

We hypothesize that H₂ recycling and consequently the negative role of Hup hydrogenase in H₂ production should be higher under microaerobic conditions, at which point an advantage of *hup*[−] strain in H₂ production should increase. In addition, higher H₂ uptake can be expected under conditions of culture shaking (mixing) and at high inoculum concentration.

The aim of this study was to verify some factors determining the improvement of H₂ production in *hup*[−] strain compared to parental strain of *Rubrivivax gelatinosus*. For this purpose, we explored the influence of substrate degree of reduction, microaerobic growth conditions, presence of N₂, inoculum concentration and culture shaking on H₂ accumulation by both strains.

Materials and methods

Bacterial strains and media

The strains of purple phototrophic bacteria *R. gelatinosus* RL2 [19] and RL2*hup*[−], were provided by K.V.P. Nagashima. The latter *hup*[−] mutant lacking *hupSL* without any insertions of antibiotics-resistant cartridges was created using the pJPCm plasmid and the plasmid pJPΔ*hupSL*-Skm

followed by kanamycin screening and by sucrose resistance screening, which will be detailed elsewhere [20]. *R. gelatinosus* RL2 was shown to synthesize reaction centers and antenna pigment complexes even under semiaerobic conditions [19]. Both strains of *R. gelatinosus*, RL2 and RL2*hup*[−], were pre-grown photosynthetically on YPS medium supplemented with Na succinate (5 g/l) and K-phosphate buffer (10 mM, pH 7.0).

H₂ production by growing cultures

For H₂ photoproduction experiments, bacteria were inoculated into Ormerod mineral medium [21] with glutamate (5 mM), yeast extract (0.4 g/l), K-phosphate buffer (20 mM, pH 7.0) and NaCl (0.23 g/l). The medium was supplied with succinate or other organic acid (as indicated in the text and Tables) with equal concentration of carbon atoms, 90 mM. Medium aliquots (8 ml) were placed in Hungate culture tubes (16 ml) supplied with butyl rubber stoppers and screw caps. For inoculum, one-day-old cultures were centrifuged aseptically in Eppendorf tubes (10,000 rpm, 3 min), the cell pellet was resuspended in Ormerod medium and added to Hungate tubes at 0.4–5% v/v, bacteriochlorophyll (BChl) concentration was specified in Tables and Figures. Depending on the aim of experiment, tubes were incubated under air or Ar gas phases (microaerobic or anaerobic conditions, correspondingly). In the latter case, tubes were repeatedly evacuated and filled with Ar or Ar + 50% N₂ using sterile filters. Cultivation was carried at 30 °C for 7–14 days until H₂ production ceased, light intensity of 30 W m^{−2} (incandescent lamps). Tubes were placed at the angle ~30° to horizon and shaken manually once a day. In some experiments tubes were placed horizontally on the platform and permanently shaken at 70 rpm (as indicated in Tables). Gas production was measured manometrically, and H₂ production was calculated on the basis of H₂ percentages measured by gas chromatography. H₂ amounted to approximately 85% of the produced gas. Each independent experiment was made in duplicates or triplicates (two or three tubes with identical composition in identical conditions). Number of experiments is specified in figure legends and table footnotes.

Short-term H₂ production/consumption

The observation of short-term H₂ production/consumption was performed in 9-ml vials. Culture aliquots (2 ml) were transferred anaerobically to the vials filled with Ar, repeatedly evacuated, refilled with Ar and supplied with ~25% H₂. Additions of N₂ or air were made as indicated in Figure legends. Vials were incubated at 30 °C under light (30 W m^{−2}) on a shaker platform (70 rpm). Experiments continued up to 10 h. The initial and final H₂ percentage was measured in each vial.

Other measurements

The total content of saccharides (as glucose residues) was analysed in the medium at the end of experiments and in cell pellet by anthrone assay [22]. BChl concentrations were measured spectrophotometrically at 772 nm following extraction in a 7:2 (v/v) acetone:methanol mixture [23].

Results

H₂ photoproduction by growing cultures of RL2 and *hup*[−] strains

Preliminary characterization of *hup*[−] strain of *R. gelatinosus* RL2 showed that bacteria grew well on lactate, malate, succinate, pyruvate. Unlike it, utilization of other short-chain fatty acids (acetate, propionate, butyrate, valerate) resulted in initial lag-period about 2 days, however, the final biomass concentration was not affected (not shown). As far as *H₂* production experiments were long-term, we used different substrates independent on the initial inhibition of growth.

Cultures of *R. gelatinosus*, RL2 and *hup*[−] strains grown under conditions described in Section “*H₂* production by growing cultures” produced *H₂* using different organic acids under the light (Table 1) like other purple non-sulfur bacteria. Under Ar phase (anaerobic conditions), *H₂* photoproduction by RL2 and *hup*[−] was quite similar independent of the substrate.

Under air gas phase (microaerobic conditions), we observed some decrease in *H₂* production in both strains. However, *hup*[−] strain demonstrated reliably higher *H₂* production compared to the parent RL2 strain when using succinate and malate

Table 1 – *H₂* photoproduction (ml/ml of culture) under Ar or air gas phase by RL2 and *hup*[−] strains of *R. gelatinosus* grown on different substrates (90 mM C). Initial BChl 0.6 ± 0.2 mg/l.^a

Growth substrate	RL2		<i>hup</i> [−]	
	Ar	Air	Ar	air
Malate	2.7 ± 0.2	1.2 ± 0.2	2.9 ± 0.3	2.2 ± 0.2
Succinate	3.0 ± 0.1	1.3 ± 0.2	2.9 ± 0.2	2.1 ± 0.2
Lactate	3.8 ± 0.4	3.2 ± 0.4	3.5 ± 0.2	3.6 ± 0.2
Acetate	3.9 ± 0.4	2.6 ± 0.6	4.0 ± 0.3	2.9 ± 0.5

^a Table represents average values (±95% confidence interval) from 8 independent experiments on succinate, 3–4 on other substrates. Values given in Table refer to maximal *H₂* production, prior to *H₂* consumption began, if any.

(Table 1). In most cases, the duration of *H₂* production was ~14 days, but it stopped in ~7–8 days and turned into *H₂* consumption under air on malate or succinate (Fig. 1).

It is well-known that oxygen causes a repression of nitrogenase synthesis. However, under microaerobic conditions employed (air gas phase), *pO₂* value in medium should be minimal due to absence of shaking, slow diffusion of gas into liquid and its consumption via respiration. That is why nitrogenase was synthesized (and *H₂* production took place) under our experimental conditions. On the other hand, under oxidized conditions *H₂* recycling is supposed to be maximal. This point is supported by kinetics of *H₂* production where we can see *H₂* consumption in the late growth phase of RL2 strain unlike to *hup*[−] strain (Fig. 1, Curve 2 vs Curve 4).

H₂ production rate by RL2 strain during 2–5 days was somewhat higher under anaerobic conditions compared to microaerobic ones (Fig. 1, Curves 1 vs 2). Unlike that, in *hup*[−] strain, the rates were about the same under anaerobic and microaerobic conditions and were close to *H₂* production rate by RL2 strain under anaerobic conditions (Fig. 1, Curves 3, 4, 1). Effect of oxygen on nitrogenase synthesis and activity is supposed to be the same in both strains. So, the decreased rate in RL2 strain under microaerobic conditions probably means that *H₂* consumption took place during the intermediate phase of the process in addition to the late growth phase. Another data on *H₂* consumption are presented below (Section “Short-term *H₂* photoproduction/consumption by cell suspensions of RL2 and *hup*[−] strains”).

The termination of *H₂* production after 6th day in *hup*[−] strain under microaerobic conditions (Fig. 1, Curve 4) was presumably determined by the shortage of substrate due to enhanced biomass synthesis.

To compare different organic acids as substrates for *H₂* production, we used the concept “degree of reduction”, γ [24]. The degree of reduction of biomass ($\text{CH}_x\text{N}_y\text{O}_z$) or organic acid (CH_xO_z) was calculated in relation to 1 C atom according to equation:

$$\gamma = 4 + x + 3y - 2z,$$

where *x*, *y*, *z* – numbers of H, N, O atoms, correspondingly, based on biomass composition [24]. For *R. capsulatus* with

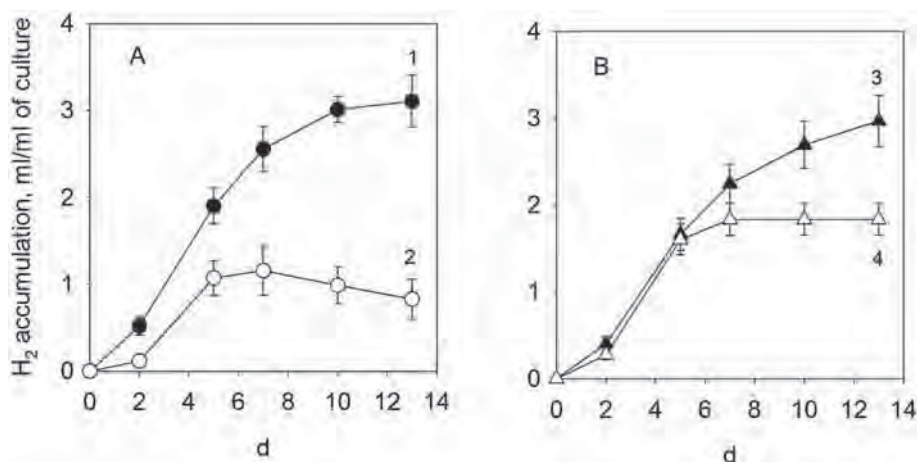


Fig. 1 – *H₂* photoproduction by growing cultures of RL2 (A) and *hup*[−] (B) strains on succinate under Ar (1, 3) or air (2, 4) gas phase (initial BChl 0.5 mg/l). The figure presents results of a typical experiment in triplicates.

Please cite this article in press as: Laurinavichene T, et al., Effect of growth conditions on advantages of *hup*[−] strain for *H₂* photoproduction by *Rubrivivax gelatinosus*, International Journal of Hydrogen Energy (2017), <http://dx.doi.org/10.1016/j.ijhydene.2016.12.074>

biomass composition $\text{CH}_{1.89}\text{O}_{0.506}\text{N}_{0.181}\text{P}_{0.048}$ the degree of reduction was earlier estimated as 4.335 [25]. The degree of reduction of organic acids was calculated in a similar way with exception of N atom. Consequently, organic acids have the following γ values:

Malic acid $\text{C}_4\text{H}_6\text{O}_5$ or $\text{CH}_{1.5}\text{O}_{1.25}$: $\gamma = 3.0$

Succinic acid $\text{C}_4\text{H}_6\text{O}_4$ or $\text{CH}_{1.5}\text{O}$: $\gamma = 3.5$

Lactic acid $\text{C}_3\text{H}_6\text{O}_3$ or CH_2O : $\gamma = 4.0$

Acetic acid $\text{C}_2\text{H}_4\text{O}_2$ or CH_2O : $\gamma = 4.0$

Assuming that *R. gelatinosus* biomass has similar degree of reduction, one can see that only malate and succinate have reliably lower degree of reduction compared to biomass. It correlated with relatively higher H_2 accumulation by *hup*⁻ strain using these two acids. Thus, in these cases, the Hup hydrogenases in RL2 strain were essential to save reducing power. For the most part, the following experiments were made with succinate-grown cultures.

Bacterial growth under different conditions was estimated by final BChl concentration. Under anaerobic conditions, BChl concentration was similar in RL2 and *hup*⁻ strains (Fig. 2A). Under microaerobic conditions, BChl concentration increased in both strains, being reliably higher in RL2. In addition, glucose content in cells (Fig. 2B) and relative glucose content per 1 mg BChl was higher in RL2. Thus, the higher H_2 production in *hup*⁻ strain under microaerobic conditions correlated with lower biomass synthesis and lower content of storage polysaccharides.

Short-term H_2 photoproduction/consumption by cell suspensions of RL2 and *hup*⁻ strains

To demonstrate the possibility of H_2 consumption by RL2 strain and to clarify conditions for this process, we took and

degassed cultures at the end of H_2 production (Fig. 1). Aliquots were incubated under Ar, Ar + 50% air, Ar + 50% N_2 with shaking. Around 25% of hydrogen was added into each vial. The rates of H_2 consumption/production varied depending on duration of growth, but the responses to air and N_2 presence in anaerobically and microaerobically grown cultures were reproducible. Typical examples are shown on Fig. 3.

H_2 consumption occurred in RL2 strain (Fig. 3A, C) in contrast to *hup*⁻ strain (Fig. 3B, D). Air addition provided maximal H_2 consumption (Fig. 3, Curves 3, 9). H_2 consumption under the Ar phase was negligible if culture was grown under Ar (Fig. 3, Curve 7). If culture was grown under air phase, H_2 consumption in previously degassed suspension took place even under 75% Ar + 25% H_2 (Fig. 3, Curve 1). It means that some non-gaseous acceptor (i.e., not O_2) was available for H_2 uptake in this case.

The question was whether O_2 or N_2 (the main air constituent) plays role in H_2 consumption process. In RL2 strain the addition of 50% N_2 somewhat stimulated this process, if endogenous H_2 consumption under the Ar was absent (Fig. 3C, Curve 8 vs 7). In contrast, N_2 did not stimulate already occurring endogenous H_2 consumption (Fig. 3A, Curve 2 vs 1).

In *hup*⁻ strain we did not observe H_2 consumption under any conditions (Fig. 3B), but in some cases H_2 production continued under Ar (Fig. 3D, Curve 10). At this point addition of air or N_2 inhibited H_2 production substantially up to complete stop of H_2 production under air-containing phase (Fig. 3D, Curve 12). This differed from results on growing culture (Table 1) where no inhibition of H_2 production by succinate-grown *hup*⁻ strain was observed under microaerobic conditions. Evidently, it was governed by distinctions between experimental conditions: permanent shaking of cell suspensions in short-term test (Fig. 3) and only periodic mixing of growing culture (Table 1; Fig. 1). Therefore, we studied the effect of shaking on growing cultures under anaerobic and microaerobic conditions, and with N_2 addition. Besides, in order to augment the difference in H_2 production between RL2 and *hup*⁻ strains we checked the effect of high inoculum concentration, suggesting that H_2 consumption in RL2 strain would grow in concentrated suspensions.

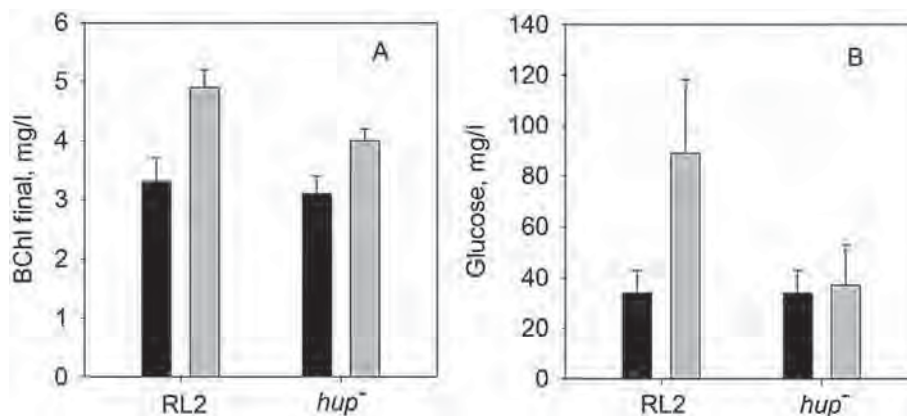


Fig. 2 – Final BChl concentration (A) and glucose equivalents measured in cell pellet (B) in RL2 and *hup*⁻ cells grown on succinate under anaerobic (dark bars) or microaerobic (light bars) conditions. Initial concentration of BChl was 0.6 mg/l. Figure presents average values ($\pm 95\%$ confidence interval) from 4 independent experiments (out of 8 given in Table 1).

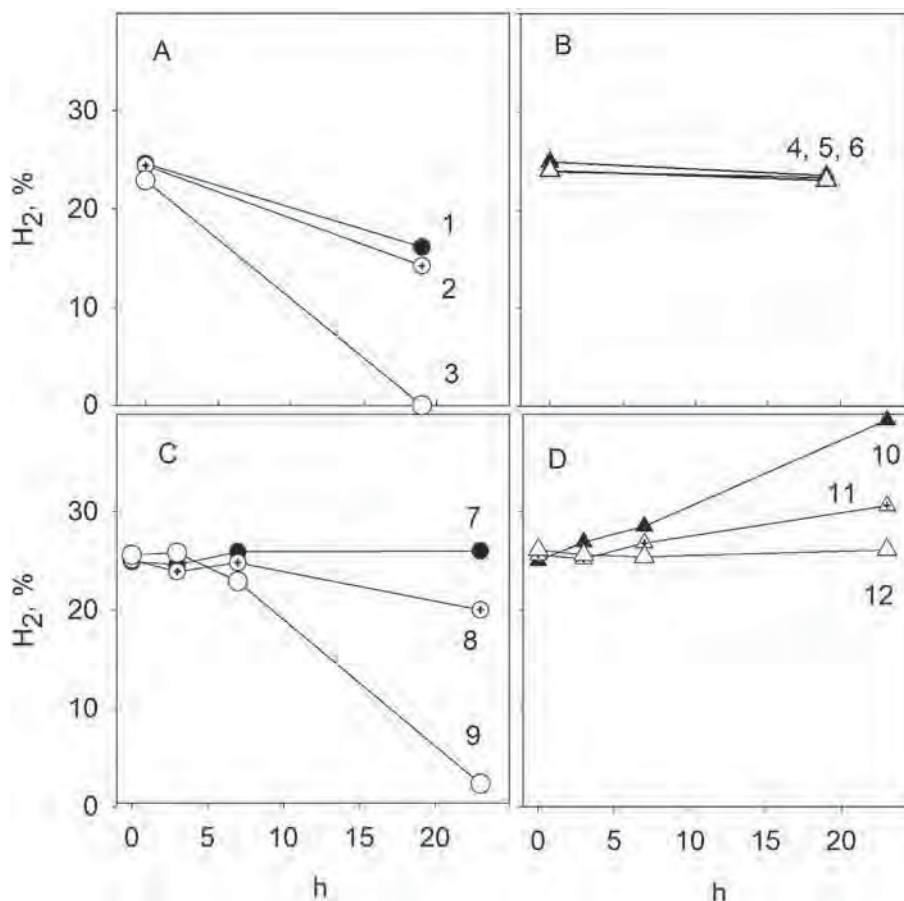


Fig. 3 – H₂ consumption/production by RL2 (A, C) and *hup*⁻ (B, D) suspensions of *R. gelatinosus* under illumination. (A, B) Cultures were grown for 17 days under air, then incubated under Ar (1, 4), Ar + 50% N₂ (2, 5) or Ar + 50% air (3, 6). (C, D) Cultures were grown for 14 days under Ar, then incubated under Ar (7, 10), Ar + 50% N₂ (8, 11) or Ar + 50% air (9, 12).

Influence of inoculum concentration, presence of N₂ and shaking on H₂ photoproduction by growing cultures of RL2 and *hup*⁻ strains

At low inoculum concentration effect of culture shaking on H₂ production under Ar gas phase was not significant in both strains (Table 2). Alternatively, the shaking of culture under microaerobic conditions suppressed H₂ production by both strains to zero. It can be due to intensive gas exchange and higher pO₂ in medium when shaking which resulted in the absence of nitrogenase synthesis and H₂ production in both strains.

As far as the main part of air is nitrogen, the effects of N₂ were also checked. Addition of N₂ to the gas phase resulted in decreased H₂ production in both strains with minor domination (if at all) in *hup*⁻ strain (Table 2). However, the effect of N₂ was weaker than that of air. Shaking the culture also enhanced negative effect of N₂ in both strains.

Under anaerobic conditions, the increase in initial BChl concentration caused a non-significant decrease in H₂ production by RL2 and *hup*⁻ strains when grown without shaking (Table 2). In contrast, the effect under microaerobic conditions was severe: ~90 and ~40% inhibition in case of high biomass concentration of RL2 and *hup*⁻ strain, respectively. Almost

Table 2 – Effect of different inoculum (BChl) concentration and culture shaking on H₂ photoproduction (ml/ml of culture) in RL2 and *hup*⁻ strains of *R. gelatinosus* grown on succinate under different gas phases.^a

Initial BChl, mg/l	Shaking	RL2			<i>hup</i> ⁻		
		Ar	air	Ar + N ₂	Ar	air	Ar + N ₂
0.6 ± 0.2	–	3.0 ± 0.1	1.3 ± 0.2	1.9 ± 0.4	2.9 ± 0.2	2.1 ± 0.2	2.2 ± 0.3
0.6 ± 0.2	+	2.8 ± 0.2	0	ns ^b	2.9 ± 0.3	0	ns ^b
1.8 ± 0.4	–	2.7 ± 0.2	0.1 ± 0.1	0.1 ± 0.1	2.5 ± 0.2	1.3 ± 0.4	0.2 ± 0.3

^a Table represents average values (±95% confidence interval) from 3 to 10 independent experiments.

^b Non-significant, <2% from maximum; the absence of oxygen in Ar + N₂ phase was proved by gas chromatography.

total inhibition was observed in both strains with high biomass content when N₂ was available. However, this effect in *hup*⁻ strain could not result from enhanced H₂ uptake. Apparently, it was not due to self-shading at high biomass concentration because there was no such inhibition by high initial BChl concentration under the Ar phase.

In both strains, the decrease in H₂ production under air or Ar + N₂ gas phase corresponded to increased biomass synthesis, maximum being in RL2 strain under microaerobic conditions (Table 3). The increase in initial BChl resulted in the increase in final BChl (Table 3). Thus, the absence of H₂ production did not correlate with absence of growth.

Furthermore, if we plotted all data on H₂ production under microaerobic conditions as a function of initial BChl concentration, gradual decrease in H₂ production with BChl increase was not observed (Fig. 4). One can see rather a stepwise decrease in both strains. In RL2 strain H₂ production dropped to ~0 (at BChl ~1.0 mg/l) while in *hup*⁻ – to ~1 ml/ml (at BChl ~1.3 mg/l). In the latter case, only initial BChl as high as 2.8 mg/l completely prevented H₂ production. It proves that the decrease in H₂ production with inoculum concentration increase was not due to the increased H₂ consumption. Results rather indicate the occurrence of some metabolic shift triggered by certain inoculum concentration. Metabolic pathways involved in such shift are unclear. Nevertheless, a reliable difference between RL2 and *hup*⁻ strains proved the role of Hup hydrogenase in H₂ uptake under microaerobic conditions over the most part of inoculum concentrations.

Discussion

Numerous data on H₂ production by *hup*⁻ mutants of PNSB clearly demonstrate their capability of enhanced H₂ production compared to parental strains. However, the stimulation effect varied in different studies and it was not clear what conditions are crucial. It should be noted, that the absolute maximum of H₂ production rate was not achieved using particularly these strains. Nevertheless, the extremely high H₂ yield of 10 mol/mol of glucose was demonstrated during continuous cultivation of *R. capsulatus* JP91 (*hup*⁻) [26] but no comparison was made with *hup*⁺ strain under the same conditions.

We studied the influence of substrate reduction degree, microaerobic conditions, presence of N₂, inoculum concentration and culture shaking on H₂ accumulation by two strains of *R. gelatinosus* (RL2 and *hup*⁻) which were not studied before. As it was expected, the stimulation of H₂ production was observed when using substrates (malate and succinate) with

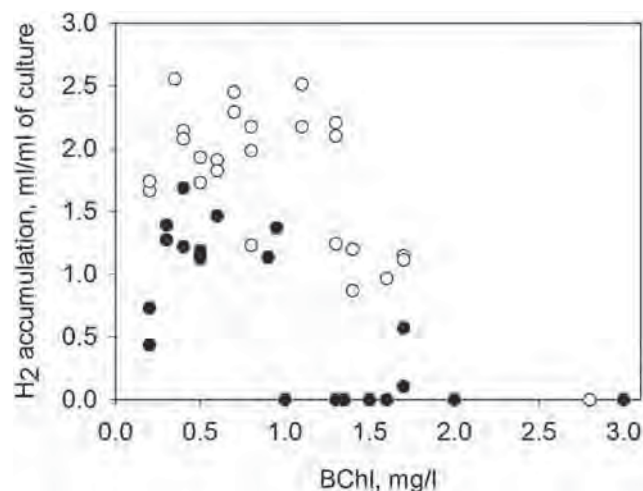


Fig. 4 – H₂ photoproduction under microaerobic conditions by RL2 (dark circles) and *hup*⁻ (open circles) strains grown on succinate and inoculated at different BChl concentrations. Figure presents results of independent experiments.

lower reduction degree than estimated biomass reduction degree. However, this was only true under microaerobic conditions (Table 1). It was not stated before while unlike to our data the stimulation effect was observed using malate or even acetate and lactate under reportedly anaerobic conditions [5,17]. Through our study, we used Hungate tubes. Even though it is far from large-scale cultivation, it still allowed to maintain strictly anaerobic conditions because these screwed tubes were designed specifically for anaerobic cultivation. Probably, it helped us to discriminate between strictly anaerobic and microaerobic conditions and find the difference in H₂ production. Nevertheless, the distinctions between various PNSB species can not be excluded.

An adverse oxygen effect on nitrogenase synthesis and activity is well-known [27]. Nevertheless, this enzyme can tolerate oxygen up to 4.6 μmol [28]. The reported H₂ production under air gas phase is probably microaerobic process in which oxygen is currently removing from suspension by respiration [29–31]. The increase in Hup-hydrogenase role in H₂ uptake under oxidative conditions is understandable. However, various air concentrations have different negative impact on H₂ production in RL2 strain. Culture shaking or stirring might transform the slight effect into the complete repression of nitrogenase synthesis, which is quite predictable. In this work, we attempted to reveal whether N₂ as a main air constituent causes an impact on H₂ production.

Table 3 – Effect of different inoculum (BChl) content on final BChl content (mg/l of culture) in RL2 and *hup*⁻ strains of *R. gelatinosus* grown on succinate under different gas phases.^a

Initial BChl, mg/l	RL2			<i>hup</i> ⁻		
	Ar	air	Ar + N ₂	Ar	Air	Ar + N ₂
0.6 ± 0.2	3.3 ± 0.4	4.9 ± 0.3	4.0 ± 0.2	3.1 ± 0.3	4.0 ± 0.2	3.9 ± 0.2
1.8 ± 0.4	4.5 ± 0.9	5.7 ± 1.4	6.2 ± 2.1	4.7 ± 0.8	6.6 ± 1.2	6.3 ± 3.2

^a Table represents average values (±95% confidence interval) from 3 to 8 independent experiments.

Previously we reported that in both growing cultures and suspensions the increase in N₂ concentration resulted in decreased H₂ production [32]. It was suggested that N₂ brings about the requirement in reductants for synthesis of N-containing compounds. Our data show that N₂ partly inhibited H₂ production in growing cultures of both strains under standard conditions (low inoculum concentration, Table 2). On the other hand, it can be governed by higher portion of organic acids utilized for biomass synthesis and lower portion for H₂ production (Table 3). In short-term experiments N₂ somewhat enhanced H₂ consumption in RL2 strain while inhibited H₂ production by *hup*⁻ strain (Fig. 3). Evidently, N₂ can reduce H₂ production due to decreased nitrogenase activity in hydrogen production under nitrogen atmosphere since 75% of electrons are allocated to ammonium formation. Also, N₂ presence can stimulate H₂ consumption due to enhanced demand of reductants for nitrogen compounds synthesis. Additionally, there is a possibility of decreased substrate availability for H₂ production. Finally, excess of nitrogen might downregulate the nitrogenase itself. The important role of Hup hydrogenase under N₂ gas phase is indirectly supported by Rey [10] where the maximal ever difference between *hup*⁻ and parental strains was demonstrated exactly under N₂ gas phase. Currently, we suggest that effect of air (microaerobic conditions) on H₂ production was partly governed by N₂.

In addition, we observed the inhibitory effect of high inoculum concentration (>1 mg BChl/l) on H₂ photoproduction in succinate-grown cultures (Table 2). This effect was low and quite similar in both strains under anaerobic conditions. Theoretically, the expenditure of substrate for biomass synthesis was similar at high and low inoculum concentration, expenditure for culture maintaining must increase with biomass increase. Thus, lower portion of substrate is available at higher inoculum concentration. However, under microaerobic conditions this effect grew, being maximal in *hup*⁺ strain. Apparently, we have the superposition of two effects: increased H₂ uptake in parental strain and metabolic shift from H₂ production to another process (possibly storage product synthesis) in both strains (Section “Influence of inoculum concentration, presence of N₂ and shaking on H₂ photoproduction by growing cultures of RL2 and *hup*⁻ strains”). Under N₂ phase, the effect of high inoculum concentration was dramatic in both strains. It should be emphasized that a similar effect was observed earlier in co-culture of *Clostridium butyricum* and *R. sphaeroides* [33] as well as in *R. sphaeroides* monoculture (our unpublished data). The inhibitory effect of high inoculum concentration was reported by Argun [34] in H₂ photoproduction experiments with co-culture containing PNSB. The authors attributed this effect to flocks formation and limited substrate penetration inside the flocks. High inoculum concentration was also found to reduce the yield and productivity of dark fermentation [35].

H₂ recycling may be important under microaerobic native conditions or under shift from anaerobic to aerobic conditions. At this point, *hup*⁺ wild type might take advantage due to higher biomass accumulation. From the other hand, in large-scale H₂ production in bioreactors the strictly anaerobic conditions are difficult to maintain. Input of air traces may be not fatal for nitrogenase synthesis but result in drastic decrease in H₂ yield when using *hup*⁺ strain, whereas *hup*⁻

strain would keep a rather high H₂ yield. Even minimal air penetration due to some drawbacks of equipment (for example, using plastic gas syringe for cultivation or bioreactor with air-permeable components) can be important. Thus, H₂ production by *hup*⁻ mutant is more tolerant to presence of air traces. However, it seems from our data that under strictly anaerobic conditions this advantage would disappear. It is the matter of future study to compare H₂ production at different pO₂ and various low-rate air flow under controlled continuous cultivation of both strains.

Conclusions

At low inoculum concentration, H₂ production by two strains of *R. gelatinosus*, RL2 and *hup*⁻, was similar under anaerobic conditions independent on the substrate. Under microaerobic conditions, *hup*⁻ strain produced more H₂ compared to RL2 strain when using only succinate and malate, substrates with lower degree of reduction than biomass. Presence of N₂ caused some decrease in H₂ production by both strains, which is partially due to enhanced H₂ consumption via Hup hydrogenase. At high inoculum concentration, H₂ production by two strains was similar under anaerobic conditions. Under microaerobic conditions, H₂ production by succinate-grown cultures decreased in both strains, especially in RL2 strain where it went to zero. Thus, the absence of Hup hydrogenase resulted in higher resistance of H₂ production process to minor air penetration.

Acknowledgments

This work was supported by RFBR and JSPS under the Russia and Japan Research Cooperative Program No. 15-54-50032 (AT) and was supported in part by grant-in-aid for JSPS KAKENHI Nos. 15K00642 and 24107004 (AnApple) to KI.

We gratefully thank Azat Abdullatypov for careful translation and editing.

REFERENCES

- [1] Tsygankov AA, Khusnutdinova AN. Hydrogen in metabolism of purple bacteria and prospects of practical application. *Microbiology* 2015;84(1):1–22.
- [2] Hallenbeck PC, Liu Y. Recent advances in hydrogen production by photosynthetic bacteria. *IJHE* 2016;41(7):4446–54.
- [3] Tichi MA, Tabita FR. Interactive control of *Rhodobacter capsulatus* redox-balancing systems during phototrophic metabolism. *J Bacteriol* 2001;183(21):6344–54.
- [4] Kondo T, Arakawa M, Hirai T, Wakayama T, Hara M, Miyake J. Enhancement of hydrogen production by a photosynthetic bacterium mutant with reduced pigment. *J Biosci Bioeng* 2002;93(2):145–50.
- [5] Kim MS, Baek JS, Lee JK. Comparison of H₂ accumulation by *Rhodobacter sphaeroides* KD131 and its uptake hydrogenase and PHB synthase deficient mutant. *IJHE* 2006;31(1):121–7.

- [6] McKinlay JB, Harwood CS. Carbon dioxide fixation as a central redox cofactor recycling mechanism in bacteria. *Proc Nat Acad Sci* 2010;107(26):11669–75.
- [7] Oh Y-K, Raj MS, Jung GY, Park S. Current status of the metabolic engineering of microorganisms for biohydrogen production. *Bioresour Technol* 2011;102:8357–67.
- [8] Hallenbeck PC, Abo-Hashesh M, Ghosh D. Strategies for improving biological hydrogen production. *Bioresour Technol* 2012;10:1–9.
- [9] Franchi E, Tosi C, Scolla G, Penna GD, Rodriguea F, Pedroni PM. Metabolically engineered *Rhodobacter sphaeroides* RV strains for improved biohydrogen photoproduction combined with disposal of food wastes. *Mar Biotechnol* 2004;6(6):552–65.
- [10] Rey FE, Oda Y, Harwood CS. Regulation of uptake hydrogenase and effects of hydrogen utilization on gene expression in *Rhodospseudomonas palustris*. *J Bacteriol* 2006;188(17):6143–52.
- [11] Kars G, Gündüz U, Yücel M, Rakhely G, Kovacs KL, Eroglu I. Evaluation of hydrogen production by *Rhodobacter sphaeroides* O.U.001 and its hupSL deficient mutant using acetate and malate as carbon sources. *IJHE* 2009;34(5):2184–90.
- [12] Liu T, Zhou Z. Improvement of hydrogen yield by hupR gene knock-out and nifA gene overexpression in *Rhodobacter sphaeroides* 6016. *IJHE* 2010;35(18):9603–10.
- [13] Kontur WS, Ziegelhoffer E, Spero MA, Donohue TJ. Pathways involved in reductant distribution during photobiological H₂ production by *Rhodobacter sphaeroides*. *Appl Environ Microbiol* 2011;77(20):7425–9.
- [14] Tao Y, Liu D, Yan X, Zhou Z, Lee JK, Yang C. Network identification and flux quantification of glucose metabolism in *Rhodobacter sphaeroides* under photoheterotrophic H₂-producing conditions. *J Bacteriol* 2012;194(2):274–83.
- [15] Wu X, Bai L, Jiang L, Liu J, Wu ML. Enhanced photo-fermentative hydrogen production from different organic substrate using hupL inactivated *Rhodospseudomonas palustris*. *Afr J Microbiol Res* 2012;6(25):5362–70.
- [16] Boran E, Özgür E, Yücel M, Gündüz U, Eroglu I. Biohydrogen production by *Rhodobacter capsulatus* HupL mutant in pilot solar tubular photobioreactor. *IJHE* 2012;37(21):16437–45.
- [17] Kars G, Gündüz U, Rakhely G, Yücel M, Eroglu I, Kovacs KL. Improved hydrogen production by uptake hydrogenase deficient mutant strain of *Rhodobacter sphaeroides* O.U.001. *IJHE* 2008;33(12):3056–60.
- [18] Uyar B, Gürkan M, Özgür E, Gündüz U, Yücel M, Eroglu I. Hydrogen production by hup(-) mutant and wild-type strains of *Rhodobacter capsulatus* from dark fermentation effluent of sugar beet thick juice in batch and continuous photobioreactors. *Bioprocess Biosyst Eng* 2015;38:1935–42.
- [19] Maki H, Matsuura K, Shimada K, Nagashima KVP. Chimeric photosynthetic reaction center complex of purple bacteria composed of the core subunits of *Rubrivivax gelatinosus* and the cytochrome subunit of *Blastochloris viridis*. *J Biol Chem* 2003;278(6):3921–8.
- [20] Sakurai S, Kitashima M, Shiraki M, Masukawa H, Sato T, Nagashima S et al. Some characteristics of nitrogenase-based photobiological hydrogen production by cyanobacteria and purple bacteria: effects of light and culture conditions. Abstract of the Hydrogen Energy Systems Society, Japan, Nov. 28–29, 2016, Tokyo, Japan.
- [21] Ormerod JG, Ormerod SK, Gest H. Light-dependent utilization of organic compounds and photoproduction of hydrogen by photosynthetic bacteria. *Arch Biochem Biophys* 1961;94(2):449–63.
- [22] Hanson R, Phillips G. Chemical composition of bacterial cell. In: Gerhardt P, Murray RGE, Costilow RN, Nester EW, Wood WA, Krieg NR, et al., editors. *Manual of methods for general bacteriology* (Russian translation). Moscow: Mir; 1984. p. 283–375.
- [23] Clayton RK. Spectroscopic analysis of bacteriochlorophylls in vitro and in vivo. *Photochem Photobiol* 1966;5(8):669–77.
- [24] Erickson LE, Minkevich IG, Eroshin VK. Application of mass and energy balance regularities in fermentation. *Biotechnol Bioeng* 1978;20(10):1595–621.
- [25] Tsygankov AA, Laurinavichene TV. Influence of degree and mode of light limitation on growth characteristics of the *Rhodobacter capsulatus* continuous cultures. *Biotechnol Bioeng* 1996;51(5):605–12.
- [26] Abo-Hashesh M, Desaunay N, Hallenbeck PC. High yield single stage conversion of glucose to hydrogen by photofermentation with continuous cultures of *Rhodobacter capsulatus* JP91. *Bioresour Technol* 2013;128:513–7.
- [27] Hochman A, Burris RH. Effect of oxygen on acetylene reduction by photosynthetic bacteria. *J Bacteriol* 1981;147(2):492–9.
- [28] Oelze J, Klein G. Control of nitrogen fixation by oxygen in purple nonsulfur bacteria. *Arch Microbiol* 1966;165(4):219–25.
- [29] Akköse S, Gündüz U, Yücel M, Eroglu I. Effects of ammonium ion, acetate and aerobic conditions on hydrogen production and expression levels of nitrogenase genes in *Rhodobacter sphaeroides* O.U.001. *IJHE* 2009;34(21):8818–27.
- [30] Merugu R, Girisham S, Reddy SM. Bioproduction of hydrogen by *Rhodobacter capsulatus* KU002 isolated from leather industry effluents. *IJHE* 2010;35(18):9591–7.
- [31] Laurinavichene T, Belokopytov B, Laurinavichius K, Khusnutdinova A, Seibert M, Tsygankov A. Towards the integration of dark- and photo-fermentative waste treatment. 4. Repeated batch sequential dark and photofermentation using starch as substrate. *IJHE* 2012;37(10):8800–10.
- [32] Laurinavichene T, Tsygankov A. The similarities and differences between the alternative and Mo-containing nitrogenases of *Rhodobacter capsulatus*. *Appl Biochem Microbiol* 1994;30(3):389–95.
- [33] Laurinavichene T, Tsygankov A. Different types of H₂ photoproduction by starch-utilizing co-culture of *Clostridium butyricum* and *Rhodobacter sphaeroides* depending on cultivation conditions. *IJHE* 2016;41(31):13419–25.
- [34] Argun H, Kargi F, Kapdan IK. Effects of the substrate and cell concentrations on biohydrogen production from ground wheat by combined dark and light fermentations. *IJHE* 2009;34(21):6181–8.
- [35] Dada O, Kalil MS, Yusoff WMW. Effect of inoculum and substrate concentration in anaerobic fermentation of treated rice bran to acetone, butanol and ethanol. *Bacteriol J* 2012;2(4):79–89.

Increased heterocyst frequency by patN disruption in *Anabaena* leads to enhanced photobiological hydrogen production at high light intensity and high cell density

Hajime Masukawa, Hidehiro Sakurai, Robert P. Hausinger & Kazuhito Inoue

Applied Microbiology and
Biotechnology

ISSN 0175-7598

Appl Microbiol Biotechnol
DOI 10.1007/s00253-016-8078-3



Your article is protected by copyright and all rights are held exclusively by Springer-Verlag Berlin Heidelberg. This e-offprint is for personal use only and shall not be self-archived in electronic repositories. If you wish to self-archive your article, please use the accepted manuscript version for posting on your own website. You may further deposit the accepted manuscript version in any repository, provided it is only made publicly available 12 months after official publication or later and provided acknowledgement is given to the original source of publication and a link is inserted to the published article on Springer's website. The link must be accompanied by the following text: "The final publication is available at link.springer.com".

Increased heterocyst frequency by *patN* disruption in *Anabaena* leads to enhanced photobiological hydrogen production at high light intensity and high cell density

Hajime Masukawa¹ · Hidehiro Sakurai² · Robert P. Hausinger^{3,4} · Kazuhito Inoue^{2,5}Received: 6 October 2016 / Revised: 26 November 2016 / Accepted: 17 December 2016
© Springer-Verlag Berlin Heidelberg 2017

Abstract The effects of increasing the heterocyst-to-vegetative cell ratio on the nitrogenase-based photobiological hydrogen production by the filamentous heterocyst-forming cyanobacterium *Anabaena* sp. PCC 7120 were studied. Using the uptake hydrogenase-disrupted mutant (Δ Hup) as the parent, a deletion-insertion mutant (PN1) was created in *patN*, known to be involved in heterocyst pattern formation and leading to multiple singular heterocysts (MSH) in *Nostoc punctiforme* strain ATCC 29133. The PN1 strain showed heterocyst differentiation but failed to grow in medium free of combined-nitrogen; however, a spontaneous mutant (PN22) was obtained on prolonged incubation of PN1 liquid cultures and was able to grow robustly on N₂. The disruption of *patN* was confirmed in both PN1 and PN22 by PCR and whole genome resequencing. Under combined-nitrogen limitation, the percentage of heterocysts to total cells in the PN22

filaments was 13–15 and 16–18% under air and 1% CO₂-enriched air, respectively, in contrast to the parent Δ Hup which formed 6.5–11 and 9.7–13% heterocysts in these conditions. The PN22 strain exhibited a MSH phenotype, normal diazotrophic growth, and higher H₂ productivity at high cell concentrations, and was less susceptible to photoinhibition by strong light than the parent Δ Hup strain, resulting in greater light energy utilization efficiency in H₂ production on a per unit area basis under high light conditions. The increase in MSH frequency shown here appears to be a viable strategy for enhancing H₂ productivity by outdoor cultures of cyanobacteria in high-light environments.

Keywords Cyanobacteria · Heterocyst · *Anabaena* · Hydrogen production · *patN* · Nitrogenase

Electronic supplementary material The online version of this article (doi:10.1007/s00253-016-8078-3) contains supplementary material, which is available to authorized users.

✉ Hajime Masukawa
masukawa@ocarina.osaka-cu.ac.jp

¹ The OCU Advanced Research Institute for Natural Science and Technology (OCARINA), Osaka City University, 3-3-138 Sugimoto, Sumiyoshi-ku, Osaka 558-8585, Japan

² Research Institute for Photobiological Hydrogen Production, Kanagawa University, Hiratsuka, Kanagawa 259-1293, Japan

³ Department of Microbiology and Molecular Genetics, Michigan State University, East Lansing, MI 48824, USA

⁴ Department of Biochemistry and Molecular Biology, Michigan State University, East Lansing, MI 48824, USA

⁵ Department of Biological Sciences, Kanagawa University, Hiratsuka, Kanagawa 259-1293, Japan

Introduction

Increasing awareness of the danger of ever-rising greenhouse gases, notably CO₂, on global climate change led the parties to the United Nations Framework Convention on Climate Change to adopt the Paris Agreement in December of 2015 (UNFCCC 2016) to hold the global average temperature increase at the above pre-industrial (1850–1900) levels. It is evident that we need to develop viable renewable energy technologies that substantially reduce CO₂ emissions from burning fossil fuels.

Photobiological production of H₂ by cyanobacteria is considered by many to be an ideal source of renewable energy because the inputs, water as the electron donor and sunlight as the energy source, are readily available and abundant (Bothe et al. 2010; Prince and Khesghi 2005; Sakurai and Masukawa 2007; Sakurai et al. 2013; Sakurai et al. 2015; Tamagnini et al. 2007). H₂ is a clean energy source that generates electricity in

fuel cells at high efficiencies while producing water as the sole product without emitting the greenhouse gas CO₂.

Cyanobacterial production of H₂ can be accomplished by hydrogenases and nitrogenases, both of which are sensitive to inactivation by O₂ (Bothe et al. 2010; Sakurai and Masukawa 2007; Sakurai et al. 2013; Tamagnini et al. 2007). In contrast to hydrogenase that catalyzes a reversible reaction ($2 e^- + 2 H^+ \leftrightarrow H_2$) without the need for ATP, nitrogenase catalyzes an irreversible reaction that requires four molecules of ATP per electron pair, essentially allowing for the unidirectional production of H₂. Under optimal conditions for N₂ reduction, nitrogenase catalyzes the following reaction: $N_2 + 8 e^- + 8 H^+ + 16 ATP \rightarrow H_2 + 2 NH_3 + 16 (ADP + P_i)$; whereas in the absence of N₂ (e.g., under Ar), all electrons are directed to H₂ production: $2 e^- + 2 H^+ + 4 ATP \rightarrow H_2 + 4 (ADP + P_i)$. Most N₂-fixing heterocyst-forming cyanobacteria possess uptake hydrogenase (Hup) which consumes H₂, thus decreasing the conversion efficiency of H₂ production by nitrogenase (Masukawa et al. 2009). Genetic inactivation of Hup (Δ Hup) in the heterocyst-forming cyanobacteria *Anabaena* and *Nostoc* leads to three to seven-fold increases in H₂ production rates (Happe et al. 2000; Masukawa et al. 2002), allowing H₂ to accumulate to high concentrations (about 7–30%) in photosynthetically growing cells under an Ar atmosphere (Kitashima et al. 2012; Masukawa et al. 2010; Yoshino et al. 2007).

Synthesis of active nitrogenase in cyanobacteria requires that the appropriate genes be expressed and that the enzyme be protected from oxygen. When a source of combined-nitrogen such as nitrate or ammonia is available from the environment, the cells do not fix nitrogen; thus, limiting combined-nitrogen is used to induce the nitrogenase genes to fix N₂. Depending on the genus, the O₂ sensitivity of nitrogenase is overcome by: 1) spatial separation of photosynthesis and nitrogenase as occurs in heterocyst-forming cyanobacteria (see below) (e.g. *Anabaena* and *Nostoc*), 2) temporal separation with photosynthesis occurring in the day time and nitrogen fixation at night as in unicellular (e.g. *Cyanothece*) or filamentous non-heterocyst-forming cyanobacteria (e.g. *Oscillatoria*), and 3) seemingly sporadic expression of photosynthesis and nitrogenase activity in some cells of the same filament by some filamentous non-heterocyst-forming cyanobacteria (e.g. *Trichodesmium*) (Finzi-Hart et al. 2009) (summarized by (Sakurai et al. 2013)).

The cyanobacterial strain used in this work is the filamentous and heterocyst-forming *Anabaena* sp. strain PCC 7120 (also called *Nostoc* sp. PCC 7120). When placed in media deprived of combined-nitrogen, the filaments develop specialized cells called heterocysts separated by approximately 10–20 vegetative cells. Heterocysts lack the O₂-evolving photosystem II, contain nitrogenase, and are surrounded by a thick cell envelope composed of glycolipids and polysaccharides

that impede the entry of O₂ and help to maintain a microoxic environment (Wolk et al. 1994). Heterocysts receive sugars as the electron donors necessary for the nitrogenase reaction from the neighboring vegetative cells that possess typical O₂-evolving photosynthetic activity. Heterocysts in turn provide the vegetative cells with fixed nitrogen, likely in the form of glutamine and a dipeptide, beta-aspartyl-arginine (Burnat et al. 2014).

Given that nitrogenase is located only in the heterocysts of *Anabaena* sp. PCC 7120 (Peterson and Wolk 1978), increasing the heterocyst frequency is a potential strategy to enhance the use of this cyanobacterium for photobiological H₂ production. Heterocyst frequency is known to increase during nitrogen starvation when using an Ar/CO₂ atmosphere, high light intensity (Sarma 2013), molybdenum deficiency (Fay and Vasconce 1974), photo-heterotrophic growth (Ungerer et al. 2008), and in symbiotic association with plants (Meeks 1998; Meeks and Elhai 2002); however, in most cases, these conditions lead to multiple contiguous heterocysts (MCH). Because vegetative cells provide photosynthate (probably in the form of sucrose (Lopez-Igual et al. 2010; Vargas et al. 2011)) to heterocysts, a regular spacing pattern of heterocysts (multiple singular heterocysts, MSH) will be more effective for photobiological H₂ production.

Heterocyst pattern formation is genetically governed. For example, an activator-inhibitor system establishes concentration gradients along the filament of the activator HetR and the two inhibitors PatS and HetN (Risser and Callahan 2009). HetR is a master transcriptional regulator protein required for the expression of many genes involved in heterocyst differentiation and pattern formation (Black et al. 1993; Buikema and Haselkorn 1991; Khudyakov and Golden 2004). Additional genes also participate in heterocyst differentiation and function (Christman et al. 2011; Ehira et al. 2003), with mutations in several of these genes resulting in increased heterocyst frequency (Herrero et al. 2013; Kumar et al. 2010); however, most of the mutants produce filaments with MCH in the absence of combined-nitrogen. In contrast, MSH filaments were observed in mutants overexpressing *patA* (Young-Robbins et al. 2010) or impaired in *patN* (Meeks et al. 2002; Meeks and Elhai 2002; Risser et al. 2012). PatA is suggested to attenuate the inhibitory effects of PatS and HetN on differentiation (Orozco et al. 2006) and PatN is thought to function as a negative regulator of differentiation by limiting the expression of *patA* (Risser et al. 2012). Mutation of *patN* induced by transposon mutagenesis was shown to uniquely cause the MSH phenotype in *Nostoc punctiforme* strain ATCC 29133 (Meeks et al. 2002). A *patN* in-frame deletion mutant of *N. punctiforme* exhibits a three-fold increase in heterocyst frequency and four-fold decrease in the vegetative cell interval between heterocysts, whereas the diazotrophic growth rates and nitrogenase activity are reduced compared with those of the wild-type cells (Risser et al. 2012).

We evaluated the effects of a MSH increase on the photobiological H₂ production of a mutant disrupted in *patN* using the parental strain *Anabaena* sp. PCC 7120 ΔHup. The initial mutant exhibited fragile filaments, but a derived isolate was similar to that from *N. punctiforme* in its MSH phenotype. On the basis of investigations comparing the effects of mutation on photosynthetic pigment composition, cell density, and light intensity on photobiological H₂ production, we demonstrated that the mutant exhibited higher H₂ productivity when grown under the conditions of high light intensity and high cell density due to a decreased susceptibility to photoinhibition than the parental ΔHup strain.

Materials and methods

Bacterial strains and growth conditions

The strains and plasmids used in this study are described in [Supplementary Table S1](#). Cyanobacterial strains derived from *Anabaena* sp. PCC 7120 were grown at 28 °C in an eight-fold dilution of Allen and Arnon (AA/8) liquid medium or non-diluted AA agar (Allen and Arnon 1955) without or with 5 or 10 mM nitrate or 2 mM NH₄Cl (final concentrations). The cultures were bubbled with air or 1% (vol/vol) CO₂-enriched air under continuous illumination using cool white fluorescent lamps at 50 or 90–100 μmol photons m⁻² s⁻¹ of photosynthetically active radiation (PAR), essentially as described previously (Masukawa et al. 2002), unless otherwise indicated. The media were supplemented with either 5 or 20 mM *N*-tris(hydroxymethyl)methyl-2-aminoethanesulfonic acid-KOH buffer (pH 8.2) for bubbling with air or 1% CO₂-enriched air, respectively. *Escherichia coli* cells were grown in lysogeny broth (Bertani 1951) medium at 37 °C.

The chlorophyll *a* (Chl *a*) concentrations of the cultures were determined by the method of Porra (Porra 1991). The absorption spectra from 400 to 750 nm of the whole cells were measured (Shimadzu UV-1800) using 2-mm path quartz cuvettes.

Construction of plasmids and creation of *Anabaena patN* mutants

Based on the complete genomic sequence of *Anabaena* sp. PCC 7120 (Kaneko et al. 2001), a *patN* (alr4812) region of 2.3 kb ([Supplementary Fig. S1a](#)) was amplified by PCR with the primer pairs alr4812-F/alr4812-R using the genomic DNA of the strain and cloned into pBluescript II SK(+), yielding pRL3724. The amplified region in pRL3724 was confirmed by sequencing. The 0.17 kb *Eco*RI internal sequence of *patN* of pRL3724 was deleted and replaced by the 1.3-kb *npt* (Km^r/Nm^r gene)-bearing *Eco*RI fragment of pUC4K, yielding plasmid pRL3730. The resulting plasmid was digested with *Xba*I,

and the 3.4-kb *Xba*I fragment containing the *patN*5'-*npt*-*patN*3' region was ligated into pRL271 (Black et al. 1993) that had been digested with the same enzyme, producing the plasmid pRL3736. This product was introduced into the ΔHup strain by conjugation. Single-crossover recombinant cells were isolated on an AA-plus-nitrate agar plate containing 5 μg/ml erythromycin (Em) and subsequent double-crossover cells were selected by sucrose insensitivity (Cai and Wolk 1990; Masukawa et al. 2002). Among the latter cells, Em-sensitive isolates were selected to identify fully segregated cells. The disruption of *patN* by insertion of the 1.3-kb *npt* sequence and complete segregation of the wild-type version of *patN* were confirmed by the presence/absence of the longer/smaller sizes of PCR-amplified DNA fragments with the primer pair alr4812-F/alr4812-R ([Supplementary Table S1b](#)) and by whole genomic resequencing. The *patN*-disrupted mutant designated PN1 was able to form heterocysts but unable to grow diazotrophically. On further incubation of PN1 cells in AA/8 liquid medium for about 1 month, a spontaneous mutant able to grow on N₂ was obtained (as described in detail in “[Results](#)” and “[Discussion](#)”) and designated PN22; disruption of *patN* in PN22 was confirmed by PCR ([Supplementary Fig. S1b](#)) and by whole genome resequencing.

H₂ production and acetylene reduction assays

Photobiological H₂ production and acetylene reduction to ethylene were measured essentially as described previously (Masukawa et al. 2002). The cells were grown in AA/8-plus-nitrate (5 mM) medium supplemented with 2 mM NH₄Cl to suppress development of heterocysts and nitrogenase activity completely while bubbling with air under illumination (cool white fluorescent lamps, 90–100 μmol photons m⁻² s⁻¹ of PAR). The cultures were subjected to a combined-nitrogen (N) step-down by washing twice, suspending in AA/8 medium to a final concentration of 0.2–0.3 mg Chl *a* liter⁻¹, and growing autotrophically while bubbling with air or 1% CO₂-enriched air. Portions (1 ml containing ca. 2–6 μg of Chl *a*) of the cultures (after N step-down at the day indicated in [Fig. 4](#)) were transferred to 7.5-ml sealed serum bottles and incubated under illumination at the same light intensity on a rotary shaker (80–90 rpm) for 1–1.5 h. The headspace gases in these vials were replaced with Ar for assay of H₂ production or with 15% (vol/vol) C₂H₂ in Ar for assay of C₂H₂ reduction, and the bottles were incubated under illumination for an additional 2–3 h. The concentrations of H₂ in the vial headspaces were measured by gas chromatography (GC; GC-2010 Plus, Shimadzu Co., Ltd., Kyoto, Japan) equipped with a thermal conductivity detector and a Rt-Msieve 5A PLOT capillary column (I.D. 0.53 mm × 50 m, Restek Co., Ltd., USA). Similarly, the

concentrations of C_2H_4 were assessed by GC (Shimadzu GC-8A) equipped with a flame-ion detector and a Porapak N-packed column (80/100 mesh, 2 m by 1/8 in.) as described previously (Masukawa et al. 2010). The activities of H_2 production and C_2H_2 reduction to C_2H_4 were normalized to Chl *a* or to the turbidity (A_{750}) of the cell suspension.

For assays of cumulative H_2 production, cells were grown in AA/8-plus-nitrate (5 mM) medium supplemented with 2 mM NH_4Cl and incubated for 1 day while bubbling with 1% CO_2 -enriched air under continuous illumination (using blue- and red-enhanced fluorescent lamps (Type FL 40 SBR-A, NEC Lighting Co., Ltd., Tokyo, Japan) at 90–100 μmol photons $m^{-2} s^{-1}$ of PAR. These cells were washed and transferred to an AA/8 medium lacking combined-nitrogen at a Chl *a* concentration of 0.5–1.0 mg liter⁻¹ and grown while bubbling with 1% CO_2 -enriched air for 2 days to induce heterocysts and nitrogenase activity. The cells were washed and suspended in BG11₀ medium (Rippka 1988), essentially as previously described (Masukawa et al. 2014). Portions of the cultures (8 ml, containing 30–100 μg of Chl *a*) were transferred into 25-ml sealed serum bottles. The bottles were flushed with Ar, followed by CO_2 addition to a final concentration of 5%. Duplicate or triplicate samples were prepared for each assay, using illumination at the intensities indicated in Figs. 5 and 6 while on a rotary shaker (70–80 rpm). The concentrations of H_2 accumulated in the headspaces were measured by GC, and the headspace gases were renewed to the initial gas composition every day.

Determination of glycogen and sucrose

The contents of glycogen in whole filaments were determined using glucoamylase from *Rhizopus* sp. (Wako Pure Chemical Industries, Ltd., Osaka, Japan) and a mixture of hexokinase/glucose-6-phosphate dehydrogenase from yeast (Roche, Mannheim, Germany). The levels of sucrose in filaments were assessed using β -fructosidase from yeast (Roche). These measurements were carried out according to (Suzuki et al. 2010).

Microscopy

Heterocysts were stained with 0.5% Alcian blue (Sigma), which binds specifically to the polysaccharide layer of heterocyst envelopes. Heterocyst frequency was determined by counting over 500 cells per sample using a microscope, with a dividing vegetative cell counted as two cells. The images were captured with a DP80 digital camera (Olympus, Tokyo, Japan) mounted on an Olympus BX53 microscope. The values are the averages of at least five independent experiments.

Genome resequencing and analysis

Six isolates of the *patN* mutants of *Anabaena* sp. PCC 7120 producing robust filaments and the PN1 reference strain were subjected to genome resequencing by the Department of Energy (DOE) Joint Genome Institute. Secondary mutations found in at least three of the isolates were analyzed by creating homology models of the encoded proteins using the Phyre2 server (data not shown) (Kelley et al. 2015).

Results

Creation of two *patN*-disrupted mutants

Two *patN*-disrupted mutants were derived from the parental ΔHup strain of *Anabaena* sp. PCC 7120 (hereafter referred to as the parental strain) by the following two steps. First, the double-crossover deletion-insertion mutant of *patN* was isolated and designated PN1. When transferred to AA/8 (N-free) medium lacking combined-nitrogen, heterocyst development was delayed by about 1 day for the PN1 mutant compared to the parental strain. This mutant strain formed MSH; however, during further incubation, the filaments fragmented, even when using static liquid culture, with the majority of the PN1 mutant cells appearing to become extinct. About 1 month after nitrogen deprivation, these cells were observed to be growing in the AA/8 (N-free) medium, and a single-colony isolate, referred to as PN22, was selected using an AA (N-free) agar plate. The disruption of *patN* in both PN1 and PN22 was confirmed by PCR (Supplementary Fig. S1b).

In an effort to identify the secondary mutation(s) that conferred a more robust phenotype on the PN1 mutant, we carried out whole genome resequencing of the PN22 and five other isolates generated in the same manner, but we could not point out the common mutation(s) thus far (data not shown).

Heterocyst frequency and diazotrophic growth of the *patN* mutant

The PN22 strain is similar to PN1 in exhibiting the MSH phenotype (Fig. 1). Of great importance, the PN22 isolate grew diazotrophically, after an initial ~2-day lag phase, at rates almost equivalent to those of the parental strain when aerated with air or 1% CO_2 -enriched air (hereafter referred to as under low and high CO_2 conditions, respectively) as measured by Chl *a* content or A_{750} (Fig. 2a–d): N_2 -fixing specific growth rate constants on the basis of Chl *a* under low and high CO_2 conditions were, respectively, 0.24 and 0.17 day⁻¹ in PN22 and 0.27 and 0.19 day⁻¹ in the parental ΔHup strain. The frequencies of heterocysts were greater in the PN22 filaments (13–15%) than in the parental strain (6.5–11%) under low CO_2 conditions (Fig. 2e). This result causes the average



Fig. 1 Heterocyst differentiation in the parental Δ Hup strain (*left*) and the PN22 mutant (*right*). The strains were grown for 2 and 3 days, respectively, in medium lacking combined-nitrogen. Alcian blue stains heterocyst-specific polysaccharide layers in the envelope, while

heterocysts in PN22, even after longer diazotrophic growth, were less stained than those in the parental strain, implying the presence of fewer polysaccharide layers in PN22

heterocyst interval in the PN22 filaments to be shorter than those of the parental strain. This MSH phenotype is essentially consistent with the previous reports on the *patN* mutants of *N. punctiforme* strain ATCC 29133, although the *N. punctiforme* mutants have double the heterocyst frequencies (26–30%) compared with those of the PN22 strain (Meeks et al. 2002; Meeks and Elhai 2002; Risser et al. 2012). Under high CO₂ conditions, the heterocyst frequencies of both *Anabaena* samples were further increased: 16–18% in the PN22 and 9.7–13% in the parental Δ Hup strain (Fig. 2f). Whereas the addition of 1% CO₂ to air resulted in an increase in the frequency of double heterocysts in the parental culture (note the bar corresponding to zero vegetative cells between heterocysts in Supplementary Fig. S2), with occasional triple heterocysts (data not shown), the PN22 filaments maintained the regular pattern of MSH (Supplementary Fig. S2).

A color change from blue-green to yellow-green, such as observed here, is well known to occur after N step-down of cyanobacterial cells due to phycobiliprotein degradation (Allen and Smith 1969; Wood and Haselkorn 1980), a phenomenon termed “nitrogen chlorosis” (Boresch 1910). After development of nitrogen fixation activity, phycobiliproteins were regained and the blue-green color was recovered in the parent Δ Hup cells, but continued bleaching was apparent in the PN22 culture, especially when grown under high CO₂ conditions (Fig. 3). The absorption peak at 620 nm associated with phycocyanin (the most abundant phycobiliprotein in *Anabaena*) gradually increased in the parental strain under both conditions after the initial loss of the absorbance. In

contrast, the peak level in the PN22 cells recovered much more slowly.

Activities of H₂ production and nitrogenase

Induction of H₂ production and nitrogenase activities (determined by acetylene reduction to ethylene) in the PN22 cells was delayed by about 1 day compared with the rates in the parental strain (Fig. 4). Thus, these activities for the PN22 strain peaked at 3–4 days under either low or high CO₂ conditions and then gradually decreased with time. Notably, the rate of the decrease after peaking was slower in the PN22 strain than in the parental strain. The maximum H₂ production and nitrogenase activities of the PN22 strain (normalized on the basis of Chl *a* content and using light intensities of 90–100 $\mu\text{mol photons m}^{-2} \text{s}^{-1}$ of PAR) under low CO₂ conditions at 3 days were approx. 75% of those of the parental strain at 2 days ($p < 0.01$, *t* test) (Fig. 4a). Under high CO₂ conditions, however, the latter strain reached the maximum activities earlier than 2 days after N step-down and the activities before 2 days were not measured (Fig. 4b); thus, we could not compare the maximum levels of the parental strain with those of the PN22.

We found that the levels of sucrose, a source of reductant for nitrogenase, when measured on the Chl *a* basis in whole filaments of the PN22 cells were less than half of those in the parental strain (Fig. 5a, b). On the other hand, the glycogen content, also a source of reductant for nitrogenase in heterocysts, exhibited a sustained higher level in whole filaments of

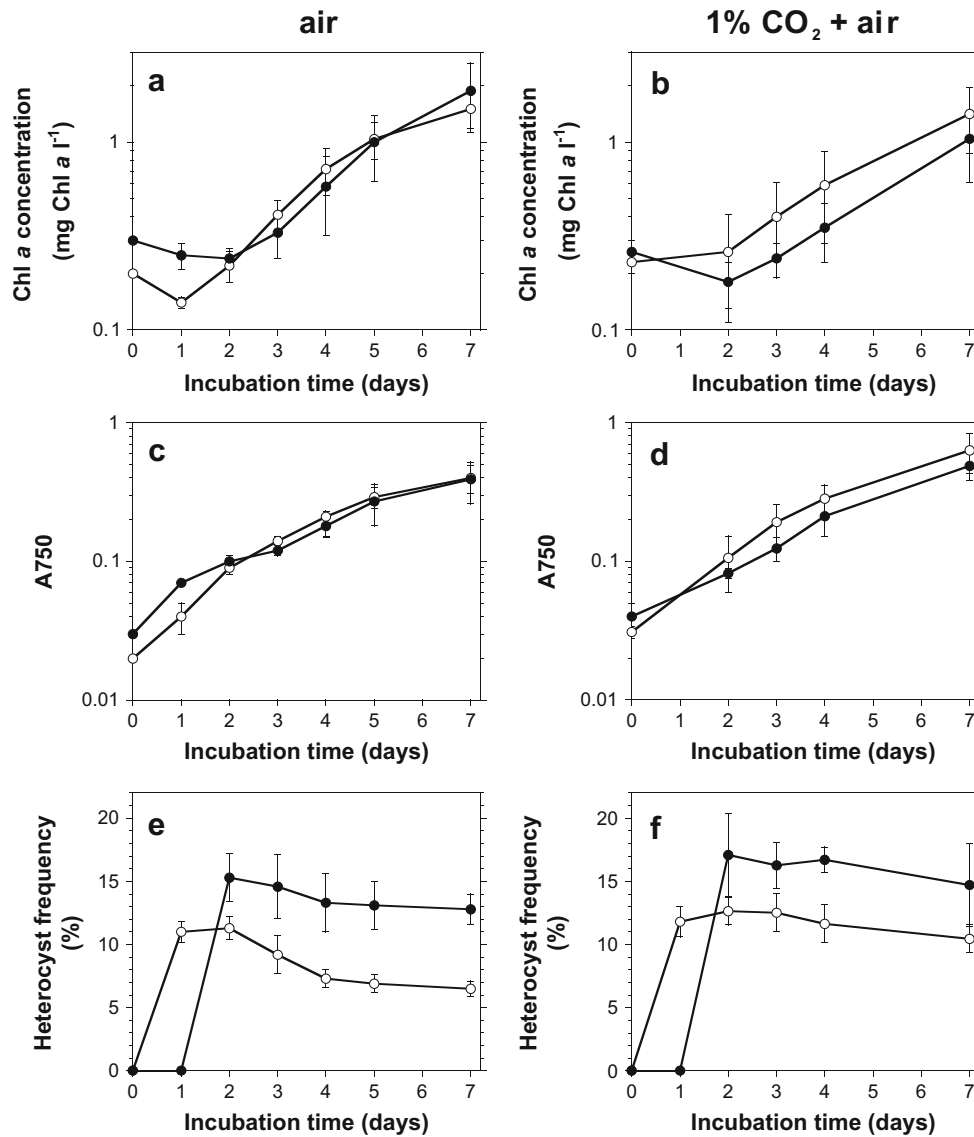


Fig. 2 Time courses of the rates of diazotrophic growth (a, b, c, d) and heterocyst frequencies (e, f) after N step-down. Cultures of the parental Δ Hup strain (open circles) and the PN22 mutant (closed circles) were grown in AA/8 (N-free) medium while bubbling with air (left column) or 1% CO₂-enriched air (right column). Diazotrophic growth was measured on the basis of Chl *a* concentrations (a, b) or by A₇₅₀ (c, d). The specific growth rate constant (i.e., 0.301/doubling time) was calculated over a

24-h period (between 2 and 3 days for the parental Δ Hup strain; 3 and 4 days for the PN22 mutant). Heterocyst frequencies were observed microscopically and the maximum frequencies under low and high CO₂ conditions were significantly higher in the PN22 than in the parental strain ($p < 0.01$, *t* test). Data points and bars represent the means \pm standard deviation of four to five independent experiments

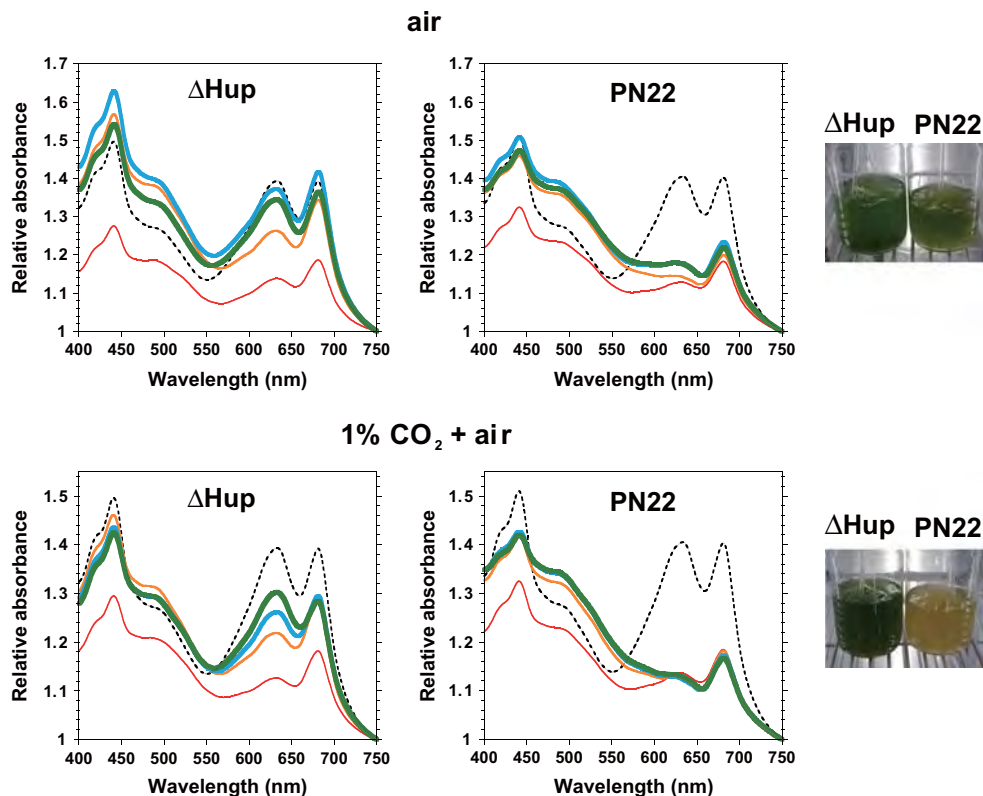
the PN22 than measured in the parental strain, with both strains showing a dramatic increase in the levels of glycogen after N step-down (Fig. 5c, d).

Effect of cell densities and light intensities on cumulative H₂ production

In order to compare the H₂ productivity per unit of illuminated area, varied amounts of Chl *a* contents (8 ml containing 30–100 μ g Chl *a* in 25-ml sealed serum bottles) were incubated in closed bottles under 5% CO₂ in Ar for 4 days, with the

headspace gas renewed every day (Fig. 6). In the absence of N₂, both the Δ Hup and PN22 cultures continued to produce H₂ at high rates over 4 days, similar to the results in our previous study using the Δ Hup cultures (Masukawa et al. 2014). H₂ production of the PN22 strain increased as the Chl *a* content increased from 30 to 100 μ g, whereas that of the parental strain leveled off when Chl *a* contents exceeded 50 μ g under the conditions tested. The cumulative volume of H₂ produced by the PN22 cultures with 100 μ g Chl *a* for 4 days was about 1.7-fold greater than that of the corresponding parental strain ($p < 0.05$, *t* test).

Fig. 3 Time courses and the effects of CO₂ on the whole cell absorption spectra after N step-down. The cultures were bubbled with air (upper row) or 1% CO₂-enriched air (lower row) and the absorption spectra were determined at 0 day (black dashed lines), 1 day (red solid lines), 2 day (orange solid lines), 3 day (green solid lines), and 4 day (blue solid lines) after N step-down. The averaged spectra (6–7 scans) were normalized to 1 at 750 nm. The pictures (right) show the cultures grown under the respective conditions at day 6



We examined the effects of varying light intensity on H₂ productivity by the two strains at different culture densities. H₂ production of the PN22 mutant was generally greater than for the ΔHup strain at the same Chl *a* concentration. Up to an initial Chl *a* content of 50 μg per bottle, the levels of cumulative H₂ produced by these two cultures under 5% CO₂ in Ar for 2 days increased for light intensities ranging from 25 to 100 μmol photons m⁻² s⁻¹ (Fig. 7). The H₂ production of both cultures was enhanced with increasing light intensity up to 100 μmol photons m⁻² s⁻¹. When further increased to 160 μmol photons m⁻² s⁻¹, H₂ production by the ΔHup strain was greatly inhibited, whereas the PN22 culture showed a relatively slight decrease in H₂ productivity.

Discussion

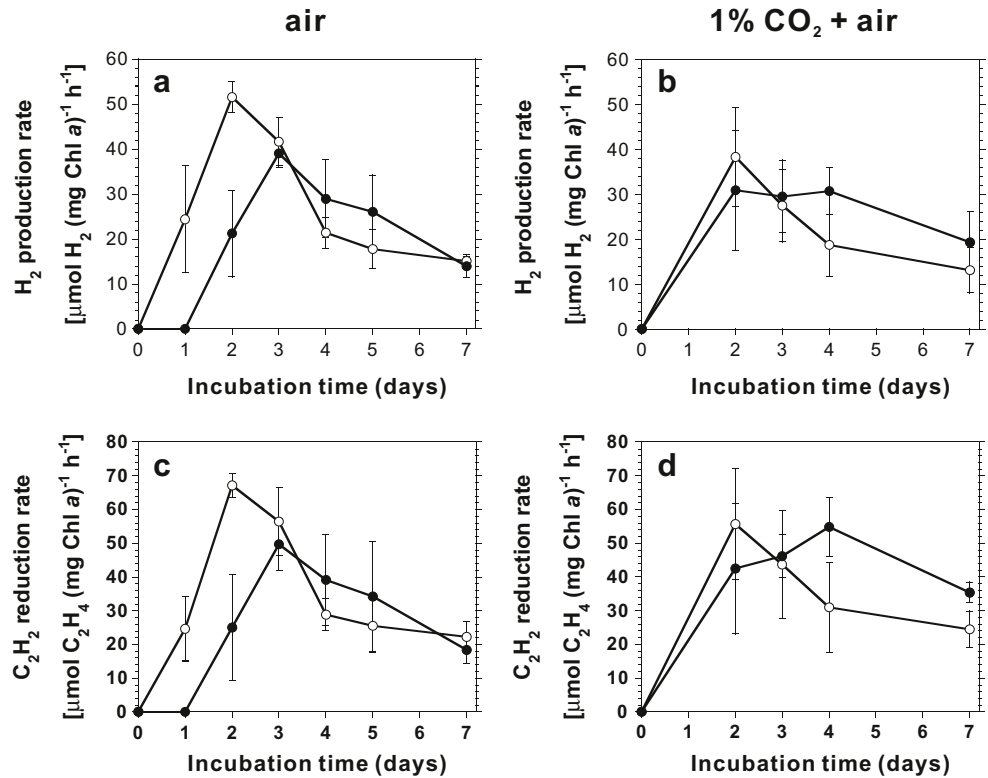
We created a *patN*-disrupted mutant using the parental strain *Anabaena* sp. PCC 7120 ΔHup. The initial mutant (PN1) exhibited fragile filaments and failed to grow in medium free of combined-nitrogen. However, a spontaneous mutant (PN22) was obtained on prolonged incubation of PN1 liquid cultures and shown to be able to grow robustly on N₂. In another heterocyst-forming cyanobacterium, *N. punctiforme* strain ATCC 29133, *patN* mutants were generated by transposon mutagenesis (Meeks et al. 2002; Meeks and Elhai 2002) or by in-frame deletion (Risser et al. 2012) with neither

situation resulting in a similar observation of filament fragility. This observation may relate to the localization and role of PatN; this protein is localized to the cytoplasmic membrane of one-half of the cell before cell division on the basis of predicted membrane spanning segments and fluorescence localization for PatN-GFP (Risser et al. 2012).

The PN22 cells exhibited about a 1-day delay in development of heterocysts and induction of nitrogenase activity compared to the parental strain and increase in the heterocyst frequency up to 16–18% under high CO₂ conditions (Fig. 2f) while maintaining the regular spacing pattern of MSH (Supplementary Fig. S2). Other investigators (Risser et al. 2012) have shown by microarray and qPCR studies of the Δ*patN* strain of *N. punctiforme* ATCC 29133 that the strain exhibits greatly decreased expression of many heterocyst-related and nitrogenase structural genes along with a significant increase in expression of *patA*, whose product is involved in proper patterning of heterocysts during the initial period (between 6 and 24 h) after N step-down (Young-Robbins et al. 2010). Similar changes in expression of the corresponding genes during early stages of differentiation of *Anabaena* sp. PCC 7120 may correspond to the observed delay in heterocyst development and may be related to the regular spacing pattern of heterocysts in the PN22 strain even under high CO₂ conditions.

The slightly lower growth rate of both the ΔHup and PN22 strains, on the basis of Chl *a* contents, under high CO₂

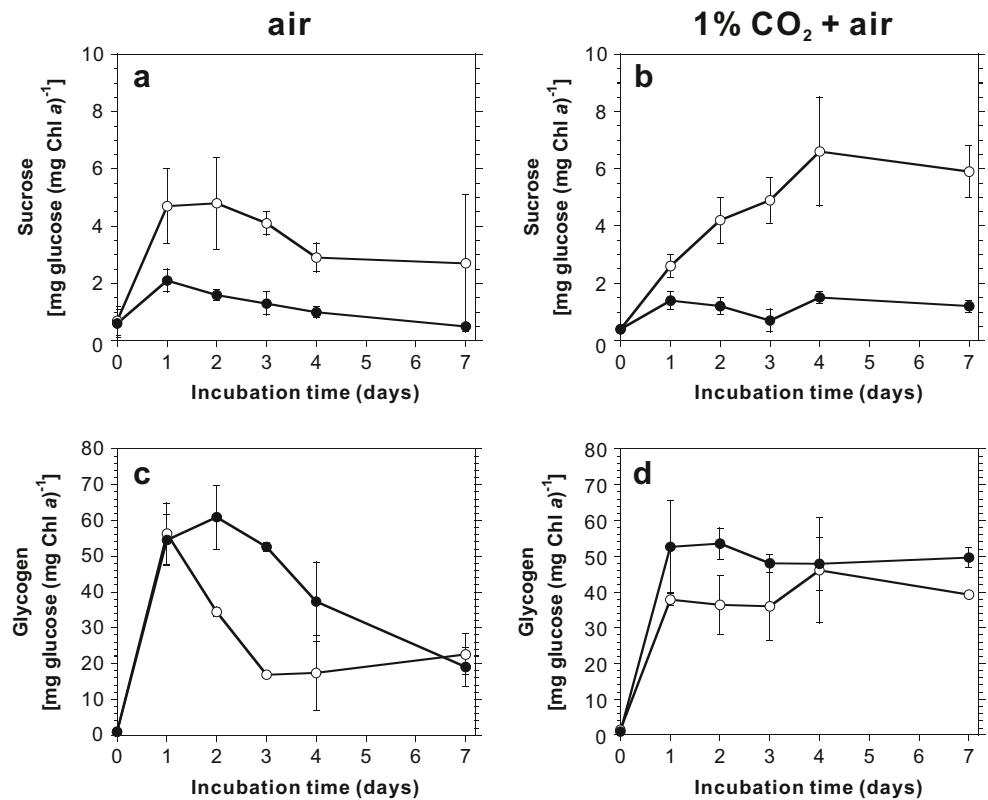
Fig. 4 Time courses of the rates for H₂ production (a, b) and the reduction of acetylene to ethylene (c, d) after N step-down. Growth conditions and the symbols are the same as in Fig. 2. Portions of the cultures were incubated under Ar for measurement of the rates of H₂ production and acetylene reduction. The respective rates were normalized on the basis of Chl *a* concentrations. Data are means ± the standard deviation of three to four independent experiments, each performed with duplicate or triplicate samples



conditions than under low CO₂ conditions (Fig. 2a, b) is likely due to the increase in the number of heterocysts that require substantial amounts of photosynthate for their development

(Murry and Wolk 1989) and also to the degradation of phycobilins (Fig. 3). After N step-down of the parental ΔHup cells, phycobiliprotein is degraded, followed by

Fig. 5 Accumulation of sucrose (a, b) and glycogen (c, d) in whole cells. Growth conditions and symbols are the same as in Fig. 2. Values are the means ± the standard deviation of two to three independent experiments



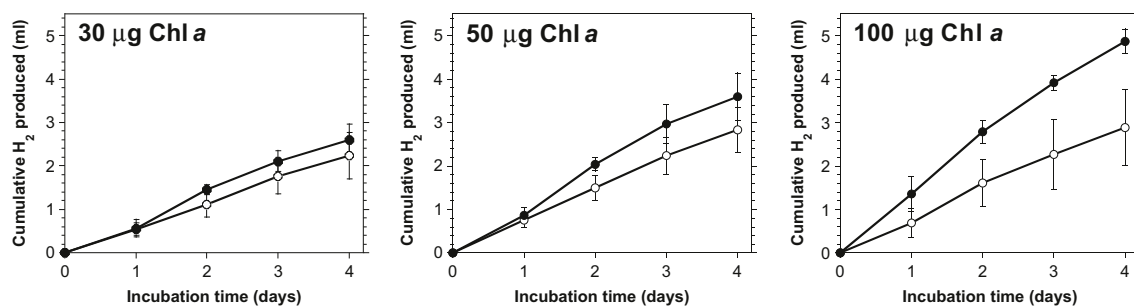


Fig. 6 Effect of cell density on cumulative H₂ production under 5% CO₂ in Ar. Cultures were pre-grown in AA/8 (N-free) medium while bubbling with 1% CO₂-enriched air for 2 days. These culture samples were subsequently incubated at a light intensity of 90–100 µmol photons m⁻² s⁻¹ under 5% CO₂ in Ar with the headspace gas renewed every

day. The initial Chl *a* contents of the cultures at the start of incubation were 30, 50, and 100 µg per vial. The symbols are the same as in Fig. 2. Values are averages of three or four independent experiments, each performed with triplicate samples

gradual increase in phycobiliprotein after development of nitrogen fixation activity (Fig. 3). In contrast, levels of phycobilin contents in the PN22 recovered much more slowly, resulting in continued bleaching especially when grown under high CO₂ conditions. The PN22 cells were capable of diazotrophic growth, so this continued bleaching is unlikely to result from severe nitrogen starvation; rather, this color effect reflects the phenomenon of phycobilin degradation that is widely observed during heterocyst development in various strains of cyanobacteria (Wolk et al. 1994).

The maximum H₂ production activities of the PN22 strain, when measured on the basis of Chl *a* content, under low and high CO₂ conditions were comparable to or not so much lower than those of the parental strain (Fig. 4a, b). As the Chl *a* and phycobilins were degraded to a greater extent in the PN22 culture than in the ΔHup cells on the turbidity basis, the H₂ production rates on the Chl *a* basis may be overestimated for the mutant cells. From the above considerations and analysis of the ratio of the activities to heterocyst frequency (Supplementary Fig. S3), the results indicate that the activity per heterocyst is probably decreased in the PN22 mutant. Nitrogenase activity in heterocysts depends on sucrose and glycogen as sources of reductant (Wolk et al. 1994). The levels of sucrose and glycogen, on the Chl *a* basis in whole filaments

of the PN22 cells, were less than half of and sustained at higher levels than those in the parental strain (Fig. 5). The diminishment in the levels of sucrose might be caused by the decrease in the frequency of vegetative cells relative to heterocysts. Glycogen is known to accumulate in heterocysts that are isolated from the filaments at about eight-fold higher levels than in the vegetative cells of *Anabaena* sp. PCC 7120 when bubbled with 1% CO₂-enriched air (Valladares et al. 2007). These results suggest that although the sucrose levels in the PN22 filaments were significantly reduced, sufficient amounts were present to allow the accumulation of glycogen at high sustained levels comparable to those in the parental strain.

It is interesting that the *patN* mutants of *N. punctiforme* strain ATCC 29133 exhibit a greater decrease in diazotrophic growth and about 60% of the maximum nitrogenase activity of the wild-type cells, on a Chl *a* basis, with a ~2-week delay in reaching the maximum enzyme level (Risser et al. 2012). The reason for the phenotypic differences in the *N. punctiforme* versus *Anabaena patN* mutants is uncertain.

The H₂ productivity per unit of illuminated area by varied amounts of Chl *a* contents under 5% CO₂ in Ar were compared (Fig. 6). H₂ production of the PN22 strain increased with increasing the Chl *a* content ranging from 30

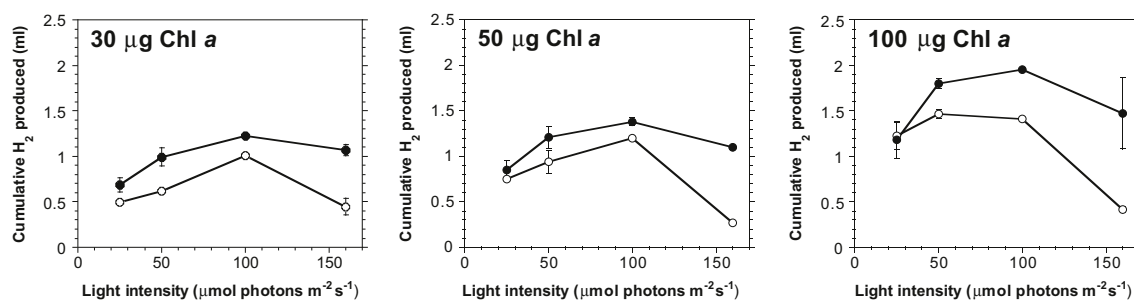


Fig. 7 Effect of light intensity on cumulative H₂ production under 5% CO₂ in Ar. Growth conditions and assays were as described in Fig. 6, with the exception that the samples were incubated at varied light intensities

for 2 days. The symbols are the same as in Fig. 2. A replicate experiment provided analogous results

100 µg, leading to about 1.7-fold greater cumulative volume of H₂ produced by the PN22 cultures with 100 µg Chl *a* for 4 days than that of the corresponding parental strain. These results are consistent with an increase in heterocyst frequency leading to increased H₂ production per unit of light-receiving area under these conditions. The effects of varying light intensity on H₂ productivity of the two strains at different culture densities were examined. The PN22 mutant generally showed greater H₂ production than the ΔHup strain at the same Chl *a* concentration (Fig. 7). In addition, when light intensity increased up to 160 µmol photons m⁻² s⁻¹, H₂ production by the ΔHup strain was greatly inhibited, whereas H₂ productivity by the PN22 culture was relatively slightly decreased. These results indicate the PN22 cells were much less susceptible to photoinhibition by strong light than the parental strain.

In order to maximize the photosynthetic efficiency and culture productivity, truncation of the antenna pigment has been shown to be an effective strategy in cyanobacteria (Nakajima et al. 1998; Nakajima and Ueda 1997) and in other photosynthetic microalgae (summarized in (Melis 2009)). It was explained that in those mutants, light absorption by individual cells is minimized, allowing for less photoinhibition and greater penetration of irradiance through the culture and consequently enhanced photosynthetic productivity by a high-density culture (Melis 2009).

In conclusion, we have shown that a non-fragile variant of the *patN* deletion mutant formed MSH and maintained heterocyst spacing even under high CO₂ conditions, in contrast to the parental ΔHup strain which formed relatively frequent double heterocysts under such conditions. The PN22 mutant was capable of normal diazotrophic growth compared to the parental strain, with about a 1-day delay in development of heterocysts and expression of nitrogenase activity. Furthermore, the PN22 strain was less susceptible to inhibition by strong light than the parent ΔHup cells. In addition, the PN22 culture showed higher light energy utilization efficiency in H₂ production activity on a per unit culture area basis compared to the ΔHup culture. The increase in heterocyst frequency shown here appears to be a viable strategy for enhancing H₂ productivity by outdoor cultures of cyanobacteria in high-light environments.

Acknowledgments This work was supported by the Precursory Research for Embryonic Science and Technology (PRESTO) and the Core Research for Evolutional Science and Technology (CREST) programs of the Japan Science and Technology Agency (JST) (to HM), the Great Lakes Bioenergy Research Center (the Department of Energy (DOE) Office of Science DE-FC02-07ER64494) (to RPH), and in part by grant-in-aid for Scientific Research on Innovative Areas (No. 24107004) and Strategic Research Base Development Program for Private Universities from the Ministry of Education Culture, Sports, Science, and Technology, Japan (to KI). We acknowledge the DOE Joint Genome Institute for resequencing the *Anabaena* sp. PCC 7120 *patN* mutant isolates and we thank Dr. Peter Wolk for the helpful discussions and assistance with our research, Dr. Akio Murakami for the

valuable comments and suggestions on the manuscript, and Miho Hosoya for the assistance with the experiments.

Compliance with ethical standards This article does not contain any studies with human participants or animals performed by any of the authors.

Conflict of interest The authors declare that they have no conflict of interest.

References

- Allen MB, Amon DI (1955) Studies on nitrogen-fixing blue-green algae. I. Growth and nitrogen fixation by *Anabaena cylindrica* Lemm. Plant Physiol 30(4):366–372. doi:10.1104/pp.30.4.366
- Allen MM, Smith AJ (1969) Nitrogen chlorosis in blue-green algae. Arch Mikrobiol 69(2):114–120. doi:10.1007/Bf00409755
- Bertani G (1951) Studies on lysogenesis. I. The mode of phage liberation by lysogenic *Escherichia coli*. J Bacteriol 62(3):293–300
- Black TA, Cai YP, Wolk CP (1993) Spatial expression and autoregulation of *hetR*, a gene involved in the control of heterocyst development in *Anabaena*. Mol Microbiol 9(1):77–84. doi:10.1111/j.1365-2958.1993.tb01670.x
- Boresch K (1910) Zur physiologie der blaulagenfarbstoffe. Lotos (Prag) 58:344–345
- Bothe H, Schmitz O, Yates MG, Newton WE (2010) Nitrogen fixation and hydrogen metabolism in cyanobacteria. Microbiol Mol Biol Rev 74(4):529–551. doi:10.1128/mmbr.00033-10
- Buikema WJ, Haselkorn R (1991) Characterization of a gene controlling heterocyst differentiation in the cyanobacterium *Anabaena* 7120. Genes Dev 5(2):321–330. doi:10.1101/gad.5.2.321
- Burnat M, Herrero A, Flores E (2014) Compartmentalized cyanophycin metabolism in the diazotrophic filaments of a heterocyst-forming cyanobacterium. Proc Natl Acad Sci U S A 111(10):3823–3828. doi:10.1073/pnas.1318564111
- Cai YP, Wolk CP (1990) Use of a conditionally lethal gene in *Anabaena* sp. strain PCC 7120 to select for double recombinants and to entrap insertion sequences. J Bacteriol 172(6):3138–3145
- Christman HD, Campbell EL, Meeks JC (2011) Global transcription profiles of the nitrogen stress response resulting in heterocyst or hormogonium development in *Nostoc punctiforme*. J Bacteriol 193(24):6874–6886. doi:10.1128/Jb.05999-11
- Ehira S, Ohmori M, Sato N (2003) Genome-wide expression analysis of the responses to nitrogen deprivation in the heterocyst-forming cyanobacterium *Anabaena* sp. strain PCC 7120. DNA Res 10(3):97–113. doi:10.1093/dnares/10.3.97
- Fay P, Vasconce L (1974) Nitrogen metabolism and ultrastructure in *Anabaena cylindrica*. II. The effect of molybdenum and vanadium. Arch Microbiol 99(3):221–230. doi:10.1007/Bf00696236
- Finzi-Hart JA, Pett-Ridge J, Weber PK, Popp R, Fallon SJ, Gunderson T, Hutcheon ID, Neelson KH, Capone DG (2009) Fixation and fate of C and N in the cyanobacterium *Trichodesmium* using nanometer-scale secondary ion mass spectrometry. Proc Natl Acad Sci U S A 106(15):6345–6350. doi:10.1073/pnas.0810547106
- Happe T, Schütz K, Böhme H (2000) Transcriptional and mutational analysis of the uptake hydrogenase of the filamentous cyanobacterium *Anabaena variabilis* ATCC 29413. J Bacteriol 182(6):1624–1631. doi:10.1128/Jb.182.6.1624-1631.2000
- Herrero A, Picossi S, Flores E (2013) Gene expression during heterocyst differentiation. Genomics of Cyanobacteria 65:281–329. doi:10.1016/B978-0-12-394313-2.00008-1
- Kaneko T, Nakamura Y, Wolk CP, Kuritz T, Sasamoto S, Watanabe A, Iriguchi M, Ishikawa A, Kawashima K, Kimura T, Kishida Y,

- Korhara M, Matsumoto M, Matsuno A, Muraki A, Nakazaki N, Shimpo S, Sugimoto M, Takazawa M, Yamada M, Yasuda M, Tabata S (2001) Complete genomic sequence of the filamentous nitrogen-fixing cyanobacterium *Anabaena* sp. strain PCC 7120. *DNA Res* 8:205–213. doi:10.1093/dnares/8.5.205
- Kelley LA, Mezulis S, Yates CM, Wass MN, Sternberg MJE (2015) The Phyre2 web portal for protein modeling, prediction and analysis. *Nat Protoc* 10(6):845–858. doi:10.1038/nprot.2015.053
- Khudyakov IY, Golden JW (2004) Different functions of HetR, a master regulator of heterocyst differentiation in *Anabaena* sp. PCC 7120, can be separated by mutation. *Proc Natl Acad Sci U S A* 101(45):16040–16045. doi:10.1073/pnas.0405572101
- Kitashima M, Masukawa H, Sakurai H, Inoue K (2012) Flexible plastic bioreactors for photobiological hydrogen production by hydrogenase-deficient cyanobacteria. *Biosci Biotechnol Biochem* 76(4):831–833. doi:10.1271/bbb.110808
- Kumar K, Mella-Herrera RA, Golden JW (2010) Cyanobacterial heterocysts. *Cold Spring Harb Perspect Biol* 2(4):ARTN a000315. doi:10.1101/cshperspect.a000315
- Lopez-Igual R, Flores E, Herrero A (2010) Inactivation of a heterocyst-specific invertase indicates a principal role of sucrose catabolism in heterocysts of *Anabaena* sp. *J Bacteriol* 192(20):5526–5533. doi:10.1128/Jb.00776-10
- Masukawa H, Inoue K, Sakurai H, Wolk CP, Hausinger RP (2010) Site-directed mutagenesis of the *Anabaena* sp. strain PCC 7120 nitrogenase active site to increase photobiological hydrogen production. *Appl Environ Microbiol* 76(20):6741–6750. doi:10.1128/AEM.01056-10
- Masukawa H, Mochimaru M, Sakurai H (2002) Disruption of the uptake hydrogenase gene, but not of the bidirectional hydrogenase gene, leads to enhanced photobiological hydrogen production by the nitrogen-fixing cyanobacterium *Anabaena* sp. PCC 7120. *Appl Microbiol Biotechnol* 58(5):618–624. doi:10.1007/s00253-002-0934-7
- Masukawa H, Sakurai H, Hausinger RP, Inoue K (2014) Sustained photobiological hydrogen production in the presence of N₂ by nitrogenase mutants of the heterocyst-forming cyanobacterium *Anabaena*. *Int J Hydrogen Energ* 39(34):19444–19451. doi:10.1016/j.ijhydene.2014.09.090
- Masukawa H, Zhang XH, Yamazaki E, Iwata S, Nakamura K, Mochimaru M, Inoue K, Sakurai H (2009) Survey of the distribution of different types of nitrogenases and hydrogenases in heterocyst-forming cyanobacteria. *Mar Biotechnol* 11(3):397–409. doi:10.1007/s10126-008-9156-z
- Meeks JC (1998) Symbiosis between nitrogen-fixing cyanobacteria and plants—the establishment of symbiosis causes dramatic morphological and physiological changes in the cyanobacterium. *Bioscience* 48(4):266–276. doi:10.2307/1313353
- Meeks JC, Campbell EL, Summers ML, Wong FC (2002) Cellular differentiation in the cyanobacterium *Nostoc punctiforme*. *Arch Microbiol* 178(6):395–403. doi:10.1007/s00203-002-0476-5
- Meeks JC, Elhai J (2002) Regulation of cellular differentiation in filamentous cyanobacteria in free-living and plant-associated symbiotic growth states. *Microbiol Mol Biol Rev* 66(1):94–121. doi:10.1128/MMBR.66.1.94-121.2002
- Melis A (2009) Solar energy conversion efficiencies in photosynthesis: minimizing the chlorophyll antennae to maximize efficiency. *Plant Sci* 177(4):272–280. doi:10.1016/j.plantsci.2009.06.005
- Murry MA, Wolk CP (1989) Evidence that the barrier to the penetration of oxygen into heterocysts depends upon two layers of the cell envelope. *Arch Microbiol* 151(6):469–474. doi:10.1007/BF00454860
- Nakajima Y, Tsuzuki M, Ueda R (1998) Reduced photoinhibition of a phycocyanin-deficient mutant of *Synechocystis* PCC 6714. *J Appl Phycol* 10(5):447–452. doi:10.1023/A:1008049901939
- Nakajima Y, Ueda R (1997) Improvement of photosynthesis in dense microalgal suspension by reduction of light harvesting pigments. *J Appl Phycol* 9(6):503–510. doi:10.1023/A:1007920025419
- Orozco CC, Risser DD, Callahan SM (2006) Epistasis analysis of four genes from *Anabaena* sp. strain PCC 7120 suggests a connection between PatA and PatS in heterocyst pattern formation. *J Bacteriol* 188(5):1808–1816. doi:10.1128/JB.188.5.1808-1816.2006
- Peterson RB, Wolk CP (1978) High recovery of nitrogenase activity and of ⁵⁵Fe-labeled nitrogenase in heterocysts isolated from *Anabaena variabilis*. *Proc Natl Acad Sci U S A* 75(12):6271–6275. doi:10.1073/pnas.75.12.6271
- Porra RJ (1991) Recent advances and re-assessments in chlorophyll extraction and assay procedures for terrestrial, aquatic, and marine organisms, including recalcitrant algae. In: Scheer H (ed) *Chlorophylls*. CRC Press, Boca Raton, FL, pp 31–57
- Prince RC, Ksheshgi HS (2005) The photobiological production of hydrogen: potential efficiency and effectiveness as a renewable fuel. *Crit Rev Microbiol* 31(1):19–31. doi:10.1080/10408410590912961
- Rippka R (1988) Isolation and purification of cyanobacteria. *Meth Enzymol* 167:3–27
- Risser DD, Callahan SM (2009) Genetic and cytological evidence that heterocyst patterning is regulated by inhibitor gradients that promote activator decay. *Proc Natl Acad Sci U S A* 106(47):19884–19888. doi:10.1073/pnas.0909152106
- Risser DD, Wong FCY, Meeks JC (2012) Biased inheritance of the protein PatN frees vegetative cells to initiate patterned heterocyst differentiation. *Proc Natl Acad Sci U S A* 109(38):15342–15347. doi:10.1073/pnas.1207530109
- Sakurai H, Masukawa H (2007) Promoting R & D in photobiological hydrogen production utilizing mariculture-raised cyanobacteria. *Mar Biotechnol* 9(2):128–145. doi:10.1007/s10126-006-6073-x
- Sakurai H, Masukawa H, Kitashima M, Inoue K (2013) Photobiological hydrogen production: bioenergetics and challenges for its practical application. *J Photoch Photobio C* 17:1–25. doi:10.1016/j.jphotochemrev.2013.05.001
- Sakurai H, Masukawa H, Kitashima M, Inoue K (2015) How close we are to achieving commercially viable large-scale photobiological hydrogen production by cyanobacteria: a review of the biological aspects. *Life* 5(1):997–1018. doi:10.3390/life5010997
- Sarma TA (2013) *Heterocyst. Handbook of cyanobacteria*. CRC Press, Boca Raton, FL, pp 165–280
- Suzuki E, Ohkawa H, Moriya K, Matsubara T, Nagaike Y, Iwasaki I, Fujiwara S, Tsuzuki M, Nakamura Y (2010) Carbohydrate metabolism in mutants of the cyanobacterium *Synechococcus elongatus* PCC 7942 defective in glycogen synthesis. *Appl Environ Microbiol* 76(10):3153–3159. doi:10.1128/Aem.00397-08
- Tamagnini P, Leitão E, Oliveira P, Ferreira D, Pinto F, Harris DJ, Heidom T, Lindblad P (2007) Cyanobacterial hydrogenases: diversity, regulation and applications. *FEMS Microbiol Rev* 31(6):692–720. doi:10.1111/j.1574-6976.2007.00085.x
- UNFCCC (2016) The Paris agreement. http://unfccc.int/paris_agreement/items/9485.php Accessed 5 Oct 2016
- Ungerer JL, Pratte BS, Thiel T (2008) Regulation of fructose transport and its effect on fructose toxicity in *Anabaena* spp. *J Bacteriol* 190(24):8115–8125. doi:10.1128/JB.00886-08
- Valladares A, Maldener I, Muro-Pastor AM, Flores E, Herrero A (2007) Heterocyst development and diazotrophic metabolism in terminal respiratory oxidase mutants of the cyanobacterium *Anabaena* sp. strain PCC 7120. *J Bacteriol* 189(12):4425–4430. doi:10.1128/JB.00220-07
- Vargas WA, Nishi CN, Giarocco LE, Salerno GL (2011) Differential roles of alkaline/neutral invertases in *Nostoc* sp. PCC 7120: Inv-B isoform is essential for diazotrophic growth. *Planta* 233(1):153–162. doi:10.1007/s00425-010-1288-5

- Wolk CP, Ernest A, Elhai J (1994) Heterocyst metabolism and development. In: Bryant DA (ed) *The molecular biology of cyanobacteria*. Springer (Kluwer Academic Publishers), Dordrecht, pp 769–823
- Wood NB, Haselkom R (1980) Control of phycobiliprotein proteolysis and heterocyst differentiation in *Anabaena*. *J Bacteriol* 141(3): 1375–1385
- Yoshino F, Ikeda H, Masukawa H, Sakurai H (2007) High photobiological hydrogen production activity of a *Nostoc* sp. PCC 7422 uptake hydrogenase-deficient mutant with high nitrogenase activity. *Mar Biotech* 9(1):101–112. doi:[10.1007/s10126-006-6035-3](https://doi.org/10.1007/s10126-006-6035-3)
- Young-Robbins SS, Risser DD, Moran JR, Haselkom R, Callahan SM (2010) Transcriptional regulation of the heterocyst patterning gene *patA* from *Anabaena* sp. strain PCC 7120. *J Bacteriol* 192(18): 4732–4740. doi:[10.1128/Jb.00577-10](https://doi.org/10.1128/Jb.00577-10)

Synthesis of ϵ -Keggin-Type Cobaltomolybdate-Based 3D Framework Material and Characterization Using Atomic-Scale HAADF-STEM and XANES

Takumi Igarashi,[†] Zhenxin Zhang,[‡] Terufumi Haioka,[†] Nao Iseki,[†] Norihito Hiyoshi,^{||} Norihito Sakaguchi,[⊥] Chisato Kato,[#] Sadafumi Nishihara,^{#,∇} Katsuya Inoue,^{#,∇} Akira Yamamoto,^{◇,○} Hisao Yoshida,^{◇,○} Nao Tsunoji,[†] Wataru Ueda,[‡] Tsuneji Sano,[†] and Masahiro Sadakane^{*,†,§,ⓧ}

[†]Department of Applied Chemistry, Graduate School of Engineering, Hiroshima University, 1-4-1 Kagamiyama, Higashi Hiroshima 739-8527, Japan

[§]JST, PRESTO, 4-1-8 Honcho, Kawaguchi, Saitama 332-0012, Japan

[‡]Faculty of Engineering, Kanagawa University, Rokkakubashi, Kanagawa-ku, Yokohama-shi, Kanagawa 221-8686, Japan

^{||}Research Institute for Chemical Process Technology, National Institute of Advanced Industrial Science and Technology (AIST), 4-2-1 Nigatake, Miyagino, Sendai 983-8551, Japan

[⊥]Faculty of Engineering, Hokkaido University, N-13, W-8, Sapporo 060-8626, Japan

[#]Graduate School of Science & Center for Chiral Science, Hiroshima University, 1-3-1. Kagamiyama, 732-8526, Higashi-Hiroshima, Japan

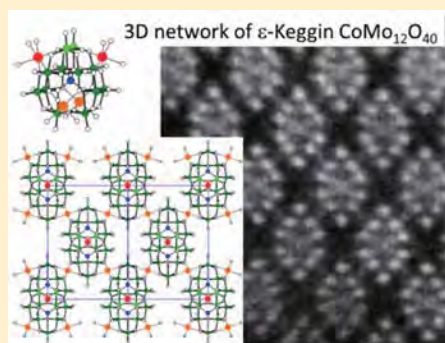
[∇]Institute for Advanced Materials Research, Hiroshima University & Natural Science Center for Basic Research and Development, 1-3-1, Kagamiyama, Higashi Hiroshima, Hiroshima 739-8526, Japan

[◇]Graduate School of Human and Environmental Studies, Kyoto University, Yoshida-nihonmatsu-cho, Sakyo-ku, Kyoto 606-8501, Japan

[○]Elements Strategy Initiative for Catalysts & Batteries (ESICB), Kyoto University, Kyotodaigaku Katsura, Nishikyo, Kyoto 615-8520, Japan

Supporting Information

ABSTRACT: We describe the preparation of ϵ -Keggin-type cobaltomolybdate-based 3D frameworks with sodium cations, $\text{NaH}_9[\epsilon\text{-Co}^{\text{II}}\text{Mo}^{\text{V}}_8\text{Mo}^{\text{VI}}_4\text{O}_{40}\text{Co}^{\text{II}}_2]$, and their characterization by high-resolution high-angle annular dark-field scanning transmission electron microscopy (HAADF-STEM) and X-ray absorption fine structure (XAFS) spectroscopy. Atomic-scale HAADF-STEM images of ϵ -Keggin compounds were obtained for the first time, and positions of Mo and Co were confirmed. Furthermore, clear evidence of the presence of a CoO_4 tetrahedron was obtained by X-ray absorption near-edge structure (XANES) analysis. Their characterization clearly revealed that ϵ -Keggin-type cobaltomolybdate units, $[\epsilon\text{-CoMo}_{12}\text{O}_{40}]^{n-}$, constructed by a central $\text{Co}^{\text{II}}\text{O}_4$ tetrahedron and 12 surrounding MoO_6 octahedra, are linked with Co^{II} to form 3D frameworks.



INTRODUCTION

Polyoxometalates (POMs) are anionic metal oxide clusters comprised of early transition metals such as tungsten (W) and molybdenum (Mo) as main metals. POMs show multielectron transfer properties and strong acidic properties, and their molecular properties are tunable by changing their structures and component elements.^{1,2} They have therefore been used as functional materials such as catalysts and electrode materials.^{1,2}

Recently, much attention has been paid to the ϵ -isomer of Keggin-type polyoxomolybdates composed of one central XO_4 tetrahedron and 12 surrounding MoO_6 octahedra with T_d symmetry (Figure 1a and 1b).³ The ϵ -isomer is formed by

rotation of four edge-sharing Mo_3O_{13} units of the most well-known α -isomer. Three oxygen atoms of four hexagonal faces of the ϵ -Keggin POM are able to bind to many metal ions such as transition metals and lanthanide metals (Figure 1c), and the rest of the coordination sites of the transition metals and lanthanide metals are bound to other ligands.

The four transition metals and lanthanide metals can also be coordinated by organic ligands, resulting in the formation of organic–inorganic hybrid materials. It is also possible to

Received: November 14, 2016

Published: February 9, 2017

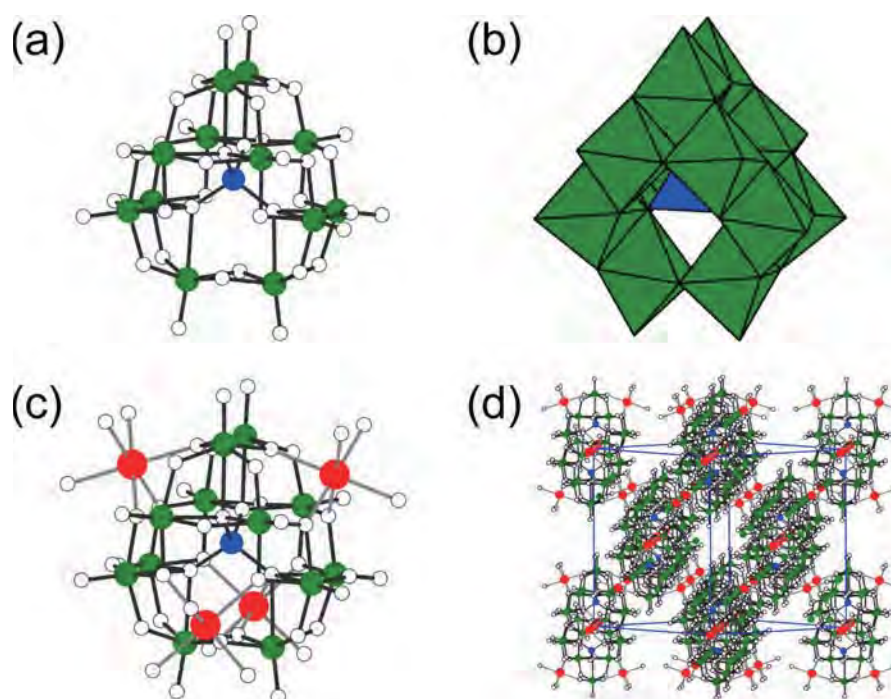


Figure 1. Structure of ϵ -Keggin-type POM: (a and c) ball-and-stick representations, (b) polyhedral representation, and (d) ball-and-stick representation of the 3D framework structure produced by connection of ϵ -Keggin-type POM with a metal linker. Blue balls, green balls, and red balls represent central sites, surrounding sites, and linker sites, respectively.

connect the ϵ -isomer of Keggin-type polyoxomolybdates by multidentate organic ligands to form a 3D framework, and Dolbecq's group and others have reported the ϵ -isomer of Keggin-type polyoxomolybdate-based organic–inorganic hybrid framework materials.^{3,4} Ohkoshi's group reported a framework material in which $[\text{Fe}(\text{CN})_6]^{4-}$ bridged the ϵ -isomer of Keggin-type $[\text{PMo}_{12}\text{O}_{36}(\text{OH})_4(\text{La}(\text{H}_2\text{O})_5)_4]$ to form $(\text{Fe}(\text{CN})_6)[\text{PMo}_{12}\text{O}_{36}(\text{OH})_4(\text{La}(\text{H}_2\text{O})_5)_4]$.⁵

Recently, we reported the first all-inorganic 3D framework composed of ϵ -Keggin polyoxovanadomolybdate, $[\epsilon\text{-VMo}_{9,4}\text{V}_{2,6}\text{O}_{40}]$, with a Bi linker (denoted as **Mo–V–Bi oxide**) (Figure 1d).^{6,7} One VO_4 tetrahedron (V occupying the central site) is surrounded by 12 MoO_6 octahedra (M occupying surrounding sites) of Mo and V to form $[\epsilon\text{-VMo}_{9,4}\text{V}_{2,6}\text{O}_{40}]$ which is linked by Bi^{III} cations (Bi occupying linker sites) to form a 3D framework. This structure was confirmed by single-crystal structure analysis, bond valence sum calculation, elemental analysis, and X-ray photoelectron spectroscopy (XPS). Ten $[\epsilon\text{-VMo}_{9,4}\text{V}_{2,6}\text{O}_{40}]$ units and Bi linkers surround a cage that is connected by channels, forming a zigzag 3D pore system. Compared with organic–inorganic POM-based framework compounds, **Mo–V–Bi oxide** is thermally more stable, and it is stable up to 350 °C, a temperature at which most organic derivatives start to decompose.⁶ Thus, water and ammonium cations present in the pores can be removed by thermal treatment, and the opened pores are analyzable by the gas adsorption–desorption technique. This compound can be used as an acid catalyst⁶ and Li-battery cathode material.⁸

One of the important properties of POMs is diversity of the elements in the structures, and it is desirable for many kinds of elements to be incorporated in the structures of ϵ -Keggin POM-based 3D frameworks. We have reported the synthesis

and characterization of ϵ -Keggin-type polyoxomolybdates with Zn and Mn (denoted as **Mo–Zn oxide** and **Mo–Mn oxide**, respectively).^{9,10} We could not grow a single crystal large enough for single-crystal structure analysis. Therefore, in these oxides, we proposed that one ZnO_4 or MnO_4 tetrahedron is surrounded by 12 MoO_6 octahedra to form ϵ -Keggin 1-zinc-12-molybdate or 1-manganese-12-molybdate that is linked by Zn^{II} or Mn^{II} , respectively, for the following two reasons. (1) Elemental ratios of Zn: Mo and Mn: Mo were 3:12 and 2.2:12 for **Mo–Zn oxide** and **Mo–Mn oxide**, respectively. These results are consistent with the surrounding site of ϵ -Keggin units being occupied by Mo and the central site and linker sites being occupied by Zn or Mn. (2) Simulated XRD profiles obtained by using the proposed models were close to the observed XRD profiles. However, it is necessary to show additional confirmation of these structures because XRD profiles are decided by the heaviest metal, Mo, and effects of relatively light elements such as Zn and Mn on the XRD profile are too small to be distinguished.

Here, we describe the preparation and structural characterization of a new member of all-inorganic ϵ -Keggin POM-based 3D frameworks with cobalt ions (Co^{II}), $\text{NaH}_9[\epsilon\text{-Co}^{\text{II}}\text{Mo}^{\text{V}}\text{Mo}^{\text{VI}}_4\text{O}_{40}\text{Co}^{\text{II}}_2]$, denoted as **Na–Mo–Co oxide**. First, the effects of synthesis conditions on formation of the desired product are described. Then the results of detailed structural analysis by using atom-level HAADF-STEM together with powder X-ray diffraction, FT-IR, Raman spectroscopy, XPS, XAFS, magnetic measurement, and elemental analysis are presented. The results clearly indicate that Co^{II} ions are located exclusively on both the central site and the linker site and that Mo is exclusively located on the surrounding sites.

EXPERIMENTAL SECTION

Materials. Chemicals were reagent grade and used as supplied, and house-made distilled water was used throughout. The **Mo–Zn oxide** ($\text{Na}_{1.5}\text{H}_{11.4}[\epsilon\text{-Zn}^{\text{II}}\text{Mo}^{\text{V}}_{10.9}\text{Mo}^{\text{VI}}_{1.1}\text{O}_{46}\text{Zn}^{\text{II}}_2]$) was prepared according to our previous paper.⁹ ZnCO_3O_4 and CoAl_2O_4 for Co-K-edge XAFS were prepared according to a previous report,¹¹ and formation of the desired phase was confirmed by powder XRD.

Synthesis of $\text{NaH}_9[\epsilon\text{-Co}^{\text{II}}\text{Mo}^{\text{V}}_8\text{Mo}^{\text{VI}}_4\text{O}_{40}\text{Co}^{\text{II}}_2]\cdot 8\text{H}_2\text{O}$ (Na–Mo–Co oxide). $\text{Na}_2\text{MoO}_4\cdot 2\text{H}_2\text{O}$ (2.823 g, 11.7 mmol based on Mo) was dissolved in 40 mL of distilled water. Metal Mo (0.2 g, 2.1 mmol) and $\text{CoCl}_2\cdot 6\text{H}_2\text{O}$ (0.785 g, 3.3 mmol) were added to the mixture sequentially, and the mixture was stirred for 10 min at room temperature, followed by adjustment of pH to 4.8 with 1 M H_2SO_4 . The mixture was introduced into a 50 mL Teflon liner of a stainless-steel autoclave (TAF-SR 50 mL, TAIATSU Techno. Japan). The autoclave was placed in an oven heated at 170 °C for 24 h. After the autoclave had been cooled down to room temperature, most of the upper solution was removed to obtain the solid on the bottom of the Teflon liner. Water was added to the solid until the amount of the mixture was ca. 90 mL. The mixture was stirred and then centrifuged at 3500 rpm for 3 min using a KOKUSAN H-27F centrifugation apparatus. Most of the upper solution was removed to obtain the solid. Water was added to the solid until the amount of mixture was ca. 90 mL. The mixture was stirred and then centrifuged at 1700 rpm for 2 min using a KOKUSAN H-27F centrifugation apparatus. Most of the upper solution was collected. Addition of water, mixing, centrifugation at 1700 rpm for 2 min, and collection of the upper solution were repeated 3 times. The collected solution was centrifuged at 1700 rpm for 60 min, and the separated solid was dried at 70 °C overnight. Then ca. 0.5 g of Na–Mo–Co oxide (yield 66% based on Mo) was obtained. Anal. Calcd for $\text{NaCo}_3\text{Mo}_{12}\text{O}_{48}\text{H}_{25}$: Co, 8.25; Mo, 53.69; Na, 1.07; H, 1.18. Found: Co, 8.24; Mo, 53.42; Na, 1.29; H, 1.19.

Characterization. XRD patterns were obtained on a D8 ADVANCE (Bruker) with $\text{Cu K}\alpha$ radiation (tube voltage: 40 kV, tube current 40 mA). Scanning electron microscopy (SEM) images were obtained with S-4800 (HITACHI). FT-IR analysis was carried out on a NICOLET 6700 FT-IR spectrometer (Thermo Fisher Scientific) as KBr pellets. Raman spectra were recorded with a T64000 (Horiba-JY). XPS was performed on a JPS-9010MC (JEOL). The spectrometer energies were calibrated using the C 1s peak at 284.8 eV. Elemental compositions were determined by an inductive coupling plasma (ICP-AES) method (ICPE-9000, Shimadzu). CHN elemental composition was determined at Instrumental Analysis Division, Equipment Management Center, Creative Research Institution, Hokkaido University. High-resolution TEM and spherical aberration (Cs)-corrected HAADF-STEM were performed by the National Institute of Advanced Industrial Science and Technology (AIST) using an ARM-200F electron microscope (JEOL, Japan) with a cold field emission gun and a CEOS probe aberration corrector.¹² High-resolution TEM images were obtained at 200 kV using an object lens with $\text{Cs} = 1$ mm. Cs-corrected HAADF-STEM images were obtained at 200 kV with a probe convergence semiangle of 14 mrad and a collection angle of 54–175 mrad. Solids were deposited on a holey carbon-coated copper grid by attaching powder directly on the grid and blowing of excess powder. Obtained images were treated with a Local 2D Wiener Filter in the HREM-Filters Pro software (HREM Research Inc., Japan) for noise removal. Image simulations were performed with the multislice simulation software WinHREM (HREM Research Inc., Japan). Nitrogen sorption isotherms were obtained by a BELSORP MAX (BEL Japan Inc.) sorption analyzer at -197 °C. Surface area was calculated by the BET method using an adsorption branch. Co K-edge XAFS spectra were measured in transmission mode using an Si(111) double-crystal monochromator at the BL9A and BL12C beamlines of the Photon Factory in the High Energy Accelerator Research Organization (KEK-PF), Japan. Magnetic susceptibility measurements were performed on a superconducting quantum interference device (SQUID) magnetometer (MPMS-5S, Quantum Design).

RESULTS AND DISCUSSION

Conditions for Preparation of Na–Mo–Co Oxides.

Mo–Zn oxide was prepared by hydrothermal reaction of a solution (pH 4.8) containing Na_2MoO_4 , Mo metal, and ZnCl_2 at 170 °C for 1 day, and **Mo–Mn oxide** was prepared by the same hydrothermal reaction with MnO. First, we performed reactions with other transition metal chlorides including CuCl_2 , NiCl_2 , CoCl_2 , FeCl_3 , and MnCl_2 . After the hydrothermal reactions, the obtained solids were collected by filtration and examined by powder XRD (Figure S1). We obtained ϵ -Keggin-based Mo oxides not only with Zn and Mn but also with Co.

We performed the reactions with different Co sources including CoSO_4 , $\text{Co}(\text{OAc})_2$, $\text{Co}(\text{NO}_3)_2$, CoO , and Co_3O_4 , and the desired ϵ -Keggin-based Mo oxides were obtained when we used CoCl_2 , CoSO_4 , and $\text{Co}(\text{OAc})_2$ (Figure 2b, Figure S2).

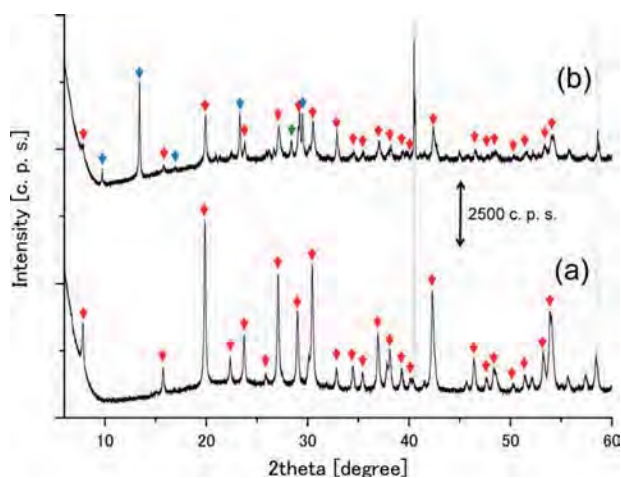


Figure 2. Powder XRD profiles of (a) purified cubic-Mo–Co oxide and (b) as-synthesized solid. Red, blue, and green arrows and black lines indicate diffraction of Mo–Co oxide, $\text{CoMoO}_4\cdot 0.75\text{H}_2\text{O}$, MoO_2 , and Mo metal, respectively.

In the case of preparation of the **Mo–Zn oxide**, the main side product was ZnMoO_4 .⁹ In the case of Co-based materials, the main side product was $\text{CoMoO}_4\cdot 0.75\text{H}_2\text{O}$.^{13–15} Eda's group reported that $\text{CoMoO}_4\cdot 0.75\text{H}_2\text{O}$ is a hydrated mixed-metal oxide with $\text{Co}^{\text{II}}\text{-O}$ octahedra and $\text{Mo}^{\text{VI}}\text{-O}$ tetrahedra.¹³

The effect of pH of the starting reaction mixture was examined by changing the pH value by addition of 1 M H_2SO_4 (Figure S3). The pH value of the reaction mixture of Na_2MoO_4 , Mo metal, and CoCl_2 without pH adjustment was ca. 6.6. Hydrothermal reaction of this solution produced $\text{NaCo}_2(\text{MoO}_4)_2\text{OH}\cdot \text{H}_2\text{O}$ ^{16,17} that has $\text{Co}^{\text{II}}\text{O}$ octahedra and $\text{Mo}^{\text{VI}}\text{O}$ tetrahedra as the main product, and a large XRD peak of Mo metal was observed (Figure S3i). Hydrothermal reactions of reaction mixtures with pH values between 1.6 and 6.0 produced the desired ϵ -Keggin-based Mo oxides. The main side products were MoO_2 and $\text{CoMoO}_4\cdot 0.75\text{H}_2\text{O}$ at lower pH values (1.6–4.2) and at higher pH values (4.8–6.0), respectively. When pH was less than 1.3, only MoO_2 was detected.

The effect of the amount of Mo metal was examined (Figure S4). Without Mo metal, $\text{CoMoO}_4\cdot 0.75\text{H}_2\text{O}$ was obtained, and an increase in the amount of Mo metal resulted in the production of ϵ -Keggin-based Mo oxides and MoO_2 . It has been reported that the valence of Mo in **Mo–V–Bi oxide**,

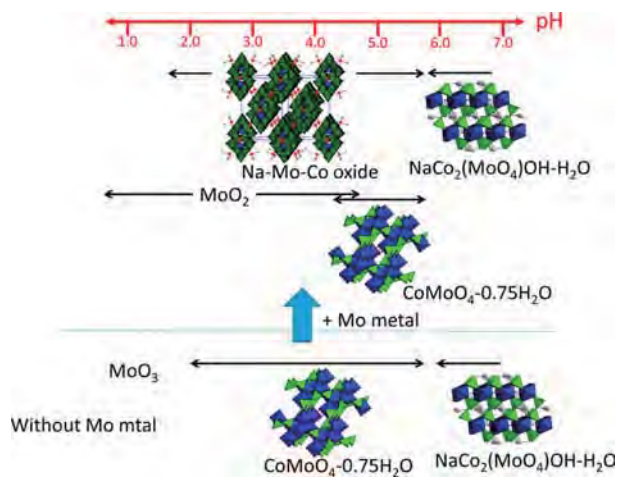
Mo–Zn oxide, and **Mo–Mn oxide** is a mixture of 5+ and 6+, and Mo metal is needed as a reducing reagent. Mo metal was a suitable reducing agent for obtaining ϵ -Keggin-based Mo oxides, and reactions with other reducing reagents such as ascorbic acid and hydrazine sulfate produced undesired amorphous products (Figure S5).

We also checked the effect of pH without Mo metal (Figure S6). Without Mo metal, MoO_3 , $\text{CoMoO}_4 \cdot 0.75\text{H}_2\text{O}$, and $\text{NaCo}_2(\text{MoO}_4)_2\text{OH} \cdot \text{H}_2\text{O}$ were obtained from the reaction mixtures with pH ranges of less than 1.0, between 1.2 and 5.5, and more than 5.5, respectively.

The effect of reaction time was also examined (Figure S7). A reaction time of more than 9 h was needed to produce the desired ϵ -Keggin-based Mo oxides. With shorter reaction time, $\text{CoMoO}_4 \cdot 0.75\text{H}_2\text{O}$ and Mo metal were detected. By increasing the reaction time, the amount of the desired ϵ -Keggin-based Mo oxides increased despite decreases in the amounts of $\text{CoMoO}_4 \cdot 0.75\text{H}_2\text{O}$ and Mo metal.

The effect of reaction temperature was also examined (Figure S8). At room temperature, only Mo was recovered after the reaction. By increasing the temperature, $\text{CoMoO}_4 \cdot 0.75\text{H}_2\text{O}$ was obtained, but the desired ϵ -Keggin-based Mo oxides were obtained only when the temperature was increased to 170 °C. These results indicate that it takes some time for Mo metal to dissolve at 170 °C and that the once-produced $\text{CoMoO}_4 \cdot 0.75\text{H}_2\text{O}$ is transformed by a reduction to the desired ϵ -Keggin-based Mo oxide (Scheme 1). Further increase of temperature to

Scheme 1. Relationship between pH and Products of Hydrothermal Reactions of Aqueous Solutions of Na_2MoO_4 and CoCl_2 at 170 °C for 24 h with and without Mo Metal



200 °C resulted in the formation of MoO_2 as the main product. We also confirmed that the once-produced $\text{CoMoO}_4 \cdot 0.75\text{H}_2\text{O}$ without Mo metal was transferred to the desired ϵ -Keggin-based Mo oxide by heating at 170 °C for 24 h in the presence of Mo metal.

Isolation of Na–Mo–Co Oxide. Despite the various reaction condition investigations, we could not find a reaction condition to produce the desired ϵ -Keggin-based Mo oxides in pure form, and the obtained solid always contained crystalline side products such as $\text{CoMoO}_4 \cdot 0.75\text{H}_2\text{O}$, MoO_2 , $\text{NaCo}_2(\text{MoO}_4)_2\text{OH} \cdot \text{H}_2\text{O}$, and Mo metal. Therefore, we purified the obtained solids by centrifugation. After purification, we obtained a solid that showed only an XRD profile

corresponding to the desired ϵ -Keggin-based Mo oxides (Figure 2).

Characterization by IR, Raman Spectroscopy, XPS, Elemental Analysis, XRD, SEM, and Gas Adsorption. IR spectra and Raman spectra of the obtained ϵ -Keggin-based Mo oxides are almost identical to those of **Mo–Zn oxide** and similar to those of $[\epsilon\text{-Mo}_{12}\text{O}_{28}(\text{OH})_{12}(\text{Co}(\text{H}_2\text{O})_3)_4]$ reported by Kögerler's group (Figure 3) in which ϵ -Keggin polyoxomolybdate has four Co ions on the four hexagonal faces,¹⁸ indicating that the obtained ϵ -Keggin-based Mo oxides have ϵ -Keggin type $[\text{Mo}_{12}\text{O}_{40}]^{n-}$ units.

XPS of the ϵ -Keggin-based Mo oxides indicated that the valence of Co is 2+ and that the valence of Mo is 5+ and 6+ with an $\text{Mo}^{5+}/\text{Mo}^{6+}$ ratio of ca. 2 (Figure S9).

Elemental analysis revealed that Mo:Co is 12:3. This result agrees with the fact that the central metal and linker metal are Co. From elemental analysis and XPS results, the formula of desired ϵ -Keggin-based Mo oxides was estimated to be $\text{NaH}_9[\epsilon\text{-Co}^{\text{II}}\text{Mo}^{\text{V}}_8\text{Mo}^{\text{VI}}_4\text{O}_{40}(\text{Co}^{\text{II}})_2]$.

Rietveld analysis with a model in which Co occupied both the central and the linker sites and Mo occupied the surrounding sites gave an XRD profile similar to the observed XRD profile of **Na–Mo–Co oxide** (Figure S10 and Table S1). Furthermore, there were no additional peaks in the experimental data, indicating that the powder sample of **Na–Mo–Co oxide** was pure. An SEM image indicates that each particle of **Na–Mo–Co oxide** has octahedral morphology that is similar to the shape of **Mo–V–Bi oxide** and **Mo–Zn oxide** particles (Figure S11).

Na–Mo–Co oxide was thermally stable after heating at 200 °C as was **Mo–Zn oxide**. N_2 , CO_2 , and CH_4 adsorption measurements indicated that **Na–Mo–Co oxide** has a micropore volume (1.77 and 0.75 molecules per one POM unit for CH_4 and CO_2 , respectively) similar to that (1.84 and 0.86 molecules per one POM unit for CH_4 and CO_2 , respectively)¹⁰ of **Mo–Zn oxide** (Figure S12 and Table S2).

Characterization by HR-TEM and HAADF-STEM. The structure of **Na–Mo–Co oxide** was further confirmed by TEM techniques. HR-TEM images of both **Mo–V–Bi oxide** and **Na–Mo–Co oxide** along the [110] direction showed an ordered arrangement of rhombic dark units that corresponds to two overlapping ϵ -Keggin units (Figure S13 and Figure 4a and 4b). The images of **Mo–V–Bi oxide** and **Na–Mo–Co oxide** were in good agreement with images simulated from the proposed structures. The 3D channel of the material can be clearly observed. These HR-TEM images are the first atomic-scale TEM images for ϵ -Keggin compounds.

HAADF-STEM is a useful method for analyzing the position of each metal because the intensity of the white spot is roughly proportional to the square of the atomic number (Z), providing an enhanced Z -contrast image.¹⁹ HAADF-STEM has been used to characterize metal positions in Mo-based oxides.^{20–22} As shown in Figure 4a and 4b, there are two kinds (indicated by red and orange circles) of linker metal sites in the [110] projection where the red linker metal is surrounded by 4 surrounding metals (light green circles), 2 central metals (blue circles), and 10 surrounding metals (dark green circles) to form the rhombus units. The rhombus units are connected by other linker sites (orange circles). The number ratio of red linker metal, orange linker metal, dark green surrounding metal, light green surrounding metal, and blue central metal along the [110] direction is 4:2:4:2:2 (Figure 4b). The white intensity of each spot increases with increasing atomic number and number

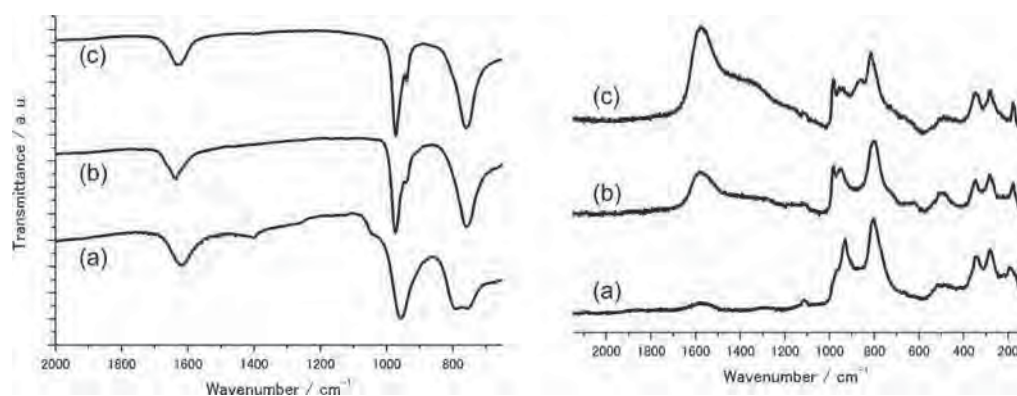


Figure 3. (Left) IR and (right) Raman spectra of (a) $[\epsilon\text{-Mo}_{12}\text{O}_{28}(\text{OH})_{12}(\text{Co}(\text{H}_2\text{O})_3)_4]$, (b) Na–Mo–Co oxide, and (c) Mo–Zn oxide.

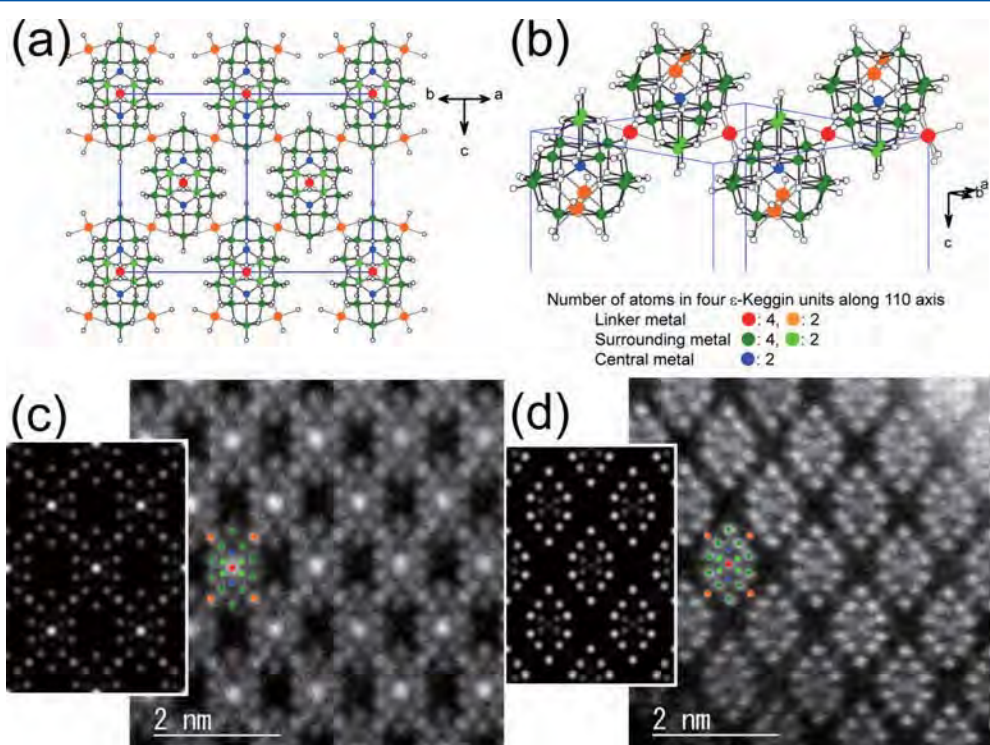


Figure 4. Ball-and-stick representation of Na–Mo–Co oxide along (a) the $[110]$ axis and (b) four ϵ -Keggin $[\text{CoMo}_{12}\text{O}_{40}]^{n-}$ units connected by Co. Dark and light green balls represent surrounding Mo, red and orange balls represent linker Co, and blue balls represent central Co. Numbers of overlapping dark green balls, light green balls, red balls, orange balls, and blue balls along the $[110]$ axis are 4, 2, 4, 2, and 2, respectively. HAADF-STEM images of (c) Mo–V–Bi oxide and (d) Na–Mo–Co oxide. (Insets) Simulated images.

of metals, and detection of the metal positions of Mo, V, Co, and Bi with atomic numbers of 42, 23, 27, and 83, respectively, is possible.

In Mo–V–Bi oxide, the presence of V and Bi in the central site and linker site, respectively, was confirmed by single-crystal X-ray structure analysis.⁶ Furthermore, it was shown that the surrounding sites are occupied by both Mo and V with an Mo:V ratio of ca. 9.4:2.6. The most intense and second most intense spots (Figures 4c and S14) correspond to Bi sites (red and orange Bi in Figure 4a and 4b) because the atomic number of Bi is much larger than those of Mo and V. Other than the most intense and second most intense spots, 10 white spots corresponding to the dark green surrounding metal were recognizable. The light green surrounding metal was not clearly observed because the number of light green surrounding metals

is one-half that of the dark green surrounding metals along the $[110]$ direction. In addition, central V was also unrecognizable because central V has a much smaller atomic number than that of Mo, and the number of central V (blue spots) along the $[110]$ direction is the same as that of the invisible light green surrounding site. The simulated image (Figure 4c, inset) obtained by using the single-crystal X-ray structure model of Mo–V–Bi oxide is similar to the observed image.

In the HAADF-STEM image of Na–Mo–Co oxide (Figure 4d), the intensities of the linker site and central site are much weaker than those of surrounding sites, indicating that the atomic number of the linker and central metal is smaller than the atomic number of the surrounding metal. These results together with the results of elemental analysis (Mo:Co = 12:3) confirm that the central and linker sites are occupied by Co and

that the surrounding site is occupied by Mo. The simulated image obtained using this model (Figure 4d, inset) is similar to the observed image.

Characterization by XAFS. In order to obtain more information about the valence and coordination environments of Co sites, we measured the Co K-edge X-ray absorption near-edge structure (XANES) spectra of **Na–Mo–Co oxide** and reference samples (Figure 5). CoO and CoAl₂O₄ were chosen

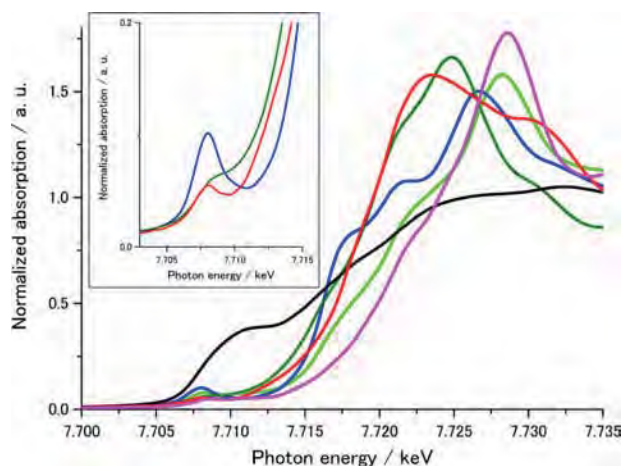


Figure 5. XANES spectra of **Na–Mo–Co oxide** and reference samples: (red line) **Na–Mo–Co oxide**, (black line) Co foil, (blue line) CoAl₂O₄, (dark green line) CoO, (light green line) Co₃O₄, and (pink) ZnCo₂O₄. (Inset) Extended spectra for pre-edge area.

for reference samples of Co^{II}, and ZnCo₂O₄ was chosen for a reference sample of Co^{III}. Co₃O₄ contains Co^{II} and Co^{III} with a 1:2 ratio. The adsorption edge shifted to higher energy (Co foil < CoO, CoAl₂O₄ < Co₃O₄ < ZnCo₂O₄) with an increase in the valence, and the adsorption edge of **Na–Mo–Co oxide** was similar to those of CoO and CoAl₂O₄, indicating that the valence of Co is 2+. In K-edge XANES spectra of 3d transition metal oxides, the pre-edge features are associated with mainly electric dipole transition from 1s to the p components in 3d–4p hybridized orbitals, and the intensity is affected by both the valence states and the coordination environments of the central metal atom.^{23–25} It is known that the pre-edge peak intensity for T_d symmetry is larger than that for O_h symmetry when comparing samples with the same valence.^{23,25} As shown in Figure 5, the pre-edge peak intensity of **Na–Mo–Co oxide** was between those of CoAl₂O₄ (Co^{II}O₄ tetrahedra, T_d symmetry)¹¹ and CoO (Co^{II}O₆ octahedra, O_h symmetry). This result supports our model of **Na–Mo–Co oxide** having two Co sites of the central site with tetrahedral coordination and the linker site with octahedral coordination.

Magnetic Measurement. Magnetic susceptibility measurements of **Mo–Zn oxide** and **Na–Mo–Co oxide** were carried out in the temperature range of 2–300 K under an external magnetic field of 10 000 Oe. Plots of $\chi_M T$ versus T, where χ_M is the molar magnetic susceptibility, are shown in Figure 6. In the case of **Mo–Zn oxide** (Na₂H₁₁[ϵ -Zn^{II}Mo^V₁₁Mo^V₁O₄₀(Zn^{II})₂]),⁹ no magnetic moment is observed, although **Mo–Zn oxide** contains paramagnetic Mo^V, indicating that there is an even number of electrons in one ϵ -Keggin ZnMo₁₂O₄₀ unit and spins of the electrons are coupled. The formula indicates that there is a single paramagnetic Mo^V in one Keggin unit but that the bulk material has no magnetic

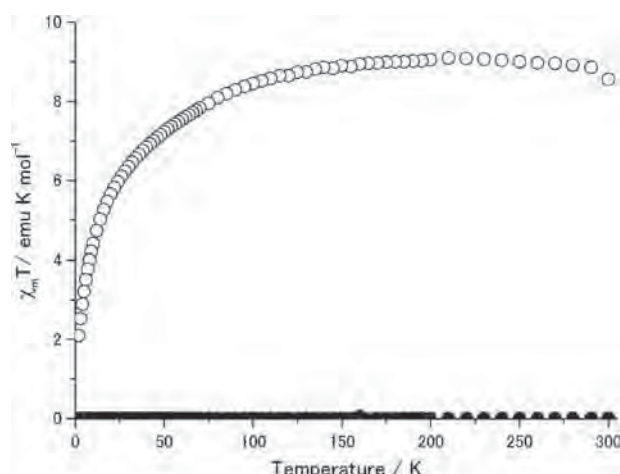


Figure 6. Plot of $\chi_M T$ product versus temperature for (white circles) **Na–Mo–Co oxide** and (black circles) **Mo–Zn oxide** in an applied field of 10000 Oe.

moment. This phenomenon can be explained by disproportionation ($2[\text{CoMo}^{\text{IV}}_{11}\text{Mo}^{\text{V}}_{1}\text{O}_{40}] \rightarrow [\text{CoMo}^{\text{IV}}_{12}\text{O}_{40}] + [\text{CoMo}^{\text{IV}}_{10}\text{Mo}^{\text{V}}_{2}\text{O}_{40}]$) and there are at least two kinds of Keggin units in the bulk material: one with two Mo^V where electrons are paired and the other without Mo^V. Couplings of spins of two electrons in one Keggin-type tungstate have been confirmed by ESR and ¹H NMR.²⁶ In the case of **Na–Mo–Co oxide**, the room-temperature $\chi_M T$ value of 8.99 emu K mol⁻¹ is much higher than that expected for three isolated Co^{II} ions (1.88 emu K mol⁻¹, S = 3/2, g = 2), indicating that a significant orbital contribution is involved at a high temperature. On lowering the temperature, the value of $\chi_M T$ gradually decreases down to the value of 5.65 emu K mol⁻¹ at 20 K, due to thermal depopulation of the excited Kramers state of the Co^{II} ion. Below 20 K, $\chi_M T$ drops rapidly to 2.10 emu K mol⁻¹ at 2 K as a result of antiferromagnetic interactions between Co^{II} ions. Thus, the even number of electrons in one ϵ -Keggin unit are coupled as in **Mo–Zn oxide**.

CONCLUSION

A new ϵ -Keggin polyoxomolybdate-based 3D framework material with Co as a heteroatom has been successfully synthesized and characterized. Structure characterization using high-resolution HAADF-STEM, XANES, IR, Raman spectra, elemental analysis, and powder XRD revealed that ϵ -Keggin cobalt-centered cobaltomolybdate, [ϵ -CoMo₁₂O₄₀], is linked by Co to form 3D diamond-like frameworks. XPS, XANES, and magnetic measurement indicated that the valence of Co is 2+. HAADF-STEM images were so clear that atomic-scale images with different spot intensities were obtained, and the positions of Mo and Co were determined. XANES spectra confirmed the presence of a CoO₄ tetrahedron. The results clearly indicated that the CoO₄ tetrahedron is surrounded by 12 MoO₆ octahedra to form the ϵ -Keggin cobaltomolybdate that was connected by CoO₆ octahedra to form the 3D framework structure. Studies to search for new ϵ -Keggin polyoxometalate-based 3D framework materials with other elements and applications as adsorption materials and for catalysis are undergoing in our group.

■ ASSOCIATED CONTENT

■ Supporting Information

The Supporting Information is available free of charge on the ACS Publications website at DOI: 10.1021/acs.inorgchem.6b02748.

Effect of metals for the synthesis of ϵ -Keggin-based Mo–M oxides; effect of cobalt sources for the synthesis of ϵ -Keggin-based Mo–Co oxides; effect of pH of the solution for the synthesis of ϵ -Keggin-based Mo–Co oxides; effect of the amount of Mo metal for the synthesis of ϵ -Keggin-based Mo–Co oxides; effect of reducing reagents for the synthesis of ϵ -Keggin-based Mo–Co oxides; effect of pH of the solution for the synthesis of Mo–Co oxides; effect of reaction time for the synthesis of ϵ -Keggin-based Mo–Co oxides; effect of reaction temperature for the synthesis of ϵ -Keggin-based Mo–Co oxides; XPS; powder XRD and Rietveld analysis; SEM; adsorption–desorption isotherm; HR-TEM; HAADF-STEM (PDF)

■ AUTHOR INFORMATION

Corresponding Author

*E-mail: sadakane09@hiroshima-u.ac.jp. Phone: +81-82-424-4456. Fax: +81-82-424-5494.

ORCID

Akira Yamamoto: 0000-0002-1329-0807

Masahiro Sadakane: 0000-0001-7308-563X

Author Contributions

All authors have given approval to the final version of the manuscript.

Notes

The authors declare no competing financial interest.

■ ACKNOWLEDGMENTS

This work was financially supported by a Grant-in-Aid for Scientific Research (A) (grant no. 2324-6135) from the Ministry of Education, Culture, Sports, Science, and Technology, Japan (MEXT), and the Center for Functional Nano Oxide at Hiroshima University. M.S. thanks PRESTO JST, Nippon Sheet Glass Foundation for Materials Science and Engineering (NSG Foundation), and the Collaborative Research Project of Materials and Structures Laboratory at the Tokyo Institute of Technology for financial support. The high-resolution electron microscopy study was supported by JSPS KAKENHI Grant no. JP16K06863. S.N. and K.I. were supported by the Japan Society for the Promotion of Science (JSPS) Core-to-Core Program; A. Advanced Research Networks, and Grants-in-Aid for Scientific Research (S) and (B) (grant nos. 25220803 and 16H04223, respectively) from MEXT. Part of this work conducted at Hokkaido University was supported by the “Nanotechnology Platform”, a program of MEXT. We thank Dr. M. Maeda and Dr. D. Kajiya at the Natural Science Center for Basic Research and Development (N-BARD), Hiroshima University, for initial TEM observation and Raman spectroscopy measurement, respectively. We thank Prof. P. Kögerler for IR spectra of $[\text{Mo}^{\text{V}}_{12}\text{O}_{28}(\text{OH})_{12}(\text{Co}^{\text{II}}(\text{H}_2\text{O})_3)_4]$ and Prof. K. Eda for a powder XRD pattern of $\text{CoMoO}_4 \cdot 0.75\text{H}_2\text{O}$. Co K-edge XAFS experiments were performed under the approval of the Photon Factory Program Advisory Committee (Proposal No. 2014G548).

■ REFERENCES

- (1) Hill, C. L. Special thematic issue on polyoxometalates. *Chem. Rev.* **1998**, *98*, 1–390.
- (2) Cronin, L.; Müller, A. Special thematic issue on polyoxometalates. *Chem. Soc. Rev.* **2012**, *41*, 7325–7648.
- (3) Dolbecq, A.; Mialane, P.; Sécheresse, F.; Keita, B.; Nadjó, L. Functionalized polyoxometalates with covalently linked bisphosphonate, N-donor or carboxylate ligands: from electrocatalytic to optical properties. *Chem. Commun.* **2012**, *48*, 8299–8316.
- (4) Rousseau, G.; Rodriguez-Albelo, L. M.; Salomon, W.; Mialane, P.; Marrot, J.; Doungmene, F.; Mbomekalle, I.; de Oliveira, P.; Dolbecq, A. Tuning the Dimensionality of Polyoxometalate-Based Materials by Using a Mixture of Ligands. *Cryst. Growth Des.* **2015**, *15*, 449–456.
- (5) Compain, J.-D.; Nakabayashi, K.; Ohkoshi, S. A Polyoxometalate-Cyanometalate Multilayered Coordination Network. *Inorg. Chem.* **2012**, *51*, 4897–4889.
- (6) Zhang, Z.; Sadakane, M.; Murayama, T.; Izumi, S.; Yasuda, N.; Sakaguchi, N.; Ueda, W. Tetrahedral Connection of ϵ -Keggin-type Polyoxometalates To Form an All-Inorganic Octahedral Molecular Sieve with an Intrinsic 3D Pore System. *Inorg. Chem.* **2014**, *53*, 903–911.
- (7) Zhang, Z.; Sadakane, M.; Murayama, T.; Ueda, W. Investigation of the formation process of zeolite-like 3D frameworks constructed with ϵ -Keggin-type polyoxovanadomolybdates with binding bismuth ions and preparation of a nano-crystal. *Dalton Trans.* **2014**, *43*, 13584–13590.
- (8) Zhang, Z.; Yoshikawa, H.; Zhang, Z.; Murayama, T.; Sadakane, M.; Inoue, Y.; Ueda, W.; Awaga, K.; Hara, M. Synthesis of V-incorporated polyoxometalate-based open frameworks and their applications to cathode-active materials. *Eur. J. Inorg. Chem.* **2016**, *2016*, 1242–1250.
- (9) Zhang, Z.; Sadakane, M.; Murayama, T.; Sakaguchi, N.; Ueda, W. Preparation, Structural Characterization, and Ion-Exchange Properties of Two New Zeolite-like 3D Frameworks Constructed by ϵ -Keggin-Type Polyoxometalates with Binding Metal Ions, $\text{H}_{11.4}[\text{ZnMo}_{12}\text{O}_{40}\text{Zn}_2]^{1.5-}$ and $\text{H}_{7.5}[\text{Mn}_{0.2}\text{Mo}_{12}\text{O}_{40}\text{Mn}_2]^{2.1-}$. *Inorg. Chem.* **2014**, *53*, 7309–7318.
- (10) Zhang, Z.; Sadakane, M.; Noro, S.-i.; Murayama, T.; Kamachi, T.; Yoshizawa, K.; Ueda, W. Selective carbon dioxide adsorption of ϵ -Keggin-type zirconomolybdate-based purely inorganic 3D frameworks. *J. Mater. Chem. A* **2015**, *3*, 746–755.
- (11) Wang, H.-Y.; Hung, S.-H.; Chen, H.-Y.; Chan, T.-S.; Chen, H.-M.; Liu, B. In Operando Identification of Geometrical-Site-Dependent Water Oxidation Activity of Spinel Co_3O_4 . *J. Am. Chem. Soc.* **2016**, *138*, 36–39.
- (12) Hiyoshi, N.; Kamiya, Y. Observation of microporous cesium salts of 12-tungstosilicic acid using scanning transmission electron microscopy. *Chem. Commun.* **2015**, *51*, 9975–9978.
- (13) Eda, K.; Uno, Y.; Nagai, N.; Sotani, N.; Whittingham, M. S. Crystal structure of cobalt molybdate hydrate $\text{CoMoO}_4 \cdot n\text{H}_2\text{O}$. *J. Solid State Chem.* **2005**, *178*, 2791–2797.
- (14) Eda, K.; Uno, Y.; Nagai, N.; Sotani, N.; Chen, C.; Whittingham, M. S. Structure-inheriting solid-state reactions under hydrothermal conditions. *J. Solid State Chem.* **2006**, *179*, 1453–1458.
- (15) Mandal, M.; Ghosh, D.; Giri, S.; Shakir, I.; Das, C. K. Polyaniline-wrapped 1D $\text{CoMoO}_4 \cdot 0.75\text{H}_2\text{O}$ nanorods as electrode materials for supercapacitor energy storage applications. *RSC Adv.* **2014**, *4*, 30832–30839.
- (16) Palacio, L. A.; Echavarria, A.; Saldarriaga, C. Crystal structure a cobalt molybdate type ϕ_x : $\text{NaCo}_2\text{OH}(\text{MoO}_4)_2$. *Int. J. Inorg. Mater.* **2001**, *3*, 367–371.
- (17) Vilminot, S.; André, G.; Bourée-Vigneron, F.; Baker, P. J.; Blundell, S. J.; Kurmoo, M. Magnetic Properties and Magnetic Structures of Synthetic Natrochalcites, $\text{NaM}^{\text{II}}_2(\text{D}_3\text{O}_2)(\text{MoO}_4)_2$, M = Co or Ni. *J. Am. Chem. Soc.* **2008**, *130*, 13490–13499.
- (18) Ellern, A.; Kögerler, P. $[\text{Co}^{\text{II}}_4\text{Mo}^{\text{VI}}_2\text{O}_{28}(\text{OH})_{12}(\text{H}_2\text{O})_{12}] \cdot 12\text{H}_2\text{O}$: facilitating single-crystal growth by deuteration. *Acta Crystallogr.* **2012**, *C68*, i17–i19.

- (19) Howie, A. Image contrast and localized signal selection techniques. *J. Microsc.* **1979**, *117*, 11–23.
- (20) Sadakane, M.; Yamagata, K.; Kodato, K.; Endo, K.; Toriumi, K.; Ozawa, Y.; Ozeki, T.; Nagai, T.; Matsui, Y.; Sakaguchi, N.; Pyrz, W. D.; Buttrey, D. J.; Blom, D. A.; Vogt, T.; Ueda, W. Synthesis of Orthorhombic Mo-V-Sb Oxide Species by Assembly of Pentagonal Mo₆O₂₁ Polyoxometalate Building Blocks. *Angew. Chem., Int. Ed.* **2009**, *48*, 3782–3786.
- (21) Pyrz, W. D.; Blom, D. A.; Sadakane, M.; Kodato, K.; Ueda, W.; Vogt, T.; Buttrey, D. J. Atomic-level imaging of Mo-V-O complex oxide phase intergrowth, grain boundaries, and defects using HAADF-STEM. *Proc. Natl. Acad. Sci. U. S. A.* **2010**, *107*, 6152–6157.
- (22) Pyrz, W. D.; Blom, D. A.; Sadakane, M.; Kodato, K.; Ueda, W.; Vogt, T.; Buttrey, D. J. Atomic-Scale Investigation of Two-Component MoVO Complex Oxide Catalysts Using Aberration-Corrected High-Angle Annular Dark-Field Imaging. *Chem. Mater.* **2010**, *22*, 2033–2040.
- (23) Westre, T. E.; Kennepohl, P.; DeWitt, J. G.; Hedman, B.; Hodgson, K. O.; Solomon, E. I. A Multiplet Analysis of Fe K-Edge 1s → 3d Pre-Edge Features on Iron Complexes. *J. Am. Chem. Soc.* **1997**, *119*, 6297–6314.
- (24) Modrow, H.; Bucher, S.; Rehr, J. J.; Ankudinov, A. L. Calculation and interpretation of K-shell x-ray absorption near-edge structure of transition metal oxides. *Phys. Rev. B: Condens. Matter Mater. Phys.* **2003**, *67*, 035123.
- (25) Yamamoto, T. Assignment of pre-edge peaks in K-edge x-ray absorption spectra of 3d transition metal compounds: electric dipole or quadrupole? *X-Ray Spectrom.* **2008**, *37*, 572–584.
- (26) Pope, M. T. *Heteropoly and Isopoly Oxometalates*; Springer-Verlag: Berlin, 1983.

Inorganic Frameworks | Hot Paper |

The Assembly of an All-Inorganic Porous Soft Framework from Metal Oxide Molecular Nanowires

Zhenxin Zhang,^{*,[a, b]} Masahiro Sadakane,^[c] Shin-ichiro Noro,^[d] Norihito Hiyoshi,^[e] Akihiro Yoshida,^[a] Michikazu Hara,^[b] and Wataru Ueda^{*,[a]}

Abstract: An all-inorganic soft framework is rare but interesting for both fundamental research and practical applications. Here, an all-inorganic soft framework based on a transition metal oxide is reported. The periodic connection of a one-dimensional anionic tungstoselenate molecular wire building block with a Co^{II} ion is used to construct the crystalline material. The crystal structure of the material was determined by high-angle annular dark-field scanning transmis-

sion electron microscopy combined with several characterization techniques. The soft framework of the material enables water adsorption/desorption with a change in its structure, leading to a high level of water adsorption. The framework of the material is flexible, and the structure of the molecular wire building block is stable during the water adsorption/desorption process.

Introduction

Crystalline materials with soft frameworks have received significant attention. The unique structural feature of a soft framework material is not only of great interest and importance in fundamental research, but also leads to various practical applications. Soft frameworks have been designed and developed in recent years. The assembly of metal ions with organic ligands provides a well-defined approach to obtain a sub-category of metal-organic frameworks (MOFs),^[1] some of which are flexible and are denoted as soft porous crystals (SPCs).^[2] The advantages of soft frameworks are a flexible structure with an easy fabrication, that is dependent on different operation conditions. These materials have the property that the crystalline

frameworks reversibly vary under external physical or chemical processes, such as molecule adsorption, temperature change, and mechanical force application. The current soft framework materials are mainly based on organic compounds (organic frameworks or metal-organic frameworks). A more inventive approach is to use an all-inorganic composition to construct soft frameworks, because an all-inorganic composition shows advantages such as structural stability, composition complexity, acidity, and redox properties. The materials are however very rare and difficult to obtain, which leaves a nearly open field that is full of challenges.

The assembly of metal-oxygen octahedra is a well-defined methodology for constructing new transition-metal oxides with unique structural features, such as crystalline porous frameworks based on metal oxides,^[3] molecular metal oxides (polyoxometalates, POMs),^[4] metal oxide molecular sheets,^[5] metal oxide molecular wires,^[6] and organic-inorganic hybrids.^[7] Among the above examples, POMs are widely used as sub-units to obtain new transition-metal oxides. There are a few examples showing the synthesis of microporous frameworks, based on transition-metal oxides by means of a bottom-up process using POMs as building blocks.^[3b,c,8] It is therefore a promising approach to obtain inorganic soft frameworks based on transition-metal oxides. To date, however, no successful example has been achieved.

We recently reported new crystalline transition-metal oxides constructed by anionic metal oxide molecular wires, $\{[\text{TeMo}_6\text{O}_{21}]^{2-}\}_n$, $\{[\text{SeMo}_6\text{O}_{21}]^{2-}\}_n$, $\{[\text{TeW}_6\text{O}_{21}]^{2-}\}_n$, and $\{[\text{SeW}_6\text{O}_{21}]^{2-}\}_n$. The molecular wires are orderly and assembled by NH_4^+ in a hexagonal fashion to form crystals (Figure 1 a–d).^[6] Our strategy for constructing all-inorganic soft framework materials is to link the molecular wires with metal cations. Here, we report the synthesis of a soft framework based on tungsten oxide and Co ions, denoted as **CoWSeO-H₂O**.

[a] Dr. Z. Zhang, Dr. A. Yoshida, Prof. Dr. W. Ueda
Faculty of Engineering, Kanagawa University, Rokkakubashi
Kanagawa-ku, Yokohama-shi, Kanagawa, 221-8686 (Japan)
E-mail: zhang.z.ag@m.titech.ac.jp
uedaw@kanagawa-u.ac.jp

[b] Dr. Z. Zhang, Prof. Dr. M. Hara
Materials and Structures Laboratory, Tokyo Institute of Technology
Nagatsuta-cho 4259, Midori-ku, Yokohama-city
Kanagawa, 226-8503 (Japan)

[c] Dr. M. Sadakane
Department of Applied Chemistry, Graduate School of Engineering
Hiroshima University, 1-4-1 Kagamiyama
Higashi Hiroshima 739-8527 (Japan)

[d] Dr. S.-i. Noro
Research Institute for Electronic Science, Hokkaido University
N21W10, Sapporo 001-0020 (Japan)

[e] Dr. N. Hiyoshi
Research Institute for Chemical Process Technology
National Institute of Advanced Industrial Science and Technology (AIST)
4-2-1 Nigatake, Miyagino, Sendai 983-8551 (Japan)

Supporting information for this article can be found under
<http://dx.doi.org/10.1002/chem.201605258>.

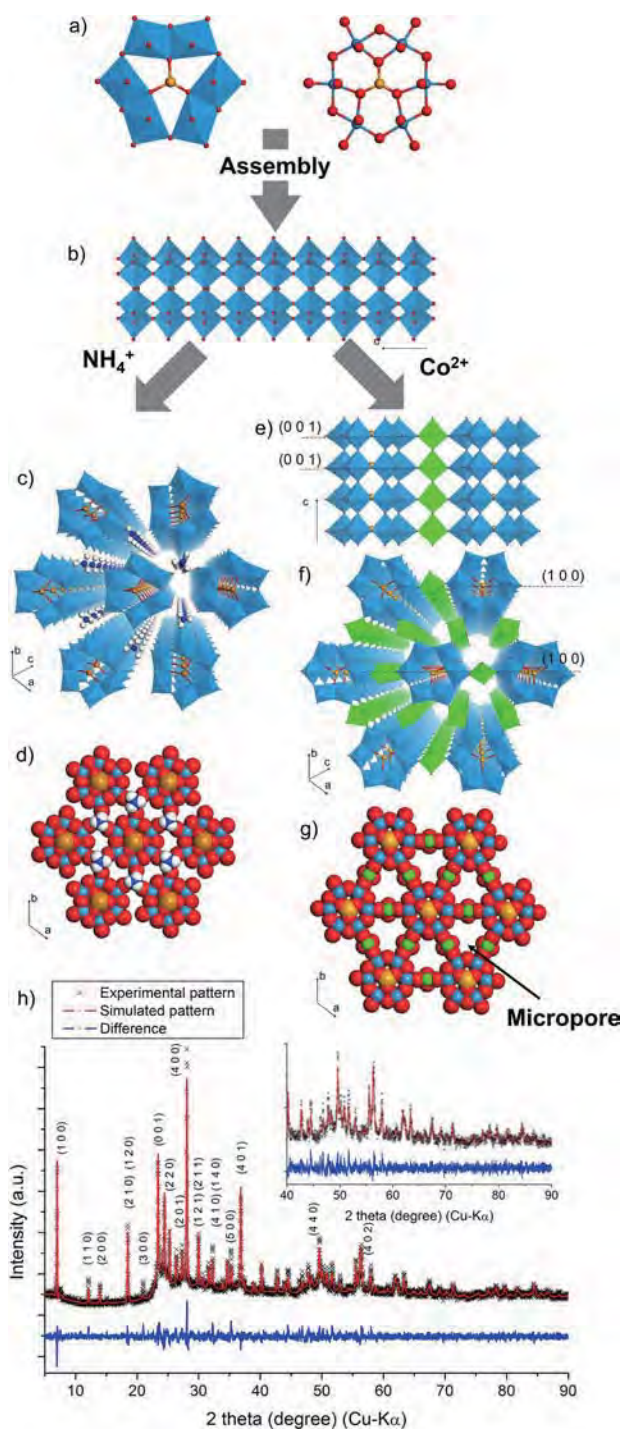


Figure 1. a) Polyhedral, and ball-and-stick representation of the hexagonal building block of $[\text{SeW}_6\text{O}_{21}]^{2-}$, b) polyhedral representation of the $\{[\text{SeW}_6\text{O}_{21}]_n\}$ molecular wire, c) 3D structure of WSeO , d) CPK (Corey, Pauling, and Koltun) representation of the ab plane of WSeO , e) the connection of the $\{[\text{SeW}_6\text{O}_{21}]_n\}$ molecular wires with Co ions, f) 3D structure of $\text{CoWSeO}\cdot\text{H}_2\text{O}$, g) CPK representation of the ab plane of $\text{CoWSeO}\cdot\text{H}_2\text{O}$; (W: light blue, Se: yellow, Co: green, O: red, N: deep blue), and h) A comparison of the experimental XRD pattern with the simulated XRD pattern of $\text{CoWSeO}\cdot\text{H}_2\text{O}$ by Rietveld refinement.

The material was constructed using building blocks of $\{[\text{SeW}_6\text{O}_{21}]^{2-}\}_n$ molecular wires linked by Co ions in a hexagonal manner. The structure of the material was confirmed using

high-angle annular dark-field scanning transmission electron microscopy (HAADF-STEM) combined with other characterizations, powder X-ray diffraction (XRD), Fourier transform infrared (FTIR) spectroscopy, X-ray photoelectron spectroscopy (XPS), thermal analysis, and scanning electron microscopy (SEM). The structure change of $\text{CoWSeO}\cdot\text{H}_2\text{O}$ is reversible during hydration and dehydration without a change in the basic structure of the building blocks.

Results and Discussion

Synthesis and characterization of $\text{CoWSeO}\cdot\text{H}_2\text{O}$ soft framework

The molecular wire-based three-dimensional (3D) framework composed of W, Se, and Co was synthesized in a hot aqueous solution. In the precursor solution, $(\text{NH}_4)_6\text{H}_2\text{W}_{12}\text{O}_{40}\cdot n\text{H}_2\text{O}$ (AMT), SeO_2 , and $\text{Co}(\text{OAc})_2$, were used as the W source, Se source, and transition metal ion linker, respectively. After heating the solution at 100°C for 17 h, $\text{CoWSeO}\cdot\text{H}_2\text{O}$ was recovered from the solution. As shown in Figure 2a, $\text{CoWSeO}\cdot\text{H}_2\text{O}$ was a well-crystallized compound, and the XRD pattern of the material was different from that of WSeO , indicating that the crystal structure of $\text{CoWSeO}\cdot\text{H}_2\text{O}$ was different.

The IR band at 1620 cm^{-1} demonstrated the existence of water in the material (Figure 2b). The peak at 1400 cm^{-1} was ascribed to NH_4^+ . $\text{CoWSeO}\cdot\text{H}_2\text{O}$ had a relatively weak NH_4^+ signal compared with that of WSeO . IR bands below 1000 cm^{-1} , which were derived from the frameworks of the metal oxide moiety, were similar to those of WSeO (Figure 2b,c),^[6b] indicating that the bonding state of the materials were similar. The Raman spectra of $\text{CoWSeO}\cdot\text{H}_2\text{O}$ and WSeO were also similar, indicating the presence of the $\{[\text{SeW}_6\text{O}_{21}]^{2-}\}_n$ building blocks in $\text{CoWSeO}\cdot\text{H}_2\text{O}$ (Figure 2d,e).

The elemental analysis of $\text{CoWSeO}\cdot\text{H}_2\text{O}$ showed N: Co: W: Se = 0.4: 1.3: 6: 1. XPS revealed that the valences of W, Se, and Co were W^{VI} , Se^{IV} , and Co^{II} , respectively (Figure S1 in the Supporting Information). The chemical composition of $\text{CoWSeO}\cdot\text{H}_2\text{O}$ can be described as $(\text{NH}_4)_{0.4}[\text{Co}^{\text{II}}_{1.3}(\text{OH})\text{Se}^{\text{IV}}\text{W}^{\text{VI}}_6\text{O}_{21}]\cdot 11\text{H}_2\text{O}$. The charge of a hexagonal unit of $[\text{Se}^{\text{IV}}\text{W}^{\text{VI}}_6\text{O}_{21}]^{2-}$ was -2 , whereas the sum of the positive charge of the counter-cations (Co^{2+} and NH_4^+) was 3. Therefore, additional negative charge was necessary. The IR spectrum and elemental analysis indicated that there was no acetate anion from the Co source ($\text{Co}(\text{OAc})_2$). Thus, OH^- was proposed to compensate the additional positive charge and might coordinate to Co.

The powder diffraction peaks of $\text{CoWSeO}\cdot\text{H}_2\text{O}$ were indexed, and the hexagonal system with $P6$ space group was obtained (Table S1 and Table S2). The charge flipping algorithm highlighted most of the atoms of the building blocks for $\text{CoWSeO}\cdot\text{H}_2\text{O}$, showing that the arrangement of the heavy metal ions in the material was likely the same as that of WSeO . There were three sites in the material with high electron densities, these are the linker site, the surrounding site, and the central site, where the ratio of the linker site: the surrounding site: the central site = 3:6:1 in the unit cell (Table S1). Elemental analysis showed that $\text{Co}/\text{W}/\text{Se} = 1.3:6:1$, and thus W and Se were esti-

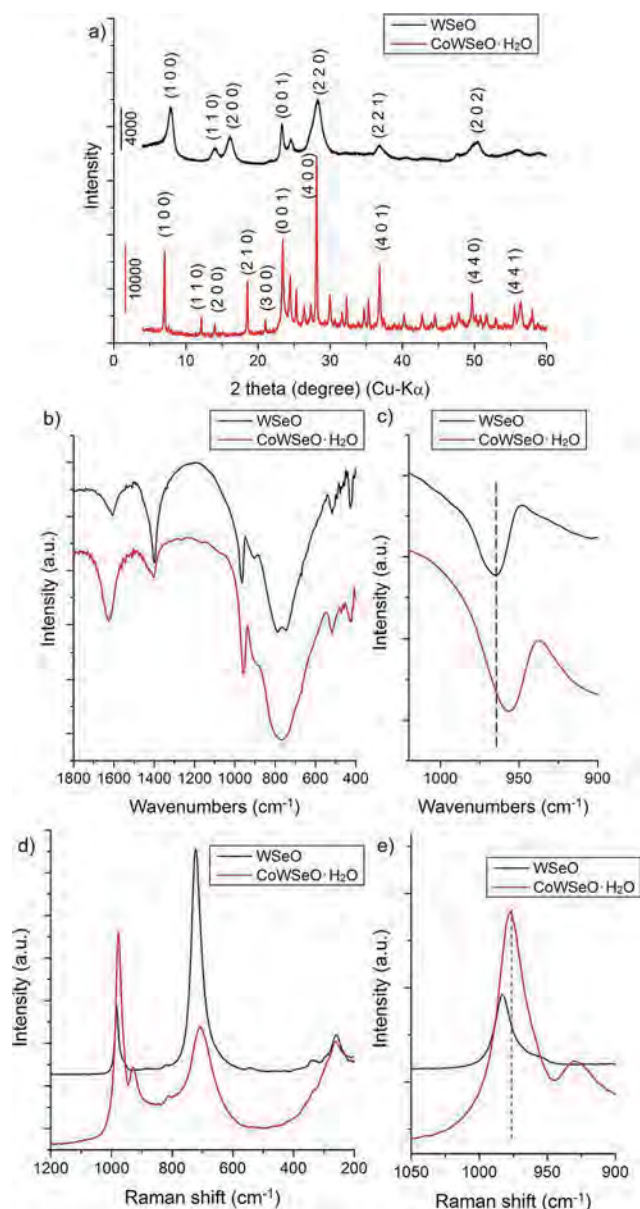


Figure 2. a) XRD patterns, b) FTIR spectra, c) enlarged FTIR spectra, d) Raman spectra, and e) enlarged Raman spectra of **WSeO** and **CoWSeO·H₂O**.

ated to be in the surrounding site and central site, respectively. Co might occupy the linker site with a partial occupancy of 0.4. The initial structure was refined by Rietveld refinement. The framework of the material is formed by the connection of the $\{[\text{Se}^{\text{IV}}\text{W}^{\text{VI}}\text{O}_{21}]^{2-}\}_n$ building blocks with the Co ions in a hexagonal fashion (Figure 1 e,f). A Co ion might connect the terminal W=O bond in the *ab* plane. The packing of the molecular wire building blocks ($\{[\text{SeW}_6\text{O}_{21}]^{2-}\}_n$) in the crystal was in a “corner-to-corner” manner (Figure S2). The micropore surrounded by three molecular wire building blocks and Co linkers (Figure 1g) was occupied by water or NH_4^+ in the original material, as indicated by FTIR (Figure 2b). The (100) plane was ascribed to the packing of the molecular wire building blocks, and the (001) plane was derived from the stacking of the hexagonal units ($[\text{SeW}_6\text{O}_{21}]^{2-}$) along the *c*-axis. The simulated XRD

pattern of the material matched the experimental pattern (Figure 1h and Table S3). No additional peaks were observed from the experimental data when compared with the simulated pattern, indicating that the powder sample of **CoWSeO·H₂O** was pure.

The IR band at 960 cm^{-1} and the Raman peak at 970 cm^{-1} corresponded to the terminal W=O bond. The IR band and Raman band of **CoWSeO·H₂O** shifted to a higher wavenumber compared with those of **WSeO** (Figure 2c,e), which indicated that the length of the W=O bond increased after the incorporation of Co ions into the structure and suggested the existence of an interaction between Co and the terminal W=O bonds of the molecular wire building blocks. Therefore, Co ions connected the molecular wires to form a 3D network of the material.

Thermal analysis (temperature-programmed desorption mass spectrometry, TPD-MS and thermogravimetric-differential thermal analysis, TG-DTA) showed the desorption of guest molecules in the original material during heating (Figures S3 and S4 in the Supporting Information). The TG-DTA of **CoWSeO·H₂O** showed two main weight loss processes (Figure S4a). The weight loss below 200°C was ascribed to water desorption, which was confirmed by TPD-MS (Figure S3a). The water content in the as-synthesized material estimated by TG was about 10%, which was in good agreement with the elemental analysis. The second weight loss at about 520°C might be due to material decomposition and SeO_2 desorption because no desorption of water or NH_3 was observed in the TPD-MS profile. The SeO_2 weight loss was estimated to be 4.7%, which was close to the elemental analysis (ca. 6.1%). Compared with **WSeO**, the water desorption of **CoWSeO·H₂O** occurred at a lower temperature.

The soft framework of **CoWSeO·H₂O** during the hydration and dehydration process

The space surrounded by the molecular wire building blocks and Co ions was originally occupied by water and NH_4^+ in **CoWSeO·H₂O**. The water and NH_4^+ in the material were removed by the heat treatment, which left micropores in the material that were suitable for the adsorption of small molecules.

CoWSeO·H₂O was treated under dehydrating conditions (together with **WSeO**) at 100°C for 24 h, and the resulting dehydrated material was denoted as **CoWSeO**. **CoWSeO** was observed by SEM, revealing a flower-shaped morphology (Figure S5 in the Supporting Information). The XRD patterns of the hydrated and dehydrated **CoWSeO** were different, indicating that the crystal structure of the material varied during the processes. This difference was investigated by in situ and ex situ XRD experiments.

The in situ XRD experiments on **CoWSeO·H₂O** were first carried out under dehydration conditions and then under hydration conditions. The material was heated with a temperature ramp increase of $10^\circ\text{C min}^{-1}$ under a nitrogen atmosphere with a flow rate of 40 mL min^{-1} . The material was monitored by powder XRD. As shown in Figure 3a,b, when the tempera-

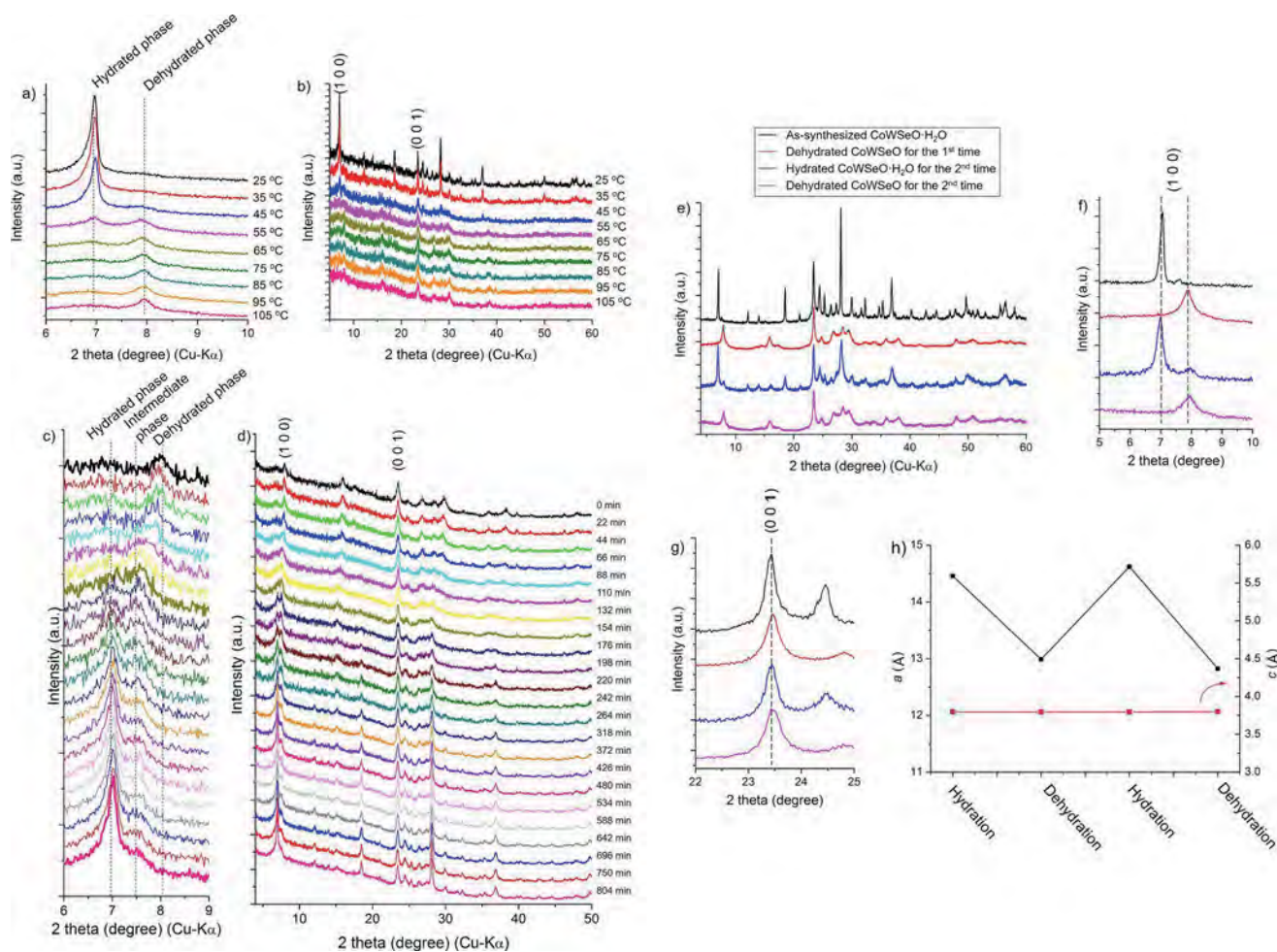


Figure 3. In situ XRD of $\text{CoWSeO}\cdot\text{H}_2\text{O}$ during heat-treatment: a) enlarged XRD patterns at low angle and b) full patterns. In situ XRD of CoWSeO during water adsorption: c) enlarged XRD patterns at low angle and d) full patterns. XRD patterns of hydrated and dehydrated CoWSeO : e) full patterns, f) enlarged patterns of the peak for the (100) plane, g) enlarged patterns of the peak for the (001) plane, and h) lattice parameter change during the hydration–dehydration process.

ture was low ($<45^\circ\text{C}$), the peak for the (100) plane was at about 7° , and the main phase was the hydrated material ($\text{CoWSeO}\cdot\text{H}_2\text{O}$). As the treatment temperature was further increased, this peak shifted to a higher angle (ca. 8°), indicating the formation of the dehydrated material (CoWSeO) and a decrease in the distance between $\{[\text{Se}^{\text{IV}}\text{W}^{\text{VI}}_6\text{O}_{21}]^{2-}\}_n$ building blocks. Other diffraction peaks also changed except for the peak for the (001) plane, which corresponded to the stacking of the hexagonal unit ($[\text{SeW}_6\text{O}_{21}]^{2-}$) in the c -axis. This indicated that the crystal structure changed, whereas the building blocks ($\{[\text{Se}^{\text{IV}}\text{W}^{\text{VI}}_6\text{O}_{21}]^{2-}\}_n$) were stable.

After the dehydrated sample had been cooled to 25°C , water vapor was introduced by N_2 bubbling ($80\text{ mL}\cdot\text{min}^{-1}$). CoWSeO was monitored by powder XRD (Figure 3c,d). As the water vapor was introduced, the diffraction peak of the (100) plane gradually shifted to a lower angle. After 132 min, an intermediate phase was generated (see below). Finally, all of the peaks returned to those of the original material ($\text{CoWSeO}\cdot\text{H}_2\text{O}$). The in situ XRD study demonstrated that the structure of the material reversibly changed with the water content in the material.

For the ex situ XRD study, when $\text{CoWSeO}\cdot\text{H}_2\text{O}$ was heated at 100°C for 24 h to form the dehydrated material, CoWSeO , the diffraction peak for the (100) plane shifted to a higher angle, indicating that the molecular wires were closer and the lattice parameter (a) of the material decreased (Figure 3e–h). CoWSeO was then placed under 100% humidity at room temperature, which caused a recovery of the original XRD peaks of $\text{CoWSeO}\cdot\text{H}_2\text{O}$. The structure of the material returned to $\text{CoWSeO}\cdot\text{H}_2\text{O}$ after the re-adsorption of water. The lattice parameter (a) changed corresponding to a reversible change in the water amount of the material. For the (001) plane, corresponding to the lattice parameter (c) (Figure 3), the water adsorption did not affect the value, maintaining a constant value of about 0.4 nm during the process; this indicated that the stacking hexagonal unit did not change and that the molecular wire building blocks were stable. The Raman spectra of $\text{CoWSeO}\cdot\text{H}_2\text{O}$ and CoWSeO were nearly the same and demonstrated that the structure of the material was stable (Figure S6 in the Supporting Information).

In contrast, WSeO , based on the same building block as $\text{CoWSeO}\cdot\text{H}_2\text{O}$ (Figure 1c,d), did not exhibit similar behavior to

CoWSeO·H₂O after the same process (Figure S7). The material was stable under heating and water vapor. The XRD peaks for the (100) plane and the (001) plane nearly remained constant. The result indicated that **WSeO** was not a soft framework material. In this case, the critical factor to form a porous soft framework might be the interaction between the transition-metal ion and molecular wire. For **CoWSeO·H₂O**, Co ions connected the molecular wire building blocks. For **WSeO**, the materials formed by attaching the molecular wire building blocks through ionic interactions between the counter-cation (NH₄⁺) and the {[Se^{VI}W^{VI}O₂₁]²⁻},_n molecular wires.

The structure of **CoWSeO** was confirmed by the atomic resolution HAADF-STEM (high-angle annular dark-field scanning transmission electron microscopy) images (Figure 4). The cross-sectional image of the (001) plane of **CoWSeO** revealed the hexagonal unit of [SeW₆O₂₁]²⁻ and its "edge-to-edge" packing manner with a periodicity of about 1.2 nm (Figure 4b). The side view of **CoWSeO** (Figure 4c) revealed that the hexagonal units, [SeW₆O₂₁]²⁻, were stacked with a layer distance of about 0.4 nm to form a molecular wire. The atomic positions in the molecular wire building blocks observed in the HAADF-STEM images were in good agreement with the structure of **CoWSeO·H₂O**. The packing of the molecular wires in **CoWSeO** (the "edge-to-edge" manner) was however different from **CoWSeO·H₂O** (the "corner-to-corner" manner). The Co site cannot be distinguished by HAADF-STEM, which might be due to the disordered distribution and low occupancy.

Water adsorption properties and flexible framework

The porous soft framework material, **CoWSeO**, was used for water adsorption at room temperature (25 °C). Before the measurement, the material was heated at 100 °C under high vacuum to remove the water molecules in the micropores. The water adsorption isotherm of **CoWSeO** (Figure 5) demonstrated that the material adsorbed water with increasing water pressure, and the total adsorbed water amount was about 11 mol mol⁻¹ (11 mol of water per 1 mol of [SeW₆O₂₁]²⁻). There were three stages during the whole process. The first stage consisted of a pressure range from 0 to 1.75 kPa. The adsorbed amount was about 3 mol mol⁻¹, and a sudden increase in the adsorbed amount indicated a strong interaction between the water and the material framework. The second stage was from 1.75 to 2.5 kPa, and the adsorbed amount was about 4.5 mol mol⁻¹. The final stage was up to 3 kPa, and the adsorbed amount was about 3.5 mol mol⁻¹. The adsorbed water could be desorbed from the material by decreasing pressure. The isotherm of water desorption from **CoWSeO·H₂O** did not overlap with the adsorption isotherm, which indicated that the adsorption process was not fully reversible. The water adsorption isotherm of **CoWSeO·H₂O** indicated a structural change during the process, and the unique adsorption isotherm was related to the soft framework of the material based on the connection of the molecular wire building blocks with the Co ions.

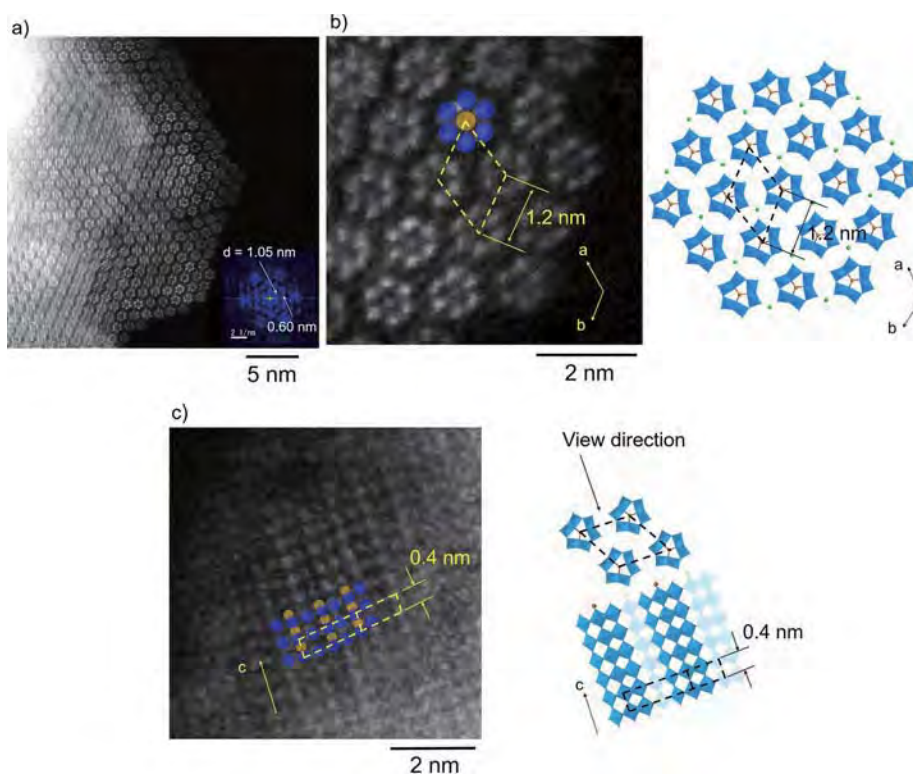


Figure 4. HAADF-STEM images of a) **CoWSeO** in the *ab* plane (Scale bar in inset = 2 nm⁻¹), b) enlarged **CoWSeO** in the *ab* plane (left) with the proposed structure (right), and c) **CoWSeO** along the *c*-axis (left) with the proposed structure (right). Dashed line indicates the unit cell of the material; W: blue, Se: yellow, Co: green.

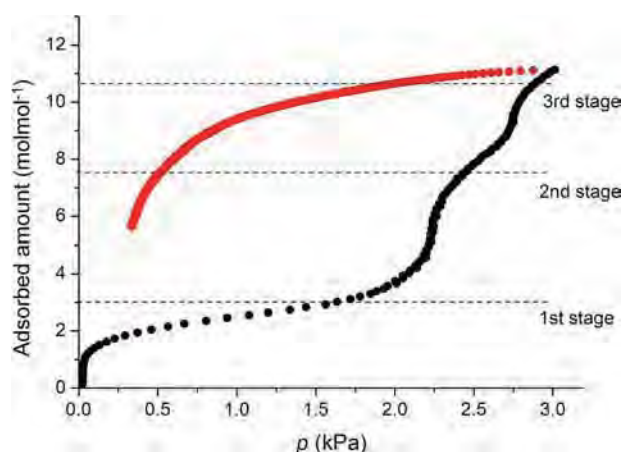


Figure 5. Water vapor adsorption (black) and desorption (red) isotherms of CoWSeO.

A relative humidity-dependent powder XRD study was carried out to understand the structural change of CoWSeO·H₂O during the water adsorption. First, CoWSeO·H₂O was dehydrated at 100 °C under high vacuum for 2.5 h. Then the dehydrated material was exposed to different relative humidity conditions for 24 h to reach the equilibrium state at 25 °C (Figure 6). The relative humidity was controlled by saturated aqueous solutions of different salts, ZnCl₂ (17%), NaBr (65%), NaCl (78%), and KBr (84%), and the corresponding water vapor pressure values at 25 °C using these aqueous solution were 0.54, 2.1, 2.5, and 2.7 kPa. There were three stable phases observed with increasing humidity. The XRD pattern of each stable phase was indexed, and the structures were refined by Rietveld refinement. Under a low humidity condition (17%), the molecular wire building blocks were arranged in the “edge-to-edge” manner, and the distance between the nanowires was close, as confirmed by the Rietveld analysis (Figure S8 and Table S4 in the Supporting Information). With the increase in humidity to 65%, another stable phase was generated with the same packing manner but an increase in lattice parameter *a* (13.4397 Å; Figure 6, Figure S9, and Table S5). The arrangement of the mo-

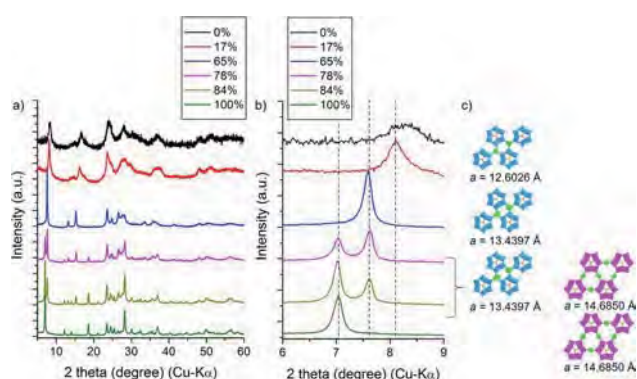


Figure 6. a) Relative humidity-dependent XRD patterns of CoWSeO. b) Enlarged XRD patterns, and c) corresponding structures of CoWSeO at different humidity values; the experiments were carried out at 25 °C. W (“edge-to-edge” manner): blue, W (“corner-to-corner” manner): purple, Se: yellow, Co: green, O: red.

lecular wires in the crystal retained the “edge-to-edge” configuration. This result demonstrated that the lattice of the material expanded with the increase in humidity. This intermediate phase was also observed in the in situ XRD study (Figure 3 c,d). A further increase in the humidity (78–85 %) produced a mixed phase, and the third stable phase did not form completely until the humidity reached 100%; the final phase had the same structure as that of CoWSeO·H₂O, and the arrangement of the {[Se^{IV}W^{VI}O₂₁]²⁻}_n molecular wires converted to the “corner-to-corner” manner. The result of the humidity-dependent powder XRD analysis demonstrated that the structure of the material changed during water adsorption.

The position of Co in CoWSeO was investigated by theoretical calculations, where the Co ion was connected to the terminal W=O bond in CoWSeO·H₂O. After dehydration, the packing of the {[Se^{IV}W^{VI}O₂₁]²⁻}_n molecular wires transitioned to the “edge-to-edge” arrangement, as shown by HAADF-STEM (Figure 4). In situ IR revealed that even the material heated at 200 °C retained the signal at about 3500 cm⁻¹, indicating that O–H (derived from OH⁻ or H₂O) probably existed as a ligand for Co (Figure S10). TPD and TG also showed that, after 100 °C, water desorption was still observed, although the amount was low (Figure S3 and Figure S4). There were two possible sites for Co in CoWSeO (Figure 7 a). The system energy calculation of the optimized structures with Co in different sites indicated that the Co ion was at position A (Figure 7 c,d). The optimized structure of CoWSeO exhibited three W=O terminal bonds and H₂O acting as ligands of Co to form a CoO₄ tetrahedron that connected the molecular wires to construct the material (Figure 7 c).

DFT calculations investigated the adsorbed structures for the initial stage of water adsorption. There were two possible sites for water adsorption, the A site (Co site) and B site (Figure 7 a). The energy of the optimized models with the water at the A site was lower than that of the water at the B site, indicating the coordination of water molecules to Co ions (Figure 7 e–h) at the beginning of the adsorption. After adsorbing two water molecules per hexagonal unit, the coordination state of Co turned from a CoO₄ tetrahedron to a CoO₆ octahedron. This simulated water coordination process was in good agreement with the adsorbed amount observed during the initial fast adsorption (2 mol mol⁻¹). Furthermore, the bond distance between Co and the W=O terminal bonds changed with an increase in the amount of coordinated water, according to the simulation (Figure 7 b). As more water adsorbed at the Co site, the W=O₁–Co became longer, and the other two became shorter. This indicated that the water adsorption changed the coordination state of Co and was probably the driving force to changing the entire crystal structure. The time-dependent DR-UV/Vis (diffuse reflectance) spectra of the material (Figure 8) at a relative humidity of about 50% showed that the absorbance changed while the sample was exposed to water vapor. The UV/Vis spectra of the material changed continuously due to the change in coordination of water at the Co site.^[9] This experiment indicated that the first step of water adsorption was Co coordination, which agreed with the result of the DFT calculation.

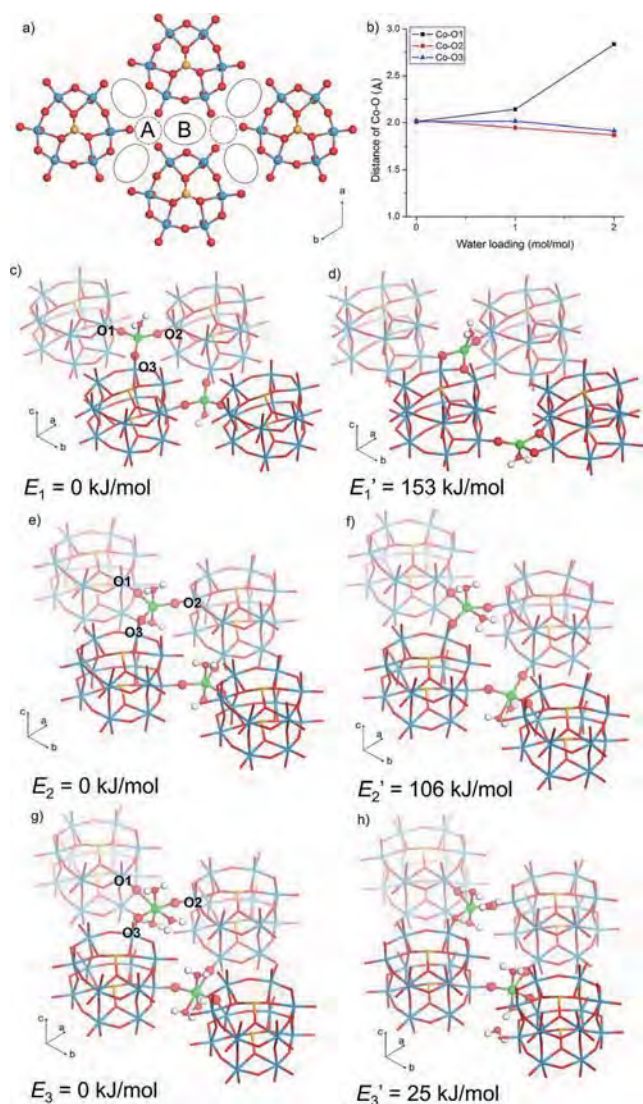


Figure 7. a) Structural representation of **CoWSeO**, A site: dashed line, B site: full line. b) Distance change of Co–O with different water loading amounts in **CoWSeO** with Co at the A site, c) **CoWSeO**, Co at the A site, d) **CoWSeO**, Co at the B site, e) **CoWSeO** adsorbed 1 mol mol^{-1} of water with Co at the A site, f) **CoWSeO** adsorbed 1 mol mol^{-1} of water with Co at the B site, g) **CoWSeO** adsorbed 2 mol mol^{-1} of water with Co at the A site, h) **CoWSeO** adsorbed 2 mol mol^{-1} of water with Co at the B site, W: blue, Se: yellow, Co: green, O: red, H: white.

A Monte Carlo (MC) simulation was carried out to further investigate the adsorbed structure of water in **CoWSeO** after the adsorption of 2 mol mol^{-1} of water (Figure 7c). The MC simulation was conducted by introducing water molecules one by one into the model of the material with the CoO_6 octahedron (Figure 7c), and water continually filled the micropores of the material (Figure S11 in Supporting Information). The adsorption energy was estimated by the MC simulation. As the water loading amount in the material was over 3 mol mol^{-1} (similar to the first stage of water adsorption) and continuously increased, the adsorption energy decreased, indicating that the structure might change upon the adsorption of more water. As indicated in the humidity-dependent XRD study, the change

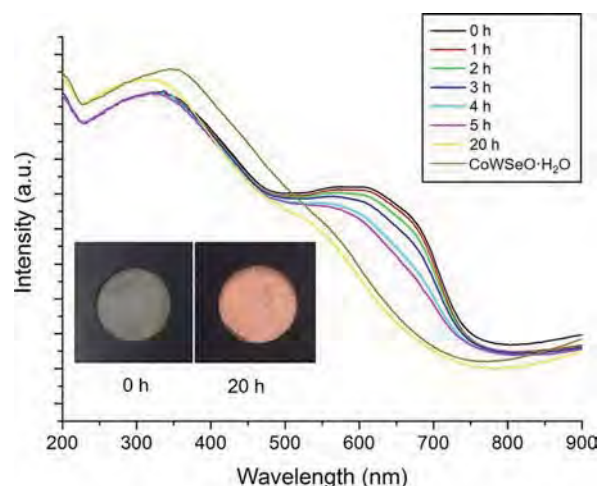


Figure 8. DR-UV/Vis spectra of **CoWSeO** during exposure to water vapor with a relative humidity of about 50%. Inserted image: photographs of **CoWSeO** (left) and **CoWSeO·H₂O** (right).

might manifest as an expansion of the lattice. When the simulated adsorbed amount reached 7 mol mol^{-1} , which approximated the second adsorption stage, the simulated adsorption energy became negative, indicating that the current structure of **CoWSeO** was unable to further adsorb water molecules. The material structure probably changed to the “corner-to-corner” structure for the adsorption of more water, as indicated in the humidity-dependent XRD study.

With consideration of the results mentioned above, a water adsorption-induced structural change of **CoWSeO** was proposed (Figure S12). First, the water molecules adsorbed at the Co site of **CoWSeO**, in which the $\{[\text{Se}^{\text{IV}}\text{W}^{\text{VI}}\text{O}_{21}]^{2-}\}_n$ building blocks were in the “edge-to-edge” manner, and the coordination state of the Co ions changed from the CoO_4 tetrahedron to the CoO_6 octahedron. As the adsorbed amount of water continually increased, the lattice parameter (a) of **CoWSeO** increased to about 13.4 \AA . Finally, when the material was fully saturated by water, the packing of $\{[\text{Se}^{\text{IV}}\text{W}^{\text{VI}}\text{O}_{21}]^{2-}\}_n$ building blocks transitioned to the “corner-to-corner” manner with a further increase of the lattice parameter (a) (ca. 14.7 \AA).

CoWSeO·H₂O was stable during the water adsorption-desorption process. After the water adsorption-desorption experiment, the used material was characterized by XRD and FTIR (Figure S13), and the results exhibited all of the characteristic peaks for **CoWSeO·H₂O**, thus demonstrating that the material structure was stable.

Conclusions

In summary, an all-inorganic 3D porous soft framework of **CoWSeO** based on a transition metal oxide was synthesized by a bottom-up approach using a 1D anionic metal oxide as a building unit and a Co ion as a linker. The structure of the material was confirmed using HAADF-STEM images combined with powder X-ray diffraction. The unique structural feature of the porous soft framework material resulted in a unique water adsorption property, and a high amount of adsorbed of water

was achieved. The Co coordination changed, the lattice parameter increased, and eventually the structure altered with the change of the water loading amount. The structure of the material changed reversibly with changes to the water content in the structure.

Materials with microporous/porous soft frameworks are abundant in the organic field of study, but they rarely appear in the inorganic field. This research provides an opportunity to further explore material science in the inorganic world to obtain new porous soft frameworks with fully inorganic compositions. Because of the combination of the unique properties of a porous soft framework and an inorganic composition, the materials are expected to have important applications in the near future.

Experimental Section

Materials

All chemicals were reagent grade and were used according to the suppliers' protocols. Homemade de-ionized water (DIRECT-Q 3UV) was used. Molecular wires of $(\text{NH}_4)_2[\text{SeW}_6\text{O}_{21}]$ (denoted as **WSeO**) were prepared according to the published procedure^[6b] and confirmed by XRD and FTIR spectroscopy.

Material synthesis

Synthesis of CoWSeO·H₂O: $(\text{NH}_4)_6\text{H}_2\text{W}_{12}\text{O}_{40} \cdot n\text{H}_2\text{O}$ (1.983 g, 7.8 mmol based on W) was dissolved in 30 mL of water, followed by the addition of SeO_2 (0.142 g, 1.3 mmol) and $\text{Co}(\text{OAc})_2 \cdot 4\text{H}_2\text{O}$ (0.198 g, 0.77 mmol) to the $(\text{NH}_4)_6\text{H}_2\text{W}_{12}\text{O}_{40} \cdot n\text{H}_2\text{O}$ solution. The solution was heated in a flask at 100 °C for 17 h with stirring. After the mixture had been cooled to room temperature, the resulting solid was recovered from the solution by filtration. The obtained solid was washed with 10 mL of water three times and dried at room temperature overnight. Finally, 0.205 g of **CoWSeO·H₂O** was obtained (yield of 9.8%). Elemental analysis: calcd for $\text{Co}_{1.3}\text{N}_{0.4}\text{W}_6\text{Se}_1\text{O}_{33}\text{H}_{24.6}$: Co, 4.22; N, 0.31; W, 60.71; Se, 4.35; H, 1.35, Found: Co, 4.12; N, 0.30; W, 60.27; Se, 4.70; H, 1.48.

Dehydration–hydration treatment: The fresh as-synthesized material was placed in an oven and dried at 100 °C for 24 h. to dehydrate. For hydration, the dried material was placed in a 100% humidity container for 24 h at 25 °C.

Characterization

XRD patterns were obtained on an Ultima IV X-ray diffractometer (Rigaku, Japan) with $\text{Cu}_{\text{K}\alpha}$ radiation (tube voltage: 40 kV, tube current: 40 mA). FTIR spectroscopy was carried out on a PerkinElmer PARAGON 1000. Diffuse-reflectance ultraviolet-visible (DR-UV/Vis) spectra were obtained using a JASCO V-570 spectrophotometer equipped with an ISN-470 reflectance spectroscopy accessory. XPS was performed on a JPS-9010MC (JEOL, Japan). The spectrometer energies were calibrated using the $\text{Au } 4f_{7/2}$ peak at 84 eV. Raman spectra were recorded using a Renishaw inVia Raman microscope. Temperature-programmed desorption mass spectrometry (TPD-MS) measurements were carried out from 40 to 600 °C at a heating rate of 10 °C min⁻¹ under He flow (flow rate: 50 mL min⁻¹). Samples were set up between two layers of quartz wool. A TPD apparatus (BEL Japan, Inc.) equipped with a quadrupole mass spectrometer (M-100QA; Anelva) was used to detect NH_3 (m/z 16) and H_2O (m/z 18). Thermal analysis (TG-DTA) was carried out up to 600 °C at

a heating rate of 10 °C min⁻¹ under nitrogen flow (flow rate: 50 mL min⁻¹) with a Thermo Plus TG-8120 (Rigaku, Japan).

HAADF-STEM images were obtained with an ARM-200F electron microscope (JEOL, Japan) operated at 200 kV with a CEOS probe aberration corrector (CEOS, Germany). The probe convergence semi-angle was 14 mrad and the collection angle of the HAADF detector was 54–175 mrad. The obtained images were treated with the Local 2D Wiener Filter in the HREM-Filters Pro software (HREM Research Inc., Japan) for noise removal. Solid samples were deposited on carbon-coated copper grids.

Elemental compositions were determined by an inductively coupled plasma (ICP-AES) method (ICPE-9000, Shimadzu). CHN elemental composition was determined at the Instrumental Analysis Division, Equipment Management Center, Creative Research Institution, Tokyo Institute of Technology.

Structure determination using powder X-ray diffraction

The structure of **CoWSeO·H₂O** was determined from powder XRD. First, the powder XRD pattern was indexed by the DICVOL06^[10] and X-cell^[11] programs. After performing a Pawley refinement, the most reasonable space group was obtained. Then, the Le Bail method^[12] was applied for intensity extraction with the EdPCR program in the FullProf software package. The initial structure was solved by a charge-flipping algorithm in JANA2006.^[13] The positions and types of atoms were obtained by analyzing the generated electron density maps (Table S1). The initial structure was refined by Rietveld analysis.

Rietveld refinement and powder diffraction pattern simulation

The structures of **CoWSeO·H₂O** and **CoWSeO** at different humidity levels were refined by powder XRD Rietveld refinements.^[14] The initial structure of **CoWSeO** at different humidity levels was obtained, by considering the **CoWSeO·H₂O** structure. The pattern and lattice parameters of the materials were refined by the Pawley method. Then, isotropic temperature factors were given for every atom in the initial structures. The Rietveld analysis was started with the initial models of the materials, and the lattice parameters and pattern parameters were from the Pawley refinement. Every atom position was refined. The occupancy of atoms in the framework was fixed without further refinement, and occupancies of atoms for water and cations were refined, with consideration of the results of the elemental analysis. Finally, the pattern parameters were refined again to obtain the lowest R_{wp} value. The crystallographic parameters and atom position of the materials are shown in Tables S2–S5. Material modeling, X-cell program, Pawley refinement, and Rietveld refinement were performed with the Materials Studio package (Accelrys Software Inc.).

DFT calculations and Monte Carlo simulation

Monte Carlo (MC) simulations were performed to predict the adsorbed structure of the guest molecule in a super cell of $(1 \times 1 \times 2)$ with the adsorption locator program in the Materials Studio package. First, the structure of **CoWSeO** and H_2O were optimized by using the DMol³ program.^[15] The optimized structure of the material is given in Table S6. We employed the Perdew–Burke–Ernzerhof (PBE) generalized gradient functional and DND basis set. The calculated Mulliken atomic charge was applied for the Monte Carlo simulation. The partial atomic charges analyzed for H_2O were $\text{H} = +0.405\text{e}$ and $\text{O} = -0.810\text{e}$. The Monte Carlo simulation and DFT

calculation were performed with the Materials Studio package (Accelrys Software Inc.).

Evaluation of water adsorption/desorption properties

The water adsorption and desorption isotherms were recorded at 25 °C on a BELSORP-aqua volumetric adsorption instrument (MicrotracBEL Corp.). Before the measurements, the samples were heated at 100 °C under reduced pressure (1–2 Pa).

Acknowledgements

This work was supported in part by the Novel Cheap and Abundant Materials for Catalytic Biomass Conversion (NOVA-CAM, FP7-NMP-2013-EU-Japan-604319) program of the Japan Science and Technology Agency (JST) and a Grants-in-Aid for Scientific Research (A) from the Ministry of Education, Culture, Sport, Science, and Technology of Japan (MEXT; grant number: 15H02318). The authors also thank the Material Analysis Suzukake-dai Center, Technical Department, Tokyo Institute of Technology, for the elemental analysis.

Keywords: adsorption · all-inorganic · flexible · polyanions · soft framework

- [1] a) S. Furukawa, J. Reboul, S. Diring, K. Sumida, S. Kitagawa, *Chem. Soc. Rev.* **2014**, *43*, 5700–5734; b) H. Furukawa, K. E. Cordova, M. O’Keeffe, O. M. Yaghi, *Science* **2013**, *341*, 1230444; c) D. J. Tranchemontagne, J. Mendoza-Cortes, M. O’Keeffe, O. M. Yaghi, *Chem. Soc. Rev.* **2009**, *38*, 1257–1283; d) O. M. Yaghi, M. O’Keeffe, N. W. Ockwig, H. K. Chae, M. Ed- daoudi, J. Kim, *Nature* **2003**, *423*, 705–714.
- [2] a) C. Serre, C. Mellot-Draznieks, S. Surblé, N. Audebrand, Y. Filinchuk, G. Férey, *Science* **2007**, *315*, 1828–1831; b) A. U. Ortiz, A. Boutin, A. H. Fuchs, F. Coudert, *Phys. Rev. Lett.* **2012**, *109*, 195502; c) S. Horike, S. Shimomura, S. Kitagawa, *Nat. Chem.* **2009**, *1*, 695–704; d) W. Cai, A. Gładysiak, M. Aniola, V. J. Smith, L. J. Barbour, A. Katrusiak, *J. Am. Chem. Soc.* **2015**, *137*, 9296–9301; e) F.-X. Coudert, C. Mellot-Draznieks, A. H. Fuchs, A. Boutin, *J. Am. Chem. Soc.* **2009**, *131*, 3442–3443; f) G. Férey, C. Serre, *Chem. Soc. Rev.* **2009**, *38*, 1380–1399; g) R. Kitaura, K. Seki, G. Akiyama, S. Kitagawa, *Angew. Chem. Int. Ed.* **2003**, *42*, 428–431; *Angew. Chem.* **2003**, *115*, 444–447; h) D. Bradshaw, J. B. Claridge, E. J. Cussen, T. J. Prior, M. J. Rosseinsky, *Acc. Chem. Res.* **2005**, *38*, 273–282; i) T. K. Maji, R. Matsuda, S. Kitagawa, *Nat. Mater.* **2007**, *6*, 142–148.
- [3] a) M. Sadakane, N. Watanabe, T. Katou, Y. Nodasaka, W. Ueda, *Angew. Chem. Int. Ed.* **2007**, *46*, 1493–1496; *Angew. Chem.* **2007**, *119*, 1515–1518; b) Z. Zhang, M. Sadakane, T. Murayama, S. Izumi, N. Yasuda, N. Sakaguchi, W. Ueda, *Inorg. Chem.* **2014**, *53*, 903–911; c) S. G. Mitchell, C. Streb, H. N. Miras, T. Boyd, D.-L. Long, L. Cronin, *Nat. Chem.* **2010**, *2*, 308–312; d) S. L. Suib, *Acc. Chem. Res.* **2008**, *41*, 479–487.
- [4] Special thematic issue on polyoxometalates: a) *Chem. Rev.* (guest ed.: C. L. Hill) **1998**, *98*, 1–390; special thematic issue on polyoxometalates: b) *Chem. Soc. Rev.* (guest eds.: L. Cronin, A. Müller) **2012**, *41*, 7333.
- [5] a) S. Balendhran, J. Deng, J. Z. Ou, S. Walia, J. Scott, J. Tang, K. L. Wang, M. R. Field, S. Russo, S. Zhuiykov, *Adv. Mater.* **2013**, *25*, 109–114; b) V. Nicolosi, M. Chhowalla, M. G. Kanatzidis, M. S. Strano, J. N. Coleman, *Science* **2013**, *340*, 1226419; c) K. Fukuda, K. Akatsuka, Y. Ebina, R. Ma, K. Takada, I. Nakai, *ACS Nano* **2008**, *2*, 1689–1695.
- [6] a) Z. Zhang, T. Murayama, M. Sadakane, H. Ariga, N. Yasuda, N. Sakaguchi, K. Asakura, W. Ueda, *Nat. Commun.* **2015**, *6*, 7731; b) Z. Zhang, M. Sadakane, N. Hiyoshi, A. Yoshida, M. Hara, W. Ueda, *Angew. Chem. Int. Ed.* **2016**, *55*, 10234–10238; *Angew. Chem.* **2016**, *128*, 10390–10394.
- [7] a) R. Kawamoto, S. Uchida, N. Mizuno, *J. Am. Chem. Soc.* **2005**, *127*, 10560–10567; b) L. Marleny Rodriguez-Albelo, A. Rabdel Ruiz-Salvador, A. Sampieri, D. W. Lewis, A. Gomez, B. Nohra, P. Mialane, J. Marrot, F. Secheresse, C. Mellot-Draznieks, *J. Am. Chem. Soc.* **2009**, *131*, 16078–16087; c) C.-Y. Sun, S.-X. Liu, D.-D. Liang, K.-Z. Shao, Y.-H. Ren, Z.-M. Su, *J. Am. Chem. Soc.* **2009**, *131*, 1883–1888.
- [8] a) M. Sadakane, K. Kodato, T. Kuranishi, Y. Nodasaka, K. Sugawara, N. Sakaguchi, T. Nagai, Y. Matsui, W. Ueda, *Angew. Chem. Int. Ed.* **2008**, *47*, 2493–2496; *Angew. Chem.* **2008**, *120*, 2527–2530.
- [9] a) S. Dzwigaj, M. Che, *J. Phys. Chem. B* **2006**, *110*, 12490–12493; b) J. Janas, T. Shishido, M. Che, S. Dzwigaj, *Appl. Catal. B* **2009**, *89*, 196–203.
- [10] A. Boulitif, D. Louer, *J. Appl. Crystallogr.* **2004**, *37*, 724–731.
- [11] M. A. Neumann, *J. Appl. Crystallogr.* **2003**, *36*, 356–365.
- [12] A. Le Bail, *Powder Diffr.* **2008**, *23*, 5–12.
- [13] L. Palatinus, G. Chapuis, *J. Appl. Crystallogr.* **2007**, *40*, 786–790.
- [14] R. A. Young, *The Rietveld Method*, Oxford University Press, Oxford, **1995**.
- [15] a) B. Delley, *J. Chem. Phys.* **2000**, *113*, 7756–7764; b) B. Delley, *J. Chem. Phys.* **1990**, *92*, 508–517.

Manuscript received: November 11, 2016

Accepted Article published: December 9, 2016

Final Article published: January 12, 2017

CrossMark
click for updatesCite this: *Catal. Sci. Technol.*, 2017,
7, 243Hydrothermal synthesis of a layered-type W–Ti–O
mixed metal oxide and its solid acid activity†Toru Murayama,^{*ab} Kiyotaka Nakajima,^{bc} Jun Hirata,^b Kaori Omata,^{bd}
Emiel J. M. Hensen^e and Wataru Ueda^{bf}

A layered-type W–Ti–O mixed oxide was synthesized by hydrothermal synthesis from an aqueous solution of ammonium metatungstate and titanium sulfate. To avoid the formation of titania, oxalic acid was used as a reductant. Optimized synthesis led to rod-like particles comprised of MO₆ (M = W, Ti) octahedra connected in a corner-sharing fashion in the *c*-direction and in the form of micropore-containing {W₆O₂₁} units in the *a*–*b* plane. The surface area, acidity and acid catalytic activity (alkylation) increased with the amount of the layered-type W–Ti–O phase. Strong Brønsted acid sites formed due to the thermal release of ammonia from the uncalcined precursor. Calcination at 400 °C led to the highest acidity and alkylation activity. Alkylation of benzyl alcohol and toluene led to heavy product formation due to over-alkylation of the product. The selectivity to the mono-alkylated product was improved by the addition of water, which competes with the selectively formed products for adsorption on the acid sites. FT-IR measurements showed that the layered-type W–Ti–O possesses Brønsted acid sites and at least two different Lewis acid sites. The stronger Lewis acid sites can be converted into Brønsted acid sites in the presence of water, and the weaker Lewis acid sites functioned in the presence of water. This water tolerance of Lewis acid sites is an important characteristic of layered-type W–Ti–O, as it allows the bifunctional catalyst to convert 1,3-DHA into lactic acid in water.

Received 18th October 2016,
Accepted 29th November 2016

DOI: 10.1039/c6cy02198k

www.rsc.org/catalysis

Introduction

Mixed metal oxides of transition metals are important inorganic materials which amongst others can serve as catalysts and ceramics. The demand for solid acid catalysts is expected to increase because such catalysts are reusable and can be readily separated from the reaction mixture. Many inorganic oxides including zeolites and metal oxides, which have Lewis acid sites, have been found to be nearly inactive for reactions in water because of the strong coordination of water to Lewis acid sites.¹ Therefore, the development of a Lewis acid catalyst that exhibits excellent catalytic activity and selectivity for

various organic reactions in the presence of water is desirable.²

An area in which solid acid catalysts operating in water are required is biomass conversion, involving reactions such as the formation of 5-hydroxymethylfurfural from hexoses and lactic acid from trioses. Furfural derivatives are raw materials for polymers. Accordingly, the conversion from sugars to furfural, which is the main component of woody biomass, has been targeted in an effort to make the transition to a sustainable economy.³ Lactic acid is also a bio-based commodity chemical with many applications, including the rapidly expanding use of polylactate as a bio-plastic.⁴ Lactic acid can be synthesized from glyceraldehyde or 1,3-dihydroxyacetone (DHA) over acid catalysts.^{5–7} These molecules are readily produced by the oxidation of glycerol, the main by-product in biodiesel production. Therefore, an efficient catalytic system that converts GLA and DHA into lactic acid would be promising for lactic acid production.⁸

One of the typical solid acid catalysts is niobium oxide, which has Lewis acidity and Brønsted acidity. Niobium oxide (or hydrated niobium oxide) has been used as a water-tolerant solid acid catalyst.^{1,9–12} Titania is also known for its combined Lewis and Brønsted acid properties. Kasuga *et al.* reported that nanotube-type titania can be easily obtained by heating titania in a concentrated aqueous alkali solution.¹³

^a Research Center for Gold Chemistry, Tokyo Metropolitan University, 1-1-F203 Minami-Osawa, Hachioji, Tokyo, 192-0397, Japan. E-mail: murayama@tmu.ac.jp

^b Institute for Catalysis, Hokkaido University, N21W10, Sapporo, Hokkaido, 001-0021, Japan

^c A Materials & Structures Laboratory, Tokyo Institute of Technology, 4259 Nagatsuta, Midori-ku, Yokohama, Kanagawa 226-8503, Japan

^d National Institute of Technology, Suzuka College, Shiroko-cho, Suzuka, Mie, 510-0294, Japan

^e Schuit Institute of Catalysis, Eindhoven University of Technology, P.O. Box 513, 5600 MB Eindhoven, The Netherlands

^f Department of Material and Life Chemistry, Faculty of Engineering, Kanagawa University, 3-27, Rokkakubashi, Kanagawa-ku, Yokohama, 221-8686, Japan

† Electronic supplementary information (ESI) available. See DOI: 10.1039/c6cy02198k

Titania nanotubes have been shown to function as acid catalysts. The structural distortion of the nanotube structure is thought to give rise to solid acidity, a feature which is absent in the nanosheet structure.^{14,15} The presence of acid sites was confirmed by ³¹P MAS NMR and CO_{ads} IR measurements, demonstrating the enhanced Brønsted acidity of the bridging Ti–OH–Ti groups in the nanotube structure. These catalysts showed already good performance in the Friedel–Crafts alkylation reactions with toluene and benzyl chloride at room temperature.

We have studied the relationship between the crystalline structure of W-based oxide mixed metal oxides (W–M–O (M = Nb, Ta, V)) and their catalytic activity.^{16–22} These catalysts were found to function as solid acids, and the acidic and structural properties have been discussed from the viewpoint of crystalline metal oxide structures. Tungsten oxides are a class of solid acids that form tungsten bronze based on W-centered oxygen octahedra.²³ The formation of mixed oxides between Ti and W or the substitution of W in WO₃ by Ti will enhance the acidity and catalytic performance,²⁴ as strong Brønsted acid sites, attributed to bridging hydroxyl groups M–(OH)–M' (M = Ti, Nb or Ta, M' = W or Mo) in previous studies^{25–27} and W–(OH)–Ti in this study, will appear in such materials.

We report herein the synthesis of a W–Ti–O mixed oxide by a hydrothermal process from ammonium metatungstate and titanium(III) sulfate precursors. The W–Ti–O mixed oxide is synthesized by the assembly of MO₆ (M = W, Ti) units, which gives rise to octahedra-based layered materials. This layered mixed W–Ti–O contains Brønsted acid and Lewis acid sites at its surface. The promise of the W–Ti–O as a Lewis acid catalyst is demonstrated in a water-mediated reaction.

Experimental

Preparation of W–Ti–O samples

W–Ti–O oxides were synthesized by a hydrothermal method from ammonium metatungstate (AMT, (NH₄)₆H₂W₁₂O₄₀·*n*H₂O, Nippon Inorganic Colour & Chemical) and titanium sulfate (Ti₂(SO₄)₃·*n*H₂O, Mitsuwa Chemical) precursors. Typically, Ti₂(SO₄)₃·*n*H₂O (1.27 mmol based on Ti) was added to 25 mL of water and stirred for about 20 min until it was dissolved. AMT (5 mmol W) was dissolved in 20 mL of deionized water, and then the W precursor solution was added to the Ti-containing solution. Oxalic acid (5 mmol, Wako) was added to the solution, and the mixture was stirred for 5 min. Then, the solution was sealed in a 60 mL Teflon liner stainless-steel autoclave. Hydrothermal reaction was carried out at 175 °C for 24 hours. The obtained solid was filtered, washed thoroughly with deionized water, and dried at 80 °C overnight and then calcined at 400 °C for 2 h.

Catalytic activity measurements

A 50 mL round-bottom three-neck flask equipped with a reflux condenser was used as a stirred bed reactor to evaluate the catalytic performance of the solids. For alkylation, a mix-

ture of benzyl alcohol (10 mmol), anisole or toluene (100 mmol), and an internal standard (decane, 5 mmol) was added to the reactor and the reaction temperature was adjusted to 100 °C. Then, 0.2 g of the catalyst and a Teflon-coated magnetic stir bar were loaded into the reactor. Aliquots (each 0.1 mL) were collected at regular intervals. The concentrations of the reactant and product were measured by gas chromatography using a flame ionization detector (GC-FID, GL science GC390B) with a ZB-1 column. To study hydrolysis, 5 wt% of an ethyl acetate aqueous solution (30 g, 17 mmol ethyl acetate) or 1 wt% *o*-troyl acetate aqueous solution (60 g, 4.03 mmol methyl phenyl acetate) with acetonitrile as an internal standard was introduced into the reactor. The reaction temperature was 60 °C and 0.8 g of the catalyst was used. The concentrations of the reactant and product were measured by GC-FID with a TC-WAX column. For pyruvaldehyde and 1,3-DHA transformations, an aqueous solution (2 mL) of the substrate (100 mM) and 0.1 g of the catalyst were used at 120 °C for 6 h by using a glass-type pressure tight vial (3 mL). The catalyst was removed after the reaction, and the solution was diluted with aqueous H₂SO₄. The concentrations of the reactant and product were measured by HPLC (JASCO, LC-2000 plus) equipped with an Aminex HPX-87 H column (diameter: 300 mm × 7.8 mm, eluent: 0.005 M H₂SO₄ 0.5 mL min⁻¹, temperature: 35 °C), with refractive index (RI) and photodiode array (PDA) detectors.

Characterization

The catalysts were characterized by the following techniques. Powder XRD patterns were measured with a diffractometer (RINT Ultima+, Rigaku) using Cu-K α radiation (tube voltage: 40 kV, tube current: 20 mA). Diffractions were recorded in the range of 4–60° with 5° min⁻¹. The morphology was investigated by using a transmission electron microscope (JEM-2100F, JEOL) at 200 kV. The samples were dispersed in ethanol by an ultrasonic treatment for several minutes, and drops of the suspension were placed on a copper grid for TEM observations. Raman spectra were obtained using a spectrometer (inVia Reflex, Renishaw, with a spectral resolution of 2 cm⁻¹) under the conditions of a wavelength of 532 nm and collection time of 10 s. N₂ adsorption isotherms at liquid N₂ temperature were measured by using an automatic physisorption apparatus (BELSORP MAX, BEL JAPAN) for the samples. Prior to N₂ adsorption, the catalysts were evacuated under vacuum at 300 °C for 2 h. The external surface area was calculated by the Brunauer–Emmett–Teller (BET) method. Temperature-programmed desorption (TPD) of ammonia (NH₃-TPD) was used to determine the acidity. These measurements were done in an automated chemisorption apparatus (BEL JAPAN). The experimental procedure was as follows. The catalyst (*ca.* 50 mg) was placed between two layers of quartz wool in a quartz reactor and pre-heated in a helium flow (50 mL min⁻¹) at 400 °C for 1 h. Then, ammonia was introduced at 100 °C for 30 min. The desorption profile from 100 to 700 °C was recorded with a mass spectrometer in a

helium flow (50 mL min^{-1}). Temperature-programmed decomposition mass spectrometry (TPD-MS) measurements were performed from 40 to $700 \text{ }^\circ\text{C}$ at a heating rate of $10 \text{ }^\circ\text{C min}^{-1}$ in a helium flow (50 mL min^{-1}). The decomposed gas molecules were monitored by a mass spectrometer (ANELVA, Quadrupole Mass Spectrometer, M-100QA, BEL Japan), collecting several mass fragments: CO_2 (44), O_2 (32), CO and N_2 (28), H_2O (18, 17, 16) and NH_3 (17, 16, 15). The acidity of the catalysts was measured by FT-IR spectroscopy (JASCO) of adsorbed pyridine or CO using a furnace cell with CaF_2 windows containing a self-supporting disk of a sample. The samples were pretreated in a vacuum at $350 \text{ }^\circ\text{C}$. Pyridine was adsorbed onto the samples at $100 \text{ }^\circ\text{C}$, and the adsorption spectrum was recorded after evacuation at $250 \text{ }^\circ\text{C}$ for 1 h. The spectrum of the adsorbed pyridine on the sample in the presence of water vapor (4.6 Torr) was also recorded. CO was adsorbed at $-183 \text{ }^\circ\text{C}$ and the adsorption spectrum was recorded with degassing.

Results and discussion

Synthesis of octahedra-layered W–Ti–O mixed metal oxide

In order to discuss the relationship between the crystalline structure of the W–Ti–O catalyst and its catalytic activity, various types of W–Ti–O mixed metal oxides and WO_3 were prepared. The synthesis conditions were optimized in an attempt to obtain as pure as possible samples of a single phase. Fig. 1 shows the XRD patterns of the most important W–Ti–O samples obtained in this study (further XRD patterns are shown in the ESI† (Fig. S1–S4)). The W/Ti ratio in the precursor solution was first investigated (Fig. S1†). The XRD pattern of W–Ti–O mixed oxides showed weak diffraction peaks at $2\theta = 23^\circ$ and 47° , when the atomic W/Ti ratio was between 3/2.84 and 3/1.42 (Fig. S1a–c†). Pure hexagonal WO_3 was obtained when there was no Ti in the precursor solution (Fig. S1f†). When Ti was added to the synthesis solution (W/Ti =

3/0.5), hexagonal W–Ti–O mixed oxides were obtained without the formation of anatase TiO_2 (Fig. S1e†). When the W/Ti ratio was lower than 3/1.42, anatase TiO_2 was formed (Fig. S1c†) and the intensity of the diffraction peaks of the hexagonal phase decreased and broadened. The diffraction peaks at $2\theta = 23^\circ$ and 47° observed in W–Ti–O mixed oxides when the atomic W/Ti ratio was between 3/1.42 and 3/2.84 were different from the peak derived from the (001) crystal plane of hexagonal WO_3 ($d_{001} = 3.898 \text{ \AA}$) and hexagonal W–Ti–O mixed oxide ($d_{001} = 3.896 \text{ \AA}$). The d -spacing corresponding to this value of the new phase W–Ti–O mixed oxides was 3.940 \AA , indicative of a new layered-type W–Ti–O mixed oxide based on MO_6 ($M = \text{W, Ti}$) octahedra connected in the c -axis direction. This conclusion is based on our earlier report on a similar W-based mixed oxide having a layered-type structure based on MO_6 octahedra and pentagonal bipyramidal $\{\text{M}_6\text{O}_{21}\}$ ($M = \text{W or Nb}$) units.^{19–22,28}

The oxidation state of Ti in the precursor ($\text{Ti}_2(\text{SO}_4)_3 \cdot n\text{H}_2\text{O}$) is $3+$, which changed to $4+$ during the mixed oxide formation as confirmed by XPS analysis. The Ti^{III} species acted as a reductant for the formation of the pentagonal bipyramidal $\{\text{W}_6\text{O}_{21}\}$ units, which are essential in the formation of the layered-type structure. Hexagonal WO_3 consists of WO_6 octahedra. The presence of a reductant is essential for the formation of the pentagonal bipyramidal $\{\text{W}_6\text{O}_{21}\}$ units. Accordingly, the presence of a reductant will suppress the formation of the hexagonal structure of tungsten oxide. The formation of pentagonal bipyramidal $\{\text{W}_6\text{O}_{21}\}$ units was confirmed by Raman spectroscopy. Fig. S5† shows the Raman spectra of the layered-type W–Ti–O and hexagonal WO_3 samples. For hexagonal WO_3 , Raman bands at 642 cm^{-1} , 688 cm^{-1} , and 817 cm^{-1} are assigned to the symmetric stretching modes of the W–O–W linkage.²⁹ The Raman band at 781 cm^{-1} of the layered-type W–Ti–O is assigned to the symmetric stretching mode of the polyhedra, supporting the formation of pentagonal bipyramidal $\{\text{W}_6\text{O}_{21}\}$ units.

Although the formation of the hexagonal tungsten oxide phase was increased by the addition of more Ti^{III} precursor, it led to the formation of anatase titania when there was too much Ti in the precursor solution. In an attempt to avoid the formation of titania, we added oxalic acid as an additional reducing agent (Fig. S2 and S3†). This greatly suppressed the formation of the crystalline hexagonal structure already by the addition of 5 mmol of oxalic acid (Fig. 1b). Ti^{IV} can form a four-coordinate structure with a carboxyl group. The Ti precursor composed of Ti^{IV} coordinated with four oxalic acid molecules accelerates the self-assembly of the mixed oxide based on octahedra under hydrothermal conditions. Fig. S4† shows the influence of the concentration of the precursor solution on the phases obtained. The W–Ti–O samples obtained with the higher precursor concentration (W/Ti ratio between 4/0.925 and 15/3.56) showed intense and sharp peaks at $2\theta = 23^\circ$ and 47° , evidencing the formation of the layered W–Ti–O without formation of hexagonal WO_3 and titania. The higher precursor concentration increases the rate of nucleation during hydrothermal synthesis and improves phase purity by

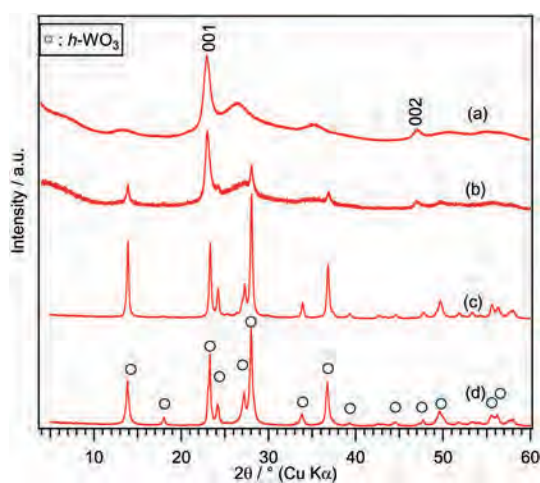


Fig. 1 XRD patterns of W–Ti–O samples: (a) W/Ti = 5/1.27 mmol (5 mmol oxalic acid), (b) W/Ti = 3/0.711 mmol (5 mmol oxalic acid), (c) W/Ti = 3/0.5 mmol, (d) W/Ti = 3/0 mmol in 45 mL of precursor solution.

avoiding the formation of other hexagonal (WO_3) and anatase (TiO_2) phases.

A representative TEM image of the layered-type W–Ti–O mixed oxide is shown in Fig. S6.† The layered-type W–Ti–O mixed oxide appeared as rod-like crystals with a diameter of 5–10 nm and lengths of 30–50 nm.

By varying the concentrations in the precursor, we were able to obtain a phase-pure layered-type structure based on octahedra MO_6 ($M = \text{W}, \text{Ti}$), showing two diffraction peaks at $2\theta = 23$ and 47° , without the formation of hexagonal WO_3 and titania (Fig. 1). The crystalline motif of the layered-type W–Ti–O in the a - b plane is due to the interconnection of MO_6 ($M = \text{W}, \text{Ti}$) octahedra and $\{\text{M}_6\text{O}_{21}\}$ ($M = \text{W}$) pentagonal units. However, the atomic ordering in the a - b plane is not sufficient to give rise to strong diffraction peaks of the sample, which is in line with the nanosized morphology of the rod-shaped particle visible by TEM.

Characterization of the W–Ti–O sample

We then proceeded to characterize the optimal phase-pure layered-type W–Ti–O sample, which was prepared at an atomic W/Ti ratio of 5/1.27 in the presence of oxalic acid. Fig. S7† shows the nitrogen adsorption–desorption isotherm and the corresponding Barrett–Joyner–Halenda (BJH) plot of the layered-type W–Ti–O mixed oxide. The adsorption isotherms displayed type IV hysteresis, suggesting the presence of mesopores. The BET surface area was $107 \text{ m}^2 \text{ g}^{-1}$. The TEM image suggests that the layered-type W–Ti–O mixed oxide sample seemed to be composed of the aggregates of nanosized crystal particles, and the mesopores are formed by the intraparticle voids. The insert highlights the adsorption at low pressure. Uptake starts at $P/P_0 = 10^{-7}$, showing that the layered-type W–Ti–O sample has micropores.^{12,30} Thus, by combining results of physisorption, XRD, Raman spectra and TEM, we demonstrate that the layered-type W–Ti–O sample contains nanosized rod-like crystals comprised of a crystalline motif of W–Ti–O in the a - b plane made up of interconnected units of MO_6 ($M = \text{W}, \text{Ti}$) octahedra and $\{\text{W}_6\text{O}_{21}\}$ pentagonal units that hold micropore channels (Fig. S8†).

In order to understand the solid acid properties of the layered W–Ti–O sample, we determined the influence of the calcination temperature on the amount of ammonia released during NH_3 -TPD. The calcined samples were also evaluated in alkylation reactions that require Brønsted acid sites. The results of these experiments are shown in Fig. 2. The highest activity for the alkylation of benzyl alcohol and anisole to benzylanisole was observed for the sample calcined at 400°C . At lower calcination temperature (300°C), ammonium cations remained in the sample originating from the precursor. This leads to a higher than expected ammonia release during NH_3 -TPD. This is supported by the TPD patterns of the uncalcined layered W–Ti–O sample and the sample after calcination at 400°C shown in Fig. S9.† The desorption peak of the ammonia derived from the ammonium cation precursor was at around 390°C for the uncalcined sample. We ar-

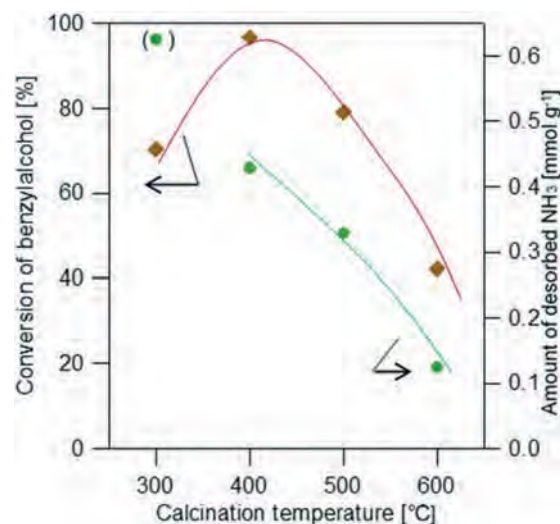


Fig. 2 Relationships of calcination temperature of the layered-type W–Ti–O catalyst with alkylation activity (cat., 0.1 g; reaction time, 1 h; anisole, 100 mmol; benzyl alcohol, 10 mmol) and the amount of NH_3 desorbed by NH_3 -TPD.

gue that the Brønsted acid sites are formed due to desorption of ammonia from the layered W–Ti–O sample. From the TPD of the sample calcined at 400°C , which shows no further release of ammonia, we infer that all ammonium cations have decomposed. Thus, the increase in alkylation activity from calcination at 300°C to 400°C is due to ammonia release, generating Brønsted acid sites. A possible reason for the decreasing catalytic activity observed for calcination temperatures higher than 400°C is the phase transition of tungsten oxide to monoclinic WO_3 . This is clear from the XRD patterns shown in the ESI.† Therefore, the layered W–Ti–O sample was calcined at 400°C for 2 h.

We also compared the performance of the layered W–Ti–O sample to that of hexagonal W–Ti–O and hexagonal WO_3 . The hexagonal W–Ti–O mixed oxide sample was obtained by using W/Ti = 3/0.5 without oxalic acid. Table 1 shows the results of alkylation reactions of anisole (or toluene) and benzyl alcohol. The alkylation activity of the layered-type W–Ti–O sample was much higher for both alkylation reactions than that of the hexagonal W–Ti–O sample. Fig. S11† shows the IR spectrum of pyridine adsorbed at 100°C followed by evacuation at 250°C for 1 h. Clearly, the layered W–Ti–O sample contains Brønsted and Lewis acid sites, whereas these sites are not observed in the hexagonal W–Ti–O sample. These results indicate that the amount of acid sites for hexagonal W–Ti–O was much smaller than that for the layered W–Ti–O sample. Hexagonal WO_3 was the least active among the three tested samples.

Solid acid reactions in the presence of water

The prospect of using the W–Ti–O mixed metal oxides as catalysts in aqueous phase reactions was investigated. First, alkylation of toluene with benzyl alcohol was investigated for

Table 1 Physical properties of catalysts and results of alkylation

Catalyst	Crystalline phase	$d(001)$	BET surface area/m ² g ⁻¹	NH ₃ desorbed amount/mmol g ⁻¹	Alkylation of anisole ^a		Alkylation of toluene ^b	
					Conv. ^c /%	Yield ^d /%	Conv. ^c /%	Yield ^d /%
W-Ti-O	Layered-type	3.940	107	0.451	48	43 (5)	78	32 (46)
h-W-Ti-O	Hexagonal	3.896	79	0.277	6	5 (1)	32	12 (20)
h-WO ₃	Hexagonal	3.898	11	0.036	4	2	—	—

^a Reaction conditions: benzyl alcohol (10 mmol), anisole (100 mmol), catalyst (0.2 g), 100 °C, 10 min. ^b Reaction conditions: toluene (10 mmol), anisole (100 mmol), catalyst (0.2 g), 100 °C, 20 min toluene. ^c Conversion of benzyl alcohol. ^d Yield of benzyl anisole or benzyl toluene. Parentheses show the yield of dibenzyl ether.

the layered W-Ti-O sample. Fig. 3 shows the influence of water on the time course of the benzyltoluene and dibenzyl ether yields. In spite of the addition of water (5 mmol) into the mixture of reactant solution with the catalyst, the substrate solution was apparently homogeneous because of the bare solubility of benzyl alcohol to water (7.15 g/100 g-H₂O at 90 °C) and an adsorptive property of the catalyst (2.35 mmol g⁻¹). For the alkylation of toluene and benzyl alcohol without the addition of water, dibenzyl ether was only obtained directly after the start of the reaction, followed by an increase of the benzyltoluene yield with reaction time. The benzyltoluene and dibenzyl ether yields stabilized after 1 h of reaction when water was not present. On the other hand, in the presence of water (5 or 10 mmol), the yield of dibenzyl ether decreased only after 30 min and the yield of benzyltoluene increased as reaction time proceeded. In another experiment shown in Fig. 3, we added 10 mmol of water after 70 min of reaction. This led to a decrease of the dibenzyl ether yield and an increase of the benzyltoluene yield. We speculate that water promotes desorption of the products from the acid sites on the layered W-Ti-O catalyst. From the TPD spectrum (Fig. S12[†]) for the layered-type W-Ti-O catalyst used in the absence of water, it is clear that the surface contains heavy products, containing toluene groups.

The peak at low temperature is due to toluene, the peak at high temperature is due to decomposition of heavier products, which likely originate from multiple alkylations. From the analysis of the reactant solution by GC-FID and GC-MS (Fig. S13[†]), heavy alkylation products such as dibenzyltoluene and tribenzyltoluene were observed. The strong Brønsted acid sites of the layered-type W-Ti-O catalyst adsorb the alkylation products on the surface of the catalyst and promote their successive alkylation. On the other hand, the addition of water to the reactant solution leads to competitive adsorption with the reactants and in this way decreases by-product formation. The other function of the addition of water would be shifting the equilibrium between benzyl alcohol and dibenzyl ether ($C_{14}H_{14}O + H_2O \rightarrow 2C_6H_5CH_2OH$), resulting in a higher alkylation rate.

Next, solid acid activity was examined by several catalytic reactions in water by using typical model reactions of hydrolysis of ethyl acetate and *o*-troyl acetate (Table 2 and Table S1[†]).³¹ Hydrolysis of ethyl acetate by using the layered-type W-Ti-O catalyst resulted in the formation of ethanol at a rate of 18.7 μmol g⁻¹ min⁻¹ for 2 h. ZSM-5 and WO₃/TiO₂ prepared by the impregnation method were tested for comparison in the same reaction conditions. The formation rates of ethanol were 19.8 μmol g⁻¹ min⁻¹ for ZSM-5 and 2.1 μmol g⁻¹ min⁻¹

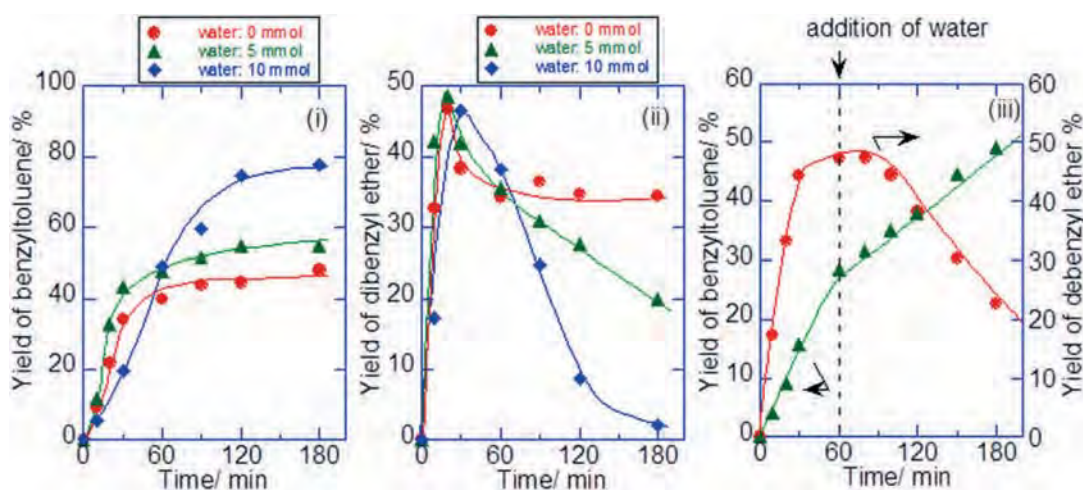
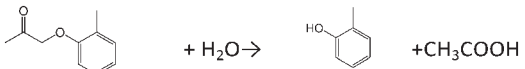
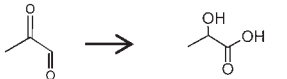
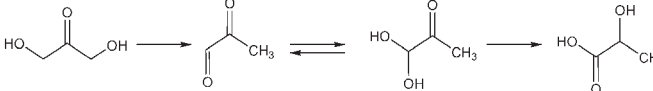


Fig. 3 Influence of the amount of water on the formation of benzyltoluene by alkylation reaction of toluene with benzyl alcohol over the layered-type W-Ti-O sample: (i) yield of benzyltoluene, (ii) yield of dibenzyl ether, (iii) and the influence of water addition on the alkylation reaction (water added after a reaction time of 70 min).

Table 2 Catalytic activity over the layered-type W-Ti-O sample in the presence of water^a

Reaction	Catalyst/g	Reaction temp./°C	Conv./%	Yield/%
$\text{CH}_3\text{COOC}_2\text{H}_5 + \text{H}_2\text{O} \rightarrow \text{CH}_3\text{COOH} + \text{C}_2\text{H}_5\text{OH}$	0.8	60	(18.7 $\mu\text{mol g}^{-1} \text{min}^{-1}$)	
	0.2	60	(8.3 $\mu\text{mol g}^{-1} \text{min}^{-1}$)	
	0.1	100 ^b	18	18
	0.1	120 ^c	70	40
	0.1	120 ^c	>99	37 (3) ^d

^a Details of reaction conditions are shown in the Experimental section. ^b Reaction time, 6 h. ^c Reaction time, 2 h. ^d Parentheses show the yield of pyruvaldehyde.

for WO_3/TiO_2 . For the hydrolysis of the more bulky ester *o*-troyl acetate, the formation rates of *o*-cresol were 8.3 $\mu\text{mol g}^{-1} \text{min}^{-1}$ for the layered-type W-Ti-O catalyst, 3.3 $\mu\text{mol g}^{-1} \text{min}^{-1}$ for WO_3/TiO_2 and 0.3 $\mu\text{mol g}^{-1} \text{min}^{-1}$ for ZSM-5. The catalytic activities based on both catalytic weight and acid site of the layered-type W-Ti-O catalyst were competitive compared to those of the other typical solid acids such as $\text{Cs}_{2.5}\text{H}_{0.5}\text{PW}_{12}\text{O}_{40}$, $\text{SO}_4^{2-}/\text{ZrO}_2$ and Nb_2O_5 .³¹ The bulkiness of the reactant, in this case, prevents diffusion into the small zeolite micropores. Yet, the layered-type W-Ti-O can act as a solid acid in an aqueous solution for the hydrolysis of both large and small esters. The reactant solution was analyzed by ICP-AES to check for possible leaching of the layered-type W-Ti-O catalyst. The results of ICP-AES showed that the amounts of leaching of the layered-type W-Ti-O catalyst were negligible.

Then, the layered-type W-Ti-O catalyst was applied to pyruvaldehyde conversion to lactic acid. The formation rate of lactic acid was slow at 100 °C. The conversion after 2 h was 18%, with nearly 100% lactic acid selectivity. The reaction at 120 °C enhanced the rate of pyruvaldehyde conversion at the expense of lactic acid selectivity. The conversion of pyruvaldehyde was 70% with 40% lactic acid yield for 2 h at 120 °C. The by-products of the reaction were dimers and trimers of the carbonyl compounds formed by the aldol condensation reaction. This performance was much better than that with sulfuric acid, which is a strong Brønsted acid (10% conversion with 6% selectivity to lactic acid at 120 °C for 2 h). Lactic acid synthesis from 1,3-DHA proceeds by dehydration reaction of 1,3-DHA to pyruvaldehyde followed by hydride transfer of pyruvaldehyde. The layered-type W-Ti-O catalyst showed full conversion with 38% selectivity to lactic acid. These values were corresponding to approximately 238 $\text{mol (m}^2 \text{mol}^{-1} \text{acid}^{-1}) \text{h}^{-1}$ of the conversion rate and 88 $\text{mol (m}^2 \text{mol}^{-1} \text{acid}^{-1}) \text{h}^{-1}$ of the formation rate based on acid density. This result shows that the layered-type W-Ti-O catalyst contains Brønsted acid sites and Lewis acid sites suitable for the transformation of 1,3-DHA. The Lewis acid sites are effective in water for pyruvaldehyde transformation.^{32,33} Below, we will show by pyridine IR that this sample contains such sites.

Solid acidity analysed by FT-IR

Fig. 4 shows the IR spectra of CO adsorbed at -183 °C on the layered-type W-Ti-O sample. The negative feature at 3660 cm^{-1} due to OH groups becomes weaker with increasing CO coverage and is replaced by a shift in the OH stretch band at 3450 cm^{-1} . This OH frequency shift upon interaction with CO, indicates that the OH groups are strongly Brønsted acidic. The absorption at 2170 cm^{-1} is attributed to the vibration of CO adsorbed on these Brønsted acid sites. The absorption band at 2179–2205 cm^{-1} is attributed to the vibrations of CO adsorbed on Lewis acid sites. The adsorption at around 2180 cm^{-1} observed at 4 Torr shifted to a higher wavenumber with the decrease in CO pressure. The presence of various absorption bands shows that the layered-type W-Ti-O sample possesses at least two kinds of Lewis acid sites of different strengths.

Fig. 5 shows the ratio of Brønsted acid sites and Lewis acid sites calculated by the integral IR absorbance of pyridine adsorbed on the layered-type W-Ti-O sample. The absorption bands at 1450 cm^{-1} and 1540 cm^{-1} were calculated as Lewis acid sites and Brønsted acid sites, respectively. After pyridine

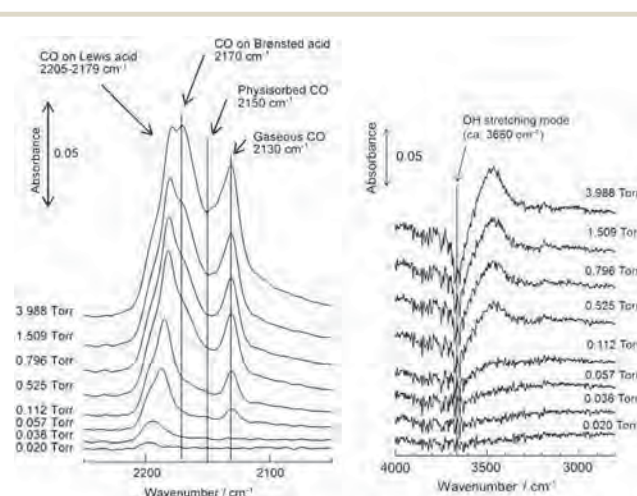


Fig. 4 FT-IR spectra of CO adsorbed (-183 °C) on the layered-type W-Ti-O catalyst.

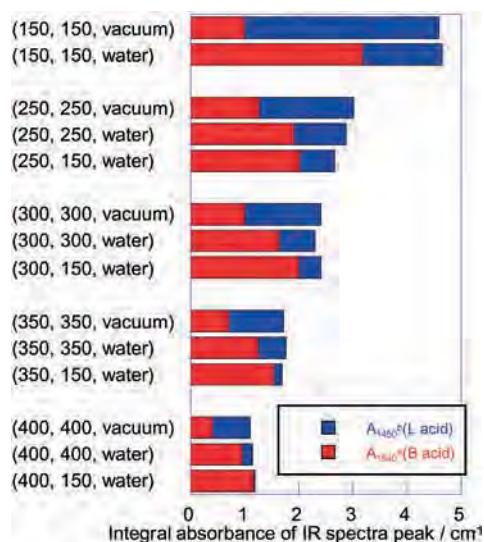


Fig. 5 Ratio of Brønsted acid sites and Lewis acid sites calculated by the peak area of pyridine-adsorbed FT-IR spectra of the layered-type W-Ti-O catalyst. (The numbers and conditions in parentheses show the desorption temperature of pyridine (°C), measurement temperature (°C) and atmosphere, respectively.)

was adsorbed onto the samples at 100 °C, the parameters of the desorbed temperature of pyridine, the measurement temperature of FT-IR and the measurement atmosphere (in a vacuum or in the presence of water) were controlled and shown as desorbed temperature/°C, measurement temperature/°C, and measurement atmosphere, respectively. A comparison of the conditions (150, 150, vacuum) with the conditions (150, 150, water) shows that the area of the adsorption peak at 1450 cm⁻¹ decreased and that of the peak at 1540 cm⁻¹ increased by the addition of water. This demonstrates that a part of the Lewis acid sites was converted to Brønsted acid sites at 150 °C upon interaction with water. Tentatively, this can be expressed by $M(L) + M=O + H_2O \rightarrow 2M-OH(B)$. The amount of Lewis acid sites that changed to Brønsted acid sites increased with increasing desorption temperature of pyridine. It is interesting to compare the IR spectra for the conditions (400, 400, vacuum), (400, 400, water) and (400, 150, water). These show that the Lewis acid sites changed to Brønsted acid sites in the presence of water and that additional Lewis acid sites were changed to Brønsted acid sites by a decrease of the temperature to 150 °C. These results suggest that weak Lewis acid sites, which were observed in the presence of water at lower temperature, act as a Lewis acid in water and that strong Lewis acid sites, which adsorbed pyridine at a higher temperature, were easily changed to Brønsted acid in the presence of water. The two peaks observed in the FT-IR spectrum of CO adsorbed corresponded to different behaviors of Lewis acid observed by FT-IR of pyridine adsorbed.

Conclusions

Layered-type W-Ti-O mixed oxides were synthesized from ammonium metatungstate and titanium sulfate precursors

with oxalic acid by a hydrothermal method. By optimization of the preparation conditions, the formation of a hexagonal structure and anatase TiO₂ was suppressed in the hydrothermal synthesis. The addition of oxalic acid as a reducing agent suppressed the formation of hexagonal W-Ti-O mixed oxide. Higher concentration of the precursors is favorable for the formation of the layered-type W-Ti-O catalyst. In general, the surface area, acidity and acid catalytic activity (alkylation) increased with the amount of the layered-type W-Ti-O phase. Strong Brønsted acid sites are obtained due to the thermal release of ammonia from the uncalcined precursor. Optimum acidity and alkylation activity were achieved by calcination at 400 °C. Alkylation of benzyl alcohol and toluene led to heavy product formation due to multiple alkylations of the product due to its strong adsorption on the catalytic surface. The selectivity could be improved by the addition of water, which competes with the products for the acid sites. FT-IR measurements showed that the layered-type W-Ti-O possesses Brønsted acid sites and at least two different Lewis acid sites. The stronger Lewis acid sites can be converted into Brønsted acid sites in the presence of water, and the weaker Lewis acid sites functioned in the presence of water. This water tolerance of Lewis acid sites is an important characteristic of layered-type W-Ti-O, as it allows the conversion of 1,3-DHA into lactic acid in water.

Acknowledgements

This work was financially supported by the European Union FP7 NMP project NOVACAM (Novel cheap and abundant materials for catalytic biomass conversion, FP7-NMP-2013-EUJapan-604319). And this study was supported by the Cooperative Research Program of Institute for Catalysis, Hokkaido University (13A1002) and the Cooperative Research Program of Materials and Structures Laboratory, Tokyo Institute of Technology (2013-53).

References

- 1 K. Nakajima, Y. Baba, R. Noma, M. Kitano, J. N. Kondo, S. Hayashi and M. Hara, *J. Am. Chem. Soc.*, 2011, **133**, 4224–4227.
- 2 S. Kobayashi and K. Manabe, *Acc. Chem. Res.*, 2002, **35**, 209–217.
- 3 M. Hara, K. Nakajima and K. Kamata, *Sci. Technol. Adv. Mater.*, 2015, **16**, 34903.
- 4 C. B. Rasrendra, B. A. Fachri, I. G. B. N. Makertihartha, S. Adisasmito and H. J. Heeres, *ChemSusChem*, 2011, **4**, 768–777.
- 5 R. M. West, M. S. Holm, S. Saravanamurugan, J. Xiong, Z. Beversdorf, E. Taarning and C. H. Christensen, *J. Catal.*, 2010, **269**, 122–130.
- 6 F. De Clippel, M. Dusselier, R. Van Rompaey, P. Vanelderden, J. Dijkmans, E. Makshina, L. Giebler, S. Oswald, G. V. Baron, J. F. M. Denayer, P. P. Pescarmona, P. A. Jacobs and B. F. Sels, *J. Am. Chem. Soc.*, 2012, **134**, 10089–10101.

- 7 E. Taarning, S. Saravanamurugan, M. S. Holm, J. Xiong, R. M. West and C. H. Christensen, *ChemSusChem*, 2009, 2, 625–627.
- 8 Y. Hayashi and Y. Sasaki, *Chem. Commun.*, 2005, 2716–2718.
- 9 T. Iizuka, K. Ogasawara and K. Tanabe, *Bull. Chem. Soc. Jpn.*, 1983, 56, 2927–2931.
- 10 C. Tagusagawa, A. Takagaki, A. Iguchi, K. Takanabe, J. N. Kondo, K. Ebitani, T. Tatsumi and K. Domen, *Chem. Mater.*, 2010, 22, 3072–3078.
- 11 I. Nowak and M. Ziolk, *Chem. Rev.*, 1999, 99, 3603–3624.
- 12 T. Murayama, J. Chen, J. Hirata, K. Matsumoto and W. Ueda, *Catal. Sci. Technol.*, 2014, 4, 4250–4257.
- 13 T. Kasuga, M. Hiramatsu, A. Hoson, T. Sekino and K. Niihara, *Langmuir*, 1998, 14, 3160–3163.
- 14 M. Kitano, K. Nakajima, J. N. Kondo, S. Hayashi and M. Hara, *J. Am. Chem. Soc.*, 2010, 132, 6622–6623.
- 15 M. Kitano, E. Wada, K. Nakajima, S. Hayashi, S. Miyazaki, H. Kobayashi and M. Hara, *Chem. Mater.*, 2013, 25, 385–393.
- 16 T. Konya, T. Katou, T. Murayama, S. Ishikawa, M. Sadakane, D. Buttrey and W. Ueda, *Catal. Sci. Technol.*, 2013, 3, 380–387.
- 17 S. Ishikawa, X. Yi, T. Murayama and W. Ueda, *Appl. Catal., A*, 2014, 474, 10–17.
- 18 S. Ishikawa, X. Yi, T. Murayama and W. Ueda, *Catal. Today*, 2014, 8–13.
- 19 K. Omata, S. Izumi, T. Murayama and W. Ueda, *Catal. Today*, 2013, 201, 7–11.
- 20 K. Omata, K. Matsumoto, T. Murayama and W. Ueda, *Chem. Lett.*, 2014, 43, 435–437.
- 21 K. Omata, K. Matsumoto, T. Murayama and W. Ueda, *Catal. Today*, 2015, 259, 205–212.
- 22 T. Murayama, N. Kuramata and W. Ueda, *J. Catal.*, 2016, 339, 143–152.
- 23 C. Yue, X. Zhu, M. Rigutto and E. Hensen, *Appl. Catal., B*, 2015, 163, 370–381.
- 24 M. Hino, M. Kurashige, H. Matsushashi and K. Arata, *Appl. Catal., A*, 2006, 310, 190–193.
- 25 T. Kitano, S. Okazaki, T. Shishido, K. Teramura and T. Tanaka, *Catal. Today*, 2012, 192, 189–196.
- 26 T. Shishido, T. Kitano, K. Teramura and T. Tanaka, *Catal. Lett.*, 2009, 129, 383–386.
- 27 T. Kitano, T. Hayashi, T. Uesaka, T. Shishido, K. Teramura and T. Tanaka, *ChemCatChem*, 2014, 6, 2011–2020.
- 28 T. Murayama, N. Kuramata, S. Takatama, K. Nakatani, S. Izumi, X. Yi and W. Ueda, *Catal. Today*, 2012, 185, 224–229.
- 29 Y. Chen and I. E. Wachs, *J. Catal.*, 2003, 217, 468–477.
- 30 T. Konya, T. Katou, T. Murayama, S. Ishikawa, M. Sadakane, D. Buttrey and W. Ueda, *Catal. Sci. Technol.*, 2013, 3, 380–387.
- 31 M. Kimura, T. Nakato and T. Okuhara, *Appl. Catal., A*, 1997, 165, 227–240.
- 32 T. Komanoya, A. Suzuki, K. Nakajima, M. Kitano, K. Kamata and M. Hara, *ChemCatChem*, 2016, 8, 1094–1099.
- 33 Y. Koito, K. Nakajima, M. Kitano and M. Hara, *Chem. Lett.*, 2013, 42, 873–875.



NH₃-efficient ammoxidation of toluene by hydrothermally synthesized layered tungsten-vanadium complex metal oxides



Yoshinori Goto^a, Ken-ichi Shimizu^{a,b,*}, Kenichi Kon^a, Takashi Toyao^{a,b}, Toru Murayama^{a,c}, Wataru Ueda^{d,*}

^a Institute for Catalysis, Hokkaido University, N-21, W-10, Sapporo 001-0021, Japan

^b Elements Strategy Initiative for Catalysts and Batteries, Kyoto University, Katsura, Kyoto 615-8520, Japan

^c Research Center for Gold Chemistry, Graduate School of Urban Environmental Sciences, Tokyo Metropolitan University, 1-1 Minami-osawa, Hachioji, Tokyo 192-0397, Japan

^d Kanagawa University, Rokkakubashi 3-27-1, Yokohama 221-8686, Japan

ARTICLE INFO

Article history:

Received 30 May 2016

Revised 26 August 2016

Accepted 16 October 2016

Available online 4 November 2016

Keywords:

Ammoxidation

Complex metal oxides

Hydrothermal synthesis

Vanadium

Tungsten

ABSTRACT

Hydrothermally synthesized W–V–O layered metal oxides (W–V–O) are studied for the vapor phase ammoxidation of toluene to benzonitrile (PhCN). Under similar conversion levels at 400 °C, W–V–O shows higher selectivity (based on toluene) to PhCN and lower selectivity to CO_x than conventional V-based catalysts (V₂O₅ and VO_x/TiO₂). Under the conditions of high contact time, W–V–O shows 99.7% conversion of toluene and 93.5% selectivity to PhCN. Another important feature of W–V–O is high NH₃-utilization efficiency in ammoxidation, which originates from the lower activity of W–V–O for NH₃ oxidation than that of V₂O₅. In situ infrared (IR) study shows that toluene is oxidized by the surface oxygen species of W83V17 to yield benzaldehyde which undergoes the reaction with adsorbed NH₃ to give benzonitrile. Model reaction studies with W–V–O suggest that the rate of NH₃ conversion to PhCN in the benzaldehyde + NH₃ + O₂ reaction is 3 times higher than the rate of NH₃ oxidation to N₂ in the NH₃ + O₂ reaction. It is shown that the high NH₃-efficiency of W–V–O is caused by the preferential reaction of NH₃ in PhCHO + NH₃ + O₂ over NH₃ + O₂ reaction.

© 2016 Elsevier Inc. All rights reserved.

1. Introduction

Ammoxidation of methyl-substituted aromatics such as toluene, xylene and methylpyridine to their corresponding nitriles is an industrially important reaction, and numerous reports have been dealt with this reaction [1–4]. The vapor phase ammoxidation of toluene to benzonitrile has been extensively studied as a model reaction [5–16]. Various metal oxide-based catalysts, including vanadium (V)-based catalysts (V₂O₅ [5], VO_x/TiO₂ [6,7], VO_x/ZrO₂ [8], V₂O₅/Nb₂O₅–TiO₂ [9], (VO)₂P₂O₇ [10–13]) and other catalysts (MoO_x/Nb₂O₅ [13], MoO_x/ZrO₂ [15], Fe-based mixed oxides [16]) have been reported to show moderate to good yields (44–77%) of benzonitrile (based on toluene) at around 400 °C [5–16]. The catalytic efficiency in the ammoxidation of toluene has been discussed in terms of the selectivity or yield of benzonitrile based on toluene. In addition to the non-selective oxidation of toluene to CO_x, another undesired side-reaction in the ammoxidation is non-selective

oxidation of ammonia (NH₃) to N₂. In order to establish a sustainable ammoxidation process, NH₃ consumption during the reaction should also be minimized. However, quite a few reports have discussed the benzonitrile selectivity based on the NH₃ consumed, or in other words, the efficiency of NH₃ utilization in ammoxidation of benzonitrile. Mechanistic studies on vanadium oxides-catalyzed ammoxidation of toluene [6,7,11–13] suggested bifunctional catalysis as a catalyst design concept. It is proposed that the VO_x sites catalyze partial oxidation of toluene to benzaldehyde-like intermediate and acid sites act as adsorption site of NH₃ [3,11–13]. If one designed a V-based mixed oxide catalyst having NH₃ adsorption sites (such as acidic WO_x sites) in close proximity to the redox sites (VO_x), the aldehyde intermediate formed on the redox site would have react preferentially with NH₃ on the acid site, resulting in high efficiency of NH₃ utilization in the ammoxidation reaction.

Our research group has focused on the hydrothermal synthesis of single crystalline Mo–V–O based catalysts [17–19]. Particularly, single phasic orthorhombic Mo₃VO_x, having a microporous and layered structure, is of importance because its structure is basically the same as that of so-called “M1 phase” which is well known as active phase in the industrial selective oxidation catalysts [18]. We have found that the Mo–V–O catalysts, as a structurally well

* Corresponding authors at: Institute for Catalysis, Hokkaido University, N-21, W-10, Sapporo 001-0021, Japan (K.-i. Shimizu).

E-mail addresses: kshimizu@cat.hokudai.ac.jp (K.-i. Shimizu), uedaw@kanagawa-u.ac.jp (W. Ueda).

defined catalytic phase for “M1 phase”, catalyzed the selective oxidative dehydrogenation of ethane at low temperature (300 °C) [18]. The single phase Mo–V–P catalyst with similar structure also catalyzed the ammoxidation of propane [19]. Recently, we have extended the hydrothermal synthetic methodology to metal oxides consisted of various groups 5 and 6 elements [20–23], and prepared a series of binary metal oxides (such as W–Ta–O [20,23], W–Nb–O [21] and W–V–O complex oxides [22]) with similar microporous and layered structure as the orthorhombic Mo_3VO_x [18]. Considering the fact that WO_x is a well known acidic co-catalyst of V-based catalysts [24–27], we have hypothesized that the W–V–O oxides act as effective catalysts for the ammoxidation. In this regard, we have recently reported the W–V–O-catalyzed highly selective ammoxidation of 3-picoline to 3-cyanopyridine [22]. We report herein a highly selective gas-phase ammoxidation of toluene by the hydrothermally prepared W–V–O layered oxides. The catalysts show high efficiency of NH_3 utilization in ammoxidation as well as high selectivity of benzonitrile based on toluene. In situ IR study shows that the reaction of benzaldehyde with NH_3 is a main pathway to benzonitrile on this catalytic system. Model reaction studies are also conducted to discuss the reason why the W–V–O catalyst shows high efficiency of NH_3 utilization.

2. Experimental

2.1. Catalyst preparation

Inorganic materials were purchased from Wako Pure Chemical Industries. According to our previous report [22], the complex metal oxide of W and V (W–V–O) with W/V molar ratio of 83/17, named W83V17, was prepared by a hydrothermal synthesis method as follows. An aqueous solution (40 mL) of $(\text{NH}_4)_6[\text{H}_2\text{W}_{12}\text{O}_{40}] \cdot n\text{H}_2\text{O}$ (10.4 mmol), $\text{VOSO}_4 \cdot n\text{H}_2\text{O}$ (4.16 mmol) and oxalic acid (0.10 mmol) was introduced into a stainless steel autoclave with a Teflon inner tube (50 mL), followed by filling the inner space of the tube by Teflon thin sheet (50 mm \times 1000 mm). Then, N_2 (20 mL min^{-1}) was fed into the solution for 10 min to remove residual oxygen. The autoclave attached to a rotating machine was installed in an oven, and the mixture underwent hydrothermal reaction at 175 °C for 24 h under mechanical rotation (1 rpm). The solid formed was filtered, washed with ion-exchanged water (1 L), dried at 80 °C overnight and then heated at 400 °C for 2 h under N_2 flow. W64V36 with W/V molar ratio of 64/36 was prepared according to the method in our previous study [22]. Bulk composition of the catalysts (Table 1) was determined by an inductively coupled plasma (ICP-AES) method (ICPE-9000, Shimadzu). Na^+ -exchanged W83V17 (designated as Na-W83V17) was prepared by mixing W–V–O (2.0 g) with 100 mL of aqueous solution of Na_2SO_4 (19.1 mmol) for 5 h at room temperature, followed by centrifuging and washing with ion-exchanged water four times, drying at 80 °C

overnight and heating at 400 °C for 2 h under N_2 flow. The Na content in Na-W83V17 (0.74 mmol g^{-1}) was determined by ICP-AES analysis. WO_3 -supported vanadia (VO_x/WO_3) with W/V molar ratio of 85/15 was prepared by impregnation method; a suspension of WO_3 (20.0 mmol) in an aqueous solution (50 mL) of NH_4VO_3 (3.5 mmol) was heated to 90 °C for 30 min to evaporate water, followed by drying at 80 °C overnight, and by heating at 400 °C for 2 h under N_2 flow. The bulk compositions and surface area of the W–V–O and VO_x/WO_3 catalysts are listed in Table 1. V_2O_5 and WO_3 for catalytic studies were commercially supplied from Wako Pure Chemical Industries. Vanadia loaded TiO_2 with V loading of 5.9 wt%, named VO_x/TiO_2 , was prepared by impregnation method [22]; a suspension of anatase TiO_2 (4 g, Wako Pure Chemical Industries) in aqueous oxalic acid solution (50 mL) of NH_4VO_3 (4.9 mmol) was evaporated at 50 °C, followed by drying at 100 °C, and by heating at 450 °C for 6 h under air.

2.2. Catalyst characterization

The BET surface areas of the catalysts were determined by N_2 adsorption at -196 °C using BELCAT (MicrotracBEL). Prior to the measurement, the samples were heated under He flow at 400 °C for 1 h. Powder X-ray diffraction (XRD) pattern of the catalysts were recorded on a Rigaku MiniFlex II/AP diffractometer with $\text{Cu K}\alpha$ radiation. Scanning electron microscope (SEM) images were taken using a JEOL JSM-7400F field emission scanning electron microscope.

The pyridine-adsorption infrared (IR) spectra were measured at 100 °C by a JASCO FT/IR-4200 spectrometer equipped with an MCT detector. The IR disk (38 \pm 1 mg, ϕ = 2 cm) of a catalyst in the flow-type IR cell. (CaF_2 windows), connected to a flow system, was first dehydrated under He flow (30 $\text{cm}^3 \text{min}^{-1}$) at 500 °C for 0.5 h, followed by cooling to the measurement temperature under He. For the adsorption of organic compounds, 0.3 mmol $\text{g}_{\text{cat}}^{-1}$ of liquid pyridine, toluene, benzaldehyde or benzonitrile was injected to the He flow preheated at 200 °C, and the vaporized organic compound was fed to the IR cell. For the adsorption of NH_3 , $\text{NH}_3(2\%)/\text{He}$ (50 $\text{cm}^3 \text{min}^{-1}$) was fed to the sample. Then, the IR disk was purged with He for 600 s, and IR measurement was carried out. Spectra were measured accumulating 15 scans at a resolution of 4 cm^{-1} . A reference spectrum of the catalyst wafer in He taken at the measurement temperature was subtracted from each spectrum.

2.3. Catalytic reactions

Vapor phase ammoxidation of toluene was carried out at atmospheric pressure using a fixed-bed flow reactor (Pyrex glass tube) with an inner diameter of 9 mm. Catalyst powders were pressed to pellets, crushed, and sieved. To maintain a constant reaction temperature, the catalyst pellets (0.25–0.50 mm size; typically 1.5 g (1.1 cm^3) of W83V17) were diluted with quartz (0.2–0.4 mm size; 1.5 cm^3) to fill the reactor (2.6 cm^3). Use of the same volume (2.6 cm^3) of the pellets with the same size range will result in the same pressure drop for different catalyst loadings. The reaction temperature was measured inside the catalyst bed by a thermocouple, whose tip was inside the upper side of the catalyst bed. The gas stream ($\text{NH}_3/\text{O}_2/\text{He}$) was fed to the reactor with mass flow controllers. Toluene was fed continuously into the gas stream at 150 °C from a syringe pump with a micro-feeder. The reactor was fed with toluene/ $\text{NH}_3/\text{O}_2/\text{He}$ mixture in the molar ratio of 1/10/4/34 with total flow rate (F) of 49 mL min^{-1} . Under the low NH_3 concentration conditions in Fig. 7, the molar ratio of toluene/ $\text{NH}_3/\text{O}_2/\text{He}$ was 1/5/4/39 (F = 49 mL min^{-1}). CH_4 was fed into outlet gas as external standard for GC-TCD analysis.

As a model reaction (Fig. 9), benzaldehyde + NH_3 + O_2 reaction by 0.1 g of the catalyst, diluted with the quartz pellets (2.5 cm^3),

Table 1
Surface area, composition and reaction rates of the catalysts.

Catalyst	S^a ($\text{m}^2 \text{g}^{-1}$)	W/V ^b	V^c ($\text{mmol h}^{-1} \text{g}^{-1}$)	V^d ($\text{mmol h}^{-1} \text{m}^{-2}$)
W64V36	27.7	64/36	1.51	0.055
W83V17	41.9	83/17	1.40	0.031
Na-W83V17	38.5	83/17	1.29	0.005
VO_x/WO_3	14.2	85/15	1.12	0.041
V_2O_5	4.8	–	3.03	0.631
WO_3	16.8	–	0.09	0.003

^a BET surface area determined by N_2 adsorption.

^b Composition determined by ICP-AES.

^c Rate of BN formation per weight of the catalysts.

^d Rate of BN formation per surface area of the catalysts.

was carried out with the same reactor which was fed with benzaldehyde/NH₃/O₂/He mixture in the molar ratio of 1/10/4/34 ($F = 49 \text{ mL min}^{-1}$). A model reaction (Fig. 9) of NH₃ + O₂ by 0.1 g of the catalyst was carried out using NH₃/O₂/He mixture in the molar ratio of 10/4/35 ($F = 49 \text{ mL min}^{-1}$).

The gas phase products (CO, CO₂ and N₂) in the outlet gas were analyzed by GC-TCD (GL Sciences GC-3200, 6 m SHINCARBON-ST packed column). Organic products, trapped in ethanol at 0 °C, followed by adding *n*-octane as an external standard, were analyzed with GC-FID (Shimadzu GC-14B with TC-5 capillary column). The carbon balance values for all the catalytic results were in a range of 95.9–101.6%.

For the ammoxidation of toluene in the present system, the nitrogen containing products were N₂ and benzonitrile (PhCN) with very small amount of benzamide (amide). GC-TCD analysis showed no formation of N₂O. Thus, the efficiency of NH₃ utilization in ammoxidation (η_{NH_3}) is defined as

$$\eta_{\text{NH}_3} = y_{\text{PhCN}} n_{\text{PhCN}} / (y_{\text{PhCN}} n_{\text{PhCN}} + y_{\text{amide}} n_{\text{amide}} + y_{\text{N}_2} n_{\text{N}_2}),$$

where y_{PhCN} , y_{amide} and y_{N_2} are the molar amounts of nitrogen containing products, and n_{PhCN} , n_{amide} and n_{N_2} are the number of nitrogen atoms in each product.

3. Result and discussion

3.1. Catalyst characterization

In our recent report [22], we synthesized a W–V–O catalyst with W/V ratio of 67/33 and studied its structure by various characterization methods: XRD, scanning transmission electron microscopy (STEM) and N₂-adsorption isotherm. Briefly, the results showed three structural features: (i) layered-type structure along *c*-axis direction characterized by diffraction peaks at $2\theta = 23^\circ$ and 46° (XRD), (ii) long rod-shaped crystal morphology due to stacking of the layers along the *c*-axis by sharing the apex oxygen (STEM), and (iii) the presence of micropore (N₂-adsorption). Considering the structural model that we have proposed for the similar binary metal oxides consisted of groups 5 and 6 elements [17–23], the structural model of W–V–O is proposed in Fig. 1. In this paper, W–V–O catalysts with different compositions (W64V36 and W83V17) were prepared. As shown in Fig. 1, their XRD patterns have essentially the same feature: two sharp diffraction peaks around 23° and 46° assignable to the (001) and (002) planes of the layered structure along *c*-axis direction. The XRD pattern of Na-W83V17 also has the same diffraction peaks at 23° and 46° . Although the intensities of Na-W83V17 are lower than those of W83V17, the XRD results indicate that the Na⁺-exchanged W83V17 (Na-W83V17) has basically the same crystal structure as W83V17. The SEM image of W83V17 (Fig. 2) showed the rod-shaped crystal probably due to stacking of the layers along the *c*-axis. Before calcination of the hydrothermally prepared binary metal oxides NH₄⁺ is located in the 6 and 7-membered ring pores, and thermal desorption of NH₃ from the precursor results in the formation of Brønsted acid sites in the pores [18]. The proton is exchangeable to various cations in aqueous solution [18].

Fig. 3 shows IR spectra (the ring-stretching region) of pyridine adsorbed on W83V17 and Na-W83V17. The spectrum for W83V17 shows the adsorption band at 1536 cm^{-1} due to pyridinium ion (PyH⁺) produced by the reaction of pyridine with Brønsted acid sites and the adsorption band at 1447 cm^{-1} due to coordinatively bound pyridine on Lewis acid sites [28]. The results indicate that the surface of W83V17 has both Brønsted and Lewis acid sites. Note that the weight of the catalyst disk for the IR experiment was the same for different catalysts, so the differences in the peak area at 1536 cm^{-1} and at 1447 cm^{-1} between samples

corresponds to the difference in the amount of Brønsted and Lewis acid sites. The spectrum for Na-W83V17 shows lower intensities of these bands, which indicates that the H⁺/Na⁺ cation exchange results in decrease in the number of Brønsted and Lewis acid sites of W83V17. It should be noted that the results of XRD show that the crystal structures of Na-W83V17 and W83V17 are similar to each other, and the surface area (Table 1) of Na-W83V17 ($38.5 \text{ m}^2 \text{ g}^{-1}$) is close to that of W83V17 ($41.9 \text{ m}^2 \text{ g}^{-1}$). These results indicate that the structure of W83V17 is essentially very close to that of Na-W83V17 except for acidity; W83V17 has larger amount of Brønsted and Lewis acid sites than Na-W83V17. The result also shows that W83V17 has larger amount of Brønsted and Lewis acid sites than V₂O₅.

3.2. Catalytic performance

Fig. 4 shows the effects of contact time on the properties of ammoxidation by W83V17 at 400 °C. Experiments were carried out by changing the catalyst weight (0.15, 0.75, 1.9, 1.5, 2.0 g) with the same inlet gas flow rate. The conversion of toluene increased with the contact time. The increase in the conversion resulted in slight decrease in the selectivity to benzonitrile (S_{PhCN}) and slight increase in the CO_x selectivity (S_{CO_x}). The selectivities to benzamide (S_{amide}) were below 0.9%. Hence, NH₃ can be consumed by two of the competitive reactions: (1) ammoxidation with toluene to produce benzonitrile and (2) NH₃ oxidation to N₂. Interestingly, the increase in the contact time resulted in the increase in the NH₃-efficiency (η_{NH_3}). This indicates a preferential promotion of the ammoxidation by W83V17 over the non-selective NH₃ oxidation.

We tested various V-based catalysts (1.5 g of W83V17, W64V36, Na-W83V17, VO_x/WO₃ and WO₃ and 0.5 g of V₂O₅) for the ammoxidation of toluene. To compare the selectivities of V₂O₅ and W–V complex oxide catalysts under the similar conversion levels, the catalyst amount of V₂O₅ was decreased. For representative catalysts, the effects of temperature on the toluene conversion, selectivity to various products and NH₃-efficiency are plotted in Fig. 5. Under the similar conversion levels, W83V17 showed higher selectivity to benzonitrile (S_{PhCN}) than the conventional V-based catalysts (V₂O₅ and VO_x/TiO₂). V₂O₅ and VO_x/TiO₂ showed higher selectivity to CO_x than W83V17.

Table 2 compares the conversions of toluene and selectivities to benzonitrile (S_{PhCN}), benzamide (S_{amide}), benzoic acid (S_{acid}), benzene (S_{B_2}) and CO_x (S_{CO_x}) at 400 °C. A conventional catalyst, V₂O₅, showed 71.2% selectivity to benzonitrile at a conversion level of 87.2%. WO₃ showed only 9.2% conversion of toluene. This indicates that vanadium is an indispensable element for this catalytic system. W83V17, W64V36 and VO_x/WO₃ show higher selectivities to benzonitrile than V₂O₅. This indicates that tungsten oxides as co-catalysts increase the selectivity to benzonitrile. The hydrothermally prepared catalysts (W83V17 and W64V36) showed higher selectivity to benzonitrile than VO_x/WO₃. Na-W83V17 showed low conversion (12.6%) than W83V17 (85.1%). Combined with the IR results in Fig. 3, we can conclude that Brønsted and/or Lewis acid sites of W83V17 significantly improve the ammoxidation activity in the present system.

Another remarkable feature of the hydrothermally prepared W–V–O catalysts (W83V17, W64V36) is highly efficient utilization of NH₃ in ammoxidation. The results in Fig. 5 and Table 2 demonstrated that W83V17 showed high NH₃-efficiency (η_{NH_3}) than other V-based catalysts. As shown in Table 2, the order of the NH₃-efficiency (η_{NH_3}) of V-based catalysts is as follows: W83V17 (56.9%) \approx W64V36 (44.8%) > VO_x/TiO₂ (42.2%) > VO_x/WO₃ (36.4%) > V₂O₅ (34.9%). The result indicates that the W–V–O catalysts (W83V17, W64V36) preferentially promote the ammoxidation over the non-selective NH₃ oxidation, while the classical and conventional V-based catalysts show moderate activity for

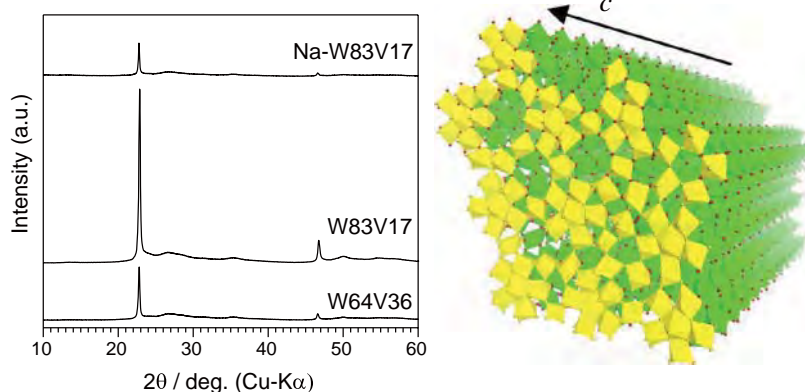


Fig. 1. XRD patterns (left) and polyhedral model (right) of microporous and layered W–V–O oxides. The top layer of the model is highlighted in yellow.

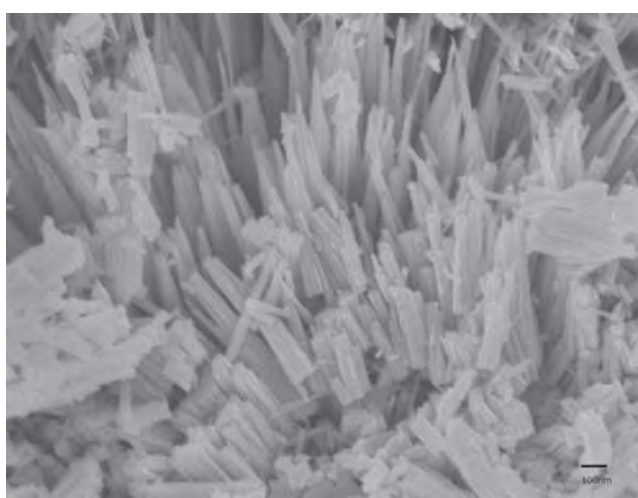


Fig. 2. SEM image of W83V17.

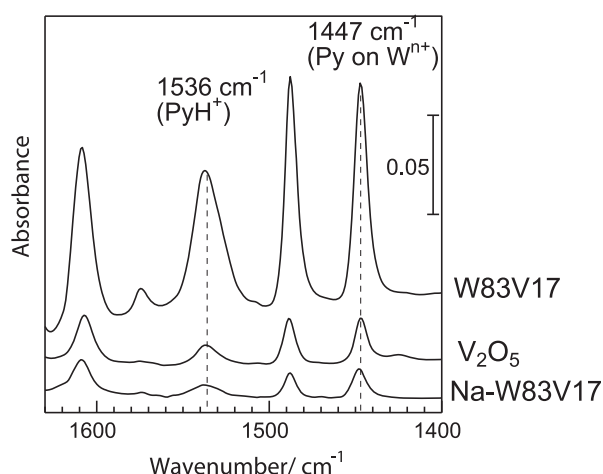


Fig. 3. IR spectra of pyridine adsorbed on the catalyst disk (38 ± 1 mg) at 100 °C.

the oxidation of NH_3 to N_2 . The catalytic results in Table 2 are converted to the rate of benzonitrile formation per surface area of the catalysts listed in Table 1. The reaction rates for W–V–O catalysts (W83V17, W64V36) are lower than those of V_2O_5 . It is obvious that the main advantages of the W–V–O catalysts are high selectivity to benzonitrile (low selectivity to CO_x) and highly efficient utilization of NH_3 .

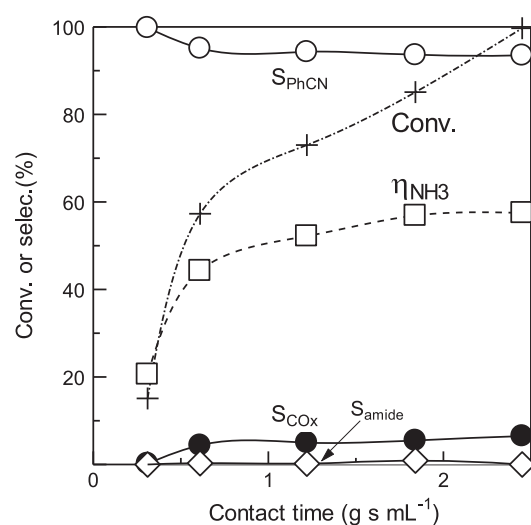


Fig. 4. Ammoxidation of toluene by W83V17 at different contact times (400 °C): conversion of toluene (+), selectivities of benzonitrile (○), benzamide (◇) and CO_x (●) and NH_3 -efficiency, η_{NH_3} , (□): toluene/ $\text{NH}_3/\text{O}_2/\text{He} = 1/10/4/34$.

Most of the previous reports on ammoxidation of toluene adopted excess NH_3 feed conditions. The reaction with lower level of NH_3 feed will lead to more sustainable and economical production of benzonitrile. Fig. 6 shows the results for the W83V17-catalyzed ammoxidation with different amounts of NH_3 (2, 5, 10 and 15 equiv. with respect to toluene). The selectivity to benzonitrile decreased with decreasing NH_3 concentration, but NH_3 -efficiency (η_{NH_3}) increased with decreasing NH_3 concentration. At the NH_3 molar ratio of 2 equiv. ($\text{NH}_3/\text{toluene} = 2/1$), the NH_3 -efficiency was 73.9% and the yield of benzonitrile was 70.2%. This indicates that the present system can produce benzonitrile with high NH_3 -efficiency and high yield under low NH_3 feed conditions. However, it is important to note that the ammonia levels required for achieving good benzonitrile yields are still several times above that required for the stoichiometric reaction. Further studies are necessary to address this issue.

Fig. 7 shows the catalytic results by 1.5 g of W83V17 and 0.5 g of V_2O_5 for the ammoxidation of toluene with lower NH_3 molar ratio (5 equiv.) than the standard conditions in Fig. 5 (10 equiv.). The general trends were basically similar to those for the standard conditions in Fig. 5, but the difference between W83V17 and V_2O_5 was more significant in Fig. 7. At 440 °C, where the toluene conversion reached 100% for both catalysts, V_2O_5 showed 52.1% selectivity to benzonitrile and 29.6% of NH_3 -efficiency, while W83V17

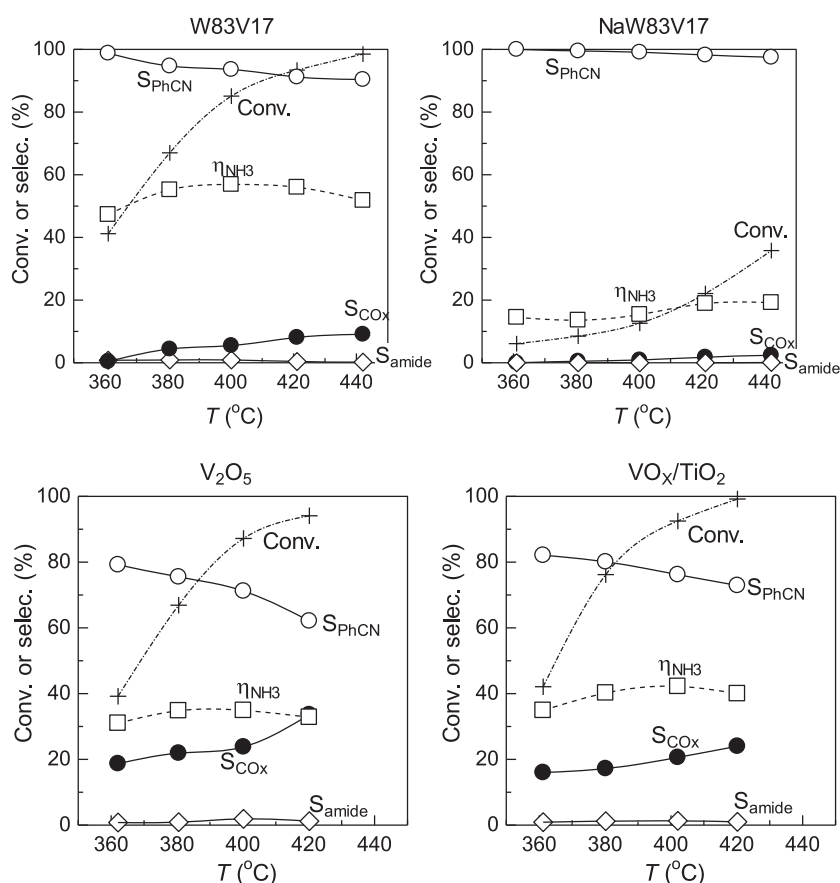


Fig. 5. Temperature dependence of the conversion of toluene (+), selectivities of benzonitrile (○), benzamide (◇) and CO_x (●) and NH₃-efficiency, η_{NH_3} , (□) for amoxidation of toluene by 1.5 g of W83V17: toluene/NH₃/O₂/He = 1/10/4/34.

Table 2

Catalytic results at 400 °C under the conditions in Fig. 5.

Catalyst	Cat. wt. (g)	Conv. (%)	S _{PhCN} (%)	S _{amide} (%)	S _{acid} (%)	S _{Bz} (%)	S _{COx} (%)	η_{NH_3} (%)
W83V17	1.5	85.1	93.6	0.9	0	0	5.5	56.9
W83V17 ^a	1.5	83.3	93.4	1.5	0	0	5.1	56.0
Na-W83V17	1.5	12.6	99.1	0	0	0	0.9	15.4
W64V36	1.5	99.9	93.0	0.3	0	0.1	6.6	44.8
VO _x /WO ₃	1.5	83.9	82.5	2.1	0	0	15.4	36.4
VO _x /TiO ₂	1.0	92.5	76.2	0.8	1.3	1.1	20.6	42.2
V ₂ O ₅	0.5	87.2	71.2	1.3	1.9	1.8	23.8	34.9
WO ₃	1.5	9.2	57.2	42.1	0	0	0.7	8.1

^a Water vapor was co-fed to the catalyst: toluene/NH₃/O₂/H₂O/He = 1/10/4/10/24 ($F = 49 \text{ mL min}^{-1}$).

showed 84.9% selectivity to benzonitrile and 80.5% of NH₃-efficiency. The results clearly demonstrate that W83V17 shows high efficiency of NH₃ utilization in amoxidation as well as high selectivity to benzonitrile based on toluene. For the reaction with W83V17 at 420 °C, the yield of benzonitrile is 85.2%, corresponding to the benzonitrile productivity of 129 g L_{cat}⁻¹ h⁻¹. The yield and the productivity of this system are not high compared with the yields (67–92%) and the productivities (52–342 g L_{cat}⁻¹ h⁻¹) of the benchmark V-based catalysts in the patents for amoxidation of toluene [1].

Fig. 8 shows the stability versus time-on-stream of W83V17-catalyzed amoxidation of toluene under the standard conditions at 400 °C. The toluene conversion slightly decreased from 98.6% to 95.1% during the 45 h of the continuous reaction. Then, the catalyst was heated at 500 °C for 1 h under He flow. The heat-treatment increased the toluene conversion to 97.6%, and the catalytic system showed high conversions (>95.9%) for the next 30 h. The benzo-

trile selectivity (90.2–90.4%) and NH₃-efficiency (50.9–53.1%) were nearly constant throughout the experiment. We also studied the effects of co-feeding of water on the catalytic performance of W83V17. As compared in Table 2, co-feeding of water vapor did not essentially change the toluene conversion, the selectivity to benzonitrile and NH₃-efficiency (η_{NH_3}). These results suggest that the present catalytic system is tolerant to water vapor.

3.3. Mechanistic and in situ IR studies

Previous studies [3,11] on the mechanism of amoxidation of toluene by V-based catalyst suggest that benzonitrile is produced via a benzaldehyde intermediate, which then reacts with NH₃ on the surface to yield benzylimine surface species. Finally, the benzylimine intermediate undergoes oxidative dehydrogenation to give benzonitrile [3,11]. We carried out a model reaction of benzaldehyde + NH₃ + O₂ by W83V17 and V₂O₅ catalysts. The results

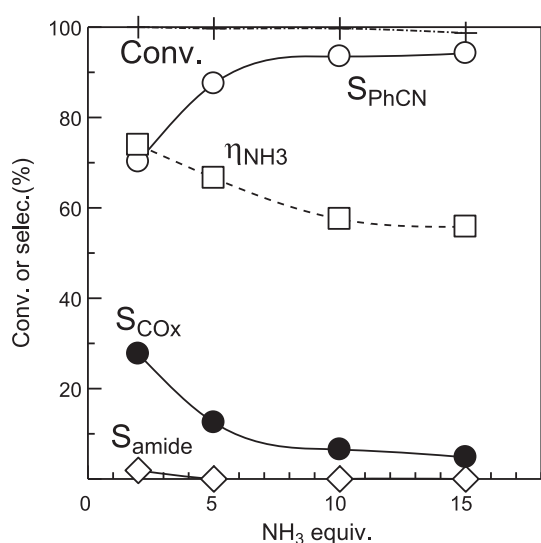
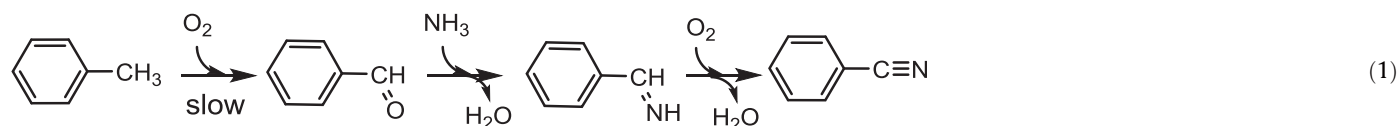


Fig. 6. Effect of the amount to NH₃ with respect to toluene on the conversion of toluene (+), selectivities of benzonitrile (○), benzamide (◇) and CO_x (●) and NH₃-efficiency, η_{NH₃}, (□) for ammoxidation of toluene by 2 g of W83V17 at 400 °C: toluene/NH₃/O₂/He = 1/10/4/34.

in Fig. 9 (left) were consistent with the proposed mechanism in the literature [3,11]; the formation rates of benzonitrile by ammoxidation of benzaldehyde were more than 6 times higher than those by ammoxidation of toluene (right) for both catalysts. This suggests that the ammoxidation of toluene by W83V17 is also driven by the proposed mechanism in the literature [3,11], Eq. (1), including the partial oxidation of toluene to benzaldehyde as a rate-limiting step.



To verify the hypothetical mechanism, we studied formation and reaction of intermediates on the W83V17 catalyst using in situ IR spectroscopy. First, adsorption of toluene and benzaldehyde was studied in order to identify the adsorbed species that

could arise on the surface of W83V17 during the ammoxidation of toluene. Gaseous toluene or benzaldehyde (0.3 mmol g_{cat}⁻¹) was introduced to the flow-type in situ IR cell at various temperatures under He flow, followed by purging with He flow for 600 s to obtain the IR spectra in Fig. 10. The spectrum of toluene adsorbed on W83V17 at ambient temperature showed two ring vibration bands of aromatics (1498 and 1588 cm⁻¹) [29] but no band due to C=O or C–O stretching modes, indicating that toluene was not oxidized by the surface oxygen of W83V17 but physically adsorbed on the surface at ambient temperature. At higher temperature (200 °C), a weak band at 1705 cm⁻¹ assignable to C=O stretching modes (ν_{CO}) of benzaldehyde [11] and ring vibration bands of aromatics (1498 and 1588 cm⁻¹) were observed. The ν_{CO} band at 1705 cm⁻¹ was also observed for benzaldehyde adsorbed on W83V17 at ambient temperature. These results indicate that toluene is oxidized by surface oxygen species of W83V17 to yield benzaldehyde even at lower temperature (200 °C) than the reaction temperature (400 °C) of the catalytic ammoxidation in this study. In the spectrum of benzonitrile on W83V17, a band at 2262 cm⁻¹ due to C≡N stretching modes (ν_{CN}) of adsorbed benzonitrile was observed.

As shown in Fig. 11, the adsorption of NH₃ at 330 °C resulted in the formation of IR bands due to protonated ammonia (NH₄⁺) on Brønsted acid sites at 1410 cm⁻¹ [28] and coordinated ammonia on Lewis acid sites at 1256 cm⁻¹ [28]. Then, we studied the reaction of the adsorbed NH₃ species with toluene at 330 °C under He flow. Soon after the introduction of gaseous toluene (0.3 mmol g_{cat}⁻¹) to the NH₃-preadsorbed W83V17, the band at 2250 cm⁻¹ due to ν_{CN} of benzonitrile was observed, and the intensity of the ν_{CN} band increased with time. The introduction of toluene decreased the intensities of the bands of NH₄⁺ (1410 cm⁻¹) and coordinated NH₃ (1256 cm⁻¹). These results indicate that benzonitrile is produced by the reaction of adsorbed NH₃

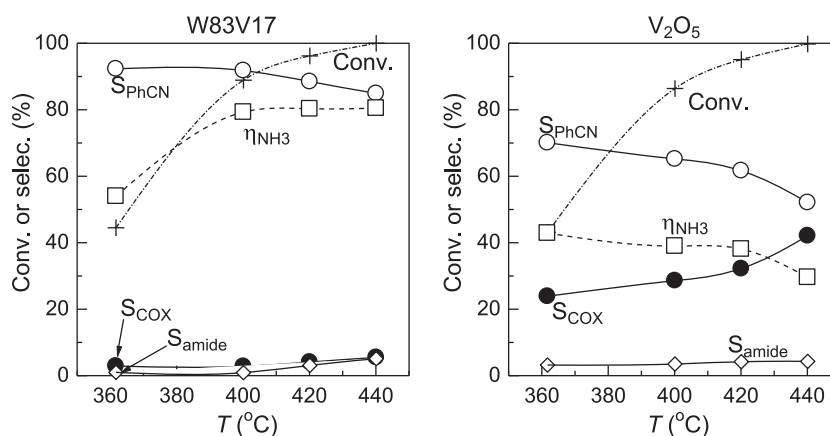


Fig. 7. Ammoxidation of toluene by 1.5 g of W83V17 and 0.5 g V₂O₅ in the low NH₃ concentration conditions (toluene/NH₃/O₂/He = 1/5/4/39): conversion of toluene (+), selectivities of benzonitrile (○), benzamide (◇) and CO_x (●) and NH₃-efficiency, η_{NH₃}, (□).

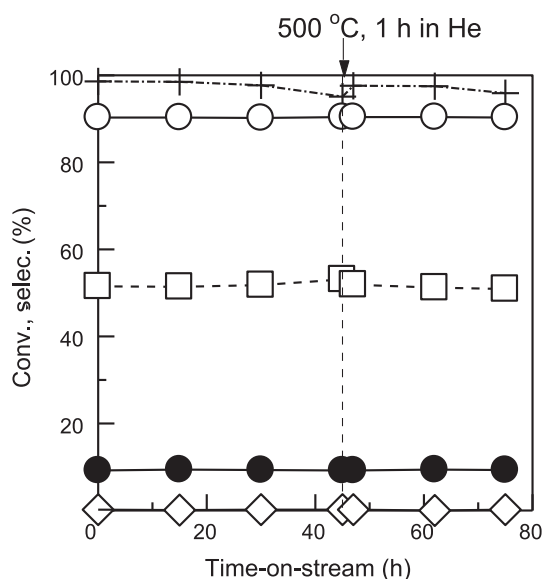


Fig. 8. Time course of ammoxidation of toluene by 1.5 g of W83V17 at 400 °C: conversion of toluene (+), selectivities of benzonitrile (O), benzamide (◇) and CO_x (●) and NH_3 -efficiency, η_{NH_3} , (□), toluene/ NH_3 / O_2 / $\text{He} = 1/10/4/34$. After 45 h of the reaction, the catalyst was heated at 500 °C for 1 h under He flow, followed by re-starting the ammoxidation reaction.

The same NH_3 adsorption experiment for V_2O_5 (Fig. 11B) shows that the amount of adsorbed NH_3 on V_2O_5 is negligible at 330 °C. Comparison of the results for W83V17 and V_2O_5 indicates that the acid sites originate from W in W83V17 act as adsorption sites of NH_3 during the ammoxidation reaction. The same experiment for VO_x/WO_3 shows that it shows adsorbed NH_3 mostly on Brønsted acid sites probably on the surface of WO_3 . However, the introduction of toluene to the adsorbed NH_3 on VO_x/WO_3 did not result in the formation of adsorbed PhCN. Considering the structural difference between the W83V17 (mixed oxide) and VO_x/WO_3 (VO_x islands supported on WO_3), one could conclude that proximity between W (acid) sites and V (redox) sites is important for the surface reaction between the adsorbed NH_3 , toluene and a reactive oxygen atom on the surface to give PhCN.

Fig. 12 shows the reaction of toluene-derived surface species with NH_3 monitored by in situ IR at 200 °C. After the observation of the benzaldehyde (1705 cm^{-1}) on W83V17, the flowing gas was switched from He to 2% NH_3 /He and the IR spectra were observed as a function of the time of NH_3 flowing at 200 °C. The ν_{CN} band of adsorbed benzonitrile species (2256 and 2232 cm^{-1}) appeared, and the intensity of the ν_{CN} band increased with time. Summarizing the IR results in Figs. 10–12, the following pathway is proposed; toluene is oxidized by the surface oxygen species of W83V17 to yield benzaldehyde which undergoes the reaction with adsorbed NH_3 to give benzonitrile possibly via benzylimine. This pathway is consistent with that proposed in the literature [3,11] shown in Eq. (1).

Fig. 9 compares the reaction rates for benzaldehyde + NH_3 + O_2 (left), NH_3 + O_2 (center) and toluene + NH_3 + O_2 (right) reactions by W83V17 and V_2O_5 . From the results in Fig. 9 and the pathway in Eq. (1), the origin of the higher NH_3 -efficiency (η_{NH_3}) of W83V17 than that of V_2O_5 is explained as follows. For V_2O_5 , the rate of NH_3 conversion to PhCN in the benzaldehyde + NH_3 + O_2 reaction is 1.5 times higher than the rate of NH_3 oxidation to N_2 in the NH_3 + O_2 reaction. For W83V17, the rate of NH_3 conversion to PhCN is 3 times higher than the rate of NH_3 oxidation to N_2 . These results indicate that, especially on W83V17, NH_3 consumption in the condensation of benzaldehyde with NH_3 is faster than NH_3

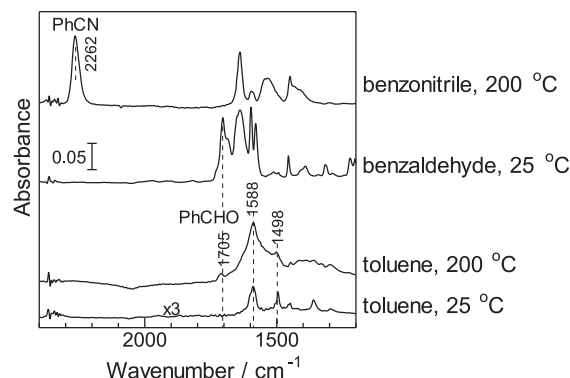


Fig. 10. IR spectra of adsorbed species on W83V17 at various temperatures.

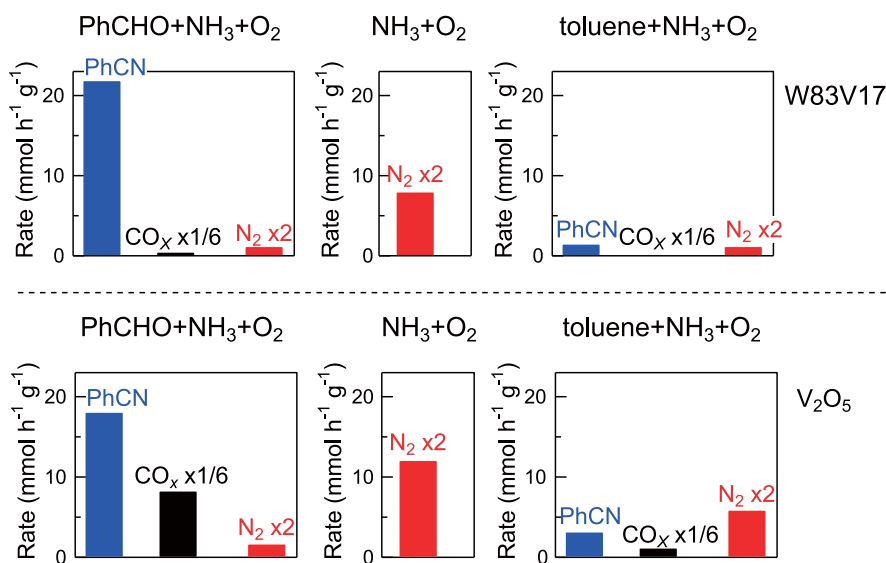


Fig. 9. Formation rates of PhCN, CO_x and N_2 for ammoxidation of benzaldehyde (left), oxidation of ammonia (center), and ammoxidation of toluene (right) by W83V17 (top) and V_2O_5 (bottom) at 400 °C.

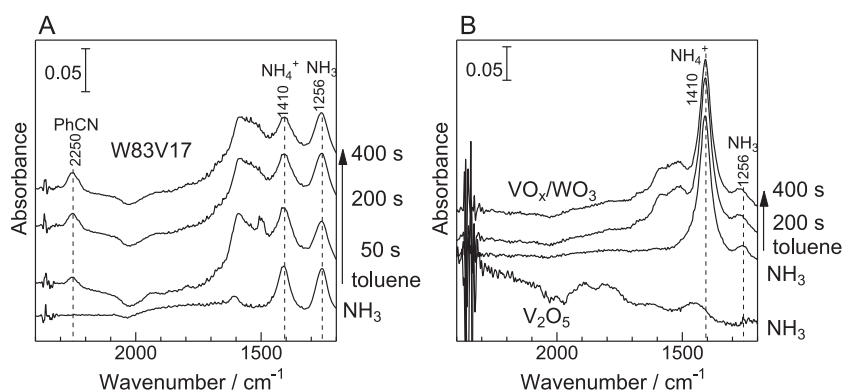


Fig. 11. IR spectra of adsorbed species on various catalyst disks (38 ± 1 mg) during the reaction of adsorbed NH_3 species with toluene-derived species at 330°C .

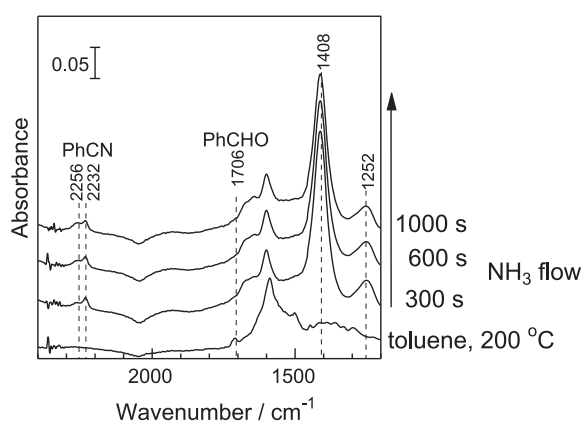
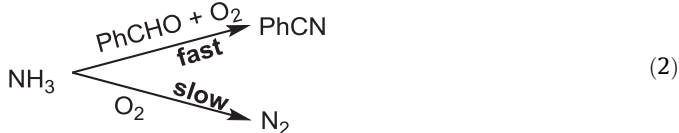


Fig. 12. IR spectra of adsorbed species on W83V17 during the reaction of toluene-derived surface species under flowing 2% NH_3/He at 200°C .

consumption in NH_3 oxidation to N_2 . Comparison of Fig. 9 (left) and Fig. 9 (center) shows that, for both catalysts, the presence of benzaldehyde in the feed decreases the rate of the unselective oxidation of NH_3 to N_2 . This indicates that ammoxidation of benzaldehyde competes with NH_3 oxidation to N_2 during ammoxidation of toluene. W83V17 showed lower rate of NH_3 oxidation in the $\text{NH}_3 + \text{O}_2$ reaction than V_2O_5 (Fig. 6, center). From these results, we could conclude that the high NH_3 -efficiency of W–V–O for ammoxidation of toluene is caused by the preferential reaction of NH_3 in the ammoxidation of benzaldehyde over NH_3 oxidation to N_2 as illustrated in Eq. (2):



On the surface of the W–V–O complex oxide, a VO_6 octahedron as a redox site is adjacent to WO_6 octahedra as NH_3 adsorption sites. The benzaldehyde adspecies, once formed by the oxidation of toluene by the VO_6 site, can react preferentially with NH_3 adspecies on the neighboring WO_6 sites, which can result in high efficiency of NH_3 utilization in the present catalytic system.

4. Conclusion

The layered-type W–V–O metal oxides (W–V–O), synthesized by hydrothermal method, selectively catalyzed the gas-phase ammoxidation of toluene to benzonitrile. Under similar conversion

levels, W–V–O showed higher selectivity to benzonitrile and lower selectivity to CO_x than conventional V-based catalysts (V_2O_5 and VO_x/TiO_2). Additionally, W–V–O was less active for the undesired oxidation of NH_3 to N_2 , resulting in the high NH_3 -utilization efficiency in ammoxidation than the conventional V-based catalysts. W–V–O showed high durability and high tolerance to co-fed water vapor, demonstrating promising catalytic properties of the present system. Model reaction studies suggested that the high NH_3 -efficiency of W–V–O was caused by the preferential reaction of NH_3 in $\text{PhCHO} + \text{NH}_3 + \text{O}_2$ over undesired $\text{NH}_3 + \text{O}_2$ reaction.

References

- [1] R.G. Rizayev, E.A. Mamedov, V.P. Vislovskii, V.E. Sheinin, *Appl. Catal. A* 83 (1992) 103–140.
- [2] A. Martin, B. Lücke, *Catal. Today* 57 (2000) 61–70.
- [3] A. Martin, V.N. Kalevaru, *ChemCatChem* 2 (2010) 1504–1522.
- [4] B. Lücke, K.V. Narayana, A. Martin, K. Jähnisch, *Adv. Synth. Catal.* 346 (2004) 1407–1424.
- [5] J.C. Otamiri, A. Andersson, *Catal. Today* 3 (1988) 211–222.
- [6] M. Sanati, A. Andersson, *Ind. Eng. Chem. Res.* 30 (1991) 312–320.
- [7] M. Sanati, A. Andersson, *Ind. Eng. Chem. Res.* 30 (1991) 320–326.
- [8] M. Sanati, A. Andersson, L.R. Wallenberg, B. Rebenstorff, *Appl. Catal. A* 106 (1993) 51–72.
- [9] C.P. Kumar, K.R. Reddy, V.V. Rao, K.V.R. Chary, *Green Chem.* 4 (2002) 513–516.
- [10] A. Martin, F. Hannour, A. Brückner, B. Lücke, *React. Kinet. Catal. Lett.* 63 (1998) 245–251.
- [11] Y. Zhang, A. Martin, H. Berndt, B. Lücke, M. Meisel, *J. Mol. Catal. A* 118 (1997) 205–214.
- [12] A. Martin, B. Lücke, M. Meisel, *Top. Catal.* 3 (1996) 377–386.
- [13] A. Martin, Y. Zhang, H.W. Zanthoff, M. Meisel, M. Baerns, *Appl. Catal. A* 139 (1996) L11–L16.
- [14] K.V.R. Chary, K.R. Reddy, T. Bhaskar, G.V. Sagar, *Green Chem.* 4 (2002) 206–209.
- [15] A. Teimouri, B. Najari, A.N. Chermahini, H. Salavati, M. Fazel-Najafabadi, *RSC Adv.* 4 (2014) 37679–37686.
- [16] E. Rombi, I. Ferino, R. Monaci, C. Picciau, V. Solinas, R. Buzzoni, *Appl. Catal. A* 266 (2004) 73–79.
- [17] M. Sadakane, N. Watanabe, T. Katou, Y. Nodasaka, W. Ueda, *Angew. Chem., Int. Ed.* 46 (2007) 1493–1496.
- [18] S. Ishikawa, W. Ueda, *Catal. Sci. Technol.* 6 (2016) 617–687.
- [19] N. Watanabe, W. Ueda, *Ind. Eng. Chem. Res.* 45 (2006) 607–614.
- [20] T. Murayama, N. Kuramata, S. Takatama, K. Nakatani, S. Izumi, X. Yi, W. Ueda, *Catal. Today* 185 (2012) 224–229.
- [21] K. Omata, S. Izumi, T. Murayama, W. Ueda, *Catal. Today* 201 (2013) 7–11.
- [22] Y. Goto, K. Shimizu, T. Murayama, W. Ueda, *Appl. Catal. A* 509 (2016) 118–122.
- [23] T. Murayama, N. Kuramata, W. Ueda, *J. Catal.* 339 (2016) 143–152.
- [24] M.D. Soriano, P. Concepcion, J.M. Lopez Nieto, F. Cavani, S. Guidetti, *C. Trevisanut, Green Chem.* 13 (2011) 2954–2962.
- [25] A. Chierigato, F. Basile, P. Concepción, S. Guidetti, G. Liosi, M.D. Soriano, C. Trevisanut, F. Cavani, J.M.L. Nieto, *Catal. Today* 197 (2012) 58.
- [26] M.D. Soriano, A. Chierigato, S. Zamora, F. Basile, F. Cavani, J.M.L. Nieto, *Top. Catal.* 59 (2016) 178–185.
- [27] X. Li, Y. Zhang, *ACS Catal.* 6 (2016) 143–150.
- [28] M. Tamura, K. Shimizu, A. Satsuma, *Appl. Catal. A* 433–434 (2012) 135–145.
- [29] G. Busca, *J. Chem. Soc., Faraday Trans.* 89 (1993) 753–755.

Deposition of Gold Nanoparticles on Niobium Pentoxide with Different Crystal Structures for Room-Temperature Carbon Monoxide Oxidation

Toru Murayama,^{*[a]} Wataru Ueda,^[b] and Masatake Haruta^[a]

Nanoparticulate gold catalysts (NPGCs) supported on niobium oxides (Nb_2O_5) were prepared by different deposition methods. Au nanoparticles (NPs) with a mean diameter of approximately 5 nm were deposited by conventional deposition methods, which include the deposition-precipitation (DP) and deposition-reduction (DR) methods, on layered-type Nb_2O_5 that possesses a deformed orthorhombic structure. Moreover, Au NPs with a mean diameter of approximately 2.7 nm could be deposited by the sol immobilization method on several crystalline forms of Nb_2O_5 (deformed orthorhombic, pseudo-hexagonal, and orthorhombic). NPGCs deposited on deformed orthorhombic Nb_2O_5 had a higher catalytic activity for CO oxidation. The temperature for 50% CO conversion was 11 °C for 1 wt% Au/ Nb_2O_5 (deformed orthorhombic) prepared by the sol immobilization method, and the CO conversion was 91% at 28 °C. As far as we know, this is the first report of highly active Au NPGCs (smaller than 3 nm in diameter) supported on Nb_2O_5 . NPGCs supported on acidic metal oxides will expand the utilization of gold catalysts for new applications.

Nanoparticulate gold catalysts (NPGCs) have attracted much attention over the past few decades.^[1–5] The most important type of Au catalyst is Au nanoparticles (NPs) supported on a base metal oxide. Small Au NPs with diameters of 5 nm or less are required to increase the surface boundary between the Au NPs and the support.^[6,7] Many kinds of supported Au catalysts have been developed as their catalytic properties are often different depending on the kind of metal oxide support used. Au catalysts are usually prepared by a deposition method, such as the deposition precipitation (DP) or deposition reduction (DR) methods, to disperse nano-scale Au particles on the support. The control of the charged state of the metal oxide surface is essential to deposit Au NPs with high and uniform dispersion. However, in previous studies, it was

difficult to prepare NPGCs if the isoelectric point of the support was below pH 5. A solid acid, which typically shows a low isoelectric point, is attractive as a support, but there have been only a few reports of Au supported on acidic oxides other than silica and zeolite supports.^[8–10]

Niobium oxide (or hydrated niobium oxide) is used widely in catalysis and in electrochromic and photoelectrochemical devices.^[11,12] Niobium oxide ($\text{Nb}_2\text{O}_5 \cdot n\text{H}_2\text{O}$, niobic acid) has been used especially as a water-tolerant solid acid catalyst for many reactions such as alkylation, esterification, hydrolysis, dehydration, and hydration.^[13,14] Niobium oxide forms different polyhedral structures and transforms its phase depending on the heat treatment performed. Recently, we reported a new crystalline niobium oxide that consists of NbO_6 octahedra, NbO_7 , and micropores based on the seven-membered ring in its structure with corner-sharing in the *c* direction.^[15] This deformed orthorhombic niobium oxide, denoted as $\text{Nb}_2\text{O}_5\text{-DO}$, was synthesized by a hydrothermal process, and the catalytic activity this crystalline structure was compared with that of pseudo-hexagonal ($\text{TT-Nb}_2\text{O}_5$), orthorhombic ($\text{T-Nb}_2\text{O}_5$), and pyrochlore (denoted as $\text{Nb}_2\text{O}_5\text{-P}$) niobium oxides. $\text{Nb}_2\text{O}_5\text{-DO}$ showed a high catalytic activity as a solid acid. A notable feature of $\text{Nb}_2\text{O}_5\text{-DO}$ is its high surface area, which exceeds $200 \text{ m}^2 \text{ g}^{-1}$. Nb_2O_5 is classified as an n-type semiconductor and has redox properties, which indicates that it could show a high catalytic activity as a support for a NPGC if Au NPs are deposited on Nb_2O_5 . We assumed that Au could be deposited on the surface of $\text{Nb}_2\text{O}_5\text{-DO}$ as nanoparticles smaller than 5 nm. Moreover, the effect of the crystalline structure will be discussed by using simple Au/ Nb_2O_5 catalysts in this work. Sobczak et al. reported Au (or Au-Cu) on Nb_2O_5 and Nb/MCF (silica) supports by modification of the niobium oxide surface by an amino group.^[16,17] Tong et al. and Ko et al. reported a simple Au/ Nb_2O_5 catalyst; however, the mean diameter of the Au particles was larger than 5 nm.^[18,19] As far as we know, this is the first report on highly active NPGCs (smaller than 5 nm) supported on Nb_2O_5 .

Several deposition methods have been used to deposit Au on an Nb_2O_5 support. Among them, the impregnation method facilitates the coagulation of Au NPs during calcination. The coprecipitation method is effective only if both Au and the support can be deposited simultaneously. Thus, the DP and DR methods, which are used commonly for the preparation for NPGCs, were used for the first time in this work to prepare Au/ Nb_2O_5 .

The results of catalytic CO oxidation over Au/ $\text{Nb}_2\text{O}_5\text{-DO}$ (DR), Au/ $\text{Nb}_2\text{O}_5 \cdot n\text{H}_2\text{O}$ (DR), and Au/ Nb_2O_5 (DR), which were prepared

[a] Prof. T. Murayama, Prof. M. Haruta
Research Center for Gold Chemistry
Tokyo Metropolitan University
1-1-F203 Minami-Osawa
Hachioji, Tokyo, 192-0397 (Japan)
E-mail: murayama@tmu.ac.jp

[b] Prof. W. Ueda
Department of Material and Life Chemistry, Faculty of Engineering
Kanagawa University
3-27, Rokkakubashi
Kanagawa-ku, Yokohama (Japan)

Supporting information for this article can be found under:
<http://dx.doi.org/10.1002/cctc.201600563>.

by the DR method, are shown in Table 1 (see also Figure S1). The Au precursor used was Au(en)₂Cl₃ (en = ethylenediamine), and the Au loading was 1 wt%. An unsupported Nb₂O₅-DO catalyst showed no activity for CO oxidation even at 400 °C.

Entry	Catalyst	$T_{1/2}$ ^[b] [°C]	Particle diameter ^[b] [nm]
1	Au/Nb ₂ O ₅ -DO(DR)	73	4.9 ± 1.4
2	Au/Nb ₂ O ₅ · <i>n</i> H ₂ O(DR)	194	13 ± 8.1
3	Au/Nb ₂ O ₅ (DR)	(29% at 250 °C) ^[c]	14 ± 6.4
4	Nb ₂ O ₅ -DO	(0% at 400 °C) ^[c]	–

[a] Catalyst, 0.15 g; Au loading, 1 wt%; flow rate, 50 mL min⁻¹ (1 vol% CO/air). [b] Measured by using TEM. [c] CO conversion.

In contrast, the activity of Au/Nb₂O₅-DO(DR) for CO oxidation was high, and the temperature for 50% CO conversion ($T_{1/2}$) was 73 °C. The catalytic activities of Au supported on the commercially available Nb₂O₅·*n*H₂O (Au/Nb₂O₅·*n*H₂O(DR)) and Nb₂O₅ (Au/Nb₂O₅(DR)) were lower than that of Au/Nb₂O₅-DO(DR). The value of $T_{1/2}$ was 194 °C for Au/Nb₂O₅·*n*H₂O(DR), and the conversion was 29% at 250 °C for Au/Nb₂O₅(DR).

TEM images of Au/Nb₂O₅-DO(DR), Au/Nb₂O₅·*n*H₂O(DR), and Au/Nb₂O₅(DR) are shown in Figure S2. The mean diameter of the Au particles on Au/Nb₂O₅-DO(DR) was 4.9 nm (standard deviation; SD, 1.4 nm), which is smaller than that of Au/Nb₂O₅·*n*H₂O(DR) (13 nm; SD, 8.1 nm) and Au/Nb₂O₅(DR) (14 nm; SD, 6.4 nm). XRD measurements showed that the mean diameter of the Au particles of Au/Nb₂O₅-DO(DR) was 4.9 nm as calculated by the Scherrer equation, which agreed well with the TEM observations. These data suggested that the morphology and the high surface area (208 m² g⁻¹) of Nb₂O₅-DO make it possible to form Au NPs dispersed on Nb₂O₅-DO. The conventional DR method was used to deposit Au as NPs (smaller than 5 nm) on Nb₂O₅-DO.

Several deposition methods were then tested by using a Nb₂O₅-DO support to obtain smaller Au NPs. The DP method, solid grinding (SG) method,^[9,20] and sol immobilization (SI) method^[21–24] were used to prepare Au/Nb₂O₅-DO catalysts. TEM images and the distribution of Au NPs on these catalysts are shown in Figure S3, and the catalytic activities for CO oxidation are shown in Figure 1. The mean diameter of the Au NPs was 7.0 nm (SD, 2.1 nm) for Au/Nb₂O₅-DO(DP), 4.1 nm (SD, 1.1 nm) for the catalyst obtained by SG, and 2.7 nm (SD, 0.7 nm) for the catalyst obtained by the SI method. The catalytic activities of these catalysts corresponded to the Au particle size, and the catalytic activity decreased in the order of SI > SG > DR > DP. The catalytic activity of Au/Nb₂O₅-DO(SG) was higher than that of the catalysts obtained by DR; however, the Au precursor dimethylacetylacetonatogold (Me₂Au(acac)) is currently too expensive to use widely. Au/Nb₂O₅-DO(SI) showed the highest catalytic activity and its particles were small with a narrow distribution. The $T_{1/2}$ was 11 °C for Au/Nb₂O₅-DO(SI), and the CO conversion was 91% at 28 °C. Nb₂O₅-DO alone showed no

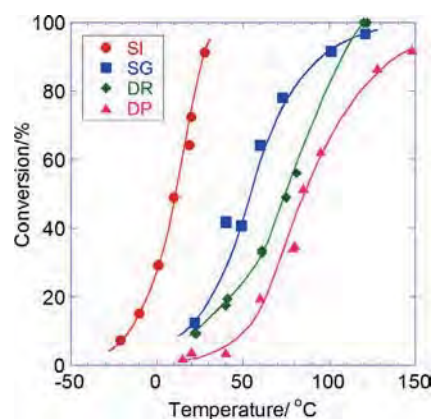


Figure 1. Effects of the deposition method on catalytic activity over Au/Nb₂O₅-DO (loading of Au, 1 wt%; catalyst, 0.15 g; 1 vol% CO in air at a flow rate of 50 mL min⁻¹).

activity even at 400 °C (Table 1); therefore, the enhancement of catalytic activity shown at room temperature by Au NPs is remarkable.

The relationship between the particle diameter and turnover frequency (TOF) and the CO conversion rate based on surface Au atoms at 20 °C is shown in Figure S4. These results show clearly that smaller Au NPs exhibit a higher catalytic activity for CO oxidation. The TOF was increased if the size of the Au NPs was minimized in a manner similar to that for other reported metal oxide supports. Therefore, as for other supported Au catalysts,^[25] active sites for CO oxidation can be assumed to be at the perimeter of the Au NPs. The results suggest that a much higher activity of the Au/Nb₂O₅ catalyst will be achieved if a catalyst with tiny cluster size particles (smaller than 2 nm in diameter)^[26] can be prepared.

As niobium oxide with several crystalline structures has been reported, the effects of the crystalline form were investigated. Four different crystalline Nb₂O₅ samples (Nb₂O₅-DO, TT-Nb₂O₅, T-Nb₂O₅, and Nb₂O₅-P) were prepared, and the XRD patterns of these supports are shown in Figure S5. Au was deposited by the SI method, and the physical properties and catalytic activities for CO oxidation of the materials are shown in Table 2 and Figure S6, respectively. Au/Nb₂O₅-DO(SI), as shown above, showed a high activity, and the loading of Au on the support was the same as the preparation amount. The mean diameters of the Au particles and the distribution of the particle diameters in the obtained catalysts are shown in Figure S7. The mean diameters of Au/TT-Nb₂O₅(SI) (2.6 nm; SD, 0.8 nm) and Au/T-Nb₂O₅(SI) (2.7 nm; SD, 0.9 nm) were almost the same as that of Au/Nb₂O₅-DO(SI) (2.7 nm; SD, 0.7 nm); however, the catalytic activity of Au/Nb₂O₅-DO(SI) for CO oxidation was much higher than that of Au/TT-Nb₂O₅(SI) and Au/T-Nb₂O₅(SI). The $T_{1/2}$ values were 11 °C for Au/Nb₂O₅-DO(SI), 79 °C for Au/TT-Nb₂O₅(SI), and 59 °C for Au/T-Nb₂O₅(SI). The TOF based on surface Au atoms at 20 °C for Au/Nb₂O₅-DO(SI) was more than three times higher than that of Au/T-Nb₂O₅(SI), and Au/Nb₂O₅-P(SI) was less active. The catalytic activity of Au supported on commercially available Nb₂O₅·*n*H₂O (entry 9) was less than that of Au/Nb₂O₅-DO(SI), which was prepared with

Table 2. Physical properties of supported Au catalysts prepared by the SI method and their catalytic activities for CO oxidation.^[a]

Entry	Support (crystalline phase)	BET surface area [m ² g ⁻¹]	Au loading [wt%]		Au [μmol m ⁻²]	T _{1/2} ^[e] [°C]	TOF@20°C ^[f] [×10 ² s ⁻¹]	Particle diameter ^[g] [nm]
			Prepared	Obtained ^[d]				
5	Nb ₂ O ₅ -DO (deformed orthorhombic)	208	1	1.01	7.69 (0.247)	11	5.5	2.7 ± 0.7
6	TT-Nb ₂ O ₅ (pseudo-hexagonal)	43	1	1.07	8.15 (1.26)	79	0.37	2.6 ± 0.8
7	T-Nb ₂ O ₅ (orthorhombic)	24	1	0.788	6.00 (1.67)	59	1.5	2.7 ± 0.9
8	Nb ₂ O ₅ -P (pyrochlore)	30	1	0.764	5.82 (1.29)	165	0.26	6.1 ± 3.1
9	Nb ₂ O ₅ ·nH ₂ O ^[b]	19	1	1.02	7.77 (2.73)	90	0.79	4.3 ± 1.4
10	Nb ₂ O ₅ ^[b]	5.8	1	0.237	1.80 (2.07)	168	0.94	3.5 ± 1.0
11	Nb ₂ O ₅ ^[c]	2.3	1	0.050	0.381 (1.10)	340	0.21	3.3 ± 0.8
12	TiO ₂ ^[h]	54	1	0.96	7.31 (0.902)	7	12	4.1 ± 2.2
13	SiO ₂ ^[h]	256	1	1.00	7.61 (0.198)	(33%, 250°C)	1.1	6.6 ± 2.7

[a] Catalyst, 0.15 g; flow rate, 50 mL min⁻¹ (1 vol% CO/air); H₂O concentration at T_{1/2}, 22–49 ppm. [b] Commercial product. [c] Ammonium niobium oxalate calcined at 400 °C. [d] Measured by using atomic absorption spectroscopy (AAS). [e] Temperature at 50% conversion. [f] Based on surface Au atoms. [g] Measured by TEM. [h] Commercial product prepared by the DP method (Au/TiO₂) and DR method (Au/SiO₂).

a 1 wt% Au loading. It was difficult to deposit all of the Au atoms on the Nb₂O₅ supports (entries 10 and 11), and their catalytic activities were lower. The catalytic activity of Au/Nb₂O₅-DO(SI) was comparable to that of Au/TiO₂ (Table 2, entry 12) and was much higher than that of Au/SiO₂ (Table 2, entry 13), which was an acidic support. These results show that the affinity of niobium oxide for the colloidal Au plays an important role in the deposition of Au on the support surfaces. The crystalline form of the support affects the reactivity even with the same Au particle diameter, which indicates that the reactivities of the active sites formed around the perimeters of the Au particles were different.

The results of the diffuse reflectance infrared Fourier transform spectroscopy (DRIFT-IR) of CO adsorbed on Au/Nb₂O₅-DO, Nb₂O₅-DO, Au/SiO₂, and Au/TiO₂ are shown in Figure 2. Both Au/Nb₂O₅-DO and Nb₂O₅-DO showed an adsorption band at $\tilde{\nu}$ = 2170 cm⁻¹, which was attributed to the adsorption of CO on the acidic sites of niobium oxide. The adsorption peaks observed at $\tilde{\nu}$ = 2130 and 2116 cm⁻¹ in the spectrum of

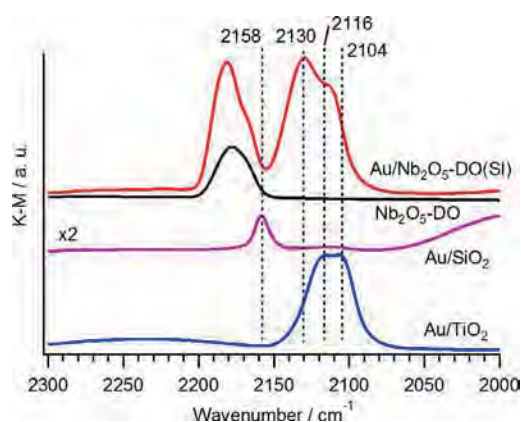


Figure 2. DRIFT-IR spectra of CO adsorbed at -190 °C on Au/Nb₂O₅-DO(SI), Nb₂O₅-DO, Au/SiO₂, and Au/TiO₂.

Au/Nb₂O₅-DO are attributed to CO adsorption on Au sites. In the case of NPGCs on an acidic support, the CO adsorption peak on Au sites shifts to a higher wavenumber.^[27] A comparison of the wavenumbers of CO adsorption on Au/Nb₂O₅-DO ($\tilde{\nu}$ = 2130, 2116 cm⁻¹), Au/SiO₂ ($\tilde{\nu}$ = 2158 cm⁻¹), and Au/TiO₂ ($\tilde{\nu}$ = 2116, 2104 cm⁻¹) suggested that Au species on Nb₂O₅-DO possessed a positive charge compared to Au/TiO₂. The results of the DRIFT-IR of adsorbed CO and X-ray photoelectron spectroscopy (XPS) for the obtained catalysts are shown in Figures S8 and S9, respectively. No FTIR adsorption peak was observed for Au/P-Nb₂O₅(SI) for adsorbed CO, which indicates the modification of the surface of Au particles by strong metal-support interactions (SMSI). The spectra of Au/T-Nb₂O₅(SI) and Au/TT-Nb₂O₅(SI) showed peaks at $\tilde{\nu}$ = 2130 and 2116 cm⁻¹, similar to Au/Nb₂O₅-DO(SI), which suggests that the same kinds of Au species were formed on these Nb₂O₅ supports. The differences of the catalytic activity for CO oxidation were thought to be because of the different redox properties based on the crystalline structure of Nb₂O₅.

To confirm the effect of the crystalline form of the niobium oxide support on the catalytic activity, the density of the Au atoms on the surface and the amount of Au used were controlled by adjusting the loading weight and the amount of the catalyst (Table 3). The order of the catalytic conversion rate and TOF based on the surface Au atoms at 20 °C is Au/Nb₂O₅-DO(SI) (0.055 s⁻¹) > Au/T-Nb₂O₅(SI) (0.028 s⁻¹) > Au/TT-Nb₂O₅(SI) (0.018 s⁻¹) > Au/Nb₂O₅-P(SI) (0.000 s⁻¹). We can conclude that the deformed orthorhombic structure of niobium oxide is favorable for the deposition of Au as NPs and for their reactivity.

The apparent activation energy of Au/Nb₂O₅-DO(SI) was 32.0 kJ mol⁻¹ and those of Au/TT-Nb₂O₅(SI), Au/T-Nb₂O₅(SI), and Au/Nb₂O₅-P(SI) were almost the same (Figure S10 and Table S1). These values are similar to those reported for other metal oxide supports, which indicates that CO oxidation takes place between lattice oxygen at the perimeters of the Au NPs

Table 3. Physical properties of supported Au catalysts prepared by the sol immobilization method and their catalytic activities for CO oxidation.^[a]

Entry	Support (Crystalline phase)	BET surface area [m ² g ⁻¹]	Au loading [wt %] Prepared	Obtained ^[b]	Catalyst amount [g]	Au [μmol m ⁻²]	<i>T</i> _{1/2} ^[c] [°C]	TOF@20 °C ^[d] [×10 ² s ⁻¹]	Particle diameter ^[e] [nm]
14	Nb ₂ O ₅ -DO (Deformed orthorhombic)	208	1	1.01	0.050	2.55 (0.247)	33	5.5	2.7 ± 0.7
15	TT-Nb ₂ O ₅ (Pseudohexagonal)	43	0.207	0.178	0.242	2.19 (0.210)	81	1.8	3.0 ± 0.8
16	T-Nb ₂ O ₅ (Orthorhombic)	24	0.117	0.113	0.426	2.44 (0.239)	65	2.8	2.3 ± 0.4
17	Nb ₂ O ₅ -P (Pyrochlore)	30	0.144	0.153	0.348	2.70 (0.259)	270	0.0	4.7 ± 1.5

[a] Flow rate, 50 mL min⁻¹ (1 vol% CO/air). [b] Measured by AAS. [c] Temperature of 50% conversion. [d] Based on surface Au atoms. [e] Measured by TEM.

and CO adsorbed on the Au NPs. Nb₂O₅-DO consists of 1D nanorods with diameters of approximately 10 nm and lengths of 50–100 nm. The *ab* plane comprises interconnected crystal structure motifs of {Nb₆O₂₁} units and micropore channels without long-range order. The side surfaces of the nanorods, which are located on the Au NPs, seem to possess coordinative unsaturation sites of niobium oxide. The lattice oxygen species of these sites will accelerate catalytic reactions.

In conclusion, Au NPs of 2.7 nm in diameter were supported on niobium oxide. The catalytic activity for CO oxidation increased with a decrease of the Au particle size. DRIFT-IR measurements showed that Lewis acid sites exist on the surface of the Au/Nb₂O₅ catalyst after the deposition of Au NPs. Therefore, the application of the Au/Nb₂O₅ catalyst can be expanded in the future to many reactions by the utilization of the combination of acidic sites and oxidation reaction sites.

Experimental Section

Different kinds of niobium oxides were prepared according to our previous study.^[15] Layered-structure-type (deformed orthorhombic) niobium oxide was synthesized by a hydrothermal method from ammonium niobium oxalate (NH₄[NbO(C₂O₄)₂(H₂O)₂]*n*H₂O, Aldrich) and was denoted as Nb₂O₅-DO. The Nb precursor was dissolved in distilled water, and the solution was treated by hydrothermal synthesis for 1 day at 175 °C. The resultant solid was separated carefully and washed with distilled water under filtration, and the solid was dried at 80 °C. The dried solid was crushed in an agate mortar and heat-treated for 2 h at 400 °C in air. Orthorhombic niobium oxide was obtained by the calcination of Nb₂O₅-DO at 650 °C for 2 h and was denoted as T-Nb₂O₅. Pseudohexagonal and pyrochlore niobium oxides were also synthesized by a hydrothermal method using a niobic acid (Nb₂O₅·*n*H₂O, Soekawa Chemicals) precursor, and they were denoted as TT-Nb₂O₅ and Nb₂O₅-P, respectively. Niobic acid was dispersed in deionized water (40 mL) at a concentration of 4 mmol, based on Nb, for Nb₂O₅-P and at a concentration of 0.25 mmol for TT-Nb₂O₅. The hydrothermal conditions and the following process were the same as those used for Nb₂O₅-DO. Commercially available Nb₂O₅ (Wako) and Nb₂O₅·*n*H₂O (Soekawa) were used for comparison.

Au catalysts were prepared by the DP and DR methods. Au(en)₂Cl₃ (0.0507 mmol) was dissolved in water (51 mL), and then niobium oxide (1 g) was added. The mixture was stirred for 1 h with the pH adjusted to 10 by using NaOH solution. In the DR method, NaBH₄

was added to the mixture, and the suspension was washed by suction filtration and dried at 80 °C. The dried catalyst was calcined at 300 °C for 4 h in air.

In the SG method, the Nb₂O₅ sample (1 g) and Me₂Au(acac) (1 wt % based on Au) were ground in an agate mortar in air for 15 min at RT followed by calcination at 300 °C for 4 h.

SI was performed according to previous reports.^[21–23] Tetraoctylammonium bromide (0.3 g) was dissolved in toluene (16 mL), and then H₂AuCl₄ solution (0.153 mmol in 5 mL deionized water) was added. The resulting solution was stirred for 10 min at RT. Dodecanethiol (72.4 μL) was added to the solution, and the solution was stirred for 10 min at 0 °C. The reaction solution was then stirred vigorously, and NaBH₄ (76 mg) in deionized water (5 mL) was added over 3 min. The solution was further stirred at 0 °C for 30 min and at RT for another 3 h. The organic phase was collected, and the solvent was removed by using a rotary evaporator. The solid was dissolved in hexane (50 mL) and filtered, and then the solvent was removed from the filtrate by using a rotary evaporator. The black product was suspended in ethanol (40 mL) and washed three times. The solid was dissolved in hexane (40 mL), and the solution was added dropwise into hexane solution in which Nb₂O₅ (3 g) was dispersed. The obtained catalyst was collected by filtration and dried at 80 °C. The dried catalyst was calcined at 300 °C for 2 h in air. Au/TiO₂ and Au/SiO₂ were purchased from HGI (Haruta Gold Incorporated).

The catalytic activity was tested for the oxidation of CO. The catalyst (0.15 g) was placed in a fixed-bed reactor, and a flow of 1 vol% CO in air was used (50 mL min⁻¹). The H₂O concentration in the gas flow was monitored by using a dew-point meter, and the concentrations were 20–100 ppm at *T*_{1/2} in all experiments. For Au/Nb₂O₅ samples prepared by the SI method, the temperature was held for 1 h at 100% CO conversion for stabilization before the measurements. The catalytic activities were compared by the reaction rate per surface Au atoms (TOF, μmol(CO) μmol(Au surface)⁻¹ s⁻¹), which was obtained under the conditions at which the conversion of CO is below 15% for a differential reactor condition. Other characterization methods are described in the Supporting Information.

Keywords: gold · heterogeneous catalysis · nanoparticles · niobium · oxidation

[1] M. Haruta, T. Kobayashi, H. Sano, N. Yamada, *Chem. Lett.* **1987**, 405–408.

[2] M. Haruta, *Catal. Today* **1997**, 36, 153–166.

- [3] A. S. K. Hashmi, G. J. Hutchings, *Angew. Chem. Int. Ed.* **2006**, *45*, 7896–7936; *Angew. Chem.* **2006**, *118*, 8064–8105.
- [4] M. Hara, K. Nakajima, K. Kamata, *Sci. Technol. Adv. Mater.* **2015**, *16*, 034903.
- [5] A. Villa, N. Dimitratos, C. E. Chan-Thaw, C. Hammond, L. Prati, G. J. Hutchings, *Acc. Chem. Res.* **2015**, *48*, 1403–1412.
- [6] T. Takei, M. Haruta, *New J. Chem.* **2011**, *35*, 2227–2233.
- [7] S. E. Davis, M. S. Ide, R. J. Davis, *Green Chem.* **2013**, *15*, 17–45.
- [8] A. Villa, S. Campisi, K. M. H. Mohammed, N. Dimitratos, F. Vindigni, M. Manzoli, W. Jones, M. Bowker, G. J. Hutchings, L. Prati, *Catal. Sci. Technol.* **2015**, *5*, 1126–1132.
- [9] J. Huang, T. Akita, J. Faye, T. Fujitani, T. Takei, M. Haruta, *Angew. Chem. Int. Ed.* **2009**, *48*, 7862–7866; *Angew. Chem.* **2009**, *121*, 8002–8006.
- [10] R. K. P. Purushothaman, J. van Haveren, A. Mayoral, I. Melián-Cabrera, H. J. Heeres, *Top. Catal.* **2014**, *57*, 1445–1453.
- [11] A. Llordés, G. Garcia, J. Gazquez, D. J. Milliron, *Nature* **2013**, *500*, 323–326.
- [12] J. Wu, J. Li, X. Lü, L. Zhang, J. Yao, F. Zhang, F. Huang, F. Xu, *J. Mater. Chem.* **2010**, *20*, 1942–1946.
- [13] K. Tanabe, S. Okazaki, *Appl. Catal. A* **1995**, *133*, 191–218.
- [14] K. Nakajima, Y. Baba, R. Noma, M. Kitano, J. N. Kondo, S. Hayashi, M. Hara, *J. Am. Chem. Soc.* **2011**, *133*, 4224–4227.
- [15] T. Murayama, J. Chen, J. Hirata, K. Matsumoto, W. Ueda, *Catal. Sci. Technol.* **2014**, *4*, 4250–4257.
- [16] I. Sobczak, K. Jagodzinska, M. Ziolek, *Catal. Today* **2010**, *158*, 121–129.
- [17] I. Sobczak, Ł. Wolski, *Catal. Today* **2015**, *254*, 72–82.
- [18] X. Tong, Z. Liu, J. Hu, S. Liao, *Appl. Catal. A* **2016**, *510*, 196–203.
- [19] H. Y. Y. Ko, M. Mizuhata, A. Kajinami, S. Deki, *J. Electroanal. Chem.* **2003**, *559*, 91–98.
- [20] T. Ishida, N. Kinoshita, H. Okatsu, T. Akita, T. Takei, M. Haruta, *Angew. Chem. Int. Ed.* **2008**, *47*, 9265–9268; *Angew. Chem.* **2008**, *120*, 9405–9408.
- [21] M. Brust, M. Walker, D. Bethell, D. J. Schiffrin, R. Whyman, *Chem. Commun.* **1994**, 801–802.
- [22] M. J. Hostetler, J. E. Wingate, C.-J. Zhong, J. E. Harris, R. W. Vachet, M. R. Clark, J. D. Londono, S. J. Green, J. J. Stokes, G. D. Wignall, et al., *Langmuir* **1998**, *14*, 17–30.
- [23] Y. Liu, H. Tsunoyama, T. Akita, S. Xie, T. Tsukuda, *ACS Catal.* **2011**, *1*, 2–6.
- [24] F. Schüth, *Phys. Status Solidi* **2013**, *250*, 1142–1151.
- [25] D. Widmann, R. J. Behm, *Angew. Chem. Int. Ed.* **2011**, *50*, 10241–10245; *Angew. Chem.* **2011**, *123*, 10424–10428.
- [26] A. Taketoshi, M. Haruta, *Chem. Lett.* **2014**, *43*, 380–387.
- [27] M. Mihaylov, H. Knözinger, K. Hadjiivanov, B. C. Gates, *Chem. Ing. Tech.* **2007**, *79*, 795–806.

Received: May 9, 2016

Published online on July 14, 2016

Available online at www.sciencedirect.com

ScienceDirect

journal homepage: www.elsevier.com/locate/he

CrossMark

Effect of the mesopores of carbon supports on the CO tolerance of Pt₂Ru₃ polymer electrolyte fuel cell anode catalyst

Napan Narischat^{a,b}, Tatsuya Takeguchi^{b,*}, Takeshi Mori^a,
Shinichiroh Iwamura^a, Isao Ogino^a, Shin R. Mukai^a, Wataru Ueda^c

^a Graduate School of Engineering, Hokkaido University, Sapporo, Japan

^b Faculty of Engineering, Iwate University, Morioka, Japan

^c Department of Material and Life Chemistry, Kanagawa University, Kanagawa, Japan

ARTICLE INFO

Article history:

Received 6 March 2016

Received in revised form

18 May 2016

Accepted 29 May 2016

Available online 24 June 2016

Keywords:

Bifunctional mechanism

Mesoporous structure

R/C ratio

Diffusivity

ABSTRACT

To investigate the effects of the porous structure of carbon support for bimetallic PtRu PEFC anode catalysts on their CO tolerance, a series of Resorcinol-formaldehyde carbon gels with different resorcinol to catalyst (R/C) ratios (i.e., 200, 800 and 1000) were synthesized and used to support Pt₂Ru₃ nanoparticles. Synthesized catalysts were characterized by powder X-ray diffraction, N₂ gas adsorption/desorption experiments, and scanning transmission electron microscopy. CO tolerances were evaluated by using a single cell in a H₂ feed in the presence of CO ranging from 100 to 2000 ppm. The potential difference of the cell using Pt₂Ru₃/RC1000ac58 anode catalyst was 0.655 V whereas the cell using a commercial Pt₂Ru₃/C catalyst showed a voltage of 0.570 V in the presence of 500 ppm CO. The results reveal that high modal size and volume of mesopore enhance diffusivity of CO resulted in effectively oxidization of CO.

© 2016 Hydrogen Energy Publications LLC. Published by Elsevier Ltd. All rights reserved.

Introduction

The most convenient way to obtain H₂ for residential polymer electrolyte fuel cell (PEFC) is through reforming of methane with steam, because the methane supply systems for residential consumption are viable everywhere. However, the generation of carbon monoxide (CO), which poisons the Pt catalyst surface and inhibits the H₂ oxidation reaction, is unavoidable. Pt–Ru alloy can enhance the CO tolerance of the catalyst presumably by the bifunctional mechanism and/or ligand effect [1,2]. However, the CO acceptant limit is lower than 100 ppm [3–6]. Many studies searching for the possibility to enhance the CO tolerance of the anode catalyst for PEFCs

have been conducted, for example by adjusting the Pt:Ru ratio [7–10], by varying PtRu particle size [11–14], and by changing the support of the bimetallic catalyst. Various materials such as carbon nanofibers and graphitic carbon (including carbon nanotubes and graphene) [15–18], surface modified carbon [19–22], and other metal oxides were tested as supports for PEFC catalysts [23–25]. Although the effect of the support still remains unclear, many studies focus on its porous structure. The effects of porous structure of many carbon supports on cell voltage were investigated and the porous structure of the support was found to significantly affect the efficiency of the electrocatalyst and its CO tolerance [26–30].

One of the most interesting materials to be used as a support is resorcinol-formaldehyde carbon gels (RFC). Their

* Corresponding author. 4-3-5 Ueda, Morioka, Iwate, 020-8551, Japan. Tel./fax: +81 19 621 6340.

E-mail address: takeguch@iwate-u.ac.jp (T. Takeguchi).

<http://dx.doi.org/10.1016/j.ijhydene.2016.05.272>

0360-3199/© 2016 Hydrogen Energy Publications LLC. Published by Elsevier Ltd. All rights reserved.

surface area, pore diameter, and structure are tunable by varying synthesis conditions. There are many reports of using RFC as supports for energy conversion and storage electrocatalysts. In addition, there are some studies using RFC as a support for electrode catalysts of the cathode [28,31,32] as well as the anode [33–38]. The two simple ways to control the porous structure of RFCs are to adjust the ratio of resorcinol to catalyst (R/C) of its starting solution and to adjust its activation degree [39,40]. The effect of activation degree has already been reported [41].

To synthesize RFC, first resorcinol and formaldehyde are polymerized using a base catalyst. The main reaction is a condensation reaction which leads to the formation of compounds. Such oligomers form clusters that agglomerate to colloidal particles. These particles coagulate and form a wet gel (hydrogel). Next the hydrogel is dried to remove the solvent trapped in its gel structure. Then the dried gel is heat-treated in an inert atmosphere and is transformed to carbon. Generally a higher carbonization temperature leads to a lower pore volume of the resulting carbon. Finally the carbon is activated by gases such as steam or CO₂ to increase its pore volume, pore size and surface area [41–45]. Moreover, activation process can also change electrochemical properties, significantly. By changing the R/C molar ratio in the starting solution used for RFC synthesis, the microstructure of the final carbons can be varied [43,45]. A lower R/C ratio results in small polymer particles (3–5 nm) which have a higher density. Polymeric RF gels, formed by small-sized polymer particles, generally have a high surface area and high compressive modulus but the gels tend to shrink when dried. Whereas RF gels synthesized at high R/C ratios are formed by large polymer particles (16–200 nm) the gels have low surface area and low compressive modulus, but they are hardly shrink when they are dried.

In this study, the effect of the R/C ratio of the starting solution on the electrochemical performance of the resulting catalyst was investigated. As the R/C ratio hardly affects the surface area of the resulting RFC, the direct effect of pore structure on electrochemical property can be clarified.

Material and methods

Resorcinol-formaldehyde carbon gel (RFC) preparation

A resorcinol–formaldehyde (RF) solution was prepared from resorcinol (R), formaldehyde (F), sodium carbonate (C), and distilled water (W). The molar ratios of resorcinol to formaldehyde (R/F) and the mass-to-volume ratio of resorcinol to water (R/W) were fixed to 0.5 mol/mol and 0.5 g mL⁻¹, respectively. The molar ratios of resorcinol to catalyst (R/C) were varied as 200, 800, and 1000 mol/mol. The prepared RF solutions were first aged and were transformed to hydrogels at room temperature. After that, RF hydrogels were aged at 60 °C for another 3 days. The water in the hydrogels was then exchanged to t-butanol by immersing the hydrogels in containers including this alcohol and placing the containers in a shaking water bath kept at 50 °C for 3 days. The t-butanol in the containers was replaced every day. Then, RF hydrogels were dried at 120 °C for 3 days before being carbonized.

Carbonization was conducted in a 100 cm³ min⁻¹ flow of nitrogen gas. Samples were heated up from 25 °C to 250 °C within 1 h, and were maintained at this temperature for 2 h. The temperature was then increased to 1000 °C at a ramp rate of 250 °C h⁻¹ and then the temperature was maintained at 1000 °C for 4 h. Activation was carried out under a 20 cm³ min⁻¹ CO₂ and 100 cm³ min⁻¹ N₂ flow at 1000 °C. Activation degree (or burn off ratio) was calculated from weight loss after activation by weight before activation.

RFC samples RC200ac58, RC800ac62 and RC1000ac58 were prepared. The number following RC (200, 800, and 1000) indicates the R/C ratio at which the samples were prepared, and that following ac (58 and 62) indicates the activation degree.

Preparation of Pt₂Ru₃ anode catalysts

First, Pt/RC1000ac58 (40 wt%Pt/C) was prepared by mixing RC1000ac58 with Pt(NH₃)₂(NO₂)₂ (4.554 wt% Pt, Tanaka Kikinzoku Kogyo), and distilled water in a three-neck flask and stirring vigorously at room temperature (20 °C) for 1 h. Pt was then reduced by ethanol and kept at 95 °C overnight. After that, the catalyst was filtered and washed with distilled water, followed by drying in air at 80 °C for 10 h. Second, RuCl₃·nH₂O (99.9%, Wako) was dissolved in distilled water and RC1000ac58 supporting Pt was added. The Pt:Ru molar ratio of was adjusted to 2:3. The mixture was kept at room temperature for 1 h. Then the Ru in the catalyst was reduced by keeping the catalyst overnight in methanol maintained at 70 °C. After that, the obtained catalyst was, again, filtered and washed with distilled water. Then the catalyst was dried in N₂ at 80 °C for 10 h. At last, the catalyst was reduced in a H₂/Ar (5% H₂) flow at room temperature for 1 h, followed by rapid heating to 880 °C within 12 min in He. The oven was turned off once the temperature reached 880 °C in order to allow the catalyst to cool down immediately. The catalyst was heated again at 150 °C for 2 h in a H₂/Ar (5% H₂) flow. Other samples (i.e., Pt₂Ru₃/RC200ac58 and Pt₂Ru₃/RC800ac62) were prepared by the same method. Commercial catalyst, Pt₂Ru₃/TKK TEC61E54 (Pt 29.6%, Ru 23.0%, Tanaka Kikinzoku Kogyo), was used as a reference.

Physical characterization

Nitrogen adsorption isotherms of all of the samples were measured at -196.15 °C using an adsorption apparatus (BELSORP-mini II surface area and pore size analyzer, BEL Japan). Specific surface area was calculated from BET plots. Pore size distributions and mesopore volumes were calculated using the Dollimore–Heal (DH) method. Here mesopores are defined as pores with a diameter between 2 and 50 nm. The diffusivity was calculated using Knudsen's equation based on the modal size of the mesopores of the catalyst after Nafion mixing. XRD patterns of PtRu metal crystallites within the catalyst were obtained by a powder X-ray diffractometer (PXRD; RIGAKU, RINT 2000). The tube current used for Cu K α radiation was 40 mA and the tube voltage was 40 kV. The angular region of the 2 θ scan was set between 10° and 85°, and the scan rate was 1° min⁻¹. The crystallite sizes were evaluated from the Scherrer equation using the peak of the (220) reflection of Pt fcc structure. Catalyst structure was investigated by using a Hitachi HD-2000 scanning transmission electron microscope

(STEM) instrument with electron energy of 200 kV and a beam current of 30 μA . Please note that the size of at least 200 PtRu particles of each sample was measured to obtain the average PtRu particle size.

MEA preparation

In the membrane electrode assembly (MEA) preparation process, carbon paper (P50T) was used as the backing layers of the anode and the cathode. Anode catalyst inks were prepared by dispersing PtRu/RFCs catalysts in distilled water and ethanol mixed with Nafion solution (5 wt% dispersion, Aldrich). Cathode catalyst ink was prepared by dissolving commercial Pt/C (46 wt%, TTK TEC10E50) in distilled water and ethanol including Nafion. In both electrodes, the catalyst ink was painted to achieve a metal loading of 0.5 mg cm^{-2} followed by a coating of 0.5 mg cm^{-2} Nafion. Finally, the anode and cathode ($22 \times 22 \text{ mm}$) were placed onto the two sides of a Nafion[®] NRE-212 membrane (Aldrich) and hot-pressed at $135 \text{ }^\circ\text{C}$ and 10 MPa for 20 min to form the MEA.

Single cell performance testing and CO tolerance experiment

The MEA was assembled into a single cell (FC05-01SP, ElectroChem, Inc.) having flow field plates made of graphite and end plates made of copper. The end plates of the cell were attached to a heater. The single cell was connected to a fuel cell test apparatus (Chino Corp.). Fig. 1 shows the setting of single cell test. Pure H_2 (or H_2/CO mixture) and O_2 were supplied at flow rates of $80 \text{ cm}^3 \text{ min}^{-1}$ to the anode and cathode, respectively, at ambient pressure. During measurements, the anode and cathode humidifiers were set at 70 and $68 \text{ }^\circ\text{C}$, respectively, and the single cell was maintained at $70 \text{ }^\circ\text{C}$. CO tolerance experiments were performed under the same conditions as single cell performance tests. The current density was set to 0.2 A cm^{-2} . First, pure H_2 was fed to the cell for 1 h and then 100 ppm of CO was mixed to H_2 . The concentration of CO was increased every 2 h to 500 ppm, 1000 ppm and finally 2000 ppm.

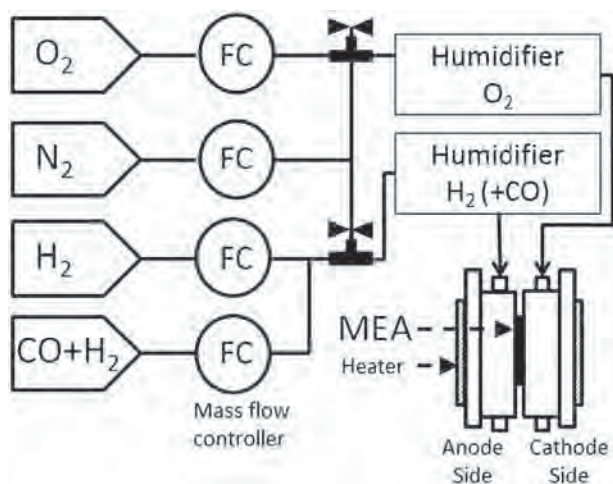


Fig. 1 – PEFC single cell performance testing and CO tolerance experiment set-up.

Results and discussion

Characterization of textural properties of synthesized carbon gels and supported Pt_2Ru_3 catalysts

Nitrogen gas adsorption data are summarized in Table 1. The synthesized RFC samples have similar BET surface areas ranging from 2140 to $2490 \text{ m}^2 \text{ g}^{-1}$, larger than the commercial catalyst ($823 \text{ m}^2 \text{ g}^{-1}$). Although the activation degree and the surface area of the samples are similar. The pore size distribution derived using the DH method differed significantly. RC800 had the largest mesopore volume among the prepared carbon supports.

PXRD and STEM characterization of supported Pt_2Ru_3 catalysts

Fig. 2 shows the PXRD (powder X-ray diffractometer) patterns of $\text{Pt}_2\text{Ru}_3/\text{RFC}$ catalysts with various R/C ratios ranging from 200 to 1000 and the commercial Pt_2Ru_3 catalyst. Diffraction peaks corresponding to the (220) plane were used to calculate PtRu crystallite sizes because there are no interference of peaks arising from the structure of carbon. The Pt (220) plane refer to the face-centered cubic (fcc) crystal structure of the Pt metal. The PXRD pattern of Pt/RC1000ac0 has been used as a reference for the Pt (220). The peak was shown at $2\theta = 67.5^\circ$. In contrast, the PXRD data for $\text{Pt}_2\text{Ru}_3/\text{RFC}$ catalysts and the commercial catalyst show similar peaks position at 69.2° . Thus, the results indicate all of the samples have a similar degree of alloying of Pt with Ru. The PtRu crystallite size is calculated by using the Scherrer equation (Table 1). The commercial catalyst has an average PtRu crystallite size of 3.4 nm . The average PtRu crystallite sizes of the synthesized $\text{Pt}_2\text{Ru}_3/\text{RFC}$ samples (1.9 – 2.7 nm) are slightly smaller than that of the commercial catalyst.

Fig. 3 shows STEM images of commercial and prepared catalysts. The average PtRu particle size of the commercial catalyst (Fig. 3A, 3.9 nm) is larger than that of $\text{Pt}_2\text{Ru}_3/\text{RC200ac58}$ (Fig. 3B, 3.2 nm) and larger than the crystallite size calculated from PXRD data. This indicates that PtRu nanoparticle consists of crystallites. The average PtRu particle size of $\text{Pt}_2\text{Ru}_3/\text{RC800ac62}$ (Fig. 3C, 2.6 nm) and $\text{Pt}_2\text{Ru}_3/\text{RC1000ac58}$ (Fig. 3E, 2.7 nm) are almost the same. However, compare with

Table 1 – The following expressions should be used. Physical properties of carbon supports and crystallite sizes of PtRu alloy.

Sample	Surface area of carbon gel support ($\text{m}^2 \text{ g}^{-1}$)	Volume of mesopore of carbon gel support ($\text{cm}^3 \text{ g}^{-1}$)	Crystallite size of alloy (nm) (As-synthesized catalyst)
RC200Ac58	2180	0.76	2.7
RC800Ac62	2470	2.29	1.9
RC1000Ac58	2140	2.08	2.3
Commercial catalyst	820	N/A	3.4

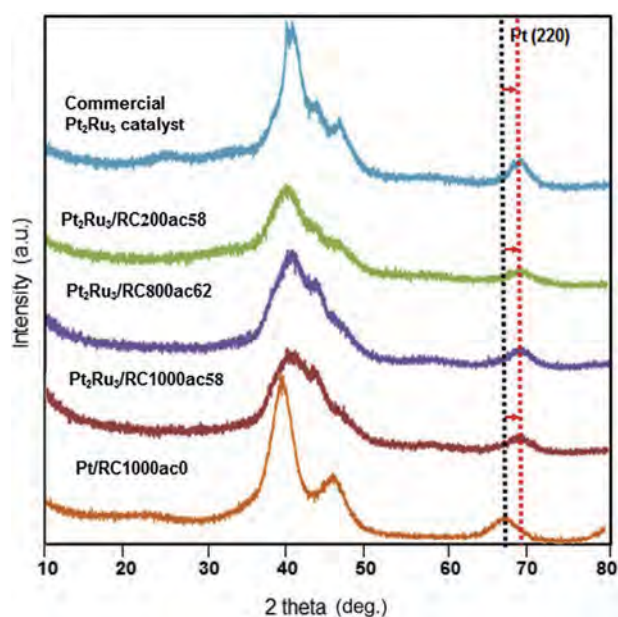


Fig. 2 – PXRD patterns of commercial Pt_2Ru_3 catalyst and prepared catalysts.

the commercial catalyst, the PtRu particle size is not much different (2.6–3.9 nm).

Single cell test and CO tolerance

Fig. 4 shows the performance of commercial and prepared catalysts. All catalysts are prepared under the same conditions

except for the R/C ratios the carbon support. The metal loading on the anode for MEA are fixed to 0.5 mg cm^{-2} . First, pure H_2 is fed to the anode side at $80 \text{ cm}^3 \text{ min}^{-1}$, and the current density is set to 0.2 A cm^{-2} . After feeding pure H_2 for 1 h, the cell using $\text{Pt}_2\text{Ru}_3/\text{RC1000ac58}$ generate the highest voltage of 0.787 V. The order of the cell voltage are as follows: 0.787 V ($\text{Pt}_2\text{Ru}_3/\text{RC1000ac58}$) > 0.775 V ($\text{Pt}_2\text{Ru}_3/\text{RC800ac62}$) > 0.748 V (commercial catalyst) > 0.666 V ($\text{Pt}_2\text{Ru}_3/\text{RC200ac58}$).

The cell using $\text{Pt}_2\text{Ru}_3/\text{RC200ac58}$ generate the lowest voltage among the catalysts tested. After 100 ppm CO is mixed with the H_2 flow. The cell voltage of $\text{Pt}_2\text{Ru}_3/\text{RC1000ac58}$ is slightly decreased by 4%, from 0.787 V to 0.758 V, after 2 h. Voltage of $\text{Pt}_2\text{Ru}_3/\text{RC800ac62}$ is also decreased by 8%, from 0.775 V to 0.721 V, after 2 h. The cell voltage of the commercial Pt_2Ru_3 catalyst and $\text{Pt}_2\text{Ru}_3/\text{RC200ac58}$ are 0.719 V and 0.287 V, respectively.

The cell voltage of the commercial catalyst significantly decreased when the CO concentration is increased to 500 ppm. Constant current density was kept at 0.2 A cm^{-2} with feeding H_2 contaminated with 500 ppm CO for 2 h. Potential difference decrease by 24%, from 0.748 V in pure H_2 to 0.567 V. Interestingly, voltage of $\text{Pt}_2\text{Ru}_3/\text{RC1000ac58}$ and $\text{Pt}_2\text{Ru}_3/\text{RC800ac62}$ slightly decrease by 8% and 11% to 0.726 V and 0.721 V, respectively. On the other hand, cell voltage of $\text{Pt}_2\text{Ru}_3/\text{RC200ac58}$ drastically decreases.

Finally, H_2 contaminated with 2000 ppm CO is fed. The cell using $\text{Pt}_2\text{Ru}_3/\text{RC1000ac58}$ showed the highest CO tolerance; potential difference decreased by 17%, from 0.787 V in pure H_2 to 0.655 V. The cell voltage of $\text{Pt}_2\text{Ru}_3/\text{RC800ac62}$ decreased from by 21%, 0.775 V–0.615 V, while the voltage for the commercial catalyst significantly decreases by 47.3%, from 0.748 V to 0.394 V.

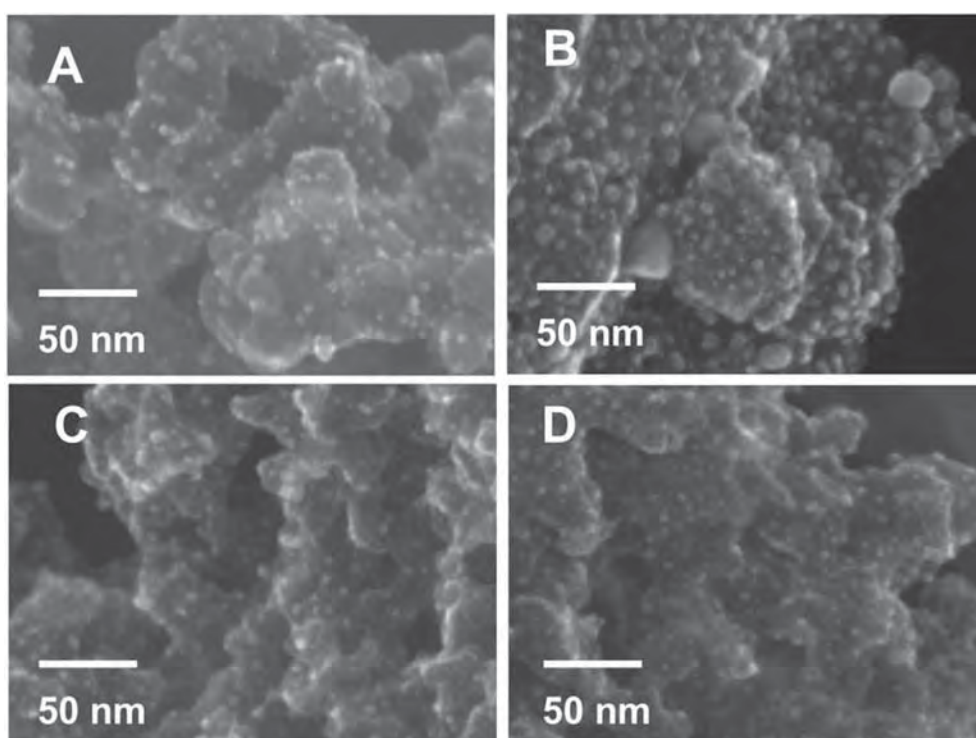


Fig. 3 – STEM images: (A) commercial $\text{Pt}_2\text{Ru}_3/\text{C}$, (B) $\text{Pt}_2\text{Ru}_3/\text{RC200ac58}$, (C) $\text{Pt}_2\text{Ru}_3/\text{RC800ac62}$ and (D) $\text{Pt}_2\text{Ru}_3/\text{RC1000ac58}$.

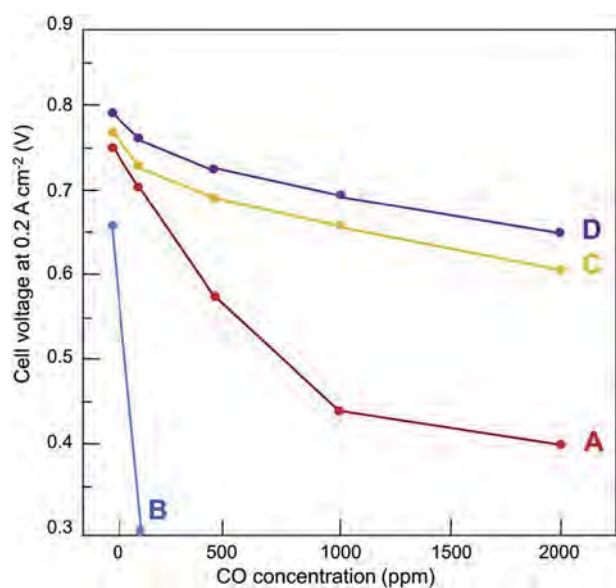


Fig. 4 – Effect of CO concentration on cell voltage at 0.2 A cm^{-2} . Cell temp.: $70 \text{ }^\circ\text{C}$; Electrolyte: Nafion[®] NRE 212; Cathode: Pt/C (0.5 mg cm^{-2}); O_2 humidified at $68 \text{ }^\circ\text{C}$; Flow rate: 80 mL min^{-1} ; Anode: $\text{Pt}_2\text{Ru}_3/\text{C}$ ($0.5 \text{ mg-PtRu cm}^{-2}$); H_2 containing 0, 100, 500, 1000 and 2000 ppm CO humidified at $70 \text{ }^\circ\text{C}$; Flow rate: 80 mL min^{-1} . (A) $\text{Pt}_2\text{Ru}_3/\text{C}$ commercial catalyst, (B) $\text{Pt}_2\text{Ru}_3/\text{RC200ac58}$, (C) $\text{Pt}_2\text{Ru}_3/\text{RC800ac58}$, (D) $\text{Pt}_2\text{Ru}_3/\text{RC1000ac58}$.

The cell voltage of $\text{Pt}_2\text{Ru}_3/\text{RC1000ac58}$ and $\text{Pt}_2\text{Ru}_3/\text{RC800ac62}$ are higher than that of the commercial catalyst at all levels of CO contamination. Especially, in the presence of 2000 ppm CO, the potential difference of $\text{Pt}_2\text{Ru}_3/\text{RC800ac62}$ is about 0.22 V higher than that of the commercial catalyst.

Effect of PtRu loading and Nafion mixing on pore volume

As the results showed above, there are no significant differences in crystallite size, alloying degree, and surface area among the catalysts, but their CO tolerance was significantly different. In order to explain this difference, the pore volume of the samples at each preparation step (carbon support, after PtRu loading and after mixing with Nafion) is measured.

As shown in Table 2, the mesopore volumes of all RFCs (calculated by DH plot) decrease by 50–60% after PtRu loading. The volume of mesopores after PtRu loading of commercial Pt_2Ru_3 catalyst ($0.77 \text{ cm}^3 \text{ g}^{-1}$) is larger than that of $\text{Pt}_2\text{Ru}_3/\text{RC200ac58}$ ($0.34 \text{ cm}^3 \text{ g}^{-1}$). The pore size distribution is shown in Fig. 5. All samples were mixed with Nafion. The mesopore volume of both the commercial Pt_2Ru_3 catalyst and $\text{Pt}_2\text{Ru}_3/$

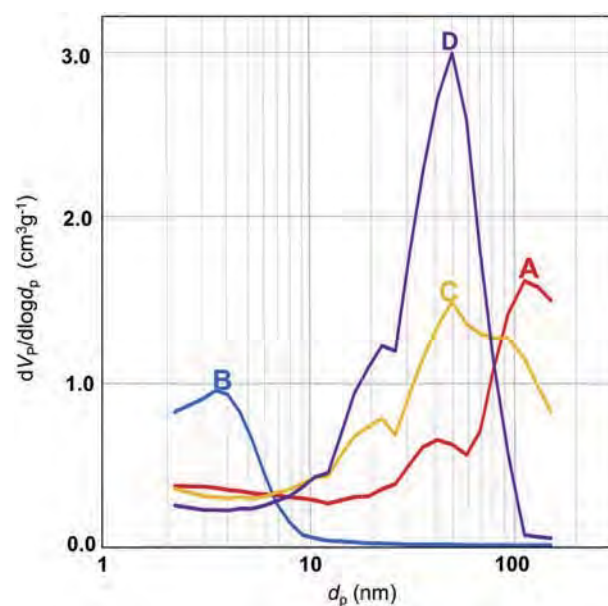


Fig. 5 – Pore size distribution of all Pt_2Ru_3 catalysts after deposition of PtRu: (A) $\text{Pt}_2\text{Ru}_3/\text{C}$ commercial catalyst, (B) $\text{Pt}_2\text{Ru}_3/\text{RC200ac58}$, (C) $\text{Pt}_2\text{Ru}_3/\text{RC800ac58}$ and (D) $\text{Pt}_2\text{Ru}_3/\text{RC1000ac58}$.

RC200ac58 decrease drastically, by 94% and 68%, respectively. On the other hand, the mesopore volumes of $\text{Pt}_2\text{Ru}_3/\text{RC800ac62}$ and $\text{Pt}_2\text{Ru}_3/\text{RC1000ac58}$ decrease by 49% and 50% after mixing with Nafion, respectively. The mesopore volumes of $\text{Pt}_2\text{Ru}_3/\text{RC800ac62}$ and $\text{Pt}_2\text{Ru}_3/\text{RC1000ac58}$ are about 5 times larger than that of $\text{Pt}_2\text{Ru}_3/\text{RC200ac58}$ at this stage. Fig. 6 shows that $\text{Pt}_2\text{Ru}_3/\text{RC800ac62}$ and $\text{Pt}_2\text{Ru}_3/\text{RC1000ac58}$ still have a large volume of mesopores after mixing with Nafion. By contrast, the mesopore volume of the commercial catalyst after mixing with Nafion is very low. $\text{Pt}_2\text{Ru}_3/\text{RC200ac58}$ contains only small mesopores (smaller than 10 nm).

Diffusivity

As explained in the previous section, catalysts on synthesized using carbons with larger mesopore volumes exhibited a higher CO tolerance. It remains elusive why the catalysts having large mesopore volume exhibit a higher CO tolerance. However, because mass transfer within mesopores is generally dictated by Knudsen diffusion, which is proportional to the diameter of mesopores, faster mass transfer of reactants and products may account for it.

After the catalyst had been mixed with Nafion, the mesopore volume increased with the increasing R/C ratio. Fig. 7

Table 2 – Mesopore volumes of the catalysts at different synthesis stages.

Sample	Volume of mesopore after PtRu loading ($\text{cm}^3 \text{ g}^{-1}$)	Decrease (%)	Volume of mesopore after Nafion mixing ($\text{cm}^3 \text{ g}^{-1}$)	Decrease (%)
RC200Ac58	0.34	55	0.11	68
RC800Ac62	0.92	60	0.47	49
RC1000Ac58	1.02	51	0.51	50
Commercial catalyst	0.77	N/A	0.05	94

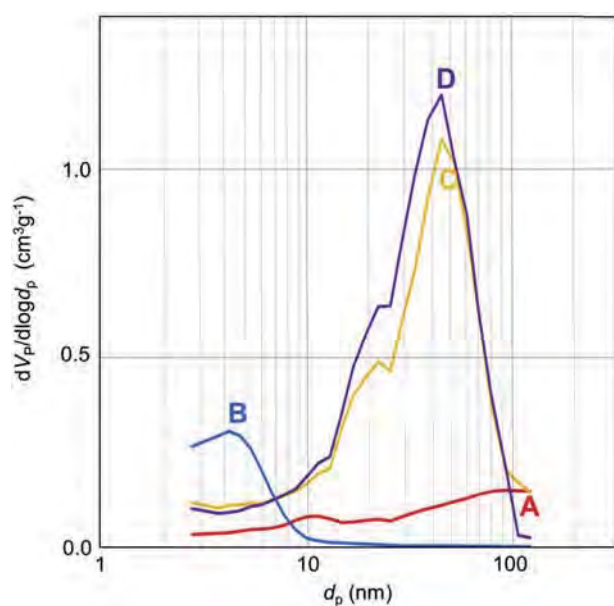


Fig. 6 – Pore size distribution of all Pt₂Ru₃ catalysts after mixing of Nafion: (A) Pt₂Ru₃/C commercial catalyst, (B) Pt₂Ru₃/RC200ac58, (C) Pt₂Ru₃/RC800ac58 and (D) Pt₂Ru₃/RC1000ac58.

shows the effect of mesopore volume on CO tolerance and diffusivity for all samples after Nafion mixing. The diffusivity shown here is calculated using Knudsen's equation based on the modal size of the mesopores of the catalyst after Nafion mixing. Diffusivity of CO within Pt₂Ru₃/RC1000ac58 and Pt₂Ru₃/RC800ac62 are much higher ($D = 0.056 \text{ cm}^2 \text{ s}^{-1}$) than that within Pt₂Ru₃/RC200ac58 ($D = 0.007 \text{ cm}^2 \text{ s}^{-1}$) and the commercial catalyst ($D = 0.014 \text{ cm}^2 \text{ s}^{-1}$).

It is clear that high-CO tolerant Pt₂Ru₃/RC1000ac58 and Pt₂Ru₃/RC800ac62 have larger mesopores. The larger size of

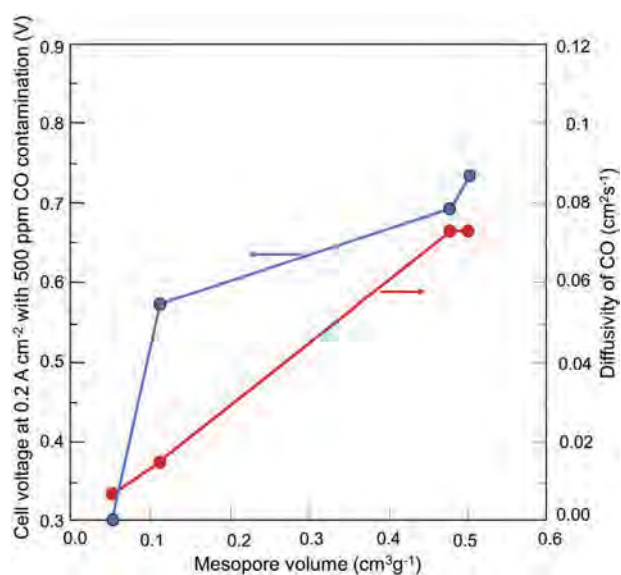


Fig. 7 – Relation between mesopore volume and diffusivity of CO after mixing of Nafion.

mesopores enables faster diffusion of all gases when compared with the mesopores in Pt₂Ru₃/RC200ac58 and the commercial catalyst. The commercial catalyst has a bimodal pore distribution, meaning it has two representative diffusion parameters, but we will focus only on that of its mesopores since macropores are not related to the diffusion near the active sites. Consider the water gas shift reaction (WGSR);



By nature of exothermic reactions, the WGSR equilibrium largely shifts to the right side at low temperature of 70 °C [46] in the presence of excess water, yielding an empty surface site on the Pt–Ru alloy [47]. Moreover, the modal size and volume of mesopores of Pt₂Ru₃/RC1000ac58 and Pt₂Ru₃/RC800ac62 are much larger than those of others, resulting in a higher diffusivity of CO. Pt₂Ru₃/RC1000ac58 has little larger volume of mesopore than Pt₂Ru₃/RC1000ac58 and also better performance than Pt₂Ru₃/RC1000ac58. Therefore, rate of water-gas shift reaction was enhanced. Since CO is effectively oxidized by this reaction, HOR progressed effectively even in the presence of high-concentration CO.

Conclusions

Pt₂Ru₃ anode catalysts were prepared using RFCs prepared at various R/C ratios (i.e., 200, 800 and 1000). The prepared catalysts have similar physical properties such as alloying degree, PtRu size and BET surface area, but the catalysts exhibited significantly different CO tolerances. In addition, the catalysts, which have large volumes of mesopores with modal size as large as 50 nm after Nafion mixing, exhibited higher CO tolerance, suggesting the importance of these mesopores for CO tolerance. Effective CO removal due to the high diffusivity in large mesopores enhances the CO tolerance of the MEA.

Acknowledgment

This research was partially funded by New Energy and Industrial Technology Development Organization (NEDO), Japan (P13400788-0).

REFERENCES

- [1] Watanabe M, Motoo S. Electrocatalysis by ad-atoms .3. Enhancement of oxidation of carbon-monoxide on platinum by ruthenium ad-atoms. *J Electroanal Chem* 1975;60:275–83.
- [2] Scott FJ, Mukerjee S, Ramaker DE. Contrast in Metal–Ligand effects on PtnM Electrocatalysts with M Equal Ru vs Mo and Sn As exhibited by in situ XANES and EXAFS measurements in methanol. *J Phys Chem C* 2010;114:442–53.
- [3] Lopes P, Freitas K, Ticianelli E. CO tolerance of PEMFC anodes: mechanisms and electrode designs. *Electrocatalysis* 2010;1:200–12.
- [4] Starz KA, Auer E, Lehmann T, Zuber R. Characteristics of platinum-based electrocatalysts for mobile PEMFC applications. *J Power Sources* 1999;84:167–72.

- [5] Amphlett JC, Mann RF, Peppley BA. On board hydrogen purification for steam reformation/PEM fuel cell vehicle power plants. *Int J Hydrogen Energy* 1996;21:673–8.
- [6] Igarashi H, Fujino T, Watanabe M. Hydrogen electro-oxidation on platinum catalysts in the presence of trace carbon monoxide. *J Electroanal Chem* 1995;391:119–23.
- [7] Muthuswamy N, de la Fuente JLG, Tran DT, Walmsley J, Tsympkin M, Raaen S, et al. Ru@Pt core-shell nanoparticles for methanol fuel cell catalyst: control and effects of shell composition. *Int J Hydrogen Energy* 2013;38:16631–41.
- [8] Li L, Xing Y. Pt–Ru nanoparticles supported on carbon nanotubes as methanol fuel cell catalysts. *J Phys Chem C* 2007;111:2803–8.
- [9] dos Santos L, Colmati F, Gonzalez ER. Preparation and characterization of supported Pt–Ru catalysts with a high Ru content. *J Power Sources* 2006;159:869–77.
- [10] Sánchez-Padilla NM, Morales-Acosta D, Morales-Acosta MD, Montemayor SM, Rodríguez-Varela FJ. Catalytic activity and selectivity for the ORR of rapidly synthesized M@Pt (M = Pd, Fe₃O₄, Ru) core-shell nanostructures. *Int J Hydrogen Energy* 2014;39:16706–14.
- [11] Sato T, Okaya K, Kunimatsu K, Yano H, Watanabe M, Uchida H. Effect of particle size and composition on CO-tolerance at Pt–Ru/C catalysts analyzed by in situ attenuated total reflection FTIR spectroscopy. *ACS Catal* 2012;2:450–5.
- [12] Yamanaka T, Takeguchi T, Wang G, Muhamad EN, Ueda W. Particle size dependence of CO tolerance of anode PtRu catalysts for polymer electrolyte fuel cells. *J Power Sources* 2010;195:6398–404.
- [13] Wang G, Takeguchi T, Muhamad EN, Yamanaka T, Ueda W. Investigation of grain boundary formation in PtRu/C catalyst obtained in a polyol process with post-treatment. *Int J Hydrogen Energy* 2011;36:3322–32.
- [14] Goto S, Hosoi S, Arai R, Tanaka S, Umeda M, Yoshimoto M, et al. Particle-size- and Ru-Core-Induced surface electronic states of Ru-Core/Pt-Shell electrocatalyst nanoparticles. *J Phys Chem C* 2014;118:2634–40.
- [15] Calderón JC, García G, Calvillo L, Rodríguez JL, Lázaro MJ, Pastor E. Electrochemical oxidation of CO and methanol on Pt–Ru catalysts supported on carbon nanofibers: the influence of synthesis method. *Appl Catal B Environ* 2015;165:676–86.
- [16] He D, Cheng K, Li H, Peng T, Xu F, Mu S, et al. Highly active platinum nanoparticles on graphene nanosheets with a significant improvement in stability and CO tolerance. *Langmuir* 2012;28:3979–86.
- [17] Jha N, Leela Mohana Reddy A, Shaijumon MM, Rajalakshmi N, Ramaprabhu S. Pt–Ru/multi-walled carbon nanotubes as electrocatalysts for direct methanol fuel cell. *Int J Hydrogen Energy* 2008;33:427–33.
- [18] Kardimi K, Tsoufis T, Tomou A, Kooi BJ, Prodromidis MI, Gournis D. Synthesis and characterization of carbon nanotubes decorated with Pt and PtRu nanoparticles and assessment of their electrocatalytic performance. *Int J Hydrogen Energy* 2012;37:1243–53.
- [19] Gupta G, Slanac DA, Kumar P, Wiggins-Camacho JD, Kim J, Ryoo R, et al. Highly stable Pt/Ordered graphitic mesoporous carbon electrocatalysts for oxygen reduction. *J Phys Chem C* 2010;114:10796–805.
- [20] Roy SC, Christensen PA, Hamnett A, Thomas KM, Trapp V. Direct methanol fuel cell cathodes with sulfur and nitrogen-based carbon functionality. *J Electrochem Soc* 1996;143:3073–9.
- [21] Yu D, Xue Y, Dai L. Vertically aligned carbon nanotube arrays Co-doped with phosphorus and nitrogen as efficient metal-free electrocatalysts for oxygen reduction. *J Phys Chem Lett* 2012;3:2863–70.
- [22] Liu S, Zhang H, Xu Z, Zhong H, Jin H. Nitrogen-doped carbon xerogel as high active oxygen reduction catalyst for direct methanol alkaline fuel cell. *Int J Hydrogen Energy* 2012;37:19065–72.
- [23] Hernández-Pichardo ML, González-Huerta RG, del Angel P, Tufiño-Velazquez M, Lartundo L. The role of the WO₃ nanostructures in the oxygen reduction reaction and PEM fuel cell performance on WO₃–Pt/C electrocatalysts. *Int J Hydrogen Energy* 2015;40:17371–9.
- [24] Xia Y, Yang Z, Mokaya R. Mesoporous hollow spheres of graphitic N-Doped carbon nanocast from spherical mesoporous silica. *J Phys Chem B* 2004;108:19293–8.
- [25] Hou Z, Yi B, Yu H, Lin Z, Zhang H. CO tolerance electrocatalyst of PtRu–HxMeO₃/C (Me = W, Mo) made by composite support method. *J Power Sources* 2003;123:116–25.
- [26] Thepkaew J, Therdthianwong S, Therdthianwong A, Kucernak A, Wongyao N. Promotional roles of Ru and Sn in mesoporous PtRu and PtRuSn catalysts toward ethanol electrooxidation. *Int J Hydrogen Energy* 2013;38:9454–63.
- [27] Salgado JRC, Paganin VA, Gonzalez ER, Montemor MF, Tacchini I, Ansón A, et al. Characterization and performance evaluation of Pt–Ru electrocatalysts supported on different carbon materials for direct methanol fuel cells. *Int J Hydrogen Energy* 2013;38:910–20.
- [28] Ouattara-Brigaudet M, Berthon-Fabry S, Beauger C, Chatenet M, Job N, Sennour M, et al. Influence of the carbon texture of platinum/carbon aerogel electrocatalysts on their behavior in a proton exchange membrane fuel cell cathode. *Int J Hydrogen Energy* 2012;37:9742–57.
- [29] Viva FA, Bruno MM, Franceschini EA, Thomas YRJ, Ramos Sanchez G, Solorza-Feria O, et al. Mesoporous carbon as Pt support for PEM fuel cell. *Int J Hydrogen Energy* 2014;39:8821–6.
- [30] Han J-H, Lee E, Park S, Chang R, Chung TD. Effect of nanoporous structure on enhanced electrochemical reaction. *J Phys Chem C* 2010;114:9546–53.
- [31] Jin H, Li J, Gao L, Chen F, Zhang H, Liu Q. Graphitic mesoporous carbon xerogel as an effective catalyst support for oxygen reduction reaction. *Int J Hydrogen Energy* 2016;36:5038–46.
- [32] Arbizzani C, Righi S, Soavi F, Mastragostino M. Graphene and carbon nanotube structures supported on mesoporous xerogel carbon as catalysts for oxygen reduction reaction in proton-exchange-membrane fuel cells. *Int J Hydrogen Energy* 2011;36:5038–46.
- [33] Alegre C, Baquedano E, Gálvez ME, Moliner R, Lázaro MJ. Tailoring carbon xerogels' properties to enhance catalytic activity of Pt catalysts towards methanol oxidation. *Int J Hydrogen Energy* 2015;40:14736–45.
- [34] Marie J, Berthon-Fabry S, Achard P, Chatenet M, Pradourat A, Chainet E. Highly dispersed platinum on carbon aerogels as supported catalysts for PEM fuel cell-electrodes: comparison of two different synthesis paths. *J Non-Crystalline Solids* 2004;350:88–96.
- [35] Job N, Marie J, Lambert S, Berthon-Fabry S, Achard P. Carbon xerogels as catalyst supports for PEM fuel cell cathode. *Energy Convers Manag* 2008;49:2461–70.
- [36] Alegre C, Calvillo L, Moliner R, González-Expósito JA, Guillén-Villafuerte O, Huerta MVM, et al. Pt and PtRu electrocatalysts supported on carbon xerogels for direct methanol fuel cells. *J Power Sources* 2011;196:4226–35.
- [37] Smirnova A, Dong X, Hara H, Vasiliev A, Sammes N. Novel carbon aerogel-supported catalysts for PEM fuel cell application. *Int J Hydrogen Energy* 2005;30:149–58.
- [38] Calderón JC, Mahata N, Pereira MFR, Figueiredo JL, Fernandes VR, Rangel CM, et al. Pt–Ru catalysts supported on carbon xerogels for PEM fuel cells. *Int J Hydrogen Energy* 2012;37:7200–11.

- [39] Chai GS, Yoon SB, Yu J-S, Choi J-H, Sung Y-E. Ordered porous carbons with tunable pore sizes as catalyst supports in direct methanol fuel cell. *J Phys Chem B* 2004;108:7074–9.
- [40] Lin M-L, Huang C-C, Lo M-Y, Mou C-Y. Well-ordered mesoporous carbon thin film with perpendicular channels: application to direct methanol fuel cell. *J Phys Chem C* 2008;112:867–73.
- [41] Narischat N, Takeguchi T, Tsuchiya T, Mori T, Ogino I, Mukai SR, et al. Effect of activation degree of resorcinol–formaldehyde carbon gels on carbon monoxide tolerance of platinum–ruthenium polymer electrolyte fuel cell anode catalyst. *J Phys Chem C* 2014;118:23003–10.
- [42] Al-Muhtaseb SA, Ritter JA. Preparation and properties of resorcinol–formaldehyde organic and carbon gels. *Adv Mater* 2003;15:101–14.
- [43] Petricević R, Reichenauer G, Bock V, Emmerling A, Fricke J. Structure of carbon aerogels near the gelation limit of the resorcinol–formaldehyde precursor. *J Non-Crystalline Solids* 1998;225:41–5.
- [44] Saliger R, Bock V, Petricevic R, Tillotson T, Geis S, Fricke J. Carbon aerogels from dilute catalysis of resorcinol with formaldehyde. *J Non-Crystalline Solids* 1997;221:144–50.
- [45] Tamon H, Ishizaka H, Mikami M, Okazaki M. Porous structure of organic and carbon aerogels synthesized by sol-gel polycondensation of resorcinol with formaldehyde. *Carbon* 1997;35:791–6.
- [46] Smith RJB, Loganathan M, Shantha Murthy S. A review of the water gas shift reaction kinetics. *Int J Chem React Eng* 2010;8:1–32.
- [47] Takeguchi T, Yamanaka T, Asakura K, Muhamad EN, Uosaki K, Ueda W. Evidence of nonelectrochemical shift reaction on a CO-tolerant high-entropy state Pt-Ru anode catalyst for reliable and efficient residential fuel cell systems. *J Am Chem Soc* 2012;134:14508–12.

Acidic Ultrafine Tungsten Oxide Molecular Wires for Cellulosic Biomass Conversion

Zhenxin Zhang,* Masahiro Sadakane, Norihito Hiyoshi, Akihiro Yoshida, Michikazu Hara, and Wataru Ueda*

Abstract: The application of nanocatalysis based on metal oxides for biomass conversion is of considerable interest in fundamental research and practical applications. New acidic transition-metal oxide molecular wires were synthesized for the conversion of cellulosic biomass. The ultrafine molecular wires were constructed by repeating $(\text{NH}_4)_2[\text{XW}_6\text{O}_{21}]$ ($X = \text{Te}$ or Se) along the length, exhibiting diameters of only 1.2 nm. The nanowires dispersed in water and were observed using high-angle annular dark-field scanning transmission electron microscopy. Acid sites were created by calcination without collapse of the molecular wire structure. The acidic molecular wire exhibited high activity and stability and promoted the hydrolysis of the glycosidic bond. Various biomasses including cellulose were able to be converted to hexoses as main products.

The construction of molecular wires by polymerizing a molecular fragment in length direction while maintaining a molecular-level size in the other two dimensions has attracted much attention. Organic molecular wires are widely used.^[1] However, inorganic molecular wires are rare and difficult to obtain.^[2] The assembly of metal–oxygen octahedra is an ideal method for preparing well-crystallized solids based on a one-dimensional (1D) molecular structure.^[3] Recent progress indicates that inorganic molecular wires can be obtained using a “top-down” approach, resulting in a new class of metal oxide molecular wires.^[4] Therefore, this new field, although full of challenges, is receiving intense investigation.

Biomass utilization is important, owing to increasing attention on energy resource consumption for a sustainable society and development.^[5] The condensation of glycosidic bonds forms a large class of cellulosic biomass, typically cellulose, and the conversion of cellulosic biomass into useful chemicals is one of the most important biomass conversion routes.^[6] The first step is hydrolysis of a glycosidic bond to form hexoses, which can be further transformed to other chemicals. Brønsted acids are active for glycosidic bond hydrolysis. Various Brønsted acids have been utilized for the hydrolysis of cellulose, including traditional liquid acids and heteropoly acids^[7] as homogeneous catalysts as well as carbon materials,^[8,10] sulfonated resins,^[9] zeolites,^[10] solid super acids,^[10] and transition-metal oxides^[11] as heterogeneous catalysts. However, the current catalytic systems suffer from many problems that need to be overcome. These limitations include low catalytic activity, high catalyst loading, high reaction temperature, long reaction time, and difficulty with catalyst recycling.

A molecular wire based on metal oxide shows promise as solid acids owing to several advantages, such as nanosize, high stability, structure diversity, composition complexity, and tunable properties. The design and development of a metal oxide molecular wire with high acidity and stability are expected to exhibit high activity for catalytic cellulosic biomass conversion.

Herein, we report the successful design and synthesis of acidic solid molecular wires based on tungstotellurate (W-Te oxide) and tungstoselenate (W-Se oxide) and their application for cellulosic biomass conversion. The structure of the materials was confirmed by high-angle annular dark-field scanning transmission electron microscopy (HAADF-STEM) combined with other characterization techniques. Single molecular wires with a diameter of 1.2 nm were observed by electron microscopy and atomic force microscopy (AFM). W-Te oxide shows high thermal and hydrothermal stability and acted as a robust acid catalyst for hydrolysis of cellulosic biomass to produce hexoses.

The hydrothermal reaction of $(\text{NH}_4)_6[\text{H}_2\text{W}_{12}\text{O}_{40}]$ and TeO_2 or SeO_2 under low pH conditions (ca. 1.5) resulted in gel-like yellow products, indicating that the particle size in the materials was small. The as-synthesized materials adsorbed a large amount of water. After the materials were dried at 80 °C, the volume of the material substantially decreased (Supporting Information, Figure S1). Powder X-ray diffraction (XRD) patterns exhibited broad peaks, indicating that the crystallinity of the materials was low (Figure 1). The precursor pH affected the resulting products. As shown in the Supporting Information, Figure S2, the W-Te oxide synthe-

[*] Dr. Z. Zhang, Dr. A. Yoshida, Prof. Dr. W. Ueda
Faculty of Engineering, Kanagawa University
Rokkakubashi, Kanagawa-ku, Yokohama-shi, Kanagawa, 221-8686
(Japan)
E-mail: zhang.z.ag@m.titech.ac.jp
uedaw@kanagawa-u.ac.jp

Dr. Z. Zhang, Prof. Dr. M. Hara
Materials and Structures Laboratory, Tokyo Institute of Technology
Nagatsuta-cho 4259, Midori-ku, Yokohama-city, Kanagawa, 226-8503
(Japan)

Dr. M. Sadakane
Department of Applied Chemistry, Hiroshima University
1-4-1 Kagamiyama, Higashi Hiroshima 739-8527 (Japan)

Dr. N. Hiyoshi
Research Institute for Chemical Process Technology, National
Institute of Advanced Industrial Science and Technology (AIST)
4-2-1 Nigatake, Miyagino, Sendai 983-8551 (Japan)

Supporting information for this article can be found under:
<http://dx.doi.org/10.1002/anie.201602770>.

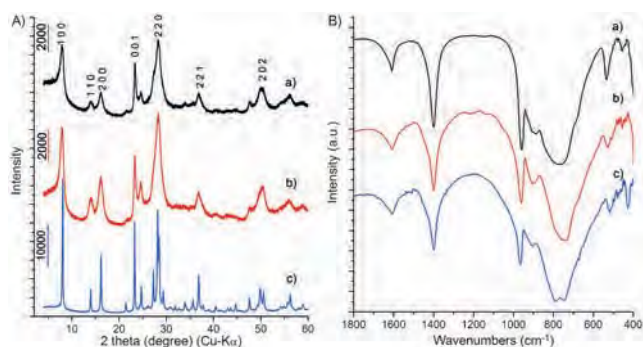
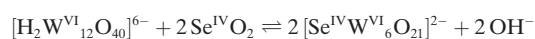
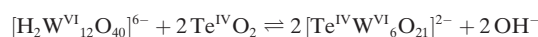


Figure 1. A) XRD patterns and B) FTIR spectra of a) W-Te oxide, b) W-Se oxide, and c) crystalline-W-Te oxide.

sized at a high pH (ca. 5) was a crystalline sample, denoted as crystalline-W-Te oxide. A decrease in the pH value of the precursor solution by less than 1.0 produced a material that had a different phase from that of W-Te oxide. For W-Se oxide, a high pH precursor did not yield a solid compound but a low pH yielded the same crystalline phase that was obtained for W-Te oxide.

The XRD pattern of the crystalline-W-Te oxide was indexed with a hexagonal cell ($a = 12.6798 \text{ \AA}$, $c = 3.8192 \text{ \AA}$), which was similar to that of Mo oxide molecular wire based crystals (Supporting Information, Figure S3).^[4] The main XRD peaks of W-Te oxide and W-Se oxide can also be indexed to nearly the same unit cell, indicating that these materials have the same structure as that of crystalline-W-Te oxide (Figure 1A). The broad diffraction peaks of the materials may be due to the small size of the particles in the material. The particle size of the materials was estimated by Scherrer's equation, showing ca. 15 nm in length along the c -axis and ca. 9 nm in diameter across the a - b plane (Supporting Information, Figure S4). The FTIR spectra of W-Te oxide, W-Se oxide, and crystalline-W-Te oxide were identical (Figure 1B), and the FTIR spectra of the W-based oxide were similar to those of the Mo-based oxide (Supporting Information, Figure S3).^[4] Therefore, the molecular structures of the materials were basically the same.

Elemental analysis indicated that the N:W:Te or Se ratio was 2:6:1. X-ray photoelectron spectroscopy (XPS; Supporting Information, Figure S5) showed that the W ions in both materials were W^{VI} , and the Te and Se ions were Te^{IV} and Se^{IV} , respectively, for the W-Te oxide and W-Se oxide, respectively. The UV/Vis spectra of the materials also indicated that the W ion in both materials was W^{VI} , because no absorbance between 500 and 800 nm was observed owing to the reduced W species (Supporting Information, Figure S6).^[12] The chemical formulae for W-Te oxide and W-Se oxide were estimated to be $(NH_4)_2[Te^{IV}W^{VI}_6O_{21}]$ and $(NH_4)_2[Se^{IV}W^{VI}_6O_{21}]$. The reactions for producing these materials can be expressed as follows:



The structure of crystalline-W-Te oxide was determined by the XRD pattern (Supporting Information, Tables S1–S3). The initial structure was refined by the Rietveld method. The simulated pattern was similar to the experimental pattern, indicating that the proposed structure was correct (Supporting Information, Figure S7).^[4]

The structure was confirmed by HAADF-STEM.^[13] The cross sectional image of the W-Te oxide (Figure 2a) shows

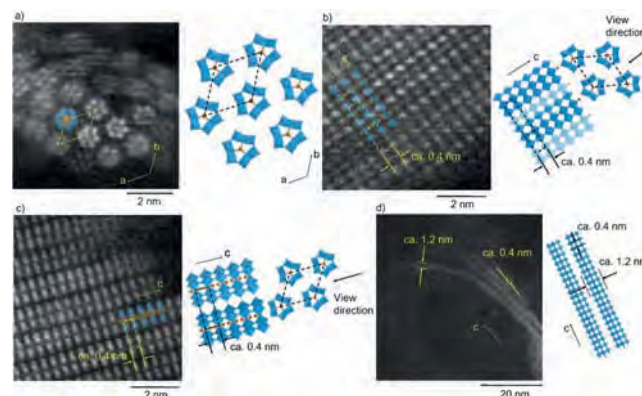


Figure 2. High-resolution HAADF-STEM images (left) and proposed structures (right) of a) W-Te oxide in the a - b plane, b) in the (100) plane, c) in the (2-10) plane, and d) W-Se oxide along the c -axis (dashed line indicates the unit cell; W blue, Te/Se brown, O red).

hexagonal units attributable to $[TeW_6O_{21}]^{2-}$ and their hexagonal array with a periodicity of ca. 1.2 nm. The side views of W-Te oxide (Figure 2b,c) show that the hexagonal units are stacked with a layer distance of ca. 0.4 nm to form a molecular wire. The atomic positions observed in Figure 2a–c are in good agreement with the proposed structures (Figure 2 right) and that of crystalline-W-Te oxide. The side view of W-Se oxide (Figure 2d) also shows a lattice fringe with a spacing of ca. 0.4 nm owing to the stack of the hexagonal units ($[SeW_6O_{21}]^{2-}$). A single molecular wire with a diameter of ca. 1.2 nm was observed in the end of a bundle of molecular wire.

The morphology of solid-state W-Te oxide and W-Se oxide was observed by scanning electron microscopy (SEM; Supporting Information, Figure S8). The crystalline-W-Te oxide had a uniform diameter of ca. 200 nm. The nanowire samples exhibited irregularly shaped particle aggregation. N_2 adsorption–desorption measurement indicated the presence of nanoparticles in the solid states (Supporting Information, Figure S9). After dispersal, the surface areas of the materials are expected to increase substantially.

W-Te oxide and W-Se oxide easily formed nanowires by simply dispersing the samples in water by ultrasound or heating. The SEM and transmission electron microscopy (TEM) images show the ultrathin nanowires after dispersal in water (Figure 3; Supporting Information, Figure S10). Single molecular wires with diameters of about 1–2 nm can be easily obtained, as shown in the typical high-resolution (HR)-TEM images (Figure 3e,f).

The diameters of the materials after dispersal were further analyzed by AFM. The AFM images of the materials after

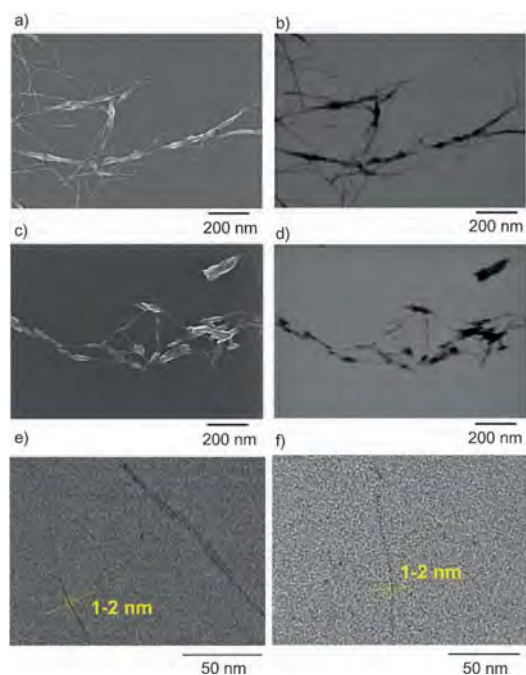


Figure 3. Electron microscopy images of the dispersed materials: a) SEM and b) TEM images of W-Te oxide; c) SEM and d) TEM images of W-Se oxide; HR-TEM images of e) W-Te oxide and f) W-Se oxide. The dispersed samples were prepared in water followed by sonication for 1 h, and then the solution was dropped on a TEM grid and dried.

dispersal indicated the presence of nanowires (Figure 4). In most cases, the nanowire consisted of an aggregation of several single molecular wires with a diameter less than 5 nm. A single molecular wire with the thickness of ca. 1.2 nm were also observed. All of the microscopy observations were conducted after the solution with the molecular wire was dried, and therefore particle aggregation could not be completely avoided.

FTIR spectra of the materials contained bands at ca. 1620 and 1400 cm^{-1} , which correspond to H_2O and NH_4^+ , respectively (Figure 1). H_2O and NH_4^+ were near the molecular wires and could be removed by calcination. Thermogravi-

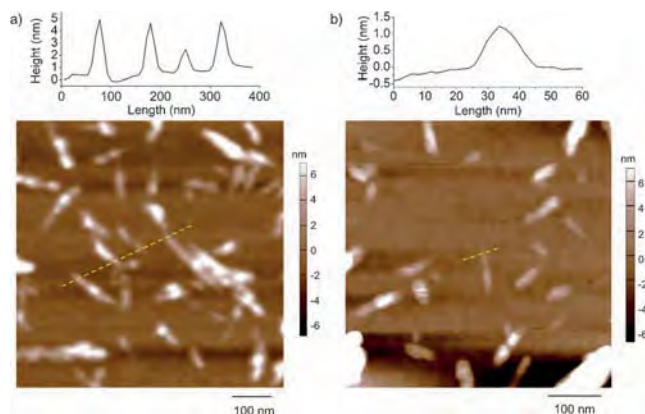


Figure 4. AFM images of a) W-Te oxide and b) W-Se oxide, top: thickness analysis indicated by yellow dashed lines in the AFM images. The sample was prepared using the same method as used for the TEM images.

metric-differential thermal analysis (TG-DTA) indicated that 8.5% and 10.7% weight losses were observed for W-Te oxide and W-Se oxide, respectively, during the heat treatment (Supporting Information, Figure S11). The desorption of NH_3 ($m/z = 16$) reached a peak maximum at 400 and 430 $^\circ\text{C}$ for W-Te oxide and W-Se oxide, respectively, in temperature-programmed desorption-mass spectrometry (TPD-MS; Supporting Information, Figure S12).

The thermal stability of W-Te oxide and W-Se oxide was evaluated. The materials were calcined under air at different temperatures for 2 h. W-Te oxide was stable at 350 $^\circ\text{C}$. The XRD patterns and FTIR spectra (Supporting Information, Figure S13 a,b) of the materials calcined below 350 $^\circ\text{C}$ did not change. A further increase in the calcination temperature generated material that exhibited different XRD peaks and IR bands, which indicated damage to the original structure. For W-Se oxide, the thermal stability was lower than that of W-Te oxide. The material started to decompose at 300 $^\circ\text{C}$ (Supporting Information, Figure S13 c,d).

The amount of NH_3 removed from W-Te oxide and W-Se oxide by calcination at 350 $^\circ\text{C}$ and 300 $^\circ\text{C}$, respectively, was estimated by TPD-MS (Supporting Information, Figure S12), and the calcined samples are referred to W-Te-AC350 and W-Se-AC300, respectively. After calcination, about 50% of the NH_3 was removed. We assume that desorption of NH_3 from the material produced proton in the materials as acid sites. The chemical formulae of the calcined materials were estimated to be $(\text{NH}_4)[\text{HTeW}_6\text{O}_{21}]$ and $(\text{NH}_4)[\text{HSeW}_6\text{O}_{21}]$ for W-Te-AC350 and W-Se-AC300, respectively.

Hydrothermal stabilities of W-Te-AC350 and W-Se-AC300, were tested at 175 $^\circ\text{C}$ for 2 h. After the treatment, the dispersed materials were recovered by evaporating all of the H_2O (Supporting Information, Figure S14). W-Te-AC350 was stable, and the structure did not change after the hydrothermal treatment. By contrast, the structure of W-Se-AC300 changed under the same conditions.

W-Te-AC350 was characterized and used as an acid catalyst for biomass hydrolysis in an aqueous solution. TEM (Supporting Information, Figure S10 e,f) and AFM (Figure S15) images indicated that W-Te-AC350 formed well-dispersed nanowires after hydrothermal treatment. Size distribution based on TEM indicated that the distribution maximum for diameter and length was 2–3 nm and 40–60 nm, respectively (Figure S16). Oxidation states of W and Te were W^{VI} and Te^{IV} (Figure S5). Elemental analysis and TG-DTA (Figure S11 c) showed the ratio N:W:Te was 1:6:1, which was identical to the formula of $(\text{NH}_4)[\text{HTe}^{\text{IV}}\text{W}^{\text{VI}}_6\text{O}_{21}]\cdot 2\text{H}_2\text{O}$. Using NH_3 as a probe molecule combined with TPD showed that the acid amount of the material was 0.41 mmol g^{-1} in solid state (Figure S17). Titration showed that the acid concentration of the dispersed material was 0.80 mmol g^{-1} .

As shown in Table 1, cellobiose was hydrolyzed by W-Te-AC350 at 130 $^\circ\text{C}$ for 4 h under hydrothermal conditions, and glucose was obtained as the main product with a high yield (90.5%). Other soluble polysaccharides, such as sucrose and starch, were converted into glucose under the same conditions (Table 1, entries 2,3). Compared with the reported catalyst, W-Te-AC350 exhibited high activity for hydrolysis of poly-

Table 1: Biomass hydrolysis by W-Te-AC350 under different conditions.^[a]

Entry	Biomass	t [h]	T [°C]	Conversion [%]	Yield based on carbon [%]				Total yield of organics [%]	
					glucose	mannose	formic acid	levulinic acid		HMF
1	cellobiose	4	130	93.1	90.5	0	0.1	0.1	0.7	91.4
2	sucrose	4	130	99	43.9	1.9	3.3	15.1	7.8	72.0
3	starch	4	130	–	78.4	0.2	0.5	1.0	1.2	81.3
4	microcrystalline cellulose ^[b]	2	175	–	8.8	2.9	0.5	1.1	0.7	14.0
5	ball-milled cellulose	2	175	–	19.0	7.2	0.7	2.5	1.2	30.6
6	ball-milled cellulose ^[c]	2	175	–	25.8	7.8	3.0	8.5	2.0	47.1
7	microcrystalline cellulose ^[d]	2	175	–	0	0	0	0	0	0

[a] Reaction conditions: biomass: 0.308 mmol based on glucose unit, W-Te-AC350: 0.05 g, water 0.5 mL. [b] Carbon balance was 86.7% (see details in the Supporting Information). [c] cellulose: 0.185 mmol. [d] Without catalyst.

saccharides (Supporting Information, Tables S4 and S5). Cellulose is more difficult to convert and was hydrolyzed at 175 °C for 2 h. Hexoses (glucose and mannose) were the primary products. Some other products were detected, such as 5-hydroxymethylfurfural (HMF), levulinic acid, and formic acid. Ball-milling can decrease the crystallinity of cellulose (Supporting Information, Figure S18) and activate the cellulose.^[14] The activity of the reaction increased using the ball-milled cellulose (Table 1, entries 5,6). In the absence of the catalyst, no products were detected (Table 1, entry 7).

The catalytic activities of different materials were investigated for comparison with W-Te-AC350. As shown in the Supporting Information, Table S6, under the same conditions, W-Te-AC350 was more active for microcrystalline cellulose conversion than other solid acids based on the amount of acid. Moreover, the activity of W-Te-AC350 was comparable to homogeneous catalysts (Supporting Information, Table S6).

The calcination temperature affected the catalytic activity of W-Te-AC350. As shown in the Supporting Information, Figure S19, the as-synthesized material exhibited low activity, and an increase in the calcination temperature enhanced the activity. When the calcination was conducted at 350 °C, the highest activity was obtained. This result demonstrated that acid sites were generated by calcination. However, a further increase in the calcination temperature (400 °C) deactivated the catalyst, which was most likely due to structural decomposition of the material at a high temperature. Therefore, maintaining the nanowire structure is a key factor for high catalytic activity.

The catalyst concentration was investigated. As the catalyst concentration increased, the total detected products increased, and hexoses tended to be further converted into other products, such as levulinic acid and formic acid. A decrease in the catalyst concentration effectively increased the selectivity to hydrolysis products (Supporting Information, Figure S20). Prolonging the reaction time yielded more organic acids and HMF, although the total yield of detected products increased (Supporting Information, Figure S21). A decrease in the reaction temperature decreased the activity and effectively suppressed the conversion of the generated hexoses. The selectivity to hexose increased at a low reaction temperature (Supporting Information, Figure S22).

The catalyst can be reused. Elemental analysis indicated that 47% of the catalyst was recovered by a low-speed centrifugation (9800 G, 1 h). The activity of the catalyst was

low (Supporting Information, Figure S23). TEM (Supporting Information, Figure S10i,j) and the size distribution (Supporting Information, Figure S16) indicated that some nanowires were still in the solution. When a high-speed centrifugation condition (48 000 G, 24 h) was used, a higher activity of the recovered catalyst was achieved.

The high catalytic activity of W-Te-AC350 was primarily due to two factors: ultrafine nanosized catalyst particles after dispersal and the strong interactions between the catalyst and the biomass. W-Te-AC350 could be well dispersed in water under hydrothermal conditions (175 °C, 2 h). After the hydrothermal treatment, the photographic images indicated that the solution containing the material became transparent and exhibited laser scattering, which indicated that the material dispersed and formed ultrafine nanowires in water (Supporting Information, Figure S24 a,b). For a sample with a low concentration, the laser scattering phenomenon still existed after the hydrothermal treatment (Figure S24 c,d), indicating that the material was not dissolved in water but dispersed. Before and after the hydrothermal treatment, dynamic light scattering (DLS) was conducted for W-Te-AC350, and the results revealed that after the hydrothermal treatment, the particle size of the material decreased (Supporting Information, Figure S25). The SEM and TEM images (Figure S10 e,f) revealed that W-Te-AC350 remained a nanowire. After the hydrothermal treatment, W-Te-AC350 was dried at –30 °C under high vacuum. The surface area of the dispersed W-Te-AC350 (15 m²g^{–1}) was higher than that of the as-synthesized W-Te oxide (Supporting Information, Figure S9). The adsorption under low pressure demonstrated the existence of micropores that may be due to the gap formed by isolated molecular wires. The calcined crystalline-W-Te oxide (Supporting Information, Figure S26) exhibited a lower activity than that of W-Te-AC350, which indicated that the nanosized material exhibited improved activity for the reaction (Supporting Information, Table S6, entry 2). All of the results demonstrated that the hydrothermal treatment promoted dispersal of the material in water and increase in the surface area.

Four oxygen sites are present in W-Te-AC350, including corner-sharing oxygen (O1), edge-sharing oxygen (O2), layer-sharing oxygen (O3), and terminal oxygen (O4), for protonation without considering the interactions between protons with NH₄⁺ (Supporting Information, Figure S27). When O2 was protonated, the system energy was the lowest among all

of the models, which indicated that O2 was the most likely position for protonation. The interaction between cellulose and the materials was simulated using cellobiose as a model molecule. The hexagonal unit with protonated O2 was used as a model for the catalyst. A Monte Carlo simulation (Supporting Information, Figure S28) showed that cellobiose interacted with the lattice oxygen, NH_4^+ , and the proton of the molecular wire with the distance between O and H shorter than 3 Å, indicating that strong or medium hydrogen bonds existed between the catalyst and cellobiose. The interaction between W-Te-AC350 and cellobiose was investigated using ^1H NMR (Supporting Information, Figure S29). When only cellobiose was present, peaks corresponding to the hydroxyl groups of cellobiose were observed by ^1H NMR.^[15] After the addition of W-Te-AC350 to the cellobiose solution, the peaks corresponding to hydroxyl group of cellobiose was broadened, indicating fast proton exchange between the molecular wire (W–OH) and cellobiose (–OH) as well as the existence of an interaction between the catalyst and the biomass.

In summary, an acidic nanocatalyst based on a W-oxide molecular wire was synthesized and characterized. The structure of the molecular wire was confirmed using an atomic-resolution HAADF-STEM image combined with XRD, FTIR, XPS, TPD, TG, and elemental analysis, and the result indicated that the growth of a hexagonal unit, $(\text{NH}_4)_2[\text{TeW}_6\text{O}_{21}]$ or $(\text{NH}_4)_2[\text{SeW}_6\text{O}_{21}]$, resulted in the formation of an inorganic 1D polymer. W-Te oxide exhibited high thermal and hydrothermal stability and was acidified by calcination. The acidic molecular wire was dispersed in water and acted as an efficient catalyst for biomass hydrolysis to produce hexoses.

Acknowledgements

This work was supported in part by the Novel Cheap and Abundant Materials for Catalytic Biomass Conversion (NOVACAM, FP7-NMP-2013-EU-Japan-604319) program of the Japan Science and Technology Agency (JST). The authors also thank Professor Atsushi Kameyama for the DLS analysis and the Material Analysis Suzukake-dai Center, Technical Department, Tokyo Institute of Technology, for the elemental analysis and NMR measurement.

Keywords: cellulosic biomass · hexose · hydrolysis · molecular wires · tungsten oxide

How to cite: *Angew. Chem. Int. Ed.* **2016**, *55*, 10234–10238
Angew. Chem. **2016**, *128*, 10390–10394

- [1] a) W. B. Davis, W. A. Svec, M. A. Ratner, M. R. Wasielewski, *Nature* **1998**, *396*, 60–63; b) H. Sakaguchi, H. Matsumura, H. Gong, *Nat. Mater.* **2004**, *3*, 551–557; c) C. M. Gothard, N. A. Rao, J. S. Nowick, *J. Am. Chem. Soc.* **2007**, *129*, 7272–7273; d) R. N. Mahato, H. Lülfi, M. H. Siekman, S. P. Kersten, P. A. Bobbert, M. P. de Jong, L. De Cola, W. G. van der Wiel, *Science* **2013**, *341*, 257–260.
- [2] M. Remskar, A. Mrzel, Z. Skraba, A. Jesih, M. Ceh, J. Demsar, P. Stadelmann, F. Levy, D. Mihailovic, *Science* **2001**, *292*, 479–481.
- [3] a) J. R. Galán-Mascarós, C. Giménez-Saiz, S. Triki, C. J. Gómez-García, E. Coronado, L. Ouahab, *Angew. Chem. Int. Ed. Engl.* **1995**, *34*, 1460–1462; *Angew. Chem.* **1995**, *107*, 1601–1603; b) L. Chen, D. Shi, J. Zhao, Y. Wang, P. Ma, J. Wang, J. Niu, *Cryst. Growth Des.* **2011**, *11*, 1913–1923; c) Y. Wang, S. Pan, H. Yu, X. Su, M. Zhang, F. Zhang, J. Han, *Chem. Commun.* **2013**, *49*, 306–308.
- [4] Z. Zhang, T. Murayama, M. Sadakane, H. Ariga, N. Yasuda, N. Sakaguchi, K. Asakura, W. Ueda, *Nat. Commun.* **2015**, *6*, 7731.
- [5] a) C. O. Tuck, E. Pérez, I. T. Horváth, R. A. Sheldon, M. Poliakoff, *Science* **2012**, *337*, 695–699; b) A. Wang, T. A. O. Zhang, *Acc. Chem. Res.* **2013**, *46*, 1377–1386; c) R. Rinaldi, F. Schüth, *Energy Environ. Sci.* **2009**, *2*, 610–626.
- [6] a) Y.-B. Huang, Y. Fu, *Green Chem.* **2013**, *15*, 1095–1111; b) T. Salmi, B. Holmbom, S. Willf, D. Y. Murzin, *Chem. Rev.* **2011**, *111*, 5638–5666; c) K. Shimizu, A. Satsuma, *Energy Environ. Sci.* **2011**, *4*, 3140–3153; d) H. Tadesse, R. Luque, *Energy Environ. Sci.* **2011**, *4*, 3913–3929.
- [7] a) K. Shimizu, H. Furukawa, N. Kobayashi, Y. Itaya, A. Satsuma, *Green Chem.* **2009**, *11*, 1627–1632; b) W. Deng, Q. Zhang, Y. Wang, *Dalton Trans.* **2012**, *41*, 9817–9831.
- [8] a) H. Kobayashi, M. Yabushita, J. Hasegawa, A. Fukuoka, *J. Phys. Chem. C* **2015**, *119*, 20993–20999; b) L. Shuai, X. Pan, *Energy Environ. Sci.* **2012**, *5*, 6889–6894; c) S. Suganuma, K. Nakajima, M. Kitano, D. Yamaguchi, H. Kato, S. Hayashi, M. Hara, *J. Am. Chem. Soc.* **2008**, *130*, 12787–12793; d) H. Kobayashi, H. Kaiki, A. Shrotri, K. Techikawara, A. Fukuoka, *Chem. Sci.* **2016**, *7*, 692–696.
- [9] R. Rinaldi, R. Palkovits, F. Schüth, *Angew. Chem. Int. Ed.* **2008**, *47*, 8047–8050; *Angew. Chem.* **2008**, *120*, 8167–8170.
- [10] A. Onda, T. Ochi, K. Yanagisawa, *Green Chem.* **2008**, *10*, 1033–1037.
- [11] A. Takagaki, C. Tagusagawa, K. Domen, *Chem. Commun.* **2008**, 5363–5365.
- [12] K. Fukuda, K. Akatsuka, Y. Ebina, R. Ma, K. Takada, I. Nakai, T. Sasaki, *ACS Nano* **2008**, *2*, 1689–1695.
- [13] N. Hiyoshi, Y. Kamiya, *Chem. Commun.* **2015**, *51*, 9975–9978.
- [14] a) C. F. Burmeister, A. Kwade, *Chem. Soc. Rev.* **2013**, *42*, 7660–7667; b) A. Shrotri, L. K. Lambert, A. Tanksale, J. Beltrami, *Green Chem.* **2013**, *15*, 2761–2768.
- [15] B. Bernet, R. Bürli, J. Xu, A. Vasella, *Helv. Chim. Acta* **2002**, *85*, 1800–1811.

Received: March 19, 2016

Revised: June 20, 2016

Published online: August 2, 2016



Hydrothermal synthesis of W–Ta–O complex metal oxides by assembling MO_6 ($M = \text{W}$ or Ta) octahedra and creation of solid acid



Toru Murayama^{a,b,*}, Nozomi Kuramata^a, Wataru Ueda^{a,c}

^a Catalysis Research Center, Hokkaido University, N21W10, Kita-ku, Sapporo, Hokkaido 001-0021, Japan

^b Research Center for Gold Chemistry, Tokyo Metropolitan University, 1-1 Minami Osawa, Hachioji, Tokyo 192-0397, Japan

^c Faculty of Engineering, Kanagawa University, 3-27-1, Rokkakubashi, Kanagawa-ku, Yokohama, Kanagawa 221-8686, Japan

ARTICLE INFO

Article history:

Received 1 December 2014

Revised 25 March 2016

Accepted 9 April 2016

Available online 8 May 2016

Keywords:

Complex metal oxide

Hydrothermal synthesis

Solid acid

W–Ta–O system

ABSTRACT

Layered-type tungsten and tantalum oxides (W–Ta–O) were synthesized by the hydrothermal method. The synthesized W–Ta–O showed characteristic peaks at $2\theta = 22.7^\circ$ and 46.2° in an X-ray diffraction pattern (Cu $K\alpha$), indicating linear corner sharing of MO_6 ($M = \text{W}, \text{Ta}$) octahedra in the c -direction. The same layered-type materials were obtained with a wide range of W and Ta composition ratios using soluble Lindqvist-type tantalum polyoxometalate ($\text{Na}_8(\text{Ta}_6\text{O}_{19})\cdot 24.5\text{H}_2\text{O}$). Na^+ cations of as-synthesized W–Ta–O were replaced with NH_4^+ and then calcined at 500°C to form Brønsted acid sites. The catalytic activity of W–Ta–O increased with increasing W ratio, suggesting that strong acid sites were generated. From Raman and adsorption measurements of W–Ta–O with various crystalline structures, it was revealed that the crystalline motif of W–Ta–O in the a – b plane was an interconnection of MO_6 ($M = \text{W}, \text{Ta}$) octahedra and $\{\text{M}_6\text{O}_{21}\}$ pentagonal units and micropore channels, but without long-range order.

© 2016 Elsevier Inc. All rights reserved.

1. Introduction

Complex metal oxides of transition metals are important inorganic materials as catalysts and ceramics. It is expected that the demand for solid acid catalysts will increase because they are reusable and readily separable from the liquid phase. One of the typical solid acid catalysts is niobium oxide. Hydrated niobium oxide ($\text{Nb}_2\text{O}_5\cdot n\text{H}_2\text{O}$, niobic acid) has high acid strength ($H_0 \leq -5.6$) and has Lewis and Brønsted acidity. Niobium oxide (or hydrated niobium oxide) has been widely used as a water-tolerant solid acid catalyst [1–5].

In parallel with studies on solid acid catalytic activity and the structure of acid sites for $\text{Nb}_2\text{O}_5\cdot n\text{H}_2\text{O}$, interest has also been shown in tantalum oxide ($\text{Ta}_2\text{O}_5\cdot n\text{H}_2\text{O}$). The formation mechanisms of acid sites are similar for $\text{Ta}_2\text{O}_5\cdot n\text{H}_2\text{O}$ and $\text{Nb}_2\text{O}_5\cdot n\text{H}_2\text{O}$ and, moreover, the strength of the acid and thermal stability of $\text{Ta}_2\text{O}_5\cdot n\text{H}_2\text{O}$ are higher than those of $\text{Nb}_2\text{O}_5\cdot n\text{H}_2\text{O}$ [6]. Ushikubo reported that a Lewis acid is formed mainly in the absence of water for $\text{Ta}_2\text{O}_5\cdot n\text{H}_2\text{O}$ and that a Brønsted acid is formed by steam treatment at 100°C [7]. Tanaka and Shishido and co-workers [8,9] reported that a $\text{Ta}_2\text{O}_5/\text{Al}_2\text{O}_3$ catalyst prepared by an impregnation method showed solid acidity and high thermal stability. Brønsted

acids were generated by a two-dimensional Ta–O–Ta network consisting of TaO_6 units having distorted octahedral symmetry.

To enhance the solid acidity, modification of $\text{Ta}_2\text{O}_5\cdot n\text{H}_2\text{O}$ by sulfate and synthesis of a complex oxide catalyst have been investigated. Domen et al. reported a W–(Nb, Ta)–O layered complex oxide synthesized by a solid state method [10]. Brønsted acid sites are formed on the monolayer surface by proton exchange treatment. Tungsten oxide is a class of solid acids, which form tungsten bronze based on octahedra structure [11]. The formation of complex oxides between M^V (Group 5 elements) and tungsten or the replacement of W in the WO_3 structure with M^V enhances the solid acidity and the catalytic performance [12]. The acidity of these catalysts has been shown to be attributable to bridging hydroxyl groups $\text{M}-(\text{OH})-\text{M}'$ ($M = \text{Nb}$ or Ta , $M' = \text{Mo}$ or W), representing a strong Brønsted acid site [9,13,14].

We have studied the relationship between the crystalline structure of complex metal oxides and their catalytic activity [15–17]. Studies on crystalline metal oxides of Mo_3VO_x have demonstrated that the oxidation activities depend on their crystalline arrangement of pentagonal $\{\text{Mo}_6\text{O}_{21}\}$ units and MO_6 octahedra in the a – b plane. These materials contain heptagonal channels in their structures. For the synthesis of these catalysts, the formation of pentagonal $\{\text{Mo}_6\text{O}_{21}\}$ units in the precursor solution was important, and the pentagonal units assembled further into a complex metal oxide under hydrothermal conditions [18]. A complex metal oxide that possess a similar layered structure in the c -direction by

* Corresponding author at: Catalysis Research Center, Hokkaido University, N21W10, Kita-ku, Sapporo, Hokkaido 001-0021, Japan.

E-mail address: murayama@tmu.ac.jp (T. Murayama).

corner sharing of MO_6 ($M = \text{Mo}, \text{W}, \text{V}, \text{Ta}, \text{Nb}$) octahedra has been synthesized by a hydrothermal method [19–21]. These catalysts were found to function as solid acids, the properties of which were understood from a structural point of view.

We report here the synthesis of W-Ta-O by a hydrothermal process from ammonium metatungstate and tantalic acid or tantalum Lindqvist-type polyoxometalate ($\text{Na}_8(\text{Ta}_6\text{O}_{19})\cdot 24.5\text{H}_2\text{O}$) precursors. The Lindqvist-type polyoxometalate is a simple structure formed by TaO_6 octahedra and it can be synthesized under basic conditions [22,23]. The complex oxide W-Ta-O having a novel crystal structure can be synthesized by the assembly of MO_6 units. The obtained W-Ta-O samples were octahedra-based layered-type materials. We demonstrated the relationships between their crystalline structure and their catalytic activity and acidity.

2. Experimental

2.1. Synthesis of $\text{Na}_8(\text{Ta}_6\text{O}_{19})\cdot 24.5\text{H}_2\text{O}$

Lindqvist-type polyoxometalate ($\text{Na}_8(\text{Ta}_6\text{O}_{19})\cdot 24.5\text{H}_2\text{O}$) was prepared according to the literature [23]. First, 2.5 g (5.7 mmol) Ta_2O_5 was calcined with 4.3 g (0.11 mol) NaOH in an alumina crucible at 400 °C for 5 h. The resulting sample was treated with 30 mL of cold water and then stirred for 30 min while cooling in an ice bath. Distilled water (120 mL) was added to the liquid, and the liquid was separated by centrifugation for 10 min at 1500 rpm. The obtained solid was dried under vacuum. The collected solid was refluxed with distilled water (80 mL) at 80–85 °C until the solution became clear. After the transparent solution was filtered, the filtrate was placed in a refrigerator for 1 day. The obtained $\text{Na}_8(\text{Ta}_6\text{O}_{19})\cdot 24.5\text{H}_2\text{O}$ crystal was filtered and dried in air overnight.

2.2. Preparation of W-Ta-O samples

W-Ta-O oxides were synthesized by a hydrothermal method from ammonium metatungstate (AMT, $(\text{NH}_4)_6\text{H}_2\text{W}_{12}\text{O}_{40}\cdot n\text{H}_2\text{O}$) and several Ta precursors. Typically, the Ta precursor (2.7 mmol based on Ta) was added to 25 mL of water and dispersed by ultrasonic agitation for 10 min. AMT (Nippon Inorganic Colour & Chemical Co.) containing 2 mmol W was dissolved in 20 mL of deionized water and then the W precursor solution was added to the Ta dispersed liquid. Then the mixture was sealed in a 60 mL Teflon liner stainless steel autoclave. Hydrothermal treatment was carried out at 175 °C for 3 days. The obtained solid was filtered, washed thoroughly with deionized water, and dried at 80 °C overnight. Lindqvist-type polyoxometalate ($\text{Na}_8(\text{Ta}_6\text{O}_{19})\cdot 24.5\text{H}_2\text{O}$), $\text{Ta}_2\text{O}_5\cdot n\text{H}_2\text{O}$ (Mitsuwa Chemical), Ta_2O_5 (Wako), TaCl_5 (Wako), TaF_5 (Wako), Ta oxalate solution (H. C. Stark), and $\text{K}(\text{TaO}_3)$ (Alfa Aesar) were used as Ta precursors, and the obtained W-Ta-O samples were denoted as $\text{W}_x\text{Ta}_y\text{O}$ (TaL), $\text{W}_x\text{Ta}_y\text{O}$ (TaA), $\text{W}_x\text{Ta}_y\text{O}$ (TaO), $\text{W}_x\text{Ta}_y\text{O}$ (TaCl), $\text{W}_x\text{Ta}_y\text{O}$ (TaF), $\text{W}_x\text{Ta}_y\text{O}$ (TaOxa), and $\text{W}_x\text{Ta}_y\text{O}$ (KTaO), respectively. The elemental ratios ($x = \text{W}/(\text{W} + \text{Ta})$, $y = \text{Ta}/(\text{W} + \text{Ta})$) were measured by ICP for the synthesized W-Ta-O samples. For W-Ta-O (TaCl), the elemental ratio of the precursor was represented because the obtained sample did not dissolve in the mixed solution of HF and HNO_3 . The samples were calcined at 500 °C for 2 h under air before use as catalysts. The rate of temperature increase was 10 °C min^{-1} from room temperature.

As-synthesized material ($\text{W}_x\text{Ta}_y\text{O}$ (TaL), 0.3 g) was dispersed in 15 mL of NaCl solution (0.1 mol L^{-1}) for ion-exchange treatment. The dispersed sample was stirred at 80 °C for 8 h. The resulting solid was collected by filtration. Then the sample was washed with water (3×100 mL) and dried at 80 °C overnight. The obtained sample was denoted as $\text{Na}^+-\text{W}_x\text{Ta}_y\text{O}$ (TaL). A $\text{W}_x\text{Ta}_y\text{O}$ (TaL) sample

treated with NH_4Cl solution was denoted as $\text{NH}_4^+-\text{W}_x\text{Ta}_y\text{O}$ (TaL). $\text{NH}_4^+-\text{W}_x\text{Ta}_y\text{O}$ (TaL) was prepared by ion-exchange treatment of $\text{W}_x\text{Ta}_y\text{O}$ (TaL) in 15 mL of NH_4Cl solution (0.1 mol L^{-1}) at 80 °C for 8 h.

To compare the relationships between crystalline structure and catalytic activity, various crystalline W-Ta-O samples were synthesized. Tetragonal $\text{Ta}_{16}\text{W}_{18}\text{O}_{94}$ was obtained by calcination of $\text{W}_{58}\text{Ta}_{42}\text{O}$ (TaA) at 1100 °C for 6 h. Orthorhombic $\text{Cs}_{0.5}[\text{Ta}_{2.5}\text{W}_{2.5}]\text{O}_{14}$ was synthesized according to the literature for orthorhombic $\text{Cs}_x(\text{Nb},\text{W})_5\text{O}_{14}$ [24]. Cs_2CO_3 , $\text{Ta}_2\text{O}_5\cdot n\text{H}_2\text{O}$, and AMT (Cs:Ta:W = 1:5:5) were dispersed in 40 mL of distilled water. The mixture was stirred and dried at 60 °C, and Cs–W–Ta powder was obtained. The powder was calcined at 1100 °C for 6 h to obtain orthorhombic $\text{Cs}_{0.5}[\text{Ta}_{2.5}\text{W}_{2.5}]\text{O}_{14}$. Pyrochlore W-Ta-O was synthesized by a hydrothermal method. AMT (W: 2 mmol) and $\text{Ta}_2\text{O}_5\cdot n\text{H}_2\text{O}$ (2.7 mmol) precursors were added to 45 mL of water and dispersed. The pH of the mixture liquid was adjusted to 10.3 using NH_3 solution. Then the mixture was sealed in a 60 mL Teflon liner stainless steel autoclave. Hydrothermal treatment was carried out at 175 °C for 3 days. Hexagonal WO_3 was synthesized by the same hydrothermal method from only the AMT precursor.

2.3. Alkylation reaction

A 50 mL round-bottomed three-necked flask equipped with a reflux condenser was used as a stirred bed reactor to test the catalytic activities. Typically, a mixture of benzyl alcohol (10 mmol), anisole (100 mmol), and an internal standard, decane (5 mmol), was added to the reactor and the reaction temperature was adjusted to 100 °C. Then 0.1 g of a catalyst and a Teflon-coated magnetic stir bar were loaded into the reactor. Aliquots (each 0.1 mL) were collected at intervals. The concentrations of the reactant and product were measured by gas chromatography using a flame ionization detector (GL Science GC390B) with a ZB-1 column.

2.4. Characterization

The catalysts were characterized by the following techniques. Elemental compositions were determined by an inductive coupling plasma (ICP-AES) method (ICPE-9000, Shimadzu). Samples were dissolved in a mixed acid solution of HF and HNO_3 . CHN powder XRD patterns were measured with a diffractometer (RINT Ultima +, Rigaku) using $\text{CuK}\alpha$ radiation (tube voltage 40 kV, tube current 20 mA). Diffractions were recorded in the range of 4–60° at 5° min^{-1} . Morphology was investigated using a scanning transmission electron microscope (HD-2000, Hitachi) at 200 kV. The samples were dispersed in ethanol with ultrasonic treatment for several minutes, and drops of the suspension were placed on a copper grid for STEM observations. Raman spectra were obtained using a spectrometer (in Via Reflex, Renishaw, 2 cm^{-1} spectral resolution) under conditions of wavelength of 532 nm and collection time of 10 s. N_2 adsorption isotherms at liquid N_2 temperature were measured using an auto adsorption system (Belsorp Max, Bel Japan) for the samples. Prior to N_2 adsorption, the catalysts were evacuated under vacuum at 300 °C for 2 h. External surface area was calculated by a multipoint Brunauer–Emmett–Teller (BET) method and the t method. Temperature-programmed desorption (TPD) of ammonia, NH_3 TPD, was used to measure oxide surface acidity. The experiment was carried out using an auto chemisorption system (Bel Japan). The experimental procedure was as follows. The catalyst (ca. 50 mg) was set between two layers of quartz wool and preheated under helium (50 mL min^{-1}) at 400 °C for 1 h. Then ammonia was introduced at 100 °C for 30 min. The desorption profile from 100 to 700 °C was recorded with a mass spectrometer under helium flow (50 mL min^{-1}). Temperature-programmed decomposition mass spectrometry

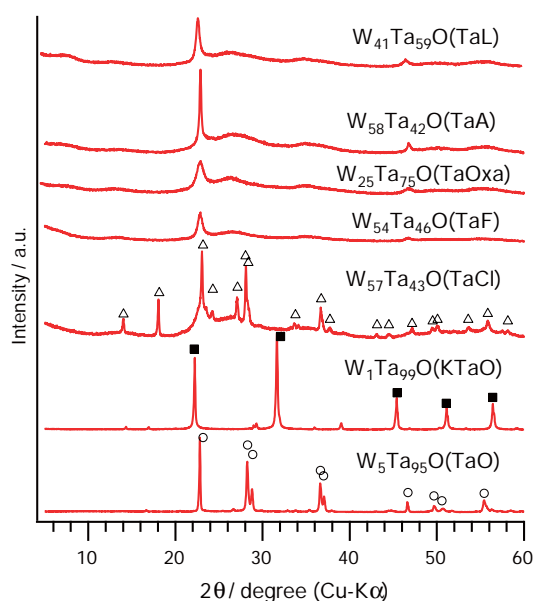


Fig. 1. XRD patterns of W-Ta-O samples synthesized from various Ta precursors under hydrothermal conditions. Δ : orthorhombic $\text{WO}_3 \cdot 0.5\text{H}_2\text{O}$; \blacksquare : cubic $\text{K}(\text{TaO}_3)$; \circ : orthorhombic Ta_2O_5 .

(TPD-MS) measurements were performed from 40 to 700 °C at a heating rate of 10 °C min⁻¹ in helium flow (50 mL min⁻¹). The decomposed gas molecules were monitored by a mass spectrometer (Anelva, quadrupole mass spectrometer, M-100QA, Bel Japan), collecting several mass fragments: CO_2 (44), O_2 (32), CO and N_2 (28), H_2O (18, 17, 16), and NH_3 (17, 16, 15).

3. Results

3.1. Effect of Ta precursor on W-Ta-O

Fig. 1 shows XRD patterns of the W-Ta-O complex oxides synthesized using ammonium metatungstate (AMT) and various tantalum precursors under hydrothermal conditions. Table 1 shows the elemental compositions measured by ICP for the obtained W-Ta-O samples. The elemental compositions of the W-Ta-O samples obtained from Lindqvist-type polyoxometalate ($\text{Na}_8(\text{Ta}_6\text{O}_{19}) \cdot 24.5\text{H}_2\text{O}$), $\text{Ta}_2\text{O}_5 \cdot n\text{H}_2\text{O}$, and TaF_5 precursors were almost the same as the precursor ratios. The $\text{W}_{41}\text{Ta}_{59}\text{O}$ (TaL), $\text{W}_{58}\text{Ta}_{42}\text{O}$ (TaA), $\text{W}_{25}\text{Ta}_{75}\text{O}$ (TaOxa), and $\text{W}_{54}\text{Ta}_{46}\text{O}$ (TaF) samples showed similar XRD patterns. These samples showed XRD peaks at $2\theta = 22.8^\circ$ and 46.8° , indicating (001) and (002) planes. These samples were composed of corner-shared octahedra along the

c-direction. The layer interval of $\text{W}_{41}\text{Ta}_{59}\text{O}$ (TaL), $\text{W}_{58}\text{Ta}_{42}\text{O}$ (TaA), $\text{W}_{25}\text{Ta}_{75}\text{O}$ (TaOxa), and $\text{W}_{54}\text{Ta}_{46}\text{O}$ (TaF) was 3.9 nm. The $\text{W}_{57}\text{Ta}_{43}\text{O}$ (TaCl), $\text{W}_1\text{Ta}_{99}\text{O}$ (KTaO), and $\text{W}_5\text{Ta}_{95}\text{O}$ (TaO) samples also showed diffraction peaks around 23° . However, these peaks were based on the (001) plane of orthorhombic $\text{WO}_3 \cdot 0.5\text{H}_2\text{O}$ for the $\text{W}_{57}\text{Ta}_{43}\text{O}$ (TaCl) sample, cubic $\text{K}(\text{TaO}_3)$ for the $\text{W}_1\text{Ta}_{99}\text{O}$ (KTaO) sample, and orthorhombic Ta_2O_5 for $\text{W}_5\text{Ta}_{95}\text{O}$ (TaO). The structure of $\text{W}_{57}\text{Ta}_{43}\text{O}$ (TaCl) seems to be a mixture of orthorhombic $\text{WO}_3 \cdot 0.5\text{H}_2\text{O}$ based on the sharp peaks and layered structure, based on the broad peaks from the XRD pattern. The pH of the precursor solution was about 1, and the low pH was the reason for the formation of orthorhombic $\text{WO}_3 \cdot 0.5\text{H}_2\text{O}$. The XRD patterns of $\text{W}_5\text{Ta}_{95}\text{O}$ (TaO) and $\text{W}_1\text{Ta}_{99}\text{O}$ (KTaO) showed diffraction peaks derived from the corresponding Ta precursor, and the elemental ratios of Ta were 95% and 99%, respectively, from ICP analysis. These precursors did not form a complex oxide because of the low solubility of the Ta precursor in water.

We have reported that solid acid catalysts that have a layered-type structure show high catalytic activity as Brønsted acids. Fig. 2 shows the results of alkylation of benzyl alcohol and anisole. All of the catalysts were calcined at 500 °C beforehand. $\text{W}_{58}\text{Ta}_{42}\text{O}$ (TaA), $\text{W}_{25}\text{Ta}_{75}\text{O}$ (TaOxa), and $\text{W}_{54}\text{Ta}_{46}\text{O}$ (TaF) showed catalytic activity, and XRD patterns showed that these catalysts had a layered structure. $\text{W}_{57}\text{Ta}_{43}\text{O}$ (TaCl) also showed catalytic activity. The conversion of the $\text{W}_1\text{Ta}_{99}\text{O}$ (KTaO) sample (cubic $\text{K}(\text{TaO}_3)$) and that of the $\text{W}_5\text{Ta}_{95}\text{O}$ (TaO) sample (orthorhombic Ta_2O_5) was very low. The $\text{W}_{41}\text{Ta}_{59}\text{O}$ (TaL) sample showed no catalytic activity; however,

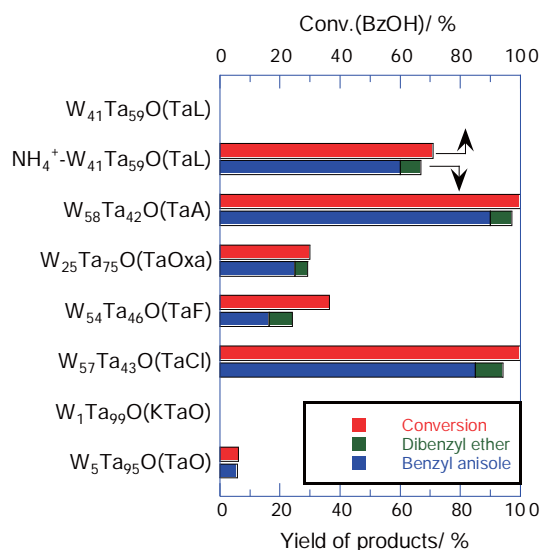


Fig. 2. Alkylation over various W-Ta-O catalysts. Reaction conditions: benzyl alcohol (10 mmol), anisole (100 mmol), catalyst (0.1 g), 100 °C, 30 min.

Table 1

Elemental compositions of the obtained W-Ta-O samples.

Catalyst	Atomic ratio of precursor		Atomic ratio of W-Ta-O ^a		Crystalline phase	<i>d</i> (001)
	W	Ta	W	Ta		
$\text{W}_{41}\text{Ta}_{59}\text{O}$ (TaL)	57	43	41	59	Octahedra-based layered type	3.889
$\text{W}_{58}\text{Ta}_{42}\text{O}$ (TaA)	57	43	58	42	Octahedra-based layered type	3.884
$\text{W}_{25}\text{Ta}_{75}\text{O}$ (TaOxa)	57	43	25	75	Octahedra-based layered type	3.887
$\text{W}_{54}\text{Ta}_{46}\text{O}$ (TaF)	57	43	54	46	Octahedra-based layered type	3.887
$\text{W}_{57}\text{Ta}_{43}\text{O}$ (TaCl)	57	43	- ^b	- ^b	Orthorhombic $\text{WO}_3 \cdot 0.5\text{H}_2\text{O}$, octahedra-based layered type	3.857
$\text{W}_1\text{Ta}_{99}\text{O}$ (KTaO)	57	43	1.4	98.6	Cubic $\text{K}(\text{TaO}_3)$	3.998
$\text{W}_5\text{Ta}_{95}\text{O}$ (TaO)	57	43	5.3	94.7	Orthorhombic Ta_2O_5	3.897

^a Measured by ICP.

^b Sample was insoluble in aqua regia.

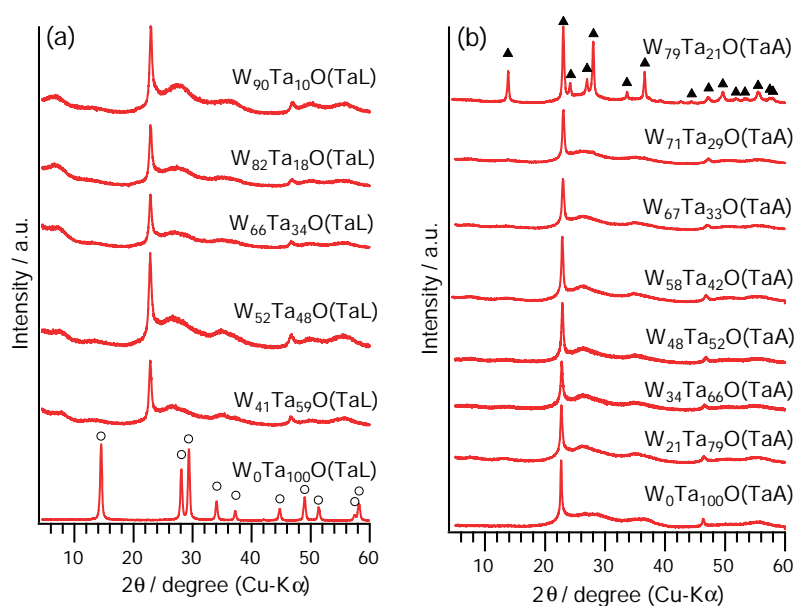


Fig. 3. Effects of W and Ta ratios on the XRD patterns of (a) W-Ta-O (TaL) and (b) W-Ta-O (TaA) samples synthesized by a hydrothermal method. ○: pyrochlore $H_4Ta_2O_7$, ▲: hexagonal WO_3 .

after ion-exchange treatment of W-Ta-O samples, NH_4 -W₄₁Ta₅₉O (TaL) showed catalytic activity, as we describe later.

3.2. Effect of ratio of W and Ta on W-Ta-O

The structures of W-Ta-O samples obtained from $Ta_2O_5 \cdot nH_2O$, TaF_5 , Ta oxalate solution, and Lindqvist-type polyoxometalate ($Na_8(Ta_6O_{19}) \cdot 24.5H_2O$) precursors were layered-type according to the XRD patterns, and these catalysts showed catalytic activity for the alkylation reaction. We focused on these layered-type materials, especially the W-Ta-O samples synthesized from $Ta_2O_5 \cdot nH_2O$ and $Na_8(Ta_6O_{19}) \cdot 24.5H_2O$ precursors. $Ta_2O_5 \cdot nH_2O$ is easy to handle and is widely available. Lindqvist-type $Na_8(Ta_6O_{19}) \cdot 24.5H_2O$, which possesses TaO_6 octahedra in its structure, can be synthesized under basic conditions. We have reported that the $\{M_6O_{21}\}$ assembly and MO_6 octahedra unit play an important role in the formation of a complex metal oxide [18,25]. Thus, these two precursors were used for detailed experiments, and their behavior was compared by changing the elemental ratios of W and Ta.

Fig. 3 shows the effects of composition ratios of W and Ta on the XRD patterns of W-Ta-O samples synthesized under hydrothermal conditions. The amount of $Na_8(Ta_6O_{19}) \cdot 24.5H_2O$ or $Ta_2O_5 \cdot nH_2O$ was fixed to 2 mmol based on Ta, and AMT concentration was changed from 0 to 0.31 M based on W. Elemental composition was analyzed by ICP for the obtained W-Ta-O samples. Peaks at $2\theta = 22.8^\circ$ and 46.8° derived from (001) and (002) were observed in the XRD patterns in the range of W ratios from 41% to 90% for the W-Ta-O (TaL) samples (Fig. 3a). Pyrochlore $H_2Ta_2O_6$ was obtained by hydrothermal treatment from only $Na_8(Ta_6O_{19}) \cdot 24.5H_2O$ (W_0Ta_{100} (TaL)). A difference between the $Na_8(Ta_6O_{19}) \cdot 24.5H_2O$ and $Ta_2O_5 \cdot nH_2O$ precursors was observed in W-Ta-O at a high W ratio. For the W-Ta-O (TaA) samples, peaks at $2\theta = 22.8^\circ$ and 46.8° were observed in the range of W ratios from 0% to 67% (Fig. 3b). Small diffraction peaks based on the hexagonal phase were observed in the $W_{71}Ta_{29}O$ (TaA) sample in addition to peaks based on the layered-type structure, and only a hexagonal phase was obtained in the $W_{79}Ta_{21}O$ (TaA) sample. The peak of the tantalum oxide ($W_0Ta_{100}O$ (TaA)) at 22.7° shifted to a lower angle. The value of d (001) for $W_0Ta_{100}O$ (TaA) was 3.910, based on the Ta octahedra.

STEM images of W-Ta-O (TaL) and W-Ta-O (TaA) are shown in Figs. 4, 5, and S1 (in the Supporting Information). For W-Ta-O (TaL), rod-shaped particles were observed regardless of the W and Ta ratio. Particle size increased with an increase in the W composition ratio. The rod-shaped particles were less than 10 nm in diameter and 50–100 nm in length for $W_{41}Ta_{59}O$ (TaL), and they were 50 nm in diameter and 100–400 nm in length for $W_{90}Ta_{10}O$ (TaL). Primary particles were also rodlike for W-Ta-O (TaA), and dandelion-type secondary particles were obtained with W ratios from 0% to 58% as shown in Fig. S1. Secondary particles irregularly formed a network between rodlike particles in the $W_{67}Ta_{33}O$ (TaA) sample. In the $W_{79}Ta_{21}O$ (TaA) sample, hexagonal WO_3 forms were observed as secondary particles. In the case of the $Ta_2O_5 \cdot nH_2O$ precursor, rod-shaped particles of tantalum oxide ($W_0Ta_{100}O$ (TaA)) were also formed. It is thought that the rodlike crystalline structure of W-Ta-O (TaA) grew from the Ta oxide core through the dis solution–crystallization mechanism. The solubility of $Ta_2O_5 \cdot nH_2O$ is low under hydrothermal conditions, and the surface concentration of W for W-Ta-O (TaA) would therefore be higher than that inside the particle. Thus, with an increase in the W ratio for W-Ta-O (TaA), the formation of a complex oxide becomes difficult and the formation of hexagonal WO_3 proceeds.

For W-Ta-O (TaL), the same layered-structure material was obtained even at higher W ratios. The following examination was carried out to determine the formation mechanism of W-Ta-O (TaL). The precursor solution (45 mL) was prepared by the mixture of AMT (W: 0.08 M) and $Na_8(Ta_6O_{19}) \cdot 24.5H_2O$ (Ta: 0.044 M). This precursor solution was colorless and transparent. Then the solution was heated at $60^\circ C$ under nitrogen bubbling. A white suspension was formed after 25 min. The white precipitate and liquid were separated by centrifugation, and both the precipitate and solution were analyzed by ICP. The W and Ta ratio of the white precipitate was W:Ta = 16:84 and that of the solution was W:Ta = 99:1. The white precipitate was amorphous according to the results of XRD, and the particle size was less than 10 nm (Figs. S2 and S3 in the Supplementary Information). The elemental ratio of $W_{52}Ta_{48}O$ (TaL) obtained by a hydrothermal method from the precursor solution was W:Ta = 52:48. From these results, small W-Ta-O particles were formed by condensation of $[Ta_6O_{19}]^{8-}$

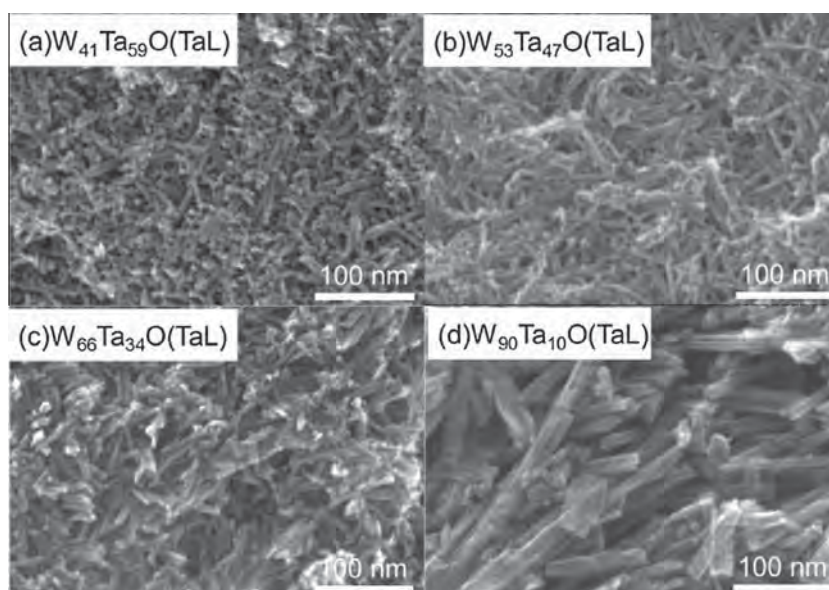


Fig. 4. STEM images of W-Ta-O (TaL).

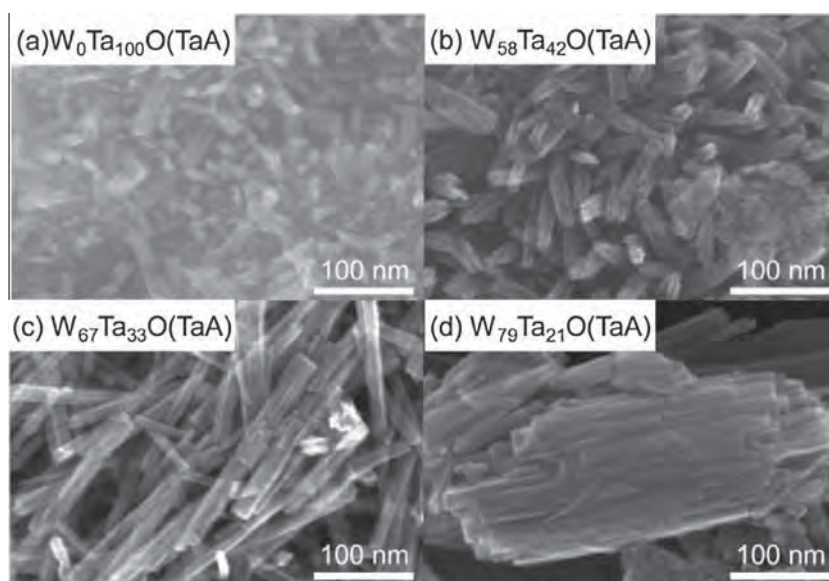


Fig. 5. STEM images of W-Ta-O (TaA).

anion and metatungstate anion as a core. Then layered-structure-type W-Ta-O was formed from the W-Ta-O core through dissolution-crystallization and tungstate anion in the solution. Thus, W and Ta of W-Ta-O (TaL) samples would be mixed well compared with W-Ta-O (TaA) samples, even at a high W ratio.

Adsorption analysis was carried out for the W-Ta-O (TaL) and W-Ta-O (TaA) samples (Figs. S4 and S5 in the Supporting Information). Figs. 6 and 7 summarize the effects of elemental ratio on surface area, mesopore volume, and micropore volume for the W-Ta-O (TaL) and W-Ta-O (TaA) samples. The surface area and micropore volume were calculated by a *t*-plot, and the mesopore volume was calculated by the BJH method. From the adsorption isotherms (Figs. S4 and S5), hysteresis loops and adsorption at low pressure ($P/P_0 < 1.0 \times 10^{-5}$) were observed, indicating the existence of mesopores and micropores, respectively. From the BJH plot (Figs. S4 and S5), the radii of mesopores of both W-Ta-O (TaL) and W-Ta-O (TaA) samples were less than 8 nm regardless

of the elemental ratio, and peak tops of the pore size distribution were also the same ($r_p \approx 2$ nm). STEM images suggested that mesopores were formed by the voids between the rod-shaped particles. The behavior of the surface area was consistent with that of the micropore volume. The micropore volume and surface area decreased with increasing ratio of W for the W-Ta-O (TaL) and W-Ta-O (TaA) samples. The surface area of W-Ta-O (TaL) became stable at a W ratio of more than 66%. In the case of W-Ta-O (TaA) samples, the formation of hexagonal WO_3 decreased the micropore volume and surface area. This is because hexagonal WO_3 does not possess micropores from a structural point of view.

3.3. Ion exchange properties of W-Ta-O (TaL) oxide

In the as-synthesized W-Ta-O (TaA) sample, ammonium cations exist on the surface and in the micropores and were formed by $\text{NH}_4\text{-OM}$ ($M = \text{W}, \text{Ta}$). These ammonium cations can be released

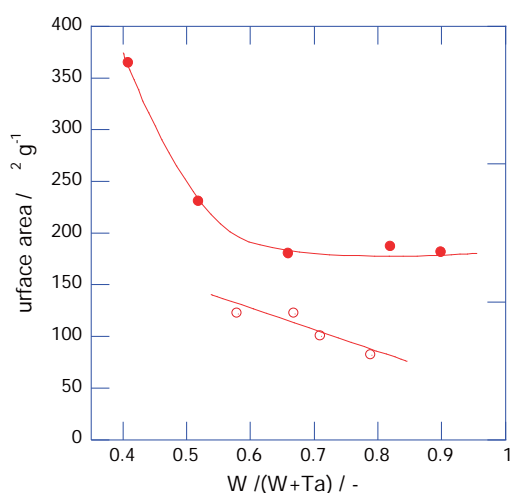


Fig. 6. Effects of ratio of W and Ta on the surface area calculated by a *t*-plot. ●: W-Ta-O (TaL), ○: W-Ta-O (TaA).

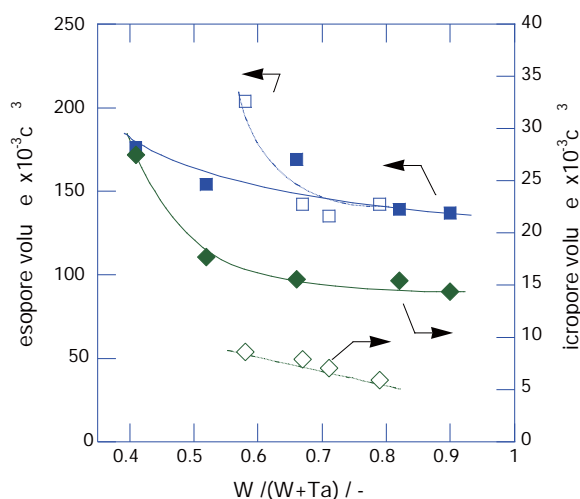


Fig. 7. Effects of ratio of W and Ta on the mesopore volume calculated by the BJH method and the micropore volume calculated by a *t*-plot. ■, ◆: W-Ta-O (TaL), □, ◇: W-Ta-O (TaA).

by calcination, and Brønsted acid sites (HO–M) will be produced. Since the precursor solution of W-Ta-O (TaL) contains NH_4^+ and Na^+ cations, as-synthesized W-Ta-O (TaL) also contains both of the cations, and Na^+ will block the Brønsted acid sites. Therefore, $\text{W}_{52}\text{Ta}_{48}\text{O}$ (TaL) did not show catalytic activity in Fig. 2. In order to exchange the Na^+ cation for NH_4^+ , the ion-exchange capacity of

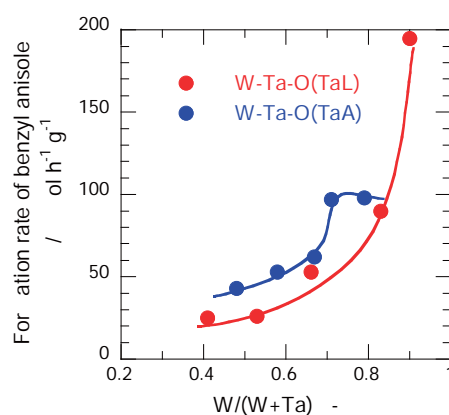


Fig. 8. Effect of ratio of W and Ta on the alkylation reaction for W-Ta-O (TaL) and W-Ta-O (TaA).

W-Ta-O (TaL) was examined. Fig. S6 in the Supporting Information shows FT-IR spectra of as-synthesized $\text{W}_{52}\text{Ta}_{48}\text{O}$ (TaL) and ion-exchanged $\text{W}_{52}\text{Ta}_{48}\text{O}$ (TaL) by NaCl or NH_4Cl . From the IR spectra of the $\text{W}_{52}\text{Ta}_{48}\text{O}$ (TaL) sample, adsorption at 1400 cm^{-1} was assigned to an asymmetric deformation vibration of the ammonium cation, which came from the AMT precursor. The intensity of the absorption band at 1400 cm^{-1} of $\text{NH}_4^+-\text{W}_{52}\text{Ta}_{48}\text{O}$ (TaL) increased and that of $\text{Na}^+-\text{W}_{52}\text{Ta}_{48}\text{O}$ (TaL) decreased. Fig. S7 shows TPD profiles of $m/z = 16$ for as-synthesized $\text{W}_{52}\text{Ta}_{48}\text{O}$ (TaL) and ion-exchanged $\text{W}_{52}\text{Ta}_{48}\text{O}$ (TaL) by NaCl or NH_4Cl . The amounts of desorbed NH_3 were 1.14 mmol g^{-1} for as-synthesized $\text{W}_{52}\text{Ta}_{48}\text{O}$ (TaL), 1.40 mmol g^{-1} for $\text{NH}_4^+-\text{W}_{52}\text{Ta}_{48}\text{O}$ (TaL), and 0.209 mmol g^{-1} for $\text{Na}^+-\text{W}_{52}\text{Ta}_{48}\text{O}$ (TaL). The results of FT-IR and TPD indicated that Na^+ and NH_4^+ cations on the $\text{W}_{52}\text{Ta}_{48}\text{O}$ (TaL) surface can be exchanged by ion-exchange treatment. After calcination treatment at 500 °C , solid acid catalytic activity was demonstrated (Table 2). The conversion of $\text{W}_{52}\text{Ta}_{48}\text{O}$ (TaL) was almost zero for 1 h, and that of $\text{NH}_4^+-\text{W}_{52}\text{Ta}_{48}\text{O}$ (TaL) was 71%. The $\text{W}_{52}\text{Ta}_{48}\text{O}$ (TaL) sample contains both NH_4^+ and Na^+ cations, and the Na^+ cation therefore prevents formation of strong acid sites. The conversion of $\text{W}_{52}\text{Ta}_{48}\text{O}$ (TaL) was 24% for 20 h by the contribution of weak Brønsted acid sites of $\text{W}_{52}\text{Ta}_{48}\text{O}$ (TaL) for the alkylation reaction. On the other hand, the $\text{Na}^+-\text{W}_{52}\text{Ta}_{48}\text{O}$ (TaL) sample showed no catalytic activity because almost all of the acid sites were blocked by Na^+ cations.

3.4. Solid acidity of $\text{NH}_4^+-\text{W-Ta-O}$ (TaL) and W-Ta-O (TaA)

Solid acid catalytic activity was examined, and the relationship between atomic ratio of W to Ta and catalytic activity was investigated. Results for Friedel–Crafts alkylation reactions of anisole with benzyl alcohol over $\text{NH}_4^+-\text{W-Ta-O}$ (TaL) and W-Ta-O (TaA) samples are presented in Fig. 8. For comparison, hexagonal WO_3

Table 2
Effects of ion-exchange treatment of the W-Ta-O (TaL) sample on solid acid catalytic activity.

Catalyst	Calcination temp./ $^{\circ}\text{C}$	Amount of desorbed $\text{NH}_3/\text{mmol g}^{-1}$	Alkylation reaction		
			Reaction time/h	Conv./% ^a	Yield/% ^b
$\text{W}_{52}\text{Ta}_{48}\text{O}$ (TaL)	500	1.14	1	0	0
			20	24	12
$\text{NH}_4^+-\text{W}_{52}\text{Ta}_{48}\text{O}$ (TaL)	500	1.40	1	71	60
			2	100	95
$\text{Na}^+-\text{W}_{52}\text{Ta}_{48}\text{O}$ (TaL)	500	0.209	1	0	0
			20	0	0

^a Conversion of benzyl alcohol.

^b Yield of benzyl anisole. Reaction conditions: benzyl alcohol (10 mmol), anisole (100 mmol), catalyst (0.1 g), 100 °C .

was synthesized by a hydrothermal method and tested for the alkylation reaction. The formation rate of benzyl anisole over the hexagonal WO_3 sample was $20 \text{ mmol h}^{-1} \text{ g}^{-1}$. For W-Ta-O (TaA), the formation rate showed a maximum for $\text{W}_{67}\text{Ta}_{33}\text{O}$ (TaA) and $\text{W}_{79}\text{Ta}_{21}\text{O}$ (TaA). $\text{W}_{79}\text{Ta}_{21}\text{O}$ (TaA) contained a hexagonal WO_3 phase in its structure (Fig. 1), and the hexagonal WO_3 would be the reason for the decrease in activity. For W-Ta-O (TaL), the formation rate of benzyl anisole increased with an increase in the W ratio. Catalytic activity drastically increased from $\text{W}_{82}\text{Ta}_{18}\text{O}$ (TaL) to $\text{W}_{90}\text{Ta}_{10}\text{O}$ (TaL). The surface area of W-Ta-O (TaL) was almost the same for both samples (Fig. 6), and another factor therefore contributes to the improvement in catalytic activity. It was reported that the alkylation reaction proceeds due to the presence of strong Brønsted acid sites. A simple comparison of NH_3 TPD (Tables S1 and S2 in the Supporting Information) does not show the relationship between acid amount from NH_3 TPD and catalytic activity because the NH_3 TPD profile of these complex oxides showed one broad peak. It is difficult to estimate the acid strength and the amount of strong acid. Therefore, we focused on the changes in alkylation activity between the NH_4^+ -W-Ta-O (TaL) and W-Ta-O (TaL) samples.

By ion-exchange treatment using NH_4Cl solution, Na^+ cations located in micropores and on the outer surface would be exchanged by NH_4^+ cations. From the results shown in Table 2, the reaction did not proceed for the heat-treated $\text{W}_{52}\text{Ta}_{48}\text{O}$ (TaL) sample but proceeded for the NH_4^+ - $\text{W}_{52}\text{Ta}_{48}\text{O}$ (TaL) sample. This suggests that the location of Na^+ over the surface of $\text{W}_{52}\text{Ta}_{48}\text{O}$ (TaL) forms an acid site after the heat treatment following ion-exchange treatment. Therefore, we considered that the amount of desorbed NH_3 of W-Ta-O (TaL) subtracted from NH_4^+ -W-Ta-O (TaL) represents the number of acid sites for alkylation activity. Thus, strong acidity of the catalyst was estimated by using the desorbed amounts of NH_3 for NH_4^+ -W-Ta-O (TaL) and W-Ta-O (TaL) samples, and the correlations of alkylation activity and acid site density were compared. The acid site density was calculated by the following equation:

$$\text{Acid site density/nm}^{-2} = \frac{(\text{Amount of desorbed } \text{NH}_3/\text{mmol g}^{-1})^a \times (\text{Na/mol}^{-1})^b \times 10^{-3}}{(\text{Surface area/m}^2 \text{ g}^{-1})^c \times (\text{Na/mol}^{-1})^2 \times 10^{18}}$$

^a Measured by TPD.

^b Avogadro's number.

^c Measured by N_2 adsorption and calculated by the BET method.

Fig. 9 shows the relationship between the acid site density of W-Ta-O (TaL) and the catalytic activity for alkylation. Alkylation

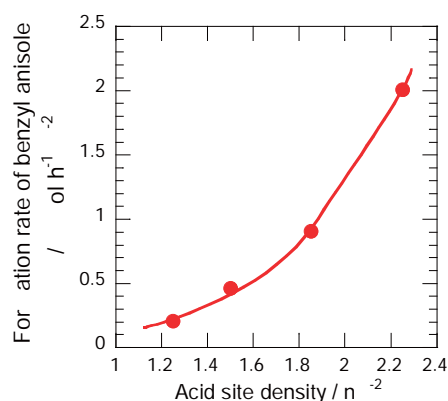


Fig. 9. Relationship between acid site density of W-Ta-O (TaL) and catalytic activity for alkylation.

activity increased with increase in acid site density, suggesting that strong Brønsted acid sites were formed on the surface of NH_4^+ -W-Ta-O (TaL) after calcination and that the locations of Na^+ of as-synthesized W-Ta-O (TaL) are the strong Brønsted acid sites. The number of strong acid sites increased with increasing W ratio, and the acid sites catalyze the alkylation reaction.

3.5. Proposed structure of W-Ta-O (TaL) and its acid sites

To discuss the relationship between crystalline structure and active sites, various crystalline W-Ta-O samples were synthesized. Fig. 10 shows the XRD patterns and Raman spectra of $\text{W}_{53}\text{Ta}_{47}\text{O}$ (TaL), $\text{W}_{58}\text{Ta}_{42}\text{O}$ (TaA), orthorhombic $\text{Cs}_{0.5}[\text{Ta}_{2.5}\text{W}_{2.5}]\text{O}_{14}$, tetragonal $\text{Ta}_{16}\text{W}_{18}\text{O}_{94}$, pyrochlore W-Ta-O, and hexagonal WO_3 . Lundberg et al. reported orthorhombic $\text{Cs}_x(\text{Nb,W})_5\text{O}_{14}$ [24] that possesses a tungsten or niobium bronze structure based on the pentagonal unit. Based on that report, orthorhombic $\text{Cs}_{0.5}[\text{Ta}_{2.5}\text{W}_{2.5}]\text{O}_{14}$ was synthesized by solid state reaction at a high temperature. Orthorhombic $\text{Cs}_{0.5}[\text{Ta}_{2.5}\text{W}_{2.5}]\text{O}_{14}$ possesses characteristic diffraction peaks at 6.5° (020), 7.6° (120), 8.8° (210), 22.8° (001), and around 27° . Tetragonal $\text{Ta}_{16}\text{W}_{18}\text{O}_{94}$ was also synthesized by heat treatment of $\text{W}_{53}\text{Ta}_{47}\text{O}$ (TaL) at 900°C . Pyrochlore W-Ta-O and hexagonal WO_3 were synthesized by a hydrothermal method. XRD patterns of the obtained samples suggested that the crystalline phase of the obtained samples was pure. Small and broad peaks were also observed at 6.8° and 8.0° for $\text{W}_{53}\text{Ta}_{47}\text{O}$ (TaL). Small and broad peaks of less than 10° for W-Ta-O (TaL) suggested the formation of a crystalline structure such as a orthorhombic phase in the a - b plane with maintenance of the layered structure [15].

From the Raman spectra of hexagonal WO_3 , the Raman bands at 160 and 250 cm^{-1} are assigned to the bending modes of the W-O-W linkage, the Raman bands at 642 , 688 , and 817 cm^{-1} are assigned to the symmetric stretching modes of the W-O-W linkage, and the Raman band at 950 cm^{-1} is assigned to the symmetric stretching mode of the W=O surface sites [26]. The Raman band at 170 cm^{-1} was assigned to translational modes of W or Ta, and the Raman bands at 870 and 960 cm^{-1} were assigned to the symmetric stretching mode of terminal Ta-O or W-O for pyrochlore W-Ta-O [27]. The Raman spectra of orthorhombic $\text{Cs}_{0.5}[\text{Ta}_{2.5}\text{W}_{2.5}]\text{O}_{14}$ and tetragonal $\text{Ta}_{16}\text{W}_{18}\text{O}_{94}$ were almost the same. The Raman bands at 931 and 998 cm^{-1} were assigned to the symmetric stretching mode of M=O (M = W, Ta). The Raman band of the symmetric stretching modes of the M-O-M (M = W, Ta) linkage was broad compared with that for hexagonal WO_3 . The Raman spectra of $\text{W}_{53}\text{Ta}_{47}\text{O}$ (TaL) and $\text{W}_{58}\text{Ta}_{42}\text{O}$ (TaA) were similar to the spectra of orthorhombic $\text{Cs}_{0.5}[\text{Ta}_{2.5}\text{W}_{2.5}]\text{O}_{14}$ and tetragonal $\text{Ta}_{16}\text{W}_{18}\text{O}_{94}$, suggesting that the framework of $\text{W}_{53}\text{Ta}_{47}\text{O}$ (TaL) and $\text{W}_{58}\text{Ta}_{42}\text{O}$ (TaA) is based on the MO_6 (M = W, Ta) octahedra and the $\{\text{M}_6\text{O}_{21}\}$ pentagonal unit.

The XRD pattern and Raman spectra of W-Ta-O (TaL) indicated that it is a layered structure composed of MO_6 octahedra and MO_7 pentagonal bipyramids interconnected in the a - b plane. This structure can be regarded as a tungsten bronze structure based on pentagonal $\{\text{W}_6\text{O}_{21}\}$ building units. Orthorhombic $\text{Cs}_{0.5}[\text{Ta}_{2.5}\text{W}_{2.5}]\text{O}_{14}$ was synthesized by solid state reaction at a high temperature. A small surface area ($3 \text{ m}^2 \text{ g}^{-1}$) is therefore inevitable, and it is difficult to remove the cesium cations in the heptagonal channel [20]. We have reported molybdenum bronze based on the pentagonal $\{\text{Mo}_6\text{O}_{21}\}$ unit of orthorhombic Mo_3VO_x obtained by a hydrothermal method. Ammonium cations derived from the precursor are located in the heptagonal channel and they can be removed as ammonia by calcination. After calcination, the heptagonal channel acts as a micropore [15]. Therefore, the presence of micropores confirms the formation of a bronze structure such as the orthorhombic phase.

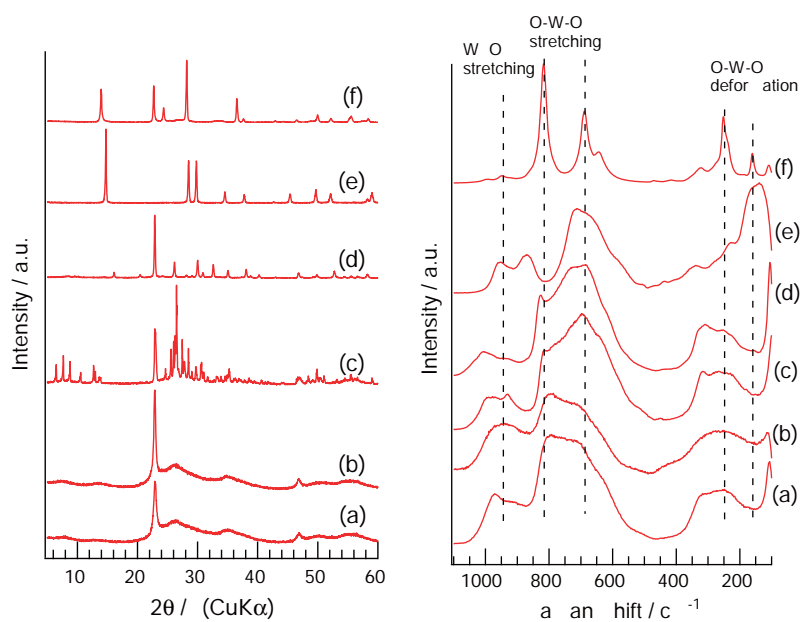


Fig. 10. (i) XRD patterns and (ii) Raman spectra of various W-Ta-O samples: (a) $W_{53}Ta_{47}O$ (TaL), (b) $W_{58}Ta_{42}O$ (TaA), (c) orthorhombic $Cs_{0.5}[Ta_{2.5}W_{2.5}]O_{14}$, (d) tetragonal $Ta_{16}W_{18}O_{94}$, (e) pyrochlore W-Ta-O, and (f) hexagonal WO_3 .

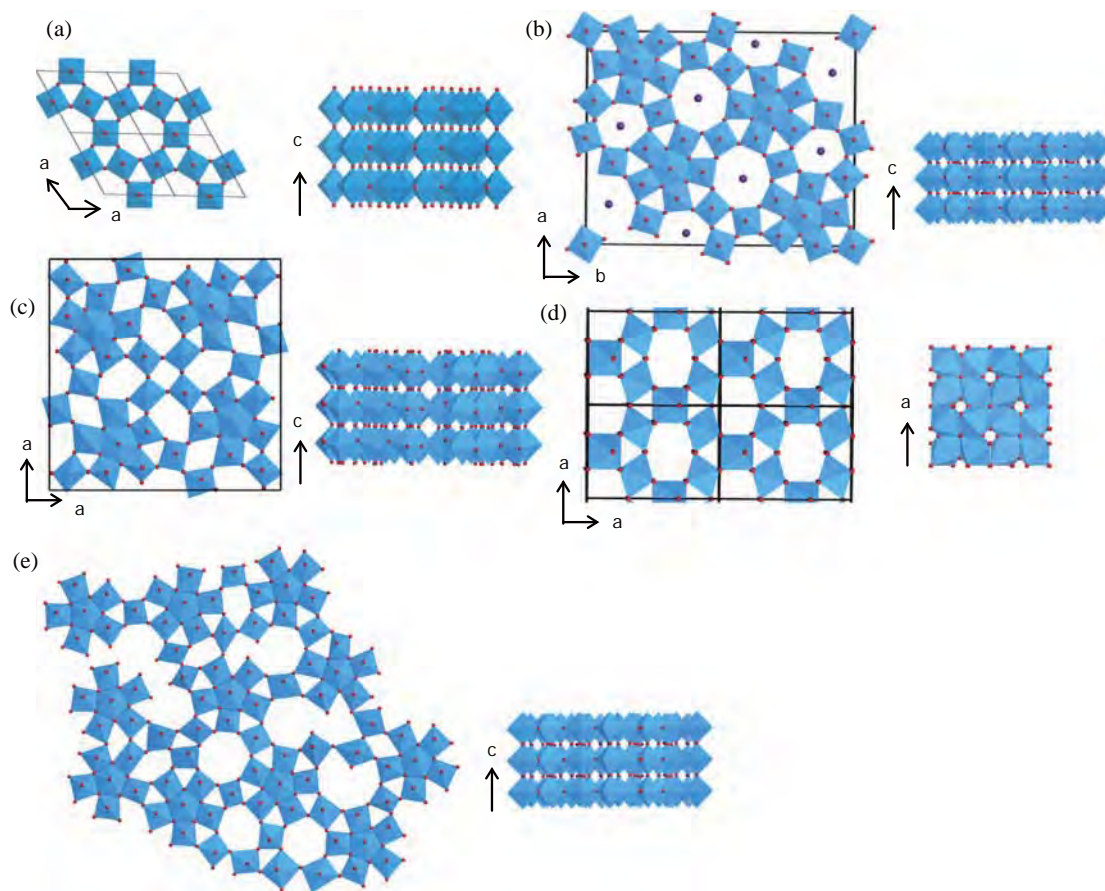


Fig. 11. Crystalline models of (a) hexagonal WO_3 , (b) orthorhombic $Cs_{0.5}[Ta_{2.5}W_{2.5}]O_{14}$, (c) tetragonal $Ta_{16}W_{18}O_{94}$, and (d) pyrochlore W-Ta-O and proposed structural model of (e) W-Ta-O (TaL). Blue polyhedra: M-O octahedra (M = Ta, W); red dots: oxygen; purple: cesium. (For interpretation of the references to color in this figure legend, the reader is referred to the web version of this article.)

The W-Ta-O (TaL) sample also showed N₂ adsorption at low pressure (1.0×10^{-6}), suggesting the formation of micropores such as heptagonal channels (Fig. S4 in the Supplementary Information). After adsorption at 1.0×10^{-6} , the amount of adsorbed nitrogen gradually increased with increasing nitrogen pressure for W-Ta-O (TaL), suggesting that the micropores formed within W-Ta-O (TaL) are partially nonuniform. However, the results of XRD, Raman, and adsorption analyses suggested that the *a*-*b* plane of W-Ta-O (TaL) is a deformed crystalline structure, as illustrated in Fig. 11. The deformed crystalline structure in the *a*-*b* plane perpendicular to the *c* axis is an interconnection of crystal structure motifs such as {M₆O₂₁} (M = W, Ta) pentagonal units and micropore channels, but without any long-range order. The arrangement of MO₆ octahedra and {M₆O₂₁} (M = W, Ta) pentagonal units may produce a disordered connection compared with a hexagonal structure (Fig. 11e).

Tetragonal Ta₁₆W₁₈O₉₄ and pyrochlore W-Ta-O samples did not show catalytic activity when these samples were used for the alkylation reaction, and the catalytic activity of hexagonal WO₃ was low. Therefore, strong Brønsted acid sites would be generated around the open mouth of the heptagonal channel after desorption of ammonia. The arrangement of MO₆ around the heptagonal channel was slightly disordered from a structural point of view [28]. A Brønsted acid site would be located around the open mouth of the heptagonal channel and would form bridging hydroxy groups (W-O(H)-Ta) connected by disordered octahedra after desorption of ammonia.

4. Conclusions

W-Ta-O samples were synthesized by a hydrothermal process. The composition ratio of W-Ta-O was changed by ammonium metatungstate and Lindqvist-type tantalum polyoxometalate (TaL) or tantallic acid (TaA) precursor. The synthesized W-Ta-O showed characteristic peaks at $2\theta = 22.7^\circ$ and 46.2° in an X-ray diffraction pattern (CuK α), indicating linear corner sharing of MO₆ (M = W, Ta) octahedra in the *c*-direction. For the tantallic acid precursor, hexagonal WO₃ was observed with an increase in the W ratio, suggesting that W and Ta were not homogeneously mixed. For the Lindqvist-type tantalum polyoxometalate precursor, the same layered-type materials were obtained with a wide range of composition ratios of W and Ta. As-synthesized W-Ta-O (TaA) contained NH₄⁺ cations in its structure, and NH₃ was desorbed by calcination at 500 °C, forming Brønsted acid without changing the structure. As-synthesized W-Ta-O (TaL) contained Na⁺ and NH₄⁺ cations. After calcination, W-Ta-O (TaL) showed weak acidity for alkylation reactions. However, after ion exchange of Na⁺ cations with NH₄⁺ and calcination treatment at 500 °C, strong Brønsted acid sites were generated. The density of the strong acid sites increased with increasing W ratio. From XRD, Raman, and adsorption measurements, a comparison of W-Ta-O (TaL) with various crystalline W-Ta-O revealed the crystalline motif of W-Ta-O (TaL). The arrangement of the *a*-*b* plane was an interconnection of MO₆ (M = W, Ta) octahedra and {M₆O₂₁} pentagonal units and micropore channels, but without long-range order. MO₆ octahedra around the open mouth of the heptagonal channel were slightly disordered, suggesting that Brønsted acid was formed as W-O(H)-Ta around the open mouth of the heptagonal channel.

Acknowledgment

This work was supported by JSPS KAKENHI Grant-in-Aid for Young Scientists 24760635.

Appendix A. Supplementary material

Supplementary data associated with this article can be found, in the online version, at <http://dx.doi.org/10.1016/j.jcat.2016.04.007>.

References

- [1] T. Iizuka, K. Ogasawara, K. Tanabe, Acidic and catalytic properties of niobium pentoxide, *Bull. Chem. Soc. Jpn.* 56 (1983) 2927–2931, <http://dx.doi.org/10.1246/bcsj.56.2927>.
- [2] C. Tagusagawa, A. Takagaki, A. Iguchi, K. Takanabe, J.N. Kondo, K. Ebitani, et al., Synthesis and characterization of mesoporous Ta–W oxides as strong solid acid catalysts, *Chem. Mater.* 22 (2010) 3072–3078, <http://dx.doi.org/10.1021/cm903767n>.
- [3] I. Nowak, M. Ziolek, Niobium compounds: preparation, characterization, and application in heterogeneous catalysis, *Chem. Rev.* 99 (1999) 3603–3624, <http://www.ncbi.nlm.nih.gov/pubmed/11849031>.
- [4] K. Nakajima, Y. Baba, R. Noma, M. Kitano, J.N. Kondo, S. Hayashi, et al., Nb₂O₅-nH₂O as a heterogeneous catalyst with water-tolerant Lewis acid sites, *J. Am. Chem. Soc.* 133 (2011) 4224–4227, <http://dx.doi.org/10.1021/ja110482r>.
- [5] T. Murayama, J. Chen, J. Hirata, K. Matsumoto, W. Ueda, Hydrothermal synthesis of octahedra-based layered niobium oxide and its catalytic activity as a solid acid, *Catal. Sci. Technol.* (2014), <http://dx.doi.org/10.1039/C4CY00713A>.
- [6] T. Ushikubo, K. Wada, Hydrated tantalum oxide as a solid acid catalyst, *Chem. Lett.* 17 (1988) 1573–1574.
- [7] T. Ushikubo, Activation of propane and butanes over niobium- and tantalum-based oxide catalysts, *Catal. Today* 78 (2003) 79–84, [http://dx.doi.org/10.1016/S0920-5861\(02\)00346-2](http://dx.doi.org/10.1016/S0920-5861(02)00346-2).
- [8] K. Kitano, S. Okazaki, T. Shishido, K. Teramura, T. Tanaka, Generation of Brønsted acid sites on alumina-supported tantalum (V) oxide calcined at 1223 K, *Chem. Lett.* 40 (2011) 1332–1334, <http://dx.doi.org/10.1246/cl.2011.1332>.
- [9] T. Kitano, S. Okazaki, T. Shishido, K. Teramura, T. Tanaka, Generation of Brønsted acid sites on Al₂O₃-supported Ta₂O₅ calcined at high temperatures, *Catal. Today* 192 (2012) 189–196, <http://dx.doi.org/10.1016/j.cattod.2012.02.035>.
- [10] C. Tagusagawa, A. Takagaki, S. Hayashi, K. Domen, Characterization of HNbWO₆ and HTaWO₆ metal oxide nanosheet aggregates as solid acid catalysts, *J. Phys. Chem. C* 113 (2009) 7831–7837.
- [11] C. Yue, X. Zhu, M. Rigutto, E. Hensen, Acid catalytic properties of reduced tungsten and niobium-tungsten oxides, *Appl. Catal. B: Environ.* 163 (2015) 370–381, <http://dx.doi.org/10.1016/j.apcatb.2014.08.008>.
- [12] M. Hino, M. Kurashige, H. Matsuhashi, K. Arata, A solid acid of tungsta-niobia more active than aluminosilicates for decompositions of cumene, ethylbenzene, and toluene, *Appl. Catal. A: Gen.* 310 (2006) 190–193, <http://dx.doi.org/10.1016/j.apcata.2006.05.038>.
- [13] T. Shishido, T. Kitano, K. Teramura, T. Tanaka, Brønsted acid generation over alumina-supported niobia by calcination at 1173 K, *Catal. Lett.* 129 (2009) 383–386, <http://dx.doi.org/10.1007/s10562-008-9837-2>.
- [14] T. Kitano, T. Hayashi, T. Uesaka, T. Shishido, K. Teramura, T. Tanaka, Effect of high-temperature calcination on the generation of Brønsted acid sites on WO₃/Al₂O₃, *ChemCatChem* 6 (2014) 2011–2020, <http://dx.doi.org/10.1002/cctc.201400053>.
- [15] T. Konya, T. Katou, T. Murayama, S. Ishikawa, M. Sadakane, D. Buttrey, et al., An orthorhombic Mo₃VO_x catalyst most active for oxidative dehydrogenation of ethane among related complex metal oxides, *Catal. Sci. Technol.* 3 (2013) 380–387, <http://dx.doi.org/10.1039/c2cy20444d>.
- [16] S. Ishikawa, X. Yi, T. Murayama, W. Ueda, Heptagonal channel micropore of orthorhombic Mo₃VO_x as catalysis field for the selective oxidation of ethane, *Appl. Catal. A: Gen.* 474 (2014) 10–17, <http://dx.doi.org/10.1016/j.apcata.2013.07.050>.
- [17] S. Ishikawa, X. Yi, T. Murayama, W. Ueda, Catalysis field in orthorhombic Mo₃VO_x oxide catalyst for the selective oxidation of ethane, propane and acrolein, *Catal. Today* (2014) 8–13, <http://dx.doi.org/10.1016/j.cattod.2013.12.054>.
- [18] M. Sadakane, K. Endo, K. Kodato, S. Ishikawa, T. Murayama, W. Ueda, Assembly of a pentagonal polyoxomolybdate building block, [Mo₆O₂₁]⁶⁻, into crystalline MoV oxides, *Eur. J. Inorg. Chem.* 2013 (2013) 1731–1736, <http://dx.doi.org/10.1002/ejic.201201142>.
- [19] T. Murayama, N. Kuramata, S. Takatama, K. Nakatani, S. Izumi, X. Yi, et al., Synthesis of porous and acidic complex metal oxide catalyst based on group 5 and 6 elements, *Catal. Today* 185 (2012) 224–229, <http://dx.doi.org/10.1016/j.cattod.2011.10.029>.
- [20] K. Omata, S. Izumi, T. Murayama, W. Ueda, Hydrothermal synthesis of W–Nb complex metal oxides and their application to catalytic dehydration of glycerol to acrolein, *Catal. Today* 201 (2013) 7–11.
- [21] K. Omata, K. Matsumoto, T. Murayama, W. Ueda, Direct oxidative transformation of glycerol into acrylic acid over phosphoric acid-added W–V–Nb complex metal oxide catalysts, *Chem. Lett.* 43 (2014) 435–437, <http://dx.doi.org/10.1246/cl.131098>.
- [22] H. Hartl, F. Pickhard, F. Emmerling, C. Rohr, Isopolyanion [Ta₆O₁₉]⁸⁻, *Z. Anorg. Allg. Chem.* 627 (2001) 2630–2638.

- [23] P.A. Abramov, A.M. Abramova, E.V. Peresyphkina, A.L. Gushchin, S.A. Adonin, M. N. Sokolov, New polyoxotantalate salt $\text{Na}_8[\text{Ta}_6\text{O}_{19}]\cdot 24.5\text{H}_2\text{O}$ and its properties, *J. Struct. Chem.* 52 (2011) 1012–1017.
- [24] M. Lundberg, M. Sundberg, New complex structures in the cesium-niobium-tungsten-oxide system revealed by HREM, *Ultramicroscopy* 52 (1993) 429–435. <<http://www.sciencedirect.com/science/article/pii/0304399193900575>> (accessed May 15, 2014).
- [25] M. Sadakane, N. Watanabe, T. Katou, Y. Nodasaka, W. Ueda, Crystalline Mo_3VO_x mixed-metal-oxide catalyst with trigonal symmetry, *Angew. Chem. Int. Ed. Engl.* 46 (2007) 1493–1496, <http://dx.doi.org/10.1002/anie.200603923>.
- [26] Y. Chen, I.E. Wachs, Tantalum oxide-supported metal oxide (Re_2O_7 , CrO_3 , MoO_3 , WO_3 , V_2O_5 , and Nb_2O_5) catalysts: synthesis, Raman characterization and chemically probed by methanol oxidation, *J. Catal.* 217 (2003) 468–477, [http://dx.doi.org/10.1016/S0021-9517\(03\)00065-4](http://dx.doi.org/10.1016/S0021-9517(03)00065-4).
- [27] M. Maćzka, A.V. Knyazev, A. Majchrowski, J. Hanuza, S. Kojima, Temperature-dependent Raman scattering study of the defect pyrochlores RbNbWO_6 and CsTaWO_6 , *J. Phys. Condens. Matter* 24 (2012) 195902, <http://dx.doi.org/10.1088/0953-8984/24/19/195902>.
- [28] M. Sadakane, K. Yamagata, K. Kodato, K. Endo, K. Toriumi, Y. Ozawa, et al., Synthesis of orthorhombic Mo–V–Sb oxide species by assembly of pentagonal Mo_6O_{21} polyoxometalate building blocks, *Angew. Chem. Int. Ed. Engl.* 48 (2009) 3782–3786, <http://dx.doi.org/10.1002/anie.200805792>.

New crystalline complex metal oxides created by unit-synthesis and their catalysis based on porous and redox properties†

Zhenxin Zhang,^a Satoshi Ishikawa,^a Yuta Tsuboi,^a Masahiro Sadakane,^b Toru Murayama^c and Wataru Ueda^{*a}

Received 13th January 2016, Accepted 28th January 2016

DOI: 10.1039/c6fd00006a

The development of new complex metal oxides having structural complexity suitable for solid-state catalysis is of great importance in fundamental catalysis research and practical applications. However, examples of these materials are rare. Herein, we report two types of crystalline complex metal oxides with new structures and their catalytic properties. The first one is an all-inorganic ϵ -Keggin polyoxometalate-based material with intrinsic microporosity. The framework of the material is formed by the assembly of ϵ -Keggin polyoxomolybdate units with metal ion linkers in a diamondoid topology. The micropores of the material can be opened without change of the structures, and the material adsorbs small molecules. This material has both redox properties and acidity and can be applied to O₂ adsorption, selective oxidation of methacrolein, and hydrolysis of cellobiose. The other material is a crystalline metal oxide based on molecular nanowires. The hexagonal POM units stack along the *c* axis to form prismatic clusters as molecular wires. The molecular wires further assemble in a hexagonal fashion to form the crystals, and NH₄⁺ and water are present in between the molecular wires. The material is active as an acid catalyst for cellobiose conversion.

Introduction

Transition metal oxides, mainly composed of metal–oxygen octahedra, show interesting properties such as multi-electron redox properties, structural stability, acidity, and elemental diversity and can be applied to many fields such as

^aDepartment of Material and Life Chemistry, Faculty of Engineering, Kanagawa University, Rokkakubashi, Kanagawa-ku, Yokohama-shi, Kanagawa, 221-8686, Japan. E-mail: uedaw@kanagawa-u.ac.jp

^bDepartment of Applied Chemistry, Graduate School of Engineering, Hiroshima University, 1-4-1 Kagamiyama, Higashi Hiroshima 739-8527, Japan

^cDepartment of Applied Chemistry, Graduate School of Urban Environmental Sciences, Tokyo Metropolitan University, 1-1 Minami-osawa, Hachioji, Tokyo 192-0397, Japan

† Electronic supplementary information (ESI) available. See DOI: 10.1039/c6fd00006a

catalysis, photocatalysis, materials science, magnetism, biology, and medicine. The design and development of new transition metal oxides with unique structural and functional features, such as porosity and nano-structure, are of great interest and particularly important for catalysis.¹

The assembly of early-transition metal–oxygen units forms inorganic molecular metal–oxygen clusters known as polyoxometalates (POMs).^{2–5} POMs are well-defined building blocks for the construction of POM-based materials,^{6,7} such as covalent POM-based organic–inorganic hybrid frameworks,^{8,9} POM-based complex metal oxides,^{10–14} and ionic porous organic–inorganic materials.^{15–19} Previous research shows that using POMs as sub-units is an effective approach to obtain transition metal oxides with new structures. Actually, we have recently succeeded in synthesizing two new kinds of structural materials of transition metal-oxides using POM units. One is an all-inorganic crystalline ϵ -Keggin POM-based framework with intrinsic microporosity^{20–24} and the other is a crystalline metal oxide based on molecular nanowires.²⁵ Their structural features are very rare in the field of metal oxides.

The all-inorganic crystalline ϵ -Keggin POM-based microporous materials are formed by the connection of ϵ -Keggin POM units with transition metal ions as linkers in a diamond-like topology (Fig. 1a–c). There are three sites in the framework: surrounding sites, central sites, and linker sites (Fig. 1a). The surrounding sites are mainly occupied by Mo ions, and the Mo ions can be substituted by V ions. The central and linker sites are occupied by other metal ions such as V, Bi, Zn, and Mn. The frameworks of the materials are anionic, and there are cations in the bulk to neutralize the negative charge of the framework. The chemical composition is readily tuned in each site mentioned above. Cages and channels form the micropores of the materials. Ten ϵ -Keggin POM units and the linker metal ions surround the cage. The cages are tetrahedrally connected with the channels to form a periodical 3D pore system as FAU-type zeolites do, and the tunnel of the pore was not straight but in a zig-zag fashion. The micropore can be opened using calcination that removes water and NH_4^+ in the micropore without collapsing the structures. The materials have interesting properties and applications such as gas adsorption,^{20,23} gas separation,²³ ion-exchange,^{20,21} and redox properties.²¹ The ϵ -Keggin POM-based microporous material, Mo–V–Bi oxide with a proton as the cation, showed catalytic activity for the etherification of benzyl alcohol.^{20,22}

Another example of the newly developed material is the crystalline metal oxides derived from molecular nanowires (Fig. 1d–f). The structures of the molecular wires are formed by the assembly of the hexagonal POM units, $[\text{XMo}_6\text{O}_{21}]^{2-}$ (X = Se or Te), along the *c* axis, which further pack in a hexagonal symmetry to form crystals with NH_4^+ and water in between the molecular wires. The molecular wires in the crystal are separable and isolable. In fact, ultrathin molecular wire-based materials can be formed and act as acid catalysts for esterification.²⁵

In our previous research, 4 iso-structural all-inorganic crystalline ϵ -Keggin POM-based microporous materials have been reported, which show different properties and have been applied to different fields.^{20–23} Herein, we extended our research and introduced two more iso-structural materials of ϵ -Keggin POM-based materials, denoted as Na–Mo–Mn oxide and NH_4 –Mo–Fe oxide. The new compositional materials were characterized using powder X-ray diffraction (XRD),

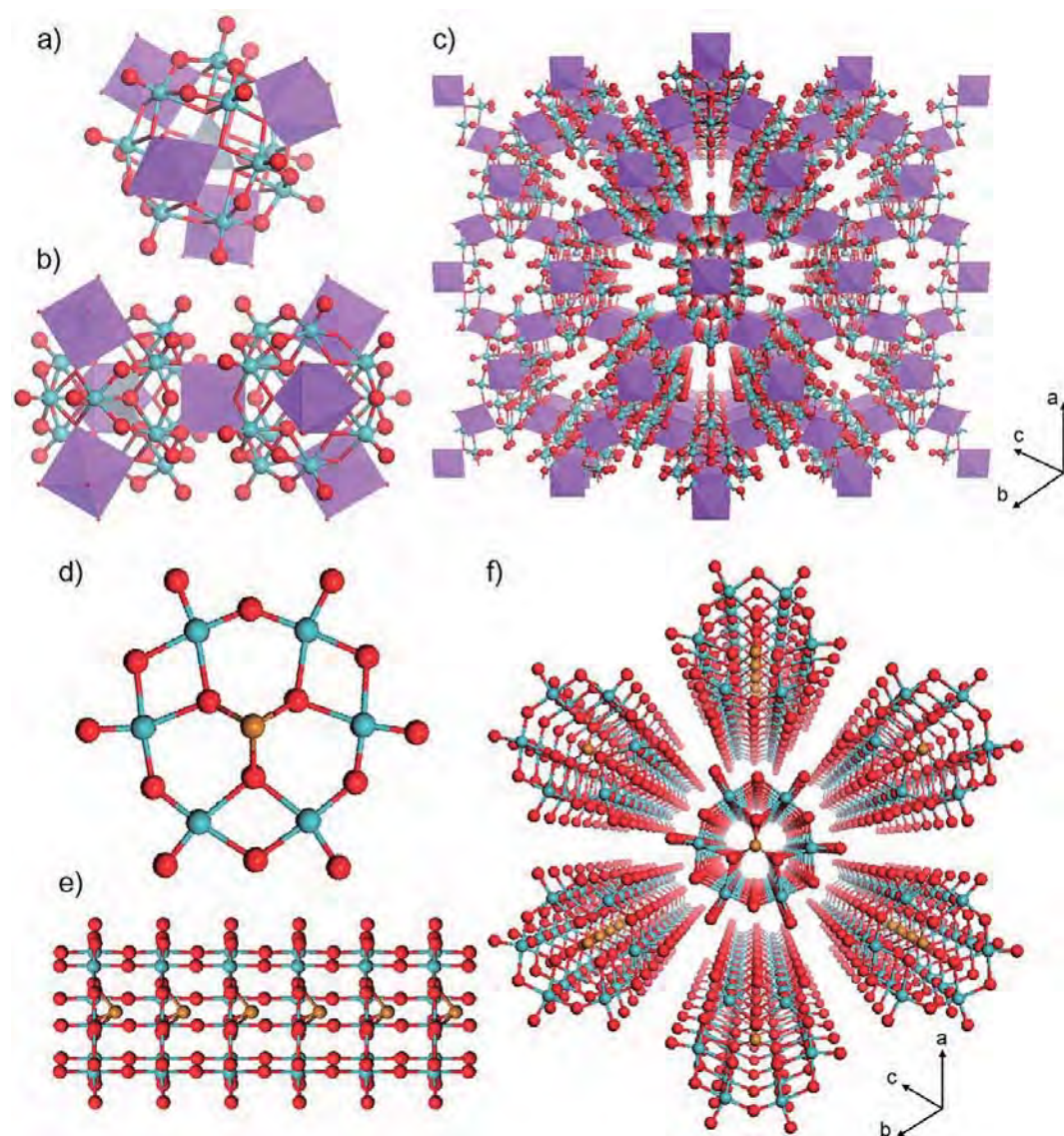


Fig. 1 Structural representation of (a) an ϵ -Keggin core with four metal ions in the linker site, (b) the connection of ϵ -Keggin POM units with linker ions, (c) the framework of porous crystalline ϵ -Keggin POM-based materials, blue sphere: surrounding site, central grey tetrahedron: central site, purple octahedron: linker site, and red sphere: O, (d) a hexagonal POM unit, (e) growing the hexagonal POM unit to form a molecular wire, and (f) the crystal structure formed by a molecular wire, blue sphere: Mo, yellow sphere: Te or Se, and red sphere: O.

Fourier transform infrared (FT-IR) spectroscopy, scanning electron microscopy (SEM), high resolution transmission electron microscopy (HR-TEM), X-ray photoelectron spectroscopy (XPS), and elemental analysis.

$\text{NH}_4\text{-Mo-Fe}$ oxide is found to adsorb O_2 in its micropores at room temperature. The unique O_2 adsorption is probably on the basis of the formation of peroxo species in the Fe site in the material as indicated in the FT-IR spectra. Mo-V-Bi oxide is found to be a new catalyst member, active and selective for methacrolein oxidation to methacrylic acid using O_2 as an oxidant. Since heat-treatment removed NH_3 from the materials to leave acid sites, the all-inorganic crystalline ϵ -Keggin POM-based microporous materials and the hexagonal POM-based molecular nanowires can be used as solid acid catalysts. Using these

catalysts, hydrolysis of cellobiose is tested as a model reaction for biomass conversion.

Experimental

All chemicals were reagent grade and used as supplied, and house made distilled water was used throughout. Mo–V–Bi oxide,²² Na–Mo–Zn oxide,²³ NH₄–Mo–Zn oxide,²³ Mo–Te oxide,²⁵ Mo–Se oxide,²⁵ and well-crystallized Mo–V–Bi oxide²⁰ were synthesized according to our previous papers.

1. Synthesis of Na–Mo–Mn oxide

Na₂MoO₄·2H₂O (2.823 g, 11.7 mmol based on Mo) was dissolved in 40 mL of distilled water. Mo (0.2 g, 2.1 mmol) metal and MnO (0.235 g, 3.3 mmol) metal were added to the solution sequentially. The pH value was adjusted to 4.8 using H₂SO₄ (1 M). The mixture was introduced into a 50 mL Teflon liner of a stainless-steel autoclave. The autoclave was placed in an oven and heated at 175 °C for 24 h with rotation (~1 rpm). After the hydrothermal reaction and cooling of the autoclave, the crude solid was transferred into a 100 mL beaker and 60 mL of water was added. For purification and solid recovery, the mixture was centrifuged (1700 rpm, 2 min), and the suspension (containing the product) solution was separated from the precipitate formed on the bottom after centrifugation. Then, after the addition of 60 mL of water to the precipitate, the solution was centrifuged and the new upper suspension solution was separated. The addition of water, centrifugation, and separation were carried out two more times. The collected suspension (containing the product) was centrifuged (3500 rpm, 30 min), and the solid on the bottom of the centrifugation tube was collected. The collected solid was washed with water by dispersion in 10 mL of water and subsequent centrifugation (3500 rpm, 30 min). After the washing process had been carried out two more times, the obtained solid was dried at 60 °C overnight. Then, 0.94 g of Na–Mo–Mn oxide (yield: 46% based on Mo) was obtained. Elemental analysis: calcd for Na₂Mn_{2.6}Mo₁₂O₄₇H_{24.8}: Mn, 6.75; Mo, 54.39; Na, 2.17; H, 1.17, found: Mn, 6.65; Mo, 54.84; Na, 2.29; H, 1.08.

2. Synthesis of NH₄–Mo–Fe oxide

(NH₄)₆Mo₇O₂₄·4H₂O (2.060 g, 11.7 mmol based on Mo) was dissolved in 40 mL of distilled water. Mo (0.2 g, 2.1 mmol) metal and Fe₃O₄ (0.258 g, 1.1 mmol) were added to the mixture sequentially (pH was 5.1). The mixture was introduced into a 50 mL Teflon liner of a stainless-steel autoclave. The autoclave was placed in an oven and heated at 175 °C for 48 h with rotation (~1 rpm). The purification process was the same to that of Na–Mo–Mn oxide. Then, 0.87 g of NH₄–Mo–Fe oxide (yield: 44% based on Mo) was obtained. Elemental analysis: calcd for N₂Fe_{2.6}Mo₁₂O₄₃H_{23.4}: Fe, 7.10; Mo, 56.29; N, 1.37; H, 1.14, found: Fe, 7.14; Mo, 56.46; N, 1.29; H, 1.00.

3. Synthesis of Mo–V–Bi oxide

Mo–V–Bi oxide was synthesized in nano-size *via* the following method.²² Bi(NO₃)₃·5H₂O (0.68 g, 1.40 mmol) was dissolved in a solution (1.7 mL) of glycerol and water with a volume ratio of 1 : 1. (NH₄)₆Mo₇O₂₄·4H₂O (1.471 g, 8.33 mmol

based on Mo) was dissolved in 20 mL of water. $\text{VOSO}_4 \cdot 5\text{H}_2\text{O}$ (0.5365 g, 2.08 mmol) was dissolved in 20 mL of water. After the solids had been completely dissolved, the solution of $\text{VOSO}_4 \cdot 5\text{H}_2\text{O}$ was rapidly poured into the solution of $(\text{NH}_4)_6\text{Mo}_7\text{O}_{24} \cdot 4\text{H}_2\text{O}$. After stirring at room temperature for 3 min, $\text{Bi}(\text{NO}_3)_3$ solution was added. Then, the mixture was stirred for 7 min. The pH of the precursor was adjusted to 3.7 with 28% of ammonia aqueous solution. After the mixture had been purged with N_2 for 10 min, the mixture was refluxed for 48 h in an oil bath with a setting temperature of 110 °C. The black solid was collected by filtration, washed with 20 mL of water 3 times, and dried at 353 K overnight. Then, 1.28 g of Mo–V–Bi oxide (yield: 56% based on Mo) was obtained.

4. Catalytic oxidation of methacrolein

The catalytic oxidation of methacrolein (MAL) to methacrylic acid (MA) was conducted over the Mo–V–Bi oxide using a fixed bed stainless tubular reactor at atmospheric pressure. Prior to the catalytic reaction, the catalyst was heat-treated at 350 °C under 40.5 mL min^{-1} of N_2 flow for 2 h (designated as Mo–V–Bi–NC350). After the heat treatment, the catalyst (0.5 g) was mixed with 2.5 g of silica sand introduced into the stainless tubular reactor. Then, the reactor was heated gradually from room temperature to 280 °C at a rate of 10 °C min^{-1} . When the temperature reached 280 °C, a reaction gas with the composition of $\text{MAL}/\text{O}_2/(\text{N}_2 + \text{He})/\text{H}_2\text{O} = 1.2/8.0/71.0/18.5$ mL min^{-1} was fed in and stabilized for 30 min before the start of the gas analysis. MAL was supplied by N_2 bubbling with a flow rate of 20.6 mL min^{-1} to a MAL liquid at 0 °C. Water was fed by He bubbling with a flow rate of 30.5 mL min^{-1} to a bottle of hot water (80 °C). The flow rates of MAL and water were determined based on gas chromatographic analysis. The catalytic reaction was carried out at setting temperatures of 280, 270, 260, 250 °C with the reaction temperature decreasing stepwise, and the real reaction temperature was monitored by the thermal-couple inserted in the middle of the catalyst zone. The reactants and the products were analyzed with three online gas chromatographs (Molecular Sieve 13X for O_2 , N_2 , and CO with a TCD detector, Gascropack54 for H_2O and CO_2 with a TCD detector, and Porapak Q for MAL, CH_3COOH , MA with an FID detector). Blank runs showed that no reaction took place without the catalyst under the experimental conditions in this study. Carbon balance was always *ca.* 97–100% and selectivity was calculated based on the sum of the products.

5. Cellobiose conversion

In a typical reaction, the catalyst (0.01 g), cellobiose (0.05 g), and H_2O (0.5 mL) were added into a 10 mL-test tube. The tube was sealed using a cap with a Teflon liner. The tube was packed in a 300 mL autoclave with a Teflon liner, followed by the addition of 20 mL of water in the autoclave to ensure the pressure-balance of the test tube. The autoclave was heated at 160 °C in an oven for 2 h. After the reaction, the solution in the tube was analyzed using high performance liquid chromatography (HPLC). The products were identified by comparison of the retention time with standard chemicals. The yield was calculated based on the carbon number.

Characterization

Nitrogen (at $-196\text{ }^{\circ}\text{C}$) and oxygen (at $25\text{ }^{\circ}\text{C}$) adsorption–desorption isotherms were obtained with a BELSORP MAX (BEL, Japan) sorption analyzer. BET surface area was calculated *via* the BET method and the external surface area was calculated by the *t*-plot method using the adsorption branch. The samples were evacuated at $200\text{ }^{\circ}\text{C}$ for 2.5 h before the measurement. The powder X-ray diffraction (XRD) pattern was obtained on a RINT2200 (Rigaku, Japan) with Cu $K\alpha$ radiation (tube voltage: 40 kV, tube current: 20 mA). SEM images were obtained with a HD-2000 (HITACHI, Japan). HR-TEM images were taken with a 200 kV TEM (JEOL, JEM-2100F, Japan). FT-IR was carried out on a PARAGON 1000, Perkin Elmer. Temperature-programmed desorption mass spectrometry (TPD-MS) measurements were carried out from $30\text{ }^{\circ}\text{C}$ to $600\text{ }^{\circ}\text{C}$ at a heating rate of $10\text{ }^{\circ}\text{C min}^{-1}$ under helium (flow rate: 50 mL min^{-1}). Samples were set up in between two layers of quartz wool. A TPD apparatus (BEL, Japan) equipped with a quadrupole mass spectrometer (M-100QA, Anelva) was used to detect NH_3 ($m/z = 16$) and H_2O ($m/z = 18$). For the TPD-MS measurements of the materials after heat treatment, the samples were heated at $200\text{ }^{\circ}\text{C}$ under high vacuum for 2.5 h in the TPD instrument before the measurements. XPS was performed on a JPS-9010MC (JEOL, Japan). The spectrometer energies were calibrated using the C 1s peak at 284.8 eV. Elemental compositions were determined using an inductive coupling plasma (ICP-AES) method (ICPE-9000, Shimadzu, Japan). CHN elemental composition was determined at the Instrumental Analysis Division, Equipment Management Center, Creative Research Institution, Hokkaido University.

1. Rietveld analysis

Rietveld refinement was performed with the Materials Studio v6.1.0 package (Accelrys Software Inc.). The initial structures of Na–Mo–Mn oxide and NH_4 –Mo–Fe oxide were refined by powder XRD Rietveld refinement.²⁶ The lattice parameters and pattern parameters of the materials were refined by Pawley refinement first. The initial structures were from Mo–V–Bi oxide.²⁰ Then, isotropical temperature factors were given for every atom in the initial structures. Rietveld analysis was started with the initial models of the materials and lattice parameters and pattern parameters from the Pawley refinement. Every atom position was refined. Occupancy of the atoms in the framework was fixed without further refinement and occupancies of atoms in micropores were refined with consideration of the elemental analysis results. Finally, the pattern parameters were refined again to obtain the lowest R_{wp} value. The crystallographic data are provided in Table S1–S3.†

Results and discussion

1. Synthesis of ϵ -Keggin POM-based porous metal oxides

The crystalline ϵ -Keggin polyoxomolybdate-based porous metal oxides were synthesized *via* the hydrothermal method. Three kinds of precursor compounds, the Mo source, the reducing agent, and the third metal ion, were necessary for the materials. As shown in Table 1, different metal ions were used as the precursors for the materials, which yielded 6 iso-structural materials with different chemical

Table 1 Comparison of the synthetic conditions for the POM-based microporous materials

	Mo source ^a	Reductant	The third metal ion	Additional process ^b	Hydrothermal conditions	Reference
Mo–V–Bi oxide	AHM	VOSO ₄	Bi(OH) ₃	—	175 °C, 48 h	20 and 22
Na–Mo–Zn oxide	Na ₂ MoO ₄	Mo	ZnCl ₂	pH ~ 4.8	175 °C, 24 h, rotation	21 and 23
NH ₄ –Mo–Zn oxide	AHM	Mo	ZnCl ₂	pH ~ 4.8	175 °C, 24 h, rotation	23
Na–Mo–Mn oxide	Na ₂ MoO ₄	Mo	MnO	pH ~ 4.8	175 °C, 24 h, rotation	This work
NH ₄ –Mo–Mn oxide	AHM	Mo	MnO	pH ~ 4.8	175 °C, 24 h	21
NH ₄ –Mo–Fe oxide	AHM	Mo	Fe ₃ O ₄	—	175 °C, 48 h, rotation	This work

^a AHM: ammonium heptamolybdate. ^b In some cases, pH was adjusted by the addition of 1 M H₂SO₄.

compositions. The Mo sources, (NH₄)₆Mo₇O₂₄·4H₂O (AHM) and Na₂MoO₄·2H₂O, with reducing agents produced ε-Keggin POMs in aqueous solution, which is well-known in POM chemistry.²⁷ The produced ε-Keggin POMs were further connected by metal ions to form the materials.

2. Structures of crystalline POM-based microporous materials

The ε-Keggin POM-based microporous materials can incorporate different transition metal ions. The chemical composition can be tuned in each site in the materials. The iso-structural materials were synthesized. As shown in Fig. 2A, the powder XRD patterns of the two new materials, Na–Mo–Mn oxide and NH₄–Mo–Fe oxide, were similar to those of the previously reported materials. The space group of the materials was *Fd* $\bar{3}$ *m* with slightly different lattice parameters (Table 2). The XRD patterns demonstrated that the basic structures of the materials were similar. FT-IR spectra of the materials were also similar, indicating that the POM molecular structures of the materials were similar (Fig. 2B).

The elemental analysis exhibited Na : Mn : Mo = 2 : 2.6 : 12 for Na–Mo–Mn oxide and N : Fe : Mo = 2 : 2.6 : 12 for NH₄–Mo–Fe oxide, respectively. The proposed structures of Na–Mo–Mn oxide and NH₄–Mo–Fe oxide were on the basis of the ε-Keggin POM units (Mn_{0.6}Mo₁₂O₄₀ or Fe_{0.6}Mo₁₂O₄₀) where the central sites were partially occupied with the Mn or Fe ions and the surrounding sites were with the Mo ions. The POM units (Mn_{0.6}Mo₁₂O₄₀ or Fe_{0.6}Mo₁₂O₄₀) were linked by Mn and Fe, respectively. Similar structure models of NH₄–Mo–Zn oxide and NH₄–Mo–Mn oxide were reported.²¹ The frameworks of the materials were negatively charged, so that there were cations, Na⁺ (Na–Mo–Mn oxide), NH₄⁺ (NH₄–Mo–Fe oxide), and water in the void spaces. The simulated XRD patterns using the Rietveld refinement were almost identical to the experimental patterns, indicating that the proposed structures were correct (Fig. S1†). There was no additional peak being observed in comparison to the experimental pattern with the simulated pattern, indicating that the powder samples were pure.

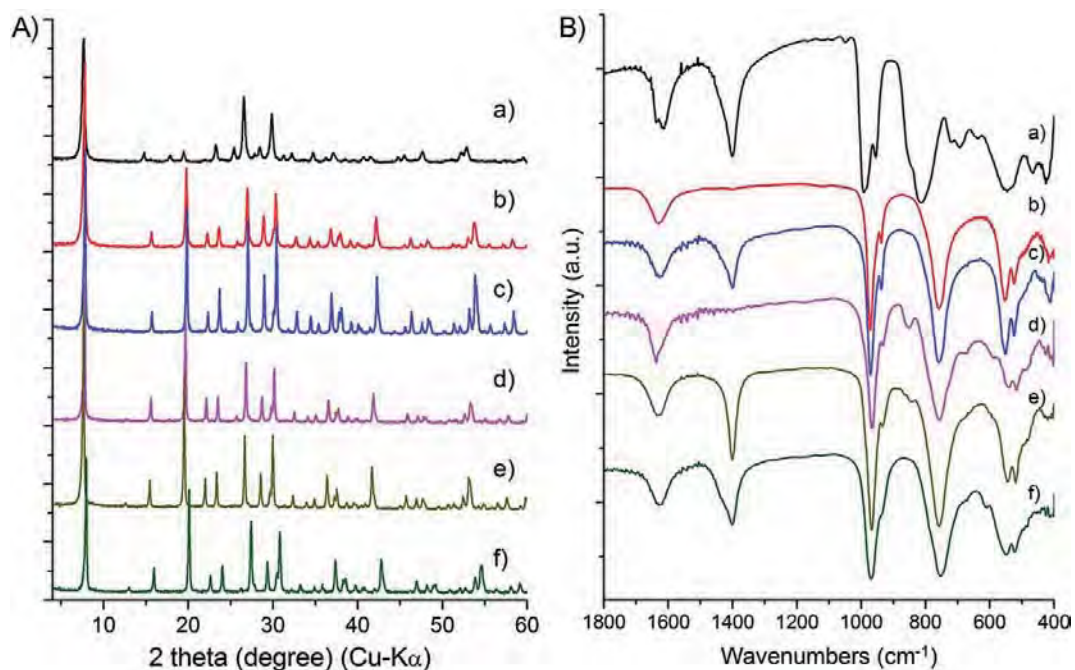


Fig. 2 (A) XRD patterns of (a) Mo–V–Bi oxide, (b) Na–Mo–Zn oxide, (c) NH₄–Mo–Zn oxide, (d) Na–Mo–Mn oxide, (e) NH₄–Mo–Mn oxide, and (f) NH₄–Mo–Fe oxide and (B) FT-IR spectra of (a) Mo–V–Bi oxide, (b) Na–Mo–Zn oxide, (c) NH₄–Mo–Zn oxide, (d) Na–Mo–Mn oxide, (e) NH₄–Mo–Mn oxide, and (f) NH₄–Mo–Fe oxide.

The oxidation states of the metal elements in Na–Mo–Mn oxide and NH₄–Mo–Fe oxide were studied using XPS (Fig. S2† and Table 2). The surrounding 12 Mo ions were mostly reduced to Mo^V. In Na–Mo–Mn oxide, Mn^{II} was present (Table 2). In the case of NH₄–Mo–Fe oxide, the ratio of Fe^{III}/Fe^{II} was 0.4/2.2. Considering the results of the elemental analysis and the oxidation state analysis, the detailed chemical formulae of the materials can be estimated (Table 2).

The SEM images (Fig. 3a and c) of Na–Mo–Mn oxide and NH₄–Mo–Fe oxide show that the materials are polyhedron-shaped crystallites with a particle size of

Table 2 The chemical properties of Na–Mo–Mn oxide and NH₄–Mo–Fe oxide

	Na–Mo–Mn oxide	NH ₄ –Mo–Fe oxide
Crystal system	Cubic	Cubic
Space group	<i>Fd3m</i>	<i>Fd3m</i>
Lattice parameter	19.7047	19.4012
Surrounding site	Mo ^{VI} /Mo ^V = 2/10	Mo ^{VI} /Mo ^V = 3/9
Central site	Mn ^{II}	Fe ^{III} /Fe ^{II} = 0.4/2.2
Linker site	Mn ^{II}	Fe ^{III} /Fe ^{II} = 0.4/2.2
Cation	Na ⁺	NH ₄ ⁺
Chemical formula	Na ₂ H _{10.8} [Mn _{2.6} Mo ₂ ^{VI} Mo ₁₀ ^V O ₄₀]·7H ₂ O	(NH ₄) ₂ H _{9.4} [Fe _{0.4} Fe _{2.2} Mo ₉ Mo ₃ ^{VI} O ₄₀]·3H ₂ O
BET surface area (m ² g ⁻¹)	22	20
Pore volume (cm ³ g ⁻¹)	0.0051	0.0058

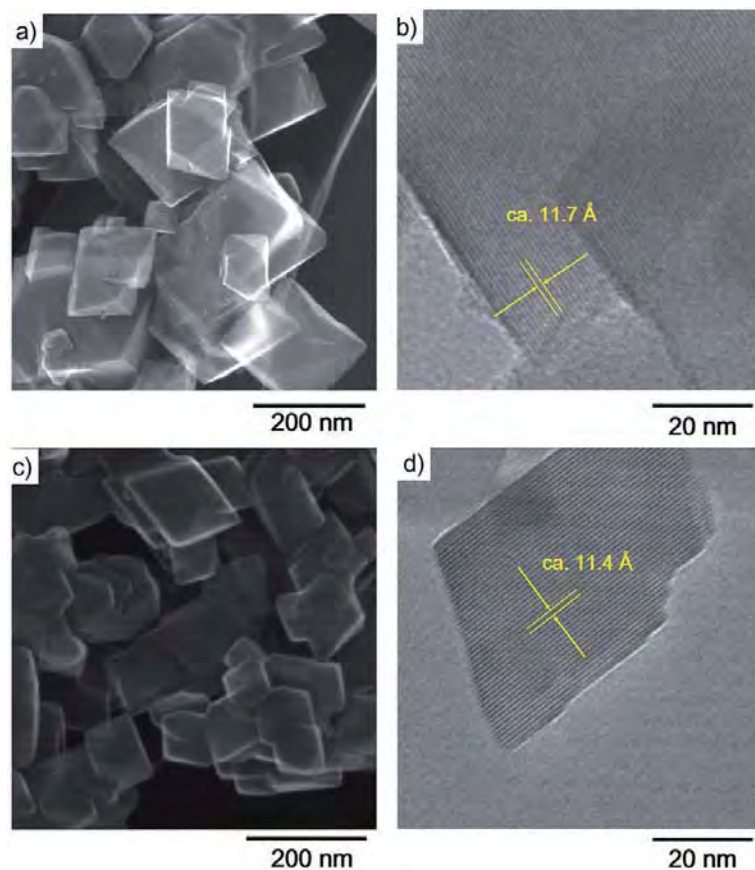


Fig. 3 (a) SEM image and (b) HR-TEM image of Na–Mo–Mn oxide and (c) SEM image and (d) HR-TEM image of NH₄–Mo–Fe oxide.

100–200 nm in diameter. The HR-TEM images further confirmed the structures of the materials (Fig. 3b and d) and showed the clear lattice images of the materials, illustrating that the materials are well-ordered sub-micrometer-sized single crystals. Layers were observed in the HR-TEM images, which corresponded to the (111) plane of the materials. The distances of the (111) plane obtained from the HR-TEM images, *ca.* 11.7 Å for Na–Mo–Mn oxide and *ca.* 11.4 Å for NH₄–Mo–Fe oxide, were in good agreement with the results from the crystal structures of the materials.

3. Microporosity of the materials

The presence of water and NH₄⁺ in the POM-based materials was confirmed by FT-IR analysis (Fig. 2B). NH₄–Mo–Fe oxide showed peak maxima at *ca.* 1630 cm⁻¹ and 1400 cm⁻¹, which corresponded to water and NH₄⁺, respectively. In Na–Mo–Mn oxide, the peak at 1630 cm⁻¹ that corresponded to water was observed. The TPD-MS analysis showed that water and NH₄⁺ in the materials desorbed during a temperature increase (Fig. S3†). The mass numbers of *m/z* = 16 and *m/z* = 18 were attributed to the signals of desorbed NH₃ and water. Water desorbed from the materials from 30 °C to 600 °C in both cases. NH₄–Mo–Fe oxide showed a peak at 320–380 °C for NH₃ desorption in the TPD profile (*m/z* = 16).

The structure of Mo–V–Bi oxide remained after calcination at 350 °C for 2 h, denoted as Mo–V–Bi-NC350.²⁰ On the other hand, Na–Mo–Mn oxide and NH₄–Mo–Fe oxide were stable after calcination at 200 °C for 2 h under a N₂ flow

(Fig. S4†), and the calcined samples were denoted as Na–Mo–Mn–NC200 and NH₄–Mo–Fe–NC200. The remaining molecules in the materials after calcination were investigated by comparison of the TPD-MS profiles before and after calcination (Fig. S3†). The peaks of water ($m/z = 18$) and NH₃ ($m/z = 16$) decreased remarkably after calcination, indicating that the guest molecules in the micropores were partly removed by the heat treatment.

Nitrogen adsorption–desorption measurements were conducted for Mo–V–Bi–NC350, Na–Mo–Mn–NC200 and NH₄–Mo–Fe–NC200 (Fig. 4). In the case of Mo–V–Bi oxide, all guest molecules were removed by calcination at 350 °C without structure collapse, and Mo–V–Bi–NC350 was a microporous material with a BET surface area of 75 m² g⁻¹.²² In the case of the Na–Mo–Mn oxide and NH₄–Mo–Fe oxide the NH₃ and water were partially removed. Nevertheless, the micropores of Na–Mo–Mn–NC200 and NH₄–Mo–Fe–NC200 were also opened (Fig. 4) and the surface areas were calculated using the BET method to be 22 m² g⁻¹ and 20 m² g⁻¹, for Na–Mo–Mn–NC200 and NH₄–Mo–Fe–NC200, respectively, which were apparently smaller than that of Mo–V–Bi–NC350. The high BET surface area of Mo–V–Bi–NC350 mainly resulted from the highly opened micropores due to the high calcination temperature. The less opened micropores of Na–Mo–Mn–NC200 and NH₄–Mo–Fe–NC200 might be ascribed to the remaining NH₄⁺ and Na⁺, which blocked the micropores.

4. Redox properties and O₂ adsorption

The ε-Keggin POM-based microporous materials show redox properties in heating conditions under an H₂ or O₂ atmosphere, because the Mo ions in the materials are a mixture of Mo^V and Mo^{VI}, which can be oxidized to Mo^{VI} and reduced to Mo^V, respectively.²¹

An interesting O₂ adsorption phenomenon of NH₄–Mo–Fe oxide was observed. The materials used for O₂ adsorption were calcined at 200 °C for 2.5 h under high

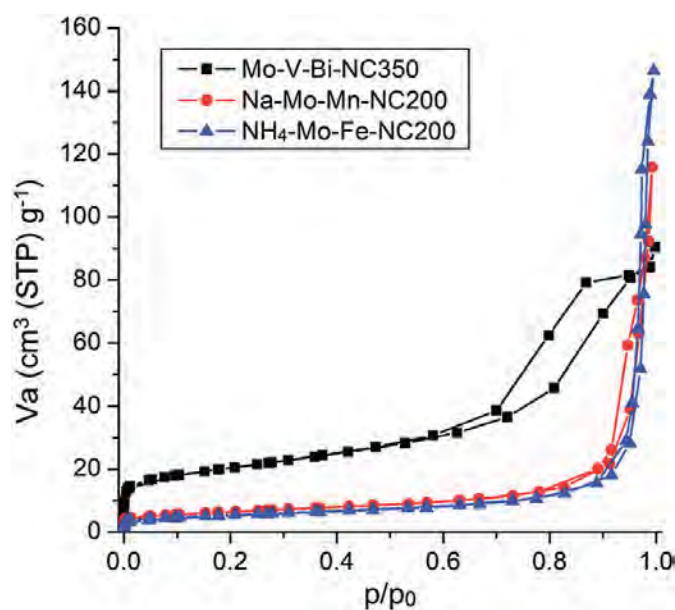


Fig. 4 The N₂ adsorption–desorption isotherms of Mo–V–Bi–NC350, Na–Mo–Mn–NC200, and NH₄–Mo–Fe–NC200.

vacuum before the experiments were conducted, denoted as $\text{NH}_4\text{-Mo-Fe-NC200}$. Calcined Na-Mo-Zn oxide and $\text{NH}_4\text{-Mo-Zn}$ oxide were denoted as Na-Mo-Zn-NC200 and $\text{NH}_4\text{-Mo-Zn-NC200}$. $\text{NH}_4\text{-Mo-Fe-NC200}$ showed an interesting O_2 adsorption property at room temperature. The adsorption-desorption of O_2 isotherms in Fig. 5a and b shows that the O_2 adsorption in $\text{NH}_4\text{-Mo-Fe-NC200}$ increased quickly in the initial adsorption step when the O_2 pressure was low. When the adsorbed amount reached the step, the O_2 uptake in the material almost stopped even when O_2 pressure was still increasing. Most of the adsorbed O_2 in $\text{NH}_4\text{-Mo-Fe-NC200}$ could not desorb from the materials. For other isostructural materials of $\text{NH}_4\text{-Mo-Fe}$ oxide, O_2 adsorption behavior was completely different from that of $\text{NH}_4\text{-Mo-Fe}$ oxide, although the surface areas (Table S4†) and basic structures were similar. The result indicated that the unique O_2 adsorption was dependent on the chemical composition, and only the Fe containing material was active for O_2 adsorption. The Fe site in the material played an important role in O_2 adsorption.

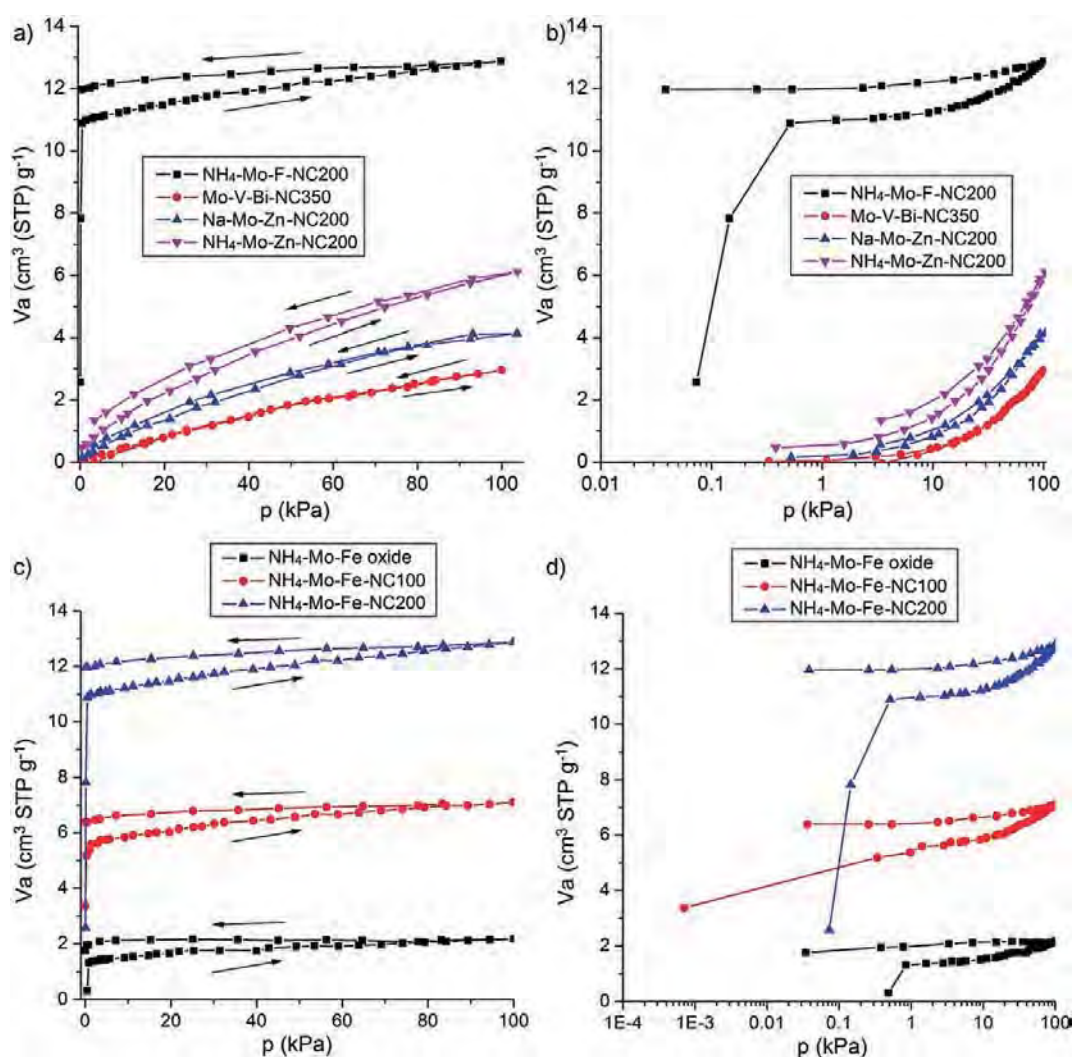


Fig. 5 O_2 adsorption isotherms of different ϵ -Keggin POM-based microporous materials under (a) normal pressure and (b) low pressure at 25 °C. O_2 adsorption isotherms of $\text{NH}_4\text{-Mo-Fe}$ oxide with different pre-treatment temperatures, at (c) normal pressure and (d) low pressure at 25 °C.

The pre-treatment temperature affected the amount of adsorbed O_2 in NH_4 -Mo-Fe oxide. As shown in Fig. 5c and d, as the pre-treatment temperature increased, the total amount of adsorbed O_2 increased. A high pre-treatment temperature removed more water and NH_3 from the material and opened the micropores of the material (Fig. S3†). The result indicated that the O_2 adsorption occurred in the micropores of NH_4 -Mo-Fe-NC200.

After O_2 adsorption, NH_4 -Mo-Fe oxide was characterized. XRD patterns (Fig. 6a) show that the basic structure of the material did not change, because all the characteristic diffraction peaks remained. The XRD peaks shifted to a higher 2θ value, indicating that the lattice parameter decreased after O_2 adsorption.

Adsorption of O_2 in NH_4 -Mo-Fe-NC200 at room temperature gave rise to a different FT-IR spectrum compared with that of the as-synthesized material in Fig. 6b, which can be explained in terms of the binding state change in the material. A new IR band emerged at *ca.* 797 cm^{-1} , corresponding to a $\nu(O-O)$ vibrational mode, which indicated the formation of a peroxy species, and it might coordinate to the Fe site (Fe-O-O).^{28,29} The band at 970 cm^{-1} corresponding to Mo=O shifted to a higher wavenumber (*ca.* 978 cm^{-1}), which demonstrated that the bond length of Mo=O shortened due to dehydration. The FT-IR spectra indicated that the O_2 adsorption in the material was not a simple oxidation process, which formed an Fe peroxy species.

5. Methacrolein oxidation by Mo-V-Bi oxide

Methacrylic acid (MA) becomes a widely used intermediate in its extensive applications to the production of methyl methacrylate and other derivatives. Selective oxidation to produce MA is a two-stage process. Firstly, isobutene oxidation of methacrolein (MAL), and then MAL to MA. For the second step of

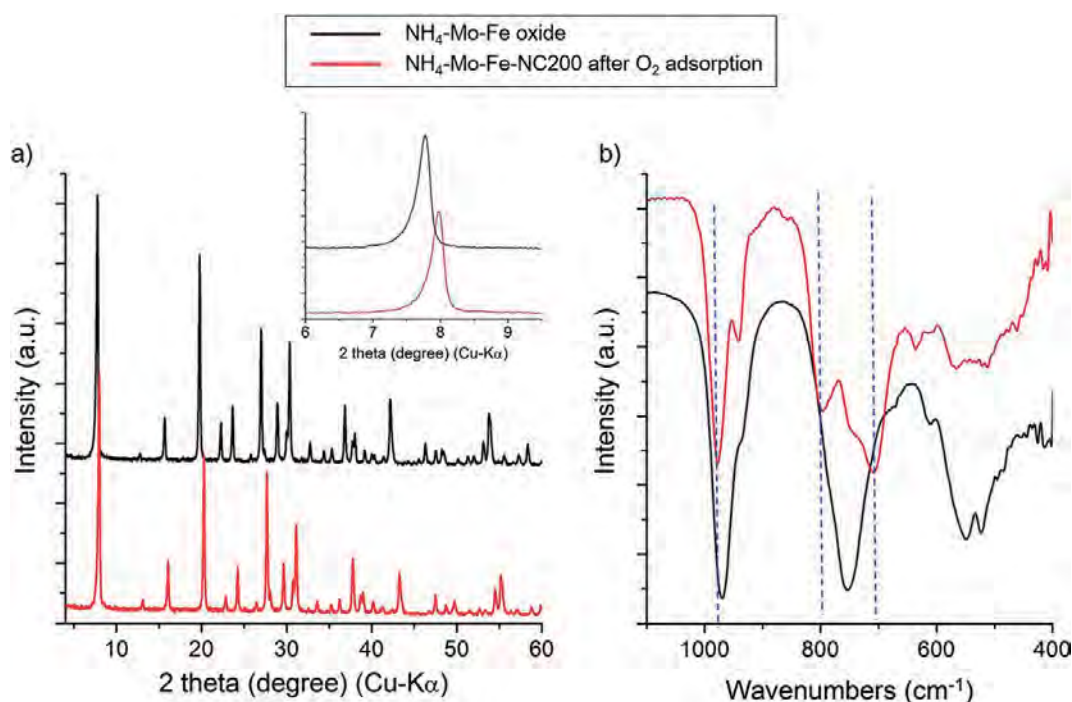


Fig. 6 (a) XRD patterns, inset figure: enlarged XRD patterns and (b) FT-IR spectra of NH_4 -Mo-Fe oxide before and after O_2 adsorption.

the reaction, both oxidation ability and solid acidity are essential, so that Keggin type POM system has been widely used. However, the catalytic performance of the POM catalysts is not satisfactory, although commercialized, and still needs improvement. Therefore, new types of oxide catalysts have been long desired for the reaction. Based on our recent discovery of a new ϵ -Keggin POM-based porous material and considering that Mo–V–Bi oxide has constituents necessary for the selective oxidation of MAL, we applied this material as a catalyst to the reaction.

We first tested the Mo–V–Bi oxide with crystal particles in nanosize (20–50 nm in diameter²²) for the MAL oxidation after calcination at 350 °C in N₂ stream (designated as Mo–V–Bi–N350(nano)). Conversions of MAL and O₂ and selectivity to MA, acetic acid (AcOH), CO, and CO₂ are shown in Fig. 7. Very interestingly, the reaction appreciably occurred over the catalyst even at 228 °C and yielded MA with 60% selectivity, which is comparable to that of a normal Keggin POM catalyst. The MAL conversion increased with increasing reaction temperature and was 28.1% at 270 °C. The MA selectivity gradually decreased as the reaction temperature increased. The AcOH selectivity, on the other hand, lineally increased with the reaction temperature and was 21.2% and 31.4% at 220 °C and 270 °C, respectively. The CO and CO₂ selectivity also increased with increasing reaction temperature. After the catalytic reaction, no changes in the XRD patterns and FT-IR spectra were observed (Fig. S5†), indicating that the basic crystal structure of the catalyst was maintained during the reaction. Evidently, the Mo–V–Bi oxide can be a new member of the oxidation catalysts for the selective oxidation of MAL.

The pore size of Mo–V–Bi oxide is 3.4 nm,²⁰ which is much smaller than the size of MAL, for which the molecular size was calculated to be 4.9 nm in minimum as calculated using the DMol³ program, and thus the reaction would take place on the external surface of the material. To test that the catalytic activity was dependent on the external surface area of the materials, a well-crystallized Mo–V–Bi–NC350 with a large particle size (1 μ m in diameter) was synthesized (Fig. S5Ac†)²⁰ and used for comparison. The activity of Mo–V–Bi–NC350 (large) was poor as expected. MAL conversion at 228 °C was *ca.* 5%, which was half of that of Mo–V–Bi–NC350(nano). The selectivity to MA was a little affected by the size of the catalyst particles.

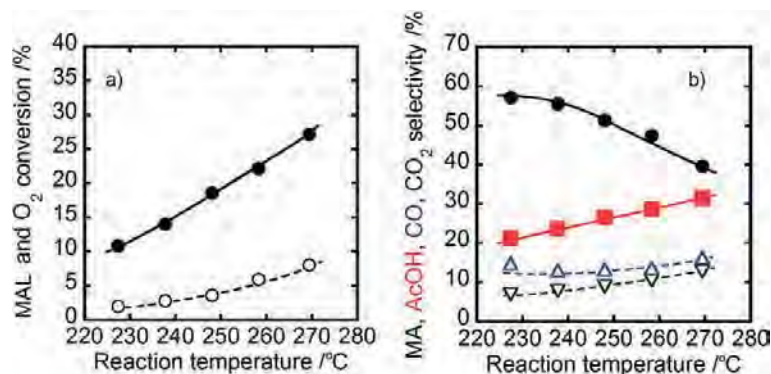


Fig. 7 MAL oxidation catalyzed by Mo–V–Bi–NC350(nano) with O₂ as an oxidant. The conversion of MAL (closed circle) and O₂ (open circle) in (a) and the selectivity (mol %) to MA (closed circle), AcOH (closed square), CO (triangle), and CO₂ (reverse triangle) in (b) as a function of the reaction temperature.

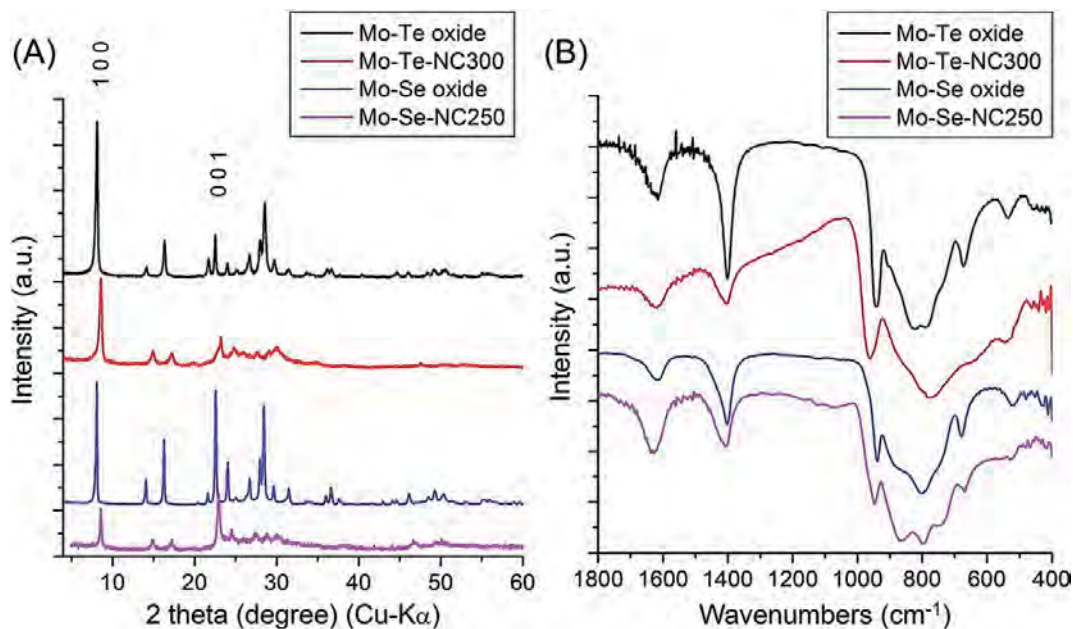


Fig. 8 (A) XRD patterns of (a) Mo–Te oxide and (b) Mo–Te–NC300 and (B) FT-IR spectra of (a) Mo–Te oxide and (b) Mo–Te–NC300.

6. Synthesis and characterization of crystalline metal oxides based on a molecular wire

Using the VI A group metal ions, such as Te and Se, a new POM-based molecular wire structure was prepared. The hydrothermal synthesis of $(\text{NH}_4)_6\text{Mo}_7\text{O}_{24} \cdot 4\text{H}_2\text{O}$ with Te^{IV} and Se^{IV} ions yielded novel metal oxides, Mo–Te oxide and Mo–Se oxide. The XRD patterns and FT-IR spectra are shown in Fig. 8. Six MoO_6 units surround one Te or Se ion in the a – b plane, which form a unit of $[\text{XMo}_6\text{O}_{21}]^{2-}$ ($X = \text{Te}$ or Se). The hexagonal units stack along the c axis to form prismatic clusters as molecular wires. The molecular wires assembled in parallel in a hexagonal fashion to form the crystalline material with NH_4^+ and water, which existed in between the molecular wires and interacted with them (Fig. 1d–f).

The existence of water and NH_4^+ in Mo–Te oxide and Mo–Se oxide was confirmed by FT-IR (Fig. 8B), which exhibited bands at *ca.* 1630 cm^{-1} for water and at *ca.* 1400 cm^{-1} for NH_4^+ . Water and NH_4^+ stabilized the crystal structures of the Mo–Te oxide and the Mo–Se oxide. Proton-exchange with NH_4^+ in the Mo–Te oxide effectively cracked the crystal of the material, keeping the structure of a molecular wire. The molecular wire can be isolated from the crystal and can be observed.²⁵

After calcination of the Mo–Te oxide at $300 \text{ }^\circ\text{C}$ and the Mo–Se oxide at $250 \text{ }^\circ\text{C}$ for 2 h under N_2 (designated as Mo–Te–NC300 and Mo–Se–NC250), the XRD patterns of the materials showed that the peaks ascribed to the (100) plane shifted to a high angle, indicating that the distance between the molecular wires decreased (Fig. 8A). The diffraction peaks for the (100) and (001) planes still remained in the calcined material, indicating that the molecular wires were still in the structures after calcination. A comparison of the FT-IR spectra before and after calcination indicated that the molecular structure of the Mo–Te oxide was stable after calcination at $300 \text{ }^\circ\text{C}$. After calcination, the IR peak for NH_4^+

(1400 cm^{-1}) decreased remarkably, and NH_3 was removed from the material to leave protons as acid sites.

7. Catalytic hydrolysis of cellobiose

Biomass utilization is of great importance, because of increasing attention to the consumption of energy resources for sustainable society and development. Cellulose is a big class of biomass, and conversion of cellulose to useful chemicals is one of the most important biomass conversion routes. The first step of cellulose conversion is hydrolysis of the glycosidic bond to form hexose that further transforms to other chemicals under certain reaction conditions. Brønsted acids are active for cellulose hydrolysis.^{30–32} Cellobiose, formed by two glucose molecules, is an ideal model substrate for the investigation of glycosidic bond hydrolysis, and the novel complex metal oxides mentioned above are expected to be active for the reaction.

After calcination, NH_3 desorbed from the porous POMs and the transition metal oxide molecular wires, and protons emerged in the materials which may act as acid sites. The materials were used as catalysts for the hydrolysis of cellobiose (Table 3). The identified products in the resulting solution are glucose, mannose, formic acid (FA), AcOH, and 5-hydroxymethylfurfural (HMF). Glucose was a direct product formed by the hydrolysis of the glycosidic bond of cellobiose. Mannose was formed by the isomerization of glucose in aqueous solution. HMF was formed by further dehydration of hexoses. The fragment molecules such as FA and AA are formed by C–C bond cleavage. The undetectable products might be ascribed to humin, which commonly forms in biomass conversion.^{33,34} Mo–V–Bi–NC350 showed the best performance among the ϵ -Keggin POM-based porous materials (Table 3, entries 1–3). For Mo–Te–NC300 and Mo–Se–NC250, the conversion of cellobiose and the yield of glucose and mannose were higher than all the ϵ -Keggin POM-based porous materials (Table 3, entries 4 and 5), which might be due to well-dispersed catalysts in the reaction media. The activity was low when no catalyst was used (Table 3, entry 6). After the reaction, the XRD patterns and FT-IR spectra of the porous POMs were identical, indicating that the materials were stable (Fig. S6†). The nanowires were too small to be recovered.

Table 3 Hydrolysis of cellobiose catalyzed by different materials^a

Entry	Catalyst	Conversion (%)	Yield based on carbon (%)					Other
			Glucose	Mannose	FA	AcOH	HMF	
1	Mo–V–Bi–NC350	50.7	14.9	12.9	2.8	0.5	1.3	18.3
2	NH_4 –Mo–Mn–NC200	37.6	4.1	4.5	0.6	0.4	0.7	27.3
3	NH_4 –Mo–Fe–NC200	50.4	10	10.3	0.9	0.3	1.0	27.9
4	Mo–Te–NC300	74.4	16.1	16.6	1.8	0.3	1.6	38.0
5	Mo–Se–NC250	90.0	18.1	20.4	1.9	0.4	2.3	46.9
6	—	7.4	6.8	0	0	0	0.6	0

^a Reaction conditions: hydrolysis of cellobiose catalyzed by different materials, reaction conditions: cellobiose (0.05 g), catalyst (0.01 g), water (0.5 mL), reaction time (2 h), and reaction temperature ($160\text{ }^\circ\text{C}$).

Conclusion

Assembly of Mo POM units with octahedra of other elements forms POM unit-structured materials. By this assembling methodology, two kinds of novel complex Mo oxides are constructed, all-inorganic ϵ -Keggin POM-based 3D microporous materials and molecular wire-based crystalline metal oxides. The results strongly indicate that the use of POM units is an effective approach for the design and development of novel transition metal oxide catalysts.

In this research, two new all-inorganic ϵ -Keggin POM-based 3D framework materials, Na–Mo–Mn oxide and NH_4 –Mo–Fe oxide, were synthesized and characterized. Structural analysis clearly demonstrates that ϵ -Keggin POMs are connected with metal ions (Mn and Fe) to form $\{\text{H}_{10.8}[\text{Mn}_{2.6}^{\text{II}}\text{Mo}_2^{\text{VI}}\text{Mo}_{10}^{\text{V}}\text{O}_{40}]\}^{2-}$ and $\{\text{H}_{9.4}[\text{Fe}_{2.6}\text{Mo}_9^{\text{V}}\text{Mo}_3^{\text{VI}}\text{O}_{40}]\}^{2-}$. These two materials are iso-structural to the reported Mo–V–Bi oxide. Furthermore, a unique O_2 adsorption phenomenon is observed in NH_4 –Mo–Fe oxide at 25 °C. The adsorption of O_2 in the Fe site may form Fe peroxo species. Mo–V–Bi oxide shows activity for MAL oxidation to produce MA with O_2 . The novel materials, ϵ -Keggin POM-based porous materials and the molecular wire-based metal oxides, are effective solid acids for the hydrolysis of cellobiose in aqueous solution. The present research provides a new approach using POM as units to construct new transition metal oxides for catalysis.

Acknowledgements

This work was financially supported by a Grant-in-Aid for Scientific Research (A) (grant No. 2324-6135) from the Ministry of Education, Culture, Sports, Science, and Technology, Japan.

References

- 1 M. Sadakane and W. Ueda, Ordered Porous Crystalline Transition Metal Oxides, in *Porous Materials*, ed. D. W. Bruce, D. O'Hare, and R. I. Walton, Wiley, 2011, vol. 11, pp. 147–216.
- 2 Y. Kamiya, M. Sadakane, and W. Ueda, Heteropoly Compounds, in *Comprehensive Inorganic Chemistry II*, ed. J. Reedijk and K. Poeppelmeier, Oxford, Elsevier, 2013, vol. 7, pp. 185–204.
- 3 M. T. Pope, *Heteropoly and Isopoly Oxometalates*, Springer-Verlag, Berlin, 1983.
- 4 Special thematic issue on polyoxometalates, *Chem. Soc. Rev.*, ed. L. Cronin and A. Müller, 2012, vol. 41, pp. 7325–7648.
- 5 Special thematic issue on polyoxometalates, *Chem. Rev.*, ed. C. L. Hill, 1998, vol. 98, pp. 1–390.
- 6 H. N. Miras, L. Vilà-Nadal and L. Cronin, *Chem. Soc. Rev.*, 2014, **43**, 5679–5699.
- 7 D.-L. Long, R. Tsunashima and L. Cronin, *Angew. Chem., Int. Ed.*, 2010, **49**, 1736–1758.
- 8 B. Nohra, H. El Moll, L. M. Rodriguez Albelo, P. Mialane, J. Marrot, C. Mellot-Draznieks, M. O'Keeffe, R. N. Biboum, J. Lemaire, B. Keita, L. Nadjo and A. Dolbecq, *J. Am. Chem. Soc.*, 2011, **133**, 13363–13374.
- 9 L. M. Rodriguez-Albelo, A. Rabdel Ruiz-Salvador, A. Sampieri, D. W. Lewis, A. Gomez, B. Nohra, P. Mialane, J. Marrot, F. Secheresse, C. Mellot-

- Draznieks, R. N. Biboum, B. Keita, L. Nadjo and A. Dolbecq, *J. Am. Chem. Soc.*, 2009, **131**, 16078–16087.
- 10 M. Sadakane, K. Kodato, T. Kuranishi, Y. Nodasaka, K. Sugawara, N. Sakaguchi, T. Nagai, Y. Matsui and W. Ueda, *Angew. Chem., Int. Ed.*, 2008, **47**, 2493–2496.
- 11 M. Sadakane, K. Yamagata, K. Kodato, K. Endo, K. Toriumi, Y. Ozawa, T. Ozeki, T. Nagai, Y. Matsui, N. Sakaguchi, W. D. Pyrz, D. J. Buttrey, D. A. Blom, T. Vogt and W. Ueda, *Angew. Chem., Int. Ed.*, 2009, **48**, 3782–3786.
- 12 M. Sadakane, N. Watanabe, T. Katou, Y. Nodasaka and W. Ueda, *Angew. Chem., Int. Ed.*, 2007, **46**, 1493–1496.
- 13 S. G. Mitchell, C. Streb, H. N. Miras, T. Boyd, D.-L. Long and L. Cronin, *Nat. Chem.*, 2010, **2**, 308–312.
- 14 S. G. Mitchell, T. Boyd, H. N. Miras, D.-L. Long and L. Cronin, *Inorg. Chem.*, 2011, **50**, 136–143.
- 15 S. Uchida, R. Eguchi and N. Mizuno, *Angew. Chem., Int. Ed.*, 2010, **49**, 9930–9934.
- 16 S. Uchida, M. Hashimoto and N. Mizuno, *Angew. Chem., Int. Ed.*, 2002, **41**, 2814–2817.
- 17 S. Uchida, S. Hikichi, T. Akatsuka, T. Tanaka, R. Kawamoto, A. Lesbani, Y. Nakagawa, K. Uehara and N. Mizuno, *Chem. Mater.*, 2007, **19**, 4694–4701.
- 18 S. Uchida and N. Mizuno, *J. Am. Chem. Soc.*, 2004, **126**, 1602–1603.
- 19 S. Uchida and N. Mizuno, *Coord. Chem. Rev.*, 2007, **251**, 2537–2546.
- 20 Z. Zhang, M. Sadakane, T. Murayama, S. Izumi, N. Yasuda, N. Sakaguchi and W. Ueda, *Inorg. Chem.*, 2014, **53**, 903–911.
- 21 Z. Zhang, M. Sadakane, T. Murayama, N. Sakaguchi and W. Ueda, *Inorg. Chem.*, 2014, **53**, 7309–7318.
- 22 Z. Zhang, M. Sadakane, T. Murayama and W. Ueda, *Dalton Trans.*, 2014, **43**, 13584–13590.
- 23 Z. Zhang, M. Sadakane, S. Noro, T. Murayama, T. Kamachi, K. Yoshizawa and W. Ueda, *J. Mater. Chem. A*, 2015, **3**, 746–755.
- 24 Z. Zhang, M. Sadakane and W. Ueda, Assembly of Epsilon-Keggin-Type Polyoxometalates to form Crystalline Microporous Metal Oxides in Trends, in *Polyoxometalates Research*, ed. L. Ruhlmann and D. Schaming, Nova Science Publishers, 2015.
- 25 Z. Zhang, T. Murayama, M. Sadakane, H. Ariga, N. Yasuda, N. Sakaguchi, K. Asakura and W. Ueda, *Nat. Commun.*, 2015, **6**, 7731.
- 26 R. A. Young, *The Rietveld method*, Oxford University Press, Oxford, 1995.
- 27 P. Mialane, A. Dolbecq, L. Lisnard, A. Mallard, J. Marrot and F. Secheresse, *Angew. Chem., Int. Ed.*, 2002, **41**, 2398–2401.
- 28 E. D. Bloch, L. J. Murray, W. L. Queen, S. Chavan, S. N. Maximo, J. P. Bigi, R. Krishna, V. K. Peterson, F. Grandjean, O. G. J. Long, B. Smit, S. Bordiga, C. M. Brown and R. Long, *J. Am. Chem. Soc.*, 2011, **133**, 14814–14822.
- 29 D. Barats, G. Leitius, R. Popovitz-Biro, L. J. W. Shimon and R. Neumann, *Angew. Chem., Int. Ed.*, 2008, **47**, 9908–9912.
- 30 K. Shimizu, H. Furukawa, N. Kobayashi, Y. Itaya and A. Satsuma, *Green Chem.*, 2009, **11**, 1627–1632.
- 31 S. Sukanuma, K. Nakajima, M. Kitano and D. Yamaguchi, *J. Am. Chem. Soc.*, 2008, **130**, 12787–12793.
- 32 Y.-B. Huang and Y. Fu, *Green Chem.*, 2013, **15**, 1095–1111.

- 33 R. Weingarten, W. C. Conner and G. W. Huber, *Energy Environ. Sci.*, 2012, **5**, 7559–7574.
- 34 R. Weingarten, Y. T. Kim, G. a. Tompsett, A. Fernández, K. S. Han, E. W. Hagaman, W. C. Conner, J. a. Dumesic and G. W. Huber, *J. Catal.*, 2013, **304**, 123–134.

Synthesis of Trigonal Mo–V–M^{3rd}–O (M^{3rd} = Fe, W) Catalysts by Using Structure-Directing Agent and Catalytic Performances for Selective Oxidation of Ethane

Satoshi Ishikawa^{1,2} · Toru Murayama³ · Masahiro Kumaki¹ · Masaya Tashiro⁴ · Zhenxin Zhang¹ · Akihiro Yoshida¹ · Wataru Ueda¹

Published online: 3 August 2016
© Springer Science+Business Media New York 2016

Abstract Crystalline Mo–V–M^{3rd}–O (M^{3rd} = Fe, W) catalysts (MoVFeO and MoVVO) with trigonal symmetry were successfully obtained by a hydrothermal method in the presence of structure-directing agents (ammonium cation and ethylammonium cation) and their catalytic performances for selective oxidation of ethane were compared with trigonal Mo₃VO_x catalyst (MoVO). Fe and W were uniformly distributed throughout the rod-shaped crystals. XRD, Raman, XRD simulation, and Rietveld analysis revealed that MoVFeO contained Fe in a heptagonal channel and W in MoVVO substituted Mo in {Mo₆O₂₁}⁶⁻ pentagonal unit in the structure. MoVVO catalyst showed comparable catalytic activity with MoVO for the selective oxidation of ethane. On the other hand, catalytic performance of MoVFeO was far less compared with those of MoVO and MoVVO. The picture that the catalytic reaction occurs at the specific part in the structure could be visualized.

Keywords Crystalline Mo–V–O catalysts · Selective oxidation · Structure–activity relationship

1 Introduction

Crystalline Mo₃VO_x catalysts (MoVO) have been attracting much attention because of its outstanding catalytic activity for the selective oxidation of ethane and acrolein [1–7]. Among these, trigonal Mo₃VO_x catalyst (Tri-MoVO) was firstly discovered by our group in 2007 which promoted a lot of researches including its physicochemical properties and catalytic properties [8–11]. Tri-MoVO is comprised of a network arrangement based on {Mo₆O₂₁}⁶⁻ pentagonal units and MO₆ (M = Mo and V) octahedral units. This arrangement forms hexagonal and heptagonal channels in their *a*-*b* basal planes, which are stacked for each other along *c*-direction to form a rod-shaped crystal (Fig. 1) [8–10]. It has been revealed that the heptagonal channel in the structure acts as a micropore to adsorb small molecules such as N₂, CO₂, CH₄, C₂H₆, and C₃H₈. Interestingly, in the selective oxidation of ethane, the reaction of ethane to ethene takes place inside the heptagonal channel [3–5, 12–14].

MoVO is formed by a hydrothermal synthesis of precursor solution containing ball-type polyoxometalate, [Mo₇₂V₃₀O₂₈₂(H₂O)₅₆(SO₄)₁₂]³⁶⁻ ({Mo₇₂V₃₀}), in which 12 {Mo₆O₂₁}⁶⁻ pentagonal units are connected with 30 [V = O]²⁺ units [3, 7, 15]. {Mo₇₂V₃₀} provides the {Mo₆O₂₁}⁶⁻ pentagonal units and MO₆ octahedra (M = Mo and V) as building units and MoVO is formed by the arrangement of these units. During the crystal formation process, NH₄⁺ cation which is provided by the Mo source ((NH₄)₆Mo₇O₂₄·4H₂O) is incorporated into the heptagonal channel [16–19]. Recently, we have shown that the counter cation in the heptagonal channel is replaceable by an

Electronic supplementary material The online version of this article (doi:10.1007/s11244-016-0666-z) contains supplementary material, which is available to authorized users.

✉ Wataru Ueda
uedaw@kanagawa-u.ac.jp

- ¹ Department of Material and Life Chemistry, Faculty of Engineering, Kanagawa University, 3-27, Rokkakubashi, Kanagawa-Ku, Yokohama 221-8686, Japan
- ² Research Fellow of Japan Society for the Promotion of Science, 5-7, Chiyoda-ku, Tokyo 102-0076, Japan
- ³ Department of Applied Chemistry, Graduate School of Urban Environmental Sciences, Tokyo Metropolitan University, 1-1 Minami-osawa, Hachioji, Tokyo 192-0397, Japan
- ⁴ Catalysis Research Center, Hokkaido University, N-21, W-10, Sapporo 001-0021, Japan

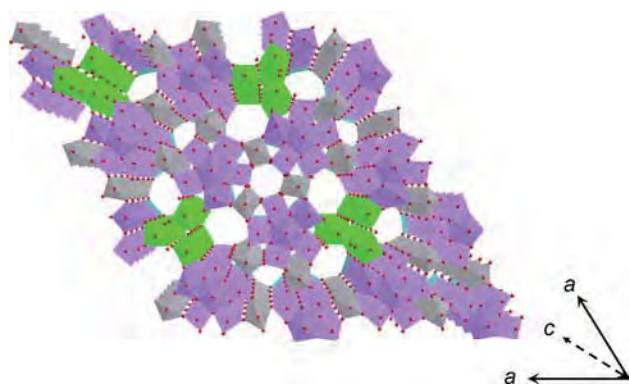


Fig. 1 Crystal structure of trigonal Mo_3VO_x . Mo, purple; V, gray; mixture of Mo and V, green

alkylammonium cation such as methylammonium cation or dimethylammonium cation [20]. We have reported that the addition of $(\text{C}_2\text{H}_5)_3\text{NHCl}$ promoted the crystallization of MoVO when additional element (ex. Al, Fe, Ga) was present together with Mo and V, although at that moment we could not know the role of $(\text{C}_2\text{H}_5)_3\text{NHCl}$ on the crystallization and the structure of MoVO [21].

We now speculate that the combination of an additional element and an alkylammonium cation can form well-crystallized MoVO having additional elements inside the structure. The incorporation of additional elements is considered to give an additional catalytic function which may result in the improvement of the catalytic activity. For example, the addition of W into the Mo–V based oxides has widely been studied to improve the catalytic performance for the selective oxidations [22, 23]. In the present study, we demonstrate that ethylammonium cation can work as a proper structure-directing agent to form trigonal Mo–V– $\text{M}^{3\text{rd}}\text{–O}$ ($\text{M}^{3\text{rd}} = \text{Fe}, \text{W}$). Obtained catalysts (MoVFeO and MoVWO) contained Fe and W uniformly in the crystal structure. The important point of these catalysts is that the additional elements (Fe, W) were located at different positions in the crystalline structure. The position of these additional elements in the crystal structure significantly influenced the catalytic activity for the selective oxidation of ethane. Strong structure–activity relationship for the selective oxidation of ethane could be observed by combining characterizations and a catalytic reaction. This findings can provide (1) the useful information to create complex mixed metal oxide with multi-functionality and (2) the molecular-level understanding of ethane oxidation which enable us to understand the strategy to design the active catalysts for selective oxidations.

2 Experimental

2.1 Synthesis of Trigonal Mo_3VO_x Oxide

Tri- Mo_3VO_x was synthesized by a hydrothermal method. 8.828 g of $(\text{NH}_4)_6\text{Mo}_7\text{O}_{24}\cdot 4\text{H}_2\text{O}$ (Mo: 50 mmol, Wako)

was dissolved in 120 mL of distilled water. Separately, an aqueous solution of VOSO_4 was prepared by dissolving 3.290 g of hydrated VOSO_4 (V: 12.5 mmol, Mitsui Chemicals) in 120 mL of distilled water. The two solutions were mixed at ambient temperature and stirred for 10 min. At the moment, pH value of the solution was 3.2. Then, 3.5 mL of 2 M H_2SO_4 solution was added to decrease the pH to 2.2 and the solution was stirred for another 10 min. The obtained mixed solution was introduced into an autoclave with a 300 mL-Teflon inner vessel and 4000 cm^2 of Teflon thin sheet to occupy about half of Teflon inner vessel space. After the introduction, N_2 was fed into the solution in the tube in order to remove residual oxygen. Then the hydrothermal reaction was started at 175 °C for 20 h under static conditions in an electric oven. Formed gray solids were washed with distilled water, and dried in air at 80 °C overnight. Obtained material was abbreviated as MoVO-A-fresh. Then, purification with oxalic acid was conducted in order to remove an impurity. To 25 mL aqueous solution (0.4 mol L^{-1} , 60 °C) of oxalic acid (Wako), 1 g of the dried material was added and stirred for 30 min, then washed with 500 mL of distilled water after filtration. The sample after the purification was abbreviated as MoVO-A. Prior to the catalytic test, MoVO-A was calcined under static air for 2 h at 400 °C with 10 °C min^{-1} ramp rate in a muffle oven. Obtained material was abbreviated as MoVO-A-AC.

2.2 Preparation of Mo–V– $\text{M}^{3\text{rd}}\text{–O}$ Oxide ($\text{M}^{3\text{rd}}: \text{Fe}, \text{W}$)

For synthesizing Mo–V– $\text{M}^{3\text{rd}}\text{–O}$ ($\text{M}^{3\text{rd}} = \text{Fe}, \text{W}$), ethylammonium trimolybdate (EATM, $(\text{CH}_3\text{CH}_2\text{NH}_3)_2\text{Mo}_3\text{O}_{10}$) was used as a Mo source instead of $(\text{NH}_4)_6\text{Mo}_7\text{O}_{24}\cdot 4\text{H}_2\text{O}$. EATM was prepared according to our previously paper [7, 20, 24]. 21.594 g of MoO_3 (0.150 mol, Kanto) was dissolved in 28.0 mL of 70 % ethylamine solution (ethylamine: 0.300 mol, Wako) diluted with 28.0 mL of distilled water. The reason for the addition of distilled water is to reduce the viscosity of the mixed solution. After being completely dissolved, the solution was evaporated under vacuum condition ($P/P_0 = 0.03$) at 70 °C and then solid powder was obtained. The powder was dried in air at 80 °C overnight.

1.799 g of EATM (Mo: 10 mmol) was dissolved in 20 mL of distilled water. Separately, an aqueous solution of VOSO_4 was prepared by dissolving 0.658 g of hydrated VOSO_4 (V: 2.5 mmol) in 20 mL of distilled water. The two solutions were mixed at ambient temperature and stirred for 10 min before the addition of 0.301 g of $\text{Fe}(\text{NH}_4)(\text{SO}_4)_2\cdot 12\text{H}_2\text{O}$ (Fe: 0.625 mmol, Wako) or 0.160 g of $(\text{NH}_4)_6[\text{H}_2\text{W}_{12}\text{O}_{40}]\cdot n\text{H}_2\text{O}$ (W: 0.625 mmol, Nippon Inorganic Colour and Chemical Co., Ltd.). The pH value changed from 2.4 to 2.0 by the addition of

$\text{Fe}(\text{NH}_4)(\text{SO}_4)_2 \cdot 12\text{H}_2\text{O}$ but no pH value change was observed by the addition of $(\text{NH}_4)_6[\text{H}_2\text{W}_{12}\text{O}_{40}] \cdot n\text{H}_2\text{O}$ (from 2.4 to 2.4). Obtained mixed solution was introduced into an autoclave with a 50 mL-Teflon inner vessel and 800 cm^2 of a Teflon thin sheet to occupy about half of Teflon inner vessel space. After being introduced, N_2 was fed into the solution in order to remove a residual oxygen. Then, the hydrothermal reaction was carried out at $175 \text{ }^\circ\text{C}$ for 48 h under static condition. Formed gray solids were separated by filtration, washed with distilled water, and dried in an air at $80 \text{ }^\circ\text{C}$ overnight. Obtained materials were abbreviated as MoVFeO-EA-fresh and MoVWO-EA-fresh, respectively. When third metals were not used in this condition, obtained material was denoted as MoVO-EA-fresh. Purification with oxalic acid was conducted for the obtained solids in order to remove an amorphous type material which was formed as an impurity. To 25 mL aqueous solution (0.4 mol L^{-1} , $60 \text{ }^\circ\text{C}$) of oxalic acid (Wako), 1 g of the dried material was added and stirred for 30 min, then washed with 500 mL of distilled water after filtration. Obtained materials were abbreviated as MoV-FeO-EA and MoVWO-EA, respectively. Prior to the catalytic test, these materials were calcined under static air for 2 h at $400 \text{ }^\circ\text{C}$ with $10 \text{ }^\circ\text{C min}^{-1}$ ramp rate in a muffle oven. The obtained materials were abbreviated as MoV-FeO-EA-AC and MoVWO-EA-AC, respectively.

As a comparison, Mo–V–M^{3rd}–O catalysts were synthesized using $(\text{NH}_4)_6\text{Mo}_7\text{O}_{24} \cdot 4\text{H}_2\text{O}$ as a Mo precursor. 1.766 g of $(\text{NH}_4)_6\text{Mo}_7\text{O}_{24} \cdot 4\text{H}_2\text{O}$ was dissolved in 20 mL of distilled water. This solution was mixed with an aqueous solution prepared by dissolving 0.658 g of hydrated VOSO_4 (V: 2.5 mmol) in 20 mL of distilled water. The two solutions were mixed at ambient temperature and stirred for 10 min before the addition of 0.301 g of $\text{Fe}(\text{NH}_4)(\text{SO}_4)_2 \cdot 12\text{H}_2\text{O}$ (Fe: 0.625 mmol) or 0.160 g of $(\text{NH}_4)_6[\text{H}_2\text{W}_{12}\text{O}_{40}] \cdot n\text{H}_2\text{O}$ (W: 0.625 mmol). pH change was observed by the addition of $\text{Fe}(\text{NH}_4)(\text{SO}_4)_2 \cdot 12\text{H}_2\text{O}$ (from 3.2 to 2.5). On the other hand, no pH change was observed by the addition of $(\text{NH}_4)_6[\text{H}_2\text{W}_{12}\text{O}_{40}] \cdot n\text{H}_2\text{O}$ (from 3.2 to 3.2) Then, pH value was controlled to 2.0 when Fe source was used and to 2.4 when W source was used by adding 2 M H_2SO_4 solution. After the N_2 bubbling for 10 min, the hydrothermal synthesis was carried out at $175 \text{ }^\circ\text{C}$ for 48 h. The formed solids were abbreviated as MoVFeO-A-fresh and MoVWO-A-fresh, respectively. In addition, we synthesized Mo–V–M^{3rd}–O with the addition of $(\text{CH}_3\text{CH}_2\text{NH}_3)\text{Cl}$ when AHM was used as a Mo source. In this preparation, 0.544 g of $(\text{CH}_3\text{CH}_2\text{NH}_3)\text{Cl}$ (EACl, 6.67 mmol, MERCK) was added into the mixed solution of Mo, V, M^{3rd} before controlling the pH. No pH change was observed by the addition of EACl. After controlling the pH of the precursor solution with 2 M H_2SO_4 (M^{3rd} = Fe, 2.0; M^{3rd} = W, 2.4), hydrothermal synthesis at $175 \text{ }^\circ\text{C}$ for 48 h

was carried out. The formed solids after the hydrothermal synthesis were abbreviated as MoVFeO-(A+EACl)-fresh and MoVWO-(A+EACl)-fresh, respectively. When third metals were not used in the presence of EACl, the formed solid was abbreviated as MoVO-(A+EACl)-fresh.

2.3 Characterization of Synthesized Materials

The synthesized materials were characterized by the following techniques: Powder XRD patterns were recorded with a diffractometer (RINT Ultima+, Rigaku) using $\text{Cu-K}\alpha$ radiation (tube voltage: 40 kV, tube current: 40 mA). For XRD measurements, the prepared samples were ground for 5 min with Si standard in order to correct peak position and to exclude an orientation effect. Diffractions were recorded in the range of 4° – 80° with $1^\circ/\text{min}$ scan speed. Raman spectra (inVia Reflex Raman spectrometer, RENISHAW) were measured in air for a static sample with Ar laser (532 nm). FT-IR analysis was carried out using a spectrometer (FT/IR-4700, JASCO) with a TGS detector. IR spectra were obtained by integrating more than 256 scans with a resolution of 4 cm^{-1} . CHN elemental composition was determined using Micro Corder JM10 (Yanaco). Elemental compositions in the bulk were determined by ICP-AES (ICPE-9000, Shimadzu). XPS (JPC-9010MC, JEOL) with a non-monochromatic $\text{Mg-K}\alpha$ radiation was used for measuring binding energy values of Mo and V. Temperature-programmed desorption (TPD) was carried out using an auto chemisorption system (BEL Japan). The catalyst (ca. 50 mg) was set between two layers of quartz wool and stabilized under helium (50 mL min^{-1}) at $400 \text{ }^\circ\text{C}$ for 10 min. Then, desorption profile from 40 to $600 \text{ }^\circ\text{C}$ was recorded with a mass spectrometer under helium flow (50 mL min^{-1}). The measurements of TPD under $\text{He}/\text{O}_2 = 45/5 \text{ mL min}^{-1}$ flow (TPO) was performed with the same apparatus. STEM-EDX analysis and mapping analysis were conducted by using HD-2000 (Hitachi). For these analyses, samples were dispersed with ethanol and treated by ultrasonic equipment. Supernatant liquid was dropped on the Cu-grid and was dried overnight for the analysis. N_2 adsorption isotherms at liq. N_2 temperature were obtained using an auto-adsorption system (BELSORP MAX, Nippon BELL). External surface areas and micropore volumes were determined using a t -plot in the t range from 0.15 to 0.90. Prior to N_2 adsorption, the catalysts were heat-treated under vacuumed condition at $300 \text{ }^\circ\text{C}$ for 2 h.

Rietveld refinement was performed for MoVO-A-AC, MoVFeO-EA-AC, and MoVWO-EA-AC using Materials Studio 7.1 (Accelrys). The XRD patterns after correcting the peak position were subjected to the refinement. First, the Rietveld refinement for MoVO-A-AC was performed using the structural model of trigonal Mo_3VO_x obtained

from our previous paper [8]. All metal atom positions were refined. After the refinement of metal positions, oxygen atom positions were refined to set a proper metal–oxygen length. The pattern parameters were refined to obtain the lowest R_{wp} value. Rietveld analysis parameters and atom positions of MoVO-A-AC are shown in Tables S1 and S2, respectively. Then, the Rietveld refinement for MoVFeO-EA-AC and MoVWO-EA-AC was carried out. For the refinement, structural model of MoVO-A-AC was used as a base structure. For MoVFeO-EA-AC, Fe was set at the heptagonal channel occupancy. For MoVWO-EA-AC, W was set at the whole $\{\text{Mo}_6\text{O}_{21}\}^{6-}$ pentagonal unit. The Rietveld refinement was performed in the same manner with MoVO-A-AC. Rietveld analysis parameters of MoVFeO-EA-AC and MoVWO-EA-AC are shown in Tables S3 and S5, respectively, and atom positions of MoVFeO-EA-AC and MoVWO-EA-AC are shown in Tables S4 and S6, respectively. XRD simulation experiments for MoVFeO-EA-AC and MoVWO-EA-AC were carried out using the same software as well as Rietveld refinement. For the experiments, structural model of MoVO-A-AC after the Rietveld refinement was used as a base structure. Atomic position and atomic occupancy were changed depending on the situation and simulated the XRD for each cases.

2.4 Catalytic Test

The selective oxidation of ethane in gas phase was carried out at atmospheric pressure in a conventional vertical flow system with a fixed bed Pyrex tubular reactor. 0.50 g of the catalyst was diluted with 2.10 g of silica and put into the tubular reactor for ethane oxidation. The reactor was

heated gradually from room temperature at a rate of $10\text{ }^\circ\text{C min}^{-1}$ to $260\text{ }^\circ\text{C}$ under nitrogen flow (40 mL min^{-1} from the top of the reactor). The temperature was measured with a thermocouple inserted in the middle of the catalyst zone. When the temperature reached $260\text{ }^\circ\text{C}$, a reactant gas with the composition of $\text{C}_2\text{H}_6/\text{O}_2/\text{N}_2 = 5/5/40\text{ mL min}^{-1}$ was fed and the reaction was started. Reaction was carried out at $260, 280, 300, 320,$ and $340\text{ }^\circ\text{C}$. Reactants and products were analyzed with three online gas chromatographs (Molecular sieve $13\times$ for O_2, N_2 and CO with a TCD detector, Gaskuropack for $\text{CO}_2, \text{C}_2\text{H}_4$ and C_2H_6 with a TCD detector, and Porapak Q for acetic acid with a FID detector). Blank runs showed that under the experimental conditions used in this study, homogeneous gas-phase reactions were negligible. Carbon balance was always ca. 98–100 %, so that the product selectivity was calculated on the basis of the product sum.

3 Results and Discussion

3.1 Synthesis of Crystalline Mo–V–M^{3rd}–O Catalysts

Figure 2 shows the XRD patterns of the obtained catalysts before the purification (see the experimental section). The amounts of ammonium cation (NH_4^+) and ethylammonium cation (EtNH_3^+) in the precursor solution in the hydrothermal synthesis are shown in Table 1. MoVO-A-fresh showed XRD peaks at $4.7^\circ, 8.3^\circ,$ and 22.2° , which are derived from (100), (110), and (001) plane of the crystalline trigonal Mo_3VO_x [1, 7, 8]. In addition to these peaks, the peak at 9.1° possibly derived from

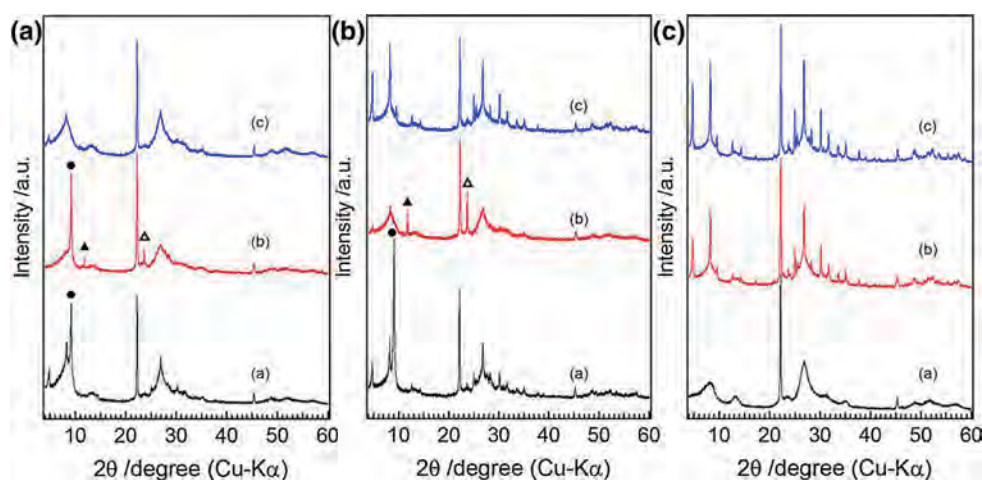


Fig. 2 **a** $(\text{NH}_4)_6\text{Mo}_7\text{O}_{24}\cdot 4\text{H}_2\text{O}$ was used as a Mo source. *a* MoVO-A-fresh, *b* MoVFeO-A-fresh, *c* MoVWO-A-fresh. **b** $(\text{NH}_4)_6\text{Mo}_7\text{O}_{24}\cdot 4\text{H}_2\text{O}$ was used as a Mo source in the presence of $(\text{C}_2\text{H}_5\text{NH}_3)\text{Cl}$. *a* MoVO-(A+EACl)-fresh, *b* MoVFeO-(A+EACl)-fresh, *c* MoVWO-

(A+EACl)-fresh. **c** $(\text{C}_2\text{H}_5\text{NH}_3)_2\text{Mo}_3\text{O}_{10}$ (EATM) was used as a Mo source. *a* MoVO-EA-fresh, *b* MoVFeO-(A+EA)-fresh, *c* MoVWO-(A+EA)-fresh. Closed circle, $(\text{NH}_4)_2\text{Mo}_4\text{O}_{13}$; closed triangle, $\text{FeO}(\text{OH})$; open triangle, $\text{Fe}(\text{OH})_3$

Table 1 Amount of counter cations in the precursor solution

Catalyst	NH ₄ ⁺ /mmol l ⁻¹	EtNH ₃ ⁺ /mmol l ⁻¹
MoVO-A	179	0
MoVFeO-A	230	0
MoVWO-A	222	0
MoVO-(A+EACl)	214	167
MoVFeO-(A+EACl)	230	167
MoVWO-(A+EACl)	222	167
MoVO-EA	0	167
MoVFeO-EA	16	167
MoVWO-EA	8	167

(NH₄)₂Mo₄O₁₃ was observed. MoVFeO-A-fresh showed the XRD peak at 22.2° which represents the layered structure, while the peaks below 10° were absent, indicating that the trigonal Mo₃VO_x was not formed. The peak at 9.1° attributed to (NH₄)₂Mo₄O₁₃ was also observed in the same manner with MoVO-A-fresh. In addition, the XRD peaks at 11.8° and 23.7°, attributable to FeO(OH) and Fe(OH)₃, respectively, were observed. MoVWO-A-fresh showed the diffraction peaks all attributed to trigonal Mo₃VO_x, although the crystallinity was poor. In the case that EACl was added into the precursor solution (Fig. 2b), MoVO-(A+EACl) showed almost the same XRD pattern with that of MoVO-A-fresh, suggesting almost no effects of (CH₃CH₂NH₃)Cl (EACl) on the crystal formation process in this synthesis. In the case of MoVFeO-(A+EACl)-fresh, the peaks attributed to trigonal phase appeared at 4.7° and 8.3° by the addition of EACl. However, the XRD peaks at 11.8° and 23.7° were still observed. In the case of MoVWO-(A+EACl)-fresh, the intensity of the peaks at 4.7° and 8.3° was clearly increased, suggesting an improvement of the crystallinity of trigonal phase by the addition of EACl. The addition of EACl was found to facilitate the formation of trigonal phase in the presence of W source.

When (EtNH₃)₂Mo₃O₁₀ (EATM) was used as a Mo source (Fig. 2c), clear differences in the XRD patterns were found. MoVO-EA-fresh showed no clear XRD peaks under 10° and the obtained XRD pattern was almost the same with that of the amorphous Mo₃VO_x material as we have reported previously [1, 20]. On the other hand, MoVFeO-EA-fresh and MoVWO-EA-fresh showed XRD peaks attributable to crystalline trigonal Mo₃VO_x and no peaks besides this phase were observed. Obviously, EtNH₃⁺ cation promoted the formation of trigonal Mo₃VO_x. For these syntheses, the role of small amount of NH₄⁺ deriving from Fe(NH₄)(SO₄)₂·12H₂O or (NH₄)₆[H₂W₁₂O₄₀]·nH₂O precursor is essential. Actually, when H₂WO₄ was used as a W source for the synthesis instead of (NH₄)₆[H₂W₁₂O₄₀]·nH₂O, no crystalline trigonal MoVWO

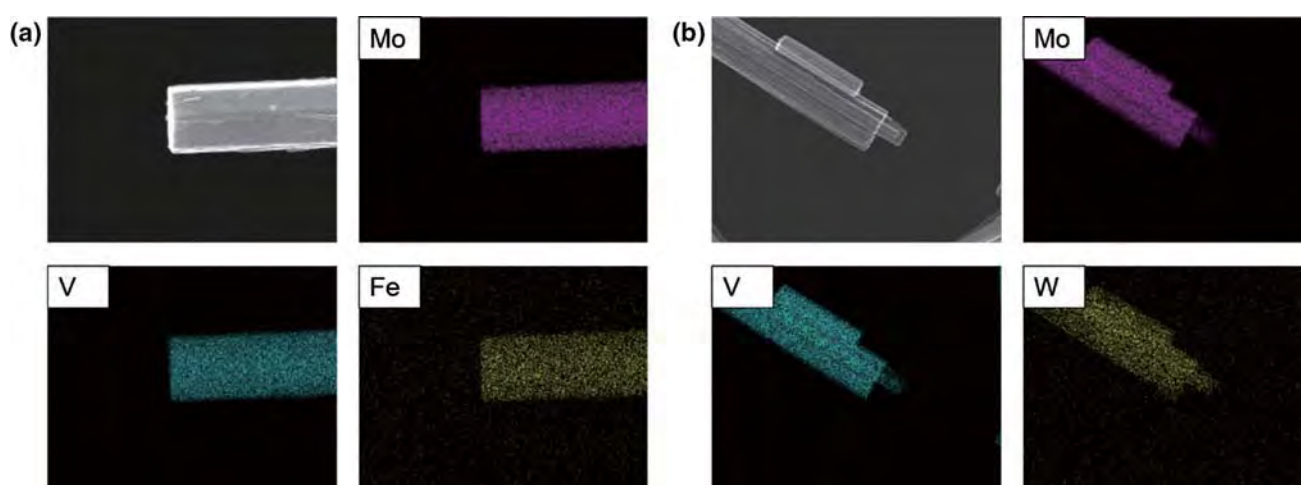
material could be obtained even though the same amount of W and the same pH value of precursor solution were applied (Fig. S1). The roles of EtNH₃⁺ and NH₄⁺ in the formation of the trigonal Mo–V–M^{3rd}–O materials will be discussed later. At this stage, we successfully obtained the crystalline Mo–V–Fe–O and Mo–V–W–O catalysts isomorphs with the trigonal Mo₃VO_x structure.

For further characterizations, MoVO-A, MoVFeO-EA, and MoVWO-EA after the purification with oxalic acid were used. Table 2 shows the results of elemental analyses of MoVO-A, MoVFeO-EA and MoVWO-EA. The bulk V/Mo ratios of MoVO-A, MoVFeO-EA and MoVWO-EA estimated by ICP were 0.32, 0.30, and 0.29, respectively, and were almost the same. For MoVFeO-EA and MoVWO-EA, Fe and W were detected by ICP and the ratios of Fe/Mo and W/Mo were 0.06 and 0.06, respectively, which are consistent with the preparative M^{3rd}/Mo ratio (0.05). STEM-mapping and STEM-EDX analyses were employed for these materials in order to estimate the elemental composition of each crystals and the results are shown in Fig. 3. The images clearly show that the elements which constitute the rods were uniformly distributed throughout the rods. The elemental compositions of the rod-shaped crystals were estimated by STEM-EDX analysis and are compared with those determined by ICP-AES. The results are listed in Table 2. The elemental compositions of the rods were almost the same with those of the bulk and were Mo/V/Fe = 1/0.30/0.07 (MoVFeO-EA) and Mo/V/W = 1/0.29/0.07 (MoVWO-EA), respectively. The coincident of the elemental composition determined by ICP (bulk) and STEM-EDX (rod-shaped crystal) indicates that these samples were highly pure with almost no impurities as implied by XRD. In addition, XPS analysis was performed for these materials in order to measure the elemental composition on their catalyst surface. The V/Mo ratios on the catalyst surface were 0.14, 0.11, and 0.14 for MoVO-A, MoVFeO-EA and MoVWO-EA, respectively, and were considerably small compared with those determined by ICP and STEM-EDX. This small V/Mo ratio at the catalyst surface have been reported in Mo–V–Te–Nb–O catalyst, crystal analogous with crystalline trigonal Mo₃VO_x catalyst [25–29]. For the third metals, XPS peak of Fe 2p_{3/2} was surprisingly negligible in MoVFeO-EA, while that of W 4f_{7/2} for MoVWO-EA could clearly be seen (Fig. S2). The obtained Fe/Mo ratio was almost 0 and the W/Mo ratio was 0.08. Since W/Mo ratio determined by ICP (bulk), STEM-EDX (rod-shaped crystal), and XPS (surface) were almost the same, W was found to be uniformly dispersed throughout the solid. On the other hand, Fe is preferentially located in the bulk for MoVFeO-EA because of the negligible Fe/Mo ratio on the surface.

IR, TPD, and TPO analyses were carried out in order to obtain information about the counter cation species in the

Table 2 Physicochemical properties of Mo–V–M^{3rd}–O materials

Catalyst	Mo/V/M ^{3rd}				CHN elemental analysis ^d /wt%		
	Preparative	Bulk ^a	Rod-shaped crystal ^b	Surface ^c	C	H	N
MoVO-A	1/0.25/–	1/0.32/–	–	1/0.14/–	0	0.76	0.80
MoVFeO-EA	1/0.25/0.05	1/0.30/0.06	1/0.30/0.07	1/0.11/0.01	1.28 (1.28)	1.10	1.01 (0.59)
MoVWO-EA	1/0.25/0.05	1/0.29/0.06	1/0.29/0.07	1/0.14/0.08	1.29 (1.29)	0.97	1.01 (0.59)

^a Determined by ICP^b Determined by STEM-EDX^c Determined by XPS^d Determined by CHN elemental analysis. Parenthesis is a calculated value derived from ethylammonium cation**Fig. 3** STEM-mapping images of MoVFeO-EA (a) and MoVWO-EA (b)

structure. Figure S3 shows the IR spectra of MoVO-A, MoVFeO-EA, and MoVWO-EA. Below 1000 cm^{-1} , all the catalysts showed the characteristic IR bands at 915 cm^{-1} attributable to V–O, 874, 840, 817, 800, 720 and 652 cm^{-1} to Mo–O–Mo, 604 cm^{-1} to V–O–Mo, and 458 cm^{-1} to Mo–O [1, 14, 20, 30–32]. The band intensity at 915 cm^{-1} was decreased in MoVFeO-EA. Possibly, the incorporation of Fe into the structure weakened the V–O bond strength. For the IR bands in the range of 1000–2000 cm^{-1} , the peak at 1620 cm^{-1} was assigned to water and the peaks in the range of 1000–1550 cm^{-1} were derived from the absorption of counter cations. Figure S3B shows the enlarged IR bands from 1000 to 1550 cm^{-1} . The absorption peak at 1401 cm^{-1} attributed to an asymmetric deformation vibration of the NH_4^+ was observed in MoVO-A [20]. The peak attributable to NH_4^+ was also observed in MoVFeO-EA and MoVWO-EA, indicating that the NH_4^+ derived from $\text{Fe}(\text{NH}_4)(\text{SO}_4)_2 \cdot 12\text{H}_2\text{O}$ or $(\text{NH}_4)_6[\text{H}_2\text{W}_{12}\text{O}_{40}] \cdot n\text{H}_2\text{O}$ precursor is located inside the structure. In addition to this band, the absorption bands at

1505 cm^{-1} attributed to a bending of NH_3^+ , 1471 cm^{-1} to CH_2 scissoring, 1449 cm^{-1} to CH_3 asymmetric deformation, 1181 cm^{-1} to CH_2 rocking, and 1037 cm^{-1} to C–N stretching were observed in MoVFeO-EA and MoVWO-EA. This strongly suggests the existing of EtNH_3^+ in the structure as well as the NH_4^+ [33–35]. This coexistence of NH_4^+ and EtNH_3^+ were further confirmed by TPD and TPO experiments. Figure S4 shows the TPD and TPO profiles of MoVFeO-EA and MoVWO-EA. TPD analysis was operated under 50 mL min^{-1} of He flow and TPO was operated under $\text{He}/\text{O}_2 = 45/5 \text{ mL min}^{-1}$ flow. Mass numbers (m/z) of 16, 44, and 45 are ascribed to the desorption of NH_3 , CO_2 , and EtNH_2 . Desorption peaks of NH_3 at 370 $^\circ\text{C}$, CO_2 at 270, 440 and 520 $^\circ\text{C}$, and EtNH_2 at 440 and 520 $^\circ\text{C}$ were observed in TPD for MoVFeO-EA. Since no C–O bond was observed in IR, the observed CO_2 desorption should be the result of the interaction between EtNH_3^+ and lattice oxygen in the structure during the TPD [20]. In the presence of oxygen (TPO), the desorption temperatures of CO_2 and EtNH_2 shifted to lower

temperature and was 260 °C for both CO₂ and EtNH₂. No NH₃ desorption was determined in TPO due to the overlapping of O₂ (m/z = 16) in a fluent gas. Desorption peaks were observed in TPD for NH₃ at 370 °C, CO₂ at 190, 320, 470 °C, and EtNH₂ at 470 °C for MoVWO-EA as well as for MoVFeO-EA. In the same manner with MoVFeO-EA, the desorption temperatures of CO₂ and EtNH₂ shifted toward low temperature in the presence of oxygen (TPO) and were around 260 °C for both the species. It has been reported that physically adsorbed species over the crystalline Mo₃VO_x materials desorb in TPD around 150 °C, which is much lower temperature than those observed in MoVFeO-EA and MoVWO-EA [13, 14]. Taking into account the desorption temperature, the detected species should be of chemisorbed on or in the structure. Combined with the IR results, the coexistence of NH₄⁺ and EtNH₃⁺ is obvious for both the catalysts.

Then, the amounts of these cations were estimated by CHN elemental analysis. As can be seen in Table 2, no C were observed in MoVO-A, thus, no oxalic acid used for the purification remained in the materials. For MoVFeO-EA and MoVWO-EA, 1.28 and 1.29 wt% of C were observed (Table 2). Since oxalic acid cannot remain in the catalysts, detected C should be all attributed to EtNH₃⁺. Based on the catalyst elemental composition and weight percent of C, the numbers of EtNH₃⁺ inside the trigonal Mo₃VO_x structure per unit cell were calculated for MoVFeO-EA and MoVWO-EA. The detailed calculation method is shown in the supplementary. The calculated numbers of EtNH₃⁺ per unit cell were 2.08 and 2.06 for MoVFeO-EA and MoVWO-EA, respectively. Since the existence of NH₄⁺ inside the structure was obvious from IR and TPD, the amount of NH₄⁺ was evaluated as well. The contributions of EtNH₃⁺ for the N weight percentages were calculated based on the weight percentages of C and were determined to be 0.59 wt% for both the catalysts. Thus, the contributions of NH₄⁺ for the N weight percentages were calculated to be 0.42 wt% for both the catalysts (Table 2). Calculated numbers of NH₄⁺ per unit cell of MoVFeO-EA and MoVWO-EA were 0.73 and 0.72, respectively. Accordingly, the numbers of counter cations (NH₄⁺ + EtNH₃⁺) of MoVFeO-EA and MoVWO-EA per unit cell were calculated as 2.81 and 2.78, respectively. In trigonal Mo₃VO_x structure unit cell, there are three heptagonal channels and two hexagonal channels. The obtained numbers of the counter cations in the MoVFeO-EA and MoVWO-EA structure unit cell were reasonably consistent with the number of the heptagonal channels in the unit cell. Since the size of the channels of the hexagonal channel (0.25 nm) is too small to accommodate these counter cation (EtNH₃⁺: 0.43 nm, NH₄⁺: 0.28 nm), it is reasonable to assume that all the counter cations are located inside the heptagonal channel (0.4 nm)

[4, 5, 12, 19]. We concluded, on the basis of these facts, that both EtNH₃⁺ and NH₄⁺ are located inside the heptagonal channel in MoVFeO-EA and MoVWO-EA.

The crystal formation of Mo–V–M^{3rd}–O might occur by the involvement of EtNH₃⁺ and NH₄⁺ during the heptagonal channel formation. EtNH₃⁺ and NH₄⁺ might work like as structure-directing agents to form trigonal Mo₃VO_x structure by entering into the heptagonal channel of the structure. The sum of H weight percents derived from EtNH₃⁺ and NH₄⁺ are calculated to be 0.49 and 0.45 wt% for MoVFeO-EA and MoVWO-EA, respectively. Since the weight percent of H in MoVFeO-EA and MoVWO-EA was determined to be 1.10 and 0.97 wt%, the rest other than those from EtNH₃⁺ and NH₄⁺ (0.61 wt% for MoVFeO-EA and 0.53 wt% for MoVWO-EA, respectively) might be derived from the water as observed in the IR analysis. The numbers of water per unit cell were calculated and were 11.6 and 9.1 for MoVFeO-EA and MoVWO-EA, respectively. These are mostly the physically adsorbed water as we have shown previously [14]. The chemical compositions of MoVFeO-EA and MoVWO-EA are now calculated as Mo_{20.8}V_{6.2}Fe_{1.2}O₇₅(EtNH₃)_{2.08}(NH₄)_{0.73}·11.6H₂O and Mo₂₀V_{5.8}W_{1.2}O₇₅(EtNH₃)_{2.06}(NH₄)_{0.72}·9.1H₂O, respectively. On the other hand, the number of NH₄⁺ per unit cell was calculated to be 2.1 for MoVO-A. The number of the counter cation in this case is obviously small compared with the number of the heptagonal channel per unit cell. Possibly, NH₄⁺ is partially exchanged with H⁺ during the purification process. The calculated chemical composition of MoVO-A was Mo_{20.4}V_{6.6}O₇₅(NH₄)_{2.1}·9.9H₂O.

3.2 Location of Third Metals in the Structure of Mo–V–M^{3rd}–O Catalysts

The location of the third metals was investigated by Rietveld analysis for the MoVFeO-EA-AC and MoVWO-EA-AC which are calcined, since the structural analysis without the counter cations is simpler than that in the presence of the cations. Figure 4 shows the Raman spectra of MoVO-A-AC, MoVFeO-EA-AC, and MoVWO-EA-AC. These catalysts showed characteristic Raman band at 871 cm⁻¹ which derived from Mo–O–Mo bond of the {Mo₆O₂₁}⁶⁻ pentagonal unit [1, 14, 16]. Almost no shift in this band was observed in MoVFeO-EA-AC compared with MoVO-A-AC, while a downward shift to 869 cm⁻¹ was observed in MoVWO-EA-AC. This fact suggests the substitution of Mo in the {Mo₆O₂₁}⁶⁻ pentagonal unit by W in MoVWO-EA-AC. On the contrary, the {Mo₆O₂₁}⁶⁻ pentagonal unit was little affected by the introduction of Fe in the structure.

Figure 5 shows the XRD patterns of MoVO-A-AC, MoVFeO-EA-AC, and MoVWO-EA-AC. The lattice parameters of these catalysts are shown in Table 3. All the

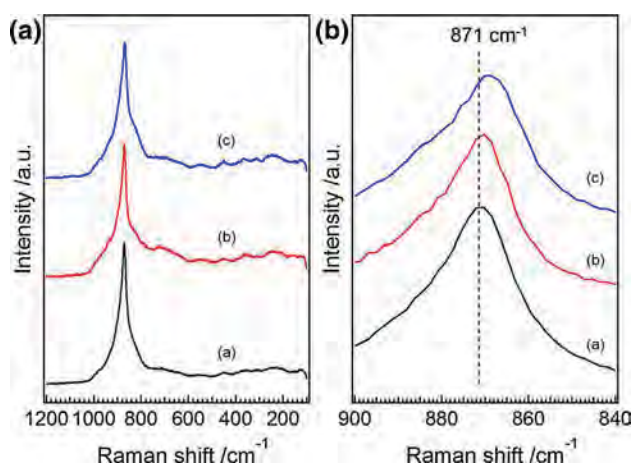


Fig. 4 **a** Raman spectra of MoVO-A-AC (a), MoVFeO-EA-AC (b), and MoVWO-EA-AC (c). **b** Enlarged Raman spectra of (a) from 840 to 900 cm^{-1}

catalysts showed no patterns related to impurities except MoVO-A-AC where small XRD peaks appeared at 6.7° and 9.0° derived from the crystalline orthorhombic Mo_3VO_x (a crystal analogous with trigonal Mo_3VO_x) [1]. As we have shown previously [10], trigonal Mo_3VO_x have a small portion of intergrowth domain with the orthorhombic Mo_3VO_x catalyst. Figure 5b shows the enlarged XRD patterns of these catalysts in the range of 21.5° – 22.5° . As can be seen from this figure that the diffraction peak of (001) plane was shifted to lower angle in MoVFeO-EA-AC compared with MoVO-A-AC, while to higher in MoVWO-EA-AC. The lattice parameter was $a = 2.131$ nm and $c = 0.4009$ nm for MoVFeO-EA-AC, indicating that the addition of Fe into the structure caused slight expansion of the lattice both in a - and c -direction. The lattice expansion by the incorporation of additional elements (Sb, Te) has

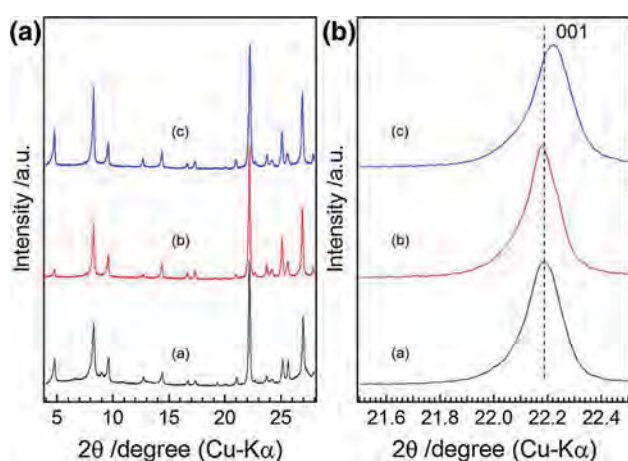


Fig. 5 **a** XRD patterns of MoVO-A-AC (a), MoVFeO-EA-AC (b), and MoVWO-EA-AC (c). **b** Enlarged XRD patterns of (a) from 21.5° to 22.5°

been observed in orthorhombic Mo_3VO_x [28]. Combined with the fact that no shift in Raman band was observed by the introduction of Fe, Fe is assumed to be located at the channels in trigonal Mo_3VO_x structure in the same manner with Te or Sb for the orthorhombic Mo_3VO_x [28]. For MoVWO-EA-AC, on the other hand, the lattice was slightly expanded in the a axis ($a = 2.129$ nm), while, the lattice parameter in the c axis was significantly decreased ($c = 0.3997$ nm). An arrangement of $\{\text{Mo}_6\text{O}_{21}\}^{6-}$ pentagonal unit comprises a network structure in the crystal structure of trigonal Mo_3VO_x . Void space generated in the network structure is filled with a trimer unit of which is comprised of three MO_6 ($M = \text{Mo}, \text{V}$), resulting in the formation of three heptagonal channels (Fig. 1) [7, 8]. Buttrey et al. has reported that the network arrangement based on the $\{\text{Mo}_6\text{O}_{21}\}^{6-}$ pentagonal unit is structurally stable compared with the oligomer unit composed by MO_6 ($M = \text{Mo}, \text{V}$) [36]. Therefore, the replacement of the atoms in the structural network comprised of the $\{\text{Mo}_6\text{O}_{21}\}^{6-}$ pentagonal unit may cause a structural parameter change preferentially to the replacement in the other parts of the crystal structure. The Raman band derived from the $\{\text{Mo}_6\text{O}_{21}\}^{6-}$ pentagonal unit was shifted by the incorporation of W. Accordingly W in MoVWO-EA-AC is considered to be located in the $\{\text{Mo}_6\text{O}_{21}\}^{6-}$ pentagonal unit by substituting Mo. In order to evaluate the lattice parameter change by the substitution of W with Mo in the pentagonal unit, we estimated the metal–oxygen bond lengths for the $\{\text{Mo}_6\text{O}_{21}\}^{6-}$ and the $\{\text{W}_6\text{O}_{21}\}^{6-}$ pentagonal unit by using the structural models of the ball type $[\text{K}_{10}\{(\text{Mo})\text{-Mo}_5\text{O}_{21}(\text{H}_2\text{O})_3(\text{SO}_4)\}_{12}(\text{VO})_{30}(\text{H}_2\text{O})_{20}]_{262}$ polyoxomolybdate ($\{\text{Mo}_{72}\text{V}_{30}\}$) and $[\text{K}_{20}\{(\text{W})\text{W}_5\text{O}_{21}(\text{SO}_4)\}_{12}(\text{VO})_{30}(\text{SO}_4)(\text{H}_2\text{O})_{63}]_{18}$ polyoxotungstate ($\{\text{W}_{72}\text{V}_{30}\}$), obtained by single crystal analysis [15, 37]. In this case, the metal–oxygen bond length only for the center atom in the pentagonal unit ($\{\text{MO}_7\}$, $M = \text{Mo}$ or W) was estimated since a disordering was observed in the edge-shared octahedral ($\{\text{MO}_6\}$, $M = \text{Mo}$ or W). In the case of $\{\text{Mo}_6\text{O}_{21}\}^{6-}$ pentagonal unit, the axial bond length (Mo-O-Mo) of $\{\text{MoO}_7\}$ was in the range of 3.996–4.027 Å and that of the equatorial bond (average of five equatorial bonds in $\{\text{MoO}_7\}$ (Mo-O)) was 2.002–2.007 Å. In the case of $\{\text{W}_6\text{O}_{21}\}^{6-}$ pentagonal unit, the axial bond length of $\{\text{WO}_7\}$ (W-O-W) was in the range of 3.922–3.940 Å and that of the equatorial bond (average of five equatorial bonds in $\{\text{WO}_7\}$ (W-O)) was 2.005–2.015 Å. Accordingly, the trigonal Mo_3VO_x lattice is expected to slightly increase to a -direction and largely decrease to c -direction when Mo in the $\{\text{Mo}_6\text{O}_{21}\}^{6-}$ pentagonal unit is substituted by W. Therefore, it is reasonable to conclude that Mo in the $\{\text{Mo}_6\text{O}_{21}\}$ pentagonal unit is substituted by W in the structure of MoVWO-EA-AC.

Table 3 XRD and N₂ adsorption for the catalysts after the air calcination

Catalyst	Int ₍₁₀₀₎ /Int ₍₁₁₀₎ ^a /-	Lattice parameter ^b /nm		External surface area ^c /m ² ·g ⁻¹	Micropore volume ^c /cm ³ ·g ⁻¹
		<i>a</i>	<i>c</i>		
MoVO-A-AC	0.44	2.125	0.4007	18.0	4.0
MoVFeO-EA-AC	0.15	2.131	0.4009	15.1	2.7
MoVWO-EA-AC	0.43	2.129	0.3997	16.7	3.6

^a Ratio of the XRD peak area between (100) and (110)

^b Calculated by Rietveld refinement

^c Calculated by *t*-plot method (*t* = 0.15–0.90)

Next, the XRD peak intensity was analyzed. The XRD peak intensity at 4.7° attributed to (100) plane was almost the same in MoVO-A-AC and in MoVWO-AC, whereas the peak intensity of MoVFeO-EA-AC was apparently weak compared with those of the other two catalysts (Fig. 5a). The XRD peak intensities ratios of 4.7° (100 plane) and 8.3° (110 plane) (Int₍₁₀₀₎/Int₍₁₁₀₎) are listed in Table 3 and were 0.44, 0.15, and 0.43 for MoVO-A-AC, MoVFeO-EA-AC, and MoVWO-EA-AC, respectively. In order to investigate the effect of the incorporation of third atoms on Int₍₁₀₀₎/Int₍₁₁₀₎ ratio, we first performed Rietveld refinement for MoVO-A-AC. Then, third atoms were incorporated into the structural model and the changes of Int₍₁₀₀₎/Int₍₁₁₀₎ ratio were evaluated. The result of Rietveld refinement for MoVO-A-AC is shown at Fig. S5 and refinement parameter, atom position, and atom occupancy are summarized in Tables S1–S2. Figure 6 shows the changes of the Int₍₁₀₀₎/Int₍₁₁₀₎ ratio as a function of Fe occupancy. XRD and Raman analyses suggested the location of Fe at the heptagonal channel or at the hexagonal channel. As can be seen in Fig. 6, the partial placement of Fe atom in the heptagonal channel decreased the Int₍₁₀₀₎/Int₍₁₁₀₎ ratio and the ratio was decreased with the increase of the Fe occupancy. On the other hand, the placement of Fe atom in the hexagonal channel increased this ratio. Although the value of Int₍₁₀₀₎/Int₍₁₁₀₎ calculated by XRD simulation was different to some extents from the experimentally obtained value, possibly due to the small difference in the structural model between MoVO-A-AC and MoVFeO-EA-AC, the simulated Int₍₁₀₀₎/Int₍₁₁₀₎ ratio changes strongly suggest that Fe is located, at least, at the heptagonal channel in the structure.

For MoVWO-EA-AC, W is suggested to be located at the {Mo₆O₂₁}⁶⁻ pentagonal unit. Figure 7 shows the XRD simulation of MoVWO-EA-AC. For the substitution of Mo by W in the {Mo₆O₂₁}⁶⁻ pentagonal, we used two structural models in which W is located either at the whole (Site 1) or at the center of the pentagonal unit (Site 2), since both the {W₆O₂₁}⁶⁻ pentagonal unit and the {W(Mo)₅O₂₁}⁶⁻ pentagonal unit have been reported [38, 39]. In addition to the pentagonal unit, we also simulated the XRD pattern by

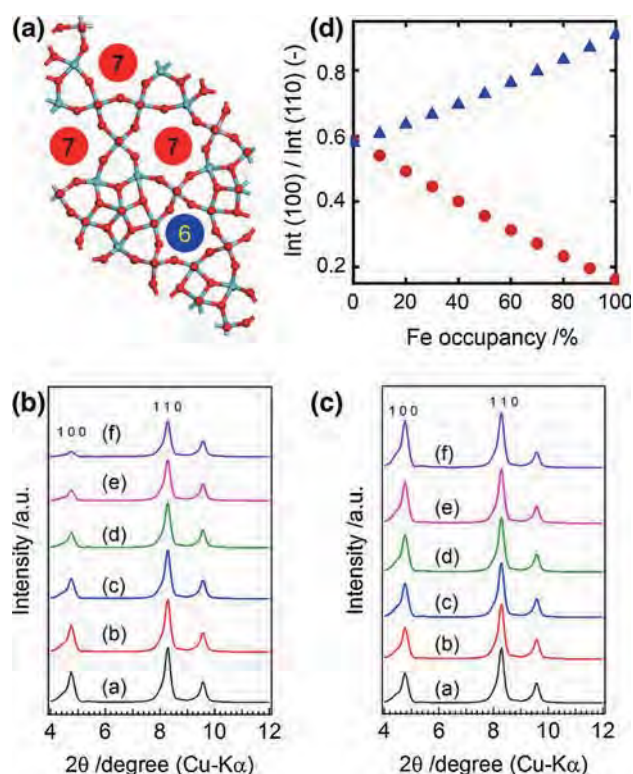


Fig. 6 **a** Structural model used for XRD simulation. Fe was set at the heptagonal channel and hexagonal channel for simulation. Mo, light green; V, gray; O, red. **b** XRD patterns from 4° to 12° simulated by setting Fe in the heptagonal channel. **c** XRD patterns from 4° to 12° simulated by setting Fe in the hexagonal channel. **a** Fe occupancy = 0 %, **b** Fe occupancy = 10 %, **c** Fe occupancy = 30 %, **d** Fe occupancy = 50 %, **e** Fe occupancy = 70 %, and **f** Fe occupancy = 100 %. **d** Int₍₁₀₀₎/Int₍₁₁₀₎ ratio changes as a function of Fe occupancy. Circle, Fe is set at the heptagonal channel; triangle, Fe is put at the hexagonal channel

replacing the atoms at the trimer unit (Site 3) and linker units, which connect two pentagonal units (Site 4, 5), by W. The occupancy of W was calculated based on the result of ICP. When W is assumed to be placed at the pentagonal unit (Site 1, 2), almost no change in Int₍₁₀₀₎/Int₍₁₁₀₎ ratio was observed, which is in good agreement with the experimental result (see the results of No W, Site 1, and

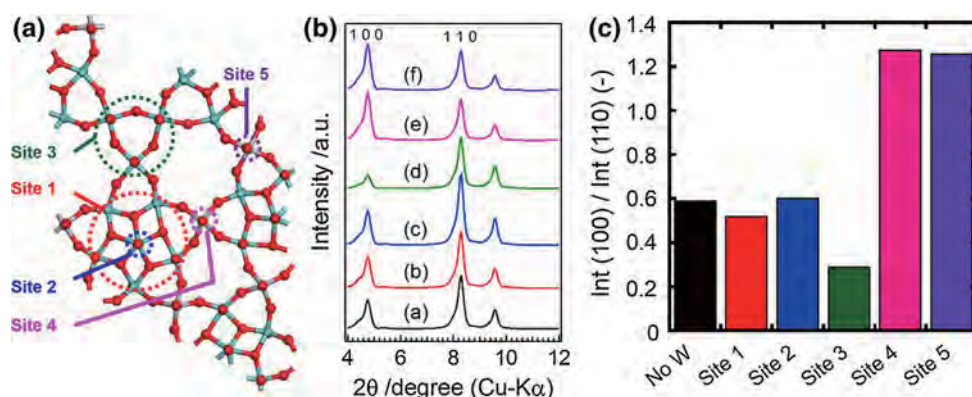


Fig. 7 **a** Structural model used for XRD simulation. W was set at the whole part of $\{\text{Mo}_6\text{O}_{21}\}^{6-}$ pentagonal unit (*Site 1*), at the center of $\{\text{Mo}_6\text{O}_{21}\}^{6-}$ pentagonal unit (*Site 2*), at the trimer unit (*Site 3*), at the linker unit facing to the hexagonal channel (*Site 4*), and at the linker unit facing to the heptagonal channel (*Site 5*). The occupancy of W was set at 7 % in *Site 1* and at 40 % in *Site 2–5*. No W in the structure

is represented as ‘No W’. Mo, light green; V, gray; O, red. **b** XRD patterns from 4° to 12° simulated by putting W at *b Site 1*, *c Site 2*, *d Site 3*, *e Site 4*, and *f Site 5*. *a* XRD pattern simulated without putting W into the structure. **c** $\text{Int}_{(100)}/\text{Int}_{(110)}$ ratio calculated based on the simulated XRD patterns as shown in (**b**)

Site 2 in Fig. 7c). On the other hand, the $\text{Int}_{(100)}/\text{Int}_{(110)}$ ratio decreased when W was located at the trimer unit (*Site 4*). In addition, the placement of W at the linker units significantly increased this ratio (*Site 5*, 6). These results strongly suggest that W substitutes Mo in the $\{\text{Mo}_6\text{O}_{21}\}^{6-}$ pentagonal unit. However, it is still unclear whether W substitutes only at the center or in the whole part of the $\{\text{Mo}_6\text{O}_{21}\}^{6-}$ pentagonal unit.

Then, Rietveld refinement was carried out for these materials in order to evaluate the validity of our proposed structure. In this experiment, Fe was set at the heptagonal channel with 40 % occupancy and W was set at the whole part of $\{\text{Mo}_6\text{O}_{21}\}^{6-}$ pentagonal unit with 7 % occupancy. The occupancies were calculated based on the result of ICP. The results of Rietveld refinement for MoVFeO-EA-AC and MoVWO-EA-AC are shown in Figs. 8, 9, respectively, and the refinement parameters, atom positions, and atom occupancies are listed in Tables S3–S6. Good agreement between simulated and observed XRD patterns were observed in both the materials and obtained R_{wp} value were 10.5 and 10.4 % for MoVFeO-EA-AC and MoVWO-EA-AC, respectively. These good agreements support the validity of our proposed structure. In the case of MoVWO-EA-AC, we also carried out Rietveld refinement using the structural model in which W is located at the center of $\{\text{Mo}_6\text{O}_{21}\}^{6-}$ pentagonal unit with 40 % occupancy. R_{wp} value obtained by the refinement was 11.4 % (data not shown). Thus, we believe that W substitutes Mo in the whole part of $\{\text{Mo}_6\text{O}_{21}\}^{6-}$ pentagonal unit, rather than that of the center. After the Rietveld refinement, Fe moved toward to the trimer unit in the structure. Since the trimer unit contains V, the decrease in V–O bond intensity observed in IR analysis might indicate that O associated with V in the trimer unit partly makes a bond with Fe.

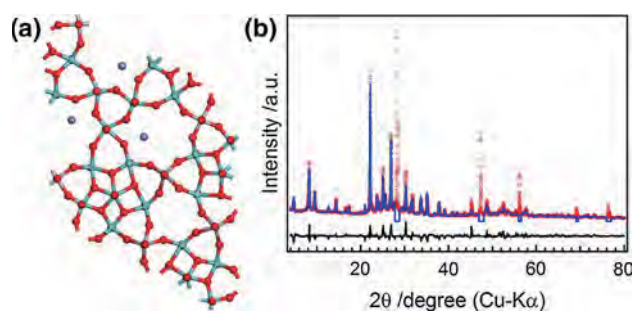


Fig. 8 **a** Structural model obtained by Rietveld refinement. Mo, light green; V, gray; Fe, purple; O, red. **b** Difference (black), calculated (blue line), and observed (red circle) patterns obtained by Rietveld refinement for MoVO-A-AC. XRD peaks of 27.8–28.8°, 47–48°, 56–56.5°, 69–69.5°, and 76–77° were attributed to Si added in order to remove orientation effects and were excluded from Rietveld refinement. R_{wp} value of the refinement was 10.5 %

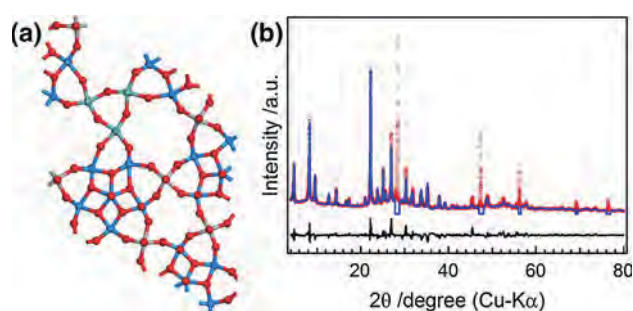


Fig. 9 **a** Structural model obtained by Rietveld refinement. Mo, light green; V, gray; mixture of Mo and W, light blue; O, red. **b** Difference (black), calculated (blue line), and observed (red circle) patterns obtained by Rietveld refinement for MoVO-A-AC. XRD peaks of 27.8–28.8°, 47–48°, 56–56.5°, 69–69.5°, and 76–77° were attributed to Si added in order to remove orientation effects and were excluded from Rietveld refinement. R_{wp} value of the refinement was 10.4 %

Configuration of Fe is still unclear so we need to investigate that for future. The different location of Fe and W in the structure may be due to the ionic and covalent character of Fe and W.

3.3 Catalytic Performances of Mo–V–M^{3rd}–O Catalysts

Table 3 also shows the external surface area and micropore volume of the catalysts measured by N₂ adsorption and estimated by t-plot method. The external surface areas of MoVO-A-AC, MoVFeO-EA-AC, and MoVWO-EA-AC were comparable for each other and were 18.0, 15.1, and 16.7 m² g⁻¹, respectively. As shown in Fig. S6, N₂ adsorption below P/P₀ < 10⁻⁵, which represents micropore adsorption, was observed for these catalysts. The micropore volumes were 4.0, 2.7, and 3.6 cm³ g⁻¹ for MoVO-A-AC, MoVFeO-EA-AC, and MoVWO-EA-AC, respectively, and the micropore volume of MoVFeO-EA-AC was smaller than those of the other two catalysts. It has been reported that the heptagonal channel in the trigonal Mo₃VO_x structure acts as the micropore to adsorb N₂. Thus, the small decrease in the micropore volume observed in MoVFeO-EA-AC might be due to the inaccessibility of N₂ into the heptagonal channel by the location of Fe [1].

Figure 10 shows the ethane conversion (a) and product selectivity (b) of the catalysts as a function of reaction temperature. MoVO-A-AC and MoVWO-EA-AC showed catalytic activity for the ethane conversion. The activity of MoVWO-EA-AC was a little bit lower than that of MoVO-A-AC. This decrease might be derived from the decrease in V amount in the unit cell (V amount in the unit cell: MoVO-A-AC, 6.6; MoVWO-EA-AC, 5.8) since C–H bond activation has been reported to takes place at the V site [14, 29]. On the other hand, the catalytic activity of MoVFeO-EA-AC was almost negligible despite of the

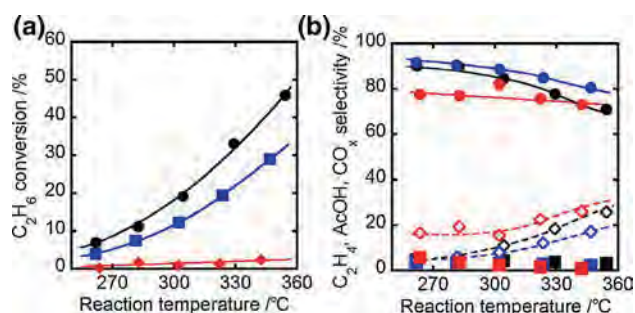


Fig. 10 Ethane conversion (a) and product selectivity (b) of the catalysts as a function of reaction temperature. **a** Circle, MoVO-A-AC; lozenge, MoVFeO-EA-AC; square, MoVWO-EA-AC. **b** Circle, C₂H₄; lozenge, CO_x; square, acetic acid. MoVO-A-AC, MoVFeO-EA-AC, and MoVWO-EA-AC were represented as black, red, and blue, respectively. Reaction condition: catalyst amount, 0.5 g; reaction gas, C₂H₆/O₂/N₂ = 5/5/40 mL min⁻¹

same basic structure of these catalysts. For selectivity, MoVO-A-AC and MoVWO-EA-AC showed almost the same product selectivity, whereas MoVFeO-EA-AC showed lower ethene selectivity and higher CO_x selectivity than those of the other two catalysts. We have reported that the ethane conversion takes place not on the catalyst surface but mostly inside the heptagonal channel [4, 5]. MoVO-A-AC and MoVWO-EA-AC have the open heptagonal channel. On the other hand, the heptagonal channel of MoVFeO-EA-AC is partially filled with Fe. This situation strongly suggests that no ethane could go through the heptagonal channel of MoVFeO-EA-AC due to the placement of Fe inside the channel, so that no ethane conversion occurs.

It was found that the location of elements significantly affects the catalytic performance. Importance of nano-scale crystal structure for the catalytic reaction could be seen. We believe this work provides useful information for designing more active catalysts for the selective reaction of ethane and more broadly for the selective oxidations.

4 Conclusion

Crystalline Mo–V–M^{3rd}–O (M^{3rd} = Fe, W) catalysts with the trigonal Mo₃VO_x structure were synthesized by a hydrothermal method when ethylammonium trimolybdate (EATM) was used as a Mo source. Obtained catalysts contained ethylammonium cation (EtNH₃⁺) and a small amount of ammonium cation (NH₄⁺), which were derived from M^{3rd} precursor, in a heptagonal channel in the structure. Obtained catalysts were pure and the third metals were uniformly distributed throughout the rod-shaped crystals. Fe was located in the heptagonal channel and W was located at the {Mo₆O₂₁}⁶⁻ pentagonal unit by substituting Mo. The placement of Fe in the heptagonal channel caused drastic decrease in the catalytic activity for the selective oxidation of ethane. On the other hand, the placement of W at the {Mo₆O₂₁}⁶⁻ pentagonal unit caused only slight change in the catalytic activity. These experimental results clearly demonstrated a structure–activity relationship for the selective oxidation of ethane.

References

- Konya T, Katou T, Murayama T, Ishikawa S, Sadakane M, Buttrey DJ, Ueda W (2013) Catal Sci Technol 3:380–387
- Chen C, Nakatani K, Murayama T, Ueda W (2013) Chem-CatChem 5:2869–2873
- Ueda W (2013) J Jpn Petrol Inst 56:122–132
- Ishikawa S, Yi X, Murayama T, Ueda W (2014) Appl Catal A Gen 474:10–17

5. Ishikawa S, Yi X, Murayama T, Ueda W (2014) *Catal Today* 238:35–40
6. Katou T, Vitry D, Ueda W (2004) *Catal Today* 91–92:237–240
7. Ishikawa S, Tashiro M, Murayama T, Ueda W (2014) *Cryst Growth Des* 14:4553–4561
8. Sadakane M, Watanabe N, Katou T, Nodasaka Y, Ueda W (2007) *Angew Chem Int Ed* 46:1493–1496
9. Pyrz WD, Blom DA, Sadakane M, Kodato K, Ueda W, Vogt T, Buttrey DJ (2010) *Chem Mater* 22:2033–2040
10. Pyrz WD, Blom DA, Sadakane M, Kodato K, Ueda W, Vogt T, Buttrey DJ (2010) *Proc Natl Acad Sci USA* 107:6152–6157
11. Chenoweth K, Duin ACT, Goddard WA (2009) *Angew Chem Int Ed* 48:7630–7634
12. Sadakane M, Kodato K, Kuranishi T, Nodasaka Y, Sugawara K, Sakaguchi N, Nagai T, Matsui Y, Ueda W (2008) *Angew Chem Int Ed* 47:2493–2496
13. Sadakane M, Ohmura S, Kodato K, Fujisawa T, Kato K, Shimidzu K, Murayama T, Ueda W (2011) *Chem Commun* 47:10812–10814
14. Ishikawa S, Kobayashi D, Konya T, Ohmura S, Murayama T, Yasuda N, Sadakane M, Ueda W (2015) *J Phys Chem C* 119:7195–7206
15. Bogdan B, Paul K, Craig LH (2005) *Chem Commun* 25:3138–3140
16. Sadakane M, Endo K, Kodato K, Ishikawa S, Murayama T, Ueda W (2013) *Eur J Inorg Chem* 10–11:1731–1736
17. Müller A, Gouzerh P (2014) *Chem Eur J* 20:4862–4873
18. Miras HN, Nadal L, Cronin L (2014) *Chem Soc Rev* 43:5679–5699
19. Sadakane M, Yamagata K, Kodato K, Endo K, Toriumi K, Ozawa Y, Ozeki T, Nagai T, Matsui Y, Sakaguchi N, Pyrz WD, Buttrey DJ, Blom DA, Vogt T, Ueda W (2009) *Angew Chem Int Ed* 48:3782–3786
20. Ishikawa S, Murayama T, Ohmura S, Sadakane M, Ueda W (2013) *Chem Mater* 25:2211–2219
21. Oshihara K, Nakamura Y, Sakuma M, Ueda W (2001) *Catal Today* 71:153–159
22. Gerhard M, József LM, Lajos V, Gábor PS, András T (2014) *Appl Catal A Gen* 474:3–9
23. Philip K, Lars G, Dominik S, Jan K, Alfons D, Frank H, Andreas HA, Joerg O, Silvia E, Guido S, Thorsten B, Manfred M, Hartmut F, Herbert V (2007) *Phys Chem Chem Phys* 9:3577–3589
24. Qiu C, Chen C, Ishikawa S, Murayama T, Ueda W (2014) *Top Catal* 57:1163–1170
25. Sanfiz AC, Hansen TW, Teschner D, Schnörch P, Girgsdies F, Trunschke A, Schlögl R, Looi MH, Hamid SBA (2010) *J Phys Chem C* 114:1912–1921
26. Heine C, Hävecker M, Sanchez MS, Trunschke A, Schlögl R, Eichelbaum M (2013) *J Phys Chem C* 117:26988–26997
27. Hävecker M, Wrabetz S, Kröhnert J, Csepei LI, Alnoncourt RN, Kolen'ko YV, Girgsdies F, Schlögl R, Trunschke A (2012) *J Catal* 285:48–60
28. Deniau B, Nguyen TT, Delichere P, Safonova O, Millet JMM (2013) *Top Catal* 56:1952–1962
29. Nguyen TT, Deniau B, Delichere P, Millet JMM (2014) *Top Catal* 57:1152–1162
30. Botella P, Concepcion P, Nieto JML, Solsona B (2003) *Catal Lett* 89:249–253
31. Botella P, Nieto JML, Solsona B, Mifsud A, Marquez F (2002) *J Catal* 209:445–455
32. Su SC, Bell AT (1998) *J Phys Chem B* 102:7000–7007
33. Fripiat JJ, Pennequin M, Poncelet G, Cloos P (1969) *Clay Miner* 8:119–134
34. Huyskens TZ, Bator G (1996) *Vib Spectrosc* 13:41–49
35. Oxtan IA (1979) *J Mol Struct* 54:11–18
36. Blom DA, Vogt T, Allard LF, Buttrey DJ (2014) *Top Catal* 57:1138–1144
37. Todea AM, Merca A, Bögge H, Glaser T, Engelhardt L, Prozorov R, Luban M, Müller A (2009) *Chem Commun* 23:3351–3353
38. Laronze NL, Marrot J, Thouvenot R, Cadot E (2009) *Angew Chem Int Ed* 121:5086–5089
39. Schäffer C, Merca A, Bögge H, Todea AM, Kistler ML, Liu T, Thouvenot R, Gouzerh P, Müller A (2009) *Angew Chem Int Ed* 121:155–159

POMs for Batteries

Synthesis of Vanadium-Incorporated, Polyoxometalate-Based Open Frameworks and Their Applications for Cathode-Active Materials

Zhenxin Zhang,^{*,[a]} Hirofumi Yoshikawa,^[b] Zhongyue Zhang,^[c] Toru Murayama,^[d] Masahiro Sadakane,^[e] Yasunori Inoue,^[f] Wataru Ueda,^{*,[a]} Kunio Awaga,^[c] and Michikazu Hara^[f]

Abstract: The tuning of the chemical composition of polyoxometalate (POM)-based open framework materials with the same structure, leading to a property change of the materials, is interesting. Here, we report the synthesis of a series of vanadium-incorporated, ϵ -Keggin polyoxometalate-based open framework materials by using a hydrothermal method. The resulting materials were characterized by powder X-ray diffraction, FTIR spectroscopy, scanning electron microscopy, energy dispersive X-ray spectroscopy, X-ray photoelectron spectroscopy, and ele-

mental analysis. Our results indicate that V is successfully incorporated into the frameworks of the materials. The introduced amount of V can be adjusted by controlling the addition of the precursor V compounds. The performances of these materials as cathode materials for Li-ion batteries have been tested. Incorporation of V can improve the cycle performance. After the 20th cycle of the charge–discharge process, the materials were transformed to the Li_2MoO_4 phase.

Introduction

Polyoxometalates (POMs) are metal–oxygen clusters that are mainly comprised of transition metal ions, such as Mo, W, V, and Nb.^[1] POMs have attracted much attention because they exhibit interesting properties. POM-based open frameworks are comprised of POM sub-building blocks and linkers that are multi-dentate organic ligands or inorganic ions.^[2] POM-based open framework materials exhibit POM-like properties, such as multi-electron redox properties, acidity, stability, and composition diversity, and they also exhibit metal–organic framework (MOF)-like properties, such as structural diversity and porosity.

Recently, POMs have attracted much attention owing to their electron storage functions. POM molecules, such as

$[\text{PMo}_{12}\text{O}_{40}]^{3-}$,^[3–6] $[\text{PW}_{12}\text{O}_{40}]^{3-}$,^[4,7] $\text{Li}_7[\text{V}_{15}\text{O}_{36}(\text{CO}_3)]$,^[8] $\text{Na}_3[\text{AlMo}_6\text{O}_{24}\text{H}_6]$,^[9] and $[\text{SiW}_{11}\text{O}_{39}]^{8-}$,^[10] have been reported to be cathode-active materials for Li-ion batteries,^[11] and large capacities have been achieved. Furthermore, porosity is beneficial for Li-ion batteries, because Li ions can easily pass through the bulk,^[12] and the introduction of porosity into POM materials is interesting for the design and development of new cathode materials for Li-ion batteries. Therefore, POM-based open framework materials are expected to be candidates for Li-ion batteries.

We have reported a new catalogue of fully inorganic POM-based open framework materials, which comprise ϵ -Keggin POM units with transition metal ion linkers (Figure 1).^[13] In our previous papers, three ϵ -Keggin POM-based framework materials, Mo–V–Bi–O,^[14] Mo–Zn–O,^[15] and Mo–Mn–O,^[15] were reported. In Mo–V–Bi–O, a V–O tetrahedron is surrounded by 12 Mo–O and V–O octahedra to form a ϵ -Keggin POM that is linked by Bi^{III} ions to form a 3-dimensional framework structure. In Mo–Zn–O and Mo–Mn–O, Zn^{II} and Mn^{II} ions are located at the center of the tetrahedron and linker site, and Mo ions are in the surrounding sites. The materials exhibit interesting properties, such as elemental diversity,^[15] ion-exchange properties,^[14,15] acidity,^[14,16] redox properties,^[15] and microporosity,^[14,17] leading to a variety of applications including adsorption, separation, ion-exchange, and catalysis. Because of the redox properties of the materials, the materials are expected to be cathode-active materials for Li-ion batteries. Furthermore, redox and electrochemical properties are expected to be tuned with changes to the chemical compositions. However, thus far, no related research has been reported.

[a] Faculty of Engineering, Kanagawa University, Rokkakubashi, Kanagawa-ku, Yokohama-shi, Kanagawa, 221-8686, Japan
E-mail: zhang.z.ag@m.titech.ac.jp
uedaw@kanagawa-u.ac.jp

<http://apchem2.kanagawa-u.ac.jp/~uedalab/index.html>

[b] School of Science and Technology, Kwansei Gakuin University, 2-1 Gakuen, Sanda, Hyogo 669-1337, Japan

[c] Department of Chemistry, Graduate School of Science, Nagoya University, Furo-cho, Chikusa-ku, Nagoya, 464-8601, Japan

[d] Department of Applied Chemistry, Graduate School of Urban Environmental Sciences, Tokyo Metropolitan University, 1-1 Minami-osawa, Hachioji, Tokyo 192-0397, Japan

[e] Department of Applied Chemistry, Graduate School of Engineering, Hiroshima University, 1-4-1 Kagamiyama, Higashi Hiroshima 739-8527, Japan

[f] Materials and Structures Laboratory, Tokyo Institute of Technology, Nagatsuta-cho 4259, Midori-ku, Yokohama-city, Kanagawa, 226-8503, Japan

Supporting information for this article is available on the WWW under <http://dx.doi.org/10.1002/ejic.201501396>.

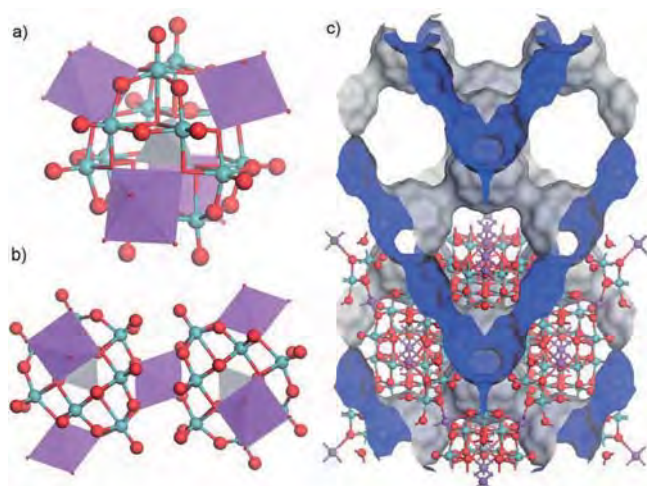


Figure 1. Ball-and-stick representation of (a) ϵ -Keggin unit with four linking metal ions, (b) the connection of two ϵ -Keggin units by linking metal ions (light blue sphere: surrounding site; gray tetrahedron: central site; purple octahedron: linker site; red sphere: oxygen), and (c) framework of the fully inorganic microporous POM-based materials and micropore system of the material indicated by the Connolly surface.

Herein, we provide a synthetic method for tuning the composition of ϵ -Keggin POM-based open framework materials by the incorporation of vanadium in both Mo-Zn-O and Mo-Mn-O, which are denoted as Mo-Zn-V_x-O and Mo-Mn-V_x-O. These materials were characterized by using powder X-ray diffraction (XRD), Fourier transform-infrared (FTIR), scanning electron microscopy (SEM), energy dispersive X-ray spectroscopy (EDX), X-ray photoelectron spectroscopy (XPS), and elemental analysis. The redox and electrochemical properties of the materials changed with the incorporation of different V contents in the materials. For the first time, the ϵ -Keggin POM-based open framework materials were successfully applied as cathode-active materials for Li-ion batteries, which performed well. The battery performance of the materials improved with the incorporation of V in the structures.

Results and Discussion

Material Synthesis and Characterization

The ϵ -Keggin POM-based open framework materials, Mo-Zn-O, Mo-Mn-O, and Mo-V-Bi-O, were synthesized according to the methods in previous papers. The XRD patterns and FTIR spectra are shown in Figure 2.

V was incorporated into the frameworks of Mo-Zn-O and Mo-Mn-O by introducing it in the starting mixture. After hydrothermal synthesis, the crude solids were recovered from the solution. A purification process was necessary to obtain pure materials. The settlement method (see the Experimental Section) was an effective approach to purify the materials. As indicated in the XRD patterns (Figure S1 in the Supporting Information), the solids recovered before purification showed the peaks of impurity phases, such as ZnMoO₄, Mo, VO₂, and V₅O₁₂, which were fully removed by the purification process. The yields of the materials for the various V contents used in the precursor solutions are shown in Figure S2. As the amount of V in the starting precursors increased, the yields of the resulting materials decreased. The synthesis of each V-incorporated sample was repeated three times to test reproducibility. XRD patterns of the materials from each synthesis are in Figure S3, which shows that the materials from each synthesis have the same structure. The yields of the materials were similar (Figure S2), demonstrating that the reproducibility of the synthesis was good.

Mo-Zn-V_x-O and Mo-Mn-V_x-O were characterized by powder XRD, which showed the characteristic powder diffraction patterns of ϵ -Keggin POM-based open framework materials (Figure 2, A, B). A diffraction peak shift was observed as the amount of V changed (Figure 2, B). As shown in Table 1, with an increase in V content to 10 %, $d_{(111)}$ of Mo-Zn-V_x-O and Mo-Mn-V_x-O decreased to 11.049 and 11.188 Å, respectively. The experimental powder XRD profiles of the V-substituted materials were fitted well by the Rietveld method using structure models of Mo-Zn-O and Mo-Mn-O^[4,15] with slight differences in the lattice parameters, the occupancies of water and cations, and the atom

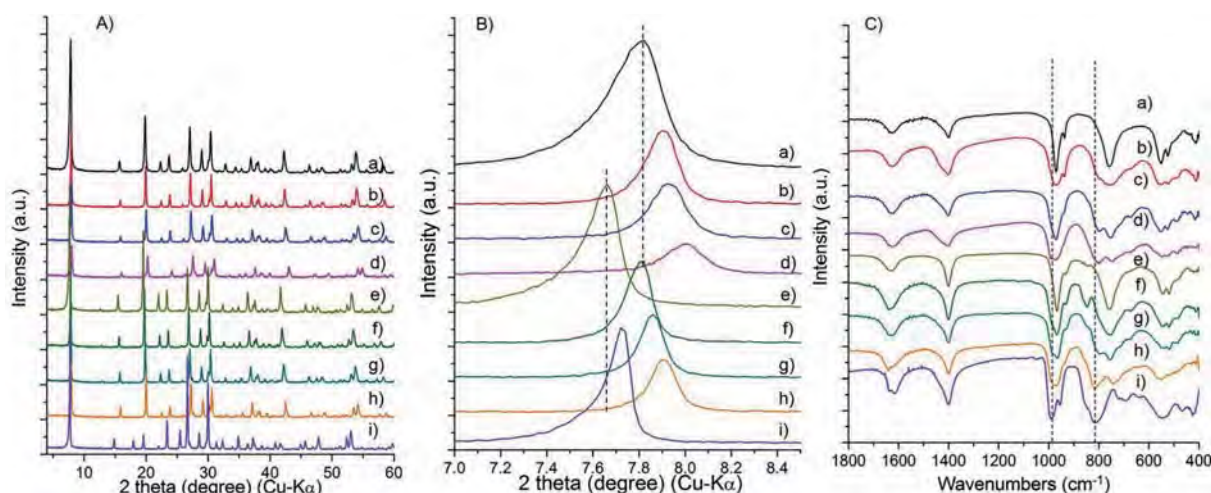


Figure 2. Powder XRD patterns of the whole 2θ range (A), enlargements of the $2\theta = 7\text{--}8.5^\circ$ region (B), and FTIR spectra (C) of the obtained materials: (a) Mo-Zn-O, (b) Mo-Zn-V_{0.01}-O, (c) Mo-Zn-V_{0.05}-O, (d) Mo-Zn-V_{0.1}-O, (e) Mo-Mn-O, (f) Mo-Mn-V_{0.01}-O, (g) Mo-Mn-V_{0.05}-O, (h) Mo-Mn-V_{0.1}-O, and (i) Mo-V-Bi-O.

Table 1. Structural information of the POM-based open framework materials.

Material	Formula	$d_{(111)}$ [Å]	a [Å]	V/(Mo+V) in precursor (V/all metal) ^[a]	V/(Mo+V) in material (V/all metal) ^[a]	Mo ^{VI} /Mo ^V	V ^V /V ^{IV}	3rd metal
Mo-V-Bi-O ^[14]	(NH ₄) _{2.8} H _{0.9} [Bi ₂ Mo _{9.4} V _{3.6} O ₄₀]·7.2H ₂ O	11.426	19.790	0.2 (0.19)	0.3 (0.26)	0.33	1	Bi ^{III}
Mo-Zn-O ^[17]	(NH ₄) _{1.5} H _{8.5} [Zn ₃ Mo ₁₂ O ₄₀]·6H ₂ O	11.240	19.468	0 (0)	0 (0)	0.5	– ^[b]	Zn ^{II}
Mo-Zn-V _{0.01} -O	(NH ₄) _{1.8} H ₁₀ [Zn ₃ Mo _{11.9} V _{0.1} O ₄₀]·6.5H ₂ O	11.169	19.345	0.01 (0.012) ^[c]	0.0083 (0.0067)	0.093	– ^[b]	Zn ^{II}
Mo-Zn-V _{0.05} -O	(NH ₄) _{1.8} H ₁₀ [Zn _{2.7} Mo _{11.6} V _{0.7} O ₄₀]·6.5H ₂ O	11.145	19.303	0.05 (0.039)	0.057 (0.047)	0.33	– ^[b]	Zn ^{II}
Mo-Zn-V _{0.1} -O	(NH ₄) _{1.8} H ₇ [Zn _{2.6} Mo _{11.2} V _{1.2} O ₄₀]·6H ₂ O	11.049	19.137	0.1 (0.078)	0.097 (0.08)	4.0	1.3	Zn ^{II}
Mo-Mn-O ^[15]	(NH ₄) _{2.1} H _{7.5} [Mn _{2.2} Mo ₁₂ O ₄₀]·4H ₂ O	11.350	19.658	0 (0)	0 (0)	1	– ^[b]	Mn ^{II}
Mo-Mn-V _{0.01} -O	(NH ₄) ₂ H ₁₄ [Mn _{2.4} Mo ₁₂ V _{0.2} O ₄₀]·5H ₂ O	11.311	19.591	0.01 (0.012) ^[c]	0.016 (0.014)	0	– ^[b]	Mn ^{II}
Mo-Mn-V _{0.05} -O	(NH ₄) _{2.2} H ₁₂ [Mn _{2.2} Mo _{11.9} V _{0.7} O ₄₀]·5H ₂ O	11.247	19.480	0.05 (0.039)	0.056 (0.047)	0.42	– ^[b]	Mn ^{II}
Mo-Mn-V _{0.1} -O	(NH ₄) _{2.2} H ₉ [Mn _{2.2} Mo _{11.6} V _{1.0} O ₄₀]·5H ₂ O	11.188	19.378	0.1 (0.078)	0.079 (0.068)	10.9	1.3	Mn ^{II}

[a] Molar ratio. [b] V content was too low for determination. [c] Each synthesis and corresponding elemental analysis were repeated three times and the elemental analysis data is in Experimental Section.

positions (Figures S4–S9 and Tables S1–S7). There were no additional peaks observed, indicating that the samples were pure. These results indicate that the basic structures of Mo-Zn-V_x-O and Mo-Mn-V_x-O were identical to those of Mo-Zn-O and Mo-Mn-O and that V was incorporated into the framework.

SEM images showed that Mo-Zn-V_x-O and Mo-Mn-V_x-O were well-crystallized materials with polyhedral morphology (Figure 3). The crystallite size was several tens of nanometers to several hundreds of nanometers. The EDX elemental mapping showed the presence of Mo, V, Zn, and Mn in the materials. Compared with the corresponding SEM images, Mo, Zn, and Mn showed strong EDX signals, with a uniform distribution of the particles, indicating that Mo, Zn, and Mn were uniformly incorporated into the corresponding materials. No V signal was detected for Mo-Zn-O and Mo-Mn-O (Figure 3, a, e), and the signal of V was weak when the content was low (Figure 3, b, c, f, g). As the V content in the materials increased, the mapping signal became stronger (Figure 3, d, h). The distribution of V in the materials was uniform, indicating that V was incorporated well into the frameworks of the materials.

The V content in the materials was further confirmed by elemental analysis. The content of metal ions for each case is listed in Table 1. The V content increased in the materials with in-

creased amounts of V source in the precursor solutions for the corresponding materials. The molar ratio of V/(Mo+V) in the materials was similar to that in the starting precursors, which demonstrates that the V content can be tuned by adjusting the amount of the V starting compounds (Table 1). In the case of V-incorporated samples with low V content (Mo-Zn-V_{0.01}-O and Mo-Zn-V_{0.05}-O), the synthesis and corresponding elemental analysis were repeated three times. The result indicated that the content of V was almost the same in the three analysis (see the Experimental Section), which indicated that the reproducibility of the materials was good. The chemical formulae based on the elemental analysis were estimated and are shown in Table 1.

There are three sites (Figure 1), the surrounding site, the central site, and the linker site, that have potential for V incorporation. The Rietveld analysis was not accurate enough to determine the position of V in the materials. The elemental analysis (Table 1) showed that introducing V into the materials decreased not only the Mo content, but also the amount of Zn ions in Mo-Zn-O, which indicated that V replaced both Mo and Zn. In Mo-Zn-O, V incorporation decreased Mo and affected the Mn content. The results indicated that V might be present in the surrounding, linker, and central sites.

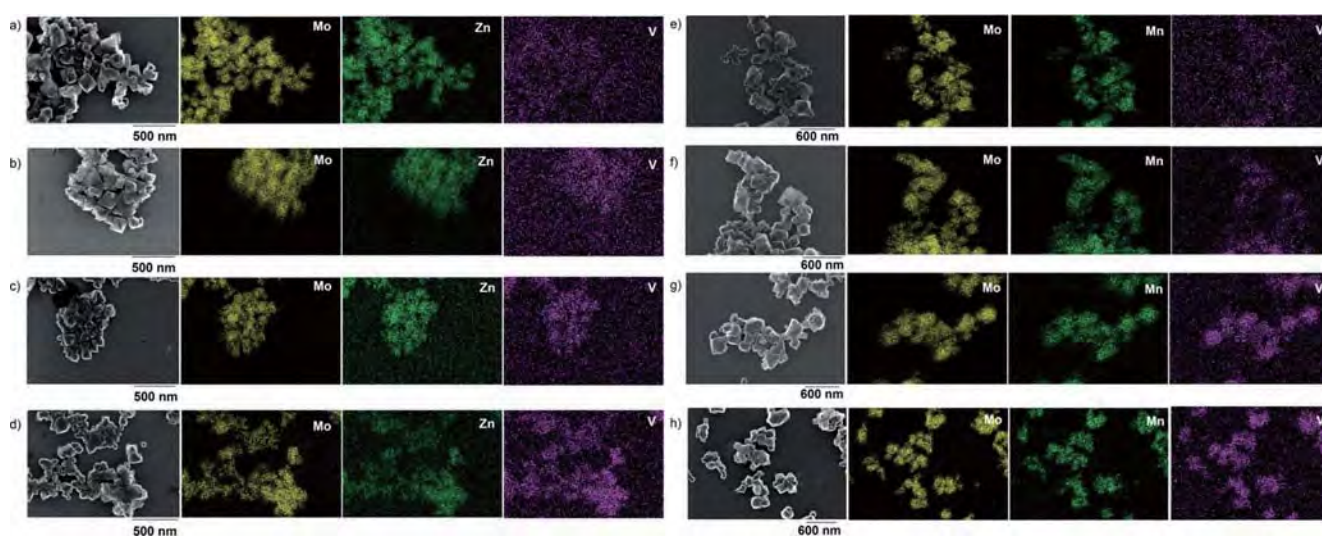


Figure 3. SEM images (left) and the corresponding EDX elemental mapping images of (a) Mo-Zn-O, (b) Mo-Zn-V_{0.01}-O, (c) Mo-Zn-V_{0.05}-O, (d) Mo-Zn-V_{0.1}-O, (e) Mo-Mn-O, (f) Mo-Mn-V_{0.01}-O, (g) Mo-Mn-V_{0.05}-O, and (h) Mo-Mn-V_{0.1}-O.

Mo-Zn-V_x-O and Mo-Mn-V_x-O were characterized by using FTIR (Figure 2, C). There are water and ammonium cations in the materials, as determined by the IR bands at 1640 cm⁻¹ and 1400 cm⁻¹, respectively. The IR peaks below 1000 cm⁻¹ were ascribed to the POM moiety. The signal at approximately 970 cm⁻¹ was ascribed to the terminal Mo=O, and the peaks between approximately 800 and 600 cm⁻¹ were ascribed to Mo-O-Mo. Compared with the V-free materials, new IR bands were observed in the materials for Mo-Zn-V_x-O and Mo-Mn-V_x-O, which were present at approximately 990 cm⁻¹ and 820 cm⁻¹,

respectively. As the amount of V increased, the intensity of the new bands increased. The IR bands at approximately 990 cm⁻¹ and 820 cm⁻¹ may be ascribed to terminal V=O and Mo-O-V, respectively, indicating that the binding state of the materials changed after V incorporation.

The metal ion valences of the POM-based open framework materials were affected by introducing V. The oxidation states of the metal elements were analyzed by XPS spectra curve fitting of Mo-Zn-V_x-O and Mo-Mn-V_x-O (Figure 4). The Mo ions were a mixture of Mo^V and Mo^{VI}. The V content in the materials

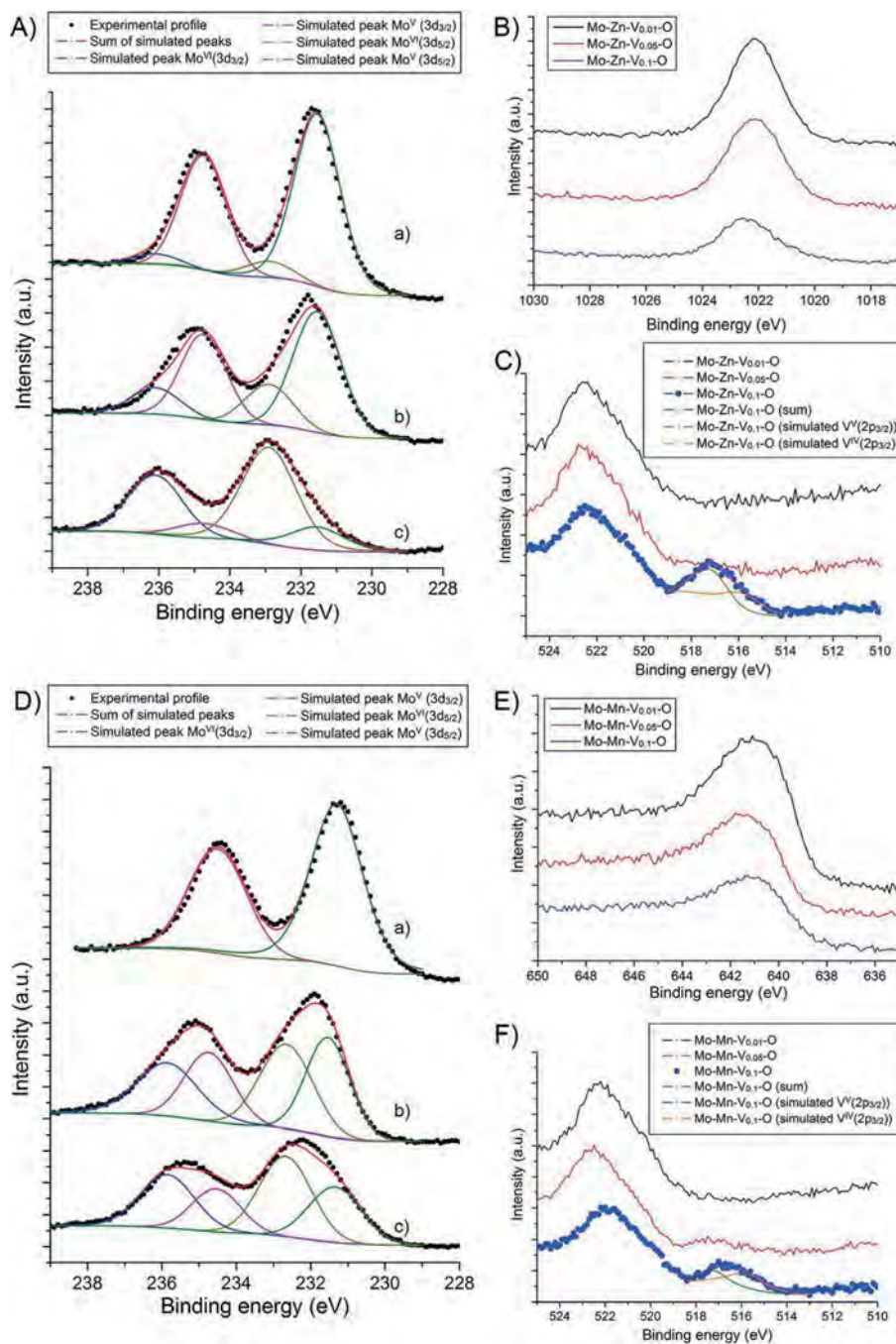


Figure 4. (A) XPS spectra of Mo ions in Mo-Zn-V_x-O: (a) Mo-Zn-V_{0.01}-O, (b) Mo-Zn-V_{0.05}-O, and (c) Mo-Zn-V_{0.1}-O. (B) XPS spectra of Zn ions in Mo-Zn-V_x-O. (C) XPS spectra of V ions in Mo-Zn-V_x-O. (D) XPS spectra of Mo ions in Mo-Mn-V_x-O: (a) Mo-Mn-V_{0.01}-O, (b) Mo-Mn-V_{0.05}-O, and (c) Mo-Mn-V_{0.1}-O. (E) XPS spectra of Zn ions in Mo-Mn-V_x-O. (F) XPS spectra of V ions in Mo-Mn-V_x-O.

affected the Mo ion valence. Most of the Mo ions were reduced to Mo^{V} when the V content was low (0.01 and 0.05 V incorporation). With increasing V content, most of the Mo ions were oxidized to Mo^{VI} . The molar ratio of $\text{Mo}^{\text{VI}}/\text{Mo}^{\text{V}}$ is provided in Table 1. The linker and central elements (Zn and Mo) were Zn^{II} and Mn^{II} , respectively, and they were not affected by V (Figure 4, B, E, and Table 1). The V_{2p} peak indicated the presence of V in the materials, and the V_{2p} peak intensity increased with increasing V content, which is in good agreement with the elemental analysis and EDX mapping (Figure 4, C, F). The valence of V in $\text{Mo-Zn-V}_{0.1}\text{-O}$ and $\text{Mo-Mn-V}_{0.1}\text{-O}$ was V^{IV} and V^{V} , and the $\text{V}^{\text{IV}}/\text{V}^{\text{V}}$ ratio was 1.3. The UV/Vis spectra of the materials showed that with increasing V content in the material, the resulting spectra continually changed (Figure S10), which also indicated that the V content affected the oxidation states of the materials.

N_2 adsorption–desorption measurements showed the materials $\text{Mo-Zn-V}_{0.1}\text{-O}$ and $\text{Mo-Mn-V}_{0.1}\text{-O}$ were microporous materials (Figure S11). The micropores of the materials are surrounded

by POM units with transition metal ion linkers (Figure 1, c). The micropores are accessible to some small molecules or cations, which results in the materials exhibiting adsorption and ion-exchange properties.^[14,15]

Electrochemical Performance

Before the charge–discharge experiments, all of the cathodes (containing 10 wt.-% of POM, 70 wt.-% of carbon black, and 20 wt.-% of binder) were characterized by powder XRD (Figure 5, a). The broad peak between 10 and 30° was ascribed to carbon black. The powder XRD showed that all the materials after being made into cathodes were well-crystallized materials, and structures of the materials were consistent with the as-prepared ones.

The charge–discharge experiments showed the performance of the batteries using the samples as cathode-active materials (the measurement conditions and devices are provided in in

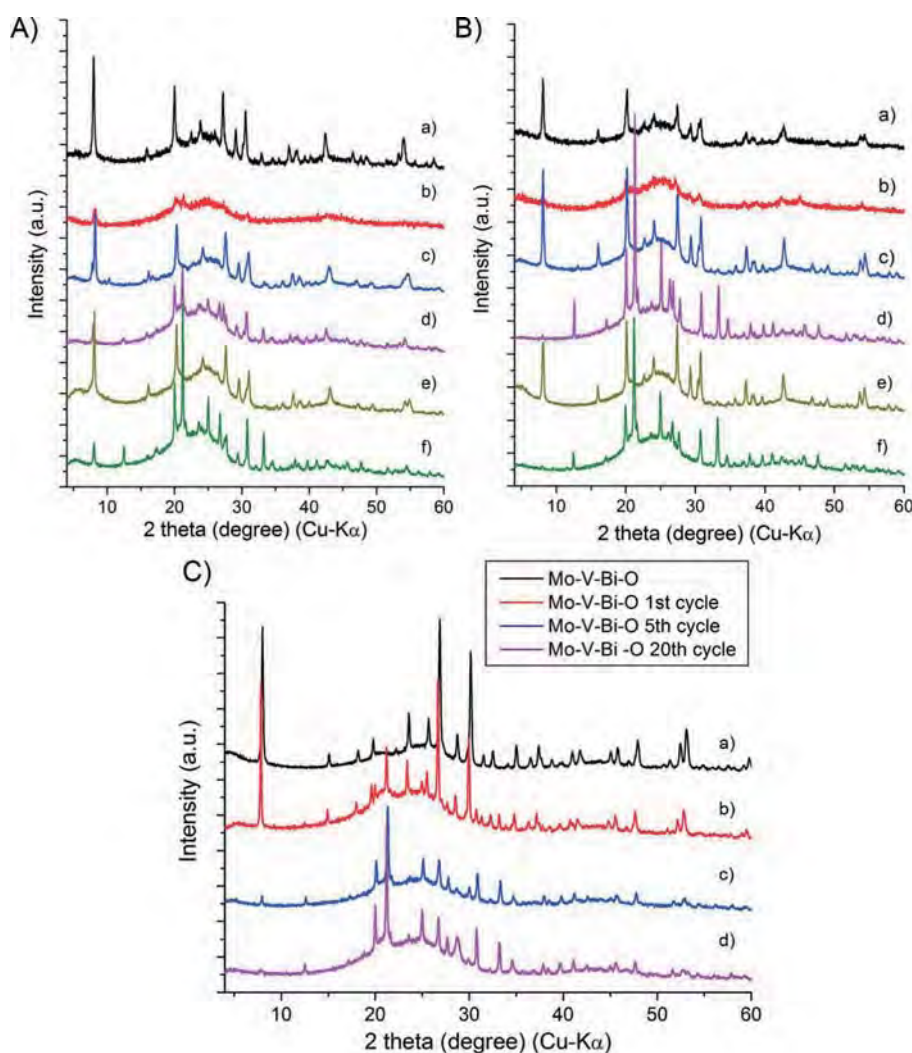


Figure 5. (A) XRD patterns of (a) fresh Mo-Zn-O , (b) used Mo-Zn-O (20 times), (c) fresh $\text{Mo-Zn-V}_{0.05}\text{-O}$, (d) used $\text{Mo-Zn-V}_{0.05}\text{-O}$ (20 times), (e) fresh $\text{Mo-Zn-V}_{0.1}\text{-O}$, and (f) used $\text{Mo-Zn-V}_{0.1}\text{-O}$ (20 times). (B) XRD patterns of (a) fresh Mo-Mn-O , (b) used Mo-Mn-O (20 times), (c) fresh $\text{Mo-Mn-V}_{0.05}\text{-O}$, (d) used $\text{Mo-Mn-V}_{0.05}\text{-O}$ (20 times), (e) fresh $\text{Mo-Mn-V}_{0.1}\text{-O}$, and (f) used $\text{Mo-Mn-V}_{0.1}\text{-O}$ (20 times). (C) XRD patterns of (a) fresh Mo-V-Bi-O , (b) used Mo-V-Bi-O (1 time), (c) used Mo-V-Bi-O (5 times), and (d) used Mo-V-Bi-O (20 times).

the Experimental Section). For the materials without V, Mo-Zn-O and Mo-Mn-O, as shown in Figure 6 and Figure S12, respectively, the first discharge curve gradually decreased, and large capacities of 270 A h kg⁻¹ and 269 A h kg⁻¹, respectively, were obtained. Assuming that all Mo ions (Mo^V and Mo^{VI}) were reduced to Mo^{IV} after discharge, the theoretical capacity for Mo-Zn-O (Mo^{VI}/Mo^V = 4:8, 16e⁻ reduction)^[17] and Mo-Mn-O (Mo^{VI}/Mo^V = 6:6, 18e⁻ reduction)^[15] were calculated to be approximately 200 A h kg⁻¹ and 230 A h kg⁻¹ (see the Experimental Section for the detailed methodology for the calculation and Table 1 for the metal ion valence of the original samples). The initial discharge capacity was slightly higher than the theoretical capacity. In the second discharge process, the capacities decreased to 171 A h kg⁻¹ and 176 A h kg⁻¹ for Mo-Zn-O and Mo-Mn-O, respectively, and after 20 cycles, they were stabilized at 110 A h kg⁻¹ and 100 A h kg⁻¹, respectively. After 20 cycles, only

38 % and 40 %, respectively, of the initial capacity remained, as shown in the cycle performance data (Table S8).

The battery performances of the V-incorporated samples were also evaluated. V was incorporated to form Mo-Zn-V_x-O and Mo-Mn-V_x-O, and the amount of V could be adjusted. V affected the Li-ion battery performance of the materials (Figure 6 and Figure S12). With increasing V content in the samples, the first discharge capacity decreased in most cases, whereas the cycle performance increased (Figure 6, a–d). Approximately 81 % and 70 % of the capacity for Mo-Zn-V_{0.1}-O and Mo-Mn-V_{0.1}-O remained, respectively, after 20 cycles of the charge–discharge experiments. The 20th discharge capacities of the V-incorporated materials were higher than those of the V-free samples.

Mo-V-Bi-O, an iso-structural material of Mo-Zn-V_x-O and Mo-Mn-V_x-O, had a capacity of approximately 320 A h kg⁻¹ during

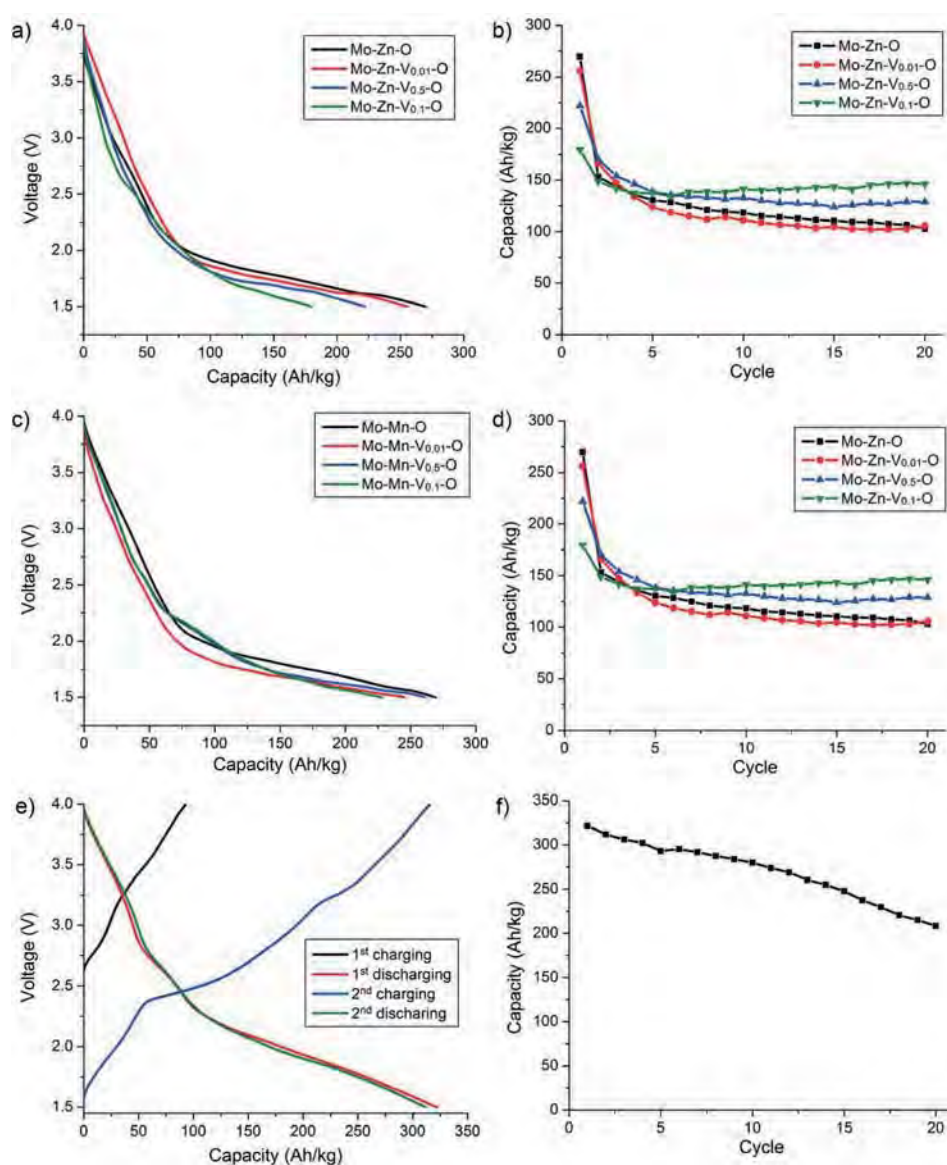


Figure 6. (a) First discharge curves of the Mo-Zn-V_x-O series. (b) Cycle performances of the Mo-Zn-V_x-O series. (c) First discharge curves of the Mo-Mn-V_x-O series. (d) Cycle performances of the Mo-Mn-V_x-O series. (e) First and second charge and discharge curves of Mo-V-Bi-O. (f) Cycle performances of Mo-V-Bi-O.

the first discharge process, which was the highest among all of the ϵ -Keggin POM-based open framework materials (Figure 6, e). The material lost some capacity after each charge–discharge cycle, which is different from other ϵ -Keggin POM-based open framework materials (Figure 6, f). After 20 cycles, approximately 70 % of the original capacity still remained. Assuming that the Mo ions (Mo^{V} and Mo^{VI}) were reduced to Mo^{IV} and the V ions (V^{IV} and V^{V}) were reduced to V^{II} , the theoretical capacity of Mo-V-Bi-O is approximately 290 A h kg^{-1} , which is similar to the experimental data. The best cycle performance might be due to the high stability of the material.^[14,15] Although the materials Mo-Zn-V_x-O, Mo-Mn-V_x-O, and Mo-V-Bi-O are isostructural, the difference in the chemical composition resulted in different electrochemical properties and Li-ion battery performances. To understand this phenomenon, the structures of the materials were characterized after using them for the Li-ion batteries.

Structure of the Materials After Use in Li-ion Batteries

After they were used as cathodes for Li-ion batteries, Mo-Zn-O and Mo-Mn-O were characterized by powder XRD (Figure 5, A, b, and B, b). The characteristic diffraction peaks for ϵ -Keggin POM-based open framework materials decreased dramatically. The V-free materials were assumed to be decomposed, forming some amorphous compounds. The capacity significantly decreased owing to the structural collapse after the charge–discharge process.

On the other hand, V affected the materials' structures after the materials were used as cathodes. In the case of Mo-V-Bi-O, some new peaks were detected in the XRD patterns after the first discharge process, indicating that a portion of Mo-V-Bi-O was transformed into other phases (Figure 5, A, b). After the fifth discharge, most of the peaks of the Mo-V-Bi-O phase disappeared, and all of the peaks that appeared represented the newly generated phase, which was the same as the phase after the 20th discharge (Figure 5, A, c, d). This result indicated that the structure of Mo-V-Bi-O changed. Mo-Zn-V_{0.05}-O, Mo-Zn-V_{0.1}-O, Mo-Mn-V_{0.05}-O, and Mo-Mn-V_{0.1}-O contained a certain amount of V after using them for the Li-ion batteries, and the structures of the materials were transformed to the same phase as that of Mo-V-Bi-O (Figure 5, B, C). The behavior of their cycle performance was similar to that of Mo-V-Bi-O. The newly generated phase was identified as a Li_2MoO_4 phase (PDF number: 01–070–8448, hexagonal, $R3c$, lattice parameters: $a = 14.27 \text{ \AA}$, $c = 9.55 \text{ \AA}$). The structure of the material was refined by Rietveld analysis. The simulated pattern was similar to that of the experimental pattern (Figure S13). The structure of the used compound (the new phase) was formed by the connection of MoO_4 tetrahedra with LiO_4 tetrahedra, which was different from the original compound (based on metal–oxygen octahedra). It has been reported that Li_2MoO_4 -type materials perform well as cathodes for Li-ion batteries.^[18] The structural transformation to the Li_2MoO_4 -phase might be why the V-incorporated sample exhibited a good cycle performance and a high capacity.

Conclusion

A series of V-incorporated, ϵ -Keggin POM-based open framework materials, Mo-Zn-V_x-O and Mo-Mn-V_x-O, were synthesized and structurally characterized. V was introduced into the framework of the materials, as indicated by XRD, FTIR, elemental analysis, and EDX-mapping. The V content can be adjusted by the initial V molar ratio in the precursor. Mo-Zn-V_x-O, Mo-Mn-V_x-O, and Mo-V-Bi-O exhibited high activities as cathode materials for Li-ion batteries. The incorporation of V resulted in a phase transformation to a stable phase (Li_2MoO_4 phase), which led to an improvement in the cycle performance of the Li-ion battery.

Experimental Section

Material Synthesis

Synthesis of Mo-Zn-V_x-O: The V-substituted, ϵ -Keggin zirconomolybdate-based materials were synthesized by using the hydrothermal method. $(\text{NH}_4)_6\text{Mo}_7\text{O}_{24}\cdot 4\text{H}_2\text{O}$ [11.7 (based on Mo) – x mmol, $x = 0.117, 0.585, \text{ or } 1.17 \text{ mmol}$] was dissolved in water (40 mL). NH_4VO_3 ($x = 0.117, 0.585, \text{ or } 1.17 \text{ mmol}$) was added to the mixture. Metal Mo (0.2 g, 2.08 mmol) and ZnCl_2 (0.453 g, 3.33 mmol) were added to the solution in succession. The mixture was introduced into the Teflon[®] liner of a stainless-steel autoclave that was fixed in a rotation oven. The hydrothermal synthesis was conducted at 448 K for 24 h with rotation (1 rpm). After the hydrothermal reaction and cooling of the autoclave, the crude solid was collected by centrifugation (3500 rpm, 5 min). For purification and solid recovery, the crude solid was dispersed in water (90 mL), and the mixture was centrifuged (1700 rpm, 2 min). Approximately 80 mL of the solution after centrifugation was collected. The addition of water (80 mL), centrifugation, and separation were performed two additional times. The collected suspension (containing the product) was centrifuged (3500 rpm, 120 min), and the solid at the bottom of the centrifugation tube was collected. The collected solid was washed with water three times by dispersing in water (10 mL), followed by subsequent centrifugation (3500 rpm, 120 min). The obtained solids are denoted as Mo-Zn-V_x-O, where $x = 0.01, 0.05, \text{ or } 0.1$, and were dried at 333 K overnight. The Mo-Zn-V_x-O (yield: 71–53 % based on Mo) compounds were then obtained.

Synthesis of Mo-Mn-V_x-O: $(\text{NH}_4)_6\text{Mo}_7\text{O}_{24}\cdot 4\text{H}_2\text{O}$ [11.7 (based on Mo) – x mmol, $x = 0.117, 0.585, \text{ or } 1.17 \text{ mmol}$] was dissolved in water (40 mL). NH_4VO_3 ($x = 0.117, 0.585, \text{ or } 1.17 \text{ mmol}$) was added to the mixture. Metal Mo (0.2 g, 2.08 mmol) and MnO (0.236 g, 3.33 mmol) were added to the solution in succession. The mixture was introduced into the Teflon[®] liner of a stainless-steel autoclave that was fixed in a rotation oven. The hydrothermal synthesis was conducted at 448 K for 24 h with rotation (≈ 1 rpm). For material purification and collection, the process was the same as that of Mo-Zn-V_x-O. The resulting materials, which are denoted as Mo-Mn-V_x-O, where $x = 0.01, 0.05, \text{ or } 0.1$ (yield: 43–35 % based on Mo) were obtained.

Synthesis of Mo-V-Bi-O: Mo-V-Bi-O was prepared according to our previous paper.^[14] $(\text{NH}_4)_6\text{Mo}_7\text{O}_{24}\cdot 4\text{H}_2\text{O}$ (8.828 g, 50 mmol based on Mo), $\text{VOSO}_4\cdot 5\text{H}_2\text{O}$ (3.219 g, 12.5 mmol), and $\text{Bi}(\text{OH})_3$ (0.438 g, 1.67 mmol) were added to water (240 mL), followed by N_2 bubbling of the solution for 10 min. The mixture was introduced into the Teflon liner of a stainless-steel autoclave, and the autoclave was placed in an oven and heated at 448 K for 48 h.

Synthesis of V-Free Samples: Mo-Zn-O and Mo-Mn-O were synthesized according to the previously reported method.^[15,17]

(NH₄)₆Mo₇O₂₄·4H₂O (2.060 g, 11.7 mmol based on Mo), Mo (0.2 g, 2.08 mmol), and ZnCl₂ or MnO (3.33 mmol) were added to water (40 mL). The mixture was introduced into the Teflon[®] liner of a stainless-steel autoclave and the autoclave was placed in an oven and heated at 448 K for 24 h.

Elemental Analysis of Mo-Zn-V_x-O and Mo-Mn-V_x-O

Mo-Zn-V_{0.01}-O: Calcd (%) for H_{30.2}N_{1.8}Mo_{11.9}Zn₃V_{0.1}O_{46.5}: N 1.18, Mo 53.29, Zn 9.16, V 0.24, H, 1.41; found: N 1.19, Mo 52.90, Zn 9.16, V 0.27 ± 0.02, (0.26, 0.29, and 0.26, for the material from each synthesis), H 1.41.

Mo-Zn-V_{0.05}-O: Calcd for H_{30.2}N_{1.8}Mo_{11.6}Zn_{2.7}V_{0.7}O_{46.5}: N 1.19, Mo 52.38, Zn 8.31, V 1.68, H 1.42; found: N 1.18, Mo 52.12, Zn 8.38, V 1.55, H 1.40.

Mo-Zn-V_{0.1}-O: Calcd for H_{26.2}N_{1.8}Mo_{11.2}Zn_{2.6}V_{1.2}O₄₆: N 1.20, Mo 51.34, Zn 8.12, V 2.92, H 1.25; found: N 1.25, Mo 51.52, Zn 8.03, V 2.91, H 1.29.

Mo-Mn-V_{0.01}-O: Calcd for H₃₂N₂Mo₁₂Mn_{2.4}V_{0.2}O₄₅: N 1.35, Mo 55.53, Mn 6.36, V 0.49, H 1.54; found: N 1.39, Mo 55.73, Mn 6.31, V 0.43 ± 0.02 (0.45, 0.41, and 0.42 for the material from each synthesis), H 1.56.

Mo-Mn-V_{0.05}-O: Calcd for H_{30.8}N_{2.2}Mo_{11.9}Mn_{2.2}V_{0.7}O₄₅: N 1.48, Mo 54.89, Mn 5.81, V 1.71, H 1.48; found: N 1.55, Mo 54.89, Mn 5.33, V 1.65, H 1.49.

Mo-Mn-V_{0.1}-O: Calcd for H_{27.8}N_{2.2}Mo_{11.6}Mn_{2.2}V₁O₄₅: N 1.49, Mo 53.94, Mn 5.86, V 2.47, H 13.5; found: N 1.52, Mo 53.51, Mn 5.78, V 2.43, H 1.32.

Electrochemical Measurements

The cathode, which included 10 wt.-% of the POM-based material, was prepared as follows: POM, carbon black, and polyvinylidene fluoride (PVDF) in the weight ratio of 1:7:2 were mixed homogeneously. Then, 1-methyl-2-pyrrolidinone (approximately 0.5 mL) was added. The mixture was pressed into a plate of a thickness of approximately 0.3 mm. The plate was cut into small discs and dried under vacuum for 2 h.

The cell used for testing the Li-ion battery performance is shown in Figure S14. Lithium metal was used as the anode material. The anode was isolated from the cathode by a polyolefin film separator. The cathode and anode were set in a coin cell with an electrolyte (LiPF₆) dissolved in a mixed solution of diethyl carbonate (DEC) and ethylene carbonate (EC) (DEC/EC = 1:1) in an inert atmosphere. The charge–discharge measurements were performed at a constant current density of 1 mA cm⁻² in the voltage range of 1.5–4.0 V.

The theoretical capacity was calculated by using the following equation:

$$\text{capacity} = (N_A \times n_e \times 1.602 \times 10^{-19}) / (3.6 M)$$

where N_A is Avogadro's constant, n_e is the number of electrons reduced, and M is the molecular weight of the material based on the formula.

Characterization: The XRD patterns were obtained with a RINT2200 (Rigaku, Japan) with Cu-K_α radiation (tube voltage: 40 kV, tube current: 20 mA). The SEM images and EDX analysis were obtained with a HD-2000 (HITACHI, Japan). Fourier transform infrared (FTIR) analysis was conducted with a PARAGON 1000 (Perkin–Elmer, USA). XPS analysis was performed with an ESCA-3400 (Shimadzu, Japan). The spectrometer energies were calibrated by using the Au(4f_{7/2}) peak at 84 eV. N₂ adsorption–desorption measurements were carried out with a Belsorp MAX (BEL, Japan). Before the measurements, the materials were calcined at 473 K for 2.5 h in high

vacuum. Surface area was calculated by the Brunauer–Emmett–Teller (BET) method by using the adsorption branch. The elemental composition was determined by using an inductively coupled plasma (ICP–AES) method (ICPE-9000, Shimadzu, Japan). The CHN elemental composition was determined at the Instrumental Analysis Division of the Equipment Management Center in the Creative Research Institution of Hokkaido University.

Rietveld Refinement: The structures of Mo-Zn-V_{0.01}-O, Mo-Zn-V_{0.05}-O, Mo-Zn-V_{0.1}-O, Mo-Mn-V_{0.01}-O, Mo-Mn-V_{0.05}-O, and Mo-Mn-V_{0.1}-O were refined by powder XRD Rietveld refinement by using the Reflex Plus program in the Materials Studio software package.^[19] The initial structures of the materials were obtained from Mo-Zn-O and Mo-Mn-O.^[15] The lattice and pattern parameters of the materials were refined by the Pawley method. Then, isotropic temperature factors were provided for every atom in the initial structures. The Rietveld analysis was started with the initial models of the materials, and the lattice and pattern parameters were obtained from the Pawley refinement. Every atom position was refined. The occupancies of the atoms in the framework was fixed without further refinement, and the occupancies of the atoms in the water molecules and cations were refined. Finally, the pattern parameters were refined again to obtain the lowest R_{wp} value. The crystallographic parameters and the atom positions of the V-substituted materials are shown in Tables S1–S7.

Acknowledgments

This research was financially supported by a Grant-in-Aid for Scientific Research (A) from the Ministry of Education, Culture, Sports, Science, and Technology of Japan (MEXT) (grant number 2324-6135).

Keywords: Redox chemistry · Batteries · Polyoxometalates · Lithium · Vanadium

- [1] a) Y. Kamiya, M. Sadakane, W. Ueda, *Heteropoly Compounds*, in: *Comprehensive Inorganic Chemistry II* (Eds.: K. Reedijk, J. Poepelmeier), Elsevier, Oxford, UK, **2013**, p. 185–204; b) D.-L. Long, R. Tsunashima, L. Cronin, *Angew. Chem. Int. Ed.* **2010**, *49*, 1736–1758; *Angew. Chem.* **2010**, *122*, 1780–1803; c) *Polyoxometalates*, C. L. Hill (Ed.), *Chem. Rev.* **1998**, *98*, 1–390; d) *Polyoxometalates*, L. Cronin, A. Müller (Eds.), *Chem. Soc. Rev.* **2012**, *41*, 7325–7648; e) M. T. Pope, *Heteropoly and Isopoly Oxometalates*, Springer-Verlag, Berlin, **1983**.
- [2] a) H. N. Miras, L. Vilà-Nadal, L. Cronin, *Chem. Soc. Rev.* **2014**, *43*, 5679–5699; b) B. Nohra, H. El Moll, L. M. Rodriguez Albelo, P. Mialane, J. Marrot, C. Mellot-Draznieks, M. O'Keeffe, R. N. Biboum, J. Lemaire, B. Keita, L. Nadjo, A. Dolbecq, *J. Am. Chem. Soc.* **2011**, *133*, 13363–13374; c) L. M. Rodriguez-Albelo, A. Rabdel Ruiz-Salvador, A. Sampieri, D. W. Lewis, A. Gomez, B. Nohra, P. Mialane, J. Marrot, F. Secheresse, C. Mellot-Draznieks, R. N. Biboum, B. Keita, L. Nadjo, A. Dolbecq, *J. Am. Chem. Soc.* **2009**, *131*, 16078–16087.
- [3] N. Kawasaki, H. Wang, R. Nakanishi, S. Hamanaka, R. Kitaura, H. Shinohara, T. Yokoyama, H. Yoshikawa, K. Awaga, *Angew. Chem. Int. Ed.* **2011**, *50*, 3471–3474; *Angew. Chem.* **2011**, *123*, 3533–3536.
- [4] M. Lira-Cantu, P. Gomez-Romero, *Chem. Mater.* **1998**, *10*, 698–704.
- [5] H. Yang, T. Song, L. Liu, A. Devadoss, F. Xia, H. Han, H. Park, W. Sigmund, K. Kwon, U. Paik, *J. Phys. Chem. C* **2013**, *117*, 17376–17381.
- [6] N. Sonoyama, Y. Suganuma, T. Kume, Z. Quan, *J. Power Sources* **2011**, *196*, 6822–6827.
- [7] M. Genovese, K. Lian, *Curr. Opin. Solid State Mater. Sci.* **2015**, *19*, 126–137.
- [8] J.-J. Chen, M. D. Symes, S.-C. Fan, M.-S. Zheng, H. N. Miras, Q.-F. Dong, L. Cronin, *Adv. Mater.* **2015**, *27*, 4649–4654.
- [9] E. Ni, S. Uematsu, N. Sonoyama, *J. Power Sources* **2014**, *267*, 673–681.

- [10] D. Ma, L. Liang, W. Chen, H. Liu, Y.-F. Song, *Adv. Funct. Mater.* **2013**, *23*, 6100–6105.
- [11] a) M. Armand, J.-M. Tarascon, *Nature* **2008**, *451*, 652–657; b) J.-M. Tarascon, M. Armand, *Nature* **2001**, *414*, 359–367; c) V. Thangadurai, S. Narayanan, D. Pinzar, *Chem. Soc. Rev.* **2014**, *43*, 4714–4727; d) J. Chen, *Chem. Soc. Rev.* **2015**, *44*, 699–728; e) P. Simon, Y. Gogotsi, *Nat. Mater.* **2008**, *7*, 845–854; f) X. Hu, W. Zhang, X. Liu, Y. Mei, Y. Huang, *Chem. Soc. Rev.* **2015**, *44*, 2376–2404.
- [12] a) Z. Zhang, H. Yoshikawa, K. Awaga, *J. Am. Chem. Soc.* **2014**, *136*, 16112–16115; b) Y. Lin, Q. Zhang, C. Zhao, H. Li, C. Kong, C. Shen, L. Chen, *Chem. Commun.* **2014**, *51*, 697–699.
- [13] Z. Zhang, M. Sadakane, W. Ueda, *Assembly of ϵ -Keggin-type Polyoxometalates to Form Crystalline Microporous Metal Oxides*, in: *Trends in Polyoxometalates Research* (Eds.: L. Ruhlmann, D. Schaming), Nova Science Publishers, Hauppauge, **2015**, p. 409–428.
- [14] Z. Zhang, M. Sadakane, T. Murayama, S. Izumi, N. Yasuda, N. Sakaguchi, W. Ueda, *Inorg. Chem.* **2014**, *53*, 903–911.
- [15] Z. Zhang, M. Sadakane, T. Murayama, N. Sakaguchi, W. Ueda, *Inorg. Chem.* **2014**, *53*, 7309–7318.
- [16] Z. Zhang, M. Sadakane, T. Murayama, W. Ueda, *Dalton Trans.* **2014**, *43*, 13584–13590.
- [17] Z. Zhang, M. Sadakane, S. Noro, T. Murayama, T. Kamachi, K. Yoshizawa, W. Ueda, *J. Mater. Chem. A* **2015**, *3*, 746–755.
- [18] a) N. Amdouni, H. Zarrouk, F. Soulette, C. M. Julien, *J. Mater. Chem.* **2003**, *13*, 2374–2380; b) X. Liu, Y. Lyu, Z. Zhang, H. Li, Y. Hu, Z. Wang, Y. Zhao, Q. Kuang, Y. Dong, Z. Liang, Q. Fan, L. Chen, *Nanoscale* **2014**, *6*, 13660–13667; c) J. Liu, Y. Lin, T. Lu, C. Du, W. Wang, S. Wang, Z. Tang, D. Qu, X. Zhang, *Electrochim. Acta* **2015**, *170*, 202–209.
- [19] R. A. Young, *The Rietveld Method*, Oxford University Press, Oxford, UK, **1995**.

Received: December 1, 2015

Published Online: February 22, 2016



Hydrothermal synthesis of microporous W–V–O as an efficient catalyst for ammoxidation of 3-picoline



Yoshinori Goto^a, Ken-ichi Shimizu^{a,b}, Toru Murayama^{a,c}, Wataru Ueda^{d,*}

^a Institute for Catalysis, Hokkaido University, N-21, W-10, Sapporo 001-0021, Japan

^b Elements Strategy Initiative for Catalysts and Batteries, Kyoto University, Katsura, Kyoto 615-8520, Japan

^c Research Center for Gold Chemistry, Graduate School of Urban Environmental Sciences, Tokyo Metropolitan University, 1-1 Minami-osawa, Hachioji, Tokyo 192-0397, Japan

^d Kanagawa University, Rokkakubashi 3-27-1, Yokohama 221-8686, Japan

ARTICLE INFO

Article history:

Received 3 August 2015

Received in revised form 7 October 2015

Accepted 7 October 2015

Available online 28 October 2015

Keywords:

Mixed metal oxide

W–V–O

Ammoxidation of 3-picoline

3-Cyanopyridine

High yield

High selectivity

ABSTRACT

W–V complex metal oxide (W–V–O) was prepared by hydrothermal synthesis method. Characterization by XRD, XPS, ICP-AES, N₂ adsorption, and STEM showed that W–V–O had a layered structure with micropore. W–V–O was tested for the vapor phase ammoxidation of 3-picoline (PIC) to 3-cyanopyridine (CP) and compared with VO_x/WO₃ catalyst prepared by impregnation method and other V-based catalysts which were reported to be efficient for this reaction. W-added vanadium oxides, W–V–O and VO_x/WO₃, showed higher CP selectivity than conventional catalysts such as VO_x/TiO₂. The W–V–O catalyst showed the highest CP selectivity of 99.5% at full PIC conversion. Kinetic studies showed that CP was the primary product and small amount of pyridine and CO₂ were produced from CP. The reaction by W–V–O in low NH₃ concentration condition or without co-feeding of water was also studied to evaluate the catalytic performance of W–V–O in industrially relevant conditions.

© 2015 Elsevier B.V. All rights reserved.

1. Introduction

Direct synthesis of nitriles via partial oxidation of hydrocarbons in the presence of ammonia (NH₃), so called ammoxidation, is an industrially important reaction [1,2]. The gas-phase ammoxidation of substituted aromatics/heteroaromatics is currently used in the production of fine chemicals and intermediates [1–18]. Especially, the ammoxidation of 3-methylpyridine (3-picoline) to nicotinonitrile (3-cyanopyridine) has been extensively studied [3–16] due to the commercial importance of 3-cyanopyridine for the industrial production of vitamin B3 (nicotinamide and nicotinic acid) as feed additives [19]. These compounds are also used as a precursor for commercial compounds such as cancer drugs, antibacterial agents, and pesticides [2]. Various metal oxide-based catalysts have been reported to be efficient for the ammoxidation of 3-methylpyridine (PIC) to 3-cyanopyridine (CP) [3–16]. Most of the reported catalysts are vanadium (V)-based catalysts, including VO_x/Nb₂O₅ [3], V₂O₅ [4], (VO)₂P₂O₇ [5,6], γ-VOHPO₄ [7], VO_x/TiO₂ [8], V–Sb–O [9], V–Cr–O [10], VZrPO [11], VZr(Al)PON [11–13], industrial VTiSbSiO_x catalyst [14], V₂O₅/MgF₂ [15], and V₂O₅/CeF₃ [16]. Mechanistic

studies on this reaction and related selective oxidation reaction of picolines [20–22], methylpyridine [23] and toluene [24] suggested bifunctional catalysis as a catalyst design concept, where the VO_x sites catalyze partial oxidation of hydrocarbons to oxygenate intermediate and acid sites originated from co-catalysts, such as PO_x, act as adsorption site of basic substrate (picolines and NH₃). Knowing the fact that oxides of tungsten (W) are well known acidic co-catalysts of V-based catalysts, one hypothesizes that W–V–O oxides can be an attractive candidate of the catalyst for the ammoxidation of picolines. To the best of our knowledge, quite a few efforts have been devoted to the development of W–V binary oxides as an attractive candidate of catalyst for the ammoxidation of picolines.

Our research group has focused on the hydrothermal synthesis of single crystalline Mo–V–O based catalysts [25–27]. Particularly, single phasic orthorhombic Mo₃VO_x, having a microporous and layered structure, is of importance because it catalyzes selective oxidative dehydrogenation of ethane even at around 300 °C [26]. The single phase Mo–V–P catalyst also catalyzes the ammoxidation of propane [27]. Recently, we extended the hydrothermal synthetic methodology to metal oxides consisted of various group 5 and 6 elements, and prepared a series of metal oxides with similar microporous and layered structure as orthorhombic Mo₃VO_x [28,29]. We hypothesized that W–V–O oxides with similar structure may show redox/acid bifunctional catalysis for ammoxidation

* Corresponding author.

E-mail address: uedaw@kanagawa-u.ac.jp (W. Ueda).

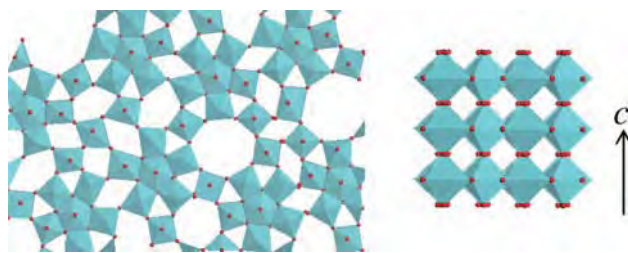


Fig. 1. Polyhedral model of the microporous and layered W-V-O oxide.

Table 1
Surface area and composition of the catalysts.

Catalyst	S.A. ^a (m ² g ⁻¹)	Bulk W/V ^b	Surface W/V ^c
V ₂ O ₅	4.8	–	–
VO _x /WO ₃	14	62/38	60/40
W-V-O	16	67/33	76/24

^a Surface area determined by the BET method.

^b W/V atomic ratio determined by ICP-AES.

^c W/V atomic ratio determined by XPS.

of 3-picoline. There are no attempts on the development of W-V binary oxides for the ammoxidation of picolines. We report herein the first example of ammoxidation of 3-picoline by hydrothermally prepared W-V-O oxide with microporous and layered structure.

2. Experimental

2.1. Catalyst preparation

Inorganic materials were purchased from Wako Pure Chemical Industries. The complex metal oxide of W and V (W-V-O) was prepared by a hydrothermal synthesis method. An aqueous solution (40 mL) of (NH₄)₆[H₂W₁₂O₄₀]-nH₂O (6.24 mmol), VOSO₄·nH₂O (4.16 mmol) and oxalic acid (0.10 mmol) was introduced into a stainless steel autoclave with a Teflon inner tube (50 mL), followed by filling the inner space of the tube by Teflon thin sheet (50 mm × 1000 mm). The presence of the sheet is important to prepare W-V-O. Then, N₂ was fed into the solution for 10 min to remove residual oxygen. The autoclave placed to rotating machine was installed in an oven. The mixture underwent hydrothermal reaction at 175 °C for 24 h under mechanical rotation (1 rpm). The formed solid was filtered, washed with ion-exchanged water, dried at 80 °C overnight and then heated at 500 °C for 2 h under N₂ flow.

V₂O₅ and WO₃ for catalytic studies were commercially supplied from Wako Pure Chemical Industries. Tungsten oxide-supported vanadia (VO_x/WO₃) was prepared by impregnation method. A suspension of WO₃ (8.01 mmol) in an aqueous solution (50 mL) of NH₄VO₃ (4.91 mmol) was heated to 90 °C for 30 min to evaporate water, followed by drying at 80 °C overnight, and by heating at 500 °C for 2 h under N₂ flow. The bulk and surface compositions and surface area of the W-V-O and VO_x/WO₃ catalysts are listed in Table 1. The composition and surface area of VO_x/WO₃ are close to those of W-V-O.

According to the literature [8], TiO₂-supported vanadia (VO_x/TiO₂) with V loading of 5.9 wt% was prepared by impregnation method. A suspension of anatase TiO₂ (4 g) in aqueous oxalic acid solution (50 mL) of NH₄VO₃ (4.9 mmol) was evaporated at 50 °C, followed by drying at 100 °C, and by heating at 450 °C for 6 h under air.

Mixed oxide of VZrPO was prepared according to the literature [11]. To aqueous solution of ZrO(NO₃)₂ (8.6 mmol, 0.02 M), aqueous HNO₃ solution of NH₄VO₃ (17.1 mmol, 0.02 M, pH 3) was added under stirring at 70 °C. After adding the corresponding amount of phosphoric acid (7.7 mmol, 3 M), a gel was formed, which was

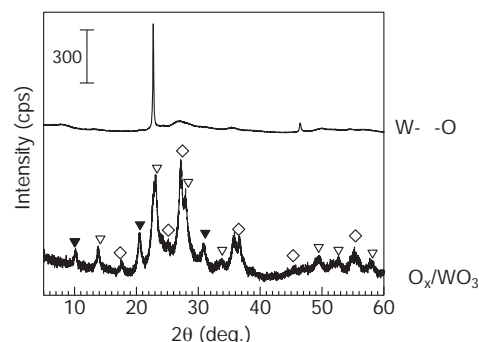


Fig. 2. XRD patterns of W-V-O and VO_x/WO₃: ▽ = WO₃ (PDF#00-033-1387), ▽ = V₂O₅ (PDF#00-040-1297), ◇ = VO₂ (PDF#43-1051).

stirred for 1 h at 70 °C, followed by adding 55 g of citric acid, stirring for 16 h at 70 °C, evaporation to dryness using a rotating evaporator, and by drying at 120 °C for 16 h. After grinding, the resulting brown powder was calcined under flowing air (6 L/h) for 16 h at 500 °C and for another 6 h at 600 °C.

Mixed oxide of V and Cr (VCrO) was prepared as follows [10]; V₂O₅ (5.28 mmol) and CrO₃ (13.2 mmol) were dissolved in an aqueous oxalic acid solution, followed by drying at 110 °C for 10 h, and by calcination in air at 500 °C for 6 h.

2.2. Catalyst characterization

Nitrogen adsorption experiments at –196 °C were carried out with a BELSORP MAX (BEL Japan Inc.) sorption analyzer. Prior to the measurement, the samples were evacuated at 200 °C for 2 h. Specific surface area of the catalysts was estimated by BET method. Powder X-ray diffraction (XRD) pattern of the catalysts was recorded on RINT2200 (Rigaku) with Cu Kα radiation (tube voltage: 40 kV, tube current: 20 mA). Scanning transmission electron microscopy (STEM) images were obtained with a HD-2000 (Hitachi High-Tech Inc.). Bulk composition of the catalysts was determined by an inductive coupling plasma (ICP-AES) method (ICPE-9000, Shimadzu). Surface composition of the catalysts was estimated by X-ray photoelectron spectroscopy (XPS) measurements using a JEOL JPS-9010MC (MgKα irradiation).

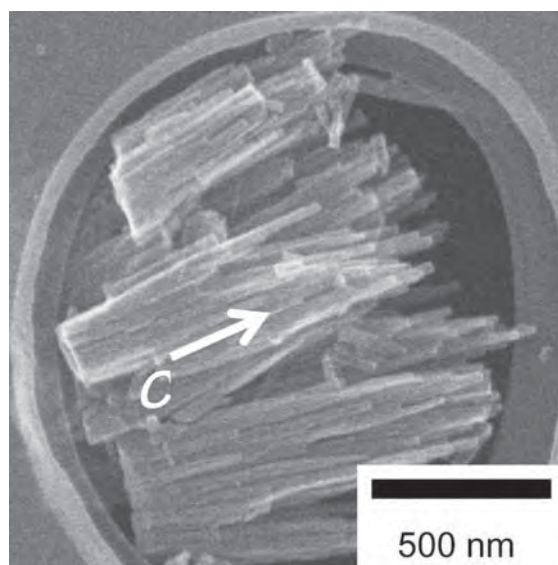


Fig. 3. STEM image of W-V-O.

Table 2
Ammonoxidation of 3-picoline.^a

Catalyst	Cat. wt. (g)	T (°C)	Conversion (%)		Selectivity (%)						
			PIC	O ₂	CP	NAc	NA	Pyr	CO	CO ₂	
WO ₃	1.00	383	0.0	11.5	0.0	0.0	0.0	0.0	0.0	0.0	0.0
VO _x /WO ₃	0.38	389	100	47.3	98.0	0.0	0.0	0.7	0.1	1.2	
W–V–O	0.75	386	100	51.7	99.5	0.0	0.0	0.2	0.0	0.3	
V ₂ O ₅	0.85	381	100	59.8	91.0	0.0	0.7	3.8	0.2	4.3	

^a Conditions: gas composition, PIC/H₂O/NH₃/O₂/He = 1/8/6/4.4/19.6.

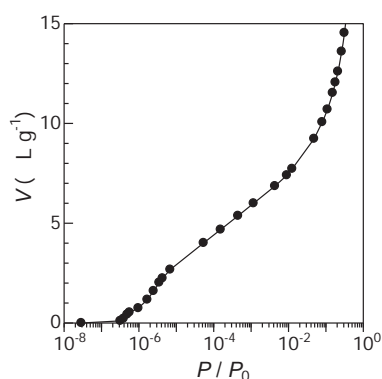


Fig. 4. N₂-adsorption isotherm of W–V–O.

2.3. Catalytic testing

Ammonoxidation of 3-picoline was carried out at atmospheric pressure using a fixed-bed flow reactor (Pyrex glass tube) with an inner diameter of 9 mm. Catalyst powders were pressed to pellets, crushed, and sieved. Catalyst pellets (0.25–0.50 mm size), diluted with quartz (0.2–0.4 mm) in a volumetric ratio of 1:6, were set in the reactor. The reaction temperature was measured inside the catalyst bed by a thermocouple. The gas stream (NH₃/O₂/He) was fed to the reactor with mass flow controller. The aqueous solution of 1.1 mol% 3-picoline (PIC) was fed continuously into the gas stream at 150 °C from a syringe pump with a micro-feeder. The volumetric composition of reaction gas was PIC:H₂O:NH₃:O₂:He = 1:8:4:4.4:19.6 (PIC/H₂O/NH₃/O₂/He = 2.7%/21.6%/10.8%/11.9%/53.0%). Total flow rate was 37 mL min⁻¹. CH₄ gas was fed into outlet gas as external standard. The gas phase products (CO and CO₂) in the outlet gas were collected in a gas bag and analyzed by TCD-GC (GL science GC-3200, 6 m SHINCARBON-ST packed column). Organic products, trapped in ethanol at 0 °C, followed by adding n-octane as external standard, were analyzed with FID-GC (Shimadzu GC-14A, 30 m 0.32 mm TC-5 capillary column). Note that carbon balance and oxygen balance for the catalytic results were 100.1 ± 0.6% and 97.5 ± 2.6%, respectively.

3. Result and discussion

3.1. Catalytic characterization

Previously, we have reported a series of studies on the hydrothermal synthesis of metal oxides consisted of group 5 and 6 elements. A group of the synthesized metal oxides have micropore due to heptagonal channel and layered structure as illustrated in Fig. 1, which is characterized by the common structural results as follows: (i) two sharp diffractions around 23° and 46° along with broad diffraction peaks around 8° and 27° observed by XRD, (ii) long rod-shaped crystal morphology, (iii) the presence of micropore. The diffractions around 23° and 46° have been attributed to the (001) and (002) planes of the layered structure in *c*-axis direction.

The rod-shaped crystal is due to stacking of the layers along the *c*-axis by sharing the apex oxygen. The microporosity is suggested to be due to the heptagonal channel structure of the *a*–*b* plane. The following results of XRD, STEM, N₂ adsorption suggest that the present W–V–O catalyst has the same structural characteristics as the porous and layered structure illustrated in Fig. 1. The XRD pattern of W–V–O (Fig. 2) showed two sharp diffraction lines at 22.7° and 46.5°. The XRD pattern of VO_x/WO₃ showed diffraction lines attributed to VO₂, V₂O₅ and WO₃.

The STEM image of W–V–O (Fig. 3) shows rod shaped crystals. The N₂-adsorption isotherm of W–V–O (Fig. 4) shows N₂ adsorption feature at low relative pressure ($P/P_0 < 10^{-6}$) which is characteristic to microporous materials. The micropore volume estimated by the *t*-plot method is 7.7×10^{-3} mL g⁻¹.

3.2. Catalytic performance

First, four catalysts (WO₃, V₂O₅, VO_x/WO₃, W–V–O) were tested for the ammonoxidation of PIC at 383–389 °C. Table 2 lists the conversions of PIC and O₂ and selectivities to cyanopyridine (CP), nicotinamide (NA), nicotinic acid (NAc), pyridine (Pyr), CO, and CO₂. As previously reported [4], V₂O₅ showed good selectivity of CP at high conversion level (99.2%), while WO₃ showed no conversion of CP. This indicates that vanadium is an indispensable element for this catalytic system. The W-added vanadium oxides, VO_x/WO₃ and W–V–O, were tested for the reaction under the conditions of full CP conversion. VO_x/WO₃ and W–V–O show higher CP selectivities than V₂O₅, which indicates that tungsten oxides as co-catalysts increase the CP selectivity of V-based ammonoxidation catalysts. Especially, the W–V–O catalyst showed the highest CP selectivity of 99.5%.

The catalytic performances of the V-based catalysts, including a well established VO_x/TiO₂ catalyst for this reaction [8], were further compared under different contact time at 380 °C. From the slope of the curve in the plot of CP conversion versus contact time (Fig. 5), the order of the catalytic activity is as follows: VO_x/WO₃ > VO_x/TiO₂ > W–V–O ≈ V₂O₅. The selectivities of the main product (CP) and byproducts (Pyr and CO₂) are plotted as a function

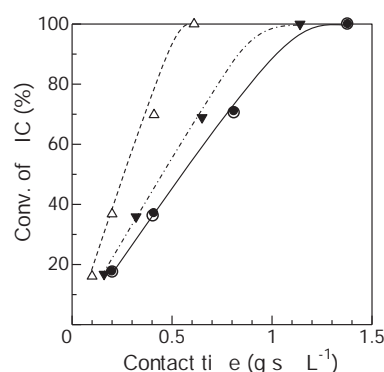


Fig. 5. Effects of contact time on PIC conversion for ammonoxidation of PIC over (○)W–V–O, (Δ) VO_x/WO₃, (●) V₂O₅, and (▼) VO_x/TiO₂. Conditions: catalyst amount = 0.5 g, T = 380 °C, gas composition, PIC/H₂O/NH₃/O₂/He = 1/8/6/4.4/19.6.

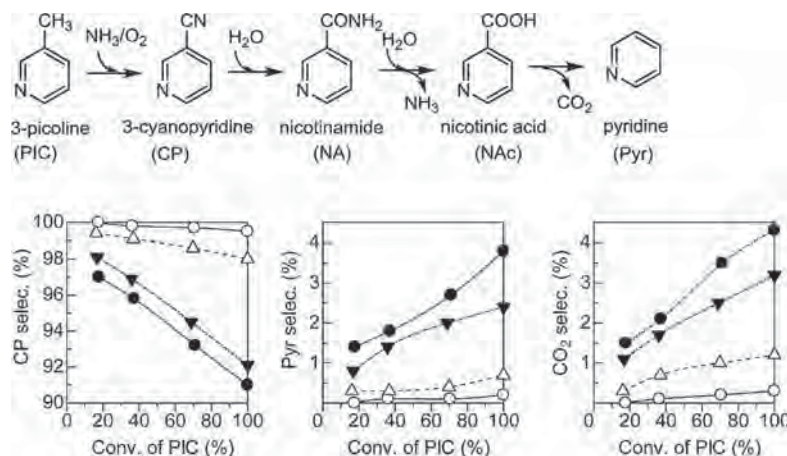


Fig. 6. Selectivity versus PIC conversion for ammoxidation of PIC over (○) W–V–O, (△) VO_x/WO₃, (▼) VO_x/TiO₂ and (●) V₂O₅. Conditions are the same as those in Fig. 5.

of the CP conversion in Fig. 6. A possible pathway of the formation of CP, NA, NAC, Pyr and CO₂ is also included in Fig. 6. Generally, Pyr and CO₂ were the main byproducts. The selectivities to NA, NAC, and CO were quite low (<0.2%) for the W–V–O and VO_x/WO₃ catalysts, while NA was also produced in 0.6–1.4% selectivity for VO_x/TiO₂ and V₂O₅ at high conversion levels. For all the catalysts tested, the CP selectivity decreased with the increase of the conversion, while the selectivities of the byproducts (Pyr and CO₂) increased. This indicates that CP is the product of the ammoxidation of PIC and Pyr and CO₂ are produced from CP probably via consecutive reactions of CP → NA → NAC → Pyr + CO₂ or via direct oxidation of CP to Pyr and CO₂. In the whole range of the conversion level, the W-added vanadium oxides (VO_x/WO₃ and W–V–O) showed higher CP selectivities than V₂O₅ and VO_x/TiO₂. Especially, the W–V–O catalyst showed the highest CP selectivity as well as the lowest selectivities of Pyr and CO₂.

To investigate the formation pathway of the byproduct in Fig. 6, we carried out hydration of CP (CP + H₂O reaction in the absence of O₂) by the W–V–O catalyst under the conditions shown Fig. 7. As shown in Fig. 7A, the conversion of CP increased with the reaction temperature. With increase in the temperature, the selectivity of NA decreased and the selectivities of Pyr and CO₂ increased. The result indicates that NA, NAC, Pyr and CO₂ are produced by hydration of the nitrile (CP) in the absence of O₂. The result in Fig. 7A is re-plotted in Fig. 7B where the selectivities are plotted as a function of the CP conversion. With increase in the conversion, the selectivity of NA decreased and the selectivities of Pyr and CO₂ increased. The selectivity of NAC increased up to 14% conversion and then decreased with the conversion. The result suggests that NA, NAC, Pyr and CO₂ are produced from CP via consecutive reactions of CP → NA → NAC → nPyr + CO₂. The hydration of the nitrile (CP) gives

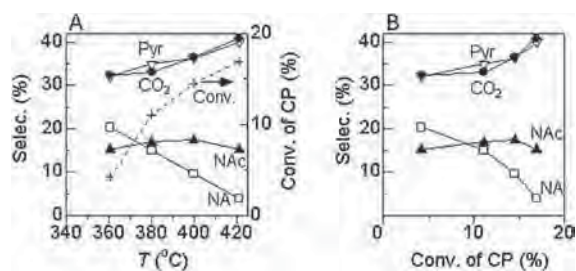


Fig. 7. Hydration of CP on W–V–O (0.5 g): gas composition, CP/H₂O/He = 1/10/10, flow rate = 21 mL min⁻¹. (A) Temperature dependence of (+) CP conversion and selectivities of (□) NA, (▲) NAC, (▼) Pyr, (●) CO₂. (B) Selectivities of (□) NA, (▲) NAC, (▼) Pyr, (●) CO₂ versus CP conversion.

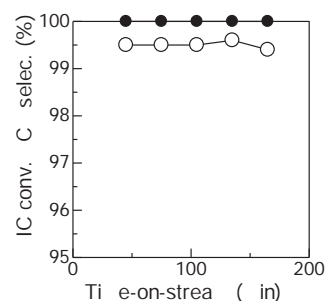


Fig. 8. (●) PIC conversion and (○) CP selectivity as a function of reaction time for ammoxidation of 3-picoline over W–V–O. Conditions: catalyst amount = 0.5 g, T = 380 °C, gas composition, PIC/H₂O/NH₃/O₂/He = 1/8/6/4.4/19.6.

the amide (NA), which undergoes further hydration to give the carboxylic acid (NAC) and NH₃. Pyr and CO₂ can be produced by the decomposition of NAC.

Next, we tested the ammoxidation of PIC with some representative catalysts (VCrO [10] and VZrPO [11]) which were reported to be efficient for this reaction in the literature (Table 3). The reactions were carried out under the same conditions (contact time, gas composition) except for the temperatures (365–410 °C). The reaction temperature for each experiment was adopted to achieve nearly full conversion of CP (98.9–100%). The result shows that VO_x/WO₃ and W–V–O exhibit higher CP selectivities than the conventional V-based catalysts, and W–V–O showed the highest CP selectivity and the lowest selectivities of Pyr and CO₂ among the catalysts tested. The above results demonstrate excellent catalytic performances of the W–V–O catalyst for the ammoxidation of PIC to CP. It should be noted that the XRD pattern of the W–V–O did not essentially change after the reaction, suggesting no change in the catalyst structure during the reaction.

From a viewpoint of industrial catalysis, long time durability and the reaction without co-feeding of water or without too much excess of NH₃ are important. The stability versus time-on-stream of the best performing W–V–O catalyst has been investigated and the result is shown in Fig. 8. The data show that the CP selectivity remains essentially constant (99.4–99.6%) during 3 h of the operation at 380 °C. Fig. 9 shows the catalytic performance of W–V–O under different NH₃ concentration. The result shows that the NH₃ partial pressure of around 12%, corresponding to 4.4 equivalent with respect to CP, is enough to give the highest selectivity at full CP conversion. Finally, we studied the effect of co-feeding of water on the catalytic performance of W–V–O. The temperature dependence

Table 3
Comparison of the catalysts for the ammoxidation of 3-picoline.^a

Catalyst	S.A (m ² g ⁻¹)	T (°C)	Conversion (%)		Selectivity (%)					
			PIC	O ₂	CP	NAC	NA	Pyr	CO	CO ₂
W–V–O	16	407	99.6	49.2	99.4	0.0	0.0	0.2	0.0	0.4
VO _x /WO ₃	14	410	100	50.0	95.8	1.6	0.6	1.0	0.0	1.0
VCrO	23	365	98.9	54.3	92.0	1.0	1.1	1.6	0.9	3.3
VZrPO	30	370	99.0	53.7	83.4	2.7	0.8	0.7	0.0	12.3

^a Conditions: catalyst amount = 0.5 g; gas composition, PIC/H₂O/NH₃/O₂/He = 1/8/6/4.4/19.6.

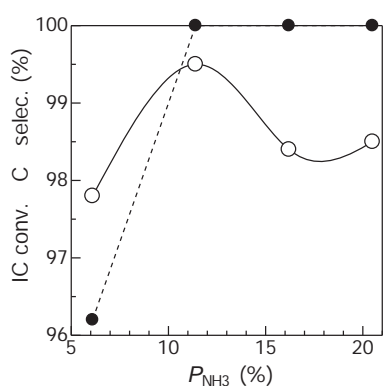


Fig. 9. (●) PIC conversion and (○) CP selectivity as a function of the concentration of NH₃ for ammoxidation of 3-picoline over W–V–O (0.5 g) at 380 °C.

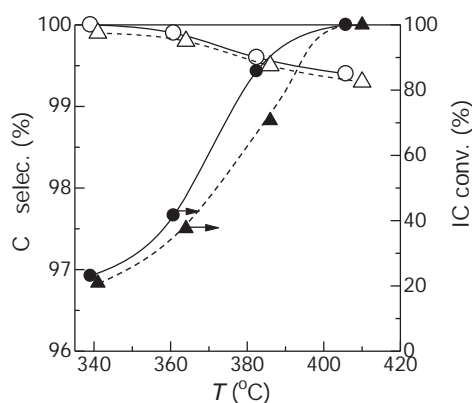


Fig. 10. (●,▲) PIC conversion and (○,△) CP selectivity as a function of temperature with water-dosing (▲,△) in the feed or without the water-dosing (●,○) over W–V–O catalyst. Gas composition, PIC/H₂O/NH₃/O₂/He = 1/8/6/4.4/19.6 or PIC/NH₃/O₂/He = 1/6/4.4/19.6.

of the reaction data with or without co-feeding of 21.6% water vapor is shown in Fig. 10. The result shows that the CP selectivity and PIC conversion without water-dosing are slightly higher than those with water-dosing. These results suggest that the present catalytic system is effective even without the additional water-dosing. Considering the fact that most of the previous catalytic systems for this reaction have been carried out under water-dosing conditions, our system is a rare example of the high yield catalytic system for the reaction without the water-dosing. The above characteristics suggest that the ammoxidation by W–V–O is important from a viewpoint of industrial production of CP from PIC.

4. Conclusion

The microporous and layered W–V metal oxide, W–V–O, was synthesized by hydrothermal method. For the vapor phase ammox-

idation of 3-picoline, the W–V–O catalyst gave an exceptionally high 3-cyanopyridine selectivity of 99.5% under full conversion conditions. The selectivity of W–V–O was higher than those of VO_x/WO₃ and other catalysts reported to be efficient for this reaction such as VCrO, VZrPO, and VO_x/TiO₂. The W–V–O catalyst gave high catalytic performance even in the absence of co-feeding of water, demonstrating that the present system can be of importance from a viewpoint of industrial production of 3-cyanopyridine from 3-picoline. Silent finding of this study was that the VO_x/WO₃ catalyst showed higher activity and selectivity for this reaction than previous V-based catalysts.

References

- [1] A. Martin, V.N. Kalevaru, *ChemCatChem* 2 (2010) 1504–1522.
- [2] A. Martin, B. Lücke, *Catal. Today* 57 (2000) 61–70.
- [3] K.V.R. Chary, G. Kishan, C.P. Kumar, G.V. Sagar, J.W. Niemantsverdriet, *Appl. Catal. A* 245 (2003) 303–316.
- [4] A. Andersson, S.T. Lundin, *J. Catal.* 58 (1979) 383–395.
- [5] V.N. Kalevaru, N. Madaan, A. Martin, *Appl. Catal. A* 391 (2011) 52–62.
- [6] A. Martin, C. Janke, V.N. Kalevaru, *Appl. Catal. A* 376 (2010) 13–18.
- [7] A. Martin, B. Lücke, H. Seeboth, G. Ladwig, *Appl. Catal.* 49 (1989) 205–211.
- [8] K.V. Narayana, A. Venugopal, K.S.R. Rao, V.V. Rao, S.K. Masthan, P.K. Rao, *Appl. Catal. A* 150 (1997) 269–278.
- [9] A. Andersson, S.L.T. Andersson, G. Centi, R.K. Grasselli, M. Sanati, F. Trifiro, *Appl. Catal. A* 43 (1994) 43–57.
- [10] F. Jiang, W. Xu, L. Niu, G. Xiao, *Catal. Lett.* 143 (2013) 1200–1206.
- [11] C. Janke, J. Radnik, U. Bentrup, A. Martin, A. Brückner, *J. Catal.* 277 (2011) 196–207.
- [12] C. Janke, J. Radnik, U. Bentrup, A. Martin, A. Brückner, *ChemCatChem* 1 (2009) 485–491.
- [13] C. Janke, J. Radnik, U. Bentrup, A. Martin, A. Brückner, *ACS Catal.* 4 (2014) 2687–2695.
- [14] A. Martin, V.N. Kalevaru, B. Lücke, A. Brückner, *Appl. Catal. A* 335 (2008) 196–203.
- [15] V.N. Kalevaru, B.D. Raju, V.V. Rao, A. Martin, *Appl. Catal. A* 352 (2009) 223–233.
- [16] V.N. Kalevaru, B. David Raju, S.K. Masthan, V.V. Rao, P. Kanta Rao, R. Subrahmanian, A. Martin, *J. Mol. Catal. A* 223 (2004) 321–328.
- [17] N. Dhachapally, V.N. Kalevaru, A. Martin, *Catal. Sci. Technol.* 4 (2014) 3306–3316.
- [18] N. Dhachapally, V.N. Kalevaru, J. Radnik, A. Martin, *Chem. Commun.* (2011) 8394–8396.
- [19] R. Chuck, *Appl. Catal. A* 280 (2005) 75–82.
- [20] Z. Song, T. Matsushita, T. Shishido, K. Takehira, *J. Catal.* 218 (2003) 32–41.
- [21] T. Shishido, Z. Song, T. Maesushita, K. Takaki, K. Takehira, *Phys. Chem. Chem. Phys.* 5 (2003) 2710–2718.
- [22] Y.A. Chesalov, T.V. Andrushkevich, V.I. Sobolev, G.B. Chernobay, *J. Mol. Catal. A* 380 (2013) 118–130.
- [23] V.M. Bondareva, T.V. Andrushkevich, E.A. Paukshtis, N.A. Paukshtis, A.A. Budneva, V.N. Parmon, *J. Mol. Catal. A* 269 (2007) 240–245.
- [24] Y. Zhang, A. Martin, H. Berndt, B. Lücke, M. Meisel, *J. Mol. Catal. A* 118 (1997) 205–214.
- [25] M. Sadakane, N. Watanabe, T. Katou, Y. Nodasaka, W. Ueda, *Angew. Chem. Int. Ed.* 46 (2007) 1493–1496.
- [26] T. Konya, T. Katou, T. Murayama, S. Ishikawa, M. Sadakane, D. Buttrey, W. Ueda, *Catal. Sci. Technol.* 3 (2013) 380–387.
- [27] N. Watanabe, W. Ueda, *Ind. Eng. Chem. Res.* 45 (2006) 607–614.
- [28] T. Murayama, N. Kuramata, S. Takatama, K. Nakatani, S. Izumi, X. Yi, W. Ueda, *Catal. Today* 185 (2012) 224–229.
- [29] K. Omata, S. Izumi, T. Murayama, W. Ueda, *Catal. Today* 201 (2013) 7–11.



Direct oxidative transformation of glycerol to acrylic acid over Nb-based complex metal oxide catalysts



Kaori Omata^a, Keeko Matsumoto^b, Toru Murayama^b, Wataru Ueda^{c,*}

^a Department of Materials Science and Engineering, Suzuka National College of Technology, Shiroko-cho, Suzuka 510-0294, Japan

^b Catalysis Research Center, Hokkaido University, N-21, W-10, Sapporo 001-0021, Japan

^c Department of Material and Life Chemistry, Kanagawa University, 3-27-1, Rokkakubashi, Kanagawa-ku, Yokohama 221-8686, Japan

ARTICLE INFO

Article history:

Received 3 March 2015

Received in revised form 4 July 2015

Accepted 13 July 2015

Available online 31 August 2015

Keywords:

Glycerol

Acrylic acid

Hydrothermal synthesis

Nb

W

V

ABSTRACT

W–V–Nb–O complex metal oxides having a structure like that of orthorhombic Mo_3VO_x were found to be an efficient catalyst for the gas-phase direct oxidative transformation of glycerol to acrylic acid. The catalysts with various compositions were facilely synthesized by hydrothermal method. The W–Nb–O catalyst without V component, mainly promoted the glycerol dehydration, giving acrolein selectively. Since Nb–O catalyst showed poor activity for the reaction, the introduction of W into the Nb–O catalysts was found effective for improving the activity for the dehydration of glycerol to acrolein. This is mainly due to the increase of Brønsted acidity by the combination of W and Nb. When V was incorporated into the framework of W–Nb–O, the resulting catalyst was found to prominently promote the formation of acrylic acid in the glycerol transformation in the presence of O_2 , while showed no effect on the dehydration of glycerol to acrolein. It was also found that V acts as an oxidation site only when glycerol is completely reacted. The optimum elemental composition for the reaction was $\text{W}_{2.2}\text{V}_{0.4}\text{Nb}_{2.4}\text{O}_{14}$ giving ca. 46% one path yield of acrylic acid and this catalytic performance was further improved by the surface modification with phosphoric acid, achieving ca. 60% one path yield of acrylic acid.

© 2015 Elsevier B.V. All rights reserved.

1. Introduction

Biomass utilization aiming at CO_2 reduction and decreasing dependency of oil has been expanding. Under this situation, the amount of biodiesel production has been increasing year after year [1]. Glycerol is a main byproduct in biodiesel production by transesterification of plant oils or animal fat with methanol, and has been produced heavily at a relatively low price. Therefore, the transformation of glycerol into other desirable chemicals by various reactions such as oxidation [2], hydrogenolysis [3], reforming [4], esterification [5,6], etherification [7] and others [8,9] has been attempted by many researchers. The dehydration of glycerol to acrolein, which is an important intermediate for chemical and agricultural industries, is one of the most valuable reactions.

Various solid acid catalysts such as zeolites [10,11], heteropoly acids [12,13] and mixed metal oxides [14–16] have been applied to this reaction in the gas phase. The main problems within this process are the formation of byproducts and deactivation of

catalysts by carbon deposition. Some zeolites or oxide catalysts give acrolein in yields of ~80% with byproducts such as hydroxyacetone, propanal and others [10,11,14–16]. On the other hand, heteropoly acid catalysts show higher yield (~98%) of acrolein [13]. However, regeneration of heteropoly acid catalysts by combustion of coke is difficult because of their low thermal stability.

Acrolein is oxidized to acrylic acid, and then used in the manufacture of plastics, coatings, adhesives and so on. Direct transformation of glycerol to acrylic acid brings about simplification of process and reduction of energy. Standard enthalpy change of the glycerol dehydration to acrolein and the acrolein oxidation to acrylic acid are 18.0 kJ mol^{-1} and $-298.3 \text{ kJ mol}^{-1}$, respectively [17]. The direct transformation of glycerol may be energy-efficient process if the energy exhausted in the latter reaction can be used for the former reaction.

As catalysts for the direct transformation of glycerol to acrylic acid, Mo–V–Te–Nb–O having an orthorhombic structure [18], W–V–O [18,19] and W–V–Nb–O [20,21] having a hexagonal tungsten bronze structure have been reported. The catalyst which gave the highest acrylic acid yield was a hexagonal W–V–Nb–O among the proposed catalysts. Chierigato et al. [20] has reported that the incorporation of Nb in W–V–O structure generates strong acid sites

* Corresponding author.

E-mail address: uedaw@kanagawa-u.ac.jp (W. Ueda).

and improves the acrylic acid yield. According to their latest report, the yield of acrylic acid reached to 50.5% by optimization of the reaction conditions [21].

Nevertheless, the values have not come up to that in the possible process with a separated glycerol dehydration and acrolein oxidation. (For example, $\text{Cs}_{2.5}\text{H}_{0.5}\text{PW}_{12}\text{O}_{40}$ catalyst gives an acrolein yield of 98% in the glycerol dehydration [13]. On the other hand, Mo–V based catalyst gives acrylic acid yield of 98% in the acrolein oxidation [22].) The direct transformation of glycerol to acrylic acid is desirable but still a challenging process because not only improvement of selectivity for each reaction by catalyst design but also tune of optimum conditions for each reaction is required to achieve higher acrylic acid yield.

We have recently reported the orthorhombic- Mo_3VO_x and trigonal- Mo_3VO_x catalysts which exhibit a high yield of acrylic acid of more than 90% in the acrolein oxidation [23]. Because the orthorhombic and trigonal phases show similar catalytic properties, we have advocated their local structure, which is the layered structure comprising 6- and 7-rings of metal-oxide octahedral and pentagonal columns, is important for high oxidation catalysis. We have also reported that W–Nb–O catalysts synthesized by hydrothermal method have a layered structure similar to orthorhombic Mo–V–O [24] and gave acrolein in high yield in gas-phase glycerol dehydration in the presence of water and oxygen [25].

If a complex oxide has both enough acidity and acrolein-oxidizing capability comparable to orthorhombic Mo–V–O, it is expected to be an efficient catalyst for the direct transformation of glycerol to acrylic acid. In the present work, we applied the complex metal oxides composed of W, Nb and V having the orthorhombic-like structure as a catalyst for the first time to the direct oxidative glycerol transformation to acrylic acid, and investigated effects of constituent materials on the selectivity for the glycerol transformation. And then we further tried to improve the catalytic performance by surface modification with phosphoric acid.

2. Experimental

2.1. Catalyst preparation

2.1.1. W–V–Nb–O by hydrothermal method

The complex metal oxide catalysts of W, V and Nb were prepared by hydrothermal synthesis method. $(\text{NH}_4)_6[\text{H}_2\text{W}_{12}\text{O}_{40}] \cdot n\text{H}_2\text{O}$ (Nippon Inorganic Color & Chemical Co., Ltd., >90.8% as WO_3), $\text{VOSO}_4 \cdot n\text{H}_2\text{O}$ (Mitsuiwa Chemical Co., Ltd., 61.9%) and $\text{Nb}_2\text{O}_5 \cdot n\text{H}_2\text{O}$ (Soekawa Chemical Co., Ltd, 70.8% as Nb_2O_5) were used as raw materials. The metal salts were added in 45 ml of ion-exchanged water under stirring. This mixed suspension was put in a stainless steel autoclave with a Teflon liner and heated at 448 K for 72 h. The formed solid was filtered, washed with ion-exchanged water, dried at 353 K and then calcined at 673 K for 4 h in air. The W/Nb ratio in the preparative materials was set to be 1.35 (W 2.7 mmol, Nb 2.0 mmol in 45 ml water) according to our previous articles [25]. W–V–Nb–O, W–V–O, and V–Nb–O were prepared from solution consisting metals with W:V:Nb = 1.35:0.1–0.6:1, W:V = 1.35:1, V:Nb = 0.4:1, respectively. Nb–O was also synthesized by the same procedure as described above.

2.1.2. Addition of P to W–Nb–O by impregnation method

Phosphoric acid-added catalysts were prepared by impregnation of uncalcined W–Nb–O (W:Nb = 1.35:1) or W–V–Nb–O (W:V:Nb = 1.35:0.3:1) with an aqueous solution of phosphoric acid, followed by calcination at 673 K in air. The content of P was set to be 2.5 wt% of the supports after optimization of P content.

2.2. Catalyst characterization

Surface area of the catalysts was estimated by BET method where nitrogen physisorption amount was measured at 77 K with a BEL max 00094 (BEL Japan Inc.). Prior to the measurement, the samples were evacuated at 473 K for 2 h. Powder X-ray diffraction (XRD) pattern of the catalysts was recorded on RINT2200 (Rigaku) with Cu K α radiation (tube voltage: 40 kV, tube current: 20 mA). Scanning transmission electron microscope (STEM) images were obtained with a HD-20000 (HITACHI). The composition of catalysts was determined by inductively coupled plasma atomic emission spectroscopy (ICP-AES). The acid amount of catalysts was measured by NH_3 -TPD with a TPD apparatus (BEL Japan Inc.). Prior to the measurement, the samples were pretreated under He flow at 673 K for 2 h. NH_3 was adsorbed on the catalysts at 473 K. Acidity of catalysts was measured by FT-IR spectroscopy (PARAGON 1000, Perkin Elmer) of adsorbed pyridine with a furnace cell with CaF_2 windows, containing a self-supporting disk of sample. The samples were pretreated in a vacuum at 623 K. Pyridine was adsorbed onto the samples at 373 K and after evacuation at 523 K for 1 h, the adsorption spectrum was recorded. The spectrum of adsorbed pyridine on sample in the presence of water vapor (4.6 Torr) was also recorded.

2.3. Catalytic testing

Transformation of glycerol was carried out in a vertical fixed-bed reactor. A mixture of 0.02–0.80 g of catalyst powder and sea sand (catalyst + sea sand = 2 ml) was set in a Pyrex glass tube with 12 mm internal diameter and pretreated at 573 K in flowing 20% O_2/N_2 for 0.5 h before the reaction. A glycerol–water 1:5 (mol/mol) solution was fed into the top of reactor with a micro feeder. Pure N_2 or O_2/N_2 was introduced with mass flow controllers. The molar composition of reaction gas was glycerol/ $\text{N}_2/\text{H}_2\text{O}$ = 5/70/25 (absence of O_2) or glycerol/ $\text{O}_2/\text{N}_2/\text{H}_2\text{O}$ = 5/14/56/25 (presence of O_2). Reaction products and unconverted glycerol in both liquid and gas phases were collected hourly in an ice trap (273 K) and a Tedlar bag connected at the end of the trap. Products in the liquid phase were analyzed with FID-GC (GL science GC353, 30 m 0.32 mm TC-WAX capillary column). Products in the gas phase were analyzed with FID-GC (Shimadzu GC14B, Gaskuropak54 column) and TCD-GC (Shimadzu GC8A, Porapak QS and MS-13X column). Glycerol conversion and product selectivities and yields were calculated by Eqs. (1)–(3).

$$\text{Glycerol conversion (\%)} = \frac{\text{Moles of glycerol reacted}}{\text{Moles of glycerol fed}} \times 100 \quad (1)$$

Product selectivity (%)

$$= \frac{\text{Moles of carbon in a product defined}}{\text{Mole of carbon in glycerol reacted}} \times 100 \quad (2)$$

$$\text{Product yield (\%)} = \frac{\text{Moles of carbon in a product defined}}{\text{Moles of carbon in glycerol fed}} \times 100(3)$$

Oxidation of acrolein was carried out in the same reactor as the transformation of glycerol. Reaction conditions were: catalyst weight, 0.2 g; reaction temperature, 458–658 K; total flow rate, 77 ml min^{-1} ; molar composition of reaction gas, acrolein/ $\text{O}_2/\text{N}_2/\text{H}_2\text{O}$ = 1/15/58/26.

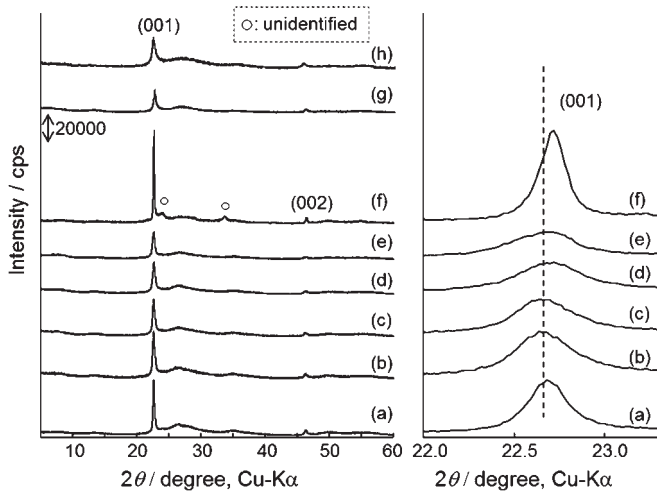


Fig. 1. XRD patterns (left: wide angle range, right: narrow range around 22°) of (a) $W_{2.8}Nb_{2.2}O_{14}$, (b) $W_{2.4}V_{0.1}Nb_{2.5}O_{14}$, (c) $W_{2.2}V_{0.4}Nb_{2.4}O_{14}$, (d) $W_{2.2}V_{0.5}Nb_{2.3}O_{14}$, (e) $W_{2.2}V_{0.9}Nb_{1.9}O_{14}$, (f) $W_{2.8}V_{2.2}O_{14}$, (g) $Nb_{5.0}O_{14}$, (h) $V_{1.0}Nb_{4.0}O_{14}$.

3. Results and discussion

3.1. Structure of W–Nb–O and W–V–Nb–O

X-ray diffraction patterns of all the samples synthesized hydrothermally are illustrated in Fig. 1 (left). The diffraction peaks in all cases were observed at 22.7° and 46.2° attributed to (001) and (002) planes of a layered structure, respectively. Since it can be considered that these peaks are due to the linear arrangement of corner-shared octahedra in *c*-direction, the appearance of these clear diffraction peaks indicates the crystal formation of *c*-direction. The other diffractions around 8° , 13° , 27° , 35° were also observed for all the samples. It should be noted that the angles of these peaks were roughly coincident with the angle region of the XRD peaks of well-crystallized $Cs_{0.5}[Nb_{2.5}W_{2.5}O_{14}]$ in the orthorhombic structure [25] which is basically the same as that of

Mo_3VO_x , as can be seen in the XRD patterns in Fig. 2. However, these diffraction peaks observed on W–Nb–O were very broad, suggesting that the crystal growth into *a* and *b* directions is very low compared to the *c*-direction. To confirm this crystal state, we collected STEM image of W–Nb–O sample and the result is shown in Fig. 2(b). Concomitantly, W–Nb–O was observed to be much small crystals with the nano-sizes of 10–30 nm in diameter (*a* and *b* direction) and of 0.1–0.3 μm in length (*c*-direction), while $Cs_{0.5}[Nb_{2.5}W_{2.5}O_{14}]$ with rod-like morphology was well-grown crystals with the sizes of 0.5–1 μm in diameter and of more than 5 μm in length (Fig. 2(a)). By taking it into account that the lattice parameters of $Cs_{0.5}[Nb_{2.5}W_{2.5}O_{14}]$, of which crystal structure is assumed here in the W–Nb–O case, are quite large (2.6 nm \times 2.1 nm in *a*–*b* plane), the observed broad peaks in XRD of the nano-sized W–Nb–O might be reasonable. These facts may suggest the formation of the orthorhombic structure in the W–Nb–O sample. In order to add more evidence to this suggestion, we conducted Rietveld analysis on the basis of the orthorhombic crystal structure of Mo_3VO_x , the lattice parameters of $Cs_{0.5}[Nb_{2.5}W_{2.5}O_{14}]$, and the crystal size of 10 nm \times 10 nm \times 300 nm as observed by STEM. As shown in Fig. 2(b), the observed and the simulated diffractions were agreed each other well (Rwp = 7.03%), while Rietveld refinement with using structure models and structural parameters of hexagonal and other layered materials did not converge. This result evidently supports the formation W–Nb–O oxide with the structure similar to that of Mo_3VO_x .

The vanadium-containing W–Nb–O, W–V–O, V–Nb–O, and Nb–O also showed the similar XRD pattern of the W–Nb–O sample (Fig. 1(left)). In the case of the vanadium-containing W–Nb–O, the diffraction peak ascribed to (001) plane shifted to higher angle depending on the V content (Fig. 1(right)). This clearly indicates that V was incorporated into the framework of W–Nb–O. XRD patterns similar to that of W–Nb–O were also observed for Nb–O, W–V–O and V–Nb–O, indicating that the same structure can be constructed in any combinations of three elements, W, Nb and V. Weak unknown peaks in W–V–O (Fig. 1(left)) may be attributed to a type of vanadium oxide which forms from hydrated vanadium oxide containing NH_4^+ ion [26] in the course of the calcination.

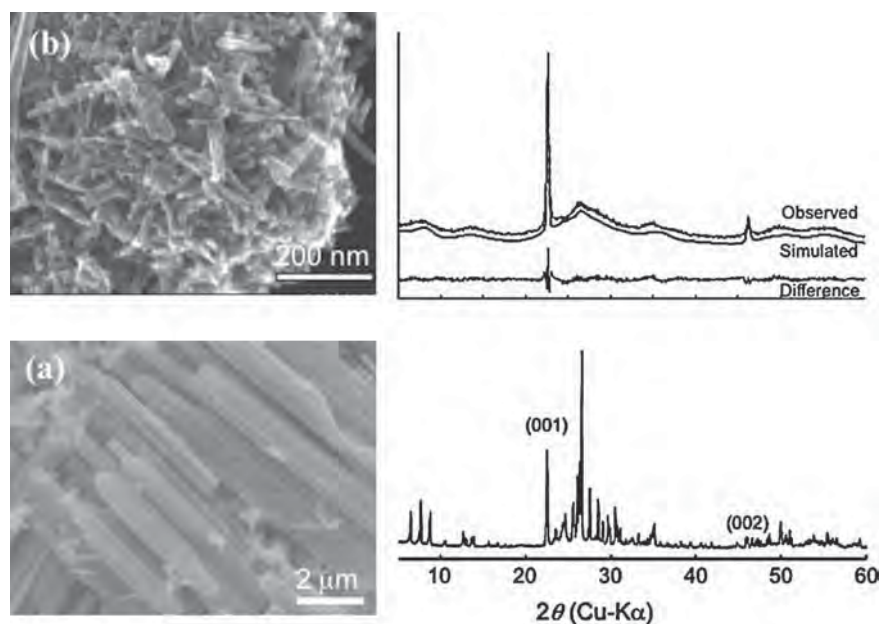


Fig. 2. STEM images of (a) $Cs_{0.5}[Nb_{2.5}W_{2.5}O_{14}]$ and (b) $W_{2.8}Nb_{2.2}O_{14}$ and their XRD patterns with Rietveld analysis.

Table 1
Catalyst surface properties and their performance for the glycerol transformation in the absence of O₂.

Catalyst	S _{BET} ^a (m ² g ⁻¹)	Acid amount (μmol g ⁻¹)	T ^b (K)	GLR ^c conv. ^d (%)	Yield ^e (%)							
					ACRL	AA	ACAL	PRAL	HACT	ACA	CO _x	Others
Nb _{5.0} O ₁₄	89	40	566	56.1	10.6	<0.1	0.3	0.1	1.9	0.1	0.4	42.6
V _{1.0} Nb _{4.0} O ₁₄	106	133	563	56.1	13.5	<0.1	1.0	0.7	3.7	0.2	0.3	36.5
W _{2.8} Nb _{2.2} O ₁₄	100	136	562	90.0	50.7	0.2	1.1	1.3	6.4	0.9	0.2	29.2
W _{2.8} V _{2.2} O ₁₄	8	5	563	9.5	3.0	<0.1	0.2	0.1	<0.1	<0.1	0.2	6.0
W _{2.2} V _{0.5} Nb ₂	118	148	563	91.7	53.8	<0.1	0.8	1.4	7.8	<0.1	0.2	27.7

^a BET surface area.

^b Reaction temperature.

^c GLR = glycerol.

^d Reaction conditions: catalyst weight, 0.2 g; flow rate, 80 ml min⁻¹; time on stream, 1–2 h; composition of reaction gas, GLR/N₂/H₂O = 5/70/25 (mol%)

^e ACRL = acrolein, AA = acrylic acid, ACAL = acetaldehyde, PRAL = propanal, HACT = hydroxyacetone, ACA = acetic acid.

On the basis of the above structural discussion, M₅O₁₄ (M = W, V, Nb) is suitable as the general chemical formula for the present materials, although net charge should be balanced by either additional proton or oxygen deficiency. We then conducted the ICP-AES analysis of all the calcined samples. Based on the analytical data, the samples are now denoted with the chemical formula as follows; W_{2.8}Nb_{2.2}O₁₄, W_{2.4}V_{0.1}Nb_{2.5}O₁₄, W_{2.2}V_{0.4}Nb_{2.4}O₁₄, W_{2.2}V_{0.5}Nb_{2.3}O₁₄, W_{2.2}V_{0.9}Nb_{1.9}O₁₄, W_{2.8}V_{2.2}O₁₄, Nb_{5.0}O₁₄, V_{1.0}Nb_{4.0}O₁₄.

3.2. Glycerol transformation in the absence of O₂

The catalytic performances in the glycerol transformation in the absence of O₂ were first examined to compare the catalytic activity of the synthesized materials for the dehydration of glycerol to acrolein. The catalytic results with specific surface area and the number of acid sites per gram (acid amount determined by NH₃-TPD) are listed in Table 1.

The role of Nb is first considered. The surface area and the acid amount of the non-Nb-containing W–V–O catalyst were lower than these of the Nb-containing catalysts. The acrolein yield over W_{2.2}V_{0.5}Nb_{2.3}O₁₄ and W_{2.8}V_{2.2}O₁₄ were 53.8 and 3.0%, respectively, indicating the introduction of Nb augmented the acrolein yield. The improvement of acrolein yield is due to the increase in the surface area and the corresponding acid amount by the introduction of Nb.

The acrolein yield over W_{2.8}Nb_{2.2}O₁₄ was 50.7%, while Nb_{5.0}O₁₄ gave acrolein yield of 10.6%. Apparently the incorporation of W to Nb_{5.0}O₁₄ improved the activity for the dehydration of glycerol. It is evident that the activity enhancement is mainly caused by the increase of surface acid amount as observed. However, according to Fig. 3 showing the plot of the acrolein yield over Nb_{5.0}O₁₄ and W_{2.8}Nb_{2.2}O₁₄ against the glycerol conversion, the acrolein yield over W_{2.8}Nb_{2.2}O₁₄ was higher than that over Nb_{5.0}O₁₄ when compared at an iso-conversion of glycerol. It can be concluded that this yield improvement was not due to the difference of the glycerol conversion but to the catalytic property changes by the combination of W and Nb in the structure. This fact also indicates that the introduction of W was improved not only activity but also acrolein selectivity.

The effect of the introduction of W to Nb_{5.0}O₁₄ on acid property was further investigated with FT-IR of adsorbed pyridine on Nb_{5.0}O₁₄ and W_{2.8}Nb_{2.2}O₁₄. Fig. 4(A) illustrates the IR spectra of pyridine on Nb_{5.0}O₁₄ and W_{2.8}Nb_{2.2}O₁₄. Both the catalysts gave the IR-bands ascribed to the adsorption of pyridine on Lewis and Brønsted acid sites at about 1450 and 1540 cm⁻¹, respectively. The ratio of Brønsted to Lewis acidity in W_{2.8}Nb_{2.2}O₁₄ was larger than that in Nb_{5.0}O₁₄. Therefore, it seems that the introduction of W increases the Brønsted acidity and hence enhances acrolein selectivity in the glycerol transformation. It has been also indicated in many papers

that Brønsted acid sites are advantageous over Lewis acid sites in the synthesis of acrolein from glycerol [1].

Effect of water addition on the acid property of W_{2.8}Nb_{2.2}O₁₄ was investigated because the glycerol transformation is carried out in the presence of additive water and formed water. Fig. 4(B) illustrates the IR spectra of adsorbed pyridine on Nb_{5.0}O₁₄ and W_{2.8}Nb_{2.2}O₁₄ in the presence of water. The addition of water decreased the intensity of the IR-band ascribed to the adsorption of pyridine on Lewis acid sites and on the other hand increased the intensity of IR-band ascribed to that on Brønsted acid sites in both Nb_{5.0}O₁₄ and W_{2.8}Nb_{2.2}O₁₄. The result indicates that Lewis acid site is hydrated and changes into Brønsted acid site in the presence of water. The ratio of Lewis acid that changed into Brønsted acid was different depending on the presence or absence of W. About 29% and 57% of Lewis acid sites changed into Brønsted acid sites in Nb_{5.0}O₁₄ and W_{2.8}Nb_{2.2}O₁₄, respectively. As a result, such high Brønsted acidity of W_{2.8}Nb_{2.2}O₁₄ should be beneficial for the catalytic reaction, since it has been widely considered that Brønsted acid sites are responsible for the glycerol transformation to acrolein.

In contrast to the prominent addition effect of W, the introduction of V into the framework of W_{2.8}Nb_{2.2}O₁₄ or Nb_{5.0}O₁₄ gave almost no effect on both the conversion of glycerol and the acrolein selectivity as can be seen in Table 1 and Fig. 3, although the acid amount of Nb_{5.0}O₁₄ largely changed. It seems that the surface acid property derived from the existence of V in the lattice and surface V itself have no ability to contribute to the glycerol dehydration steps. This speculation will be evident from the results in the glycerol transformation in the presence of O₂ as shown in the next.

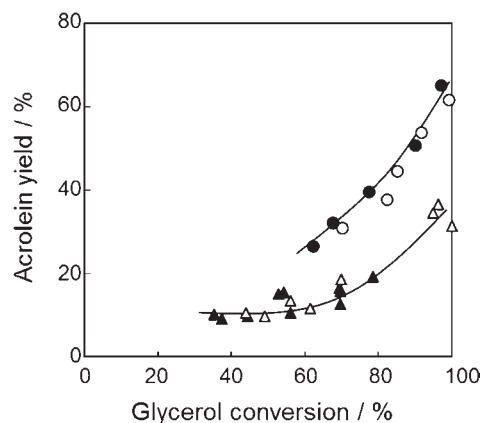


Fig. 3. Acrolein yield against glycerol conversion in the glycerol transformation. Symbols: W_{2.8}Nb_{2.2}O₁₄ ●; W_{2.2}V_{0.5}Nb_{2.3}O₁₄ ○; Nb_{5.0}O₁₄ ▲; V_{1.0}Nb_{4.0}O₁₄ △. Composition of reaction gas, GLR/N₂/H₂O = 5/70/25 (mol%).

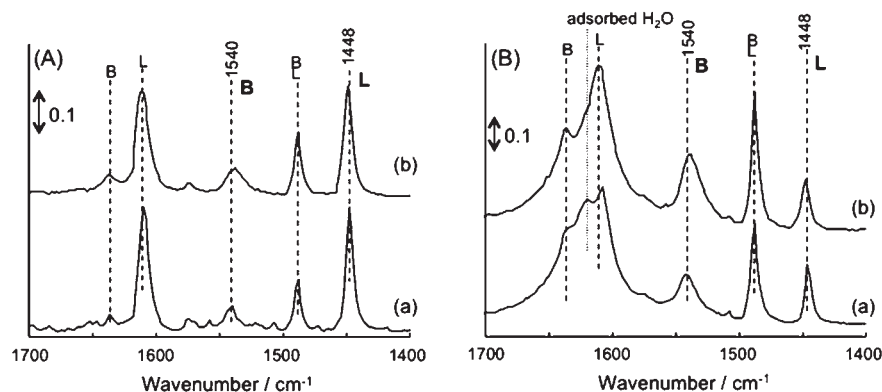


Fig. 4. IR spectra of adsorbed pyridine on (a) $\text{Nb}_{5.0}\text{O}_{14}$ and (b) $\text{W}_{2.8}\text{Nb}_{2.2}\text{O}_{14}$ in the absence (A) and presence (B) of water.

3.3. Glycerol transformation in the presence of O_2

The catalytic results of the glycerol transformation in the presence of O_2 are listed in Table 2. The $\text{W}_{2.8}\text{Nb}_{2.2}\text{O}_{14}$ catalyst gave acrolein mainly in better yield compared to the reaction in the absence of O_2 . Obviously oxygen assists the dehydration and maintains the catalytic activity. When V was incorporated into the $\text{W}_{2.8}\text{Nb}_{2.2}\text{O}_{14}$ catalyst ($\text{W}_{2.2}\text{V}_{0.5}\text{Nb}_{2.3}\text{O}_{14}$), acrylic acid yield greatly increased and acrolein formation was suppressed. This result clearly demonstrates that the incorporated V can promote the acrolein oxidation process to acrylic acid. Since the addition of V into $\text{Nb}_{5.0}\text{O}_{14}$ ($\text{V}_{1.0}\text{Nb}_{4.0}\text{O}_{14}$) simply promoted over oxidation to CO_x , W as a component seems essential for the formation of acrylic acid. In fact, $\text{W}_{2.8}\text{V}_{2.2}\text{O}_{14}$ showed appreciable activity for the formation of acrylic acid as shown in Table 2. However, the yield values over this catalyst were inferior to that achieved over $\text{W}_{2.2}\text{V}_{0.5}\text{Nb}_{2.3}\text{O}_{14}$, suggesting that co-existence of three components in the framework of orthorhombic type structure is important.

The presence of V is also important for the catalytic activity durability. We tested the time courses of acrolein and acrylic acid yield in the glycerol transformation over $\text{W}_{2.8}\text{Nb}_{2.2}\text{O}_{14}$ and $\text{W}_{2.2}\text{V}_{0.5}\text{Nb}_{2.3}\text{O}_{14}$ in the presence of O_2 . The yield of acrylic acid over $\text{W}_{2.2}\text{V}_{0.5}\text{Nb}_{2.3}\text{O}_{14}$ was kept constant during 5 h of the reaction although acrolein yield over $\text{W}_{2.8}\text{Nb}_{2.2}\text{O}_{14}$ decreased from 74.5% to 57.7%. The amounts of carbon deposition after the reaction over $\text{W}_{2.8}\text{Nb}_{2.2}\text{O}_{14}$ and $\text{W}_{2.2}\text{V}_{0.5}\text{Nb}_{2.3}\text{O}_{14}$ catalysts measured by TG were about 193.6 and 30.3 $\text{mg g}_{\text{cat}}^{-1}$, respectively. It is clear that V sites decrease the carbon deposition that may cause deactivation of the catalysts in the dehydration of glycerol. The materials causing catalytic deactivation may be oxidatively decomposed at the V sites under the reaction conditions.

The effect of constituent materials is summarized as follows: Nb increased the surface area and the acid amount of the catalysts and improved the activity for the dehydration of glycerol to acrolein. W increased the Brönsted acidity of the catalysts and improved the activity for the dehydration of glycerol to acrolein. V was the essential element for the oxidation of acrolein to acrylic acid. The introduction of V into the framework of $\text{Nb}_{5.0}\text{O}_{14}$ or $\text{W}_{2.8}\text{Nb}_{2.2}\text{O}_{14}$ little affects the acrolein formation from glycerol. The co-existence of three components in the framework of orthorhombic type structure is most indispensable for achieving high acrylic acid in the direct oxidative transformation of glycerol.

3.4. Effect of V content on the yield of acrylic acid

The W–V–Nb–O catalysts with different V contents were tested in order to further elucidate the role of added V on the

catalytic performance. Fig. 5 illustrates the yield of acrolein, acrylic acid and CO_x in the glycerol transformation in the presence of O_2 under the various contact times over the W–V–Nb–O catalysts. The $\text{W}_{2.8}\text{Nb}_{2.2}\text{O}_{14}$ catalyst gave maximum acrolein yield at $W/F=2.5 \times 10^{-3} \text{ g min ml}^{-1}$. At contact time above $W/F=2.5 \times 10^{-3} \text{ g min ml}^{-1}$, the yield of acrolein decreased and the yield of CO_x increased with increasing the contact time. Acrylic acid was not observed at all over the $\text{W}_{2.8}\text{Nb}_{2.2}\text{O}_{14}$ catalyst. In a separate experiment of acrolein oxidation over this catalyst, it was found that acrolein was directly oxidized to CO_x without formation of acrylic acid. The results indicate that acrolein was directly oxidized to CO_x also under the glycerol transformation. On the other hand, acrylic acid was formed over the V-containing catalysts. The catalysts containing larger amount of V tend to give maximum yields of acrylic acid at shorter contact time. Over the $\text{W}_{2.4}\text{V}_{0.1}\text{Nb}_{2.5}\text{O}_{14}$ catalyst, the formations of acrolein, acrylic acid and CO_x were formed and these product yield changes indicate a consecutive reaction profile. In addition to this, the direct conversion of acrolein to CO_x should be contributed to the profile, since the formation of CO_x from acrolein on W–Nb–O sites

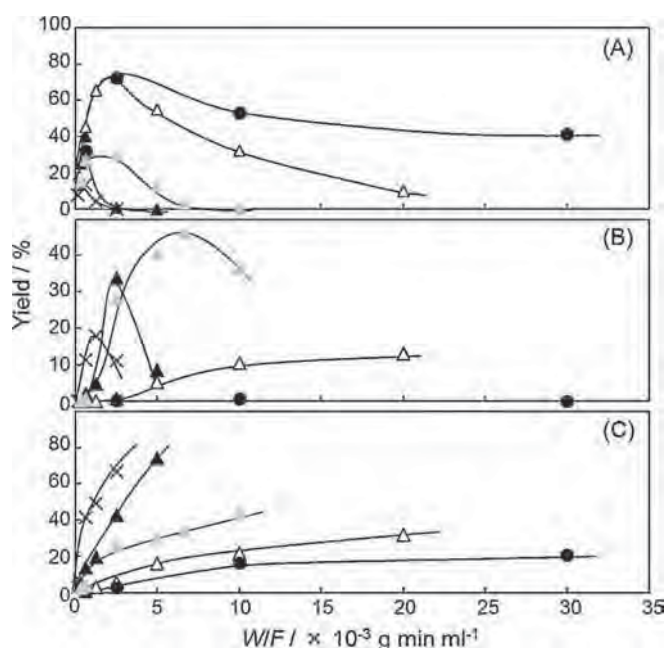


Fig. 5. Effect of contact time on yield of (A) acrolein, (B) acrylic acid and (C) CO_x in the glycerol transformation in the presence of O_2 over $\text{W}_{2.8}\text{Nb}_{2.2}\text{O}_{14}$ ●; $\text{W}_{2.4}\text{V}_{0.1}\text{Nb}_{2.5}\text{O}_{14}$ ▲; $\text{W}_{2.2}\text{V}_{0.5}\text{Nb}_{2.3}\text{O}_{14}$ △; $\text{W}_{2.2}\text{V}_{0.9}\text{Nb}_{1.9}\text{O}_{14}$ ×.

Table 2
Catalytic performance in the glycerol transformation in the presence of O₂.

Catalyst	T ^a (K)	GLR conv. ^b (%)	O ₂ conv. (%)	Yield (%)							
				ACRL	AA	ACAL	PRAL	HACT	ACA	CO _x	Others
W _{2.8} Nb _{2.2} O ₁₄	565	97.2	4.9	72.3	<0.1	1.8	0.7	1.6	0.4	2.9	17.5
V _{1.0} Nb _{4.0} O ₁₄	628	100	80.0	4.4	1.4	0.8	<0.1	<0.1	3.5	83.7	6.0
W _{2.8} V _{2.2} O ₁₄	628	100	55.0	3.3	18.2	0.8	<0.1	<0.1	14.0	53.2	10.5
W _{2.2} V _{0.5} Nb _{2.3} O ₁₄	596	100	51.9	0.9	33.7	0.5	<0.1	<0.1	15.2	42.7	7.0

^a Reaction temperature.

^b Reaction conditions: catalyst weight, 0.2 g; flow rate, 80 ml min⁻¹; time on stream, 1–2 h; composition of reaction gas, GLR/O₂/N₂/H₂O = 5/14/56/25 (mol%).

Table 3
Glycerol transformation over phosphoric acid-added W–Nb–O and W–V–Nb–O catalysts.

Catalyst	W/F _{gcat} (min ml ⁻¹)	GLR conv. ^a (%)	O ₂ conv. (%)	Yield (%)							
				ACRL	AA	ACAL	PRAL	HACT	ACA	CO _x	Others
W _{2.8} Nb _{2.2} O ₁₄	2.5 × 10 ⁻³	98.9	6.5	74.5	0.1	2.9	1.0	0.4	0.7	3.8	15.5
2.5 wt%PO ₄ /W _{2.8} Nb _{2.2} O ₁₄	2.5 × 10 ⁻³	100	5.6	81.8	0.3	2.1	0.6	0.5	0.3	2.7	11.7
W _{2.2} V _{0.4} Nb _{2.4} O ₁₄	6.7 × 10 ⁻³	100	48.6	3.5	46.2	1.4	<0.1	<0.1	12.7	33.8	2.4
	1.0 × 10 ⁻²	100	53.4	0.5	36.6	0.4	<0.1	<0.1	14.2	44.8	4.0
2.5 wt%PO ₄ /W _{2.2} V _{0.4} Nb _{2.4} O ₁₄	6.7 × 10 ⁻³	100	33.0	15.3	44.8	2.6	0.1	<0.1	7.8	21.5	7.9
	1.0 × 10 ⁻²	100	45.3	0.5	59.2	0.3	<0.1	<0.1	8.2	22.3	9.5

^a Reaction conditions: set temperature of the furnace, 558 K; composition of reactant gas, glycerol/O₂/N₂/H₂O = 5/14/56/25 (mol%).

is unavoidable. The catalyst which exhibited the maximum yield of acrylic acid was W_{2.2}V_{0.4}Nb_{2.4}O₁₄ and gave an acrylic acid yield of 46.2% at W/F = 6.7 × 10⁻³ g min ml⁻¹. The further addition of V resulted in large CO_x formation.

In Fig. 6, the conversion of oxygen and the yields of acrylic acid, acrolein and CO_x are plotted against the glycerol conversion. Over W_{2.2}V_{0.9}Nb_{1.9}O₁₄, the conversion of oxygen more than 20% was observed even under the condition that glycerol conversion was less than 100%. The W_{2.2}V_{0.5}Nb_{2.3}O₁₄ catalyst also showed a similar catalytic result. This oxygen consumption should be of the oxidation of glycerol because acrylic acid was formed after glycerol conversion reached 100%. In W_{2.8}Nb_{2.2}O₁₄, W_{2.4}V_{0.1}Nb_{2.5}O₁₄ and W_{2.2}V_{0.4}Nb_{2.4}O₁₄, on the other hand, the conversion of oxygen was much less than 5% even under the condition that glycerol conversion was almost 100%. That is to say, the oxidation of glycerol hardly proceeds over these catalysts. This is the reason why W_{2.2}V_{0.4}Nb_{2.4}O₁₄ gave higher acrylic acid yield than W_{2.2}V_{0.5}Nb_{2.3}O₁₄ or W_{2.2}V_{0.9}Nb_{1.9}O₁₄ where excess V may have a strong activity for the oxidation of glycerol as well as the desired products to unidentified products.

More interesting points from Fig. 6 is that the formation of acrylic acid and CO_x began just after glycerol was converted completely. This result strongly suggests that glycerol having high boiling point (563 K) can exclusively adsorb on the surface V oxidative sites and inhibit the access of acrolein. This is why W–Nb–O site can work for dehydration independently until glycerol is completely consumed and then V in the framework of W–Nb–O starts working for the oxidation of accumulated acrolein to acrylic acid.

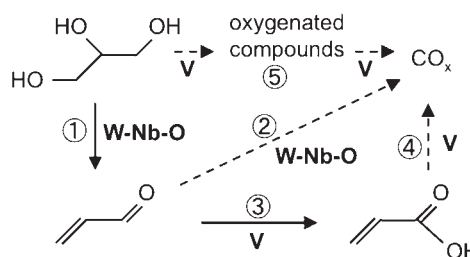
3.5. Reaction pathway of the glycerol transformation over W–V–Nb–O catalysts

Reaction pathways of the glycerol transformation on W–V–Nb–O are shown in Scheme 1. On W–Nb–O framework site, two pathways, pathway 1 where acrolein is formed by the dehydration of glycerol and pathway 2 where the formed acrolein is oxidized to CO_x, subsequently proceed. On V sites in the W–Nb–O framework, pathway 3 where acrylic acid is formed by the oxidation of acrolein can take place, followed by pathway 4 where acrylic acid is oxidized to CO_x. Pathway 5 is the oxidation of glycerol proceeding on V site. As shown in Fig. 5, over W_{2.4}V_{0.1}Nb_{2.5}O₁₄, acrolein forms in a relatively high yield

because the reaction rate of the glycerol dehydration to acrolein (pathway 1) is much higher than that of the glycerol oxidation (pathway 5). Then, to yield acrylic acid by the oxidation of acrolein (pathway 3), the high reaction temperature or the long contact time is required. Under the high reaction temperature or long contact time, however, a high yield of acrylic acid cannot be expected due to the occurrence of the direct formation of CO_x from acrolein (pathway 2) over much available W–Nb–O site. On the other hand, although W_{2.2}V_{0.9}Nb_{1.9}O₁₄ gives acrylic acid in a high selectivity in the acrolein oxidation, the oxidation of glycerol to CO_x (pathway 4) inevitably proceeds over excess V sites. W_{2.2}V_{0.4}Nb_{2.4}O₁₄ exhibited the highest yield of acrylic acid as a whole because undesirable oxidation pathways (pathway 2, 4 and 5) are retarded by well-balanced cooperation of the W–Nb–O network and the incorporated V.

3.6. Oxidative glycerol transformation over phosphoric acid-added W–V–Nb–O

Based on the above results and discussion on the role of each catalytic element, one may think that a control of oxidation activity of V site is still necessary for improving acrylic acid yield in the oxidative glycerol transformation. We, therefore, tried to introduce phosphate anions on the surface of the W–V–Nb–O catalyst [27] because we can expect an interaction between V site and phosphate anions to form vanadium phosphate like species and also another interaction between W site and phosphate anions to form heteropoly-type unit in the framework.



Scheme 1. Reaction scheme for the transformation of glycerol to acrylic acid over W–V–Nb–O catalysts.

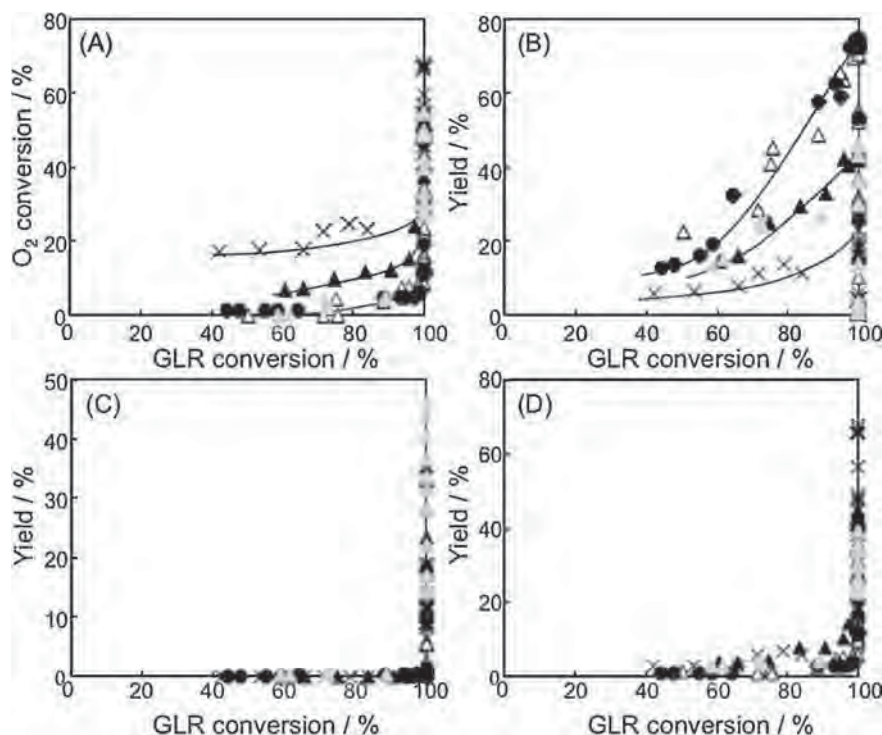


Fig. 6. O₂ conversion (A) and yield of acrolein (B), acrylic acid (C) and CO_x (D) as the function of the glycerol conversion. Reaction conditions: temperature, 558 K; composition of reaction gas, glycerol/O₂/N₂/H₂O = 5/14/56/25 (mol%). Symbols: W_{2.8}Nb_{2.2}O₁₄ ●; W_{2.4}V_{0.1}Nb_{2.5}O₁₄ ▲; W_{2.2}V_{0.4}Nb_{2.4}O₁₄ △; W_{2.2}V_{0.5}Nb_{2.3}O₁₄ ○; W_{2.2}V_{0.9}Nb_{1.9}O₁₄ ×.

We simply synthesized two materials, 2.5 wt%PO₄/W_{2.8}Nb_{2.2}O₁₄ and 2.5 wt%PO₄/W_{2.2}V_{0.4}Nb_{2.4}O₁₄, by impregnation method as described in Section 2. The catalytic performance of W_{2.8}Nb_{2.2}O₁₄ and 2.5 wt%PO₄/W_{2.8}Nb_{2.2}O₁₄ in the glycerol transformation was first examined and the results are shown in Table 3. Both the glycerol conversion and the acrolein yield were appreciably increased by the phosphoric acid addition, and the 2.5 wt%PO₄/W_{2.8}Nb_{2.2}O₁₄ catalyst achieved the acrolein yield of 81.8%. This improvement seems due to the changes of surface acidity. It was observed that the number of acid sites per gram largely increased by the addition of phosphoric acid to 244 μmol g⁻¹ and the ratio of Brönsted to Lewis acidity increased from 0.4 to 1.5. This is probably due to a formation of heteropolytype unit over the surface. Moreover, it was observed in the FT-IR study that water substantially decreased the Lewis acid sites and on the other hand increased the Brönsted acid sites (B/L ratio to be 23.4 over 2.5 wt%PO₄/W_{2.8}Nb_{2.2}O₁₄). This result indicates that Lewis acid sites change into Brönsted acid sites in the presence of water.

The same effect of the phosphoric acid addition was also observed in the W_{2.2}V_{0.4}Nb_{2.4}O₁₄ and 2.5 wt%PO₄/W_{2.2}V_{0.4}Nb_{2.4}O₁₄ for the direct glycerol transformation to acrylic acid and the results are also shown in Table 3. The addition effect is prominent and the attained maximum yield of acrylic acid was 59.2% under a suitable contact time condition, which is the highest reported for the direct transformation of glycerol to acrylic acid [18–21]. Of additional importance is that the yield of acrylic acid was kept almost constant during 5 h of the reaction.

In order to elucidate the role of phosphoric acid in this course of the transformation, we conducted acrolein oxidation over W_{2.2}V_{0.4}Nb_{2.4}O₁₄ and 2.5 wt%PO₄/W_{2.2}V_{0.4}Nb_{2.4}O₁₄. It was observed that the maximum acrylic acid yield was 64.4% (581 K) over W_{2.2}V_{0.4}Nb_{2.4}O₁₄ and 71.7% (577 K) over 2.5 wt%PO₄/W_{2.2}V_{0.4}Nb_{2.4}O₁₄, indicating that phosphoric acid enhances the selectivity to acrylic acid in the acrolein oxidation as

well as the acrolein formation. Phosphoric acid seems to interact with surface V site to moderate the oxidation ability and to suppress the pathway 4 mainly.

4. Conclusions

While the orthorhombic-like W–Nb–O gives acrolein selectively in the glycerol transformation, acrylic acid formed from glycerol directly in the presence of oxygen by the introduction of V into the W–Nb–O. W increased the Brönsted acidity of the catalysts, so that the activity for the dehydration of glycerol to acrolein was enhanced. V in the framework little affected the acrolein formation from glycerol but exhibited high selectivity of acrylic acid in the oxidation of acrolein. V appears to be essential element for the oxidation of acrolein to acrylic acid. By changing the V content in W–Nb–O, a maximum yield of acrylic acid from glycerol 46.2% was achieved over W_{2.2}V_{0.4}Nb_{2.4}O₁₄ under W/F = 6.7 × 10⁻³ g min ml⁻¹ at the reaction temperature of 580 K. The addition of phosphoric acid to W_{2.8}Nb_{2.2}O₁₄ increased the acid amount and the Brönsted acidity of the W_{2.8}Nb_{2.2}O₁₄ catalyst. In addition to the acidity change, phosphoric acid interacts with V sites for suppressing the sequential oxidation of acrylic acid to CO_x. As a result, acrylic acid yield in the glycerol transformation increased significantly. The 2.5 wt%PO₄/W_{2.2}V_{0.4}Nb_{2.4}O₁₄ catalyst gave acrylic acid yield of 59.2% directly from glycerol under oxidative condition (W/F = 1.0 × 10⁻² g min ml⁻¹, reaction temperature 594 K). The catalytic performance evidences provided in the present work may prove a possibility of the industrial realization of the direct transformation of glycerol to acrylic acid.

References

- [1] B. Katryniok, S. Paul, V. Bellière-Baca, P. Reye, F. Dumeignil, *Green Chem.* 12 (2010) 2079.

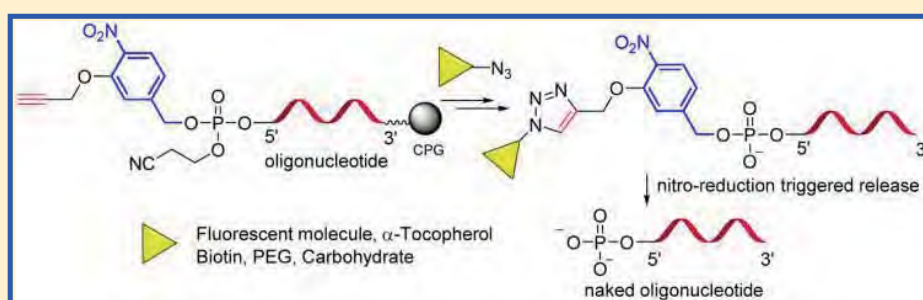
- [2] S. Gil, M. Marchena, L. S-Silva, A. Romero, P. Sánchez, J.L. Valverde, *Chem. Eng. J.* 178 (2011) 423.
- [3] Y. Kusunoki, T. Miyazawa, K. Kunimori, K. Tomishige, *Catal. Commun.* 6 (2005) 645.
- [4] A.C.-C. Chang, W.-H. Lin, K.-H. Lin, C.-H. Hsiao, H.-H. Chen, H.-F. Chang, *Int. Hydrogen Energy J.* 37 (2012) 13110.
- [5] M.S. Khayoon, B.H. Hameed, *Appl. Catal. A* 433 (2012) 152.
- [6] M. Kapoor, M.N. Gupta, *Process Biochem.* 47 (2012) 503.
- [7] H.J. Lee, D. Seung, K.S. Jung, H. Kim, I.N. Filimonov, *Appl. Catal. A* 390 (2010) 235.
- [8] A. Martin, M. Richter, *Eur. J. Lipid Sci. Technol.* 113 (2011) 100.
- [9] T. Tago, T. Masuda, *WO 2011108509* (2011).
- [10] Y.T. Kim, K.-D. Jung, E. Duck Park, *Appl. Catal. A* 393 (2011) 275.
- [11] C.-J. Jia, Y. Liu, W. Schmidt, A.-H. Lu, F. Schüth, *J. Catal.* 269 (2010) 71.
- [12] E. Tsukuda, S. Sato, R. Takahashi, T. Sodesawa, *Catal. Commun.* 8 (2007) 1349.
- [13] A. Alhanash, E.F. Kozhevnikova, I.V. Kozhevnikov, *Appl. Catal. A* 378 (2010) 11.
- [14] M. Massa, A. Andersson, E. Finocchio, G. Busca, F. Lenrick, L.R. Wallenberg, *J. Catal.* 297 (2013) 93.
- [15] A. Ulgen, W.F. Hoelderich, *Appl. Catal. A* 400 (2011) 34.
- [16] F. Cavani, S. Guidetti, L. Marinelli, M. Piccinini, E. Ghedini, M. Signoretto, *Appl. Catal. B* 100 (2010) 197.
- [17] J.A. Dean, *Lange's Handbook of Chemistry*, 1985, pp. 1–9.
- [18] J. Deleplanque, J.-L. Dubois, J.-F. Devaux, W. Ueda, *Catal. Today* 157 (2010) 351.
- [19] M.D. Soriano, P. Concepción, J.M.L. Nieto, F. Cavani, S. Guidetti, C. Trevisanut, *Green Chem.* 13 (2011) 2954.
- [20] A. Chierogato, F. Basile, P. Concepción, S. Guidetti, G. Liosi, M.D. Soriano, C. Trevisanut, F. Cavani, J.M.L. Nieto, *Catal. Today* 197 (2012) 58.
- [21] A. Chierogato, M.D. Soriano, F. Basile, G. Liosi, S. Zamora, P. Concepción, F. Cavani, J.M.L. Nieto, *Appl. Catal. B* 150 (2014) 37.
- [22] Y. Moro-oka, W. Ueda, *Adv. Catal.* 40 (1994) 233.
- [23] M. Sadakane, K. Kodato, T. Kuranishi, Y. Nodasaka, K. Sugawara, N. Sakaguchi, T. Nagai, Y. Matsui, W. Ueda, *Angew. Chem. Int. Ed.* 47 (2008) 2493.
- [24] T. Murayama, N. Kuramata, S. Takatama, K. Nakatania, S. Izumia, X. Yi, W. Ueda, *Catal. Today* 185 (2012) 224.
- [25] K. Omata, S. Izumi, T. Murayama, W. Ueda, *Catal. Today* 201 (2013) 7.
- [26] Y. Oka, T. Yao, N. Yamamoto, *Nippon Seramikkusu Kyokai Gakujutsu Ronbunshi* 98 (1990) 1365.
- [27] K. Omata, K. Matsumoto, T. Murayama, W. Ueda, *Chem. Lett.* 43 (2014) 435.

Conjugatable and Bioreduction Cleavable Linker for the 5'-Functionalization of Oligonucleotides

Hisao Saneyoshi,*¹ Yuta Yamamoto, Kazuhiko Kondo, Yuki Hiyoshi, and Akira Ono*

Department of Material and Life Chemistry, Faculty of Engineering, Kanagawa University, 3-27-1 Rokkakubashi, Kanagawa-ku, Yokohama 221-8686, Japan

S Supporting Information



ABSTRACT: An efficient conjugatable and bioreduction cleavable linker was designed and synthesized for the 5'-terminal ends of oligonucleotides. A phosphoramidite reagent bearing this linker was successfully applied to solid phase synthesis and incorporated at the 5'-terminal ends of oligonucleotides. The controlled pore glass (CPG)-supported oligonucleotides were subsequently conjugated to a diverse range of functional molecules using a CuAAC reaction. The synthesized oligonucleotide conjugates were then cleaved using a nitroreductase/NADH bioreduction system to release the naked oligonucleotides.

The conjugation of oligonucleotides with functional molecules is an important strategy for the construction of modified oligonucleotides with various applications in medicinal chemistry, diagnostics, and biological science.^{1–6} Functional molecules can be attached to other compounds using a postsynthetic modification strategy, which requires the presence of a reactive group in the parent compound as a handle for the attachment of the functional molecule. This strategy has been widely used to attach a broad range of functional molecules (i.e., from small molecules to macromolecules) to various compounds and represents a simple and low-cost method for introducing functionality.^{5–7} Several postsynthetic modification reactions have been reported in the literature,^{5,6} including, most notably, the Cu(I)-catalyzed alkyne azide cycloaddition (CuAAC) reaction,^{8–10} which has been used extensively in the field of nucleic acid chemistry^{11–19} because of its high reaction efficacy and orthogonal reactivity profile.

Stimulus-responsive linkers are highly desired for the development of drug delivery systems for nucleic acid-based drugs.^{20,21} To date, various cleavable linkers have been reported with numerous applications in the life sciences.^{22,23} One of the most commonly used types of cleavable linkers are disulfide linkers, which can be cleaved by intracellular glutathione,²⁴ and linkers belonging to this class have been applied to several nucleic acid-based drugs.^{20,25,26} As part of our research toward the development of new reduction-responsive cleavable linkers for oligonucleotides, we became interested in 4-nitrobenzyl-type structures²⁷ because we envisaged that they would be

cleaved by a reductive-elimination reaction in cancer cells or bacterial cells.^{28–30}

Herein, we report the design and synthesis of a phosphoramidite reagent bearing a 4-nitrobenzyl-type linker with an alkyne moiety. This reagent was used in a final capping reaction at the 5'-terminal end of an oligonucleotide prepared using a DNA/RNA synthesizer. The subsequent CuAAC reaction of this moiety with various functional molecules⁶ could then be used to achieve the efficient preparation of oligonucleotide conjugates (Figure 1). These procedures could therefore be used to synthesize a diverse range of 5'-modified oligonucleotides from one parent oligonucleotide precursor. Furthermore, this linker can be readily cleaved under bioreductive conditions to release the naked oligonucleotide.

The synthesis of our phosphoramidite bearing a clickable/biocleavable linker started from the commercially available aldehyde **1**, which was reduced with NaBH₄ to give the known alcohol **2**.³¹ The phenolic group of **2** was selectively alkylated with propargyl bromide in the presence of K₂CO₃ to give compound **3**, which was converted to phosphoramidite **4** for solid phase DNA synthesis using standard procedures (Scheme 1).

Phosphoramidite **4** was incorporated at the 5'-end of a series of model oligonucleotides (oligothymidylate and mixed sequence) using standard phosphoramidite chemistry (Scheme 2). Next, prior to the release and deprotection, we conducted

Received: October 18, 2016

Published: January 23, 2017



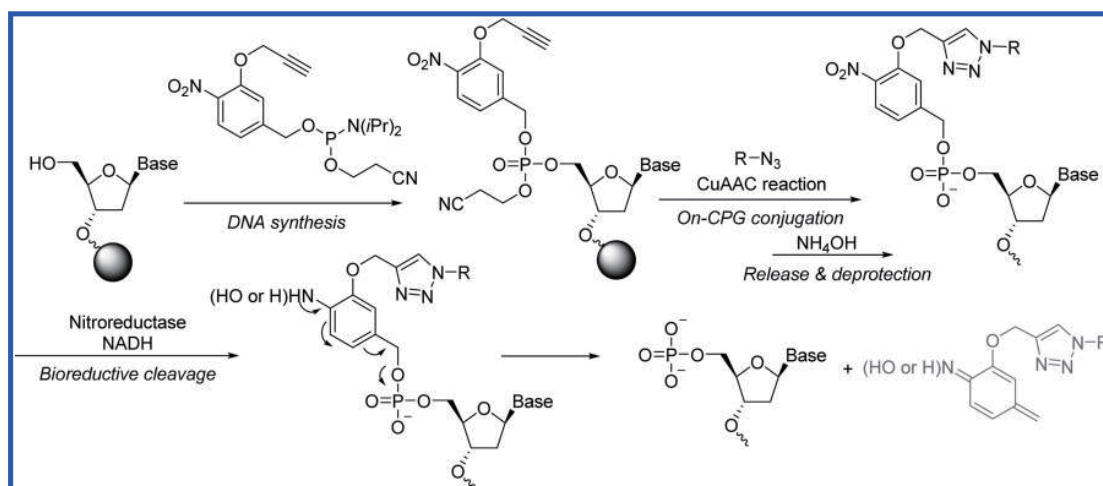
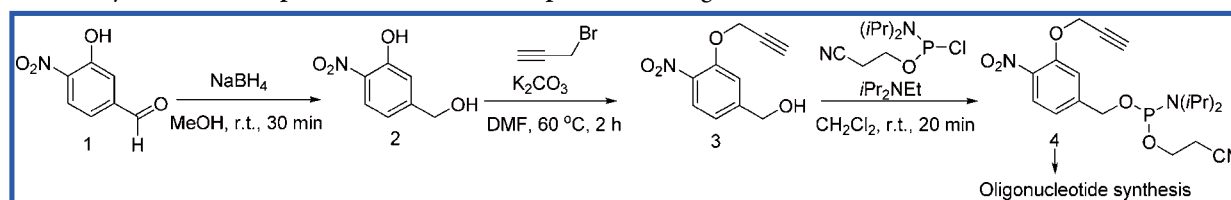
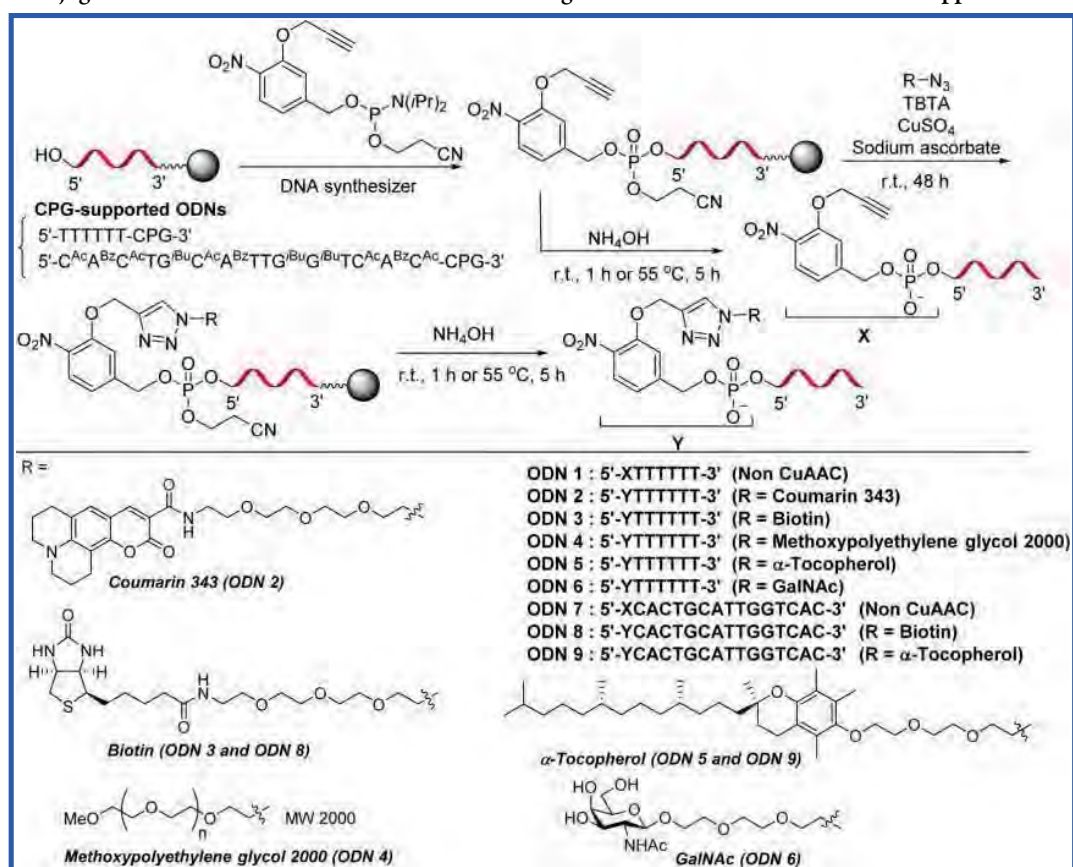


Figure 1. Conjugation/bioreductive cleavage strategy for nucleic acid.

Scheme 1. Synthesis of Phosphoramidite and Its Incorporation in Oligonucleotides



Scheme 2. Conjugation with Various Functional Molecules Using a CuAAC Reaction on the CPG Support



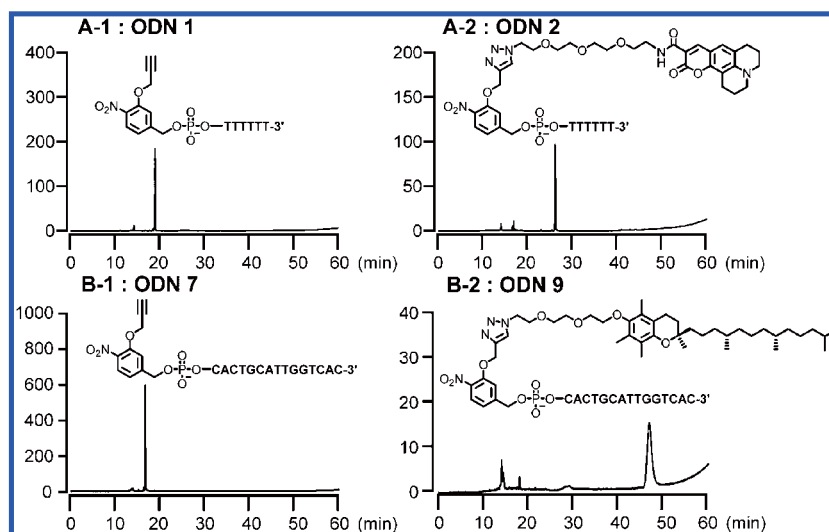


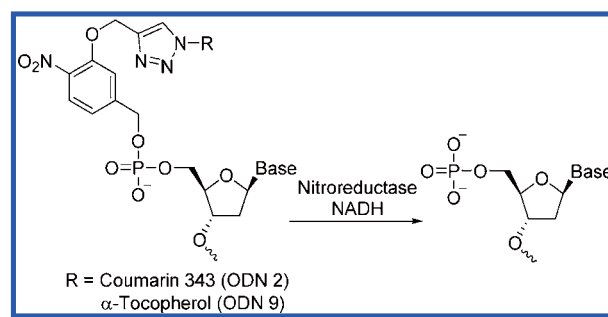
Figure 2. RP HPLC profiles of the crude conjugated ODNs before HPLC purification, which were prepared using an on-solid support CuAAC reaction. Panel A-1: ODN 1; Panel A-2: ODN 2; Panel B-1: ODN 7; Panel B-2: ODN 9. HPLC conditions: A buffer (0.1 M TEAA containing 5% CH₃CN), B buffer (CH₃CN), gradient (B) 0 to 100% (60 min). Flow rate: 1 mL/min.

an on-solid support CuAAC reaction^{11,15,18} to allow for the attachment of several functional molecules, including biotin,³² α -tocopherol,³³ *N*-acetylgalactosamine (GalNAc),³⁴ and polyethylene glycol (PEG)³⁵ to the oligonucleotide. These molecules were selected because they have been reported to enhance cellular uptake and prolong blood circulation. With the exception of the commercially available materials, the procedure used to prepare the azide described in this study is shown in Scheme S1. Upon completion of the reaction (48 h, r.t.), the remaining reagents were washed out of the reaction mixture, and the conjugated oligonucleotides were released from the CPG support and deprotected with aqueous NH₄OH. The resulting oligonucleotides (ODNs) were analyzed by reversed-phase HPLC (RP-HPLC), and the typical results are shown in Figure 2.

Panels A-1 and B-1 show the HPLC chromatograms of the nonconjugated oligonucleotides ODN 1 and ODN 7 before HPLC purification, which were used as controls. These chromatograms revealed that the linker was stable to the DNA synthesis and deprotection conditions. Panels A-2 and B-2 show the HPLC profiles of the conjugated oligonucleotides ODN 2 and ODN 9 before HPLC purification, respectively. The coupling yields for these reactions were generally good, and several other conjugates were also prepared in good yield, as described in Figure S1. The crude compound mixtures were purified by preparative HPLC, and the structures of the pure compounds were confirmed by MALDI-TOF mass spectroscopy (Figure S2).

We then proceeded to investigate the cleavability of the linker to determine whether the functional molecules could be readily separated from the conjugated oligonucleotides by bioreduction (Scheme 3). The conjugates were treated with nitroreductase (from *Escherichia coli*) and NADH, which were selected as model reductive conditions, and the reaction was monitored by HPLC. Time-course profiles for the deprotection reaction are shown in Figure 3. Panels A (bottom) and B (bottom) show the peaks for the DNA conjugates ODN 2 and ODN 9 as well as the internal standard (asterisk) and NADH (5–12 min). The addition of the enzyme led to the cleavage of the linker to give the corresponding 5'-phosphorylated ODNs

Scheme 3. Release of the Naked Oligonucleotide via a Nitro-Reduction Reaction



(Panel A, upper; Panel B, upper) in a time-dependent manner. The conversion yields were estimated from the HPLC data, and the results were determined to be as follows: 15 min, 35%; 30 min, 53%; 60 min, 69%; 120 min, 85% for panel A and 15 min, 22%; 30 min, 32%; 60 min, 38%; 120 min, 46% for panel B. The newly formed peak (naked ODN, as indicated by the black arrow) was isolated by preparative HPLC, and its structure was confirmed by MALDI-TOF mass spectroscopy. The linker was stable in a buffer containing NADH or enzyme (Figure S3). These results indicated that the reduction-elimination reaction performed effectively for the elimination of the functionalized molecules attached to the oligonucleotides. Several other conjugate molecules (ODN 3–6 and 8) were also cleaved under the same conditions, as shown in Figure S4. To assess the applicability of these functionalized oligonucleotides to in vivo systems, we need to investigate the cleavage reaction under the hypoxic conditions typically observed in tumor cells. These studies go beyond the scope of the current study but are currently in progress in our laboratory and will be reported elsewhere in due course.

To summarize, a phosphoramidite monomer bearing a conjugatable and bioreduction cleavable linker was prepared to functionalize the 5'-terminal ends of oligonucleotides. This system was successfully applied to solid phase synthesis and incorporated at the 5'-terminal ends of oligonucleotides. The

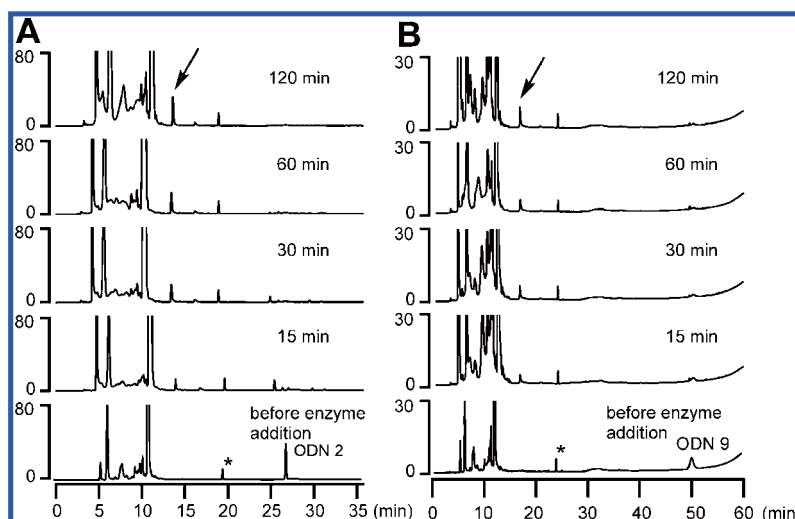


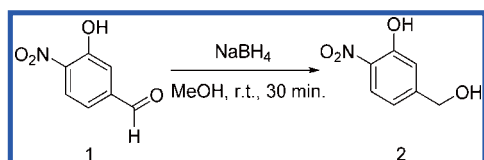
Figure 3. Time-dependent RP-HPLC profiles for the nitroreductase-triggered cleavage of the linkers in the ODNs: Panel A: ODN 2; Panel B: ODN 9; *internal standard (N6-Bz-2'-dA). HPLC conditions: Panel A: A buffer (0.1 M TEAA containing 5% CH₃CN), B buffer (CH₃CN), gradient (B) 0 to 60% (36 min). Flow rate: 1 mL/min. Panel B: A buffer (0.1 M TEAA containing 5% CH₃CN), B buffer (CH₃CN), gradient (B) 0 to 20% (20 min) and then 20 to 100% (40 min). Flow rate: 1 mL/min.

subsequent conjugation of these CPG-supported oligonucleotides with a diverse range of functional molecules was achieved using an on-CPG CuAAC reaction. The resulting oligonucleotide-functionalized conjugates were successfully cleaved using a nitroreductase/NADH system to release the naked oligonucleotides. This new method could be used for the functionalization of oligonucleotides and bioactive nucleotides at their 5'-termini, and the biocleavable properties could be useful for medicinal chemistry and biotechnology applications. For example, the linker reported in this study could be used like a prodrug for bioreductive cleavage leading to the release of a 5'-phosphorylated guide strand RNA, which is a component of the siRNA used for selective RNA interference in cancer cells.

EXPERIMENTAL SECTION

General Experimental Procedure. Chemicals were purchased from a commercial supplier and used without further purification. NMR spectra were recorded at 500 or 600 MHz for ¹H NMR, 126 or 151 MHz for ¹³C NMR, and 243 MHz for ³¹P NMR. Chemical shifts were measured from tetramethylsilane for ¹H NMR spectra and ¹³C NMR spectra and 85% phosphoric acid (0.0 ppm) for ³¹P NMR spectra. The coupling constant (*J*) was reported in hertz. Abbreviations for multiplicity were: s, singlet; d, doublet; t, triplet; sext, sextet; m, multiplet; br, broad. Column chromatography was carried out with a silica gel C-60 or NH silica gel. Thin-layer chromatography (TLC) analyses were carried out on preparative TLC.

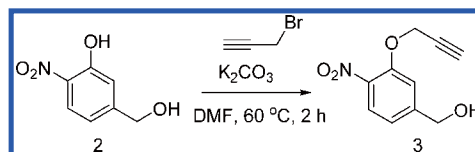
5-(Hydroxymethyl)-2-nitrophenol³¹ 2. 3-Hydroxy-4-nitrobenzaldehyde (1.02 g, 6.11 mmol) was dissolved in MeOH (20 mL). To



the solution was carefully added NaBH₄ (462 mg, 12.2 mmol), and the solution was stirred at room temperature for 30 min. The solution was quenched with 1 M HCl aq. evaporated in vacuo, dissolved in EtOAc, and washed with H₂O. The organic solution was dried (Na₂SO₄), filtered, and evaporated in vacuo. The residue was purified by column chromatography on a silica gel eluted with CHCl₃/MeOH (95:5, v/v)

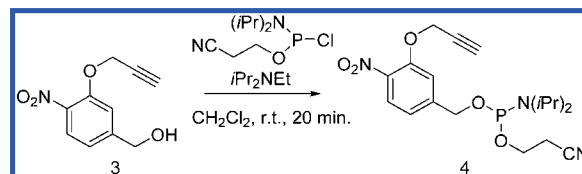
to give (967 mg, 94%) as a yellow solid: mp 96.5–97.0 °C; ¹H NMR (600 MHz, CDCl₃) δ 10.66 (1H, s), 8.10 (1H, d, *J* = 8.3 Hz), 7.18 (1H, s), 6.98 (1H, dd, *J* = 8.2, 1.4 Hz), 4.77 (2H, d, *J* = 5.5 Hz), 1.89 (1H, t, *J* = 5.5 Hz).

(4-Nitro-3-(prop-2-yn-1-yloxy)phenyl)methanol 3. Compound 2 (580 mg, 3.43 mmol) and K₂CO₃ (1.42 g, 10.3 mmol)



were dissolved in DMF (10 mL), and a solution was stirred at 60 °C for 1 h. To the solution was added propargyl bromide (368 μL, 4.12 mmol), and the solution was stirred at 60 °C for 1 h. The solution was diluted with EtOAc and washed with H₂O (twice). The organic solution was dried (MgSO₄), filtered, and evaporated in vacuo. The residue was purified by column chromatography on a silica gel eluted with hexane:EtOAc (80:20 → 70:30, v/v) to give 3 (670 mg, 94%) as a pale yellow solid: mp 83.5–84.5 °C; ¹H NMR (600 MHz, CDCl₃) δ 7.86 (1H, d, *J* = 8.6 Hz), 7.28 (1H, s), 7.05 (1H, d, *J* = 8.3 Hz), 4.86 (2H, d, *J* = 2.4 Hz), 4.79 (2H, d, *J* = 5.5 Hz), 2.60 (1H, t, *J* = 2.4 Hz), 2.23 (1H, t, *J* = 5.8 Hz); ¹³C NMR (151 MHz, CDCl₃) δ 151.2, 148.2, 139.0, 126.1, 118.9, 113.0, 77.2, 77.1, 64.0, 57.2; HRMS (ESI-TOF) *m/z*: [M + Na⁺] calcd for C₁₀H₉N NaO₄⁺: 230.0424, found: 230.0426.

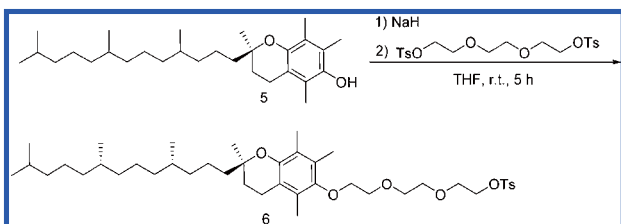
2-Cyanoethyl (4-Nitro-3-(prop-2-yn-1-yloxy)benzyl) Diisopropylphosphoramidite 4. Compound 3 (52 mg, 250 μmol) was



coevaporated with pyridine (5 times) and toluene (twice) and dissolved in CH₂Cl₂ (5 mL). To the solution were added *i*Pr₂NEt (87 μL, 500 μmol) and 2-cyanoethyl *N,N*-diisopropylchlorophosphoramidite (83 μL, 375 μmol) under argon. The mixture was stirred at room temperature for 20 min and diluted with CH₂Cl₂, dried (Na₂SO₄), filtered, and evaporated in vacuo. The residue was purified by column chromatography on a NH-silica gel eluted with hexane:EtOAc (50:50, v/v) to give 4 (52 mg, 53%) as a clear oil; ¹H NMR (500 MHz,

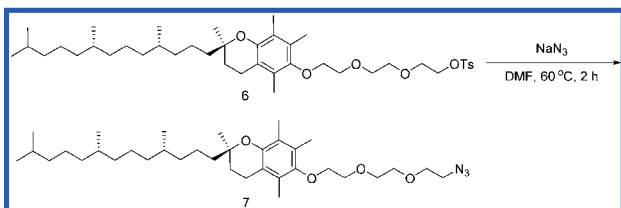
CDCl₃) δ 7.87 (1H, d, J = 8.6 Hz), 7.29 (1H, brs), 7.05–7.03 (1H, m), 4.86 (2H, d, J = 2.6 Hz), 4.83–4.73 (2H, m), 3.95–3.89 (1H, m), 3.86–3.80 (1H, m), 3.74–3.63 (2H, m), 2.67 (2H, t, J = 6.6 Hz), 2.59 (1H, t, J = 2.3 Hz), 1.23–1.21 (12H, m); ¹³C NMR (126 MHz, CDCl₃) δ 151.1, 146.52, 146.47, 139.1, 125.9, 119.1, 117.6, 113.3, 77.26, 77.02, 64.5, 64.3, 58.5, 58.3, 57.2, 43.4, 43.3, 24.74, 24.68, 24.6, 20.52, 20.46; ³¹P NMR (243 MHz, CDCl₃) δ 149.7 HRMS (ESI-TOF) m/z : [M + Na⁺] calcd for C₁₉H₂₆N₃NaO₅P⁺: 430.1502, found: 430.1506.

2-(2-(2-(((R)-2,5,7,8-Tetramethyl-2-((4S,8S)-4,8,12-trimethyltridecyl)chroman-6-yl)oxy)ethoxy)ethoxy)ethyl 4-

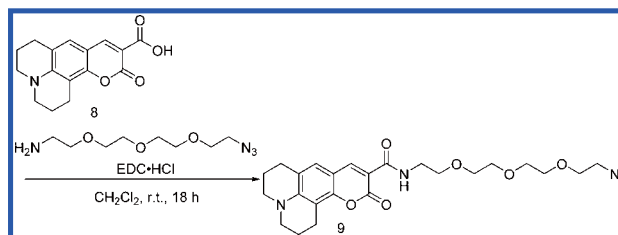


Methylbenzenesulfonate 6. α -Tocopherol (312 mg, 0.724 mmol) was dissolved in THF (10 mL) under argon. To the solution was added 55% NaH (65 mg, 1.46 mmol), and the solution was stirred at room temperature for 5 min. To the mixture was added triethylene glycol bis(*p*-toluenesulfonate) (995 mg, 2.17 mmol), and it was stirred at room temperature for 5 h. Crushed ice was added to the reaction mixture, which was extracted with EtOAc. The organic solution was washed with brine, dried (Na₂SO₄), filtered, and evaporated in vacuo. The residue was purified by column chromatography on a silica gel eluted with hexane:EtOAc (90:10 \rightarrow 80:20, v/v) to give **6** (495 mg, 95%) as a yellow syrup. ¹H NMR (600 MHz, CDCl₃) δ 7.81 (2H, d, J = 8.3 Hz), 7.33 (2H, d, J = 8.3 Hz), 4.18 (2H, t, J = 4.8 Hz), 3.80–3.77 (4H, m), 3.74 (1H, t, J = 4.8 Hz), 3.69–3.67 (2H, m), 3.65–3.63 (2H, m), 2.57 (2H, t, J = 6.2 Hz), 2.43 (3H, s), 2.16 (3H, s), 2.12 (3H, s), 2.07 (3H, s), 1.83–1.72 (2H, m), 1.56–1.04 (24H, m), 0.87–0.84 (12H, m); ¹³C NMR (151 MHz, CDCl₃) δ 148.0, 147.8, 144.8, 133.0, 129.8, 128.0, 127.8, 125.8, 122.8, 117.5, 74.8, 72.1, 70.9, 70.6, 69.3, 68.8, 40.1, 39.4, 37.49, 37.47, 37.44, 37.3, 32.8, 32.7, 31.3, 28.0, 24.8, 24.5, 23.9, 22.7, 22.6, 21.6, 21.1, 20.6, 19.8, 19.7, 12.7, 11.84, 11.79; HRMS (ESI-TOF) m/z : [M + Na⁺] calcd for C₄₂H₆₈NaO₇S⁺: 739.4578, found: 739.4588.

(R)-6-(2-(2-(2-Azidoethoxy)ethoxy)ethoxy)-2,5,7,8-tetramethyl-2-((4S,8S)-4,8,12-trimethyltridecyl)chromane 7. Com-

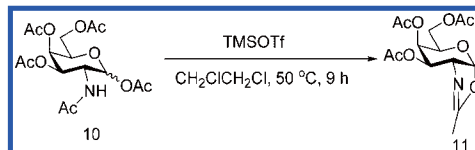


ound **6** (120 mg, 0.167 mmol) was dissolved in DMF (2 mL). To a solution was added NaN₃ (109 mg, 1.68 mmol), and the solution was stirred at 60 °C for 2 h. The reaction mixture was diluted with EtOAc and washed with H₂O and brine. The organic solution was dried (Na₂SO₄), filtered, and evaporated in vacuo. The residue was purified by column chromatography on a silica gel eluted with hexane:EtOAc (9:1, v/v) to give azide derivative **7** (79 mg, 81%) as a yellow syrup. ¹H NMR (600 MHz, CDCl₃) δ 3.83 (4H, s), 3.77–3.76 (2H, m), 3.73–3.71 (4H, m), 3.41 (2H, t, J = 4.8 Hz), 2.58 (2H, t, J = 6.9 Hz), 2.18 (3H, s), 2.14 (3H, s), 2.07 (3H, s), 1.83–1.72 (2H, m), 1.56–1.04 (24H, m), 0.87–0.83 (12H, m); ¹³C NMR (151 MHz, CDCl₃) δ 148.1, 147.8, 127.8, 125.8, 122.8, 117.5, 74.8, 72.1, 71.0, 70.8, 70.7, 70.2, 50.8, 40.1, 39.4, 37.5, 37.4, 37.3, 32.8, 32.7, 31.3, 28.0, 24.8, 24.5, 23.9, 22.7, 22.6, 21.0, 20.7, 19.8, 19.7, 12.7, 11.84, 11.79; HRMS (ESI-TOF) m/z : [M + Na⁺] calcd for C₃₃H₆₁N₃NaO₄⁺: 610.4554, found: 610.4569.



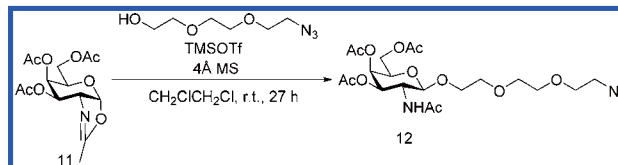
N-(2-(2-(2-Azidoethoxy)ethoxy)ethoxy)ethyl)-11-oxo-2,3,6,7-tetrahydro-1H,5H,11H-pyrano[2,3-f]pyrido[3,2,1-ij]-quinoline-9-carboxamide 9. Coumarin 343 (50 mg, 0.175 mmol) and 1-amino-11-azido-3,6,9-trioxundecane (50 mg, 0.229 mmol) were dissolved in CH₂Cl₂ (2 mL). To the solution was added EDC·HCl (38 mg, 0.198 mmol). The resulted mixture was stirred at room temperature for 18 h. The mixture was evaporated in vacuo. The residue was purified by column chromatography on a silica gel eluted with CHCl₃/MeOH (50:1, v/v) to give **9** (83 mg, 98%) as a yellow syrup. ¹H NMR (600 MHz, CDCl₃) δ 9.08–9.07 (1H, m), 8.58 (1H, s), 7.00 (1H, s), 3.70–3.63 (14H, m), 3.40 (2H, t, J = 4.8 Hz), 3.34 (4H, t, J = 6.9 Hz), 2.89 (2H, t, J = 6.2 Hz), 2.78 (2H, t, J = 6.2 Hz), 2.00 (4H, sext, J = 6.9 Hz); ¹³C NMR (151 MHz, CDCl₃) δ 163.4, 162.9, 152.7, 148.1, 148.0, 127.0, 119.6, 109.0, 108.2, 105.6, 70.74, 70.68, 70.6, 70.0, 69.9, 50.7, 50.2, 49.8, 39.4, 27.5, 21.1, 20.2, 20.1; HRMS (ESI-TOF) m/z : [M + Na⁺] calcd for C₂₄H₃₁N₅NaO₆⁺: 508.2167, found: 508.2174.

Compound 11. ³⁴D-Galactosamine pentaacetate **10** (2.00 g, 5.14 mmol) was dissolved in 1,2-dichloroethane (20 mL) under argon.



TMSOTf (1 mL, 5.53 mmol) was added to the mixture, which was stirred at 50 °C for 9 h. Saturated NaHCO₃ aq was added to the mixture, which was washed with saturated NaHCO₃ aq (twice) and brine (twice). The organic solution was dried (Na₂SO₄), filtered, and evaporated in vacuo. The residue was purified by column chromatography on a silica gel eluted with CHCl₃/MeOH (50:1, v/v) to give oxazoline derivative **11** (925 mg, 54%) as a clear syrup. ¹H NMR (600 MHz, CDCl₃) δ 6.00 (1H, d, J = 6.9 Hz), 5.47 (1H, t, J = 3.1 Hz), 4.92 (1H, dd, J = 7.6, 3.4 Hz), 4.26 (1H, td, J = 6.9, 2.8 Hz), 4.21 (1H, dd, J = 11.7, 7.6 Hz), 4.13 (1H, dd, J = 11.7, 6.2 Hz), 4.01 (1H, td, J = 7.6, 1.4 Hz), 2.13 (3H, s), 2.07 (6H, s), 2.06 (3H, d, J = 1.4 Hz).

2-(2-(2-Azidoethoxy)ethoxy)ethyl-2-acetamido-3,4,6-tri-O-acetyl-2-deoxy- α -D-galactopyranoside 12. ³⁴Compound **11** (847



mg, 2.57 mmol) and 0.5 M 2-(2-azidoethoxy)ethoxyethan-1-ol in *t*-butyl methyl ether (7.7 mL, 3.35 mmol) was coevaporated with pyridine (thrice) and toluene (thrice) and dissolved in 1,2-dichloroethane (10 mL) under argon. To the solution was added 4 Å molecular sieves (1 g), and the mixture was stirred at room temperature for 30 min. TMSOTf (232 μ L, 1.29 mmol) was added, and the mixture was stirred at room temperature for 19 h, and TMSOTf (232 μ L, 1.29 mmol) was further added. The mixture was stirred at same temperature for 8 h, and Et₃N was added. The mixture was evaporated in vacuo. The residue was purified by column chromatography on a silica gel eluted with hexane:EtOAc (1:9, v/v) to give **12** (796 mg, 61%) as a clear syrup. ¹H NMR (600 MHz, CDCl₃)

δ 6.35 (1H, d, $J = 8.9$ Hz), 5.34 (1H, d, $J = 3.4$ Hz), 5.10 (1H, dd, $J = 11.0, 3.4$ Hz), 4.78 (1H, d, $J = 8.3$ Hz), 4.24–4.11 (3H, m), 3.93–3.91 (2H, m), 3.88–3.84 (1H, m), 3.75–3.64 (9H, m), 3.50–3.48 (2H, m), 2.17 (3H, s), 2.05 (3H, s), 2.00 (3H, s), 1.99 (3H, s).

Oligonucleotide Synthesis and On-CPG Conjugation by CuAAC Reaction. Oligonucleotide synthesis was carried out on the Applied Biosystems 394 DNA/RNA Synthesizer according to the manufacturer's recommendations. 2-Cyanoethyl phosphoramidite (dT, dC, dA, and dG) and phosphoramidite **4** were used as 0.1 M solutions in dry acetonitrile. Synthesized solid-supported ODNs were used for conjugation as described below.

Condition A (5'-XTTTTT-3'). CPG support (135 nmol on the 5 mg CPG), azide (1 μ mol), copper(II) sulfate pentahydrate (10 nmol), Tris[1-benzyl-1H-1,2,3-triazol-4-yl]methylamine (10 nmol), and sodium ascorbate (200 nmol) in 100 μ L of a mixed solution (MeOH:THF:H₂O:tBuOH (50:25:24.5:0.5)) were allowed to stand at room temperature for 48 h.

Condition B (5'-YCACTCGATTGGTCAC-3'). CPG support (135 nmol on the 5 mg CPG), azide (1 μ mol), copper(II) sulfate pentahydrate (144 nmol), Tris[1-benzyl-1H-1,2,3-triazol-4-yl]methylamine (430 nmol), and sodium ascorbate (430 nmol) in 100 μ L of a mixed solution (MeOH:THF:H₂O:tBuOH (50:25:21:4)) were allowed to stand at room temperature for 48 h.

After the conjugation reaction was completed, excess reagents were washed out using CH₃CN (1 mL \times 5) and CH₂Cl₂ (1 mL \times 5). Then, CPG-supported ODN was dried in vacuo and released from the CPG support and deprotected by NH₄OH at room temperature for 1 h (ODN 1–6) or at 55 $^{\circ}$ C for 5 h (ODN 7–9). ODNs were purified by HPLC with a reversed-phase silica gel column.

The structure of each ODN was confirmed by MALDI-TOF mass spectrometry using reflection negative mode. (Matrix for ionizing samples was used as a mixture (10:1:1; saturated 3-hydroxy-2-picolinic acid, 2-picolinic acid/H₂O (50 mg/mL), and ammonium citrate/H₂O (50 mg/mL)). MALDI-TOF mass data: ODN 1: calcd [M – H]: 2030.32; found: 2030.16; ODN 2: calcd [M – H]: 2515.55; found 2514.81; ODN 3: calcd [M – H]: 2474.54; found 2474.88; ODN 4: calcd [M – H]: 3830–4230; found 3761–4250; ODN 5: calcd [M – H]: 2617.79; found 2618.37; ODN 6: calcd [M – H]: 2408.50; found 2408.20; ODN 7: calcd [M – H]: 4793.80; found 4795.80; ODN 8: calcd [M – H]: 5238.01; found 5240.54; ODN 9: calcd [M – H]: 5381.25; found 5384.89

Bioreductive Cleavage of Linker for Releasing Naked Oligonucleotides. ODN (10 μ M), NADH (10 mM), and nitroreductase (20 or 80 μ g for ODN 4) in 200 μ L of 50 mM sodium phosphate (pH 7.0) were incubated at 37 $^{\circ}$ C. Aliquots of sample solution were analyzed by reverse-phase HPLC at appropriate times. The appeared peak was fractionized and identified by MALDI-TOF mass spectroscopy. 5'-PO₄-TTTTTT-3' (calcd [M – H]: 1841.28; found: 1841.73). 5'-PO₄-CACTCGATTGGTCAC-3' (calcd [M – H]: 4604.75; found: 4597.49).

ASSOCIATED CONTENT

Supporting Information

The Supporting Information is available free of charge on the ACS Publications website at DOI: 10.1021/acs.joc.6b02527.

HPLC profiles, stability under various conditions, synthetic routes, and copies of ¹H, ¹³C, and ³¹P NMR spectra (PDF)

AUTHOR INFORMATION

Corresponding Authors

*E-mail: saneyoshih@kanagawa-u.ac.jp.

*E-mail: akiraono@kanagawa-u.ac.jp.

ORCID

Hisao Saneyoshi: 0000-0003-4061-101X

Notes

The authors declare no competing financial interest.

ACKNOWLEDGMENTS

This work was supported by the Strategic Research Base Development Program for Private Universities (Kanagawa University, 2012–2016) from the Ministry of Education, Culture, Sports, Science and Technology, Japan (A.O.) and the Takahashi Industrial and Economic Research Foundation (H.S.).

REFERENCES

- Juliano, R. L.; Ming, X.; Nakagawa, O. *Acc. Chem. Res.* **2012**, *45*, 1067.
- Jeong, J. H.; Mok, H.; Oh, Y.-K.; Park, T. G. *Bioconjugate Chem.* **2009**, *20*, 5.
- Olejnik, J.; Krzymanska-Olejnik, E.; Rothschild, K. I. *Nucleic Acids Res.* **1996**, *24*, 361.
- Kolpashchikov, D. M. *Chem. Rev.* **2010**, *110*, 4709.
- Singh, Y.; Murat, P.; Defrancq, E. *Chem. Soc. Rev.* **2010**, *39*, 2054.
- Winkler, J. *Ther. Delivery* **2013**, *4*, 791.
- Patterson, D. M.; Nazarova, L. A.; Prescher, J. A. *ACS Chem. Biol.* **2014**, *9*, 592.
- Huisgen, R. *Angew. Chem.* **1963**, *75*, 604.
- Tornøe, C. W.; Christensen, C.; Meldal, M. *J. Org. Chem.* **2002**, *67*, 3057.
- Rostovtsev, V. V.; Green, L. G.; Fokin, V. V.; Sharpless, K. B. *Angew. Chem., Int. Ed.* **2002**, *41*, 2596.
- Bouillon, C.; Meyer, A.; Vidal, S.; Jochum, A.; Chevlot, Y.; Cloarec, J. P.; Praly, J. P.; Vasseur, J. J.; Morvan, F. *J. Org. Chem.* **2006**, *71*, 4700.
- Gogoi, K.; Mane, M. V.; Kunte, S. S.; Kumar, V. A. *Nucleic Acids Res.* **2007**, *35*, e139.
- Nakane, M.; Ichikawa, S.; Matsuda, A. *J. Org. Chem.* **2008**, *73*, 1842.
- Lonnberg, H. *Bioconjugate Chem.* **2009**, *20*, 1065.
- Jayaprakash, K. N.; Peng, C. G.; Butler, D.; Varghese, J. P.; Maier, M. A.; Rajeev, K. G.; Manoharan, M. *Org. Lett.* **2010**, *12*, 5410.
- Pujari, S. S.; Xiong, H.; Seela, F. *J. Org. Chem.* **2010**, *75*, 8693.
- Pourceau, G.; Meyer, A.; Chevlot, Y.; Souteyrand, E.; Vasseur, J. J.; Morvan, F. *Bioconjugate Chem.* **2010**, *21*, 1520.
- Yamada, T.; Peng, C. G.; Matsuda, S.; Addepalli, H.; Jayaprakash, K. N.; Alam, M. R.; Mills, K.; Maier, M. A.; Charisse, K.; Sekine, M.; Manoharan, M.; Rajeev, K. G. *J. Org. Chem.* **2011**, *76*, 1198.
- Willibald, J.; Harder, J.; Sparrer, K.; Conzelmann, K. K.; Carell, T. *J. Am. Chem. Soc.* **2012**, *134*, 12330.
- Jeong, J. H.; Mok, H.; Oh, Y. K.; Park, T. G. *Bioconjugate Chem.* **2009**, *20*, 5.
- Ji, Y.; Yang, J.; Wu, L.; Yu, L.; Tang, X. *Angew. Chem., Int. Ed.* **2016**, *55*, 2152.
- Leriche, G.; Chisholm, L.; Wagner, A. *Bioorg. Med. Chem.* **2012**, *20*, 571.
- Wong, P. T.; Choi, S. K. *Chem. Rev.* **2015**, *115*, 3388.
- Saito, G.; Swanson, J. A.; Lee, K. D. *Adv. Drug Delivery Rev.* **2003**, *55*, 199.
- Mintzer, M. A.; Simanek, E. E. *Chem. Rev.* **2009**, *109*, 259.
- Lee, Y. S.; Kim, S. W. *J. Controlled Release* **2014**, *190*, 424.
- Yamazoe, S.; McQuade, L. E.; Chen, J. K. *ACS Chem. Biol.* **2014**, *9*, 1985.
- Lin, T. S.; Wang, L.; Antonini, I.; Cosby, L. A.; Shiba, D. A.; Kirkpatrick, D. L.; Sartorelli, A. C. *J. Med. Chem.* **1986**, *29*, 84.
- Wilson, W. R.; Hay, M. P. *Nat. Rev. Cancer* **2011**, *11*, 393.
- Wong, R. H.; Kwong, T.; Yau, K. H.; Au-Yeung, H. Y. *Chem. Commun. (Cambridge, U. K.)* **2015**, *51*, 4440.
- Katayama, S.; Ae, N.; Kodo, T.; Masumoto, S.; Hourai, S.; Tamamura, C.; Tanaka, H.; Nagata, R. *J. Med. Chem.* **2003**, *46*, 691.
- Ren, W. X.; Han, J.; Uhm, S.; Jang, Y. J.; Kang, C.; Kim, J. H.; Kim, J. S. *Chem. Commun. (Cambridge, U. K.)* **2015**, *51*, 10403.
- Nishina, K.; Unno, T.; Uno, Y.; Kubodera, T.; Kanouchi, T.; Mizusawa, H.; Yokota, T. *Mol. Ther.* **2008**, *16*, 734.

- (34) Prakash, T. P.; Graham, M. J.; Yu, J.; Carty, R.; Low, A.; Chappell, A.; Schmidt, K.; Zhao, C.; Aghajani, M.; Murray, H. F.; Riney, S.; Booten, S. L.; Murray, S. F.; Gaus, H.; Crosby, J.; Lima, W. F.; Guo, S.; Monia, B. P.; Swayze, E. E.; Seth, P. P. *Nucleic Acids Res.* **2014**, *42*, 8796.
- (35) Iversen, F.; Yang, C.; Dagnaes-Hansen, F.; Schaffert, D. H.; Kjems, J.; Gao, S. *Theranostics* **2013**, *3*, 201.

Synthesis and Characterization of Cell-Permeable Oligonucleotides Bearing Reduction-Activated Protecting Groups on the Internucleotide Linkages

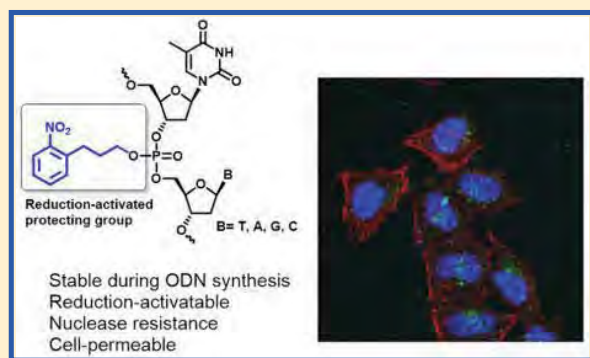
Hisao Saneyoshi,^{*,†} Koichi Iketani,[†] Kazuhiko Kondo,[†] Takeo Saneyoshi,[‡] Itaru Okamoto,[†] and Akira Ono^{*,†}

[†]Department of Material and Life Chemistry, Faculty of Engineering, Kanagawa University, 3-27-1 Rokkakubashi, Kanagawa-ku, Yokohama 221-8686, Japan

[‡]Brain Science Institute RIKEN, 2-1 Hirosawa, Wako City, Saitama 351-0198, Japan

Supporting Information

ABSTRACT: Cell-permeable oligodeoxyribonucleotides (ODNs) bearing reduction-activated protecting groups were synthesized as oligonucleotide pro-drugs. Although these oligonucleotides were amenable to solid-phase DNA synthesis and purification, the protecting group on their phosphodiester moiety could be readily cleaved by nitroreductase and NADH. Moreover, these compounds exhibited good nuclease resistance against 3'-exonuclease and endonuclease and good stability in human serum. Fluorescein-labeled ODNs modified with reduction-activated protecting groups showed better cellular uptake compared with that of naked ODNs.



INTRODUCTION

Synthetic oligonucleotides such as antisense oligonucleotides and siRNAs can be used as biological tools and therapeutic agents to develop a better understanding of pharmacological processes and treat various human diseases.^{1–5}

However, the application of naked oligonucleotides as therapeutic agents has been limited by their polyanionic and hydrophilic properties, which can prevent them from being adsorbed into cells. Furthermore, naked oligonucleotides are rapidly degraded in the biological fluid. The development of an efficient strategy capable of delivering oligonucleotides to a specific target site is therefore highly desirable for the therapeutic application of these systems. Various delivery systems including liposomes, micelles, and nanoparticles have been developed to date to allow for the efficient delivery of oligonucleotides.^{6–10} The direct conjugation of oligonucleotides with carbohydrates, peptides, vitamins, lipids, and antibodies has also been used to facilitate the efficient delivery of these agents to specific target sites via receptor-mediated mechanisms or direct penetration.^{11–18} An alternative pro-oligonucleotide approach was developed by Imbach and co-workers in the 1990s.^{19–24} This particular strategy is based on the use of biodegradable protecting groups for the phosphodiester moieties between the internucleotide linkages of the oligonucleotides. The resulting pro-oligonucleotides (pro-oligos) are bioreversible phosphotriester-type oligonucleotides, which can be readily adsorbed into the cytoplasm without the need for a transfection reagent. Following their uptake into

the cytoplasm, the protecting groups on these pro-oligos can be deprotected by endogenous esterases releasing the active oligonucleotides. The main advantages of this strategy are as follows: (i) there is no need for transfection reagents; (ii) these systems are typically resistant to nucleases; and (iii) several protecting groups are amenable to this approach with different deprotection triggers.^{25–47}

We are particularly interested in using the hypoxic conditions found in the tumor microenvironment to develop targeted pro-oligo systems as therapeutic agents that can be activated by the hypoxic conditions found in advanced solid tumors.⁴⁸ Several hypoxia-activated prodrugs based on a nitro reduction mechanism have been reported in the literature.⁴⁹ Furthermore, nitrothienyl and nitrofuranyl protecting groups have been applied to nucleic acids to protect their internucleotide linkages, leading to improved cellular uptake and nuclease resistance.³⁸ However, this strategy has only ever been applied to oligo thymidylates.

Mixed-sequence oligonucleotides bearing bioreductively sensitive protecting groups would be valuable tools for biological research, with a wide range of potential applications in cancer biology and medicinal studies. Furthermore, these systems could be used without the need for a transfection reagent. In this study, we used a 3-(2-nitrophenyl)propyl

Received: July 7, 2016

Revised: August 20, 2016

Published: September 6, 2016

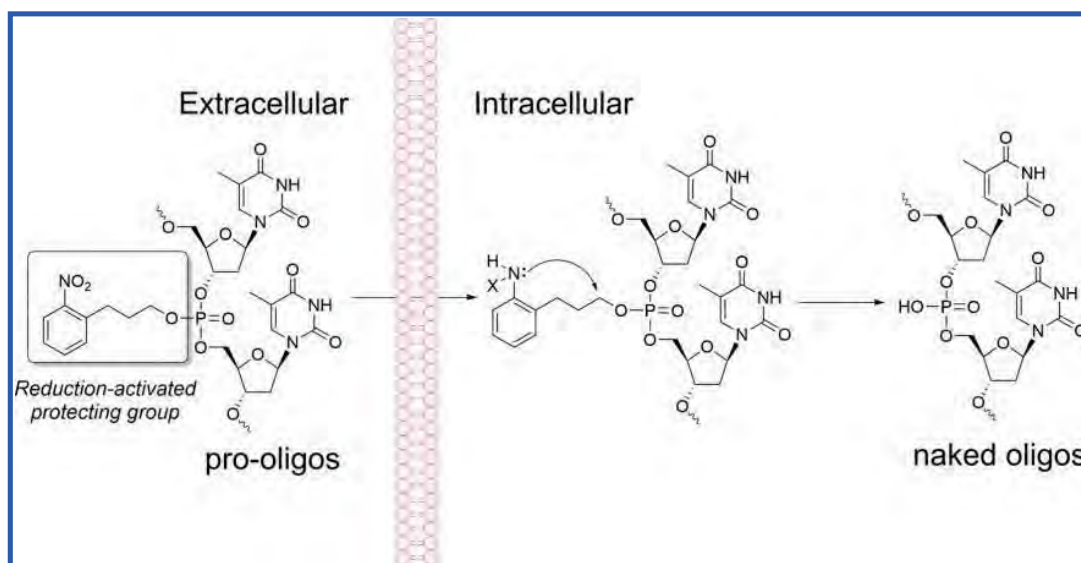


Figure 1. Schematic representation of the behavior expected of the pro-oligos.

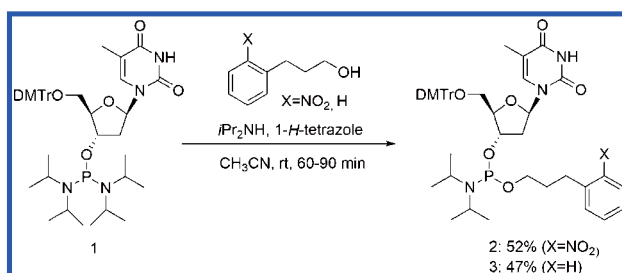
(NPP) group as a new hypoxia-labile protecting group for the phosphodiester bonds of oligonucleotides. From a structural perspective, this protecting group contains aliphatic and aromatic groups with no acyl groups, and it was therefore envisaged that this group would be stable for standard chemical synthesis. It was also envisaged that this group would remain stable in biological fluids except for those found in hypoxic environments. The most likely mechanism for the deprotection of the NPP group is an intramolecular cyclization, which would be triggered by the bioreduction of the nitro group to release the active oligonucleotides (Figure 1).

In this study, we synthesized pro-oligos bearing an NPP group and investigated the deprotection of these systems under model bioreductive conditions. We also evaluated the nuclease resistance, duplex formation, and cellular uptake properties of these NPP-protected pro-oligos.

RESULTS AND DISCUSSION

For the synthesis of the monomer unit, we coupled the known phosphorodiamidite derivative **1**³⁶ with 3-(2-nitrophenyl)propan-1-ol^{50,51} and 3-phenylpropan-1-ol to give the desired coupling products **2** and **3**, respectively (Scheme 1). A series of oligodeoxyribonucleotides (ODN 1–7) incorporating **2** or **3** was synthesized on a DNA synthesizer system using standard methods. The release of the oligonucleotide from the CPG support and the reactions for the deprotection of the base and

Scheme 1. Synthesis of Nucleoside Phosphoroamidites Bearing NPP and 3-Phenylpropyl Groups



phosphate protecting groups were performed under standard conditions (e.g., NH_4OH , rt, 2 h or 55°C , 4 h). The oligothymidylates (ODN 1, 2, and 5–7) and oligonucleotides with mixed sequences incorporating **2** or **3** (ODN 4 and 5) were successfully synthesized according to the route shown in Scheme 2.

Typical reverse-phase high-performance liquid chromatography (HPLC) profiles are shown in Figure 2 (upper: before purification; bottom: after purification). These data showed that the NPP groups were stable to the sequential deprotection and purification steps involved in the synthesis of the oligonucleotide, with the desired products providing double peaks that are derived from diastereoisomers. It is noteworthy that purified ODN 1 remained unchanged after being treated with NH_4OH at 55°C for 6 h (Figure S1).

As a model, an experiment was conducted under bioreductive conditions to evaluate the deprotection of the NPP groups in the ODNs (Scheme 3). ODN 1 ($5'$ -TTT X TTT- $3'$; X = modified T unit) was treated with nitroreductase (from *Escherichia coli*) in the presence of NADH, and the reaction was monitored by HPLC. Time-course HPLC chromatograms are shown in Figure 3A. A peak corresponding to ODN 1 was observed in the HPLC chromatogram prior to the addition of the enzyme along with a peak corresponding to NADH. After incubation with the enzyme for 30 min, the intensity of the peak corresponding to ODN 1 decreased considerably. As the reaction proceeded, so too did the reduction in the intensity of the peak corresponding to ODN 1 until it had been finally converted to the deprotected product (as indicated by the black arrow in the figure). The conversion yields for each time line are shown in Figure 3B.

An oligonucleotide bearing PP groups on its internucleotide linkages (ODN 2) was also synthesized as a noncleavable substrate. This oligonucleotide was also treated with nitroreductase and NADH under the same conditions as those described above for the NPP protected oligonucleotide. The results revealed that ODN 2 was completely stable under the enzymatic conditions for 6 h. The stability of this system was attributed to the absence of a nitro group on the protecting group (Figure 3C,D).

Scheme 2. Synthesis of ODNs Bearing NPP and 3-Phenylpropyl Groups

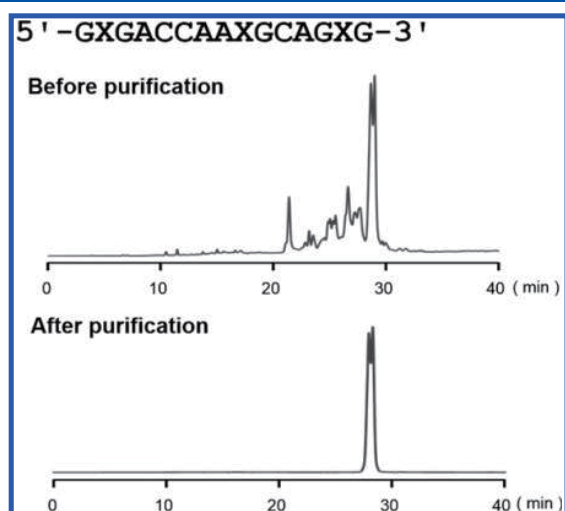
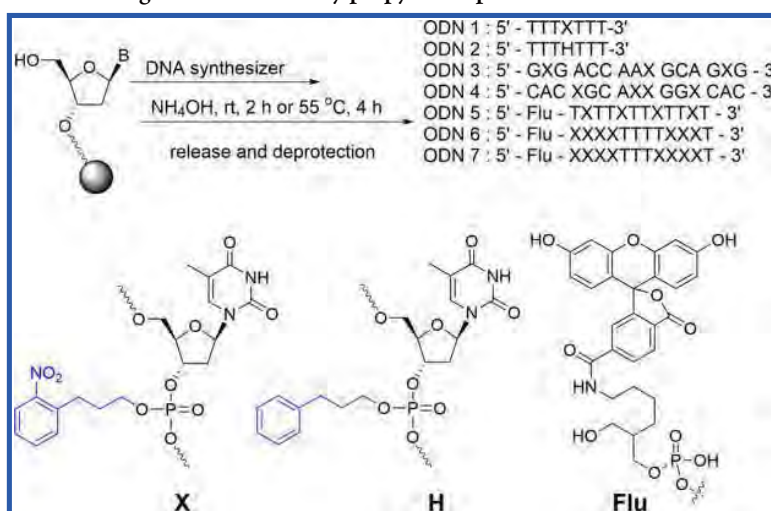
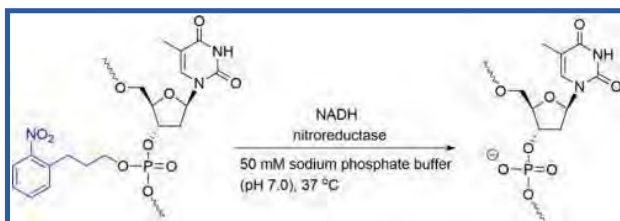


Figure 2. Crude reverse-phase HPLC profiles of a typical ODN with a mixed sequence after DNA synthesis. The purities of the synthesized oligonucleotides were determined by HPLC and their structures were confirmed by MALDI-TOF mass spectroscopy (Table S1).

Scheme 3. Bioreductive Deprotection of the 3-(2-Nitrophenyl)propyl Groups in the ODNs



ODN 1 was found to be stable in buffer, both with and without NADH or nitroreductase, for at least 6 h. HPLC profiles for all of the control experiments are shown in Figure S1.

Next, hybridization affinities of pro-oligonucleotides with mixed sequences were investigated. The sequences used in this study and thermal denaturation profiles are shown in Figure 4. Each ODN has three or four phosphotriester linkages.

Introduction of protecting groups at the internucleotide linkage induced destabilization of duplex formation.

Next, the susceptibility of the synthesized ODNs to nucleolytic enzymes was examined. A total of two kinds of nucleases, *Crotalus adamanteus* venom phosphodiesterase (CAVP) and DNase I, were used as models for a 3'-exonuclease and an endonuclease, respectively. The stability of the ODNs in human serum was also tested.

The ODN 5 containing four residues of each nucleotide analogue were labeled with fluorescein at the 5'-end and incubated with CAVP, DNase I, or 50% human serum. The reactions were then analyzed by polyacrylamide gel electrophoresis under denaturing conditions.

The results for the denature gel analysis of the ODNs treated with CAVP are shown in Figure 5. The control oligonucleotides were completely converted to a series of short nucleotide fragments after being incubated with CAVP for 30 min. Conversely, ODN 5 remained unchanged after being incubated with enzyme for 120 min. ODN 5 also exhibited good nuclease resistance against endonuclease. Furthermore, ODN 5 remained intact after being incubated with DNase I for 72 h, whereas naked ODN was completely consumed after 3 h under the same conditions (Figure 6). ODN 5 also exhibited much greater stability in 50% human serum than did the naked ODN. Taken together, these results showed that ODN 5 was resistant to the effects of several nucleases, including human serum (Figure 7).

Next, we investigated the cellular uptake properties of the ODNs in HeLa cells. ODNs 5–7 were labeled with fluorescein at their 5'-end containing phosphotriester. HeLa cells were treated with individual solutions of the different ODNs (10 μ M) for 1 h and washed with PBS before being fixed with paraformaldehyde and dyed with Alexa594-phalloidin and Hoechst 33258.

The fixed cells were observed by confocal microscopy (Figure 8A). The intensity of the fluorescence of the labeled pro-oligos in the cells increased as the number of protecting groups increased. The maximum intensity was observed for ODN 7, which contained 67% phosphotriester moieties (Figure 8B). This result indicated that the pro-oligos bearing reduction-responsive protecting groups were cell-permeable.

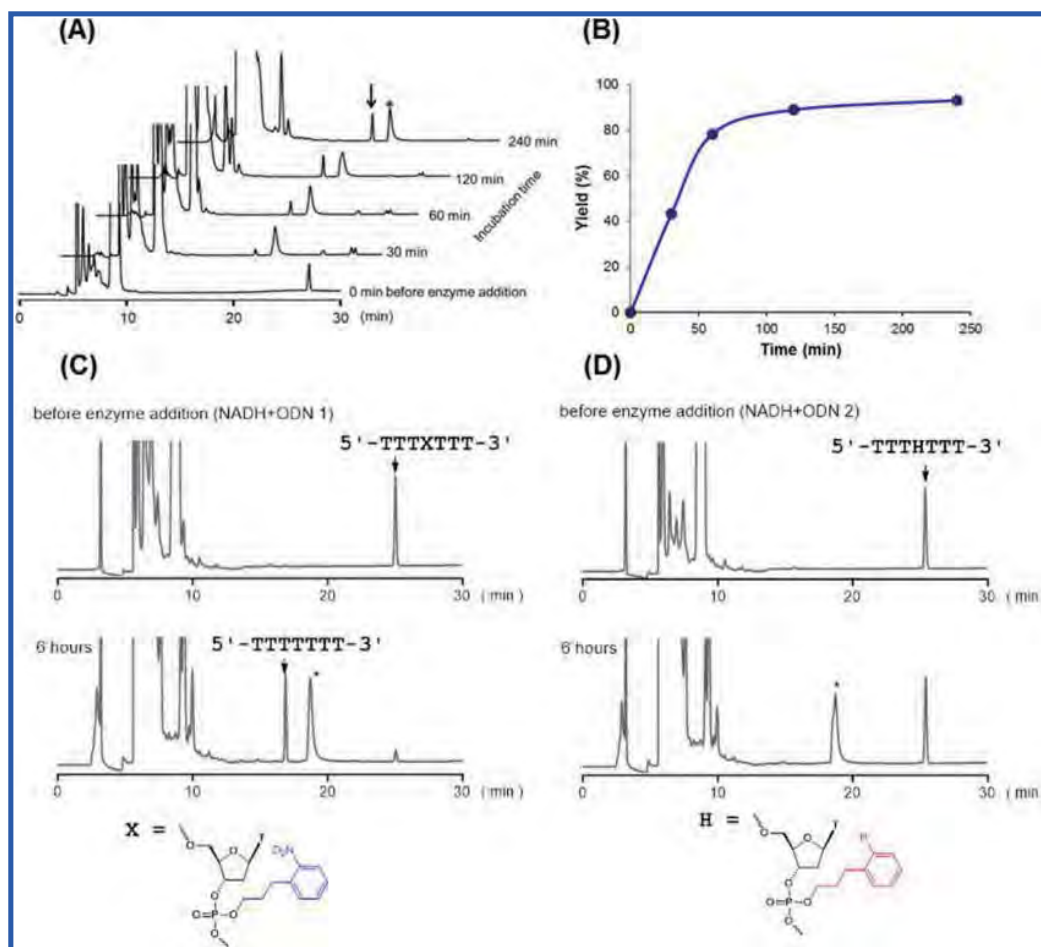


Figure 3. Reverse-phase HPLC chromatograms for the nitroreductase-mediated deprotection of the ODNs. Panel A: reverse-phase HPLC profiles showing the time course for the deprotection reaction; panel B: deprotection yield; panel C: reverse-phase HPLC for the deprotection of NPP after 6 h; panel D: reverse-phase HPLC profile for the deprotection of PP after 6 h. The asterisk indicates a contamination peak from the enzyme solution. The yields were estimated by HPLC analysis based on peak area.

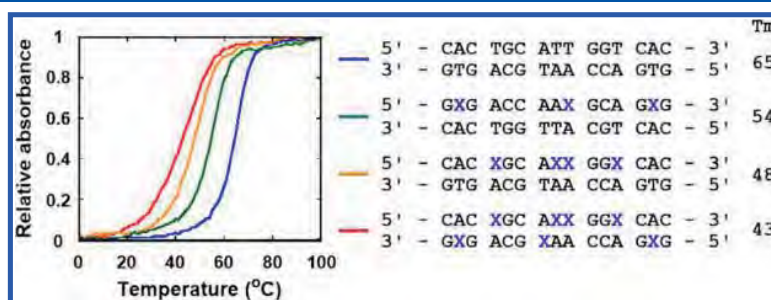


Figure 4. Thermal denaturation profiles of pro-oligos. Conditions: duplex (2 μ M), 100 mM NaCl in 10 mM MOPS (pH 7.0).

CONCLUSIONS

In summary, we have designed and synthesized a series of new pro-oligos, which were activated under bioreductive conditions. We also succeeded in the synthesis of pro-oligos consisting of mixed sequences, which were evaluated in terms of their thermal stabilities. The protecting group in these pro-oligos was readily cleaved by nitroreductase and NADH. These pro-oligos exhibited good nuclease resistance against 3'-exonucleases and endonucleases and good stability in human serum. Notably, ODN 7 showed much better cellular uptake in HeLa cells compared with that of naked ODN, as well as slightly better

uptake than ODN 5 and ODN 6. These results therefore indicate that the pro-oligos described in this study could be used as pro-drugs for the delivery of oligonucleotide-based therapeutics in hypoxic cells.

EXPERIMENTAL SECTION

General Procedures. Chemicals were purchased from Wako Pure Chemicals (Osaka, Japan), Sigma-Aldrich (St. Louis, MO), Tokyo Chemical Industry (Tokyo, Japan), and Glen Research (Sterling, VA) and used without further purification. NMR spectra were recorded on a JEOL (Tokyo,

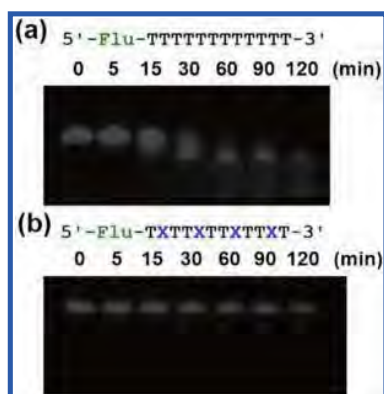


Figure 5. Polyacrylamide gel electrophoresis of 5'-fluorescein labeled ODNs hydrolyzed by CAVP (a 3'-exonuclease). (a) Unmodified oligonucleotide. (b) ODN 5. ODNs were incubated with snake venom phosphodiesterase for 0 min (lane 1), 5 min (lane 2), 15 min (lane 3), 30 min (lane 4), 60 min (lane 5), 90 min (lane 6), and 120 min (lane 7). The experimental conditions are described in the [Experimental section](#).



Figure 6. Polyacrylamide gel electrophoresis of 5'-fluorescein labeled ODNs hydrolyzed by DNase I (an endonuclease). (a) Unmodified oligonucleotide. (b) ODN 5. ODNs were incubated with DNase I for 0 min (lane 1), 3 h (lane 2), 6 h (lane 3), 12 h (lane 4), 24 h (lane 5), 48 h (lane 6), and 72 h (lane 7). The experimental conditions are described in the [Experimental section](#).

Japan) instrument at 600 MHz for ^1H NMR, 125 MHz for ^{13}C NMR, and 172 MHz for ^{31}P NMR. Chemical shifts were measured from tetramethylsilane for ^1H NMR spectra, CDCl_3 (77.0 ppm) for ^{13}C NMR spectra, and 85% phosphoric acid (0.0 ppm) for ^{31}P NMR spectra. The coupling constant (J) was reported in hertz. Abbreviations for multiplicity were: s, singlet; d, doublet; t, triplet; m, multiplet; br, broad. Column chromatography was carried out with a silica gel C-60 (Kanto, Japan) or NH silica gel (Fuji Silysia Chemical; Kasugai, Japan). Thin-layer chromatography (TLC) analyses were carried out on Kieselgel 60-F254 plates (Merck). Reverse-phase HPLC was carried out with Intersil ODS-3 (4.6 \times 250 mm; GL Sciences). The UV-VIS spectrum was recorded on a UV-1650PC Spectrophotometer (Shimadzu, Kyoto, Japan). The HPLC system consisted of a controller, a pump, a UV monitor (SPD-10AVP; Shimadzu), and a recorder (CR6A; Shimadzu).

Oligonucleotide Synthesis. Oligonucleotides synthesis was carried out on the Applied Biosystems 394 DNA/RNA synthesizer according to the manufacturer's recommendations. 2-Cyanoethyl phosphoramidite (dT, dC, dA, and dG) and



Figure 7. Polyacrylamide gel electrophoresis of the 5'-fluorescein labeled ODNs treated with 50% human serum. (a) Unmodified oligonucleotide. (b) ODN 5. ODNs were incubated with 50% human serum for 0 min (lane 1), 1 h (lane 2), 2 h (lane 3), 3 h (lane 4), 4 h (lane 5), 5 h (lane 6), and 6 h (lane 7). Experimental conditions are described in the [Experimental section](#).

phosphoramidite 2 and 3 are used as 0.1 M solutions in dry acetonitrile. Synthesized ODNs were released from CPG support and deprotected by NH_4OH at room temperature for 2 h or 55 $^\circ\text{C}$ for 4 h. The CPG solid support was filtered off, and the filtrate was concentrated in vacuo. Crude ODNs were purified by C-18 cartridge. Each sample was further purified by using reverse-phase HPLC. The structures of each ODN were confirmed by measurement of matrix-assisted laser desorption and ionization time-of-flight (MALDI-TOF) mass spectrometry on the AXIMA-CFR plus (Shimadzu) by using reflection-negative mode. (Matrix for ionizing samples was used as a mixture (10:1:1; saturated 3-hydroxy-2-picolonic acid, 2-picolonic acid- H_2O (50 mg/mL), and ammonium citrate- H_2O (50 mg/mL)).

Thermal Denaturation. Each sample containing a duplex (2 μM) in a buffer of 10 mM MOPS (pH 7.0) with 100 mM NaCl was used this study. The thermally induced transitions of the duplexes were monitored at 260 nm on a UV-1650PC spectrophotometer (Shimadzu) with the T_m analysis accessory (TMSPC-8). The temperature was ramped at 1.0 $^\circ\text{C}$ min $^{-1}$.

Enzymatic Deprotection of Protecting Groups at the Internucleotide Linkage. ODN 1 (6 μM), NADH (10 mM), and nitroreductase (from *E. coli*, 160 μg) in 200 μL of 50 mM sodium phosphate buffer (pH 7.0) was incubated at 37 $^\circ\text{C}$. Aliquots of sample solution were analyzed by reverse-phase HPLC at appropriate times. HPLC conditions: A buffer (0.1 M TEAA containing 5% CH_3CN), B buffer (0.1 M TEAA containing 50% CH_3CN); gradient (B) 5% \rightarrow 60% (30 min). Column: Intersil ODS-3 (4.6 \times 250 mm) (GL Sciences).

Hydrolysis of ODN 5 with CAVP. ODN 5 labeled with fluorescein at the 5'-end (10 μM) was incubated with phosphodiesterase I (0.1 μg , *C. adamanteus* venom; SIGMA) in a buffer containing 50 mM Tris-HCl (pH 8.0) and 10 mM MgCl_2 (total volume of 500 μL) at 37 $^\circ\text{C}$. At the appropriate time, aliquots (20 μL) of the reaction mixture were separated, and the mixture was heated for 5 min at 90 $^\circ\text{C}$. The solutions were analyzed by electrophoresis on 20% polyacrylamide gel containing 7 M urea. The gels were visualized by an AE-9000 E-Graph (ATTO).

Hydrolysis of ODN 5 with DNase 1. ODN 5 labeled with fluorescein at the 5'-end (10 μM) was incubated with

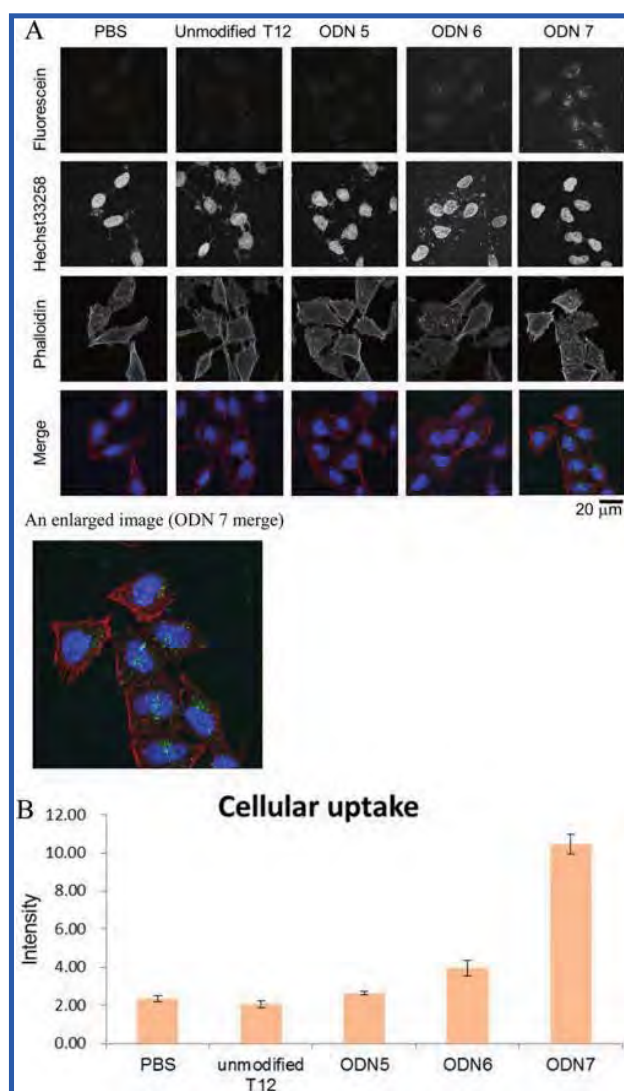


Figure 8. Confocal images showing the cellular uptake of the 5'-fluorescein labeled pro-ODNs in HeLa cells (panel A) and analysis of the amount of fluorescein-labeled pro-oligos in the cells (panel B). The numbers of protecting groups increased from the left side to the right side (ODN 5–7).

recombinant DNase I (100 units; Takara) in a buffer containing 100 mM sodium acetate (pH 6.0) and 5 mM MgCl₂ (total volume of 100 μ L) at 37 $^{\circ}$ C. At the appropriate time, aliquots (10 μ L) of the reaction mixture were separated, and the mixture was added to 5 mM EDTA and heated for 5 min at 90 $^{\circ}$ C. The solutions were analyzed by electrophoresis on 20% polyacrylamide gel containing 7 M urea. The gels were visualized by an AE-9000 E-Graph.

Stability of ODN 5 in the 50% Human Serum. ODN 5 labeled with fluorescein at the 5'-end (10 μ M) was incubated with human serum (Sigma)/PBS (1:1, v/v, total volume of 100 μ L) at 37 $^{\circ}$ C. At the appropriate time, aliquots (10 μ L) of the reaction mixture were separated, and the mixture was added to 10 M urea and heated for 5 min at 90 $^{\circ}$ C. The solutions were analyzed by electrophoresis on 20% polyacrylamide gel containing 7 M urea. The gels were visualized by an AE-9000 E-Graph.

Cell Culture, Oligonucleotide Treatment, and Imaging

Analysis. HeLa cells were cultured in Dulbecco's modified Eagle's medium (Invitrogen), 10% fetal bovine serum, and penicillin–streptomycin at 37 $^{\circ}$ C in 5% CO₂ and 95% air. Cells were plated on glass coverslip in a 24 well culture plate at 2×10^4 cells per well overnight. The following day, cells were washed once with 400 μ L of OptiMEM I (Invitrogen) and preincubated in OptiMEM I for 20 min at 37 $^{\circ}$ C and 5% CO₂. Cells were treated with the pro-oligo solution at the 10 μ M concentration in OptiMEM I for 60 min. After being washed three times with 400 μ L of OptiMEM I for 5 min at 37 $^{\circ}$ C, 5% CO₂ cells were fixed for 20 min in 4% paraformaldehyde in PHEMS buffer (60 mM PIPES, 25 mM HEPES (pH 7.4), 5 mM EGTA, 1 mM MgCl₂, and 3% sucrose) at room temperature, washed three times for 5 min in PBS, and stained with Alexa594 phalloidin (1:100) and Hoechst 33258 (10 μ g/mL) in TBST for 20 min at room temperature. After being washed with PBS, coverslips were mounted on glass slides with Prolong gold (Invitrogen) and imaged using a confocal microscope (FV1200; Olympus). The amount of fluorescein-labeled pro-oligos in the cells was analyzed with Atto Image Analysis Software CS Analyzer 4.

ASSOCIATED CONTENT

Supporting Information

The Supporting Information is available free of charge on the ACS Publications website at DOI: 10.1021/acs.bioconjchem.6b00368.

Figures showing reverse-phase HPLC profiles of synthesized ODNs and HPLC profiles of control experiments of ODN 1 and ODN 2. A table showing the oligonucleotide sequence and MALDI-TOF mass analysis of synthesized oligonucleotides. Additional details on synthetic procedures for all compounds and copies of ¹H, ¹³C, and ³¹P NMR spectra. (PDF)

AUTHOR INFORMATION

Corresponding Authors

*E-mail: saneyoshih@kanagawa-u.ac.jp.

*E-mail: akiraono@kanagawa-u.ac.jp.

Notes

The authors declare no competing financial interest.

ACKNOWLEDGMENTS

This work was supported by the Strategic Research Base Development Program for Private Universities (Kanagawa University, 2012–2016) from the Ministry of Education, Culture, Sports, Science, and Technology, Japan (A.O.) and Takahashi Industrial and Economic Research Foundation (H.S.).

REFERENCES

- (1) Takeshita, F., and Ochiya, T. (2006) Therapeutic potential of RNA interference against cancer. *Cancer Sci.* 97, 689–696.
- (2) Devi, G. R. (2006) siRNA-based approaches in cancer therapy. *Cancer Gene Ther.* 13, 819–829.
- (3) Bennett, C. F., and Swayze, E. E. (2010) RNA targeting therapeutics: molecular mechanisms of antisense oligonucleotides as a therapeutic platform. *Annu. Rev. Pharmacol. Toxicol.* 50, 259–293.
- (4) Mescalchin, A., and Restle, T. (2011) Oligomeric Nucleic Acids as Antivirals. *Molecules* 16, 1271–1296.

- (5) Evers, M. M., Toonen, L. J., and van Roon-Mom, W. M. (2015) Antisense oligonucleotides in therapy for neurodegenerative disorders. *Adv. Drug Delivery Rev.* **87**, 90–103.
- (6) Mintzer, M. A., and Simanek, E. E. (2009) Nonviral vectors for gene delivery. *Chem. Rev.* **109**, 259–302.
- (7) Ku, S. H., Kim, K., Choi, K., Kim, S. H., and Kwon, I. C. (2014) Tumor-targeting multifunctional nanoparticles for siRNA delivery: recent advances in cancer therapy. *Adv. Healthcare Mater.* **3**, 1182–1193.
- (8) Lee, Y. S., and Kim, S. W. (2014) Bioreducible polymers for therapeutic gene delivery. *J. Controlled Release* **190**, 424–439.
- (9) Ozpolat, B., Sood, A. K., and Lopez-Berestein, G. (2014) Liposomal siRNA nanocarriers for cancer therapy. *Adv. Drug Delivery Rev.* **66**, 110–116.
- (10) Yang, J., Liu, H., and Zhang, X. (2014) Design, preparation and application of nucleic acid delivery carriers. *Biotechnol. Adv.* **32**, 804–817.
- (11) Chiu, Y. L., Ali, A., Chu, C. Y., Cao, H., and Rana, T. M. (2004) Visualizing a correlation between siRNA localization, cellular uptake, and RNAi in living cells. *Chem. Biol.* **11**, 1165–1175.
- (12) Winkler, J. (2013) Oligonucleotide conjugates for therapeutic applications. *Ther. Delivery* **4**, 791–809.
- (13) Akinc, A., Querbes, W., De, S., Qin, J., Frank-Kamenetsky, M., Jayaprakash, K. N., Jayaraman, M., Rajeev, K. G., Cantley, W. L., Dorkin, J. R., et al. (2010) Targeted Delivery of RNAi Therapeutics With Endogenous and Exogenous Ligand-Based Mechanisms. *Mol. Ther.* **18**, 1357–1364.
- (14) Madani, F., Lindberg, S., Langel, U., Futaki, S., and Graslund, A. (2011) Mechanisms of cellular uptake of cell-penetrating peptides. *J. Biophys.* **2011**, 414729.
- (15) Jarver, P., Coursindel, T., Andaloussi, S. E., Godfrey, C., Wood, M. J., and Gait, M. J. (2012) Peptide-mediated Cell and In Vivo Delivery of Antisense Oligonucleotides and siRNA. *Mol. Ther.–Nucleic Acids* **1**, e27.
- (16) Raouane, M., Desmaële, D., Urbinati, G., Massaad-Massade, L., and Couvreur, P. (2012) Lipid Conjugated Oligonucleotides: A Useful Strategy for Delivery. *Bioconjugate Chem.* **23**, 1091–1104.
- (17) Spinelli, N., Defranco, E., and Morvan, F. (2013) Glycoclusters on oligonucleotide and PNA scaffolds: synthesis and applications. *Chem. Soc. Rev.* **42**, 4557–4573.
- (18) Cuellar, T. L., Barnes, D., Nelson, C., Tanguay, J., Yu, S. F., Wen, X., Scales, S. J., Gesch, J., Davis, D., van Brabant Smith, A., et al. (2015) Systematic evaluation of antibody-mediated siRNA delivery using an industrial platform of THIOMAB-siRNA conjugates. *Nucleic Acids Res.* **43**, 1189–1203.
- (19) Périgaud, C., Gosselin, G., Lefebvre, I., Girardet, J.-L., Benzaria, S., Barber, I., and Imbach, J.-L. (1993) Rational design for cytosolic delivery of nucleoside monophosphates: “SATE” and “DTE” as enzyme-labile transient phosphate protecting groups. *Bioorg. Med. Chem. Lett.* **3**, 2521–2526.
- (20) Barber, I., Rayner, B., and Imbach, J.-L. (1995) The prooligonucleotide approach. I: Esterase-mediated reversibility of dithymidine S-alkyl-phosphorothiolates to dithymidine phosphorothioates. *Bioorg. Med. Chem. Lett.* **5**, 563–568.
- (21) Mignet, N., Morvan, F., Rayner, B., and Imbach, J.-L. (1997) The pro-oligonucleotide approach. V: Influence of the phosphorus atom environment on the hydrolysis of enzymolabile dinucleoside phosphotriesters. *Bioorg. Med. Chem. Lett.* **7**, 851–854.
- (22) Tosquellas, G., Alvarez, K., Dell’Aquila, C., Morvan, F., Vasseur, J.-J., Imbach, J.-L., and Rayner, B. (1998) The pro-oligonucleotide approach: Solid phase synthesis and preliminary evaluation of model pro-dodecathymidylates. *Nucleic Acids Res.* **26**, 2069–2074.
- (23) Bologna, J. C., Morvan, F., and Imbach, J. L. (1999) The prooligonucleotide approach: Synthesis of mixed phosphodiester and SATE phosphotriester prooligonucleotides using H-phosphonate and phosphoramidite chemistries. *Eur. J. Org. Chem.* **1999**, 2353–2358.
- (24) Bologna, J. C., Vives, E., Imbach, J. L., and Morvan, F. (2002) Uptake and quantification of intracellular concentration of lipophilic pro-oligonucleotides in HeLa cells. *Antisense Nucleic Acid Drug Dev.* **12**, 33–41.
- (25) Iyer, R. P., Yu, D., and Agrawal, S. (1994) Stereospecific bio-reversibility of dinucleoside S-alkyl phosphorothiolates to dinucleoside phosphorothioates. *Bioorg. Med. Chem. Lett.* **4**, 2471–2476.
- (26) Iyer, R. P., Yu, D., and Agrawal, S. (1995) Prodrugs of Oligonucleotides - the Acyloxyalkyl Esters of Oligodeoxyribonucleoside Phosphorothioates. *Bioorg. Chem.* **23**, 1–21.
- (27) Iyer, R. P., Yu, D., Devlin, T., Ho, N.-h., and Agrawal, S. (1996) Acyloxyaryl prodrugs of oligonucleoside phosphorothioates. *Bioorg. Med. Chem. Lett.* **6**, 1917–1922.
- (28) Krise, J. P., and Stella, V. J. (1996) Prodrugs of phosphates, phosphonates, and phosphinates. *Adv. Drug Delivery Rev.* **19**, 287–310.
- (29) Wilk, A., Chmielewski, M. K., Grajkowski, A., Phillips, L. R., and Beaucage, S. L. (2002) The 3-(N-tert-Butylcarboxamido)-1-propyl Group as an Attractive Phosphate/Thiophosphate Protecting Group for Solid-Phase Oligodeoxyribonucleotide Synthesis. *J. Org. Chem.* **67**, 6430–6438.
- (30) Cieślak, J., Grajkowski, A., Livengood, V., and Beaucage, S. L. (2004) Thermolytic 4-Methylthio-1-butyl Group for Phosphate/Thiophosphate Protection in Solid-Phase Synthesis of DNA Oligonucleotides. *J. Org. Chem.* **69**, 2509–2515.
- (31) Ausin, C., Grajkowski, A., Cieślak, J., and Beaucage, S. L. (2005) An efficient reagent for the phosphorylation of deoxyribonucleosides, DNA oligonucleotides, and their thermolytic analogues. *Org. Lett.* **7**, 4201–4204.
- (32) Kröck, L., and Heckel, A. (2005) Photoinduced Transcription by Using Temporarily Mismatched Caged Oligonucleotides. *Angew. Chem., Int. Ed.* **44**, 471–473.
- (33) Pöijärvi, P., Heinonen, P., Virta, P., and Lönnberg, H. (2005) 2,2-Bis(ethoxycarbonyl)- and 2-(Alkylaminocarbonyl)-2-cyano-Substituted 3-(Pivaloyloxy)propyl Groups as Biodegradable Phosphate Protections of Oligonucleotides. *Bioconjugate Chem.* **16**, 1564–1571.
- (34) Shah, S., Rangarajan, S., and Friedman, S. H. (2005) Light-activated RNA interference. *Angew. Chem., Int. Ed.* **44**, 1328–1332.
- (35) Grajkowski, A., Ausin, C., Kauffman, J. S., Snyder, J., Hess, S., Lloyd, J. R., and Beaucage, S. L. (2007) Solid-phase synthesis of thermolytic DNA oligonucleotides functionalized with a single 4-hydroxy-1-butyl or 4-phosphato-/thiophosphato-1-butyl thiophosphate protecting group. *J. Org. Chem.* **72**, 805–815.
- (36) Grajkowski, A., Cieślak, J., Kauffman, J. S., Duff, R. J., Norris, S., Freedberg, D. I., and Beaucage, S. L. (2008) Thermolytic release of covalently linked DNA oligonucleotides and their conjugates from controlled-pore glass at near neutral pH. *Bioconjugate Chem.* **19**, 1696–1706.
- (37) Ora, M., Taherpour, S., Linna, R., Leisvuori, A., Hietamäki, E., Pöijärvi-Virta, P., Beigelman, L., and Lönnberg, H. (2009) Biodegradable Protections for Nucleoside 5'-Monophosphates: Comparative Study on the Removal of O-Acetyl and O-Acetyloxymethyl Protected 3-Hydroxy-2,2-bis(ethoxycarbonyl)propyl Groups. *J. Org. Chem.* **74**, 4992–5001.
- (38) Zhang, N., Tan, C., Cai, P., Zhang, P., Zhao, Y., and Jiang, Y. (2009) The design, synthesis and evaluation of hypoxia-activated pro-oligonucleotides. *Chem. Commun. (Cambridge, U. K.)* **0**, 3216–3218.
- (39) Ausin, C., Kauffman, J. S., Duff, R. J., Shivaprasad, S., and Beaucage, S. L. (2010) Assessment of heat-sensitive thiophosphate protecting groups in the development of thermolytic DNA oligonucleotide prodrugs. *Tetrahedron* **66**, 68–79.
- (40) Grajkowski, A., Cieślak, J., Gapeev, A., and Beaucage, S. L. (2010) Hydroxyalkylated phosphoramidate, phosphoramidothioate and phosphorodiamidothioate derivatives as thiophosphate protecting groups in the development of thermolytic DNA prodrugs. *New J. Chem.* **34**, 880–887.
- (41) Kiuru, E., Ora, M., Beigelman, L., Blatt, L., and Lönnberg, H. (2011) Synthesis and enzymatic deprotection of biodegradably protected dinucleoside-2',5'-monophosphates: 3-(acetyloxy)-2,2-bis(ethoxycarbonyl)propyl phosphoesters of 3'-O-(acyloxymethyl)-adenyl-2',5'-adenosines. *Chem. Biodiversity* **8**, 266–286.

- (42) Kiuru, E., Ahmed, Z., Lönnberg, H., Beigelman, L., and Ora, M. (2013) 2,2-Disubstituted 4-Acylthio-3-oxobutyl Groups as Esterase- and Thermolabile Protecting Groups of Phosphodiester. *J. Org. Chem.* **78**, 950–959.
- (43) Jain, H. V., Takeda, K., Tami, C., Verthelyi, D., and Beaucage, S. L. (2013) Assessment of the cellular internalization of thermolytic phosphorothioate DNA oligonucleotide prodrugs. *Bioorg. Med. Chem.* **21**, 6224–6232.
- (44) Meade, B. R., Gogoi, K., Hamil, A. S., Palm-Apergi, C., van den Berg, A., Hagopian, J. C., Springer, A. D., Eguchi, A., Kacsinta, A. D., Dowdy, C. F., et al. (2014) Efficient delivery of RNAi prodrugs containing reversible charge-neutralizing phosphotriester backbone modifications. *Nat. Biotechnol.* **32**, 1256–1261.
- (45) Leisvuori, A., Lonnberg, H., and Ora, M. (2014) 4-Acetylthio-2,2-dimethyl-3-oxobutyl Group as an Esterase- and Thermo-Labile Protecting Group for Oligomeric Phosphodiester. *Eur. J. Org. Chem.* **2014**, 5816–5826.
- (46) Saneyoshi, H., Shimamura, K., Sagawa, N., Ando, Y., Tomori, T., Okamoto, I., and Ono, A. (2015) Development of a photolabile protecting group for phosphodiester in oligonucleotides. *Bioorg. Med. Chem. Lett.* **25**, 2129–2132.
- (47) Saneyoshi, H., Kondo, K., Sagawa, N., and Ono, A. (2016) Glutathione-triggered activation of the model of pro-oligonucleotide with benzyl protecting groups at the internucleotide linkage. *Bioorg. Med. Chem. Lett.* **26**, 622–625.
- (48) Hockel, M., and Vaupel, P. (2001) Tumor hypoxia: definitions and current clinical, biologic, and molecular aspects. *J. Natl. Cancer Inst.* **93**, 266–276.
- (49) Wilson, W. R., and Hay, M. P. (2011) Targeting hypoxia in cancer therapy. *Nat. Rev. Cancer* **11**, 393–410.
- (50) Chiou, W. H., Kao, C. L., Tsai, J. C., and Chang, Y. M. (2013) Domino Rh-catalyzed hydroformylation-double cyclization of o-amino cinnamyl derivatives: applications to the formal total syntheses of physostigmine and physovenine. *Chem. Commun. (Cambridge, U. K.)* **49**, 8232–8234.
- (51) Rawat, V., Kumar, B. S., and Sudalai, A. (2013) Proline catalyzed sequential alpha-aminoxylation or -amination/reductive cyclization of o-nitrohydrocinnamaldehydes: a high yield synthesis of chiral 3-substituted tetrahydroquinolines. *Org. Biomol. Chem.* **11**, 3608–3611.

Bioinorganic Chemistry

Structure Determination of an Ag^I-Mediated Cytosine–Cytosine Base Pair within DNA Duplex in Solution with ¹H/¹⁵N/¹⁰⁹Ag NMR Spectroscopy

Takenori Dairaku,^{*[a, b]} Kyoko Furuita,^[c] Hajime Sato,^[d] Jakub Šebera,^[e] Katsuyuki Nakashima,^[f] Jiro Kondo,^[g] Daichi Yamanaka,^[b] Yoshinori Kondo,^[b] Itaru Okamoto,^[h] Akira Ono,^[h] Vladimír Sychrovský,^{*[e, i]} Chojiro Kojima,^{*[c]} and Yoshiyuki Tanaka^{*[b, f]}

Abstract: The structure of an Ag^I-mediated cytosine–cytosine base pair, C–Ag^I–C, was determined with NMR spectroscopy in solution. The observation of 1-bond ¹⁵N–¹⁰⁹Ag *J*-coupling (¹*J*(¹⁵N, ¹⁰⁹Ag): 83 and 84 Hz) recorded within the C–Ag^I–C base pair evidenced the N3–Ag^I–N3 linkage in C–Ag^I–C. The triplet resonances of the N4 atoms in C–Ag^I–C demonstrated that each exocyclic N4 atom exists as an amino group (–NH₂), and any isomerization and/or N4–Ag^I bonding can be excluded. The 3D structure of Ag^I–DNA complex determined with NOEs was classified as a B-form conformation with a notable propeller twist of C–Ag^I–C (–18.3 ± 3.0°). The ¹⁰⁹Ag NMR chemical shift of C–Ag^I–C was recorded for cytidine/Ag^I complex (δ(¹⁰⁹Ag): 442 ppm) to completed full NMR characterization of the metal linkage. The structural interpretation of NMR data with quantum mechanical calculations corroborated the structure of the C–Ag^I–C base pair.

polymorphism detection,^[5] nanomachine,^[6] conductivity,^[7] and response to enzymes^[8].

In our previous study, we discovered that cytosine–cytosine (C–C) mismatch selectively captured an Ag⁺ ion and C–Ag^I–C base pair was formed in DNA duplex.^[3a] Although, many metal-base pairs composed of artificial and/or natural nucleobases have been reported to date,^[2] virtual usability of C–Ag^I–C in nanotechnologies has been particularly highlighted in the fields of nanotechnology due to its easy sample preparation.^[2c,g] Our previous studies revealed the 1:1 stoichiometry between C–C mismatch and Ag⁺ ion,^[3a] and the thermodynamic parameters describing C–Ag^I–C formation (*K_a*, Δ*H*, Δ*S*, Δ*G*)^[9a] were determined. The reported *K_a* values for C–Ag^I–C base pair (~10⁶ m⁻¹)^[9a] were significantly larger than the *K_a* for the normal G–C base pair (8.3 × 10⁴ m⁻¹).^[9b] By contrast to negative Δ*S* that is usually obtained for complexation of biomolecules,^[9c,d] the positive Δ*S* was recorded for the C–Ag^I–C base pair formation with isothermal titration calorimetry.^[9a] However, rational explanation of the positive Δ*S* has not been reported due to the lack of structural information on the C–Ag^I–C base pair.

Several hypothetical structures of the C–Ag^I–C have been presented to date (Figure 1). Previously, we proposed a structure with an N3–Ag^I–N3 linkage as an analogy of the T–Hg^{II}–T base pair (Figure 1 a).^[3a,10] As another possible structure of the C–Ag^I–C base pair, a structure with an N3–Ag^I–O2 linkage

Since the formation of Hg^{II}-mediated thymine–thymine base pair (T–Hg^{II}–T) in DNA duplex was solidly proven by using synthetic oligonucleotides,^[1] the metal-mediated base pairs (metal-base pairs) have been utilized for various applications^[2] such as metal-ion sensors,^[3] Hg²⁺-trapping,^[4] single-nucleotide-

[a] Dr. T. Dairaku
School of Pharmaceutical Sciences, Ohu University
31-1 Misumido, Tomita-machi, Koriyama, Fukushima 963-8611 (Japan)
E-mail: t-dairaku@pha.ohu-u.ac.jp

[b] Dr. T. Dairaku, D. Yamanaka, Prof. Y. Kondo, Prof. Y. Tanaka
Graduate School of Pharmaceutical Sciences, Tohoku University
6-3 Aza-Aoba, Aramaki, Aoba-ku, Sendai, Miyagi 980-8578 (Japan)

[c] Dr. K. Furuita, Dr. C. Kojima
Institute for Protein Research, Osaka University
3-2 Yamadaoka, Suita, Osaka 565-0871 (Japan)
E-mail: kojima@protein.osaka-u.ac.jp

[d] Dr. H. Sato
Application, Bruker BioSpin K.K.
3-9 Moriya-cho, Kanagawa-ku, Yokohama
Kanagawa 221-0022 (Japan)

[e] Dr. J. Šebera, Dr. V. Sychrovský
Institute of Organic Chemistry and Biochemistry
Academy of Sciences of the Czech Republic, v.v.i.
Flemingovo náměstí 2, 16610 Praha 6 (Czech Republic)
E-mail: vladimir.sychrovsky@marge.uochb.cas.cz

[f] Dr. K. Nakashima, Prof. Y. Tanaka
Faculty of Pharmaceutical Sciences, Tokushima Bunri University
Yamashiro-cho, Tokushima 770-8514 (Japan)
E-mail: tanakay@ph.bunri-ac.jp

[g] Dr. J. Kondo
Department of Materials and Life Sciences
Faculty of Science and Technology, Sophia University
7-1 Kioi-cho, Chiyoda-ku, Tokyo 102-8554 (Japan)

[h] Dr. I. Okamoto, Prof. A. Ono
Department of Material & Life Chemistry, Faculty of Engineering
Kanagawa University, 3-27-1 Rokkakubashi, Kanagawa-ku
Yokohama, Kanagawa 221-8686 (Japan)

[i] Dr. V. Sychrovský
Czech Technical University in Prague
Faculty of Electrical Engineering, Department of Electrotechnology
Technická 2, 166 27 Praha 6 (Czech Republic)

Supporting information for this article can be found under
<http://dx.doi.org/10.1002/chem.201603048>.

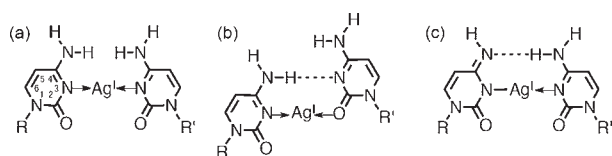


Figure 1. a) Structure of C–Ag^I–C proposed in accordance with T–Hg^{II}–T^[3a,10] and assuming the N3–Ag^I–N3 linkage observed for Ag^I–RNA complex in the crystal.^[12] b) Structure of C–Ag^I–C predicted by Wang et al.^[11] c) The most probable isomerized (deprotonated) structure of (a). R and R' denote the sugar of the nucleotide units within DNA.

(Figure 1 b) was also proposed by Wang et al.^[11] The discrepancy between the Figure 1 a-type structure and 1 b-type structure is becoming a matter of debate.

The structure with the N3–Ag^I–N3 linkage was found recently in the crystal structure of an RNA duplex with C–Ag^I–C base pairs (PDB-ID: 5AY2).^[12] However, several issues concerning C–Ag^I–C structure remained unclear even with the crystal structure. First, the Figure 1 a-type structure might be isomerized into the Figure 1 c-type structure in which unfavorable amino–amino repulsion is converted into favorable hydrogen bonding through the deprotonation of one of the amino groups. However, the structural discrimination between Figure 1 a,c was impossible in the crystal structure of the RNA duplex^[12] since the coordinates of hydrogen atoms were not determined due to its resolution. Second, the typical helical arrangements of DNA and RNA are different by nature and the chemical structure of C–Ag^I–C in respective duplexes should be, therefore, studied independently. Third, it should be also mentioned that the geometry of Figure 1 a may have steric/electrostatic repulsions between amino groups of the paired cytosine residues. Therefore, if the C–Ag^I–C takes the Figure 1 a-type structure, one should explain how to avoid unfavorable steric/electrostatic amino–amino repulsions in a DNA duplex. Thus, the local base-pairing mode of C–Ag^I–C has not been unambiguously determined yet. Therefore, considering these three structures as structural candidates, the base-pairing mode of C–Ag^I–C must be determined.

To determine the chemical structure of C–Ag^I–C in solution, ¹⁵N NMR spectroscopy was employed. The 1-bond N–metal *J*-coupling^[13a,b] and 2-bond N–N *J*-coupling across a metal mediated linkage^[1c] provided solid evidence of the metal binding mode in similar metallo–base pairs. In addition, the N–H *J*-coupling of the amino group was used for exact determination of the state of the amino group(s) in C–Ag^I–C. Lastly, ¹H NMR spectroscopy was used for determination of the 3D structure of DNA duplex containing metallo–base pair(s).^[13a,14]

In the present study, we recorded the 1D ¹⁵N NMR spectra of DNA duplexes containing a C–Ag^I–C base pair to determine its base-pairing mode in solution. The structural interpretation of observed NMR parameters was corroborated with their theoretical calculations. The determined structure of C–Ag^I–C was then employed in an NOE-based calculation of the 3D structure of Ag^I–DNA duplex.

To determine the chemical structure of C–Ag^I–C and the 3D structure of the DNA duplex including the C–Ag^I–C, we synthesized DNA1 and DNA2, respectively (Figure 2 a,b). Details of

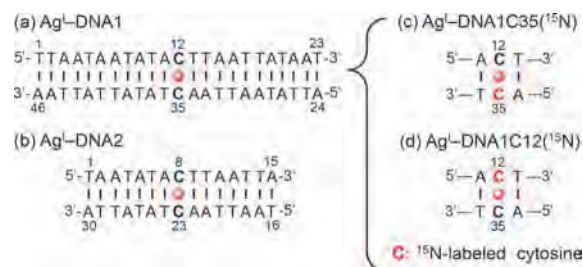


Figure 2. a) The Ag^I–DNA1 complex. b) The Ag^I–DNA2 complex. c) C35-specific ¹⁵N-labeled Ag^I–DNA1 complex (Ag^I–DNA1C35(¹⁵N)). d) C12-specific ¹⁵N-labeled Ag^I–DNA1 complex (Ag^I–DNA1C12(¹⁵N)). Ag^I is shown as a red sphere. To obtain ¹J(¹⁵N,¹⁰⁹Ag) steadily, more stable sequence, DNA1, was employed. To avoid heavy signal overlaps, shorter sequence, DNA2 was employed for the 3D structure calculations.

the design of these DNA sequences can be found in the legend to Figure 2 and in the Supporting Information, Materials and Methods section. The 1D ¹⁵N NMR spectra of cytosine residue-specific ¹⁵N-labeled Ag^I–DNA1 complexes (Figure 2 c,d) were recorded.

In the ¹⁵N NMR spectra, the N3 signals of both C12 and C35 of the C12–Ag^I–C35 base pairs were observed as a doublet due to the ¹J(¹⁵N,¹⁰⁹Ag) = 84 and 83 Hz, respectively (Figure 3). Further structural interpretation of 1-bond ¹⁵N–¹⁰⁹Ag *J*-coupling was provided by theoretical calculations. The ¹J(¹⁵N,¹⁰⁹Ag) = 84.8 Hz was calculated for Figure 1 a-type structure involving the N3–Ag^I–N3 linkage (Table 1). For the Figure 1 b-type structure involving the N3–Ag^I–O2 linkage, one of the ¹⁵N–¹⁰⁹Ag *J*-couplings becomes 3-bond *J*-coupling through the Ag^I–O2 = C2–N3 linkage the theoretical value of which is |³J(¹⁵N,¹⁰⁹Ag)| = 6.4 Hz (Supporting Information, Table S1). The calculations thus demonstrated that occurrence of the Ag^I–O2 linkage in C–Ag^I–C is inconsistent with the experiment.

Further, the state of the exocyclic N4 atom of the cytosine residue was determined with ¹⁵N NMR spectroscopy. From the 1D ¹⁵N NMR spectra, the N4 signals of both C12 and C35 residues were observed as a triplet resonance (Figure 3). These

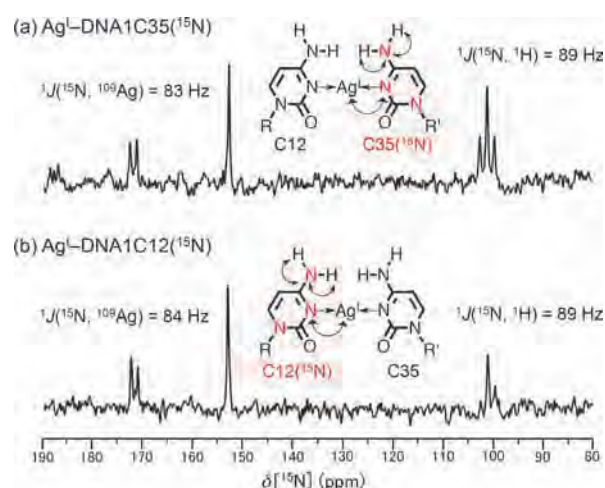


Figure 3. a) 1D ¹⁵N NMR spectrum of the Ag^I–DNA1C35(¹⁵N). b) 1D ¹⁵N NMR spectrum of the Ag^I–DNA1C12(¹⁵N). Solution conditions are 2.0 mM DNA1C35(¹⁵N) or DNA1C12(¹⁵N), 2.0 mM ¹⁰⁹AgNO₃, 100 mM NaNO₃ in water (H₂O/D₂O = 9:1), pH 7.2–7.3 by using the shigemim-NMR tube.

Table 1. $^1J(^{15}\text{N}, ^{109}\text{Ag})$ and $\delta(^{109}\text{Ag})$ values.		
	$^1J(^{15}\text{N}, ^{109}\text{Ag})$ [Hz]	$\delta(^{109}\text{Ag})$ [ppm]
Experimental	83, ^[a] 84 ^[b]	442 ^[c]
Theoretical	84.8 ^[d]	359 ^[d]

[a] The observed $^1J(^{15}\text{N}, ^{109}\text{Ag})$ in Ag^I-DNA1C35(¹⁵N). [b] The observed $^1J(^{15}\text{N}, ^{109}\text{Ag})$ in Ag^I-DNA1C12(¹⁵N). [c] Obtained using the 2:1 complex of cytidine/Ag^I (0.5 M cytidine, 0.24 M AgNO₃ in D₂O). [d] The theoretical values. The $^1J(^{15}\text{N}, ^{109}\text{Ag})$ was calculated as average for two *J*-couplings in C–Ag^I–C. The $\delta(^{109}\text{Ag})$ was calculated as an average value of $\delta(^{109}\text{Ag})$ shifts calculated for mutual rotation of cytosine bases over N3–Ag^I–N3 linkage ($\delta(^{109}\text{Ag})$ varied from 308.0 to 381.5 ppm) in correspondence with assumed flexibility of the 2:1 complex of cytidine/Ag^I. The details concerning theoretical calculations can be found in the Supporting Information, Tables S1, S6–S8, and Figures S7–S9.

coupling patterns provided direct evidence that both the N4 atoms of C12 or C35 exist as an amino group (–NH₂). Isomerization of cytosine after the formation of a C–Ag^I–C base pair in DNA1 was safely excluded. In addition, the two protons of N4 amino groups of C12 and C35 were observed in the ¹⁵N-filtered ¹H NMR spectra (Supporting Information, Figure S1). These data also provide evidence that each exocyclic N4 atom exists as an amino group (–NH₂). In total, it was concluded that the symmetric structure shown in Figure 1 a is the base-pairing mode of C–Ag^I–C in DNA duplex.

The base-pairing mode of C–Ag^I–C was completely determined by NMR spectroscopically revealing the state of the amino groups, which were not resolved crystallographically. This is also the first structure of the C–Ag^I–C base pair within a DNA duplex in solution. The magnitudes of $^1J(^{15}\text{N}, ^{109}\text{Ag})$ in C–Ag^I–C (Table 1) were similar to magnitudes of $^1J(^{15}\text{N}, ^{109}\text{Ag})$ in imidazole–Ag^I–imidazole (Im–Ag^I–Im) base pairs recorded in DNA duplex^[13a] and also to other *J*-couplings in similar compounds (Supporting Information, Table S2). The theoretical $^1J(^{15}\text{N}, ^{109}\text{Ag})$ in C–Ag^I–C calculated with DFT including relativistic effects were in good agreement with experiment (Table 1).

The 3D structure of Ag^I-DNA2 complex was calculated by employing NOE data. The assignments and structure calculations are reported in the Supporting Information, Materials and Methods section (Tables S3–S5 and Figures S2–S4). Out of 100 structures derived from the NOE-based 3D structure calculation, the 10 lowest-energy structures that complied with the experimental and empirical structural constraints were obtained (Figure 4a). The top view of the Ag^I-DNA2 complex with the lowest energy is shown in Figure 4b and a side view is shown in Figure S5 (Supporting Information). The global 3D structure was converged into an anti-parallel double helical structure that was not disordered owing to C–Ag^I–C. The Ag⁺ ion captured within the metallo-base pair was located near the helical axis (Figure 4a,b). Although the sugar pucker of C–Ag^I–C was C3'-endo-like,^[10] the Ag^I-DNA2 complex maintained a B-form conformation. The C1'–C1' distance for C–Ag^I–C (10.2 ± 0.1 Å) was a little shorter than the typical distance in the canonical Watson–Crick (W–C) base pairs (~10.7 Å). Therefore, the structural feature of the C–Ag^I–C base pair is similar to T–Hg^{II}–T base pair that behaves as a structural mimic of the W–C base pair.^[14] This fact explains why both C–Ag^I–C and T–

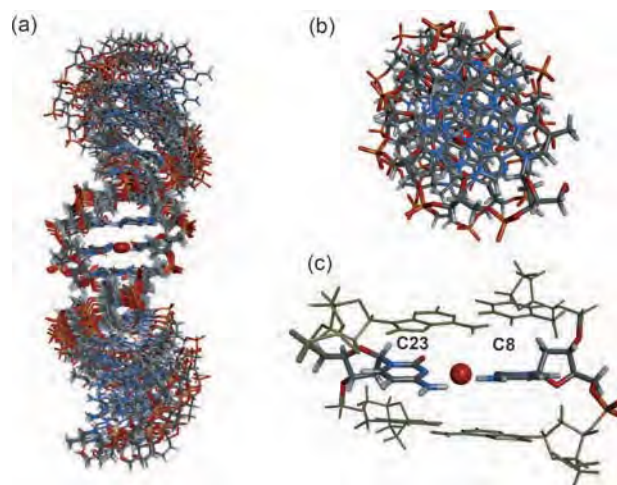


Figure 4. a) Overlay of the 10 low-energy structures of the Ag^I-DNA2. The structures are deposited at the Protein Data Bank under PDB-ID: 2rvp. b) The top view on the Ag^I-DNA2. c) The local structure of Ag^I-DNA2 showing propeller twist of C–Ag^I–C. The Ag^I atom is depicted as a red sphere.

Hg^{II}–T are recognized by DNA polymerase^[8a–d] and DNA ligase^[8e].

The plausibility of proximity of amino groups in C–Ag^I–C despite their repulsion was rationalized with the NOE-calculated 3D structure of Ag^I-DNA2 complex. The propeller twist angle of the C8–Ag^I–C23 base pair was $-18.3 \pm 3.0^\circ$ and the distance between respective protons of the amino groups was thus 2.2 ± 0.1 Å. This is how the amino–amino repulsion in C8–Ag^I–C23 was notably suppressed (Figure 4c). Interestingly, similar propeller twist angles were also observed in the crystals of C–Ag^I–C (-29 – -27°)^[12] and T–Hg^{II}–T (-22 , -20°).^[15]

The NMR structure of Ag^I-DNA rationalized extraordinary thermodynamic parameters describing the formation of C–Ag^I–C. It particularly concerns the relationship of the Ag^I-DNA structure and “positive” entropy for C–Ag^I–C base pairing. The C–Ag^I–C structure demonstrated entire metal dehydration that explains the measured positive ΔS as dehydration entropy owing to removal of structural water molecules within the hydration shell of the Ag⁺ ion that occurs during C–Ag^I–C formation.

Lastly, the ¹⁰⁹Ag NMR chemical shift of C–Ag^I–C was measured to complete the *J*/ δ NMR dataset for characterization of the metallo-base pair. Unfortunately, the sensitivity of ¹⁰⁹Ag NMR was too low to allow $\delta(^{109}\text{Ag})$ measurement in Ag^I-DNA complex. Therefore, the 1D ¹⁰⁹Ag NMR spectrum was recorded for 2:1 complex of cytidine/Ag^I complex in D₂O (Supporting Information, Figure S6). The ¹⁰⁹Ag signal was observed at $\delta = 442$ ppm; however, the ¹⁵N-¹⁰⁹Ag *J*-coupling was not recorded owing to Ag^I-ligand exchange that can be postulated outside the DNA scaffold. This was the first measurement of $\delta(^{109}\text{Ag})$ in C–Ag^I–C employing cytidine/Ag^I complex. The $\delta(^{109}\text{Ag})$ was consistent as regards its magnitude with those of coordination complexes including N–Ag^I–N linkages (Supporting Information, Table S2). These related experiments support our assumption that the observed ¹⁰⁹Ag signal was acquired for C–Ag^I–C in the 2:1 complex of cytidine/Ag^I. To confirm this assumption, $\delta(^{109}\text{Ag})$ was also DFT calculated. The $\delta(^{109}\text{Ag})$ calculated for the 2:1 complex of cytidine/Ag^I was $\delta = 359$ ppm, whereas $\delta(^{109}\text{Ag})$

calculated for the 1:1 complex of cytidine/Ag^I was $\delta = 200$ ppm (Table 1 and Table S1 and S6–S8 in the Supporting Information). Hence, according to theoretical calculations, the $\delta(^{109}\text{Ag})$ was recorded in C–Ag^I–C that was formed as a 2:1 complex of cytidine/Ag^I. All the NMR parameters acquired for the C–Ag^I–C base pair are fundamental reference data employable in future structural studies on Ag^I complexes.

In summary, we determined the chemical structure of the C–Ag^I–C metallo-base pair composed of natural nucleobases and the 3D structure of anti-parallel DNA duplex including the C–Ag^I–C pair. Remarkably, the state of amino protons in the C–Ag^I–C base pair was precisely defined at the atomic level for the first time, which allowed unambiguous determination of chemical structure of C–Ag^I–C. The structural data and description of methods for NMR measurements and structural interpretation of NMR parameters will be employable in future rational design of molecular devices utilizing the metallo-DNA platform.

Acknowledgements

This work was performed using the NMR spectrometer under the Cooperative Research Program of the Institute for Protein Research, Osaka University. This work was supported by the Platform for Drug Discovery, Informatics, and Structural Life Science from the Ministry of Education, Culture, Sports, Science and Technology (MEXT), Japan. This work was supported by grants-in-aid for Scientific Research (A) (24245037 to J.K., A.O., and Y.T), (B) (24310163 to Y.T and C.K.), and (C) (18550146 to Y.T) from MEXT, Japan; a Human Frontier Science Program (HFSP) Young Investigator Grant from HFSP, France (Y.T. and V.S.); and GAČR (13-27676S to V.S.) from the Czech Republic. Y.T. and V.S. were further supported by an Invitation Fellowship for Research in Japan (Short-Term) from JSPS. This work was also supported by Grant-in-Aid for JSPS Fellows (263684 to T.D.).

Keywords: bioinorganic chemistry · DNA · metallo-base-pair · NMR spectroscopy · silver

- [1] a) A. Ono, H. Togashi, *Angew. Chem. Int. Ed.* **2004**, *43*, 4300–4302; *Angew. Chem.* **2004**, *116*, 4400–4402; b) Y. Miyake, H. Togashi, M. Tashiro, H. Yamaguchi, S. Oda, M. Kudo, Y. Tanaka, Y. Kondo, R. Sawa, T. Fujimoto, T. Machinami, A. Ono, *J. Am. Chem. Soc.* **2006**, *128*, 2172–2173; c) Y. Tanaka, S. Oda, H. Yamaguchi, Y. Kondo, C. Kojima, A. Ono, *J. Am. Chem. Soc.* **2007**, *129*, 244–245.
- [2] a) G. H. Clever, C. Kaul, T. Carell, *Angew. Chem. Int. Ed.* **2007**, *46*, 6226–6236; *Angew. Chem.* **2007**, *119*, 6340–6350; b) G. H. Clever, M. Shionoya, *Coord. Chem. Rev.* **2010**, *254*, 2391–2402; c) A. Ono, H. Torigoe, Y. Tanaka, I. Okamoto, *Chem. Soc. Rev.* **2011**, *40*, 5855–5866; d) Y. Takezawa, M. Shionoya, *Acc. Chem. Res.* **2012**, *45*, 2066–2076; e) P. Scharf, J. Müller, *ChemPlusChem* **2013**, *78*, 20–34; f) K. S. Park, H. G. Park, *Curr. Opin. Biotechnol.* **2014**, *28*, 17–24; g) Y. Tanaka, J. Kondo, V. Sychrovský, J. Šebera, T. Dairaku, H. Saneyoshi, H. Urata, H. Torigoe, A. Ono, *Chem. Commun.* **2015**, *51*, 17343–17360.
- [3] a) A. Ono, S. Cao, H. Togashi, M. Tashiro, T. Fujimoto, T. Machinami, S. Oda, Y. Miyake, I. Okamoto, Y. Tanaka, *Chem. Commun.* **2008**, 4825–4827; b) P. D. Selid, H. Y. Xu, E. M. Collins, M. S. Face-Collins, J. X. Zhao, *Sensors* **2009**, *9*, 5446–5459; c) G. Aragay, J. Pons, A. Merkoçi, *Chem. Rev.* **2011**, *111*, 3433–3458; d) D. L. Ma, D. S.-H. Chan, B. Y.-W. Man, C.-H. Leung, *Chem. Asian J.* **2011**, *6*, 986–1003; e) M. Li, H. Gou, I. Al-Ogaidi, N. Wu, *ACS Sustainable Chem. Eng.* **2013**, *1*, 713–723; f) D.-L. Ma, H.-Z. He, K.-H. Leung, H.-J. Zhong, D. S.-H. Chan, C.-H. Leung, *Chem. Soc. Rev.* **2013**, *42*, 3427–3440.
- [4] a) X. Liu, C. Qi, T. Bing, X. Cheng, D. Shangguan, *Talanta* **2009**, *78*, 253–258; b) Y. S. Wang, C.-C. Cheng, J.-K. Chen, F.-H. Ko, F.-C. Chang, *J. Mater. Chem. A* **2013**, *1*, 7745–7750; c) N. Dave, M. Y. Chan, P.-J. J. Huang, B. D. Smith, J. Liu, *J. Am. Chem. Soc.* **2010**, *132*, 12668–12673; d) P.-J. J. Huang, J. Liu, *Chem. Eur. J.* **2011**, *17*, 5004–5010; e) Y. Yu, B. W. Zhang, M. Yu, B. Deng, L. F. Li, C. H. Fan, J. Y. Li, *Sci. China Chem.* **2012**, *55*, 2202–2208; f) M. Kuriyama, K. Haruta, T. Dairaku, T. Kawamura, S. Kikkawa, K. Inamoto, H. Tsukamoto, Y. Kondo, H. Torigoe, I. Okamoto, A. Ono, E. H. Morita, Y. Tanaka, *Chem. Pharm. Bull.* **2014**, *62*, 709–712.
- [5] a) Y.-W. Lin, H.-T. Ho, C.-C. Huang, H.-T. Chang, *Nucleic Acids Res.* **2008**, *36*, e123; b) H. Torigoe, A. Ono, T. Kozasa, *Transition Met. Chem.* **2011**, *36*, 131–144.
- [6] a) J. Liu, Y. Lu, *Angew. Chem. Int. Ed.* **2007**, *46*, 7587–7590; *Angew. Chem.* **2007**, *119*, 7731–7734; b) Z.-G. Wang, J. Elbaz, F. Remacle, R. D. Levine, I. Willner, *Proc. Natl. Acad. Sci. USA* **2010**, *107*, 21996–22001; c) Z.-G. Wang, J. Elbaz, I. Willner, *Nano Lett.* **2011**, *11*, 304–309; d) D. Li, A. Wieckowska, I. Willner, *Angew. Chem. Int. Ed.* **2008**, *47*, 3927–3931; *Angew. Chem.* **2008**, *120*, 3991–3995; e) S. Shimron, J. Elbaz, A. Henning, I. Willner, *Chem. Commun.* **2010**, *46*, 3250–3252; f) F. Wang, R. Orbach, I. Willner, *Chem. Eur. J.* **2012**, *18*, 16030–16036; g) K. S. Park, C. Jung, H. G. Park, *Angew. Chem. Int. Ed.* **2010**, *49*, 9757–9760; *Angew. Chem.* **2010**, *122*, 9951–9954.
- [7] a) B. Liu, A. J. Bard, C. Z. Li, H. B. Kraatz, *J. Phys. Chem. B* **2005**, *109*, 5193–5198; b) H. Isobe, N. Yamazaki, A. Asano, T. Fujino, W. Nakanishi, S. Seki, *Chem. Lett.* **2011**, *40*, 318–319; c) S. Liu, G. H. Clever, Y. Takezawa, M. Kaneko, K. Tanaka, X. Guo, M. Shionoya, *Angew. Chem. Int. Ed.* **2011**, *50*, 8886–8890; *Angew. Chem.* **2011**, *123*, 9048–9052; d) I. Kratochvílová, M. Golan, M. Vala, M. Špérová, M. Weiter, O. Páv, J. Šebera, I. Rosenberg, V. Sychrovský, Y. Tanaka, F. M. Bickelhaupt, *J. Phys. Chem. B* **2014**, *118*, 5374–5381; e) E. Toomey, J. Xu, S. Vecchioni, L. Rothschild, S. Wind, G. E. Fernandes, *J. Phys. Chem. C* **2016**, *120*, 7804–7809.
- [8] a) K. S. Park, C. Jung, H. G. Park, *Angew. Chem. Int. Ed.* **2010**, *49*, 9757–9760; *Angew. Chem.* **2010**, *122*, 9951–9954; b) H. Urata, E. Yamaguchi, T. Funai, Y. Matsumura, S.-i. Wada, *Angew. Chem. Int. Ed.* **2010**, *49*, 6516–6519; *Angew. Chem.* **2010**, *122*, 6666–6669; c) T. Funai, Y. Miyazaki, M. Aotani, E. Yamaguchi, O. Nakagawa, S. Wada, H. Torigoe, A. Ono, H. Urata, *Angew. Chem. Int. Ed.* **2012**, *51*, 6464–6466; *Angew. Chem.* **2012**, *124*, 6570–6572; d) T. Funai, J. Nakamura, Y. Miyazaki, R. Kiri, O. Nakagawa, S. Wada, A. Ono, H. Urata, *Angew. Chem. Int. Ed.* **2014**, *53*, 6624–6627; *Angew. Chem.* **2014**, *126*, 6742–6745; e) S. Bi, B. Ji, Z. P. Zhang, J. J. Zhu, *Chem. Sci.* **2013**, *4*, 1858–1863.
- [9] a) H. Torigoe, I. Okamoto, T. Dairaku, Y. Tanaka, A. Ono, T. Kozasa, *Biochimie* **2012**, *94*, 2431–2440; b) H. Arakawa, J. F. Neault, H. A. Tajmir-Riahi, *Biophys. J.* **2001**, *81*, 1580–1587; c) D. H. Turner, N. Sugimoto, S. M. Freier, *Annu. Rev. Biophys. Chem.* **1988**, *17*, 167–192; d) E. B. Starikov, B. Nordén, *Chem. Phys. Lett.* **2012**, *538*, 118–120.
- [10] T. Dairaku, K. Furuita, H. Sato, Y. Kondo, C. Kojima, A. Ono, Y. Tanaka, *Nucleosides Nucleotides Nucleic Acids* **2015**, *34*, 887–900.
- [11] Y. Wang, B. Ritzo, L. Q. Gu, *RSC Adv.* **2015**, *5*, 2655–2658.
- [12] J. Kondo, Y. Tada, T. Dairaku, H. Saneyoshi, I. Okamoto, Y. Tanaka, A. Ono, *Angew. Chem. Int. Ed.* **2015**, *54*, 13323–13326; *Angew. Chem.* **2015**, *127*, 13521–13524.
- [13] a) S. Johannsen, N. Megger, D. Böhme, R. K. O. Sigel, J. Müller, *Nat. Chem.* **2010**, *2*, 229–234; b) T. Dairaku, K. Furuita, H. Sato, J. Šebera, D. Yamanaka, H. Otaki, S. Kikkawa, Y. Kondo, R. Katahira, F. M. Bickelhaupt, C. F. Guerra, A. Ono, V. Sychrovský, C. Kojima, Y. Tanaka, *Chem. Commun.* **2015**, *51*, 8488–8491.
- [14] H. Yamaguchi, J. Šebera, J. Kondo, S. Oda, T. Komuro, T. Kawamura, T. Dairaku, Y. Kondo, I. Okamoto, A. Ono, J. V. Burda, C. Kojima, V. Sychrovský, Y. Tanaka, *Nucleic Acids Res.* **2014**, *42*, 4094–4099.
- [15] J. Kondo, T. Yamada, C. Hirose, I. Okamoto, Y. Tanaka, A. Ono, *Angew. Chem. Int. Ed.* **2014**, *53*, 2385–2388; *Angew. Chem.* **2014**, *126*, 2417–2420.

Received: June 27, 2016

Published online on August 9, 2016



Contents lists available at ScienceDirect

Inorganica Chimica Acta

journal homepage: www.elsevier.com/locate/ica

Review

Hg^{II}/Ag^I-mediated base pairs and their NMR spectroscopic studies

Takenori Dairaku^{a,b}, Kyoko Furuita^c, Hajime Sato^d, Jakub Šebera^{e,f}, Katsuyuki Nakashima^g, Akira Ono^h, Vladimír Sychrovský^e, Chojiro Kojima^c, Yoshiyuki Tanaka^{a,g,*}

^a Graduate School of Pharmaceutical Sciences, Tohoku University, 6-3 Aza-Aoba, Aramaki, Aoba-ku, Sendai, Miyagi 980-8578, Japan

^b School of Pharmaceutical Sciences, Ohu University, 31-1 Misumido, Tomita-machi, Koriyama, Fukushima 963-8611, Japan

^c Institute for Protein Research, Osaka University, 3-2 Yamadaoka, Suita, Osaka 565-0871, Japan

^d Application, Bruker BioSpin K.K., 3-9 Moriya-cho, Kanagawa-ku, Yokohama, Kanagawa 221-0022, Japan

^e Institute of Organic Chemistry and Biochemistry, Academy of Sciences of the Czech Republic, v.v.i., Flemingovo náměstí 2, 16610 Praha 6, Czech Republic

^f Institute of Physics, Academy of Sciences of the Czech Republic, v.v.i., Na Slovance 2, CZ-182 21 Prague 8, Czech Republic

^g Faculty of Pharmaceutical Sciences, Tokushima Bunri University, Yamashiro-cho, Tokushima 770-8514, Japan

^h Department of Material & Life Chemistry, Kanagawa University, 3-27-1 Rokkakubashi, Kanagawa-ku, Yokohama, Kanagawa 221-8686, Japan

ARTICLE INFO

Article history:

Received 3 December 2015

Received in revised form 10 March 2016

Accepted 12 March 2016

Available online 5 April 2016

Keywords:

Metallo-base-pair

¹⁹⁹Hg NMR spectroscopy

¹⁵N NMR spectroscopy

¹⁰⁹Ag NMR spectroscopy

ABSTRACT

Modern nucleic acids chemistry enabled us to create various types of metal-mediated base pairs (metallo-base-pairs). Nowadays, their structural/spectroscopic data have been accumulated. From the NMR spectroscopic point of view, data on Hg^{II}/Ag^I-mediated base pairs are most accumulated. Accordingly, it would be informative to review a current state of the NMR spectroscopic data of the Hg^{II}/Ag^I-mediated base pairs for subsequent structural studies on other metallo-base-pairs.

© 2016 Elsevier B.V. All rights reserved.



Takenori Dairaku was received his BSc degree (Ohu University, 2009), MSc degree (Tohoku University, 2011), and Ph.D. (Tohoku University, 2015). Afterward, he became a post-doctoral fellow of the Laboratory of Molecular Transformation, Graduate School of Pharmaceutical Sciences, Tohoku University (Professor Yoshinori Kondo's laboratory). Since 2014, he is Research Fellow of Japan Society for the Promotion of Science (JSPS Research Fellow). His current research interests are nucleic acids–metal interactions and development of DNA-based molecular-devices.



Kyoko Furuita received her BSc degree from Tsukuba University in 2005, and MS degree from Nara Institute of Science and Technology (NAIST) in 2007. She received Ph.D. in Bioscience from NAIST in 2010. She worked at Institute for Protein Research (IPR), Osaka University as a post-doctoral fellow in 2010–2014. From 2013 to 2014, she received Research Fellowship for Young Scientist from Japan Society for the Promotion of Science. She worked at Bruker Biospin K.K. as an application scientist in 2014–2015. From 2015, she belongs to IPR, Osaka University as a post-doctoral fellow. Her main research area is NMR structural biology of proteins and nucleic acids.

* Corresponding author at: Faculty of Pharmaceutical Sciences, Tokushima Bunri University, Yamashiro-cho, Tokushima 770-8514, Japan.

E-mail address: tanakay@ph.bunri-ac.jp (Y. Tanaka).



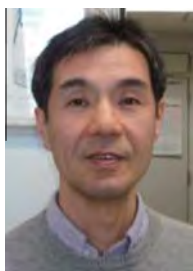
Hajime Sato received a bachelor's degree (Yokohama National University, 1991) and a master's degree (Yokohama National University, 1993). Afterward, he joined to Bruker BioSpin Japan. He received a Ph.D. (Yokohama City University, 2011) while working in Bruker BioSpin.



Jakub Šebera received his MSc degree from Charles University in Prague in 2003 and Ph.D. degree from Czech Technical University in Prague in 2008 (with Dr. Stanislav Zálaiš at J. Heyrovský Institute of Physical Chemistry AS CR). Since 2010 he worked as a post-doctoral fellow in Institute of Physics of the AS CR and in the Institute of Organic Chemistry and Biochemistry of the AS CR. In 2014, he became associated scientist at Institute of Organic Chemistry and Biochemistry AS CR. His research interests include theoretical modeling of chemically modified nucleic acids, enzymatic DNA repair, and material properties in relation to nanotechnologies.



Katsuyuki Nakashima received his B.S. degree (Tokushima Bunri University, 1991) and M.S. degree (Tokushima Bunri University, 1993). Afterward, He was working at the institute of Kyorin Pharmaceutical (1993–1997). From 1997, he belonged to the Faculty of Pharmaceutical Sciences, Tokushima Bunri University as a research assistant (1997–2007), received Ph.D. (Tokushima Bunri University, 2006), an assistant professor (2007–2014) and a lecturer (2014-). His current research interests are total synthesis of biologically active compounds, and structure determination of natural products.



Akira Ono was born in 1957 in Saijo-shi, Ehime-ken, Japan. He received his BSc degree in 1981, MSc degree in 1983, and Ph.D. in 1986 from the Faculty of Pharmaceutical Sciences, Hokkaido University under the supervision of Professor Tohru Ueda. Afterward, He joined the Faculty of Pharmaceutical Sciences, Hokkaido University as an assistant professor in Professor T. Ueda's group. In 1993, he moved to the Graduate School of Sciences, Tokyo Metropolitan University as an Associate Professor. In 2005, he moved to Department of Material & Life Chemistry, Faculty of Engineering, Kanagawa University as a Professor. His current research interests are synthesis of bioactive nucleic acids, nucleic acids-metal interactions, development of nucleic acids based functional materials.



Vladimír Sychrovský received his Ph.D. degree in 1998 from Charles University in Prague, Czech Republic (with Prof. Petr Čárský at J. Heyrovský Institute of Physical Chemistry AS CR). Then he worked in University of Gothenburg, Sweden with Prof. Dieter Cremer (Postdoctoral) from 1998 to 2000. He became associated scientist at Heyrovský Institute of Physical Chemistry AS CR during 2000–2004 and senior scientist at Institute of Organic Chemistry and Biochemistry AS CR since 2004. He received Young Investigator Award by the Human Frontier Science Program in 2008 and award by Daiichi-Sankyo Foundation Of Life-Science in 2011. He became JSPS fellow since 2012. His research interest is focused on theoretical modeling of general properties of nucleic acids including spectroscopic and charge transport properties and chemical reaction pathways.



Chojiro Kojima, male, NMR spectroscopist and biophysicist, graduated from inorganic and physical chemistry department, Osaka University in 1995 under the supervision of Professor Yoshimasa Kyogoku (Institute for Protein Research, Osaka, Japan). He worked with Professor Thomas L. James (University of California, San Francisco, USA) in 1995–1998 and Professor Masatsune Kainosho (Tokyo Metropolitan University, Tokyo, Japan) in 1998–2001 as a postdoctoral fellow. He was an associate professor of Nara Institute of Science and Technology (Nara, Japan) in 2001–2010. Since 2010, he is an associate professor of Osaka University (Osaka, Japan). He is a board member of NMR society of Japan and protein society of Japan. In recent years he focused on NMR structural biology developing new techniques for proteins and nucleic acids.



Yoshiyuki Tanaka received his BSc degree (Osaka University, 1991) and MSc degree (Osaka University, 1993), and received Ph.D. (Osaka University, 1998). Afterward, He joined AIST-Tsukuba as a post-doctoral fellow. From 2001, he belonged to the Graduate School of Pharmaceutical Sciences, Tohoku University as a Research Instructor (2001–2002), an Assistant Professor (2002–2007) and an Associate Professor (2007–2015). Now he became a full Professor of the Laboratory of Analytical Chemistry at the Faculty of Pharmaceutical Sciences, Tokushima Bunri University. During his scientific carrier, he received several awards like the “Young Investigator Award” of the “Human Frontier Science Program (HFSP, Strasbourg)” in 2008. His current research interests are nucleic acids-metal interactions and mechanistic studies on functional RNA/DNA molecules.

Contents

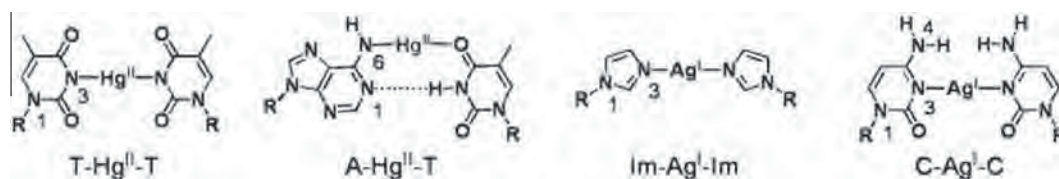
1. Introduction	36
2. Structural analyses of Hg ^{II} /Ag ^I -mediated base pairs with heteronuclear NMR spectroscopy	37
3. Three-dimensional (3D) structures of DNA duplexes including metallo-base-pairs	38
4. Selectivity of ligands for Hg ²⁺ /Ag ⁺	40
5. Conclusion	41
Acknowledgements	41
References	42

1. Introduction

The occurrence/incorporation of metal-mediated base pairs (metallo-base-pairs) into DNA molecules had been studied for a long time by Lippert's group and were followed by a proposal that hydrogen bonds of base pairs could be substituted with coordination bonds with metal cations as functionalizations of DNA molecules by K. Tanaka and Shionoya [1]. Such metallo-base-pairs were actually incorporated into DNA duplexes [2–4]. Since then, many metal-mediated base pairs were created by using artificial metal chelators or other ligands [1–9]. Later, it was discovered/re-discovered that natural nucleobases also have an ability to form metallo-base-pairs, such as Hg^{II}-mediated thymine–thymine (T–Hg^{II}–T) [10,11] and Ag^I-mediated cytosine–cytosine (C–Ag^I–C) [12] base pairs (Scheme 1). This finding stimulated application

studies of metallo-base-pairs as metal sensors, single-nucleotide-polymorphism (SNP) detectors, heavy-metal trappers, nanomachines, etc [13–16].

Simultaneously with these application studies, novel metallo-base-pairs were extensively explored, and there exist more than 50 independent metallo-base-pairs to the best of our knowledge [16]. However, little is known about their structures even if crystallographic [17–23] and NMR spectroscopic [24–40] structures are considered. In the case of NMR spectroscopic studies, Hg^{II}-mediated adenine–thymine (A–Hg^{II}–T) [25], T–Hg^{II}–T [31] and Ag^I-mediated imidazole–imidazole (Im–Ag^I–Im) [35] base pairs (Scheme 1) were intensely studied at the level of heteronuclear multi-dimensional NMR spectroscopy. Since the NMR spectroscopic data include not only structural information but also information regarding electronic structures, we review here the



Scheme 1. Metallo-base-pairs dealt with in this article.

current state of the art on NMR spectroscopic studies on the A–Hg^{II}–T, T–Hg^{II}–T and Im–Ag^I–Im base pairs.

2. Structural analyses of Hg^{II}/Ag^I-mediated base pairs with heteronuclear NMR spectroscopy

Heteronuclear NMR spectroscopy is a critical and indispensable technique for the determination of base-pairing modes of metallo-base-pairs. This is because metallo-base-pairs are formed through coordination bonds generally involving N, O, or S donor atoms (some of them may be regarded covalent bonds). Without observing NMR signals from the corresponding metal ions or coordination sites, it is impossible to conclude their coordination geometries (base-pairing modes) firmly.

In this sense, three metallo-base-pairs satisfy this criterion, namely, A–Hg^{II}–T [25], T–Hg^{II}–T [31] and Im–Ag^I–Im [35] base pairs. In all cases, ¹⁵N NMR spectroscopic techniques were effectively employed, and the base-pairing modes of these metallo-base-pairs were accurately determined beyond any doubt.

In the case of the A–Hg^{II}–T base pair, ¹⁵N chemical shift changes were used to deduce the Hg^{II}-binding site on the adenine base. According to the data by Frøystein and Sletten, they observed large downfield chemical shift changes of the N1 atoms of adenine residues (N1(A)) by 9.4–15.3 ppm (Table 1) [25]. They carefully interpreted these data and concluded that the Hg^{II}-binding site is N6 (amino group) despite the fact that large chemical shift changes were observed at N1(A) [25].

To understand this interpretation, the background of how to interpret ¹⁵N chemical shift changes needs to be explained (Table 2). Based on the theory of heteronuclear NMR chemical shifts, the shielding constant (σ) is expressed as a sum of diamagnetic (σ^D) and paramagnetic (σ^P) terms [33,34].

$$\sigma = \sigma^D + \sigma^P \quad (1)$$

σ^D : the diamagnetic term increases total shielding constant σ ;

$$\sigma^D > 0$$

σ^P : the paramagnetic term decreases total shielding constant σ ;

$$\sigma^P < 0$$

Table 2
Nitrogen-15 chemical shift changes.^a

Bond	Direction	$\Delta\delta(^{15}\text{N})^b/$ ppm	Refs.
N–H... ¹⁵ N (hydrogen-bond)	Upfield	–2.6 to –8.7	[54–56]
¹⁵ N: → ¹⁵ N ⁺ –H (protonation)	Upfield	–40 to –70	[57]
¹⁵ N–M ^{II} (coordination-bond)	Upfield	~–20	[51,58–61]
¹⁵ N–M ^{II} (proton-metal exchange)	Downfield	~+30	[31,33,34]

^a Nitrogen-15 chemical shift changes are listed in ppm.

^b Positive and negative values represent downfield and upfield shifts, respectively.

From empirical knowledge, the $|\sigma^P|$ is typically larger than $|\sigma^D|$ (Eq. (2)). In addition, the $|\sigma^P|$ is proportional to $\frac{1}{\Delta E_{\text{ave}}}$, where ΔE_{ave} is average electronic excitation energy (Eq. (3)).

$$|\sigma^D| < |\sigma^P| \quad (2)$$

$$|\sigma^P| \propto \frac{1}{\Delta E_{\text{ave}}} \quad (3)$$

Here, by defining energies of molecular orbitals (MOs) that describe ground state and excited state of lone-pair electrons E_{lp} and E^* , we can derive the following very rough estimate of average excitation energy (ΔE_{ave}).

$$\Delta E_{\text{ave}} \approx E^* - E_{\text{lp}} \quad (4)$$

When the E_{lp} of the observed site is lowered, ΔE_{ave} becomes larger [33,34]. For example, a bond-formation such as metalation or protonation onto a nitrogen atom produces a bonding MO with a lower energy than that of the lone pair electrons of the nitrogen atom. As a result, E_{lp} is lowered (lone-pair electrons are shifted to the lower bonding MO). This phenomenon can be correlated with the ¹⁵N chemical shift (δ_{N}), as follows

Bond-formation (increase in covalency):

$$E_{\text{lp}} \downarrow \Rightarrow \Delta E_{\text{ave}} (\approx E^* - E_{\text{lp}}) \uparrow \Rightarrow |\sigma^P| \downarrow \Rightarrow \sigma \uparrow \Rightarrow \delta_{\text{N}} \downarrow \text{ (upfield shift)} \quad (5)$$

Table 1
NMR spectroscopic parameters for Hg^{II}/Ag^I-mediated base pairs.

Base pair/solvent/additive	Site	$\delta(\text{metal})/$ ppm	J/Hz		$\Delta\delta(^{15}\text{N})/\text{ppm}^a$			$\Delta\delta(^{13}\text{C})/\text{ppm}^a$				
			$^1J_{\text{N-M}}^b$	$^2J_{\text{NN}}$	N1	N3	N7	C2	C4	C5	C6	C8
A–Hg ^{II} –T(DNA) ^c /H ₂ O/–	N6	–	–	N.A.	+9.4 to +15.3	–3.3 to +2.4	–0.5 to –0.7	–	–	–	–	–
T–Hg ^{II} –T(DNA) ^d /H ₂ O/–	N3	–	–	2.4	–	+29.9 to +35.3	N.A.	–	–	–	–	N.A.
T–Hg ^{II} –T(nucleoside) ^e /DMSO/–	N3	–1784	1050	–	–	–	N.A.	+2.7	+2.4	–0.2	0.0	N.A.
T–Hg ^{II} –T(TpT)/H ₂ O/–	N3	–	–	–	–	–	N.A.	~+2	~+2	–	–	N.A.
Im–Ag ^I –Im(DNA) ^f /H ₂ O/–	N3	–	86	–	–3.2 to –5.1	–14.5 to –15.9	N.A.	–	–	–	–	–
Guanosine(0.5 M)–Hg ^{II} ^h /DMSO/–	N7	–	–	–	~0	~0.5	~–20	–	–	–	–	–
Guanosine(0.2 M)–Hg ^{II} ⁱ /DMSO/–	N7	–	–	–	–	–	–	+0.69	–1.24	–2.63	–1.04	+1.61
Guanosine(0.2 M)–Hg ^{II} ^j /DMSO/Et ₃ N	N1	–	–	–	–	–	–	+3.90	–0.48	–1.78	+2.75	+1.04

^a Positive and negative values represent down-field and up-field shifts, respectively.

^b One-bond ¹⁵N–metal J -coupling ($^1J(^{15}\text{N},^{199}\text{Hg})$ and $^1J(^{15}\text{N},^{107/109}\text{Ag})$).

^c Sample: d(CGCGAAATTCGCG)₂ (4.8 mM) at pH 7. Reference: all data [25].

^d Sample: d(CGCGTTGTCC).d(GGACTTCGCG) (2.0 mM) at pH 6. Reference: all data [31,33,34].

^e Sample: Isolated thymidine–Hg^{II}–thymidine in DMSO. Reference: $\delta(\text{metal})$ [39,43]; $^1J_{\text{N-M}}$ [39]; $\Delta\delta(^{13}\text{C})$ [42].

^f Sample: Hg^{II}–[thymidyl (3'–5') thymidine (TpT)] complex at pH 6.5. Ref. [41].

^g Sample: d(TTAATT Im Im AAATTA)₂ (0.5–1.4 mM) at pH 7.2. Reference: all data [35]. Since this measurement was performed with the Ag^I-source under the natural abundance (¹⁰⁷Ag/¹⁰⁹Ag = 51.839: 48.161) and two isotopes are spin quantum number $I = 1/2$ with similar gyromagnetic ratios ($\gamma(^{107}\text{Ag})/\gamma(^{109}\text{Ag}) = 1: 1.15$), two kinds of J -couplings, namely $^1J(^{15}\text{N},^{107}\text{Ag})$ and $^1J(^{15}\text{N},^{109}\text{Ag})$, are overlapped each other. As a result, the derive J -coupling value became an approximately average values between $^1J(^{15}\text{N},^{107}\text{Ag})$ and $^1J(^{15}\text{N},^{109}\text{Ag})$.

^h Reference: all data [51].

ⁱ Reference: all data [52].

Bond-dissociation/destabilization (decrease in covalency):

$$E_{\text{lp}} \uparrow \Rightarrow \Delta E_{\text{ave}} (\approx E^* - E_{\text{lp}}) \downarrow \Rightarrow |\sigma^{\text{p}}| \uparrow \Rightarrow \sigma \downarrow \Rightarrow \delta_{\text{N}} \uparrow \quad (\text{downfield shift}) \quad (6)$$

Thus, any bond-formation which restricts the excitation of the lone pair/shared electrons of a nitrogen atom (i.e. metalation or protonation) induces an upfield shift of the ^{15}N resonances (Table 2) (see also the Refs. [33,34] for theoretical background).

When we look into the data by Frøystein and Sletten [25] keeping this principle in mind, the “downfield” shifts of the N1(A) resonances are inconsistent with the interpretation of Hg^{II} -binding at N1(A). This is the reason why the data were interpreted as Hg^{II} -binding at N6(A). Furthermore, the imino proton signals of the complementary thymine residue suggest additional Hg^{II} -binding at O4 of the thymine residue [25].

Next, in the case of the T- Hg^{II} -T base pair, its structure was deduced from 2-bond ^{15}N - ^{15}N J -coupling across Hg^{II} ($^2J(^{15}\text{N}, ^{15}\text{N}) = 2.4 \text{ Hz}$) within a DNA duplex (Table 1) [31]. In principle, J -couplings are observed between covalently linked atoms, and the observed $^2J(^{15}\text{N}, ^{15}\text{N})$ represents experimental evidence for the N3- Hg^{II} -N3 linkage within the T- Hg^{II} -T base pair. The observed $\sim 30 \text{ ppm}$ downfield shifts of ^{15}N signals also supported the Hg^{II} -binding at N3 through a proton- Hg^{II} exchange [33,34]. These large downfield shifts might be explained from the difference in the nature of N-H and N- Hg^{II} bonds. On the basis of Eqs. (5) and (6), the N3 atom in the T- Hg^{II} -T base pair resonates downfield with respect to N3 atom in thymine base [33,34] because the N3- Hg^{II} bond in T- Hg^{II} -T is more ionic and less covalent than the N3-H bond in thymine [39,41].

The Eqs. (5) and (6) should be, however, applied with caution since the relationships were derived neglecting “Heavy-Atom effect on the NMR shielding constants of the nearby Light Atoms (HALA)” relativistic effects. The interpretation of perturbation of N3 chemical shift owing to Hg^{II} -linkage may be therefore misleading when the HALA effect on N3 shielding constant is not negligible. Here, the calculated spin-orbit contribution (σ^{SO}) to NMR shielding represented the HALA term. Plausibility of the Eqs. (5) and (6) for explaining general trends in NMR shifts of nucleobase-metal complexes may be nevertheless assumed since the experimental chemical shift perturbations owing to Hg^{II} -linkage for the T- Hg^{II} -T base pair (Table 1) were coherent with trends described by the relationships. The σ^{SO} contribution calculated for N3 atom in T- Hg^{II} -T was -8.6 ppm whereas the σ^{D} and σ^{P} contribution was 312.3 ppm and -275.4 ppm , respectively. For a comparison, the σ^{SO} contribution calculated for N1 atom of thymine in T- Hg^{II} -T was only 0.6 ppm since the HALA propagates the most onto the light atom(s) proximal to heavy atom. The observed change in chemical shift of N3 atom of thymine owing to Hg^{II} -linkage was $\sim 20 \text{ ppm}$ upfield. The Eqs. (5) and (6) can be used for the interpretation of N3 NMR shift changes in terms of altered N3-H/N3- Hg^{II} bonding since the absolute magnitude of σ^{SO} represents roughly 3% of the absolute magnitudes of σ^{D} and σ^{P} .

In addition to these ^{15}N NMR spectroscopic data, ^{199}Hg NMR spectra were recorded for the T- Hg^{II} -T base pair [39]. At first, trials to detect a ^{199}Hg signal from the T- Hg^{II} -T-embedded DNA duplex were performed, but were not successful due to the low sensitivity of the ^{199}Hg nucleus. In order to overcome this issue from the sample concentration, a Hg^{II} -thymidine (1:2) complex was prepared according to the literature by Buncl et al. [42]. Then, its ^{199}Hg NMR spectrum was recorded in an organic solvent (dimethyl sulfoxide (DMSO)) to suppress Hg^{II} -ligand exchanges. In order to detect the 1-bond ^{15}N - ^{199}Hg J -coupling ($^1J(^{15}\text{N}, ^{199}\text{Hg})$), ^{15}N -labeled thymidine was employed [39].

In the ^{199}Hg NMR spectrum, a signal was observed at a chemical shift ($\delta(^{199}\text{Hg})$) of -1784 ppm (Fig. 1 and Table 1) [39]. The δ

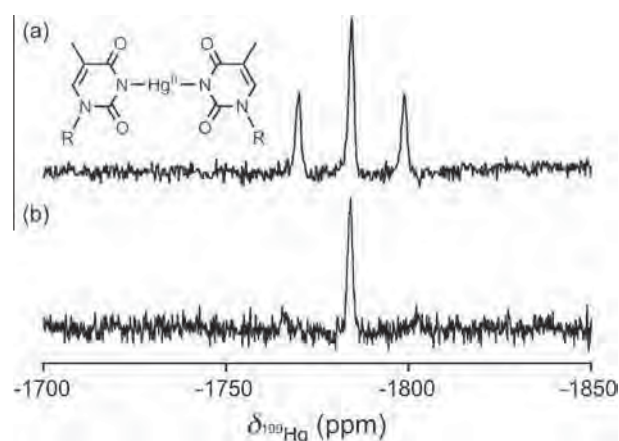


Fig. 1. One-dimensional ^{199}Hg NMR spectra (71.667 MHz for ^{199}Hg frequency). (a) One-dimensional ^{199}Hg NMR spectrum without ^{15}N -decoupling. (b) One-dimensional ^{199}Hg NMR spectrum with ^{15}N -decoupling. The ^{199}Hg NMR chemical shifts are referenced to dimethylmercury (0 ppm) using 1.0 M HgCl_2 in $\text{DMSO}-d_6$ as a secondary reference (-1501 ppm) [62]. Reproduced under a Creative Commons Attribution-NonCommercial 3.0 Unported Licence from [Ref. [39]] Dairaku, T. et al., Chem. Commun., 2015, 51, 8488] – Published by The Royal Society of Chemistry.

(^{199}Hg) value was consistent with a previous observation [43] in the same system. More importantly, the ^{199}Hg signal was a triplet resonance with $^1J(^{15}\text{N}, ^{199}\text{Hg}) = 1050 \text{ Hz}$ (Fig. 1 and Table 1) [39]. This splitting disappeared upon ^{15}N -decoupling (Fig. 1) [39], which is solid evidence that the observed splitting of the ^{199}Hg signal was indeed due to a $^1J(^{15}\text{N}, ^{199}\text{Hg})$ coupling. The observed $^1J(^{15}\text{N}, ^{199}\text{Hg})$ value was surprisingly larger than those observed before (~ 3 times as large as the preexisting data), which demonstrated that the range of $^1J(^{15}\text{N}, ^{199}\text{Hg})$ is wider than those observed previously. With these data, a complete set of chemical shift and J -coupling values was collected for the T- Hg^{II} -T system.

As the last example for an NMR spectroscopically characterized metallo-base-pair, we would like to review the Im- Ag^{I} -Im base pair [35]. The base-pairing mode of the Im- Ag^{I} -Im base pair was determined by observing a 1-bond ^{15}N - $^{107/109}\text{Ag}$ J -coupling ($^1J(^{15}\text{N}, ^{107/109}\text{Ag})$) under natural abundance ($^{107}\text{Ag}/^{109}\text{Ag} = 51.839:48.161$) [35] (see the footnote to Table 1 for details). The derived $^1J(^{15}\text{N}, ^{107/109}\text{Ag})$ value was 86 Hz [35]. Notably, the Im- Ag^{I} -Im base pair was the first one whose base-pairing mode was determined by means of 1-bond N-metal J -coupling ($^1J_{\text{N-M}}$). In addition, the ^{15}N chemical shift changes upon Ag^{I} -binding to the imidazole base (Im) were approximately -15 ppm (upfield shift) (Table 1) as predicted from the principle in Table 2 for a coordination bond.

In summary, the heteronuclear NMR technique is a powerful and indispensable tool for the determination of chemical structures of metallo-base-pairs.

3. Three-dimensional (3D) structures of DNA duplexes including metallo-base-pairs

In the case of DNA duplexes including Im- Ag^{I} -Im or T- Hg^{II} -T base pairs, their 3D structures were determined NMR-spectroscopically in solution (Fig. 2) [35,38]. In both structures, the derived 3D structures belonged to a B-form conformation. Notably, both Im- Ag^{I} -Im and T- Hg^{II} -T base pairs were stacked within respective double helical structures without any severe distortion of the duplexes. Both metallo-base-pairs act as mimics of Watson-Crick base pairs. Such a structural matching of Im- Ag^{I} -Im and T- Hg^{II} -T base pairs with B-form duplex makes these metallo-base-pairs stable within DNA molecules.

The structural match contributes to the negative ΔH for the formation of Im- Ag^{I} -Im and T- Hg^{II} -T base pairs [44]. In addition, it

was demonstrated that the formation of these metallo-base-pairs is entropically favorable [44]. The same trend was further observed for the C–Ag^I–C base pair [36]. As a result, high affinities of Hg²⁺ to the T–T mismatch and those of Ag⁺ to Im–Im/C–C mismatches (low K_d values) were observed [44] (As a related data, K_d values for

thymidine/uridine-cation and adenosine(pyridine-type ligand)-cation systems were reported [45]). The positive entropy changes (ΔS) for the metallo-base-pair formation can be regarded as a “dehydration-entropy” which is often observed for the chelation of metal ions [36,38,44]. Actually, from the 3D structures of both

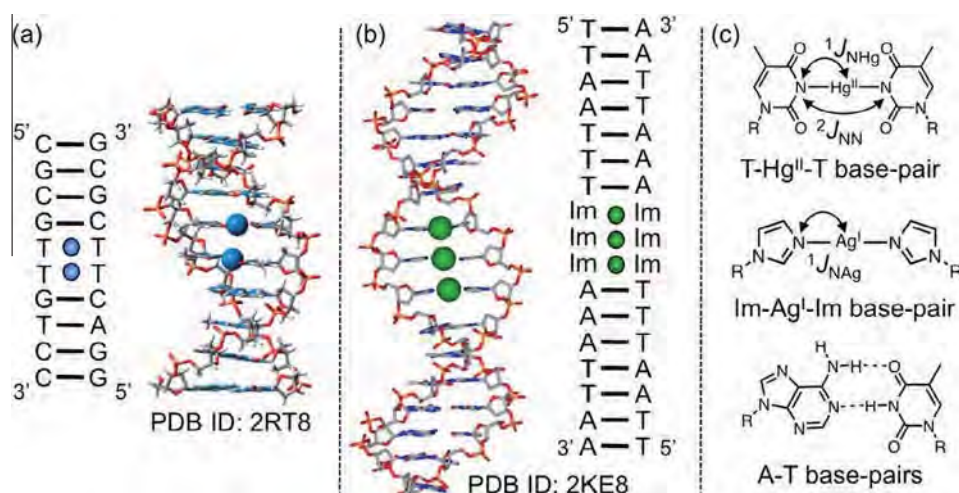


Fig. 2. Three-dimensional structures of metallo-DNA molecules. R denotes deoxyribose. (a) The 3D structure of the DNA duplex with consecutive T-Hg^{II}-T base pairs and its sequence [38]. This sequence was selected since the T_m value of the selected sequence was the highest of all T_m values for the examined sequences [38]. (b) The 3D structure of the DNA duplex with consecutive Im-Ag^I-Im base pairs and its sequence [35]. This sequence was selected since Im-Ag^I-Im base-pairing and the resulting duplex formation was confirmed [35]. The authors also demonstrated that the 1,2,4-triazole formed Ag^I-mediated base pair, and the substitution of 1,2,4-triazole with imidazole resulted in better Ag^I-binding [35]. The 3D graphics are adopted from Ref. [16] with permission from The Royal Society of Chemistry.

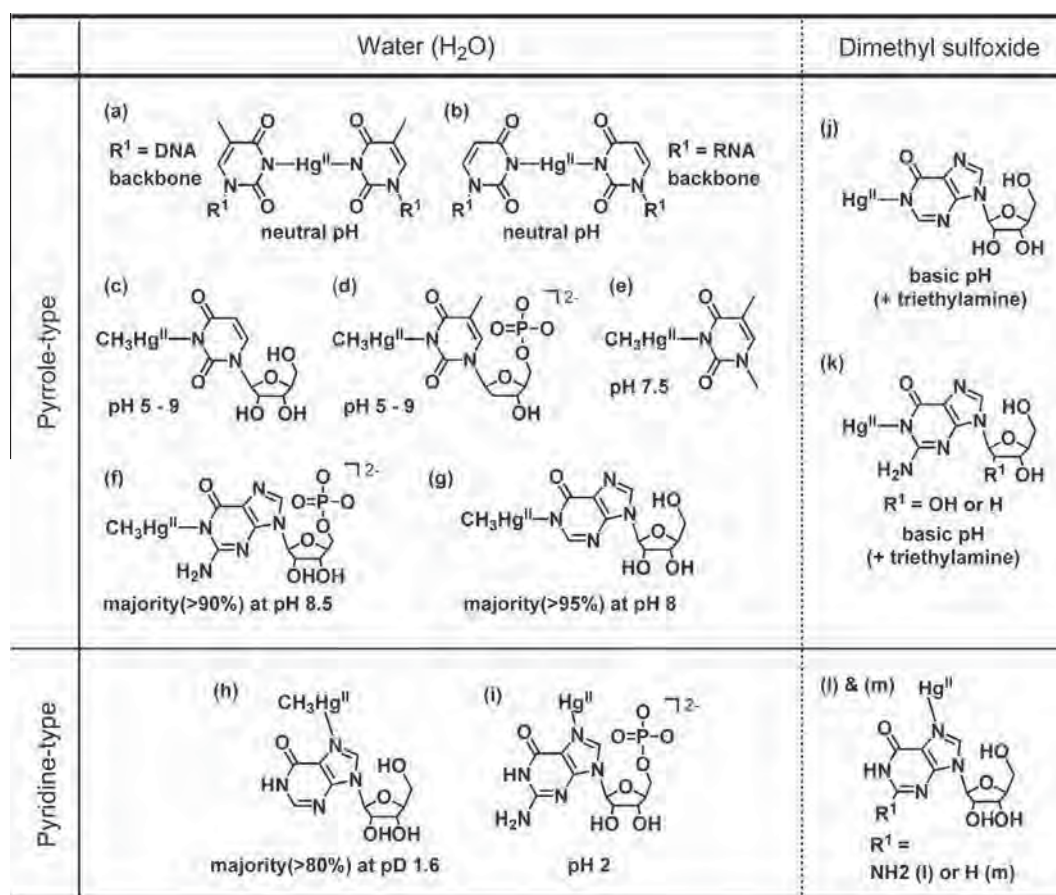


Fig. 3. Hg^{II}-complexes in solution classified in terms of ligand-types. References for the respective complexes are as follows. (a) [11,31], (b) [32], (c) [63], (d) [64], (e) [64], (f) [65], (g) [66], (h) [66], (i) [65], (j) [52], (k) [52], (l) [51], (m) [61].

Im–Ag^I–Im and T–Hg^{II}–T base pairs, metal cations were completely shielded from a bulk water solvent, and the “dehydration-entropy” hypothesis was demonstrated from their 3D structures [35,38].

In addition, the metal cations of Im–Ag^I–Im and T–Hg^{II}–T base pairs are located along the helical axes of the respective DNA duplexes [35,38]. As a result, the neighboring metal cations are located close to one another in spite of a possible repulsion due to their positive charge. However, their close contacts can be rationalized if argentophilic interaction/metallophilic attraction [46,47] between heavy elements is considered [35,37,38,48–50].

Thus, the 3D structures of DNA duplexes with metallo-base-pairs have provided data for fundamental chemistry, and they will be a chemical basis for creating novel applications of these metallo-base-pairs.

4. Selectivity of ligands for Hg²⁺/Ag⁺

There is an unanswered question as to why Hg²⁺ preferentially binds to thymine/uracil (Figs. 3a, b and 4a, b) and why Ag⁺ preferentially binds to cytosine and imidazole (Fig. 5a, b, and e).

question can be converted into why Hg²⁺ favors an anionic ligand (deprotonated pyrrole-type nitrogen) and why Ag⁺ favors a electrically neutral ligand (pyridine-type nitrogen). At the moment, there is no clear answer to this question, and there is only the experimentally observed trend (see also Figs. 3–5 for other examples of Hg²⁺/Ag⁺-nucleobase complexes).

In order to consider this question, we would like to focus on Hg²⁺ first. According to the “Hard and Soft Acids and Bases (HSAB) rule”, Hg²⁺ belongs to a canonical soft Lewis acid that tends to form a covalent bond. However, the bonds between Hg^{II} and N3 of thymine (N3(T)) in the T–Hg^{II}–T base pair were found to possess high ionicity and low covalency [33,34,41]. This experimental/theoretical insight slightly deviates from the prediction from the HSAB rule. However, this point itself might be a key-point to explain the ligand-selectivity of Hg²⁺. Although this idea is just tentative at the moment, it might be worthwhile to examine it to clarify this issue.

In relation to the unanswered question, it should be noted that in an organic solvent such as DMSO, Hg²⁺ binds to the pyridine-type N7 atom of guanosine (N7(G)) rather than the pyrrole-type

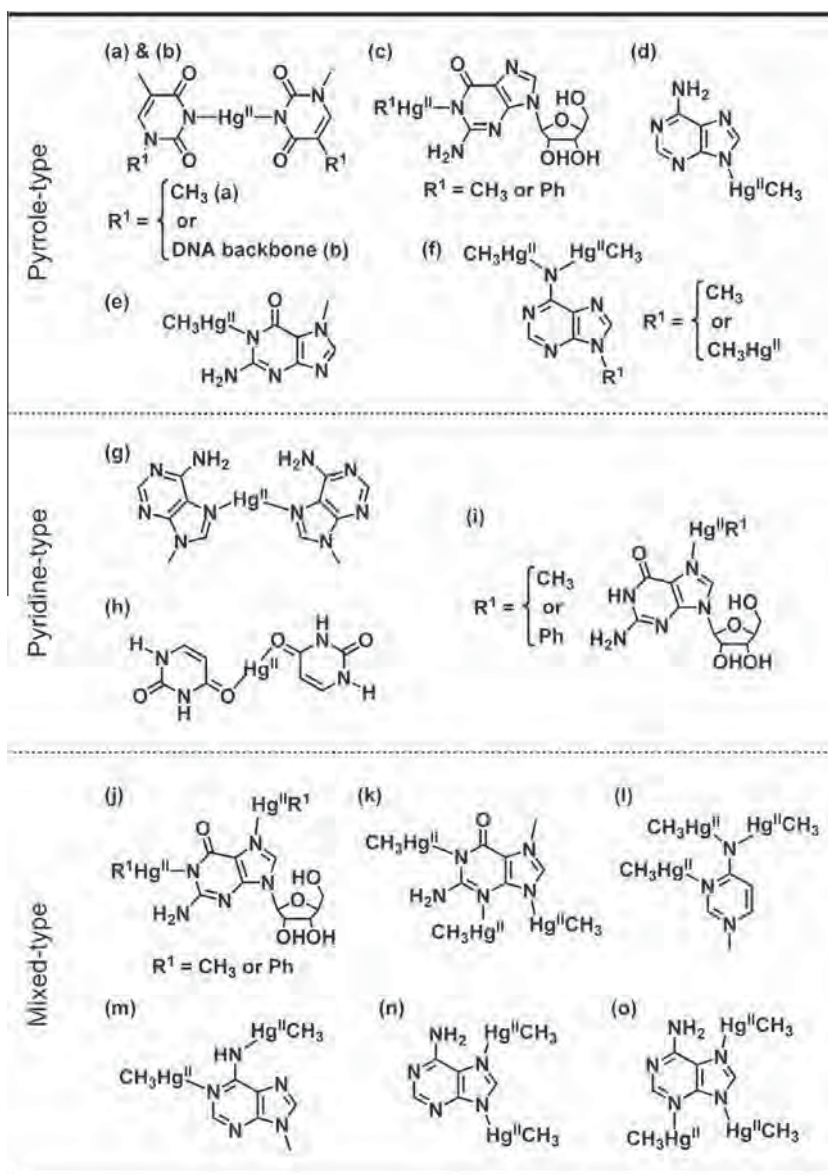


Fig. 4. Crystalline/solid Hg^{II}-complexes classified in terms of ligand-types. References for the respective complexes are as follows. (a) [64,21,67], (b) [22], (c) [68], (d) [69], (e) [70], (f) [71], (g) [72], (h) [73,74], (i) [68], (j) [68], (k) [70], (l) [71], (m) [75], (n) [69,75], (o) [69].

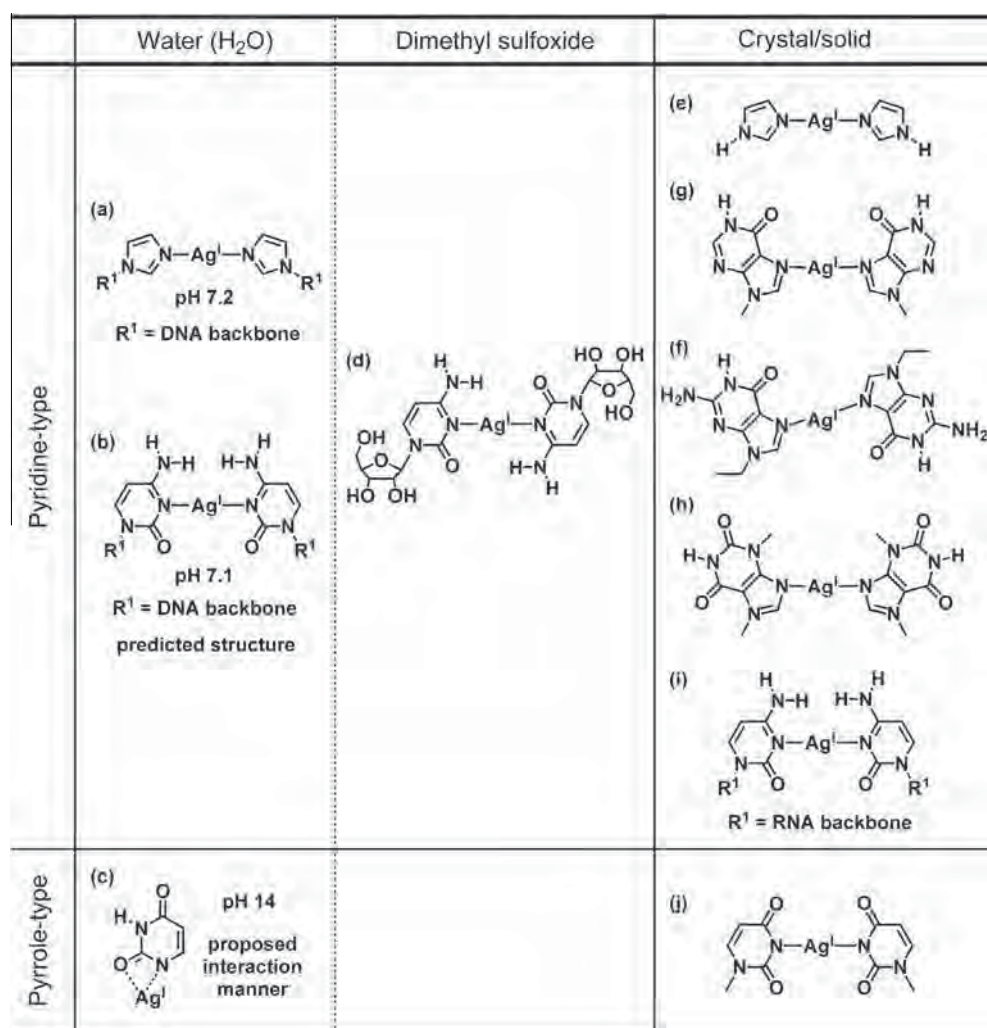


Fig. 5. Ag^I-mediated base pairs. References for the respective complexes are as follows. (a) [35,37], (b) [12], (c) [76], (d) [36], (e) [77,78], (f) [79,80], (g) [81], (h) [82], (i) [23], (j) [83]. For (c), the binding site is simply proposed one in the literature, and the Ag^I-binding manner might be different (i.e. N3).

N1 atom of guanosine (N1(G)) (Fig. 3l and m) [51]. Therefore, the preference for pyrrole-type nitrogen atoms by Hg²⁺ is a phenomenon specific for aqueous solutions. Interestingly, this preference by Hg²⁺ is reversed in the presence of a base (triethylamine) (Hg²⁺ again bound to N1(G) even in DMSO) (Fig. 3j and k) [52]. This indicates that a proton acceptor (base) is indispensable for Hg²⁺-binding to pyrrole-type nitrogen atoms like N1(G), and suggests that water and OH⁻ (a ligand of Hg²⁺ other than H₂O) would act as a proton acceptor (H⁺ + H₂O → H₃O⁺; H⁺ + HO⁻ → H₂O) in aqueous solutions [41,53]. On the other hand, even in water solution under low pH (pH < 2), the Hg^{II}-binding to N1(G) was inhibited owing to competitive binding of proton and Hg²⁺ (Fig. 3h and i). In addition, exceptional pyrrole–nitrogen-binding of Ag^I occurred only under extreme basic condition (pH 14) (Fig. 5c). Furthermore, for some complexes, one can find other metal binding modes, which deviated from the ligand-preferences of Hg^{II} and Ag^I discussed above, but they were observed only in crystals (Figs. 4 and 5j). Therefore, we should keep this fact in mind, and construct a unified interpretation for the selectivity of ligands by Hg²⁺/Ag⁺. In any case, such understanding of fundamental physicochemical properties of metallo-base-pairs may represent a general guideline for the creation of novel metallo-base-pairs.

5. Conclusion

Here, we reviewed NMR spectroscopic/structural data for Hg^{II}/Ag^I-mediated base pairs. Notably, all possible *J*-coupling and chemical shift values for the T–Hg^{II}–T base pair were obtained, owing to the determination of the $|J(^{15}\text{N}, ^{199}\text{Hg})|$ value which is a rarely observed parameter in general. Because 3D structures of the T–Hg^{II}–T-embedded DNA duplexes were also determined, the NMR spectroscopic parameters for the T–Hg^{II}–T base pair will serve as a standard reference for structural studies on other metallo-base-pairs. In addition, other pioneering works on Im–Ag^I–Im and the A–Hg^{II}–T base pairs also provide well-defined reference data of NMR parameters. Especially, the Im–Ag^I–Im base pair provides precise data for Ag^I. Here we note that another example of Ag^I-mediated base pairs, the C–Ag^I–C system, has also been studied NMR-spectroscopically, and its structure will be published elsewhere. Accumulated and growing spectroscopic data will be chemical basis for constructing molecular devices and novel applications.

Acknowledgements

This work was supported by Grants-in-aid for Scientific Research (A) (24245037 to A.O. and Y.T.), (B) (24310163 to Y.T.)

and Challenging Exploratory Research (15K13734 to Y.T.) from the Ministry of Education, Culture, Sports, Science, and Technology (MEXT), Japan; a Human Frontier Science Program (HFSP) Young Investigator Grant from HFSP, France (Y.T. and V.S.); and GACR (P205/10/0228 and 15-21387S to V.S.) from the Czech Republic. T.D. and K.F. are the recipients of a Research Fellowship for Young Scientists from the Japan Society for the Promotion of Science (JSPS). Y.T. and V.S. were further supported by an Invitation Fellowship for Research in Japan (Short-Term) from JSPS.

References

- [1] (a) S. Menzer, M. Sabat, B. Lipper, *J. Am. Chem. Soc.* 114 (1992) 4644; (b) O. Krizanovic, M. Sabat, *J. Am. Chem. Soc.* 115 (1993) 5538; (c) B. Lippert, *J. Chem. Soc., Dalton Trans.* (1997) 3971; (d) J. Müller, R.K.O. Sigel, B. Lippert, *J. Inorg. Biochem.* 79 (2000) 261; (e) K. Tanaka, M. Shionoya, *J. Org. Chem.* 64 (1999) 5002.
- [2] E. Meggers, P.L. Holland, W.B. Tolman, F.E. Romesberg, P.G. Schultz, *J. Am. Chem. Soc.* 122 (2000) 10714.
- [3] K. Tanaka, A. Tengeji, T. Kato, N. Toyama, M. Shiro, M. Shionoya, *J. Am. Chem. Soc.* 124 (2002) 12494.
- [4] K. Tanaka, A. Tengeji, T. Kato, N. Toyama, M. Shionoya, *Science* 299 (2003) 1212.
- [5] T. Carell, C. Behrens, J. Gierlich, *Org. Biomol. Chem.* 1 (2003) 2221. and reference cited therein.
- [6] H.-A. Wagenknecht, *Angew. Chem.* 115 (2003) 3322. *Angew. Chem., Int. Ed.* 2003, 42, 3204 and reference cited therein.
- [7] G.H. Clever, C. Kaul, T. Carell, *Angew. Chem.* 119 (2007) 6340. *Angew. Chem., Int. Ed.* 2007, 46, 6226 and reference cited therein.
- [8] Y. Takezawa, M. Shionoya, *Acc. Chem. Res.* 45 (2012) 2066. and reference cited therein.
- [9] P. Scharf, J. Müller, *ChemPlusChem* 78 (2013) 20. and reference cited therein.
- [10] A. Ono, H. Togashi, *Angew. Chem.* 116 (2004) 4400. *Angew. Chem., Int. Ed.* 2004, 43, 4300.
- [11] Y. Miyake, H. Togashi, M. Tashiro, H. Yamaguchi, S. Oda, M. Kudo, Y. Tanaka, Y. Kondo, R. Sawa, T. Fujimoto, T. Machinami, A. Ono, *J. Am. Chem. Soc.* 128 (2006) 2172.
- [12] A. Ono, S. Cao, H. Togashi, M. Tashiro, T. Fujimoto, T. Machinami, S. Oda, Y. Miyake, I. Okamoto, Y. Tanaka, *Chem. Commun.* (2008) 4825.
- [13] X. Liu, C.-H. Lu, I. Willner, *Acc. Chem. Res.* 47 (2014) 1673. and reference cited therein.
- [14] F. Wang, C.-H. Lu, I. Willner, *Chem. Rev.* 114 (2014) 2881. and reference cited therein.
- [15] A. Ono, H. Torigoe, Y. Tanaka, I. Okamoto, *Chem. Soc. Rev.* 40 (2011) 5855. and reference cited therein.
- [16] Y. Tanaka, J. Kondo, V. Sychrovský, J. Šebera, T. Dairaku, H. Saneyoshi, H. Urata, H. Torigoe, A. Ono, *Chem. Commun.* 51 (2015) 17343. and reference cited therein.
- [17] S. Atwell, E. Meggers, G. Spraggon, P.G. Schultz, *J. Am. Chem. Soc.* 123 (2001) 12364.
- [18] C. Kaul, M. Müller, M. Wagner, S. Schneider, T. Carell, *Nat. Chem.* 3 (2011) 79.
- [19] M.K. Schlegel, L.-O. Essen, E. Meggers, *J. Am. Chem. Soc.* 130 (2008) 8158.
- [20] E. Ennifar, P. Walter, P. Dumas, *Nucleic Acids Res.* 31 (2003) 2671.
- [21] L.D. Kosturko, C. Folzer, R.F. Stewart, *Biochemistry* 13 (1974) 3949.
- [22] J. Kondo, T. Yamada, C. Hirose, I. Okamoto, Y. Tanaka, A. Ono, *Angew. Chem.* 126 (2014) 2417. *Angew. Chem., Int. Ed.* 2014 53, 2385.
- [23] J. Kondo, Y. Tada, T. Dairaku, H. Saneyoshi, I. Okamoto, Y. Tanaka, A. Ono, *Angew. Chem., Int. Ed.* 54 (2015) 13323.
- [24] P.R. Young, U.S. Nandi, N.R. Kallenbach, *Biochemistry* 21 (1982) 62.
- [25] N.A. Frøystein, E. Sletten, *J. Am. Chem. Soc.* 116 (1994) 3240.
- [26] S. Steinkopf, W. Nerdal, A. Kolstad, E. Sletten, *Acta Chem. Scand.* 50 (1996) 775.
- [27] E. Sletten, N.A. Frøystein, in: A. Sigel, H. Sigel (Eds.), *Metal Ions in Biological Systems*, vol. 32, Marcel Dekker, 1996, pp. 397–418.
- [28] Z. Kuklennyik, L.G. Marzilli, *Inorg. Chem.* 35 (1996) 5654.
- [29] E. Sletten, W. Nerdal, in: A. Sigel, H. Sigel (Eds.), *Metal Ions in Biological Systems*, vol. 34, Marcel Dekker, 1997, pp. 479–500.
- [30] Y. Tanaka, H. Yamaguchi, S. Oda, M. Nomura, C. Kojima, Y. Kondo, A. Ono, *Nucleosides Nucleotides Nucleic Acids* 25 (2006) 613.
- [31] Y. Tanaka, S. Oda, H. Yamaguchi, Y. Kondo, C. Kojima, A. Ono, *J. Am. Chem. Soc.* 129 (2007) 244.
- [32] S. Johannsen, S. Paulus, N. Düpre, J. Müller, R.K.O. Sigel, *J. Inorg. Biochem.* 102 (2008) 1141.
- [33] Y. Tanaka, A. Ono, *Dalton Trans.* (2008) 4965.
- [34] Y. Tanaka, A. Ono, in: N. Hadjilidiadis, E. Sletten (Eds.), *Metal Complexes – DNA Interactions*, Wiley & Sons, John, 2009, pp. 439–462.
- [35] S. Johannsen, N. Megger, D. Böhme, R.K.O. Sigel, J. Müller, *Nat. Chem.* 2 (2010) 229.
- [36] H. Torigoe, I. Okamoto, T. Dairaku, Y. Tanaka, A. Ono, T. Kozasa, *Biochimie* 94 (2012) 2431.
- [37] S. Kumbhar, S. Johannsen, R.K.O. Sigel, M.P. Waller, J. Müller, *J. Inorg. Biochem.* 127 (2013) 203.
- [38] H. Yamaguchi, J. Šebera, J. Kondo, S. Oda, T. Komuro, T. Kawamura, T. Daraku, Y. Kondo, I. Okamoto, A. Ono, J.V. Burda, C. Kojima, V. Sychrovský, Y. Tanaka, *Nucleic Acids Res.* 42 (2014) 4094.
- [39] T. Dairaku, K. Furuita, H. Sato, J. Šebera, D. Yamanaka, H. Otaki, S. Kikkawa, Y. Kondo, R. Katahira, F.M. Bickelhaupt, C.F. Guerra, A. Ono, V. Sychrovský, C. Kojima, Y. Tanaka, *Chem. Commun.* 51 (2015) 8488.
- [40] T. Dairaku, K. Furuita, H. Sato, Y. Kondo, C. Kojima, A. Ono, Y. Tanaka, *Nucleosides Nucleotides Nucleic Acids* 34 (2015) 877.
- [41] T. Uchiyama, T. Miura, H. Takeuchi, T. Dairaku, T. Komuro, T. Kawamura, Y. Kondo, L. Benda, V. Sychrovský, P. Bouř, I. Okamoto, A. Ono, Y. Tanaka, *Nucleic Acids Res.* 40 (2012) 5766.
- [42] E. Buncel, C. Boone, H. Joly, R. Kumar, A.R. Norris, *J. Inorg. Biochem.* 25 (1985) 61.
- [43] A.R. Norris, R. Kumar, *Inorg. Chim. Acta* 93 (1984) 33.
- [44] (a) H. Torigoe, A. Ono, T. Kozasa, *Chem. Eur. J.* 16 (2010) 13218; (b) K. Petrovec, B.J. Ravoo, J. Müller, *Chem. Commun.* 48 (2012) 11844.
- [45] (a) H. Lönnberg, J. Arpalahiti, *Inorg. Chim. Acta* 55 (1980) 39; (b) B. Knobloch, W. Linert, H. Sigel, *Proc. Natl. Acad. Sci. USA* 102 (2005) 7459.
- [46] P. Pyykkö, *Chem. Rev.* 97 (1997) 597.
- [47] P. Pyykkö, M. Straka, *Phys. Chem. Chem. Phys.* 2 (2000) 2489.
- [48] D.A. Megger, C. Fonseca Guerra, J. Hoffmann, B. Brutschy, F.M. Bickelhaupt, J. Müller, *Chem. Eur. J.* 17 (2011) 6533.
- [49] L. Benda, M. Straka, Y. Tanaka, V. Sychrovský, *Phys. Chem. Chem. Phys.* 13 (2011) 100.
- [50] L. Benda, M. Straka, V. Sychrovský, P. Bouř, Y. Tanaka, *J. Phys. Chem. A* 116 (2012) 8313.
- [51] G.W. Buchanan, J.B. Stothers, *Can. J. Chem.* 60 (1982) 787.
- [52] L.G. Marzilli, B. de Castro, C. Solorzano, *J. Am. Chem. Soc.* 104 (1982) 461.
- [53] J. Šebera, J. Burda, M. Straka, A. Ono, C. Kojima, Y. Tanaka, V. Sychrovský, *Chem. Eur. J.* 19 (2013) 9884.
- [54] X. Gao, R.A. Jones, *J. Am. Chem. Soc.* 109 (1987) 3169.
- [55] B.L. Gaffney, P.-P. Kung, C. Wang, R.A. Jones, *J. Am. Chem. Soc.* 117 (1995) 12281.
- [56] X. Zhang, B.L. Gaffney, R.A. Jones, *J. Am. Chem. Soc.* 120 (1998) 6625.
- [57] Y. Kyogoku, *Appl. Spectrosc. Rev.* 17 (1981) 279.
- [58] Y. Tanaka, C. Kojima, E.H. Morita, Y. Kasai, K. Yamasaki, A. Ono, M. Kainosho, K. Taira, *J. Am. Chem. Soc.* 124 (2002) 4595.
- [59] (a) Y. Tanaka, Y. Kasai, S. Mochizuki, A. Wakisaka, E.H. Morita, C. Kojima, A. Toyozawa, Y. Kondo, M. Taki, Y. Takagi, A. Inoue, K. Yamasaki, K. Taira, *J. Am. Chem. Soc.* 126 (2004) 744; (b) Y. Tanaka, K. Taira, *Chem. Commun.* (2005) 2069.
- [60] G. Wang, B.L. Gaffney, R.A. Jones, *J. Am. Chem. Soc.* 126 (2004) 8908.
- [61] G.W. Buchanan, M. Bell, *Can. J. Chem.* 61 (1983) 2445.
- [62] S.S. Lemos, D.U. Martins, V.M. Deflon, J. Elena, *J. Organomet. Chem.* 694 (2009) 253.
- [63] S. Mansy, T.E. Wood, J.C. Sprowles, R.S. Tobias, *J. Am. Chem. Soc.* 96 (1974) 1762.
- [64] R.W. Chrisman, S. Mansy, H.J. Peresie, A. Ranade, T.A. Berg, R.S. Tobias, *Bioinorg. Chem.* 7 (1977) 245.
- [65] S. Mansy, R.S. Tobias, *J. Am. Chem. Soc.* 96 (1974) 6874.
- [66] S. Mansy, R.S. Tobias, *Biochemistry* 14 (1975) 2952.
- [67] B. Morzyk-Ociepa, D. Michalska, *J. Mol. Struct.* 598 (2001) 133.
- [68] A.J. Canty, R.S. Tobias, *Inorg. Chem.* 18 (1979) 413.
- [69] R. Savoie, J.-J. Jutier, L. Prizant, A.L. Beauchamp, *Spectrochim. Acta, Part A* 38 (1982) 561.
- [70] W.S. Sheldrick, P. Gross, *Inorg. Chim. Acta* 153 (1988) 247.
- [71] J.-P. Charland, M. Simard, A.L. Beauchamp, *Inorg. Chim. Acta* 80 (1983) L57.
- [72] F. Zamora, M. Sabat, B. Lippert, *Inorg. Chim. Acta* 267 (1998) 87.
- [73] J.A. Carrabine, M. Sundaralingam, *Biochemistry* 10 (1971) 292.
- [74] S. Mansy, R.S. Tobias, *Inorg. Chem.* 14 (1975) 287.
- [75] L. Prizant, M.J. Olivier, R. Rivest, A.L. Beauchamp, *J. Am. Chem. Soc.* 101 (1979) 2765.
- [76] J.R. DeMember, Fr.A. Wallace, *J. Am. Chem. Soc.* 97 (1975) 6240.
- [77] C.-A. Antti, B.N.K. Lundberg, *Acta Chim. Scand.* 25 (1971) 1758.
- [78] F. Effendy, C. Marchetti, R. Pettinari, A. Pettinari, B.W. Pizzabocca, A.H. Skelton, *Inorg. Chim. Acta* 359 (2006) 1504.
- [79] F. Belanger-Gariepy, A.L. Beauchamp, *J. Am. Chem. Soc.* 102 (1980) 3461.
- [80] K. Aoki, W. Saenger, *Acta Crystallogr., Sect. C* 40 (1984) 772.
- [81] S. Menzer, E.C. Hillgeris, B. Lippert, *Inorg. Chim. Acta* 211 (1993) 221.
- [82] V. Kulikov, G. Meyer, *Cryst. Growth Des.* 13 (2013) 2916.
- [83] M. Barceló-Oliver, B.A. Baquero, A. Bauzá, Á. García-Raso, R. Vich, I. Mata, E. Molins, À. Terróna, A. Frontera, *Dalton Trans.* 42 (2013) 7631.



Short communication

Synthesis and characterizations of a paddlewheel-type dirhodium-based photoactive porous metal-organic framework



Yusuke Kataoka^{a,*}, Konomi S. Kataoka^b, Hidenobu Murata^c, Makoto Handa^a,
Wasuke Mori^b, Tatsuya Kawamoto^{b,*}

^a Department of Chemistry, Interdisciplinary Graduate School of Science and Engineering, Shimane University, 1060 Nishikawatsu, Matsue, Shimane 690-8504, Japan

^b Department of Chemistry, Faculty of Science, Kanagawa University, 2946 Tsuchiya, Hiratsuka, Kanagawa 259-1293, Japan

^c Department of Materials System Science, Yokohama City University, 22-2 Seto, Kanazawa-ku, Yokohama 236-0027, Japan

ARTICLE INFO

Article history:

Received 27 February 2016

Received in revised form 10 April 2016

Accepted 13 April 2016

Available online 22 April 2016

Keywords:

Coordination polymer

Rhodium complex

Paddlewheel-type complex

ABSTRACT

A paddlewheel-type dirhodium-based, photoactive, porous metal-organic framework, $[\text{Rh}_2(\text{ZnTCPP})(\text{H}_2\text{O})_{7.5}]$ (**1**; ZnTCPP = zinc tetra(4-carboxyphenyl)porphyrin), was prepared and characterized via synchrotron X-ray analyses (X-ray powder diffraction, extended X-ray absorption fine structure, and X-ray absorption near-edge structure), elemental analysis, infrared spectroscopy, and N_2 gas adsorption isotherm analysis. Spectroscopic study revealed a drastic decrease in the emission intensity of **1** compared with [ZnTCPP], although features present in the absorption spectra of the two complexes were almost the same. This indicated that **1** underwent the photo-induced intramolecular charge transfer and/or energy transfer from the ZnTCPP moiety to dirhodium moiety.

© 2016 Elsevier B.V. All rights reserved.

1. Introduction

Paddlewheel-type dirhodium tetracarboxylates, $[\text{Rh}_2(\text{O}_2\text{CR})_4(\text{L})_2]$ (R = aromatic ring or alkyl chain, L = axially coordinated ligand) [1–2], and their related analogous complexes [3–5] have attracted much attention because of their interesting structures and potential functional properties such as catalytic [6–7], molecular sensing [8], and antitumor activities [9–11]. These functional properties are performed in the solvated or dispersed conditions in the solvent media. Recently, these types of complexes have been utilized as robust building blocks for porous metal-organic frameworks (MOFs) [12–14], extended coordination polymers (CPs) [15–19], and supramolecular complexes [20–21]. The merits of a paddlewheel-type dirhodium unit as an MOF building block are (1) the unit's axial site availability, i.e., the open metal site, as a potential site for functional solid-state activities, and (2) the structural robustness compared with other paddlewheel-type dimetal units (such as Cu_2 and Zn_2) because of the existence of the Rh–Rh single bond. However, previously reported examples of dirhodium-based MOFs with open metal sites are quite limited because of their low level of crystallinity (making them unsuitable for X-ray powder diffraction (XRD)) [22] and difficulties observed in both their synthesis and structural characterization. In fact, most dirhodium-based MOFs have not been satisfactorily characterized. To enable the further development of dirhodium-based MOFs, characterization

methods that are typically used for X-ray amorphous samples, such as X-ray absorption fine structure (XAFS) are indispensable.

As rare examples of dirhodium-based MOFs, Mori's group reported dirhodium-based MOFs connected by dicarboxylate or tetracarboxylate bridging units, which have open-porous structures and open metal sites. These MOFs were reported to exhibit highly efficient catalytic performance for both H–D exchange reactions [12] and olefin hydrogenation [13] even at a low-temperature (e.g., 200 K); moreover, they were reported to be useful as catalysts for photochemical H_2 evolution in the presence of a photosensitizer and an electron relay [14]. Interestingly, the catalytic performances of these MOFs were remarkably superior compared with related discrete dirhodium complexes such as $[\text{Rh}_2(\text{O}_2\text{CCH}_3)_4(\text{H}_2\text{O})_2]$, indicating that the immobilization of a dirhodium unit as a building block of a porous MOF is advantageous for the development of effective catalysts and functional materials.

As mentioned above, although dirhodium-based MOFs with open metal sites are promising catalysts, there is no example of dirhodium-based “photoactive” MOFs, which have some potential as photocatalysts. In this study, a dirhodium-based, photoactive, porous MOF, $[\text{Rh}_2(\text{ZnTCPP})(\text{H}_2\text{O})_{7.5}]$ (Fig. 1; ZnTCPP = zinc tetra(4-carboxyphenyl)porphyrin), which utilizes a ZnTCPP photosensitizer as a building unit, was synthesized and fully characterized via synchrotron X-ray analyses (XRD and XAFS).

2. Results and discussion

A solvothermal reaction of $[\text{Rh}_2(\text{O}_2\text{CCH}_3)_4(\text{H}_2\text{O})_2]$ (0.20 mmol) with ZnTCPP (0.20 mmol) in degassed EtOH under N_2 atmosphere gave

* Corresponding authors.

E-mail addresses: kataoka@riko.shimane-u.ac.jp (Y. Kataoka), karaoka@riko.shimane-u.ac.jp (T. Kawamoto).

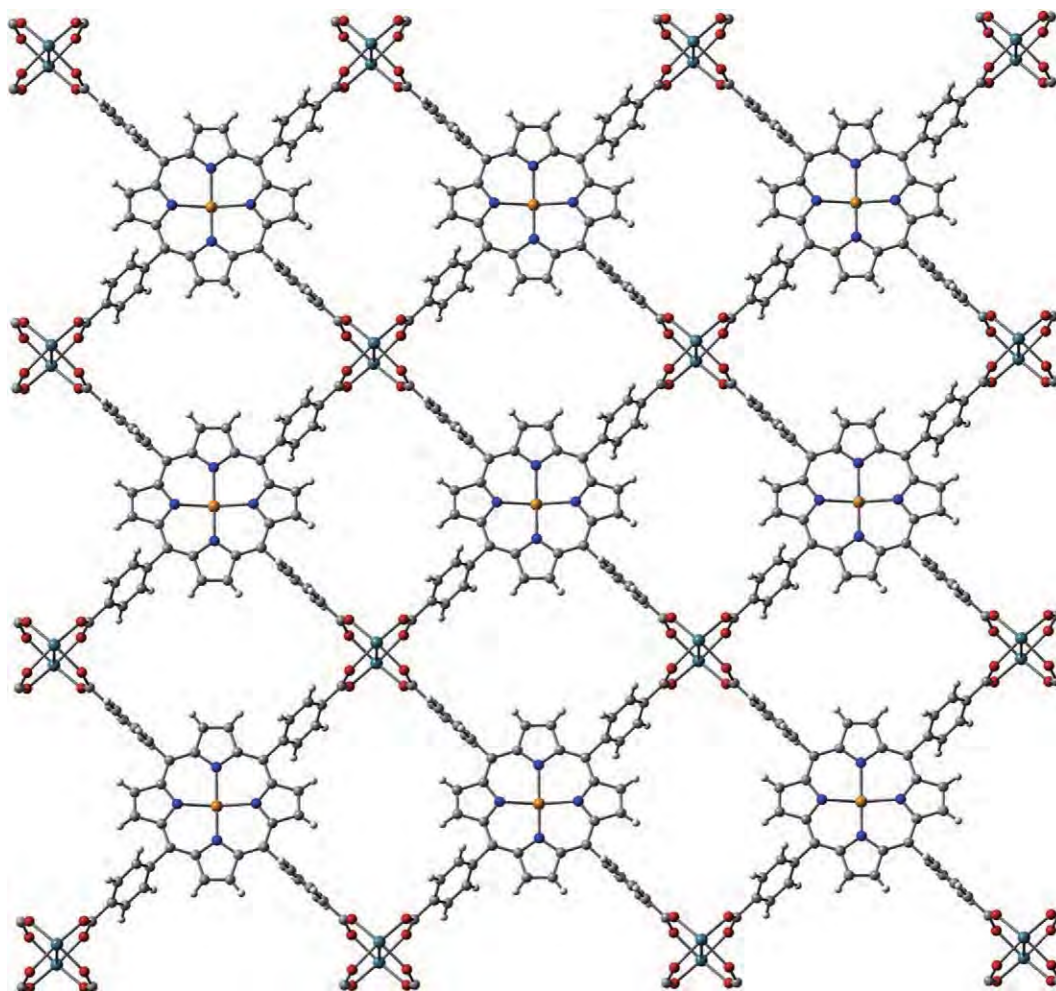


Fig. 1. Deduced two-dimensional structure of [1]. (Rh: green, Zn: orange, O: red, N: blue, C: Gray, H: white.)

$[\text{Rh}_2(\text{ZnTCPP})(\text{H}_2\text{O})_{7.5}]$ (**[1]**) as a low-crystalline, dark-purple, hygroscopic powder (80.4% yield). Scanning electron microscope images revealed that **[1]** particles were polyhedral in shape with sizes of 0.5–1.3 μm (Fig. S1 in the Electronic supporting information (ESI)). Thus, **[1]** is a submicron-scale MOF, such a compound has recently received attention as an efficient heterogeneous catalyst [23–24]. Similar solvothermal reactions for the preparation of **[1]** using (i) degassed *N,N*-dimethylformamide instead of degassed EtOH or (ii) RhCl_3 instead of $[\text{Rh}_2(\text{O}_2\text{CCH}_3)_4(\text{H}_2\text{O})_2]$ were attempted; both reaction methods gave only amorphous black powders of a non-porous structure mixed with colloidal Rh particles [25]. As is often reported in a paddlewheel-type dirhodium complex synthesis, the amount of colloidal rhodium particles as a side product in **[1]** increased when the reaction time was greater than 6 h in the purification of **[1]**.

The preparatory XRD analysis of **[1]** was performed with generally used laboratory-based XRD equipment, and no significant peak corresponding to **[1]** was observed, i.e., only two broad diffraction curves were observed. As in previously reported cases, this result does not provide any meaningful information concerning the structure of dirhodium-based MOFs [22]. To obtain useful information regarding the structure of **[1]**, synchrotron XRD measurements were performed at the Spring-8 BL19B2 beamline ($\lambda = 1.00 \text{ \AA}$). As shown in Fig. 2, the diffraction pattern of **[1]** displayed several distinctive intense peaks whose positions approximately agreed with the superposition of the peak positions of the simulated XRD pattern of $[\text{Zn}_2(\text{ZnTCPP})]$ [26], which was determined using a single-crystal X-ray structure. Therefore,

it is obvious that the overall framework and packing structures of **[1]** were similar to that of $[\text{Zn}_2(\text{ZnTCPP})]$.

If rhodium ions in **[1]** are in the typical paddlewheel-type motif, the two-dimensional structure of **[1]** may be isostructural with that of $[\text{Zn}_2(\text{ZnTCPP})]$, which has a porous, two-dimensional grid sheet

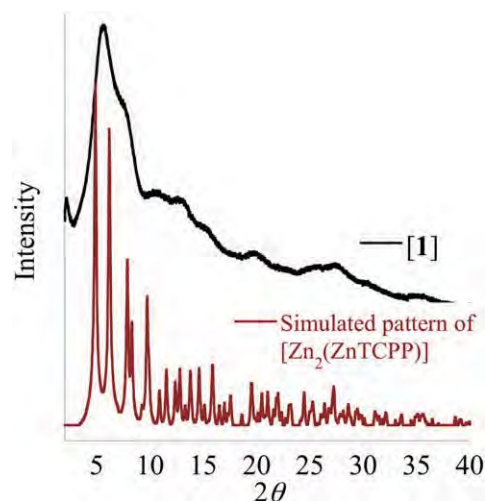


Fig. 2. Synchrotron XRD pattern of **[1]** and simulated pattern of $[\text{Zn}_2(\text{ZnTCPP})]$.

structure. Thus, to completely understand the coordination environment of rhodium ions in **[1]**, it is very important to clarify the molecular structure of **[1]**. To facilitate this, synchrotron extended X-ray absorption fine structure (EXAFS) analysis was performed at the SAGA Light Source (SAGA LS) BL07 beamline. Fig. 3(a) shows the Rh K-edge spectra of both **[1]** and $[\text{Rh}_2(\text{O}_2\text{CCH}_3)_4(\text{H}_2\text{O})_2]$. The obtained EXAFS spectra are of good resolution and can be used to assign specific chemical bonds. In addition, radial distribution functions are clearly resolved up to approximately 4.0 Å. Notably, up to 3.0 Å, the spectral features of **[1]** agree well with those of $[\text{Rh}_2(\text{O}_2\text{CCH}_3)_4(\text{H}_2\text{O})_2]$. From these results, the radial peaks at approximately 1.10–1.22 (shoulder) and 1.50 Å are assigned as sum of Rh–O (coordinated oxygen in water and carboxylate) and Rh–Rh bonds and sum of Rh...C (detached carbonyl carbon in carboxylate) and Rh...O (detached oxygen in water and carboxylate) distances, respectively. Thus, the coordination environment around rhodium ions in **[1]** is almost the same as that in $[\text{Rh}_2(\text{O}_2\text{CCH}_3)_4(\text{H}_2\text{O})_2]$ not only in the first coordination sphere but also in the second and third coordination spheres. These results clearly demonstrate that rhodium ions in **[1]** form a paddlewheel-type dimetallic core.

To investigate the oxidation state and electronic environment of a dirhodium unit in **[1]**, a high-resolution X-ray absorption near-edge structure (XANES) spectrum of **[1]** was also obtained at the SAGA LS BL07 beamline and compared with the spectra of $[\text{Rh}_2(\text{O}_2\text{CCH}_3)_4(\text{H}_2\text{O})_2]$ and Rh_2O_3 . As shown in Fig. 3(c), the Rh K-edge XANES spectrum of **[1]** is in good agreement with that of $[\text{Rh}_2(\text{O}_2\text{CCH}_3)_4(\text{H}_2\text{O})_2]$; moreover it does not agree with that of Rh_2O_3 . This indicates that (i) the electronic environment of **[1]** is similar to that of $[\text{Rh}_2(\text{O}_2\text{CCH}_3)_4(\text{H}_2\text{O})_2]$ and (ii) Rh ions in **[1]** are divalent.

The oxidation number assigned to Rh ions in **[1]** is also supported by the infrared spectrum. The symmetric $[\nu_{\text{sym}}(\text{CO}_2^-)]$ and asymmetric $[\nu_{\text{asym}}(\text{CO}_2^-)]$ stretching modes of **[1]** are clearly observed in the typical region (1400 – 1650 cm^{-1}). For **[1]**, the values of $\nu_{\text{sym}}(\text{CO}_2^-)$, $\nu_{\text{asym}}(\text{CO}_2^-)$, and their separation [i.e., $\Delta\nu(\text{CO}_2^-) = \nu_{\text{asym}}(\text{CO}_2^-) - \nu_{\text{sym}}(\text{CO}_2^-)$] are 1394, 1554, and 160 cm^{-1} , respectively. The value of $\Delta\nu(\text{CO}_2^-)$ observed for **[1]** is similar to those of typical dirhodium(II, II) complexes (160–190 cm^{-1}) [15].

To investigate the permanent porosity of **[1]**, N_2 gas adsorption measurements were performed at 77 K. Fig. 4 shows the N_2 gas adsorption isotherm for **[1]**. The measurements show (i) a significant amount of N_2 adsorption at a low-pressure and (ii) gently sloping N_2 adsorption

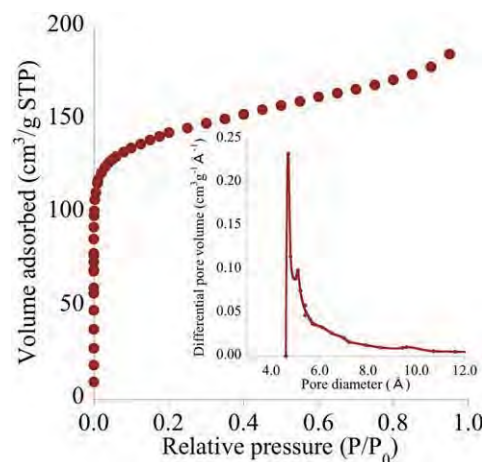


Fig. 4. N_2 adsorption isotherm of **[1]** at 77 K. Insert graph is distribution of pore diameter of **[1]** estimated using the Horvath-Kawazoe method. Here, STP is standard temperature and pressure.

in the region from 20 to 740 Torr. From these results, we concluded that the recorded isotherm can be classified as showing IUPAC-I behavior, which corresponds to a single-layer physical adsorption of the N_2 gas onto the surface of **[1]**. Specific Langmuir surface area and pore volume calculated from the N_2 adsorption isotherm of activated **[1]** were 689.8 m^2/g and 0.22 cm^3/g , respectively. The distribution of pore diameter, estimated using the Horvath-Kawazoe (HK) method, suggested that **[1]** has pores of approximately 4.7 Å in size similar to $[\text{Zn}_2(\text{ZnTCPP})]$ (ca. 4.4 Å) of which value was estimated from the single crystal X-ray structures [26–27]. These results clearly indicated that **[1]** has a porous framework structure and sufficient micropores to permit N_2 gas adsorption.

To investigate the photophysical properties of **[1]**, diffuse reflectance (DR) UV–visible and emission spectra of both **[1]** and $[\text{ZnTCPP}]$ in the solid state were recorded. As shown in Fig. 5(a), the UV–visible spectral features of **[1]** were almost identical to that of $[\text{ZnTCPP}]$, indicating that the ground (S_0) state electronic interaction between dirhodium and ZnTCPP moieties was negligibly small and that direct photoinduced intramolecular excitations between these moieties were not generated.

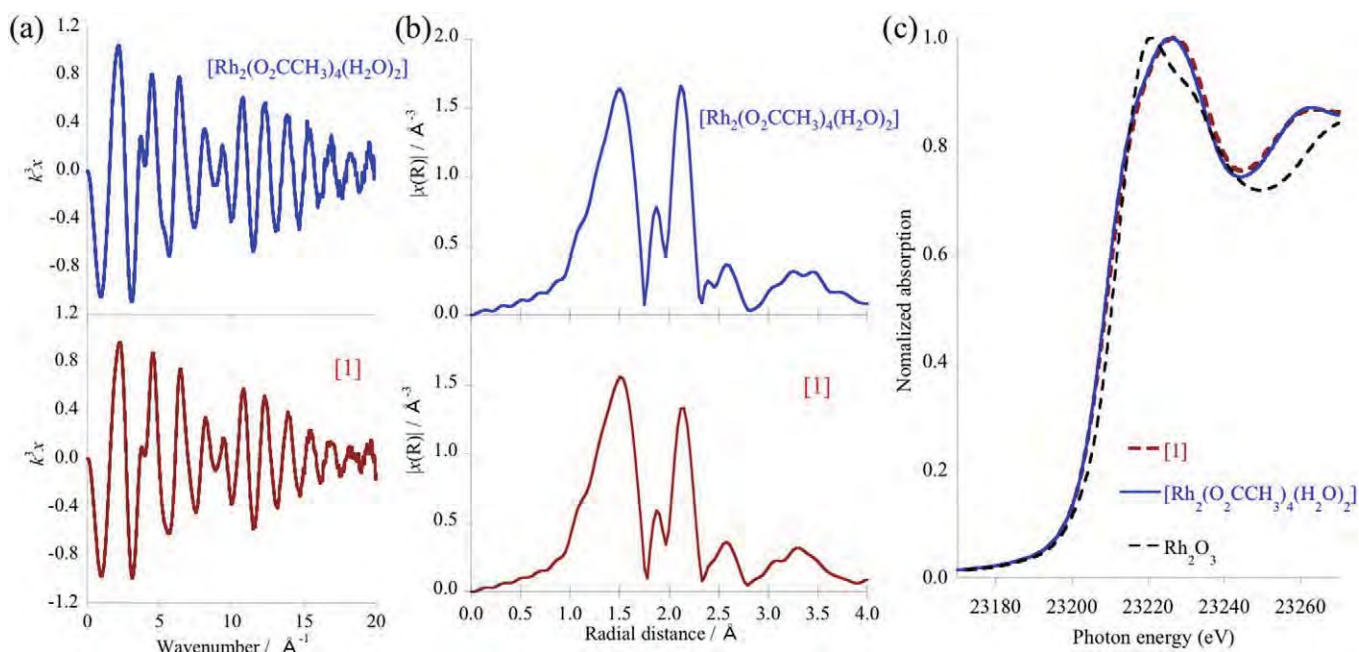


Fig. 3. Rh K-edge XAFS spectra of **[1]** and $[\text{Rh}_2(\text{O}_2\text{CCH}_3)_4(\text{H}_2\text{O})_2]$. (a) EXAFS spectra, (b) Fourier-transform EXAFS spectra, and (c) XANES spectra.

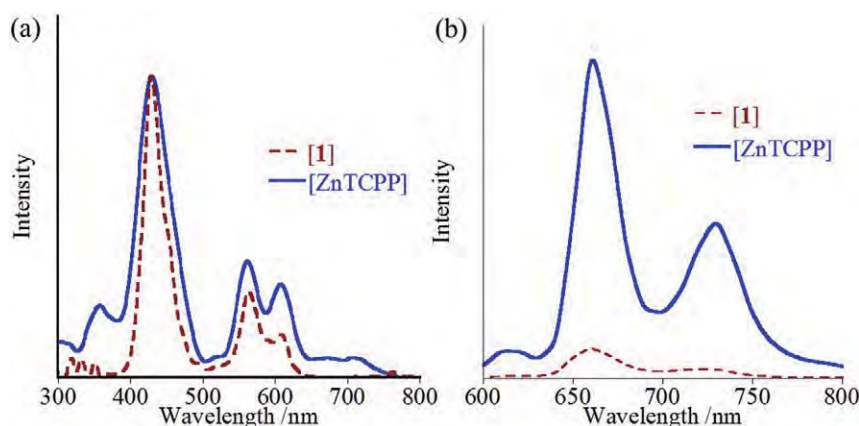


Fig. 5. (a) Absorption and (b) emission spectra of [1] and [ZnTCPP].

The weak d-d transition bands of a dirhodium moiety ($d\pi Rh_2 \rightarrow d\sigma Rh_2$) were obscured by the intense zinc porphyrin Q (612 and 563 nm) and Soret (430 nm) bands. The most intense emission bands in the spectra were observed at 660 nm for both [1] and [ZnTCPP], and while the emission energies of [1] and [ZnTCPP] were almost identical, band intensities of the observed bands for [1] were much weaker than those of [ZnTCPP] (Fig. 5(b)). These results indicated that an efficient photoinduced intramolecular charge transfer (CT) and/or energy transfer (ET) from an excited ZnTCPP moiety to dirhodium moiety occurred in [1].

3. Conclusion

In summary, the photoactive dirhodium-based porous MOF, $[Rh_2(ZnTCPP)(H_2O)_n]$, was synthesized and carefully characterized. The XAFS (EXAFS and XANES) spectra clearly indicated that the building block of [1] is a paddlewheel-type dirhodium(II,II)-unit. The amount of N_2 adsorption, estimated surface area, and pore diameters of [1] were compatible with the proposed molecular structure, which is roughly isostructural with $[Zn_2(ZnTCPP)]$. From the results of the DR UV–visible and emission spectra, it is cleared that [1] exhibits potential absorption property arising from the presence of ZnTCPP units, which cause a photoinduced CT and/or ET from the ZnTCPP moiety to dirhodium moiety. Thus, it is anticipated that [1] may be applied as a photocatalyst. Further study is now in progress in our laboratories.

4. Experimental

4.1. Materials

$[Rh_2(O_2CCH_3)_4(H_2O)_2]$ and [ZnTCPP] were prepared according to the reported methods with slight modifications. All of the other reagents (reagent grade quality) were purchased from the commercial source and were used without further purification.

4.2. Synthesis of [1]

A mixture of $[Rh_2(O_2CCH_3)_4(H_2O)_2]$ (95.6 mg, 0.20 mmol), ZnTCPP (174.4 mg, 0.20 mmol), and degassed EtOH (15 mL) was sealed in a Teflon-lined autoclave under N_2 atmosphere and heated at 423 K for 3 h. After cooling to room temperature, purple powders were collected on membrane filter and were washed with EtOH and THF and were dried under vacuum at room temperature for 1 day to obtain the porous MOF [1]. Yield: 191.5 mg (80.4%).

EA: calcd. For $C_{48}H_{24}N_4O_8Rh_2Zn \cdot (H_2O)_{7.5}$: C 48.40, H 3.30, N 4.70%. Found: C 48.58, H 2.98, N 4.22%.

4.3. General procedures

A synchrotron XRD measurement was carried out by use of a large Debye-Scherrer camera with an imaging plate (IP) as detectors at BL19B2 beamline in Spring-8. The wavelength of incident X-ray beam was set to 1.00 Å. Synchrotron extended X-ray absorption fine structure (EXAFS) measurements were performed at BL07 beamline of the SAGA Light Source. Infrared spectrum was recorded on a JASCO 4100 spectrometer on a KBr disk at room temperature. The diffuse reflectance spectra were measured using a JASCO V-560 spectrophotometer equipped with a 60 mm integrating sphere. N_2 adsorption isotherm at 77 K was carried out using an ASAP2010 volumetric adsorption analyzer (Shimadzu Co.). A sample was dried at 300 K for overnight and 393 K for 3 h to remove the solvated water. Ultra-high-purity grades (99.9999%) of N_2 (for gas analysis) and He (for gas analysis in free space) were used in this adsorption study. Powders of [1] were observed using Scanning Electron Microscope (SEM; FE-SEM S-4000, Hitachi Co.).

Supplementary data to this article can be found online at <http://dx.doi.org/10.1016/j.inoche.2016.04.009>.

Acknowledgements

This work has been supported by Grant-in-Aid for Scientific Research (Nos. 15K17897, 15H00877, 25620145) and the Strategic Research Base Development Program for Private University of the Ministry of Education, Culture, Sports and Technology (MEXT), Japan. Y.K. acknowledges the JAPAN PRIZE Foundation, and the Electronic Technology Research Foundation of Chugoku. The synchrotron radiation experiments were performed at the BL19B2 beamline of Spring-8 with the approval of the Japan Synchrotron Radiation Research Institute (JASRI) (Proposal No. 2012B1828). The XAFS experiments were performed at the BL07 beamline with the proposal No. 1405035PT.

References

- [1] F.A. Cotton, B.G. Deboer, M.D. LaPrade, J.R. Pipal, D.A. Ucko, *Acta Crystallogr., Sect. B* 27 (1971) 1664–1671.
- [2] H.T. Chifotides, K.R. Dunber, Rhodium compounds, in: F.A. Cotton, C.A. Murillo, R.A. Walton (Eds.), *Multiple Bonds between Metal Atoms*, third ed. Springer Science and Business Media, New York 2005, pp. 465–589.
- [3] Y. Kataoka, N. Yano, T. Kawamoto, M. Handa, *Eur. J. Inorg. Chem.* 34 (2015) 5650–5655.
- [4] G. Pimblett, C.D. Garner, W. Clegg, *Dalton Trans.* 6 (1986) 1257–1263.
- [5] C.A. Crawford, J.H. Matonic, J.H. Huffman, K. Folting, K.R. Dunber, G. Christou, *Inorg. Chem.* 36 (1997) 2361–2371.
- [6] J. Hansen, H.M.L. Davies, *Coord. Chem. Rev.* 252 (2008) 545–555.
- [7] P.M. Gois, A.F. Trindade, L.F. Veiros, V. Andre, M.T. Duarte, C.A.M. Afonso, S. Caddick, F.G.N. Cloke, *Angew. Chem. Int. Ed.* 46 (2007) 5750–5753.
- [8] S.A. Hilderbrand, M.H. Lim, S.J. Lippard, *J. Am. Chem. Soc.* 126 (2004) 4972–4978.
- [9] H.T. Chifotides, K.R. Dunber, *Acc. Chem. Res.* 38 (2005) 146–156.
- [10] R.A. Howard, T.G. Spring, J.L. Bear, *Cancer Res.* 36 (1976) 4402–4405.

- [11] A.M. Angeles-Boza, H.T. Chifotides, J.D. Aguirre, A. Chouai, P.K.-L. Fu, K.R. Dunbar, C. Turro, *J. Med. Chem.* 49 (2006) 6841–6847.
- [12] S. Naito, T. Tanibe, E. Saito, T. Miyao, W. Mori, *Chem. Lett.* 30 (2001) 1178.
- [13] T. Sato, W. Mori, C.N. Kato, T. Ohmura, T. Sato, K. Yokoyama, S. Takamizawa, S. Naito, *Chem. Lett.* 32 (2003) 854–855.
- [14] Y. Kataoka, K. Sato, Y. Miyazaki, Y. Suzuki, H. Tanaka, Y. Kitagawa, T. Kawakami, M. Okumura, W. Mori, *Chem. Lett.* 39 (2010) 358–359.
- [15] M. Handa, M. Watanabe, D. Yohioka, S. Kawabata, R. Nukada, M. Mikuriya, H. Azuma, K. Kasuga, *Bull. Chem. Soc. Jpn.* 72 (1999) 2681–2686.
- [16] F.A. Cotton, Y. Kim, J. Lu, *Inorg. Chim. Acta* 221 (1994) 1–4.
- [17] S. Takamizawa, E. Nakata, H. Yokoyama, K. Mochizuki, W. Mori, *Angew. Chem. Int. Ed.* 42 (2003) 4331–4334.
- [18] A.S. Filatov, A.Y. Rogachev, M.A. Petrukhina, *Cryst. Growth Des.* 6 (2006) 1479–1484.
- [19] M.A. Petrukhina, *Coord. Chem. Rev.* 251 (2007) 1690–1698.
- [20] R.P. Bonar-Law, T.D. McGrath, N. Singh, J.F. Bickley, A. Steiner, *Chem. Commun.* 24 (1999) 2457–2458.
- [21] M.W. Cooke, G.S. Hanan, F. Loiseau, S. Campagna, M. Watanabe, Y. Tanaka, *Angew. Chem. Int. Ed.* 44 (2005) 4881–4884.
- [22] G. Nickerl, U. Stoeck, U. burkhardt, I. Senkovska, S. Kaskel, *J. Mater. Chem. A* 2 (2014) 144–148.
- [23] J.Y. Lee, O.K. Farha, J. Roberts, K.A. Scheidt, S.T. Nguyen, J.T. Hupp, *Chem. Soc. Rev.* 38 (2009) 1450–1459.
- [24] A. Dhakshinamoorthy, H. Garcia, *Chem. Soc. Rev.* 43 (2014) 5750–5765.
- [25] M. Ebihara, M. Nomura, S. Sakai, T. Kawamura, *Inorg. Chim. Acta* 360 (2007) 2345–2352.
- [26] E.-Y. Choi, C.A. Wray, C. Hu, W. Choe, *CrystEngComm* 11 (2009) 553–555.
- [27] R. Makiura, R. Usui, E. Pohl, K. Prassides, *Chem. Lett.* 43 (2014) 1161–1163.

Coordination Polymers

Paddlewheel-Type Dirhodium Tetrapivalate Based Coordination Polymer: Synthesis, Characterization, and Self-Assembly and Disassembly Transformation Properties

Yusuke Kataoka,^{*,[a]} Natsumi Yano,^[a] Takashi Shimodaira,^[b] Yin-Nan Yan,^[b] Mikio Yamasaki,^[c] Hidekazu Tanaka,^[a] Kohji Omata,^[a] Tatsuya Kawamoto,^[b] and Makoto Handa^{*,[a]}

Abstract: An extended one-dimensional chain-type coordination polymer, $[\text{Rh}_2(\text{piv})_4(\text{tpy})]_n$ (**1**; piv = pivalate, tpy = 2,2':6',2''-terpyridine), has been synthesized and characterized by single-crystal and powder X-ray diffraction analyses, elemental analysis, IR spectroscopy, thermogravimetric analysis, UV/Vis diffuse reflectance spectroscopy, and magnetic measurements at 300 K. This complex shows unique repeatable self-assembly and

disassembly transformation properties. Polymer **1** readily decomposed to its constituent building blocks, that is, $[\text{Rh}_2(\text{piv})_4]$ and tpy, in organic solvents at 300 K, but the disassembly product of **1** readily re-self-assembled to give **1** as a crystalline product in aqueous ethanol solution at 373 K. In addition, **1** was obtained as a crystalline powder by a water-assisted mechanochemical synthesis route.

Introduction

The paddlewheel-type dirhodium(II) tetracarboxylates^[1] and their related complexes^[2] have attracted much interest because of their intriguing molecular structures and their excellent functional properties, for example, as catalysts,^[3] sensors,^[4] and anti-tumor drugs.^[5] Recently, these types of complexes have been utilized as robust building blocks for coordination polymers (CPs)^[6] and supramolecular complexes.^[7] Several of these exhibit interesting inherent properties that discrete metal complexes absolutely cannot show.^[8] The most general strategy for the synthesis of paddlewheel-type dirhodium-based CPs is to coordinate bidentate organic ligands such as diimines,^[9] quinones,^[10] and halides^[11] to the axial site of the dirhodium unit. This synthetic strategy usually affords one-dimensional (1D) robust CPs with high durability towards organic solvents. The most famous CP of this type, which was independently reported by the groups of Mori and Takamizawa^[12] and Handa and Mikuriya,^[13] is the 1D chain-type CP $[\text{Rh}_2(\text{Ba})_4(\text{pyz})]$ (Ba = benzoate, pyz = pyrazine), which can adsorb various gases and organic vapors into its coordination spaces.^[14] Although several extensive studies inspired by the above-mentioned work can be found in the literature,^[15] examples of paddlewheel-type di-

rhodium-based CPs are still limited compared with other paddlewheel-type dimetal-based CPs.

As mentioned above, although several examples of CPs synthesized from paddlewheel-type dirhodium tetracarboxylates and diimine or bipyridyl ligands have already been reported,^[16] there is no example of a CP connected by terpyridyl ligands. In concrete terms, it has been reported that the reaction of the dirhodium tetraacetate complex $[\text{Rh}_2(\text{O}_2\text{CCH}_3)_4]$ with 2,2':6',2''-terpyridine (tpy), which is the most common and well-used tridentate ligand, affords a discrete anchor-shaped dirhodium acetate complex, $[\text{Rh}_2(\text{O}_2\text{CCH}_3)(\text{tpy})_2]^{3+}$,^[17] that is, in the case of $[\text{Rh}_2(\text{O}_2\text{CCH}_3)_4]$, the tpy ligands are bonded to the rhodium ions in a tridentate chelate coordination mode rather than in an axial coordination mode. On the other hand, we incidentally discovered that the reaction of the dirhodium tetrapivalate complex $[\text{Rh}_2(\text{piv})_4]$ (piv = pivalate) and the tpy ligand affords purple single crystals of 1D CPs.

Herein we describe the synthesis, characterization, and self-assembly and disassembly transformation properties of a new 1D CP, $[\text{Rh}_2(\text{piv})_4(\text{tpy})]$ (**1**; piv = pivalate), which is fabricated from the paddlewheel-type dirhodium(II) tetrapivalate $[\text{Rh}_2(\text{piv})_4]$ and the flexible tridentate tpy ligand (Figure 1). In this article we describe three important findings. First, the framework structure of **1** is stable in water, but is easily disassembled into $[\text{Rh}_2(\text{piv})_4]$ and tpy in organic solvents. This solvent durability is in contrast to CPs in general as well as metal-organic frameworks (MOFs). Secondly, dissociated **1** is easily re-self-assembled to **1** in hot aqueous ethanol (EtOH) solution. To the best of our knowledge, the absolute self-assembly and disassembly transformations of polymeric compounds are very limited for CPs as well as organic polymers. Finally, **1** can also be prepared by a mechanochemical synthesis. A successful example of a mechanochemical synthesis of a paddlewheel-type

[a] Department of Chemistry, Interdisciplinary Graduate School of Science and Engineering, Shimane University, 1060 Nishikawatsu, Matsue, Shimane 690-8504, Japan
E-mail: kataoka@riko.shimane-u.ac.jp
<https://www.shimane-u.ac.jp/en/>

[b] Department of Chemistry, Faculty of Science, Kanagawa University, 2946 Tsuchiya, Kanagawa 259-1293, Japan

[c] RIGAKU Corporation, Matsubarasho, Akishima, Tokyo 196-8666, Japan

Supporting information for this article is available on the WWW under <http://dx.doi.org/10.1002/ejic.201600197>.

dirhodium-based CP has never previously been reported in the literature.

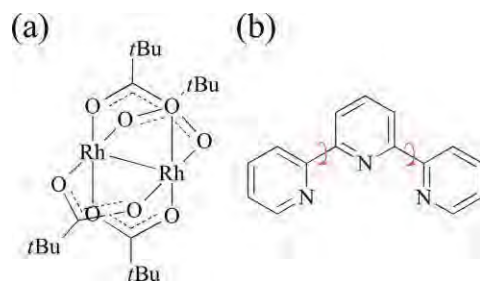


Figure 1. Molecular structures of (a) $[\text{Rh}_2(\text{piv})_4]$ and (b) tpy. The bent arrows indicate rotating sites of the pyridyl rings.

Results and Discussion

Synthesis and Characterization of $[\text{Rh}_2(\text{piv})_4(\text{tpy})]$ (**1**)

Single crystals of **1** suitable for single-crystal X-ray diffraction analysis were solvothermally synthesized from the self-assembly of $[\text{Rh}_2(\text{piv})_4]$ (0.60 mmol) and tpy (0.60 mmol) in the mixed solvent of EtOH (10.5 mL) and H_2O (1.5 mL). After heating at 373 K under N_2 for 1 h, deep-purple crystals of **1** were deposited on the bottom of the reaction vessel in relatively good yield (72.8 %). It is worth mentioning that **1** was not obtained when H_2O was omitted from the reaction system. Thus, it is speculated that H_2O participates as an assistant reagent in the polymerization of **1**. Although paddlewheel-type dirhodium-based CPs can generally be easily synthesized, that is, they readily polymerize at room temperature, complex **1** is not synthesized under the same reaction conditions. In addition, although we attempted the reaction of $[\text{Rh}_2(\text{piv})_4]$ with various ligands derived from tpy, such as 4,4',4''-tri-*tert*-butyl-2,2':6',2''-terpyridine, 4'-(4-bromophenyl)-2,2':6',2''-terpyridine, and trimethyl 2,2':6',2''-terpyridine-4,4',4''-tricarboxylate, under similar reaction conditions, no polymeric products were obtained. This is presumably due to the steric repulsion between the piv- and tpy-derived ligands.

The crystal structure of **1** was determined by single-crystal X-ray diffraction at 100 K and refined satisfactorily [$R_1(\text{all}) = 4.56\%$, $wR_2(\text{all}) = 10.68\%$], although small disordering of the methyl groups in the pivalate ligands was observed. Complex **1** crystallizes in the monoclinic space group $C2/c$. The asymmetric unit consists of an Rh ion, two piv[−] anionic ligands, and half a tpy ligand (Figure 2a). The substructure (structure surrounding the Rh_2 unit) of **1** is shown in Figure 2b. The Rh ions are in a distorted octahedral environment formed by four carboxylate oxygen atoms from different piv[−] ligands, the pyridyl nitrogen atom of a tpy ligand, and an Rh ion. The Rh–Rh single bond in **1** is confirmed, with a bond length of 2.409 Å, which is in the expected range for a dirhodium tetracarboxylate coordinated axially to aromatic nitrogen donor ligands. {For example, the Rh–Rh bond length of $[\text{Rh}_2(\text{piv})_4(4,4'\text{-bpy})]_n$ is 2.395 Å.} The two terminal pyridyl rings of one tpy ligand are bonded to the axial sites of the Rh–Rh bond, whereas the central pyridyl ring in the tpy ligand is not coordinated to the Rh ions. The Rh–O bond

lengths are in the range of 2.025–2.057 Å, and the Rh–N bond length is 2.345 Å. These bonds are clearly longer than those of $[\text{Rh}_2(\text{piv})_4(4,4'\text{-bpy})]_n$ (Rh–O 2.014–2.040 Å; Rh–N 2.225–2.264 Å), which indicates that the binding energy between $[\text{Rh}_2(\text{piv})_4]$ and tpy in **1** is lower than that between $[\text{Rh}_2(\text{piv})_4]$ and 4,4'-bpy in $[\text{Rh}_2(\text{piv})_4(4,4'\text{-bpy})]_n$. Interestingly, as shown in Figure 2c, intramolecular CH...O interactions are formed between the H atoms of the tpy ligands and the O atoms of the piv[−] ligands (H17...O4 ca. 2.27 Å, C17...O4 ca. 3.09 Å, H11...O3 ca. 2.66 Å, and C11...O3 ca. 2.93 Å).

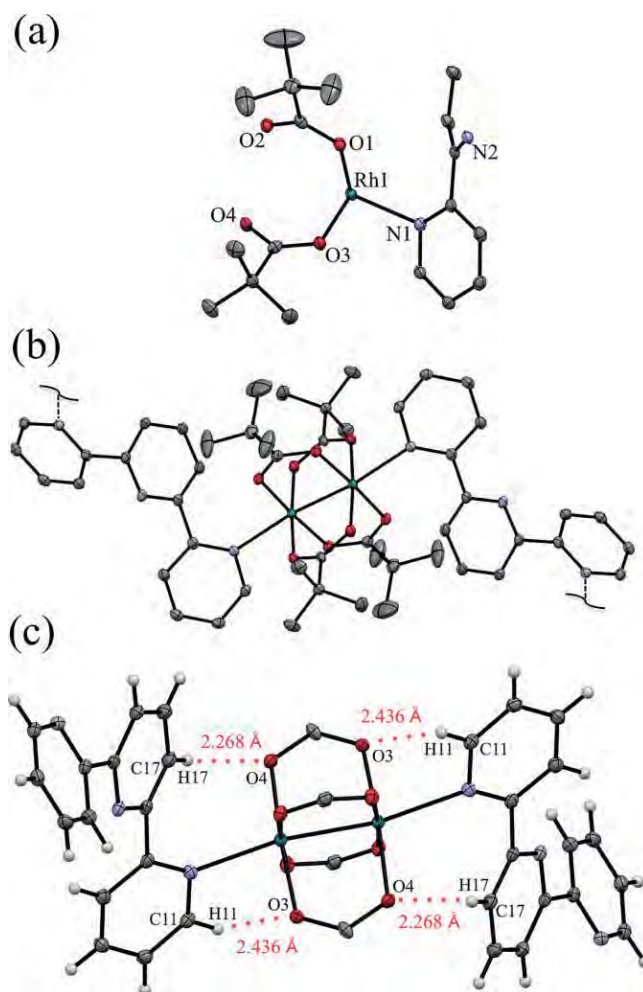


Figure 2. Crystal structure of **1**: (a) asymmetric unit structure, (b) substructure, and (c) fragment molecular structure showing intramolecular CH–O interactions. In (a) and (b), hydrogen atoms have been omitted for clarity. Ellipsoids are drawn at the 30 % probability level.

Figure 3a shows the 1D extended structure of **1**. The tpy ligands in **1** are heavily twisted because of the repulsion between the piv[−] and tpy ligands. Therefore, as a result, **1** forms a 1D zig-zag chain-type structure. As depicted in Figure 3b, guest spaces are not present in the three-dimensional (3D) packing structure of **1** for the inclusion of solvent (e.g., EtOH or H_2O) or other molecules. The void volume and residual electron count of the crystal structure of **1** estimated by using the Platon SQUEEZE program are only 223.0 Å³ and two electrons per unit cell, respectively, which indicates that there is not sufficient vol-

ume for guest inclusion into **1** (total volume of the crystal structure and the Z value of **1** are 3916.4 \AA^3 and 4, respectively), that is, the packing structure of **1** is closely self-assembled.

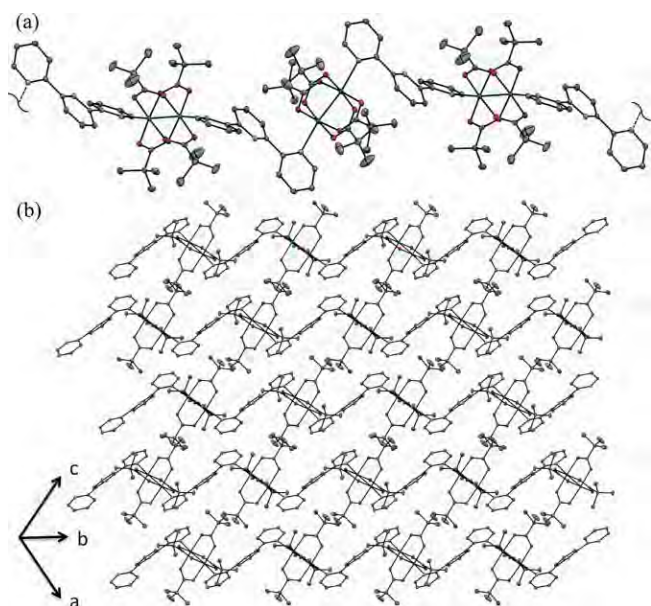


Figure 3. (a) One-dimensional extended structure and (b) 3D packing structure of **1**. Hydrogen atoms have been omitted for clarity. Ellipsoids are drawn at the 30% probability level.

The phase purity of the crystalline powder of **1** was confirmed by CHN elemental analysis, thermogravimetry (TG), and powder X-ray diffraction (PXRD) analysis. Guest solvents are not observed in the CHN elemental and TG analyses of **1**. This is consistent with the crystal structure of **1**. In addition, the combination of TG and differential thermal analysis (DTA) revealed that the initial thermal decomposition of **1** occurs at ca. 500 K in air. As depicted in Figure 4, the PXRD pattern of **1** is very sharp and agrees well with the simulated pattern derived from the crystal structure of **1**. This strongly indicates that **1** is obtained as a single phase.

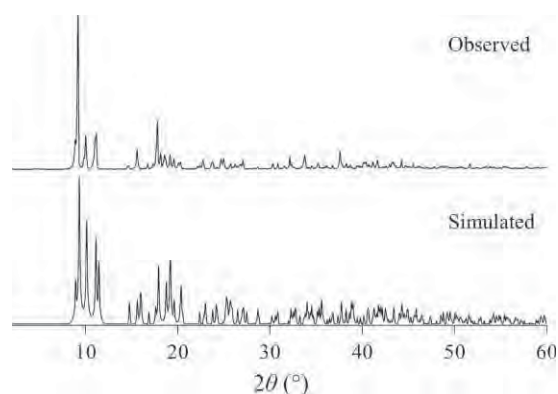


Figure 4. Observed (top) and simulated (bottom) XRD patterns of **1**.

The valence of the rhodium ions in **1** was confirmed IR spectroscopy and magnetic analysis (Evans method) at 300 K. In the IR spectrum (KBr disk), the symmetric $[\nu_{\text{sym}}(\text{COO}^-)]$ and asym-

metric $[\nu_{\text{asym}}(\text{COO}^-)]$ stretching modes of **1** appear at 1415 and 1587 cm^{-1} , respectively (see Figure S1 in the Supporting Information). Because the difference between the symmetric and asymmetric stretching modes, that is, $\Delta\nu(\text{COO}^-)$, of **1** (172 cm^{-1}) is similar to those of $[\text{Rh}_2(\text{piv})_4(\text{pyridine})_2]$ (170 cm^{-1}) and $[\text{Rh}_2(\text{piv})_4(4,4'\text{-bpy})_2]$ (168 cm^{-1} ; $4,4'\text{-bpy} = 4,4'\text{-bipyridine}$), the valence of the rhodium ions in **1** was concluded to be divalent. This oxidation state is strongly supported by magnetic measurements. The effective magnetic moment (μ_{eff}) of **1** is 0.56 B.M. at 300 K, which indicates that **1** is diamagnetic. From these results, we determined that the rhodium ions in **1** are divalent and that **1** has a closed-shell electronic structure.

In addition to the above characterization, we measured the UV/Vis diffuse reflectance spectrum at 300 K. In the visible region, the absorption maxima for **1** appear at 439 and 569 nm (see Figure S2 in the Supporting Information). This contrasts with the absorption maxima at 439 and 686 nm for $[\text{Rh}_2(\text{piv})_4]$ and at 430 and 520 nm for $[\text{Rh}_2(\text{piv})_4(4,4'\text{-bpy})]$. Therefore, the electronic structure of complex **1**, specifically the molecular orbital interactions between $[\text{Rh}_2(\text{piv})_4]$ and the pyridyl ligands and their energies, may differ somewhat to those of $[\text{Rh}_2(\text{piv})_4]$ and typical dirhodium-based CPs.

Solvent Durability of **1**

As is well known, almost all CPs and MOFs synthesized from paddlewheel-type dimetal units are stable in common organic solvents, whereas they readily decompose in water. In general, the decomposed building blocks of CPs and MOFs cannot re-self-assemble to the original CPs and MOFs. In this context, we confirm that **1** is unique in its solvent-resistance properties. As depicted in Figure 5a,b, although **1** is stable in hexane, it readily

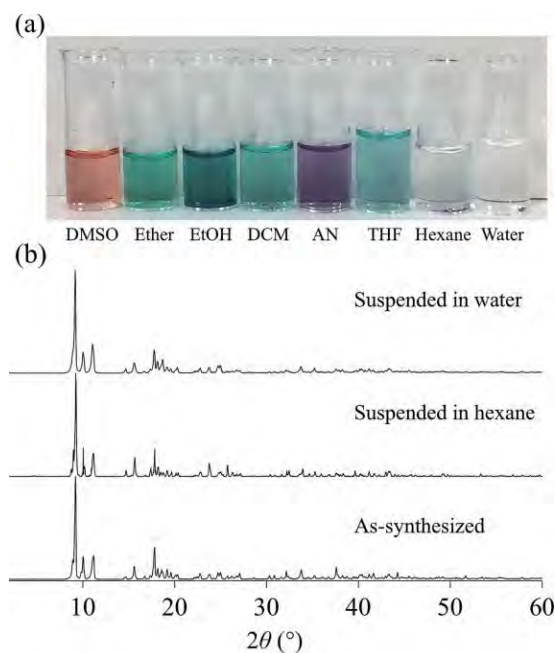


Figure 5. Suspensions of **1** in various solvents. (a) Photograph of the suspensions and (b) XRD patterns of as-synthesized **1** (bottom) and **1** suspended in hexane (middle) or water (top).

decomposes not only in donor solvents such as dmsO, diethyl ether, EtOH, acetonitrile, and thf, but also in nondonor solvents such as CH₂Cl₂. In dmsO solution, the color of decomposed **1** is rose-pink, which is similar to that of [Rh₂(piv)₄] dissolved in dmsO. Because the absorption wavelength in the visible region of decomposed **1** in dmsO (501 nm) is similar to that of [Rh₂(piv)₄] dissolved in dmsO, it can be deduced that **1** is decomposed into its discrete building blocks, that is, [Rh₂(piv)₄] and tpy, in organic solvents (see Figure S3 in the Supporting Information). Unexpectedly, **1** is very stable in water; the XRD pattern of water-suspended **1** (suspended in water for 12 h) is in good agreement with that of as-synthesized **1**.

To clarify the reason for the decomposition of **1** in various organic solvents but not in water and hexane, we investigated the solubility of [Rh₂(piv)₄], which is a building block of **1**. We confirmed that [Rh₂(piv)₄] readily dissolves in dmsO, diethyl ether, EtOH, acetonitrile, and thf, whereas it is insoluble in water and hexane, that is, [Rh₂(piv)₄] dissolves in the same organic solvents in which complex **1** decomposes. Thus, we concluded that the [Rh₂(piv)₄] unit in **1** is very easily dissociated from the framework of **1** in various common organic solvents because of its high solubility in those solvents.

Self-Assembly and Disassembly Transformations of **1**

To investigate whether the disassembled material of **1** re-self-assembles to crystalline **1**, we carried out the following experiment. First, the crystalline powder of **1** was dissolved in thf and completely dried at room temperature. The obtained product, that is, the disassembled material of **1**, is a blue powder that is clearly different to the solid color of as-synthesized **1**. As shown in Figure 6, the XRD pattern of the disassembled material of **1** is clearly dissimilar to those of as-synthesized **1**, [Rh₂(piv)₄(thf)₂], and tpy. This indicates that the framework structure in the disassembled material of **1** has absolutely collapsed. We then heated the disassembled material of **1** in a mixture of EtOH and H₂O at 373 K under N₂. During this process purple single crystals were deposited on the bottom of the Schlenk flask, and these crystals gave a PXRD pattern in good agreement with that of as-synthesized **1**. These results demon-

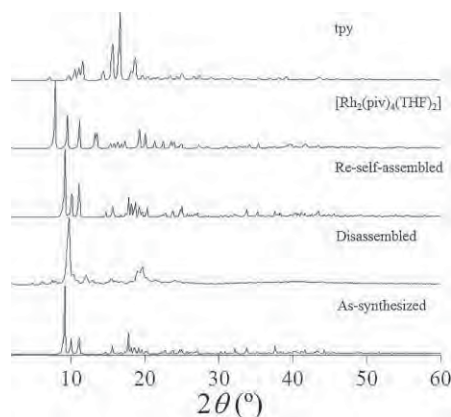
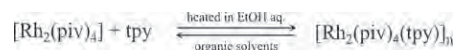


Figure 6. PXRD patterns of as-synthesized **1**, disassembled **1**, re-self-assembled **1**, [Rh₂(piv)₄(thf)₂], and tpy.

strate that the disassembled material of **1** re-self-assembled to again afford crystalline **1**, as depicted in Scheme 1. It is worth mentioning that this self-assemble/disassemble transformation of **1** is repeatable. In general, it is very difficult for disassembled MOFs and CPs to re-self-assemble, because they typically break down into their constituent components, such as metal ions and organic ligands, that is, because most transition-metal-complex-based building blocks are unstable and decompose in solvent. However, in the case of **1**, reconstruction of the framework is relatively easy, because the molecular structure of the [Rh₂(piv)₄] moiety is very rigid and stable in the same solvents.



Scheme 1. Structural transformation of **1**.

Mechanochemical Synthesis of **1**

Finally, we successfully synthesized **1** mechanochemically by water-assisted grinding using a typical mortar and pestle. Fine powders of [Rh₂(piv)₄] and tpy in a molar ratio of 1:1 were ground for 4 h, with water (0.10 mL) added to the reaction system every 15 min. [Rh₂(piv)₄] and tpy are insoluble in water. PXRD patterns and macro-images of the ground materials are shown in Figure 7 for different grinding times. We can easily

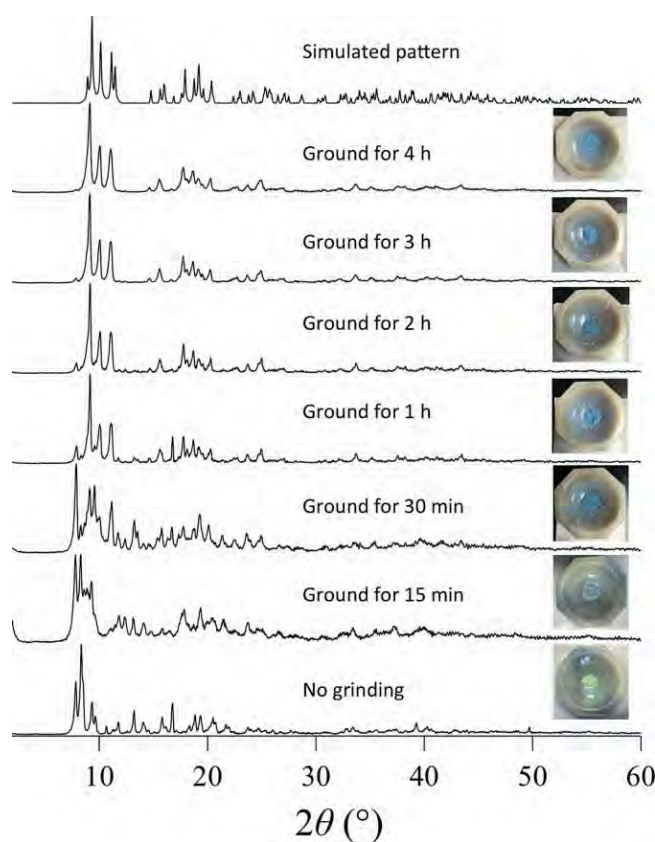


Figure 7. PXRD patterns and macro-images of the ground materials of [Rh₂(piv)₄] and tpy at different grinding times. The simulated pattern of **1** is shown for comparison (top).

confirm that the color of the powders changed from green to purple during grinding. In addition, the PXRD patterns gradually changed to the unique XRD pattern of **1** with increasing grinding time, and the PXRD pattern of the ground sample at 4 h is highly consistent with that of **1** synthesized under solvothermal conditions. As depicted in Figure S4 in the Supporting Information, scanning electron microscopy (SEM) revealed that the particle size of the ground powders gradually decreased. Note that addition of water to the reaction system is essential to form the crystalline phase of **1**; mechanochemical grinding of $[\text{Rh}_2(\text{piv})_4]$ and tpy without the addition of water afforded only an amorphous material with no intense XRD peaks. Thus, even in the mechanochemical synthesis of **1**, water is necessary as an assistant material for polymerization to give **1**.

Conclusions

In this study the extended 1D chain-type coordination polymer $[\text{Rh}_2(\text{piv})_4(\text{tpy})]_n$ (**1**) was obtained by the solvothermal reaction of $[\text{Rh}_2(\text{piv})_4]$ and tpy in aqueous EtOH solution. The crystalline powder of **1** was also obtained by a water-assisted mechanochemical synthesis route by using $[\text{Rh}_2(\text{piv})_4]$ and tpy. To the best of our knowledge, this is the first successful example of a mechanochemical synthesis of a paddlewheel-type dirhodium-based CP. The addition of water to the reaction system was essential for both synthetic methods to obtain the crystalline product of **1**, which indicates that water is required as an assistant reagent for the polymerization of **1**. We speculate that the atypical non-anchor-shape of the dirhodium complex arises from the strong electron-donating effect of the piv ligands, that is, the Rh–O bonds are stronger in $[\text{Rh}_2(\text{piv})_4]$ than in $[\text{Rh}_2(\text{O}_2\text{CCH}_3)_4]$. The repeatable self-assembly and disassembly transformation of **1** was clearly demonstrated. Such absolute transformation properties are very limited in not only CPs but also organic polymers. At this stage, we assume that the disassembly of **1** occurs, because $[\text{Rh}_2(\text{piv})_4]$ is very easily dissociated from the framework of **1** as a result of the relatively low binding energy between the $[\text{Rh}_2(\text{piv})_4]$ and tpy units and because $[\text{Rh}_2(\text{piv})_4]$ dissolves in the same organic solvents in which complex **1** decomposes. The functional applications of **1** are currently limited because of the close-packed nonporous structure of **1**. However, the unique structural transformation properties and solvent durability of **1** are important for creating paddlewheel-type dirhodium-based porous CPs and MOFs. We are now developing this study for the construction of porous CPs and MOFs based on paddlewheel-type dirhodium units and tpy-derived ligands with a view to creating soft porous materials with various functional properties and structural stability.

Experimental Section

Materials and Instruments: All reagents and solvents used in this study were purchased from commercial sources and used without further purification. The PXRD measurements were performed with a RIGAKU MiniFlex II (30 kV, 15 mA) diffractometer using $\text{Cu-K}\alpha$ radi-

ation at room temperature. TG/DTA analysis was carried out by using a RIGAKU Thermo Plus 2 series TG/DTA 8120 instrument. Absorption and UV/Vis diffuse reflectance spectra were recorded with JASCO V-670 and JASCO V-570 spectrophotometers equipped with an ISV-469 integration sphere, respectively. CHN elemental analysis was conducted by using a Perkin-Elmer PE2400 series II CHNS/O analyzer. The magnetic moment at 300 K was determined by Evans' method using an MSB-MKI magnetic susceptibility balance (SSL, Cambridge). The IR spectrum was recorded by using a JASCO FT-IR 660-plus spectrometer in KBr disk at room temperature. SEM images were taken by using a HITACHI TM3030Plus Miniscope.

Solvothermal Synthesis of 1: A mixture of $[\text{Rh}_2(\text{piv})_4]$ (366.2 mg, 0.60 mol) and tpy (140.0 mg, 0.60 mmol) was dissolved in ethanol/water (10.5:1.5 mL) and transferred to a 50 mL Schlenk flask. The mixture was heated at reflux under N_2 for 1 h. Once cooled to room temperature, the deep-purple crystals formed at the bottom of the flask were collected on a membrane filter, washed with ethanol, and dried under vacuum at 343 K for 1 h. Yield: 72.8 % (368.6 mg, 0.437 mmol). $\text{C}_{35}\text{H}_{47}\text{N}_3\text{O}_8\text{Rh}_2$ (843.58): calcd. C 49.83, H 5.62, N 4.98; found C 49.85, H 5.66, N 5.02.

Mechanochemical Synthesis of 1: A mixture of $[\text{Rh}_2(\text{piv})_4]$ (122.0 mg, 0.20 mmol) and tpy (46.7 mg, 0.20 mmol) was ground with a typical mortar and pestle for 4 h with the addition of water (0.1 mL) every 15 min. The deep-purple powder was collected and dried under air at 343 K for 1 h. Yield: 92.0 % (154.1 mg). $\text{C}_{35}\text{H}_{47}\text{N}_3\text{O}_8\text{Rh}_2$ (843.58): calcd. C 49.83, H 5.62, N 4.98; found C 49.71, H 5.38, N 5.13.

Single-Crystal X-ray Diffraction Analysis: Single crystals of **1** suitable for X-ray diffraction analysis were obtained as described above. A single crystal was attached to a Cryoloop by using paraffin oil (HAMPTON RESEARCH). Diffraction data were collected at 100 K with a RIGAKU Mercury 70 diffractometer equipped with an Mo rotating-anode X-ray generator with monochromated $\text{Mo-K}\alpha$ radiation. The diffraction data were processed by using the CrystalClear-SM Expert 2.1 b45 software (RIGAKU). The structure was solved by direct methods (SHELXS) and refined by using the full-matrix least-squares technique on F^2 with SHELXL in the CrystalStructure 4.2 software. Non-hydrogen atoms were refined with anisotropic displacement parameters, and all hydrogen atoms were located at calculated positions and refined by using a riding model. The residual electron density in the void spaces of the final refined structure was evaluated using the PLATON SQUEEZE program. Crystal data for **1**: $\text{C}_{35}\text{H}_{47}\text{N}_3\text{O}_8\text{Rh}_2$, $M_r = 843.58$, $T = 100$ K, monoclinic, space group $C2/c$ (no. 15), $a = 18.760(5)$, $b = 11.982(3)$, $c = 18.665(5)$ Å, $\beta = 111.020(6)^\circ$, $V = 3916.4(18)$ Å³, $D_{\text{calcd.}} = 1.431$ g/cm³, $Z = 4$, $R_1(\text{all}) = 0.0456$, $R_1(I > 2\sigma) = 0.0412$, $wR_2(\text{all}) = 0.1068$, $wR_2(I > 2\sigma) = 0.1016$, GOF = 1.065, total reflections: 3575. CCDC 1453319 (for **1**) contains the supplementary crystallographic data for this paper. These data can be obtained free of charge from The Cambridge Crystallographic Data Centre.

Acknowledgments

This work has been supported by a Grant-in-Aid for Scientific Research (grant nos. 15K17897, 15H00877, 25620145, 26420739) and the Strategic Research Base Development Program for Private Universities of the Ministry of Education, Culture, Sports and Technology (MEXT), Japan. Y. K. acknowledges the JAPAN PRIZE Foundation and the Electronic Technology Research Foundation of Chugoku.

Keywords: Rhodium · Polymers · X-ray diffraction · Tridentate ligands

- [1] a) F. A. Cotton, B. G. Deboer, M. D. LaPrade, J. R. Pipal, D. A. Ucko, *Acta Crystallogr., Sect. B* **1971**, 27, 1664; b) H. T. Chifotides, K. R. Dunber in *Multiple Bonds between Metal Atoms* (Eds.: F. A. Cotton, C. A. Murillo, R. A. Walton), Springer Science and Business Media, New York, **2005**, p. 465.
- [2] a) G. Pimblett, C. D. Garner, W. Clegg, *J. Chem. Soc., Dalton Trans.* **1986**, 6, 1257; b) A. R. Chakravarty, F. A. Cotton, D. A. Tocher, J. H. Tocher, *Organometallics* **1985**, 4, 8; c) F. J. Lahoz, A. Martin, M. A. Esteruelas, E. Sola, J. L. Serrano, L. A. Oro, *Organometallics* **1991**, 10, 1794; d) C. A. Crawford, J. H. Matonic, J. H. Huffman, K. Folting, K. R. Dunber, G. Christou, *Inorg. Chem.* **1997**, 36, 2361; e) Y. Kataoka, N. Yano, T. Kawamoto, M. Handa, *Eur. J. Inorg. Chem.* **2015**, 34, 5650.
- [3] a) J. Hansen, H. M. L. Davies, *Coord. Chem. Rev.* **2008**, 252, 545; b) M. P. Doyle, E. Duffy, M. Ratnikov, L. Zhou, *Chem. Rev.* **2010**, 110, 704; c) P. M. Gois, A. F. Trindade, L. F. Veiros, V. Andre, M. T. Duarte, C. A. M. Afonso, S. Caddick, F. G. N. Cloke, *Angew. Chem. Int. Ed.* **2007**, 46, 5750; *Angew. Chem.* **2007**, 119, 5852.
- [4] a) S. A. Hilderbrand, M. H. Lim, S. J. Lippard, *J. Am. Chem. Soc.* **2004**, 126, 497; b) S. L. Schiavo, P. Piraino, A. Bonavita, G. Micali, G. Rizzo, G. Neri, *Sens. Actuators B* **2008**, 129, 772; c) R. C. Smith, A. G. Tennyson, S. J. Lippard, *Inorg. Chem.* **2006**, 45, 6222; d) J. Esteban, J. V. Ros-Lis, R. Martinez-Manez, M. D. Marcos, M. Moragues, J. Soto, F. Sancenon, *Angew. Chem. Int. Ed.* **2010**, 49, 4934; *Angew. Chem.* **2010**, 122, 5054.
- [5] a) H. T. Chifotides, K. R. Dunber, *Acc. Chem. Res.* **2005**, 38, 146; b) R. A. Howard, T. G. Spring, J. L. Bear, *Cancer Res.* **1976**, 36, 4402; c) A. M. Angeles-Boza, H. T. Chifotides, J. D. Aguirre, A. Chouai, P. K.-L. Fu, K. R. Dunbar, C. Turro, *J. Med. Chem.* **2006**, 49, 6841.
- [6] a) T. Sato, W. Mori, C. N. Kato, E. Yanaoka, T. Kuribayashi, R. Ohtera, Y. Shiraishi, *J. Catal.* **2005**, 232, 186; b) Y. Kataoka, K. Sato, Y. Miyazaki, Y. Suzuki, H. Tanaka, Y. Kitagawa, T. Kawakami, M. Okumura, W. Mori, *Chem. Lett.* **2010**, 39, 358; c) K. Uemura, M. Ebihara, *Inorg. Chem.* **2011**, 50, 7919; d) H. Miyasaka, C. S. Campos-Fernandez, J. R. Galan-Mascaros, K. R. Dunbar, *Inorg. Chem.* **2000**, 39, 5870.
- [7] a) R. P. Bonar-Law, T. D. McGrath, N. Singh, J. F. Bickley, A. Steiner, *Chem. Commun.* **1999**, 24, 2457; b) M. W. Cooke, G. S. Hanan, F. Loiseau, S. Campagna, M. Watanabe, Y. Tanaka, *Angew. Chem. Int. Ed.* **2005**, 44, 4881; *Angew. Chem.* **2005**, 117, 4959; c) F. A. Cotton, P. Lei, C. Lin, C. A. Murillo, X. Wang, S.-Y. Yu, Z.-X. Zhang, *J. Am. Chem. Soc.* **2004**, 126, 1518.
- [8] S. Takamizawa, E. Nakata, T. Saito, *Angew. Chem. Int. Ed.* **2004**, 43, 1368; *Angew. Chem.* **2004**, 116, 1392.
- [9] N. Fritsch, C. R. Wick, T. Waidmann, P. O. Dral, J. Tucher, F. W. Heinemann, T. E. Shubina, T. Clark, N. Burzlaff, *Inorg. Chem.* **2014**, 53, 12305.
- [10] a) M. Handa, T. Nakao, M. Mikuriya, T. Kotera, R. Nukada, K. Kasuga, *Inorg. Chem.* **1998**, 37, 149; b) M. Handa, M. Mikuriya, Y. Sato, T. Kotera, R. Nukada, D. Yoshioka, K. Kasuga, *Bull. Chem. Soc. Jpn.* **1996**, 69, 3438.
- [11] F. A. Cotton, E. V. Dikarev, M. A. Petrukhina, *Angew. Chem. Int. Ed.* **2000**, 39, 2362; *Angew. Chem.* **2000**, 112, 2452.
- [12] a) W. Mori, H. Hoshino, Y. Nishimoto, S. Takamizawa, *Chem. Lett.* **1999**, 28, 331; b) S. Takamizawa, T. Hiroki, E. Nakata, K. Mochizuki, W. Mori, *Chem. Lett.* **2002**, 12, 1208.
- [13] M. Mikuriya, M. Higashiguchi, T. Sakai, D. Yoshioka, M. Handa in *Progress in Coordination and Bioinorganic Chemistry* (Eds.: M. Melnik, A. Sirota), Slovak Technical University Press, Bratislava, **2003**, p. 213.
- [14] a) S. Takamizawa, E. Nakata, H. Yokoyama, K. Mochizuki, W. Mori, *Angew. Chem. Int. Ed.* **2003**, 42, 4331; *Angew. Chem.* **2003**, 115, 4467; b) S. Takamizawa, E. Nakata, T. Saito, T. Akatsuka, *Inorg. Chem.* **2005**, 44, 1362; c) S. Takamizawa, C. Kachi-Terajima, M. Kohbara, T. Akatsuka, T. Jin, *Chem. Asian J.* **2007**, 2, 837.
- [15] a) F. A. Cotton, Y. Kim, J. Lu, *Inorg. Chim. Acta* **1994**, 221, 1; b) F. A. Cotton, Y. Kim, *J. Am. Chem. Soc.* **1993**, 115, 8511; c) Y. Kataoka, K. Sato, Y. Miyazaki, Y. Suzuki, H. Tanaka, Y. Kitagawa, T. Kawakami, M. Okumura, W. Mori, *Chem. Lett.* **2010**, 39, 358; d) A. S. Filatov, A. Y. Rogachev, M. A. Petrukhina, *Cryst. Growth Des.* **2006**, 6, 1479; e) M. A. Petrukhina, *Coord. Chem. Rev.* **2007**, 251, 1690.
- [16] M. Handa, M. Watanabe, D. Yoshioka, S. Kawabata, R. Nukada, M. Mikuriya, H. Azuma, K. Kasuga, *Bull. Chem. Soc. Jpn.* **1999**, 72, 2681.
- [17] F. P. Pruchnik, F. Robert, Y. Jeannin, S. Jeannin, *Inorg. Chem.* **1996**, 35, 4261.

Received: February 26, 2016
Published Online: April 24, 2016

Dinuclear Ruthenium(III)–Ruthenium(IV) Complexes, Having a Doubly Oxido-Bridged and Acetato- or Nitrate-Capped Framework

Tomoyo Suzuki,[†] Yutaka Suzuki,[†] Tatsuya Kawamoto,[‡] Ryo Miyamoto,[§] Shinkoh Nanbu,[†] and Hirotaka Nagao^{*,†}[†]Department of Materials and Life Sciences, Faculty of Science and Technology, Sophia University, 7-1 Kioi-cho, Chiyoda-ku, Tokyo 102-8554 Japan[‡]Department of Chemistry, Faculty of Science, Kanagawa University, Hiratsuka, Kanagawa 259-1293, Japan[§]Graduate School of Science and Technology, Hirosaki University, Bunkyo-cho, Hirosaki 036-8561, Japan

Supporting Information

ABSTRACT: Dinuclear ruthenium complexes in a mixed-valence state of Ru^{III}–Ru^{IV}, having a doubly oxido-bridged and acetato- or nitrate-capped framework, [$\{\text{Ru}^{\text{III,IV}}(\text{ebpma})\}_2(\mu\text{-O})_2(\mu\text{-L})\](\text{PF}_6)_2$ [ebpma = ethylbis(2-pyridylmethyl)amine; L = CH₃COO[−] (1), NO₃[−] (2)], were synthesized. In aqueous solutions, the diruthenium complex 1 showed multiple redox processes accompanied by proton transfers depending on the pH. The protonated complex of 1, which is described as I_{H+}, was obtained.

Conversion of small molecules into more useful and higher-energy chemicals using a metal complex catalyst under mild conditions has been paid much attention from the viewpoint of environmental concerns.^{1,2} Multinuclear frameworks of metal complexes that function as multielectron transferring sites and have appropriate electronic structures for the nature of targeting substrates are useful for material conversion systems. Singly and doubly oxido-bridged dinuclear complexes have been well studied as homogeneous catalysts for water oxidation³ and as biomimetic soluble methane monooxygenase,⁴ respectively. Several dinuclear complexes having a doubly oxido-bridged core, M₂(μ-O)₂, e.g., Mn–Mn,⁵ Fe–Mn,⁶ Fe–Fe,⁷ and Co–Co,⁸ have been synthesized and characterized in relation to oxidation reactions catalyzed by metal complexes. Diruthenium complexes having a doubly oxido- or hydroxido-bridged core, Ru₂(μ-O)₂ or Ru₂(μ-OH)₂,^{9,10} and triply bridged diruthenium complexes, in which a bidentate ligand is capped between metal centers with the doubly oxido- or hydroxido-bridged core, have been reported.^{11,12} In our previous work on dinuclear frameworks using a tridentate ancillary ligand, ethylbis(2-pyridylmethyl)amine (ebpma), triply chlorido- and/or methoxido-bridged diruthenium complexes of Ru^{II}–Ru^{III}, [$\{\text{Ru}(\text{ebpma})\}_2(\mu\text{-Cl})_n(\mu\text{-OMe})_{3-n}\]^{2+}$ ($n = 1, 3$),^{13,14} and singly oxido-bridged complexes of Ru^{III}–Ru^{IV}, [$\{\text{RuX}_2(\text{ebpma})\}_2(\mu\text{-O})\]^+$ ($X = \text{Cl}, \text{Br}$),¹⁴ have been synthesized. Their structures and reactivities, as well as their competency for functioning as molecular conversion reaction sites, have been of interest. In this work, diruthenium complexes of Ru^{III}–Ru^{IV} having the doubly oxido-bridged core with capping of acetato or nitrate, [$\{\text{Ru}^{\text{III,IV}}(\text{ebpma})\}_2(\mu\text{-O})_2(\mu\text{-L})\](\text{PF}_6)_2$ [L = CH₃COO[−] (1), NO₃[−] (2)], have been

synthesized. The structure of the doubly oxido-bridged and nitrate-capped framework is determined by X-ray crystallography. The electronic structures, electrochemical and spectroscopic properties, reactions with Brønsted acids, and electrochemical behaviors in aqueous solutions were studied.

Reactions of the singly oxido-bridged halogeno diruthenium complex, [$\{\text{Ru}^{\text{III,IV}}\text{Cl}_2(\text{ebpma})\}_2(\mu\text{-O})\]\text{PF}_6$, with four equimolar amounts of AgL (L = CH₃COO, NO₃) in water–acetone under air afforded a triply bridged diruthenium complex having a doubly oxido-bridged and acetato- or nitrate-capped framework, 1 and 2, by the addition of NH₄PF₆ as the precipitant. The structure of 2 was determined by X-ray structural analysis, as shown in Figure 1 (Figure S1 and Table S1). For 1, a preliminary

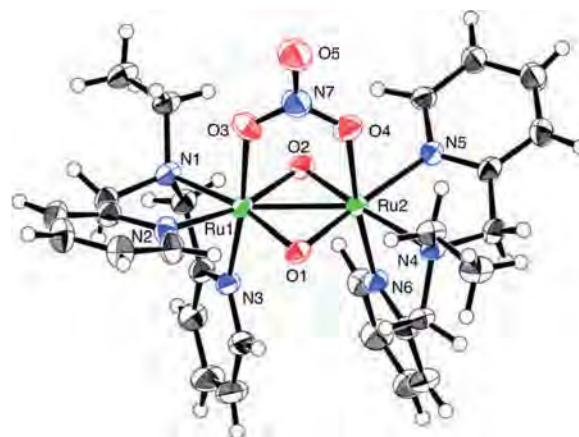


Figure 1. Thermal ellipsoid plots of the crystal structure of 2 shown at the 50% probability level. For clarity, H atoms and two PF₆[−] counteranions are omitted.

structure similar to that of 2 was obtained because of the size and quality of the single crystals. The structural parameters of the Ru₂(μ-O)₂ core [Ru–O, 1.929(3)–1.933(3) Å; Ru–O–Ru, 78.15(10) and 78.10(10)°; O–Ru–O, 101.65(11) and 101.76(11)°] were similar to those of the reported diruthenium complex of Ru^{III}–Ru^{IV} having a doubly oxido-bridged and

Received: April 11, 2016

Published: June 24, 2016

carbonato-capped framework, $[\{\text{Ru}(\text{dtne})\}(\mu\text{-O})_2(\mu\text{-O}_2\text{CO})]\text{PF}_6$ [dtne = 1,2-bis(1,4,7-triazacyclononan-1-yl)ethane].¹¹ Comparison of structural parameters between **2** and reported triply bridged complexes of $\text{Ru}^{\text{III}}\text{-Ru}^{\text{III}}$ having the $\text{Ru}_2(\mu\text{-OH})_2$ core, $[\{\text{Ru}(\text{tacn})\}(\mu\text{-OH})_2(\mu\text{-O}_2\text{CCH}_3)]\text{I}_3$ (tacn = 1,4,7-triazacyclononane)^{12d} and $[\{\text{Ru}(\text{tacn})\}(\mu\text{-OH})_2(\mu\text{-O}_2\text{CO})]\text{Br}_2$,¹¹ revealed longer Ru–O lengths and similar Ru–O–Ru and O–Ru–O angles. The present diruthenium complex had a shorter Ru–Ru distance [2.4334(4) Å] compared to that of the diruthenium complexes described above, suggesting interaction between two Ru centers. The capping nitrate anion coordinated without much distortion (O–N–O, 118.56, 120.71, and 120.72°) to form the triply bridged framework.

The values of the effective magnetic moment μ_{eff} at 295 K were 2.19 μ_{B} for **1** and 2.17 μ_{B} for **2**, accounting for one unpaired electron (Table S3). Electron spin resonance (ESR) spectra were measured at 77 K in frozen acetone–toluene solutions (Figure S2). Clear ESR signals were obtained with *g* values of 2.22, 2.10, and 2.00 for **1** and 2.17, 2.11, and 2.00 for **2**. From these measurements, one unpaired electron was confirmed and the electronic structure was identified to be $\text{Ru}^{\text{III}}\text{-Ru}^{\text{IV}}$ with antiferromagnetic electronic coupling. Density functional theoretical (DFT) calculations for **2** were performed using the Gaussian 09 program with unrestricted B3LYP/LANL2DZ/cc-pVDZ (Table S4). The result suggested that the electron density of the highest occupied frontier molecular orbital (161a^a; see Figure S3) of **2** was contributed by the diruthenium core, $\text{Ru}_2(\mu\text{-O})_2$.

Cyclic voltammetry (CV) curves of **1** and **2** in acetonitrile show one reversible oxidation process and stepwise reversible and irreversible reduction ones (Figure 2). Analysis of the

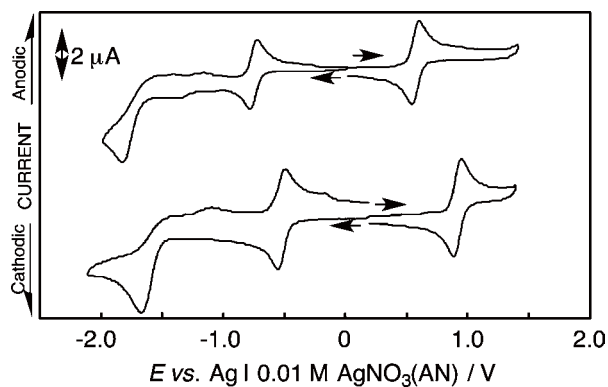


Figure 2. CV curves of **1** (upper) and **2** (bottom) in acetonitrile containing tetraethylammonium perchlorate at 25 °C.

hydrodynamic voltammetry (Figures S4–S7) and controlled potential electrolysis (CPE) experiments for reversible oxidation and reduction waves (Figures S8–S11) indicated that these processes were assigned to one-electron redox couples, $\text{Ru}^{\text{III}}\text{-Ru}^{\text{IV}}/\text{Ru}^{\text{III}}\text{-Ru}^{\text{III}}$ and $\text{Ru}^{\text{IV}}\text{-Ru}^{\text{IV}}/\text{Ru}^{\text{III}}\text{-Ru}^{\text{IV}}$, respectively. Thus, the formal oxidation state of both complexes is concluded to be $\text{Ru}^{\text{III}}\text{-Ru}^{\text{IV}}$. The large difference of the redox potentials between two reversible waves reveals a stable mixed-valence state ($K_{\text{C}} = 2.7 \times 10^{22}$ for **1** and 3.7×10^{24} for **2**; Table S5), classified into class III according to Robin and Day classification.¹⁵ The $\text{Ru}^{\text{III}}\text{-Ru}^{\text{III}}$ species in CH_3CN changed and ligand-substitution reactions occurred (Figure S9), and the $\text{Ru}^{\text{IV}}\text{-Ru}^{\text{IV}}$ state was stable during the oxidative CPE experiment (Figure S11).

In UV–vis and NIR spectroscopy in CH_3CN (Figure S14), two intense absorption bands and one broad weak band were observed. Spectroelectrochemical measurements of **1** and **2** were performed in CH_3CN using an optically transparent thin-layer electrode cell. The $\text{Ru}^{\text{III}}\text{-Ru}^{\text{III}}$ complexes that were formed by one-electron reduction of **1** and **2** were unstable and gradually changed during reductive CPE. In oxidative CPE, similar spectral changes of both complexes with isosbestic points were observed, indicating that the oxidized forms of the $\text{Ru}^{\text{IV}}\text{-Ru}^{\text{IV}}$ state were stable during these experiments (Figures S15 and S16). Weak broad bands at 677 nm for **1** and 586 nm for **2** were newly observed with a decreasing weak broad band at 762 nm for **2**. The broad band around 700 nm was observed for a similar $\text{Ru}^{\text{IV}}\text{-Ru}^{\text{IV}}$ complex having the $\text{Ru}_2(\mu\text{-O})_2$ core.¹¹ Thus, the bands of **1** and **2** at 339 and 318 nm were assigned to metal-to-ligand charge transfer, those at 977 and 762 nm represented a transition from the highest occupied frontier orbital to the lowest unoccupied molecular orbital, which were both mainly contributed by the $\text{Ru}_2(\mu\text{-O})_2$ core.⁵

CV curves of **1** in 2:1 (v/v) water–acetonitrile mixed solutions, as shown in Figure S12, revealed three or four distinctive redox waves in all pH regions. These waves were attributed to stepwise one- or two-electron redox processes of the metal centers. The redox potentials depend on the pH of the solutions, explained by the contribution of proton transfer(s) with reduction and oxidation processes. Profiles of CV reversibly changed in the pH region between 1.5 and 12.5, indicating that the complex was stable without decomposition. For complex **2**, electrochemical measurements in aqueous solutions could not be identified in detail because of the reactivity of **2**. A Pourbaix diagram, a plot of the redox potential versus pH, is described in Figure 3.¹⁶ The expected oxidation states of the Ru centers and

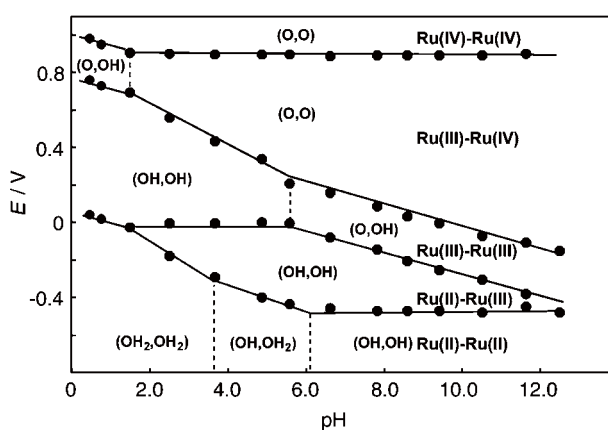


Figure 3. Pourbaix diagram of **1**.

chemical states of the bridging moieties were described in the diagram [**1** is shown as $\text{Ru}^{\text{III}}\text{-Ru}^{\text{IV}}$ and (O,O)]. The pH-independent regions reveal only a change of the oxidation states, and the slopes of the linear relationship in the pH-dependent regions indicate the number of protons and electrons in the redox processes. The diagram indicates that nine species having a $(\mu\text{-O})_2$, $(\mu\text{-O})(\mu\text{-OH})$, $(\mu\text{-OH})_2$, $(\mu\text{-OH})(\mu\text{-OH}_2)$, or $(\mu\text{-OH}_2)_2$ bridging core are expected to exist in the pH regions of the diagram with oxidation states of $\text{Ru}^{\text{IV}}\text{-Ru}^{\text{IV}}$, $\text{Ru}^{\text{III}}\text{-Ru}^{\text{IV}}$, $\text{Ru}^{\text{III}}\text{-Ru}^{\text{III}}$, $\text{Ru}^{\text{II}}\text{-Ru}^{\text{III}}$, and $\text{Ru}^{\text{II}}\text{-Ru}^{\text{II}}$. Notably, in a pH lower than 1.5, a protonated complex of **1**, $[\{\text{Ru}^{\text{III,IV}}(\text{ebpma})\}_2(\mu\text{-O})(\mu\text{-OH})(\mu\text{-O}_2\text{CCH}_3)]^{3+}$ (**1**_{H⁺}), exists and can be isolated.

Reactions of **1** with Brønsted acids HX ($X^- = \text{Cl}^-, \text{ClO}_4^-, \text{CF}_3\text{SO}_3^-$, or $^{1/2}\text{SO}_4^{2-}$) in water–acetone under air were investigated. The protonated species I_{H^+} was isolated from a 3:7 (v/v) water–acetone solution containing Brønsted acid and identified as the $\text{Ru}^{\text{III}}-\text{Ru}^{\text{IV}}$ state by the magnetic susceptibility measurement at room temperature ($\mu_{\text{eff}} = 1.92 \mu_{\text{B}}$; Table S3). In the CV measurements in CH_3CN , the protonated complex I_{H^+} showed three waves at a more positive region than those of **1** (Figure S13a). By the addition of Bu_4NOH to the solution of I_{H^+} , a similar CV profile of **1** was obtained, and the further addition of $\text{CF}_3\text{SO}_3\text{H}$ reversibly afforded the original CV (Figure S13). These CV changes agreed with the results of electrochemical measurements in a water–acetonitrile solution. In reactions of **2** with Brønsted acids, decomposition of the nitrate-capped framework occurred to give a nitrosylruthenium complex. Studies of the details of the products and differences of the reactivities between **1** and **2** are in progress.

New dinuclear ruthenium complexes of $\text{Ru}^{\text{III}}-\text{Ru}^{\text{IV}}$, composed of a doubly oxido-bridged $\text{Ru}_2(\mu\text{-O})_2$ core and one capped anion, $[\{\text{Ru}^{\text{III,IV}}(\text{ebpma})\}_2(\mu\text{-O})_2(\mu\text{-L})]^{2+}$ ($\text{L} = \text{CH}_3\text{COO}^-$ and NO_3^-), were synthesized and fully characterized. Detailed studies of the redox behaviors in aqueous solutions of **1** provided stability of the expected forms at certain pH conditions. The protonated complex I_{H^+} having the oxido- and hydroxido-bridged and acetato-capped framework $(\mu\text{-O})(\mu\text{-OH})(\mu\text{-O}_2\text{CCH}_3)$ in the state of $\text{Ru}^{\text{III}}-\text{Ru}^{\text{IV}}$ could be isolated under acidic conditions. The properties of the diruthenium complexes having a doubly oxido-bridged core are important in order to understand the rules of multinuclear metal complexes and to develop a multielectron and multicenter reaction site that functions as a redox reaction mediator for material conversion reactions. Further reactions of these diruthenium complexes and syntheses of diruthenium complexes in alternative oxidation states are in progress.

■ ASSOCIATED CONTENT

Supporting Information

The Supporting Information is available free of charge on the ACS Publications website at DOI: 10.1021/acs.inorgchem.6b00890.

Synthetic procedures, characterization data, X-ray crystallographic data, magnetic susceptibility, ESR spectra, DFT calculations, electrochemical measurements, and spectroscopic properties (PDF)

X-ray crystallographic data in CIF format (CIF)

■ AUTHOR INFORMATION

Corresponding Author

*E-mail: h-nagao@sophia.ac.jp.

Notes

The authors declare no competing financial interest.

■ REFERENCES

- (1) (a) Blakemore, J. D.; Crabtree, R. H.; Brudvig, G. W. *Chem. Rev.* **2015**, *115*, 12974–13005. (b) Meyer, F.; Tolman, W. B. *Inorg. Chem.* **2015**, *54*, 5039. (c) Kärkäs, M. D.; Verho, O.; Johnston, E. V.; Åkermarck, B. *Chem. Rev.* **2014**, *114*, 11863–12001.
- (2) Special Issue on Cooperative & Redox Non-Innocent Ligands in Directional Organometallic Reactivity: *Eur. J. Inorg. Chem.* **2012**, 340–580.
- (3) For example, see: Jurss, J. W.; Concepcion, J. J.; Butler, J. M.; Omberg, K. M.; Baraldo, L. M.; Thompson, D. G.; Lebeau, E. L.; Hornstein, B.; Schoonover, J. R.; Jude, H.; Thompson, J. D.;

Dattelbaum, D. M.; Rocha, R. C.; Templeton, J. L.; Meyer, T. J. *Inorg. Chem.* **2012**, *51*, 1345–1358.

- (4) (a) Banerjee, R.; Proshlyakov, Y.; Lipscomb, J. D.; Proshlyakov, D. *A. Nature* **2015**, *518*, 431–441. (b) Wang, W.; Liang, A. D.; Lippard, S. J. *Acc. Chem. Res.* **2015**, *48*, 2632–2639. (c) Stoian, S. A.; Xue, G.; Bominaar, E. L.; Que, L., Jr.; Münck, E. *J. Am. Chem. Soc.* **2014**, *136*, 1545–1558. (d) Xue, G.; Geng, C.; Ye, S.; Fiedler, A. T.; Neese, F.; Que, L., Jr. *Inorg. Chem.* **2013**, *52*, 3976–3984. (e) Tinberg, C. E.; Lippard, S. J. *Acc. Chem. Res.* **2011**, *44*, 280–288.

- (5) (a) Sankaralingam, M.; Jeon, S. H.; Lee, Y.-M.; Seo, M. S.; Ohkubo, K.; Fukuzumi, S.; Nam, W. *Dalton Trans.* **2016**, *45*, 376–383. (b) Pal, S.; Olmstead, M. M.; Armstrong, W. H. *Inorg. Chem.* **1995**, *34*, 4708–4715. (c) Younker, J. M.; Krest, C. M.; Jiang, W.; Krebs, C.; Bollinger, J. M., Jr.; Green, M. T. *J. Am. Chem. Soc.* **2008**, *130*, 15022–15027.

- (7) Xue, G.; Wang, D.; De Hont, R.; Fiedler, A. T.; Shan, X.; Münck, E.; Que, L., Jr. *Proc. Natl. Acad. Sci. U. S. A.* **2007**, *104*, 20713–20718.

- (8) Netto, C. G. C. M.; Toma, H. E. *Eur. J. Inorg. Chem.* **2013**, *2013*, 5826–5830.

- (9) (a) Power, J. M.; Evertz, K.; Henling, L.; Marsh, R.; Schaefer, W. P.; Labinger, J. A.; Bercaw, J. E. *Inorg. Chem.* **1990**, *29*, 5058–5065. (b) Dengel, A. C.; El-Hendawy, A. M.; Griffith, W. P.; O'Mahoney, C. A.; Williams, D. J. *J. Chem. Soc., Dalton Trans.* **1990**, 737–742.

- (10) (a) Kuroiwa, K.; Yoshida, M.; Masaoka, S.; Kaneko, K.; Sakai, K.; Kimizuka, N. *Angew. Chem., Int. Ed.* **2012**, *51*, 656–659. (b) Liu, P. N.; Wen, T. B.; Ju, K. D.; Sung, H. H.-Y.; Williams, I. D.; Jia, G. *Organometallics* **2011**, *30*, 2571–2580. (c) Auzias, M.; Therrien, B.; Süß-Fink, G. *Inorg. Chem. Commun.* **2007**, *10*, 1239–1243. (d) Standfest-Hauser, C. M.; Schmid, R.; Kirchner, K.; Mereiter, K. *Monatsh. Chem.* **2004**, *135*, 911–917. (e) Svetlanova-Larsen, A.; Zoch, C. R.; Hubbard, J. L. *Organometallics* **1996**, *15*, 3076–3087. (f) Shapley, P. A.; Schwab, J. J.; Wilson, S. R. *J. Coord. Chem.* **1994**, *32*, 213–232.

- (11) Geilenkirchen, A.; Neubold, P.; Schneider, R.; Wieghardt, K.; Flörke, U.; Haupt, H.-J.; Nuber, B. *J. Chem. Soc., Dalton Trans.* **1994**, 457–464.

- (12) (a) Zhang, Q.-F.; Adams, R. D.; Leung, W.-H. *Inorg. Chim. Acta* **2006**, *359*, 978–983. (b) Kelson, E. P.; Henling, L. M.; Schaefer, W. P.; Labinger, J. A.; Bercaw, J. E. *Inorg. Chem.* **1993**, *32*, 2863–2873. (c) Carmona, D.; Mendoza, A.; Ferrer, J.; Lahoz, F. J.; Oro, L. A. *J. Organomet. Chem.* **1992**, *431*, 87–102. (d) Wieghardt, K.; Herrmann, W.; Köppen, M.; Jibril, I.; Huttner, G. *Z. Naturforsch., B: J. Chem. Sci.* **1984**, *39*, 1335–1343.

- (13) Matsuya, K.; Fukui, S.; Hoshino, Y.; Nagao, H. *Dalton Trans.* **2009**, 7876–7878.

- (14) Suzuki, T.; Matsuya, K.; Kawamoto, T.; Nagao, H. *Eur. J. Inorg. Chem.* **2014**, *2014*, 722–727.

- (15) *Mixed Valency Systems—Applications in Chemistry, Physics and Biology*; Prassides, K., Ed.; Kluwer Academic Publishers: Dordrecht, The Netherlands, 1991.

- (16) Slattery, S. J.; Blaho, J. K.; Lehnes, J.; Goldsby, K. A. *Coord. Chem. Rev.* **1998**, *174*, 391–416.

Inorganic Chemistry

A New Paddlewheel-Type Dirhodium-Based Metal-Organic Framework with Deprotonated 2,6-Bis(2-benzimidazolyl)pyridine

Natsumi Yano,^[a] Yusuke Kataoka,^{*[a]} Hidekazu Tanaka,^[a] Tatsuya Kawamoto,^[b] and Makoto Handa^{*[a]}

The reaction of $[\text{Rh}_2(\text{OAc})_4(\text{H}_2\text{O})_2]$ ($\text{OAc} = \text{acetate}$) and 2,6-bis(2-benzimidazolyl)pyridine (bzimpy2H) in EtOH affords two different crystals, orange-red chips (1) and purple blocks (2). Single crystal X-ray diffraction analyses revealed that complex 1 forms a porous two-dimensional framework constructed from $[\text{Rh}_2(\text{OAc})_4]$ and $[\text{Rh}(\text{bzimpyH})(\text{bzimpy})]$, whereas complex 2 forms a

bis-bzimpy2H-adducted discrete complex, $[\text{Rh}_2(\text{OAc})_4(\text{bzimpy2H})_2]$. Interestingly, the color of the crystalline powder of complex 1 changes from orange-red to yellow-brown immediately upon removal of guest solvents from the pores of complex, and dried complex 1 (yellow-brown state) can recover to its orange-red state by soaking in EtOH at room temperature.

Introduction

Considerable attention has been focused on the synthesis and characterization of paddlewheel-type dirhodium(II) tetracarboxylate complexes, $[\text{Rh}_2(\text{O}_2\text{CR})_4(\text{L})_2]$ ($\text{R} = \text{alkyl chain, aromatic ring, etc.}$, $\text{L} = \text{axially coordinated ligands}$),^[1] and their related complexes^[2] over the past forty years because of their intriguing electronic structures^[3] and applications, such as catalysis,^[4] chemical sensing,^[5] and antitumor agents.^[6] In recent years, the utilization of these complexes has expanded to "building blocks" and "corner connectors" for supramolecular complexes^[7] and polymeric complexes, such as one-dimensional (1D) coordination polymers (CPs)^[8] and two- or three-dimensional (2D or 3D) metal-organic frameworks (MOFs),^[9] because of the structural robustness conferred by the Rh–Rh single bond. One successful strategy for the synthesis of dirhodium-based polymeric complexes utilizes the two linear-coordinated sites of the Rh–Rh bond axis. This strategy affords the various series of 1D chain-type dirhodium-based CPs which are connected by bidentate organic or organometallic ligands. For example, the slow diffusion reactions of $[\text{Rh}_2(\text{O}_2\text{CR})_4(\text{L})_2]$ with bidentate linear N -donor organic ligands ($N \sim N$) such as pyrazine and 4,4'-bipyridine afford crystalline 1D chain-type CPs, $[\text{Rh}_2(\text{O}_2\text{CR})_4(N \sim N)]$, some of which have interesting gas and vapor adsorption properties at low temperature.^[10]

As mentioned above, although several examples of 1D chain-type CPs constructed from paddlewheel-type dirhodium units and $N \sim N$ ligands have already been reported and the knowledge of their synthesis is well established, examples of dirhodium-based polymeric complexes connected by V-shaped tridentate N -donor organic ligands, such as terpyridine (tpy) analogous ligands, are still extremely limited.^[11] Although tpy analogous ligands are geometrically flexible and potentially suitable as polydentate organic linkers for the synthesis of 2D or 3D MOFs, a previously reported dirhodium-based polymeric complex connected by a tpy analogous linker is only a quasi-1D CP^[11]; 2D or 3D dirhodium-based MOFs connected by tpy analogous linkers have never been reported. Therefore, our group has focused on the utilization of tpy analogous ligands as organic linkers for the dirhodium-based polymeric complexes to create the functional porous MOFs. During the development of this study, we incidentally discovered that the reaction of dirhodium tetraacetate (Figure 1(a)) and an imidazole-

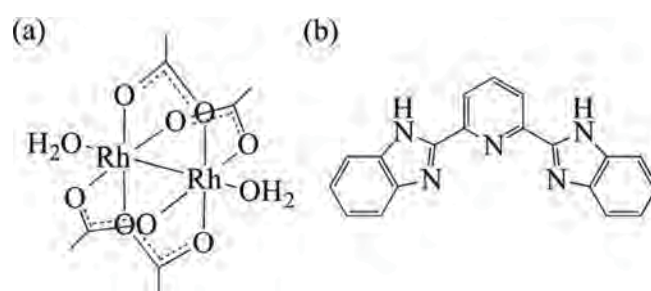


Figure 1. Molecular structures of (a) $[\text{Rh}_2(\text{OAc})_4(\text{H}_2\text{O})_2]$ and (b) bzimpy2H.

modified terpyridine analogous ligand, 2,6-bis(2-benzimidazolyl)pyridine (bzimpy2H; see Figure 1(b)), affords a 2D sheet structure; the sheets are closely self-assembled, with 1D pores.

[a] N. Yano, Dr. Y. Kataoka, Prof. H. Tanaka, Prof. M. Handa
Department of Chemistry, Interdisciplinary Graduate School of Science and Technology
Shimane University
1060 Nishikawatsu, Matsue, Shimane, 690–8504, Japan
E-mail: kataoka@riko.shimane-u.ac.jp

[b] Prof. T. Kawamoto
Department of Chemistry, Faculty of Science
Kanagawa University
2946 Tsuchiya, Hiratsuka, Kanagawa, 259–1293, Japan

Supporting information for this article is available on the WWW under <http://dx.doi.org/10.1002/slct.201600617>

In this study, we describe the synthesis and structural characterization of a new paddlewheel-type dirhodium-based MOF with coincidentally formed octahedral secondary building block [Rh(bzimpyH)(bzimpy)], which rhodium ion is coordinated by two deprotonated bzimpy2H, $\{[\text{Rh}_2(\text{OAc})_4]_3[\text{Rh}(\text{bzimpyH})(\text{bzimpy})]_2\}$ (complex 1; OAc = acetate). Discrete bis-bzimpy2H adducted dirhodium tetraacetate complex, $[\text{Rh}_2(\text{OAc})_4(\text{bzimpy}2\text{H})_2]$ (complex 2), which is a reasonable intermediate complex in the synthetic process of complex 1, is also isolated and structurally characterized. To the best of our knowledge, complex 1 is the first example of a 2D dirhodium-based MOF with an imidazole-modified tpy analogous ligand. Interestingly, complex 1 shows repetitive color-changing behavior depending on the presence of a guest solvent in the pores of complex 1; this is also an unprecedented behavior for a dirhodium-based polymeric complex.

Results and Discussion

Syntheses of complexes 1 and 2

A mixture of $[\text{Rh}_2(\text{OAc})_4(\text{H}_2\text{O})_2]$ (0.10 mmol) and bzimpy2H (0.10 mmol) in 4.0 mL EtOH was refluxed for 2 h under N_2 atmosphere, and the resulting reaction solution was left at room temperature for 6 days in the air. The small orange-red chip (complex 1) and purple block (complex 2) crystals were slowly grown from the brown-red solution and deposited on the bottom of the reaction vessel. The grown crystals were collected on a membrane filter and were washed with *N,N*-dimethylformamide (DMF) and tetrahydrofuran (THF) to remove soluble complex 2 and unreacted $[\text{Rh}_2(\text{OAc})_4(\text{H}_2\text{O})_2]$ and bzimpy2H. The residual orange-red crystals of complex 1 were dried under vacuum at 300 K for 3 h (Yield: 14.3% (9.9 mg)). We also observed that the room temperature reaction of $[\text{Rh}_2(\text{OAc})_4(\text{H}_2\text{O})_2]$ and bzimpy2H in EtOH only gave complex 2 in high yield (99.1%). This indicates that complex 2 is one of the intermediates to synthesize complex 1. It was noticed that (i) prolonging the reaction (reflux) time did not increase the yield of complex 1, giving the mixture of undesired rhodium colloid particles with the desired complex 1 and that (ii) when the reacting solution was left less than 6 days, the yield of complex 1 decreased to 2.6–7.9 mg (3.8%–11.4%); meanwhile, the yield of complex 1 did not increase when the reacting solution was left more than 6 days. Electrospray ionization mass spectrometry (ESI-MS) of the reaction solution exposed in the air shows the presence of the mononuclear rhodium(III) complex [Rh(bzimpyH)(bzimpy)] (Found: 723.1 m/z, Calcd.(M+H⁺): 723.1 m/z). This result indicated that the reaction solution oxidized by air-oxygen affords [Rh(bzimpyH)(bzimpy)], which is slowly connected to $[\text{Rh}_2(\text{OAc})_4]$ to form the complex 1. Although we attempted other reaction methods with various organic solvents, such as DMF and THF, the yield of complex 1 was not improved. From these results, we concluded that the present synthetic method of complex 1 is reasonable, although the yield is relatively low.

Crystal structures of complexes 1 and 2

Single-crystal X-ray diffraction analyses were carried out for the as-synthesized crystals of complexes 1 and 2, and their crystallographic data are summarized in Table S1. Complex 1 crystallizes in the triclinic space group *P*-1. Figure 2(a) and (b) show

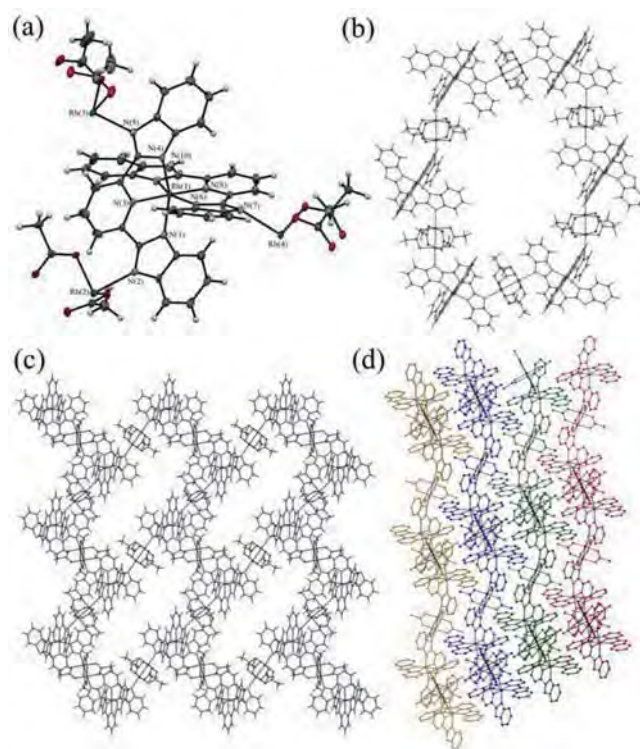


Figure 2. Crystal structures of complex 1; (a) asymmetric unit, (b) expand structure, (c) two-dimensional structure, and (d) packing structure of complex 1. In Figure 2 (a), the thermal ellipsoids are drawn at 20% probability level. In Figure 2 d), H atoms are omitted for clarify and different 2D sheet layers are classified.

the asymmetric unit and expanded structure of complex 1, respectively. As confirmed from Figure 2(a), the asymmetric unit of complex 1 contains three crystallographically independent halves of the $[\text{Rh}_2(\text{OAc})_4]$ units and one [Rh(bzimpyH)(bzimpy)] unit, which have singly and doubly deprotonated bzimpy2H ligands, i.e., bzimpyH and bzimpy ligands, respectively. The three deprotonated nitrogen atoms of the [Rh(bzimpyH)(bzimpy)] unit are all coordinated to the axial positions of three different $[\text{Rh}_2(\text{OAc})_4]$ units. That is, the two-axial positions of the $[\text{Rh}_2(\text{OAc})_4]$ units in complex 1 are occupied and utilized as a part of the connection with the [Rh(bzimpyH)(bzimpy)] units. Therefore, complex 1 forms an infinite polymeric structure. The average Rh–Rh and N–Rh₂ bond lengths in complex 1 are 2.412 Å and 2.283 Å, respectively, and are relatively long compared with those reported for dirhodium tetracarboxylate complexes with axial aromatic nitrogen donor ligands, such as $[\text{Rh}_2(\text{O}_2\text{CCMe}_3)_4(4,4'\text{-bipyridine})]$ (Rh–Rh: 2.395 Å, N–Rh₂: 2.245 Å).^[10a] These longer bond lengths are considered to be due to the

electron donating nature of the $[\text{Rh}(\text{bzimpyH})(\text{bzimpy})]$ moiety. The effects of the axial coordination on the equatorial Rh–O bonds in $[\text{Rh}_2(\text{OAc})_4]$ moieties are negligibly small, with average Rh–O bond lengths of 2.042 Å for complex **1** and 2.042 Å for $[\text{Rh}_2(\text{OAc})_4(\text{H}_2\text{O})_2]$. Although the X-ray analytical data shows no trace of a peak for the hydrogen atom belonging to a secondary amine group, the nitrogen moiety is deduced to be the secondary amine group when taking the C–N bond lengths and the total balance of the electronic charge into account, like the cases of the other reported metal complexes with bzimpyH ligands.^[12] The average C–N bond length in the deprotonated imidazole moieties in the bzimpyH and bzimpy ligands is 1.369 Å, similar to that of the protonated imidazole group in the bzimpyH ligand (1.365 Å), indicating that electrons in the bzimpyH and bzimpy ligands are not localized in a specific part of imidazole moiety.^[12] That is, it is assumed that the N(10) atom in the bzimpyH ligand is not deprotonated. As depicted in Figure 2 (c), the expanded structure of complex **1** forms two-dimensional (2D) sheets with ca. $19.4 \times 11.9 \text{ \AA}^2$ pores that are constructed from six $[\text{Rh}_2(\text{OAc})_4]$ and six $[\text{Rh}(\text{bzimpyH})(\text{bzimpy})]$ units (see Figure 2(b)). These 2D sheets are non-interpenetrating and self-assemble with an A–A packing pattern (see Figure 2(d)). The hydrogen atoms of the secondary amine group in the bzimpyH ligands are located in the direction of the pore wall of complex **1**. Since the guest solvents in complex **1** could not be structurally determined because of their disorders, the final structure model of complex **1** was refined without residual electron density of guest solvents using the PLATON program (the final R_1 and wR_2 [$I > 2\sigma$] values were 6.82 and 16.80%, respectively).^[13] The estimated solvent-accessible void volume and residual electron count per unit cell of complex **1** by using the PLATON SQUEEZE program are 1480.0 \AA^3 and $116.4 e^-$, respectively. From the total volume of complex **1** (3678.4 \AA^3), the effective pore volume of complex **1** is estimated to be 40.2%.

Complex **2** crystallizes in the monoclinic space group $P2_1/c$ with an asymmetric unit containing a half of the $[\text{Rh}_2(\text{OAc})_4]$ unit and one bzimpy2H ligand. As depicted in Figure 3, the

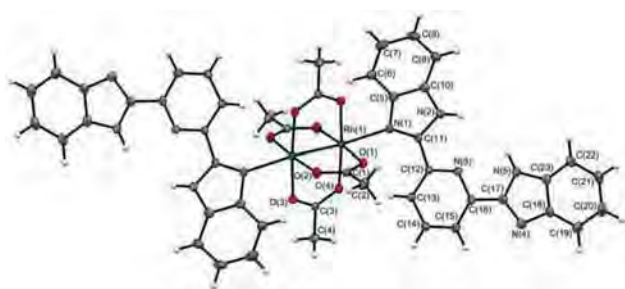


Figure 3. Crystal structures of complex **2**. Here, the thermal ellipsoids are drawn at 30% probability levels. (a) $[\text{Rh}_2(\text{OAc})_4(\text{H}_2\text{O})_2]$ and (b) bzimpy2H.

overall structure of complex **2** is a typical discrete paddlewheel-type dinuclear structure wherein two bzimpy2H ligands are co-

ordinated to the axial sites of the $[\text{Rh}_2(\text{OAc})_4]$ unit, having the crystallographic inversion center in the midpoint of the Rh–Rh bond. The Rh–Rh bond length (2.403 Å) of complex **2** is slightly shorter than that of complex **1**, whereas the N–Rh₂ bond length (2.306 Å) is slightly longer. This is because the electron-donating nature of $[\text{Rh}(\text{bzimpyH})(\text{bzimpy})]$ in complex **1** is stronger than that of bzimpy2H in complex **2**, coming from the electron-rich bzimpyH and bzimpy ligands. The C–N bond lengths in the secondary amine groups of the bzimpy2H ligands in complex **2** are in the region from 1.358 Å to 1.378 Å, which is similar to those of the secondary amine groups of the bzimpyH ligand in complex **1**.

Absorption spectral features of complexes **1** and **2**

As depicted in Figure 4(a), the color of the crystalline powder of complex **1** immediately changed from orange-red to yellow-

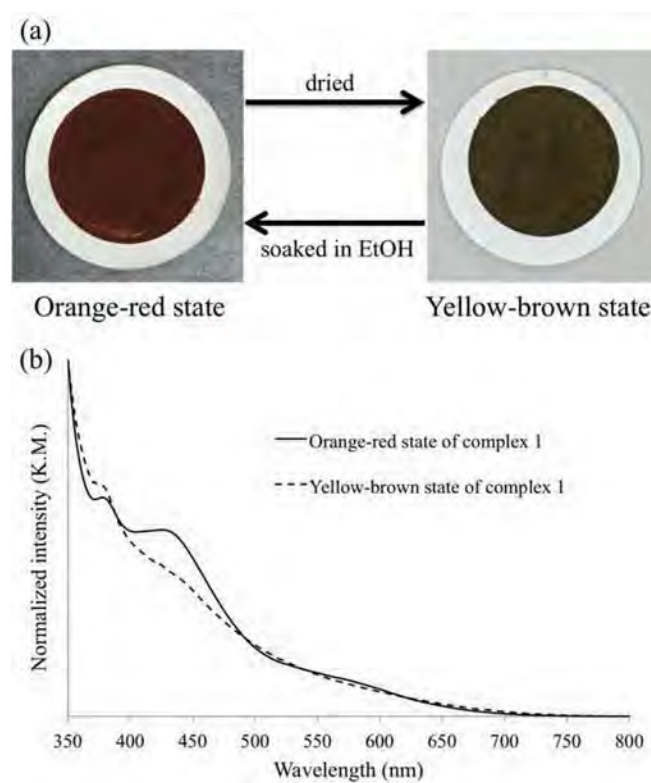


Figure 4. (a) Pictures of orange-red and brown-yellow states of complex **1**. (b) Solid-state absorption spectra of orange-red and brown-yellow states of complex **1**.

brown when the crystal solvents or washing solvents, i.e., DMF and THF, were removed from the complex **1**. Interestingly, the yellow-brown state of complex **1** is easily recovered to the orange-red state by soaking in the EtOH at room temperature. This interconversion between the yellow-brown and orange-red states of complex **1** is repeatable. Figure 4(b) shows the solid-state absorption spectra (transmission spectra with liquid paraffin) of yellow-brown and orange-red states of complex **1**.

In the orange-red state of complex **1**, absorption bands observed at 430 and 380 nm are ascribed to the metal-to-ligand charge transfer (MLCT) mixed with $\pi(\text{bzimpyH}) \rightarrow \pi^*(\text{bzimpyH})$ and $\sigma(\text{Rh}_2) \rightarrow \sigma^*(\text{Rh}_2)$ excitations, respectively. The shoulder band, assigned as $\pi^*(\text{Rh}_2) \rightarrow \sigma^*(\text{Rh}_2)$, is also observed in the region from 550 to 680 nm. On the contrary, in the yellow-brown state of complex **1**, although a lower absorption band (380 nm) and broad shoulder band were clearly observed, the absorption band around 430 nm is notably decreased compared with that of orange-red state of complex **1**. We speculated that this absorption spectral change between yellow-brown and orange-red states of complex **1** originated from both (i) collapse of the framework structure of complex **1** due to the removal of guest solvents from the pores of complex **1** and (ii) break-down of the hydrogen-bonding interaction between the secondary amine group in the bzimpyH ligand (host) of complex **1** and EtOH or H₂O in the guest spaces. Similar hydrogen-bonding interaction-induced color-changing behavior of an imidazole-based Zn-MOF was recently reported in the literature.^[14]

Characterizations of complexes **1** and **2**

The infrared spectra of dried complexes **1** and **2** show weak N–H vibrations at 3186 and 3229 cm⁻¹, respectively. The values of the symmetric ($\nu_{\text{sym}}(\text{COO}^-)$) and asymmetric stretching modes ($\nu_{\text{asym}}(\text{COO}^-)$) of the bridging carboxylates and their separation, i.e., $\Delta\nu(\text{COO}^-) = \nu_{\text{asym}}(\text{COO}^-) - \nu_{\text{sym}}(\text{COO}^-)$, of complex **1** are 1434, 1588, and 154 cm⁻¹, respectively. These values are similar not only to those of complex **2** ($\nu_{\text{sym}}(\text{COO}^-) = 1438$ cm⁻¹, $\nu_{\text{asym}}(\text{COO}^-) = 1591$ cm⁻¹, and $\Delta\nu(\text{COO}^-) = 153$ cm⁻¹) but also those of $[\text{Rh}_2(\text{OAc})_4(\text{H}_2\text{O})_2]$ ($\nu_{\text{sym}}(\text{COO}^-) = 1437$ cm⁻¹, $\nu_{\text{asym}}(\text{COO}^-) = 1587$ cm⁻¹, and $\Delta\nu(\text{COO}^-) = 150$ cm⁻¹).

Finally, to clarify the porosity and framework stability of dried complex **1**, N₂ gas adsorption at 77 K and X-ray diffraction (XRD) analyses were performed. Figure S1 in the ESI shows the N₂ adsorption isotherms of complex **1**. The obtained isotherm, which has no significant micropore-filling at very low relative pressure (P/P_0) and slight surface adsorption in the region of $0.03 < P/P_0 < 0.3$, is classified as IUPAC type II, which is commonly observed as physical adsorption by non-porous materials. The calculated BET surface area of dried complex **1** is only 37.9 m²/g. This result indicated that the structural framework and significant porosity of dried complex **1** are collapsed by removing the crystalline solvents from the guest spaces of complex **1**. This is supported by X-ray diffraction analyses of dried complex **1** (XRD analyses in this study were performed with paraffin oil because the obtained amount of complex **1** is very small; thus, only relatively low diffraction angles are measured and discussed to avoid the intense broad diffraction of paraffin oil); the observed XRD pattern of yellow-brown state of complex **1** is considerably different from the simulated pattern of the crystal structure of complex **1**, whereas the XRD patterns of two orange-red states, i.e., as-synthesized and recovered states, of complex **1** are similar to the simulated pattern of the crystal structure of complex **1** (see Figure 5).

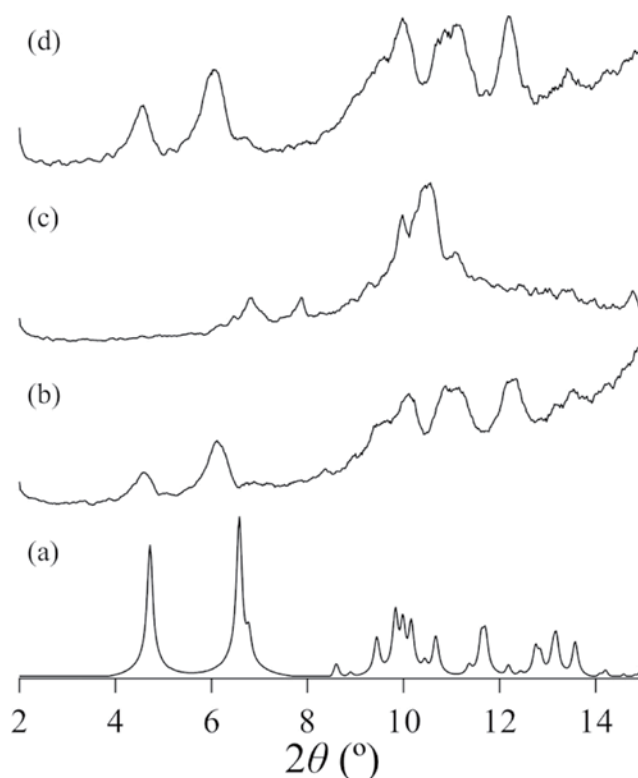


Figure 5. Simulated and observed XRD patterns of complex **1**; (a) simulated pattern based on single-crystal structure, (b) as-synthesized state, (c) dried state, and (d) recovered state of complex **1**. (XRD analyses in this study were performed with paraffin oil because the obtained amount of complex **1** is very small; thus, only relatively low diffraction angles are measured and discussed to avoid the intense broad diffraction of paraffin oil.)

Conclusions

In this study, a new 2D MOF $\{[\text{Rh}_2(\text{OAc})_4]_3[\text{Rh}(\text{bzimpyH})(\text{bzimpy})]_2\}$ (complex **1**) was synthesized by the reaction of $[\text{Rh}_2(\text{OAc})_4(\text{H}_2\text{O})_2]$ and bzimpy2H. ESI-MS revealed that although $[\text{Rh}(\text{bzimpyH})(\text{bzimpy})]$ is generated in the reaction solution (EtOH) immediately after the reaction by refluxing, the formation of the structural framework of complex **1** proceeds slowly at room temperature. Single crystal X-ray structure analyses revealed that complex **1** and **2** form self-assembly 2D sheet structures with 1D pores and discrete bis-bzimpy2H adducted dirhodium complex, respectively. We also confirmed that complex **2** is easily and rapidly formed by the room temperature reaction of $[\text{Rh}_2(\text{OAc})_4]$ and bzimpy2H. The proposed mechanism of formation of complex **1** is as shown in Figure 6.

In addition, the color of the crystalline powder of complex **1** changed from orange-red to yellow-brown immediately after guest solvents were removed from the pores of complex **1**. XRD analyses revealed that this color-changing behavior of complex **1** originates from both (i) the collapse of the framework structure of complex **1** due to the removal of guest solvents from the pores of complex **1** and (ii) the break-down of the hydrogen-bonding interaction between the secondary amine group in the bzimpyH ligand (host) of complex **1** and EtOH or H₂O in the guest spaces. Interestingly, the structural

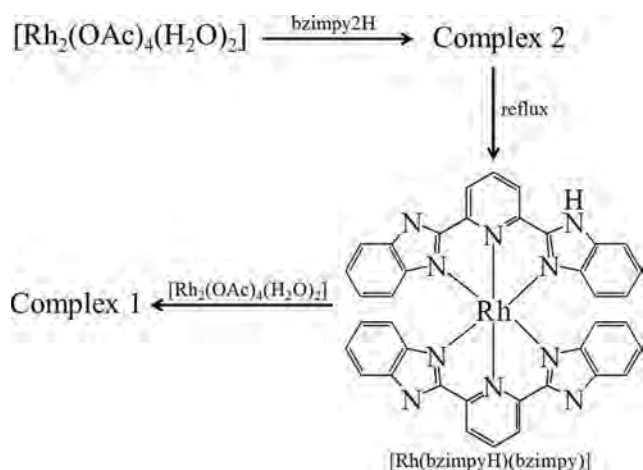


Figure 6. Deduced synthetic mechanism of complex 1.

changes between the orange-red and yellow-brown states of complex 1 are repeatable. Although the color-changing behaviors, i.e., chromism behaviors, of discrete paddlewheel-type dirhodium complexes are well known, those of a dirhodium-based polymeric structure have been never reported. Therefore, this is the first example of a polymeric complex with paddlewheel-type dirhodium-unit showing chromism behavior.

Supporting Information

Experimental details, crystallographic data of complexes 1 and 2, N_2 adsorption isotherm of complex 1, and CIF files of complexes 1 and 2 can be found in the Supporting Information available online.

Acknowledgements

This work has been supported by Grant-in-Aid for Scientific Research (Nos. 15 K17897, 15H00877, 25620145) and the Strategic Research Base Development Program for Private University of the Ministry of Education, Culture, Sports and Technology (MEXT), Japan. Y.K. acknowledges the JAPAN PRIZE Foundation, and the Electronic Technology Research Foundation of Chugoku. The authors are grateful to Ms. Michiko Egawa (Shimane University) for her measurements of elemental analysis and Dr. Mikio Yamasaki (Rigaku Co.) for helpful comments about the refinement of single crystal X-ray structure analysis.

Keywords: Paddlewheel-type Dirhodium Complex · Metal-Organic Framework · Color Changing Behavior · Crystal Structures

- [1] a) F.A. Cotton, B.G. Deboer, M.D. LaPrade, J.R. Pipal, D.A. Ucko, *Acta Crystallogr. Sect. B*, **1971**, 27, 1664–1671; b) T.R. Felthouse, in *Progress in In-*

organic Chemistry, Volume 29, (Eds.: S.J. Lippard), John Wiley & Sons, Inc., Hoboken, 1982, pp. 73–166; c) H.T. Chifotides, K.R. Dunber, in *Multiple Bonds between Metal Atoms*, third ed., (Eds.: F.A. Cotton, C.A. Murillo, R.A. Walton), Springer Science and Business Media, New York, 2005, pp. 465–589.

- [2] a) T.P. Zhu, M.Q. Ahsan, T. Malinski, K.M. Kadish, J.L. Bear, *Inorg. Chem.* **1984**, 23, 3–10; b) J.L. Bear, C.L. Yao, R.S. Lifsey, J.D. Korp, K.M. Kadish, *Inorg. Chem.* **1991**, 30, 336–340; c) Y. Kataoka, N. Yano, T. Kawamoto, M. Handa, *Eur. J. Inorg. Chem.* **2015**, 34, 5650–5655; d) C.A. Crawford, J.H. Matonic, J.H. Huffman, K. Foltling, K.R. Dunber, G. Christou, *Inorg. Chem.* **1997**, 36, 2361–2371.
- [3] a) J.G. Norman Jr, H.J. Kolari, *J. Am. Chem. Soc.* **1978**, 100, 791–799; b) Y. Kataoka, Y. Kitagawa, T. Saito, Y. Nakanishi, T. Matsui, K. Sato, Y. Miyazaki, T. Kawakami, M. Okumura, W. Mori, K. Yamaguchi, *Bull. Chem. Soc. Jpn.* **2010**, 83, 1481–1488.
- [4] a) J. Hansen, H.M.L. Davies, *Coord. Chem. Rev.* **2008**, 252, 545–555; b) M.P. Doyle, *J. Org. Chem.* **2006**, 71, 9253–9260; c) Y. Kataoka, K. Sato, Y. Miyazaki, Y. Suzuki, H. Tanaka, Y. Kitagawa, T. Kawakami, M. Okumura, W. Mori, *Chem. Lett.* **2010**, 39, 358–359.
- [5] a) S.A. Hilderbrand, M.H. Lim, S.J. Lippard, *J. Am. Chem. Soc.* **2004**, 126, 4972–4978; b) M.E. Moragues, J. Esteban, J.V. Ros-Lis, R. Martinez-Manez, M.D. Marcos, M. Martinez, J. Soto, F. Sancenon, *J. Am. Chem. Soc.* **2011**, 133, 15762–15772; c) S.L. Schiavo, P. Cardiano, N. Donato, M. Latino, G. Neri, *J. Mater. Chem.* **2011**, 21, 18034–18041.
- [6] a) R.A. Howard, T.G. Spring, J.L. Bear, *Cancer Res.* **1976**, 36, 4402–4405; b) H.T. Chifotides, K.R. Dunber, *Acc. Chem. Res.* **2005**, 38, 146–156; c) A.M. Angeles-Boza, H.T. Chifotides, J.D. Aguirre, A. Chouai, P.K.-L. Fu, K.R. Dunber, C. Turro, *J. Med. Chem.* **2006**, 49, 6841–6847.
- [7] a) R.P. Bonar-Law, T.D. McGrath, N. Singh, J.F. Bickley, A. Steiner, *Chem. Commun.* **1999**, 24, 2457–2458; b) M.W. Cooke, G.S. Hanan, F. Loiseau, S. Campagna, M. Watanabe, Y. Tanaka, *Angew. Chem. Int. Ed.* **2005**, 44, 4881–4884; c) F.A. Cotton, C.A. Murillo, S.-E. Stiriba, X. Wang, R. Yu, *Inorg. Chem.* **2005**, 44, 8223–8233.
- [8] a) M. Handa, T. Nakao, M. Mikuriya, T. Kotera, R. Nukada, K. Kasuga, *Inorg. Chem.* **1998**, 37, 149–152; b) F.A. Cotton, E.V. Dikarev, M.A. Petrukina, S.-E. Stiriba, *Polyhedron* **2000**, 19, 1829–1835; c) C.T. Chapman, A.M. Goforth, N.G. Pschier, M.D. Smith, U.H.F. Bunz, H.-C.Z. Loye, *J. Chem. Crystallogr.* **2003**, 33, 885–890; d) K. Uemura, M. Ebihara, *Inorg. Chem.* **2011**, 50, 7919–7921; e) P. Amo-Ochoa, S. Delgado, A. Gallego, C.J. Gomez-Garcia, R. Jimenez-Aparicio, G. Martinez, J. Perles, M.R. Torres, *Inorg. Chem.* **2012**, 51, 5844–5849.
- [9] a) S. Naito, T. Tanibe, E. Saito, T. Miyao, W. Mori, *Chem. Lett.* **2001**, 30, 1178–1179; b) T. Sato, W. Mori, C.N. Kato, E. Yanaoka, T. Kuribayashi, R. Ohtera, Y. Shiraishi, *J. Catal.* **2005**, 232, 186–198; c) G. Nickerl, U. Stoeck, U. burkhardt, I. Senkovska, S. Kaskel, *J. Mater. Chem. A* **2014**, 2, 144–148; d) Y. Kataoka, K.S. Kataoka, H. Murata, M. Handa, W. Mori, T. Kawamoto, *Inorg. Chem. Commun.* in press.
- [10] a) M. Handa, M. Watanabe, D. Yoshioka, S. Kawabata, R. Nukada, M. Mikuriya, H. Azuma, K. Kasuga, *Bull. Chem. Soc. Jpn.* **1999**, 72, 2681–2686; b) W. Mori, H. Hoshino, Y. Nishimoto, S. Takamizawa, *Chem. Lett.* **1999**, 28, 331–332; c) S. Takamizawa, E. Nakata, H. Yokoyama, K. Mochizuki, W. Mori, *Angew. Chem. Int. Ed.* **2003**, 42, 4331–4334; d) S. Takamizawa, C. K.-Terajima, M. Kohbara, T. Akatsuka, T. Jin, *Chem. Asian. J.* **2007**, 2, 837–848.
- [11] Y. Kataoka, N. Yano, T. Shimodaira, Y.-N. Yan, M. Yamasaki, H. Tanaka, K. Omata, T. Kawamoto, M. Handa, *Eur. J. Inorg. Chem.* in press.
- [12] M. Boca, R.F. Jameson, W. Linert, *Coord. Chem. Rev.* **2011**, 255, 290–317.
- [13] A.L. Spek, *Acta Cryst. D* **2009**, 65, 148–155.
- [14] Y. Yu, J.-P. Ma, C.-W. Zhao, J. Yang, Z.-M. Zhang, Q.-K. Liu, Y.-B. Dong, *Inorg. Chem.* **2015**, 54, 11590–11592.

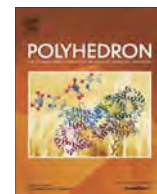
Submitted: May 27, 2016

Accepted: June 1, 2016



Contents lists available at ScienceDirect

Polyhedron

journal homepage: www.elsevier.com/locate/poly

A neutral paddlewheel-type diruthenium(III) complex with benzamidinato ligands: Synthesis, crystal structure, magnetism, and electrochemical and absorption properties

Yusuke Kataoka^{a,*}, Saki Mikami^a, Hiroshi Sakiyama^b, Minoru Mitsumi^c, Tatsuya Kawamoto^d, Makoto Handa^{a,*}

^a Department of Chemistry, Interdisciplinary Graduate School of Science and Engineering, Shimane University, 1060 Nishikawatsu, Matsue, Shimane 690-8504, Japan

^b Department of Material and Biological Chemistry, Faculty of Science, Yamagata University, Kojirakawa, Yamagata 990-8560, Japan

^c Department of Chemistry, Faculty of Science, Okayama University of Science, 1-1 Ridaicho, Kita-ku, Okayama 700-005, Japan

^d Department of Chemistry, Faculty of Science, Kanagawa University, 2946 Tsuchiya, Hiratsuka, Kanagawa 259-1293, Japan

ARTICLE INFO

Article history:

Received 29 December 2016

Accepted 6 March 2017

Available online xxxxx

Keywords:

Diruthenium complex

Paddlewheel-type structure

Electronic structure

Magnetic property

DFT calculation

ABSTRACT

A new neutral diruthenium(III) complex coordinated with benzamidinato (bam) ligands, $[\text{Ru}_2(\text{bam})_4\text{Cl}_2]\cdot\text{H}_2\text{O}$ (**1**), was synthesized and characterized, and its electronic structure was closely investigated via magnetic susceptibility, absorption spectrum, cyclic voltammetry, and density functional theory (DFT) calculations. Single crystal X-ray diffraction analysis revealed that complex **1** has a typical paddlewheel-type structure with a Ru–Ru bond (bond length: 2.342(1) Å), in which the diruthenium (Ru_2) core is coordinated by four equatorially μ -bridging bam ligands and two axial Cl^- ions. The magnetic study and DFT calculations proved that complex **1** has a triplet spin state ($S = 1$) and a unique electronic structure ($\pi^4\delta^2\pi^2\sigma^2$). Absorption spectral feature and electrochemical property of complex **1** were also carefully investigated both experimentally and theoretically in this study.

© 2017 Elsevier Ltd. All rights reserved.

1. Introduction

In the past few decades, the paddlewheel-type diruthenium (Ru_2) complexes have become one of the most extensively investigated families of dinuclear complexes with multiple metal–metal bonding [1–10]. This type of Ru_2 complexes generally show unique electronic structures with degenerate molecular orbitals (MOs) [11,12] and display unique redox [13,14], spectroscopic [15], magnetic [16,17], and catalytic characteristics [18,19]. Recently, the paddlewheel-type Ru_2 units have also been employed as robust paramagnetic building blocks for the supramolecular complexes [20,21], coordination polymers [22,23], and porous metal-organic frameworks [24,25]. It is well known that the paddlewheel-type Ru_2 complexes typically take three different paramagnetic oxidation states: $\text{Ru(II)}\text{--}\text{Ru(II)}$, $\text{Ru(II)}\text{--}\text{Ru(III)}$, and $\text{Ru(III)}\text{--}\text{Ru(III)}$. However, the most reported species is the mixed-valent $\text{Ru(II)}\text{--}\text{Ru(III)}$ oxidation state with a spin state (S) of 3/2, because it is thermodynamically preferred and highly stable in air when normally used bidentate ligands such as carboxylate ions bridge the Ru metals.

The electronic structure and magnetic and redox properties of Ru_2 complexes with $\text{Ru(II)}\text{--}\text{Ru(III)}$ oxidation state have been well investigated so far and already reviewed in the literatures by few groups [1,26–28]. In addition, study of Ru_2 complexes with the $\text{Ru(II)}\text{--}\text{Ru(II)}$ oxidation state has also progressed well recently because of their strong electron-donating properties, oxidation reactivity, and interesting magnetic properties [29–31]. In contrast, the electronic structure and chemical and physical properties of Ru_2 complexes with the $\text{Ru(III)}\text{--}\text{Ru(III)}$ oxidation state [1,32–34], which are still a rare species, are not yet sufficiently understood and established.

Among the various types of bridging organic ligands already utilized for the synthesis of paddlewheel-type Ru_2 complexes, amidinate is considered to be a suitable ligand because of the formation of a robust Ru_2 complex due to the strong Ru–N bond. However, the oxidation states and electronic structures of the Ru_2 complex with amidinate ligands are not sufficiently clear yet; they easily change depending on the Ph- and H-substituted positions in the amidinate ligands, as depicted in Fig. 1. In concrete terms, it is known that the Ru_2 complex coordinated with *N,N*-diphenylformamidinate (dpf), $[\text{Ru}_2(\text{dpf})_4\text{Cl}]$, has the $\text{Ru(II)}\text{--}\text{Ru(III)}$ oxidation state with $S = 3/2$ [35], while the Ru_2 complex coordinated with *N,N*-dimethylbenzamidinate (dmba), $[\text{Ru}_2(\text{dmba})_4\text{Cl}_2]$, has the Ru

* Corresponding authors.

E-mail addresses: kataoka@riko.shimane-u.ac.jp (Y. Kataoka), handam@riko.shimane-u.ac.jp (M. Handa).

<http://dx.doi.org/10.1016/j.poly.2017.03.005>

0277-5387/© 2017 Elsevier Ltd. All rights reserved.

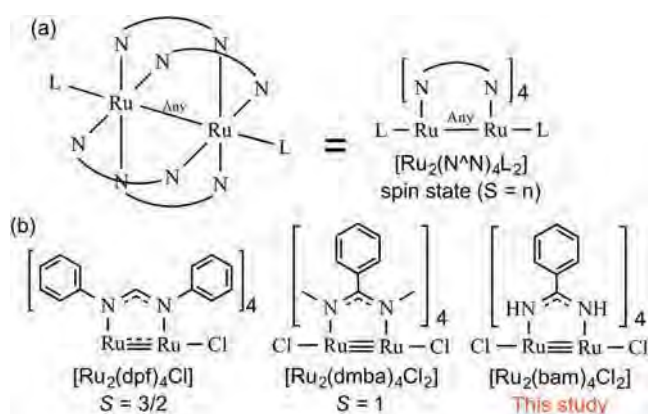


Fig. 1. Schematic representation for (a) simplified molecular geometry of diruthenium complex, $[\text{Ru}_2(\text{N}^{\wedge}\text{N})_4\text{L}_2]$, where $\text{N}^{\wedge}\text{N}$ and L are bridging amidinate and axial halogen ions, respectively and (b) simplified molecular geometries and their thermodynamically preferred spin state (S) of $[\text{Ru}_2(\text{dpf})_4\text{Cl}]$, $[\text{Ru}_2(\text{dmmba})_4\text{Cl}_2]$, and $[\text{Ru}_2(\text{bam})_4\text{Cl}_2]$ (complex **1**).

(III)–Ru(III) oxidation state with $S = 1$ [36]. For a deeper understanding of the relationship between the substitution position in amidinate ligands and the oxidation state (electronic structure) of the Ru_2 complexes with amidinate ligands, the study of the electronic structure and oxidation state of the Ru_2 complex coordinated with benzamidinate (bam) is indispensable.

Herein, we describe the detailed synthesis and characterization of the paddlewheel-type Ru_2 complex with bam ligands, $[\text{Ru}_2(\text{bam})_4\text{Cl}_2] \cdot \text{H}_2\text{O}$ (**1**). To determine the oxidation state and electronic structure of complex **1**, variable-temperature magnetic susceptibility measurement study and density functional theory (DFT) calculations were performed. In addition, the redox and spectroscopic properties of complex **1** were carefully investigated, both experimentally and theoretically, in this study.

2. Experimental

2.1. Materials and instruments

All the chemicals and reagents were purchased from commercial sources and used without further purification. $[\text{Ru}_2(\text{O}_2\text{CCH}_3)_4\text{Cl}]$ was prepared according to a previously reported method with slight modifications [2]. Elemental analyses for carbon, hydrogen, and nitrogen were conducted using a Yanaco CHN CORDER MT-6 installed at Shimane University, Japan. The fourier transform infrared (FT-IR) spectrum was measured using a JASCO FT-IR 660-plus spectrometer in KBr disks at room temperature. Electrospray ionization mass spectrometry (ESI-MS) was conducted using a Bruker micro-TOF analyzer. Variable-temperature magnetic susceptibility measurement was carried out using a superconducting quantum interference device (SQUID) MPMS XL-5 from Quantum Design installed at Okayama University of Science, Japan. UV-Vis absorption spectrum was measured in CHCl_3 using a JASCO V-670 spectrometer. Cyclic voltammetry (CV) was measured in dried CHCl_3 containing tetra-*n*-butylammonium hexafluorophosphate (TBAPF_6) as an electrolyte using BAS ALS-DY 2325 Electrochemical Analyzer. A glassy carbon disk (1.5 mm radius), Pt wire, and saturated calomel electrode (SCE) were used as the working, counter, and reference electrodes, respectively.

2.2. Synthesis of $[\text{Ru}_2(\text{bam})_4\text{Cl}_2] \cdot \text{H}_2\text{O}$ (**1**)

A 20.0 mL aqueous solution of $[\text{Ru}_2(\text{O}_2\text{CCH}_3)_4\text{Cl}]$ (0.50 mmol, 236.7 mg) was mixed with a 30.0 mL aqueous solution containing

benzamidinate hydrochloride (Hbam-HCl: 25.0 mmol, 200.6 mg) and NaOH (5.0 mmol, 3915.2 mg) at room temperature, and the resulting solution was refluxed at 373 K under N_2 atmosphere for 2 days. The precipitated green crude solid was collected by filtration and dried under vacuum at 343 K. The dried crude powder was then purified by column chromatography on silica gel (Wako gel, Wako Pure Chemical Industries Ltd.) with $\text{CH}_3\text{Cl}-\text{CH}_3\text{OH}$ (19:1) as an eluent. The reddish-brown band was collected and evaporated to dryness. The resulting residue was collected on a membrane filter, washed with diethylether, and dried at 343 K for 6 h to give a black powder of complex **1**. The obtained yield was 83.4 mg (21.7%). *Anal. Calc.* for $\text{Ru}_2\text{H}_{30}\text{C}_{28}\text{N}_8\text{Cl}_2\text{O}$: C, 43.81; H, 3.94; N, 14.60. *Found*: C, 43.80; H, 3.93; N, 14.46%. IR (KBr pellet, cm^{-1}): 3447 (m), 3365 (s), 3278 (m), 2925 (vw), 1636 (vw), 1513 (vs), 1470 (vs), 1290 (w), 1259 (m), 1029 (vw), 785 (vw), 699 (s), 676 (s), 530 (m). ESI-MS: *Calcd.* for $[\text{M}-\text{Cl}]^+$ 715.0207 *m/z*; *found* 715.0212 *m/z*.

2.3. Single crystal X-ray diffraction analyses

X-ray diffraction data of complex **1** was collected at 150 K on a RIGAKU Saturn 724 CCD system equipped with Mo rotating-anode X-ray generator with Monochromated Mo $K\alpha$ radiation ($\lambda = 0.71075 \text{ \AA}$) installed in Kanagawa university and were processed with using CrystalClear program (RIGAKU). The structure of complex **1** was solvated by direct method (SIR-2004) and refined using the full-matrix least-squares technique F^2 with SHELXL2014 equipped in the CrystalStructure 4.2.1 software (RIGAKU). Non-hydrogen atoms were refined with anisotropic displacement and almost all of hydrogen atoms were located at the calculated positions and refined as riding models. The residual electron density in the void spaces of final refined structure of complex **1** was evaluated using PALTON SQUEEZE program. Crystal data as well as the details of data collection and refinement for complex **1** is summarized in Table 1 and is obtained as CIF file from Cambridge Crystallographic Data Center (CCDC). Deposition numbers of complex **1** is CCDC-1523719.

2.4. Details of DFT calculations

All the DFT calculations were performed using the GAUSSIAN 09 C.01 program package [37]. The hybrid DFT functional method, B3LYP, with the Los Alamos effective core potential (ECP) basis set, LANL2DZ, for Ru atoms and the double zeta polarized basis set, 6-31G*, for the other atoms. In this study, we used the unrestricted broken-symmetry approach for determining the

Table 1
Crystallographic data for complex **1**.

Crystal size (mm^3)	$0.05 \times 0.05 \times 0.02$
Chemical formula	$\text{C}_{28}\text{H}_{28}\text{Cl}_2\text{N}_8\text{Ru}_2$
T (K)	150
Formula weight (g/mol)	749.63
Crystal system	triclinic
Space group	$P\bar{1}$
a (\AA)	8.476(3)
b (\AA)	10.600(3)
c (\AA)	10.735(4)
α ($^\circ$)	74.805(13)
β ($^\circ$)	81.287(15)
γ ($^\circ$)	70.549(15)
V (\AA^3)	875.4(5)
Z	1
D_{calc} (g cm^{-3})	1.422
$F(000)$	374
Final R_1 indices [$I > 2\sigma(I)$]	$R_1 = 0.0232$, $wR_2 = 0.0616$
R indices (all data)	$R_1 = 0.0266$, $wR_2 = 0.0631$
Goodness of fit (GOF) on F^2	1.115

open-shell electronic structure of complex **1**. The solvent effect of CHCl_3 was considered by the polarizable continuum model. Full geometry optimization without symmetry constraints was performed in CHCl_3 , and the resulting geometry was confirmed to be a potential energy minimum by vibrational frequency analysis (no imaginary frequencies were observed). The spin-allowed excitations were calculated by the time-dependent DFT (TDDFT) method.

3. Results and discussion

3.1. Synthesis and characterization of complex **1**

Complex **1** was prepared by the general ligand-exchange reaction between $[\text{Ru}_2(\text{O}_2\text{CCH}_3)_4\text{Cl}]$ and 50 times excess of Hbam-HCl in NaOH aqueous solution. Here, the pH of the reaction solution was increased from 5.86 to 11.10 by adding NaOH. Thus, in this reaction, NaOH served as a reagent for both increasing the pH and deprotonating Hbam. By purifying the reaction crude products via silica-gel column chromatography, the pure form of complex **1** was obtained as a black powder with 21.7% yield. It was noticed that (i) the reaction of $[\text{Ru}_2(\text{O}_2\text{CCH}_3)_4\text{Cl}]$ and Hbam-HCl in an aqueous solution without NaOH did not occur because of the low reactivity of Hbam, and (ii) although we altered the reaction conditions for the synthesis by prolonging the reflux time and increasing the concentration of NaOH, the final yields of complex **1** did not increase. Therefore, we concluded that the present synthetic method should be a reasonable scheme for the synthesis of complex **1**.

The obtained powder of complex **1** was characterized by ESI-MS, elemental analysis, and infrared spectroscopy. In the ESI-MS with positive ion mode, an intense signal was detected at 715.0212 m/z , which was consistent with the theoretical value of $[\text{Ru}_2(\text{bam})_4\text{Cl}]^+$ ($[\text{M}-\text{Cl}]^+$: 715.0217 m/z). As shown in Fig. S1 in electronic supplementary data (SD), the signals observed around 715.0212 m/z , i.e., the isotropic signals of $[\text{Ru}_2(\text{bam})_4\text{Cl}]^+$, agreed well with those of the simulated signal pattern of $[\text{Ru}_2(\text{bam})_4\text{Cl}]^+$. The purity of complex **1** was assessed by elemental analysis; the observed CHN ratios of complex **1** were in good agreement with the calculated values of $[\text{Ru}_2(\text{bam})_4\text{Cl}_2] \cdot \text{H}_2\text{O}$. The FT-IR spectral data for complex **1** clearly indicated the presence of the bridging C=N moieties with $\nu(\text{C}=\text{N})$ vibrations at 1636, 1513, and 1470 cm^{-1} (see Fig. S2 in SD). In addition, the N-H vibration frequency of the bam ligands appeared sharply at 3365 cm^{-1} .

3.2. Crystal structure of complex **1**

Single crystal X-ray diffraction analysis was carried out for a single crystal of complex **1**, which was obtained by recrystallization from a MeOH/ H_2O / CHCl_3 mixed solution. The crystallographic data of complex **1** are summarized in Table 1, the selected structural parameters of complex **1** are listed in Table S1 in SI, and the ORTEP structure (30% ellipsoid) and the packing structures of complex **1** are depicted in Fig. 2. Complex **1** crystallized in the triclinic space group $P\bar{1}$, the asymmetric unit comprising one-half of the molecule, i.e., one Ru ion, one Cl ion, and two bam ligands. Hence, the inversion center is located at the middle of the Ru–Ru bond. As confirmed from Fig. 2(a), complex **1** formed a typical paddlewheel-type structure with a Ru–Ru bond (2.342(1) Å) in which the Ru_2 core was coordinated by four equatorially μ -bridging bam ligands and two axial Cl^- ions. The Ru–Cl and averaged Ru–N bond lengths were 2.527(1) and 2.021 [2] Å, respectively. The bonding parameters of the primary coordination sphere of complex **1** were approximately equal to those reported for the $[\text{Ru}_2(\text{L})_4\text{Cl}_2]$ -type diruthenium(III) complexes (Ru–Ru: ca. 2.32 Å,

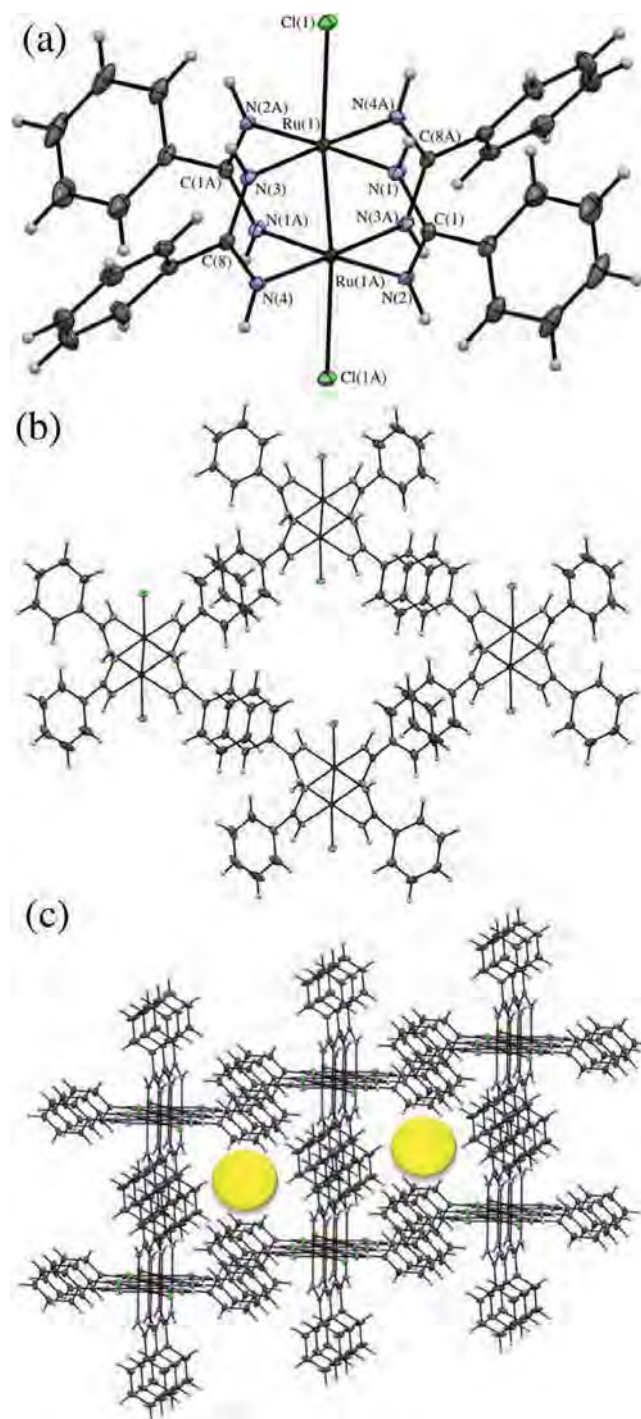


Fig. 2. Crystal structure of complex **1**: (a) ortep diagram of complex **1** (thermal ellipsoids were drawn at 30% probability level), (b) expanded supramolecular structure of complex **1**, and (c) self-assembly packing structure of complex **1** (Here, yellow balls indicate the one-dimensional channels for solvent-guest inclusion.) (Color online.)

Ru–Cl: ca. 2.56 Å, and Ru–N: 2.04 Å) [35], while the Ru–Ru–Cl bond angle of complex **1** ($172.80(2)^\circ$) was slightly bent compared with that reported for the diruthenium(III) complex (180.0°). This difference indicated that the electronic structure of complex **1** is somewhat different from those of the previously reported diruthenium(III) complexes with amidinate ligands, while the spin state ($S = 1$) is identical.

As shown in Fig. 2(b), four phenyl groups of complex **1** in the crystal packing form intermolecular π – π interactions with the phenyl groups of the four surrounding complex **1** molecules; the distance (4.009 Å) between the mean planes of the Ph rings is short enough to be considered as a result of the π – π stacking. This affords self-assembling supramolecular structures with one-dimensional channels for solvent inclusion (see Fig. 2(c)). Unfortunately, the presence of the solvent molecules –MeOH, H₂O and CHCl₃– in the packing space (the above-mentioned one-dimensional channels) of complex **1**, could not be structurally determined because of high disorders of the solvent molecules. Thus, the final structure model of complex **1** was refined without residual electron density of their solvents using the PALTON program [38]. The final R_1 and wR_2 [$I > 2\sigma(1)$] values were 2.32% and 6.16%, respectively. The solvent volume and residual electron count of complex **1** estimated by the PALTON SQUEEZE program were 212.7 Å³ and 27.8 e[–], respectively (this crystal system had $Z = 1$ and $V = 875.4$ Å³), indicating that the guest solvent molecules in the packing space of complex **1** are deduced as one MeOH and one H₂O molecules.

3.3. Magnetic susceptibility of complex **1**

To determine the oxidation state of complex **1**, the magnetic susceptibility of as-synthesized black powder of complex **1** was measured at temperatures ranging from 2 to 300 K. Fig. 3 shows the variable-temperature molar magnetic susceptibility (χ_m) and the effective magnetic moments (μ_{eff}) of complex **1**. The μ_{eff} value (2.89 μ_B) for complex **1** at room temperature is comparable with the spin-only value of 2.83 μ_B , expected for a system of $S = 1$ system and with the reported values of the Ru₂ complexes with Ru(III)–Ru(III) oxidation state. In addition, the μ_{eff} value of complex **1** gradually decreases with decreasing temperature owing to a large zero-field splitting (ZFS) of the Ru₂ core. The magnetic parameters, i.e., D (ZFS) and g (g factor), of complex **1** were estimated by fitting the obtained magnetic data to Eq. (1).

$$\chi_m = (1 - \rho) \left[\frac{2N\beta^2 g^2}{3kT} \frac{\{e^{-D/kT} + \frac{(2kT)}{D}(1 - e^{-D/kT})\}}{(1 + 2e^{-D/kT})} \right] + \rho \left(\frac{5Ng_{\text{imp}}^2 \beta^2}{4kT} \right) \quad (1)$$

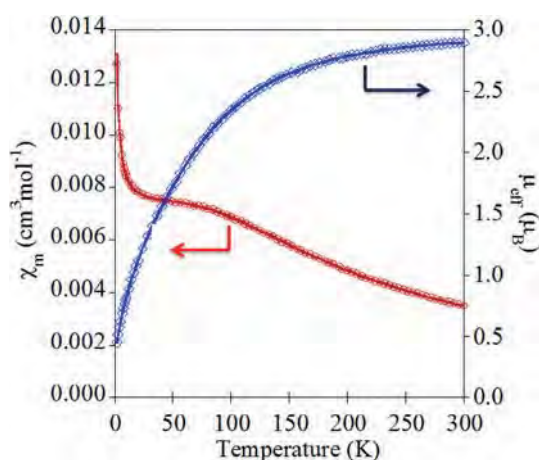


Fig. 3. Variable-temperature magnetic susceptibility (\diamond) and moment (\circ) of complex **1**. Red and blue lines are drawn for the magnetic susceptibility and moment, respectively, with the parameter values obtained by fitting to the Eq. (1) in the text.

where, k is the Boltzmann constant, N is the Avogadro's number, and β is the Bohr magneton. Eq. (1) includes the correction terms for a small amount of paramagnetic impurity (ρ) with $S = 3/2$ [Ru₂ (II, III)] species, g_{imp} being assumed to be equal to g ($=2.11$ (see below)) by convention. The data fitting results gave $D = 213$ cm^{–1} and $g = 2.11$ ($\rho = 0.0056$), which were consistent with those of the earlier works on the Ru₂ complex with Ru(III)–Ru(III) oxidation state ($D = 227$ – 261 cm^{–1}) [35,39]. The obtained magnetic results support that complex **1** has a Ru(III)–Ru(III) oxidation state with $S = 1$.

3.4. Molecular orbitals and spin density distribution of complex **1**

To investigate the electronic structure and spin density distribution of complex **1**, the DFT calculations were performed. Initially, we carried out the geometry optimization for complex **1** in CHCl₃; the optimized geometry of complex **1** was well reproduced in the X-ray structure of complex **1**, as shown in Table S1. Fig. 4 shows the electronic structure with the selected molecular orbitals (MOs) of complex **1**.

Remarkably, the electronic structure of complex **1** is somewhat unique in comparison with those of the other diruthenium(III) complexes (typically, $\sigma^2\pi^4\delta^2\pi^{*2}$ configuration). The energy ordering of the MOs between the Ru ions in complex **1** becomes $\pi^4\delta^2\pi^{*2}\sigma^2$, in which energy of the σ -bonding orbital between the Ru ions is located at the singly occupied MO(SOMO)-1. The energy of the σ -bonding orbital is significantly more destabilized than that of the antibonding π^* orbitals between the Ru ions because of the large orbital interactions with Cl ions. It is also remarkable that energy of the p orbitals of N atoms in bam ligands appears at highest SOMO. These unique characteristics of the electronic structure of complex **1** were not observed in the previously reported diruthenium(III) complex. In the occupied antibonding orbitals between the Ru ions, two unpaired electrons of complex **1** occupy two individual π^* orbitals, similarly to those of the general diruthenium(III) complexes. In the unoccupied MO space, the lowest unoccupied MO of complex **1** is localized on the antibonding π^* orbitals between the Ru ions.

The spin density distribution of complex **1** was estimated from the spin density difference between α and β orbital densities. As depicted in Fig. 5, the spin density of complex **1** is mainly localized

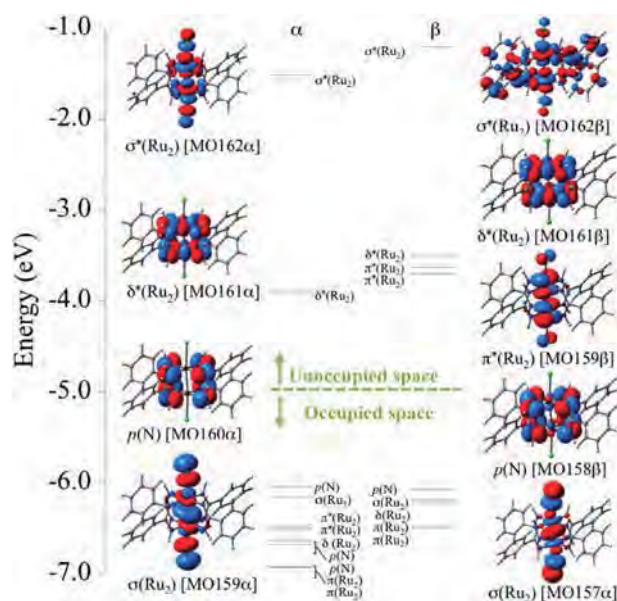


Fig. 4. Molecular orbital diagram and selected MOs of complex **1**.

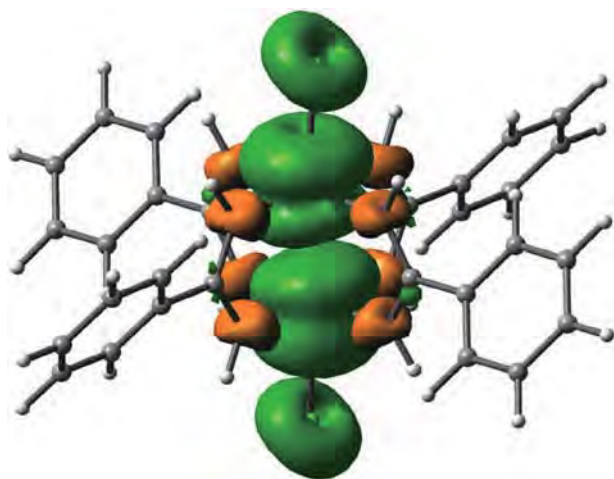


Fig. 5. Spin density distribution of complex **1**.

on the primary coordination sphere of the Ru₂ core, and leakage of the spin density from the Ru₂ core to the Ph groups in bam ligands is negligibly small. The spin density populations of complex **1** (total spin = 2) at Ru₂ core, Cl ions, and bam ligands of complex **1** were 2.02, 0.13, and -0.15, respectively. Thus, the magnetism of complex **1** mainly originates from the localized spin of the Ru₂ core.

3.5. Electrochemical property of complex **1**

The electrochemical redox behavior of complex **1** in dried CHCl₃ was measured by the CV technique. As shown in Fig. 6, complex **1** exhibited only one reversible redox wave at E_{1/2} = -0.231 V versus SCE, which is ascribed to a Ru⁶⁺/Ru⁵⁺ couple. This redox potential was nearly consistent with the Ru⁶⁺/Ru⁵⁺ redox potential of [Ru₂(dmba)₄Cl₂] (-0.321 V versus Ag/AgCl), while it significantly shifted to anodic and cathodic sides compared with those of [Ru₂(hpp)₄Cl₂] (hpp = 1,3,4,6,7,8-Hexahydro-2H-pyrimido[1,2-a]pyrimidine; E_{1/2} = -0.60 V versus SCE) [39,40] and [Ru₂(dpf)₄Cl] (E_{1/2} = 0.54 V versus SCE) [35], respectively. This result indicated that the donor ability of the bam ligand is much stronger than that of [Ru₂(dpf)₄Cl], but relatively weaker than that of [Ru₂(hpp)₄Cl₂].

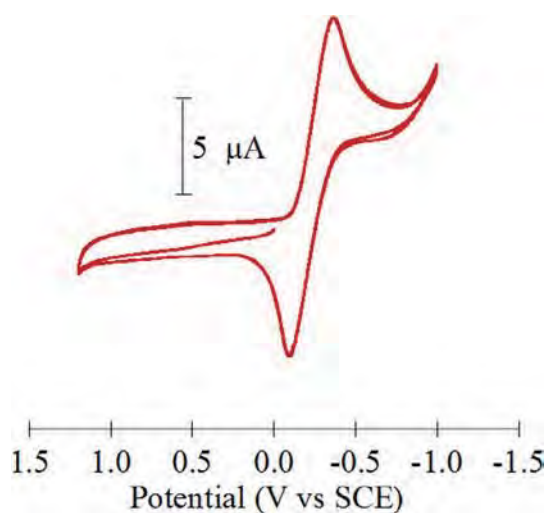


Fig. 6. Cyclic voltammogram of complex **1** recorded in 0.10 M CHCl₃ solution of Bu₄NPF₆ at a scan rate of 0.1 V/s. Here, open circuit potential was 0.169 V vs. SCE.

The redox property of complex **1** was further investigated by the DFT calculations. The one-electron reduced species of complex **1**, i.e. complex [1]⁻, was calculated with different two spin states S = 3/2 and 1/2, and their results afford that total energy of complex [1]⁻ with S = 3/2 is 5.0 kcal/mol more stable compared with that with S = 1/2. That is, it is expected that complex [1]⁻ possesses a spin state of S = 3/2. Since the difference in orbital occupations between the Ru ions in complexes **1** and [1]⁻ (S = 3/2) is the occupation of only π* orbital, we were able to prove the observed redox couple with a potential of -0.231 V versus SCE as the Ru⁶⁺/Ru⁵⁺ redox couple, though it is not a ligand-centered redox couple.

3.6. Absorption spectral features of complex **1**

Finally, we measured the absorption spectrum of complex **1** in CHCl₃. As depicted in Fig. 7, the spectrum of complex **1** shows a low-lying shoulder at 858 nm and two intense bands at 568 and 459 nm. Noteworthy, the absorption coefficients of their bands are higher than those for typical d-d transition bands of Ru₂ complexes. These spectral features of complex **1** were absolutely different from those of the previously reported diruthenium(III) complex with amidinato ligands (the absorption bands of [Ru₂(dmba)₄Cl₂] appeared at 726 and 438 nm). It seemed that this difference could be owing to the different absorption characters of complex **1** and the other diruthenium(III) complexes with amidinate ligands. Thus, to determine the absorption characters of complex **1**, investigation of the spectral features of complex **1** was carried out by means of time-dependent DFT (TDDFT) calculation. Table S2 and Fig. S3 in SD show the summary of the absorption characters and simulated absorption spectrum of complex **1**, respectively. In general, although conventional TDDFT method cannot provide the reasonable results (e.g. excitation energies and absorption intensities) for the excitation of molecules with open-shell electronic structure because of the spin-contamination error, the obtained calculation result in this study was approximately able to interpret the observed spectrum of complex **1**. The experimentally observed shoulder band at 858 nm is considered to comprise mainly two excitation characters [p(N) → π*(Ru₂) and p(N) → δ*(Ru₂)]. Thus, shoulder band is assigned to be ligand-to-metal charge transfer (LMCT) transition. The experimentally observed band at 568 nm, which corresponds to the calculated excitation energies at 541, 516 and 507 nm, is identified as the LMCT [p(N) → δ*(Ru₂)] character mixed with minor d-d [δ(Ru₂) → δ*(Ru₂)] transition. In the wavelength region shorter than 460 nm, several intense excitations are calculated, and their energies absolutely reproduced the observed absorption band at 459 nm. Since these are mainly excited from π(Ph) to π*(Ru₂) and from p(Cl)/π(Ph) to δ*(Ru₂), this band is also assigned as the LMCT transition. Although our calculation results included d-d transition characters similarly to

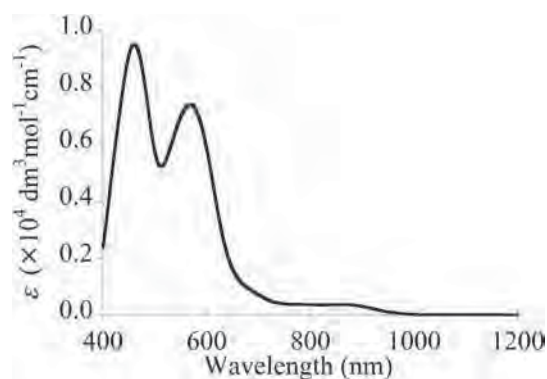


Fig. 7. Absorption spectrum of complex **1** in CHCl₃.

[Ru₂(dmba)₄Cl₂], their intensity is negligibly small. It seems that these unique transition characters of complex **1**, which has dominant LMCT characters, are origin of the different absorption spectrum feature between complex **1** and other Ru₂(III) complexes.

4. Conclusion

In this study, a new diruthenium(III) complex, [Ru₂(bam)₄Cl₂·(H₂O)] (**1**), was synthesized by the reaction of diruthenium(II,III) tetracetate chloride and benzamidine hydrochloric acid in a basic aqueous solution and was fully characterized by infrared spectroscopy, ESI-MS, elemental analysis, and single crystal X-ray diffraction analysis. Variable-temperature magnetic susceptibility measurement revealed that of complex **1** has an open-shell electronic structure with $S = 1$, Ru(III)–Ru(III) oxidation state, and a large ZFS value of $D = 213 \text{ cm}^{-1}$. The DFT calculations suggested that the electronic structure of the Ru₂ core in complex **1** is $\pi^4\delta^2-\pi^*\sigma^2$. The absorption spectral features and redox property of complex **1** were experimentally investigated and theoretically verified. From these results, we found that complex **1** has a potential application as the paramagnetic building block for supramolecular complexes and porous metal-organic frameworks. Further study on the synthesis of this type of complexes is now in progress in our group.

Acknowledgements

This work has been supported by Grant-in-Aid for Scientific Research (Nos. 15K17897, 15H00877, 16K05722) and the Strategic Research Base Development Program for Private University of the Ministry of Education, Culture, Sports and Technology (MEXT), Japan. Y.K. acknowledges the JAPAN PRIZE Foundation, and the Electronic Technology Research Foundation of Chugoku. The authors are grateful to Ms. Michiko Egawa (Shimane University) for her measurements of elemental analysis.

Appendix A. Supplementary data

CCDC 1523719 contains the supplementary crystallographic data for complex **1**. These data can be obtained free of charge via <http://www.ccdc.cam.ac.uk/conts/retrieving.html>, or from the Cambridge Crystallographic Data Centre, 12 Union Road, Cambridge CB2 1EZ, UK; fax: (+44) 1223-336-033; or e-mail: deposit@ccdc.cam.ac.uk. Supplementary data associated with this article can be found, in the online version, at <http://dx.doi.org/10.1016/j.poly.2017.03.005>.

References

- [1] F.A. Cotton, C.A. Murillo, R.A. Walton, *Multiple Bonds Between Metal Atoms*, third ed., Springer Science and Business Media, New York, 2005.
- [2] T.A. Stephenson, G. Wilkinson, *J. Inorg. Nucl. Chem.* **28** (1966) 2285.
- [3] M. Mukaida, T. Nomura, T. Ishimori, *Bull. Chem. Soc. Jpn.* **40** (1967) 2462.
- [4] T. Malinski, D. Chang, F.N. Feldmann, J.L. Bear, K.M. Kadish, *Inorg. Chem.* **22** (1983) 3225.
- [5] S. Takamizawa, K. Yamaguchi, W. Mori, *Inorg. Chem. Commun.* **1** (1998) 177.
- [6] H. Miyasaka, R. Clerac, C.S.C. Fernandez, K.R. Dunbar, *Inorg. Chem.* **40** (2001) 1663.
- [7] D. Yoshioka, M. Mikuriya, M. Handa, *Bull. Chem. Soc. Jpn.* **77** (2004) 2205.
- [8] J.-W. Ying, I.P.-C. Liu, B. Xi, Y. Song, C. Campana, J.-L. Zuo, T. Ren, *Angew. Chem. Int. Ed.* **49** (2010) 954.
- [9] D. Yoshioka, M. Mikuriya, M. Handa, *Chem. Lett.* **31** (2002) 1044.
- [10] M. Manowong, B. Han, T.R. McAloon, J. Shao, I.A. Guzei, S. Ngubane, E.V. Caemelbecke, J.K. Bear, K.M. Kadish, *Inorg. Chem.* **53** (2014) 7416.
- [11] J.G. Norman Jr., H.J. Kolari, *J. Am. Chem. Soc.* **100** (1978) 791.
- [12] O.V. Sizova, L.V. Skripnikov, A.Y. Sokolov, O.O. Lyubimova, *J. Struct. Chem.* **48** (2007) 28.
- [13] F.A. Cotton, E. Pedersen, *Inorg. Chem.* **14** (1975) 388.
- [14] Y. Hiraoka, T. Ikeue, H. Sakiyama, F. Guegan, D. Luneau, B. Gillon, I. Hiromitsu, D. Yoshioka, M. Mikuriya, Y. Kataoka, M. Handa, *Dalton Trans.* **44** (2015) 13439.
- [15] M.A. Castro, A.E. Roltberg, F.D. Cukiernik, *Inorg. Chem.* **47** (2008) 4682.
- [16] H. Miyasaka, C.S.C. Fernandez, R. Clerac, K.R. Dunbar, *Angew. Chem. Int. Ed.* **39** (2000) 3831.
- [17] M.C. Barral, S. Herrero, R.J. Aparicio, R. Torres, F.A. Urbanos, *Angew. Chem. Int. Ed.* **44** (2004) 305.
- [18] Y. Kataoka, K. Sato, Y. Miyazaki, K. Masuda, H. Tanaka, S. Naito, W. Mori, *Energy Environ. Sci.* **2** (2009) 397.
- [19] K. Sato, Y. Kataoka, W. Mori, *J. Nanosci. Nanotech.* **12** (2012) 585.
- [20] P. Angaridis, J.F. Berry, F.A. Cotton, C.A. Murillo, X. Wang, *J. Am. Chem. Soc.* **125** (2003) 10327.
- [21] M.D. Young, Q. Zhang, H.-C. Zhou, *Inorg. Chim. Acta* **424** (2015) 216.
- [22] G. Arribas, M.C. Barral, R.G. Prieto, R.J. Aparicio, J.L. Priego, M.R. Torres, F.A. Urbanos, *Inorg. Chem.* **44** (2005) 5770.
- [23] D. Matoga, M. Mikuriya, M. Handa, J. Szklarewicz, *Chem. Lett.* **34** (2005) 1550.
- [24] S. Furukawa, N. Ohba, S. Kitagawa, *Chem. Commun.* **7** (2005) 865.
- [25] B.S. Kennon, J.-H. Her, P.W. Stephens, J.S. Miller, *Inorg. Chem.* **48** (2009) 6117.
- [26] M.A.S. Aquino, *Coord. Chem. Rev.* **120** (1998) 141.
- [27] M.A.S. Aquino, *Coord. Chem. Rev.* **248** (2004) 1025.
- [28] M. Mikuriya, D. Yoshioka, M. Handa, *Coord. Chem. Rev.* **250** (2006) 2194.
- [29] S. Ring, A.J.H.M. Meijer, N.J. Patmore, *Polyhedron* **103** (2016) 87.
- [30] E.V. Dikarev, A.S. Filatov, R. Clerac, M.S. Petrukhina, *Inorg. Chem.* **45** (2006) 744.
- [31] S. Furukawa, S. Kitagawa, *Inorg. Chem.* **43** (2004) 6464.
- [32] M. Ebihara, N. Nagaya, N. Kawashima, T. Kawamura, *Inorg. Chim. Acta* **351** (2003) 305.
- [33] B. Liu, T. Ding, W.-J. Hua, Z.-M. Liu, H.-M. Hu, S.-H. Li, L.-M. Zheng, *Dalton Trans.* **42** (2013) 3429.
- [34] W.-Z. Chen, T. Ren, *Inorg. Chem.* **42** (2003) 8847.
- [35] J.L. Bear, B. Han, S. Huang, K.M. Kadish, *Inorg. Chem.* **35** (1996) 3012.
- [36] G. Xu, C. Campana, T. Ren, *Inorg. Chem.* **41** (2002) 3521.
- [37] Gaussian 09, Revision C.01, M.J. Frisch, G.W. Trucks, H.B. Schlegel, G.E. Scuseria, M.A. Robb, J.R. Cheeseman, G. Scalmani, V. Barone, B. Mennucci, G.A. Petersson, H. Nakatsuji, M. Caricato, X. Li, H.P. Hratchian, A.F. Izmaylov, J. Bloino, G. Zheng, J.L. Sonnenberg, M. Hada, M. Ehara, K. Toyota, R. Fukuda, J. Hasegawa, M. Ishida, T. Nakajima, Y. Honda, O. Kitao, H. Nakai, T. Vreven, J.A. Montgomery, Jr., J.E. Peralta, F. Ogliaro, M. Bearpark, J.J. Heyd, E. Brothers, K.N. Kudin, V.N. Staroverov, R. Kobayashi, J. Normand, K. Raghavachari, A. Rendell, J. C. Burant, S.S. Iyengar, J. Tomasi, M. Cossi, N. Rega, J.M. Millam, M. Klene, J.E. Knox, J.B. Cross, V. Bakken, C. Adamo, J. Jaramillo, R. Gomperts, R.E. Stratmann, O. Yazyev, A.J. Austin, R. Cammi, C. Pomelli, J.W. Ochterski, R.L. Martin, K. Morokuma, V.G. Zakrzewski, G.A. Voth, P. Salvador, J.J. Dannenberg, S. Dapprich, A.D. Daniels, Ö. Farkas, J.B. Foresman, J.V. Ortiz, J. Cioslowski, and D.J. Fox, Gaussian Inc, Wallingford CT, 2009.
- [38] A.L. Spek, *Acta Cryst. D65* (2009) 148.
- [39] J.K. Bear, Y. Li, B. Han, K.M. Kadish, *Inorg. Chem.* **35** (1996) 1395.
- [40] F.A. Cotton, C.A. Murillo, J.H. Reibenspies, D. Villagran, X. Wang, C.C. Wilkinson, *Inorg. Chem.* **43** (2004) 8373.



Synthesis, characterization, and structure–activity relationship of the antimicrobial activities of dinuclear *N*-heterocyclic carbene (NHC)–silver(I) complexes



Ryosuke Sakamoto, Soichiro Morozumi, Yuki Yanagawa, Mizuki Toyama, Akihiko Takayama, Noriko Chikaraishi Kasuga, Kenji Nomiya *

Department of Chemistry, Faculty of Science, Kanagawa University, Tsuchiya, Hiratsuka, Kanagawa 259-1293, Japan

ARTICLE INFO

Article history:

Received 12 April 2016

Received in revised form 20 June 2016

Accepted 28 June 2016

Available online 29 June 2016

Keywords:

Dinuclear silver(I) complexes

N-heterocyclic carbene (NHC) ligands

Molecular structures

Antimicrobial activities

Structure–activity relationship

ABSTRACT

The three dinuclear silver(I) complexes of *N*-heterocyclic carbene (NHC) ligands, $[\text{Ag}_2(\mathbf{L-1a})](\text{PF}_6)_2 \cdot 2\text{CH}_3\text{CN}$ (**Ag-1a**), $[\text{Ag}_2(\mathbf{L-2})_2](\text{PF}_6)_2 \cdot \text{H}_2\text{O}$ (**Ag-2**), and $[\text{Ag}_2(\mathbf{L-4})_2](\text{PF}_6)_2 \cdot 2\text{CH}_3\text{CN}$ (**Ag-4**), were synthesized by reactions of Ag_2O with the corresponding PF_6^- salt of the NHC precursors indicated as $\text{H}_4\mathbf{L-1}(\text{PF}_6)_4$, $\text{H}_2\mathbf{L-2}(\text{PF}_6)_2$, and $\text{H}_2\mathbf{L-4}(\text{PF}_6)_2$. $\text{H}_4\mathbf{L-1}(\text{PF}_6)_4$, which is the precursor of ligand **L-1**, was formed as mixed crystals of two geometric isomers, i.e., $\text{H}_4\mathbf{L-1a}(\text{PF}_6)_4$ (major) and $\text{H}_4\mathbf{L-1b}(\text{PF}_6)_4$ (minor), each of which was not isolated as single species. Ag_2O reacted with the mixed isomers of $\text{H}_4\mathbf{L-1}(\text{PF}_6)_4$ to give a single, pure crystalline silver(I) complex **Ag-1a** with one isomer (**L-1a**) as the major product. The molecular structures of the precursors and their silver(I) complexes were determined by X-ray crystallography. A mononuclear NHC–silver(I) complex (**Ag-3**) was prepared by the reaction of Ag_2O with the precursor **HL-3Cl**. The silver(I) complexes and NHC precursors prepared here were characterized by CHN elemental analysis, FTIR, Thermogravimetry/Differential thermal analysis, X-ray crystallography and solution (^1H and ^{13}C) NMR spectroscopy. Organometallic silver(I) complexes **Ag-1a**, **Ag-2**, and **Ag-4** were dinuclear C–Ag–C bonding complexes, whereas **Ag-3** was a mononuclear C–Ag–Cl bonding complex. These complexes are highly soluble in organic solvents such as acetone, acetonitrile, and dimethyl sulfoxide, and light-stable in the solid-state and in solution over one year. The antimicrobial activities of four silver(I) complexes and their NHC precursors against selected bacteria, yeasts, and molds in water-suspension systems were evaluated via the minimum inhibitory concentration; the activities were strongly dependent on the molecular structures of the dinuclear silver(I) complexes, which suggests a structure–activity relationship.

© 2016 Elsevier Inc. All rights reserved.

1. Introduction

Silver(I) complexes are well-known to possess antimicrobial activities [1–4]. Also, as model compounds for silver(I)–peptide and silver(I)–protein interactions, silver(I) complexes with amino acids have been intensively studied [5–16]. Several crystal structures of silver(I) complexes with amino-acids have been reported to date; $[\text{Ag}(\alpha\text{-ala})_n]$ [5], $\{[\text{Ag}(\beta\text{-ala})\text{NO}_3]_2\}$ [6,7], $[\text{Ag}(\text{gly})_n]$ [8], $\{[\text{Ag}(\text{Hglygly})\text{NO}_3]_2\}$ [8], $\{[\text{Ag}(\text{gly})_2 \cdot \text{H}_2\text{O}]_n\}$ [9], $[\text{Ag}(D\text{- or }L\text{-asn})_n]$ [9], $[\text{Ag}_2(D\text{-asp})(L\text{-asp}) \cdot 1.5\text{H}_2\text{O}]_n$ [9], $[\text{Ag}(L\text{-Hhis})_n]$ [10], $[\text{Ag}_2(D\text{-Hhis})(L\text{-Hhis})_n]$ [11], $\{[\text{Ag}(L\text{-H}_3\text{his})(\text{NO}_3)_2]_2 \cdot \text{H}_2\text{O}\}_n$ [12], $\{[\text{Ag}_2(D\text{-H}_3\text{his})(L\text{-H}_3\text{his})(\text{NO}_3)_4]_n\}$ [12], $\{\text{Na}[\text{Ag}_3(L\text{-his})_2] \cdot n\text{H}_2\text{O}\}_n$ ($n = 1\text{--}5$) [13], $[\text{Ag}_2(D\text{-met})(L\text{-met})_n]$ [14] and $\{[\text{Ag}(L\text{-Harg})\text{NO}_3]_2 \cdot \text{H}_2\text{O}\}_n$ [15] (Hala = alanine, Hgly = glycine, Hglygly = glycylglycine, Hasn = asparagine, H₂asp = aspartic acid, H₂his = histidine, Hmet = methionine and Harg = arginine). The bonding modes of the silver(I) centers in these complexes have been classified into four types: Type I, which contains only Ag–O bonds; type II, which feature alternatively repeating two-

coordinate O–Ag–O and N–Ag–N bonding units; type III, which feature repeating two-coordinate N–Ag–O bonding units; and type IV, which contains only Ag–N bonds [9]. To date, we have suggested that ligand-exchangeability plays a key role in the wide spectrum of antimicrobial activities of Werner-type silver(I) complexes [16–18]. For example, complexes featuring Ag–N and Ag–O bonding exhibit a wide spectrum of effective antimicrobial activities against microorganisms, while the Ag–S bonding complexes showed a narrow spectrum of activities and the Ag–P bonding complexes are inactive [4,18].

On the other hand, with respect to organometallic Ag–C bonding complexes, silver(I) complexes of *N*-heterocyclic carbenes (NHCs) have been extensively investigated because of their successful applications in bioorganometallic chemistry and effectiveness as carbene-transfer agents [19–27]. Biological studies of silver(I)–NHC complexes are based on the knowledge that elemental silver and its salts have long been known to protection of the eyes of newborns from infection; they also feature antimicrobial properties, predominantly against chronic ulcers, extensive burns, and wounds [28,29]. Youngs' group has attributed the antimicrobial activities of several stable NHC–silver(I) complexes to the slow release of Ag^+ ions from such complexes [30–35]. In contrast, the antimicrobial activities of the C–Ag–C and C–Ag–

* Corresponding author.

E-mail address: nomiya@kanagawa-u.ac.jp (K. Nomiya).

Cl bonding have been explained by the effects of substituents of the N-atoms, i.e., the lipophilicity of the complexes [36–38]. In particular, it should be noted that a structure-activity relationship of the anticancer activities of NHC-silver(I) complexes was recently proposed [39–41]. Thus, in order to study the structure-activity relationship of the antimicrobial activities of NHC-silver(I) complexes, we selected several NHC precursors (Scheme 1) for the preparation of light-stable and inert Ag–C bonding complexes [39,42–45].

In this work, we prepared such inert Ag–C bonding complexes, i.e., **Ag-1a**, **Ag-2**, **Ag-3**, and **Ag-4** (Scheme 2). These silver(I) complexes and their NHC precursors were characterized by CHN elemental analysis, FTIR, Thermogravimetry/Differential thermal analysis (TG/DTA), and solution (^1H and ^{13}C) NMR spectroscopy, X-ray crystallography, except for **Ag-3** [43,44] and **Ag-4** [45], the molecular structures of which have been recently reported in the literature. Their antimicrobial activities in the water-suspension system were estimated by minimum inhibitory concentration (MIC). Herein, we report the molecular and crystal structures of the NHC precursors and the two novel silver(I) complexes, **Ag-1a** and **Ag-2**, and propose the structure-activity relationships in the antimicrobial activities of the dinuclear NHC-silver (I) complexes.

2. Experimental

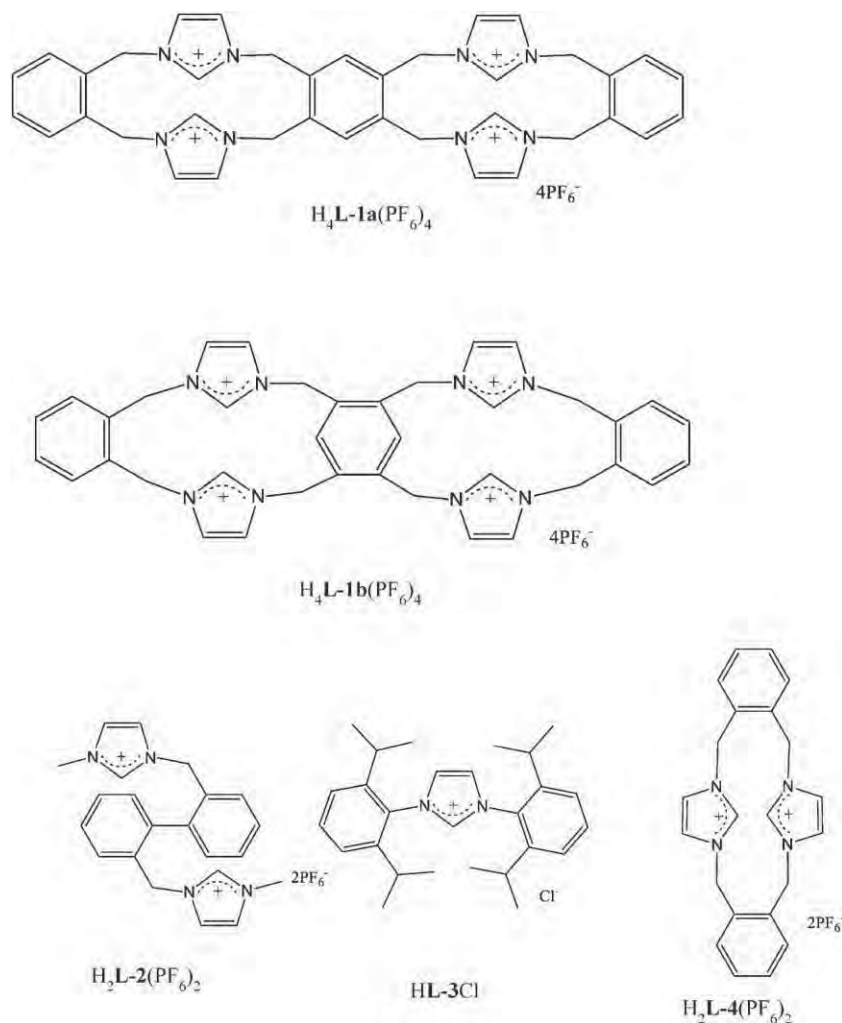
2.1. Materials

The following reagent-grade chemicals were used as received: Ag_2O , imidazole, 1-methylimidazole, potassium hexafluorophosphate,

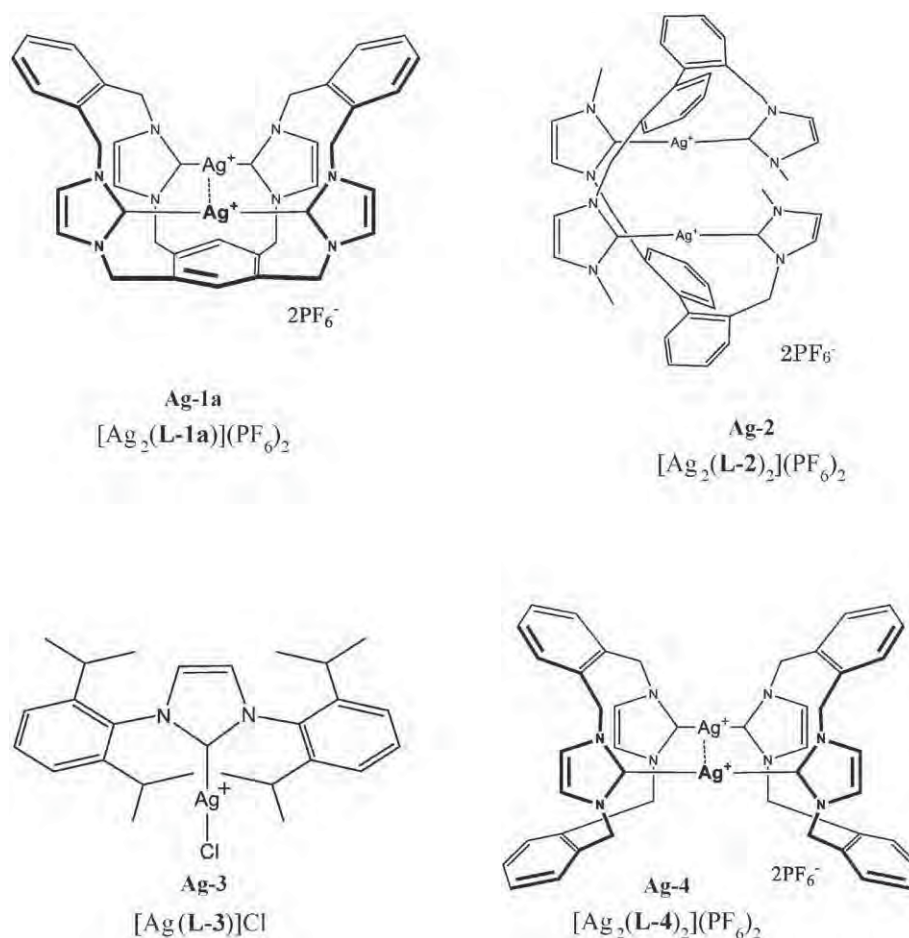
sodium hydroxide, 1,3-bis(2,6-diisopropylphenyl)imidazolium chloride (**HL-3Cl**), dimethyl sulfoxide (DMSO), EtOH, Et₂O, CH₂Cl₂, MeOH, CH₃CN, THF, pentane, toluene and acetone (Wako); 2,2'-bis(bromomethyl)-1,1'-biphenyl, α,α' -dibromo-*o*-xylene and tetrakis(bromomethyl)benzene (Aldrich); CDCl₃-*d*₆ (99.8 D atom %, Kanto Kagaku) and DMSO-*d*₆ (99.9 D atom %, Isotec). The precursors of NHC (**L-1**, **L-2** and **L-4**) ligands, i.e., H₄**L-1**(PF₆)₄ [42], H₂**L-2**(PF₆)₂ [42] and H₂**L-4**(PF₆)₂ [39,46] were prepared according to the literatures, and characterized by CHN elemental analysis, TG/DTA, FTIR, X-ray crystallography (Supporting information), and ^1H and ^{13}C NMR in DMSO-*d*₆.

2.2. Measurements

CHN elemental analyses were performed using a Perkin-Elmer PE2400 series II CHNS/O analyzer. TG/DTA were performed under air with a temperature ramp of 4 °C min⁻¹ between 30 and 500 °C using a Rigaku Thermo Plus 2 TG 8120 instrument. Infrared spectra were recorded on a JASCO FTIR 4100 spectrometer at room temperature using KBr disks. ^1H and $^{13}\text{C}\{^1\text{H}\}$ NMR spectra in solution were recorded at ambient temperature on a JEOL ECP500 NMR spectrometer. ^1H and $^{13}\text{C}\{^1\text{H}\}$ NMR spectra of the complexes were measured in DMSO-*d*₆, CDCl₃, or CD₃CN solutions with an internal tetramethylsilane reference. Distorsionless Enhancement by Polarization Transfer (DEPT) measurements were used for assignment of $^{13}\text{C}\{^1\text{H}\}$ NMR spectra of the precursors of the ligands and their silver(I) complexes.



Scheme 1. NHC precursors H₄**L-1**(PF₆)₄ as a mixture of geometrical isomers (H₄**L-1a**(PF₆)₄ and H₄**L-1b**(PF₆)₄), H₂**L-2**(PF₆)₂, **HL-3Cl**, and H₂**L-4**(PF₆)₂.



Scheme 2. NHC-silver(I) complexes Ag-1a–Ag-4.

2.2.1. Synthesis of the precursor H₄L-1(PF₆)₄·0.5CH₃CN of the ligand L-1 (major component) and L-1b (minor component)

Tetrakis(bromomethyl)benzene (0.450 g, 1 mmol) was added to a solution of 1,2'-bis(*N*-imidazole-1-ylmethyl) benzene (0.476 g, 2 mmol) in 50 mL of CH₃CN. The solution was stirred overnight at room temperature. The resultant white powder was collected using a membrane filter (JV 0.1 μm) and re-dissolved in 100 mL of water. A solution of potassium hexafluorophosphate (0.736 g, 4 mmol) in 25 mL of water was then added. The resultant white powder was collected using a membrane filter (JV 0.1 μm), washed with water (20 mL × 2) and Et₂O (20 mL × 2), and dried thoroughly by suction (0.868 g, 73%). The compound was crystallized by vapor diffusion of an internal solution of the powder (0.53 g, 0.6 mmol) dissolved in 40 mL of CH₃CN with Et₂O as an external solvent. After three days, colorless clear block crystals formed were collected using a membrane filter (JV 0.1 μm), washed with Et₂O (20 mL × 2), and dried in vacuo for 2 h. Yield: 0.256 g (48.0%). The crystals obtained were soluble in acetone, acetonitrile and DMSO, but insoluble in water, MeOH, EtOH, CH₂Cl₂, CHCl₃, Et₂O and hexane. Anal. calc. for C₄₀H_{39.5}N_{8.5}F₁₂P₂ or H₄L-1(PF₆)₄·0.5CH₃CN: C, 38.80; H, 3.30; N, 9.86. Found: C, 38.92; H, 3.71; N, 10.11%. TG/DTA data: a weight loss of 2.20% was observed at below 60.9 °C due to the desolvation of 0.5 CH₃CN molecules; calc. 1.82% for 0.5 CH₃CN molecules. An endothermic peak was observed at 48 °C and decomposition began at around 256 °C with exothermic peaks at 350, 496 °C and an endothermic peak at 496 °C. Prominent IR bands in the 1800–400 cm⁻¹ region (KBr disk): 1625 w, 1557 m, 1500 vw, 1471 w, 1458 w, 1419 w, 1350 vw, 1319 vw, 1286 vw, 1228 vw, 1213 vw, 1147 m, 1021 vw, 840 vs, 760 w, 731 m, 560 s, 500 vw, 416 vw cm⁻¹. The ¹H and ¹³C NMR signals were broad. ¹H NMR (DMSO-*d*₆, 26.2 °C): δ_H 5.49–5.70 (CH₂, br, m, 16H), 7.19–8.18 (CH, br,

m, 16H), and 8.19–9.38 (CH, br, 4H). ¹³C NMR (DMSO-*d*₆, 28.0 °C): δ_C 49.63 (CH₂), 50.48 (CH₂), 121.84 (CH), 122.57 (CH), 131.08 (CH), 132.36 (CH), 134.05 (CH), 134.87 (C), 135.80 (C), 139.73 (CH).

The ligand L-1 was found to be a mixture of two geometrical isomers, i.e., L-1a and L-1b by X-ray crystallography (Supporting information), but they could not be separated, e.g. by partial crystallization. Most signals of ¹H and ¹³C NMR were too broad to be assigned. Only the area of CH₂ in ¹H NMR showed two independent peaks, and the ratio of L-1a and L-1b was estimated as 3:1.

2.2.2. Synthesis of the precursor H₂L-2(PF₆)₂ of the ligand L-2

1-Methylimidazole (158 μL, 2 mmol) was added to a solution of 2,2'-bis(bromomethyl)-1,1'-biphenyl (0.340 g, 1 mmol) in 50 mL of acetone. The solution was stirred overnight at room temperature. The resultant white powder was collected using a membrane filter (JV 0.1 μm) and dissolved in 50 mL of water. A solution of potassium hexafluorophosphate (0.368 g, 2 mmol) in 10 mL water was then added dropwise. The resultant white powder was collected using a membrane filter (JV 0.1 μm), washed with water (20 mL × 2) and Et₂O (20 mL × 2), and dried thoroughly by suction. The compound was crystallized by vapor diffusion of an internal solution of the powder (0.063 g, 0.1 mmol) dissolved in 5 mL of acetone with Et₂O as an external solvent. After one day, colorless clear plate crystals formed and were collected using a membrane filter (JV 0.1 μm), washed with Et₂O (20 mL × 2), and dried in vacuo for 2 h. Yield: 0.03 g (43.2%). The crystals obtained were soluble in acetone, acetonitrile and DMSO, but insoluble in water, MeOH, CH₂Cl₂, CHCl₃, Et₂O and hexane. Anal. calc. for C₂₂H₂₄N₄F₁₂P₂ or H₂L-2(PF₆)₂: C, 41.65; H, 3.81; N, 8.83. Found: C, 41.58; H, 4.08; N, 8.62%. TG/DTA data: no weight loss was observed before decomposition temperature.

Decomposition began at around 271 °C with an endothermic peak at 187 °C and an exothermic peak at 500 °C. Prominent IR bands in the 1800–400 cm⁻¹ region (KBr disk): 1636 m, 1580 w, 1567 w, 1541 vw, 1520 vw, 1507 vw, 1487 w, 1457 w, 1428 vw, 1394 vw, 1367 vw, 1338 vw, 1201 vw, 1166 w, 1114 vw, 1092 vw, 1058 vw, 1031 vw, 1010 vw, 936 w, 868 vs, 847 vs, 827 vs, 776 m, 762 m, 750 m, 741 m, 715 w, 703 w, 665 w, 624 m, 557 s, 468 w, 451 w, 423 vw, 414 w cm⁻¹. ¹H NMR (DMSO-*d*₆, 26.1 °C): δ_H 3.78 (CH₃, s, 6H), 5.07–5.20 (CH₂, m, 4H), 7.08 (CH, d, *J* = 7.6 Hz, 2H), 7.37 (CH, t, *J* = 1.8 Hz, 2H), 7.40 (CH, d, *J* = 7.6 Hz, 2H), 7.46 (CH, t, *J* = 7.6 Hz, 2H), 7.53 (CH, t, *J* = 7.6 Hz, 2H), 7.63 (CH, t, *J* = 1.8 Hz, 2H) and 8.67 (CH, s, 2H). ¹³C NMR (DMSO-*d*₆, 28.1 °C): δ_C 35.68 (CH₃), 50.37 (CH₂), 122.30 (CH), 123.72 (CH), 128.75 (CH), 128.95 (CH), 129.39 (CH), 129.71 (CH), 131.83 (C), 136.60 (CH), 138.37 (C).

2.2.3. Synthesis of the precursor H₂L-4(PF₆)₂·CH₃CN of the ligand L-4

This precursor was prepared by slightly modified method of the literatures [39,46]. The details of synthesis and characterization were described in Supporting information.

2.2.4. Synthesis of [Ag₂(L-1a)](PF₆)₂·2CH₃CN (Ag-1a)

Ag₂O (0.092 g, 0.4 mmol) was added to a solution of H₄L-1(PF₆)₄ (0.237 g, 0.2 mmol) in 40 mL of CH₃CN. The black suspension was refluxed overnight in an oil bath at 90 °C. The suspension was passed through Celite (Wako No. 503). The pale-yellow clear filtrate was evaporated to dryness using a rotary evaporator at ca 30 °C, and the resultant solid was dissolved in 10 mL of acetonitrile. Reprecipitation was performed by adding the solution to 100 mL of Et₂O. The resultant white powder was collected with a membrane filter (JV 0.1 μm), washed with Et₂O (20 mL × 2), and dried thoroughly by suction.

The compound was crystallized by vapor diffusion of an internal solution of the powder (0.12 g, 0.1 mmol) dissolved in 10 mL of CH₃CN with Et₂O as an external solvent. After four days, colorless clear block crystals formed and were collected using a membrane filter (JV 0.1 μm), washed with Et₂O (20 mL × 2), and dried in vacuo for 2 h. Yield: (0.05 g, 41.8%). The crystals obtained were soluble in acetone, acetonitrile, and DMSO, but insoluble in water, MeOH, EtOH, CH₂Cl₂, CHCl₃, Et₂O, and hexane; they were light-stable for more than one year in the solid-state. Anal. calc. for C₄₄H₄₀N₁₀F₁₂P₂Ag₂O or [Ag₂(L-1)](PF₆)₂·2CH₃CN: C, 42.37; H, 3.39; N, 11.77. Found: C, 42.09; H, 3.21; N, 11.75%. TG/DTA data: a weight loss of 6.02% was observed at below 256 °C due to desolvation of two CH₃CN molecules; calc. 6.82% for 2 CH₃CN molecules. Decomposition began at around 256 °C with exothermic peaks at 296, 313 and 478 °C. Prominent IR bands in the 1800–400 cm⁻¹ region (KBr disk): 1636 w, 1571 w, 1542 vw, 1507 vw, 1480 w, 1455 w, 1400 w, 1336 vw, 1302 vw, 1246 vw, 1210 vw, 1192 w, 1161 vw, 1120 vw, 1082 vw, 1037 vw, 925 vw, 848 vs, 769 w, 755 w, 743 w, 653 vw, 622 vw, 558 m, 505 vw, 481 vw, 439 vw, 423 vw cm⁻¹. ¹H NMR (DMSO-*d*₆, 25.8 °C): δ_H 5.13 (CH₂, d, 4H, *J* = 13.5 Hz), 5.32 (CH₂, d, 4H, *J* = 13.5 Hz), 5.85 (CH₂, t, 8H, *J* = 13.5 Hz), 6.29 (CH, s, 4H), 7.11 (CH, s, 4H), 7.61 (CH, m, 4H), 7.75 (CH, m, 4H), 8.19 (CH, s, 2H). ¹³C NMR (DMSO-*d*₆, 28.0 °C): δ_C 51.14 (CH₂), 54.72 (CH₂), 119.28 (CH), 123.70 (CH), 129.83 (CH), 133.58 (CH), 135.13 (CH), 136.02 (C), 140.75 (C), 183.53 (C, d, ¹J_{C-Ag} = 186 Hz, ¹J_{C-Ag} = 215 Hz).

As a matter of fact, we obtained only the crystals of Ag-1a, but no crystals of Ag-1b. In fact, we never obtained the mixture of Ag-1a and Ag-1b both in the solid state and the reaction solution. Probably, Ag-1b is low soluble in organic solvents, and in the workup, when the black suspension was passed through Celite, Ag-1b will be filtered off together with unreacted Ag₂O. Thus, we can neither estimate the yield nor present the spectroscopic data of Ag-1b.

2.2.5. Synthesis of [Ag₂(L-2)](PF₆)₂·H₂O (Ag-2)

Ag₂O (0.232 g, 1.0 mmol) was added to a solution of H₂L-2(PF₆)₂ (0.317 g, 0.5 mmol) in 25 mL of CH₃CN. The black suspension was

refluxed overnight in an oil bath at ca 65 °C. The suspension was filtered through Celite (Wako No. 503). The colorless clear filtrate was evaporated to dryness using a rotary evaporator at ca 30 °C. Then, 3 mL of acetonitrile was added, and the white powder was reprecipitated by adding the solution to 25 mL of Et₂O. The resultant white powder was collected using a membrane filter (JV 0.1 μm) and washed with Et₂O (30 mL × 2). The compound was crystallized by vapor diffusion of an internal solution of the powder (0.119 g, 0.1 mmol) dissolved in 5 mL of CH₃CN with Et₂O as an external solvent. After one day, colorless clear granular crystals formed were collected using a membrane filter (JV 0.1 μm), washed with Et₂O (30 mL × 2). At this stage, the crystalline sample, which was contaminated with small amounts of black material, was dissolved in 5 mL of CH₃CN, and the black materials were removed via filtration through a folded filter paper (Whatman #5). Vapor diffusion was again carried out using the clear filtrate as an internal solution and Et₂O as an external solvent. After one day, the colorless, needle crystals formed were collected using a membrane filter (JV 0.1 μm), washed with Et₂O (30 mL × 2) and dried in vacuo for 2 h. Yield: (0.1034 g, 34.2%).

The colorless needle crystals were soluble in acetone, acetonitrile, CH₂Cl₂, and DMSO, but insoluble in water, MeOH, EtOH, CHCl₃, Et₂O, light petroleum, ethyl acetate, and hexane; they were light-stable for more than one year in the solid-state. This complex did not undergo ligand exchange with PPh₃ in CH₃CN solution under the Ag-2: PPh₃ = 1:2 molar ratio conditions. Anal. calc. for C₄₄H₄₆N₈F₁₂P₂Ag₂O or [Ag₂(L-2)](PF₆)₂·H₂O: C, 43.73; H, 3.84; N, 9.27. Found: C, 43.83; H, 3.99; N, 9.10%. TG/DTA data: a weight loss of 1.61% was observed at below 199 °C due to the desolvation of H₂O molecule; calc. 1.49% for one H₂O molecule. Decomposition began at around 199 °C with exothermic peaks at 307 and 490 °C. Prominent IR bands in the 1800–400 cm⁻¹ region (KBr disk): 1733 vw, 1698 vw, 1684vw, 1653 vw, 1568 w, 1474 w, 1461 w, 1440 w, 1408 w, 1363 w, 1337 w, 1261 w, 1245 w, 1198 w, 1162 vw, 1118 vw, 1045 vw, 1008 vw, 968 vw, 843 vs, 758 w, 738 w, 677 vw, 624 vw, 557 m, 498 vw, 477 vw, 464 vw, 440 vw, 439 w, 418 vw, 404 vw cm⁻¹. ¹H NMR (DMSO-*d*₆, 22.0 °C): δ_H 3.78 (CH₃, s, 6H), 5.08 (CH₂, d, 2H, *J* = 15.4 Hz), 5.38 (CH₂, d, 2H, *J* = 15.5 Hz), 7.19 (CH, m, 2H), 7.27 (CH, d, 2H, *J* = 13.4 Hz), 7.44 (CH, m, 2H), 7.45 (CH, m, 2H), 7.48 (CH, s, 2H), 7.89 (CH, s, 2H). ¹³C NMR (DMSO-*d*₆, 24.1 °C): δ_C 36.90 (CH₂), 50.93 (CH₂), 121.79 (CH), 122.13 (CH), 124.01 (CH), 126.96 (CH), 127.96 (CH), 128.49 (CH), 131.13 (CH), 136.30 (C), 137.03 (C), 180.72 (C, d, ¹J_{C-Ag} = 205 Hz, ¹J_{C-Ag} = 177 Hz).

2.2.6. Synthesis of [Ag(L-3)Cl] (Ag-3)

The mononuclear NHC-silver(I) complex [Ag(L-3)Cl] (Ag-3) was prepared by the reaction of commercially available Ag₂O and HL-3Cl in CH₂Cl₂. Synthetic conditions and characterization data of Ag-3 were described in Supporting Information. The NMR spectroscopic data for Ag-3 was in accordance with those in the reference [43]. The molecular structure of Ag-3 has been reported in the literature [44].

2.2.7. Synthesis of [Ag₂(L-4)](PF₆)₂·2CH₃CN (Ag-4)

The dinuclear NHC-silver(I) complex [Ag₂(L-4)](PF₆)₂·2CH₃CN (Ag-4) was obtained by the reaction of Ag₂O and H₂L-4(PF₆)₂ in acetonitrile. Synthetic conditions and characterization data of Ag-4 were described in Supporting Information. The NMR spectroscopic data for Ag-4 was in accordance with those in the reference [45]. The molecular structure of Ag-4 has been reported in the literature [45].

2.3. X-ray crystallography

Single crystals with dimensions of 0.10 × 0.10 × 0.07 mm³ for Ag-1a and 0.05 × 0.02 × 0.01 mm³ for Ag-2 as well as the NHC precursors, H₄L-1(PF₆)₄ as a mixture of H₄L-1a(PF₆)₄ and H₄L-1b(PF₆)₄, and H₂L-2(PF₆)₂, were mounted on cryoloops using Paratone N and cooled by a stream of cooled N₂ gas. Data collection was performed on a Bruker SMART APEX

CCD diffractometer at 100 K for **Ag-1a**, $H_4L-1(PF_6)_4$ and $H_2L-2(PF_6)_2$, and a Rigaku VariMax with Saturn CCD diffractometer at 120 K for **Ag-2**. The intensity data were automatically collected for Lorentz and polarization effects during integration. The structure was solved by direct methods (program SHELXS-97) [47] followed by subsequent difference Fourier calculations and refined using a full-matrix, least-squares procedure on F^2 (program SHELXL-97) [48]. Absorption correction was performed with SADABS (empirical absorption correction) for **Ag-1a** [49] and CrystalClear (multi-scan absorption correction) for **Ag-2** [50]. All non-hydrogen atoms were refined anisotropically. The hydrogen atoms were placed geometrically. Details of the crystallographic data for **Ag-1a** and **Ag-2** are listed in Table 1, and those for $H_4L-1a(PF_6)_4$, $H_4L-1b(PF_6)_4$, and $H_2L-2(PF_6)_2$ are listed in Table S1. The details of the crystal data have been deposited with the Cambridge Crystallographic Data Centre as supplementary publication nos. CCDC 1035994 and 1405678 for complexes **Ag-1a** and **Ag-2**, respectively.

2.4. Antimicrobial activity

The antimicrobial activities of complexes (**Ag-1a–Ag-4**) and the precursors of NHC ligands (**L-1–L-4**), i.e., $H_4L-1(PF_6)_4$, $H_2L-2(PF_6)_2$, **HL-3Cl**, and $H_2L-4(PF_6)_2$, were estimated via the minimum inhibitory concentration (MIC; $\mu\text{g mL}^{-1}$) in a water-suspension system, as described in the literature [51].

3. Results and discussion

3.1. Synthesis and characterization of the NHC precursors, $H_4L-1(PF_6)_4$, $H_2L-2(PF_6)_2$ and $H_2L-4(PF_6)_2$

Three NHC precursors, i.e., $H_4L-1(PF_6)_4$ [42], $H_2L-2(PF_6)_2$ [42] and $H_2L-4(PF_6)_2$ [39,46] as shown in Scheme 1 were prepared as PF_6^- salts according to literature methods and, obtained in yields of 48.0%, 43.2% and 63.9%, respectively. The compounds were rigorously characterized by CHN elemental analysis, TG/DTA, FTIR, 1H , ^{13}C NMR, and single-crystal X-ray analysis. The three salts were stable in air below the decomposition temperature and soluble in polar organic solvents such as CH_3CN , acetone, and DMSO. The molecular structures of $H_4L-1a(PF_6)_4$, $H_4L-1b(PF_6)_4$ and $H_2L-2(PF_6)_2$ were determined (Figs. S1 and S3), and their crystallographic data and selected distances (Å) and angles ($^\circ$) are given in Tables S1 and S2, respectively. The **HL-3Cl** NHC precursor

is commercially available and was used as received. Characteristic signals for imidazolium protons of carbene protons of $H_4L-1(PF_6)_4$, $H_2L-2(PF_6)_2$, and $H_2L-4(PF_6)_2$ were observed in the 8 to 10 ppm region in the 1H NMR spectra in $DMSO-d_6$; these disappeared upon the formation of the silver(I) complexes. The molecular structures of $H_4L-1a(PF_6)_4$, $H_4L-1b(PF_6)_4$, $H_2L-2(PF_6)_2$, and $H_2L-4(PF_6)_2$, were open and terrace-like compared to those of the silver(I) complexes, as described below.

3.2. Synthesis and characterization of the NHC-silver(I) complexes, **Ag-1a–Ag-4**

Three NHC-silver(I) complexes (i.e., **Ag-1a**, **Ag-2** and **Ag-4**) were synthesized by reactions of the corresponding NHC precursors with PF_6^- anions and Ag_2O in organic solvents (CH_3CN or acetone), but **Ag-3** was prepared by a reaction of **HL-3Cl** and Ag_2O in CH_2Cl_2 . All the compounds (**Ag-1a–Ag-4**) shown in Scheme 2 were crystallized by vapor diffusion and obtained in yields of 67.2%, 34.2%, 66.4% and 40.8%, respectively. The formation of NHC-silver(I) complexes was confirmed by the disappearance of the characteristic imidazolium protons of the NHC precursors, which were observed at around 8 to 10 ppm in the 1H NMR spectra of the compounds in $DMSO-d_6$. Further, in the ^{13}C NMR spectra of **Ag-1a**, **Ag-2**, and **Ag-4**, in $DMSO-d_6$ and **Ag-3** in $CDCl_3$, the carbene carbon signals of the precursors observed in the 130–140 ppm region were shifted down-field to the 180–190 ppm region upon complexation. The crystals of the four NHC-silver(I) complexes were highly soluble in acetone and CH_3CN and light-stable for more than one year in the solid-state. The molecular and crystal structures of **Ag-1a** and **Ag-2** were determined (see Section 3.3); however, those of **Ag-3** [43,44] and **Ag-4** [45] were recently reported in the literatures.

3.3. Molecular and crystal structures

Single crystals of complexes, $[Ag_2(L-1a)](PF_6)_2 \cdot 2CH_3CN$ (**Ag-1a**) and $[Ag_2(L-2)](PF_6)_2 \cdot H_2O$ (**Ag-2**), were formed by vapor diffusion of an internal CH_3CN solution of the silver(I) complex with an external solvent (diethyl ether) at room temperature. Colorless rod crystals of **Ag-1a** and granular ones of **Ag-2** were obtained in 41.8% (119 mg scale) and 34.2% (103 mg scale) yields, respectively. The composition and molecular formula of **Ag-1a** and **Ag-2** were consistent with the elemental analysis, TG/DTA, and FTIR.

X-ray structural analysis revealed that **Ag-1a** formed a basket-like cage structure of **L-1a** containing two silver ions (Fig. 1). Apparently, two intramolecular C–Ag–C bonding and one $Ag \cdots Ag$ interaction brought about the structural change, compared to terrace-like planar structure of the NHC precursors, $H_4L-1a(PF_6)_4$ and $H_4L-1b(PF_6)_4$ (Figs. S1 and S2). The two silver atoms are in a T-shaped geometry, as reported for complexes of methyl- and phenyl-substituted tetrapodal imidazolium ligands [45]. Each silver atom was coordinated to two carbon atoms and featured one arene interaction ($Ag1-C16$ 2.102(3), $Ag1-C36$ 2.109(3), $Ag1 \cdots C11$ 2.796(3), $Ag2-C17$ 2.095(3), $Ag2-C37$ 2.096(3) and $Ag2 \cdots C8$ 2.766(3) Å). In addition, an intramolecular $Ag \cdots Ag$ interaction ($Ag1 \cdots Ag2$ 3.0460(4) Å) is evident in Fig. 1; the $Ag \cdots Ag$ distance is less than the van der Waals diameter of 3.44 Å [52], but larger than twice the metallic radius of silver (2.88 Å) [53]. The number of CH_3CN molecules was determined based on the elemental and thermal analyses. No coordination of CH_3CN to Ag^+ was observed in the crystal of **Ag-1a**.

In contrast, **Ag-2**, which consists of **L-2** and two silver(I) ions, exhibited a helical structure because of the twisted nature of the biphenyl moiety (Fig. 2). Two carbon atoms coordinated to each silver(I) ion in a linear fashion. The $Ag \cdots Ag$ distance (3.2918(5) Å) indicates the absence of an intramolecular $Ag \cdots Ag$ interaction in **Ag-2**. Crystallographic data for **Ag-1a** and **Ag-2** are shown in Table 1, and selected distances (Å) and angles ($^\circ$) for **Ag-1a–Ag-4** are shown in Table 2.

The molecular structure of **Ag-3** shows a linear 2-coordinated mononuclear silver(I) complex [43,44]. The molecular structure of **Ag-4**

Table 1
Crystallographic data for $[Ag_2(L-1a)](PF_6)_2 \cdot 2CH_3CN$ (**Ag-1a**) and $[Ag_2(L-2)](PF_6)_2$ (**Ag-2**).

	$[Ag_2(L-1a)](PF_6)_2 \cdot 2CH_3CN$ (Ag-1a)	$[Ag_2(L-2)](PF_6)_2$ (Ag-2)
Empirical formula	$C_{42}H_{40}N_{10}P_2F_{12}Ag_2$	$C_{44}H_{44}N_8P_2F_{12}Ag_2$
Formula weight	1190.52	1190.55
Crystal system	Monoclinic	Orthorhombic
Space group	$P2_1/c$ (No. 14)	$Pcca2_1$ (No. 29)
$a/\text{Å}$	14.1737(8)	20.507(2)
$b/\text{Å}$	22.3856(13)	12.8857(15)
$c/\text{Å}$	14.3009(8)	17.727(2)
$\alpha/^\circ$	90	90
$\beta/^\circ$	101.7460(10)	90
$\gamma/^\circ$	90	90
$V/\text{Å}^3$	4442.5(4)	4684.4(10)
$D_{\text{calcd}}/\text{g cm}^{-3}$	1.78	1.69
Z	4	4
T/K	100	120
μ/mm^{-1}	1.050	0.995
No. of reflections total	32,894	10,631
Unique	11,031	10,631
No. of observations ($I > 2\sigma(I)$)	8181	10,302
R_{int}	0.0450	0.0447
R	0.0391	0.0295
R_w	0.0896	0.0910
GOF	0.952	0.779

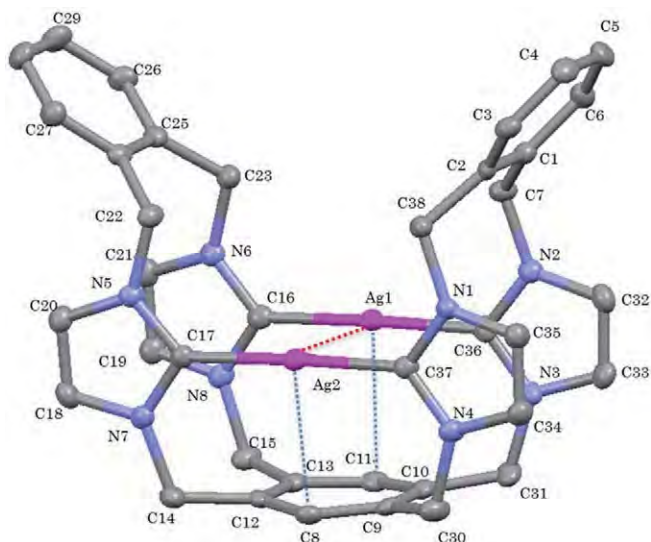


Fig. 1. Molecular structure of $[Ag_2(L-1a)](PF_6)_2 \cdot 2CH_3CN$ (**Ag-1a**). Hydrogen atoms, two PF_6^- anions and two CH_3CN molecules are omitted for clarity.

reported in the literature [45] is similar to that of **Ag-1a**, except that the bottom of the cage is absent. The $Ag \cdots Ag$ distance of 2.9620(6) Å in **Ag-4** indicates that a weak intramolecular $Ag \cdots Ag$ interaction exists.

A comparison of the environments around the silver(I) ions in the synthesized complexes is summarized as follows: i) All silver(I) complexes exhibit linear 2-coordination according to the C–Ag–C angle; ii) the Ag–C bond length of the silver(I) complexes increases in the order of **Ag-3** (2.077(2) Å), **Ag-2** (2.081(3)–2.096(3) Å), **Ag-3** (2.093(3)–2.095(3) Å) and **Ag-1a** (2.095(3)–2.109(3) Å); and the strength of the intramolecular $Ag \cdots Ag$ interactions is in the order of **Ag-4** > **Ag-1a** >> **Ag-2**.

3.4. Antimicrobial activities

The antimicrobial activities (Table 3) of the four NHC–silver(I) complexes (i.e., **Ag-1a–Ag-4**) together with the NHC precursors, against

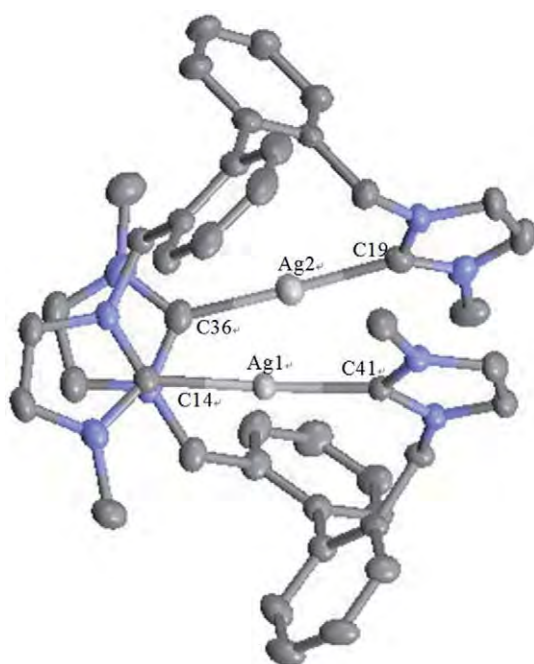


Fig. 2. Molecular structure of $[Ag_2(L-2)](PF_6)_2$ (**Ag-2**). Hydrogen atoms and two PF_6^- anions are omitted for clarity.

selected bacteria, yeasts and molds in a water-suspension system, as evaluated via the MIC, were strongly dependent upon their molecular structures; this demonstrates the structure–activity relationship.

The antimicrobial activities of several NHC–silver(I) complexes that have been reported to date were attributed to the slow release of Ag^+ ions from the Ag–NHC complexes. For example, Youngs and coworkers proposed that the strong binding ability of NHCs to silver(I) ions results in stable complexes that slowly release silver ions, thus retaining the antimicrobial effect over longer periods of time; they also suggested that the NHC–silver(I) complexes slowly decompose in aqueous culture media to form imidazolium cations and biologically active silver species [30–35]. It has been also suggested that the substituents on the N-atoms of the NHC–silver(I) complexes may play a crucial role in the antimicrobial activity, i.e., enable tuning of the lipophilicity of the complexes and their transport across the cell wall barrier [36,37]. It has also been reported that dinuclear silver(I) complexes bearing a pyridine-functionalized NHC system were active as antimicrobial agents [38].

On the other hand, it should be noted that a structure–activity relationship with respect to the anticancer activities of NHC–silver(I) complexes has recently been proposed by Budagumpi's group [39–41]: They found that (1) dinuclear complexes of benzimidazole-derived NHC–silver(I) complexes present anticancer potentials many times greater than those of their mononuclear counterparts. Moreover, in the case of some dinuclear silver(I) complexes, (2) a short silver–silver distance seems to play an important role in enhancing the activity, and (3) the presence of the substituents is therefore fundamental. Such dinuclear silver(I) complexes have (4) slightly longer silver–carbene carbon distances, and (5) the planar central spacer unit would be the best choice for the design of biologically potent benzimidazole-based silver(I)–NHC complexes.

Since the antimicrobial spectra by dinuclear NHC–silver(I) complexes **Ag-1a–Ag-4** are different from each other, and the antimicrobial activities are strongly dependent on the silver(I) complexes (Table 3), the mode of antimicrobial action would be attributable to the silver(I) complexes, but not to the silver(I) ions present in solution. This work reveals the first example of a structure–activity relationship in the antimicrobial activities of **Ag-1a–Ag-4**, which seems to parallel that proposed for the anticancer activities of NHC–silver(I) complexes proposed by Budagumpi's group [39–41]. Thus, we proposed that the planar central spacer moiety of **Ag-1a** would play an important role in inhibition of growth of the test organisms, as the reason of the great difference in the activities of **Ag-2** and **Ag-4** without such moieties. Our proposal may be related to that the through-space interactions of **Ag-1a**, but not the through-bond interactions, with amino acids and peptides to denature enzymes or forming breaks of cell walls (so called pits) resulting in the antimicrobial action [54].

The wide spectrum of antimicrobial activities of the inert and extremely stable dinuclear NHC–silver(I) complex, **Ag-1a**, can be compared with the narrow spectrum with poor activities or no activity of water-insoluble phosphane silver(I) complexes such as $[Ag_2(R-Hpyrrld)_2(H_2O)(PPh_3)_2]$ [51], $[Ag(R-Hpyrrld)(PPh_3)_2]$ [51] ($H_2pyrrld = 2$ -pyrrolidone-5-carboxylic acid), and can also be compared with the wide spectrum of modest activities of water-insoluble Ag–N bonding complex $[Ag(L-Hhis)]_n$ [10] (Table 3).

The antimicrobial spectrum of the organometallic complex **Ag-1a** is also quite different from the wide antimicrobial spectrum of the Werner-type Ag–N and Ag–O bonding complexes, inactivity of the Ag–P bonding complexes, and narrow spectrum of the Ag–S bonding complexes; these antimicrobial spectra have been interpreted so far to be based on their ligand-exchangeability [4,16,18]. It is unlikely that the antimicrobial activities of dinuclear NHC–silver(I) complexes are caused by slow release of silver(I) ions, because this would lead to similar antimicrobial spectra for all NHC–silver(I) complexes. Also, on understanding the antimicrobial activities evaluated in a water-suspension system, not only the molecular structures of the silver(I) complexes, but also the crystal structures should be taken into account.

Table 2
Selected distances (Å) and angles (°) of [Ag₂(L-1a)](PF₆)₂·2CH₃CN (**Ag-1a**) and [Ag₂(L-2)₂](PF₆)₂ (**Ag-2**), together with the literature data of [Ag(L-3)Cl] (**Ag-3**) and [Ag₂(L-4)₂](PF₆)₂ (**Ag-4**).

[Ag ₂ (L-1a)](PF ₆) ₂ ·2CH ₃ CN (Ag-1a)		[Ag ₂ (L-2) ₂](PF ₆) ₂ (Ag-2)		[Ag(L-3)Cl] (Ag-3) [44]	
Ag1–C16	2.102(3)	Ag1–C14	2.096(3)	Ag1–C1	2.077(2)
Ag1–C36	2.109(3)	Ag1–C41	2.096(3)	Ag1–C11	2.3038(7)
Ag2–C37	2.096(3)	Ag2–C19	2.089(3)		
Ag2–C17	2.095(3)	Ag2–C36	2.081(3)		
Ag1...Ag2	3.0460(4)	Ag1...Ag2	3.4918(5)		
Ag1...C11	2.796(3)				
Ag2...C8	2.766(3)				
C16–Ag1–C36	176.69(12)	C14–Ag1–C41	173.66(11)	C1–Ag1–C11	180.0
C37–Ag2–C17	177.22(11)	C19–Ag2–C36	177.55(14)		
C11...Ag1–Ag2	86.66(7)				
C37–Ag2–Ag1	89.10(8)				
[Ag ₂ (L-4) ₂](PF ₆) ₂ (Ag-4) [45]					
Ag–C22	2.095(3)				
Ag–C42	2.093(3)				
Ag...Ag ⁱ	2.9620(6)				
C22–Ag–C42 ⁱ	176.3(1)				
Symmetry operation i; 2 – x, 1 – y, 1 – z					

4. Conclusion

In summary, three dinuclear NHC-silver(I) complexes with C–Ag–C bonding modes (i.e., **Ag-1a**, **Ag-2** and **Ag-4**) and one mononuclear NHC-silver(I) complex with a C–Ag–Cl bonding mode (i.e., **Ag-3**) were synthesized, and the molecular structures of **Ag-1a** and **Ag-2** were

Table 3
Antimicrobial activities of **Ag-1a** to **Ag-4** and the NHC precursors as well as the relating silver(I) complexes evaluated by minimum inhibitory concentration (MIC; µg mL⁻¹).

	Ag-1a	Ag-2	Ag-3	Ag-4
<i>Escherichia coli</i>	15.7	500	>1000	250
<i>Bacillus subtilis</i>	31.3	1000	>1000	250
<i>Staphylococcus aureus</i>	31.3	250	>1000	125
<i>Pseudomonas aeruginosa</i>	62.5	500	>1000	125
<i>Candida albicans</i>	62.5	>1000	>1000	1000
<i>Saccharomyces cerevisiae</i>	31.3	1000	>1000	125
<i>Aspergillus brasiliensis</i> (<i>niger</i>)	62.5	>1000	>1000	>1000
<i>Penicillium citrinum</i>	125	>1000	>1000	>1000
	[Ag ₂ (R-Hpyrrld) ₂ (H ₂ O)(PPh ₃) ₂] [51]	[Ag(R-Hpyrrld)(PPh ₃) ₂] [51]	[Ag(L-Hhis)] _n [10]	
<i>E. coli</i>	62.5	>1000	125	
<i>B. subtilis</i>	62.5	>1000	250	
<i>S. aureus</i>	125	>1000	250	
<i>P. aeruginosa</i>	250	>1000	250	
<i>C. albicans</i>	500	>1000	125	
<i>S. cerevisiae</i>	500	>1000	125	
<i>A. brasiliensis</i> (<i>niger</i>)	>1000	>1000	250	
<i>P. citrinum</i>	250	>1000	250	
	H ₄ L-1(PF ₆) ₄	H ₂ L-2(PF ₆) ₂	HL-3Cl	H ₂ L-4(PF ₆) ₂
<i>E. coli</i>	62.5	>1000	1000	500
<i>B. subtilis</i>	125	>1000	15.7	500
<i>S. aureus</i>	1000	>1000	15.7	500
<i>P. aeruginosa</i>	>1000	>1000	>1000	>1000
<i>C. albicans</i>	125	>1000	>1000	>1000
<i>S. cerevisiae</i>	31.3	>1000	1000	>1000
<i>A. brasiliensis</i> (<i>niger</i>)	>1000	>1000	>1000	>1000
<i>P. citrinum</i>	>1000	>1000	>1000	>1000

H₂pyrrld = 2-pyrrolidone-5-carboxylic acid.

The MIC tests of the silver(I) complexes above were conducted under suspension conditions.

determined. The antimicrobial activities of the dinuclear NHC-silver(I) complexes, as evaluated by MIC in a water-suspension system, were strongly dependent upon their molecular structures. This structure–activity relationship of the antimicrobial activities of dinuclear NHC-silver(I) complexes was first observed herein and appears to parallel that of the anticancer activities of NHC-silver(I) complexes recently proposed by Budagumpi's group. In particular, the planar central spacer unit of the inert and stable dinuclear silver(I) complex, **Ag-1a**, which shows a wide spectrum of effective antimicrobial activities, may play an important role in the antimicrobial activities. The antimicrobial activities of these dinuclear NHC-silver(I) complexes are quite different from those of the previously reported Ag–P, Ag–S, Ag–N and Ag–O bonding Werner-type complexes, the antimicrobial spectra of which have been well-explained based on their ligand-exchangeability. This work proposes that the planar central spacer units of **Ag-1a** play an important role in the through-space interactions with the organisms. Studies regarding this concept are currently in progress. Also, the cytotoxic effects on the human normal cell line and the therapeutic potential of **Ag-1a** would be objective of our future work.

5. Supporting information

Synthetic conditions and characterization data of the precursor H₂L-4(PF₆)₂·CH₃CN of the ligand **L-4** and NHC-silver(I) complexes (**Ag-3** and **Ag-4**) and molecular structures of the NHC precursors, i.e., H₄L-1a(PF₆)₄, H₄L-1b(PF₆)₄ and H₂L-2(PF₆)₂ (Figs. S1–S3), their crystallographic data (Table S1), and their selected distances (Å) and angles (°) (Table S2).

Abbreviations

(1) NHC-silver(I) complexes:

Ag-1a [Ag₂(L-1a)](PF₆)₂·2CH₃CN

Ag-2 [Ag₂(L-2)₂](PF₆)₂·H₂O

Ag-3 [Ag(L-3)Cl]

Ag-4 [Ag₂(L-4)₂](PF₆)₂·2CH₃CN

NHC-silver(I) complexes as their abbreviations and geometries in the forms without solvated molecules are depicted in Scheme 2.

(2) Precursors of the NHC ligands:

H₄L-1(PF₆)₄ as a precursor of a mixture of **L-1a** and **L-1b** ligands, H₂L-2(PF₆)₂, HL-3Cl and H₂L-4(PF₆)₂ are depicted in Scheme 1.

(3) Others:

TG/DTA Thermogravimetry/Differential thermal analysis
 DEPT Distorsionless Enhancement by Polarization Transfer
 MIC Minimum inhibitory concentration ($\mu\text{g mL}^{-1}$)
 DMSO Dimethyl sulfoxide
 H₂pyrrld 2-Pyrrolidone-5-carboxylic acid

Acknowledgements

This work was supported by the Strategic Research Base Development Program for Private Universities of the Ministry of Education, Culture, Sports, Science, and Technology of Japan and also by a grant from the Research Institute for Integrated Science, Kanagawa University (RIIS201505).

Appendix A. Supplementary data

Supplementary data to this article can be found online at <http://dx.doi.org/10.1016/j.jinorgbio.2016.06.031>.

References

- [1] M.C. Gimeno, A. Laguna, *Comprehensive Coordination Chemistry II*, Vol. 6, Elsevier, Oxford, (2004), 911–1145.
- [2] C.F. Shaw III, *Chem. Rev.* 99 (1999) 2589–2600.
- [3] S. Ahmad, A.A. Isab, S. Ali, A.R. Al-Arfaj, *Polyhedron* 25 (2006) 1633–1645.
- [4] K. Nomiya, N.C. Kasuga, A. Takayama, A. Muñoz-Bonilla, M. Cerrada, M. Fernández-García (Eds.), *Polymeric Materials with Antimicrobial Activity*, RSC (2014), pp. 156–207.
- [5] P.A. Demaret, F. Abraham, *Acta Crystallogr. Sect. C43* (1987) 1519–1521.
- [6] M.E. Kamwaya, E. Papavinasam, S.G. Teoh, R.K. Rajaram, *Acta Crystallogr. Sect. C40* (1984) 1318–1320.
- [7] M.E. Kamwaya, E. Papavinasam, S.G. Teoh, R.K. Rajaram, *Z. Kristallogr.* 169 (1984) 51–56.
- [8] C.B. Acland, H.C. Freeman, *Chem. Commun.* (1971) 1016–1017.
- [9] K. Nomiya, H. Yokoyama, *J. Chem. Soc. Dalton Trans.* (2002) 2483–2490.
- [10] K. Nomiya, S. Takahashi, R. Noguchi, S. Nemoto, T. Takayama, M. Oda, *Inorg. Chem.* 39 (2000) 3301–3311.
- [11] N.C. Kasuga, Y. Takagi, S. Tsuruta, W. Kuwana, R. Yoshikawa, K. Nomiya, *Inorg. Chim. Acta* 368 (2011) 44–48.
- [12] L. Mirolo, T. Schmidt, S. Eckhardt, M. Meuwly, K.M. Fromm, *Chem. Eur. J.* 19 (2013) 1754–1761.
- [13] A. Takayama, Y. Takagi, K. Yanagita, C. Inoue, R. Yoshikawa, N.C. Kasuga, K. Nomiya, *Polyhedron* 80 (2014) 151–156.
- [14] N.C. Kasuga, R. Yoshikawa, Y. Sakai, K. Nomiya, *Inorg. Chem.* 51 (2012) 1640–1647.
- [15] A. Takayama, R. Yoshikawa, S. Iyoku, N.C. Kasuga, K. Nomiya, *Polyhedron* 52 (2013) 844–847.
- [16] K. Nomiya, I. Azumaya, N.C. Kasuga, T. Kato, *Curr. Top. Biochem. Res.* 10 (2008) 1–11.
- [17] K. Nomiya, K. Tsuda, N.C. Kasuga, *J. Chem. Soc. Dalton Trans.* (1998) 1653–1660.
- [18] K. Nomiya, K. Tsuda, T. Sudoh, M. Oda, *J. Inorg. Biochem.* 68 (1997) 39–44.
- [19] L. Mercs, M. Albrecht, *Chem. Soc. Rev.* 39 (2010) 1903–1912.
- [20] A. Biffis, M. Cipani, C. Tubaro, M. Basato, M. Costante, E. Bressan, A. Venzo, C. Graiff, *New J. Chem.* 37 (2013) 4176–4184.
- [21] S. Budagumpi, R.A. Haque, A.W. Salman, *Coord. Chem. Rev.* 256 (2012) 1787–2126.
- [22] S. Budagumpi, K.-H. Kim, I. Kim, *Coord. Chem. Rev.* 255 (2011) 2785–3066.
- [23] I.J.B. Lin, C.S. Vasam, *Coord. Chem. Rev.* 251 (2007) 642–670.
- [24] E.A.B. Kantchev, C.J. Orien, M. G. Organ, *Angew. Chem.* 119 (2007) 2824–2870; *Angew. Chem. Int. Ed.* 46 (2007) 2768–2813.
- [25] G.C. Fortman, S.P. Nolan, *Chem. Soc. Rev.* 40 (2011) 5151–5169.
- [26] A. Correa, S.P. Nolan, L. Cavallo, *Top. Curr. Chem.* 302 (2011) 131–155.
- [27] S. Diez-Gonzalez, S.P. Nolan, *Coord. Chem. Rev.* 251 (2007) 874–883.
- [28] A. Melaiye, Z. Sun, K. Hindi, A. Milsted, D. Ely, D.H. Reneker, C.A. Tessier, W.J. Youngs, *J. Am. Chem. Soc.* 127 (2005) 2285–2291.
- [29] J.C. Garrison, C.A. Tessier, W.J. Youngs, *J. Organomet. Chem.* 690 (2005) 6008–6020.
- [30] A. Kascatan-Nebioglu, M.J. Panzner, C.A. Tessier, C.L. Cannon, W.J. Youngs, *Coord. Chem. Rev.* 251 (2007) 884.
- [31] K.M. Hindi, M.J. Panzner, C.A. Tessier, C.L. Cannon, W.J. Youngs, *Chem. Rev.* 109 (2009) 3859–3884.
- [32] A. Kascatan-Nebioglu, A. Melaiye, K. Hindi, S. Durmus, M.J. Panzner, L.A. Hogue, R.J. Mallet, C.E. Hovis, M. Coughenour, S.D. Crosby, A. Milsted, D.L. Ely, C.A. Tessier, C.L. Cannon, W.J. Youngs, *J. Med. Chem.* 49 (2006) 6811–6818.
- [33] K.M. Hindi, T.J. Siciliano, S. Durmus, M.J. Panzner, D.A. Medvetz, D.V. Reddy, L.A. Hogue, C.E. Hovis, J.K. Hilliard, R.J. Mallet, C.A. Tessier, C.L. Cannon, W.J. Youngs, *J. Med. Chem.* 51 (2008) 1577–1583.
- [34] B.D. Wright, P.N. Shah, L.J. McDonald, M.L. Shaeffer, P.O. Wagers, M.J. Panzner, J. Smolen, J. Tagaev, C.A. Tessier, C.L. Cannon, W.J. Youngs, *Dalton Trans.* 41 (2012) 6500–6506.
- [35] M.J. Panzner, A. Deeraksa, A. Smith, B.D. Wright, K.M. Hindi, A. Kascatan-Nebioglu, A.G. Torres, B.M. Judy, C.E. Hovis, J.K. Hilliard, R.J. Mallett, E. Cope, D.M. Estes, C.L. Cannon, J.G. Leid, W.J. Youngs, *Eur. J. Inorg. Chem.* (2009) 1739–1745.
- [36] I. Ozdemir, E.O. Ozcan, S. Gunal, N. Gurubuz, *Molecules* 15 (2010) 2499–2508.
- [37] R.A. Haque, P.O. Asekunowo, M.R. Razali, F. Moharmad, *Heteroat. Chem.* 25 (2014) 194–204.
- [38] R.A. Haque, P.O. Asekunowo, S. Budagumpi, *Inorg. Chem. Commun.* 47 (2014) 56–59.
- [39] S. Budagumpi, R.A. Haque, S. Endud, G.U. Rehman, A.W. Salman, *Eur. J. Inorg. Chem.* (2013) 4367–4388.
- [40] R.A. Haque, M.Z. Ghadhayeb, A.W. Salman, S. Budagumpi, M.B.K. Ahamed, A.M.S.A. Majid, *Inorg. Chem. Commun.* 22 (2012) 113–119.
- [41] R.A. Haque, S. Budagumpi, H.Z. Zulikha, N. Hasanudin, M.B.K. Ahamed, A.M.S.A. Majid, *Inorg. Chem. Commun.* 24 (2014) 128–133.
- [42] B.N. Ahamed, R. Dutta, P. Ghosh, *Inorg. Chem.* 52 (2013) 4269–4276.
- [43] P. de Frémont, N.M. Scott, E.D. Stevens, T. Ramnial, O.C. Lightbody, C.L.B. Macdonald, J.A.C. Clyburne, C.D. Abernethy, S.P. Nolan, *Organometallics* 24 (2005) 6301–6309.
- [44] X.-Y. Yu, B.O. Patric, B.R. James, *Organometallics* 25 (2006) 2359–2363.
- [45] M.V. Baker, D.H. Brown, R.A. Haque, B.W. Skelton, A.H. White, *Dalton Trans.* (2004) 3756–3764.
- [46] M.V. Baker, B. Skelton, A.H. White, *J. Chem. Soc. Dalton Trans.* (2001) 111–120.
- [47] G.M. Sheldrick, *Acta Crystallogr. Sect. A* 46 (1990) 467–473.
- [48] G.M. Sheldrick, *SHELXL-97 Program for Crystal Structure Refinement*, University of Göttingen, Göttingen, Germany, 1997.
- [49] G.M. Sheldrick, *SADABS*, University of Göttingen, Göttingen, Germany, 1996.
- [50] Rigaku, *CrystalClear*, Rigaku Corporation, Tokyo, Japan, 2005.
- [51] R. Noguchi, A. Sugie, Y. Okamoto, A. Hara, K. Nomiya, *Bull. Chem. Soc. Jpn.* 78 (2005) 1953–1962.
- [52] A. Bondi, *J. Phys. Chem.* 68 (1964) 441–451.
- [53] A.F. Wells, *Structural Inorganic Chemistry*, fourth ed. Oxford University Press, London, 1975 1022.
- [54] S. Eckhardt, P.S. Brunetto, J. Gagnon, M. Priebe, B. Giese, K.M. Fromm, *Chem. Rev.* 113 (2013) 4708–4754.



Crystal structure of *catena*-poly[silver(I)- μ -L-valinato- κ^2 N:O]

Yoshitaka Takagi, Youhei Okamoto, Chisato Inoue, Noriko Chikaraishi
Kasuga and Kenji Nomiya

Acta Cryst. (2017). E73, 354–357



IUCr Journals

CRYSTALLOGRAPHY JOURNALS ONLINE

This open-access article is distributed under the terms of the Creative Commons Attribution Licence <http://creativecommons.org/licenses/by/2.0/uk/legalcode>, which permits unrestricted use, distribution, and reproduction in any medium, provided the original authors and source are cited.



Crystal structure of *catena*-poly[silver(I)- μ -L-valinato- κ^2 N:O]

Yoshitaka Takagi, Youhei Okamoto, Chisato Inoue, Noriko Chikaraishi Kasuga and Kenji Nomiya*

Department of Chemistry, Faculty of Science, Kanagawa University, Tsuchiya, Hiratsuka, Kanagawa 259-1293, Japan.
*Correspondence e-mail: nomiya@kanagawa-u.ac.jp

The reaction of Ag₂O with L-valine (L-Hval, C₅H₁₁NO₂) in a 1:2 molar ratio in water, followed by vapour diffusion, afforded a coordination polymer of the title compound, [Ag(C₅H₁₀NO₂)]_n, with N–Ag–O repeat units, which is classified as a type III silver(I) complex with amino acid ligands. The asymmetric unit consists of two independent units of [Ag(L-val)]. In the crystal, the polymeric chains run along [101], and neighbouring chains are linked *via* a weak Ag...Ag interaction and N–H...O hydrogen bonds. The title complex exhibited antimicrobial activity against selected bacteria (*Escherichia coli*, *Bacillus subtilis*, *Staphylococcus aureus* and *Pseudomonas aeruginosa*).

1. Chemical context

Silver(I) complexes with amino acid ligands have been of interest not only due to their numerous medicinal applications but also as model protein–silver(I) interaction compounds (Banti & Hadjikakou, 2013; Eckhardt *et al.*, 2013). Aside from S-containing amino acids, such as cysteine which forms an insoluble S-bridging silver(I) complex (Leung *et al.*, 2013), we have focused on ligand-exchangeable silver(I) complexes with N and O donor atoms. Although many of them are difficult to crystallize and light-sensitive, several crystals of silver(I) complexes have been prepared (Nomiya *et al.*, 2014). In comparison to gold(I) ions, silver(I) ions show various coordination numbers and modes with N and O atoms and tend to form polymeric structures. The polymeric structures of silver(I) complexes with non-S amino acid ligands are classified into four types based on the bonding modes of the silver(I) atom: type I contains only Ag–O bonds, *e.g.*, silver(I) with aspartic acid (Hasp), {[Ag₂(D-asp)(L-asp)]1.5H₂O}_n; type II contains O–Ag–O and N–Ag–N bonds, *e.g.*, silver(I) with glycine (Hgly), [Ag(gly)]_n; type III contains N–Ag–O units, *e.g.*, silver(I) complexes with glycine, [Ag(gly)]_n, and L-asparagine (L-Hasn), [Ag(L-asn)]_n; type IV contains only Ag–N bonds, *e.g.*, silver(I) with L-histidine (L-H₂his), [Ag(L-Hhis)]_n (Nomiya *et al.*, 2000; Nomiya & Yokoyama, 2002). Two types of complexes (types II and III) have been reported for [Ag(gly)]_n. Here, we report the preparation and crystal structure of silver(I) with L-valine (L-Hval).

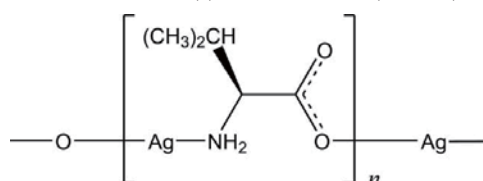


Table 1
 Selected geometric parameters (Å, °).

Ag1—N1	2.136 (4)	Ag2—O3	2.142 (4)
Ag1—O2 ⁱ	2.124 (3)	Ag2—N2 ⁱ	2.155 (4)
O2 ⁱ —Ag1—N1	176.13 (16)	O3—Ag2—N2 ⁱ	165.79 (18)

 Symmetry code: (i) $x - 1, y, z - 1$.

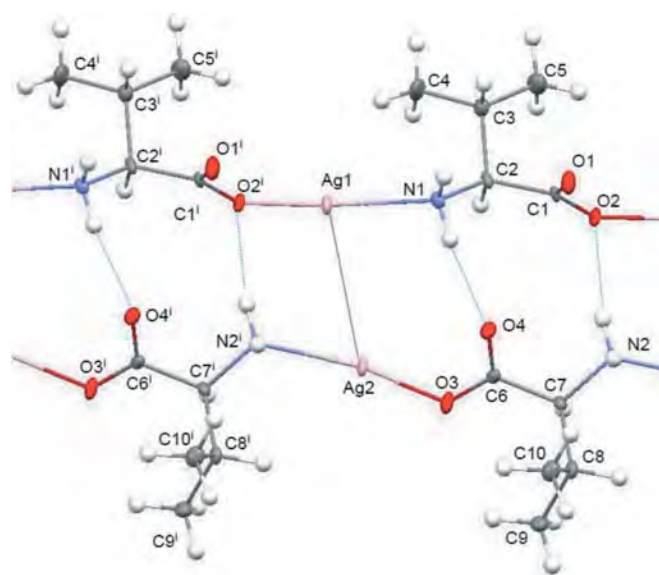
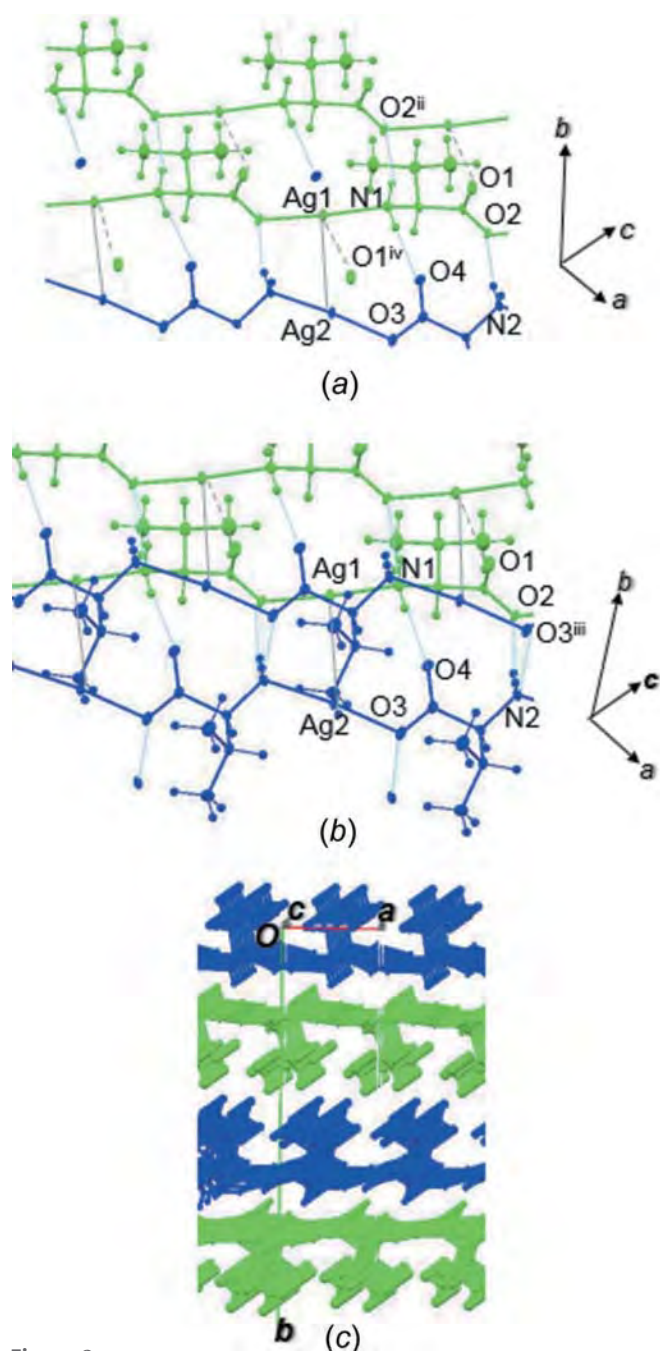
Table 2
 Hydrogen-bond geometry (Å, °).

$D-H\cdots A$	$D-H$	$H\cdots A$	$D\cdots A$	$D-H\cdots A$
N1—H1B \cdots O4	0.87 (3)	2.04 (3)	2.907 (6)	169 (5)
N2—H2B \cdots O2	0.87 (3)	2.19 (3)	3.053 (7)	171 (6)
N1—H1A \cdots O2 ⁱⁱ	0.86 (3)	2.10 (3)	2.935 (5)	164 (6)
N2—H2A \cdots O3 ⁱⁱⁱ	0.86 (3)	2.13 (4)	2.924 (5)	153 (6)

 Symmetry codes: (ii) $x - 1, y, z$; (iii) $x, y, z + 1$.

2. Structural commentary

The local coordination around the silver(I) atom of the title compound is shown in Fig. 1. The asymmetric unit consists of two units of $[\text{Ag}(\text{L-val})]$, which separately form polymeric chains along [101]. In each chain, the N and O atoms coordinate almost linearly to the silver(I) atom (Table 1), resulting in repeating N—Ag—O units. Since the $\text{Ag1}\cdots\text{O1}^{\text{iv}}$ distance [2.654 (4) Å; symmetry code: (iv) $x, y, z - 1$] is much longer than those of $\text{Ag1}-\text{O2}^{\text{i}}$ [2.124 (3) Å] and $\text{Ag2}-\text{O3}$ [2.142 (4) Å], $[\text{Ag}(\text{L-val})]_n$ is classified as being a type III linear N—Ag—O polymer, as found in the silver(I) complexes with glycine (Acland & Freeman, 1971), with α -alanine (Démaret & Abraham, 1987) and with asparagine (Nomiya & Yokoyama, 2002).


Figure 1
 Part of the polymeric structure of the title compound showing the local coordination around the silver(I) atoms. Displacement ellipsoids are drawn at the 50% probability level. The weak Ag \cdots Ag interaction is displayed as a grey line and the N—H \cdots O hydrogen bonds are drawn as blue dotted lines. [Symmetry code: (i) $x - 1, y, z - 1$.]

Figure 2
 (a) Weak interactions around the polymeric chains containing Ag1 [symmetry codes: (ii) $x - 1, y, z$; (iv) $x, y, z - 1$]. (b) Weak interactions around the coordination polymers containing Ag2 [symmetry code: (iii) $x, y, z + 1$]. (c) Packing diagram of $[\text{Ag}(\text{L-val})]_n$.

Although the polymeric structures of N—Ag—O repeated units of $[\text{Ag}(\text{L-val})]_n$ and $[\text{Ag}(\text{L-asp})]_n$ are similar to each other, the Ag \cdots Ag distance [3.3182 (6) Å] between the neighbouring chains in $[\text{Ag}(\text{L-val})]_n$ is slightly shorter than that [3.4371 (9) Å] in $[\text{Ag}(\text{L-asp})]_n$. This indicates the presence of a weak Ag \cdots Ag interaction between the two independent N—Ag—O chains in the title complex, considering the metallic and van der Waals radii of 1.44 and 1.72 Å, respectively, for Ag (Wells, 1975; Bondi, 1964).

Table 3
Experimental details.

Crystal data	
Chemical formula	[Ag(C ₅ H ₁₀ NO ₂)]
<i>M_r</i>	224.01
Crystal system, space group	Monoclinic, <i>P</i> 2 ₁
Temperature (K)	90
<i>a</i> , <i>b</i> , <i>c</i> (Å)	5.4475 (5), 22.545 (2), 5.5411 (5)
β (°)	95.446 (2)
<i>V</i> (Å ³)	677.47 (11)
<i>Z</i>	4
Radiation type	Mo <i>K</i> α
μ (mm ⁻¹)	2.90
Crystal size (mm)	0.36 × 0.16 × 0.09
Data collection	
Diffractometer	Bruker SMART APEXII CCD
Absorption correction	Multi-scan (<i>SADABS</i> ; Bruker, 2009)
<i>T_{min}</i> , <i>T_{max}</i>	0.422, 0.780
No. of measured, independent and observed [<i>I</i> > 2 σ (<i>I</i>)] reflections	4981, 3034, 3013
<i>R_{int}</i>	0.016
(<i>sin</i> θ / λ) _{max} (Å ⁻¹)	0.666
Refinement	
<i>R</i> [<i>F</i> ² > 2 σ (<i>F</i> ²)], <i>wR</i> (<i>F</i> ²), <i>S</i>	0.022, 0.054, 1.15
No. of reflections	3034
No. of parameters	179
No. of restraints	7
H-atom treatment	H atoms treated by a mixture of independent and constrained refinement
$\Delta\rho_{\max}$, $\Delta\rho_{\min}$ (e Å ⁻³)	1.13, -1.11
Absolute structure	Flack <i>x</i> determined using 1275 quotients [(<i>I</i> ⁺ − <i>I</i> [−])/(<i>I</i> ⁺ + <i>I</i> [−])] (Parsons <i>et al.</i> , 2013)
Absolute structure parameter	0.048 (19)

Computer programs: *APEX2* and *SAINT* (Bruker, 2008), *SIR2004* (Burla *et al.*, 2005), *SHELXL2016* (Sheldrick, 2015) and *Mercury* (Macrae *et al.*, 2008).

3. Supramolecular features

The two independent polymeric chains containing Ag1 and Ag2, respectively, are represented as green and blue in Fig. 2. The chains of Ag1 are connected to each other by N—H···O hydrogen bonds [N1—H1A···O2ⁱⁱ; symmetry code: (ii) *x* − 1, *y*, *z*] into a sheet structure. The chains of Ag2 are also linked into a sheet structure by N—H···O hydrogen bonds [N2—H2A···O3ⁱⁱⁱ; symmetry code: (iii) *x*, *y*, *z* + 1]. Both sheets are parallel to the *ac* plane and the two sheets are stacked alternately along the *b* axis through the weak Ag···Ag interactions and N—H···O hydrogen bonds (N1—H1B···O4 and N2—H22B···O2; Table 2).

4. Synthesis and crystallization

To a suspension of 232 mg (1.0 mmol) of Ag₂O in 20 ml of water was added 234 mg of L-valine (2.0 mmol), followed by stirring for 2 h at room temperature. The resulting grey suspension was filtered. Vapour diffusion was performed at room temperature by using the colourless filtrate as the inner solution and ethanol as the external solvent. The platelet crystals formed were collected and washed with acetone (30 ml) and ether (30 ml) to afford 0.5 mg of colourless crys-

tals of [Ag(L-val)]. The colour of the crystals gradually changed to brown in a few days at ambient temperature. Analysis calculated for C₅H₁₀NO₂Ag: C 26.81, H 4.50, N 6.25%. Found: C 27.01, H 4.40, N 6.34%. Prominent IR bands in 1800–400 cm⁻¹ (KBr disk): 1577*vs*, 1471*m*, 1414*s*, 1359*m*, 1184*w*, 987*w*, 892*w*, 827*m*, 716*m*, 651*m*, 547*m*, 443*m*.

5. Antimicrobial activity

The title silver(I) complex exhibits antimicrobial activity for selected bacteria. The minimum inhibitory concentration (MIC, μ mL⁻¹) values of the complex for four bacteria, *E. coli*, *B. subtilis*, *S. aureus*, *P. aeruginosa* are 31.3, 62.5, 125 and 31.3, respectively. [Ag(L-val)]_{*n*} did not inhibit the growth of two yeasts (*C. albicans* and *S. cerevisiae*) and two molds [*A. brasiliensis* (*niger*) and *P. citrinum*] in water-suspension systems. [Ag(L-val)]_{*n*} is insoluble in H₂O and other organic solvents (MeOH, DMSO, acetone, EtOH, CH₃CN, CH₂Cl₂, CHCl₃, ether, and EtOAc).

6. Refinement

Crystal data, data collection and structure refinement details are summarized in Table 3. C-bound H atoms were positioned geometrically and refined using a riding model with *U*_{iso}(H) = 1.2 or 1.5*U*_{eq}(C). H atoms of the amino groups were found in a difference Fourier map and their positions were refined with restraints of N—H = 0.86 (2) Å and H···H = 1.40 (4) Å, and with *U*_{iso}(H) = 1.2*U*_{eq}(N).

Funding information

Funding for this research was provided by: Research Institute for Integrated Science, Kanagawa University (award No. RIIS201604).

References

- Acland, C. B. & Freeman, H. C. (1971). *J. Chem. Soc. D*, pp. 1016–1017.
- Banti, C. N. & Hadjikakou, S. K. (2013). *Metallomics*, **5**, 569–596.
- Bondi, A. (1964). *J. Phys. Chem.* **68**, 441–451.
- Bruker (2008). *APEX2* and *SAINT*. Bruker AXS Inc., Madison, Wisconsin, USA.
- Bruker (2009). *SADABS*. Bruker AXS Inc., Madison, Wisconsin, USA.
- Burla, M. C., Caliandro, R., Camalli, M., Carrozzini, B., Cascarano, G. L., De Caro, L., Giacovazzo, C., Polidori, G. & Spagna, R. (2005). *J. Appl. Cryst.* **38**, 381–388.
- Démaret, A. & Abraham, F. (1987). *Acta Cryst.* **C43**, 1519–1521.
- Eckhardt, S., Brunetto, P. S., Gagnon, J., Priebe, M., Giese, B. & Fromm, K. M. (2013). *Chem. Rev.* **113**, 4708–4754.
- Leung, B. O., Jalilehvand, F., Mah, V., Parvez, M. & Wu, Q. (2013). *Inorg. Chem.* **52**, 4593–4602.
- Macrae, C. F., Bruno, I. J., Chisholm, J. A., Edgington, P. R., McCabe, P., Pidcock, E., Rodriguez-Monge, L., Taylor, R., van de Streek, J. & Wood, P. A. (2008). *J. Appl. Cryst.* **41**, 466–470.
- Nomiya, K., Kasuga, N. C. & Takayama, K. (2014). *RSC Polymer Chemistry Series*, Vol. 10, edited by A. Munoz-Bonilla, M. L. Cerrada and M. Fernandez-Garcia, pp. 156–207. Cambridge: RSC publishing.

- Nomiya, K., Takahashi, S., Noguchi, R., Nemoto, S., Takayama, T. & Oda, M. (2000). *Inorg. Chem.* **39**, 3301–3311.
- Nomiya, K. & Yokoyama, H. (2002). *J. Chem. Soc. Dalton Trans.* pp. 2483–2490.
- Parsons, S., Flack, H. D. & Wagner, T. (2013). *Acta Cryst.* **B69**, 249–259.
- Sheldrick, G. M. (2015). *Acta Cryst.* **C71**, 3–8.
- Wells, A. F. (1975). *Structural Inorganic Chemistry*, 4th ed. p. 1015. London: Oxford University Press.

supporting information

Acta Cryst. (2017). E73, 354-357 [https://doi.org/10.1107/S2056989017001815]

Crystal structure of *catena*-poly[silver(I)- μ -L-valinato- κ^2 N:O]

Yoshitaka Takagi, Youhei Okamoto, Chisato Inoue, Noriko Chikaraishi Kasuga and Kenji Nomiya

Computing details

Data collection: *APEX2* (Bruker, 2008); cell refinement: *SAINTE* (Bruker, 2008); data reduction: *SAINTE* (Bruker, 2008); program(s) used to solve structure: *SIR2004* (Burla *et al.*, 2005); program(s) used to refine structure: *SHELXL2016* (Sheldrick, 2015); molecular graphics: *Mercury* (Macrae *et al.*, 2008); software used to prepare material for publication: *SHELXL2016* (Sheldrick, 2015).

catena-Poly[silver(I)- μ -L-valinato- κ^2 N:O]

Crystal data

[Ag(C₅H₁₀NO₂)]
 $M_r = 224.01$
 Monoclinic, $P2_1$
 $a = 5.4475$ (5) Å
 $b = 22.545$ (2) Å
 $c = 5.5411$ (5) Å
 $\beta = 95.446$ (2)°
 $V = 677.47$ (11) Å³
 $Z = 4$

$F(000) = 440$
 $D_x = 2.196$ Mg m⁻³
 Mo $K\alpha$ radiation, $\lambda = 0.71073$ Å
 Cell parameters from 4323 reflections
 $\theta = 3.6$ – 28.3 °
 $\mu = 2.90$ mm⁻¹
 $T = 90$ K
 Needle, colorless
 $0.36 \times 0.16 \times 0.09$ mm

Data collection

Bruker SMART APEXII CCD
 diffractometer
 Radiation source: Sealed Tube
 Detector resolution: 8.366 pixels mm⁻¹
 ω scans
 Absorption correction: multi-scan
 (SADABS; Bruker, 2009)
 $T_{\min} = 0.422$, $T_{\max} = 0.780$

4981 measured reflections
 3034 independent reflections
 3013 reflections with $I > 2\sigma(I)$
 $R_{\text{int}} = 0.016$
 $\theta_{\max} = 28.3$ °, $\theta_{\min} = 1.8$ °
 $h = -7 \rightarrow 3$
 $k = -28 \rightarrow 30$
 $l = -7 \rightarrow 7$

Refinement

Refinement on F^2
 Least-squares matrix: full
 $R[F^2 > 2\sigma(F^2)] = 0.022$
 $wR(F^2) = 0.054$
 $S = 1.15$
 3034 reflections
 179 parameters
 7 restraints
 H atoms treated by a mixture of independent
 and constrained refinement

$w = 1/[\sigma^2(F_o^2) + (0.0258P)^2 + 0.4276P]$
 where $P = (F_o^2 + 2F_c^2)/3$
 $(\Delta/\sigma)_{\max} = 0.001$
 $\Delta\rho_{\max} = 1.13$ e Å⁻³
 $\Delta\rho_{\min} = -1.11$ e Å⁻³
 Absolute structure: Flack x determined using
 1275 quotients $[(I^+) - (I^-)] / [(I^+) + (I^-)]$ (Parsons *et al.*, 2013)
 Absolute structure parameter: 0.048 (19)

Special details

Geometry. All esds (except the esd in the dihedral angle between two l.s. planes) are estimated using the full covariance matrix. The cell esds are taken into account individually in the estimation of esds in distances, angles and torsion angles; correlations between esds in cell parameters are only used when they are defined by crystal symmetry. An approximate (isotropic) treatment of cell esds is used for estimating esds involving l.s. planes.

Refinement. Refinement of F^2 against ALL reflections. The weighted R-factor wR and goodness of fit S are based on F^2 , conventional R-factors R are based on F, with F set to zero for negative F^2 . The threshold expression of $F^2 > 2\text{sigma}(F^2)$ is used only for calculating R-factors(gt) etc. and is not relevant to the choice of reflections for refinement. R-factors based on F^2 are statistically about twice as large as those based on F, and R- factors based on ALL data will be even larger.

Fractional atomic coordinates and isotropic or equivalent isotropic displacement parameters (\AA^2)

	<i>x</i>	<i>y</i>	<i>z</i>	$U_{\text{iso}}^*/U_{\text{eq}}$
Ag1	0.62135 (6)	0.72712 (2)	0.36519 (6)	0.01288 (9)
C1	1.1756 (9)	0.7379 (2)	1.0188 (9)	0.0097 (10)
C2	1.0368 (9)	0.7590 (2)	0.7813 (9)	0.0112 (9)
H2C	1.149003	0.755936	0.649045	0.013*
C3	0.9626 (9)	0.8245 (2)	0.8085 (10)	0.0146 (10)
H3	0.837026	0.826310	0.928715	0.018*
C4	0.8460 (11)	0.8514 (3)	0.5695 (11)	0.0244 (12)
H4A	0.962402	0.848370	0.445617	0.037*
H4B	0.806760	0.893266	0.594925	0.037*
H4C	0.694559	0.829836	0.515562	0.037*
C5	1.1823 (11)	0.8626 (3)	0.9056 (12)	0.0236 (12)
H5A	1.309746	0.861056	0.792249	0.035*
H5B	1.249657	0.847404	1.063895	0.035*
H5C	1.128339	0.903713	0.922864	0.035*
O1	1.0588 (6)	0.7234 (2)	1.1919 (6)	0.0166 (7)
O2	1.4109 (6)	0.73698 (16)	1.0246 (6)	0.0125 (7)
N1	0.8165 (8)	0.7214 (2)	0.7175 (7)	0.0115 (8)
H1A	0.721 (9)	0.726 (3)	0.830 (8)	0.014*
H1B	0.877 (10)	0.6856 (15)	0.732 (11)	0.014*
Ag2	0.89815 (6)	0.60339 (2)	0.21275 (6)	0.01329 (10)
C6	1.2547 (9)	0.5896 (2)	0.6450 (10)	0.0107 (9)
C7	1.5054 (9)	0.5750 (2)	0.7793 (9)	0.0102 (9)
H7	1.635708	0.590634	0.680772	0.012*
C8	1.5466 (9)	0.5077 (2)	0.8113 (9)	0.0120 (9)
H8	1.686570	0.502380	0.939835	0.014*
C9	1.6241 (10)	0.4791 (3)	0.5799 (10)	0.0185 (10)
H9A	1.487275	0.481332	0.451923	0.028*
H9B	1.667499	0.437482	0.611812	0.028*
H9C	1.767197	0.500216	0.527632	0.028*
C10	1.3225 (10)	0.4764 (2)	0.8998 (10)	0.0168 (10)
H10A	1.365825	0.435354	0.943053	0.025*
H10B	1.186513	0.476776	0.770720	0.025*
H10C	1.271796	0.497164	1.042428	0.025*
N2	1.5353 (7)	0.6050 (2)	1.0205 (7)	0.0118 (7)
H2A	1.442 (10)	0.587 (2)	1.112 (10)	0.014*

H2B	1.494 (11)	0.6423 (13)	1.004 (11)	0.014*
O3	1.2360 (7)	0.57934 (18)	0.4188 (7)	0.0154 (8)
O4	1.0857 (6)	0.61000 (18)	0.7610 (6)	0.0140 (7)

Atomic displacement parameters (Å²)

	U^{11}	U^{22}	U^{33}	U^{12}	U^{13}	U^{23}
Ag1	0.00939 (17)	0.01968 (19)	0.00880 (17)	0.00032 (14)	-0.00310 (11)	-0.00117 (15)
C1	0.010 (2)	0.012 (3)	0.007 (2)	-0.0023 (17)	-0.0027 (17)	-0.0017 (17)
C2	0.008 (2)	0.017 (3)	0.008 (2)	-0.0015 (18)	-0.0004 (17)	-0.0040 (18)
C3	0.013 (2)	0.015 (2)	0.016 (2)	-0.0009 (18)	-0.0019 (19)	-0.0001 (19)
C4	0.031 (3)	0.020 (3)	0.020 (3)	0.006 (3)	-0.012 (2)	0.004 (2)
C5	0.024 (3)	0.016 (3)	0.029 (3)	-0.003 (2)	-0.006 (2)	-0.002 (2)
O1	0.0121 (16)	0.027 (2)	0.0102 (16)	-0.0014 (16)	-0.0009 (12)	0.0029 (17)
O2	0.0035 (14)	0.021 (2)	0.0123 (16)	0.0017 (12)	-0.0014 (12)	-0.0017 (14)
N1	0.0099 (18)	0.014 (2)	0.0104 (18)	-0.0014 (16)	0.0010 (14)	-0.0020 (17)
Ag2	0.00789 (17)	0.0215 (2)	0.00975 (18)	0.00137 (14)	-0.00313 (12)	-0.00090 (15)
C6	0.009 (2)	0.008 (2)	0.015 (2)	-0.0007 (16)	-0.0017 (18)	0.0003 (16)
C7	0.010 (2)	0.012 (2)	0.008 (2)	0.0006 (17)	0.0005 (17)	-0.0026 (17)
C8	0.008 (2)	0.017 (2)	0.011 (2)	-0.0003 (18)	-0.0017 (17)	-0.0003 (18)
C9	0.019 (3)	0.019 (3)	0.017 (2)	0.007 (2)	0.000 (2)	-0.004 (2)
C10	0.014 (2)	0.018 (2)	0.019 (3)	-0.002 (2)	0.002 (2)	0.004 (2)
N2	0.0130 (19)	0.0164 (19)	0.0054 (18)	0.0006 (18)	-0.0028 (14)	0.0000 (18)
O3	0.0088 (16)	0.027 (2)	0.0099 (17)	0.0028 (14)	-0.0009 (13)	0.0020 (15)
O4	0.0092 (15)	0.0187 (19)	0.0142 (18)	0.0034 (14)	0.0006 (13)	-0.0009 (15)

Geometric parameters (Å, °)

Ag1—N1	2.136 (4)	Ag2—O3	2.142 (4)
Ag1—O2 ⁱ	2.124 (3)	Ag2—N2 ⁱ	2.155 (4)
C1—O1	1.245 (6)	C6—O4	1.259 (6)
C1—O2	1.280 (6)	C6—O3	1.269 (7)
C1—C2	1.530 (7)	C6—C7	1.527 (7)
C2—N1	1.485 (6)	C7—N2	1.493 (6)
C2—C3	1.543 (7)	C7—C8	1.541 (7)
C2—H2C	1.0000	C7—H7	1.0000
C3—C5	1.528 (8)	C8—C10	1.530 (7)
C3—C4	1.538 (7)	C8—C9	1.530 (7)
C3—H3	1.0000	C8—H8	1.0000
C4—H4A	0.9800	C9—H9A	0.9800
C4—H4B	0.9800	C9—H9B	0.9800
C4—H4C	0.9800	C9—H9C	0.9800
C5—H5A	0.9800	C10—H10A	0.9800
C5—H5B	0.9800	C10—H10B	0.9800
C5—H5C	0.9800	C10—H10C	0.9800
N1—H1A	0.86 (3)	N2—H2A	0.86 (3)
N1—H1B	0.87 (3)	N2—H2B	0.87 (3)

O2 ⁱ —Ag1—N1	176.13 (16)	O3—Ag2—N2 ⁱ	165.79 (18)
O1—C1—O2	124.1 (5)	O4—C6—O3	125.2 (5)
O1—C1—C2	119.9 (4)	O4—C6—C7	119.5 (5)
O2—C1—C2	116.0 (4)	O3—C6—C7	115.2 (4)
N1—C2—C1	110.4 (4)	N2—C7—C6	110.8 (4)
N1—C2—C3	110.9 (4)	N2—C7—C8	109.9 (4)
C1—C2—C3	109.1 (4)	C6—C7—C8	112.4 (4)
N1—C2—H2C	108.8	N2—C7—H7	107.8
C1—C2—H2C	108.8	C6—C7—H7	107.8
C3—C2—H2C	108.8	C8—C7—H7	107.8
C5—C3—C4	109.1 (5)	C10—C8—C9	111.5 (4)
C5—C3—C2	111.6 (4)	C10—C8—C7	112.2 (4)
C4—C3—C2	112.6 (5)	C9—C8—C7	111.5 (4)
C5—C3—H3	107.8	C10—C8—H8	107.1
C4—C3—H3	107.8	C9—C8—H8	107.1
C2—C3—H3	107.8	C7—C8—H8	107.1
C3—C4—H4A	109.5	C8—C9—H9A	109.5
C3—C4—H4B	109.5	C8—C9—H9B	109.5
H4A—C4—H4B	109.5	H9A—C9—H9B	109.5
C3—C4—H4C	109.5	C8—C9—H9C	109.5
H4A—C4—H4C	109.5	H9A—C9—H9C	109.5
H4B—C4—H4C	109.5	H9B—C9—H9C	109.5
C3—C5—H5A	109.5	C8—C10—H10A	109.5
C3—C5—H5B	109.5	C8—C10—H10B	109.5
H5A—C5—H5B	109.5	H10A—C10—H10B	109.5
C3—C5—H5C	109.5	C8—C10—H10C	109.5
H5A—C5—H5C	109.5	H10A—C10—H10C	109.5
H5B—C5—H5C	109.5	H10B—C10—H10C	109.5
C2—N1—Ag1	120.3 (3)	C7—N2—H2A	107 (4)
C2—N1—H1A	107 (4)	C7—N2—H2B	110 (4)
C2—N1—H1B	102 (4)	H2A—N2—H2B	112 (5)
H1A—N1—H1B	108 (5)	C6—O3—Ag2	117.7 (3)

Symmetry code: (i) $x-1, y, z-1$.

Hydrogen-bond geometry (\AA , $^\circ$)

$D-H\cdots A$	$D-H$	$H\cdots A$	$D\cdots A$	$D-H\cdots A$
N1—H1B \cdots O4	0.87 (3)	2.04 (3)	2.907 (6)	169 (5)
N2—H2B \cdots O2	0.87 (3)	2.19 (3)	3.053 (7)	171 (6)
N1—H1A \cdots O2 ⁱⁱ	0.86 (3)	2.10 (3)	2.935 (5)	164 (6)
N2—H2A \cdots O3 ⁱⁱⁱ	0.86 (3)	2.13 (4)	2.924 (5)	153 (6)

Symmetry codes: (ii) $x-1, y, z$; (iii) $x, y, z+1$.

Aluminum- and Gallium-Containing Open-Dawson Polyoxometalates

Satoshi Matsunaga,^[a] Yusuke Inoue,^[a] Takuya Otaki,^[a] Hironori Osada,^[a] and Kenji Nomiya*^[a]

Keywords: Polyoxometalates; Open-Dawson structural POM; Aluminum; Gallium

Abstract. Al- and Ga-containing open-Dawson polyoxometalates (POMs), $K_{10}[\{Al_4(\mu-OH)_6\}\{\alpha,\alpha-Si_2W_{18}O_{66}\}]\cdot 28.5H_2O$ (**Al₄-open**) and $K_{10}[\{Ga_4(\mu-OH)_6\}\{\alpha,\alpha-Si_2W_{18}O_{66}\}]\cdot 25H_2O$ (**Ga₄-open**) were synthesized by the reaction of trilacunary Keggin POM, $[A-\alpha-SiW_9O_{34}]^{10-}$, with $Al(NO_3)_3\cdot 9H_2O$ or $Ga(NO_3)_3\cdot nH_2O$, and unequivocally characterized by single-crystal X-ray analysis, ^{29}Si and ^{183}W NMR, and FT-IR spectroscopy as well as elemental analysis and TG/DTA. Single-crystal X-ray analysis revealed that the $\{M_4(\mu-OH)_6\}^{6+}$ ($M = Al, Ga$) clusters were included in an open pocket of the open-

Dawson polyanion, $[\alpha,\alpha-Si_2W_{18}O_{66}]^{16-}$, which was constituted by the fusion of two trilacunary Keggin POMs via two W–O–W bonds. These two open-Dawson structural POMs showed clear difference of the bite angles depending on the size of ionic radii. In cases of both compounds, the solution ^{29}Si and ^{183}W NMR spectra in D_2O showed only one signal and five signals, respectively. These spectra were consistent with the molecular structures of **Al₄-** and **Ga₄-open**, suggesting that these polyoxoanions were obtained as single species and maintained their molecular structures in solution.

Introduction

Polyoxometalates (POMs) are discrete metal oxide clusters that are of current interest as soluble metal oxides and for their applications in catalysis, medicine, and materials science.^[1] The preparation of POM-based materials is therefore an active field of research.

Recently, the open-Dawson POMs have been reported as an emerging class of POMs.^[2] The conventional Dawson structural POMs are regarded as an assembly of two trilacunary Keggin POMs via six W–O–W bonds. In 2014, Mizuno et al. reported that the conventional Dawson POM with highly charged guest SiO_4^{4-} , $TBA_8[\alpha-Si_2W_{18}O_{62}]\cdot 3H_2O$, was synthesized by dimerization of a trilacunary Keggin POM, $[SiW_9O_{34}]^{10-}$, in an organic solvent.^[3a] However, in aqueous media, the electrostatic repulsion between the halves, induced by the highly charged guest XO_4^{4-} ($X = Si, Ge$), is so strong that it inhibits the assembly of the usual Dawson structure.^[3b] Therefore, the two trilacunary Keggin units with XO_4^{4-} ($X = Si, Ge$) are linked by only two W–O–W bonds, forming open-Dawson structural POMs. The open pocket of the open-Dawson POMs can accommodate multiple metals (1 to 6 metals), and several compounds have been reported so far that contain metal ions in the open pocket, e.g., V^{5+} ,^[2f] Mn^{2+} ,^[2c,2h] Fe^{3+} ,^[2f] Co^{2+} ,^[2a,2c,2g,2h,2i,2n] Ni^{2+} ,^[2c,2h,2k,2n] Cu^{2+} ,^[2b,2c,2d]

Zn^{2+} .^[2j] In particular, the Ni_5 open-Dawson POM reported by Hill et al. is an efficient catalyst for water oxidation (WOC) both in the dark and under irradiation with 455 nm LED light with $[Ru(bpy)_3]^{2+}$ as photosensitizer and $Na_2S_2O_8$ as sacrificial electron acceptor.^[2k] The open-Dawson POMs could constitute a promising platform for the development of metal-substituted-POM-based materials and catalysts.

On the other hand, trivalent group 13 ions exist as a wide and dynamic range of cluster species in aqueous solution.^[4] Especially, aluminum is the third most abundant element in the terrestrial environment, and therefore, the complex solution speciation of Al^{3+} clusters can provide not only a clear understanding of aluminum in natural water systems, but also the basis for commercial applications. The synthetic and structural studies of Al- and Ga-containing POMs can provide valuable molecular models of the clusters and metal oxides of group 13 metals with a well-defined structure. Furthermore, the Al sites in Al-containing POMs act as Lewis acid sites,^[5b,5e] and Al-containing POMs are expected to be used as the Lewis-acid catalysis. Despite their importance, only a few Al- and Ga-containing POMs, in which addenda tungsten ions are substituted by Al^{3+} and Ga^{3+} ions, have been fully structurally characterized.^[5,6e] The Al-substituted POMs whose structures are determined by X-ray crystallography include $K_6H_3[ZnW_{11}O_{40}Al]\cdot 9.5H_2O$,^[5a] $TBA_3H[\gamma-SiW_{10}O_{36}\{Al(OH)_2\}_2(\mu-OH)_2]\cdot 4H_2O$, $TBA_3[(C_5H_5N)H][\gamma-SiW_{10}O_{36}\{Al(C_5H_5N)\}_2(\mu-OH)_2]\cdot 2H_2O$ (TBA = tetrabutylammonium),^[5b] $K_6Na[(A-PW_9O_{34})_2\{W(OH)(OH)_2\}\{Al(OH)(OH)_2\}\{Al(\mu-OH)(OH)_2\}_2]\cdot 19H_2O$,^[5c] $TBA_9[\{\gamma-H_2SiW_{10}O_{36}Al_2(\mu-OH)_2(\mu-OH)\}_3]$, $TBA_6Li_3[\{\gamma-H_2SiW_{10}O_{36}Al_2(\mu-OH)_2(\mu-OH)\}_3]\cdot 18H_2O$,^[5d] $Rb_2Na_2[Al_4(H_2O)_{10}(\beta-As^{III}W_9O_{33}H)_2]\cdot 20H_2O$, $(NH_4)_2Na_2[Al_4(H_2O)_{10}(\beta-Sb^{III}W_9O_{33}H)_2]\cdot 20H_2O$,^[5e] $TBA_6[\alpha-PW_{11}Al(OH)O_{39}ZrCp_2]_2$,^[5f] and $TMA_{14}Na_2[B-\alpha-$

* Prof. Dr. K. Nomiya
E-Mail: nomiya@kanagawa-u.ac.jp

[a] Department of Chemistry
Faculty of Science
Kanagawa University
2946 Tsuchiya
Hiratsuka, Kanagawa 259–1293, Japan

Supporting information for this article is available on the WWW under <http://dx.doi.org/10.1002/zaac.201500794> or from the author.

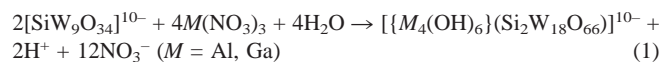
$\text{H}_3\text{P}_2\text{W}_{15}\text{O}_{59}\{\text{Al}(\text{OH})_2\}_2\{\text{Al}(\text{OH}_2)\}_2\cdot 39\text{H}_2\text{O}$ (TMA = tetramethylammonium).^[5g] Ga-substituted POMs have been studied for their potential applications as radiopharmaceuticals and antivirals, and several Ga-substituted POMs have been reported so far.^[6] However, the structurally characterized Ga-substituted POMs by X-ray crystallography are still one of the least reported compounds. Recently, Patzke et al. reported the synthesis of tri- and di-Ga-substituted Keggin POM dimers, i.e., $[\text{Ga}_6(\text{H}_2\text{O})_x\{\alpha\text{-SiW}_9\text{O}_{34}(\text{OH})_y\}_2]^{n-}$ (**Ga₆-dimer**) and $[\text{Ga}_4(\text{H}_2\text{O})_2\{\alpha\text{-SiW}_{10}\text{O}_{38}\}_2]^{12-}$ (**Ga₄-dimer**).^[6e] In this context, Al- and Ga-substituted POMs remain challenging targets from the synthetic and structural point of view. However, Al- and Ga-containing open-Dawson structural POMs have never been reported so far.

In this paper, the Al- and Ga-containing open-Dawson POMs, $\text{K}_{10}[\{\text{Al}_4(\mu\text{-OH})_6\}(\alpha,\alpha\text{-Si}_2\text{W}_{18}\text{O}_{66})]\cdot 28.5\text{H}_2\text{O}$ (**Al₄-open**) and $\text{K}_{10}[\{\text{Ga}_4(\mu\text{-OH})_6\}(\alpha,\alpha\text{-Si}_2\text{W}_{18}\text{O}_{66})]\cdot 25\text{H}_2\text{O}$ (**Ga₄-open**) were synthesized and unequivocally characterized by X-ray crystallography, ²⁹Si and ¹⁸³W NMR and FT-IR spectroscopy as well as elemental analysis, and TG/DTA.

Results and Discussion

Synthesis and Characterization

The potassium salts of aluminum(III)- and gallium(III)-containing open-Dawson POMs, $\text{K}_{10}[\{\text{Al}_4(\mu\text{-OH})_6\}(\alpha,\alpha\text{-Si}_2\text{W}_{18}\text{O}_{66})]\cdot 28.5\text{H}_2\text{O}$ (**Al₄-open**) and $\text{K}_{10}[\{\text{Ga}_4(\mu\text{-OH})_6\}(\alpha,\alpha\text{-Si}_2\text{W}_{18}\text{O}_{66})]\cdot 25\text{H}_2\text{O}$ (**Ga₄-open**), as crystalline samples, were obtained with 13.7% and 26.2% yields, respectively. **Al₄-open** was prepared by the 1:2 molar ratio reaction of the separately prepared $\text{Na}_{10}[\text{A-}\alpha\text{-SiW}_9\text{O}_{34}]\cdot 18\text{H}_2\text{O}$ with $\text{Al}(\text{NO}_3)_3\cdot 9\text{H}_2\text{O}$, followed by stirring the solution at 80 °C for 30 min. **Ga₄-open** was prepared by the 1:2 molar ratio reaction of the separately prepared $\text{K}_{10}[\text{A-}\alpha\text{-SiW}_9\text{O}_{34}]\cdot 10\text{H}_2\text{O}$ with $\text{Ga}(\text{NO}_3)_3\cdot n\text{H}_2\text{O}$, followed by stirring the solution at 80 °C for 30 min. The samples were characterized using elemental analysis, i.e., H, Al or Ga, Cl, K, Si, W analyses, FT-IR, TG/DTA, ²⁹Si and ¹⁸³W NMR in D₂O, and X-ray crystallography. The formation of polyoxoanions, $[\{M_4(\text{OH})_6\}(\alpha,\alpha\text{-Si}_2\text{W}_{18}\text{O}_{66})]^{10-}$ ($M = \text{Al}, \text{Ga}$) is represented by Equation (1).



Al₄-open was prepared at pH 2–3, and was crystallized at pH 6.5. At the early stage of crystallization, minor products were formed together with **Al₄-open**. The minor product was the Keggin POM tetramer containing Al₁₆-hydroxide cluster, i.e., $[\{\alpha\text{-Al}_3\text{SiW}_9\text{O}_{34}(\mu\text{-OH})_6\}_4\{\text{Al}_4(\mu\text{-OH})_6\}]^{22-}$ (**Al₁₆-tetramer**).^[7] The pure **Al₄-open** can be obtained from the mother liquor after removal of the crude crystals by filtration and addition of saturated KCl aqueous solution.

The reaction condition of **Ga₄-open** was similar to that of **Al₄-open** with the exception of the metal source, $\text{Ga}(\text{NO}_3)_3\cdot n\text{H}_2\text{O}$ instead of $\text{Al}(\text{NO}_3)_3\cdot 9\text{H}_2\text{O}$, and the counter cations of the precursor of trilauncary Keggin POM, i.e., K⁺ vs. Na⁺. Patzke's group has previously obtained **Ga₄-open** only as a by-

product of the trigallium(III)-substituted dimer, $[\text{Ga}_6(\text{H}_2\text{O})_x\{\alpha\text{-SiW}_9\text{O}_{34}(\text{OH})_y\}_2]^{n-}$ (**Ga₆-dimer**) and the di-gallium(III) substituted dimer, $[\text{Ga}_4(\text{H}_2\text{O})_2\{\alpha\text{-SiW}_{10}\text{O}_{38}\}_2]^{12-}$ (**Ga₄-dimer**).^[6e] By using their synthetic method, **Ga₄-open** was not isolated as main product.

In contrast to Patzke's method, our method allows the isolation of **Ga₄-open** as main product. There are two major differences between our method and theirs: (1) the order of addition of reagents, i.e., $[\text{A-}\alpha\text{-SiW}_9\text{O}_{34}]^{10-}$ vs. $\text{Ga}(\text{NO}_3)_3\cdot n\text{H}_2\text{O}$; (2) the counter cations of the precursor of trilauncary Keggin POM, i.e., K⁺ vs. Na⁺. In our method, $\text{Ga}(\text{NO}_3)_3\cdot n\text{H}_2\text{O}$ was added to the solution of $[\text{A-}\alpha\text{-SiW}_9\text{O}_{34}]^{10-}$ adjusted to pH 7.5, whereas in their method $[\text{A-}\alpha\text{-SiW}_9\text{O}_{34}]^{10-}$ was added to the solution of $\text{Ga}(\text{NO}_3)_3$. Because the solution of $\text{Ga}(\text{NO}_3)_3$ has a low pH, their reaction conditions were more acidic than ours. In addition, the potassium salt of trilauncary Keggin POM, $\text{K}_{10}[\text{A-}\alpha\text{-SiW}_9\text{O}_{34}]\cdot \text{H}_2\text{O}$ was used as starting material, whereas others used the sodium salt, $\text{Na}_{10}[\text{A-}\alpha\text{-SiW}_9\text{O}_{34}]\cdot 15\text{H}_2\text{O}$, as precursor. Hill et al. noted that the open-Dawson POM structures are more easily maintained using the potassium salt of $[\text{SiW}_9\text{O}_{34}]^{10-}$, whereas the sandwich structures are more often obtained using the sodium salt of $[\text{SiW}_9\text{O}_{34}]^{10-}$.^[21] The crystal structure of **Ga₄-open** also indicated that K⁺ ions play an important role in the formation of the open-Dawson structural POMs (see the molecular structure section). Although **Al₄-open** can be synthesized even if the sodium salt of trilauncary Keggin POM, $\text{Na}_{10}[\text{A-}\alpha\text{-SiW}_9\text{O}_{34}]\cdot 18\text{H}_2\text{O}$ was used as starting material, the addition of excess KCl was needed.

At the early stage of crystallization of **Ga₄-open**, a few crystals of **Ga₆-dimer** were also occasionally formed as minor product, together with **Ga₄-open**, and the presence of the **Ga₆-dimer** was also confirmed by ¹⁸³W NMR (see the NMR section). **Ga₄-open** in pure form can be obtained even after contamination with small amounts of **Ga₆-dimer** crystals, after removal of the mixed crystals from the mother liquor by filtration, and addition of saturated KCl aqueous solution.

The solid FT-IR spectra of **Al₄-open** and **Ga₄-open**, measured in KBr disks, are shown in Figures S1 and S2 (Supporting Information), respectively. The peaks at 1010, 958 cm⁻¹ for **Al₄-open** and 1007, 958 cm⁻¹ for **Ga₄-open** correspond to $\nu_{\text{as}}(\text{Si-O})$ and $\nu_{\text{as}}(\text{W-O}_i)$, respectively. The characteristic bands at 900–600 cm⁻¹ of both compounds are associated with $\nu(\text{W-O}_c)$, $\nu(\text{W-O}_b)$, and $\nu(\text{W-O-W})$.^[2f] The IR spectra are very similar to those of the common open-Dawson POMs.^[2]

Molecular Structures

The molecular structure of the polyoxoanion of **Al₄-open**, its polyhedral representation, and the Al₄ moieties are shown in Figure 1a, b, and c, respectively.

The composition and formula of **Al₄-open**, which contains 10 potassium counter cations, and 28.5 crystallization water molecules, were determined by elemental analysis and TG analysis. In X-ray crystallography, one open-Dawson polyoxoanion, 8 potassium cations, and 24 crystallization water molecules per formula unit were identified in the crystal structure. As in the case of other structural investigations of crystals

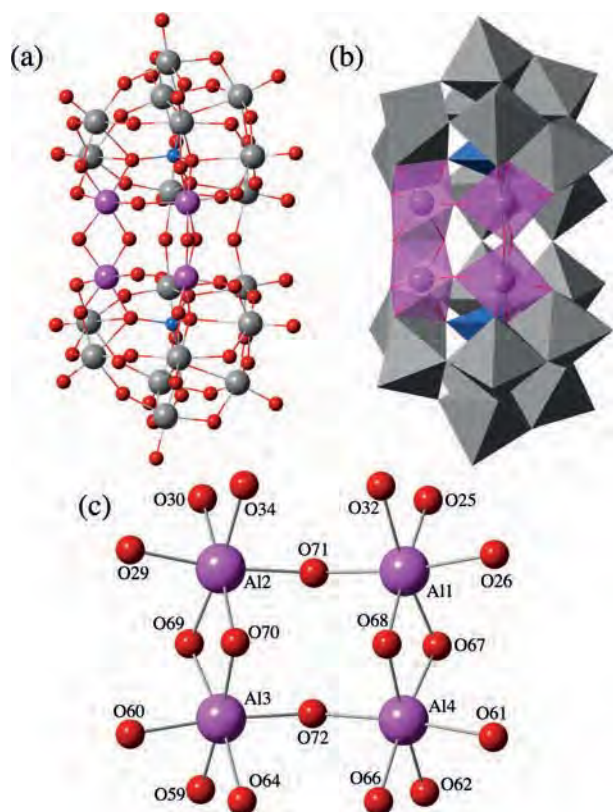


Figure 1. (a) Molecular structure of the polyoxoanion, $[(\text{Al}_4(\mu\text{-OH})_6)(\alpha,\alpha\text{-Si}_2\text{W}_{18}\text{O}_{66})]^{10-}$ of **Al₄-open**, (b) its polyhedral representation, and (c) the partial structure around the Al₄ center. Color code: Al, pink; O, red; Si, blue; W, gray.

of highly hydrated large polyoxometalate complexes, it was not possible to locate every potassium cation and crystalline water molecules in the crystal structure.

X-ray crystallography of **Al₄-open** revealed that the $\{\text{Al}_4(\mu\text{-OH})_6\}^{6+}$ cluster was included in an open pocket of the open-Dawson polyanion, $[\alpha,\alpha\text{-Si}_2\text{W}_{18}\text{O}_{66}]^{16-}$ (Figure 1a). The open-Dawson polyanion is formed by the fusion of two trilacunary Keggin POMs, $[\alpha\text{-}\alpha\text{-Si}_2\text{W}_9\text{O}_{34}]^{10-}$, by two W–O–W bonds. The four central aluminum(III) atoms in the $\{\text{Al}_4(\mu\text{-OH})_6\}^{6+}$ cluster unit are arranged in a rectangular array with Al \cdots Al distances of 2.858(5) (Al1–Al4), 2.880(5) (Al2–Al3), 3.528(5) (Al1–Al2), and 3.498(5) (Al3–Al4) Å. This metal ion arrangement is similar to that of $[\{\text{Fe}_4(\text{OH})_6\}(\text{Si}_2\text{W}_{18}\text{O}_{66})]^{10-}$ reported previously by Her et al.^[2f] The Fe \cdots Fe distances of $[\{\text{Fe}_4(\text{OH})_6\}(\text{Si}_2\text{W}_{18}\text{O}_{66})]^{10-}$ are 3.039(5) (Fe1–Fe4), 3.025(5) (Fe2–Fe3), 3.632(5) (Fe1–Fe2), and 3.660(5) (Fe3–Fe4), and are slightly longer than those of **Al₄-open**. All aluminum atoms are connected to neighboring aluminum atoms through corner sharing oxygen atoms (O71 and O72) and edge sharing oxygen atoms (O67, O68, O69, and O70). Bond valence sum (BVS) calculations^[11] have strongly suggested that the oxygen atoms (O67, O68, O69, O70, O71, and O72) are protonated, i.e., they are ascribed to the OH[−] groups (the BVS value; O67, 0.992; O68, 0.945; O69, 0.965; O70, 0.974; O71, 0.958; O72, 0.984; Table S1). Each Al atom is bonded to three oxygen atoms of the lacunary site in the open-Dawson polyanion, $[\alpha,\alpha\text{-}$

$\text{Si}_2\text{W}_{18}\text{O}_{66}]^{16-}$ [Al–O average 1.940 Å]. Thus, four Al atoms can be considered to be six-coordinate.

The molecular structure of the polyoxoanion of **Ga₄-open**, its polyhedral representation, and the partial structure around the Ga₄ centers are shown in Figure 2a, b, and c, respectively.

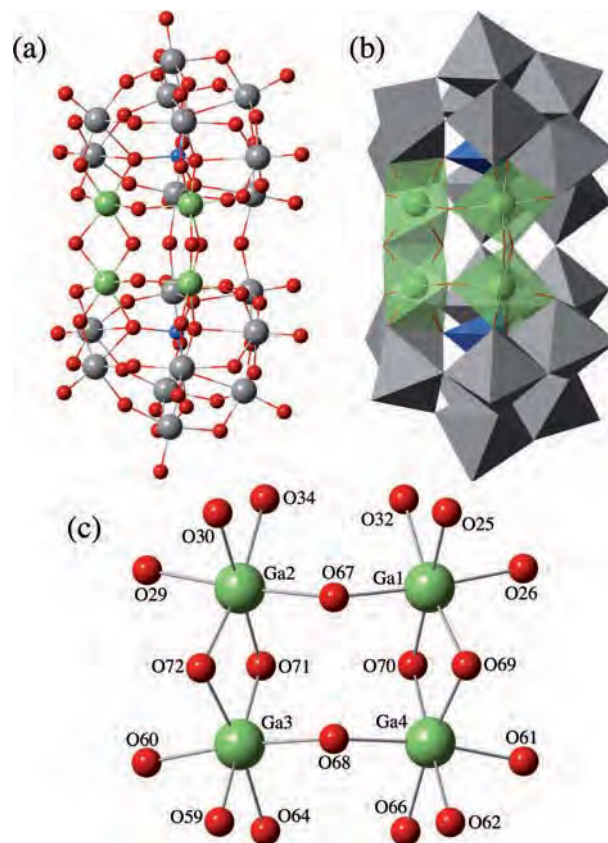


Figure 2. (a) Molecular structure of the polyoxoanion, $[(\text{Ga}_4(\mu\text{-OH})_6)(\alpha,\alpha\text{-Si}_2\text{W}_{18}\text{O}_{66})]^{10-}$ of **Ga₄-open**, (b) its polyhedral representation, and (c) the partial structure around the Ga₄ center. Color code: Ga, green; O, red; Si, blue; W, gray.

The composition and formula of **Ga₄-open**, which contains 10 potassium counteranions and 25 crystallization water molecules, were determined by elemental analysis and TG analysis. In X-ray crystallography, one open-Dawson polyoxoanion, 7 potassium cations, and 21 crystallization water molecules per formula unit were identified in the crystal structure. As in the case of other structural investigations of crystals of highly hydrated large polyoxometalate complexes, it was not possible to locate every potassium cation and crystalline water molecules. The structure of **Ga₄-open** is isostructural with **Al₄-open** (Figure 2). Bond valence sum (BVS) calculations^[11] suggested that the oxygen atoms (O67, O68, O69, O70, O71, and O72) are protonated (the BVS value; O67, 1.111; O68, 1.116; O69, 1.111; O70, 0.995; O71, 1.024; O72, 1.083; Table S2, Supporting Information). In contrast, it should be noted that Patzke's group reported that the corner- and edge-sharing oxygen atoms connecting to neighboring gallium atoms were di-protonated, i.e., $[\{\text{Ga}_4(\text{H}_2\text{O})_6\}\text{Si}_2\text{W}_{18}\text{O}_{66}]^{n-}$.^[6e] Each Ga atom is bonded to three oxygen atoms of the lacunary site in the open-Dawson

polyanion, $[\alpha, \alpha\text{-Si}_2\text{W}_{18}\text{O}_{66}]^{16-}$ [Ga–O average 2.014 Å]. Thus, four Ga atoms can be considered to be six-coordinate.

In open-Dawson POMs, the bite angle can be defined as the dihedral angle between the planes passing through the six oxygen atoms of the lacunary site of each trilacunary Keggin units. The bite angle changes depending upon the metal cluster included in the open pocket of the $[\alpha, \alpha\text{-Si}_2\text{W}_{18}\text{O}_{66}]^{16-}$ unit (Figure 3). The bite angles are 54.274° for **Al₄-open** and 56.110° for **Ga₄-open**. The difference of the bite angles between **Al₄-open** and **Ga₄-open** is caused by the difference of ionic radii between Al (0.53 Å) and Ga (0.76 Å) ions.^[12] The bite angles in these open-Dawson POMs can be compared with those of previously reported open-Dawson structural POMs; the bite angles of **Al₄-open** (54.274°) and **Ga₄-open** (56.110°) are narrower than those of the high-nuclear metal-substituted open-Dawson POMs, including Co_6 (60.045°),^[2n] Zn_6 dimer (60.308°),^[2j] Cu_5 (61.663°),^[2b,2d] and Ni_5 (58.925°)^[2k] clusters. On the other hand, the low-nuclear metal-substituted open-Dawson POMs such as Ni_2 (53.3941°)^[2i] and Co_2 (53.3625° ,^[2a] 53.4437°)^[2c] showed narrower bite angles than those of our **Al₄-open** and **Ga₄-open**. These results indicate that the bite angle increases with the increase in the number of inserted metals.

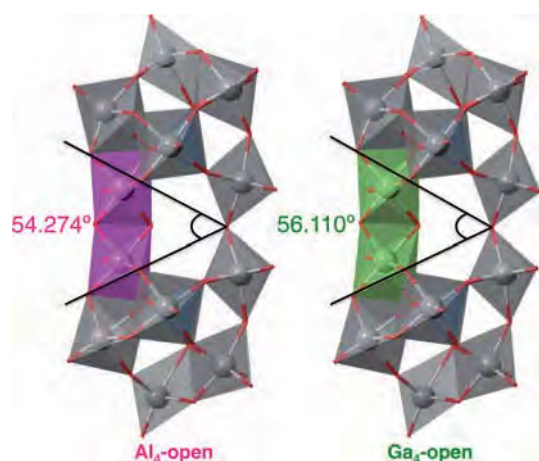


Figure 3. Bite angles of **Al₄-open** (left) and **Ga₄-open** (right).

There are many interactions between the oxygen atoms of the polyanion moiety and the K^+ cations in the crystal structures of both compounds. In particular, the terminal (O16, O49) and the edge-sharing (O21, O55) oxygen atoms of the WO_6 polyhedra serving as a hinge between the two trilacunary Keggin units interacted with K^+ cations (K1, K4 for **Al₄-open**; K1, K3 for **Ga₄-open**) [K1–O16, 2.661(8); K1–O49, 2.810(8); K4–O21, 2.717(8); K4–O55, 2.904(8) Å for **Al₄-open**; K1–O16, 2.784(10); K1–O49, 2.658(10); K3–O21, 2.895(9); K3–O55, 2.740(9) Å for **Ga₄-open**] (Figure 4). These interactions between K^+ ions and oxygen atoms in open-Dawson POM appear to play an important role in the formation of the open-Dawson structural POMs. In fact, most of the previously reported open-Dawson POMs adopted K^+ ions as counteranions, and this type of interaction was observed in most open-Dawson structural POMs, such as V_2 ,^[2f] Zn_6 dimer,^[2j] Ni_5 ,^[2k] and Cu_5 .^[2b,2d] Inter-POM interactions via K^+ cations and

crystallization water molecules were also observed in the crystal structures of **Al₄-open** and **Ga₄-open**, forming a 3D network structure in the crystal (Figure 5).

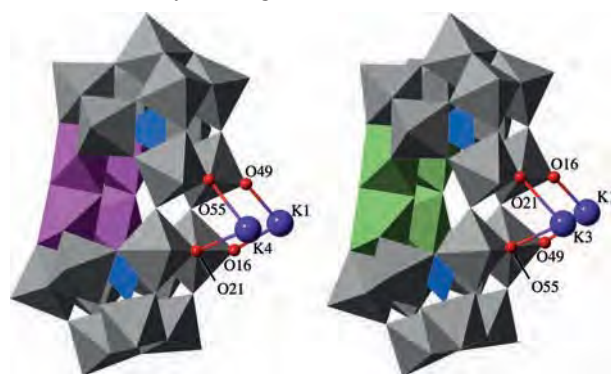


Figure 4. Interactions with K^+ cations of the terminal and the edge-sharing oxygen atoms of the WO_6 polyhedra serving as a hinge between the two trilacunary Keggin units of **Al₄-open** (left) and **Ga₄-open** (right).

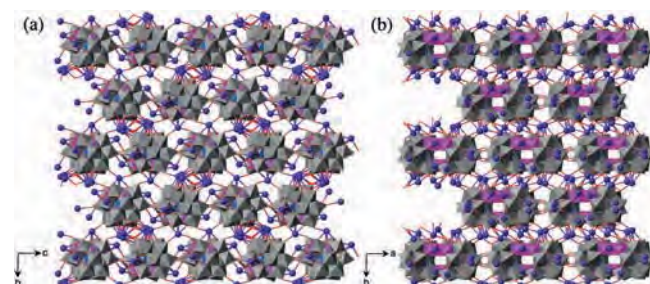


Figure 5. Packing structures of **Al₄-open**, viewed along (a) the crystallographic *a* axis and (b) the *b* axis.

Solution ^{29}Si , ^{183}W NMR

The solution ^{29}Si NMR spectra of **Al₄-open** and **Ga₄-open** in D_2O showed only one resonance, at -82.55 and -82.31 ppm, respectively (Figure 6).

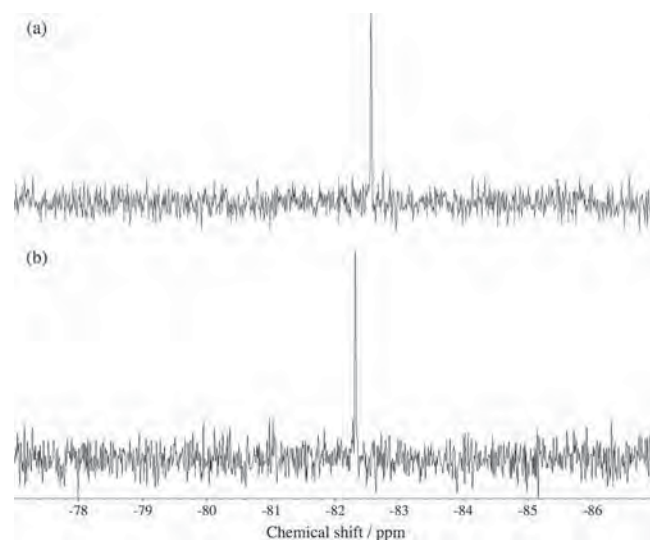


Figure 6. Solution ^{29}Si NMR spectra of (a) **Al₄-open** and (b) **Ga₄-open** dissolved in D_2O .

It has been recognized that ^{183}W NMR chemical shifts are extremely sensitive to tiny structural changes. The ^{183}W NMR spectra of **Al₄-open** in D₂O (Figure 7a) showed a five-line spectrum at -79.67 (2 W), -83.33 (2 W), -149.84 (2 W), -175.17 (1 W), and -197.67 (2 W) ppm. The five-line spectrum is consistent with the molecular structure of **Al₄-open**. The ^{183}W NMR spectra of **Ga₄-open** in D₂O (Figure 7b) also showed a five-line spectrum at -64.31 (2 W), -72.52 (2 W), -151.79 (2 W), -167.10 (1 W), and -194.70 (2 W) ppm. The trigallium(III)-substituted dimer, **Ga₆-dimer**, and the di-gallium(III)-substituted dimer, **Ga₄-dimer**, reported by Patzke et al. showed a two-line spectrum (-81.289 , -160.571 ppm) and a six-line spectrum (-70.754 , -85.283 , -117.227 , -156.435 , -164.894 , and -169.969 ppm), respectively.^[6e] The five-line spectra are characteristic of **Al₄-** and **Ga₄-open**, suggesting that **Al₄-** and **Ga₄-open** existed as a single species and maintained their structures in solution. In addition, **Ga₄-open** was clearly distinguishable from tri- and di-gallium(III)-substituted dimers by ^{183}W NMR spectroscopy.

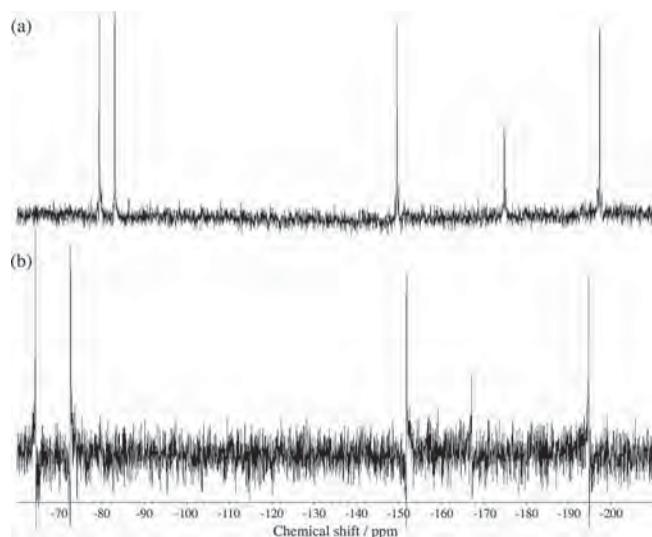


Figure 7. Solution ^{183}W NMR spectra of (a) **Al₄-open** and (b) **Ga₄-open** dissolved in D₂O.

The sample obtained in the early stage of crystallization of **Ga₄-open** showed two minor ^{183}W NMR peaks at -80.73 and -159.67 ppm, together with the main five peaks of **Ga₄-open** (Figure S3, Supporting Information). The chemical shifts of the minor peaks were in accordance with those of the **Ga₆-dimer**, and, in fact, the **Ga₆-dimer** was formed as a minor product under our reaction conditions. The sample contaminated with **Ga₆-dimer** can be easily purified by recrystallization from water.

Conclusions

The open-Dawson structural POMs containing aluminum or gallium, i.e., $\text{K}_{10}[\{\text{Al}_4(\mu\text{-OH})_6\}(\alpha,\alpha\text{-Si}_2\text{W}_{18}\text{O}_{66})]\cdot 28.5\text{H}_2\text{O}$ (**Al₄-open**), and $\text{K}_{10}[\{\text{Ga}_4(\mu\text{-OH})_6\}(\alpha,\alpha\text{-Si}_2\text{W}_{18}\text{O}_{66})]\cdot 25\text{H}_2\text{O}$ (**Ga₄-open**) were synthesized and characterized. The solution ^{29}Si and ^{183}W NMR spectra in D₂O indicated that both **Al₄-**

open and **Ga₄-open** were obtained as a single species and their structures were maintained in solution. Single-crystal X-ray analyses revealed that the $\{\text{M}_4(\mu\text{-OH})_6\}^{6+}$ ($\text{M} = \text{Al}, \text{Ga}$) cluster is included in an open pocket of the open-Dawson polyanion. There are many interactions between the oxygen atoms of the open-Dawson units and the K^+ cations in the crystal structures of **Al₄-** and **Ga₄-open**, and these interactions appear to play an important role in the formation of open-Dawson structural POMs. Synthesis and structural characterization of the open-Dawson POMs family, which contains tetranuclear Al and Ga moieties in the open pocket, elucidated clear difference of the bite angles. The Al and Ga sites in **Al₄-** and **Ga₄-open** would act as Lewis acid sites, and **Al₄-** and **Ga₄-open** are expected to be used as the Lewis-acid catalysis. In addition, this work can be extended to future molecular design of novel open-Dawson POMs containing different transition metal ions with varying nuclearities beyond group 13 elements. Studies of the open-Dawson structural POMs containing other group 13 metal such as In^{3+} are in progress.

Experimental Section

Materials The following reagents were used as received: $\text{Al}(\text{NO}_3)_3\cdot 9\text{H}_2\text{O}$, $\text{Ga}(\text{NO}_3)_3\cdot n\text{H}_2\text{O}$ ($n = 7\text{--}9$), HCl, KOH, KCl (all from Wako Pure Chemical Industries), and D₂O (Kanto Chemical). The trilacunary Keggin POMs, i.e., $\text{Na}_{10}[\text{A-}\alpha\text{-SiW}_9\text{O}_{34}]\cdot 18\text{H}_2\text{O}$ and $\text{K}_{10}[\text{A-}\alpha\text{-SiW}_9\text{O}_{34}]\cdot 10\text{H}_2\text{O}$, were prepared according to the literature methods,^[8,9] and identified by TG/DTA and FT-IR analysis.

Instrumentation and Analytical Procedures Elemental analyses were carried out by Mikroanalytisches Labor Pascher (Remagen, Germany). The samples were dried overnight at room temperature in the range of 10^{-3} to 10^{-4} Torr before analysis. The ^{29}Si NMR (99.4 MHz) spectra in D₂O solution were recorded in 5-mm outer diameter tubes with a JEOL JNM ECP 500 FTNMR spectrometer and a JEOL ECP-500 NMR spectroscopic data processing system. The ^{29}Si NMR spectra were referenced to an internal standard of DSS. The ^{183}W NMR (20.8 MHz) spectra were recorded in 10-mm outer diameter tubes, with a JEOL JNM-ECP 500 FT-NMR spectrometer equipped with a JEOL NM-50T10L low-frequency tunable probe and a JEOL ECP-500 NMR spectroscopic data processing system. These spectra were referenced to an external standard (saturated $\text{Na}_2\text{WO}_4/\text{D}_2\text{O}$ solution) by the substitution method. Chemical shifts were reported on the δ scale with resonances upfield of Na_2WO_4 ($\delta = 0$ ppm) as negative. Infrared spectra were recorded with a Jasco 4100 FTIR spectrometer by using KBr disks at room temperature. Thermogravimetric (TG) and differential thermal analyses (DTA) were acquired with a Rigaku Thermo Plus 2 series TG8120 instrument. TG/DTA measurements were run under air with a temperature ramp of 4.0°C per min between 20 (for **Al₄-open**) or 22 (for **Ga₄-open**) and 500°C .

Al₄-open $\text{Na}_{10}[\text{A-}\alpha\text{-SiW}_9\text{O}_{34}]\cdot 18\text{H}_2\text{O}$ (6.0 g, 2.16 mmol) was suspended in 120 mL of water. The pH was adjusted to 7.5 using HCl_{aq} (0.1 M). $\text{Al}(\text{NO}_3)_3\cdot 9\text{H}_2\text{O}$ (1.62 g, 4.32 mmol) was added to the solution, and the solution was heated to 80°C for 30 min. The pH dropped to 2.00. Subsequently the pH was adjusted to 6.5 by KOH_{aq} (1 M) and saturated KCl_{aq} (6 mL) was added to the solution. After 1 d, colorless crystals formed, which were removed by a membrane filter (JG 0.2 μm). Saturated KCl_{aq} (6 mL) was added to the filtrate, and the solution was left undisturbed at room temperature. After 1 d, colorless needle crystals formed,

which were collected on a membrane filter (JG 0.2 μm), washed with cold water, and dried in vacuo for 2 h. The yield was 0.818 g (0.148 mmol, 13.7% based on $\text{Na}_{10}[\text{A-}\alpha\text{-SiW}_9\text{O}_{34}]\cdot 18\text{H}_2\text{O}$).

The crystalline sample was soluble in water but insoluble in organic solvents such as methanol, ethanol, and diethyl ether. $\text{H}_{28}\text{Al}_4\text{K}_{10}\text{O}_{83}\text{Si}_2\text{W}_{18}$ or $\text{K}_{10}[\{\text{Al}_4(\text{OH})_6\}(\text{Si}_2\text{W}_{18}\text{O}_{66})]\cdot 11\text{H}_2\text{O}$: calcd. H 0.54, Al 2.07, K 7.49, O 25.44, Si 1.08, W 63.39%; found: H 0.46, Al 1.90, K 7.64, O 24.9, Si 1.05, W 63.2%, total 99.15%. A weight loss of 3.93% (solvated water) was observed during overnight drying at room temperature, at 10^{-3} – 10^{-4} Torr before analysis, suggesting the presence of 12 water molecules. TG/DTA under atmospheric conditions: a weight loss of 9.26% was observed at below 500 $^\circ\text{C}$; calcd. 9.27% for $x = 28.5$ in $\text{K}_{10}[\{\text{Al}_4(\text{OH})_6\}(\text{Si}_2\text{W}_{18}\text{O}_{66})]\cdot x\text{H}_2\text{O}$. **R** (KBr): $\tilde{\nu}$ = (polyoxometalate region): 1623 (m), 1385 (w), 1010 (m), 958 (s), 907 (vs), 801 (vs), 755 (s), 710 (s), 657 (m), 523 (m) cm^{-1} . **² i R** (40.0 $^\circ\text{C}$, D_2O , DSS, ppm): $\delta = -82.55$. **¹ R** (D_2O , ppm): $\delta = -79.67$ (2 W \times 2), -83.33 (2 W \times 2), -149.84 (2 W \times 2), -175.17 (1 W \times 2), -197.67 (2 W \times 2).

¹⁰ Ga₄ ₆ $\alpha\alpha$ -i₂ ₁ ₆₆ $\cdot 25$ ₂ Ga₄-open $\text{K}_{10}[\text{A-}\alpha\text{-SiW}_9\text{O}_{34}]\cdot 10\text{H}_2\text{O}$ (3.0 g, 1.07 mmol) was suspended in 60 mL of water. The pH was adjusted to 7.5 using HCl_{aq} (0.1 M). $\text{Ga}(\text{NO}_3)_3\cdot n\text{H}_2\text{O}$ (0.86 g, 2.14 mmol calculated based on octahydrate) was added to the solution, and the solution was heated to 80 $^\circ\text{C}$ for 30 min. The pH dropped to 1.78. Subsequently the pH was adjusted to 6.5 by KOH_{aq} (1 M) and saturated KCl_{aq} (1.8 mL) was added to the solution. After 1 d, colorless needle crystals formed, which were collected on a membrane filter (JG 0.2 μm), and dried in vacuo for 2 h. The yield was 0.79 g (0.140 mmol, 26.2% based on $\text{K}_{10}[\text{A-}\alpha\text{-SiW}_9\text{O}_{34}]\cdot 10\text{H}_2\text{O}$).

The crystalline sample was soluble in water but insoluble in organic solvents such as methanol, ethanol, and diethyl ether. $\text{H}_{16}\text{Ga}_4\text{K}_{10}\text{O}_{77}\text{Si}_2\text{W}_{18}$ or $\text{K}_{10}[\{\text{Ga}_4(\text{OH})_6\}(\text{Si}_2\text{W}_{18}\text{O}_{66})]\cdot 5\text{H}_2\text{O}$: calcd. H 0.31, Ga 5.28, K 7.40, Si 1.06, W 62.63%; found: H 0.32, Ga 4.94, K 7.75, Si 1.04, W 62.7%. A weight loss of 5.32% (solvated water) was observed during overnight drying at room temperature, at 10^{-3} – 10^{-4} Torr, before analysis, suggesting the presence of 18 water molecules. TG/DTA under atmospheric conditions: a weight loss of 7.96% was observed at below 500 $^\circ\text{C}$; calcd. 8.09% for $x = 25$ in $\text{K}_{10}[\{\text{Ga}_4(\text{OH})_6\}(\text{Si}_2\text{W}_{18}\text{O}_{66})]\cdot x\text{H}_2\text{O}$. **R** (KBr): $\tilde{\nu}$ = (polyoxometalate region): 1623 (m), 1007 (m), 958 (m), 925 (s), 898 (vs), 785 (vs), 740 (s), 675 (m), 638 (m), 545 (m), 521 (m), 494 (m) cm^{-1} . **² i R** (40.0 $^\circ\text{C}$, D_2O , DSS, ppm): $\delta = -82.31$. **¹ R** (D_2O , ppm): $\delta = -64.31$ (2 W \times 2), -72.52 (2 W \times 2), -151.79 (2 W \times 2), -167.10 (1 W \times 2), -194.70 (2 W \times 2).

-ra r stallo rap Single crystals with dimensions of $0.24 \times 0.09 \times 0.05$ mm^3 for **Al₄-open**, and $0.40 \times 0.08 \times 0.08$ mm^3 for **Ga₄-open** were surrounded by liquid paraffin (Paratone-N) and analyzed at 150(2) K. All measurements were performed with a Rigaku MicroMax-007HF with Saturn CCD diffractometer. The structures were solved by direct methods (SHELXS-97),^[10a] followed by difference Fourier calculation and refinement by a full-matrix least-squares procedure on ² (program SHELXL-97).^[10b] Most atoms in the main part of the structure were refined anisotropically, while the rest (as crystallization solvents) were refined isotropically because of the presence of disorder. The composition and formula of the POM containing many counteranions and many crystallization water molecules were determined by elemental analysis and TG analysis. As with other structural investigations of crystals of highly hydrated large polyoxometalate complexes, it was not possible to locate every counteranion and crystallization water molecule. This frequently encountered situation is attributed to extensive disorder of the cations and many of the

crystallization water molecules. The details of the crystallographic data for **Al₄-open** and **Ga₄-open** are listed in Table 1.

Table 1. Crystallographic data and structure refinement results for **Al₄-open** and **Ga₄-open**.

	Al₄ open-Dawson	Ga₄ open-Dawson
Formula	$\text{Al}_4\text{K}_8\text{O}_{96}\text{Si}_2\text{W}_{18}$	$\text{Ga}_4\text{K}_7\text{O}_{93}\text{Si}_2\text{W}_{18}$
Formula weight	5322.20	5406.06
Color, shape	colorless, prism	colorless, needle
Crystal system	monoclinic	monoclinic
Space group	$P2_1/$	$P2_1/$
Z	150(2)	150(2)
$a/\text{\AA}$	18.015(3)	18.170(2)
$b/\text{\AA}$	20.254(3)	20.226(3)
$c/\text{\AA}$	24.115(4)	24.007(3)
$\beta/^\circ$	111.4877(19)	111.8525(16)
$V/\text{\AA}^3$	8187(2)	8212.2(18)
Z	4	4
$D_{\text{calc}}/\text{g}\cdot\text{cm}^{-3}$	4.318	4.373
(000)	9328	9444
GOF	1.075	1.109
χ^2 ($I > 2.00\sigma(I)$)	0.0430	0.0527
(all data)	0.0466	0.0584
χ^2 (all data)	0.1067	0.1253

Further details of the crystal structures investigations may be obtained from the Fachinformationszentrum Karlsruhe, 76344 Eggenstein-Leopoldshafen, Germany (Fax: +49-7247-808-666; E-Mail: crysdata@fiz-karlsruhe.de, <http://www.fiz-karlsruhe.de/request> for deposited data.html) on quoting the depository numbers CSD-429730 for **Al₄-open** (Identification code; 1403252) and CSD-428783 for **Ga₄-open** (Identification code; 1401212).

Supporting Information (see footnote on the first page of this article): Bond valence sum (BVS) calculations of **Al₄-** and **Ga₄-open** (Tables S1, S2), FT-IR spectra of **Al₄-** and **Ga₄-open** (Figures S1 and S2), ¹⁸³W NMR of the sample obtained in early stage of crystallization of **Ga₄-open** (Figure S3), TG/DTA data of **Al₄-** and **Ga₄-open** (Figures S4 and S5).

Ac no led ements

This study was supported by JSPS KAKENHI Grant number 22550065, by the Strategic Research Base Development Program for Private Universities of the Ministry of Education, Culture, Sports, Science and Technology of Japan, and also by a grant from Research Institute for Integrated Science, Kanagawa University (RIIS201505).

Re erences

- [1] a) M. T. Pope, A. Müller, *Angew. Chem. Int. Ed.* **1**, 34–48; b) M. T. Pope, *Heteropoly and Isopolyoxometalates*, Springer-Verlag: New York, **1**; A series of 12 reviews in a volume: c) C. L. Hill (Ed.), *Chem. Rev.* **1**, 1–390; d) T. Okuhara, N. Mizuno, M. Misono, *Acc. Chem. Res.* **1**, 113–252; e) C. L. Hill, C. M. Prosser-McCartha, *Coord. Chem. Rev.* **1**, 407–455; A series of 34 papers in a volume devoted to *Polyoxoanions in Catalysis*: f) C. L. Hill (Ed.), *Mol. Catal. A* **1**, 1–371; g) R. Neumann, *Prog. Inorg. Chem.* **1**, 317–370; h) M. T. Pope, A. Müller (Eds.), *Polyoxometalate Chemistry from Molecular Assemblies to Materials*, Kluwer Academic Publishers, Netherlands, **2001**; i) T. Yamase, M. T. Pope (Eds.), *Polyoxometalate Chemistry and Catalysis*, Wiley, 2001.

- Kluwer Academic Publishers, Netherlands, **2002**; j) M. T. Pope, *Polyoxo Anions synthesis and structure*, in *Comprehensive Coordination Chemistry*, (Ed.: A. G. Wedd), Elsevier, New York, **2004**, Vol. 4, p. 635; k) C. L. Hill, *Polyoxometalates synthesis*, in *Comprehensive Coordination Chemistry* (Ed.: A. G. Wedd), Elsevier Science: New York, **2004**, Vol. 4, p. 679; A series of 32 papers in a volume devoted to *Polyoxometalates in Catalysis*, l) C. L. Hill (Ed.), *Mol. Catal. A* **200**, , 1–242; m) A. Proust, R. Thouvenot, P. Gouzerh, *Chem. Comm. n.* **200**, 1837–1852; n) B. Hasenkopf, K. Micoine, E. Lacôte, S. Thorimbert, M. Malacria, R. Thouvenot, *Chem. Comm. n.* **200**, 5001–5013; o) D.-L. Long, R. Tsunashima, L. Cronin, *Angew. Chem. nt.* **2010**, 1736–1758; p) K. Nomiyama, Y. Sakai, S. Matsunaga, *Chem. Comm. n.* **2011**, 179–196; q) M. T. Pope, U. Kortz, *Polyoxometalates, in synthesis and applications in inorganic Chemistry*, Wiley, Weinheim, **2012**; r) N. V. Izarova, M. T. Pope, U. Kortz, *Angew. Chem. nt.* **2012**, 9492–9510; s) Y.-F. Song, R. Tsunashima, *Chem. Comm. n.* **2012**, 7384–7402; t) A. Bijelic, A. Rempel, *Coord. Chem. Rev.* **2015**, 22–38; u) S.-S. Wang, G.-Y. Yang, *Chem. Comm. n.* **2015**, 4893–4962; v) A. Blazevic, A. Rempel, *Coord. Chem. Rev.* **2016**, 42–64.
- [2] a) N. Laronze, J. Marrot, G. Hervé, *Chem. Comm. n.* **200**, 2360–2361; b) L.-H. Bi, U. Kortz, *Chem. Comm. n.* **2004**, 7961–7962; c) N. Leclerc-Laronze, J. Marrot, G. Hervé, *Chem. Comm. n.* **2005**, 1275–1281; d) S. Nellutla, J. van Tol, N. S. Dalal, L.-H. Bi, U. Kortz, B. Keita, L. Nadjo, G. A. Khitrov, A. G. Marshall, *Inorg. Chem.* **2005**, 9795–9806; e) N. Leclerc-Laronze, M. Haouas, J. Marrot, F. Taulelle, G. Hervé, *Angew. Chem. nt.* **2006**, 139–142; f) N. Leclerc-Laronze, J. Marrot, G. Hervé, *Chim. Ind. (Milan)* **2006**, 1467–1471; g) C.-Y. Sun, S.-X. Liu, C.-L. Wang, L.-H. Xie, C.-D. Zhang, B. Gao, Z.-M. Su, H.-Q. Jia, *Mol. Cryst. Liq. Cryst.* **2006**, 170–175; h) C.-L. Wang, S.-X. Liu, C.-Y. Sun, L.-H. Xie, Y.-H. Ren, D.-D. Liang, H.-Y. Cheng, *Mol. Cryst. Liq. Cryst.* **200**, 88–95; i) L. Ni, F. Hussain, B. Spingler, S. Weyeneth, G. R. Patzke, *Inorg. Chem.* **2011**, 4944–4955; j) G. Zhu, Y. V. Geletii, C. Zhao, D. G. Musaev, J. Song, C. L. Hill, *Alton Rans.* **2012**, 9908–9913; k) G. Zhu, E. N. Glass, C. Zhao, H. Lv, J. W. Vickers, Y. V. Geletii, D. G. Musaev, J. Song, C. L. Hill, *Alton Rans.* **2012**, 13043–13049; l) G. Zhu, Y. V. Geletii, J. Song, C. Zhao, E. N. Glass, J. Bacsa, C. L. Hill, *Inorg. Chem.* **201**, 1018–1024; m) L. Ni, B. Spingler, S. Weyeneth, G. R. Patzke, *Inorg. Chem.* **201**, 1681–1692; n) J. Guo, D. Zhang, L. Chen, Y. Song, D. Zhu, Y. Xu, *Alton Rans.* **201**, 8454–8459.
- [3] a) T. Minato, K. Suzuki, K. Kamata, N. Mizuno, *Chem. Comm. n.* **2014**, 5946–5952; b) F.-Q. Zhang, W. Guan, L.-K. Yan, Y.-T. Zhang, M.-T. Xu, E. Hayfron-Benjamin, Z.-M. Su, *Inorg. Chem.* **2011**, 4967–4977.
- [4] a) P. A. Jordan, N. J. Clayden, S. L. Heath, G. R. Moore, A. K. Powell, A. Tapparo, *Coord. Chem. Rev.* **1** **6**, 281–309; b) W. H. Casey, *Chem. Comm. n.* **2006**, 1–16; c) Z. L. Mensinger, W. Wang, D. A. Keszler, D. W. Johnson, *Chem. Comm. n.* **2012**, 1019–1030.
- [5] a) Q. H. Yang, D. F. Zhou, H. C. Dai, J. F. Liu, Y. Xing, Y. H. Lin, H. Q. Jia, *Polyhedron* **1**, 3985–3989; b) Y. Kikukawa, S. Yamaguchi, Y. Nakagawa, K. Uehara, S. Uchida, K. Yamaguchi, N. Mizuno, *Am. Chem. Soc.* **200**, 15872–15878; c) C. N. Kato, Y. Katayama, M. Nagami, M. Kato, M. Yamasaki, *Alton Rans.* **2010**, 11469–11474; d) Y. Kikukawa, K. Yamaguchi, M. Hibino, N. Mizuno, *Inorg. Chem.* **2011**, 12411–12413; e) M. Carraro, B. S. Bassil, A. Sorarù, S. Berardi, A. Surchopar, U. Kortz, M. Bonchio, *Chem. Comm. n.* **201**, 7914–7916; f) C. N. Kato, Y. Makino, W. Unno, H. Uno, *Alton Rans.* **201**, 1129–1135; g) C. N. Kato, T. Kashiwagi, W. Unno, M. Nakagawa, H. Uno, *Inorg. Chem.* **2014**, 4823–4832.
- [6] a) F. Zonnevillje, C. M. Tourné, G. F. Tourné, *Inorg. Chem.* **1** **2**, 2742–2750; b) N. Yamamoto, D. Schols, E. de Clercq, Z. Debyser, R. Pauwels, J. Balzarini, H. Nakashima, M. Baba, M. Ho-soya, R. Snoeck, *Mol. Pharm. ol.* **1** **2**, 1109–1117; c) J. Liu, F. Ortega, P. Sethuraman, D. E. Katsoulis, C. E. Costello, M. T. Pope, *Chem. Comm. n.* **1** **2**, 1901–1906; d) L. Meng, J.-F. Liu, Y.-J. Wu, Y.-W. Xiao, D.-Q. Zhao, *Chin. Chem. Lett.* **1** **5**, 334–339; e) K. Allmen, P.-E. Car, O. Blacque, T. Fox, R. Müller, G. R. Patzke, *Z. Anorg. Allg. Chem.* **2014**, 781–789; f) M. A. Fedotov, L. P. Kazanskii, *Il. A. A. i. Chem. i. ngl. ransl.* **1**, 1789–1792; g) B. Lihua, P. Jun, C. Yaguang, L. Jingfu, Q. Lunyu, *Polyhedron* **1** **4**, 2421–2424; h) J. Liu, X. Zhan, Y. Chen, G. Li, J. Wang, *Ransition Met. Chem.* **1** **5**, 327–329; i) J.-Y. Niu, M.-X. Li, J.-P. Wang, Y. Bo, *Chem. Crystallogr.* **200**, 799–803; j) D. Drewes, E. M. Limanski, B. Krebs, *Inorg. Chem.* **2005**, 1542–1546; k) S. Himeno, S. Murata, K. Eda, *Alton Rans.* **200**, 6114–6119.
- [7] Y. Inoue, S. Matsunaga, K. Nomiyama, *Chem. Lett.* **2015**, 1649–1651.
- [8] A. Tézé, G. Hervé, in: *Inorganic Syntheses* (Ed.: A. P. Ginsberg), John Wiley and Sons, New York, **1** **0**, vol. 27, pp. 85–96.
- [9] N. Laronze, J. Marrot, G. Herve, *Inorg. Chem.* **200**, 5857–5862.
- [10] a) G. M. Sheldrick, *Acta Crystallogr. Sect. A* **1** **0**, 467–473; b) G. M. Sheldrick, *H*, Program for Crystal Structure Refinement; University of Göttingen: Göttingen, Germany, **1**.
- [11] a) I. D. Brown, D. Altermatt, *Acta Crystallogr. Sect. A* **1** **5**, 244–247; b) I. D. Brown, R. D. Shannon, *Acta Crystallogr. Sect. A* **1** **2**, 266–282; c) I. D. Brown, *Acta Crystallogr. Sect. A* **1** **2**, 553–572; d) I. D. Brown, *Acta Crystallogr.* **1** **6**, 479–480.
- [12] a) R. D. Shannon, C. T. Prewitt, *Acta Crystallogr. Sect. A* **1** **6**, 925–946; b) R. D. Shannon, *Acta Crystallogr. Sect. A* **1** **6**, 751–761.

Received: November 27, 2015
Published Online: April 5, 2016

Article

β,β -Isomer of Open-Wells–Dawson Polyoxometalate Containing a Tetra-Iron(III) Hydroxide Cluster: $[\{\text{Fe}_4(\text{H}_2\text{O})(\text{OH})_5\}(\beta,\beta\text{-Si}_2\text{W}_{18}\text{O}_{66})]^{9-}$

Satoshi Matsunaga, Eriko Miyamae, Yusuke Inoue and Kenji Nomiya *

Department of Chemistry, Faculty of Science, Kanagawa University, Hiratsuka, Kanagawa 259-1293, Japan; matsunaga@kanagawa-u.ac.jp (S.M.); miyamae.527@gmail.com (E.M.); r201470042gl@jindai.jp (Y.I.)

* Correspondence: nomiya@kanagawa-u.ac.jp; Tel.: +81-463-59-4111

Academic Editor: Duncan H. Gregory

Received: 15 April 2016; Accepted: 9 May 2016; Published: 17 May 2016

Abstract: The β,β -isomer of open-Wells–Dawson polyoxometalate (POM) containing a tetra-iron(III) cluster, $\text{K}_9[\{\text{Fe}_4(\text{H}_2\text{O})(\text{OH})_5\}(\beta,\beta\text{-Si}_2\text{W}_{18}\text{O}_{66})] \cdot 17\text{H}_2\text{O}$ (potassium salt of $\beta,\beta\text{-Fe}_4\text{-open}$), was synthesized by reacting $\text{Na}_9\text{H}[\text{A-}\beta\text{-SiW}_9\text{O}_{34}] \cdot 23\text{H}_2\text{O}$ with $\text{FeCl}_3 \cdot 6\text{H}_2\text{O}$ at pH 3, and characterized by X-ray crystallography, FTIR, elemental analysis, TG/DTA, UV–Vis, and cyclic voltammetry. X-ray crystallography revealed that the $\{\text{Fe}^{3+}_4(\text{H}_2\text{O})(\text{OH})_5\}^{7+}$ cluster was included in the open pocket of the β,β -type open-Wells–Dawson polyanion $[\beta,\beta\text{-Si}_2\text{W}_{18}\text{O}_{66}]^{16-}$ formed by the fusion of two trilacunary β -Keggin POMs, $[\text{A-}\beta\text{-SiW}_9\text{O}_{34}]^{10-}$, via two W–O–W bonds. The β,β -open-Wells–Dawson polyanion corresponds to an open structure of the standard γ -Wells–Dawson POM. $\beta,\beta\text{-Fe}_4\text{-open}$ is the first example of the compound containing a geometrical isomer of α,α -open-Wells–Dawson structural POM.

Keywords: polyoxometalates; open-Wells–Dawson structural POM; iron; geometrical isomer

1. Introduction

Polyoxometalates (POMs) are discrete metal oxide clusters that are of interest as soluble metal oxides, with applications in catalysis, medicine, and materials science [1–13]. Recently, the open-Wells–Dawson POMs have been an emerging class of POMs [14–28]. The standard Wells–Dawson structural POM is regarded as an assembly of two trilacunary Keggin POMs via six W–O–W bonds. In 2014, Mizuno *et al.* reported the synthesis of a standard Wells–Dawson structural POM with a highly charged guest SiO_4^{4-} , $\text{TBA}_8[\alpha\text{-Si}_2\text{W}_{18}\text{O}_{62}] \cdot 3\text{H}_2\text{O}$, by dimerization of a trilacunary Keggin POM, $[\alpha\text{-SiW}_9\text{O}_{34}]^{10-}$, in an organic solvent [29]. However, in aqueous media, the electrostatic repulsion induced by the highly charged guest XO_4^{4-} ($\text{X} = \text{Si}, \text{Ge}$) inhibits the assembly of the standard Wells–Dawson structure [30]. Therefore, the two trilacunary Keggin units with XO_4^{4-} ($\text{X} = \text{Si}, \text{Ge}$) are linked by two W–O–W bonds, forming open-Wells–Dawson structural POMs. The open pocket of these POMs can accommodate up to six metals. Thus, these compounds constitute a promising platform for the development of metal-substituted POM-based materials and catalysts. To date, many compounds with various metal ions in their open pocket have been reported. For example, V^{5+} [19], Mn^{2+} [16,21], Fe^{3+} [19], Co^{2+} [14,16,20,21,25,27], Ni^{2+} [16,21,24,27], Cu^{2+} [15–17], Zn^{2+} [23], Al^{3+} [28], Ga^{3+} [28], and lanthanoid (Eu^{3+} , Gd^{3+} , Tb^{3+} , Dy^{3+} , Ho^{3+}) [22,26].

The standard Wells–Dawson structural POM is one of the most deeply studied POMs. Baker and Figgis predicted the existence of six possible structural isomers of the Wells–Dawson POM (α , β , γ , α^* , β^* , γ^*) [31]. So far, only the α -, β -, γ -, and γ^* - isomers have been experimentally confirmed [32–37]. The α -Wells–Dawson POM has D_{3h} symmetry (Figure 1, upper left). The β - and γ -Wells–Dawson isomers exhibit C_{3v} and D_{3h} symmetries, respectively, and are derived from the α -Wells–Dawson

isomer by a 60° rotation of one (β -isomer) or two (γ -isomer) $\{M_3O_{13}\}$ caps about the three-fold axis of the α -Wells–Dawson isomer (Figure 1, upper middle and right). Likewise, the α^* -, β^* -, and γ^* -Wells–Dawson isomers are derived from the α -, β -, and γ -isomer by a 60° rotation of half $\{XM_9\}$ units.

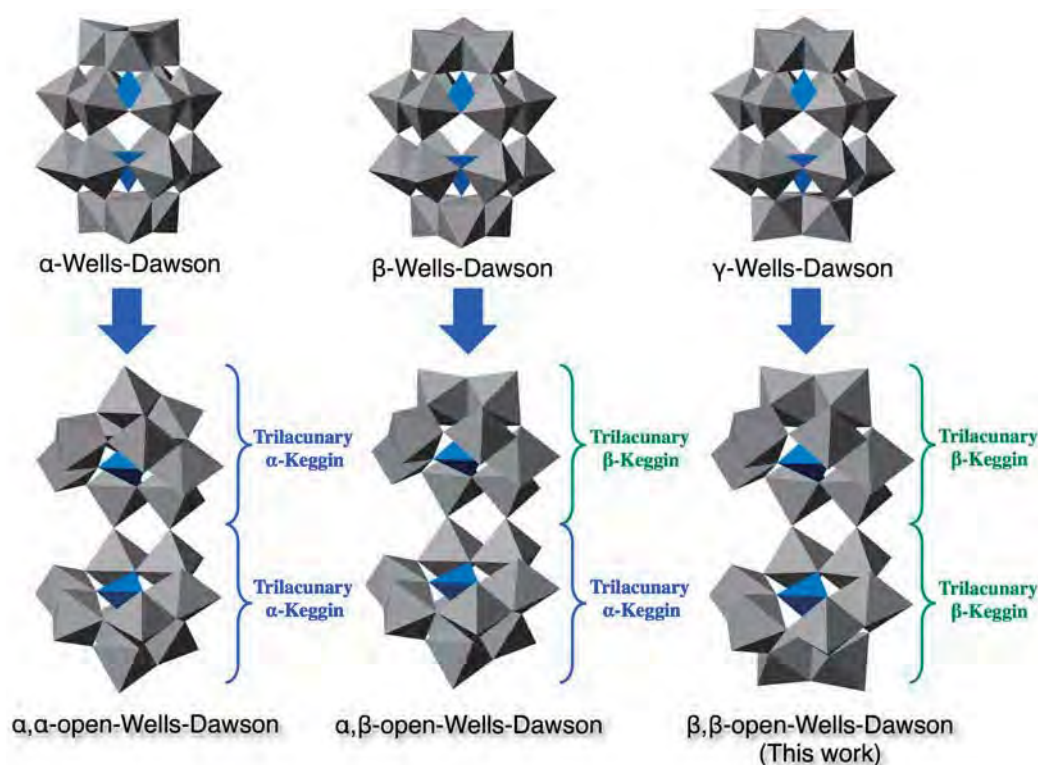


Figure 1. The isomers of the usual Wells–Dawson structural POMs and the open-Wells–Dawson POMs. Color code: XO_4 , blue; WO_6 , gray.

On the basis of the analogy with the standard Wells–Dawson isomers, the isomers of the open-Wells–Dawson POMs are possible. The well-known α, α -open-Wells–Dawson POM [α, α - $X_2W_{18}O_{66}$] $^{16-}$, built from two trilacunary α -Keggin units [A - α - XW_9O_{34}] $^{10-}$ by two W–O–W bonds, corresponds to an open structure of the conventional α -Wells–Dawson POM (Figure 1, lower left). A similar assembly of two trilacunary β -Keggin units prompts the β, β -open-Wells–Dawson isomer, which is viewed as an open structure of the γ -Wells–Dawson POM (Figure 1, lower right). Likewise, an assembly of the trilacunary α - and β -Keggin POMs leads to the α, β -open-Wells–Dawson isomer corresponding to an open structure of the β -Wells–Dawson POM. However, only the α, α -isomer of the open-Wells–Dawson structural POM has been reported so far.

Herein, we report the synthesis of the β, β -isomer of the open-Wells–Dawson POM containing a tetra-iron(III) cluster, $K_9[\{Fe_4(H_2O)(OH)_5\}(\beta, \beta-Si_2W_{18}O_{66})] \cdot 17H_2O$ (potassium salt of β, β - Fe_4 -open) and its characterization by X-ray crystallography, FTIR, elemental analysis, TG/DTA, UV–Vis, and cyclic voltammetry. The β, β - Fe_4 -open is the first example of the compound containing a geometrical isomer of the α, α -open-Wells–Dawson structural POM.

2. Results and Discussion

2.1. Synthesis and Characterization

The potassium salts of β, β - Fe_4 -open, $K_9[\{Fe_4(H_2O)(OH)_5\}(\beta, \beta-Si_2W_{18}O_{66})] \cdot 17H_2O$, were prepared by the reaction of the separately prepared $Na_9H[A-\beta-SiW_9O_{34}] \cdot 23H_2O$ with $FeCl_3 \cdot 6H_2O$ in a 1:2 molar ratio at pH 3, followed by stirring the solution at $80^\circ C$ for 30 min. The β, β -type

open-Wells–Dawson POM containing a tetra-iron(III) cluster was obtained as crystalline sample with 22.2% yield.

Equation (1) represents the formation of the polyoxoanion $[\{\text{Fe}_4(\text{H}_2\text{O})(\text{OH})_5\}(\beta,\beta\text{-Si}_2\text{W}_{18}\text{O}_{66})]^{9-}$.



In the case of the α,α -analogue, *i.e.*, $\text{K}_2\text{Na}_8[\{\text{Fe}_4(\text{OH})_6\}(\text{Si}_2\text{W}_{18}\text{O}_{66})] \cdot 44\text{H}_2\text{O}$ ($\alpha,\alpha\text{-Fe}_4\text{-open}$) [19], the K^+ ions incorporating the open-Wells–Dawson POM, *i.e.*, $\text{K}_{13}[\{\text{K}(\text{H}_2\text{O})_3\}_2\{\text{K}(\text{H}_2\text{O})_2\}(\alpha,\alpha\text{-Si}_2\text{W}_{18}\text{O}_{66})] \cdot 19\text{H}_2\text{O}$ (**K-open**), were used as a precursor, whereas the potassium salt of $\beta,\beta\text{-Fe}_4\text{-open}$ was prepared from the trilacunary β -Keggin POM, *i.e.*, $\text{Na}_9\text{H}[\text{A-}\beta\text{-SiW}_9\text{O}_{34}] \cdot 23\text{H}_2\text{O}$. Both α,α - and $\beta,\beta\text{-Fe}_4\text{-open}$ were prepared at *ca.* pH 3. Excess K^+ ions are required for the formation of the α,α -open-Wells–Dawson POM [25,28], indicating that K^+ ions play an important role in the synthesis. In the case of the present β,β -open-Wells–Dawson POM, the addition of excess KCl was needed, indicating that K^+ ions also play an important role in the formation of the β,β -open-Wells–Dawson structural POMs.

The potassium salt of $\beta,\beta\text{-Fe}_4\text{-open}$ was characterized via elemental analysis. Prior to analysis, the sample was dried overnight at room temperature under a vacuum of 10^{-3} – 10^{-4} Torr. All elements (H, Fe, K, O, Si, and W) were analyzed for a total of 99.74%, indicating that the obtained compound was highly pure. The observed data was in accordance with the calculated values for the formula constituting four water molecules, *i.e.*, $\text{K}_9[\{\text{Fe}_4(\text{H}_2\text{O})(\text{OH})_5\}(\beta,\beta\text{-Si}_2\text{W}_{18}\text{O}_{66})] \cdot 4\text{H}_2\text{O}$ (see Experimental Section). The weight loss observed during drying was 4.23% corresponding to *ca.* 13 crystallized water molecules (calcd. 4.33%), and therefore, the sample contained a total of 17 crystallized water molecules. On the other hand, during the TG/DTA measurements carried out under atmospheric conditions (Figure S2), a weight loss of 6.10%, observed at temperatures below 500 °C, corresponded to *ca.* 18 water molecules (calcd. 5.98%). Thus, the elemental analysis and TG/DTA displayed a presence of a total of 17–18 water molecules for the sample under atmospheric conditions. The formula for the potassium salt of $\beta,\beta\text{-Fe}_4\text{-open}$ presented herein is decided as $\text{K}_9[\{\text{Fe}_4(\text{H}_2\text{O})(\text{OH})_5\}(\beta,\beta\text{-Si}_2\text{W}_{18}\text{O}_{66})] \cdot 17\text{H}_2\text{O}$ based on the results of the complete elemental analysis.

2.2. Molecular Structure

X-ray crystallography of $\beta,\beta\text{-Fe}_4\text{-open}$ revealed that a β,β -type open-Wells–Dawson polyanion is formed by the fusion of two trilacunary β -Keggin POMs, $[\text{A-}\beta\text{-SiW}_9\text{O}_{34}]^{10-}$, via two W–O–W bonds, and the $\{\text{Fe}^{3+}_4(\text{H}_2\text{O})(\text{OH})_5\}^{7+}$ cluster is included in the open pocket of the β,β -type open-Wells–Dawson polyanion, $[\beta,\beta\text{-Si}_2\text{W}_{18}\text{O}_{66}]^{16-}$ (Figure 2). The structure of the β,β -open-Wells–Dawson polyanion moiety is derived by a 60° rotation of two $\{\text{M}_3\text{O}_{13}\}$ caps of the α,α -type isomer, corresponding to an open structure of the γ -Wells–Dawson POM; it is the first example of the isomer of the α,α -open-Wells–Dawson POM.

The four iron(III) centers in the open pocket were arranged in a rectangular array, and were connected to the neighboring iron atoms through edge-sharing oxygen atoms (O67, O68, O69, and O70) and corner-sharing oxygen atoms (O71 and O72). Bond valence sum (BVS) calculations [38] of the oxygen atoms connected to the iron atoms suggested that four of the oxygen atoms (O67, O69, O71, and O72) are protonated, *i.e.*, they are ascribed to the hydroxide groups (the BVS values: O67, 1.106; O69, 1.157; O71, 1.170; O72, 1.255; Table S1). On the other hand, the BVS values of two inner edge-sharing oxygen atoms (O68, 0.796 and O70, 0.660; Table S1) were slightly lower than those of other oxygen atoms connected to the iron atoms. These results suggested that there is one proton between two oxygen atoms (O68 and O70), *i.e.*, the iron(III) cluster in the open pocket can be represented as $\{\text{Fe}_4(\text{H}_2\text{O})(\text{OH})_5\}^{7+}$. All the iron atoms were in the +3 oxidation state (the BVS values: Fe1, 2.981; Fe2, 3.030; Fe3, 3.018; Fe4, 3.148; Table S1). These results were consistent with elemental analysis of the potassium salt of $\beta,\beta\text{-Fe}_4\text{-open}$. The Fe...Fe distances connected through edge-sharing oxygen atoms were 3.103(4) (Fe1–Fe3) and 3.114(4) (Fe2–Fe4) Å, and through corner-sharing oxygen atoms were

3.648(5) (Fe1–Fe2) and 3.646(5) (Fe3–Fe4). This metal ion arrangement was similar to that of previously reported α,α -Fe₄-open [19], and $[[M_4(OH)_6](\alpha,\alpha\text{-Si}_2W_{18}O_{66})]^{10-}$ (M = Al, Ga) [28].

The bite angle of β,β -Fe₄-open was 58.736°, similar to that of α,α -Fe₄-open (58.147°), and as for the structure around the open pocket, no clear difference was observed between the α,α - and β,β -Fe₄-open.

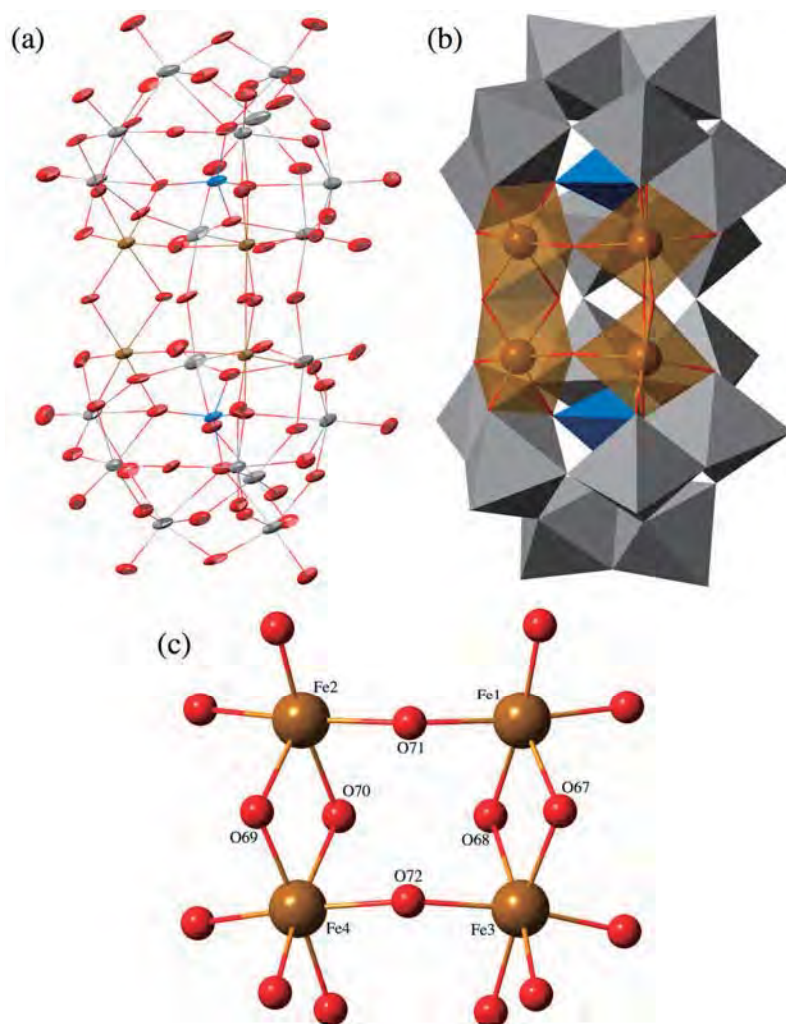


Figure 2. (a) Molecular structure of the polyoxoanion $[\text{Fe}_4(\text{H}_2\text{O})(\text{OH})_5](\beta,\beta\text{-Si}_2\text{W}_{18}\text{O}_{66})^{9-}$ of potassium salt of β,β -Fe₄-open; (b) its polyhedral representation; and (c) the partial structure around the Fe₄ center. Color code: Fe, brown; O, red; Si, blue; W, gray.

There are many interactions between the oxygen atoms of the polyanion moiety and K^+ in the crystal structure of β,β -Fe₄-open. In particular, the terminal (O15, O16, O37, O38) oxygen atoms of the WO_6 polyhedra serve as a hinge between the two trilacunary Keggin units interacting with K^+ cations (K1) (K1-O15, 2.800(14); K1-O16, 2.689(12); K1-O37, 2.685(14); K1-O38, 2.819(14) Å; Figure 3). These interactions play an important role in the formation of the β,β -type open-Wells–Dawson structural POMs and have been previously reported for the α,α -open-Wells–Dawson POMs [28].

2.3. Absorption Spectrum

The absorption spectrum of β,β -Fe₄-open in H_2O is shown in Figure 4. The shoulder band due to the O to Fe^{3+} charge transfer [39] was observed around 450 nm ($\epsilon = 98 \text{ M}^{-1} \cdot \text{cm}^{-1}$). This spectrum was similar to that of α,α -Fe₄-open (Figure S3).

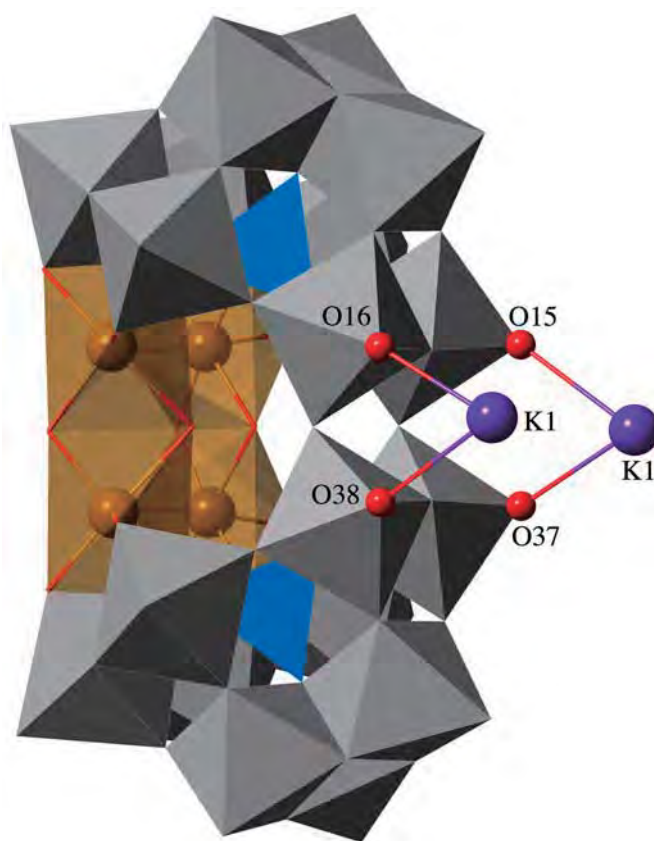


Figure 3. Interactions with K^+ ions of the terminal oxygen atoms of the WO_6 polyhedra serving as a hinge between the two trilacunary β -Keggin units of $\beta,\beta\text{-Fe}_4\text{-open}$.

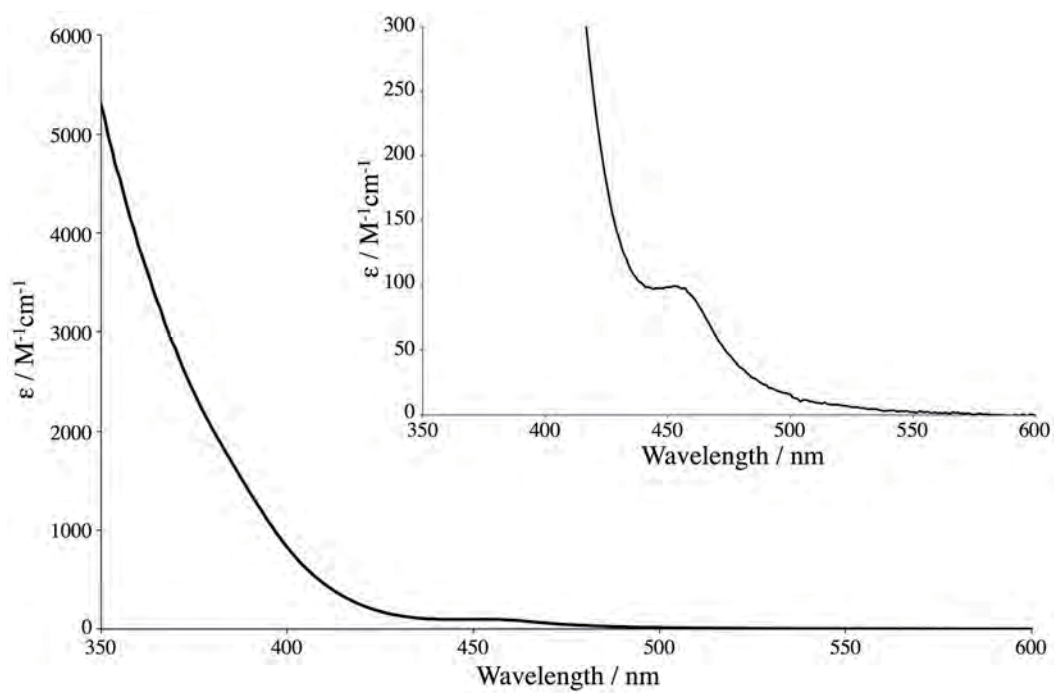


Figure 4. UV/Vis absorption spectrum of potassium salt of $\beta,\beta\text{-Fe}_4\text{-open}$ in H_2O . Inset shows enlarged view.

2.4. Electrochemistry

The cyclic voltammogram of 0.5 mM $\beta,\beta\text{-Fe}_4\text{-open}$ conducted in 0.5 M KOAc/HOAc buffer (pH 4.8) solution at a scan rate of $25\text{ mV}\cdot\text{s}^{-1}$ showed three characteristic peaks at -0.665 , -0.794 , and -0.939 V (*vs.* Ag/AgCl), respectively. These peaks were associated with W^{6+} centered reduction processes (Figure 5). Hill *et al.* have reported similar redox processes based on Zn-containing open-Wells–Dawson POMs [23], and noted that the second reduction wave associated with W^{6+} is a two-electron process. The cyclic voltammogram of 0.5 mM $\alpha,\alpha\text{-Fe}_4\text{-open}$ in 0.5 M KOAc/HOAc buffer (pH 4.8) solution at a scan rate of 25 mV/s was similar to that of $\beta,\beta\text{-Fe}_4\text{-open}$ (Figure S4). However, the reduction processes of $\alpha,\alpha\text{-Fe}_4\text{-open}$ based on W^{6+} were observed at a slightly more negative potential *i.e.*, (-0.704 , -0.866 , -0.936 V *vs.* Ag/AgCl) (Figure S4).

On the other hand, the redox waves observed at -0.212 and 0.380 V can be attributed to the redox processes of Fe^{3+} centers, since the Zn-containing open-Wells–Dawson POM displayed no redox waves in this region [23]. The area ratio between the second reduction wave of W^{6+} (two-electron process, $E = -0.794\text{ V}$) and the reduction of Fe^{3+} ($E = -0.212\text{ V}$) is *ca.* 1:2, *i.e.*, 2:4 electrons. Based on the comparison of the area ratio, the wave is likely to be the simultaneous one-electron redox of the four- Fe^{3+} center.

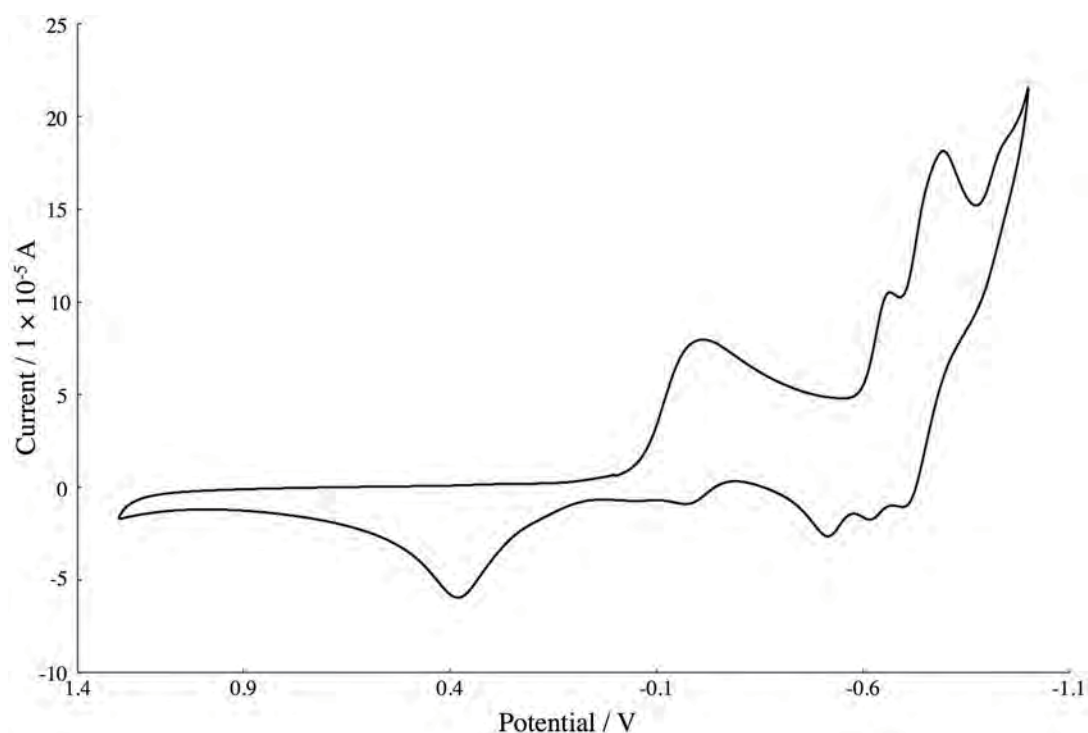


Figure 5. Cyclic voltammograms (CV) of 0.5 mM potassium salt of $\beta,\beta\text{-Fe}_4\text{-open}$ in 0.5 M potassium acetate buffer, pH 4.8, scan rate $25\text{ mV}\cdot\text{s}^{-1}$, under N_2 .

3. Experimental Section

3.1. Materials

The following reagents were used as received: $\text{FeCl}_3\cdot 6\text{H}_2\text{O}$, HCl, KOH, and KCl (from Wako Pure Chemical Industries, Osaka, Japan). The sodium salt of trilaicary Keggin POM, *i.e.*, $\text{Na}_9\text{H}[\text{A-}\beta\text{-SiW}_9\text{O}_{34}]\cdot 23\text{H}_2\text{O}$, and $\alpha,\alpha\text{-Fe}_4\text{-open}$ were prepared according to the literature method [19,40], and identified by X-ray crystallography, TG/DTA, FT-IR, UV/Vis absorption spectra, and cyclic voltammetry.

3.2. Instrumentation and Analytical Procedures

Elemental analyses were carried out by Mikroanalytisches Labor Pascher (Remagen, Germany). The sample was dried overnight at room temperature under 10^{-3} – 10^{-4} Torr before analysis. Infrared spectra were recorded on a Jasco 4100 FTIR spectrometer (Jasco, Hachioji, Japan) using KBr disks at room temperature. Thermogravimetric (TG) and differential thermal analyses (DTA) were acquired using a Rigaku Thermo Plus 2 series TG8120 instrument (Rigaku, Akishima, Japan). TG/DTA measurements were run under air with a temperature ramp of 4.0 °C/min between 20 and 500 °C. Absorption spectra in H₂O were obtained on a JASCO V-630 spectrophotometer (Jasco). Cyclic voltammetry was performed with ALS/CH Instruments (BAS, Sumida-ku, Japan), a Model 610E electrochemical analyzer with a three electrode cell in 0.5 M KOAc/HOAc buffer (pH 4.8) under N₂ atmosphere. A glassy carbon working electrode, a Pt auxiliary electrode and a Ag/AgCl reference electrode were employed. The scan rate was 25 mV · s⁻¹.

3.3. Synthesis of K₉[{Fe₄(H₂O)(OH)₅}(β,β-Si₂W₁₈O₆₆)] · 17H₂O (Potassium Salt of β,β-Fe₄-Open)

Na₉H[A-β-SiW₉O₃₄] · 23H₂O (1.00 g, 0.351 mmol) was suspended in 50 mL of water. The pH was adjusted to 3.0 using 1.0 M HCl_{aq}, and 1.0 mL of saturated KCl_{aq} was added to the solution. Upon addition of FeCl₃ · 6H₂O (0.190 g, 0.703 mmol) to the solution, the pH dropped to 1.57. Subsequently, the pH was adjusted to 3.0 using 1.0 M KOH_{aq}. Thereafter, the solution was heated to 80 °C for 30 min and the pH was re-adjusted to 3.0 using 1.0 M KOH_{aq}. The resulting solution was left to stand undisturbed at room temperature for one week. The resulting yellow plate crystals were collected on a membrane filter (JG 0.2 μm), and dried *in vacuo* for 2 h to obtain a yield of 0.211 g (0.0390 mmol, 22.2% based on Na₉H[A-β-SiW₉O₃₄] · 23H₂O).

The crystalline sample was soluble in water, but insoluble in organic solvents such as methanol, ethanol, and diethyl ether. Complete elemental analysis (%) calcd. for H₁₅Fe₄K₉O₇₆Si₂W₁₈ or K₉[{Fe₄(H₂O)(OH)₅}(β,β-Si₂W₁₈O₆₆)] · 4H₂O: H, 0.29; Fe, 4.32; K, 6.80; O, 23.51; Si, 1.09; W, 63.99. Found: H, 0.29; Fe, 4.25; K, 6.57; O, 23.6; Si, 1.23; W, 63.8; total ~99.74%. A weight loss of 4.23% (solvated water) was observed during overnight drying at room temperature, at 10^{-3} – 10^{-4} Torr before analysis, suggesting the presence of 13 water molecules (calcd. 4.33%). TG/DTA under atmospheric conditions: a weight loss of 6.10% was observed below 500 °C; calc. 5.98% for x = 18 in K₉[{Fe₄(H₂O)(OH)₅}(β,β-Si₂W₁₈O₆₆)] · xH₂O. IR (KBr, cm⁻¹): 1615 (w), 1090 (w), 1008 (w), 962 (s), 906 (vs), 879 (vs), 810 (vs), 761 (vs), 716 (s), 643 (m), 520 (w), 483 (w), 407 (w).

3.4. X-ray Crystallography

For the potassium salt of β,β-Fe₄-open, a single crystal with dimensions of 0.11 × 0.08 × 0.07 mm³ was surrounded by liquid paraffin (Paratone-N) and analyzed at 100(2) K. Measurement was performed using a Bruker SMART APEX CCD diffractometer. The structure was solved by direct methods (SHELXS-97), followed by difference Fourier calculations and refinement by a full-matrix least-squares procedure on F² (program SHELXL-97) [41].

Crystal data: triclinic, space group P-1, a = 12.560(2), b = 19.013(3), c = 20.359(4) Å, α = 92.925(3), β = 98.002(3), γ = 93.086(3)°, V = 4799.1(15) Å³, Z = 2, D_{calcd} = 3.694 g · cm⁻³, μ(Mo-Kα) = 22.371 mm⁻¹. R₁ (I > 2.00σ(I)) = 0.0605, R (all data) = 0.0751, wR₂ (all data) = 0.1642, GOF = 1.032. Most atoms in the main part of the structure were refined anisotropically, while the rest (as crystallization solvents) were refined isotropically, because of the presence of disorder. The composition and formula of the POM, containing countercations and crystalline water molecules, were determined by the complete elemental and TG analyses. Similar to other structural investigations of crystals of highly hydrated large polyoxometalate complexes, it was not possible to locate every countercation and hydrated water molecule, due to the extensive disorder of the cations and crystalline water molecules. Further details of the crystal structure investigations may be obtained from the Fachinformationszentrum Karlsruhe, 76344 Eggenstein-Leopoldshafen, Germany (Fax: +49-7247-808-666; E-Mail: crysdata@fiz-karlsruhe.de,

http://www.fiz-karlsruhe.de/request_for_deposited_data.html?&L=1) on quoting the depository number CSD-431049 (Identification code; em1-6-3c).

4. Conclusions

In summary, we prepared a β,β -isomer of open-Wells–Dawson POM containing a tetra-iron(III) cluster, $K_9[\{Fe_4(H_2O)(OH)_5\}(\beta,\beta-Si_2W_{18}O_{66})] \cdot 17H_2O$ (potassium salt of β,β -Fe₄-open), by reacting trilacunary β -Keggin POM, $Na_9H[A-\beta-SiW_9O_{34}] \cdot 23H_2O$, with $FeCl_3 \cdot 6H_2O$. This compound is the first example containing the isomer of α,α -open-Wells–Dawson structural POM. Studies on the α,β -isomers of open-Wells–Dawson POMs, regarded as an open structure of the standard β -Wells–Dawson POM, are in progress.

Supplementary Materials: The following are available online at www.mdpi.com/2304-6740/4/2/15/s1, Table S1: Bond valence sum (BVS) calculations of Fe and O atoms of the $\{Fe_4(H_2O)(OH)_5\}$ cluster moieties of β,β -Fe₄-open; Figure S1: FT-IR spectrum of potassium salt of β,β -Fe₄-open (KBr disk); Figure S2: TG/DTA data of potassium salt of β,β -Fe₄-open; Figure S3: UV/Vis absorption spectra of α,α - and β,β -Fe₄-open in H₂O; Figure S4: Cyclic voltammograms (CV) of 0.5 mM potassium salt of α,α - and β,β -Fe₄-open in 0.5 M potassium acetate buffer, pH 4.8, scan rate 25 mV · s⁻¹, under N₂; checkCIF/PLATON report.

Acknowledgments: This study was supported by the Strategic Research Base Development Program for Private Universities of the Ministry of Education, Culture, Sports, Science and Technology of Japan, and also by a grant from Research Institute for Integrated Science, Kanagawa University (RIIS201505).

Author Contributions: Satoshi Matsunaga and Kenji Nomiya conceived and designed the experiments, and wrote the paper; Eriko Miyamae and Yusuke Inoue synthesized and characterized the compound.

Conflicts of Interest: The authors declare no conflict of interest.

Abbreviations

The following abbreviations are used in this manuscript:

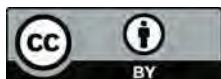
POM	Polyoxometalate
TG/DTA	Thermogravimetric/differential thermal analyses
BVS	Bond valence sum

References

1. Pope, M.T.; Müller, A. Polyoxometalate chemistry: An old field with new dimensions in several disciplines. *Angew. Chem. Int. Ed.* **1991**, *30*, 34–48. [[CrossRef](#)]
2. Pope, M.T. *Heteropoly and Isopolyoxometalates*; Springer-Verlag: New York, NY, USA, 1983.
3. Hill, C.L.; Prosser-McCartha, C.M. Homogeneous catalysis by transition metal oxygen anion clusters. *Coord. Chem. Rev.* **1995**, *143*, 407–455. [[CrossRef](#)]
4. Neumann, R. Polyoxometalate complexes in organic oxidation chemistry. *Prog. Inorg. Chem.* **1998**, *47*, 317–370.
5. Proust, A.; Thouvenot, R.; Gouzerh, P. Functionalization of polyoxometalates: Towards advanced applications in catalysis and materials science. *Chem. Commun.* **2008**, 1837–1852. [[CrossRef](#)] [[PubMed](#)]
6. Hasenknopf, B.; Micoine, K.; Lacôte, E.; Thorimbert, S.; Malacria, M.; Thouvenot, R. Chirality in polyoxometalate chemistry. *Eur. J. Inorg. Chem.* **2008**, 5001–5013. [[CrossRef](#)]
7. Long, D.-L.; Tsunashima, R.; Cronin, L. Polyoxometalates: Building blocks for functional nanoscale systems. *Angew. Chem. Int. Ed.* **2010**, *49*, 1736–1758. [[CrossRef](#)] [[PubMed](#)]
8. Nomiya, K.; Sakai, Y.; Matsunaga, S. Chemistry of group IV metal ion-containing polyoxometalates. *Eur. J. Inorg. Chem.* **2011**, 179–196. [[CrossRef](#)]
9. Izarova, N.V.; Pope, M.T.; Kortz, U. Noble metals in polyoxometalates. *Angew. Chem. Int. Ed.* **2012**, *51*, 9492–9510. [[CrossRef](#)] [[PubMed](#)]
10. Song, Y.-F.; Tsunashima, R. Recent advances on polyoxometalate-based molecular and composite materials. *Chem. Soc. Rev.* **2012**, *41*, 7384–7402. [[CrossRef](#)] [[PubMed](#)]
11. Bijelic, A.; Rompel, A. The use of polyoxometalates in protein crystallography—An attempt to widen a well-known bottleneck. *Coord. Chem. Rev.* **2015**, *299*, 22–38. [[CrossRef](#)] [[PubMed](#)]

12. Wang, S.-S.; Yang, G.-Y. Recent advances in polyoxometalate-catalyzed reactions. *Chem. Rev.* **2015**, *115*, 4893–4962. [[CrossRef](#)] [[PubMed](#)]
13. Blazevic, A.; Rompel, A. The Anderson–Evans polyoxometalate: From inorganic building blocks via hybrid organic–inorganic structures to tomorrows “Bio-POM”. *Coord. Chem. Rev.* **2016**, *307*, 42–64. [[CrossRef](#)]
14. Laronze, N.; Marrot, J.; Hervé, G. Synthesis, molecular structure and chemical properties of a new tungstosilicate with an open Wells–Dawson structure, α -[Si₂W₁₈O₆₆]¹⁶⁻. *Chem. Commun.* **2003**, 2360–2361. [[CrossRef](#)]
15. Bi, L.-H.; Kortz, U. Synthesis and structure of the pentacopper(II) substituted tungstosilicate [Cu₅(OH)₄(H₂O)₂(A- α -SiW₉O₃₃)₂]¹⁰⁻. *Inorg. Chem.* **2004**, *43*, 7961–7962. [[CrossRef](#)] [[PubMed](#)]
16. Leclerc-Laronze, N.; Marrot, J.; Hervé, G. Cation-directed synthesis of tungstosilicates. 2. Synthesis, structure, and characterization of the open Wells–Dawson anion α -[K(H₂O)₂](Si₂W₁₈O₆₆)¹⁵⁻ and its transition-metal derivatives [[M(H₂O)](μ -H₂O)₂K(Si₂W₁₈O₆₆)]¹³⁻ and [[M(H₂O)](μ -H₂O)₂K{M(H₂O)₄}(Si₂W₁₈O₆₆)]¹¹⁻. *Inorg. Chem.* **2005**, *44*, 1275–1281. [[PubMed](#)]
17. Nellutla, S.; Tol, J.V.; Dalal, N.S.; Bi, L.-H.; Kortz, U.; Keita, B.; Nadjo, L.; Khitrov, G.A.; Marshall, A.G. Magnetism, electron paramagnetic resonance, electrochemistry, and mass spectrometry of the pentacopper(II)-substituted tungstosilicate [Cu₅(OH)₄(H₂O)₂(A- α -SiW₉O₃₃)₂]¹⁰⁻, A model five-spin frustrated cluster. *Inorg. Chem.* **2005**, *44*, 9795–9806. [[CrossRef](#)] [[PubMed](#)]
18. Leclerc-Laronze, N.; Haouas, M.; Marrot, J.; Taulelle, F.; Hervé, G. Step-by-step assembly of trivacant tungstosilicates: Synthesis and characterization of tetrameric anions. *Angew. Chem. Int. Ed.* **2006**, *45*, 139–142. [[CrossRef](#)] [[PubMed](#)]
19. Leclerc-Laronze, N.; Marrot, J.; Hervé, G. Dinuclear vanadium and tetranuclear iron complexes obtained with the open Wells–Dawson [Si₂W₁₈O₆₆]¹⁶⁻ tungstosilicate. *C. R. Chim.* **2006**, *9*, 1467–1471. [[CrossRef](#)]
20. Sun, C.-Y.; Liu, S.-X.; Wang, C.-L.; Xie, L.-H.; Zhang, C.-D.; Gao, B.; Su, Z.-M.; Jia, H.-Q. Synthesis, structure and characterization of a new cobalt-containing germanotungstate with open Wells–Dawson structure: K₁₃[{Co(H₂O)](μ -H₂O)₂K(Ge₂W₁₈O₆₆)]. *J. Mol. Struct.* **2006**, *785*, 170–175. [[CrossRef](#)]
21. Wang, C.-L.; Liu, S.-X.; Sun, C.-Y.; Xie, L.-H.; Ren, Y.-H.; Liang, D.-D.; Cheng, H.-Y. Bimetals substituted germanotungstate complexes with open Wells–Dawson structure: Synthesis, structure, and electrochemical behavior of [{M(H₂O)](μ -H₂O)₂K{M(H₂O)₄}(Ge₂W₁₈O₆₆)]¹¹⁻ (M = Co, Ni, Mn). *J. Mol. Struct.* **2007**, *841*, 88–95. [[CrossRef](#)]
22. Ni, L.; Hussain, F.; Spingler, B.; Weyeneth, S.; Patzke, G.R. Lanthanoid-containing open Wells–Dawson silicotungstates: Synthesis, crystal structures, and properties. *Inorg. Chem.* **2011**, *50*, 4944–4955. [[CrossRef](#)] [[PubMed](#)]
23. Zhu, G.; Geletii, Y.V.; Zhao, C.; Musaev, D.G.; Song, J.; Hill, C.L. A dodecanuclear Zn cluster sandwiched by polyoxometalate ligands. *Dalton Trans.* **2012**, *41*, 9908–9913. [[CrossRef](#)] [[PubMed](#)]
24. Zhu, G.; Glass, E.N.; Zhao, C.; Lv, H.; Vickers, J.W.; Geletii, Y.V.; Musaev, D.G.; Song, J.; Hill, C.L. A nickel containing polyoxometalate water oxidation catalyst. *Dalton Trans.* **2012**, *41*, 13043–13049. [[CrossRef](#)] [[PubMed](#)]
25. Zhu, G.; Geletii, Y.V.; Song, J.; Zhao, C.; Glass, E.N.; Bacsá, J.; Hill, C.L. Di- and tri-cobalt silicotungstates: Synthesis, characterization, and stability studies. *Inorg. Chem.* **2013**, *52*, 1018–1024. [[CrossRef](#)] [[PubMed](#)]
26. Ni, L.; Spingler, B.; Weyeneth, S.; Patzke, G.R. Trilacunary Keggin-type POMs as versatile building blocks for lanthanoid silicotungstates. *Eur. J. Inorg. Chem.* **2013**, 1681–1692. [[CrossRef](#)]
27. Guo, J.; Zhang, D.; Chen, L.; Song, Y.; Zhu, D.; Xu, Y. Syntheses, structures and magnetic properties of two unprecedented hybrid compounds constructed from open Wells–Dawson anions and high-nuclear transition metal clusters. *Dalton Trans.* **2013**, *42*, 8454–8459. [[CrossRef](#)] [[PubMed](#)]
28. Matsunaga, S.; Inoue, Y.; Otaki, T.; Osada, H.; Nomiya, K. Aluminum- and Gallium-Containing Open-Dawson Polyoxometalates. *Z. Anorg. Allg. Chem.* **2016**, *642*, 539–545. [[CrossRef](#)]
29. Minato, T.; Suzuki, K.; Kamata, K.; Mizuno, N. Synthesis of α -Dawson-type silicotungstate [α -Si₂W₁₈O₆₂]⁸⁻ and protonation and deprotonation inside the aperture through intramolecular hydrogen bonds. *Chem. Eur. J.* **2014**, *20*, 5946–5952. [[CrossRef](#)] [[PubMed](#)]
30. Zhang, F.-Q.; Guan, W.; Yan, L.-K.; Zhang, Y.-T.; Xu, M.-T.; Hayfron-Benjamin, E.; Su, Z.-M. On the origin of the relative stability of Wells–Dawson isomers: A DFT study of α -, β -, γ -, α^* -, β^* -, and γ^* -[(PO₄)₂W₁₈O₅₄]⁶⁻ anions. *Inorg. Chem.* **2011**, *50*, 4967–4977. [[CrossRef](#)] [[PubMed](#)]

31. Baker, L.C.W.; Figgis, J.S. New fundamental type of inorganic complex: Hybrid between heteropoly and conventional coordination complexes. Possibilities for geometrical isomerisms in 11-, 12-, 17-, and 18-heteropoly derivatives. *J. Am. Chem. Soc.* **1970**, *92*, 3794–3797. [[CrossRef](#)]
32. Dawson, B. The structure of the 9(18)-heteropoly anion in potassium 9(18)-tungstophosphate, $K_6(P_2W_{18}O_{62}) \cdot 14H_2O$. *Acta Crystallogr.* **1953**, *6*, 113–126. [[CrossRef](#)]
33. Neubert, H.; Fuchs, J. Crystal structures and vibrational spectra of two isomers of octadecatungsto-diarsenate $(NH_4)_6As_2W_{18}O_{62} \cdot nH_2O$. *Z. Naturforsch.* **1987**, *42b*, 951–958. [[CrossRef](#)]
34. Contant, R.; Thouvenot, R. A reinvestigation of isomerism in the Dawson structure: Syntheses and ^{183}W NMR structural characterization of three new polyoxotungstates $[X_2W_{18}O_{62}]^{6-}$ ($X = P^V, As^V$). *Inorg. Chim. Acta* **1993**, *212*, 41–50. [[CrossRef](#)]
35. Richardt, P.J.S.; Gable, R.W.; Bond, A.M.; Wedd, A.G. Synthesis and redox characterization of the polyoxo Anion, $\gamma^*-[S_2W_{18}O_{62}]^{4-}$: A unique fast oxidation pathway determines the characteristic reversible electrochemical behavior of polyoxometalate anions in acidic media. *Inorg. Chem.* **2001**, *40*, 703–709. [[CrossRef](#)] [[PubMed](#)]
36. Zhang, J.; Bond, A.M. Voltammetric reduction of α - and $\gamma^*-[S_2W_{18}O_{62}]^{4-}$ and α -, β -, and γ - $[SiW_{12}O_{40}]^{4-}$: Isomeric dependence of reversible potentials of polyoxometalate anions using data obtained by novel dissolution and conventional solution-phase processes. *Inorg. Chem.* **2004**, *43*, 8263–8271. [[CrossRef](#)] [[PubMed](#)]
37. Sun, Y.-X.; Zhang, Z.-B.; Sun, Q.; Xu, Y. Syntheses, characterization and catalytic properties of two new Wells–Dawson molybdosulfates. *Chin. J. Inorg. Chem.* **2011**, *27*, 556–560.
38. Brown, I.D.; Altermatt, D. Bond-valence parameters obtained from a systematic analysis of the Inorganic Crystal Structure Database. *Acta Crystallogr.* **1985**, *B41*, 244–247. [[CrossRef](#)]
39. Zonnevijlle, F.; Tourné, C.M.; Tourné, G.F. Preparation and Characterization of Iron(III)- and Rhodium(III)-Containing Heteropolytungstates. Identification of Novel Oxo-Bridged Iron(III) Dimers. *Inorg. Chem.* **1982**, *21*, 2751–2757. [[CrossRef](#)]
40. Tézé, A.; Hervé, G. α -, β -, and γ -Dodecatungstosilicic acids: Isomers and related lacunary compounds. *Inorg. Synth.* **1990**, *27*, 85–96.
41. Sheldrick, G.M. A short history of SHELX. *Acta Crystallogr.* **2008**, *64*, 112–122. [[CrossRef](#)] [[PubMed](#)]



© 2016 by the authors; licensee MDPI, Basel, Switzerland. This article is an open access article distributed under the terms and conditions of the Creative Commons Attribution (CC-BY) license (<http://creativecommons.org/licenses/by/4.0/>).



Article

Synthesis, Structure, and Characterization of In₁₀-Containing Open-Wells–Dawson Polyoxometalate

Satoshi Matsunaga, Takuya Otaki, Yusuke Inoue, Kohei Mihara and Kenji Nomiya *

Department of Chemistry, Faculty of Science, Kanagawa University, Hiratsuka, Kanagawa 259-1293, Japan; matsunaga@kanagawa-u.ac.jp (S.M.); toatkaukyia1@gmail.com (T.O.); r201470042gl@jindai.jp (Y.I.); r201203938gu@jindai.jp (K.M.)

* Correspondence: nomiya@kanagawa-u.ac.jp; Tel.: +81-463-59-4111

Academic Editor: Greta Ricarda Patzke

Received: 12 April 2016; Accepted: 10 May 2016; Published: 17 May 2016

Abstract: We have successfully synthesized $K_{17}\{[\{KIn_2(\mu-OH)_2\}(\alpha,\alpha-Si_2W_{18}O_{66})]_2[In_6(\mu-OH)_{13}(H_2O)_8]\} \cdot 35H_2O$ (potassium salt of **In₁₀-open**), an open-Wells–Dawson polyoxometalate (POM) containing ten indium metal atoms. This novel compound was characterized by X-ray crystallography, ²⁹Si NMR, FTIR, complete elemental analysis, and TG/DTA. X-ray crystallography results for $\{[\{KIn_2(\mu-OH)_2\}(\alpha,\alpha-Si_2W_{18}O_{66})]_2[In_6(\mu-OH)_{13}(H_2O)_8]\}^{17-}$ (**In₁₀-open**) revealed two open-Wells–Dawson units containing two In³⁺ ions and a K⁺ ion, $[\{KIn_2(\mu-OH)_2\}(\alpha,\alpha-Si_2W_{18}O_{66})]^{11-}$, connected by an In₆-hydroxide cluster moiety, $[In_6(\mu-OH)_{13}(H_2O)_8]^{5+}$. **In₁₀-open** is the first example of an open-Wells–Dawson POM containing a fifth-period element. Moreover, to the best of our knowledge, it exhibits the highest nuclearity among the indium-containing POMs reported to date.

Keywords: polyoxometalates; open-Wells–Dawson structural polyoxometalate; Indium

1. Introduction

Polyoxometalates (POMs) are discrete metal oxide clusters that are of current interest as soluble metal oxides, as well as for their application in catalysis, medicine, and materials science [1–13]. Recently, open-Wells–Dawson POMs have been reported as an emerging class of POMs [14–28]. These compounds are a dimerized species of the trilacunary Keggin POMs, $[XW_9O_{34}]^{10-}$ (X = Si, Ge). Standard Wells–Dawson structural POMs are regarded as two trilacunary Keggin POM units assembled together via six W–O–W bonds. However, the electrostatic repulsion between the two units in $[XW_9O_{34}]^{10-}$ (X = Si and Ge), induced by the highly charged guest XO_4^{4-} (X = Si, Ge) ion, is assumed to be so strong that it inhibits the assembly of the standard Wells–Dawson structure in aqueous media. Therefore, when the two trilacunary Keggin units comprise an XO_4^{4-} (X = Si, Ge) ion, they are linked by only two W–O–W bonds. This results in the formation of an open-Wells–Dawson structural POM [29]. The open pocket of these POMs can accommodate multiple metal ions (one to six metal ions). Thus, this class of compounds may constitute a promising platform for the development of metal-substituted-POM-based materials and catalysts. To date, many compounds that contain various metal ions in their open pocket, e.g., V⁵⁺ [19], Mn²⁺ [16,21], Fe³⁺ [19], Co²⁺ [14,16,20,21,25,27], Ni²⁺ [16,21,24,27], Cu²⁺ [15–17], and Zn²⁺ [23] have been reported. Some lanthanoid (Eu³⁺, Gd³⁺, Tb³⁺, Dy³⁺, and Ho³⁺)-containing open-Wells–Dawson POMs have also been reported [22,26]. However, the large ionic radii of these lanthanoid atoms inhibit their complete insertion within the open pocket. This results in a weak coordination, similar to that of the K ions in K-containing open-Wells–Dawson POMs. Recently, we synthesized the Al₄- and Ga₄-containing open-Wells–Dawson POMs: $[\{Al_4(\mu-OH)_6\}(\alpha,\alpha-Si_2W_{18}O_{66})]^{10-}$ (**Al₄-open**) and $[\{Ga_4(\mu-OH)_6\}(\alpha,\alpha-Si_2W_{18}O_{66})]^{10-}$ (**Ga₄-open**), respectively, and successfully determined their molecular structures by single crystal X-ray crystallography [28]. X-ray structure analyses of **Al₄-** and

Ga₄-open revealed that the $\{M_4(\mu\text{-OH})_6\}^{6+}$ ($M = \text{Al}^{3+}, \text{Ga}^{3+}$) clusters are included in the open pocket of the open-Wells–Dawson unit.

In general, trivalent group 13 ions are found as various oligomeric hydroxide species in aqueous solution [30–32]. Synthetic and structural studies of group 13 ion-containing POMs provide informative and definitive molecular models of group 13 metal clusters in solution. However, among all the Al-, Ga-, and In-containing POMs, formed by the substitution of several tungsten ions in the parent POMs with trivalent group 13 ions [28,33–40], few well-characterized In-containing POMs have been reported to date [41–43]. Thus, In-containing POMs are intriguing target compounds from both a synthetic and a structural point of view.

In this study, we successfully synthesized an open-Wells–Dawson POM containing ten indium metal ions, $\text{K}_{17}[\{[\text{KIn}_2(\mu\text{-OH})_2](\alpha,\alpha\text{-Si}_2\text{W}_{18}\text{O}_{66})\}_2[\text{In}_6(\mu\text{-OH})_{13}(\text{H}_2\text{O})_8]\} \cdot 35\text{H}_2\text{O}$ (potassium salt of **In₁₀-open**), and characterized it by X-ray crystallography, ²⁹Si NMR, FTIR, complete elemental analysis, and thermogravimetric/differential thermal analyses (TG/DTA). In contrast to **Al₄-** and **Ga₄-open**, **In₁₀-open** showed a dimer structure bridged by a deca-indium-hydroxide cluster.

2. Results and Discussion

2.1. Synthesis

The crystalline sample of potassium salt of **In₁₀-open**, was afforded in 17.9% yield. This complex was prepared from a 1:5 molar ratio reaction of $\text{K}_{13}[\{[\text{K}(\text{H}_2\text{O})_3\}_2[\text{K}(\text{H}_2\text{O})_2](\alpha,\alpha\text{-Si}_2\text{W}_{18}\text{O}_{66})\} \cdot 19\text{H}_2\text{O}$ with InCl_3 . The sample was characterized using complete elemental analysis (H, In, K, O, Si, and W analyses), FTIR, TG/DTA, ²⁹Si NMR in D_2O , and X-ray crystallography.

The FTIR spectrum of potassium salt of **In₁₀-open** (Figure S1) displays peaks at 1000 and 945 cm^{-1} that correspond to $\nu_{\text{as}}(\text{Si-O})$ and $\nu_{\text{as}}(\text{W-O}_t)$, respectively. The characteristic bands at 900–600 cm^{-1} are associated with $\nu(\text{W-O}_c)$, $\nu(\text{W-O}_b)$, and $\nu(\text{W-O-W})$. The IR spectrum is very similar to those of the common open-Wells–Dawson POMs.

Before elemental analysis, the sample of **In₁₀-open** was dried overnight at room temperature under vacuum (10^{-3} – 10^{-4} Torr). All elements (H, In, K, O, Si, and W) were observed for a total analysis of 100.37%. The recorded data were in good accordance with the calculated values for the formula without water of crystallization, $\text{K}_{17}[\{[\text{KIn}_2(\mu\text{-OH})_2](\alpha,\alpha\text{-Si}_2\text{W}_{18}\text{O}_{66})\}_2[\text{In}_6(\mu\text{-OH})_{13}(\text{H}_2\text{O})_8]$ (see Experimental section). The weight loss observed during drying, before analysis, was 5.28% corresponding to ca. 35 crystalline water molecules. On the other hand, during the TG/DTA measurements carried out under atmospheric conditions, a weight loss of 6.40%, observed at temperatures below 500 °C, corresponding to a total of ca. 42 water molecules, *i.e.*, 8 coordinated water molecules and 34 molecules of water of crystallization (Figure S2). Thus, the elemental analysis and TG/DTA displayed a presence of a total of 34–35 water molecules for the sample under atmospheric conditions. The formula for potassium salt of **In₁₀-open** presented herein was determined as $\text{K}_{17}[\{[\text{KIn}_2(\mu\text{-OH})_2](\alpha,\alpha\text{-Si}_2\text{W}_{18}\text{O}_{66})\}_2[\text{In}_6(\mu\text{-OH})_{13}(\text{H}_2\text{O})_8] \cdot 35\text{H}_2\text{O}$ based on the results of the complete elemental analysis.

2.2. Molecular Structure

The molecular structure of the polyoxoanion of potassium salt of **In₁₀-open** and its polyhedral representation are shown in Figure 1a,b, respectively. X-ray crystallographic data of **In₁₀-open** reveal that the two open-Wells–Dawson units that include two In^{3+} ions and a K^+ ion, $[\{[\text{KIn}_2(\mu\text{-OH})_2](\alpha,\alpha\text{-Si}_2\text{W}_{18}\text{O}_{66})\}]^{11-}$, are connected by a central In_6 -hydroxide cluster moiety, $[\text{In}_6(\mu\text{-OH})_{13}(\text{H}_2\text{O})_8]^{5+}$, to form a dimeric open-Wells–Dawson polyanion, $\{[\{[\text{KIn}_2(\mu\text{-OH})_2](\alpha,\alpha\text{-Si}_2\text{W}_{18}\text{O}_{66})\}_2[\text{In}_6(\mu\text{-OH})_{13}(\text{H}_2\text{O})_8]\}^{17-}$ (Figure 1).

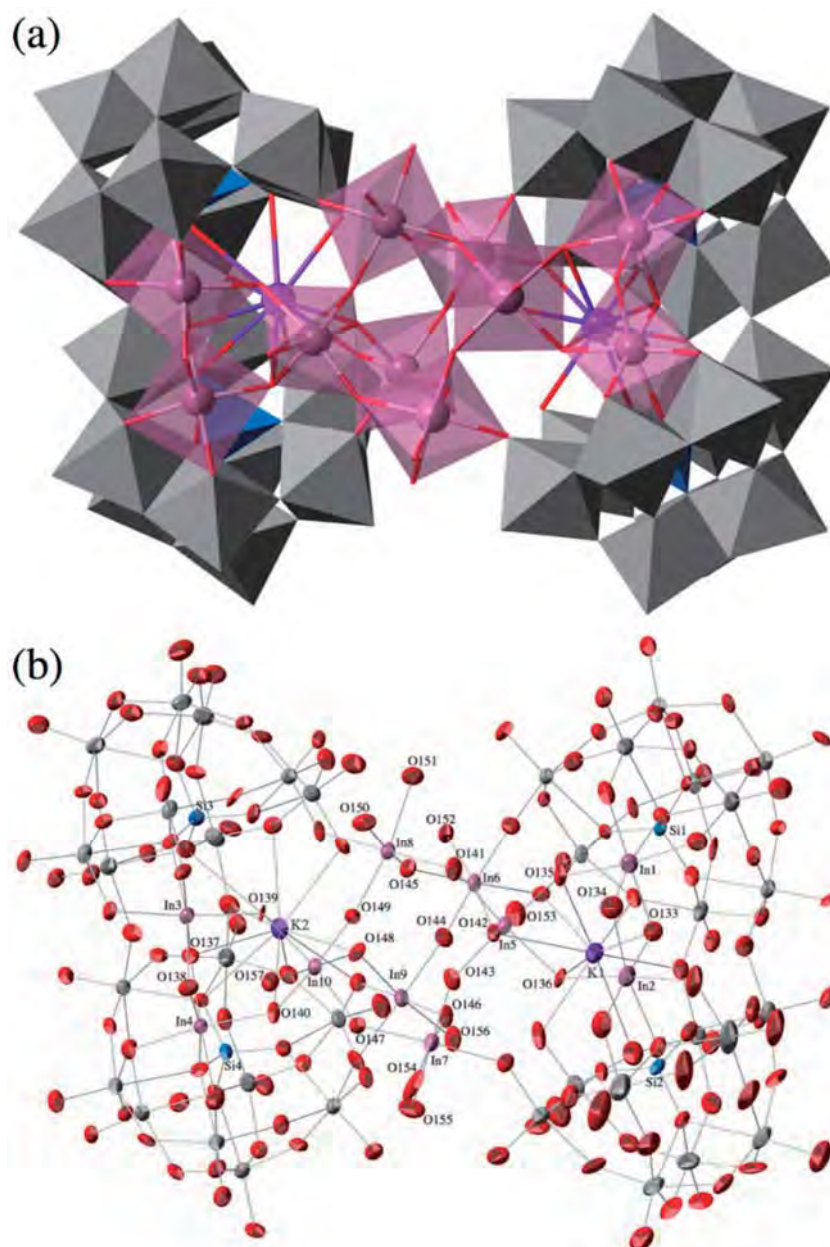


Figure 1. Molecular structure of the polyoxoanion, $\{[KIn_2(\mu-OH)_2](\alpha,\alpha-Si_2W_{18}O_{66})_2[In_6(\mu-OH)_{13}(H_2O)_8]\}^{17-}$ of potassium salt of **In₁₀-open**. (a) Its polyhedral representation; and (b) thermal ellipsoidal plot. Color code: In, pink; K, purple; O, red; Si, blue; W, gray.

The two indium atoms in the open pocket of the open-Wells–Dawson POM units are connected through edge-sharing oxygen atoms (O133, O134 for In1, In2; O137, O138 for In3, In4) with In···In distances of 3.266(2) (In1···In2) and 3.299(2) (In3···In4) (Figure 2a). Each Indium atom in the open pocket is bonded to three oxygen atoms of the lacunary site in the open-Wells–Dawson polyanion [In–O average = 2.2011 Å]. Open-Wells–Dawson POMs that include two metal atoms in the open pocket have been previously reported, e.g., $K_{11}[\{KV_2O_3(H_2O)_2\}(Si_2W_{18}O_{66})] \cdot 40H_2O$ (**V₂-open**) [19]. In contrast to our **In₁₀-open**, the two vanadium atoms in the open pocket of **V₂-open** are bound to only one half {SiW₉} of the open-Wells–Dawson unit, and are linked in a corner-sharing fashion (Figure 2b). Therefore, **In₁₀-open** is the first example of an open-Wells–Dawson POM that includes two metal atoms with edge-sharing fashion.

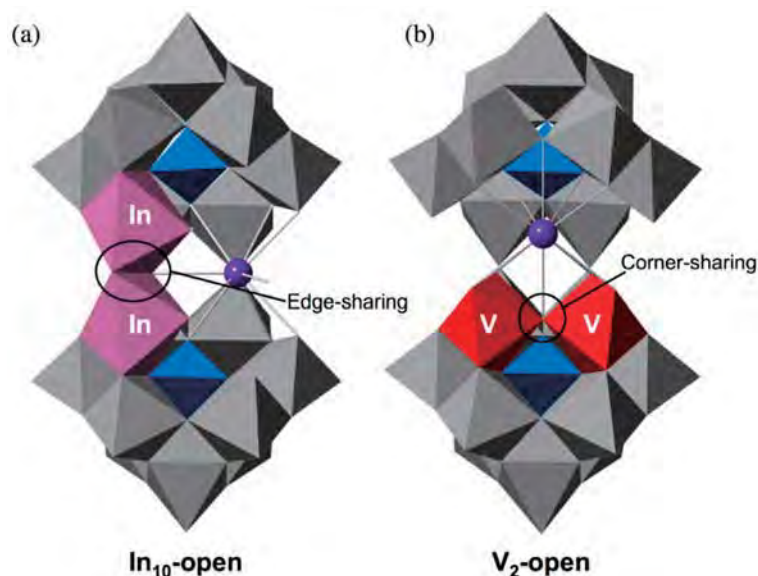


Figure 2. The metal arrangement of (a) **In₁₀-open** and (b) **V₂-open** in the open pocket.

In addition to the indium atoms in the open-pocket, the complex contains six indium atoms in the bridging hydroxide cluster. The indium atoms in the bridging cluster are connected to each other in a corner-sharing fashion. Moreover, the In atoms in the open-pocket and the W atoms of the open-Wells–Dawson POM units are also linked to the In atoms of the bridging cluster in a corner-sharing fashion. Thus, all the Indium atoms can be considered to be 6-coordinated. Bond valence sum (BVS) [44] calculations suggest that the corner- and edge-sharing oxygen atoms that are linked to the In atoms (corner-sharing: O135, O136, O139, O140, O141, O142, O143, O144, O145, O146, O147, O148, and O149; edge-sharing: O133, O134, O137, and O138) are protonated, *i.e.*, they are ascribed to the hydroxide groups. On the other hand, the terminal oxygen atoms on the indium atoms (O150, O151, O152, O153, O154, O155, O156, and O157) are ascribed to the water groups (Table S1).

In₁₀-open has a dimeric structure composed of two indium-containing open-Wells–Dawson POM moieties bridged by **In₆** hydroxide clusters. Dimeric open-Wells–Dawson POMs, similar to **In₁₀-open**, have also been reported for $\{[\text{Zn}_6(\mu\text{-OH})_7(\text{H}_2\text{O})(\alpha,\alpha\text{-Si}_2\text{W}_{18}\text{O}_{66})_2]\}^{22-}$ (**Zn₁₂-open**) by Hill *et al.* [23]. In this complex, the six zinc atoms are included in the open pocket of the open-Wells–Dawson unit, and the two **Zn₆**-containing open-Wells–Dawson units are connected through the two edge-sharing oxygen atoms. The arrangement and the number of metal ions in the open-pocket of the **In₁₀-open** are different from those of the **Zn₁₂-open** reported previously.

In open-Wells–Dawson POMs, the bite angle can be defined as the dihedral angle between the planes that pass through the six oxygen atoms of the lacunary site of each trilacunary Keggin unit. The bite angle varies, depending on the metal cluster included in the open pocket of the open-Wells–Dawson unit. The bite angles of **In₁₀-open** are 64.363° and 65.139° (Figure 3). These values are wider than those of other open-Wells–Dawson POMs, including other group 13 ions, such as **Al₄-** (54.274°) and **Ga₄-open** (56.110°) [28]. The difference between the bite angles of **Al₄-**, **Ga₄-**, and **In₁₀-open** is caused by the difference in the ionic radii of the Al (0.53 Å), Ga (0.76 Å), and In (0.94 Å) ions [45,46]. **In₁₀-open** displays the widest bite angles when compared to previously reported open-Wells–Dawson POMs, including the **Co₆** (60.045°) [27], **Zn₆** dimer (60.308°) [23], **Ni₅** (58.925°) [24], and **Cu₅** (61.663°) [15,17] clusters. The open-Wells–Dawson POM containing a **Cu₅** cluster (**Cu₅-open**) exhibits a large bite angle (61.663°) due to the long bond lengths between the copper and the edge-sharing oxygen atom, caused by Jahn–Teller distortion [15,17]. The bite angles of **In₁₀-open** are ca. 3° wider than that of **Cu₅-open**. This increase appears to be caused by the large ionic radius of the indium ions incorporated in the open pocket.

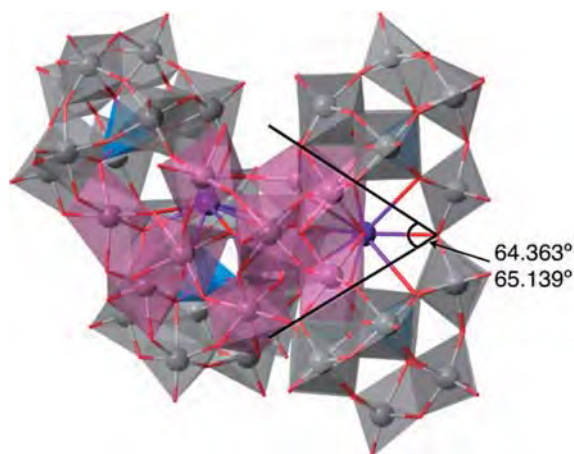


Figure 3. Bite angles of **In₁₀-open**.

The previously reported open-Wells–Dawson POMs mainly accommodated the fourth-period elements. Except for the lanthanoid-containing open-Wells–Dawson POMs, whose open-pockets weakly coordinate to the lanthanoid ions, open-Wells–Dawson POMs that accommodate the larger fifth- and sixth-period elements have not been reported to date. Thus, **In₁₀-open** indicates that elements (such as indium) having large ionic radii (0.94 Å) can be incorporated in the open-pocket of an open-Wells–Dawson unit.

2.3. Solution ²⁹Si NMR

The solution ²⁹Si NMR spectrum of **In₁₀-open** in D₂O displays a two-line spectrum at −82.415 and −83.159 ppm in a 1:1 ratio (Figure 4). The two Si atoms in one open-Wells–Dawson unit are nonequivalent due to the configuration of the other open-Wells–Dawson unit, even though the two units are equivalent. The adjacent two ²⁹Si NMR peaks are consistent with the structure of **In₁₀-open** observed by X-ray crystallography. This suggests that **In₁₀-open** exists as a single species and maintains its structure in solution.

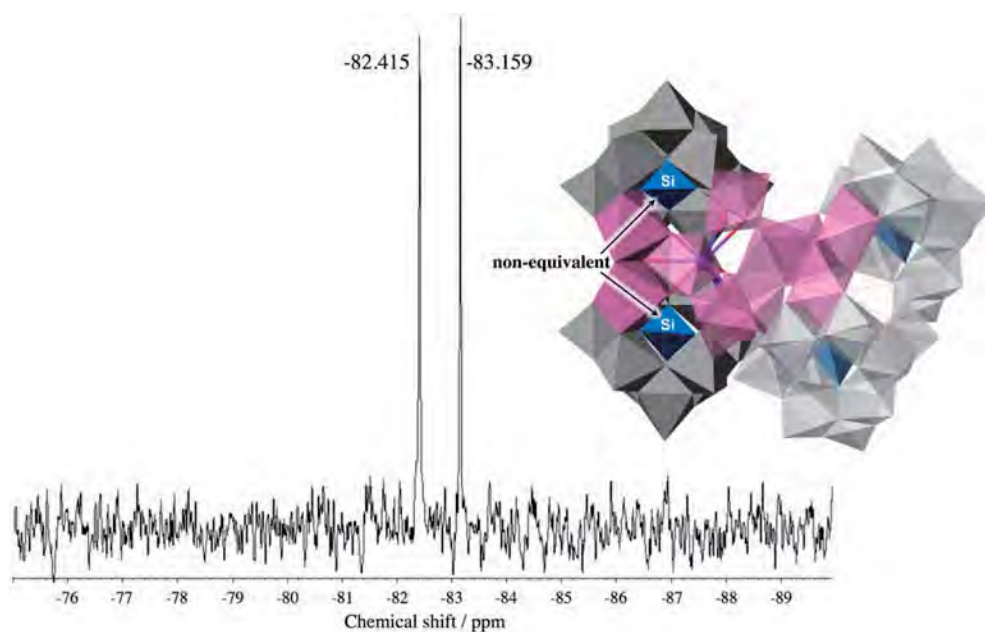


Figure 4. Solution ²⁹Si NMR spectrum of potassium salt of **In₁₀-open** dissolved in D₂O.

3. Experimental Section

3.1. Materials

The following reagents were used as received: InCl_3 (from Sigma-Aldrich Japan, Shinagawa, Japan), KOH , KCl (from Wako Pure Chemical Industries, Osaka, Japan), and D_2O (Kanto Chemical, Tokyo, Japan). The K ion-incorporating open-Wells–Dawson POM, $\text{K}_{13}[\{\text{K}(\text{H}_2\text{O})_3\}_2\{\text{K}(\text{H}_2\text{O})_2\}(\alpha,\alpha\text{-Si}_2\text{W}_{18}\text{O}_{66})\}\cdot 19\text{H}_2\text{O}$, was prepared according to literature [14], and identified by TG/DTA and FT-IR analysis.

3.2. Instrumentation and Analytical Procedures

A complete elemental analysis was carried out by Mikroanalytisches Labor Pascher (Remagen, Germany). The sample was dried overnight at room temperature under a pressure of 10^{-3} – 10^{-4} Torr before analysis. The ^{29}Si NMR (119.24 MHz) spectra in D_2O solution were recorded in 5-mm outer diameter tubes, on a JEOL JNM ECP 500 FTNMR spectrometer with a JEOL ECP-500 NMR data-processing system (JEOL, Akishima, Japan). The ^{29}Si NMR spectrum was referenced to an internal standard of DSS. Infrared spectra were recorded on a Jasco 4100 FTIR spectrometer (Jasco, Hachioji, Japan) by using KBr disks at room temperature. TG/DTA measurements were performed using a Rigaku Thermo Plus 2 series TG8120 instrument (Rigaku, Akishima, Japan), under air flow with a temperature ramp of 4.0 °C per min at a temperature ranging between 26 and 500 °C.

3.3. Synthesis of $\text{K}_{17}[\{\{\text{KIn}_2(\mu\text{-OH})_2\}(\alpha,\alpha\text{-Si}_2\text{W}_{18}\text{O}_{66})\}_2[\text{In}_6(\mu\text{-OH})_{13}(\text{H}_2\text{O})_8]\}\cdot 35\text{H}_2\text{O}$ (Potassium Salt of **In₁₀-open**)

InCl_3 (398 mg, 1.80 mmol) was dissolved in water (40 mL). A separate solution of $\text{K}_{13}[\{\text{K}(\text{H}_2\text{O})_3\}_2\{\text{K}(\text{H}_2\text{O})_2\}(\alpha,\alpha\text{-Si}_2\text{W}_{18}\text{O}_{66})\}\cdot 19\text{H}_2\text{O}$ (2.00 g, 0.361 mmol) dissolved in 100 mL of distilled water was added dropwise to the resulting solution. The pH of this solution was adjusted to 4.0 using 0.1 M KOH_{aq} . Next, 4 mL of saturated KCl_{aq} were added to the solution. The resulting solution was left to stand undisturbed at room temperature for 3 days. The afforded colorless needle crystals were collected on a membrane filter (JG 0.2 μm), and dried *in vacuo* for 2 h. Yield = 0.381 g (0.0323 mmol, 17.9% based on $\text{K}_{13}[\{\text{K}(\text{H}_2\text{O})_3\}_2\{\text{K}(\text{H}_2\text{O})_2\}(\alpha,\alpha\text{-Si}_2\text{W}_{18}\text{O}_{66})\}\cdot 19\text{H}_2\text{O}$).

The crystalline sample was soluble in water, but insoluble in organic solvents such as methanol, ethanol, and diethyl ether. Elemental analysis (%) calcd. for $\text{H}_{33}\text{In}_{10}\text{K}_{19}\text{O}_{157}\text{Si}_4\text{W}_{36}$ or $\text{K}_{17}[\{\{\text{KIn}_2(\mu\text{-OH})_2\}(\alpha,\alpha\text{-Si}_2\text{W}_{18}\text{O}_{66})\}_2[\text{In}_6(\mu\text{-OH})_{13}(\text{H}_2\text{O})_8]\}\cdot 34\text{H}_2\text{O}$: H 0.30, In 10.28, K 6.65, O 22.49, Si 1.01, W 59.27; Found: H 0.23, In 10.0, K 6.42, O 23.4, Si 1.02, W 59.3 (total 100.37%). A weight loss of 5.28% (solvated water) was observed during overnight drying at room temperature, at a pressure of 10^{-3} – 10^{-4} Torr before analysis. This suggested the presence of 35 water molecules. From TG/DTA air flow, a weight loss of 6.40% was observed at a temperature below 500 °C; calc. 6.42% for a total of 42 water molecules, *i.e.*, 34 solvated water molecules and 8 coordinated water molecules in $\text{K}_{17}[\{\{\text{KIn}_2(\mu\text{-OH})_2\}(\alpha,\alpha\text{-Si}_2\text{W}_{18}\text{O}_{66})\}_2[\text{In}_6(\mu\text{-OH})_{13}(\text{H}_2\text{O})_8]\}\cdot 34\text{H}_2\text{O}$; IR (KBr, cm^{-1}): 1622 (m), 1000 (w), 945 (m), 890 (vs), 786 (vs), 730 (vs), 649 (s), 548 (m), 523 (m); ^{29}Si NMR (50.0 °C, D_2O , DSS, ppm): $\delta = -82.415, -83.159$.

3.4. X-Ray Crystallography

For **In₁₀-open**, a single crystal with dimensions of $0.21 \times 0.06 \times 0.05 \text{ mm}^3$ was surrounded by liquid paraffin (Paratone-N) and analyzed at 150(2) K. All measurements were performed on a Rigaku MicroMax-007HF with a Saturn CCD diffractometer (Rigaku). The structure was solved by direct methods (SHELXS-97), followed by difference Fourier calculations and refinement by a full-matrix least-squares procedure on F^2 (program SHELXL-97) [47].

Crystal data: monoclinic, space group $\text{P2}(1)/a$, $a = 23.525(5)$, $b = 32.926(7)$, $c = 25.424(6)$ Å, $\beta = 93.273(2)^\circ$, $V = 19661(7)$ Å³, $Z = 4$, $D_{\text{calcd}} = 3.857 \text{ g cm}^{-3}$, $\mu(\text{Mo-K}\alpha) = 22.491 \text{ mm}^{-1}$; $R_1[I > 2.00\sigma(I)] = 0.0829$, R (all data) = 0.1012, wR_2 (all data) = 0.2296, GOF = 1.056. Most atoms

in the main part of the structure were refined anisotropically, while the rest (as crystallization solvents) were refined isotropically, because of the presence of disorder. The composition and formula of the POM (containing many counteranions and many crystalline water molecules) were determined from complete elemental and TG analyses. Similar to structural investigations of other crystals of highly hydrated large POM complexes, it was not possible to locate every counteranion and hydrated water molecule in the complex. This frequently encountered situation is attributed to the extensive disorder of the cations and many of the crystalline water molecules. Further details on the crystal structure investigations may be obtained from: Fachinformationszentrum Karlsruhe, 76344 Eggenstein-Leopoldshafen, Germany (Fax: +49-7247-808-666; E-Mail: crysdata@fiz-karlsruhe.de, http://www.fiz-karlsruhe.de/request_for_deposited_data.html?&L=1) on quoting the depository number CSD-430962 (Identification code; 56_11_1).

4. Conclusions

In summary, we prepared and characterized an open-Wells–Dawson structural POM, potassium salt of **In₁₀-open**, containing ten indium ions, *i.e.*, $K_{17}\{[\{KIn_2(\mu-OH)_2\}(\alpha,\alpha-Si_2W_{18}O_{66})]_2 [In_6(\mu-OH)_{13}(H_2O)_8] \cdot 35H_2O$ (potassium salt of **In₁₀-open**). Single-crystal X-ray analyses revealed that two open-Wells–Dawson units that include two In^{3+} ions and a K^+ ion are connected by an In_6 -hydroxide cluster moiety to form a dimeric open-Wells–Dawson polyanion. **In₁₀-open** displayed the widest bite angles among the previously reported open-Wells–Dawson POMs. This is mainly due to the large ionic radius of the indium ion. The solution ^{29}Si spectrum in D_2O indicated that **In₁₀-open** was obtained as a single species and that its structure was maintained in solution. **In₁₀-open** is the first example of an open-Wells–Dawson POM containing a fifth-period element, and it exhibits the highest nuclearity of any indium-containing POM reported to date. This work can be extended to the future molecular design of novel open-Wells–Dawson POMs containing large fifth- and sixth-period elements, such as Ru, Rh, Pd, Pt. Studies of open-Wells–Dawson structural POMs containing larger metal atoms are in progress.

Supplementary Materials: The following are available online at www.mdpi.com/2304-6740/4/2/16/s1, Figure S1: FT-IR spectrum of potassium salt of **In₁₀-open** (KBr disk), Figure S2: TG/DTA data of potassium salt of **In₁₀-open** (from 22 to 500 °C), Table S1: Bond valence sum (BVS) calculations of In and O atoms of the Indium-cluster moieties of **In₁₀-open**: checkCIF/PLATON report.

Acknowledgments: This study was supported by the Strategic Research Base Development Program for Private Universities of the Ministry of Education, Culture, Sports, Science and Technology of Japan, and also by a grant from the Research Institute for Integrated Science, Kanagawa University (RIIS201505).

Author Contributions: Satoshi Matsunaga and Kenji Nomiya conceived and designed the experiments, and wrote the paper; Takuya Otaki and Yusuke Inoue synthesized and characterized the compound; Kohei Mihara assisted characterization of the compound.

Conflicts of Interest: The authors declare no conflict of interest.

Abbreviations

The following abbreviations are used in this manuscript:

POM	Polyoxometalate
TG/DTA	Thermogravimetric/differential thermal analyses
BVS	Bond valence sum

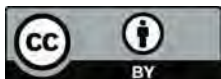
References

1. Pope, M.T.; Müller, A. Polyoxometalate chemistry: An old field with new dimensions in several disciplines. *Angew. Chem. Int. Ed.* **1991**, *30*, 34–48. [[CrossRef](#)]
2. Pope, M.T. *Heteropoly- and Isopolyoxometalates*; Springer-Verlag: New York, NY, USA, 1983.
3. Hill, C.L.; Prosser-McCartha, C.M. Homogeneous catalysis by transition metal oxygen anion clusters. *Coord. Chem. Rev.* **1995**, *143*, 407–455. [[CrossRef](#)]

4. Neumann, R. Polyoxometalate complexes in organic oxidation chemistry. *Prog. Inorg. Chem.* **1998**, *47*, 317–370.
5. Proust, A.; Thouvenot, R.; Gouzerh, P. Functionalization of polyoxometalates: Towards advanced applications in catalysis and materials science. *Chem. Commun.* **2008**, 1837–1852. [[CrossRef](#)] [[PubMed](#)]
6. Hasenknopf, B.; Micoine, K.; Lacôte, E.; Thorimbert, S.; Malacria, M.; Thouvenot, R. Chirality in polyoxometalate chemistry. *Eur. J. Inorg. Chem.* **2008**, *2008*, 5001–5013. [[CrossRef](#)]
7. Long, D.-L.; Tsunashima, R.; Cronin, L. Polyoxometalates: Building blocks for functional nanoscale systems. *Angew. Chem. Int. Ed.* **2010**, *49*, 1736–1758. [[CrossRef](#)] [[PubMed](#)]
8. Nomiya, K.; Sakai, Y.; Matsunaga, S. Chemistry of group IV metal ion-containing polyoxometalates. *Eur. J. Inorg. Chem.* **2011**, *2011*, 179–196. [[CrossRef](#)]
9. Izarova, N.V.; Pope, M.T.; Kortz, U. Noble metals in polyoxometalates. *Angew. Chem. Int. Ed.* **2012**, *51*, 9492–9510. [[CrossRef](#)] [[PubMed](#)]
10. Song, Y.-F.; Tsunashima, R. Recent advances on polyoxometalate-based molecular and composite materials. *Chem. Soc. Rev.* **2012**, *41*, 7384–7402. [[CrossRef](#)] [[PubMed](#)]
11. Bijelic, A.; Rompel, A. The use of polyoxometalates in protein crystallography—An attempt to widen a well-known bottleneck. *Coord. Chem. Rev.* **2015**, *299*, 22–38. [[CrossRef](#)] [[PubMed](#)]
12. Wang, S.-S.; Yang, G.-Y. Recent advances in polyoxometalate-catalyzed reactions. *Chem. Rev.* **2015**, *115*, 4893–4962. [[CrossRef](#)] [[PubMed](#)]
13. Blazevic, A.; Rompel, A. The Anderson–Evans polyoxometalate: From inorganic building blocks via hybrid organic–inorganic structures to tomorrows “Bio-POM”. *Coord. Chem. Rev.* **2016**, *307*, 42–64. [[CrossRef](#)]
14. Laronze, N.; Marrot, J.; Hervé, G. Synthesis, molecular structure and chemical properties of a new tungstosilicate with an open Wells–Dawson structure, α -[Si₂W₁₈O₆₆]¹⁶⁻. *Chem. Commun.* **2003**, *21*, 2360–2361. [[CrossRef](#)]
15. Bi, L.-H.; Kortz, U. Synthesis and structure of the pentacopper(II) substituted tungstosilicate [Cu₅(OH)₄(H₂O)₂(A- α -SiW₉O₃₃)₂]¹⁰⁻. *Inorg. Chem.* **2004**, *43*, 7961–7962. [[CrossRef](#)] [[PubMed](#)]
16. Leclerc-Laronze, N.; Marrot, J.; Hervé, G. Cation-directed synthesis of tungstosilicates. 2. Synthesis, structure, and characterization of the open Wells–Dawson anion α -[K(H₂O)₂(Si₂W₁₈O₆₆)]¹⁵⁻ and its transition-metal derivatives [M(H₂O)](μ-H₂O)₂K(Si₂W₁₈O₆₆)]¹³⁻ and [M(H₂O)](μ-H₂O)₂K{M(H₂O)₄(Si₂W₁₈O₆₆)]¹¹⁻. *Inorg. Chem.* **2005**, *44*, 1275–1281. [[PubMed](#)]
17. Nellutla, S.; Tol, J.V.; Dalal, N.S.; Bi, L.-H.; Kortz, U.; Keita, B.; Nadjjo, L.; Khitrov, G.A.; Marshall, A.G. Magnetism, electron paramagnetic resonance, electrochemistry, and mass spectrometry of the pentacopper(II)-substituted tungstosilicate [Cu₅(OH)₄(H₂O)₂(A- α -SiW₉O₃₃)₂]¹⁰⁻, A model five-spin frustrated cluster. *Inorg. Chem.* **2005**, *44*, 9795–9806. [[CrossRef](#)] [[PubMed](#)]
18. Leclerc-Laronze, N.; Haouas, M.; Marrot, J.; Taulelle, F.; Hervé, G. Step-by-step assembly of trivacant tungstosilicates: Synthesis and characterization of tetrameric anions. *Angew. Chem. Int. Ed.* **2006**, *45*, 139–142. [[CrossRef](#)] [[PubMed](#)]
19. Leclerc-Laronze, N.; Marrot, J.; Hervé, G. Dinuclear vanadium and tetranuclear iron complexes obtained with the open Wells–Dawson [Si₂W₁₈O₆₆]¹⁶⁻ tungstosilicate. *C. R. Chim.* **2006**, *9*, 1467–1471. [[CrossRef](#)]
20. Sun, C.-Y.; Liu, S.-X.; Wang, C.-L.; Xie, L.-H.; Zhang, C.-D.; Gao, B.; Su, Z.-M.; Jia, H.-Q. Synthesis, structure and characterization of a new cobalt-containing germanotungstate with open Wells–Dawson structure: K₁₃[{Co(H₂O)}(μ-H₂O)₂K(Ge₂W₁₈O₆₆)]. *J. Mol. Struct.* **2006**, *785*, 170–175. [[CrossRef](#)]
21. Wang, C.-L.; Liu, S.-X.; Sun, C.-Y.; Xie, L.-H.; Ren, Y.-H.; Liang, D.-D.; Cheng, H.-Y. Bimetals substituted germanotungstate complexes with open Wells–Dawson structure: Synthesis, structure, and electrochemical behavior of [M(H₂O)](μ-H₂O)₂K{M(H₂O)₄(Ge₂W₁₈O₆₆)]¹¹⁻ (M = Co, Ni, Mn). *J. Mol. Struct.* **2007**, *841*, 88–95. [[CrossRef](#)]
22. Ni, L.; Hussain, F.; Spingler, B.; Weyeneth, S.; Patzke, G.R. Lanthanoid-containing open Wells–Dawson silicotungstates: Synthesis, crystal structures, and properties. *Inorg. Chem.* **2011**, *50*, 4944–4955. [[CrossRef](#)] [[PubMed](#)]
23. Zhu, G.; Geletii, Y.V.; Zhao, C.; Musaev, D.G.; Song, J.; Hill, C.L. A dodecanuclear Zn cluster sandwiched by polyoxometalate ligands. *Dalton Trans.* **2012**, *41*, 9908–9913. [[CrossRef](#)] [[PubMed](#)]
24. Zhu, G.; Glass, E.N.; Zhao, C.; Lv, H.; Vickers, J.W.; Geletii, Y.V.; Musaev, D.G.; Song, J.; Hill, C.L. A nickel containing polyoxometalate water oxidation catalyst. *Dalton Trans.* **2012**, *41*, 13043–13049. [[CrossRef](#)] [[PubMed](#)]

25. Zhu, G.; Geletii, Y.V.; Song, J.; Zhao, C.; Glass, E.N.; Bacsá, J.; Hill, C.L. Di- and tri-cobalt silicotungstates: Synthesis, characterization, and stability studies. *Inorg. Chem.* **2013**, *52*, 1018–1024. [[CrossRef](#)] [[PubMed](#)]
26. Ni, L.; Spingler, B.; Weyeneth, S.; Patzke, G.R. Trilacunary Keggin-type POMs as versatile building blocks for lanthanoid silicotungstates. *Eur. J. Inorg. Chem.* **2013**, *2013*, 1681–1692. [[CrossRef](#)]
27. Guo, J.; Zhang, D.; Chen, L.; Song, Y.; Zhu, D.; Xu, Y. Syntheses, structures and magnetic properties of two unprecedented hybrid compounds constructed from open Wells–Dawson anions and high-nuclear transition metal clusters. *Dalton Trans.* **2013**, *42*, 8454–8459. [[CrossRef](#)] [[PubMed](#)]
28. Matsunaga, S.; Inoue, Y.; Otaki, T.; Osada, H.; Nomiya, K. Aluminum- and gallium-containing open-Dawson polyoxometalates. *Z. Anorg. Allg. Chem.* **2016**, *642*, 539–545. [[CrossRef](#)]
29. Zhang, F.-Q.; Guan, W.; Yan, L.-K.; Zhang, Y.-T.; Xu, M.-T.; Hayfron-Benjamin, E.; Su, Z.-M. On the origin of the relative stability of Wells–Dawson isomers: A DFT study of α -, β -, γ -, α^* -, β^* -, and γ^* -[(PO₄)₂W₁₈O₅₄]⁶⁻ anions. *Inorg. Chem.* **2011**, *50*, 4967–4977. [[CrossRef](#)] [[PubMed](#)]
30. Jordan, P.A.; Clayden, N.J.; Heath, S.L.; Moore, G.R.; Powell, A.K.; Tapparo, A. Defining speciation profiles of Al³⁺ complexed with small organic ligands: The Al³⁺-heidi system. *Coord. Chem. Rev.* **1996**, *149*, 281–309. [[CrossRef](#)]
31. Casey, W.H. Large aqueous aluminum hydroxide molecules. *Chem. Rev.* **2006**, *106*, 1–16. [[CrossRef](#)] [[PubMed](#)]
32. Mensinger, Z.L.; Wang, W.; Keszler, D.A.; Johnson, D.W. Oligomeric group 13 hydroxide compounds—A rare but varied class of molecules. *Chem. Soc. Rev.* **2012**, *41*, 1019–1030. [[CrossRef](#)] [[PubMed](#)]
33. Kikukawa, Y.; Yamaguchi, S.; Nakagawa, Y.; Uehara, K.; Uchida, S.; Yamaguchi, K.; Mizuno, N. Synthesis of a dialuminum-substituted silicotungstate and the diastereoselective cyclization of citronellal derivatives. *J. Am. Chem. Soc.* **2008**, *130*, 15872–15878. [[CrossRef](#)] [[PubMed](#)]
34. Kato, C.N.; Katayama, Y.; Nagami, M.; Kato, M.; Yamasaki, M. A sandwich-type aluminium complex composed of tri-lacunary Keggin-type polyoxotungstate: Synthesis and X-ray crystal structure of [(A-PW₉O₃₄)₂{W(OH)(OH₂)}{Al(OH)(OH₂)}{Al(μ -OH)(OH₂)₂}]⁷⁻. *Dalton Trans.* **2010**, *39*, 11469–11474. [[CrossRef](#)] [[PubMed](#)]
35. Kikukawa, Y.; Yamaguchi, K.; Hibino, M.; Mizuno, N. Layered assemblies of a dialuminum-substituted silicotungstate trimer and the reversible interlayer cation-exchange properties. *Inorg. Chem.* **2011**, *50*, 12411–12413. [[CrossRef](#)] [[PubMed](#)]
36. Carraro, M.; Bassil, B.S.; Sorarù, A.; Berardi, S.; Suchopar, A.; Kortz, U.; Bonchio, M. A Lewis acid catalytic core sandwiched by inorganic polyoxoanion caps: Selective H₂O₂-based oxidations with [Al^{III}₄(H₂O)₁₀(β -XW₉O₃₃H)₂]⁶⁻ (X = As^{III}, Sb^{III}). *Chem. Commun.* **2013**, *49*, 7914–7916. [[CrossRef](#)] [[PubMed](#)]
37. Kato, C.N.; Makino, Y.; Unno, W.; Uno, H. Synthesis, molecular structure, and stability of a zirconocene derivative with α -Keggin mono-aluminum substituted polyoxotungstate. *Dalton Trans.* **2013**, *42*, 1129–1135. [[CrossRef](#)] [[PubMed](#)]
38. Kato, C.N.; Kashiwagi, T.; Unno, W.; Nakagawa, M.; Uno, H. Syntheses and molecular structures of monomeric and hydrogen-bonded dimeric Dawson-type trialuminum-substituted polyoxotungstates derived under acidic and basic conditions. *Inorg. Chem.* **2014**, *53*, 4823–4832. [[CrossRef](#)] [[PubMed](#)]
39. Inoue, Y.; Matsunaga, S.; Nomiya, K. Al₁₆-hydroxide cluster-containing tetrameric polyoxometalate, [(α -Al₃SiW₉O₃₄(μ -OH)₆]₄{Al₄(μ -OH)₆}]²²⁻. *Chem. Lett.* **2015**, *44*, 1649–1651. [[CrossRef](#)]
40. Allmen, K.; Car, P.-E.; Blacque, O.; Fox, T.; Müller, R.; Patzke, G.R. Structure and properties of new gallium-containing polyoxotungstates with hexanuclear and tetranuclear cores. *Z. Anorg. Allg. Chem.* **2014**, *640*, 781–789. [[CrossRef](#)]
41. Limanski, E.M.; Drewes, D.; Krebs, B. Sandwich-like polyoxotungstates with indium(III) as a heteroatom synthesis and characterization of the first examples of a new type of anions. *Z. Anorg. Allg. Chem.* **2004**, *630*, 523–528. [[CrossRef](#)]
42. Hussain, F.; Reicke, M.; Janowski, V.; Silva, S.D.; Futuwi, J.; Kortz, U. Some indium(III)-substituted polyoxotungstates of the Keggin and Dawson types. *C. R. Chim.* **2005**, *8*, 1045–1056. [[CrossRef](#)]
43. Zhao, D.; Ye, R.-H. Solvothermal synthesis and structure of a new indium-substituted polyoxotungstate: [(CH₃)₂NH₂]₄[In₃(H₂O)₃(NO₃)(A- α -H₃PW₉O₃₄)₂·H₂O]. *J. Clust. Sci.* **2011**, *22*, 563–571. [[CrossRef](#)]
44. Brown, I.D.; Altermatt, D. Bond-valence parameters obtained from a systematic analysis of the Inorganic Crystal Structure Database. *Acta Crystallogr.* **1985**, *B41*, 244–247. [[CrossRef](#)]

45. Shannon, R.D.; Prewitt, C.T. Effective ionic radii in oxides and fluorides. *Acta Cryst.* **1969**, *B25*, 925–946. [[CrossRef](#)]
46. Shannon, R.D. Revised effective ionic radii and systematic studies of interatomic distances in halides and chalcogenides. *Acta Cryst.* **1976**, *A32*, 751–761. [[CrossRef](#)]
47. Sheldrick, G.M. A short history of SHELX. *Acta Crystallogr.* **2008**, *64*, 112–122. [[CrossRef](#)] [[PubMed](#)]



© 2016 by the authors; licensee MDPI, Basel, Switzerland. This article is an open access article distributed under the terms and conditions of the Creative Commons Attribution (CC-BY) license (<http://creativecommons.org/licenses/by/4.0/>).

Silver- and Acid-Free Catalysis by Polyoxometalate-Assisted Phosphanegold(I) Species for Hydration of Diphenylacetylene

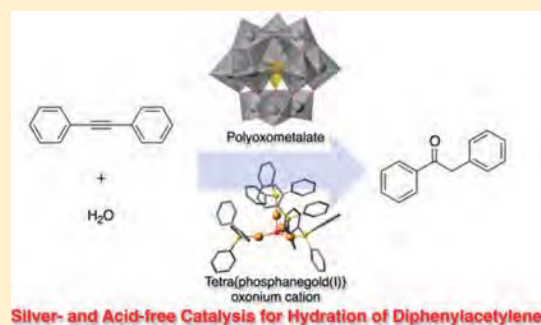
Hidekazu Arai,[†] Takuya Yoshida,^{†,‡,§} Eri Nagashima,[†] Akifumi Hatayama,[†] Shogo Horie,[†] Satoshi Matsunaga,[†] and Kenji Nomiya^{*,†}

[†]Department of Chemistry, Faculty of Science, Kanagawa University, Hiratsuka, Kanagawa 259-1293, Japan

[‡]Research Center for Gold Chemistry and [§]Department of Applied Chemistry, Tokyo Metropolitan University, Minami-osawa 1-1, Hachioji, Tokyo 192-0397, Japan

Supporting Information

ABSTRACT: A DMSO-soluble intercluster compound consisting of a tetra{phosphanegold(I)}oxonium cation and an α -Keggin polyoxometalate (POM) anion, $[\{\text{Au}(\text{PPh}_3)_4(\mu_4\text{-O})\}_3[\alpha\text{-PW}_{12}\text{O}_{40}]_2$ (**1**), was found to be an effective precatalyst for the silver- and acid-free catalysis of diphenylacetylene hydration (0.67 mol % catalyst; conversions 36.1%, 55.2%, and 93.7% after 4, 6, and 24 h reactions, respectively). The reaction proceeded in the suspended system in 6 mL of 1,4-dioxane/water (4:1) at 80 °C because of the low solubility of **1**. Similar POM-based phosphanegold(I) compounds $[\{\{\text{Au}(\text{PPh}_3)_4(\mu_4\text{-O})\}\{\text{Au}(\text{PPh}_3)_3(\mu_3\text{-O})\}\}[\alpha\text{-PW}_{12}\text{O}_{40}]\cdot\text{EtOH}$ (**5**), which is composed of a heptakis{triphenylphosphanegold(I)}-dioxonium cation and an α -Keggin POM anion, and $[\text{Au}(\text{CH}_3\text{CN})(\text{PPh}_3)_3][\alpha\text{-PMo}_{12}\text{O}_{40}]$ (**6**), which consists of an acid-free monomeric phosphanegold(I) acetonitrile cation and an α -Keggin molybdo-POM anion, also exhibited acid-free catalysis for the hydration of diphenylacetylene. An induction period was observed in the catalysis by **5**. On the other hand, their component species, or phosphanegold(I) species without the POM anion, such as $[\{\text{Au}(\text{PPh}_3)_4(\mu_4\text{-O})\}(\text{BF}_4)_2$ (**2**) and $[\{\text{Au}(\text{PPh}_3)_3(\mu_3\text{-O})\}\text{BF}_4$ (**3**), and the monomeric phosphanegold(I) complex $[\text{Au}(\text{RS-pyrrld})(\text{PPh}_3)]$ (**4**) (RS-Hpyrrld = RS-2-pyrrolidone-5-carboxylic acid), the last of which has been used as a precursor for the preparation of **1**, **5**, and **6**, showed poor activities in this reaction (0.67 mol % catalysts; conversions 1.8%, 1.7%, and 0.5% after 24 h reactions, respectively). However, upon adding the free-acid form of Keggin POM, i.e., $\text{H}_3[\alpha\text{-PW}_{12}\text{O}_{40}]\cdot 7\text{H}_2\text{O}$ (H-POM; 0.67 mol %), **2**–**4** exhibited remarkably enhanced activities (conversion 97.6% each after 24 h reactions). In contrast, the activities were not enhanced after adding either the sodium salt of the Keggin POM, $\text{Na}_3[\alpha\text{-PW}_{12}\text{O}_{40}]\cdot 8\text{H}_2\text{O}$ (Na-POM; 0.67 mol %), or a Brønsted acid 10% HBF_4 aqueous solution (0.67 mol %). Both H-POM and Na-POM themselves exhibited no activity. Catalysis by the phosphanegold(I) species for diphenylacetylene hydration was influenced significantly under the free-acid form or sodium salt of the Keggin POM. Acid-free catalytic hydration by **1** of other alkynes, such as phenylacetylene and 1-phenyl-1-butyne, was also examined.



INTRODUCTION

Polyoxometalates (POMs) are anionic, molecular metal–oxygen bonding clusters that resemble the discrete fragments of solid metal oxides and mimic soluble metal oxides. These properties have led to a range of applications in different fields, especially in catalysis, medicine, biology, electrochromism, magnetism, and material science.¹ A combination of POMs with cluster cations or macrocations has resulted in the formation of various interesting intercluster compounds from the viewpoints of ionic crystals, crystal growth, crystal engineering, structure, sorption properties, etc.^{2–4}

Recently, we reported the formation of a novel intercluster compound consisting of a tetrakis{triphenylphosphanegold(I)}oxonium cluster cation and the Keggin POM anion, i.e., $[\{\text{Au}(\text{PPh}_3)_4(\mu_4\text{-O})\}_3[\alpha\text{-PW}_{12}\text{O}_{40}]_2$ (**1**).^{5a} This compound resulted from the POM-mediated clusterization of *in situ*-generated monomeric phosphanegold(I) units, $[\text{Au}(\text{PPh}_3)]^+$ or

$[\text{Au}(\text{L})(\text{PPh}_3)]^+$ (L = solvent), during the carboxylate elimination of a monomeric phosphanegold(I) carboxylate, $[\text{Au}(\text{RS-pyrrld})(\text{PPh}_3)]$ (**4**) (RS-Hpyrrld = RS-2-pyrrolidone-5-carboxylic acid),⁶ in the presence of the free-acid form of the Keggin POM, $\text{H}_3[\alpha\text{-PW}_{12}\text{O}_{40}]\cdot 7\text{H}_2\text{O}$ (H-POM). In addition, we reported the formation of a heptakis{triphenylphosphanegold(I)}dioxonium cluster cation, $[\{\{\text{Au}(\text{PPh}_3)_4(\mu_4\text{-O})\}\{\text{Au}(\text{PPh}_3)_3(\mu_3\text{-O})\}\}^{3+}$,^{5b} by the reaction of $[\text{Au}(\text{RS-pyrrld})(\text{PPh}_3)]$ with the sodium salt of the Keggin POM, i.e., $\text{Na}_3[\alpha\text{-PW}_{12}\text{O}_{40}]\cdot 9\text{H}_2\text{O}$ (Na-POM). These reactions were strongly dependent on the acidity, bulkiness, and high charge density of the POM. Such reactions were also affected by the substituents on the phosphane ligands.^{5c,e,f} For example, novel intercluster compounds $[\{\{\text{Au}\{p\text{-RPh}\}_3\}_2(\mu\text{-OH})\}_2]_3[\alpha\text{-}$

Received: February 11, 2016

Published: May 18, 2016

$\text{PM}_{12}\text{O}_{40}]_2 \cdot n\text{EtOH}$ ($R = \text{Me}$, $M = \text{W}$; $R = \text{Me}$, $M = \text{Mo}$; $R = \text{F}$, $M = \text{Mo}$) have been synthesized at room temperature^{5c} by reactions between $[\text{Au}(\text{RS-pyrrld})\{\text{P}(p\text{-RPh})_3\}]$ ($R = \text{Me}$, F) in CH_2Cl_2 and $\text{H}_3[\alpha\text{-PM}_{12}\text{O}_{40}] \cdot n\text{H}_2\text{O}$ ($M = \text{W}$, $n = 7$; $M = \text{Mo}$, $n = 14$) in mixed $\text{EtOH}/\text{H}_2\text{O}$ solvents. Novel intercluster compounds, i.e., $[\{\text{Au}(\text{PPh}_3)_4(\mu_4\text{-O})\}][\alpha\text{-XW}_{12}\text{O}_{40} \{\text{Au}(\text{PPh}_3)_3\}_3 \cdot 3\text{EtOH}$ ($X = \text{Al}$, B), composed of the tetrakis-triphenylphosphane-gold(I) oxonium cluster cation and a saturated Keggin POM, together with three monomeric phosphane-gold(I) units coordinated to the OW_2 oxygen atoms of the edge-shared WO_6 octahedra of the POM, were also reported.^{5d}

Several phosphane-gold(I) complexes have been reported to be effective homogeneous catalysts for organic synthesis.⁷ One of the most straightforward ways of synthesizing compounds with carbon–oxygen bonds is the hydration of unsaturated organic compounds. In particular, the synthesis of carbonyl compounds by the addition of water to alkynes is not only environmentally benign but also economically attractive.^{8a} For alkyne hydration, active catalytic systems composed of a highly toxic mercury salt and either a Lewis or Brønsted acid have traditionally been used. Therefore, the development of less toxic methods has attracted considerable interest.

In 2002, Tanaka et al. reported alkyne hydration, from 1-octyne to 2-octanone, in MeOH at 70 °C catalyzed by an organogold complex, $[(\text{PPh}_3)\text{AuMe}]$, that was activated by a strong acid, such as H_2SO_4 , $\text{CF}_3\text{SO}_3\text{H}$, or $\text{H}_3[\text{PW}_{12}\text{O}_{40}]$.^{8b} In 2004, Schmidbauer's group reported that (phosphane)gold(I) carboxylates and sulfonates are highly active and reusable catalysts for the hydration of 3-hexyne by the addition of water.^{8a}

With regard to gold catalysis, the “silver effect”^{9a,b} and “counterion effect”^{9c–e} need to be considered. For example, it has been claimed that gold-catalyzed alkyne hydration cannot be catalyzed only by $[\text{Au}]^+$ and that the presence of silver is required for the reaction to proceed.^{9a} However, the role of the counterion, such as OTf , SbF_6^- , and BF_4^- , or the “counterion effect”, rather than the role of the silver salt has been pointed out.^{9c–e} In 2009, Corma et al. reported the first incidence of acid- and silver-free gold(I)-catalyzed alkyne hydration using gold(I) complexes with phosphane ligands combined with a soft noncoordinating anion, e.g., $[\text{Au}(\text{L})]\text{NTf}_2$ ($\text{L} = \text{SPhos}$, PPh_3 , PtBu_3 ; $\text{NTf}_2^- = \text{bis}(\text{trifluoromethanesulfonyl})\text{imide}$), at room temperature.^{8c} In 2011, however, Nolan et al. revealed the hydration of terminal and internal alkynes by NHC-gold(I) precatalysts ($\text{NHC} = \text{N-heterocyclic carbene}$), e.g., $[(\text{IPr})\text{AuOH}]$ ($\text{IPr} = 1,3\text{-bis}(2,6\text{-diisopropylphenyl})\text{imidazol-2-ylidene}$), which can generate the active catalytic species $[(\text{IPr})\text{Au}]^+$ by protonolysis in the presence of a Brønsted acid, such as HSbF_6 , HNTf_2 , or HBF_4 .^{8d} They recently reported a diaurated species, $[\{\text{Au}(\text{IPr})_2(\mu\text{-OH})\}]\text{BF}_4^-$, as a silver- and acid-free catalyst for alkyne hydration, nitrile hydration, and some organic transformations with relatively low catalyst loadings (0.5 mol %).^{9b} On the other hand, Corma et al. recently observed a clear induction time in the gold(I)–carbene-catalyzed hydration of diphenylacetylene and suggested that the gold(I)–carbene decomposes under these reaction conditions. Moreover, the latter could be the catalytically active gold species because 3–5-atom gold–alkyne clusters were formed after an induction period.^{8e}

Sicilia et al. discussed the theoretical aspects of the $[\text{Au}(\text{PR}_3)]^+$ -catalyzed hydration of diphenylacetylene.¹⁰ The calculations suggested that the rate-determining step of the

entire process is the addition of a second nucleophile molecule to the formed enol ether to yield the final ketone product.

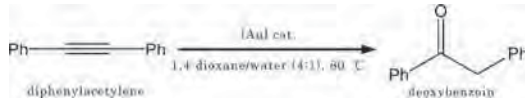
Regarding POM-based gold(I) catalysts, Blanc et al. reported that proton-containing hybrid complexes $[\text{Au}(\text{CH}_3\text{CN})\text{-}(\text{PPh}_3)_x\text{H}_{4-x}[\text{SiW}_{12}\text{O}_{40}]]$ ($x = 1\text{--}4$; **B1–B4**) exhibited effective catalytic activity and selectivity as heterogeneous catalysts for the conversion of enyne acetate to cyclopentenone and the rearrangement of propargylic *gem*-diester to (*E*)-3-oxycarbonyl enone derivatives.^{11a} In addition, the related proton-containing hybrid complexes $[\text{Au}(\text{CH}_3\text{CN})(\text{PR}_3)][\text{POM-H}]$ ($R = \text{Ph}$, Me ; $\text{POM-H} = \text{H}_3\text{SiW}_{12}\text{O}_{40}$, $\text{H}_2\text{PM}_{12}\text{O}_{40}$ ($M = \text{Mo}$, W), $\text{H}_3\text{P}_2\text{W}_{18}\text{O}_{62}$) also exhibited bifunctional catalytic properties for the tandem aza-Prins cyclization/enol ether hydrolysis.^{11b}

In this work, we have examined diphenylacetylene hydration catalyzed by acid-free intercluster compounds of phosphane-gold(I) cluster species with Keggin POMs, i.e., $[\{\text{Au}(\text{PPh}_3)_4(\mu_4\text{-O})\}_3[\alpha\text{-PW}_{12}\text{O}_{40}]_2 \cdot 4\text{EtOH}$ (**1**) and $[\{\{\text{Au}(\text{PPh}_3)_4(\mu_4\text{-O})\}\{\{\text{Au}(\text{PPh}_3)_3(\mu_3\text{-O})\}\}][\alpha\text{-PW}_{12}\text{O}_{40}] \cdot \text{EtOH}$ (**5**), as well as $[\text{Au}(\text{CH}_3\text{CN})(\text{PPh}_3)_3][\alpha\text{-PMo}_{12}\text{O}_{40}]$ (**6**), consisting of an acid-free monomeric phosphane-gold(I) cation and α -Keggin molybdo-POM anion, under the following conditions: catalysts (0.67 mol %), diphenylacetylene (1.5 mmol), toluene (4.7 mmol) as an internal standard, 1,4-dioxane/water (4:1 v/v) mixed solvent, reaction temperature 80 °C. Complexes **1**, **5**, and **6** were the effective precatalysts of the silver- and acid-free catalysis for diphenylacetylene hydration. In addition, as control experiments, alkyne hydration catalysis by two phosphane-gold(I) cluster species without a POM anion, $([\{\text{Au}(\text{PPh}_3)_4(\mu_4\text{-O})\}](\text{BF}_4)_2$ (**2**) and $[\{\text{Au}(\text{PPh}_3)_3(\mu_3\text{-O})\}]\text{BF}_4$ (**3**), as well as by the monomeric phosphane-gold(I) complex $[\text{Au}(\text{RS-pyrrld})(\text{PPh}_3)]$ (**4**) (all 0.67 mol %) was examined in the presence or absence of additives (0.67 mol % each), such as $\text{H}_3[\alpha\text{-PW}_{12}\text{O}_{40}] \cdot 7\text{H}_2\text{O}$ (H-POM), $\text{Na}_3[\alpha\text{-PW}_{12}\text{O}_{40}] \cdot 8\text{H}_2\text{O}$ (Na-POM), or aqueous HBF_4 solution (Table 1). This paper reports silver- and acid-free catalysis using *in situ*-generated POM-assisted phosphane-gold(I) species from **1** and related compounds for diphenylacetylene hydration.

EXPERIMENTAL SECTION

Materials. The following reactants were used as received: diphenylacetylene, deoxybenzoin, phenylacetylene, acetophenone, 1,4-dioxane (Wako), 1-phenyl-1-butyne, butyrophenone, 1-phenyl-2-butanone (TCI), $[\{\text{Au}(\text{PPh}_3)_3(\mu_3\text{-O})\}]\text{BF}_4$ (**3**) (Aldrich), and CD_2Cl_2 and $\text{DMSO-}d_6$ (Isotec). Keggin POMs, such as $\text{H}_3[\alpha\text{-PW}_{12}\text{O}_{40}] \cdot 7\text{H}_2\text{O}$ (H-POM), $\text{H}_3[\alpha\text{-PMo}_{12}\text{O}_{40}] \cdot 14\text{H}_2\text{O}$, $\text{Na}_3[\alpha\text{-PW}_{12}\text{O}_{40}] \cdot 8\text{H}_2\text{O}$ (Na-POM), $\text{H}_4[\alpha\text{-SiW}_{12}\text{O}_{40}] \cdot 17\text{H}_2\text{O}$, $\text{H}_5[\alpha\text{-BW}_{12}\text{O}_{40}] \cdot 15\text{H}_2\text{O}$, $\text{H}_5[\alpha\text{-AlW}_{12}\text{O}_{40}] \cdot 11\text{H}_2\text{O}$, and $\text{H}_6[\alpha\text{-ZnW}_{12}\text{O}_{40}] \cdot 9\text{H}_2\text{O}$, were prepared using the procedures reported elsewhere.^{5d,12} The compounds were identified by Fourier transform infrared (FTIR) spectroscopy, thermogravimetric and differential thermal analysis (TG/DTA), and solution (^{27}Al , ^{31}P) nuclear magnetic resonance (NMR) spectroscopy. The precursor $[\text{Au}(\text{RS-pyrrld})(\text{PPh}_3)]$ (**4**) was synthesized using the literature procedure⁶ and identified by CHN elemental analysis, FTIR spectroscopy, TG/DTA, and solution (^1H , $^{13}\text{C}\{^1\text{H}\}$, $^{31}\text{P}\{^1\text{H}\}$) NMR spectroscopy.

The precatalysts $[\{\text{Au}(\text{PPh}_3)_4(\mu_4\text{-O})\}_3[\alpha\text{-PW}_{12}\text{O}_{40}]_2 \cdot 4\text{EtOH}$ (**1**) and $[\{\{\text{Au}(\text{PPh}_3)_4(\mu_4\text{-O})\}\{\{\text{Au}(\text{PPh}_3)_3(\mu_3\text{-O})\}\}][\alpha\text{-PW}_{12}\text{O}_{40}] \cdot \text{EtOH}$ (**5**) were prepared as crystalline samples using liquid–liquid diffusion methods of the reaction systems consisting of $[\text{Au}(\text{RS-pyrrld})(\text{PPh}_3)]$ (**4**) in CH_2Cl_2 and $\text{H}_3[\alpha\text{-PW}_{12}\text{O}_{40}] \cdot 7\text{H}_2\text{O}$ (H-POM) or $\text{Na}_3[\alpha\text{-PW}_{12}\text{O}_{40}] \cdot 8\text{H}_2\text{O}$ (Na-POM) dissolved in an $\text{EtOH}/\text{H}_2\text{O}$ mixed solvent, respectively,^{5a,b} and characterized by elemental analysis, FTIR spectroscopy, TG/DTA, and $^{31}\text{P}\{^1\text{H}\}$ NMR spectroscopy. $[\{\text{Au}(\text{PPh}_3)_4(\mu_4\text{-O})\}](\text{BF}_4)_2$ (**2**) was prepared in BF_4^- form from **1**

Table 1. Results of the Hydration of Diphenylacetylene Catalyzed by Phosphanegold(I) Species^a


entry	catalyst/additive	conversion (%)		
		after 4 h	after 6 h	after 24 h
1-1(1)	[{Au(PPh ₃) ₄ (μ ₄ -O)} ₃][α-PW ₁₂ O ₄₀] ₂ (1)	36.1	55.2	93.7
1-1(2)	1 + HBF ₄ (aq)	71.2	84.0	>99
1-1(3)	1 + NaBF ₄	17.4	22.9	54.0
1-1(4)	1 + KBF ₄	21.5	27.1	68.0
1-2	[{Au(PPh ₃) ₃ (μ ₄ -O)}(BF ₄) ₂] (2)	2.1	2.0	1.8
1-3	2 + H-POM	72.3	84.7	97.6
1-4	2 + Na-POM	1.5	2.3	9.7
1-5	2 + HBF ₄ (aq)	6.0	7.0	7.2
1-6	[{Au(PPh ₃) ₃ (μ ₃ -O)}]BF ₄ (3)	2.0	1.4	1.7
1-7	3 + H-POM	73.1	87.0	97.6
1-8	3 + Na-POM	2.8	3.6	16.3
1-9	3 + HBF ₄ (aq)	3.1	3.0	3.4
1-10	[Au(RS-pyrrld)(PPh ₃) ₂] (4)	0.7	1.1	0.5
1-11	4 + H-POM	71.5	84.9	97.6
1-12 ^b	4 + Na-POM	1.4	2.1	4.9
1-13	4 + HBF ₄ (aq)	1.2	1.2	2.2
1-14	H ₃ [α-PW ₁₂ O ₄₀]-7H ₂ O (H-POM)	0	0	0
1-15	Na ₃ [α-PW ₁₂ O ₄₀]-8H ₂ O (Na-POM)	0	0	0
1-16(1)	[{Au(PPh ₃) ₃ (μ ₄ -O)} ₃][{Au(PPh ₃) ₃ (μ ₃ -O)}][α-PW ₁₂ O ₄₀]-EtOH (5)	2.0	4.2	89.0
1-16(2)	5 + HBF ₄ (aq)	14.9	24.1	87.3
1-16(3)	5 + NaBF ₄	0.3	0.5	8.4
1-16(4)	5 + KBF ₄	2.7	3.1	19.0
1-17	[Au(CH ₃ CN)(PPh ₃) ₃][α-PMo ₁₂ O ₄₀] (6)	71.8	84.9	91.6

^aReaction conditions: main catalysts (0.67 mol %), additives (0.67 mol %), substrate diphenylacetylene 1.5 mmol, toluene (4.7 mmol) as an internal standard, solvent 6 mL of solvent mixture of 1,4-dioxane and water (4:1), temperature 80 °C. ^bIn entry 1-12, the reaction was followed after 24 h until 1 week, but their conversions were unchanged (conversions 9.1% after 48 h, 8.7% after 72 h, and 9.7% after 168 h), suggesting that the Na⁺ ion inhibits catalysis by the heptaphoshanegold(I) cluster compound 5 or significantly lengthens the induction period.

using an anion-exchange resin (Amberlyst A-27) via a batch method, and the [PW₁₂O₄₀]³⁻-free powder sample obtained was confirmed by ³¹P{¹H} NMR in CD₂Cl₂.^{5a}

[Au(PPh₃)₂]BF₄ was prepared^{13e} and characterized by elemental analysis, TG/DTA, and ³¹P{¹H} NMR spectroscopy. Phosphanegold(I) cluster compounds, [Au₉(PPh₃)₈](NO₃)₃^{14a} and [Au₉(PPh₃)₈][α-PW₁₂O₄₀]₂^{2a} were prepared using the methodology reported in the literature and characterized by elemental analysis, TG/DTA, FTIR spectroscopy, ³¹P{¹H} NMR spectroscopy, and X-ray crystallography.

Instrumentation/Analytical Procedures. CHN elemental analyses were carried out using a PerkinElmer 2400 CHNS elemental analyzer II (Kanagawa University). IR spectra were recorded on a Jasco 4100 FT-IR spectrometer in KBr disks at room temperature. TG/DTA was performed using a Rigaku Thermo Plus 2 series TG/DTA TG 8120 instrument.

The ¹H NMR (500.00 MHz) and ³¹P{¹H} NMR (202.00 MHz) spectra in a DMSO-*d*₆ solution were recorded in 5 mm-outer-diameter tubes on a JEOL JNM-ECP 500 FT-NMR spectrometer using a JEOL ECP-500 NMR data processing system. The ¹³C{¹H} NMR (99 MHz) spectra were recorded in 5 mm-outer-diameter tubes on a JEOL

JNM-ECA 400 FT-NMR or a JEOL JNM-ECS-400 FT-NMR spectrometer and a JEOL ECA-400 NMR or ECS-400 NMR data processing system, respectively. The ¹H and ¹³C{¹H} NMR spectra were referenced to an internal standard, tetramethylsilane (SiMe₄). The ³¹P{¹H} NMR spectra were referenced to the external standard 25% H₃PO₄ in H₂O in a sealed capillary. The ³¹P{¹H} NMR data with the usual 85% H₃PO₄ reference were shifted to +0.544 ppm from the data.

The high-performance liquid chromatography (HPLC) apparatus and conditions are as follows: Shimadzu LC-20AD with Shimadzu SPD-20A (wavelength 260 nm) detector, using a VP-ODS (150 mm × 4.6 mm) column, flow rate 0.7 mL per min, and the solvent MeOH/water (30:17).

Preparation of [Au(CH₃CN)(PPh₃)₃][PMo₁₂O₄₀] (6). Compound 6 was obtained by a liquid–liquid diffusion method using a CH₃CN/water (5:1) mixed solvent, instead of the EtOH/H₂O (5:1) mixed solvent used in the synthesis of 1. [Au(RS-pyrrld)(PPh₃)₂] (70.5 mg, 0.120 mmol) was dissolved in CH₂Cl₂ (10 mL). A yellow clear solution of H₃[α-PMo₁₂O₄₀]-14H₂O (41.5 mg, 20 μmol) dissolved in 6 mL of a CH₃CN/H₂O (5:1, v/v) mixed solvent was added slowly along the interior wall of a round-bottomed flask containing the colorless clear solution of [Au(RS-pyrrld)(PPh₃)₂]. The round-bottomed flask containing two layers, i.e., the gold(I) complex solution in the lower layer and the POM solution in the upper layer, was sealed and left in the dark at room temperature. After 3 days, yellow block crystals were formed, collected using a membrane filter (JG 0.2 μm), washed with CH₃CN (20 mL × 2) and Et₂O (20 mL × 2), and dried *in vacuo* over a 2 h period. Yield: 30 mg (45.1%). The crystalline samples were soluble in DMSO but insoluble in H₂O, CH₃CN, and Et₂O. Anal. Calcd for C₆₀H₅₄N₃O₄₀P₄Au₃Mo₁₂ or [Au(CH₃CN)(PPh₃)₃][PMo₁₂O₄₀]: C, 21.69; H, 1.64; N, 1.26. Found: C, 21.80; H, 1.33; N, 1.26. TG/DTA under atmospheric conditions: a 3.02% weight loss due to desorption of CH₃CN molecules below 141.9 °C was observed with an endothermic peak at 143.4 °C; calcd 3.57% for three coordinated CH₃CN molecules in 6. FTIR (KBr): 1637 (m), 1479 (w), 1436 (m), 1312 (vw), 1181 (vw), 1158 (vw), 1102 (w), 1064 (s), 1027 (vw), 962 (vs), 874 (s), 803 (vs), 753 (s), 713 (s), 692 (s), 597 (m), 545 (s), 500 (s) cm⁻¹. ³¹P{¹H} NMR [22.9 °C, DMSO-*d*₆]: δ -3.32, 27.32 ppm. ¹H NMR [22.2 °C, DMSO-*d*₆]: δ 2.08 (s, CH₃CN), 5.76 (s, CH₂Cl₂), 7.56–7.70 (m, Ph) ppm. Crystal data for 6: C₆₀H₅₄Au₃Mo₁₂N₃O₄₀P₄; *M* = 3323.12; rhombohedral, space group R3; *a* = 19.2205(6) Å, *c* = 19.179(12) Å, *V* = 6134.4(5) Å³, *Z* = 3, *D*_c = 2.699 g cm⁻³, μ(Mo Kα) = 19.399 mm⁻¹. *R*₁ = 0.0274, *wR*₂ = 0.0648 (for all data). *R*_{int} = 0.0194, *R*₁ = 0.0271, *wR*₂ = 0.0647, GOF = 1.033 (14 433 total reflections, 5185 unique reflections where *I* > 2σ(*I*)). The same compound was recently synthesized from a reaction of [Au(Me)(PPh₃)₃] (1.0 equiv) with H₃[PMo₁₂O₄₀]-*n*H₂O (1.0 equiv) in CH₃CN (2.5 mL) at room temperature, and reported together with the crystal data (CCDC 1407462) by Blanc et al.,^{11b} even though their expected structure was based on the proton-containing, bifunctional catalyst [Au(CH₃CN)(PPh₃)₃][H₂PMo₁₂O₄₀].

Species Formed in the Catalyst System 3 + H-POM (Entries 1–7). A colorless clear solution of H₃[α-PW₁₂O₄₀]-7H₂O (H-POM) (0.060 g, 0.02 mmol) dissolved in 6 mL of an EtOH/H₂O (5:1, v/v) mixed solvent was added slowly to a colorless clear solution of [{Au(PPh₃)₃(μ₃-O)}]BF₄ (3) (0.0592 g, 0.040 mmol) dissolved in 10 mL of CH₂Cl₂. The vial containing two layers was sealed and left in the dark at room temperature. After a few days, pale yellow block crystals formed. A portion was used for X-ray crystallography, and the remainder was collected with a membrane filter (JG 0.2 μm), washed with EtOH (4 mL × 2) and Et₂O (6 mL × 2), and dried *in vacuo* for 2 h. Yield of crystals: 55.6 mg (48.7%). Yellow block crystals were also characterized by TG/DTA, X-ray crystallography, and ³¹P{¹H} NMR in DMSO-*d*₆.

TG/DTA under atmospheric conditions: a 0.61% weight loss due to two desorbed EtOH molecules was observed below 212.3 °C; calcd 0.41% for one EtOH molecule and 0.81% for two EtOH molecules. ³¹P{¹H} NMR [21.7 °C, DMSO-*d*₆]: δ -14.89, 24.90 ppm. X-ray crystallography revealed the formation of a tetrakis{phosphanegold-

Table 2. Effect of Various Amounts of Diphenylacetylene in Catalysis by 1^a

entry	deoxybenzoin formed (TON)				conversion (%) = yield			
	after 4 h	after 6 h	after 24 h	after 48 h	after 4 h	after 6 h	after 24 h	after 48 h
2-1 ^b	214.4	233.9	396.5	521.5	28.6	31.2	52.9	69.5
2-2 ^c	54.2	82.7	140.6		36.1	55.2	93.7	
2-3 ^d	141.1	134.7	140.3		47.0	44.9	46.8	

^aReaction conditions: catalyst [$\{\text{Au}(\text{PPh}_3)_4(\mu_4\text{-O})\}_3[\alpha\text{-PW}_{12}\text{O}_{40}]_2$ ·4EtOH (1) 0.01 mmol, toluene (4.7 mmol) as an internal standard, solvent 6 mL of a mixed solvent of 1,4-dioxane and water (4:1), temperature 80 °C. ^bEntry 2-1. Catalyst 1 (0.13 mol %), substrate diphenylacetylene 7.5 mmol, max TON = 750.0. ^cEntry 2-2. Catalyst 1 (0.67 mol %), substrate diphenylacetylene 1.5 mmol, max TON = 150.0. ^dEntry 2-3. Extra substrate (1.5 mmol) was added to the solution (entry 2-2) after 24 h of reaction by 1, max TON = 300.

(I)}oxonium cation [$\{\text{Au}(\text{PPh}_3)_4(\mu_4\text{-O})\}_3$] as a counterion of the [$\alpha\text{-PW}_{12}\text{O}_{40}$]³⁻ anion. Crystal data: $\text{C}_{216}\text{H}_{180}\text{Au}_{12}\text{O}_{83}\text{P}_{14}\text{W}_{24}$; $M = 11313.18$; monoclinic, space group $\text{C}2/c$; $a = 28.653(6)$ Å, $b = 19.107(4)$ Å, $c = 32.601(7)$ Å, $\alpha = 90^\circ$, $\beta = 107.31(3)^\circ$, $\gamma = 90^\circ$, $V = 17040(6)$ Å³, $Z = 2$, $D_c = 2.205$ g cm⁻³, $\mu(\text{Mo K}\alpha) = 13.326$ mm⁻¹. $R_1 = 0.0715$, $wR_2 = 0.1662$ (for all data). $R_{\text{int}} = 0.0548$. $R_1 = 0.0681$, $wR_2 = 0.1636$ ($I > 2\sigma(I)$). GOF = 1.033.

Species Formed in the Catalyst System 3 + Na-POM (Entries 1–8). A colorless clear solution of $\text{Na}_3[\alpha\text{-PW}_{12}\text{O}_{40}] \cdot 8\text{H}_2\text{O}$ (Na-POM) (0.030 g, 0.010 mmol) dissolved in 3 mL of an EtOH/H₂O (5:1, v/v) mixed solvent was added slowly to a colorless clear solution of [$\{\text{Au}(\text{PPh}_3)_3(\mu_3\text{-O})\}_3\text{BF}_4$] (3) (0.036 g, 0.024 mmol) in 5 mL of CH₂Cl₂. The vial containing two layers was sealed and left in the dark at room temperature. After a few days, colorless plate crystals formed. A portion was used for X-ray crystallography, and the remainder was collected with a membrane filter (JG 0.2 μm), washed with EtOH (2 mL × 2) and Et₂O (2 mL × 2), and dried *in vacuo* for 2 h. Yield of crystals: 40.1 mg (64.5%).

The crystals were unsuitable for X-ray crystallography, but CHN elemental analysis, TG/DTA, and ³¹P{¹H} NMR spectroscopy in DMSO-*d*₆ identified them as an intercluster compound between the heptakis(triphenylphosphane)gold(I)}dioxonium cation and the [$\alpha\text{-PW}_{12}\text{O}_{40}$]³⁻ anion. This compound was obtained previously by a reaction of [$\{\text{Au}(\text{RS-pyrrld})(\text{PPh}_3)\}_3$] (4) in CH₂Cl₂ with $\text{Na}_3[\alpha\text{-PW}_{12}\text{O}_{40}] \cdot 8\text{H}_2\text{O}$ (Na-POM) dissolved in an EtOH/H₂O mixed solvent.^{5b}

Anal. Calcd for $\text{C}_{130}\text{H}_{117}\text{O}_{44}\text{P}_8\text{Au}_7\text{W}_{12}$ or [$\{\{\text{Au}(\text{PPh}_3)_4(\mu_4\text{-O})\}_3[\alpha\text{-PW}_{12}\text{O}_{40}]_2\}_3$]·2EtOH: H, 1.90; C, 25.12. Found: H, 1.97; C, 24.74. TG/DTA under atmospheric conditions: a 1.20% weight loss due to two desorbed EtOH molecules was observed below 206.2 °C; calcd 0.75% for one EtOH molecule and 1.48% for two EtOH molecules. ³¹P{¹H} NMR [22.3 °C, DMSO-*d*₆]: δ -14.94, 24.35.

Catalytic Reaction. The catalytic reaction was carried out under the conditions reported elsewhere (Table 1).^{8f} Diphenylacetylene (0.267 g, 1.5 mmol) and toluene (100 μL, 0.94 mmol), as an internal standard, were added to the precatalyst [$\{\text{Au}(\text{PPh}_3)_4(\mu_4\text{-O})\}_3[\alpha\text{-PW}_{12}\text{O}_{40}]_2$ ·4EtOH (1) (0.115 g, 0.01 mmol) suspended in 6 mL of a solvent mixture of 1,4-dioxane and water (4:1). After the dark yellow suspension was flushed with N₂ gas for 5 min, it was stirred in an oil bath at approximately 80 °C for 1, 4, 6, 18, 20, and 24 h reactions. The heterogeneous reaction mixture in each reaction time was cooled to room temperature. The catalyst was allowed to settle in the bottom of the vial. The supernatant solution of 100 μL was transferred to a 10 mL volumetric flask and diluted to 10 mL with MeOH. The homogeneous MeOH solution of 5 μL was analyzed by HPLC. Deoxybenzoin as the hydration product was produced exclusively and evaluated.

RESULTS AND DISCUSSION


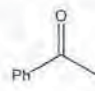

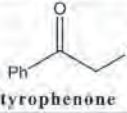
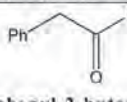
Synthesis and Characterization of 6. The reaction of [$\{\text{Au}(\text{RS-pyrrld})(\text{PPh}_3)\}_3$] dissolved in CH₂Cl₂ with H₃[$\alpha\text{-PMo}_{12}\text{O}_{40}$]·14H₂O dissolved in a CH₃CN/H₂O (5:1, v/v) mixed solvent resulted in the formation of the compound consisting of the monomeric phosphane-gold(I) acetonitrile complex cation and Keggin molybdo-POM anion [$\text{Au}(\text{CH}_3\text{CN})(\text{PPh}_3)_3[\alpha\text{-PMo}_{12}\text{O}_{40}]$] (6) as a DMSO-soluble crystalline sample. The compound was characterized by CHN elemental analysis, FTIR spectroscopy, X-ray crystallography, and solution (¹H, ³¹P{¹H}) NMR spectroscopy. Compound 1 has been obtained by a similar reaction of [$\{\text{Au}(\text{RS-pyrrld})(\text{PPh}_3)\}_3$] dissolved in CH₂Cl₂ with H₃[$\alpha\text{-PW}_{12}\text{O}_{40}$]·*n*H₂O dissolved in an EtOH/H₂O (5:1) mixed solvent.^{5a} Compounds 6 and 1 were formed only in a different solvent system using the same reagents. Compound 6 did not contain a proton in the counterion, but it showed acid-free effective catalysis for the hydration of diphenylacetylene, which is in contrast to the bifunctional catalysis by the proton-containing hybrid complexes [$\{\text{Au}(\text{CH}_3\text{CN})(\text{PR}_3)\}_3[\text{POM-H}]$] (R = Ph, Me; POM-H = H₃SiW₁₂O₄₀, H₂PM₁₂O₄₀ (M = Mo, W), H₃P₂W₁₈O₆₂).^{11b}

The solution ³¹P{¹H} NMR spectrum of 6 in DMSO-*d*₆ revealed two sharp signals at -3.32 and 27.32 ppm due to the α -Keggin POM [$\text{PMo}_{12}\text{O}_{40}$]³⁻ and the PPh₃ ligand in the [$\text{Au}(\text{CH}_3\text{CN})(\text{PPh}_3)_3$]⁺, respectively. The signal of the PPh₃ ligand at 27.32 ppm was similar to the signal observed at 27.61 ppm of the [$\{\text{Au}(\text{RS-pyrrld})(\text{PPh}_3)\}_3$] precursor. The tendency toward the ³¹P{¹H} NMR spectroscopic resonance of the oligomeric phosphane-gold(I) clusters appeared at a higher field than that of the monomeric phosphane-gold(I) complexes. This suggests that the monomeric structure of 6 had been maintained in the solution.⁵ The ³¹P{¹H} NMR spectrum of 6 in DMSO-*d*₆ was comparable to the reported ³¹P NMR spectrum reported for [$\text{Au}(\text{MeCN})(\text{PPh}_3)_3[\text{H}_2\text{PMo}_{12}\text{O}_{40}]$] (-4.1 and 26.6 ppm).^{11b}

Catalysis by the Intercluster Compound 1 and the Effect of HBF₄(aq), NaBF₄, and KBF₄ Addition (Entries 1-1(1)–(4)). The intercluster compound [$\{\text{Au}(\text{PPh}_3)_4(\mu_4\text{-O})\}_3[\alpha\text{-PW}_{12}\text{O}_{40}]_2$ ·4EtOH (1) showed acid-free, effective catalysis for the hydration of diphenylacetylene (0.67 mol %, entry 1-1(1), Table 1), in which its conversion to deoxybenzoin was 36.1% after a 4 h reaction, 55.2% after a 6 h reaction, and 93.7% after a 24 h reaction, in 6 mL of 1,4-dioxane/water (4:1) at 80 °C. Compound 1 is soluble in DMSO, but sparingly soluble in the reaction solvent of 1,4-dioxane/water (4:1). Therefore, the reaction appears to proceed in the suspension/heterogeneous system. Compound 1 itself is not a catalyst, but dissolved species generated in the dynamic process of 1, i.e., the monomeric [$\text{Au}(\text{PPh}_3)_3$]⁺ or [$\text{Au}(\text{L})(\text{PPh}_3)_3$]⁺ species (L = solvent), will be the catalyst precursor. This was observed as an averaged single peak in the solution ³¹P{¹H} NMR spectrum of 1 in DMSO-*d*₆.^{5a} This significant feature is suggested by the catalytic reaction by [$\text{Au}(\text{CH}_3\text{CN})(\text{PPh}_3)_3[\alpha\text{-PMo}_{12}\text{O}_{40}]$] (6) (entry 1-17). Therefore, the actual reaction will proceed through the homogeneous system by the dissolved [$\text{Au}(\text{PPh}_3)_3$]⁺ or [$\text{Au}(\text{L})(\text{PPh}_3)_3$]⁺ species.

Interestingly, catalysis by 1 was influenced significantly by the addition of HBF₄(aq), NaBF₄, and KBF₄ (entries 1-1(1)–(4)).

Table 3. Hydration of Phenylacetylene and 1-Phenyl-1-butyne Catalyzed by **1**^c

Entry	Alkynes	Products	TON	Yield (%)
3-1	 phenylacetylene	 acetophenone	141.5	94.3 ^a
3-2	 1-phenyl-1-butyne	 butyrophenone	58.2	38.8 ^b
		 1-phenyl-2-butanone	85.5	57.0 ^b

^aReaction time: 24 h. ^bReaction time: 2 h. ^cReaction conditions: Catalyst 0.01 mmol (0.67 mol %), substrate 1.50 mmol, 1,4-dioxane/water = 4:1 mixed solvent 6 mL, N₂ 1 atm, temperature 80 °C. Max TON = 150.0.

The catalytic activity of **1** (entry 1-1(1)) was enhanced further by the addition of HBF₄(aq), which was comparable to those of **2** + H-POM (entry 1-3), **3** + H-POM (entry 1-7), **4** + H-POM (entry 1-11), and compound **6** alone. In contrast, it was decreased by the addition of NaBF₄ (entry 1-1(3)) and KBF₄ (1-1(4)). A similar tendency was observed in the catalytic systems of **5** by the addition of HBF₄(aq), NaBF₄, and KBF₄ (entries 1-16(1)–(4)). This suggests that the generation of the catalyst precursor [Au(PPh₃)⁺ or [Au(L)(PPh₃)⁺ (L = solvent) from **1** and **5** is influenced significantly by the addition of HBF₄(aq), NaBF₄, and KBF₄. The catalytic activities observed here strongly suggest that the catalyst precursor is the solvent-coordinating species [Au(L)(PPh₃)⁺, such as the counteraction of **6** rather than the hypothetical, coordinating unsaturated species [Au(PPh₃)⁺. If this is the case, the catalytically active species will be attributed to the alkyne-coordinating species [Au(alkyne)(PPh₃)⁺ that is stabilized by the POM anion.

Under the conditions of increased amounts (7.5 mmol) of diphenylacetylene using **1** (0.13 mol %), the conversion of 69.5% was observed after 48 h of reaction (Table 2, entry 2-1), showing that the substrate still remains, and the hydration reaction proceeded after 24 h. This shows that the catalyst precursor (L = solvent) or the active species (L = alkyne) of the [Au(L)(PPh₃)⁺ species stabilized by [PW₁₂O₄₀]³⁻ can work only when the substrate is present. However, after the substrate has almost been completely consumed, the active species readily changes to the inactive form, such as [Au(PPh₃)₂]⁺. Therefore, the reaction continues until the substrate has almost been totally consumed.

Under the conditions of diphenylacetylene (1.5 mmol) and **1** (0.67 mol %) (entry 2-2 = entry 1-1); the conversion was 93.7% after a 24 h reaction, suggesting that the substrate is almost completely consumed. Extra amounts of diphenylacetylene (1.5 mmol) were added to the solution of entry 2-2 after a 24 h reaction, in which the active species had already changed to the inactive form [Au(PPh₃)₂]⁺. Time denotes the time after the extra substrate had been added. The results are shown in entry 2-3, in which conversions were unchanged, i.e., 47.0% after 4 h, 44.9% after 6 h, and 46.8% after 24 h, indicating that new deoxybenzoin has not accumulated. This means that the active species cannot be recovered from the once formed, inactive form and the reaction does not proceed further.

Effects of other mixed solvent systems (acetonitrile/water (4:1), DMF/water (4:1)) on the catalytic activities of diphenylacetylene hydration by **1** were also evaluated (Table S1). The acetonitrile/water (4:1) system exhibited effective activities (Table S1, entry 2), even though the activity was found to be lower than that of the 1,4-dioxane/water (4:1) system. The activity of the DMF/water (4:1) system (Table S1, entry 3) was lower than those of the 1,4-dioxane/water (4:1) and acetonitrile/water (4:1) systems.

Catalysis by 1 for Hydration of Other Alkynes. The hydration of phenylacetylene and 1-phenyl-1-butyne as an alkyne by **1** was also examined (Table 3). The hydration of phenylacetylene by **1** resulted in the formation of acetophenone with a TON of 141.5 (conversion 94.3%) after a 24 h reaction at 80 °C (entry 3-1). These results revealed much more effective catalysis by **1** under milder conditions compared to the literature data (conversion 81%) using the catalyst system NHC-gold(I) complex [Au(IPr)(OH)] (0.02 μmol) in the presence of aqueous HSBF₆ (0.06 μmol), in 2 mL of 1,4-dioxane/water (2:1) after a 24 h reaction at 120 °C.^{8d}

On the other hand, the hydration of 1-phenyl-1-butyne by **1** resulted in the formation of butyrophenone with a TON of 58.2 (conversion 38.8%) and 1-phenyl-2-butanone with a TON of 85.5 (conversion 57.0%) after a 24 h reaction at 80 °C (entry 3-2). The conversion of more than 90% in the hydration of diphenylacetylene and phenylacetylene by **1** was achieved after a 24 h reaction, whereas the hydration of 1-phenyl-1-butyne was complete within a 2 h reaction.

The hydration of 1-phenyl-1-butyne by **1** can be compared with the formation of butyrophenone (15%) and 1-phenyl-2-butanone (50%) via the catalyst system of [Au(IPr)(OH)] (0.02 μmol) plus aqueous HSBF₆ (0.06 μmol) after a 24 h reaction at 120 °C.^{8d} Therefore, compound **1** generates an acid-free, effective catalyst under milder conditions.

The distribution of the products by **1**, i.e., butyrophenone (38.8%) and 1-phenyl-2-butanone (57.0%), shows that coordination of the alkyne substrate in the [Au(L)(PPh₃)⁺ species/POM and the subsequent nucleophilic attack of water molecules are comparatively selective. Therefore, the [Au(PPh₃)⁺ unit tends to coordinate to the site closer to the Ph group of the alkyne and the water molecule attacks the opposite site, i.e., the site closer to the Et group.

Catalysis by Related Compounds 5 and 6 for Diphenylacetylene Hydration. The related, intercluster compound consisting of the heptaphosphanegold(I) dioxonium cation and Keggin POM, $[\{\{\text{Au}(\text{PPh}_3)\}_4(\mu_4\text{-O})\}\{\{\text{Au}(\text{PPh}_3)\}_3(\mu_3\text{-O})\}][\alpha\text{-PW}_{12}\text{O}_{40}]\cdot\text{EtOH}$ (**5**), also showed effective catalytic activity (0.67 mol %, entry 1-16, Table 1); that is, its conversion to deoxybenzoin was 2.0% after a 4 h reaction, 4.2% after a 6 h reaction, and 89.0% after a 24 h reaction. Note that an induction period was observed in the early stages of the reaction.

The heptaphosphanegold(I) cluster cation in **5** was formed only in the presence of POM.^{5b} Indeed, the heptaphosphanegold(I) cluster was not found, when the anion of **5** was exchanged with BF_4^- using anion-exchange resin, but the tetraphosphanegold(I) cluster was observed in solution due to decomposition.

On the other hand, another related compound, which was composed of the monomeric phosphanegold(I) cation and Keggin molybdo-POM, i.e., $[\text{Au}(\text{CH}_3\text{CN})(\text{PPh}_3)_3][\alpha\text{-PMo}_{12}\text{O}_{40}]$ (**6**), also showed effective catalysis (0.67 mol %, entry 1-17, Table 1); the conversion was 71.8% after a 4 h reaction, 84.9% after a 6 h reaction, and 91.6% after a 24 h reaction. Compound **6** was prepared by the reaction between $[\text{Au}(\text{RS-pyrrld})(\text{PPh}_3)]$ and $\text{H}_3[\alpha\text{-PMo}_{12}\text{O}_{40}]\cdot 14\text{H}_2\text{O}$ in the $\text{CH}_3\text{CN}/\text{water}$ solvent mixture, whereas compound **1** was prepared using the same reagents in a different solvent system, i.e., EtOH/water solvent mixture [see Experimental Section]. Although compound **6** also does not contain any acidic species, it can work as an acid-free catalyst precursor.

In catalytic processes by **1** and **5**, the catalyst precursor will actually be the same as **6**, i.e., $[\text{Au}(\text{L})(\text{PPh}_3)]^+$ (L = solvent), and the active species is the L = alkyne compound derived from it. In the catalysis by **1** and **5**, the catalyst precursor will originate from a “dynamic” process (or including fluxional or scrambling of $[\text{Au}(\text{PPh}_3)]^+$ species in solution).^{5a,b}

Regarding the POM-based phosphanegold(I) catalysts, Blanc et al. recently reported that the proton-containing hybrid complexes $[\text{Au}(\text{CH}_3\text{CN})(\text{PR}_3)_3][\text{POM-H}]$ (R = Ph, Me; POM-H = $\text{H}_3\text{SiW}_{12}\text{O}_{40}$, $\text{H}_2\text{PM}_{12}\text{O}_{40}$ (M = Mo, W), $\text{H}_3\text{P}_2\text{W}_{18}\text{O}_{62}$) showed catalytic properties for the rearrangement of the enyne esters to cyclopentenones and the cyclization of *N*-propargylcarboxamides.^{11b} They also reported bifunctional catalytic properties for aza-Prins cyclization/enol ether hydrolysis.^{11a} They also reported the X-ray structures of $[\text{Au}(\text{CH}_3\text{CN})(\text{PPh}_3)_3][\text{PM}_{12}\text{O}_{40}]$ (M = Mo, W) without acidic protons, together with the related POM compounds, but none of them had the expected structures.

Control Experiments 1: Catalysis by Phosphanegold(I) Species without POM. For diphenylacetylene hydration, the component species constituting **1** and **5**, i.e., the tetra- and triphosphanegold(I) cluster species $[\{\{\text{Au}(\text{PPh}_3)\}_4(\mu_4\text{-O})\}(\text{BF}_4)_2$ (**2**, entry 1-2) and $[\{\{\text{Au}(\text{PPh}_3)\}_3(\mu_3\text{-O})\}]\text{BF}_4$ (**3**, entry 1-6) and the POMs $\text{H}_3[\alpha\text{-PW}_{12}\text{O}_{40}]\cdot 7\text{H}_2\text{O}$ (H-POM, entry 1-14) and $\text{Na}_3[\alpha\text{-PW}_{12}\text{O}_{40}]\cdot 8\text{H}_2\text{O}$ (Na-POM, entry 1-15), showed poor activities (0.67 mol % each; conversions of 1.8%, 1.7%, 0%, and 0% after 24 h reactions, respectively). In other words, the phosphanegold(I) species without POM showed no activity. The complex precursor without POM, i.e., $[\text{Au}(\text{RS-pyrrld})(\text{PPh}_3)]$ (**4**, entry 1-10), also showed only poor activity (0.67 mol %; conversion of 0.5% after 24 h reaction). Therefore, the activities of **1** and **5** suggest that the phosphanegold(I) species exhibit catalytic activities only in the presence of POM.

Control Experiments 2: Catalysis by Phosphanegold(I) Species Brought about in the Presence of the Free-Acid Form of Keggin POM (H-POM). Upon the addition of the free-acid form of α -Keggin POM, $\text{H}_3[\alpha\text{-PW}_{12}\text{O}_{40}]\cdot 7\text{H}_2\text{O}$ (H-POM; 0.67 mol %), compounds **2–4** (0.67 mol %) showed remarkably enhanced activities (conversions of 72.3% (entry 1-3), 73.1% (entry 1-7), 71.5% (entry 1-11) after 1 h reactions; 84.7% (entry 1-3), 87.0% (entry 1-7), 84.9% (entry 1-11) after 4 h reactions; and 97.6% each (entries 1-3, 1-7, and 1-11) after 24 h reactions). That is, all phosphanegold(I) species **2–4** showed effective activities for diphenylacetylene hydration only under the conditions assisted by the free-acid form of Keggin POM (H-POM). The observed activities were comparable to those of the monomeric phosphanegold(I) cation with the POM anion (**6**, entry 1-17) and of the system **1** + $\text{HBF}_4(\text{aq})$ (entry 1-1(2)). Note that all reactions of entries 1-3, 1-7, and 1-11 actually form the tetraphosphanegold(I) cluster cation $[\{\{\text{Au}(\text{PPh}_3)\}_4(\mu_4\text{-O})\}]^{2+}$ in the solution (see Experimental Section). Therefore, these reaction systems consist of $[\{\{\text{Au}(\text{PPh}_3)\}_4(\mu_4\text{-O})\}]^{2+}$, $[\alpha\text{-PW}_{12}\text{O}_{40}]^{3-}$, and acidic H^+ , or they are compatible with the system of **1** plus H^+ (entry 1-1(2)). Their catalytic activities were higher than those of **1** only after 4 h and 6 h reactions (entry 1-1(1)). This suggests that the catalyst precursor, $[\text{Au}(\text{L})(\text{PPh}_3)]^+/\text{POM}$ (L = solvent), may be generated more easily from **1** in the presence of acidic H^+ .

A combination of **4** and the free-acid form of various Keggin POMs $[\text{XW}_{12}\text{O}_{40}]^{n-}$ (X = Si, B, Al, Zn) was also used for diphenylacetylene hydration (Table 4). All catalyst systems

Table 4. Hydration of Diphenylacetylene Catalyzed by Combination of $[\text{Au}(\text{RS-pyrrld})(\text{PPh}_3)]$ (4**) + Free-Acid Form of Various Keggin POMs**

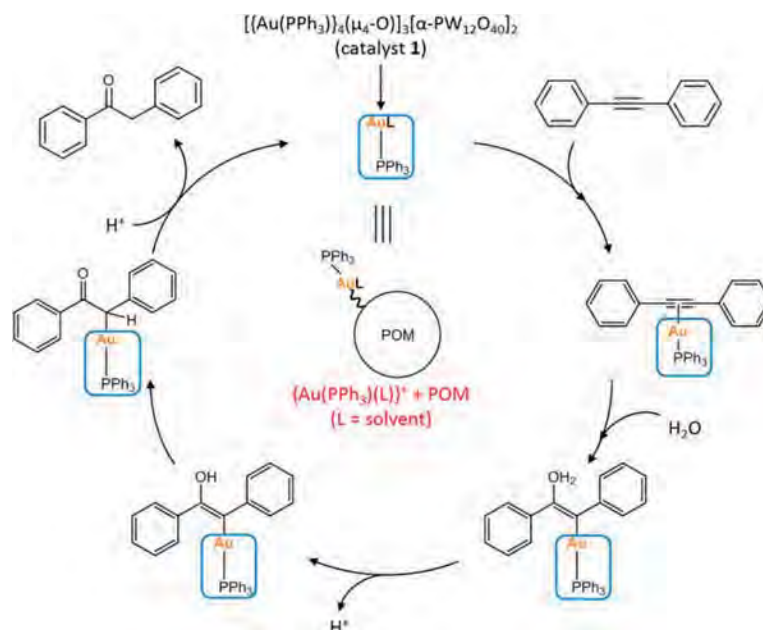
entry	main catalyst [0.67 mol %], additives [0.67 mol %]	conversion (%)		
		after 4 h	after 6 h	after 24 h
4-1	4 + $\text{H}_3[\alpha\text{-PW}_{12}\text{O}_{40}]\cdot 7\text{H}_2\text{O}$	71.5	84.9	97.6
4-2	4 + $\text{H}_4[\alpha\text{-SiW}_{12}\text{O}_{40}]\cdot 17\text{H}_2\text{O}$	34.0	44.7	61.6
4-3	4 + $\text{H}_3[\alpha\text{-BW}_{12}\text{O}_{40}]\cdot 15\text{H}_2\text{O}$	44.5	52.6	75.7
4-4	4 + $\text{H}_3[\alpha\text{-AlW}_{12}\text{O}_{40}]\cdot 11\text{H}_2\text{O}$	36.7	51.7	56.8
4-5	4 + $\text{H}_6[\alpha\text{-ZnW}_{12}\text{O}_{40}]\cdot 9\text{H}_2\text{O}$	38.1	49.0	62.1

exhibited effective activities (entries 4-2–4-5), even though the activities of X = Si, B, Al, and Zn were found to be lower than that of X = P (entry 1-11 = entry 4-1). The origin of the observed differences is unclear.

Control Experiments 3: Catalysis by Phosphanegold(I) Species in the Presence of Sodium Salt of Keggin POM (Na-POM). No enhancement of their original activities was observed (entries 1-4, 1-8, 1-12) after adding the sodium salt of the Keggin POM, $\text{Na}_3[\alpha\text{-PW}_{12}\text{O}_{40}]\cdot 8\text{H}_2\text{O}$ (Na-POM; 0.67 mol %), to compounds **2–4**.

All the reactions of **2** + Na-POM (entry 1-4), **3** + Na-POM (entry 1-8), and **4** + Na-POM (entry 1-12) resulted in the formation of the heptaphosphanegold(I) cluster cation in the solution (see Experimental Section). Therefore, these reaction systems are composed of $[\{\{\text{Au}(\text{PPh}_3)\}_4(\mu_4\text{-O})\}\{\{\text{Au}(\text{PPh}_3)\}_3(\mu_3\text{-O})\}]^{3+}$, $[\alpha\text{-PW}_{12}\text{O}_{40}]^{3-}$, and Na^+ , or they are compatible with the system of **5** plus Na^+ ion (entry 1-16(2)). Catalysis by **5** itself was achieved after a clear induction period (entry 1-16(1)), suggesting that it takes a longer time to generate the catalyst precursor $[\text{Au}(\text{L})(\text{PPh}_3)]^+$. The catalytic reaction by **5** is retarded by the presence of alkaline (Na^+ and

Scheme 1



K^+) ions (entries 1-16(3) and 1-16(4)), or the induction period is lengthened remarkably, as shown in entry 1-12 [footnote b; the reaction was followed from 24 h until 1 week, but their conversions were unchanged (the conversions were 9.1% after 48 h, 8.7% after 72 h, and 9.7% after 168 h)]. Therefore, the activities of the systems consisting of **5** plus Na^+ ion (entry 1-16(3)) are consistent with the results of entries 1-4, 1-8, and 1-12. A similar tendency was found in the systems of **1** plus $NaBF_4$ and KBF_4 (entries 1-1(3) and 1-1(4)).

Furthermore, the addition of an aqueous solution of the Brønsted acid, 10% HBF_4 (0.67 mol %), to compounds **2–4** did not have any effects on their original activities (entries 1-5, 1-9, 1-13). This shows that the free-acid form of POM, but not the acidic proton without POM, significantly assists catalysis by the monomeric phosphanegold(I) species $[Au(L)(PPh_3)]^+$ ($L = \text{solvent or alkyne}$).

$^{31}P\{^1H\}$ NMR Characterization of the Reaction Systems by **1, **5**, and **6**.** (1) The reaction solution after a 6 h reaction at 80 °C using **1** (0.67 mol %, entry 1-1(1)), in which sufficient amounts of diphenylacetylene still remained (conversion 55.2%), was evaporated to dryness. The residue was then dissolved in CD_2Cl_2 . The $^{31}P\{^1H\}$ NMR spectrum of a CD_2Cl_2 solution revealed a broad signal that was assigned to the $[Au(\text{diphenylacetylene})(PPh_3)]^+$ species at 36.1 ppm, in addition to the inactive $[Au(PPh_3)_2]^+$ species¹³ at 45.1 ppm and $[PW_{12}O_{40}]^{3-}$ at -14.6 ppm (Figure S1a). The signal at 36.1 ppm was consistent with a ^{31}P NMR signal at 36.1 ppm in CD_2Cl_2 of $[Au(\text{alkyne})(PPh_3)]^+SbF_6^-$ reported in the literature.¹⁵ $^{31}P\{^1H\}$ NMR spectra in CD_2Cl_2 of the residues obtained from the reaction systems after hydration reactions at 80 °C of other alkynes (phenylacetylene and 1-phenyl-1-butyne) using **1** were also measured (Figure S1b,c): after 6 h hydration reaction ($[\alpha-PW_{12}O_{40}]^{3-}$, -14.7 ppm; $[Au(\text{phenylacetylene})(PPh_3)]^+$, 37.2 ppm; $[Au(PPh_3)_2]^+$, 45.2 ppm) and after 1 h hydration reaction ($[\alpha-PW_{12}O_{40}]^{3-}$; -15.0 ppm, $[Au(1\text{-phenyl-1-butyne})(PPh_3)]^+$; 34.4 and 36.2 ppm, $[Au(PPh_3)_2]^+$; 44.9 ppm). On the other hand, the DMSO- d_6 solution of the residue collected after a 6 h reaction

at 80 °C revealed a signal assignable to $[Au(\text{DMSO})(PPh_3)]^+$ at 27.30 ppm, as well as signals due to the inactive $[Au(PPh_3)_2]^+$ at 43.8 ppm and $[PW_{12}O_{40}]^{3-}$ at -14.93 ppm (Figure S2).

The insoluble materials recovered by filtering off the reaction solution after a 24 h reaction were dissolved in DMSO- d_6 , and a $^{31}P\{^1H\}$ NMR spectrum of the solution was measured. In such materials, the starting compound **1**, which is observed as a signal at 24.98 ppm, was absent, but the $^{31}P\{^1H\}$ NMR spectrum revealed characteristic signals due to several catalytically inactive compounds, such as $[PW_{12}O_{40}]^{3-}$ at -14.85 ppm, $[Au(PPh_3)_2]^+$ at 43.68 ppm, and mixed-valence phosphanegold(I) cluster cations, such as $[Au_9(PPh_3)_8]^{3+}$, as signals at approximately 57–58 ppm.^{14a} The filtrate obtained after a 24 h reaction was evaporated to dryness, and the residue was dissolved in DMSO- d_6 . The $^{31}P\{^1H\}$ NMR spectrum of the solution showed no signal, suggesting that the reaction solution after a 24 h reaction does not contain any materials originating from PPh_3 and $[PW_{12}O_{40}]^{3-}$. On the other hand, the 1H NMR spectrum of the solution revealed the signals for a CH_2 group (4.28 ppm) and the phenyl groups of deoxybenzoin as the hydration product (7.22–8.02 ppm). Because the conversion was 93.7% after a 24 h reaction, the signals of diphenylacetylene would be very small in the reaction solution.

(2) The solution $^{31}P\{^1H\}$ NMR spectrum of **5** in DMSO- d_6 revealed two sharp signals at -14.92 and 24.46 ppm. The former peak was assigned to the phosphorus heteroatom in the α -Keggin POM, whereas the latter peak was assigned to the averaged signal of PPh_3 groups due to fluxional motion in the solution of the heptaphosphanegold(I) cluster, which corresponds to one broad signal at 24.6 ppm in the CPMAS ^{31}P NMR spectrum.^{5b} The solid-state broad single peak was attributed to the fact that all PPh_3 groups are in an approximately equivalent state, but they are not fluxional in the solid state. The heptaphosphanegold(I) cluster would probably be present in solution only in the presence of POM; that is, it cannot exist without POM.^{5b} The solution $^{31}P\{^1H\}$ NMR signal at 24.46 ppm shifted slightly to a higher field from

the single peak observed at 24.84 ppm of the tetraphosphanegold(I) cluster in solution.^{5a}

The $^{31}\text{P}\{^1\text{H}\}$ NMR measurements in DMSO- d_6 of the insoluble materials recovered by filtering off the reaction solution after a 24 h reaction showed that the signal of the starting compound **5** had disappeared. However, the inactive $[\text{Au}(\text{PPh}_3)_2]^+$ species as the major signal at 43.84 ppm and the mixed-valence phosphanegold clusters,^{14a} such as $[\text{Au}_9(\text{PPh}_3)_8]^{3+}$, as the minor signals at 54.45 and 58.13 ppm appeared, in addition to the signal of $[\text{PW}_{12}\text{O}_{40}]^{3-}$ at -14.84 ppm. The $^{31}\text{P}\{^1\text{H}\}$ NMR spectrum of the reaction solution after a 24 h reaction of **5** was similar to that of **1**. The catalyst precursor in the catalysis by **5** was also the $[\text{Au}(\text{L})(\text{PPh}_3)]^+$ species (L = solvent), but an induction period was required for its generation.

(3) The $^{31}\text{P}\{^1\text{H}\}$ NMR measurements in DMSO- d_6 of **6** before the reaction showed a signal at 27.32 ppm. The $^{31}\text{P}\{^1\text{H}\}$ NMR measurements in DMSO- d_6 of the insoluble materials recovered after the 24 h reaction showed that the starting compound **6** disappeared with the concomitant appearance of the major signal at 43.55 ppm due to $[\text{Au}(\text{PPh}_3)_2]^+$ species and many smaller signals at 56.19, 57.24, 57.85 (main peak), and 58.06 ppm due to the mixed-valence gold cluster species,^{14a} such as $[\text{Au}_9(\text{PPh}_3)_8]^{3+}$. In addition, the signal due to $[\text{PMo}_{12}\text{O}_{40}]^{3-}$ at -3.32 ppm before the reaction changed to that at -5.96 ppm after a 24 h reaction, which was attributed to the partially reduced molybdo-POM. This shows that the reaction contains a redox process, which will be brought about together by the oxidation of PPh_3 liberated from **6**.

Reaction Scheme. The reaction scheme of diphenylacetylene hydration catalyzed by **1** is depicted in Scheme 1. The generation of monomeric phosphanegold(I) species $[\text{Au}(\text{L})(\text{PPh}_3)]^+$ (L = solvent; catalyst precursor) in the presence of the POM anion from **1** initiates alkyne coordination to the Au(I) site by ligand exchange of L (catalytically active species), followed by the subsequent nucleophilic attack of a water molecule on the coordinated alkyne and the deprotonation of coordinated water, resulting in the formation of the enol form of deoxybenzoin and a transformation to the keto form on the Au(I) site. By subsequent protonation, the catalytic cycle would be completed. This is consistent with the theoretical discussion of alkyne hydration catalyzed by gold(I) species.¹⁰ In this catalytic cycle, the catalytically active, monomeric phosphanegold(I) species $[\text{Au}(\text{L})(\text{PPh}_3)]^+$ (L = alkyne) would be accompanied by the POM anion throughout the process. The generation of the catalyst precursor $[\text{Au}(\text{L})(\text{PPh}_3)]^+$ (L = solvent) from **1** would be accelerated by the acidic proton, as indicated by the reaction **1** + aqueous HBF_4 (entry 1-1(2)), but may be retarded by alkaline (Na^+ or K^+) ions (entries 1-1(3) and 1-1(4)). In the catalysis by **5** (entry 1-16(1)), the induction period would also be related to the process of generating the catalyst precursor $[\text{Au}(\text{L})(\text{PPh}_3)]^+$ (L = solvent), which may be accelerated by the acidic proton (entry 1-16(2)), but affected seriously by alkaline (Na^+ and K^+) ions (entries 1-16(3) and -4)).

CONCLUSION

Both compounds **1** and **6** exhibited acid-free, effective catalytic activity for diphenylacetylene hydration (entries 1-1(1) and 1-17, respectively). Compounds **1** and **6** were synthesized by the same reaction process of **4** + H-POM using only different solvent systems, EtOH/ H_2O vs $\text{CH}_3\text{CN}/\text{H}_2\text{O}$, respectively. In both catalytic processes by **1** and **6**, the active species was

attributed to the monomeric gold(I)-alkyne species stabilized by POM, i.e., $[\text{Au}(\text{L})(\text{PPh}_3)]^+/\text{POM}$ (L = alkyne). Indeed, the reaction systems without POM, such as **2**–**4** (entries 1-2, 1-6, and 1-10, respectively), exhibited poor activities. In catalysis by **1**, the catalyst precursor $[\text{Au}(\text{L})(\text{PPh}_3)]^+$ (L = solvent) is originated from the “dynamic” process (or the fluxional or scrambling process of $[\text{Au}(\text{PPh}_3)]^+$ species in solution, as shown in the $^{31}\text{P}\{^1\text{H}\}$ NMR spectrum of **1** in DMSO- d_6 ^{5a}), whereas in catalysis by **6**, it gave rise to ligand exchange with the solvent used. The acidic proton enhances the activity of **1** (entry 1-1(2)), suggesting that the generation of the catalyst precursor is accelerated by an acidic proton. Because the catalyst systems of **2** + H-POM (entry 1-3), **3** + H-POM (entry 1-7), and **4** + H-POM (entry 1-11) generate the same tetraphosphanegold(I) species in solution, such catalytic systems are actually the same as that of **1** plus a proton, the activities of which are higher than that of **1** itself (entry 1-1(1)). In contrast, catalysis by **5** showed an induction period (entry 1-16(1)), suggesting that it takes a longer time to generate the catalyst precursor $[\text{Au}(\text{L})(\text{PPh}_3)]^+$. However, because the catalyst systems of **2** + Na-POM (entry 1-4), **3** + Na-POM (entry 1-8), and **4** + Na-POM (entry 1-12) form the same heptakis{phosphanegold(I)} species in solution, their catalytic activities are actually the same as the system of **5** plus a Na^+ ion (entry 1-16(3)). The catalytic reaction by **5** is retarded by the presence of alkaline (Na^+ and K^+) ions. The induction period may be lengthened markedly, as shown in entries 1-12 [footnote b] and 1-16(3) and -(4). Further work in this area is currently under way. The influence of the stoichiometry of the gold catalyst **4** versus the amount of POM (Table 4) will be studied in our next plan. We have synthesized other types of intercluster compounds consisting of the dimers of dinuclear units in parallel-edge and crossed-edge arrangements of phosphanegold(I) units and Keggin POMs and determined their molecular structures.^{5c} Catalytic behaviors of such POM-based compounds will also be studied as future work.

ASSOCIATED CONTENT

Supporting Information

The Supporting Information is available free of charge on the ACS Publications website at DOI: 10.1021/acs.organomet.6b00114.

Figures S1 and S2 ($^{31}\text{P}\{^1\text{H}\}$ NMR data of the residues obtained from the reaction systems) and Table S1 (effect of mixed solvent system on the catalytic activities) (PDF)

AUTHOR INFORMATION

Corresponding Author

*Phone: 81-463-59-4111. Fax: 81-463-58-9684. E-mail: nomiya@kanagawa-u.ac.jp (K. Nomiya).

Notes

The authors declare no competing financial interest.

ACKNOWLEDGMENTS

This study was supported by JSPS KAKENHI grant number 225S0065 and by the Strategic Research Base Development Program for Private University of the Ministry of Education, Culture, Sports, Science and Technology of Japan.

REFERENCES

- (1) (a) Pope, M. T.; Müller, A. *Angew. Chem., Int. Ed. Engl.* **1991**, *30*, 34–48. (b) Pope, M. T. *Heteropoly and Isopoly Oxometalates*; Springer-Verlag: New York, 1983. (c) Day, V. W.; Klemperer, W. G. *Science* **1985**, *228*, 533–541. (d) Hill, C. L. *Chem. Rev.* **1998**, *98*, 1–390. (e) Okuhara, T.; Mizuno, N.; Misono, M. *Adv. Catal.* **1996**, *41*, 113–252. (f) Hill, C. L.; Prosser-McCarthy, C. M. *Coord. Chem. Rev.* **1995**, *143*, 407–455. (g) Pope, M. T. Polyoxo Anions: Synthesis and Structure. In *Comprehensive Coordination Chemistry II*; Wedd, A. G., Ed.; Elsevier Science: New York, 2004; Vol. 4, pp 635–678. (h) Hill, C. L. Polyoxometalates: Reactivity. In *Comprehensive Coordination Chemistry II*; Wedd, A. G., Ed.; Elsevier Science: New York, 2004; Vol. 4, pp 679–759. (i) Nomiya, K.; Sakai, Y.; Matsunaga, S. *Eur. J. Inorg. Chem.* **2011**, *2011*, 179–196.
- (2) (a) Schulz-Dobrick, M.; Jansen, M. *Eur. J. Inorg. Chem.* **2006**, *2006*, 4498–4502. (b) Schulz-Dobrick, M.; Jansen, M. *Inorg. Chem.* **2007**, *46*, 4380–4382. (c) Schulz-Dobrick, M.; Jansen, M. *Z. Anorg. Allg. Chem.* **2007**, *633*, 2326–2331. (d) Schulz-Dobrick, M.; Jansen, M. *Z. Anorg. Allg. Chem.* **2008**, *634*, 2880–2884. (e) Gruber, F.; Jansen, M. *Z. Anorg. Allg. Chem.* **2010**, *636*, 2352–2356. (f) Gruber, F.; Jansen, M. *Z. Anorg. Allg. Chem.* **2011**, *637*, 1450.
- (3) (a) Gao, G.-G.; Cheng, P.-S.; Mak, T. C. W. *J. Am. Chem. Soc.* **2009**, *131*, 18257–18259. (b) Gruber, F.; Schulz-Dobrick, M.; Jansen, M. *Chem. - Eur. J.* **2010**, *16*, 1464–1469. (c) Gruber, F.; Jansen, M. *Inorg. Chim. Acta* **2010**, *363*, 4282–4286. (d) Xiao, Y.; Wang, Q.-M. *Chem. - Eur. J.* **2012**, *18*, 11184–11187.
- (4) (a) Mizuno, N.; Uchida, S. *Chem. Lett.* **2006**, *35*, 688–693. (b) Uchida, S.; Kawamoto, R.; Mizuno, N. *Inorg. Chem.* **2006**, *45*, 5136–5144. (c) Uchida, S.; Mizuno, N. *Coord. Chem. Rev.* **2007**, *251*, 2537–2546. (d) Ogasawara, Y.; Uchida, S.; Mizuno, N. *J. Phys. Chem. C* **2007**, *111*, 8218–8227. (e) Lesbani, A.; Kawamoto, R.; Uchida, S.; Mizuno, N. *Inorg. Chem.* **2008**, *47*, 3349–3357. (f) Uchida, S.; Lesbani, A.; Ogasawara, Y.; Mizuno, N. *Inorg. Chem.* **2012**, *51*, 775–777.
- (5) (a) Nomiya, K.; Yoshida, T.; Sakai, Y.; Nanba, A.; Tsuruta, S. *Inorg. Chem.* **2010**, *49*, 8247–8254. (b) Yoshida, T.; Nomiya, K.; Matsunaga, S. *Dalton Trans.* **2012**, *41*, 10085–10090. (c) Yoshida, T.; Matsunaga, S.; Nomiya, K. *Dalton Trans.* **2013**, *42*, 11418–11425. (d) Yoshida, T.; Matsunaga, S.; Nomiya, K. *Chem. Lett.* **2013**, *42*, 1487–1489. (e) Yoshida, T.; Yasuda, Y.; Nagashima, E.; Arai, H.; Matsunaga, S.; Nomiya, K. *Inorganics* **2014**, *2*, 660–673. (f) Yoshida, T.; Nagashima, E.; Arai, H.; Matsunaga, S.; Nomiya, K. *Z. Anorg. Allg. Chem.* **2015**, *641*, 1688–1695.
- (6) Noguchi, R.; Hara, A.; Sugie, A.; Nomiya, K. *Inorg. Chem. Commun.* **2006**, *9*, 355–359. The representation of H₂pyrrld is changed to Hpyrrld; thus, the formulation of [Au(RS-Hpyrrld)(PPh₃)] used so far is also changed to [Au(RS-pyrrld)(PPh₃)].
- (7) (a) Schmidbaur, H.; Schier, A. *Z. Naturforsch., B: J. Chem. Sci.* **2011**, *66b*, 329–350. (b) Gorin, D. J.; Toste, F. D. *Nature* **2007**, *446*, 395–403. (c) Hashmi, A. S. K. *Chem. Rev.* **2007**, *107*, 3180–3211. (d) Li, Z.; Brouwer, C.; He, C. *Chem. Rev.* **2008**, *108*, 3239–3265. (e) Hashmi, A. S. K.; Rudolph, M. *Chem. Soc. Rev.* **2008**, *37*, 1766–1775. (f) Gorin, D. J.; Sherry, B. D.; Toste, F. D. *Chem. Rev.* **2008**, *108*, 3351–3378. (g) Rudolph, M.; Hashmi, A. S. K. *Chem. Soc. Rev.* **2012**, *41*, 2448–2462. (h) Sherry, B. D.; Toste, F. D. *J. Am. Chem. Soc.* **2004**, *126*, 15978–15979. (i) Sherry, B. D.; Maus, L.; Laforteza, B. N.; Toste, F. D. *J. Am. Chem. Soc.* **2006**, *128*, 8132–8133. (j) Sakaguchi, K.; Okada, T.; Shinada, T.; Ohfune, Y. *Tetrahedron Lett.* **2008**, *49*, 25–28. (k) Mauleón, P.; Krinsky, J. L.; Toste, F. D. *J. Am. Chem. Soc.* **2009**, *131*, 4513–4520. (l) Aponick, A.; Li, C.-Y.; Palmes, J. A. *Org. Lett.* **2009**, *11*, 121–124. (m) Mauleón, P.; Krinsky, J. L.; Toste, F. D. *J. Am. Chem. Soc.* **2009**, *131*, 4513–4520. (n) Sengupta, S.; Shi, X. *ChemCatChem* **2010**, *2*, 609–619. (o) de Almeida, M. P.; Carabineiro, S. A. C. *ChemCatChem* **2012**, *4*, 18–29.
- (8) (a) Roembke, P.; Schmidbaur, H.; Cronje, S.; Raubenheimer, H. *J. Mol. Catal. A: Chem.* **2004**, *212*, 35–42. (b) Mizushima, E.; Sato, K.; Hayashi, T.; Tanaka, M. *Angew. Chem., Int. Ed.* **2002**, *41*, 4563–4565. (c) Leyva, A.; Corma, A. *J. Org. Chem.* **2009**, *74*, 2067–2074. (d) Nun, P.; Ramón, R. S.; Gaillard, S.; Nolan, S. P. *J. Organomet. Chem.* **2011**, *696*, 7–11. (e) Oliver-Meseguer, J.; Leyva-Pérez, A.; Corma, A. *ChemCatChem* **2013**, *5*, 3509–3515. (f) Gaillard, S.; Bosson, J.; Ramón, R. S.; Nun, P.; Slawin, A. M. Z.; Nolan, S. P. *Chem. - Eur. J.* **2010**, *16*, 13729–13740. (g) Wang, W.; Zheng, A.; Zhao, P.; Xia, C.; Li, F. *ACS Catal.* **2014**, *4*, 321–327.
- (9) (a) Wang, D.; Cai, R.; Sharma, S.; Jirak, J.; Thummanapelli, S. K.; Akhmedov, N. G.; Zhang, H.; Liu, X.; Petersen, J. L.; Shi, X. *J. Am. Chem. Soc.* **2012**, *134*, 9012–9019. (b) Gómez-Suárez, A.; Oonishi, Y.; Meiries, S.; Nolan, S. P. *Organometallics* **2013**, *32*, 1106–1111. (c) Jia, M.; Bandini, M. *ACS Catal.* **2015**, *5*, 1638–1652. (d) Ciancaleoni, G.; Belpassi, L.; Zuccaccia, D.; Tarantelli, F.; Belanzoni, P. *ACS Catal.* **2015**, *5*, 803–814. (e) Biasiolo, L.; Zotto, A. D.; Zuccaccia, D. *Organometallics* **2015**, *34*, 1759–1765.
- (10) (a) Mazzone, G.; Russo, N.; Sicilia, E. *J. Chem. Theory Comput.* **2010**, *6*, 2782–2789. (b) Mazzone, G.; Russo, N.; Sicilia, E. *Organometallics* **2012**, *31*, 3074–3080.
- (11) (a) Hueber, D.; Hoffmann, M.; Louis, B.; Pale, P.; Blanc, A. *Chem. - Eur. J.* **2014**, *20*, 3903–3907. (b) Hueber, D.; Hoffmann, M.; de Frémont, P.; Pale, P.; Blanc, A. *Organometallics* **2015**, *34*, 5065–5072. (c) Dupré, N.; Brazel, C.; Fensterbank, L.; Malacria, M.; Thorimbert, S.; Hasenknopf, B.; Lacôte, E. *Chem. - Eur. J.* **2012**, *18*, 12962–12965. (d) An, D.; Ye, A.; Deng, W.; Zhang, Q.; Wang, Y. *Chem. - Eur. J.* **2012**, *18*, 2938–2947.
- (12) (a) North, E. O.; Haney, W. *Inorg. Synth.* **1939**, *1*, 127–129. (b) Tézé, A.; Hervé, G. *Inorg. Synth.* **1990**, *27*, 85–96. (c) Aoki, S.; Kurashina, T.; Kasahara, Y.; Nishijima, T.; Nomiya, K. *Dalton Trans.* **2011**, *40*, 1243–1253. (d) Nakajima, K.; Eda, K.; Himeno, S. *Inorg. Chem.* **2010**, *49*, 5212–5215.
- (13) (a) Zhang, J.; Yang, C.-G.; He, C. *J. Am. Chem. Soc.* **2006**, *128*, 1798–1799. (b) Attar, S.; Bearden, W. H.; Alcock, N. W.; Alyea, E. C.; Nelson, J. H. *Inorg. Chem.* **1990**, *29*, 425–433. (c) Carriedo, G. A.; López, S.; Suárez-Suárez, S.; Presa-Soto, D.; Presa-Soto, A. *Eur. J. Inorg. Chem.* **2011**, *2011*, 1442–1447. (d) Casado, R.; Contel, M.; Laguna, M.; Romero, P.; Sanz, S. *J. Am. Chem. Soc.* **2003**, *125*, 11925–11935. (e) Wang, J.-C. *Acta Crystallogr., Sect. C: Cryst. Struct. Commun.* **1996**, *52*, 611–613.
- (14) (a) Wen, F.; Englert, U.; Gutrath, B.; Simon, U. *Eur. J. Inorg. Chem.* **2008**, *2008*, 106–111. (b) Gutrath, B. S.; Englert, U.; Wang, Y.; Simon, U. *Eur. J. Inorg. Chem.* **2013**, *2013*, 2002–2006.
- (15) Brooner, R. E. M.; Brown, T. J.; Widenhoefer, R. A. *Chem. - Eur. J.* **2013**, *19*, 8276–8284.

Cite this: *Dalton Trans.*, 2016, **45**, 13565

The effect of counteranions on the molecular structures of phosphanegold(i) cluster cations formed by polyoxometalate (POM)-mediated clusterization†

Eri Nagashima,^a Takuya Yoshida,^{a,b,c} Satoshi Matsunaga^a and Kenji Nomiya^{*a}

The effect of counteranions on the molecular structures of phosphanegold(i) cluster cations formed by polyoxometalate (POM)-mediated clusterization was investigated. A novel intercluster compound, $[\{(AuL_{Cl})_2(\mu-OH)\}_2]_3[\alpha-PMo_{12}O_{40}]_2 \cdot 3EtOH$ (**1-PMO₁₂**), was obtained as orange-yellow plate crystals in 12.0% yield from a 6 : 1 molar ratio reaction of the monomeric phosphanegold(i) carboxylato complex $[Au(RS-pyrrld)(L_{Cl})]$ ($RS-Hpyrrld = RS-2$ -pyrrolidone-5-carboxylic acid; $L_{Cl} = tris(4$ -chlorophenyl)phosphane) in CH_2Cl_2 with the free acid-form of Keggin polyoxometalate (POM), $H_3[\alpha-PMo_{12}O_{40}] \cdot 14H_2O$. An EtOH/ H_2O (5 : 1, v/v) solvent mixture was used. The dimeric cation $[\{(AuL_{Cl})_2(\mu-OH)\}_2]^{2+}$ in **1-PMO₁₂** was in a parallel-edge arrangement that was formed by self-assembly through the inter-cationic aurophilic interactions of the μ -OH-bridged dinuclear phosphanegold(i) cation. The POM anion in **1-PMO₁₂** was successfully exchanged with a smaller PF_6^- anion by the use of an anion-exchange resin. POM-free, colorless block crystals of $[\{(AuL_{Cl})_3(\mu_3-O)\}_2](PF_6)_2 \cdot 4CH_2Cl_2$ (**2-PF₆**) were obtained by vapor diffusion in 14.1% yield. During the synthesis of **2-PF₆**, a compound with mixed counteranions (one POM and one PF_6^- anion), *i.e.* $[\{(AuL_{Cl})_4(\mu_4-O)\}_2](\alpha-PMo_{12}O_{40})PF_6$ (**3-PMO₁₂PF₆**), was obtained in 66.4% yield. Both products were characterized by elemental analysis, TG/DTA, FT-IR, $^{31}P\{^1H\}$ NMR, 1H NMR, and X-ray crystallography. X-ray crystallography revealed that the counteranion in **2-PF₆** was the dimeric cation of the μ_3 -O-bridged tris(phosphanegold(i)) species, whereas that in **3-PMO₁₂PF₆** consisted of an unusual μ_4 -O-bridged tetragonal-pyramidal tetrakis(phosphanegold(i)) cation. Therefore, we concluded that the POM anion significantly contributed to the stabilization of these counteranions (parallel-edged arrangement in **1-PMO₁₂** and μ_4 -O-bridged tetragonal-pyramid in **3-PMO₁₂PF₆**). Moreover, the previously reported yellow crystals of $[\{(AuL_F)_2(\mu-OH)\}_2]_3[PMo_{12}O_{40}]_2 \cdot 3EtOH$ (**4-PMO₁₂**; $L_F = tris(4$ -fluoro phenyl)phosphane) were successfully converted to the POM-free crystalline OTf^- salt $[\{(AuL_F)_2(\mu-OH)\}_2](OTf)_2 \cdot 0.5Et_2O$ (**4-OTf**) by the use of an anion-exchange resin. X-ray crystallography also revealed that the parallel-edge arrangement of the dimeric cation in **4-PMO₁₂** was converted to the crossed-edge arrangement of that in **4-OTf**. These results illustrate that the $Au \cdots O_{POM}$ and hydrogen-bonding ($C-H \cdots O_{POM}$ and $O-H \cdots O_{POM}$) interactions between the phosphanegold(i) cluster cation and the Keggin POM anion in the solid state significantly contribute to the structure, composition, and stability of the phosphane gold(i) cluster cations in **4-PMO₁₂**.

Received 6th July 2016,
Accepted 26th July 2016
DOI: 10.1039/c6dt02670b

www.rsc.org/dalton

Introduction

Polyoxometalates (POMs) are discrete metal oxide clusters that are of current interest as soluble metal oxides, and for their application in catalysis, medicine, and materials science.¹ The preparation of POM-based materials is therefore an active field of research. Notably, a combination of POMs with cluster cations or macrocations has resulted in the formation of various intercluster compounds that are interesting from the viewpoints of conducting research on ionic crystals, crystal growth, crystal engineering, structure, sorption

^aDepartment of Chemistry, Faculty of Science, Kanagawa University, Tsuchiya, Hiratsuka, Kanagawa 259-1293, Japan. E-mail: nomiya@kanagawa-u.ac.jp

^bResearch Center for Gold Chemistry, Graduate School of Urban Environmental Sciences, Tokyo Metropolitan University, 1-1 Minami-osawa, Hachioji, Tokyo 192-0397, Japan

^cDepartment of Applied Chemistry, Graduate School of Urban Environmental Sciences, Tokyo Metropolitan University, 1-1 Minami-osawa, Hachioji, Tokyo 192-0397, Japan. E-mail: nomiya@kanagawa-u.ac.jp

†CCDC 1485425 (**1-PMO₁₂**), 1485428 (**2-PF₆**), 1485433 (**3-PMO₁₂PF₆**) and 1485430 (**4-OTf**). For crystallographic data in CIF or other electronic format see DOI: 10.1039/c6dt02670b

properties, and so on. In many intercluster compounds, POMs have been combined with separately prepared cluster cations.²

Recently, we discovered that POM-mediated clusterization of monomeric $[\text{Au}(\text{PR}_3)]^+$ units results in the formation of an intercluster compound containing the tetra{phosphanegold(i)}-oxonium cluster cation $[\{\text{Au}(\text{PPh}_3)_4(\mu_4\text{-O})\}_3[\alpha\text{-PW}_{12}\text{O}_{40}]_2 \cdot 4\text{EtOH}$ (**5-PW₁₂**). This discovery was made during the carboxylate elimination of $[\text{Au}(\text{RS-pyrrld})(\text{PPh}_3)]$ (*RS*-Hpyrrld = *RS*-2-pyrrolidone-5-carboxylic acid),³ in the presence of the free-acid form of the α -Keggin POM, $\text{H}_3[\alpha\text{-PW}_{12}\text{O}_{40}] \cdot 7\text{H}_2\text{O}$.^{4a} The tetra{phosphanegold(i)}oxonium cluster cation in **5-PW₁₂** exhibited the C_{3v} symmetry. Here, it should be noted that the abbreviations of the compounds are based on the combination of phosphane-gold(i) cations and counteranions, in which different compositions of the phosphane-gold(i) cations are abbreviated as different, boldfaced numbers such as **1**, **2**, **3** and so on, and the Keggin POM $[\text{PMo}_{12}\text{O}_{40}]^{3-}$, PF_6^- and trifluoromethanesulfonate (OTf^-) anions are abbreviated as **PMo₁₂**, **PF₆** and **OTf**, respectively (see Abbreviations listed at the end of the text).

We also discovered that the reaction of $[\text{Au}(\text{RS-pyrrld})(\text{PPh}_3)]$ with the sodium salt of the α -Keggin POM, $\text{Na}_3[\alpha\text{-PW}_{12}\text{O}_{40}] \cdot 9\text{H}_2\text{O}$ afforded the heptakis{triphenylphosphanegold(i)}dioxonium cation $[\{\{\text{Au}(\text{PPh}_3)_4(\mu_4\text{-O})\}\{\{\text{Au}(\text{PPh}_3)_3(\mu_3\text{-O})\}\}^{3+}$.^{4b} This was confirmed only in the presence of POM anions.

Phosphane ligands in the carboxylatophosphanegold(i) precursors were found to have significant influence on the POM-mediated clusterization of monomeric $[\text{Au}(\text{PR}_3)]^+$ units. For example, the $[\{\{\text{Au}\{P(p\text{-RPh})_3\}_2(\mu\text{-OH})\}_2\}_3[\alpha\text{-PM}_{12}\text{O}_{40}]_2$ series ($\text{R} = \text{Me}$, $\text{M} = \text{W}$; $\text{R} = \text{Me}$, $\text{M} = \text{Mo}$; $\text{R} = \text{F}$, $\text{M} = \text{Mo}$ (**4-PMo₁₂**)) has recently been synthesized from the reactions between $[\text{Au}(\text{RS-pyrrld})\{P(p\text{-RPh})_3\}]$ in CH_2Cl_2 and $\text{H}_3[\alpha\text{-PM}_{12}\text{O}_{40}] \cdot n\text{H}_2\text{O}$ ($\text{M} = \text{W}$, $n = 7$ and $\text{M} = \text{Mo}$, $n = 14$) in mixed EtOH/ H_2O solvents.^{4c,d} In each cluster cation, the OH-bridging dimer of the diphosphanegold(i) units, $[\{\{\text{Au}\{P(p\text{-RPh})_3\}_2(\mu\text{-OH})\}\}^+]$, was formed as a crossed-edge arrangement for $\text{R} = \text{Me}$, whereas a parallel-edge arrangement was formed for $\text{R} = \text{F}$, depending upon the substituent on the aryl group of the triarylphosphanes.

Novel intercluster compounds $[\{\{\text{Au}(\text{PPh}_3)_4(\mu_4\text{-O})\}\}[\alpha\text{-XW}_{12}\text{O}_{40}\{\text{Au}(\text{PPh}_3)_3\}_3] \cdot 3\text{EtOH}$ ($\text{X} = \text{Al}$, **B**) have been prepared from the reactions between $[\text{Au}(\text{RS-pyrrld})(\text{PPh}_3)]$ in CH_2Cl_2 and the free-acid form of the highly negatively charged Keggin POM, $\text{H}_5[\alpha\text{-XW}_{12}\text{O}_{40}] \cdot n\text{H}_2\text{O}$ ($\text{X} = \text{Al}$, $n = 12$; $\text{X} = \text{B}$, $n = 14$), in EtOH/ H_2O at room temperature ($\text{Au} : \text{POM}$ molar ratio = 7 : 1).^{4e} Hence, the POM-mediated clusterization of $[\text{Au}(\text{PR}_3)]^+$ units provides an effective synthetic route for the preparation of novel phosphane-gold(i) cluster cations.

In addition, element-centered gold(i) clusters $[\text{E}(\text{AuL})_n]^{m+}$ have been studied extensively by Schmidbaur,^{5a-d} and Laguna.^{5e} For example, a tris{phosphanegold(i)} oxonium cluster $[\{\{\text{Au}(\text{PMe}_3)_3(\mu_3\text{-O})\}\}^+]$ was found to be a structural motif for chalcogen-centered gold(i) clusters, where the monomeric units are aggregated through crossed edges.^{5b} Element-centered gold(i) clusters are also apt models for the isolobal protic species $[\text{H}_3\text{O}]^+$ and $[\text{H}_4\text{O}]^{2+}$ that are currently of great interest.⁶ As for their applications, several phosphane-gold(i) complexes

have been proven to work as effective catalysts for organic transformation reactions.^{4f,7,8}

The tetra{phosphanegold(i)}oxonium cluster cation $[\{\{\text{Au}(\text{PPh}_3)_4(\mu_4\text{-O})\}\}^{2+}$ in **5-PW₁₂** was confirmed to exhibit the C_{3v} symmetry,^{4a} but the X-ray structure of the POM-free compound $[\{\{\text{Au}(\text{PPh}_3)_4(\mu_4\text{-O})\}\}(\text{BF}_4)_2$ (**5-BF₄**, T_d symmetry) has not been determined to date.^{5a,9b} Nevertheless, it has been discussed that the molecular structures (C_{3v} vs. T_d symmetry) in the solid state of the tetra{phosphanegold(i)}oxonium cation are significantly influenced by the presence of large POM anions.⁵ On the other hand, the POM-free $[\{\{\text{Au}\{P(o\text{-MePh})_3\}_4(\mu_4\text{-O})\}\}^{2+}$ cation in the BF_4^- salt (**6-BF₄**) has been determined to exhibit T_d symmetry.^{9b} Unfortunately, X-ray structure analysis to confirm the C_{3v} symmetry in $[\{\{\text{Au}\{P(o\text{-MePh})_3\}_4(\mu_4\text{-O})\}\}_3[\alpha\text{-PW}_{12}\text{O}_{40}]_2$ (**6-PW₁₂**) has been unsuccessful.

We focused on the effect of POM anions on the structure of the phosphane-gold(i) cluster cation in solid state intercluster compounds. To investigate this effect, we needed to prepare the crystalline compounds of the phosphane-gold(i) cluster cations (both with and without the presence of POM anions), and determine their molecular structures. Therefore, in this study, we report the preparation of the intercluster compound $[\{\{\text{AuL}_{\text{Cl}}\}_2(\mu\text{-OH})\}_2\}_3[\alpha\text{-PMo}_{12}\text{O}_{40}]_2 \cdot 3\text{EtOH}$ (**1-PMo₁₂**) and its POM-free salt $[\{\{\text{AuL}_{\text{Cl}}\}_3(\mu_3\text{-O})\}_2](\text{PF}_6)_2 \cdot 4\text{CH}_2\text{Cl}_2$ (**2-PF₆**) using an anion-exchange resin. During the synthetic process from **1-PMo₁₂** to **2-PF₆**, we unexpectedly obtained a novel compound with mixed anions $[\{\{\text{AuL}_{\text{Cl}}\}_4(\mu_4\text{-O})\}\}_2[\alpha\text{-PMo}_{12}\text{O}_{40}]\text{PF}_6$ (**3-PMo₁₂PF₆**). The molecular structures of all the afforded products were determined by X-ray crystallography. Interestingly, the unusual $\mu_4\text{-O}$ -bridged tetragonal-pyramidal cation structure in **3-PMo₁₂PF₆** belonged to a class of electron-deficient species stabilized by both $[\alpha\text{-PMo}_{12}\text{O}_{40}]^{3-}$ and PF_6^- anions. Moreover, using the previously reported **4-PMo₁₂** moiety,^{4c} we successfully obtained the POM-free, OTf^- salt $[\{\{\text{AuL}_{\text{F}}\}_2(\mu\text{-OH})\}\}_2(\text{OTf})_2 \cdot 0.5\text{Et}_2\text{O}$ (**4-OTf**), and determined its molecular structure.

Herein, we demonstrate that the molecular structures of the phosphane-gold(i) cations in **1-PMo₁₂**, **2-PF₆**, **3-PMo₁₂PF₆**, and **4-OTf** are strongly dependent on the POM anions.

Results and discussion

Syntheses and composition characterization

The intercluster compounds obtained from the phosphane-gold(i) cluster and the Keggin POM anion, and their anion-exchanged compounds were obtained as follows: **1-PMo₁₂** in 12.0% (0.032 g scale) yield, **2-PF₆** in 14.1% (0.017 g scale) yield, **3-PMo₁₂PF₆** in 66.4% (0.061 g scale) yield, and **4-OTf** in 56.0% (0.040 g scale) yield.

The compound **1-PMo₁₂** was prepared from a reaction between $[\text{Au}(\text{RS-pyrrld})(\text{L}_{\text{Cl}})]$ in CH_2Cl_2 and the free-acid form of the α -Keggin POM, $\text{H}_3[\alpha\text{-PMo}_{12}\text{O}_{40}] \cdot 14\text{H}_2\text{O}$ in a mixed EtOH/ H_2O solvent. Crystallization was carried out by slow evaporation at room temperature in the dark. The CHN elemental analysis and TG/DTA of **1-PMo₁₂** indicated that **1-PMo₁₂** con-

sisted of three $[(AuL_{Cl})_2(\mu-OH)]_2^{2+}$ cations, two Keggin $[\alpha-PMo_{12}O_{40}]^{3-}$ POM anions, and three EtOH solvent molecules. These results were consistent with the X-ray crystallographic data (see the molecular structure). In the $^{31}P\{^1H\}$ NMR analysis in $DMSO-d_6$, the signals for phosphanegold(i) cluster cations and Keggin POM anions were observed at 25.08 ppm and -3.29 ppm, respectively. The three EtOH solvent molecules were also confirmed by a weight loss of 1.54% observed by TG/DTA, and by a signal at 1.09 ppm (t, $J = 6.9$ Hz, CH_3CH_2OH) in the 1H NMR analysis in $DMSO-d_6$. The solid-state IR spectrum of **1-PMo₁₂** displayed characteristic vibrational bands owing to the coordinating L_{Cl} ligand, and prominent vibrational bands from the α -Keggin molybdo-POM moiety with a P heteroatom (1062, 957, 879, and 802 cm^{-1}).¹⁰ In the IR spectrum, the carbonyl vibrational bands of the anionic *RS*-pyrrld ligand in the $[Au(RS\text{-pyrrld})(L_{Cl})]$ precursor disappeared. Elimination of the carboxylate ligand was also confirmed by 1H NMR analysis in $DMSO-d_6$.

The POM-free powder compounds **2-PF₆** and **4-OTf** were prepared from the intercluster compounds **1-PMo₁₂** and **4-PMo₁₂**, respectively, using anion-exchange resins (PF_6^- and OTf^- forms). This was followed by crystallization in a refrigerator by vapor diffusion in a solvent system (CH_2Cl_2 internal solution and Et_2O external solvent). The X-ray crystallographic data indicated the formation of oxygen-bridged gold(i) cluster cations $[(AuL_{Cl})_3(\mu_3-O)]_2^{2+}$ in **2-PF₆**, and $[(AuL_F)_2(\mu-OH)]_2^{2+}$ in **4-OTf**. The use of an anion-exchange method resulted in the transformation of the original dimer-of-dinuclear cluster in **1-PMo₁₂** to the dimer-of-trinuclear-cluster cation $[(AuL_{Cl})_3(\mu_3-O)]_2^{2+}$ in **2-PF₆**. On the other hand, this same method trans-

formed the parallel-edge arrangement in **4-PMo₁₂** into the crossed-edge arrangement of $[(AuL_F)_2(\mu-OH)]_2^{2+}$ in **4-OTf**. The CHN elemental analysis results and the TG/DTA data for **2-PF₆** and **4-OTf** were consistent with the X-ray crystallographic results. The solid-state IR spectra of **2-PF₆** and **4-OTf** exhibited characteristic vibrational bands due to the coordinating triarylphosphane ligands. The prominent vibrational bands of the POM anions in **1-PMo₁₂** and **4-PMo₁₂** disappeared, suggesting that the POM anions were completely exchanged. This suggestion was also confirmed by the $^{31}P\{^1H\}$ NMR spectra.

The compound **3-PMo₁₂PF₆** was prepared from **1-PMo₁₂** using a small amount of an anion-exchange resin (PF_6^- , 1 mL). The resulting product was then crystallized. The X-ray crystallographic data of **3-PMo₁₂PF₆** revealed a discrete intercluster compound containing two $[(AuL_{Cl})_4(\mu_4-O)]^{2+}$ cations, one $[\alpha-PMo_{12}O_{40}]^{3-}$, and one PF_6^- anion. The structure of $[(AuL_{Cl})_4(\mu_4-O)]^{2+}$ in **3-PMo₁₂PF₆** was found to be an unusual μ_4 -O-bridged tetragonal-pyramid with the C_{4v} symmetry. This was a first example of electron-deficient oxygen-bridged gold(i) cluster species (see the molecular structures). The solid-state IR spectrum of **3-PMo₁₂PF₆** displayed characteristic vibrational bands owing to the $[\alpha-PMo_{12}O_{40}]^{3-}$ (1062, 957, 878, and 803 cm^{-1}) and PF_6^- anions.

Molecular structure of the $[(AuL_{Cl})_2(\mu-OH)]_2^{2+}$ cation in **1-PMo₁₂**

Single-crystal X-ray analysis revealed that **1-PMo₁₂** crystallizes in the triclinic $P\bar{1}$ space group, and is composed of three tetragold(i) cluster cations $[(AuL_{Cl})_2(\mu-OH)]_2^{2+}$, and two saturated α -Keggin POMs $[\alpha-PMo_{12}O_{40}]^{3-}$ as counteranions (Fig. 1). The

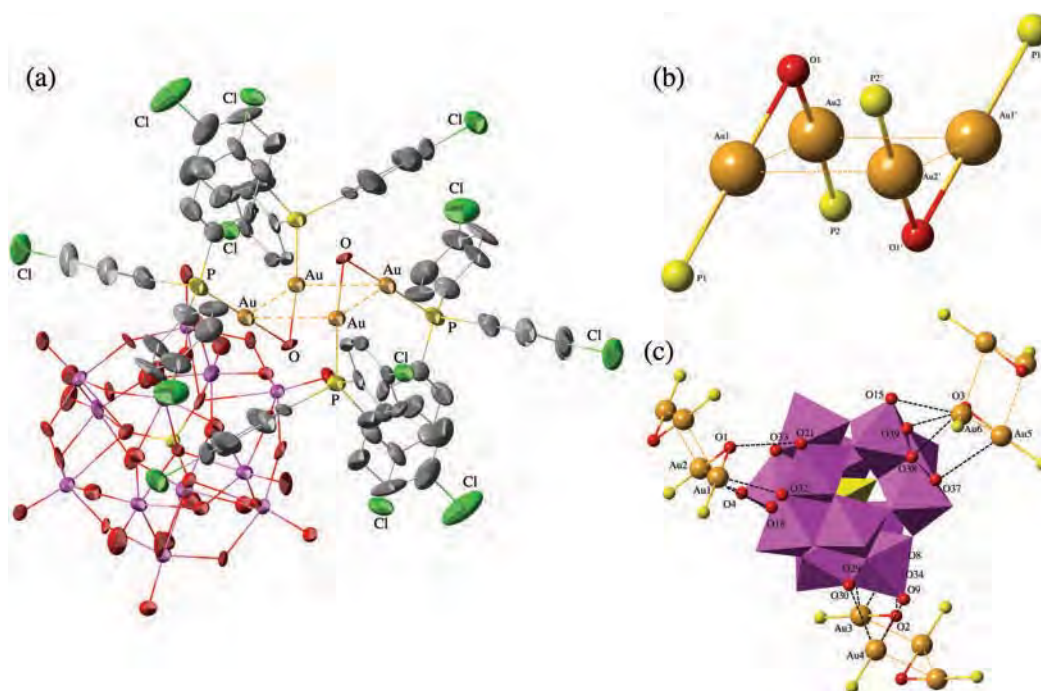


Fig. 1 (a) Molecular structure of $[(AuL_{Cl})_2(\mu-OH)]_2[\alpha-PMo_{12}O_{40}]_2 \cdot 3EtOH$ (**1-PMo₁₂**), (b) the partial structure around the tetragold(i) cluster core of **1-PMo₁₂** in a parallel-edge fashion, and (c) the short interactions between the tetragold(i) unit and the α -Keggin POM unit.

digold(i) unit consists of two $\{(\text{AuL}_{\text{Cl}})_2(\mu\text{-OH})\}$ monomers linked by a $\mu\text{-OH}$ ligand, and the two digold(i) units dimerized by aurophilic interactions [Au1–Au2, 3.166(5) Å; Au3–Au4, 3.253(5) Å; and Au5–Au6, 3.395(7) Å] to form the tetragold(i) cluster cation $[\{(\text{AuL}_{\text{Cl}})_2(\mu\text{-OH})\}_2]^{2+}$. Three crystallographically independent tetragold(i) cations were present in the unit cell. The digold(i) cations of **1-PMo**₁₂ dimerized in a parallel-edge arrangement, leading to a rectangular array of four gold(i) atoms (Fig. 1(b)). Parallel-edge tetragold(i) cations similar to those observed in **1-PMo**₁₂ have been reported for $[\{(\text{AuL}_{\text{F}})_2(\mu\text{-OH})\}_2]_3[\alpha\text{-PMo}_{12}\text{O}_{40}]_3\cdot 3\text{EtOH}$,^{4c} $[\{\text{Au}\{\text{P}(m\text{-FPh})_3\}_4(\mu_4\text{-O})\}_2]_2[\{(\text{Au}\{\text{P}(m\text{-FPh})_3\}_2(\mu\text{-OH})\}_2)]_2[\alpha\text{-PMo}_{12}\text{O}_{40}]_2\cdot \text{EtOH}$,^{4d} and $[\{(\text{AuL}_{\text{Cl}})_2(\mu\text{-OH})\}_2]_3[\alpha\text{-SiMo}_{12}\text{O}_{40}(\text{AuL}_{\text{Cl}})_2]\cdot \text{EtOH}$.^{4g} With the exception of the substituent of the phosphane ligand (Cl vs. F), the composition of $[\{(\text{AuL}_{\text{F}})_2(\mu\text{-OH})\}_2]_3[\alpha\text{-PMo}_{12}\text{O}_{40}]_3\cdot 3\text{EtOH}$ ^{4c} was similar to that of **1-PMo**₁₂, i.e., three parallel-edge tetragold(i) clusters, and two $[\alpha\text{-PMo}_{12}\text{O}_{40}]^{3-}$ anions. On the other hand, $[\{\text{Au}\{\text{P}(m\text{-FPh})_3\}_4(\mu_4\text{-O})\}_2]_2[\{(\text{Au}\{\text{P}(m\text{-FPh})_3\}_2(\mu\text{-OH})\}_2)]_2[\alpha\text{-PMo}_{12}\text{O}_{40}]_2\cdot \text{EtOH}$ ^{4d} was synthesized with the same POM $[\alpha\text{-PMo}_{12}\text{O}_{40}]^{3-}$ as **1-PMo**₁₂, but contained two types of tetragold(i) cluster cations. These were the oxo-centered tetragold(i) cluster cations $[\{\text{Au}\{\text{P}(m\text{-FPh})_3\}_4(\mu_4\text{-O})\}_2]^{2+}$, as well as one parallel-edge tetragold(i) cluster $[\{(\text{Au}\{\text{P}(m\text{-FPh})_3\}_2(\mu\text{-OH})\}_2)]_2$. In the case of $[\{(\text{AuL}_{\text{Cl}})_2(\mu\text{-OH})\}_2]_3[\alpha\text{-SiMo}_{12}\text{O}_{40}(\text{AuL}_{\text{Cl}})_2]\cdot \text{EtOH}$, two mononuclear phosphane-gold(i) cations, $[\text{AuL}_{\text{Cl}}]^+$, linking to the OMo₂ oxygen atoms of the Keggin POM anion, co-existed with the parallel-edge tetragold(i) clusters.

The parallel-edge tetragold(i) cluster $[\{(\text{Au}(\text{PR}_3)_2(\mu\text{-OH})\}_2]^{2+}$ has never been synthesized without POM anions. The structure of the parallel-edge arrangement, without the POM, has only been reported for the thiolato-bridged cations, $[\{(\text{Au}(\text{PR}^1_3)_2(\mu\text{-SR}^2)\}_2]^{2+}$ ($\text{R}^1 = \text{Ph}, \text{Me}$; $\text{R}^2 = \text{CMe}_3, 2\text{-H}_2\text{NC}_6\text{H}_4, \text{CH}_2\text{CMe}_3, 4\text{-MeC}_6\text{H}_4, 2,3,4,6\text{-tetraacetyl-1-thio-D-glucopyranosato}$).¹¹

Molecular structure of the $[\{(\text{AuL}_{\text{Cl}})_3(\mu_3\text{-O})\}_2]$ cation in 2-PF₆

X-ray crystallography revealed that the cation containing the $\mu_3\text{-O}$ atom (2) $[\{(\text{AuL}_{\text{Cl}})_3(\mu_3\text{-O})\}_2]^{2+}$, in 2-PF₆, is dimeric in the crystalline form (Fig. 2). The species $[\{(\text{AuL}_{\text{Cl}})_3(\mu_3\text{-O})\}]^+$ has a pyramidal structure, and the $\mu_3\text{-O}$ atom is outside the Au₃ plane.

The Au...O distances in (2) (1.997–2.070 Å; average 2.043 Å) were slightly longer than those of the related compound $[\{(\text{AuPPh}_3)_3(\mu_3\text{-O})\}_2](\text{BF}_4)_2$ (1.93–2.04 Å; average 1.97 Å).^{9a} Both were slightly shorter than the sum of the singly bound Au and O covalent radii (2.10 Å). The Au...P bond lengths in (2) (2.216–2.224 Å) were close to those of $[\{(\text{AuPPh}_3)_3(\mu_3\text{-O})\}_2](\text{BF}_4)_2$ (2.25–2.27 Å).^{9a} Both were shorter than the sum of the Au and P covalent radii. The phosphorus coordination was close to tetrahedral.

Both intra- and intermolecular Au...Au contacts existed, and the intermolecular interactions led to a dimeric structure in which two pyramidal $[\{(\text{AuPR}_3)_3(\mu_3\text{-O})\}]^+$ units, related by an inversion center, are edge-bridged through two gold atoms. The intra- and intermolecular Au...Au distances in (2) are comparable (3.003–3.193 Å; average 3.109 Å and 3.073 Å, respectively). Both were significantly longer than the distances in the Au metal (2.884 Å),¹² but shorter than the sum of the Au van der Waals radii (3.32 Å).¹³ The intramolecular Au...Au distances in (2) were close to those of $[\{(\text{AuPPh}_3)_3(\mu_3\text{-O})\}_2](\text{BF}_4)_2$ (3.032–3.215 Å; average 3.094 Å),^{9a} but the intermolecular Au...Au distance in (2) was significantly shorter than that (3.162(6) Å) in the $[\{(\text{AuPPh}_3)_3(\mu_3\text{-O})\}_2]^{2+}$ cation.

These Au...Au distances can be compared to those of the $\mu_3\text{-S}$ analogues. The intramolecular Au...Au distances in the dimeric cation $[\{(\text{AuPPh}_2\text{Me})_3(\mu_3\text{-S})\}_2]^{2+}$ with an OTf[−] anion¹⁴ are in the range of 3.0187(12)–3.2534(13) Å (average 3.114 Å). These values are comparable to those of $[\{(\text{AuPPh}_3)_3(\mu_3\text{-S})\}]^+$

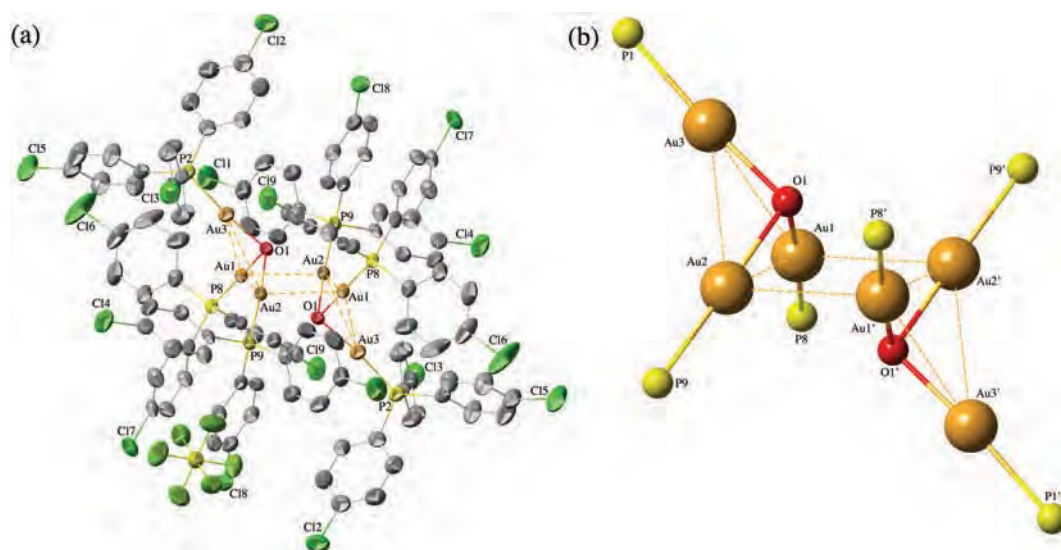


Fig. 2 (a) Molecular structure of $[\{(\text{AuL}_{\text{Cl}})_3(\mu_3\text{-O})\}_2](\text{PF}_6)_2$ (2-PF₆), and (b) the partial structure around the dimeric tris(phosphane-gold(i))oxonium cluster cation (2).

(3.071–3.409 Å).^{15a,b} The most pronounced difference was found in the intermolecular Au...Au contacts: 3.0774(1) Å in $[(AuPPh_2Me)_3(\mu_3-S)]_2^{2+}$ against 3.236 and 3.361 Å in $[(AuPPh_3)_3(\mu_3-S)]^+$.^{15a,b}

Molecular structure of the $[(AuLCl)_4(\mu_4-O)]^{2+}$ cation in $3-PMo_{12}PF_6$

The $[(AuLCl)_4(\mu_4-O)]^{2+}$ cation (**3**) crystallized with one $[\alpha-PMo_{12}O_{40}]^{3-}$ anion and one PF_6^- anion ($3-PMo_{12}PF_6$, Fig. 3). The structure of cation **3** in $3-PMo_{12}PF_6$ consisted of a tetragonal-pyramidal framework, with the oxygen atom occupying the apical position (Fig. 3(b)). The distances between the adjacent Au atoms [2.8708(7)–2.8709(7) Å] were close to or slightly shorter than the distances in the Au metal (2.88 Å),¹² and significantly shorter than the sum of the Au van der Waals radii (3.32 Å).¹³ The distances between the diagonally opposed Au atoms were 4.0599(6) (Au1–Au1) and 4.0570(6) Å (Au2–Au2). The O atom was 0.612 Å (O12) and 0.503 Å (O13) out of the Au_4 plane. The Au–O distances are 2.120(4) (Au1–O12) and 2.090(4) (Au2–O13) Å, and the Au–O–Au angles are 85.2(2)° and 146.4(8)° (Au1–O12–Au1), and 86.7(2)° and 152.2(9)° (Au2–O13–Au2).

These data can be compared to those of the μ_4-S analogous $[(AuPPh_3)_4(\mu_4-S)]^{2+}$ cation with a ClO_4^- anion.¹⁴ The distances between the adjacent Au atoms are 2.883(2)–2.901(2) Å, and those between the diagonally opposed Au atoms are 4.079 Å

and 4.102 Å. The S atom lies 1.25 Å out of the Au_4 plane. The Au–S distances are in the range of 2.392(7)–2.408(7) Å, and the Au–S–Au angles are in the range of 73.8(2)–74.5(2)°.

The bonding mode of the μ_4-O atom and the gold(i) centers in the $[(AuLCl)_4(\mu_4-O)]^{2+}$ cation (**3**) can be described by a simple MO diagram, similar to that of the S-analogous $[(AuPPh_3)_4(\mu_4-S)]^{2+}$ with C_{4v} symmetry.¹⁴ Three bonding orbitals are filled by six available valence electrons, and the non-bonding orbital a_1 , as the HOMO, is occupied by two electrons. The bonding mode can be identified as an electron-deficient species with a bond order of 3/4 for four O–AuPR₃ bonds, and a μ_4-O ion with one lone pair. This compound is in contrast to the previously reported C_{3v} symmetry compound, $[(Au(PR_3)_4)(\mu_4-O)]^{2+}$ (R = Ph, *m*-FPh, *m*-Me),^{4a,d} in which the four O–AuPR₃ bonds can be regarded as a single bond with a bond order of 1. Thus, the present cation (**3**) is of a class of hypercoordinated species, together with $[(AuPPh_3)_5(\mu_5-C)]^+$,^{15c} $[(AuPPh_3)_6(\mu_6-C)]^{2+}$,^{15d} $[(AuPPh_3)_5(\mu_5-N)]^{2+}$,^{15e,f} $[(AuPPh_3)_5(\mu_5-P)]^{2+}$,^{15g} $[(AuL)_6(\mu_6-P)]^{3+}$ (L = P^tBu_3 , P^iPr_3),^{15h} $[(AuPPh_3)_4(\mu_4-S)]^{2+}$,^{14,15i} and $[(AuPPh_3)_3(\mu_3-S)]^+$.^{15a,b}

Molecular structure of the $[(AuLF)_2(\mu-OH)]_2^{2+}$ cation in 4-OTf

Single-crystal X-ray analysis revealed that **4-OTf** crystallizes in the tetragonal $P4(2)/n$ space group and is composed of one tetragold(i) cluster cation, $[(AuLF)_2(\mu-OH)]_2^{2+}$, and two OTf[−] anions (Fig. 4). The digold(i) unit consists of two

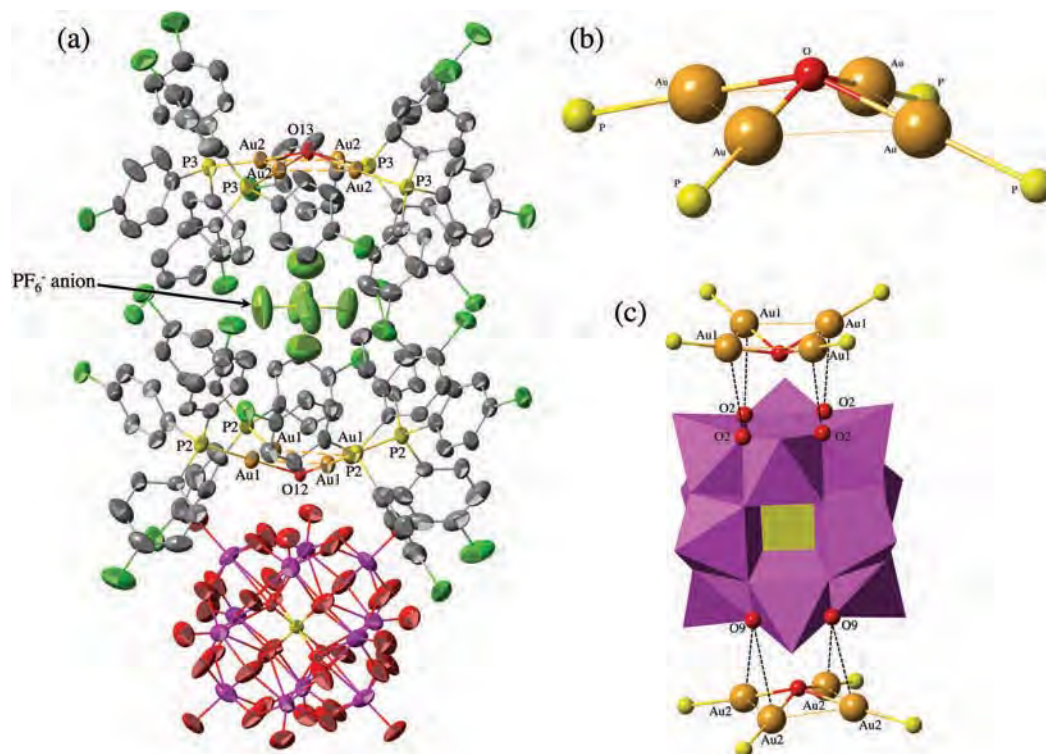


Fig. 3 (a) Molecular structure of $[(AuLCl)_4(\mu_4-O)]_2[\alpha-PMo_{12}O_{40}]PF_6$ ($3-PMo_{12}PF_6$), (b) the partial structure around the tetragold(i) cluster core of $[(AuLCl)_4(\mu_4-O)]^{2+}$ (**3**), and (c) the short interactions between the tetragold(i) unit and the α -Keggin POM unit.

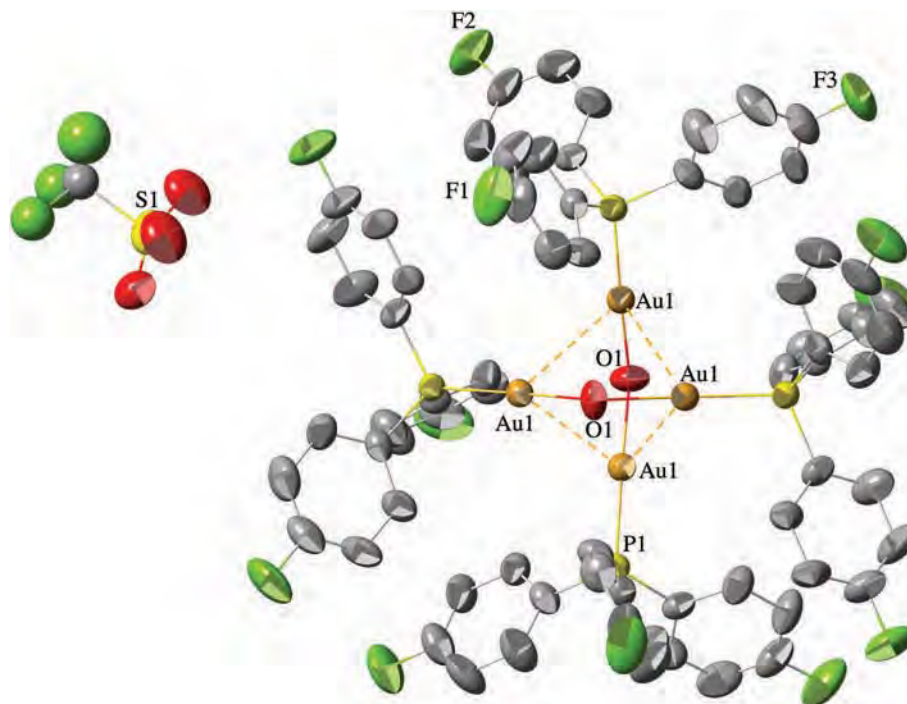


Fig. 4 Molecular structure of $\{[(AuL_F)_2(\mu-OH)]_2(OTf)_2 \cdot 0.5Et_2O$ (**4-OTf**).

$\{(AuL_F)_2(\mu-OH)\}$ monomers linked by a $\mu-OH$ ligand, and the two digold(i) units dimerized in a crossed-edge arrangement by aurophilic interactions ($Au-Au$, 3.2530(4) Å) to form the tetragold(i) cluster cation $\{[(AuL_F)_2(\mu-OH)]_2\}^{2+}$. The crossed-edge cluster cation $\{[(AuL_F)_2(\mu-OH)]_2\}^{2+}$ in **4-OTf** was converted from the original parallel-edge cluster in **4-PMo₁₂** during the anion-exchange procedure. This suggests that the counteranion plays an important role in the formation of the gold(i)phosphane cluster cations. Crossed-edge tetragold(i) cations $\{[(Au(PR_3))_2(\mu-OH)]_2\}^{2+}$ similar to that observed in **4-OTf** have been reported for $\{[(Au\{P(p-MePh)_3\})_2(\mu-OH)]_2\}_3[\alpha-PM_{12}O_{40}]_2 \cdot nEtOH$ ($M = W$, $n = 1$; $M = Mo$, $n = 0$),^{4c} and $\{[(Au(PPh_3))_2(\mu-OH)]_2\}-(OTf)_2$.¹⁶ Halide-bridged tetragold(i) cations with a crossed-edge arrangement, $\{[(Au(PR)_2(\mu-X)]_2\}[(SbF_6)_2]$ ($X = Cl, Br, I$; $R = Ph_3, \{(MeO)_2C_6H_3\}Ph_2$) have also been reported.¹⁷

Solution ($^{31}P\{^1H\}$ and 1H) NMR

The solution $^{31}P\{^1H\}$ NMR spectrum of **1-PMo₁₂** in $DMSO-d_6$ (Fig. 5(a)) exhibited a sharp peak at 25.08 ppm owing to the $P(p-ClPh)_3$ ligands (L_{Cl}) of the gold(i) cluster cation, and another peak at -3.29 ppm owing to the heteroatom phosphorus in the Keggin molybdo-POM anion. In addition to these main peaks, several minor peaks attributed to the decomposition of the gold(i) cluster cation (41.79 ppm) and the Keggin molybdo-POM anion (-0.04 , -0.46 ppm) were also observed, because of the instability of **1-PMo₁₂** in $DMSO-d_6$. In general, $^{31}P\{^1H\}$ NMR peaks of the oxygen-centered phosphane-gold(i) clusters are observed at higher field values when compared to those of the precursor $[Au(RS-pyrrld)(L_{Cl})]$; 27.40 ppm in $CDCl_3$.

In the solution $^{31}P\{^1H\}$ NMR spectrum of **2-PF₆** in $DMSO-d_6$ (Fig. 5(b)), a singlet attributed to the L_{Cl} ligands of the gold(i) cluster cation, and a quintet attributed to the PF_6^- counteranion were observed at 22.43 and -143.41 (coupling constant $J_{PF} = 711$ Hz) ppm, respectively. The peak due to the L_{Cl} ligands of the gold(i) cluster cation was observed in a higher field than that of **1-PMo₁₂** (25.08 ppm).

In the solution $^{31}P\{^1H\}$ NMR spectrum of **3-PMo₁₂PF₆** in $DMSO-d_6$ (Fig. 5(c)), the peaks attributed to the L_{Cl} ligands of the pyramidal gold(i) cluster cation, the heteroatom phosphorus in the Keggin molybdo-POM anion, and the PF_6^- anion were observed at 24.83, -3.46 , and -143.75 (coupling constant $J_{PF} = 711$ Hz) ppm, respectively. In addition to these peaks, several peaks (-0.61 , 41.63 ppm) attributed to the decomposition of the gold(i) cluster cation and the Keggin molybdo-POM anion (-0.61 ppm) were also observed because of the instability of **3-PMo₁₂PF₆** in $DMSO-d_6$. The decomposition species of the gold(i) cluster cation at 41.63 ppm was assigned to the diphosphane gold(i) complex $[Au(L_{Cl})_2]^+$. The solid-state CP-MAS ^{31}P NMR of **3-PMo₁₂PF₆** displayed signals owing to the L_{Cl} ligands of the pyramidal gold(i) cluster cation, the heteroatom phosphorus in the Keggin molybdo-POM anion, and the PF_6^- anion (24.09, -3.57 , and -144.29 (coupling constant $J_{PF} = 707$ Hz) ppm, respectively) (Fig. 6). In contrast to the solution $^{31}P\{^1H\}$ NMR spectrum of **3-PMo₁₂PF₆** in $DMSO-d_6$, the peaks due to the decomposition of the gold(i) cluster cation and the Keggin molybdo-POM anion were not observed.

Because **4-OTf** is soluble in CD_2Cl_2 , the solution $^{31}P\{^1H\}$ NMR spectrum of **4-OTf** was measured in CD_2Cl_2 (Fig. 5(d)).

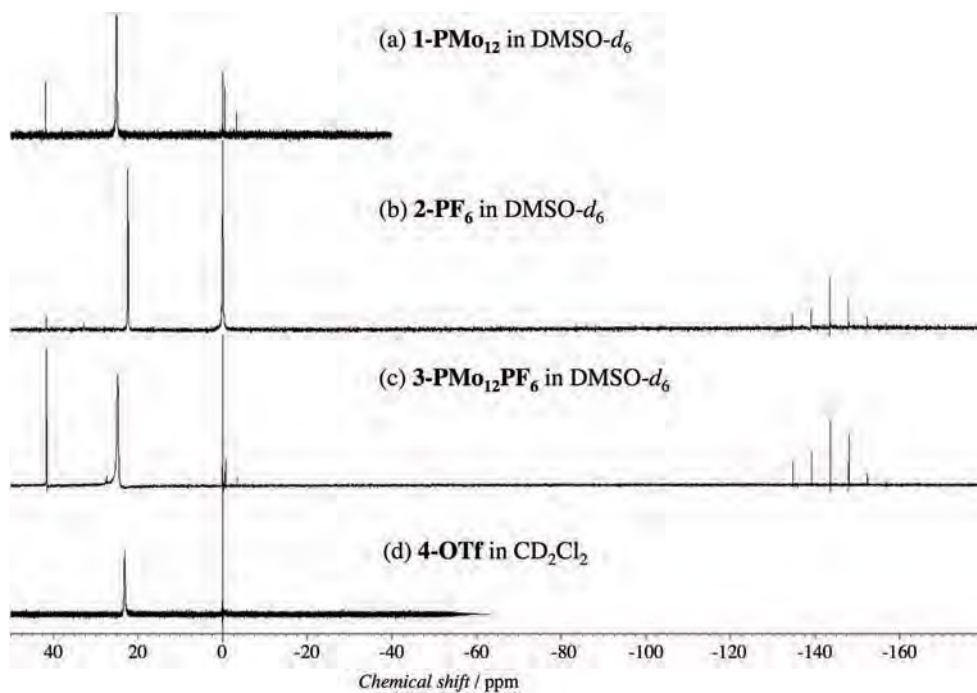


Fig. 5 $^{31}\text{P}\{^1\text{H}\}$ NMR spectra of (a) **1-PMo₁₂** in DMSO-*d*₆, (b) **2-PF₆** in DMSO-*d*₆, (c) **3-PMo₁₂PF₆** in DMSO-*d*₆, and (d) **4-OTf** in CD₂Cl₂.

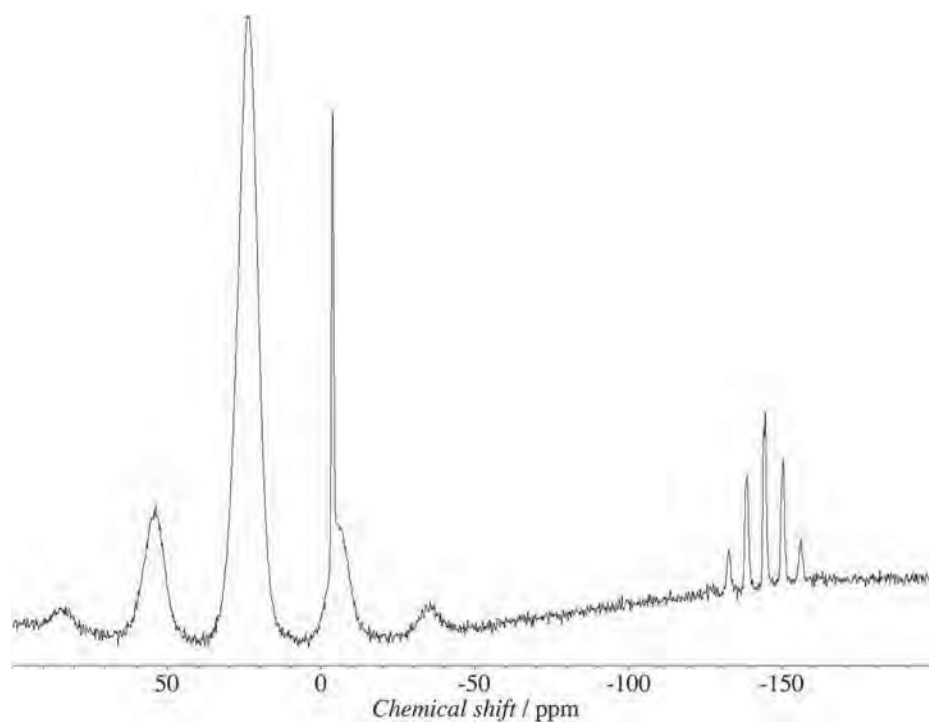


Fig. 6 Solid-state CP-MAS ^{31}P NMR spectrum of **3-PMo₁₂PF₆**.

A peak owing to the $\text{P}(p\text{-FPh})_3$ ligands (L_F) of the crossed-edge tetragold(i) cluster cation was observed at 23.17 ppm. No peaks attributed to the decomposition species of the gold(i) cluster cation were observed in CD₂Cl₂.

Conclusions

During the anion exchange of **1-PMo₁₂** and PF_6^- , two types of phosphanegold(i) cluster cations were formed. These were the

monomeric tetrakis{phosphanegold(i)} species (3) with both POM and PF_6^- anions (**3-PMo₁₂PF₆**), and the dimeric tris{phosphanegold(i)} species (2) with only the PF_6^- anion (**2-PF₆**). X-ray crystallography revealed that the cationic species containing the $\mu_4\text{-O}$ atom (3) showed an unusual geometry (a square-pyramidal structure with the local C_{4v} symmetry). The bonding mode can be described as an electron-deficient species with a bond order of 3/4 for four O-AuPR_3 bonds, and a $\mu_4\text{-O}$ ion with one lone pair. This species was first formed in the presence of both POM and PF_6^- anions, while the dimeric tris{phosphanegold(i)}($\mu_3\text{-O}$) species (2) was formed as a PF_6^- salt in a system without a POM anion. The previously reported intercluster compound **4-PMo₁₂** was successfully converted to the POM-free, crystalline OTf^- salt, **4-OTf**, by using an anion-exchange resin. The crossed-edge cluster cation $[\{(\text{AuL}_F)_2(\mu\text{-OH})\}_2]^{2+}$ in **4-OTf** was converted from the original parallel-edge cluster in **4-PMo₁₂** during the anion-exchange. This suggested that the counteranion plays an important role in the formation of gold(i)phosphane cluster cations.

Experimental

Materials

The following reactants were used as received: EtOH, CH_2Cl_2 , Et_2O (Wako), and DMSO- d_6 , CD_2Cl_2 (Isotec). The free-acid form of α -Keggin POM, $\text{H}_3[\alpha\text{-PMo}_{12}\text{O}_{40}]\cdot 14\text{H}_2\text{O}$ was prepared according to the ether extraction method,¹⁸ and identified by FT-IR, TG/DTA, and solution ^{31}P NMR. The phosphanegold(i) carboxylate precursors, $[\text{Au}(\text{RS-pyrrld})(\text{L}_X)]$ ($X = \text{Cl}, \text{F}$), were synthesized using L_X ($X = \text{Cl}, \text{F}$) in the reported preparation of $[\text{Au}(\text{RS-pyrrld})(\text{PPh}_3)]$,³ and identified by CHN elemental analysis, FT-IR, TG/DTA, and (^1H , $^{13}\text{C}\{^1\text{H}\}$ and $^{31}\text{P}\{^1\text{H}\}$) NMR spectroscopy. The intercluster compound containing the $\mu\text{-OH}$ -bridged parallel-edge dimer cations, **4-PMo₁₂**, was prepared according to a recently reported method,^{4c} and its yellow plate crystals (27.9% yield) were identified by CHN elemental analysis, FT-IR, TG/DTA, and (^1H , $^{31}\text{P}\{^1\text{H}\}$) NMR spectroscopy.

Instrumentation/analytical procedures

CHN elemental analyses were carried out with a Perkin-Elmer 2400 CHNS Elemental Analyzer II (Kanagawa University). The IR spectra were recorded on a Jasco 4100 FT-IR spectrometer using KBr disks at room temperature. The TG/DTA data were acquired using a Rigaku Thermo Plus 2 series TG 8120 instrument. Both the ^1H NMR (500.00 MHz) and $^{31}\text{P}\{^1\text{H}\}$ NMR (202.00 MHz) spectra of the samples were recorded in 5 mm-outer-diameter tubes on a Jeol JNM-ECP 500 FT-NMR spectrometer equipped with a Jeol ECP-500 NMR data processing system. The ^1H NMR spectra were referenced to an internal standard of tetramethylsilane (SiMe_4). The $^{31}\text{P}\{^1\text{H}\}$ NMR spectra were referenced to an external standard of 25% H_3PO_4 in H_2O in a sealed capillary. The $^{31}\text{P}\{^1\text{H}\}$ NMR data with the usual 85% H_3PO_4 reference are shifted to +0.544 ppm from our data. Solid-state CP-MAS ^{31}P NMR (121.00 MHz) spectra were recorded using 6 mm-outer-diameter rotors with a Jeol

JNM-ECP 300 FT-NMR spectrometer equipped with a Jeol ECP-300 NMR spectroscopic data processing system.

Syntheses

$[\{(\text{AuL}_{\text{Cl}})_2(\mu\text{-OH})\}_2]_3[\alpha\text{-PMo}_{12}\text{O}_{40}]_2\cdot 3\text{EtOH}$ (**1-PMo₁₂**). A solution of $[\text{Au}(\text{RS-pyrrld})(\text{L}_{\text{Cl}})]$ (0.192 g, 0.300 mmol) dissolved in 25 mL of CH_2Cl_2 was slowly added to a yellow clear solution of $\text{H}_3[\alpha\text{-PMo}_{12}\text{O}_{40}]\cdot 14\text{H}_2\text{O}$ (0.104 g, 0.050 mmol) dissolved in 15 mL of an EtOH/ H_2O (5 : 1, v/v) mixed solvent. After stirring for 1 h at room temperature, the reaction solution was filtered through a folded filter paper (Whatman no. 5). The resulting yellow clear solution was slowly evaporated at room temperature in the dark. Orange-yellow plate crystals were formed after 10 days. They were collected on a membrane filter (JG 0.2 μm), washed with EtOH (20 mL \times 2) and Et_2O (20 mL \times 2), and dried *in vacuo* for 2 h [yield = 32 mg (12.0%)]. The crystalline samples were soluble in DMSO, but insoluble in H_2O , EtOH, and Et_2O . Calcd for $\text{C}_{222}\text{H}_{168}\text{O}_{89}\text{P}_{14}\text{Cl}_{36}\text{Mo}_{24}\text{Au}_{12}$ or $[\{(\text{AuL}_{\text{Cl}})_2(\mu\text{-OH})\}_2]_3[\alpha\text{-PMo}_{12}\text{O}_{40}]_2\cdot 3\text{EtOH}$: C, 25.07; H, 1.59%. Found: C, 24.81; H, 1.77%. TG/DTA under atmospheric conditions: a weight loss of 1.54% due to desorption of EtOH was observed at temperatures <191.1 $^\circ\text{C}$; calcd 1.30% for three EtOH molecules. IR (KBr): 1575 m, 1560 w, 1479 m, 1388 m, 1301 vw, 1183 vw, 1088 s, 1062 m, 1012 m, 957 s, 879 m, 802 vs, 751 s, 705 w, 631 vw, 572 w, 496 m, 454 vw cm^{-1} . $^{31}\text{P}\{^1\text{H}\}$ NMR (25.2 $^\circ\text{C}$, DMSO- d_6): δ (ppm): -3.29, 25.08 (main), -0.46, -0.04, 41.79 (minor). ^1H NMR (24.5 $^\circ\text{C}$, DMSO- d_6): δ (ppm): 1.09 (t, $J = 6.9$ Hz, $\text{CH}_3\text{CH}_2\text{OH}$), 7.54-7.59 (m, Aryl). Note: the ^1H NMR signals owing to $\text{CH}_3\text{CH}_2\text{OH}$ overlapped with those attributed to the H_2O present in DMSO- d_6 .

$[\{(\text{AuL}_{\text{Cl}})_3(\mu_3\text{-O})\}_2](\text{PF}_6)_2$ (**2-PF₆**). An orange-yellow crystalline sample of **1-PMo₁₂** (0.100 g, 9.44 μmol) was added to the anion-exchange resin (PF_6^- , 5 mL) suspended in 20 mL of a $\text{CH}_2\text{Cl}_2/\text{CH}_3\text{CN}$ (1 : 1, v/v) mixed solvent. After stirring for 30 min at room temperature, the suspension was filtered through a membrane filter (JV 0.1 μm). The filtrate was evaporated to dryness with a rotary evaporator at 30 $^\circ\text{C}$, and the residue was dried *in vacuo* for 2 h. The afforded colorless white powder was dissolved in 8 mL of CH_2Cl_2 . Vapor diffusion in a solvent system (CH_2Cl_2 internal solution and an Et_2O external solvent) was performed in a refrigerator (~ 3 $^\circ\text{C}$). After three days, colorless block crystals were formed. X-ray diffraction measurements were performed for some of the crystals, and the remaining crystals were collected on a membrane filter (JG 0.2 μm), washed with Et_2O (20 mL \times 2), and dried *in vacuo* for 2 h. A colorless white powder, soluble in CH_2Cl_2 , CHCl_3 , DMSO, and DMF, and insoluble in Et_2O , was obtained [yield = 16.9 mg (14.1%)]. Calcd for $\text{C}_{108}\text{H}_{72}\text{O}_2\text{F}_{12}\text{P}_8\text{Cl}_{18}\text{Au}_6$ or $[\{(\text{AuL}_{\text{Cl}})_3(\mu_3\text{-O})\}_2](\text{PF}_6)_2$: C, 35.08; H, 1.96%. Found: C, 34.81; H, 1.65%. TG/DTA under atmospheric conditions: no weight loss was observed before decomposition. IR (KBr): 1646 m, 1575 s, 1559 s, 1479 vs, 1389 s, 1301 m, 1183 m, 1141 w, 1088 vs, 1012 s, 847 s, 816 s, 751 s, 724 w, 702 w, 632 w, 572 m, 557 m, 540 m, 503 m, 495 m, 469 w, 451 m, 420 w cm^{-1} . $^{31}\text{P}\{^1\text{H}\}$ NMR (21.9 $^\circ\text{C}$, DMSO- d_6): δ (ppm): -143.41 ($J_{\text{PF}} =$

711 Hz, owing to PF₆), 22.43. ¹H NMR (22.9 °C, DMSO-*d*₆): δ (ppm): 7.46–7.76 (m, *Aryl*).

[{(AuLCl)₄(μ₄-O)}₂][α-PMo₁₂O₄₀]PF₆ (3-PMo₁₂PF₆). An anion-exchange resin (PF₆⁻, 1 mL) was used in the synthesis of **2-PF₆**. Yellow needle-shaped crystals were formed. X-ray diffraction measurement was performed on part of the crystals, and the remaining crystals were collected on a membrane filter (JG 0.2 μm), washed with Et₂O (20 mL × 2), and dried *in vacuo* for 2 h. A yellow powder that was soluble in DMSO and DMF, slightly soluble in CH₂Cl₂ and CHCl₃, and insoluble in Et₂O, was obtained [yield = 61.1 mg (66.4%)]. Calcd for C₁₄₄H₉₆O₄₂F₆P₁₀Cl₂₄Mo₁₂Au₈ or [(AuLCl)₄(μ₄-O)]₂[α-PMo₁₂O₄₀]⁻PF₆: C, 26.61; H, 1.49%. Found: C, 26.66; H, 1.45%. TG/DTA under atmospheric conditions: no weight loss was observed before decomposition. IR (KBr): 1636 w, 1575 m, 1559 w, 1480 s, 1388 m, 1301 vw, 1184 vw, 1141 vw, 1088 vs, 1062 m, 1012 m, 957 s, 878 m, 803 vs, 751 vs, 743 s, 704 w, 633 w, 573 m, 495 m, 452 w, 421 vw, 405 w cm⁻¹. Solid-state CP-MAS ³¹P NMR (RT): δ (ppm): -144.29 (*J*_{PF} = 707 Hz, owing to PF₆), -3.57, 24.09. ³¹P{¹H} NMR (22.9 °C, DMSO-*d*₆): δ (ppm): -143.75 (*J*_{PF} = 711 Hz, owing to PF₆), -3.46, 24.83 (main), -0.61, 41.63 (minor). ¹H NMR (23.8 °C, DMSO-*d*₆): δ (ppm): 1.09 (t, *J* = 6.9 Hz, Et₂O), 3.39 (q, *J* = 7.1 Hz, Et₂O), 7.52–7.75 (m, *Aryl*).

[{(AuLF)₂(μ-OH)}₂](OTf)₂·0.5Et₂O (4-OTf). An anion-exchange resin (OTf⁻, 5 mL) and **4-PMo₁₂** (0.100 g, 10.0 mmol) were used in the synthesis of **2-PF₆** to afford a yellow-white powder [yield = 66.0 mg]. The powder was dissolved in 5 mL of CH₂Cl₂. Vapor diffusion in a solvent system (CH₂Cl₂ internal solution and an Et₂O external solvent) was performed in the dark, at room temperature. Colorless block crystals were deposited after five days. X-ray diffraction measurements were performed on part of the crystals, and the remaining crystals were collected on a membrane filter (JG 0.2 μm), washed with Et₂O (20 mL × 2), and dried *in vacuo* for 2 h. During the process, the crystals were converted into a white powder that

was soluble in CH₂Cl₂, DMSO, and DMF, and insoluble in EtOH and Et₂O [yield = 39.5 mg (56.0%)]. Calcd for C₇₆H₅₅O_{8.5}F₁₈S₂P₄Au₄ or [(AuLF)₂(μ-OH)]₂-(OTf)₂·0.5Et₂O: C, 37.69; H, 2.29%. Found: C, 37.03; H, 2.39%. TG/DTA under atmospheric conditions: no weight loss was observed before decomposition. IR (KBr): 1589 vs, 1496 vs, 1396 vs, 1349 w, 1265 vs, 1159 vs, 1102 vs, 1032 vs, 1013 s, 709 m, 638 vs, 618 m, 575 m, 534 vs, 524 vs, 450 vs, 441 vs cm⁻¹. ³¹P{¹H} NMR (24.3 °C, CD₂Cl₂): δ (ppm): 23.17. ¹H NMR (23.8 °C, CD₂Cl₂): δ (ppm): 1.15 (t, *J* = 8.5, 9.0 Hz, Et₂O), 3.43 (q, *J* = 17.5 Hz, Et₂O), 7.11–7.54 (m, *Aryl*).

X-ray crystallography

Single crystals with dimensions of 0.26 × 0.09 × 0.03 mm³ (**1-PMo₁₂**), 0.12 × 0.10 × 0.03 mm³ (**2-PF₆**), 0.17 × 0.04 × 0.02 mm³ (**3-PMo₁₂PF₆**), and 0.23 × 0.19 × 0.19 mm³ (**4-OTf**) were mounted on cryoloops using liquid paraffin, and cooled by using a stream of cooled N₂ gas. Data collection was performed on a Bruker SMART APEX CCD diffractometer at 100 K for **1-PMo₁₂** and **4-OTf**, and a Rigaku VariMax with a Saturn CCD diffractometer at 150 K for **2-PF₆** and **3-PMo₁₂PF₆**. The intensity data were automatically collected for Lorentz and polarization effects during integration. The structure was solved by direct methods (program SHELXS-97),^{19a} followed by subsequent difference Fourier calculations, and refined by a full-matrix, least-squares procedure on *F*² (program SHELXL-97).^{19b} Absorption corrections were performed with SADABS^{19c} for **1-PMo₁₂** and **4-OTf**, and with the CrystalClear program^{19d} for **2-PF₆** and **3-PMo₁₂PF₆**. The composition and formula of the POM moiety containing the solvated molecule were determined by CHN elemental analysis, TG/DTA, and ¹H NMR. Solvent molecules in the structure were highly disordered and impossible to refine by using conventional discrete-atom models. To resolve these issues, the contribution of the solvent electron density was removed by using the

Table 1 Crystallographic data for **1-PMo₁₂**, **2-PF₆**, **3-PMo₁₂PF₆**, and **4-OTf**

Parameters	1-PMo₁₂	2-PF₆	3-PMo₁₂PF₆	4-OTf
Formula	C ₂₁₆ H ₁₄₄ Au ₁₂ Cl ₃₆ Mo ₂₄ O ₈₆ P ₁₄	C ₁₀₈ H ₇₂ Au ₆ Cl ₁₈ F ₁₂ O ₂ P ₈	C ₁₆₄ H ₁₄₄ Au ₈ Cl ₃₂ F ₆ Mo ₁₂ O ₅₀ P ₁₀	C ₇₄ H ₄₈ Au ₄ F ₁₈ O ₈ P ₄ S ₂
Formula weight	10 491.25	3697.32	7199.90	2382.99
Color, shape	Yellow, plate	Colorless, block	Yellow, needle	Colorless, block
Crystal system	Triclinic	Triclinic	Tetragonal	Tetragonal
Space group	<i>P</i> $\bar{1}$	<i>P</i> $\bar{1}$	<i>P4/n</i>	<i>P4(2)/n</i>
<i>T</i> /K	100	150	150	100
<i>a</i> /Å	17.823(3)	15.019(3)	22.6489(7)	15.9305(3)
<i>b</i> /Å	22.894(4)	15.422(3)	22.6489(7)	15.9305(3)
<i>c</i> /Å	24.124(4)	15.667(3)	23.3214(9)	17.0830(8)
<i>α</i> /°	68.125(3)	74.16(3)	90	90
<i>β</i> /°	83.712(3)	64.13(3)	90	90
<i>γ</i> /°	82.884(3)	64.20(3)	90	90
<i>V</i> /Å ³	9043(3)	2924.2(10)	11 963.2(7)	4335.3(2)
<i>Z</i>	1	1	2	2
<i>D</i> _{calc} /g cm ⁻³	1.926	2.100	1.999	1.825
<i>F</i> ₀₀₀	4906	1744	6824	2252
GOF	0.990	1.072	1.033	1.111
<i>R</i> ₁ (<i>I</i> > 2.00σ(<i>I</i>))	0.0743	0.0497	0.0824	0.0522
<i>R</i> (all data)	0.1685	0.0553	0.0882	0.0647
w <i>R</i> ₂ (all data)	0.1868	0.1259	0.2888	0.1586

SQUEEZE routine in PLATON for **1-PMo₁₂**.^{19e} The details of the crystallographic data for **1-PMo₁₂**, **2-PF₆**, **3-PMo₁₂PF₆**, and **4-OTf** are listed in Table 1.

Abbreviations

L _{Cl}	P(<i>p</i> -ClPh) ₃
L _F	P(<i>p</i> -FPh) ₃
1-PMo₁₂	[{(AuL _{Cl}) ₂ (μ-OH)} ₂] ₃ [α-PMo ₁₂ O ₄₀] ₂ ·3EtOH
2-PF₆	[{(AuL _{Cl}) ₃ (μ ₃ -O)} ₂](PF ₆) ₂ ·4CH ₂ Cl ₂
2	[{(AuL _{Cl}) ₃ (μ ₃ -O)} ₂] ²⁺
3-PMo₁₂PF₆	[{(AuL _{Cl}) ₄ (μ ₄ -O)} ₂][α-PMo ₁₂ O ₄₀]PF ₆
3	[{(AuL _{Cl}) ₄ (μ ₄ -O)} ₂] ²⁺
4-PMo₁₂	[{(AuL _F) ₂ (μ-OH)} ₂] ₃ [α-PMo ₁₂ O ₄₀] ₂ ·3EtOH
4-OTf	[{(AuL _F) ₂ (μ-OH)} ₂](OTf) ₂ ·0.5Et ₂ O
5-PW₁₂	[{Au(PPh ₃) ₃ (μ ₄ -O)} ₃][α-PW ₁₂ O ₄₀] ₂ ·4EtOH
6-PW₁₂	[{Au{P(<i>o</i> -MePh) ₃ } ₄ (μ ₄ -O)} ₃][α-PW ₁₂ O ₄₀] ₂
6-BF₄	[{Au{P(<i>o</i> -MePh) ₃ } ₄ (μ ₄ -O)} ₃](BF ₄) ₂

Acknowledgements

This work was supported by JSPS KAKENHI Grant number 22550065, by a grant from the Research Institute for Integrated Science, Kanagawa University (RIIS201505), and also by the Strategic Research Base Development Program for Private Universities of the Ministry of Education, Culture, Sports, Science and Technology of Japan.

References

- (a) M. T. Pope and A. Müller, *Angew. Chem., Int. Ed. Engl.*, 1991, **30**, 34–48; (b) M. T. Pope, *Heteropoly and Isopoly Oxometalates*, Springer-Verlag, New York, 1983; (c) A. Proust, R. Thouvenot and P. Gouzerh, *Chem. Commun.*, 2008, 1837–1852; (d) B. Hasenknopf, K. Micoine, E. Lacôte, S. Thorimbert, M. Malacria and R. Thouvenot, *Eur. J. Inorg. Chem.*, 2008, 5001–5013; (e) D. Laurencin, R. Thouvenot, K. Boubekour, F. Villain, R. Villanneau, M.-M. Rohmer, M. Bernard and A. Proust, *Organometallics*, 2009, **28**, 3140–3151; (f) D.-L. Long, R. Tsunashima and L. Cronin, *Angew. Chem., Int. Ed.*, 2010, **49**, 1736–1758; (g) K. Nomiya, Y. Sakai and S. Matsunaga, *Eur. J. Inorg. Chem.*, 2011, 179–196.
- (a) M. Schulz-Dobrick and M. Jansen, *Eur. J. Inorg. Chem.*, 2006, 4498–4502; (b) S. Uchida and N. Mizuno, *Coord. Chem. Rev.*, 2007, **251**, 2537–2546.
- R. Noguchi, A. Hara, A. Sugie and K. Nomiya, *Inorg. Chem. Commun.*, 2006, **9**, 355–359.
- (a) K. Nomiya, T. Yoshida, Y. Sakai, A. Nanba and S. Tsuruta, *Inorg. Chem.*, 2010, **49**, 8247–8254; (b) T. Yoshida, K. Nomiya and S. Matsunaga, *Dalton Trans.*, 2012, **41**, 10085–10090; (c) T. Yoshida, S. Matsunaga and K. Nomiya, *Dalton Trans.*, 2013, **42**, 11418–11425; (d) T. Yoshida, Y. Yasuda, E. Nagashima, H. Arai, S. Matsunaga and K. Nomiya, *Inorganics*, 2014, **2**, 660–673; (e) T. Yoshida, S. Matsunaga and K. Nomiya, *Chem. Lett.*, 2013, **42**, 1487–1489; (f) H. Arai, T. Yoshida, E. Nagashima, A. Hatayama, S. Horie, S. Matsunaga and K. Nomiya, *Organometallics*, 2016, **35**, 1658–1666; (g) T. Yoshida, E. Nagashima, H. Arai, S. Matsunaga and K. Nomiya, *Z. Anorg. Allg. Chem.*, 2015, **641**, 1688–1695.
- (a) H. Schmidbaur and A. Schier, *Chem. Soc. Rev.*, 2012, **41**, 370–412; (b) K. Angermaier and H. Schmidbaur, *Inorg. Chem.*, 1994, **33**, 2069–2070; (c) K. Angermaier and H. Schmidbaur, *Chem. Ber.*, 1994, **127**, 2387–2391; (d) H. Schmidbaur and A. Schier, *Chem. Soc. Rev.*, 2008, **37**, 1931–1951; (e) M. C. Gimeno and A. Laguna, *Chem. Soc. Rev.*, 2008, **37**, 1952–1966.
- (a) H. G. Raubenheimer and H. Schmidbaur, *Organometallics*, 2012, **31**, 2507–2522; (b) E. S. Stoyanov, G. Gunbas, N. Hafezi, M. Mascal, I. V. Stoyanova, F. S. Tham and C. A. Reed, *J. Am. Chem. Soc.*, 2012, **134**, 707–714.
- (a) D. J. Gorin and F. D. Toste, *Nature*, 2007, **446**, 395–403; (b) A. S. K. Hashmi, *Chem. Rev.*, 2007, **107**, 3180–3211; (c) Z. Li, C. Brouwer and C. He, *Chem. Rev.*, 2008, **108**, 3239–3265; (d) A. S. K. Hashmi and M. Rudolph, *Chem. Soc. Rev.*, 2008, **37**, 1766–1775; (e) D. J. Gorin, B. D. Sherry and F. D. Toste, *Chem. Rev.*, 2008, **108**, 3351–3378; (f) H. Schmidbaur and A. Schier, *Z. Naturforsch., B: Chem. Sci.*, 2011, **66**, 329–350; (g) M. Rudolph and A. S. K. Hashmi, *Chem. Soc. Rev.*, 2012, **41**, 2448–2462; (h) D. Hueber, M. Hoffmann, B. Louis, P. Pale and A. Blanc, *Chem. – Eur. J.*, 2014, **20**, 3903–3907; (i) S. Sengupta and X. Shi, *ChemCatChem*, 2010, **2**, 609–619; (j) M. P. de Almeida and S. A. C. Carabineiro, *ChemCatChem*, 2012, **4**, 18–29; (k) N. Dupré, C. Brazel, L. Fensterbank, M. Malacria, S. Thorimbert, B. Hasenknopf and E. Lacôte, *Chem. – Eur. J.*, 2012, **18**, 12962–12965.
- (a) B. D. Sherry and F. D. Toste, *J. Am. Chem. Soc.*, 2004, **126**, 15978–15979; (b) B. D. Sherry, L. Maus, B. N. Laforteza and F. D. Toste, *J. Am. Chem. Soc.*, 2006, **128**, 8132–8133; (c) K. Sakaguchi, T. Okada, T. Shinada and Y. Ohfuné, *Tetrahedron Lett.*, 2008, **49**, 25–28; (d) P. Mauleón, J. L. Krinsky and F. D. Toste, *J. Am. Chem. Soc.*, 2009, **131**, 4513–4520.
- (a) A. N. Nesmeyanov, E. G. Perevalova, Y. T. Struchkov, M. Y. Antipin, K. I. Grandberg and V. P. Dyadchenko, *J. Organomet. Chem.*, 1980, **201**, 343–349; (b) H. Schmidbaur, S. Hofreiter and M. Paul, *Nature*, 1995, **377**, 503–504.
- C. Rocchiccioli-Deltcheff, R. Thouvenot and R. Franck, *Spectrochim. Acta, Part A*, 1976, **32**, 587–597.
- (a) S. Wang and J. P. Fackler Jr., *Inorg. Chem.*, 1990, **29**, 4404–4407; (b) A. Sladek and H. Schmidbaur, *Chem. Ber.*, 1995, **128**, 907–909; (c) J. M. López-de-Luzuriaga, A. Sladek, W. Schneider and H. Schmidbaur, *Chem. Ber./Recl.*, 1997, **130**, 641–646; (d) J. Chen, T. Jiang, G. Wei, A. A. Mohamed, C. Homrighausen, J. A. Krause Bauer, A. E. Bruce and M. R. M. Bruce, *J. Am. Chem. Soc.*, 1999, **121**, 9225–9226; (e) A. A. Mohamed, J. Chen, A. E. Bruce, M. R. M. Bruce,

- J. A. Krause Bauer and D. T. Hill, *Inorg. Chem.*, 2003, **42**, 2203–2205; (f) A. Battisti, O. Bellina, P. Diversi, S. Losi, F. Marchetti and P. Zanello, *Eur. J. Inorg. Chem.*, 2007, 865–875.
- 12 A. F. Wells, *Structural Inorganic Chemistry*, Oxford University Press, London, 4th edn, 1975, p. 1022.
- 13 A. Bondi, *J. Phys. Chem.*, 1964, **68**, 441–451.
- 14 F. Canales, C. Gimeno, A. Laguna and M. D. Villacampa, *Inorg. Chim. Acta*, 1996, **244**, 95–103.
- 15 (a) P. G. Jones, G. M. Sheldrick and E. Hadicke, *Acta Crystallogr., Sect. B: Struct. Crystallogr. Cryst. Chem.*, 1980, **36**, 2777–2779; (b) H. Schmidbaur, A. Kolb, E. Zeller, A. Schier and H. Beruda, *Z. Anorg. Allg. Chem.*, 1993, **619**, 1575–1579; (c) F. Scherbaum, A. Grohmann, G. Muller and H. Schmidbaur, *Angew. Chem., Int. Ed. Engl.*, 1989, **28**, 463–465; (d) F. Scherbaum, A. Grohmann, B. Huber, C. Krüger and H. Schmidbaur, *Angew. Chem., Int. Ed. Engl.*, 1988, **27**, 1544–1546; (e) A. Grohmann, J. Riede and H. Schmidbaur, *Nature*, 1990, **345**, 140–142; (f) A. Schier, A. Grohmann, J. M. Lopez-de-Luzuriaga and H. Schmidbaur, *Inorg. Chem.*, 2000, **39**, 547–554; (g) H. Schmidbaur, G. Weidenhiller and O. Steigelmann, *Angew. Chem., Int. Ed. Engl.*, 1991, **30**, 433–435; (h) E. Zeller and H. Schmidbaur, *J. Chem. Soc., Chem. Commun.*, 1993, 69–70; (i) F. Canales, M. C. Gimeno, P. G. Jones and A. Laguna, *Angew. Chem., Int. Ed. Engl.*, 1994, **33**, 769–770.
- 16 Y. Tang and B. Yu, *RSC Adv.*, 2012, **2**, 12686–12689.
- 17 (a) A. Hamel, N. W. Mitzel and H. Schmidbaur, *J. Am. Chem. Soc.*, 2001, **123**, 5106–5107; (b) H. Schmidbaur, A. Hamel, N. W. Mitzel, A. Schier and S. Nogai, *Proc. Natl. Acad. Sci. U. S. A.*, 2002, **99**, 4916–4921.
- 18 E. O. North and W. Haney, *Inorg. Synth.*, 1939, **1**, 127.
- 19 (a) G. M. Sheldrick, *Acta Crystallogr., Sect. A: Found. Crystallogr.*, 1990, **46**, 467–473; (b) G. M. Sheldrick, *SHELXL-97 program for crystal structure refinement*, University of Göttingen, Göttingen, Germany, 1997; (c) G. M. Sheldrick, *SADABS*, University of Göttingen, Göttingen, Germany, 1996; (d) Molecular Structure Corporation & Rigaku, *CrystalClear, Version 1.4. MSC*, 9009 New Trails Drive, The Woodlands, TX 77381-5209, USA, and Rigaku Corporation, 3-9-12 Akishima, Tokyo, Japan, 2000; (e) A. L. Spek, *Acta Crystallogr., Sect. A: Found. Crystallogr.*, 1990, **46**, c34.



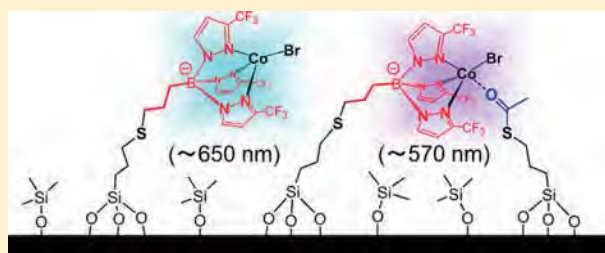
Immobilization of a Boron Center-Functionalized Scorpionate Ligand on Mesoporous Silica Supports for Heterogeneous Tp-Based Catalysts

Ayaka Nakamizu, Takeshi Kasai, Jun Nakazawa,* and Shiro Hikichi*^{1b}

Department of Material and Life Chemistry, Faculty of Engineering, Kanagawa University, Kanagawa-ku, Yokohama 221-8686, Japan

Supporting Information

ABSTRACT: To develop novel immobilized metallocomplex catalysts, allyltris(3-trifluoromethylpyrazol-1-yl)borate (allyl-Tp^{CF3}) was synthesized. A boron-attached allyl group reacts with thiol to afford the desired mesoporous silica-immobilized Tp^{CF3}. Cobalt(II) is an efficient probe for estimating the structures of the immobilized metallocomplexes. The structures of the formed cobalt(II) complexes and their catalytic activity depended on the density of the organic thiol groups and on the state of the remaining sulfur donors on the supports.



1. INTRODUCTION

Hydrotris(pyrazolyl)borates (Tp^R) and related multidentate “scorpionate” ligands have been utilized extensively in coordination chemistry, with applications in areas such as organometallic and biomimetic catalysis.¹ An attractive characteristic of Tp^R is the feasibility for molecular designing by incorporation of the appropriate substituent groups on the pyrazolyl rings. Both electronic and structural properties of the substituent groups on the R³–R⁵ positions of the pyrazolyl rings influence the reactivity at the metal center of the resulting complex.^{1,2} Recently, interest in the modification of the boron center of Tp^R has increased. Replacement of a boron-attached hydride to a suitable functional group might yield a corresponding boron center-functionalized ligand (FG-Tp^R) that is applicable to various conjugate materials, with retention of the facially capping tridentate metal-supporting scaffolds.^{3–5}

Immobilization of FG-Tp^R on organic polymer-based supports has been achieved. Notably, the molecular structures of Tp^R–metal complexes correlate with the flexibility of the base polymer.⁵ On the flexible polymer support, metalation of the immobilized Tp^R yields a coordinatively saturated [M(Tp^R)₂] species because the flexible polymer backbone results in two approaching Tp^R moieties. Although the formed [M(Tp^R)₂] sites function as cross-linking points of the polymers,^{3b} these sites appear to be catalytically inert. By contrast, Tp^R can be immobilized while retaining a high-dispersion state on the rigid supports. In fact, the Tp ligand immobilized on the less flexible, highly cross-linked polystyrene resin support yields the desired coordinatively unsaturated [M(Tp^R)(L)_n] species, some of which exhibit catalytic activity.^{5c} Even in the successful resin-supported compounds, the correlation between the structure of the formed metal–Tp^R complexes and the local environments of the immobilized Tp^R ligands (which are affected by the morphology of the support,

density of Tp^R, interaction of metals with functional groups other than immobilized ligands, etc.) has never been examined. A few Tp^R-based heterogeneous metallocomplex catalysts in which the boron centers of Tp^R are not functionalized (i.e., in which a hydride group remains) and silica and resin beads are used as supports have been reported thus far.⁶ Also, iron complexes of tris(pyrazolyl)methane, which is a carbon-centered Tp analogue, have been immobilized on zeolite and carbon materials with similar manner, and catalytic activities of the immobilized complexes are higher than those of the corresponding homogeneous parent.⁷ By contrast, immobilization of FG-Tp^R on rigid inorganic supports has not been reported so far.⁸ Controlling the three-dimensional environments surrounding the immobilized FG-Tp^R and its metallocomplexes can be achieved using these inorganic supports with an ordered structure. In this context, we have been developing ordered mesoporous, silica-immobilized metallocomplex catalysts based on FG-Tp^R, as reported herein.

2. RESULTS AND DISCUSSION

2.1. Synthesis and Characterization of Allyl-Tp^{CF3} and Its Complexes of Cobalt(II). Our imidazole-based scorpionate analogue, allylbis(imidazolyl)methylborate (L^{allyl}), can be immobilized onto thiol-functionalized inorganic supports using thiol–ene coupling.⁹ A similar ligand immobilization method has also been used with the N,N,O-type carbon-based scorpionate compound.^{8c} Therefore, we have designed an allyl-functionalized tris(3-trifluoromethylpyrazol-1-yl)borate (allyl-Tp^{CF3}) as a metal-supporting ligand for a biomimetic

Received: January 10, 2017

Accepted: March 6, 2017

Published: March 17, 2017

oxidation catalyst because fluoroalkyl groups resist oxidation.¹⁰ Thus far, a nonsubstituted pyrazole-based ligand, allyl-Tp^H, has been synthesized by Camerano et al.¹¹ Our target ligand, allyl-Tp^{CF₃}, can be synthesized in a similar manner: condensation of allylbis(alkoxy)borane with two equiv of 3-trifluoromethylpyrazole (pz^{CF₃}H) and nucleophilic addition of a potassium salt of pz^{CF₃}.

Before immobilization of the synthesized allyl-Tp^{CF₃} onto inorganic supports, we examined coordination properties of the ligand toward cobalt(II) and characterized the resulting complexes. We selected cobalt(II) because of its usefulness as a structural probe stemming from the rich chemistry associated with the correlation between coordination geometries of cobalt(II) centers and their UV–vis spectral patterns. Reaction of the potassium salt of allyl-Tp^{CF₃} and CoBr₂·6H₂O in tetrahydrofuran (THF) yielded a blue solution. From this solution, blue crystalline solids of a bromide complex, [CoBr(allyl-Tp^{CF₃})] (1), were obtained as the major product. In addition, a small amount of a pale-pink compound, the homoleptic complex [Co(allyl-Tp^{CF₃})₂] (2), was also obtained. The molecular structures of 1 and 2 were determined using X-ray crystallography (Figure 1). The geometries of the cobalt(II)

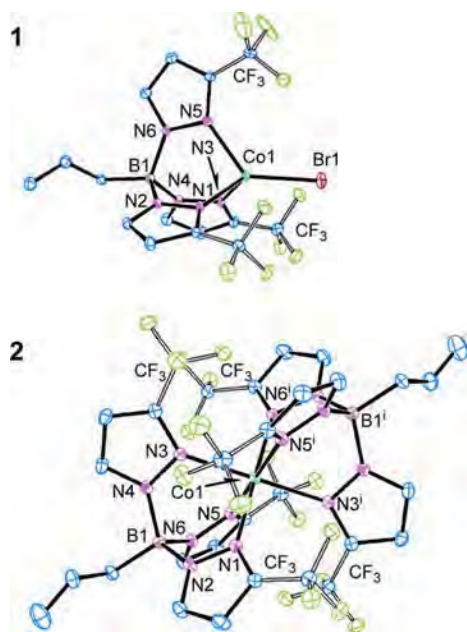


Figure 1. ORTEP drawings of complexes 1 and 2 at the 30% probability level. For clarity, covalent bonds in CF₃ groups are displayed by white lines and the hydrogen atoms are omitted.

centers of 1 and 2 were pseudotetrahedral and octahedral, respectively. In both 1 and 2, the allyl-Tp^{CF₃} coordinated to the cobalt(II) centers in a facially capping tridentate mode through three pyrazolyl nitrogen donors. No flipping from 3-CF₃-pyrazolyl to 5-CF₃-pyrazolyl occurred.¹² The allyl groups in 1 and 2 did not coordinate to the cobalt centers, although coordination of a boron-attached allyl group in a hybrid scorpionate ligand, [(allyl)B(pz^H)₂(CH₂PPh₂)][−], to an iridium(I) center has been reported by Camerano et al.¹³ Compounds 1 and 2 retained their molecular structures when dissolved in appropriate solvents, as indicated by the similarity of the spectral features of visible-light absorption by the solutions (1 in CH₂Cl₂ and 2 in THF) and the solids. Reaction of allyl-

Tp^{CF₃} with Co(OAc)₂·4H₂O yielded a violet-colored compound 3, which exhibited a λ_{max} of approximately 580 nm in both solid and solution states.¹⁴ Although attempts to obtain single crystals suitable for X-ray analysis were not successful, compound 3 is tentatively assigned as a κ²-acetate complex with a penta-coordinated cobalt(II) center.

2.2. Synthesis and Characterization of Immobilized Cobalt Complex Catalysts.

Allyl-Tp^{CF₃} was anchored onto organothiol-functionalized silica using a thiol–ene coupling reaction. As we reported previously, the structural properties of the support, such as the support surface morphology and the loading density of the organic linker group, are the dominant factors controlling the structure and performance of the resulting metallocomplex active sites of the immobilized catalysts.^{15–17} Therefore, in this study, SBA-15-type mesoporous SiO₂ with controlled thiol group (SBA^{SH}) loadings was used as the support. This support was prepared through one-pot condensation of tetraethoxysilane (TEOS) and 3-mercaptopropyltrimethoxysilane (MPTMS) in the presence of a polymer micelle template.^{16–18} The condensation ratios of TEOS and MPTMS were controlled as TEOS:MPTMS = (100 − *x*):*x*, where *x* = 0.5 or 1.0. The resultant thiol-functionalized SBA-15-type supports (SBA^{SH}(*x*)), which were obtained by removing the template using Soxhlet extraction, had a desired mesoporous structure, as confirmed by XRD analysis and N₂ isotherm absorption/desorption behavior. Remaining Si–OH groups on the surface of the mesopore walls were end-capped by treatment with 1,1,1,3,3,3-hexamethyldisilazane (HMDS) at 323 K. The end-capping of the Si–OH groups led to a decrease in the acidity and an increase in the hydrophobicity of the silica support; these characteristics should avoid degradation of the Tp^{CF₃} moiety through hydrolysis of the B–N linkages. The loading amount of the thiol groups was consistent with the value of *x* estimated by ¹H NMR analysis of the alkyl groups. The densities of the loaded thiol on SBA^{SH}(*x*) were approximately 0.06 molecules/nm² for *x* = 0.5 and 0.12 molecules/nm² for *x* = 1.0.

The coupling reaction of SBA^{SH}(*x*) with a CHCl₃ solution of allyl-Tp^{CF₃}, which gave SBA^{SH-Tp}(*x*), was initiated by adding a small amount of AIBN under heating. The immobilized amount of Tp^{CF₃} for SBA^{SH-Tp}(0.5) was approximately the same as the loadings of thiol groups. For SBA^{SH-Tp}(1.0), some of the loaded thiol groups were not connected with Tp^{CF₃}. Further reaction of the remaining thiol groups for SBA^{SH-Tp}(1.0) with additional allyl-Tp^{CF₃} did not occur. The steric bulkiness of allyl-Tp^{CF₃} resulted in a saturation of the ligand loadings. Therefore, to prevent the formation of thiolato complexes, the remaining thiol groups were transformed to thioacetate ester by the reaction with acetyl chloride and the resultant supports were named as SBA^{SAc-Tp}(*x*).

Reaction of the Tp^{CF₃}-anchored supports with an MeCN solution of CoBr₂·6H₂O yielded the corresponding immobilized cobalt complex catalysts Co/SBA^{SH-Tp}(*x*) (4; *x* = 0.5 and 5; *x* = 1.0) and Co/SBA^{SAc-Tp}(*x*) (4'; *x* = 0.5 and 5'; *x* = 1.0) (Scheme 1). Loading amounts of the cobalt ion on the catalysts varied depending on the initial SH loadings and on the state of the non-Tp-anchored sulfur groups as SH or SAc (see Table S2). Coordination environments of the cobalt(II) center of the immobilized complexes were explored using diffuse reflectance UV–vis spectrophotometry; the results are shown in Figure 2. Comparison of the spectral patterns of the immobilized complexes and those of 1–3 in the solid state revealed the

Scheme 1. Preparation of the Supports and Catalysts

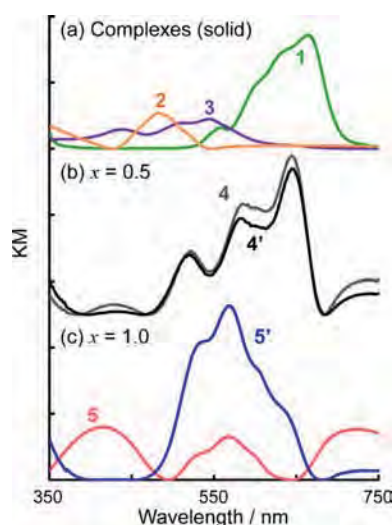
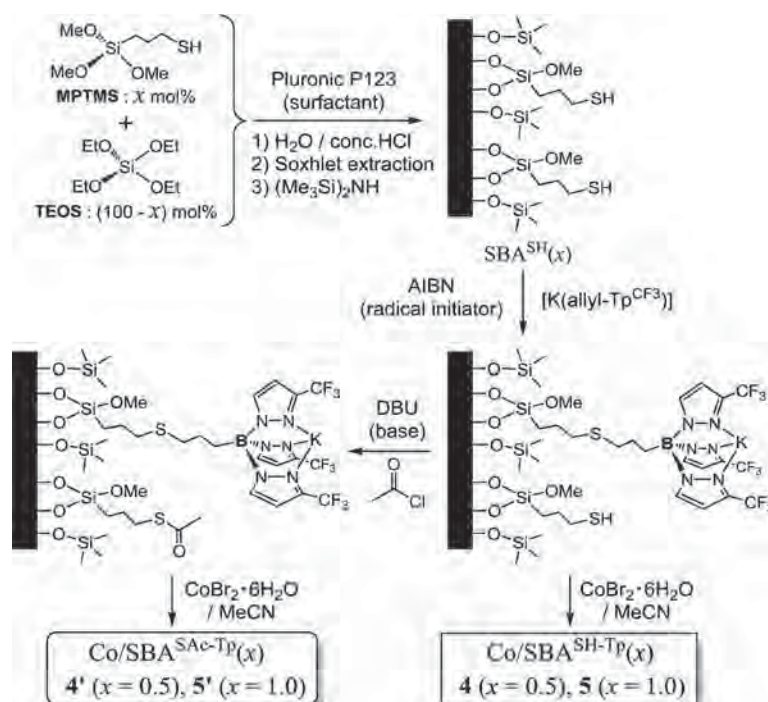


Figure 2. Diffuse-reflectance UV-vis spectra of the solid of the cobalt complexes 1–3 (a) and the immobilized cobalt complex catalysts with an initial thiol-loading ratio with $x = 0.5$ (b) and 1.0 (c).

coordination number of the cobalt(II) centers of the immobilized complexes.

For the lower thiol loading supports (where $x = 0.5$), a tetrahedral cobalt(II) species was mainly formed, as suggested by the similarity between the spectral patterns of 1 and those of the catalysts 4 and 4'. Although the loading amounts of cobalt and the states of the remaining sulfur groups on 4 and 4' were somewhat different, the similar spectral patterns of 4 and 4' indicated that the dispersive immobilization of Tp^{CF_3} resulted in the formation of the tetrahedral cobalt species.

The spectral patterns of the higher-thiol-loaded catalysts ($x = 1.0$) clearly differed from that of the catalysts with $x = 0.5$ and

that of tetrahedral complex 1. The spectrum of 5 ($\text{SBA}^{\text{SH-Tp}}$ derivative) appears to contain both hexa- and penta-coordinated cobalt(II), similar to the mixture of 2 and 3. The cobalt loadings on 5 were higher than the amounts of the immobilized Tp^{CF_3} (see Table S2). Notably, only trace amounts of cobalt were immobilized onto the reaction of non- Tp^{CF_3} -anchored support $\text{SBA}^{\text{SH}}(1.0)$ and the MeCN solution of $\text{CoBr}_2 \cdot 6\text{H}_2\text{O}$. Therefore, the co-existence of Tp^{CF_3} and the thiol groups would lead to the formation of some multinuclear cobalt complexes on the support. By contrast, the UV-vis spectrum of the $\text{SBA}^{\text{SAC-Tp}}$ derivative 5' suggested that the major species was the penta-coordinate species and that small amounts of hexa- and tetra-coordinate species also existed. From the densities of the loaded thiol groups, their average distances were estimated to be 2.9 nm for $\text{SBA}^{\text{SH}}(1.0)$ and 4.1 nm for $\text{SBA}^{\text{SH}}(0.5)$. In such situations, the immobilized Tp^{CF_3} appears to be isolated even on $\text{SBA}^{\text{SH}}(1.0)$, and it might be difficult to access the other groups (SH, SAc, and Tp^{CF_3}) of the formed $\text{Tp}^{\text{CF}_3}\text{Co}$ moieties on the supports ($\text{SBA}^{\text{SH-Tp}}$ and $\text{SBA}^{\text{SAC-Tp}}$). However, the location of the immobilized complexes was not a flat surface but a curved inner wall of the straight pore. As a result, the distances between the functional groups and the cobalt center of $\text{Tp}^{\text{CF}_3}\text{Co}$ were sufficiently small for them to coordinate and form the penta-coordinate complexes. Therefore, the structures of the immobilized complexes were affected by the structures of the supports, the density of the organic functional groups, and the state of the remaining sulfur donors.

We also examined $\text{Co}(\text{OAc})_2 \cdot 4\text{H}_2\text{O}$ as the metal source instead of $\text{CoBr}_2 \cdot 6\text{H}_2\text{O}$ (Table S2 and Figure S6). In the reaction of the non- Tp^{CF_3} -immobilized support SBA^{SH} with an MeCN solution of $\text{Co}(\text{OAc})_2 \cdot 4\text{H}_2\text{O}$, some cobalt species were anchored on the support. By contrast, no cobalt species was anchored onto $\text{SBA}^{\text{SH}}(0.5)$ when $\text{CoBr}_2 \cdot 6\text{H}_2\text{O}$ was used as a precursor. Additionally, the reaction of $\text{SBA}^{\text{SAC-Tp}}(x)$ with an

MeCN solution of $\text{Co}(\text{OAc})_2 \cdot 4\text{H}_2\text{O}$ resulted in the immobilized cobalt ions were in excess of the amount of the anchored Tp^{CF_3} . The spectral patterns of the cobalt species on each of the supports [i.e., $\text{SBA}^{\text{SH}}(0.5)$, $\text{SBA}^{\text{SH}-\text{Tp}^{\text{CF}_3}}(0.5 \text{ and } 1.0)$, and $\text{SBA}^{\text{SAC}-\text{Tp}^{\text{CF}_3}}(0.5 \text{ and } 1.0)$ shown in Figure S6] varied depending on the anion of the precursor. These different behaviors of the cobalt species when anchoring to the functionalized supports imply that the counteranions of cobalt(II) dominate control of the structure of the immobilized cobalt compounds. The acetate anions tend to become bridging ligands that yield multinuclear cobalt species that interact with the Tp^{CF_3} and even with the SH groups on the supports.

2.3. Correlation between the Structure and Activity of Immobilized Cobalt Complex Catalysts. Substrate-oxidizing activities of the obtained immobilized cobalt complex catalysts were examined by using cyclohexene as a substrate.

First, we compared the activity of the catalysts prepared from $\text{CoBr}_2 \cdot 6\text{H}_2\text{O}$ to clarify the performance of the cobalt centers supported by the Tp^{CF_3} scaffold. When aqueous H_2O_2 was used as the oxidant, the immobilized catalysts exhibited catalase-like H_2O_2 degradation activity, with the formation of O_2 bubbles. On the contrary, when *tert*-BuOOH was used as the oxidant, catalytic allylic oxygenation of cyclohexene occurred. No leaching of the cobalt species was observed under these reaction conditions. The major product was dialkylperoxide in all reactions, which indicated the reactions proceeded through a Haber–Weiss mechanism. Similar reactivity toward cyclohexene oxidation with *tert*-BuOOH has been observed on a cobalt-based MOF catalyst.¹⁹ The turnover number (TON) order of the cobalt centers was $4' > 5' > 4 > 5 > 1$ (homogeneous conditions). It is worth noting that the immobilized $\text{Tp}^{\text{CF}_3}\text{Co}$ complex catalysts exhibited higher activity compared with the homogeneous cobalt species derived from genuine cobalt(II) salts ($\text{CoBr}_2 \cdot 6\text{H}_2\text{O}$ and $\text{Co}(\text{OAc})_2 \cdot 4\text{H}_2\text{O}$; Table S3). The higher activities of the immobilized catalysts are attributed to the suppression of bimolecular reactions that lead to catalyst decomposition. The differences in the TONs of the immobilized catalysts indicate that the structures of the cobalt centers affect the catalytic efficiencies. The most active catalyst was $4'$, which was composed of isolated $\text{Tp}^{\text{CF}_3}\text{Co}$ sites without free thiol groups. The remaining thiol groups suppress the catalytic activity, as clearly demonstrated by comparisons with the activities of 5 and $5'$. The lowest activity of 5 suggests that the hexa-coordinated cobalt center is less reactive than the coordinatively unsaturated tetra- and penta-coordinated cobalt species formed on the other immobilized catalysts. Catalyst $5'$, the second-most active catalyst, exhibited better selectivity toward epoxidation than that observed for $4'$ (Figure 3).

The activities of the immobilized cobalt complex catalysts derived from $\text{Co}(\text{OAc})_2 \cdot 4\text{H}_2\text{O}$ were also examined (Table S3). The non- Tp^{CF_3} -coordinated cobalt species formed on SBA^{SH} also exhibited better activity and epoxidation selectivity. In the catalysts derived from $\text{Co}(\text{OAc})_2 \cdot 4\text{H}_2\text{O}$, the supports of the most active and the second-most active catalysts were $\text{SBA}^{\text{SAC}-\text{Tp}^{\text{CF}_3}}(0.5)$ and $\text{SBA}^{\text{SH}-\text{Tp}^{\text{CF}_3}}(1.0)$, respectively. Trends of the product selectivity of these catalysts were similar to those observed for $4'$ and $5'$ (derived from $\text{CoBr}_2 \cdot 6\text{H}_2\text{O}$). The catalysts supported on the highly dispersed Tp^{CF_3} (i.e., $x = 0.5$) exhibited a strong radical character that is sufficient to induce the oxygenation of the allylic position. For the catalysts formed on the support with higher loadings of Tp^{CF_3} and thiol (i.e., $x = 1.0$), a small increase in epoxide selectivity was observed.

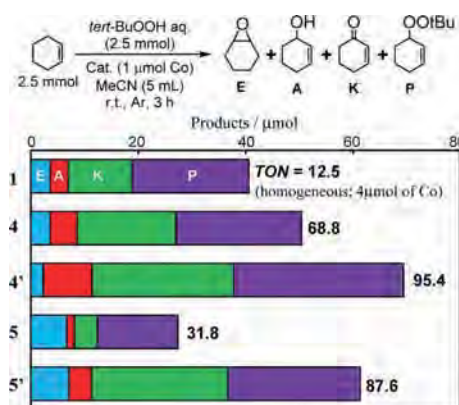


Figure 3. Cyclohexene oxidation with TBHP catalyzed by the compounds derived from $\text{CoBr}_2 \cdot 6\text{H}_2\text{O}$. TONs were estimated on the basis of the oxidizing equivalent of the products according to the following equation: $\text{TON} = (\text{cyclohexene oxide (E)} + \text{cyclohexen-1-ol (A)} + 2 \times \text{cyclohexen-1-one (K)} + \text{tert-butyl-cyclohexenyl-1-peroxide (P)})/\text{cobalt}$.

Therefore, the local structure of the functionalized supports might be a controlling factor for the structures and activities of the metal centers. In the case of the cobalt-acetate-based catalysts, however, the nature of acetate makes selective formation of the isolated cobalt centers supported by Tp^{CF_3} difficult.

3. CONCLUSIONS

The boron-functionalized scorpionate ligand was successfully immobilized onto mesoporous silica through covalent bonds. The structures of the formed cobalt(II) complexes and their catalytic activities depended on the density of the organic thiol groups and on the state of the remaining sulfur donors on the inner wall of the mesopores. Additionally, the nature of the anions of the metal sources was a dominant factor affecting the structures of the immobilized metal complexes. As demonstrated herein, cobalt(II) is an efficient probe for estimating the structures of the immobilized species.

4. EXPERIMENTAL SECTION

4.1. Materials and Methods. All solvents used for the synthesis of the ligand and catalytic reaction (THF, toluene, CH_2Cl_2 , and MeCN) were purified over a Glass Contour Solvent Dispensing System under an Ar atmosphere. Other reagents of the highest grade that were commercially available were used without further purification. Atomic absorption analysis was performed on a Shimadzu AA-6200. Elemental analysis was performed on a Perkin-Elmer CHNS/O Analyzer 2400II. GC analysis was performed on a Shimadzu GC2010 gas chromatograph with an Rtx-5 column (Restek, length = 30 m, i.d. = 0.25 mm, and thickness = 0.25 μm). IR spectra were recorded on a JASCO FT/IR 4200 spectrometer. NMR spectra were recorded on a JEOL ECA-600 spectrometer. UV–vis spectra of solution samples were recorded on a JASCO V650 spectrometer, and solid reflectance spectra were recorded on the same instrument with a PIN-757 integrating sphere attachment for solid. Nitrogen sorption studies were performed at liquid nitrogen temperature (77 K) using Micromeritics TriStar 3000. Before the adsorption experiments, the samples were outgassed under reduced pressure for 3 h at 333 K.

4.2. Synthesis of Potassium Salt of Allyltris(3-trifluoromethylpyrazol-1-yl)borate (= [K(allyl-Tp^{CF3})₃]). Potassium salt of 3-trifluoromethylpyrazole (=pz^{CF3}K) was obtained by the condensation reaction of KOH (0.33 g, 5.0 mmol) with pz^{CF3}H (0.68 g, 5.0 mmol) in dry methanol (30 mL) at ambient temperature for 1 h and the volatiles were removed by evaporation. The obtained white solids of pz^{CF3}K, pz^{CF3}H (2.66 g, 19.0 mmol), and allyldiisopropoxyborane (=B(allyl)(OiPr)₂; 1.0 mL, 4.89 mmol) were dissolved in toluene (125 mL) and refluxed for 24 h using Dean–Stark equipment. Crude products obtained by evaporation were washed with pentane. An analytically pure product was obtained as a pale yellow solid (0.60 g, 26% yield). ¹H NMR (C₃D₆O, rt): δ (ppm) = 2.40 (d, 2H, CH₂=CHCH₂-), 4.46–4.70 (dd, 2H, CH₂=CHCH₂-), 5.92 (m, 1H, CH₂=CHCH₂-), 6.39 (s, 3H, pz-4H), and 7.34 (s, 3H, pz-5H). ¹³C NMR (THF-*d*₆, rt): δ (ppm) = 30.30 (CH₂=CHCH₂-), 102.16 (pz-4C), 112.54 (CH₂=CHCH₂-), 120.24–125.56 (CF₃), 135.28 (pz-5C), 139.50 (CH₂=CHCH₂-), and 141.82–142.54 (pz-3C). ¹⁹F NMR (C₃D₆O, rt): δ (ppm) = -60.18 (CF₃). ESI-TOF MS (MeOH solution, negative mode): *m/z* = 457 ([M - K]⁻).

4.3. Reaction of [K(allyl-Tp^{CF3})] and CoBr₂·6H₂O (Formation of [Co^{II}Br(allyl-Tp^{CF3})] (1) and [Co^{II}(allyl-Tp^{CF3})₂] (2)). A THF (100 mL) solution of [K(allyl-Tp^{CF3})] (1.00 g, 2.02 mmol) was added slowly to CoBr₂·6H₂O (0.529 g, 2.42 mmol) dissolved in THF (90 mL) at ambient temperature. After stirring for 1 h, volatiles were removed under reduced pressure. The resultant solids were suspended in pentane and then decanted. The resultant solids were dissolved in CH₂Cl₂, and insoluble materials were removed by filtration through a Celite plug. From the filtrate, the volatiles were removed under reduced pressure, and the resultant solids were dissolved in a mixture of CH₂Cl₂ and *n*-hexane. Refrigeration of this solution at 243 K afforded a small amount of pale yellow crystalline solids of the homoleptic complex 2. After the removal of 2 by filtration, the resultant solution was concentrated and stored at 243 K, yielding a blue powder of the desired bromide complex 1 (220 mg, 0.369 mmol, 18% yield). ¹H NMR (CDCl₃, rt): δ (ppm) = 47.00 (s, 3H, pz-4H) and 68.19 (s, 3H, pz-5H). IR (KBr): ν_{C-H} = 3263 cm⁻¹; ν_{B-C} = 1260 cm⁻¹. ESI-TOF MS (MeOH solution, positive mode): *m/z* = 548 [M - Br + MeOH]⁺. UV-vis (CH₂Cl₂, rt): λ (nm (M⁻¹ cm⁻¹)) = 669 (330).

4.4. Reaction of [K(allyl-Tp^{CF3})] and Co(OAc)₂·4H₂O (Formation of [Co^{II}(OAc)(allyl-Tp^{CF3})] (3)). A THF (90 mL) solution of [K(allyl-Tp^{CF3})] (0.870 g, 1.75 mmol) was added slowly to an MeOH (60 mL) solution of Co(OAc)₂·4H₂O (0.371 g, 2.10 mmol) at ambient temperature. After stirring for 1 h, volatiles were removed under reduced pressure. The resultant solids were suspended in pentane and then decanted. The resultant solids were dissolved in CH₂Cl₂, and insoluble materials were removed by filtration through a Celite plug. From the filtrate, the volatiles were removed under reduced pressure, and purple species were obtained from the resultant solids by extraction with MeCN. From this solution, MeCN was removed by evaporation, and the resultant solids were dissolved in a mixture of CH₂Cl₂ and *n*-hexane. Refrigeration of this solution at 243 K yielded reddish purple solids of 3. IR (KBr): ν_{C-H} = 3161 cm⁻¹; ν_{C=O} = 1605 cm⁻¹; ν_{B-C} = 1258 cm⁻¹. UV-vis (CH₂Cl₂, rt): λ (nm (M⁻¹ cm⁻¹)) = 561 (56).

4.5. Preparation of SBA^{SH}(*x*). Thiol-functionalized mesoporous silica supports (=SBA^{SH}(*x*)) were prepared by a similar

manner for the previously reported organoazide-functionalized SBA-15 by Nakazawa and Stack.¹⁸ Condensation ratio of mercaptopropyltrimethoxysilane (=MPTMS; *x* mol % of Si) and tetraethoxysilane (=TEOS; (100 - *x*) mol % of Si) were defined as *x* = 0.5 or 1. In a flask, 8.0 g of the surfactant Pluronic P123 [=triblock copolymer EO₂₀PO₇₀EO₂₀, where EO = poly(ethylene glycol) and PO = poly(propylene glycol)] was placed and then dissolved in 260 mL of water with 40 mL of conc. HCl solution (35 wt %) by stirring at 313 K for 4 h. To the resultant solution, 18.4 mL (81.3 mmol) of TEOS and appropriate amounts of MPTMS (76.0 μL when *x* = 0.5 or 155 μL when *x* = 1.0) were added. The mixture was stirred at 323 K for 24 h and subsequently heated at 363 K for 24 h. Once cooled, the solid product was filtered and washed with deionized H₂O and EtOH. The P123 surfactant was removed using Soxhlet extraction with a mixture of 200 mL of H₂O and 200 mL of EtOH over 24 h. The resultant white solid was dried under vacuum. Then the remaining silanol groups on the as-prepared thiol-functionalized SBA-15 were end-capped by the trimethylsilyl group. A suspension of the dried solid of the precursor of SBA^{SH}(*x*) (5.4 g) and 1,1,1,3,3,3-hexamethyldisilazane (=HMDS; 10 mL) in toluene (100 mL) was stirred at 323 K for 1 h. The resultant solid was collected by filtration then washed with toluene and CH₂Cl₂. Dryness under evacuation yielded 5.3 g of end-capped support, namely, SBA^{SH}(*x*). Loading amounts of the thiol groups were determined using ¹H NMR spectrometry as follows: 10 mg of SBA^{SH}(*x*) was dissolved in 2 mL of D₂O solution containing a small amount of NaOH under heating. To this solution, 10 mg (0.072 mmol) of *p*-nitrophenol was added as an internal standard. The loading amounts of the thiol groups were estimated by a comparison of the integration values of ¹H NMR signals of ethylene and phenyl groups.

4.6. Preparation of SBA^{SH-Tp}(*x*). To a suspension of SBA^{SH}(*x*) (2.0 g) in CHCl₃ (30 mL), [K(allyl-Tp^{CF3})] (180 mg, 0.38 mmol) and AIBN (10 mg) were added. The resultant mixture was refluxed for 6 h. The white solid of SBA^{SH-Tp} was obtained by filtration. The resultant solid was washed with CHCl₃ and then dried under evacuation. The loading amounts of Tp were estimated from the contents of nitrogen (wt % of N) using CHN elemental analysis (data are shown in Table S2).

4.7. Preparation of SBA^{SAC-Tp}(*x*). In 30 mL of toluene, an appropriate amount of SBA^{SH-Tp}(*x*) was suspended. To this suspension, acetyl chloride (2.0 equiv with respect to the loading amounts of thiol) and DBU (2.5 equiv) were added, and the resultant mixture was refluxed for 6 h. The white filtrates of SBA^{SAC-Tp}(*x*) were washed with toluene and then dried under evacuation.

4.8. Preparation of Catalysts. In 20 mL of CH₂Cl₂, 0.20 g of the support [SBA^{SH-Tp}(*x*) or SBA^{SAC-Tp}(*x*)] was suspended. To this suspension, an acetonitrile (10 mL) solution of CoBr₂·6H₂O (13 mg, 0.039 mmol) was added, and the resultant mixture was stirred at room temperature for 2 h. Filtration, washing with MeCN and methanol, and then drying under evacuation yielded a pale blue solid of the catalysts Co/SBA^{SH-Tp}(*x*) (4 (*x* = 0.5) and 5 (*x* = 1.0)) or Co/SBA^{SAC-Tp}(*x*) (4' (*x* = 0.5) and 5' (*x* = 1.0)). Loading amounts of cobalt on the catalysts were determined as follows. The catalyst (10 mg) was dissolved into 1 mL of aqueous solution of KOH (0.04 g/mL) under heating. Then, the solution was acidified with 2 mL of conc. aq. HNO₃ and diluted with H₂O to 50 mL volume.

The solution was passed through syringe filter before being introduced into an atomic absorption spectrometer.

4.9. Catalytic Reactions. Typical procedure for the heterogeneous reaction is as follows: In Schlenk flask, an appropriate amount of the catalyst (1 μmol cobalt on the immobilized catalyst) was suspended in 5 mL of MeCN. Cyclohexene (0.25 mL, 2.5 mmol), nitrobenzene (10 μL , 0.10 mmol; as internal standard), and 70 wt % aqueous *tert*-BuOOH (2.5 mmol) were added to this suspension. All reactions were carried under Ar, and the products were analyzed using GC with an internal standard.

■ ASSOCIATED CONTENT

Supporting Information

The Supporting Information is available free of charge on the ACS Publications website at DOI: 10.1021/acsomega.7b00022.

Characterizations of the SBA supports and the catalysts, comparison of the catalytic activities, spectroscopic data of $[\text{K}(\text{allyl-Tp}^{\text{CF}_3})]$, UV–vis spectra of the solutions of 1–3, diffuse reflectance UV–vis spectra of the immobilized cobalt species derived from $\text{CoBr}_2 \cdot 6\text{H}_2\text{O}$ and $\text{Co}(\text{OAc})_2 \cdot 4\text{H}_2\text{O}$, and crystallographic files in CIF format for 1 and 2 (PDF)

Crystallographic data of cobalt(II) complexes (CIF)

■ AUTHOR INFORMATION

Corresponding Authors

*E-mail: jnaka@kanagawa-u.ac.jp (J.N.).

*E-mail: hikichi@kanagawa-u.ac.jp (S.H.).

ORCID

Shiro Hikichi: 0000-0001-6001-9780

Notes

The authors declare no competing financial interest.

■ ACKNOWLEDGMENTS

This work was supported in part by a Grants-in-Aid for Scientific Research (no. 26420788) and a Strategic Development of Research Infrastructure for Private Universities (no. S1201017) from the Ministry of Education, Culture, Sports, Science, and Technology (MEXT), Japan.

■ REFERENCES

- (1) (a) Trofimenko, S. *Scorpionates—The Coordination Chemistry of Polypyrazolylborate Ligands*; Imperial College Press: London, England, 1999. (b) Pettinari, C. *Scorpionates II: Chelating Borate Ligands*; Imperial College Press: London, England, 2008.
- (2) Hikichi, S.; Kobayashi, C.; Yoshizawa, M.; Akita, M. *Chem.—Asian J.* **2010**, *5*, 2086–2092.
- (3) (a) Reger, D. L.; Gardinier, J. R.; Gemmill, W. R.; Smith, M. D.; Shahin, A. M.; Long, G. J.; Rebbouh, L.; Grandjean, F. *J. Am. Chem. Soc.* **2005**, *127*, 2303–2316. (b) Reger, D. L.; Gardinier, J. R.; Smith, M. D.; Shahin, A. M.; Long, G. J.; Rebbouh, L.; Grandjean, F. *Inorg. Chem.* **2005**, *44*, 1852–1866.
- (4) (a) Kuchta, M. C.; Gemel, C.; Metzler-Nolte, N. *J. Organomet. Chem.* **2007**, *692*, 1310–1314. (b) Kuchta, M. C.; Gross, A.; Pinto, A.; Metzler-Nolte, N. *Inorg. Chem.* **2007**, *46*, 9400–9404. (c) Zagermann, J.; Kuchta, M. C.; Merz, K.; Metzler-Nolte, N. *Eur. J. Inorg. Chem.* **2009**, 5407–5412.
- (5) (a) Qin, Y.; Cui, C.; Jäkle, F. *Macromolecules* **2008**, *41*, 2972–2974. (b) Qin, Y.; Shipman, P. O.; Jäkle, F. *Macromol. Rapid Commun.* **2012**, *33*, 562–567. (c) Desrochers, P. J.; Pearce, A. J.; Rogers, T. R.; Rodman, J. S. *Eur. J. Inorg. Chem.* **2016**, 2465–2473.

- (6) (a) Díaz-Requejo, M. M.; Belderráin, T. R.; Nicasio, M. C.; Pérez, P. J. *Organometallics* **2000**, *19*, 285–289. (b) Díaz-Requejo, M. M.; Belderráin, T. R.; Pérez, P. J. *Chem. Commun.* **2000**, 1853–1854. (c) Casagrande, A. C. A.; Tavares, T. T. d. R.; Kuhn, M. C. A.; Casagrande, O. L., Jr.; dos Santos, J. H. Z.; Teranishi, T. *J. Mol. Catal. A: Chem.* **2004**, *212*, 267–275. (d) Desrochers, P. J.; Besel, B. M.; Corken, A. L.; Evanov, J. R.; Hamilton, A. L.; Nutt, D. L.; Tarkka, R. M. *Inorg. Chem.* **2011**, *50*, 1931–1941.

- (7) (a) Martins, L. M. D. R. S.; Pombeiro, A. J. L. *Eur. J. Inorg. Chem.* **2016**, 2236–2252. (b) Martins, L. M. D. R. S.; Pombeiro, A. J. L. *Coord. Chem. Rev.* **2014**, *265*, 74–88. (c) Martins, L. M. D. R. S.; Martins, A.; Alegria, E. C. B. A.; Carvalho, A. P.; Pombeiro, A. J. L. *Appl. Catal., A* **2013**, *464–465*, 43–50. (d) Martins, L. M. D. R. S.; de Almeida, M. P.; Carabineiro, S. A. C.; Figueiredo, J. L.; Pombeiro, A. J. L. *ChemCatChem* **2013**, *5*, 3847–3856.

- (8) Functionalized carbon-based scorpionate ligands, namely alkynyltris(pyrazolyl)methane, 2,2,2-tris(pyrazolyl)ethanol and allyl-bis(pyrazolyl)acetate, have been immobilized onto silica supports so far: (a) Dördelmann, G.; Pfeiffer, H.; Birkner, A.; Schatzschneider, U. *Inorg. Chem.* **2011**, *50*, 4362–4367. (b) Machado, K.; Mukhopadhyay, S.; Mishra, G. S. *J. Mol. Catal. A: Chem.* **2015**, *400*, 139–146. (c) Hübner, E.; Haas, T.; Burzlaff, N. *Eur. J. Inorg. Chem.* **2006**, 4989–4997.

- (9) Hikichi, S.; Kaneko, M.; Miyoshi, Y.; Mizuno, N.; Fujita, K.; Akita, M. *Top. Catal.* **2009**, *52*, 845–851.

- (10) Oxidation catalysis of cobalt(II) and nickel(II) complexes with $\text{Tp}^{\text{CF}_3, \text{Me}}$ have been reported: (a) Gorun, S. M.; Hu, Z.; Stibrany, R. T.; Carpenter, G. *Inorg. Chim. Acta* **2000**, *297*, 383–388. (b) Nakazawa, J.; Terada, S.; Yamada, M.; Hikichi, S. *J. Am. Chem. Soc.* **2013**, *135*, 6010–6013.

- (11) Camerano, J. A.; Casado, M. A.; Ciriano, M. A.; Oro, L. A. *Dalton Trans.* **2006**, 5287–5293.

- (12) Trofimenko, S.; Calabrese, J. C.; Domaille, P. J.; Thompson, J. S. *Inorg. Chem.* **1989**, *28*, 1091–1101.

- (13) Camerano, J. A.; Casado, M. A.; Ciriano, M. A.; Tejel, C.; Oro, L. A. *Chem.—Eur. J.* **2008**, *14*, 1897–1905.

- (14) Hikichi, S.; Sasakura, Y.; Yoshizawa, M.; Ohzu, Y.; Moro-oka, Y.; Akita, M. *Bull. Chem. Soc. Jpn.* **2002**, *75*, 1255–1262.

- (15) Akashi, T.; Nakazawa, J.; Hikichi, S. *J. Mol. Catal. A: Chem.* **2013**, *371*, 42–47.

- (16) Tsuruta, T.; Yamazaki, T.; Watanabe, K.; Chiba, Y.; Yoshida, A.; Naito, S.; Nakazawa, J.; Hikichi, S. *Chem. Lett.* **2015**, *44*, 144–146.

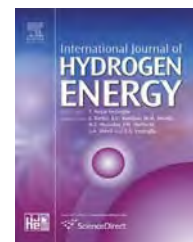
- (17) (a) Nakazawa, J.; Hori, T.; Stack, T. D. P.; Hikichi, S. *Chem.—Asian J.* **2013**, *8*, 1191–1199. (b) Nakazawa, J.; Yata, A.; Hori, T.; Stack, T. D. P.; Naruta, Y.; Hikichi, S. *Chem. Lett.* **2013**, *42*, 1197–1199.

- (18) One-pot synthesis of organoazide-functionalized SBA: (a) Nakazawa, J.; Stack, T. D. P. *J. Am. Chem. Soc.* **2008**, *130*, 14360–14361. (b) Nakazawa, J.; Smith, B. J.; Stack, T. D. P. *J. Am. Chem. Soc.* **2012**, *134*, 2750–2759.

- (19) Tonigold, M.; Lu, Y.; Bredenkötter, B.; Rieger, B.; Bahnmüller, S.; Hitzbleck, J.; Langstein, G.; Volkmer, D. *Angew. Chem., Int. Ed.* **2009**, *48*, 7546–7550.

Available online at www.sciencedirect.com

ScienceDirect

journal homepage: www.elsevier.com/locate/ijhydene

Formation of Ru active species by ion-exchange method for aqueous phase reforming of acetic acid



Toshiaki Nozawa, Yuichi Mizukoshi, Akihiro Yoshida, Shiro Hikichi, Shuichi Naito*

Department of Material and Life Chemistry, Kanagawa University, 3-27-1 Rokkakubashi, Kanagawa-ku, Yokohama, 221-8686, Japan

ARTICLE INFO

Article history:

Received 1 May 2016

Received in revised form

3 October 2016

Accepted 4 October 2016

Available online 15 November 2016

Keywords:

Aqueous phase reforming

Acetic acid

Ruthenium

Zeolite

Ion-exchanging

ABSTRACT

NaY-zeolite was employed as a support of ruthenium catalysts for aqueous phase reforming of acetic acid. Catalytic activities of the supported ruthenium species on NaY-zeolite depended on oxidation state controlled by preparation conditions. Catalyst NaY(exc), whose 5 wt% ruthenium precursors were supported through cation-exchanging process, produced H₂ continuously for 10 h when the catalysts were used without reducing by H₂ prior to usage. Decreasing the loading amounts of ruthenium on NaY(exc) led to improve the selectivity toward complete reforming of acetic acid giving H₂ and CO₂ because of the strong interaction between positively charged ruthenium particle and the support. However, contents of sodium cations controlled by the pH of precursor solutions did not affect the catalytic performances.

© 2016 Hydrogen Energy Publications LLC. Published by Elsevier Ltd. All rights reserved.

Introduction

It has been generally accepted that hydrogen fuel cells are environmentally clean and highly efficient devices for electrical power generation [1–3]. They cannot have, however, a high impact on solving environmental problems without overcoming the shortage of hydrogen production from high-temperature steam reforming of non-renewable hydrocarbon feedstock [4–6]. The full environmental benefit of generating power from hydrogen fuel cells is achieved when hydrogen is produced from renewable sources such as solar power and biomass which are promising major challenges as the global energy generation moves toward a “hydrogen society”.

Fifteen years ago, it was reported for the first time that the liquid phase reactions of methanol, ethylene glycol, glycerol and other oxygenates with water were catalyzed by supported Pt and Ni metals, which can be a model catalytic reaction for biomass conversion [7,8]. The mechanism of H₂ production from ethylene glycol was recognized to involve the cleavages of C–C and C–H bonds to form adsorbed CO followed by water-gas shift to H₂ and CO₂ formation [9,10]. Consequently, a good catalyst for aqueous phase reforming (APR) process must be active in the cleavage of C–C bonds and water-gas shift reaction, but it must inhibit the cleavage of C–O bond and methanation reactions. It has been generally accepted that alcohols such as methanol, ethylene glycol and glycerol, where the C–H bond of each carbon atom is activated by adjacent OH groups, might be converted selectively to H₂ and CO₂ [7,11–13].

* Corresponding author.

E-mail address: naitos01@kanagawa-u.ac.jp (S. Naito).

<http://dx.doi.org/10.1016/j.ijhydene.2016.10.028>

0360-3199/© 2016 Hydrogen Energy Publications LLC. Published by Elsevier Ltd. All rights reserved.

For ethanol, however, it is rather difficult to obtain H₂ and CO₂ selectively as complete reforming products because of the non-activated methyl group, which is easily transformed to CH₄ [14–16]. Accordingly we will obtain a 1:1 ratio of CH₄ and CO₂ together with acetic acid, and formed CO or CO₂ is transformed into CH₄ through a methanation reaction which results in an excess CH₄ compared to CO₂ [17]. However, a possibility of reforming acetic acid in steam reforming (SR) as well as APR reactions exists at lower temperatures.

Recently we have studied APR reactions of ethanol (EtOH) and acetic acid (AcOH) as model compounds of biomass for hydrogen production over various supported precious metal catalysts [17]. In the case of EtOH-APR over TiO₂ supported 5 wt % metal catalysts, the activity as well as the selectivity differ depending on the kind of metals with the following activity order: Ru > Rh > Pt > Ir. Over Pt/TiO₂ and Ir/TiO₂, a large amount of AcOH was formed by the hydration of acetaldehyde (AcH) with smaller amounts of CO₂ and CH₄ (1:1 ratio), indicating the absence of complete reforming process with water. On the other hand, over Rh/TiO₂ and Ru/TiO₂ catalysts, major products were CH₄ and CO₂ with a small amount of liquid phase products and excess CH₄ was formed afterward indicating the operation of an unfavorable methanation reaction.

We have also studied the metal particle size effects upon the APR reactions of ethanol and acetic acid over Ru/TiO₂ catalysts to clarify the controlling factors for the selectivity of this reaction [18]. Decomposition processes from AcH and AcOH occurred over larger Ru metals, forming 1:1 ratio CH₄ and CO (or CO₂). On the other hand, positively charged (Ru^{δ+}) Ru species would be the active sites for the hydration of AcH where CO₂ methanation was inhibited completely. From AcH and AcOH, a certain extent of complete reforming process to form H₂ and CO₂ was observed especially over smaller Ru metal catalysts. At this stage, however, detailed active site structure and the mechanism of the complete reforming process were not clarified yet.

In the present study, we have designed Ru/NaY-zeolite catalysts for APR reaction of AcOH. NaY zeolite has unique three-dimensional ordered porous structure as well as cation-exchangeable ability. Such characteristics would be efficient for controlling the structural and electronic properties of supported ruthenium species. As we have expected, Ru/NaY-zeolite catalysts exhibit high selectivity for complete reforming. In this work, we have tried to characterize the efficient active site formed on NaY zeolite.

Experimental

Preparation of catalysts and reaction procedures

Supported ruthenium catalysts were prepared by simple impregnation of a precursor compound or cation-exchanging method. A cationic ruthenium(III) complex, [Ru(NH₃)₆]Cl₃, was employed as a precursor of all the supported ruthenium catalysts.

Impregnation method

The supports (NaY zeolite, Al₂O₃, SiO₂, and SiO₂-Al₂O₃) were dispersed in pure water and stirred for 30 min. To this slurry,

an aqueous solution of [Ru(NH₃)₆]Cl₃ (5 wt% of the support) was added and the resulting mixture was stirred for 30 min at room temperature. After additional stirring for 1 h at 333 K, volatiles were evaporated. The obtained solids were dried overnight at 373 K and grinded. Prior to employ as catalyst, the solids were reduced at 623 K under H₂ stream.

Cation-exchanging method

NaY zeolite (2.95 g) was dispersed to de-ionized water (400 mL) and stirred for 30 min at room temperature. To this slurry, aqueous HCl (1 mol L⁻¹) was added to adjust the pH to a desired value (4.5–7.0). In another vessel, [Ru(NH₃)₆]Cl₃ (an appropriate amount of ruthenium regarding to the support; 0.5 wt%–5 wt%) was dissolved in water (50 mL). This solution was stirred for 30 min at ambient temperature and then dilute aqueous HCl (0.1 mol L⁻¹) was added to adjust the pH as 4.5. The resulting ruthenium precursor solution was added to the support-dispersed solution. After stirring the mixture at room temperature for 24 h, solid materials were collected by centrifugation. The resulting catalysts were washed with water (300 mL × 3) and dried by vacuum at room temperature overnight. The loading amounts of ruthenium and sodium were quantified by inductively coupled plasma mass spectrometry (ICP-MS) and atomic absorption spectroscopy (AAS), respectively. The resulting catalysts, x wt % Ru/NaY(exc) (pH y) [where x = 5, 2, 1, or 0.5 on y = 4.5 (changing the loading amounts of ruthenium), and, y = 4.5, 5.0, 5.5, 6.0, 6.5, or 7.0 when x = 5 (changing the pH of the catalyst-preparing solution)] were applied to the reaction with or without pre-reduction treatment under H₂ streaming at 623 K.

Catalyst SA(exc), namely SiO₂-Al₂O₃ based ruthenium catalysts, was also prepared by cation-exchanging method via similar manner. The support SA, whose cation was exchanged from H⁺ to NH₄⁺, was dispersed in pure water. To this support-dispersed slurry, the precursor solution was added immediately and stirred for 24 h at room temperature. Then the solids were collected by filtration and washed with 1 L of de-ionized water. Contents of ruthenium in the washed water were quantified by ICP-MS to estimate the exchanged ratio of cations. The resulting catalysts were evacuated at room temperature overnight. The resulting 3.4 wt% Ru/SA(exc) was applied to the reaction with or without pre-reduction treatment.

Aqueous phase reforming of acetic acid with water

The catalyst (0.5 g) was put into a stainless steel autoclave (400 mL). After purging by pure N₂, 80 mL of degassed aqueous solution of acetic acid (1 vol%: AcOH = 28.0 mmol g_{cat.}⁻¹) was introduced into the reactor under nitrogen atmosphere. The reforming reaction was conducted in a batch mode, which was connected to an online TCD gas chromatograph to analyze the gas phase products during the reaction (molecular sieve 13X column and Porapak Q column). After quick heating (about 60 min), the reaction was started at 473 K under 2.5–3.0 MPa pressure. During the reaction, the liquid phase content of the autoclave was stirred vigorously by a magnetic stirrer. A small part of the liquid phase products was sampled using an online sampling tube (1 mL) and analyzed using an FID gas chromatograph (CP PoraBond Q column).

Characterization of catalysts

A transmission electron microscope (JEM-2010, JEOL) with an acceleration voltage of 200 kV and LaB₆ cathode was applied to observe the images of the supported catalysts. Samples were prepared by suspending the catalyst powder ultrasonically in methanol and depositing a drop of the suspension on a standard copper grid covered with carbon monolayer film. X-ray photoelectron spectroscopy (JPS-9010, JEOL) with a MgK α X-ray source (10 kV, 10 mA) was applied for the analysis of the chemical states of the catalysts. The catalyst was pressed into a 20 mm diameter disk. Then the disk was mounted on the sample holder of the XPS preparation chamber and reduced by H₂ at 473 K or 623 K and transferred to the analysis chamber without exposure to air. The observed binding energy was calibrated by using a O_{1s} transition peak.

The amount of CO adsorption was measured by a static volumetric adsorption apparatus (Omnisorp100CX, Beckmann Coulter) at room temperature and used for TOF estimation. The metal dispersion (D (%); percentage of metal atoms exposed to the surface) on the support was evaluated from the amount of chemisorbed CO by assuming the stoichiometry of CO(a)/M = 1.

Fourier transform infrared spectroscopy (FT-IR) measurements were carried out by use of a self-support catalyst disk mounted in a transmission cell and a FT-IR spectrometer (FT-IR/6100, JASCO) equipped with a closed gas circulation system. Similar pretreatment as the reaction procedure was carried out before CO adsorption measurements.

Results and discussion

Comparison of different preparation methods upon the activity and selectivity of AcOH-H₂O reaction over NaY-zeolite, Al₂O₃, SiO₂ and SiO₂-Al₂O₃ supported Ru catalysts

NaY zeolite is one of the ordered structured aluminosilicates. In order to estimate the support effect, AcOH conversion activities of supported ruthenium catalysts on the related Si-Al-O based supports (NaY zeolite, SiO₂-Al₂O₃, SiO₂, and Al₂O₃) were examined as summarized in Table 1 and Fig. 1. To NaY zeolite and SiO₂-Al₂O₃ (abbreviated as NaY and SA, respectively), a ruthenium precursor, [Ru^{III}(NH₃)₆]³⁺, was loaded by two different methods, that is, simple impregnation and cation-exchanging. Such difference of the preparation methods would affect the structure of the resulting supported ruthenium species. On these catalysts except SA(exc), 5 wt% of ruthenium was supported. Immobilization of [Ru^{III}(NH₃)₆]³⁺ on SiO₂-Al₂O₃ by cation-exchange method resulted in loading of ruthenium with 3.4 wt% due to the limitation of exchangeable amounts of cation. SiO₂- and Al₂O₃-supported catalysts were prepared by impregnation of the same precursor. The supported ruthenium species of these catalysts were treated with H₂ stream at 623 K prior to applying to the catalytic reaction. Also, the catalysts prepared by cation-exchanging method (i.e. NaY(exc) and SA(exc)) were applied to the catalytic reaction without pre-reducing treatment.

The catalyst NaY(imp), which was prepared by impregnation method, exhibited highest AcOH conversion. The products were H₂, CO₂ and CH₄ and no other product was detected in

either liquid- or gas phase. If ideal complete reforming of AcOH (CH₃COOH + 2H₂O → 4H₂ + 2CO₂) occurred, no CH₄ would be yielded and the ratio of formed H₂ to CO₂ would be 2:1. After 10 h of the reaction, almost same amounts of CO₂ and CH₄ were formed, whereas the production of H₂ was terminated apparently. In the initial stage, however, the ratios of products H₂/CO₂ and CO₂/CH₄, estimated from the formation rates of each surface ruthenium site (TOF), were 0.93 and 1.68, respectively. These time-dependence reaction profiles (Fig. 1(a)) imply the complete reforming of AcOH catalyzed by the ruthenium sites on NaY(imp), although degradation of AcOH (CH₃COOH → CH₄ + CO₂) occurred concomitantly and the catalysis of the ruthenium sites was changed during the reaction. The observed reaction profiles on NaY(imp) were similar to those found on the TiO₂ supported 5 wt% ruthenium catalyst as we had reported previously. In contrast, other catalysts whose ruthenium species were supported by impregnation method (SA(imp), SiO₂ and Al₂O₃) exhibited similar reaction profiles to those found on 1 wt% Ru over TiO₂ support. Although AcOH conversion activities were lower, the major product was H₂ after 10 h reaction and the values of the both H₂/CO₂ and CO₂/CH₄ on each catalysts were higher than those on NaY(imp).

The catalytic activities of the supported ruthenium species on NaY-zeolite remarkably depended on the immobilization methods of the precursor and oxidation state controlled by treatment procedures. NaY(exc), whose ruthenium precursors were supported through cation-exchanging process, produced H₂ continuously for 10 h when supported ruthenium species was not treated with H₂ prior to the catalytic reaction. Although AcOH conversion activity was lower, the formation of CH₄ was suppressed over NaY(exc) compared to that observed over NaY(imp). On the contrary, when it was reduced by H₂ at 623 K prior to the reaction, the profile was similar to that found for the reaction catalyzed by NaY(imp). These observations might suggest obvious difference of catalytic active sites for reforming and degradation, and dynamic structural changing of the immobilized ruthenium species during the reduction by H₂ at high temperature.

Changes of the catalytic performance of the supported ruthenium were also observed on the SA-based catalysts. The conversion of AcOH over SA(exc) was somewhat lower than that over SA(imp). On the other hand, the reaction selectivity toward complete reforming became higher over the catalyst prepared by the cation-exchanging method. In the case of SA(exc), no pre-reduction of the supported ruthenium led to somewhat lowering the activity and selectivity compared to those of the corresponding pre-reduced catalyst. Such difference between NaY(exc) and SA(exc) might suggest that not only the structure and electronic state of the supported ruthenium but also the components of the support were dominant factors for the catalysis.

Structural differences between impregnated and ion-exchanged catalysts and their correlation to catalytic behaviors

Since catalytic activity and selectivity of AcOH reforming reaction were strongly affected by the kinds of the supports and the way of loading and pretreatments, the characterization of employed catalysts was carried out.

Table 1 – Results of AcOH + H₂O reaction at 473 K for 10 h over various 5 wt% supported Ru catalysts.

Entry	Catalysts ^a	Disp./% ^b	Amounts of products/mmol g _{cat.} ⁻¹			H ₂ /CO ₂ (10 h)	CO ₂ /CH ₄ (10 h)	Conv./% (10 h)
			H ₂	CO ₂	CH ₄			
1	NaY (imp)	25.0	8.42	24.37	23.38	0.35	1.04	85.3
2	SA (imp)	13.9	9.50	6.20	2.73	1.53	2.27	15.9
3	SiO ₂	7.8	6.05	4.16	1.08	1.45	3.87	9.4
4	Al ₂ O ₃	5.0	8.67	4.90	2.33	1.77	2.10	12.9
5	NaY (exc)	64.7	8.14	18.08	17.33	0.45	1.04	63.2
6	SA (exc)	79.9	8.32	5.19	2.36	1.60	2.20	13.5
7 ^c	NaY (exc)	(64.7)	10.65	6.14	2.50	1.74	2.46	15.4
8 ^c	SA (exc)	(79.9)	6.45	4.51	1.63	1.43	2.77	11.0

Entry	Catalysts ^a	Disp./% ^b	Initial formation rates/mmol g _{cat.} ⁻¹ h ⁻¹			TOF/×10 ⁻³ s ⁻¹			H ₂ /CO ₂ (Initial)	CO ₂ /CH ₄ (Initial)
			H ₂	CO ₂	CH ₄	H ₂	CO ₂	CH ₄		
1	NaY (imp)	25.0	3.71	3.98	2.37	8.32	8.95	5.33	0.93	1.68
2	SA (imp)	13.9	1.92	1.20	0.20	7.75	4.85	0.83	1.60	5.87
3	SiO ₂	7.8	2.62	1.37	0.13	18.89	9.89	0.97	1.91	10.19
4	Al ₂ O ₃	5.0	2.32	0.95	0.33	26.04	10.67	3.74	2.44	2.85
5	NaY (exc)	64.7	3.88	3.20	1.92	3.36	2.77	1.67	1.21	1.66
6	SA (exc)	79.9	1.59	0.85	0.12	1.65	0.88	0.12	1.88	7.04
7 ^c	NaY (exc)	(64.7)	2.03	1.10	0.37	1.76	0.95	0.32	1.85	2.94
8 ^c	SA (exc)	(79.9)	1.88	1.11	0.17	1.94	1.14	0.18	1.70	6.35

Reaction conditions: Amount of catalyst; 0.5 g, Catalyst pretreatment; H₂ reduction at 623 K for 2 h, Internal standard gas; N₂ 1 atm, Reactant solution; 1 vol% AcOH/aq 80 mL (AcOH = 28.0 mmol g_{cat.}⁻¹), Reaction temp.; 423 K.

^a Ru loading amount; 5 wt% except Ru/SA(exc), Ru loading of Ru/SA(exc) = 3.4 wt%.

^b Dispersion; calculated by chemisorbed CO.

^c As-prepared.

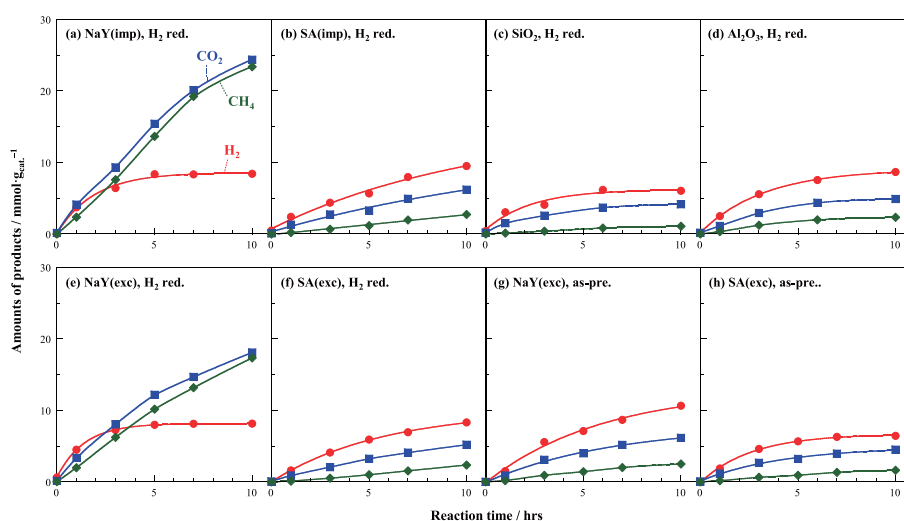


Fig. 1 – Time courses of AcOH + H₂O reaction at 473 K for 10 h over various supported Ru catalysts, (a) NaY(imp), (b) SA(imp), (c) SiO₂, (d) Al₂O₃, (e) NaY(exc), (f) SA(exc) after H₂ reduction at 623 K, (g) NaY(exc), (h) SA(exc), as-prepared.

As estimated from the amount of adsorbed CO (i.e. dispersion of ruthenium) shown in Table 1, ruthenium metal particle sizes were dependent on the method of the loading as well as on the kinds of the supports. Especially on the cation-exchangeable support (i. e. NaY or SA), the size of the supported particles became smaller when the catalysts prepared by ion exchange method rather than impregnation. These results may be explained by the electrostatic interaction between support and the ruthenium complex cations, $[\text{Ru}(\text{NH}_3)_6\text{Cl}_{3-n}]^{n+}$, derived from the precursor.

Fig. 2 shows the TEM images of 5 wt% supported Ru catalysts after H₂ reduction at 623 K for 2 h. As shown in Fig. 2(a), in the case of NaY(imp)-zeolite, together with well dispersed uniform 2 nm Ru clusters, 2–10 nm larger Ru particles were observed randomly, which may be formed on the outer-surface of NaY-zeolite. In the case of impregnated Ru over other supports, broad distributions of the 2–3 to 10–20 nm Ru nano-clusters and their coagulated metal particles were observed as shown in Fig. 2(b)–(d). These tendencies were well correlated with those estimated by CO adsorption. On the

contrary, in the case of cation exchanged NaY-zeolite, bigger Ru particles were rarely observed as shown in Fig. 2(e), and none in the case of SA(exc) catalysts(Fig. 2(f)).

Fig. 3 shows the XPS analyses of Ru 3d transitions of the various Ru catalysts after *in-situ* pretreatments in the preparation chamber of the spectrometer. Spectra (a) summarize the Ru 3d transition of as-prepared catalysts. Because of overlapping of C 1s and Ru 3d_{3/2} transitions around 285 eV, the states of Ru were estimated on the basis Ru 3d_{5/2} transitions appeared in the lower energy region. In the case of impregnation catalysts, all the catalysts exhibit the same peak at 282.4 eV, which can be assigned to Ru³⁺ of physisorbed [Ru(NH₃)₆]³⁺ complexes. When these catalysts were reduced at 473 K, this peak shifted to 279.5 eV, which can be assigned to Ru⁰. Accordingly, in the cases of impregnated catalysts, the interaction between the precursor complex with supports is very weak and easily reduced to Ru metal.

The situation was rather different in the cases of cation-exchanged NaY and SA catalysts. As shown in the top part of Fig. 3(a), Ru 3d_{5/2} transition peaks shifted to the lower binding energy position (NaY: 280.9 and SA: 281.9 eV), indicating stronger interaction of precursor complexes with supports. However, the successive reduction by H₂ at 473 K did not cause the change of the peak position very much (NaY: 280.6 and SA: 281.9), indicating lower reducibility of these catalysts.

Fig. 4 shows the IR spectra of CO adsorption at r.t over impregnated and cation-exchanged catalysts after H₂ reduction at indicated temperatures. In the cases of impregnated catalysts (Fig. 4(a)), three characteristic CO(a) adsorption bands were observed at around 2150, 2080 and 2030 cm⁻¹. The former two bands can be assigned to the germinal Ru^{δ+}(CO)₂ species and the third one, to zero-valent Ru⁰-CO band whose intensity ratios were decreased with the increase of reduction temperatures from 473 K to 623 K.

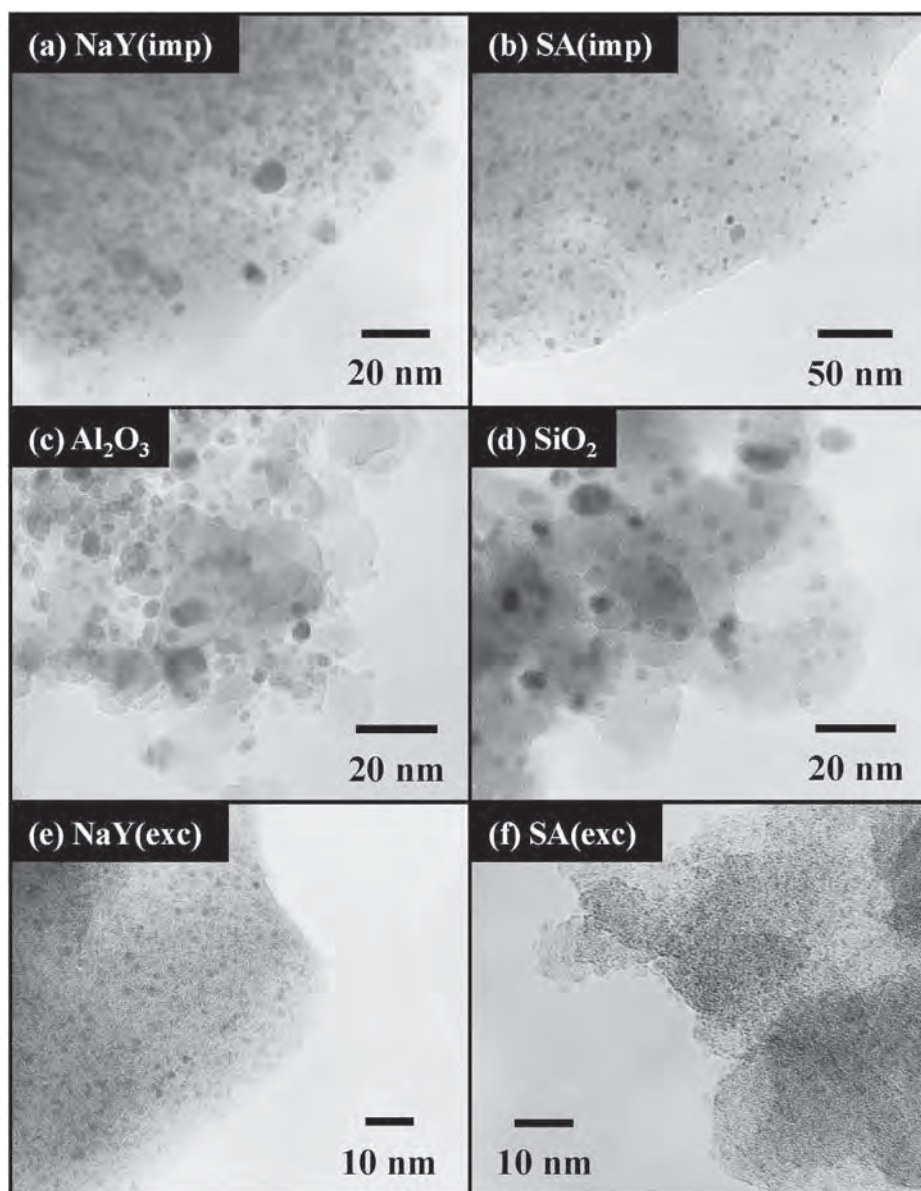


Fig. 2 – TEM images of various supported Ru catalysts after H₂ reduction at 623 K for 2 h, (a) NaY(imp), (b) SA(imp), (c) SiO₂, (d) Al₂O₃, (e) NaY(exc), (f) SA(exc).

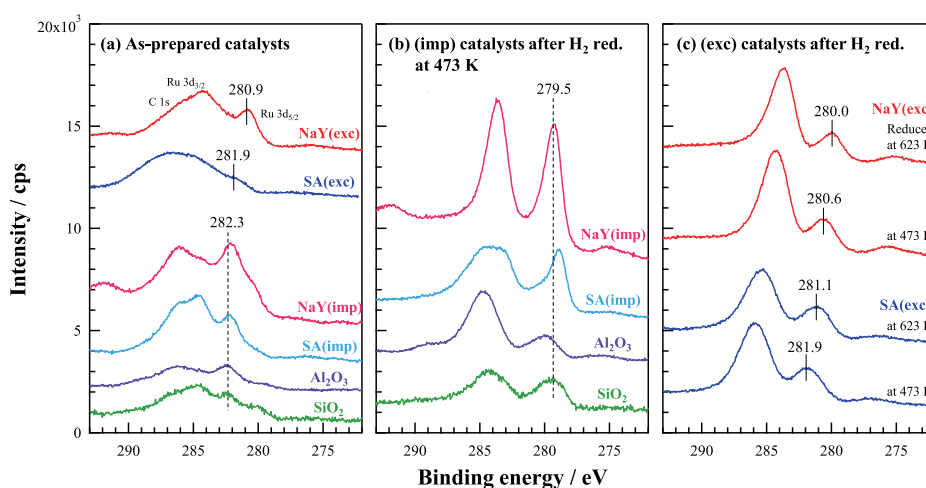


Fig. 3 – XPS analyses of Ru 3d transitions of various supported Ru catalysts, (a) (exc) and (imp) catalysts as-prepared, (b) (imp) catalysts reduced by H₂ at 473 K, (c) (exc) catalysts reduced by H₂ at 473 K and 623 K.

On the other hand, the situation was rather different in the cases of cation exchanged catalysts. As shown in Fig. 4(b), over NaY(exc) catalyst the peak intensities of adsorbed CO increased extraordinarily suggesting sudden occurrence of the precursor complex reduction at around 473 K. Amiridis et al. investigated the adsorption of CO over Al₂O₃- and SiO₂-supported Ru catalysts through FT-IR spectroscopy [19]. According to their discussion, two kinds of pair peaks at [1980, 2062 cm⁻¹] and [2011, 2105 cm⁻¹] can be assigned to two Ru dicarbonyl adsorbed species, Ru⁰(CO)₂ and Ru²⁺(CO)₂, respectively. By raising the reduction temperature up to 623 K, these dicarbonyl peaks decreased gradually, and a new peak emerged at around 2029 cm⁻¹, which can be assigned to linearly adsorbed CO(a) on top of Ru⁰ species.

In the case of SA catalysts, similar spectral changes were observed as shown in Fig. 4(c). Until at 323 K, four main peaks were observed at 1970, 2017, 2082 and 2160 cm⁻¹, which can be assigned to weakly adsorbed tricarbonyl species (Ru³⁺-(CO)₃; n = 1–3) and linear species Ru^{δ+}-(CO). At 473 K, tricarbonyl species decreased gradually, and additional peaks were observed at 1990, 2017 and 2090 cm⁻¹, which can be assigned

to Ru²⁺ dicarbonyl and linear CO(a) on top of small Ru⁰ clusters. Accordingly, the reduction of Ru precursor complexes started at around 473 K, which corresponded well to the occurrence of complete AcOH reforming reaction. Further reduction up to 623 K caused the appearance of large peaks at 2026–2043 cm⁻¹, which can be assigned to the linearly adsorbed CO on the larger Ru nanoparticles.

These characterization results indicate that cation-exchange preparation method is much more efficient than impregnation method to control the metal particle sizes of supported catalysts. Moreover, cation-exchanged Ru species on the supports are more stable and less reducible than impregnated ones, which exhibit higher selectivity for complete reforming of aqueous AcOH reforming reaction.

Correlation between the activities and preparation conditions of NaY catalyst

In the case of TiO₂ supported ruthenium catalysts, the decreasing of the loadings of ruthenium leads to reduce the particle size of the supported ruthenium species due to strong

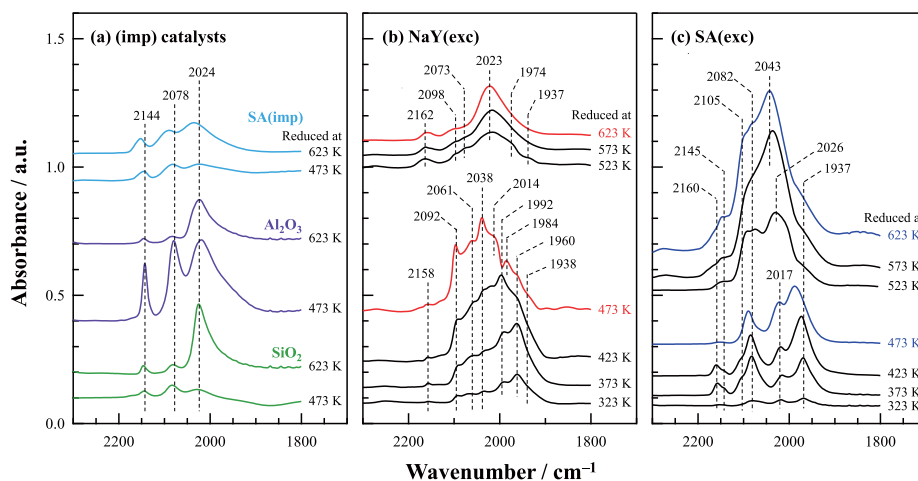


Fig. 4 – FT-IR spectra of CO adsorption at r.t. over supported Ru catalysts after H₂ reduction at each temperature, (a) (imp) catalysts, (b) NaY(exc) catalyst, (c) SA(exc) catalyst.

Table 2 – Ru dispersion and loading amounts of Ru and Na on the NaY supported Ru catalysts prepared by cation-exchanging method.

Applied Ru/wt%	pH	Ru loadings/wt %	Ru dispersion/%	Na loadings/wt%
0.5	4.5	0.49	113.5	6.95
1.0	4.5	0.99	94.7	6.08
2.0	4.5	1.99	67.0	4.86
5.0	4.5	4.96	64.7	2.79
5.0	5.0	4.98	90.3	3.34
5.0	5.5	4.99	108.4	5.74
5.0	6.0	4.99	126.0	5.89
5.0	6.5	4.99	114.8	6.07
5.0	7.0	4.99	41.8	6.06

interaction between the TiO₂ support and the impregnated ruthenium species. The resulting small ruthenium particles are positively charged and such Ru^{δ+} species are proposed as the active sites for the complete reforming of AcOH on the basis of improvement of the products selectivity, that is, higher H₂/CO₂ and CO₂/CH₄. Therefore, we examined changing the loadings of ruthenium in the present NaY zeolite catalysts.

A lower ruthenium loading amount catalyst, 0.5 wt% Ru/NaY(exc), was prepared by cation-exchanging method at pH 4.5 same as the corresponding 5 wt% Ru/NaY(exc). On the pre-reduced 0.5 wt% catalyst, the dispersion of the supported ruthenium estimated by CO absorption was increased

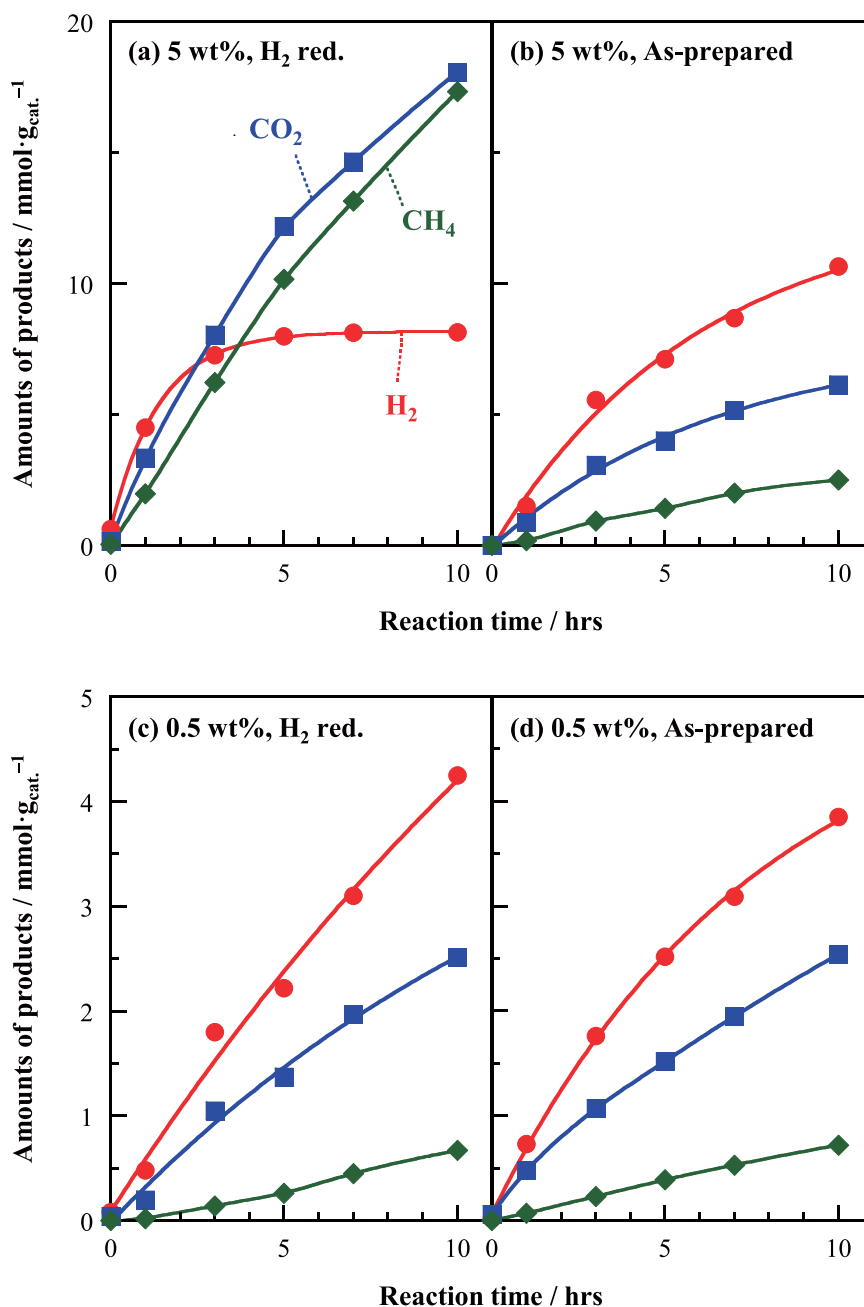


Fig. 5 – Time courses of AcOH + H₂O reaction at 473 K for 10 h over various Ru/NaY(exc) catalysts, (a) Ru loading amounts: 5 wt%, catalyst conditions: H₂ red., (b) 5 wt%, as-pre, (c) 0.5 wt%, H₂ red., (d) 0.5 wt%, as-pre.

compared to the 5 wt% one (65% on 5 wt% Ru catalyst whereas 114% on 0.5 wt% Ru one; see Table 2). Over 0.5 wt% Ru/NaY(exc), CH₄ formation was tremendously suppressed, although the AcOH conversion was low (3.1%). Moreover, H₂ generation was continuous with almost the same and constant rate for 10 h. After 10 h, the values of H₂/CO₂ and CH₄/CO₂ were 1.7 and 3.8, respectively. In the case of the 0.5 wt% Ru-loading catalysts, the catalytic activity of a non-reduced catalyst (Fig. 5(d)) was essentially identical with that of the pre-reduced one (Fig. 5(c)), whereas those of the 5 wt% Ru-loading catalysts were different whether pre-reduced (Fig. 5(a)) or not (Fig. 5(b)).

Fig. 6 summarized the trends of the changes of the initial formation rates of the products over reduced and non-reduced catalysts with respect to the loading amounts of ruthenium on NaY through ion-exchange immobilization method. Drastic change of the initial reaction rates and the selectivity dependency on the Ru loading manner was observed on the pre-reduced catalysts. The higher ruthenium loading catalysts exhibited the lower values of the ratio of the CO₂/CH₄ formation rates although the formation rates of all gaseous products were high. Such inverse trends between the ratio of CO₂/CH₄ and the respective formation rates of the products would arise from the increase of the activity toward AcOH decomposition rather than reforming over the pre-reduced higher Ru loading catalysts. In the case of non-

reduced catalysts, the trend of the decrease of the products formation rates was similar to that observed on the pre-reduced catalysts. However, the ratios of the CO₂/CH₄ formation rates exhibited similar values on the catalysts despite of the different Ru loadings. Therefore, distributions of the active sites toward reforming or degradation have varied depending on the combination of the loading amounts and the electronic structures of ruthenium.

Generally speaking, addition of basic sites onto the reforming catalysts would be efficient for the improvement of the catalytic activity because such basic sites take a role in H₂O activation. Therefore, we explored the correlation between the contents of Na⁺, as well as Ru, and the catalytic performances. The catalysts 5 wt% NaY(exc at pH *y*; where *y* = 5.0, 5.5, 6.0), which were prepared at pH 5.0, 5.5, 6.0 and 7.0, contained higher amount of sodium compared to those of the corresponding catalyst prepared at pH 4.5 (5 wt% NaY(exc at pH 4.5)). Therefore, the contents of sodium depended on the acidity of the catalyst-preparing media because partial exchanging of Na⁺ to H⁺ occurred at lower pH. The initial formation rates of the gaseous products were compared as shown in Fig. 6. Both on the pre-reduced and non-reduced catalysts, the rates as well as the CO₂/CH₄ ratios were similar to each other, although the dispersions of the ruthenium were varied (see Table 2). On the higher ruthenium loading catalysts, the pH of the precursor solutions did not

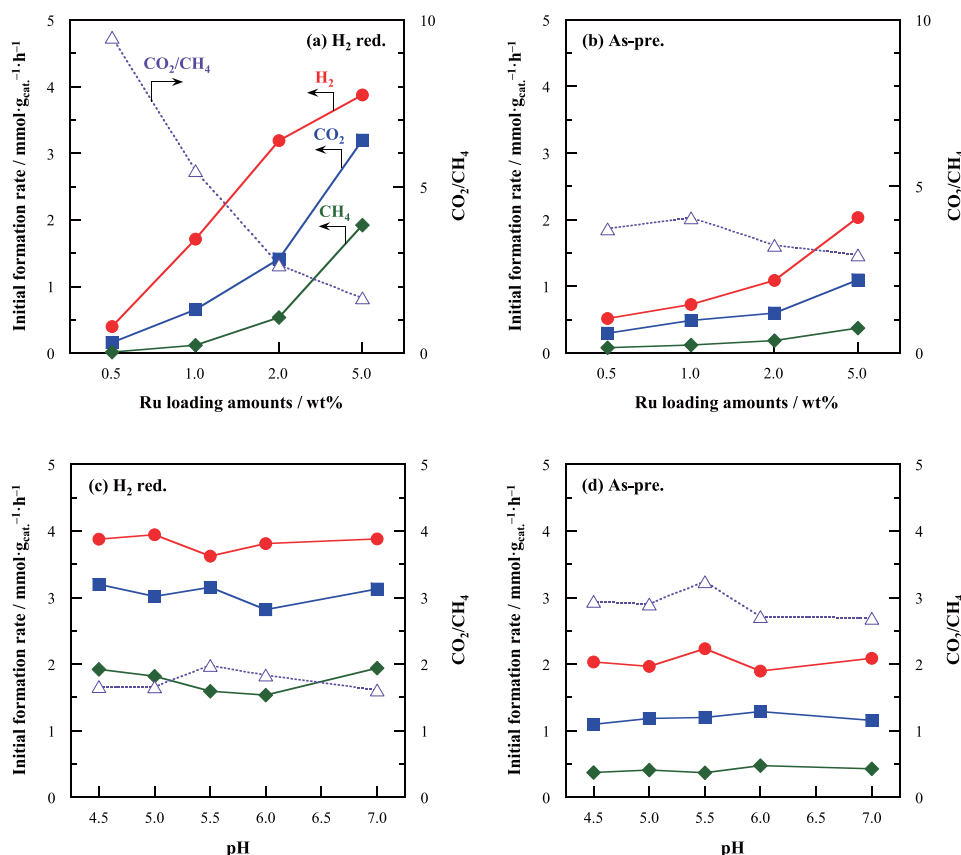


Fig. 6 – Initial formation rates of products and reforming selectivity (= CO₂/CH₄) for AcOH + H₂O reaction at 473 K over various *x* wt% Ru/NaY (exc, pH *y*) catalysts prepared by cation-exchanging method, (*x* = 0.5, 1.0, 2.0, 5.0 wt%, *y* = pH 4.5, 5.0, 5.5, 6.0, 6.5, 7.0). The dependence of Ru loading amounts (a: after H₂ reduced at 623 K, b: as-prepared) and preparation pH conditions (c: after H₂ reduced at 623 K, d: as-prepared).

influence the catalytic performances although the partial catalyst structures, i.e., the contents of sodium as well as the dispersion of ruthenium were varied. XPS spectra of the 5 wt% NaY(exc) catalysts prepared at pH 6.0 were similar to those of the catalysts prepared at pH 4.5. In both pH 6.0 and 4.5 catalysts, H₂ treatment at 473 K led to partial reduction of Ru(III) to some cationic Ru^{δ+} species, whereas complete reduction of Ru(III) to Ru(0) occurred at high temperature. Therefore, electronic states would be a dominant factor for emergence of the reforming activity.

Conclusions

Catalytic activities of the supported ruthenium species on NaY-zeolite depended on immobilization conditions of [Ru(NH₃)₆]³⁺ and oxidation state controlled by treatment procedures. The catalyst NaY(exc), whose 5 wt% ruthenium precursors were supported through cation-exchanging process, produced H₂ continuously for 10 h when the catalysts were used without being reduced by H₂ prior to usage. Decreasing the loading amounts of ruthenium led to improve the selectivity toward complete reforming of acetic acid giving H₂ and CO₂. Spectroscopic analyses of the surface ruthenium species formed on NaY suggest that the cationic Ru^{δ+} sites formed via partial reduction of Ru(III) catalyze the reforming of CH₃COOH with H₂O yielding H₂ and CO₂, while the metallic Ru(0) sites catalyze the decomposition of acetic acid giving CH₄ and CO₂. Reducing the loading amounts of [Ru(NH₃)₆]³⁺ on NaY(exc) might result in stabilization of the Ru^{δ+} sites through electrostatic interaction between NaY.

Acknowledgements

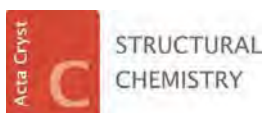
The authors are grateful for financial support through a Strategic Development of Research Infrastructure for Private Universities (S1201017) from the Ministry of Education, Culture, Sports, Science, and Technology (MEXT), Japan.

Appendix A. Supplementary data

Supplementary data related to this article can be found at <http://dx.doi.org/10.1016/j.ijhydene.2016.10.028>.

REFERENCES

- [1] Alaswad A, Baroutaji A, Achour H, Carton J, Makky AA, Olabi AG. Developments in fuel cell technologies in the transport sector. *Int J Hydrogen Energy* 2016;41:16499–508.
- [2] Fletcher T, Thring R, Watkinson M. An Energy Management Strategy to concurrently optimise fuel consumption & PEM fuel cell lifetime in a hybrid vehicle. *Int J Hydrogen Energy* 2016;41(46):21503–15. <http://dx.doi.org/10.1016/j.ijhydene.2016.08.157>.
- [3] Dodds PE, Staffell I, Hawkes AD, Li F, Grunewald P, McDowall W, et al. Hydrogen and fuel cell technologies for heating: a review. *Int J Hydrogen Energy* 2015;40:2065–83.
- [4] Haryanto A, Fernando S, Murali N, Adhikari S. Current status of hydrogen production techniques by steam reforming of ethanol: a review. *Energy Fuels* 2005;19:2098–106.
- [5] Vaidya PD, Rodrigues AE. Glycerol reforming for hydrogen production: a review. *Chem Eng Technol* 2009;32:1463–9.
- [6] Trane R, Dahl S, Skjøth-Rasmussen MS, Jensen AD. Catalytic steam reforming of bio-oil. *Int J Hydrogen Energy* 2012;37:6447–72.
- [7] Cortright RD, Davda RR, Dumesic JA. Hydrogen from catalytic reforming of biomass-derived hydrocarbons in liquid water. *Nature* 2002;418:964–7.
- [8] Shabaker JW, Huber GW, Dumesic JA. Aqueous-phase reforming of oxygenated hydrocarbons over Sn-modified Ni catalysts. *J Catal* 2004;222:180–91.
- [9] Shabaker JW, Davda RR, Huber GW, Cortright RD, Dumesic JA. Aqueous-phase reforming methanol and ethylene glycol over alumina-supported platinum catalysts. *J Catal* 2003;215:344–52.
- [10] Shabaker JW, Dumesic JA. Kinetics of aqueous-phase reforming of oxygenated hydrocarbons: Pt/Al₂O₃ and Sn-modified Ni catalysts. *Ind Eng Chem Res* 2004;43:3105–12.
- [11] Sakamoto T, Miyao T, Yoshida A, Naito S. Effect of Re and Mo addition upon liquid phase methanol reforming with water over SiO₂, ZrO₂ and TiO₂ supported Ir catalysts. *Int J Hydrogen Energy* 2010;35:6203–9.
- [12] Sakamoto T, Kikuchi H, Miyao T, Yoshida A, Naito S. Effect of transition metal element addition upon liquid phase reforming of methanol with water over TiO₂ supported Pt catalysts. *Appl Catal A Gen* 2010;375:156–62.
- [13] Kunkes EL, Soares RR, Simonetti DA, Dumesic JA. An integrated catalytic approach for the production of hydrogen by glycerol reforming coupled with water-gas shift. *Appl Catal B Env* 2009;90:693–8.
- [14] Tang Z, Monroe J, Dong J, Nenoff T, Weinkauff D. Platinum-loaded NaY zeolite for aqueous-phase reforming of methanol and ethanol to hydrogen. *Int Eng Chem Res* 2009;48:2728–33.
- [15] Cruz IO, Ribeiro NFP, Aranda DAG, Souza MMVM. Hydrogen production by aqueous-phase reforming of ethanol over nickel catalysts prepared from hydrotalcite precursors. *Catal Comm* 2008;9:2606–11.
- [16] Xiong H, DeLaRiva A, Wang Y, Datye AK. Low-temperature aqueous-phase reforming of ethanol on bimetallic PdZn catalysts. *Catal Sci Technol* 2015;5:254.
- [17] Nozawa T, Yoshida A, Hikichi S, Naito S. Effects of Re addition upon aqueous phase reforming of ethanol over TiO₂ supported Rh and Ir catalysts. *Int J Hydrogen Energy* 2015;40:4129–40.
- [18] Nozawa T, Mizukoshi Y, Yoshida A, Naito S. Aqueous phase reforming of ethanol and acetic acid over TiO₂ supported Ru catalysts. *Appl Catal B Env* 2014;146:221–6.
- [19] Chin AY, Williams CT, Amiriadis MD. FTIR studies of CO adsorption on Al₂O₃- and SiO₂-supported Ru catalysts. *J Phys Chem B* 2006;110:871–82.



ISSN: 2053-2296

journals.iucr.org/c

A pseudotetrahedral nickel(II) complex with a tridentate oxazoline-based scorpionate ligand: chlorido[tris(4,4-dimethyloxazolin-2-yl)phenylborato]nickel(II)

Tomoaki Takayama, Jun Nakazawa and Shiro Hikichi

Acta Cryst. (2016). **C72**, 842–845



IUCr Journals
CRYSTALLOGRAPHY JOURNALS ONLINE

Copyright © International Union of Crystallography

Author(s) of this paper may load this reprint on their own web site or institutional repository provided that this cover page is retained. Republication of this article or its storage in electronic databases other than as specified above is not permitted without prior permission in writing from the IUCr.

For further information see <http://journals.iucr.org/services/authorrights.html>

A pseudotetrahedral nickel(II) complex with a tridentate oxazoline-based scorpionate ligand: chlorido[tris(4,4-dimethyloxazolin-2-yl)phenylborato]nickel(II)

Tomoaki Takayama, Jun Nakazawa and Shiro Hikichi*

Department of Material & Life Chemistry, Faculty of Engineering, Kanagawa University, 3-27-1 Rokkakubashi, Kanagawa-ku, Yokohama City 222-8686, Japan. *Correspondence e-mail: hikichi@kanagawa-u.ac.jp

Received 20 April 2016

Accepted 27 July 2016

Edited by G. P. A. Yap, University of Delaware, USA

Keywords: oxazoline-based scorpionate; nickel compound; coordination compound; crystal structure.

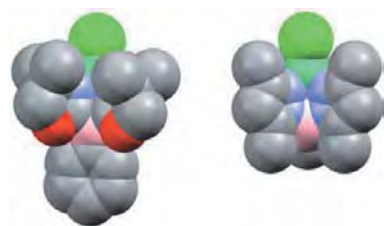
CCDC reference: 1496281

Supporting information: this article has supporting information at journals.iucr.org/c

Poly(pyrazol-1-yl)borates have been utilized extensively in coordination compounds due to their high affinity toward cationic metal ions on the basis of electrostatic interactions derived from the mononegatively charged boron centre. The original poly(pyrazol-1-yl)borates, christened ‘scorpionates’, were pioneered by the late Professor Swiatoslaw Trofimenko and have expanded to include various borate ligands with N-, P-, O-, S-, Se- and C-donors. Scorpionate ligands with boron–carbon bonds, rather than the normal boron–nitrogen bonds, have been developed and in these new types of scorpionate ligands, amines and azoles, such as pyridines, imidazoles and oxazolines, have been employed as N-donors instead of pyrazoles. Furthermore, a variety of bis- and tris(oxazolin-yl)borate ligands, including chiral ones, have been developed. Tris(oxazolin-2-yl)borates work as facially capping tridentate chelating ligands in the same way as tris(pyrazol-1-yl)borates. In the title compound, $[\text{Ni}(\text{C}_{21}\text{H}_{29}\text{BN}_3\text{O}_3)\text{Cl}]$, the Ni^{II} ion is coordinated by three N atoms from the facially capping tridentate chelating tris(4,4-dimethyloxazolin-2-yl)phenylborate ligand and a chloride ligand in a highly distorted tetrahedral geometry. The Ni–Cl bond length [2.1851 (5) Å] is comparable to those found in a previously reported tris(3,5-dimethylpyrazol-1-yl)hydroborate derivative [2.1955 (18) and 2.150 (2) Å]. The molecular structure deviates from C_{3v} symmetry due to the structural flexibility of the tris(4,4-dimethyloxazolin-2-yl)phenylborate ligand.

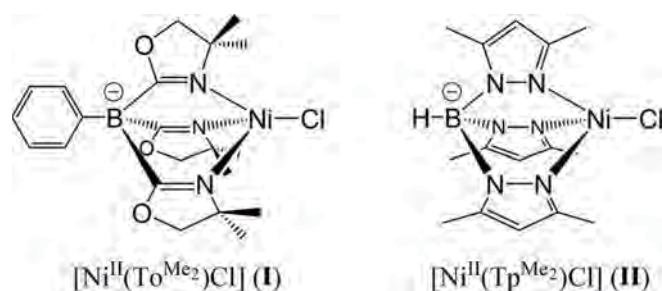
1. Introduction

Poly(pyrazol-1-yl)borates, $[\text{B}(\text{pz}^R)_n\text{X}_{4-n}]^-$ ($n = 2-4$; $R =$ substituent groups on the pyrazoles; $X = \text{H}$, alkyl, phenyl *etc.*), have been utilized extensively in various coordination compounds due to their high affinity toward cationic metal ions on the basis of electrostatic interactions derived from the mononegatively charged boron centre, as well as for their chelating effect (Trofimenko, 1999). The types of borate-based chelating ligands, namely ‘scorpionates’, have been growing, since the original poly(pyrazol-1-yl)borates were pioneered by the late Professor Swiatoslaw Trofimenko (Trofimenko, 1966), and include various borate ligands with N- (other than pyrazole, see below), P- (Barney *et al.*, 1999; Thomas & Peters, 2001), O- (Al-Harbi *et al.*, 2011), S- (Garner *et al.*, 1996; Ge *et al.*, 1994; Riordan, 2010), Se- (Minoura *et al.*, 2006) and C-donors (Fränkel *et al.*, 2001; Cowley *et al.*, 2006). Some scorpionate ligands with boron–carbon bonds, rather than the normal boron–nitrogen bonds, had appeared after the mid-1990s (Pettinari, 2008). In such new types of scorpionate ligands, amines (Betley & Peters, 2002) and azoles, such as pyridines (Hodgkins & Powell, 1996; Khaskin *et al.*, 2006),



© 2016 International Union of Crystallography

imidazoles (Fujita *et al.*, 2000) and oxazolines (Mazet *et al.*, 2005; Dunne *et al.*, 2008), have been employed as N-donors instead of pyrazoles. Furthermore, a variety of bis- and tris-(oxazolyl)borate ligands, including chiral ones, have been developed because various oxazoline derivatives are available. Tris(oxazolin-2-yl)borates, namely To^R (where R denotes substituent groups on the oxazoline rings), work as facially capping tridentate chelating ligands in the same way as tris-(pyrazol-1-yl)borates (Tp^R). In the tris(oxazolin-2-yl)borates, substituent groups at the 4-position of oxazoline would be as effective in controlling the coordination environment of a metal centre as those at the 3-position of the pyrazoles in Tp^R . In this study, tris(4,4-dimethyloxazolin-2-yl)phenylborate, which is abbreviated as To^{Me_2} (Dunne *et al.*, 2008), was employed as a coordinating ligand in a chloride complex of nickel(II). The molecular structure of the resulting complex, $[Ni^{II}(To^{Me_2})Cl]$, (I), was compared with that of the related tris(3,5-dimethylpyrazol-1-yl)hydroborate (abbreviated as Tp^{Me_2}) derivative, *i.e.* $[Ni^{II}(Tp^{Me_2})Cl]$, (II) (Desrochers *et al.*, 2003).



2. Experimental

2.1. Synthesis and crystallization

The title compound, $[Ni^{II}(To^{Me_2})Cl]$, (I), was prepared by reaction of nickel(II) dichloride and the sodium salt $NaTo^{Me_2}$, which was synthesized from the protonated ligand HTo^{Me_2} (Dunne *et al.*, 2008). A solution of HTo^{Me_2} (1.472 g, 3.84 mmol) in tetrahydrofuran (THF, 40 ml) was added slowly to sodium hydride (0.153 g, 3.82 mmol) suspended in THF (40 ml) through a cannula at 273 K. The reaction mixture was stirred for 2 h after the generation of hydrogen gas had ceased. The solvent was removed under reduced pressure. The resulting solid was suspended in pentane, with stirring for 10 min, and then the liquid was decanted. This was repeated twice to yield a pale-yellow powder of $NaTo^{Me_2}$. $NaTo^{Me_2}$ is hygroscopic (*i.e.* hydrolyzed to HTo^{Me_2}) and so the solid obtained was used in the following reactions without further purification. A solution of $NaTo^{Me_2}$ (345 mg, 0.852 mmol) in THF (15 ml) was added slowly to nickel(II) chloride (anhydrous, 118 mg, 0.908 mmol) suspended in anhydrous MeOH (15 ml), and the resultant mixture was stirred for 30 min at ambient temperature. After removal of the solvent under reduced pressure, the resulting solid was dissolved in CH_2Cl_2 and insoluble materials were removed by filtration through a Celite plug. The solvent was evaporated under reduced pressure and the resulting solid was

Table 1
Experimental details.

Crystal data	
Chemical formula	$[Ni(C_{21}H_{29}BN_3O_3)Cl]$
M_r	476.44
Crystal system, space group	Monoclinic, $P2_1/c$
Temperature (K)	113
a, b, c (Å)	10.8792 (17), 13.221 (2), 15.972 (3)
β (°)	96.899 (2)
V (Å ³)	2280.7 (7)
Z	4
Radiation type	Mo $K\alpha$
μ (mm ⁻¹)	1.00
Crystal size (mm)	0.35 × 0.35 × 0.20
Data collection	
Diffractometer	Saturn70 (4 × 4 bin mode)
Absorption correction	Numerical [<i>CrystalClear</i> (Rigaku, 2007) and <i>ABSCOR</i> (Higashi, 1995)]
T_{min}, T_{max}	0.761, 0.861
No. of measured, independent and observed [$I > 2\sigma(I)$] reflections	16162, 5168, 4140
R_{int}	0.029
$(\sin \theta/\lambda)_{max}$ (Å ⁻¹)	0.649
Refinement	
$R[F^2 > 2\sigma(F^2)], wR(F^2), S$	0.024, 0.061, 0.99
No. of reflections	5168
No. of parameters	277
H-atom treatment	H-atom parameters constrained
$\Delta\rho_{max}, \Delta\rho_{min}$ (e Å ⁻³)	0.37, -0.25

Computer programs: *CrystalClear* (Rigaku, 2007), *SORTAV* (Blessing, 1995), *SIR92* (Altomare *et al.*, 1994), *SHELXL2014* (Sheldrick, 2015), *ORTEP-3 for Windows* (Farrugia, 2012) and *WinGX* (Farrugia, 2012).

dissolved in MeCN. Refrigeration of this MeCN solution at 243 K afforded a pink powder of (I) (yield 384 mg, 0.807 mmol, 94%). Pale-red–pink single crystals of (I) suitable for X-ray analysis were obtained by the vapour diffusion method, *i.e.* hexane vapour was diffused into a $CHCl_3$ solution of (I) at 243 K. Analysis calculated for $C_{21}H_{29}BCIN_3NiO_3$: C 52.94, H 6.14, N 8.82%; found: C 53.07, H 6.21, N 8.80%. ESI-MS⁺ (m/z): $[M + H]^+$ calculated for $C_{21}H_{30}BCIN_3NiO_3$: 476.1; found: 476.0. IR (KBr pellet, ν , cm⁻¹): 3075, 3048, 3035, 2968, 2930, 2899, 2871, 1600, 1570, 1496, 1461, 1434, 1388, 1369, 1352, 1278, 1253, 1194, 1166, 1038, 1018, 990, 957, 918, 894, 846, 817, 751, 713, 670, 658, 648, 640, 619. UV–vis [CH_2Cl_2 solution, room temperature, nm, (ϵ , M⁻¹ cm⁻¹): 309 (220), 483 (315), 818 (93).

2.2. Refinement

Crystal data, data collection and structure refinement details are summarized in Table 1. The H atoms were placed in geometrically idealized positions and constrained to ride on their parent atoms, with C–H distances of 0.95 (aryl), 0.99 (methylene) or 0.98 Å (methyl) and with $U_{iso}(H) = 1.5U_{eq}(C)$ for the methyl groups and $1.2U_{eq}(C)$ otherwise.

3. Results and discussion

The Ni^{II} centre of (I) displays a highly distorted tetrahedral geometry, with a terminal chloride anion and three facially

scorpionates

Table 2

Comparison of the structural parameters (Å, °) of $[\text{Ni}^{\text{II}}(\text{To}^{\text{Me}_2})\text{Cl}]$, (I), and its Tp^{Me_2} analogue, (II).

	$[\text{Ni}^{\text{II}}(\text{To}^{\text{Me}_2})\text{Cl}]$, (I)	$[\text{Ni}^{\text{II}}(\text{Tp}^{\text{Me}_2})\text{Cl}]$, (II)	
		Molecule 1	Molecule 2
Ni—Cl	2.1851 (5)	2.1955 (18)	2.150 (2)
Ni—N1	2.0002 (11)	1.964 (3)	1.992 (3)
Ni—N2	1.9982 (11)	1.964 (3)	1.992 (3)
Ni—N3	1.9825 (11)	1.962 (5)	1.992 (5)
Cl—Ni—N1	136.75 (3)	123.66 (10)	125.44 (11)
Cl—Ni—N2	119.62 (4)	123.66 (10)	125.44 (11)
Cl—Ni—N3	114.91 (3)	122.39 (16)	121.63 (15)
Cl—Ni—B	167.03 (3)	178.7	177.5
N1—Ni—N2	89.79 (5)	91.47 (18)	90.30 (19)
N1—Ni—N3	92.22 (4)	93.51 (14)	92.16 (14)
N2—Ni—N3	93.12 (5)	93.51 (14)	92.16 (14)

arranged N-atom donors from the oxazolinyll (ox) groups of the To^{Me_2} ligand, as shown in Fig. 1. As summarized in Table 2, the Ni—Cl bond length in (I) is comparable to those found in the two crystallographically independent molecules of the previously reported analogous Tp^{Me_2} derivative, *i.e.* $[\text{Ni}^{\text{II}}(\text{Tp}^{\text{Me}_2})\text{Cl}]$, (II). The average Ni—N bond length of (I) [1.994 (1) Å] is also close to the Ni—N bond lengths of (II). However, the three Ni— $\text{N}_{\text{oxazolinyll}}$ bond lengths of (I) are slightly different from each other; in contrast, the three Ni— N_{pyz} bond lengths (pyz is pyrazolyl) in the molecules of (II) are almost identical. Also, the three Cl—Ni— N_{ox} angles in (I) are substantially different, ranging from 114.91 (3) to 136.75 (3)°, while the Cl—Ni— N_{pyz} angles in (II) are similar [121.63 (15)–125.44 (11)°]. The dihedral angles between the

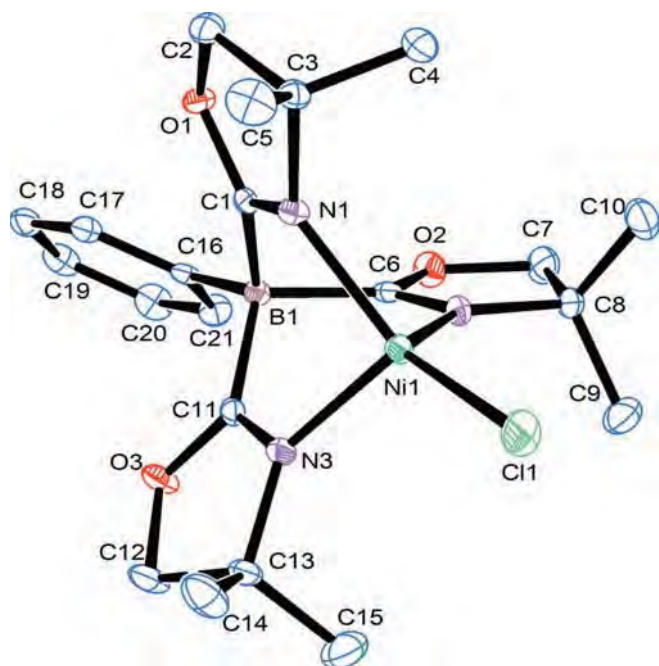


Figure 1
The molecular structure of $[\text{Ni}^{\text{II}}(\text{To}^{\text{Me}_2})\text{Cl}]$, (I), showing the atom-labelling scheme. Displacement ellipsoids are drawn at the 50% probability level. H atoms have been omitted for clarity.

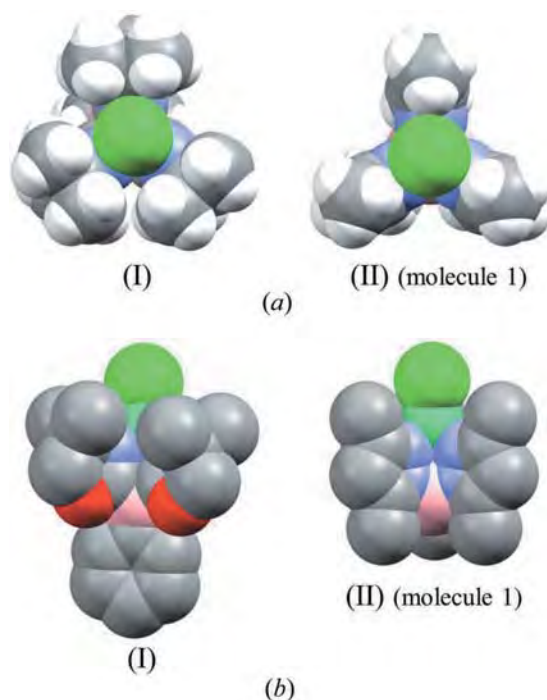


Figure 2
Space-filling diagrams of (I) and (II), viewed (a) along the Ni...B axis and (b) from the side with H atoms omitted.

planes of adjacent oxazoline rings are 102.80 (7), 125.25 (8) and 131.84 (8)° in complex (I) (the oxazoline rings are planar to within 0.090 Å). In contrast, the dihedral angles between planes of adjacent pyrazole rings in (II) are 125.77, 117.12 and 117.12° for the molecule 1 and 119.83, 120.08, 120.08° for the molecule 2. Therefore, the molecular structure of (I) is highly distorted compared to the pseudo- C_{3v} -symmetric structures of (II). Clear evidence of the distortion of (I) is that the Cl—Ni...B angle [167.03 (3)°] deviates greatly from 180°. In contrast, the facially capping tridentate Tp^{Me_2} ligand of (II) is located on a pseudo- C_{3v} axis, as indicated by the Cl—Ni...B angles of 177.5 and 178.7°. The calculated equivalent cone angles (ECA) of the scorpionate ligands, which are derived from the atomic coordinates of (I) and (II), are 211.70° for To^{Me_2} , and 204.13 and 201.37° for Tp^{Me_2} (Guzei & Wendt, 2006). As shown in the space-filling model of compound (I) in Fig. 2, six methyl groups surround the metal centre. Steric repulsion between the methyl groups would form the cavity surrounded by the rigid and bulky Me— C_{ox} —Me groups which results in the larger ECA value of To^{Me_2} . Some Tp^{R} ligands with large cone angles (*i.e.* Tp^{R} with bulky substituent groups surrounding the metal centre) are recognized to be enforcing tetrahedral geometry giving pseudo- C_{3v} -symmetric structures. In the To^{Me_2} complex, (I), however, the chloride ligand was not forced to lie on the extension of the Ni...B axis. The distance between the chloride ligand of (I) and the least-squares plane defined by the six methyl C atoms at the 4-positions of the oxazolonyl groups is 2.1201 (3) Å, whereas the distance between the Cl atom and the plane defined by the three methyl C atoms at the 3-positions of the pyrazolyl

groups of Tp^{Me_2} in (II) are 1.655 and 1.662 Å. Therefore, the bowl-shaped cavity derived from the six methyl substituents of To^{Me_2} is shallower than that made from the three methyl groups of Tp^{Me_2} , and the extent of the protrusion of the chloride ligand from the bowl-shaped cavity in (I) is larger than that found in (II).

To date, several molecular structures of tetracoordinated zinc(II) complexes with To^{Me_2} have been reported (Mukherjee *et al.*, 2010). A chloride complex, $[\text{Zn}^{\text{II}}\text{Cl}(\text{To}^{\text{Me}_2})]$, has pseudo- C_{3v} symmetry, as evidenced by an almost linear arrangement of the Cl, Zn and B atoms [$\text{Cl}-\text{Zn}\cdots\text{B} = 174.27 (2)^\circ$]. In a *tert*-butoxide (*O*'Bu) complex, $[\text{Zn}^{\text{II}}(\text{O}'\text{Bu})(\text{To}^{\text{Me}_2})]$, the $\text{O}-\text{Zn}\cdots\text{B}$ angle is significantly nonlinear [$166.03 (6)^\circ$], as found here for chloridonickel(II) complex (I). These observations seem to indicate a structurally flexible tendency of the tridentate To^{Me_2} complexes.

We have also reported a related chloride complex of nickel(II) with tris(3,5-dimethyl-4-bromopyrazol-1-yl)hydroborate, *i.e.* $[\text{Ni}^{\text{II}}\text{Cl}(\text{Tp}^{\text{Me}_2,\text{Br}})]$ (Hikichi *et al.*, 2013). Remarkably, this brominated ligand complex has a dimeric structure with pentacoordinated nickel(II) formulated as $[\{\text{Ni}(\text{Tp}^{\text{Me}_2,\text{Br}})\}_2(\mu\text{-Cl})_2]$ in the solid state, as revealed by X-ray crystallography. In CH_2Cl_2 , however, the UV-vis spectrum of this brominated complex was similar to that of complex (I) and to those of a series of $\text{Ni}-X$ ($X = \text{Cl}, \text{Br}$ and I) complexes with Tp^{Me_2} (Desrochers *et al.*, 2006), suggesting that in solution all complexes are tetrahedrally coordinated, with pseudo- C_{3v} symmetry, and that the varying degrees of distortions in the solid state arise from crystal-packing effects.

While it is known that divalent metal ions of group 10 elements (*i.e.* Ni^{II} , Pd^{II} and Pt^{II}) favour a square-planar geometry, all the chloride complexes of nickel(II) with various Tp^R and To^{Me_2} ligands are tetrahedral, with the ligand coordinating in a facially capping tridentate manner. In contrast, in the palladium analogues $[\text{Pd}^{\text{II}}\text{Cl}(\kappa^2\text{-Tp}^{\text{iPr}_2})(\text{py})]$ and $[\{\text{Pd}^{\text{II}}(\kappa^3\text{-Tp}^{\text{iPr}_2})_2(\mu\text{-Cl})_2\}][\text{Tp}^{\text{iPr}_2}$ denotes tris(3,5-diisopropylpyrazol-1-yl)hydroborate and py is pyridine], the coordination geometry of palladium is square planar, with only two of the pyrazole N atoms of the Tp^{iPr_2} ligand coordinating to the metal (Akita *et al.*, 2000).

Acknowledgements

This work was supported in part by a Grant in-Aid for Scientific Research (No. 26420788) and a Strategic Development of Research Infrastructure for Private Universities from the Ministry of Education, Culture, Sports, Science, and

Technology (MEXT), Japan. SH and JN also thank Kanagawa University for financial support.

References

- Akita, M., Miyaji, T., Muroga, N., Mock-Knoblauch, C., Adam, W., Hikichi, S. & Moro-oka, Y. (2000). *Inorg. Chem.* **39**, 2096–2102.
- Al-Harbi, A., Sattler, W., Sattler, A. & Parkin, G. (2011). *Chem. Commun.* **47**, 3123–3125.
- Altomare, A., Cascarano, G., Giacovazzo, C., Guagliardi, A., Burla, M. C., Polidori, G. & Camalli, M. (1994). *J. Appl. Cryst.* **27**, 435.
- Barney, A. A., Heyduk, A. F. & Nocera, D. G. (1999). *Chem. Commun.* pp. 2379–2380.
- Betley, T. A. & Peters, J. C. (2002). *Inorg. Chem.* **41**, 6541–6543.
- Blessing, R. H. (1995). *Acta Cryst.* **A51**, 33–38.
- Cowley, R. E., Bontchev, R. P., Duesler, E. N. & Smith, J. M. (2006). *Inorg. Chem.* **45**, 9771–9779.
- Desrochers, P. J., LeLievre, S., Johnson, R. J., Lamb, B. T., Phelps, A. L., Cordes, A. W., Gu, W. & Cramer, S. P. (2003). *Inorg. Chem.* **42**, 7945–7950.
- Desrochers, P. J., Telser, J., Zvyagin, S. A., Ozarowski, A., Krzystek, J. & Vivic, D. A. (2006). *Inorg. Chem.* **45**, 8930–8941.
- Dunne, J. F., Su, J., Ellern, A. & Sadow, A. D. (2008). *Organometallics*, **27**, 2399–2401.
- Farrugia, L. J. (2012). *J. Appl. Cryst.* **45**, 849–854.
- Fränkel, R., Kernbach, U., Bakola-Christianopoulou, M., Plaia, U., Suter, M., Ponikwar, W., Nöth, H., Moinet, C. & Fehllhammer, W. P. (2001). *J. Organomet. Chem.* **617–618**, 530–545.
- Fujita, K., Hikichi, S., Akita, M. & Moro-oka, Y. (2000). *J. Chem. Soc. Dalton Trans.* pp. 117–119.
- Garner, M., Reglinski, J., Cassidy, I., Spicer, M. D. & Kennedy, A. R. (1996). *Chem. Commun.* pp. 1975–1976.
- Ge, P., Haggerty, B. S., Rheingold, A. L. & Riordan, C. G. (1994). *J. Am. Chem. Soc.* **116**, 8406–8407.
- Guzei, I. A. & Wendt, M. (2006). *Dalton Trans.* pp. 3991–3999.
- Higashi, T. (1995). *ABSCOR*. Rigaku Corporation, Tokyo, Japan.
- Hikichi, S., Hanaue, K., Fujimura, T., Okuda, H., Nakazawa, J., Ohzu, Y., Kobayashi, C. & Akita, M. (2013). *Dalton Trans.* **42**, 3346–3356.
- Hodgkins, T. G. & Powell, D. R. (1996). *Inorg. Chem.* **35**, 2140–2148.
- Khaskin, E., Zavalij, P. Y. & Vedernikov, A. N. (2006). *J. Am. Chem. Soc.* **128**, 13054–13055.
- Mazet, C., Köhler, V. & Pfaltz, A. (2005). *Angew. Chem. Int. Ed.* **44**, 4888–4891.
- Minoura, M., Landry, V. K., Melnick, J. G., Pang, K., Marchiò, L. & Parkin, G. (2006). *Chem. Commun.* pp. 3990–3992.
- Mukherjee, D., Ellern, A. & Sadow, A. D. (2010). *J. Am. Chem. Soc.* **132**, 7582–7583.
- Pettinari, C. (2008). In *Scorpionates II: Chelating Borate Ligands*. London: Imperial College Press.
- Rigaku (2007). *CrystalClear*. Rigaku Corporation, Tokyo, Japan.
- Riordan, C. G. (2010). *Coord. Chem. Rev.* **254**, 1815–1825.
- Sheldrick, G. M. (2015). *Acta Cryst.* **C71**, 3–8.
- Thomas, J. C. & Peters, J. C. (2001). *J. Am. Chem. Soc.* **123**, 5100–5101.
- Trofimenko, S. (1966). *J. Am. Chem. Soc.* **88**, 1842–1844.
- Trofimenko, S. (1999). In *Scorpionates: The Coordination Chemistry of Polypyrazolylborate Ligands*. London: Imperial College Press.

supporting information

Acta Cryst. (2016). C , 842-845 [https://doi.org/10.1107/S2053229616012183]

A pseudotetrahedral nickel(II) complex with a tridentate oxazoline-based scorpionate ligand: chlorido[tris(4,4-dimethyloxazolin-2-yl)phenylborato]nickel(II)

Tomoaki Takayama, Jun Nakazawa and Shiro Hikichi

Computing details

Data collection: *CrystalClear* (Rigaku, 2007); cell refinement: *CrystalClear* (Rigaku, 2007); data reduction: *CrystalClear* (Rigaku, 2007), *SORTAV* (Blessing, 1995); program(s) used to solve structure: *SIR92* (Altomare *et al.*, 1994); program(s) used to refine structure: *SHELXL2014* (Sheldrick, 2015); molecular graphics: *ORTEP-3 for Windows* (Farrugia, 2012); software used to prepare material for publication: *WinGX* publication routines (Farrugia, 2012).

Ni(Ph-To)Cl

Crystal data

$C_{21}H_{29}BCIN_3NiO_3$
 $M_r = 476.44$
 Monoclinic, $P2_1/c$
 $a = 10.8792$ (17) Å
 $b = 13.221$ (2) Å
 $c = 15.972$ (3) Å
 $\beta = 96.899$ (2)°
 $V = 2280.7$ (7) Å³
 $Z = 4$

$F(000) = 1000$
 $D_x = 1.388$ Mg m⁻³
 Mo $K\alpha$ radiation, $\lambda = 0.71073$ Å
 Cell parameters from 6816 reflections
 $\theta = 1.9$ – 27.5 °
 $\mu = 1.00$ mm⁻¹
 $T = 113$ K
 Block, red
 $0.35 \times 0.35 \times 0.20$ mm

Data collection

Saturn70 (4x4 bin mode)
 diffractometer
 Radiation source: Rotating Anode
 Detector resolution: 28.5714 pixels mm⁻¹
 ω scans
 Absorption correction: numerical
 [CrystalClear (Rigaku, 2007) and ABSCOR
 (Higashi, 1995)]
 $T_{\min} = 0.761$, $T_{\max} = 0.861$

16162 measured reflections
 5168 independent reflections
 4140 reflections with $I > 2\sigma(I)$
 $R_{\text{int}} = 0.029$
 $\theta_{\max} = 27.5$ °, $\theta_{\min} = 1.9$ °
 $h = -10 \rightarrow 14$
 $k = -16 \rightarrow 16$
 $l = -20 \rightarrow 20$

Refinement

Refinement on F^2
 Least-squares matrix: full
 $R[F^2 > 2\sigma(F^2)] = 0.024$
 $wR(F^2) = 0.061$
 $S = 0.99$
 5168 reflections

277 parameters
 0 restraints
 Hydrogen site location: inferred from
 neighbouring sites
 H-atom parameters constrained

$$w = 1/[\sigma^2(F_o^2) + (0.0354P)^2]$$

where $P = (F_o^2 + 2F_c^2)/3$
 $(\Delta/\sigma)_{\max} < 0.001$

$$\Delta\rho_{\max} = 0.37 \text{ e } \text{\AA}^{-3}$$

$$\Delta\rho_{\min} = -0.25 \text{ e } \text{\AA}^{-3}$$

Special details

Geometry. All esds (except the esd in the dihedral angle between two l.s. planes) are estimated using the full covariance matrix. The cell esds are taken into account individually in the estimation of esds in distances, angles and torsion angles; correlations between esds in cell parameters are only used when they are defined by crystal symmetry. An approximate (isotropic) treatment of cell esds is used for estimating esds involving l.s. planes.

Fractional atomic coordinates and isotropic or equivalent isotropic displacement parameters (\AA^2)

	<i>x</i>	<i>y</i>	<i>z</i>	$U_{\text{iso}}^*/U_{\text{eq}}$
Ni1	0.81347 (2)	0.22126 (2)	0.46290 (2)	0.01215 (6)
Cl1	0.99249 (3)	0.25093 (3)	0.53634 (2)	0.02534 (9)
O1	0.58962 (8)	0.07426 (6)	0.28034 (6)	0.01325 (19)
O2	0.47256 (9)	0.13747 (7)	0.52167 (6)	0.0182 (2)
O3	0.54481 (8)	0.41357 (7)	0.36278 (6)	0.0176 (2)
N3	0.72065 (10)	0.34364 (8)	0.42058 (7)	0.0128 (2)
N1	0.75107 (10)	0.14194 (8)	0.35986 (7)	0.0124 (2)
N2	0.67335 (10)	0.16895 (8)	0.52071 (7)	0.0140 (2)
C8	0.66903 (13)	0.12461 (10)	0.60568 (8)	0.0159 (3)
C11	0.60804 (12)	0.32907 (10)	0.38978 (8)	0.0119 (3)
C7	0.53129 (14)	0.09517 (11)	0.60120 (9)	0.0218 (3)
H7A	0.5217	0.0207	0.6018	0.026*
H7B	0.4941	0.1240	0.6495	0.026*
C6	0.56418 (12)	0.17442 (9)	0.47998 (8)	0.0123 (3)
C4	0.83302 (14)	-0.02671 (10)	0.39302 (9)	0.0203 (3)
H4A	0.8900	0.0028	0.4387	0.030*
H4B	0.8712	-0.0866	0.3708	0.030*
H4C	0.7559	-0.0463	0.4147	0.030*
C3	0.80490 (12)	0.05100 (10)	0.32263 (8)	0.0136 (3)
C2	0.69696 (12)	0.01915 (10)	0.25686 (9)	0.0159 (3)
H2A	0.7137	0.0379	0.1993	0.019*
H2B	0.6832	-0.0548	0.2589	0.019*
C12	0.63387 (13)	0.49687 (10)	0.37142 (10)	0.0204 (3)
H12A	0.6008	0.5548	0.4010	0.024*
H12B	0.6528	0.5198	0.3154	0.024*
C10	0.75462 (15)	0.03299 (11)	0.61774 (9)	0.0249 (3)
H10A	0.7318	-0.0159	0.5724	0.037*
H10B	0.7466	0.0013	0.6723	0.037*
H10C	0.8405	0.0547	0.6163	0.037*
C21	0.30135 (13)	0.24998 (10)	0.38473 (9)	0.0187 (3)
H21	0.3166	0.2558	0.4444	0.022*
C13	0.75064 (13)	0.45344 (10)	0.42343 (9)	0.0158 (3)
C18	0.25241 (13)	0.23450 (10)	0.21099 (9)	0.0184 (3)
H18	0.2366	0.2286	0.1514	0.022*
C5	0.92108 (13)	0.07726 (11)	0.28313 (10)	0.0237 (3)
H5A	0.9020	0.1301	0.2405	0.036*

H5B	0.9513	0.0169	0.2564	0.036*
H5C	0.9850	0.1017	0.3269	0.036*
C16	0.39976 (12)	0.22645 (9)	0.33932 (8)	0.0129 (3)
C1	0.63387 (12)	0.14514 (9)	0.33751 (8)	0.0114 (3)
C19	0.15687 (13)	0.25763 (10)	0.25776 (10)	0.0212 (3)
H19	0.0754	0.2683	0.2305	0.025*
C9	0.70621 (15)	0.20563 (11)	0.67177 (9)	0.0255 (3)
H9A	0.7910	0.2280	0.6671	0.038*
H9B	0.7019	0.1777	0.7282	0.038*
H9C	0.6497	0.2633	0.6625	0.038*
C17	0.37173 (12)	0.21982 (9)	0.25145 (8)	0.0147 (3)
H17	0.4364	0.2048	0.2184	0.018*
C14	0.86871 (14)	0.47303 (11)	0.38378 (11)	0.0255 (3)
H14A	0.9381	0.4381	0.4164	0.038*
H14B	0.8854	0.5459	0.3837	0.038*
H14C	0.8588	0.4477	0.3257	0.038*
C20	0.18157 (13)	0.26514 (11)	0.34502 (10)	0.0223 (3)
H20	0.1166	0.2806	0.3777	0.027*
C15	0.76375 (16)	0.48866 (12)	0.51477 (10)	0.0298 (4)
H15A	0.6853	0.4783	0.5379	0.045*
H15B	0.7852	0.5607	0.5174	0.045*
H15C	0.8292	0.4497	0.5478	0.045*
B1	0.54017 (13)	0.21873 (11)	0.38307 (9)	0.0116 (3)

Atomic displacement parameters (\AA^2)

	U^{11}	U^{22}	U^{33}	U^{12}	U^{13}	U^{23}
Ni1	0.01108 (9)	0.01108 (9)	0.01357 (9)	-0.00066 (7)	-0.00151 (6)	0.00106 (7)
Cl1	0.01819 (18)	0.0260 (2)	0.0285 (2)	-0.00325 (14)	-0.01106 (15)	0.00344 (15)
O1	0.0131 (5)	0.0119 (5)	0.0145 (5)	0.0008 (4)	0.0004 (4)	-0.0035 (4)
O2	0.0176 (5)	0.0204 (5)	0.0175 (5)	-0.0041 (4)	0.0057 (4)	0.0032 (4)
O3	0.0143 (5)	0.0094 (5)	0.0277 (6)	0.0000 (4)	-0.0035 (4)	0.0030 (4)
N3	0.0139 (6)	0.0103 (6)	0.0138 (6)	-0.0020 (4)	0.0004 (4)	0.0006 (4)
N1	0.0125 (5)	0.0100 (5)	0.0148 (6)	0.0006 (4)	0.0016 (4)	-0.0007 (4)
N2	0.0174 (6)	0.0130 (6)	0.0114 (6)	-0.0013 (5)	0.0014 (4)	0.0018 (4)
C8	0.0243 (8)	0.0138 (7)	0.0099 (6)	-0.0017 (6)	0.0030 (6)	0.0018 (5)
C11	0.0147 (7)	0.0116 (6)	0.0095 (6)	0.0019 (5)	0.0020 (5)	0.0010 (5)
C7	0.0275 (8)	0.0225 (8)	0.0159 (7)	-0.0054 (6)	0.0049 (6)	0.0039 (6)
C6	0.0156 (6)	0.0075 (6)	0.0143 (6)	-0.0024 (5)	0.0042 (5)	-0.0025 (5)
C4	0.0241 (8)	0.0145 (7)	0.0209 (8)	0.0037 (6)	-0.0029 (6)	0.0000 (6)
C3	0.0137 (7)	0.0119 (6)	0.0153 (6)	0.0024 (5)	0.0024 (5)	-0.0009 (5)
C2	0.0162 (7)	0.0156 (7)	0.0159 (7)	0.0044 (5)	0.0024 (5)	-0.0026 (5)
C12	0.0191 (7)	0.0093 (7)	0.0314 (8)	-0.0023 (5)	-0.0028 (6)	0.0026 (6)
C10	0.0344 (9)	0.0212 (8)	0.0193 (8)	0.0055 (7)	0.0038 (7)	0.0055 (6)
C21	0.0170 (7)	0.0193 (7)	0.0201 (7)	0.0009 (6)	0.0035 (6)	-0.0015 (6)
C13	0.0177 (7)	0.0088 (6)	0.0198 (7)	-0.0020 (5)	-0.0015 (6)	0.0005 (5)
C18	0.0196 (7)	0.0132 (7)	0.0208 (7)	-0.0025 (6)	-0.0042 (6)	0.0010 (6)
C5	0.0160 (7)	0.0251 (8)	0.0313 (8)	0.0020 (6)	0.0083 (6)	-0.0002 (7)

C16	0.0130 (6)	0.0063 (6)	0.0192 (7)	-0.0014 (5)	0.0013 (5)	-0.0002 (5)
C1	0.0157 (7)	0.0090 (6)	0.0097 (6)	-0.0026 (5)	0.0019 (5)	0.0027 (5)
C19	0.0123 (7)	0.0162 (7)	0.0335 (9)	-0.0020 (5)	-0.0044 (6)	0.0036 (6)
C9	0.0350 (9)	0.0252 (8)	0.0163 (7)	-0.0053 (7)	0.0027 (6)	-0.0043 (6)
C17	0.0143 (6)	0.0109 (6)	0.0185 (7)	0.0003 (5)	0.0008 (5)	-0.0007 (5)
C14	0.0199 (8)	0.0197 (8)	0.0364 (9)	-0.0050 (6)	0.0016 (7)	0.0081 (7)
C20	0.0132 (7)	0.0231 (8)	0.0314 (8)	0.0011 (6)	0.0054 (6)	0.0019 (6)
C15	0.0358 (10)	0.0242 (8)	0.0275 (9)	0.0036 (7)	-0.0041 (7)	-0.0111 (7)
B1	0.0115 (7)	0.0100 (7)	0.0131 (7)	-0.0005 (6)	0.0011 (6)	0.0001 (6)

Geometric parameters (Å, °)

Ni1—N3	1.9825 (11)	C12—H12A	0.9900
Ni1—N2	1.9982 (11)	C12—H12B	0.9900
Ni1—N1	2.0002 (11)	C10—H10A	0.9800
Ni1—C11	2.1851 (5)	C10—H10B	0.9800
O1—C1	1.3559 (15)	C10—H10C	0.9800
O1—C2	1.4631 (15)	C21—C20	1.394 (2)
O2—C6	1.3546 (15)	C21—C16	1.3984 (19)
O2—C7	1.4627 (16)	C21—H21	0.9500
O3—C11	1.3550 (15)	C13—C14	1.521 (2)
O3—C12	1.4624 (16)	C13—C15	1.522 (2)
N3—C11	1.2788 (16)	C18—C19	1.385 (2)
N3—C13	1.4875 (16)	C18—C17	1.3923 (19)
N1—C1	1.2827 (16)	C18—H18	0.9500
N1—C3	1.4919 (17)	C5—H5A	0.9800
N2—C6	1.2859 (17)	C5—H5B	0.9800
N2—C8	1.4842 (16)	C5—H5C	0.9800
C8—C9	1.5241 (19)	C16—C17	1.4027 (18)
C8—C10	1.5259 (19)	C16—B1	1.6049 (19)
C8—C7	1.542 (2)	C1—B1	1.6412 (19)
C11—B1	1.6327 (19)	C19—C20	1.391 (2)
C7—H7A	0.9900	C19—H19	0.9500
C7—H7B	0.9900	C9—H9A	0.9800
C6—B1	1.6462 (19)	C9—H9B	0.9800
C4—C3	1.5267 (19)	C9—H9C	0.9800
C4—H4A	0.9800	C17—H17	0.9500
C4—H4B	0.9800	C14—H14A	0.9800
C4—H4C	0.9800	C14—H14B	0.9800
C3—C5	1.5191 (19)	C14—H14C	0.9800
C3—C2	1.5373 (18)	C20—H20	0.9500
C2—H2A	0.9900	C15—H15A	0.9800
C2—H2B	0.9900	C15—H15B	0.9800
C12—C13	1.5427 (19)	C15—H15C	0.9800
N3—Ni1—N2	93.12 (5)	H10A—C10—H10B	109.5
N3—Ni1—N1	92.22 (4)	C8—C10—H10C	109.5
N2—Ni1—N1	89.79 (5)	H10A—C10—H10C	109.5

N3—Ni1—C11	114.91 (3)	H10B—C10—H10C	109.5
N2—Ni1—C11	119.62 (4)	C20—C21—C16	121.89 (14)
N1—Ni1—C11	136.75 (3)	C20—C21—H21	119.1
C1—O1—C2	106.68 (10)	C16—C21—H21	119.1
C6—O2—C7	107.12 (10)	N3—C13—C14	110.27 (11)
C11—O3—C12	106.60 (10)	N3—C13—C15	108.84 (11)
C11—N3—C13	110.81 (11)	C14—C13—C15	111.13 (12)
C11—N3—Ni1	115.69 (9)	N3—C13—C12	100.57 (10)
C13—N3—Ni1	133.26 (8)	C14—C13—C12	113.23 (12)
C1—N1—C3	109.90 (11)	C15—C13—C12	112.25 (12)
C1—N1—Ni1	116.07 (9)	C19—C18—C17	119.91 (13)
C3—N1—Ni1	129.78 (8)	C19—C18—H18	120.0
C6—N2—C8	110.86 (11)	C17—C18—H18	120.0
C6—N2—Ni1	117.14 (9)	C3—C5—H5A	109.5
C8—N2—Ni1	131.99 (9)	C3—C5—H5B	109.5
N2—C8—C9	108.71 (11)	H5A—C5—H5B	109.5
N2—C8—C10	110.07 (11)	C3—C5—H5C	109.5
C9—C8—C10	111.30 (12)	H5A—C5—H5C	109.5
N2—C8—C7	101.23 (10)	H5B—C5—H5C	109.5
C9—C8—C7	112.66 (12)	C21—C16—C17	116.42 (12)
C10—C8—C7	112.37 (12)	C21—C16—B1	122.43 (12)
N3—C11—O3	115.12 (11)	C17—C16—B1	120.85 (12)
N3—C11—B1	124.38 (12)	N1—C1—O1	115.17 (11)
O3—C11—B1	120.50 (11)	N1—C1—B1	123.08 (11)
O2—C7—C8	105.34 (10)	O1—C1—B1	121.27 (11)
O2—C7—H7A	110.7	C18—C19—C20	119.28 (13)
C8—C7—H7A	110.7	C18—C19—H19	120.4
O2—C7—H7B	110.7	C20—C19—H19	120.4
C8—C7—H7B	110.7	C8—C9—H9A	109.5
H7A—C7—H7B	108.8	C8—C9—H9B	109.5
N2—C6—O2	114.86 (12)	H9A—C9—H9B	109.5
N2—C6—B1	121.89 (11)	C8—C9—H9C	109.5
O2—C6—B1	123.19 (11)	H9A—C9—H9C	109.5
C3—C4—H4A	109.5	H9B—C9—H9C	109.5
C3—C4—H4B	109.5	C18—C17—C16	122.29 (13)
H4A—C4—H4B	109.5	C18—C17—H17	118.9
C3—C4—H4C	109.5	C16—C17—H17	118.9
H4A—C4—H4C	109.5	C13—C14—H14A	109.5
H4B—C4—H4C	109.5	C13—C14—H14B	109.5
N1—C3—C5	111.55 (11)	H14A—C14—H14B	109.5
N1—C3—C4	107.60 (11)	C13—C14—H14C	109.5
C5—C3—C4	110.88 (11)	H14A—C14—H14C	109.5
N1—C3—C2	100.89 (10)	H14B—C14—H14C	109.5
C5—C3—C2	112.60 (12)	C19—C20—C21	120.22 (14)
C4—C3—C2	112.82 (11)	C19—C20—H20	119.9
O1—C2—C3	104.85 (10)	C21—C20—H20	119.9
O1—C2—H2A	110.8	C13—C15—H15A	109.5
C3—C2—H2A	110.8	C13—C15—H15B	109.5

O1—C2—H2B	110.8	H15A—C15—H15B	109.5
C3—C2—H2B	110.8	C13—C15—H15C	109.5
H2A—C2—H2B	108.9	H15A—C15—H15C	109.5
O3—C12—C13	105.30 (10)	H15B—C15—H15C	109.5
O3—C12—H12A	110.7	C16—B1—C11	111.78 (11)
C13—C12—H12A	110.7	C16—B1—C1	117.01 (11)
O3—C12—H12B	110.7	C11—B1—C1	104.99 (10)
C13—C12—H12B	110.7	C16—B1—C6	117.86 (11)
H12A—C12—H12B	108.8	C11—B1—C6	103.70 (10)
C8—C10—H10A	109.5	C1—B1—C6	99.73 (10)
C8—C10—H10B	109.5		
C6—N2—C8—C9	-113.21 (13)	O3—C12—C13—C14	129.85 (12)
Ni1—N2—C8—C9	65.54 (15)	O3—C12—C13—C15	-103.32 (13)
C6—N2—C8—C10	124.64 (13)	C20—C21—C16—C17	0.6 (2)
Ni1—N2—C8—C10	-56.60 (15)	C20—C21—C16—B1	174.30 (12)
C6—N2—C8—C7	5.59 (14)	C3—N1—C1—O1	-6.50 (15)
Ni1—N2—C8—C7	-175.65 (9)	Ni1—N1—C1—O1	-165.66 (8)
C13—N3—C11—O3	3.59 (16)	C3—N1—C1—B1	165.61 (11)
Ni1—N3—C11—O3	178.61 (8)	Ni1—N1—C1—B1	6.46 (16)
C13—N3—C11—B1	-175.62 (11)	C2—O1—C1—N1	-4.34 (14)
Ni1—N3—C11—B1	-0.61 (16)	C2—O1—C1—B1	-176.61 (11)
C12—O3—C11—N3	5.09 (15)	C17—C18—C19—C20	-0.5 (2)
C12—O3—C11—B1	-175.66 (11)	C19—C18—C17—C16	0.7 (2)
C6—O2—C7—C8	7.07 (14)	C21—C16—C17—C18	-0.76 (19)
N2—C8—C7—O2	-7.40 (13)	B1—C16—C17—C18	-174.60 (12)
C9—C8—C7—O2	108.52 (13)	C18—C19—C20—C21	0.3 (2)
C10—C8—C7—O2	-124.79 (12)	C16—C21—C20—C19	-0.4 (2)
C8—N2—C6—O2	-1.40 (15)	C21—C16—B1—C11	-85.36 (15)
Ni1—N2—C6—O2	179.64 (8)	C17—C16—B1—C11	88.09 (14)
C8—N2—C6—B1	-178.93 (11)	C21—C16—B1—C1	153.55 (12)
Ni1—N2—C6—B1	2.11 (16)	C17—C16—B1—C1	-32.99 (17)
C7—O2—C6—N2	-3.84 (15)	C21—C16—B1—C6	34.61 (18)
C7—O2—C6—B1	173.66 (11)	C17—C16—B1—C6	-151.93 (12)
C1—N1—C3—C5	133.38 (12)	N3—C11—B1—C16	-178.65 (12)
Ni1—N1—C3—C5	-71.20 (14)	O3—C11—B1—C16	2.18 (16)
C1—N1—C3—C4	-104.79 (13)	N3—C11—B1—C1	-50.82 (16)
Ni1—N1—C3—C4	50.63 (15)	O3—C11—B1—C1	130.00 (12)
C1—N1—C3—C2	13.59 (14)	N3—C11—B1—C6	53.38 (16)
Ni1—N1—C3—C2	169.01 (9)	O3—C11—B1—C6	-125.79 (12)
C1—O1—C2—C3	12.67 (13)	N1—C1—B1—C16	171.15 (12)
N1—C3—C2—O1	-15.31 (12)	O1—C1—B1—C16	-17.21 (17)
C5—C3—C2—O1	-134.34 (11)	N1—C1—B1—C11	46.57 (16)
C4—C3—C2—O1	99.21 (12)	O1—C1—B1—C11	-141.79 (11)
C11—O3—C12—C13	-11.02 (14)	N1—C1—B1—C6	-60.57 (15)
C11—N3—C13—C14	-129.72 (12)	O1—C1—B1—C6	111.08 (12)
Ni1—N3—C13—C14	56.45 (16)	N2—C6—B1—C16	-177.58 (12)
C11—N3—C13—C15	108.13 (13)	O2—C6—B1—C16	5.10 (18)

supporting information

Ni1—N3—C13—C15	-65.69 (15)	N2—C6—B1—C11	-53.47 (15)
C11—N3—C13—C12	-9.95 (14)	O2—C6—B1—C11	129.21 (12)
Ni1—N3—C13—C12	176.23 (10)	N2—C6—B1—C1	54.71 (15)
O3—C12—C13—N3	12.23 (14)	O2—C6—B1—C1	-122.62 (12)



Oxidation Catalysts

Synthesis, Characterization and Aerobic Alcohol Oxidation Catalysis of Palladium(II) Complexes with a Bis(imidazolyl)borate Ligand

Kenta Ando,^[a] Jun Nakazawa,^{*[a]} and Shiro Hikichi^{*[a]}

Abstract: Chloro- and hydroxo-palladium(II) complexes with an imidazole-based scorpionate ligand bis(1-methylimidazolyl)methylphenylborate, $[\text{B}(\text{Im}^{\text{N-Me}})_2\text{MePh}]^- (= \text{L}^{\text{Ph}})$, have been synthesized. Reaction of a lithium salt of L^{Ph} with $[\text{PdCl}_2(\text{NPh})_2]$ yields a miscellaneous mixture involving a homoleptic complex $[\text{Pd}(\text{L}^{\text{Ph}})_2]$. Replacement of the neutral ligand (benzotrile) in the starting material with pyridine leads to the desired chloride complex **1**. X-ray crystallographic analysis reveals the formula of **1** to be $[\text{PdCl}(\text{L}^{\text{Ph}})(\text{py})]$ with a square-planar palladium(II) center

supported by the bidentate L^{Ph} ligand. Treatment of **1** with NaOH yields non-pyridine-containing hydroxo species with L^{Ph} such as $[\text{Pd}(\text{OH})(\text{L}^{\text{Ph}})(\text{H}_2\text{O})]$ and $[(\text{PdL}^{\text{Ph}})_2(\mu\text{-OH})_2]$. The hydroxo species **2** can convert into active species for catalytic secondary alcohol oxidation with O_2 in the absence of extra base. The utility of **2** as a catalyst precursor and the inertness of chloride complex **1** suggest that the basic nature of the co-ligand (i.e. OH^-) on the palladium center supported by L^{Ph} is essential to the formation of a putative palladium-alkoxide intermediate.

Introduction

Poly(pyrazolyl)borates, $[\text{B}(\text{pz}^{\text{R}})_n\text{X}_{4-n}]^-$ ($n = 2-4$; R = substituent groups on the pyrazole ring; X = H, alkyl, phenyl, etc.), have been extensively utilized in various coordination compounds ranging from bioinorganic models to organometallics.^[1,2] In addition to these authentic “scorpionate” ligands, interests in other borate-based chelating ligands with N-,^[3-6] P-,^[7] S-^[8] and C-donors^[9] have been growing in recent years. As N-donating ligands, azoles such as pyridines,^[4] oxazolines,^[5] and imidazoles^[6] have been employed instead of pyrazoles. In such N-donating ligands, except for the poly(pyrazolyl)borates, the azoles are connected to a boron atom through carbon–boron bonds. The higher covalency of B–C linkages makes such species resistant to hydrolytic degradation. Consequently, these new types of scorpionate ligands are expected to be extensively applied to various organometallic and biomimetic catalysts.

Many complexes of group 10 elements with a family of poly(pyrazolyl)borates including hydrotris(pyrazolyl)borates (= Tp^{R}) have been reported thus far. In Pd^{II} complexes, Tp^{R} behaves as bidentate ligand, because Pd^{II} favors a square-planar geometry forming metastable $16e^-$ species.^[10-13] Therefore, bidentate $4e^-$ donating ligands would be suitable to obtain Pd^{II} complexes. In fact, bis(pyrazolyl)borates (= Bp^{R}) have been employed as supporting ligands for Pd^{II} , and a few such molecular structures are known.^[10,14] Our developed imidazole-based -1

charged scorpionate ligands, namely bis(1-methyl-2-imidazolyl)methylborate, $[\text{B}(\text{Im}^{\text{N-Me}})_2\text{MeX}]^- (= \text{L}^{\text{X}})$, would be applicable as supporting ligands of Pd^{II} as predicted from the established formation of square-planar Ni^{II} complexes with a series of L^{X} .^[6c,6d] In L^{X} , X can represent various functional groups such as alkoxy, alkyl, carboxy, chloride, hydride and phenyl on the boron center. Interestingly, the bulkiness of X affects the dihedral angle of two imidazolyl groups contained within L^{X} coordinating to a metal center. Although the phenyl group is a two-dimensional planar component based on sp^2 -hybridized carbon atoms, it is less bulky than alkyl groups composed of sp^3 -hybridized carbon atoms with respect to three-dimensional occupancy.^[6d] Therefore, the arrangement of the phenyl group on L^{Ph} is one of the critical factors dictating the molecular structure of resulting metal complexes. In this study, N2-donating L^{Ph} complexes of Pd^{II} have been synthesized. Additionally, the catalytic activities of the newly synthesized Pd^{II} complexes in alcohol oxidation reactions have been examined.

Results and Discussion

Synthesis, Characterization and Reactivity of Chloropalladium(II) Complexes with L^{Ph}

Reaction of the benzonitrile adduct of dichloropalladium(II), $[\text{PdCl}_2(\text{PhCN})_2]$, and 1 equiv. of LiL^{Ph} , generated in situ by treatment of HL^{Ph} with $n\text{BuLi}$, yielded a mixture of L^{Ph} complexes of palladium(II) as suggested by moderately complicated ^1H NMR data. ESI-MS analysis of this product mixture displayed several ion peaks attributed to fragments containing a $[\text{Pd}(\text{L}^{\text{Ph}})]^+$ component. Formation of a desired chloropalladium(II) complex, $[\text{Pd}^{\text{II}}\text{Cl}(\text{L}^{\text{Ph}})(\text{PhCN})]$, was suggested by elemental analysis data as

[a] Department of Material and Life Chemistry, Faculty of Engineering, Kanagawa University

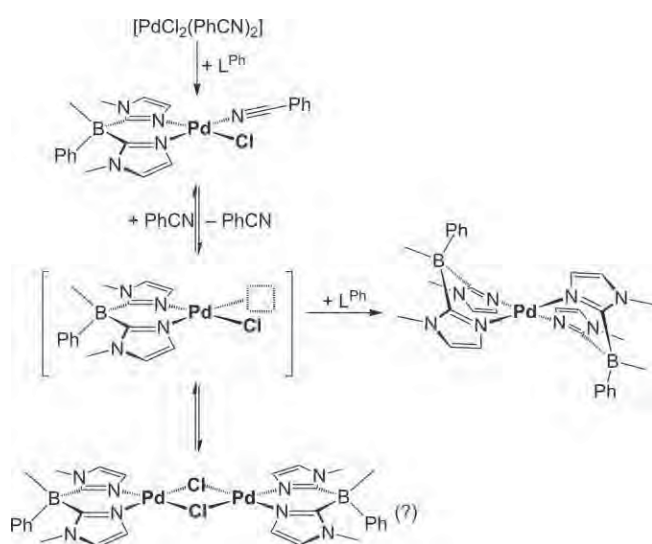
3-27-1 Rokkakubashi, Kanagawa-ku, Yokohama 221-8686, Japan

E-mail: hikichi@kanagawa-u.ac.jp

<http://apchem2.kanagawa-u.ac.jp/~hikichilab/>

Supporting information for this article is available on the WWW under <http://dx.doi.org/10.1002/ejic.201600206>.

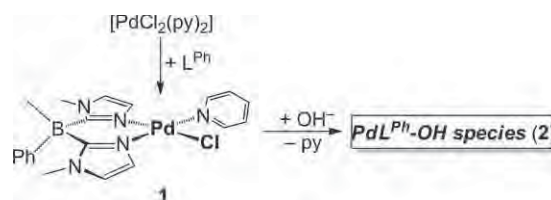
well as the observation of ion peaks assigned as $\{[\text{Pd}^{\text{II}}\text{Cl}(\text{L}^{\text{Ph}})(\text{NCPH})] + \text{Li} + \text{H}_2\text{O}\}^+$ in the ESI mass spectrum and an IR peak consistent with CN stretching that could be attributed to a Pd-binding benzonitrile molecule. From this crude product mixture, however, only a trace amount of crystalline solid could be isolated. Preliminary X-ray crystallographic analysis revealed the molecular structure of the isolated solid to be homoleptic complex $[\text{Pd}^{\text{II}}(\text{L}^{\text{Ph}})_2]$ (see Supporting Information). Notably, this homoleptic complex would be one of the anticipated equilibrium products formed through dissociation of benzonitrile as proposed in Scheme 1. In the case of Tp^{iPr_2} complexes, a dinuclear Pd^{II} -chlorido species without any neutral ligand [i.e. $[\text{PdTp}^{\text{iPr}_2}]_2(\mu\text{-Cl})_2$], has been generated by acetonitrile dissociation from starting compound $[\text{PdCl}_2(\text{MeCN})_2]$.^[12] Our attempts to isolate putative chlorido complexes such as dinuclear bis- μ -chloride species and the mononuclear benzonitrile adduct have, thus far, failed.



Scheme 1. Reaction of $[\text{PdCl}_2(\text{PhCN})_2]$ with $\text{Li}\cdot\text{L}^{\text{Ph}}$ affords a product mixture in equilibrium.

The chloropalladium complex with L^{Ph} could be trapped by changing the neutral benzonitrile co-ligand to pyridine (Scheme 2). The molecular structure of the pyridine adduct, $[\text{Pd}^{\text{II}}\text{Cl}(\text{L}^{\text{Ph}})(\text{py})]$ (**1**), was solved by X-ray crystallography (Figure 1). The palladium center has a square-planar geometry supported by an N_3Cl donor set, and the bond lengths of Pd–N are different due to a *trans* influence. The Pd–N3 bond, of which one of two nitrogen donors from L^{Ph} is located *trans* to the Cl ligand, is somewhat longer than the Pd–N1 one, another N-donor from the L^{Ph} *trans* to the pyridine ligand. The overall structure of the coordination sphere of the palladium center is similar to that of a previously reported Tp^{iPr_2} complex, namely $[\text{Pd}^{\text{II}}\text{Cl}(\kappa^2\text{-Tp}^{\text{iPr}_2})(\text{py})]$ (Table 1). In the Tp^{iPr_2} complex, two of the three pyrazolyl N-donors coordinate to the Pd center, and a remaining pyrazolyl group is *not* directed towards the palladium atom.^[12] In L^{Ph} of **1**, the planar phenyl substituent on the boron center is located in the cleft between the two *N*-methyl groups of the imidazolyl donors. As a result, the dihedral angle of the two imidazolyl rings (154.7°) is wider than that found in $[\text{Pd}^{\text{II}}(\text{L}^{\text{Ph}})_2]$ (122.0°), in which the boron-coordinated phenyl

group faces the Pd center and the boron-associated methyl group resides between two *N*-methyl groups.^[6d] A CDCl_3 solution of **1** displayed two sets of ^1H NMR signals for the imidazolyl groups of L^{Ph} . In addition, ^1H NMR signals attributed to the Pd-binding pyridine of **1** were moderately shifted relative to those of $[\text{Pd}^{\text{II}}\text{Cl}_2(\text{py})_2]$. These observations support the notion that the coordination structure of **1** is maintained in the solution state. In an ESI mass spectrum of an $\text{MeOH}/\text{CH}_2\text{Cl}_2$ solution of **1**, ion peaks assigned to $[\text{Pd}(\text{L}^{\text{Ph}})]^+$ were observed as major signals. In addition to the ion peaks of several mononuclear Pd species, minor signals representative of $[\text{Pd}^{\text{II}}_2\text{Cl}(\text{L}^{\text{Ph}})_2]^+$ ($m/z = 777.8$), a putative Cl^- dissociated cation from the putative dinuclear palladium(II)-bis(μ -chlorido) complex, were observed. This observation suggests that dissociation of the neutral ligand (e.g. benzonitrile and pyridine) leads to dimerization of the $[\text{Pd}^{\text{II}}\text{X}(\text{L}^{\text{Ph}})]$ moiety.



Scheme 2. Formation of chlorido (**1**) and hydroxo (**2**) complexes.

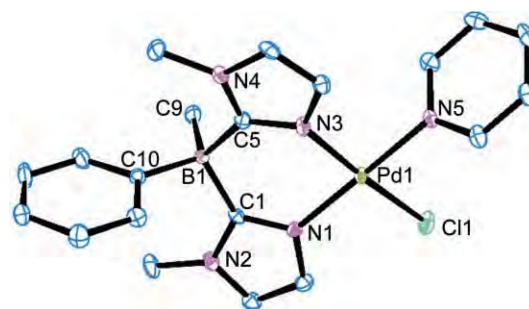


Figure 1. Molecular structure of **1** (30% probability).

Table 1. Selected structural parameters of **1** and $[\text{PdCl}(\kappa^2\text{-Tp}^{\text{iPr}_2})(\text{py})]$.^[12]

Complex:	1	$[\text{PdCl}(\kappa^2\text{-Tp}^{\text{iPr}_2})(\text{py})]$
N2 ligand:	L^{Ph}	Tp^{iPr_2}
Bond lengths [Å]		
Pd–Cl	2.3065(10)	2.285(1)
Pd–N1	2.011(3)	2.002(3)
Pd–N3	2.031(3)	2.015(3)
Pd–N5	2.034(3)	2.032(3)
Bond angles [°]		
N1–Pd1–Cl	92.41(10)	92.59(9)
N1–Pd1–N3	91.04(13)	86.2(1)
N1–Pd1–N5	178.48(13)	176.7(1)
N3–Pd1–Cl	176.35(9)	177.72(9)
N3–Pd1–N5	89.67(12)	92.1(1)
N5–Pd1–Cl	86.84(10)	89.01(9)

The present chloride complex **1** was converted into hydroxo species **2** through reaction with NaOH in a $\text{THF}/\text{toluene}$ mixture. An ESI mass spectrum of an $\text{MeOH}/\text{CH}_2\text{Cl}_2$ solution of **2** exhibited ion peaks attributable to not only monomeric species

such as $[\text{Pd}(\text{L}^{\text{Ph}})]^+$ and its MeOH adducts, but also dinuclear Pd species assigned as Na^+ adducts of $[\text{Pd}^{\text{II}}_2(\text{L}^{\text{Ph}})_2(\text{OH})(\text{OMe})]$ and $[\text{Pd}^{\text{II}}_2(\text{L}^{\text{Ph}})_2(\text{OMe})_2]$. In the ^1H NMR spectrum (Figure S7, Supporting Information), no signals attributed to pyridine were observed. Two sets of signals representing methyl groups bound to the boron center and the imidazolyl 1-nitrogen atom of L^{Ph} were observed in a ratio of 3:2. Also, the ratio of peak areas for two signals at $\delta = -2.63$ and -2.52 ppm was 3:2. These higher-magnetic-field signals disappeared upon addition of D_2O due to fast H/D exchange involving the hydroxide ligands. In the mononuclear and dinuclear hydroxo complexes of palladium(II) with $\text{Tp}^{\text{Pr}2}$, the signals of the proton of the OH group were observed at $\delta = -1.79$ ppm for $[\text{Pd}^{\text{II}}(\text{OH})(\kappa^2\text{-Tp}^{\text{Pr}2})(\text{py})]$ and $\delta = -1.71$ ppm for $[\{\text{Pd}^{\text{II}}(\kappa^2\text{-Tp}^{\text{Pr}2})(\text{H}_2\text{O})\}_2(\mu\text{-OH})_2]$, respectively.^[12] Therefore, **2** is likely a mixture of non-pyridine-containing hydroxo complexes. A possible explanation for the existence of two sets of ^1H NMR signals for OH and L^{Ph} is that **2** is a mixture of a mononuclear hydroxo complex with an aqua ligand, $[\text{Pd}^{\text{II}}(\text{OH})(\text{L}^{\text{Ph}})(\text{H}_2\text{O})]$ (**2a**), and a dinuclear complex without neutral ligands, $[\{\text{Pd}^{\text{II}}(\text{L}^{\text{Ph}})\}_2(\mu\text{-OH})_2]$ (**2b**), as shown in Figure 2. At this stage, we cannot exclude another possibility, the existence of structural isomers arising from orientational differences involving the Ph group in L^{Ph} {i.e. "facing towards the metal center" as found in $[\text{Pd}^{\text{II}}(\text{L}^{\text{Ph}})]$ or "sitting between two N-methyl groups" as in complex **1**}. Additionally, such orientational differences may involve different arrangements of L^{Ph} {i.e. "syn" versus "anti" with respect to the boron-linked methyl groups} in complex **2b**.

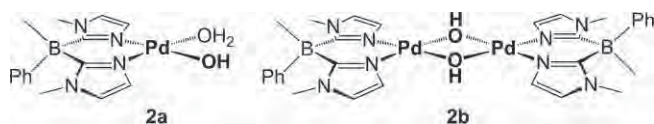


Figure 2. Plausible structures of the hydroxo species **2**.

Alcohol Oxidation Catalysis

Interest in oxidative transformations of organic substrates employing O_2 as the terminal oxidant has been growing substantially. To date, many palladium species have been employed as catalysts for various oxidative reactions.^[15,16] Several palladium complexes have been reported as catalysts for aerobic alcohol oxidation reactions. Among successful ligands employed for such palladium-based catalysts are N2-chelating phenanthroline derivatives.^[17] The present L^{Ph} ligand is also an N2-chelating species consisting of the π -accepting imidazole. Therefore, the

possible application of L^{Ph} complexes **1** and **2** as precursors of a catalyst for alcohol oxidations with O_2 was examined. In addition to synthetic L^{Ph} -containing compounds **1** and **2**, precursor species $[\text{PdCl}_2(\text{py})_2]$ and $[\text{PdCl}_2(\text{PhCN})_2]$ along with addition of HL^{Ph} to these precursors were examined in such oxidative assays.

In this study, solvent-free oxidation of 1-phenylethanol under relatively mild conditions (353 K, 1 atm of O_2 , no additive) was tested. A product formed under these conditions was acetophenone, although bis(1-phenylethyl) ether was also detected in one exceptional case (see below). Time courses and yields of acetophenone production with all the systems examined are summarized in Figure 3 and Table 2, respectively. Hydroxo species **2** clearly served as a precursor to the alcohol-oxidizing catalyst. An initial reaction rate for the **2**-based system was the fastest of all those evaluated. In contrast, chlorido complex **1** seemed to serve as an inhibitor for alcohol autoxidation. Also, the mixture of $[\text{PdCl}_2(\text{PhCN})_2]$ and HL^{Ph} appeared to induce only a small extent of catalysis. These observations indicate that the hydroxide ligand may work efficiently in the $\text{Pd}^{\text{II}}\text{-L}^{\text{Ph}}$ compounds. Metal-alkoxide species are often proposed to be important intermediates in alcohol oxidation reactions; examples include many catalytic systems such as homogeneous metallo-complex catalysts, enzymes, and heterogeneous supported

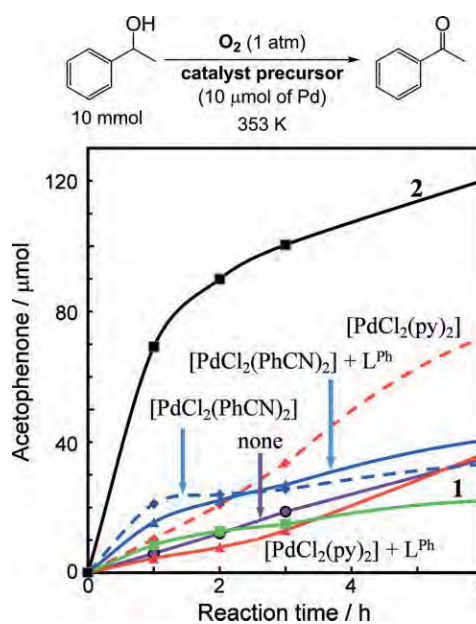
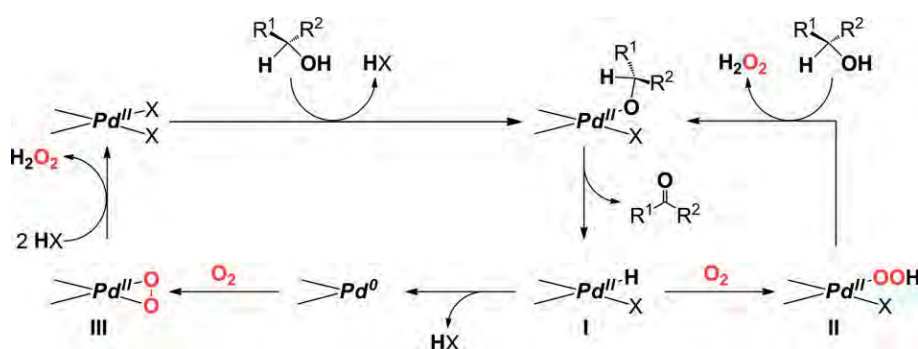


Figure 3. Time course of 1-phenylethanol oxidation with O_2 .

Table 2. Activities for the solvent-free oxidation of 1-phenylethanol with O_2 .

Compound	Amount of acetophenone [μmol]		TON per palladium 24 h
	6 h	24 h	
none	34.8	61.0	–
1	22.0	27.8	2.8
2	120.1	129.6	13.0
$[\text{PdCl}_2(\text{py})_2]$	72.0	194.1	19.4
$[\text{PdCl}_2(\text{py})_2] + \text{HL}^{\text{Ph}}$	36.3	181.9	18.2
$[\text{PdCl}_2(\text{PhCN})_2]$	33.2	59.6	6.0
$[\text{PdCl}_2(\text{PhCN})_2] + \text{HL}^{\text{Ph}}$	40.5	84.1	8.4



Scheme 3. Proposed reaction mechanisms for 1-phenylethanol oxidation.

metal catalysts.^[18–20] In our system, dehydrative condensation of hydroxo species **2** with the alcohol substrate would yield a palladium(II) alkoxide intermediate; this might explain why such reactions did not require a base additive. As we have reported previously, palladium(II)-hydroxo complexes $[\text{Pd}^{\text{II}}(\text{OH})(\kappa^2\text{-Tp}^{\text{Pr}2})(\text{py})]$ and $[\{\text{Pd}^{\text{II}}(\kappa^2\text{-Tp}^{\text{Pr}2})(\text{H}_2\text{O})\}_2(\mu\text{-OH})_2]$ react with various protic compounds HA to give the corresponding A^- complexes, where HA may represent an alcohol (= MeOH), phenol, or hydroperoxide (= H_2O_2 , *t*BuOOH).^[12,13] In fact, we noted that the present L^{Ph} complexes **2** were readily converted into their corresponding alkoxide species during ESI-MS ionization as described above. The chloride ligand of **1** proved inert with respect to the presence of alcohol, and the coordinating pyridine ligand in **1** was insufficient in terms of driving the reaction. In contrast, starting compound $[\text{PdCl}_2(\text{py})_2]$ was an efficient precursor to the oxidative catalyst. Although the initial reaction rate of the system with $[\text{PdCl}_2(\text{py})_2]$ was slower than that measured for **2**, the yield of acetophenone after 24 h proved optimal among the systems evaluated. Analogous complex $[\text{PdCl}_2(\text{PhCN})_2]$ failed to serve as a catalyst precursor due to formation of palladium black (Pd^0). In this system, a dehydrative coupling of 1-phenylethanol substrate was noted to afford the corresponding symmetric ether. Notably, the addition of L^{Ph} to $[\text{PdCl}_2(\text{PhCN})_2]$ suppressed the precipitation of Pd^0 but did little to improve the desired catalytic oxidation chemistry.

For the Pd^{II} complex catalyzed alcohol oxidation, two possible reaction mechanisms are proposed as shown in Scheme 3. One mechanism invokes a putative palladium(II) hydride intermediate (**I** in Scheme 3) that reacts with O_2 giving a palladium(II)-hydroperoxo species (**II**). Another mechanistic possibility entails reductive elimination of HX from the $\text{Pd}(\text{H})(\text{X})$ species **I** to yield the corresponding Pd^0 compound and subsequent reaction with O_2 giving palladium(II)-peroxo species **III**. In the former mechanism, the oxidation state of the palladium center remains +2 throughout the catalyst turnover process.^[15,16,21] Our -1 -charged L^{Ph} ligand might favor palladium(II) rather than palladium(0), as suggested by the absence of peaks during the initial reductive scan within -1.1 V (v.s. Fc/Fc^+) in the CV data for **1** and **2** (see Supporting Information). However, in the reaction mediated by complex **2**, the rate of formation for acetophenone was seen to gradually diminish, and the conversion of 1-phenylethanol was almost completely stopped at a reaction time of 6 h (Figure 3 and Table 2). During this reaction the color of the reaction mixture turned from pale yellow to brown during the

initial stages, and the brown color darkened with further progress of the reaction. These observations suggest that the catalytically active species formed from **2** might react with H_2O_2 generated during catalytic turnover.^[21] Such a reaction with H_2O_2 may lead to a less basic and effectively inert species, thereby serving as a means of catalyst quenching. To gain further insight into our catalytic reaction mechanism, the reactivity of **2** with H_2O_2 warrants further investigation. Towards this end, the results of ongoing work will be reported in due course.

Conclusions

Imidazole-based scorpionate ligand L^{Ph} was employed as a bidentate support for palladium(II). Reaction of $[\text{PdCl}_2(\text{PhCN})_2]$ with L^{Ph} yielded a miscellaneous mixture including the homoleptic complex $[\text{Pd}^{\text{II}}(\text{L}^{\text{Ph}})_2]$. The mononuclear chloropalladium(II) complex with pyridine as co-ligand (= **1**) was synthesized from the $[\text{PdCl}_2(\text{py})_2]$ precursor and characterized by X-ray crystallography. Hydrolysis of pyridine-containing chloride complex **1** gave non-pyridine-containing hydroxo species **2**, an efficient precursor of the catalyst for secondary alcohol oxidations with O_2 . Moreover, hydroxo species **2** is a promising precursor of catalysts for various oxygen-coupled oxidation reactions such as oxidative functionalization of alkenes.^[15]

Experimental Section

Instrumentation: Elemental analyses were performed with a Perkin–Elmer CHNS/O Analyzer 2400II. IR measurements of KBr pellets of solid compounds were carried out by using JASCO FT/IR 4200 spectrometers. NMR spectra were recorded with a JEOL ECA-600 (^1H , 600.0 MHz) spectrometer. Chemical shifts (δ) are reported in ppm downfield from the signal of internal SiMe_4 . Mass spectra were measured with a JEOL JMS-T100LC using the electrospray ionization (ESI) method (positive mode). Gas chromatographic (GC) analyses were carried out with a Shimadzu GC-2010 instrument with a flame ionization detector equipped with a RESTEK Rtx-Wax (30 m, 0.25 mmID, 0.25 μm df) capillary column.

Materials and Methods: All manipulations were performed under argon using standard Schlenk techniques. THF, Et_2O , pentane, toluene, CH_2Cl_2 , and MeCN were purified by means of a Glass Contour Solvent Dispensing System under Ar. Other reagents of high grade commercially available were used without further purification. $[\text{PdCl}_2(\text{PhCN})_2]$ ^[22] and $\text{H}\cdot\text{L}^{\text{Ph}[\text{6b}]}$ were prepared according to the methods described in the literature.

Synthesis of the Compounds

[PdCl(L^{Ph})(py)] (1): In a 100 mL Schlenk tube, addition of pyridine (0.23 mL, 2.8 mmol) to a reddish-brown CH₂Cl₂ (40 mL) solution of [PdCl₂(PhCN)₂] (216 mg, 0.56 mmol) yielded a pale yellow solution of [PdCl₂(py)₂]. In another Schlenk tube, a 1.6 M *n*-hexane solution of *n*-butyllithium (0.43 mL, 0.68 mmol) was slowly added to a THF (20 mL) solution of H-L^{Ph} (180 mg, 0.68 mmol) at -80 °C. The resulting mixture containing lithium the salt of L^{Ph} was warmed gradually to ambient temperature, and stirring was continued for 30 min. This Li-L^{Ph} solution was slowly added to the prepared THF solution of [PdCl₂(py)₂], and the resultant mixture was stirred at room temperature for 1 h, then heated at reflux for 3 h. After removal of the volatiles under reduced pressure, the resulting solid was dissolved in CH₂Cl₂, and insoluble materials were removed by filtration through a Celite plug. From the filtrate, the volatiles were removed under reduced pressure to yield **1** as a yellow powder. C₂₀H₂₃BClN₅Pd (486.12): calcd. C 49.42, H 4.77, N 14.41; found C 49.61, H 4.81, N 14.60. IR (KBr): $\tilde{\nu}$ = 3132 (w, ν_{CH}), 3062 (w, ν_{CH}), 2993 (s, ν_{CH}), 2908 (s, ν_{CH}), 1605 (s, ν_{CN}), 1547 (w), 1449 (s), 1283 (s, ν_{BC}), 1136 (s), 942 (s), 745 (s), 712 (s), 689 (s) cm⁻¹. ¹H NMR (CDCl₃): δ = 0.54 (s, 3 H, *Me*-B), 2.94 (s, 3 H, *Me*-N), 2.95 (s, 3 H, *Me*-N), 5.66 (d, *J* = 1.4 Hz, 1 H, 4-*H*_{im}), 6.38 (d, *J* = 1.4 Hz, 1 H, 5-*H*_{im}), 6.52 (d, *J* = 1.4 Hz, 1 H, 4-*H*_{im}), 7.06 (t, *J* = 7.2 Hz, 1 H, 4-*H*_{Ph}), 7.15 (t, *J* = 7.2 Hz, 2 H, 3,5-*H*_{Ph}), 7.21 (d, *J* = 6.9 Hz, 2 H, 2,6-*H*_{Ph}), 7.39 (t, *J* = 7.2 Hz, 2 H, 3,5-*H*_{py}), 7.46 (d, *J* = 2.1 Hz, 1 H, 5-*H*_{im}), 7.84 (t, *J* = 7.6 Hz, 1 H, 4-*H*_{py}), 8.72 (d, *J* = 4.8 Hz, 2 H, 2,6-*H*_{py}) ppm. ESI-MS (positive; MeOH/CH₂Cl₂): *m/z* = 370.9 [Pd + L]⁺, 402.9 [Pd + L + MeOH]⁺, 449.9 [Pd + L + Py]⁺, 482.0 [Pd + L + Py + MeOH]⁺, 777.8 [2 Pd + 2 L + Cl]⁺.

Hydroxo Species 2: In a 50 mL Schlenk tube, **1** (48.6 mg, 0.10 mmol) was dissolved in a mixture of THF (2 mL) and toluene (10 mL) at ambient temperature under Ar. To this solution, a powder of NaOH (100 mg, 2.5 mmol) was added, and the mixture was stirred at room temperature for 15 h. Then insoluble compounds were removed by filtration through a Celite plug, and the volatiles were removed from the filtrate by evaporation to give **2** as a pale-yellow powder. IR (KBr): $\tilde{\nu}$ = 3378 (w), 3133 (w), 3060 (w, ν_{CH}), 3041 (w, ν_{CH}), 2993 (s, ν_{CH}), 2923 (s, ν_{CH}), 1589 (w, ν_{CN}), 1572 (s, ν_{CN}), 1443 (s), 1431 (s), 1415 (s), 1285 (s, ν_{BC}), 1141 (s), 938 (s), 736 (s), 713 (s), 523 (s) cm⁻¹. ¹H NMR (CDCl₃): δ = -2.63 (s, 0.6 H, *OH*), -2.52 (s, 0.4 H, *OH*), 0.29 (s, 1.2 H, *Me*-B), 0.29 (s, 1.8 H, *Me*-B), 3.00 (s, 3.6 H, *Me*-N), 3.08 (s, 2.4 H, *Me*-N), 6.48 (d, *J* = 1.8 Hz, 1.2 H, 4-*H*_{im}), 6.49 (d, *J* = 1.8 Hz, 0.8 H, 4-*H*_{im}), 6.76 (d, *J* = 1.8 Hz, 2 H, 5-*H*_{im}), 7.12 (m, 1 H, 4-*H*_{Ph}), 7.14 (m, 2 H, 3,5-*H*_{Ph}), 7.18 (m, 2 H, 2,6-*H*_{Ph}) ppm. ESI-MS (positive; MeOH/CH₂Cl₂): *m/z* = 371.0 [Pd + L]⁺, 403.0 [Pd + L + MeOH]⁺, 452.0 [Pd + L + OH + 2 MeOH]⁺, 484.1 [Pd + L + OH + 3 MeOH]⁺, 815.0 [2 Pd + 2 L + OH + MeO + Na]⁺, 829.0 [2 Pd + 2 L + 2 MeO + Na]⁺.

Catalytic Alcohol Oxidation with O₂: To 1-phenylethanol (1.2 mL, 10 mmol), the examined Pd compounds (10 μ mol of Pd) and naphthalene (12.8 mg, 100 μ mol; as an internal standard for GC analyses) were added. All reactions were carried at 353 K under 1 atm of O₂, and the products were analyzed by GC.

X-ray Data Collections and Structural Determinations: Single crystals of [Pd(L^{Ph})₂] and chloride complex **1** were obtained by application of the vapor diffusion method; to CH₂Cl₂ solutions of the complexes, the vapor of hexane was diffused. Diffraction data were collected using a Rigaku Satarn 70 CDD area detector system with graphite-monochromated Mo-K α radiation. The crystals were mounted on loops using liquid paraffin flash-cooled to 113 K, and the data collections were carried at the same temperature. Crystallographic data and the results of refinement are summarized in

Table S-1. Structure analyses were performed by using the Win-GX program package.^[23] The structures of the complexes were solved by direct methods using the SIR-92 program.^[24] The structures were refined on F² with full-matrix least-squares methods using SHELXL-2014/7.^[25] All non-hydrogen atoms were refined anisotropically. Hydrogen atoms on the pyrazolyl and phenyl groups were added in the riding mode with C-H 0.96 Å (for methyl groups) or 0.93 Å (for aromatic rings) with U_{iso}(H) = 1.2 U_{iso}(attached atom). CCDC 1434363 (for [Pd(L^{Ph})₂]), and 1434364 (for **1**) contain the supplementary crystallographic data for this paper. These data can be obtained free of charge from The Cambridge Crystallographic Data Centre.

Supporting Information (see footnote on the first page of this article): Reaction procedures for [PdCl₂(PhCN)₂] with L^{Ph} and spectroscopic data of [Pd(L^{Ph})₂]; procedures and results of cyclic voltammetry of **1** and **2**; ORETP diagram and selected structural parameters of [Pd(L^{Ph})₂]; ¹H NMR, ESI mass and IR spectra of [Pd(L^{Ph})₂], **1**, and **2**.

Acknowledgments

This work was supported in part by a Grant in-Aid for Scientific Research (No. 26420788) and a Strategic Development of Research Infrastructure for Private Universities from the Ministry of Education, Culture, Sports, Science, and Technology (MEXT), Japan. S. H. and J. N. also thank Kanagawa University for financial support.

Keywords: Borates · Palladium · N ligands · Oxidation

- [1] S. Trofimenko, *Scorpionates – The Coordination Chemistry of Polypyrazolylborate Ligands*, Imperial College Press, London, **1999**.
- [2] C. Pettinari, *Scorpionates II: Chelating Borate Ligands*, Imperial College Press, London, **2008**.
- [3] For an amide-based borate ligand, see: T. A. Betley, J. C. Peters, *Inorg. Chem.* **2002**, *41*, 6541–6543.
- [4] For examples of borate ligands based on pyridine donors, see: a) T. G. Hodgkins, D. R. Powell, *Inorg. Chem.* **1996**, *35*, 2140–2148; b) E. Khaskin, P. Y. Zavalij, A. N. Vedernikov, *J. Am. Chem. Soc.* **2006**, *128*, 13054–13055; c) E. Khaskin, P. Y. Zavalij, A. N. Vedernikov, *Angew. Chem. Int. Ed.* **2007**, *46*, 6309–6312; *Angew. Chem.* **2007**, *119*, 6425; d) E. Khaskin, P. Y. Zavalij, A. N. Vedernikov, *J. Am. Chem. Soc.* **2008**, *130*, 10088–10089; e) E. Khaskin, D. L. Lew, S. Pal, A. N. Vedernikov, *Chem. Commun.* **2009**, 6270–6272; f) C. Cui, R. A. Lalancette, F. Jäkle, *Chem. Commun.* **2012**, *48*, 6930–6932.
- [5] For examples of borate ligands based on oxazolines, see: a) C. Mazet, V. Köhler, A. Pfaltz, *Angew. Chem. Int. Ed.* **2005**, *44*, 4888–4891; *Angew. Chem.* **2005**, *117*, 4966; b) V. Köhler, C. Mazet, A. Toussaint, K. Kulicke, D. Häussinger, M. Neuburger, S. Schaffner, S. Kaiser, A. Pfaltz, *Chem. Eur. J.* **2008**, *14*, 8530–8539; c) J. F. Dunne, J. Su, A. Ellern, A. D. Sadow, *Organometallics* **2008**, *27*, 2399–2401; d) B. Baird, A. V. Pawlikowski, J. Su, J. W. Wiench, M. Pruski, A. D. Sadow, *Inorg. Chem.* **2008**, *47*, 10208–10210; e) A. V. Pawlikowski, A. Ellern, A. D. Sadow, *Inorg. Chem.* **2009**, *48*, 8020–8029; f) J. F. Dunne, K. Manna, J. W. Wiench, A. Ellern, M. Pruski, A. D. Sadow, *Dalton Trans.* **2010**, *39*, 641–653.
- [6] For examples of borate ligands based on imidazolyl donors, see: a) K. Fujita, S. Hikichi, M. Akita, Y. Moro-oka, *J. Chem. Soc., Dalton Trans.* **2000**, 117–119; b) K. Fujita, S. Hikichi, M. Akita, Y. Moro-oka, *J. Chem. Soc., Dalton Trans.* **2000**, 1255–1260; c) K. Fujita, M. Akita, S. Hikichi, *Inorg. Chim. Acta* **2009**, *362*, 4472–4479; d) S. Hikichi, K. Fujita, Y. Manabe, M. Akita, J. Nakazawa, H. Komatsuzaki, *Eur. J. Inorg. Chem.* **2010**, 5529–5537; e) F. Odon, Y. Chiba, J. Nakazawa, T. Ohta, T. Ogura, S. Hikichi, *Angew. Chem. Int. Ed.* **2015**, *54*, 7336–7339; *Angew. Chem.* **2015**, *127*, 7444–7447; f) S. Hikichi, M. Kaneko, Y. Miyoshi, N. Mizuno, K. Fujita, M. Akita, *Top. Catal.* **2009**, *52*, 845–851; g) T. Tsuruta, T. Yamazaki, K. Watanabe, Y.

- Chiba, A. Yoshida, S. Naito, J. Nakazawa, S. Hikichi, *Chem. Lett.* **2015**, *44*, 144–146.
- [7] For examples of borate ligands based on phosphines, see: a) A. A. Barney, A. F. Heyduk, D. G. Nocera, *Chem. Commun.* **1999**, 2379–2380; b) J. C. Thomas, J. C. Peters, *J. Am. Chem. Soc.* **2001**, *123*, 5100–5101.
- [8] For examples of borate ligands based on thioethers, see: a) C. G. Riordan, *Coord. Chem. Rev.* **2010**, *254*, 1815–1825; b) P. Ge, B. S. Haggerty, A. L. Rheingold, C. G. Riordan, *J. Am. Chem. Soc.* **1994**, *116*, 8406–8407; c) C. Ohrenberg, P. Ge, P. Schebler, C. G. Riordan, G. P. A. Yap, A. L. Rheingold, *Inorg. Chem.* **1996**, *35*, 749–754; d) C. Ohrenberg, L. M. Liable-Sands, A. L. Rheingold, C. G. Riordan, *Inorg. Chem.* **2001**, *40*, 4276–4283.
- [9] For examples of borate ligands based on NHCs, see: a) R. Fränkel, U. Kernbach, M. Bakola-Christianopoulou, U. Plaia, M. Suter, W. Ponikwar, H. Nöth, C. Moinet, W. P. Fehlhammer, *J. Organomet. Chem.* **2001**, *617–618*, 530–545; b) R. E. Cowley, R. P. Bontchev, E. N. Duesler, J. M. Smith, *Inorg. Chem.* **2006**, *45*, 9771–9779; c) I. Nieto, R. P. Bontchev, J. M. Smith, *Eur. J. Inorg. Chem.* **2008**, 2476–2480.
- [10] P. K. Byers, A. J. Canty, R. T. Honeyman, *Adv. Organomet. Chem.* **1992**, *34*, 1–65.
- [11] a) A. J. Canty, N. J. Minchin, L. M. Engelhardt, B. W. Skelton, A. H. White, *J. Chem. Soc., Dalton Trans.* **1986**, 645–650; b) A. L. Rheingold, L. M. Liable-Sands, C. L. Incarvito, S. Trofimenko, *J. Chem. Soc., Dalton Trans.* **2002**, 2297–2301.
- [12] For chlorido and hydroxo complexes of Pd^{II} with Tp^{Pr}2, see: M. Akita, T. Miyaji, N. Muroga, C. Mock-Knoblauch, S. Hikichi, W. Adam, Y. Moro-oka, *Inorg. Chem.* **2000**, *39*, 2096–2102.
- [13] For other Pd^{II} complexes with Tp^{Pr}2, see: a) T. Miyaji, M. Kujime, S. Hikichi, Y. Moro-oka, M. Akita, *Inorg. Chem.* **2002**, *41*, 5286–5295; b) M. Akita, T. Miyaji, S. Hikichi, Y. Moro-oka, *Chem. Commun.* **1998**, 1005–1006; c) M. Akita, T. Miyaji, S. Hikichi, Y. Moro-oka, *Chem. Lett.* **1999**, 813–814; d) M. Kujime, S. Hikichi, M. Akita, *Organometallics* **2001**, *20*, 4049–4060; e) M. Kujime, S. Hikichi, M. Akita, *Chem. Lett.* **2003**, *32*, 486–487; f) M. Kujime, S. Hikichi, M. Akita, *Dalton Trans.* **2003**, 3506–3515.
- [14] a) E. Gutiérrez, M. C. Nicasio, M. Paneque, C. Ruiz, V. Salazar, *J. Organomet. Chem.* **1997**, *549*, 167–176; b) M. M. Díaz-Requejo, M. C. Nicasio, T. R. Belderrain, P. J. Pérez, M. C. Puerta, P. Valerga, *Eur. J. Inorg. Chem.* **2000**, 1359–1364.
- [15] a) S. S. Stahl, *Angew. Chem. Int. Ed.* **2004**, *43*, 3400–3420; *Angew. Chem.* **2004**, *116*, 3480–3501; b) S. S. Stahl, *Science* **2005**, *309*, 1824–1826.
- [16] a) K. M. Gligorich, M. S. Sigman, *Angew. Chem. Int. Ed.* **2006**, *45*, 6612–6615; *Angew. Chem.* **2006**, *118*, 6764–6767; b) K. M. Gligorich, M. S. Sigman, *Chem. Commun.* **2009**, 3854–3867.
- [17] R. A. Sheldon, I. W. C. E. Arends, G.-J. Ten Brink, A. Dijkman, *Acc. Chem. Res.* **2002**, *35*, 774–781.
- [18] a) M. Fontecave, S. Ollagnier-de-Choudens, E. Mulliez, *Chem. Rev.* **2003**, *103*, 2149–2166; b) J. W. Whittaker, *Chem. Rev.* **2003**, *103*, 2347–2363; c) D. Rokhsana, E. M. Shepard, D. E. Brown, D. M. Dooley, in *Copper-oxygen chemistry* (Eds.: K. D. Karlin, S. Itoh), John Wiley & Sons, Inc., Hoboken, New Jersey, **2011**, pp. 53–106.
- [19] a) J. M. Hoover, B. L. Ryland, S. S. Stahl, *J. Am. Chem. Soc.* **2013**, *135*, 2357–2367; b) M. Königsmann, N. Donati, D. Stein, H. Schönberg, J. Harmer, A. Sreekanth, H. Grützmacher, *Angew. Chem. Int. Ed.* **2007**, *46*, 3567–3570; *Angew. Chem.* **2007**, *119*, 3637–3640.
- [20] a) A. Corma, H. Garcia, *Chem. Soc. Rev.* **2008**, *37*, 2096–2126; b) K. Yamaguchi, N. Mizuno, *Chem. Eur. J.* **2003**, *9*, 4353–4361.
- [21] A. J. Ingram, K. L. Walker, R. N. Zare, R. M. Waymouth, *J. Am. Chem. Soc.* **2015**, *137*, 13632–13646.
- [22] G. K. Anderson, M. Lin, *Inorg. Synth.* **1990**, *28*, 61.
- [23] L. J. Farrugia, *J. Appl. Crystallogr.* **1999**, *32*, 837–838.
- [24] A. Altomare, M. C. Burla, M. Camalli, M. Cascarano, C. Giacovazzo, A. Guagliardi, G. Polidori, *J. Appl. Crystallogr.* **1994**, *27*, 435–436.
- [25] a) G. M. Sheldrick, *SHELXL, Program for Crystal Structure Refinement*, version 2014/7, University of Göttingen, Germany, **2014**; b) G. M. Sheldrick, *Acta Crystallogr., Sect. A* **2008**, *64*, 112–122.

Received: February 29, 2016
Published Online: April 24, 2016

Enhancement of the electrocatalytic oxygen reduction reaction on Pd₃Pb ordered intermetallic catalyst in alkaline aqueous solutions

Arockiam John Jeevagan, Takao Gunji, Fūma Ando, Toyokazu Tanabe, Shingo Kaneko & Futoshi Matsumoto

Journal of Applied Electrochemistry

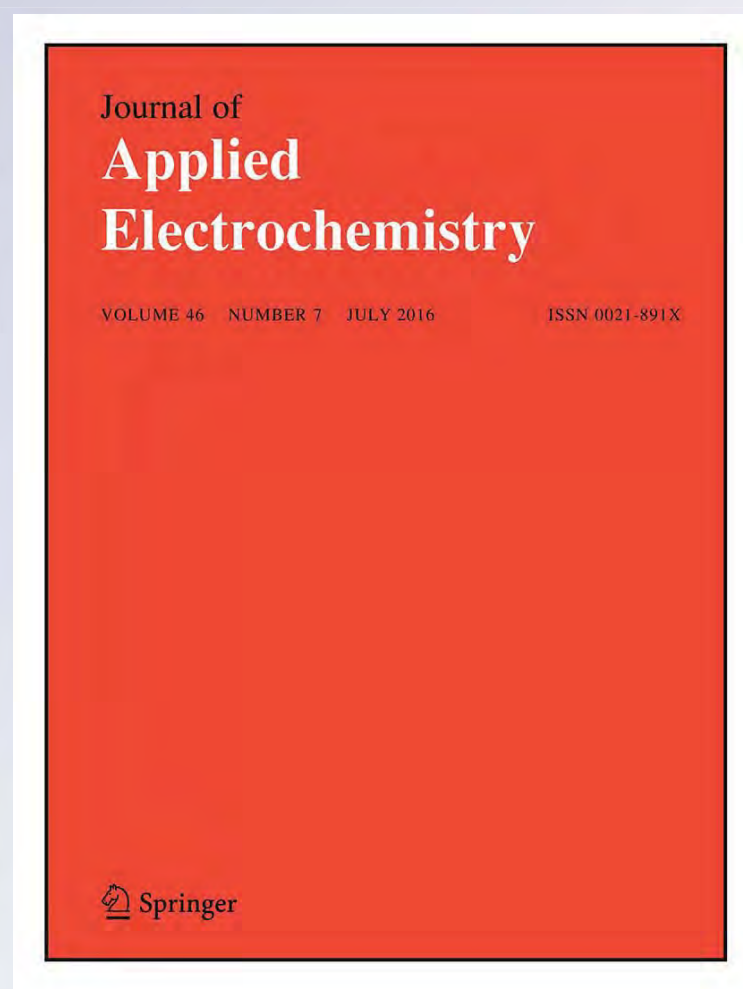
ISSN 0021-891X

Volume 46

Number 7

J Appl Electrochem (2016) 46:745-753

DOI 10.1007/s10800-016-0968-7



Your article is protected by copyright and all rights are held exclusively by Springer Science +Business Media Dordrecht. This e-offprint is for personal use only and shall not be self-archived in electronic repositories. If you wish to self-archive your article, please use the accepted manuscript version for posting on your own website. You may further deposit the accepted manuscript version in any repository, provided it is only made publicly available 12 months after official publication or later and provided acknowledgement is given to the original source of publication and a link is inserted to the published article on Springer's website. The link must be accompanied by the following text: "The final publication is available at link.springer.com".

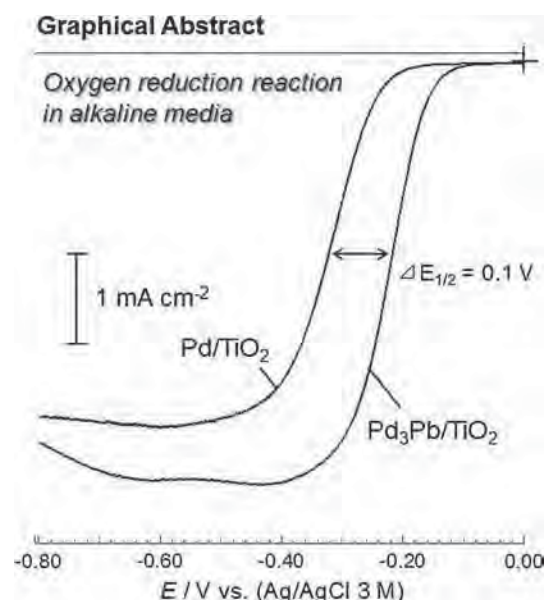
Enhancement of the electrocatalytic oxygen reduction reaction on Pd₃Pb ordered intermetallic catalyst in alkaline aqueous solutions

Arockiam John Jeevagan¹ · Takao Gunji¹ · Fūma Ando¹ · Toyokazu Tanabe¹ · Shingo Kaneko² · Futoshi Matsumoto¹

Received: 13 January 2016 / Accepted: 19 April 2016 / Published online: 7 May 2016
 © Springer Science+Business Media Dordrecht 2016

Abstract Enhancement of the oxygen reduction reaction (ORR) was examined with Pd₃Pb ordered intermetallic nanoparticles (NPs) supported on titania (Pd₃Pb/TiO₂). The Pd₃Pb/TiO₂ catalyst was synthesized by a conventional wet chemical method with Pd and Pb ion precursors, a reducing agent and TiO₂ powder under ambient temperature. X-ray diffraction, transmission electron microscopy, and X-ray photoelectron spectroscopy measurements indicated the formation of the ordered intermetallic phase of Pd₃Pb in the NP form on the TiO₂ surface. Electrochemical measurements showed that the Pd₃Pb/TiO₂ catalyst markedly enhanced the ORR in an alkaline environment due to the unique surface of Pd₃Pb NPs and the strong interaction between Pd₃Pb and TiO₂ compared with TiO₂-supported Pd, Pt, and PtPb NPs. The onset potential of Pd₃Pb/TiO₂ was shifted toward a higher potential by 110–150 mV compared with Pd/TiO₂, PtPb/TiO₂, and Pt/TiO₂.

Graphical Abstract



Keywords Electrocatalysis · Oxygen reduction reaction · Ordered intermetallic phase · Alkaline media

✉ Futoshi Matsumoto
 ft101828zr@kanagawa-u.ac.jp

¹ Department of Materials and Life Chemistry, Kanagawa University, 3-27-1, Rokkakubashi, Kanagawa-ku, Yokohama, Kanagawa 221-8686, Japan

² Research Institute for Engineering, Kanagawa University, 3-27-1, Rokkakubashi, Kanagawa-ku, Yokohama, Kanagawa 221-8686, Japan

1 Introduction

The direct conversion of chemical energy to electrical energy via fuel cells plays a vital role in the development of sustainable technologies to decrease the consumption of fossil fuels and to mitigate climate warming [1, 2]. Among the different types of fuel cells, polymer electrolyte membrane fuel cells (PEMFCs) have attracted enormous

attention due to their high energy conversion efficiency with zero emissions. Hence, significant efforts have been put into the design and synthesis of metal-based nanostructures for PEMFC catalysts to increase their catalytic activity and stability. Sluggish kinetics are associated with the oxygen reduction reaction (ORR) at PEMFCs [3, 4]. Platinum (Pt) is the most efficient catalyst for the ORR at PEMFCs, but the high cost and poor poison resistance of Pt-based PEMFC technology are major problems hindering its commercialization [5–7]. Therefore, it is urgent to develop a low-cost electrocatalyst with highly improved kinetics toward the ORR [8]. To achieve these requirements, several methods have been developed, such as using nanostructures to increase the surface-to-volume ratio [9], using an alloying technique to incorporate non-precious metals into the nanostructures, and replacing core atoms in Pt nanoparticles (NPs) with a non-precious metal [10]. These approaches have not achieved the performance necessary to satisfy the requirements of customers. In the development of electrocatalysts for PEMFCs and the search for the next promising electrocatalyst, the development of alkaline cation exchange membranes has drawn increasing attention to electrocatalysis in an alkaline environment because the overpotential for the ORR is significantly reduced in an alkaline environment [11]. Thus, researchers have focused on a wider selection of elements as electrocatalysts instead of Pt in an alkaline environment [11, 12]. Palladium (Pd) is a promising substitute for Pt because the Pd catalyst possesses intrinsic electrocatalytic performance toward the ORR in alkaline media [8, 13, 14]. Other attractive aspects are that Pd is much more abundant and is less expensive than Pt [15]. Furthermore, Pd has similar properties to Pt (same FCC crystal structure and atomic size), and it also possesses respectable oxygen reduction activity, as well as catalytic durability [16, 17]. Thus, significant efforts have been focused on promoting the electrocatalytic activity of Pd toward the ORR in alkaline media [18]. The catalytic activity and stability of Pd catalysts can be further improved by forming Pd-alloyed bimetallic catalysts [19, 20]. Alloying Pd with other metals improves the catalytic activity and reduces the Pd loading and cost [11]. Pd-based alloys with transition metals (Co, Cu, Ni, Fe) or less expensive metals, such as Pb and Bi, showed enhanced catalytic activities. These alloys include Pd-Ni [18, 21], Pd-Cu [22], Pd-Fe [19, 23], Pd-Co [20, 24], Pd-Bi [25], Pd-Au [26–28], and Pd-Ag [29]. These materials can be used as low-cost materials for different fuel-cell applications. Recently, transition metal oxide-supported metal nanocatalysts have been widely examined as oxidation and reduction electrocatalysts in PEMFCs. Transition metal oxides (TiO_2 , CeO_2 , Nb_2O_5 , WO_3 , ZrO_2) play an important role in catalytic reactions to accelerate the reaction rate

because of the strong interaction of the electrocatalyst with the transition metal oxides [30]. We have also reported the enhancement of the ORR on ordered intermetallic PtPb NPs supported on TiO_2 [31] and considered that the surfaces of ordered intermetallic PtPb NPs have intrinsic high ORR activity due to the electronic interaction between Pt and Pb atoms in the PtPb NPs. However, the Pb metal at the PtPb surface can be dissolved by electrochemical polarization during the ORR, and the TiO_2 support materials prevent the electrochemical dissolution of Pt from the PtPb NPs due to the strong interaction between the PtPb NPs and TiO_2 support. As a result, the PtPb surface has an important role in the ORR on the electrocatalyst surface without the electrochemical dissolution of Pb metal from the PtPb NPs. We expected that the same phenomenon would also occur on the Pd_3Pb NPs supported on TiO_2 to enhance the ORR in an alkaline environment. Herein, we report the synthesis of a Pd_3Pb intermetallic catalyst on TiO_2 and examine its catalytic activity toward the ORR in an alkaline environment to find promising electrocatalysts for the ORR in alkaline media. The ultrafine intermetallic Pd_3Pb was prepared on the TiO_2 surface ($\text{Pd}_3\text{Pb}/\text{TiO}_2$) using sodium borohydride as the reductive agent of the Pd and Pb precursors in a methanol medium under an Ar atmosphere. The resultant catalysts were characterized by X-ray diffraction (XRD), energy-dispersive X-ray analysis (EDX), scanning transmission electron microscopy (STEM), transmission electron microscopy (TEM), X-ray photoelectron spectroscopy (XPS), and inductively coupled plasma-mass spectrometry (ICP-MS). In addition, the electrocatalytic performance, kinetics and stability of the ordered intermetallic Pd_3Pb catalyst on TiO_2 for the ORR under alkaline conditions were examined by linear sweep voltammetry and chronoamperometry. The electrocatalytic activity of $\text{Pd}_3\text{Pb}/\text{TiO}_2$ for the ORR was compared with the activities of Pd/TiO_2 , PtPb/TiO_2 , and Pt/TiO_2 as reference catalysts.

2 Experimental

2.1 Synthesis of $\text{Pd}_3\text{Pb}/\text{TiO}_2$, Pd/TiO_2 , Pt/TiO_2 , and PtPb/TiO_2

The Pd precursor, $\text{Pd}(\text{CH}_3\text{COO})_2$; Pb precursor, $\text{Pb}(\text{CH}_3\text{COO})_2$; and Pt precursor, $\text{H}_2\text{PtCl}_6 \cdot 6\text{H}_2\text{O}$ were purchased from Wako Pure Chemical Industries, Ltd., Japan, and were used as received without further purification. Pd_3Pb NPs on TiO_2 supports were synthesized through a wet chemical route using the borohydride reduction method. Briefly, 0.5 g of TiO_2 (anatase, particle size <25 nm, 99.7 %, Sigma-Aldrich) was suspended in 15 mL of anhydrous methanol (99.8 %, Sigma-Aldrich) for 15 min

in a two-neck round-bottom flask. The Pd precursor (0.26 mmol) and Pb precursor (0.082 mmol) were dissolved in a 15-mL shielded vial under an Ar atmosphere and were subsequently transferred to the TiO₂ suspension. Then, the solution was stirred for 30 min to yield a homogeneous reddish-yellow solution. After 30 min, 5.2 mmol of freshly prepared NaBH₄ (Sigma-Aldrich) in methanol was injected into the solution by cannula. The color of the solution immediately turned dark gray after the addition of NaBH₄, indicating the formation of Pd₃Pb NPs on the TiO₂ support. The products were washed with anhydrous methanol three times and dried under vacuum. Pd/TiO₂, Pt/TiO₂, and PtPb/TiO₂ were synthesized using the Pd precursor (or Pt, Pb precursors) and TiO₂ support under the same synthetic conditions.

2.2 Physical characterization

XRD measurements were performed between the diffraction angles (2θ) of 20° and 80°, and the structural patterns were collected using a Rigaku RINT-ULTIMA III X-ray powder diffractometer with CuK_α radiation ($\lambda = 0.1548$ nm). The XPS measurements were used to examine the chemical states of the catalyst, and the spectra were collected using a JPS-9010 JEOL instrument. An MgK α X-ray source with an anodic voltage of 10 kV and a current of 10 mA was used for the XPS spectral measurements. TEM images were obtained with a JEOL 2100-F microscope with an operating voltage of 200 kV. STEM was performed, and the composition of Pd₃Pb NPs/TiO₂ was analyzed by an energy-dispersion spectrometer (EDS, Oxford link system), which was connected to the TEM. The samples for TEM were prepared by dropping a methanol suspension of the catalyst powder onto a copper grid (150 mesh). The metal (Pd, Pt, Pb) contents of the products were determined by inductively coupled plasma-mass spectrometry (ICP-MS, Agilent, 7700 \times).

2.3 Electrochemical measurements

The NP/support material samples were coated on a glassy carbon (GC) electrode (diameter = 5 mm) from a suspension prepared by the ultrasonic mixing of Pd₃Pb/TiO₂ (5.0 wt%), Pb/TiO₂ (5.0 wt%), or Pt/TiO₂ (5.0 wt%) samples (1 mg) with Milli-Q water (995 μ L), isopropanol (250 μ L, 99.7 %, Wako Pure Chemical Industries Ltd., Japan), and Nafion solution (5 μ L, 5 wt%, EW: 1100, Sigma-Aldrich) for 30 min. The loadings of NP on the TiO₂ support material were evaluated by ICP-MS. A 12 μ L aliquot of catalyst suspension was dropped onto the cleaned GC electrode and was dried under vacuum. The loading of Pd₃Pb/TiO₂ (or Pd/TiO₂, PtPb/TiO₂, and Pt/TiO₂) on the GC electrode was 50.0 μ g cm⁻². Prior to modification of the GC electrode, the GC electrode was mirror-polished with a 0.05 μ m alumina

slurry for 10 min, sonicated for 5 min to remove any adsorbed impurities on the GC electrode and dried under Ar. The electrochemical measurements were performed in a conventional two-compartment, three-electrode cell with the catalyst-coated GC electrode as the working electrode, a platinum wire as the auxiliary electrode and NaCl (3 M) Ag/AgCl as the reference electrode. All potentials were referenced to the reversible hydrogen electrode (RHE). The electrochemical measurements were performed on a Bio-Logic SAS workstation (Model, VMP3). Oxygen gas was purged for 30 min into a 0.1 M aqueous KOH solution to prepare an O₂-saturated solution. The catalyst-coated electrode was rotated using an electrode rotator (Hokuto Denko, Japan, HR-30) at 2000 rpm. The ORR polarization curves were recorded using linear sweep voltammetry in an O₂-saturated 0.1 M KOH aqueous solution with a scan rate of 10 mV s⁻¹. Stability tests were performed by chronoamperometry at 0.85 V (vs. RHE) with a rotation speed of 2000 rpm in an O₂-saturated 0.1 M KOH aqueous solution. The current densities shown in the voltammograms were normalized by the geometric surface area of the GC electrode (0.20 cm²).

3 Results and discussion

3.1 Physical characterization

XRD measurements were used to analyze the crystal structure of the synthesized Pd₃Pb NPs on the TiO₂ surface. Figure 1 shows the XRD profiles for TiO₂ (a), Pd NPs/TiO₂ (b), and Pd₃Pb NPs/TiO₂ (c). The XRD profile for the Pd NPs (Fig. 1b) shows barely recognized reflection peaks

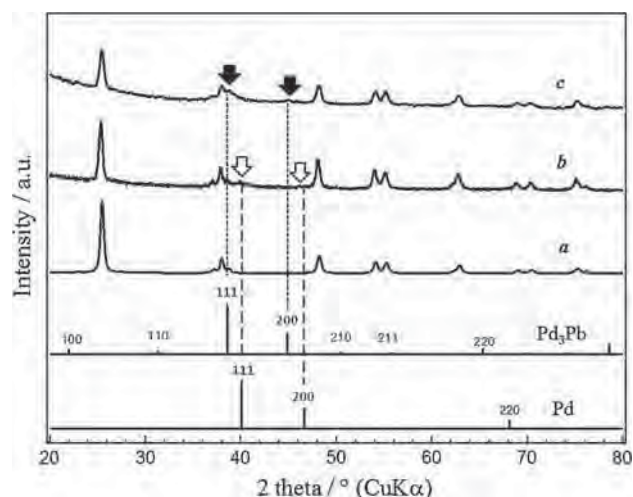


Fig. 1 XRD patterns of the synthesized nanoparticles: TiO₂ (a), Pd/TiO₂ (b), and Pd₃Pb/TiO₂ (c). The XRD profiles for the simulated XRD lines for Pd and Pd₃Pb are shown for reference. Open circle and filled circle correspond to the peaks of Pd and Pd₃Pb

at 39.6° and 46.8° that are assigned to the (111) and (200) reflection planes corresponding to the Pd as well as the peaks originating from TiO_2 , as shown in Fig. 1a. In the profile, the broadening of the peaks for Pd/ TiO_2 is due to nano-sized particles of Pd on the TiO_2 support. The XRD profile (Fig. 1c) for the products prepared with Pd and Pb precursors on TiO_2 also shows very small reflection peaks at 38.6° and 44.8° that can be assigned to the (111) and (200) reflection planes of an ordered intermetallic Pd_3Pb phase (Cu_3Au , $\text{Pm}\bar{3}m$, $a = b = c = 0.4035$ nm), respectively, with the peaks originating from TiO_2 . Compared with the Pd/ TiO_2 , the characteristic peaks of $\text{Pd}_3\text{Pb}/\text{TiO}_2$ ((111) and (200)) are noticeably shifted toward lower diffraction angles, indicating an increase in the lattice constant of Pd atoms due to the incorporation of Pb atoms into the Pd lattice [32]. The average crystallite sizes of the Pd and Pd_3Pb NPs were estimated based on the diffraction peaks of the (200) plane using the Scherrer equation and were approximately 3.5 and 3.8 nm, respectively.

Because there is a problem with the identification of the Pd_3Pb ordered intermetallic NPs based on the XRD results, TEM measurements were used to confirm the formation of Pd_3Pb ordered intermetallic phase in the NPs and to investigate the morphology and particle size distribution of the Pd_3Pb NPs on TiO_2 . Figure 2A shows the TEM images of the $\text{Pd}_3\text{Pb}/\text{TiO}_2$. The prepared NPs with a diameter of 2–5 nm are finely dispersed on the TiO_2 support. The histogram (Fig. 2B) of the particle diameter evaluated from the TEM image showed a symmetrical distribution on the TiO_2 . From the histogram, the average diameter of the

prepared Pd_3Pb NPs on the TiO_2 is 4.0 nm. The prepared Pd, Pt, and PtPb NPs on the TiO_2 have average sizes of 3.8, 3.9, and 4.2 nm. From the HR-TEM image (Fig. 2C) of the $\text{Pd}_3\text{Pb}/\text{TiO}_2$ catalyst, the d -spacings of the lattice fringes were 0.283 and 0.313 nm, which correspond to the (110) and (101) planes of the ordered intermetallic Pd_3Pb , respectively. The corresponding FFT pattern showed sharp (110) and (101) super lattice spots characteristic of the ordered Cu_3Au -type structure (D) of a Pd_3Pb compound. Compositional mapping by STEM-EDS analysis was used to determine the elemental distribution in the Pd_3Pb NPs (Fig. 3). STEM (A)-energy-dispersive spectroscopy (EDS) mappings (B–D) also indicated that the NPs are composed of Pd and Pb atoms on TiO_2 and demonstrated that the average mole ratio of Pd to Pb for the Pd_3Pb NPs is consistent with the desired value (Pd:Pb = 75.0:25.0 for Pd_3Pb), namely Pd:Pb = 73.6:26.4, as determined by the STEM image captured in the area of $50\text{ nm} \times 50\text{ nm}$. Figure 3E displays the profiles of the EDS line scans (point resolution of EDX beam: 0.2 nm) along with the lines presented in Fig. 3A. The average mole ratios of Pd to Pb, which were evaluated using the STEM-EDS mappings, were consistent with the desired value for Pd_3Pb (Pd:Pb = $75.0 \pm 3:25.0 \pm 3$), which was predicted from stoichiometric ratio of 3:1 in the Pd_3Pb compound, at all points for the Pd_3Pb NPs. The TEM/STEM results indicate that both Pd and Pb atoms are distributed throughout the particles, and the Pd and Pb atoms form an ordered intermetallic phase in the NP, although the formation of a Pd_3Pb ordered intermetallic phase could not be confirmed from the XRD profile.

XPS measurements were used to investigate the electronic environment of Pd in the $\text{Pd}_3\text{Pb}/\text{TiO}_2$. Figure 4 shows the XPS spectral profiles of Pd NPs (a, commercially available product, E-TEK), Pd/ TiO_2 (b), and $\text{Pd}_3\text{Pb}/\text{TiO}_2$ (c) in the Pd 3d region. The two peaks around the binding energies of 335 and 340 eV are assigned to the Pd $3d_{5/2}$ and Pd $3d_{3/2}$ emission peaks of Pd and reveal that the Pd in the samples of (A–C) is metallic Pd (0). The binding energies for Pd metal (A) are Pd $3d_{5/2}$, 335.1 ± 0.2 eV, and Pd $3d_{3/2}$, 340.6 ± 0.2 eV. On the other hand, two coupled peaks for Pd/ TiO_2 (b) appear at the binding energies of 335.2 ± 0.2 and 340.6 ± 0.2 eV in the Pd 3d signal region. Compared with the binding energy levels of Pd NPs, the two peaks for Pd/ TiO_2 shifted to higher binding energy due to the electronic interaction between the Pd NPs and TiO_2 support. The XPS spectral profiles of $\text{Pd}_3\text{Pb}/\text{TiO}_2$ (c) also exhibit a peak shift of the Pd 3d emission peaks to higher binding energy. The peaks can be observed at 335.8 ± 0.20 and 341.0 ± 0.20 eV. The large peak shift is caused by the change in the electronic structure of Pd from the interaction between the Pd and inserted Pb atoms, as well as between the Pd atoms in the

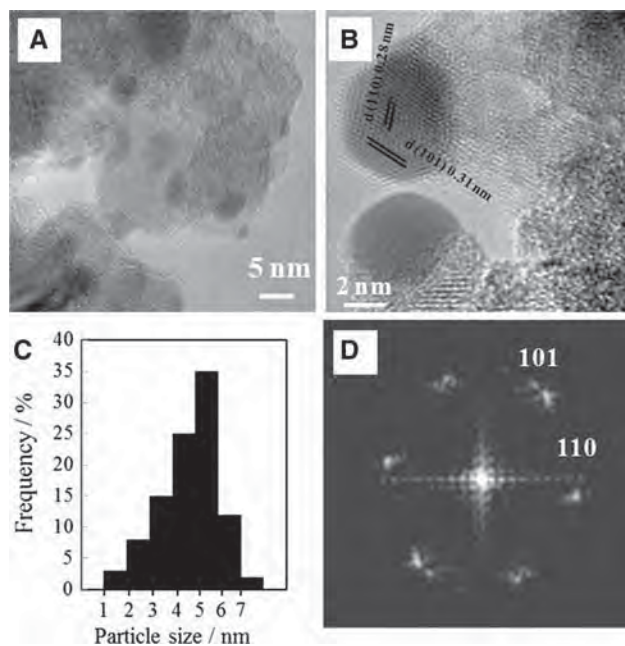


Fig. 2 TEM (A) and HR-TEM (B) images of $\text{Pd}_3\text{Pb}/\text{TiO}_2$, as well as the particle size distribution (C) of Pd_3Pb NPs. D FFT pattern obtained from (B)

Fig. 3 STEM (A) image and EDS mapping images of Pd₃Pb/TiO₂: Pd (B), Pb (C), and mixture (D) of images (B) and (C) for the Pd₃Pb sample. E Line-scanning profile across Pd₃Pb NPs on TiO₂

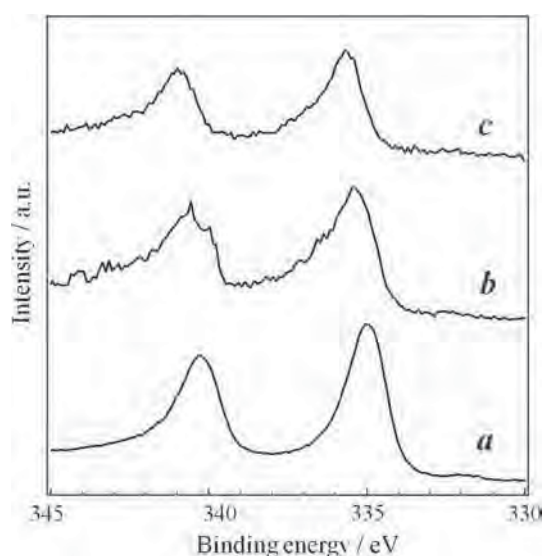
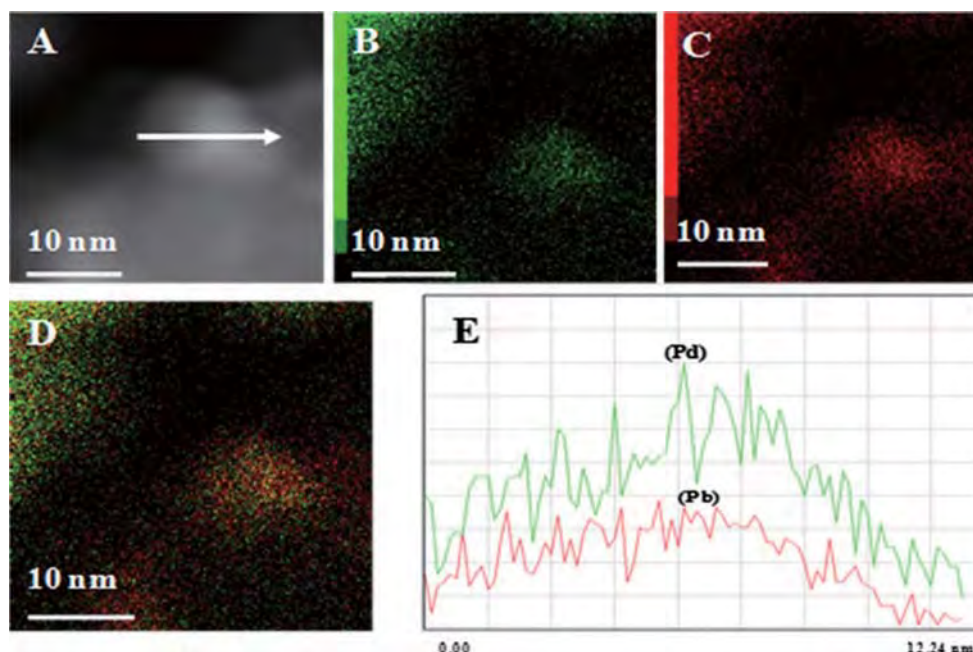


Fig. 4 XPS spectral profiles for Pd 3d in Pd (a) NPs, Pd (b) on TiO₂, and Pd₃Pb (c) on TiO₂

Pd₃Pb NPs and the TiO₂ support. Although the results are not shown here, XPS signals of Pb in the Pd₃Pb NPs were also detected in the Pb 3d region. The atomic ratio of Pd to Pb (3:1), based on the comparison between the XPS peak areas of Pd and Pb atoms and the peak shift in the Pb 3d region to the low binding energy side, confirms the formation of the Pd₃Pb ordered intermetallic phase.

3.2 Electrochemical measurements

Catalyst-coated GC electrodes were used to study the ORR activities and kinetics at the Pd/TiO₂ and Pd₃Pb/TiO₂

electrodes. Figure 5 shows the ORR polarization curves of the Pd/TiO₂ (a), Pd₃Pb/TiO₂ (b), Pt/TiO₂ (c), and PtPb/TiO₂ (d) catalysts obtained in an O₂-saturated 0.1 M KOH aqueous solution at a rotation speed of 2000 rpm. The onset potential (potential where the reduction current passed through -0.01 mA cm^{-2}) of the Pd/TiO₂ (a) for the ORR is 0.90 V (vs. RHE). On the other hand, the curve of Pd₃Pb/TiO₂ (b) has an onset potential at 0.98 V, which is more positive than that of Pd/TiO₂, indicating that the

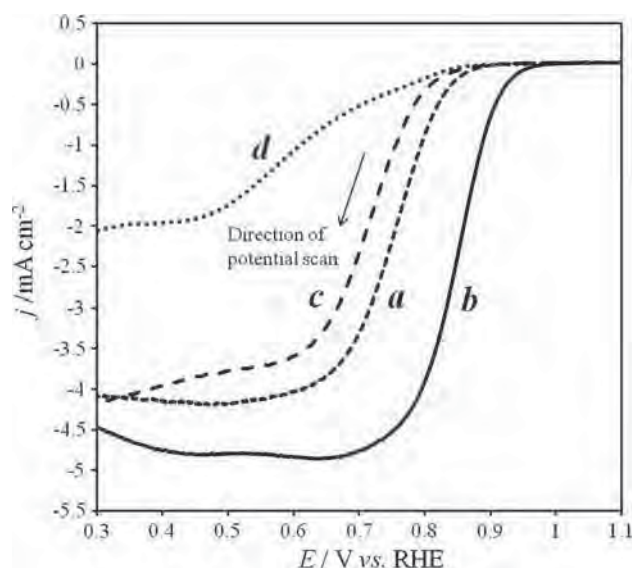


Fig. 5 ORR polarization curves of Pd/TiO₂ (a), Pd₃Pb/TiO₂ (b), Pt/TiO₂ (c), and PtPb/TiO₂ (d) catalysts in an O₂-saturated 0.1 M KOH solution at a scan rate of 10 mV s^{-1} and an electrode rotation rate of 2000 rpm

Pd₃Pb NPs feature significant enhancement in electrocatalytic ORR in an alkaline environment compared with Pd/TiO₂. Furthermore, the electrocatalytic ORR activity of Pd₃Pb/TiO₂ was also compared with that of the Pt/TiO₂ (c) and PtPb/TiO₂ (d) catalysts. The Pt/TiO₂ and PtPb/TiO₂ catalysts have onset potentials of 0.88 and 0.86 V. The PtPb/TiO₂, which exhibits superior ORR activity in acidic aqueous solution, [31] displayed degradation behavior in alkaline media. The Pd₃Pb/TiO₂ sample has the highest onset potential; in other words, the ORR was enhanced to the greatest extent on the Pd₃Pb/TiO₂ among the four samples examined in this study. The polarization curves for the Pd₃Pb/TiO₂ show a well-defined diffusion-limited current near -4.8 mA cm^{-2} in the region from 0.3 to 0.7 V. The value of the theoretical diffusion-limited current density for ORR in 0.1 M KOH aqueous solution is approximately -6 mA cm^{-2} at the electrode rotation speed of 2000 rpm. The Pd/TiO₂, Pt/TiO₂, and PtPb/TiO₂ also exhibit lower diffusion-limited currents than the expected diffusion-limited current density due to the use of low electron-conductive TiO₂ as a support material. If the low conductivity of the TiO₂ support influences the ORR curves, the shape of the ORR voltammograms become less sharp, namely the potential where the reduction current density reaches the diffusion-limited region shifts toward negative potential, and the value of the diffusion-limited current density does not decrease. However, the Pd₃Pb/TiO₂ caused diffusion plateaus lower than the theoretical value and flattened the shape of the voltammogram. There are several discussions on influencing the diffusion-limited current density level [33–35]. The much lower electrical conductivity of TiO₂ as the support decreases the diffusion-limited current density, as confirmed by Popov (see the supporting information section of [35]). Although they did not mention the reason for the decreased diffusion-limited current in the paper, we believe that the agglomerate formation of the TiO₂ support is related to the decrease in the diffusion-limited currents. Highly agglomerated NPs/TiO₂ inhibits O₂ diffusion to the NP surfaces; as a result, the lack of O₂ has a negative effect on the diffusion-limited current density.

The catalyst loading on the GC electrode, the surface area of the catalysts, and the mass- and surface area-specific activities for Pd₃Pb/TiO₂, Pd/TiO₂, Pt/TiO₂, and PtPb/TiO₂ are summarized in Table 1. The electrochemical surface area of the Pd₃Pb NPs could not be measured using the monolayer PdO reduction peak ($405 \mu\text{C cm}^{-2}$ [36]) observed by cyclic voltammetry in acidic aqueous solution because of the insertion of Pb atoms in the Pd crystal structure and the electronic interaction between Pt and Pb atoms in the ordered intermetallic NPs, as has been reported in the case of PtPb ordered intermetallic NPs [37]. Therefore, the surface area of the NPs was calculated based

on the observed average NP's diameter and the NP loading on TiO₂. The NPs on TiO₂ were considered to have the form of a hemisphere and the density (13.41 g cm^{-3}) [38] of Pd₃Pb for the calculation of the surface area. In Table 1, all samples have almost the same loading weight and diameter on the TiO₂ support. The geometric factor of the NPs on the TiO₂ support does not result in the difference of the electrocatalytic activities observed for the Pd₃Pb, Pd, Pt, and PtPb NPs/TiO₂ samples. In the aspect of both the mass- and surface area-specific activities measured at 0.85 V, Pd₃Pb/TiO₂ exhibits superior activities compared to Pd/TiO₂, PtPb/TiO₂, and Pt NPs/TiO₂. Kim reported high catalytic activity for the ORR with the graphene-supported Pd (Pd/GNS) catalyst in alkaline aqueous solutions [39]. Our Pd₃Pb sample exhibits comparable ORR activities (-0.81 mA cm^{-2} and $-0.90 \text{ mA } \mu\text{g}^{-1}$ at 0.85 V) with their results (-1.52 mA cm^{-2} and $-0.84 \text{ mA } \mu\text{g}^{-1}$ with Pd/GNS at 0.85 V). From the viewpoint of mass activity, our sample is superior to Pd/GNS. The defeat of the Pd₃Pb/TiO₂ with respect to the surface area activity is caused by overestimation of the surface area of the Pd₃Pb NPs. In reality, the active surfaces are lower than the estimated surface area because of the strong aggregation of Pd₃Pb/TiO₂. A portion of NPs on the TiO₂ was blocked by other Pd₃Pb/TiO₂, and the feed of O₂ to the blocked NP surfaces is reduced. Therefore, the working surface areas of the NPs are smaller than the surface areas of the NPs summarized in Table 1. The inherent surface area activity is therefore higher than the estimated values.

To evaluate the kinetic parameters (kinetic current density and the number of transferred electrons) on the Pd₃Pb surface on TiO₂ during the course of the ORR, the polarization curves were recorded at different disk rotation rates in a rotating disk electrode (RDE) experiment. Figure 6A depicts the dependence of the ORR curves on the disk rotation rate for the Pd₃Pb/TiO₂-coated GC. The j^{-1} versus $\omega^{-1/2}$ plots at different potentials are presented in Fig. 6B. The number of electrons involved in the ORR can be determined from the slope of the Koutecky–Levich (K–L) plot [40]

$$j = 1/j_k + (1/B)/\omega^{0.5} \quad (1)$$

$$B = 0.2 nF(D_{\text{O}_2})^{2/3}(\nu)^{-1/6}C_{\text{O}_2}, \quad (2)$$

where j is the measured current density, j_k is the kinetic current, ω is the electrode rotation rate, n is the number of electrons, F is the Faraday constant, D_{O_2} is the diffusion coefficient of O₂ ($D_{\text{O}_2} = 1.9 \times 10^{-5} \text{ cm}^2 \text{ s}^{-1}$) [41], ν is the kinetic viscosity of the solution ($0.01 \text{ cm}^2 \text{ s}^{-1}$) [41], and C_{O_2} is the bulk concentration of O₂ ($C_{\text{O}_2} = 1.2 \times 10^{-6} \text{ mol cm}^{-3}$) [41]. From the straight lines shown in the K–L plots (Fig. 6B), the number of electrons transferred in the

Table 1 Summary of the NP particle size, surface area, electrocatalytic activities characterized by TEM, and electrochemical analyses for Pd₃Pb/TiO₂, Pd/TiO₂, PtPb/TiO₂, and Pt/TiO₂

	Catalyst (NP/TiO ₂) loading on the GC electrode (μg m ⁻²)	Average diameter of NP (nm)	Density of metal (g m ⁻³)	Surface area of metal NP (m ² g ⁻¹)	Mass-specific activity mAμg ⁻¹ (of NP) at 0.85 V vs. RHE	Surface area-specific activity (mA m ⁻²) at 0.85 V vs. RHE
Pd ₃ Pb/TiO ₂	50 × 10 ⁴	4.0	13.4 × 10 ⁶	111	−0.90	8.1 × 10 ³
Pd/TiO ₂	50 × 10 ⁴	3.8	12.0 × 10 ⁶	250	−0.034	1.4 × 10 ²
Pt/TiO ₂	50 × 10 ⁴	3.9	21.5 × 10 ⁶	92	−0.030	3.2 × 10 ²
PtPb/TiO ₂	50 × 10 ⁴	4.2	15.5 × 10 ⁶	71	−0.018	2.5 × 10 ²

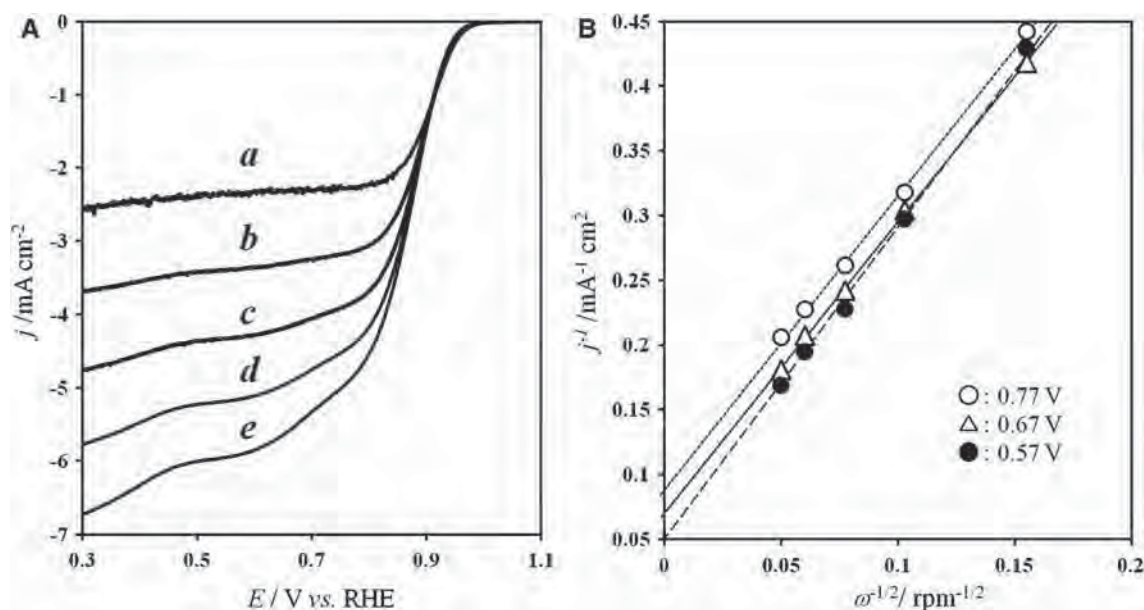


Fig. 6 The dependence of the ORR current density of the Pd₃Pb/TiO₂-coated GC electrode in a 0.1 M KOH solution on the electrode rotation rate: 400 (a), 900 (b), 1600 (c), 2500 (d), and 3600 (e) rpm

ORR was calculated to be 3.65–3.76 at approximately 0.57–0.77 V, indicating that the ORR is relatively dominated by the four-electron reduction of O₂ in the potential region from 0.57 to 0.77 V. In the j^{-1} versus $\omega^{-1/2}$ plots, the kinetic current for the Pd₃Pb/TiO₂ was calculated from the intercept of the plots. At 0.77 V, the kinetic current density was evaluated to be 11.7 mA cm⁻². Our prepared Pd₃Pb/TiO₂ exhibits comparable kinetic current density with those observed for benchmarked Pd/carbon black (CB) (3 mA cm⁻² at 0.77 V [42]) and Pt/CB (12.5 mA cm⁻² at 0.8 V [43]), although the TiO₂ support material has high electron resistivity.

A chronoamperometric study was conducted to investigate the durability of the catalyst for the ORR. The current-time curves on Pd₃Pb/TiO₂ (a) and Pd/TiO₂ (b) catalysts in an O₂ saturated 0.1 M KOH(aq) solution are shown in Fig. 7. For the ORR on Pd₃Pb/TiO₂ (a) at constant applied potential of 0.85 V, the current densities of the catalysts change quickly initially, and after reaching −5 mA cm⁻²,

the current density decreases slowly. After 50 min, the current density decreased to −4.2 mA cm⁻² (to 84 %). In contrast, for Pd/TiO₂, the current rapidly decreased to −0.9 mA cm⁻² in 50 min. The above results indicate that Pd₃Pb/TiO₂ is more stable than Pd/TiO₂ in terms of their catalytic activities for the ORR.

The synergistic effect of the inherent electrocatalytic activity of the Pd₃Pb ordered intermetallic surfaces and the electronic interaction [44, 45] between Pd₃Pb NPs and TiO₂, which was taken from the XPS results, produces superior ORR activity. The electronic interaction between Pd and TiO₂ via the Ti–O–Pd bridging, as mentioned in the XPS results, contributes to the enhancement of ORR with the following two factors: (1) OH adsorbed on the Pd surface in the Pd₃Pb NPs is spilled over to the TiO₂ (reduction of the formation of OH on the Pd surface) [46, 47] and (2) the *d* orbital electron in the Pd atoms is donated to Ti atoms through the bridging Ti–O–Pd bond (*d* orbital vacancy, resulting in enhanced 2π electron donation from

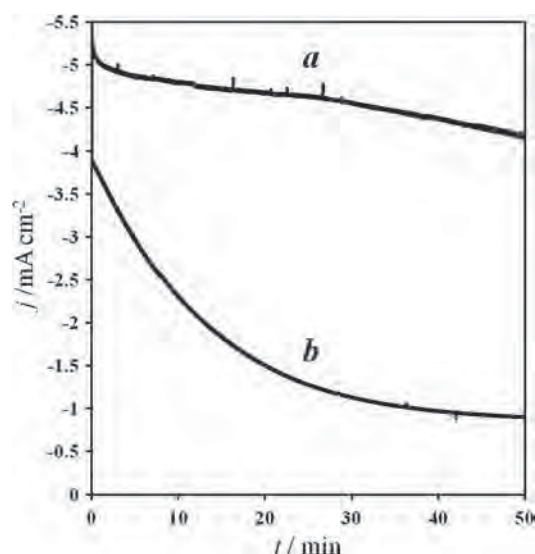


Fig. 7 Chronoamperometry curves of Pd₃Pb/TiO₂ (a) and Pd/TiO₂ (b) catalysts in O₂-saturated 0.1 M KOH aqueous solution at an electrode potential of 0.85 V

O₂ to the surface of Pd₃Pb and back donation of the electrons [47, 48], both of which facilitate O₂ adsorption on the Pd surface, that is, the first step of the ORR, to rapidly produce two desirable H₂O molecules.

4 Conclusions

We have described the synthesis of finely dispersed Pd₃Pb NPs on TiO₂, which were prepared by the co-reduction of Pd and Pb precursors through a wet chemical synthetic route. The formation of Pd₃Pb NPs on TiO₂ was confirmed by XRD, XPS, and TEM/STEM. The HR-TEM images showed that the synthesized NPs are intermetallic, with an average size of 4.0 nm. The nanostructured Pd₃Pb has better catalytic properties toward the ORR compared with the Pd and Pt catalysts. The kinetics of the ORR principally involves a four-electron reduction with first-order kinetics. The stability and kinetics of the catalyst are reasonable; therefore, the catalyst is a low-cost candidate to replace Pt as a fuel-cell catalyst. The incorporation of Pb into the Pd catalyst modifies the electronic properties of Pd and promotes the electrocatalytic ORR activity.

References

- Liu ZL, Zhao B, Guo CL, Sun Y, Shi Y, Yang HY, Li Z (2010) *J Colloid Interface Sci* 351:233–238
- Chen DJ, Zhou ZY, Wang Q, Xiang DM, Tian N, Sun SG (2010) *Chem Commun* 46:4252–4254
- Wu G, Mack NH, Gao W, Ma S, Zhong R, Han J, Baldwin JK, Zelenay P (2012) *ACS Nano* 6:9764–9776
- Debe MK (2012) *Nature* 486:43–51
- Liang YY, Li YG, Wang HL, Zhou JG, Wang J, Regier T, Dai H (2011) *J Nat Mater* 10:780–786
- Cheng FY, Shen JA, Peng B, Pan YD, Tao ZL, Chen J (2011) *Nat Chem* 3:79–84
- Hong JW, Kang SW, Choi BS, Kim D, Lee SB, Han SW (2012) *ACS Nano* 6:2410–2419
- Zhou RF, Jaroniec M, Qiao SZ (2015) *Chem Cat Chem* 7:3808–3817
- Polarz S (2011) *Adv Funct Mater* 21:3214
- Lee JS, Park GS, Lee HI, Kim ST, Cao RG, Liu ML, Cho J (2011) *Nano Lett* 11:5362–5366
- Zhang Z, More KL, Sun K, Wu Z, Li W (2011) *Chem Mater* 23:1570–1577
- Sekol RC, Li X, Cohen P, Doubek G, Carmo M, Taylor AD (2013) *Appl Catal B* 138:285–293
- Shim JH, Kim J, Lee C, Lee Y (2011) *Chem Mater* 23:4694–4700
- Sun W, Hsu A, Chen R (2011) *J Power Sources* 196:4491–4498
- Antolini E (2009) *Energy Environ Sci* 2:915–931
- Lu Y, Jiang Y, Gao X, Wang X, Chen W (2014) *J Am Chem Soc* 136:11687–11697
- Wang D, Lu S, Jiang S (2010) *Chem Commun* 46:2058
- Wang M, Zhang W, Wang J, Wexler D, Poynton SD, Slade RCT, Liu H, Jensen BW, Kerr R, Shi D, Chen J (2013) *ACS Appl Mater Interfaces* 5:12708–12715
- Kang YS, Choi KH, Ahn D, Lee MJ, Baik J, Chung DY, Kim MJ, Minhyoung L, Kim SY, Shin H, Lee KU, Sung YE (2016) *J Power Sources* 303:234–242
- Wei YC, Liu CW, Wang KW (2011) *Chem Commun* 47:11927–11929
- Chen L, Guo H, Fujita T, Hirata A, Zhang W, Inoue A, Chen M (2011) *Adv Funct Mater* 21:4364–4370
- Wu J, Shan S, Luo J, Joseph P, Petkov P, Zhong CJ (2015) *ACS Appl Mater Interfaces* 7(46):25906–25913
- Tang W, Zhang L, Henkelman G (2011) *J Phys Chem Lett* 2:1328–1331
- Yin S, Cai M, Wang C, Shen PS (2011) *Energy Environ Sci* 4:558–563
- Wang D, Xin HL, Wang H, Yu Y, Rus E, Muller DA, DiSalvo FJ, Abruña HD (2012) *Chem Mater* 24:2274–2281
- Cai J, Huang Y, Guo Y (2013) *Electrochim Acta* 99:22–29
- Tian M, Malig M, Chen S, Chen A (2011) *Electrochem Commun* 13:370–373
- Yin Z, Chi M, Zhu Q, Ma D, Sun J, Bao X (2013) *J Mater Chem A* 1:9157–9163
- Simonet J (2010) *Electrochem Commun* 12:1475–1478
- Liu M, Lu Y, Chen W (2013) *Adv Funct Mater* 23:1289–1296
- Gunji T, Saravanan G, Tanabe T, Tsuda T, Miyauchi M, Kobayashi G, Abe H, Matsumoto F (2014) *Catal. Sci Technol* 4:1436–1445
- Furukawa S, Suga A, Komatsu T (2014) *Chem Commun* 50:3277–3280
- Mayrhofer KJJ, Strmcnik D, Blizanac BB, Stamenkovic V, Arenz M, Markovic NM (2008) *Electrochim Acta* 53:3181–3188
- Bonnacaze RT, Mano N, Nam B, Heller A (2007) *J Electrochem Soc* 154:F44–F47
- Huang SY, Ganesan P, Park S, Popov BN (2009) *J Am Chem Soc* 131:13898–13899
- Chierchie T, Mayer C, Lorenz WJ (1982) *J Electroanal Chem* 135:211–220
- Matsumoto F, Roychowdhury C, DiSalvo FJ, Abruña HD (2008) *J Electrochem Soc* 155:B148–B154
- Massalski TB (Editor-in-Chief) (1990) *Binary Phase Diagrams*, 2nd ed., Vol. 1, ASM International, Materials Park, OH
- Seo MH, Choi SM, Kim HJ, Kim WB (2011) *Electrochem Commun* 13:182–185

40. Bard AJ, Faulkner LR (1980) *Electrochemical methods: fundamentals and applications*. Wiley, New York
41. Park S-A, Lim H, Kim Y-T (2015) *ACS Catal* 5:3995–4002
42. Wu Q, Rao Z, Yuan L, Jiang L, Sun G, Ruan J, Zhou Z, Sang S (2014) *Electrochim Acta* 150:157–166
43. Sahraie NR, Kramm UI, Steinberg J, Zhang Y, Thomas A, Reier T, Paraknowitsch JP, Strasser P (2015) *Nat Commun* 6:8618
44. Bruix A (2012) *J Am Chem Soc* 134:8968–8974
45. Campbell CT (2012) *Nat Chem* 4:597–598
46. Awaludin Z, Suzuki M, Masud J, Okajima T, Ohsaka T (2011) *J Phys Chem C* 115:25557–25567
47. Jaksic JM, Labou D, Papakonstantinou GD, Siokou A, Jaksic MM (2010) *J Phys Chem C* 114:18298–18312
48. Hyun K, Lee JH, Yoon CW, Kwon Y (2013) *Int J Electrochem Sci* 8:11752–11767



Site-selective deposition of binary Pt–Pb alloy nanoparticles on TiO₂ nanorod for acetic acid oxidative decomposition



Toyokazu Tanabe^{a,*}, Wataru Miyazawa^a, Takao Gunji^a, Masanari Hashimoto^a, Shingo Kaneko^b, Toshiaki Nozawa^a, Masahiro Miyauchi^c, Futoshi Matsumoto^{a,*}

^a Department of Material & Life Chemistry, Kanagawa University, Yokohama, Japan

^b Research Institute for Engineering, Kanagawa University, Yokohama, Japan

^c Department of Metallurgy and Ceramics Science, Tokyo Institute of Technology, Meguro-ku, Tokyo, Japan

ARTICLE INFO

Article history:

Received 8 January 2016

Revised 28 May 2016

Accepted 31 May 2016

Keywords:

Bimetallic alloy nanoparticles

Alloy co-catalyst

Site-selective deposition

Rutile TiO₂

Acetic acid decomposition

ABSTRACT

Alloy nanoparticles (NPs) loaded TiO₂ photocatalysts have attracted considerable attention in the recent years as a promoter of highly active photocatalysts under ultraviolet (UV) irradiation. Many synthetic techniques have been utilized in preparation of binary alloy NPs loaded TiO₂. However, control of deposition site for alloy NPs on TiO₂ is one of the challenging themes in TiO₂ study. Herein, we present that site-selective Pt–Pb NPs deposition on rutile TiO₂ nanorod by successive reduction in metal ions, photo-reduction of Pt⁴⁺ and followed by microwave assisted polyol reduction of Pb²⁺ (2-step method). The Pt–Pb NPs were site-selectively deposited on the reduction site on (110) surface of the rutile TiO₂ nanorod. The photocatalytic activity of rutile TiO₂ was significantly enhanced after Pt–Pb NPs loading for oxidative decomposition of AcOH in aqueous phase. The AcOH was completely oxidized to CO₂ and the CO₂ evolution of the site-selectively Pt–Pb NPs deposited TiO₂ was nearly six times higher than that of a bare rutile TiO₂ and three times higher than randomly Pt–Pb NPs deposited TiO₂. The well mating of the reduction reaction site on photocatalyst, TiO₂, and deposition site for co-catalyst, Pt–Pb NPs, induces efficient electron injection from photocatalyst TiO₂ to co-catalyst Pt–Pb NPs, promoting oxygen reduction reaction and reduction process of AcOH oxidative decomposition. The accelerated electron consumption in reduction process leads to smooth oxidative decomposition of AcOH at oxidation site. These findings suggest that the site-selective deposition of alloy NPs is a predominant way to bring out catalytic performance of co-catalyst alloy NPs on TiO₂.

© 2016 Elsevier Inc. All rights reserved.

1. Introduction

Titanium dioxide (TiO₂) is one of the most important photocatalysts in the area of environmental purification, hydrogen generation, and CO₂ photoreduction [1,2]. Application of a bare TiO₂ is limited, due to their low quantum conversion efficiency. The photocatalytic activities of TiO₂ are usually limited by rapid recombination of photogenerated electron–hole pairs. In order to reduce the electron–hole recombination, one of the effective ways is to load surface modifiers as co-catalyst on TiO₂ photocatalyst. If trace co-catalyst is loaded onto photocatalyst surfaces, the photogenerated electron–hole pairs could be spatially separated, because

electrons and holes could be respectively localized onto the surfaces of photocatalyst and co-catalyst. Consequently, the recombination of photogenerated electron–hole pairs could be inhibited, and the oxidation and reduction reactions could occur at different surface positions. Among various organic and inorganic compounds are used as co-catalyst, metal and/or metal oxide particles were widely used as co-catalysts on TiO₂ in the past, since they enhance the electron transfer prolonging the lifetime of charge carriers [3]. For example, Zhao reported Pt loading suppresses the recombination and promotes the absorption of visible light of TiO₂ [4]. Miyauchi reported the grafting of Cu_xO clusters on TiO₂ achieves the efficient photocatalytic VOCs decomposition and anti-pathogenic effect in in-door condition [5–7]. So far, monometals, such as Pt, have been extensively studied as co-catalyst. Recently, bimetallic alloy has attracted considerable attention as a class of highly active co-catalyst [8]. In particular, Pt alloy NPs loaded TiO₂ can exhibit interesting photocatalytic properties for organic oxidation and CO₂ reduction that are absent in the monometallic

* Corresponding authors at: Department of Material & Life Chemistry, Kanagawa University, 3-27-1 Rokkakubashi, Yokohama, Kanagawa 221-8686, Japan. Fax: +81 45 413 9770.

E-mail addresses: ft101933wb@kanagawa-u.ac.jp (T. Tanabe), ft101828zr@kanagawa-u.ac.jp (F. Matsumoto).

Pt NPs loaded TiO₂ [8]. In addition, Pt alloy co-catalyst is more cost efficient due to the decrease in the usage of Pt. Several bimetallic alloy loaded TiO₂ was applied for photocatalytic reactions under UV irradiation. Alloying with Pt changes the surface chemical composition, crystalline and valence structures of original Pt, promoting electron transfer and absorption strengthen between Pt and reactant. It is acknowledged that metal/semiconductor heterojunction creates a Schottky barrier (Φ_b) at the interface. Photogenerated electron in semiconductor must jump this barrier and is transferred to metal. The Φ_b at Pt/TiO₂ junction is relatively high because of the large difference between the work function of Pt ($\Phi_{Pt} = 5.6$ eV) [9] and the electron affinity of TiO₂ conduction band ($\chi_{TiO_2} = 3.8$ eV) [10]. The high barrier at Pt/TiO₂ junction can prevent more electrons from flowing from TiO₂ to Pt, and more energy is needed for the electrons to flow, which suppresses electron transfer, although large barrier enhances electron–hole separation. Therefore, a moderate barrier height that allows smooth electron transfer and efficient electron–hole separation is necessary for efficient photocatalytic reaction in TiO₂. Alloying of other metal with a lower work function is an effective way to decrease work function of Pt [11,12], leading to decrease Φ_b . Shiraishi et al. reported that Pt alloying with Cu decreases the work function of Pt NPs and decreases the height of Schottky barrier at the Pt–Cu/TiO₂ heterojunction, and this leads to enhance photocatalytic activity [11]. These findings indicate that Pt–*M* alloy loaded TiO₂, in which *M* is metal with lower work function than that of Pt such as Pb, Bi and Cu, has a potential as a high active photocatalyst. Recently, our group has reported that Pt–Pb and Pt–Cu alloy loaded TiO₂ exhibited higher electrocatalytic activity toward oxygen reduction reaction [13,14] and intermetallic PtPb or PtTi₃ loaded WO₃ showed enhanced photocatalytic activity toward acetic aldehyde and acetic acid (AcOH) decomposition under visible light irradiation [15–18]. Beside, photocatalytic properties for co-catalyst deposited TiO₂ are significantly affected by deposition site of co-catalyst on the exposed crystal faces on TiO₂ particles. In the case of single metal loading, photoreduction method using hole scavenger (e.g., methanol) is often used to site-selectively immobilize metal nanoparticles on the reduction site of photocatalyst [19,20]. However, site-selective deposition has not been developed for alloy NPs loading on photocatalyst yet. Alloy NPs are usually prepared by simultaneous reduction in metal ions (e.g., impregnation or precipitation method) [8]. These conventional preparation methods lead to random deposition of alloy NPs irrespective of reactive sites on photocatalyst surface. Therefore, the control of deposition site of Pt alloy NPs on exposed crystal faces of TiO₂ would be crucial for the enhancement of the photocatalytic activity of TiO₂. To obtain the most out of the enhancement effect by alloy NPs loading, it is required to advance preparation method achieving site-selective deposition of alloy NPs on target reaction site of TiO₂.

Herein, we present the site-selective deposition method of Pt–Pb alloy NPs on rutile TiO₂ nanorod (TiO₂-rod). We select rectangular shaped rutile TiO₂-rod with clear automorphism as a photocatalyst, since it is hard to identify reaction sites on TiO₂ spherical particles or polycrystalline aggregated particles. Ohno et al. reported that rutile TiO₂-rod with specific exposed crystal faces are prepared by hydrothermal treatment of titanium trichloride (TiCl₃) solution and its surfaces exposed (110) crystal faces act as reductive face while (001), (111) act as oxidative faces for photocatalytic reaction [19,21,22]. The exposed crystal faces facilitate the separation of electrons and holes, resulting in improvement in photocatalytic activity. Using well-crystallized rutile TiO₂-rod, one can confirm the site-selection of alloy NPs deposition on TiO₂-rod. In this study, site-selective deposition of Pt–Pb NPs on the reduction site on (110) surface for TiO₂-rod is accomplished by 2-step reduction method of metal ions, i.e., photoreduction of

Pt⁴⁺ and followed by microwave assisted polyol reduction of Pb²⁺. The Pt–Pb NPs/TiO₂ prepared by the 2-step enhances significantly photocatalytic activity for AcOH decomposition, much higher than conventional co-reduction method (1-step) and monometal Pt/TiO₂. We show a great efficiency for the site-selective deposition of alloy NPs on TiO₂.

2. Materials and methods

2.1. Chemicals

All chemical reagents were commercial products used without further treatment. Titanium trichloride (TiCl₃), sodium chloride (NaCl), methanol (CH₃OH), potassium hydroxide (KOH), ethylene glycol (C₂H₆O₂), hexachloroplatinic acid (H₂PtCl₆·6H₂O), lead acetate trihydrate (Pb(CH₃COO)₂·3H₂O), lead nitrate (Pb(NO₃)₂), nitric acid (HNO₃) and ammonia solution (2.5%NH₃) were purchased from Wako Pure Chemical Industries, Ltd., and acetic acid (CH₃COOH) was purchased from Kanto Chemical Co., Inc., and dichloro (cycloocta-1,5-diene) platinum (Pt(COD)Cl₂) was purchased from Strem Chemicals Inc., and hydrogen peroxide (30%H₂O₂) was purchased from Junsei Chemical Co., Ltd. (all are of reagent grades). TiO₂ (MT-600B, TAYCA), a rutile with an average surface area (S_{BET}) of 35 m² g⁻¹, was used as a reference photocatalyst.

2.2. Procedure for preparation of rutile TiO₂ nanorods

Exposed-crystal-face-controlled rutile TiO₂ nanorods were prepared by hydrothermal synthesis, following a modified version of the previous reports [19]. 14.61 g of sodium chloride (5 M) was added to 45.73 cm³ of Milli-Q water with vigorous stirring and then 4.27 cm³ of titanium trichloride (0.15 M) was added. The solution was put in a sealed Teflon-lined autoclave reactor (Sanai Kagaku Co., HU-100) and heated at 190 °C for 6 h in an oven. After hydrothermal treatment, the residue in the Teflon bottle was washed with Milli-Q water and dried under reduced pressure at 70 °C for 12 h. Surface modified rutile TiO₂ nanorods were prepared by H₂O₂–NH₃ chemical etching. A synthesized rutile TiO₂ nanorods (250 mg) were added to a H₂O₂–NH₃ mixed solutions (25 mL of 30% H₂O₂ and 2.5 mL of 2.5%NH₃) according to the literature [21] and stirred for 1–4 h at room temperature. After etching treatment, the TiO₂ nanorods were filtered and washed with Milli-Q water.

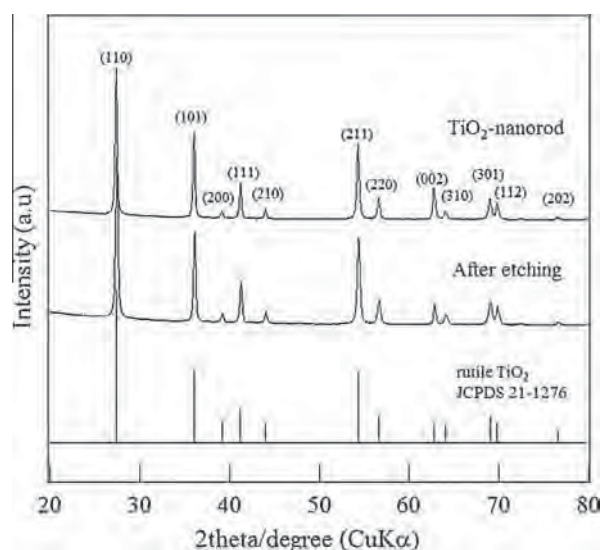


Fig. 1. XRD pattern for the prepared rutile TiO₂ nanorod and after etching for 4 h.

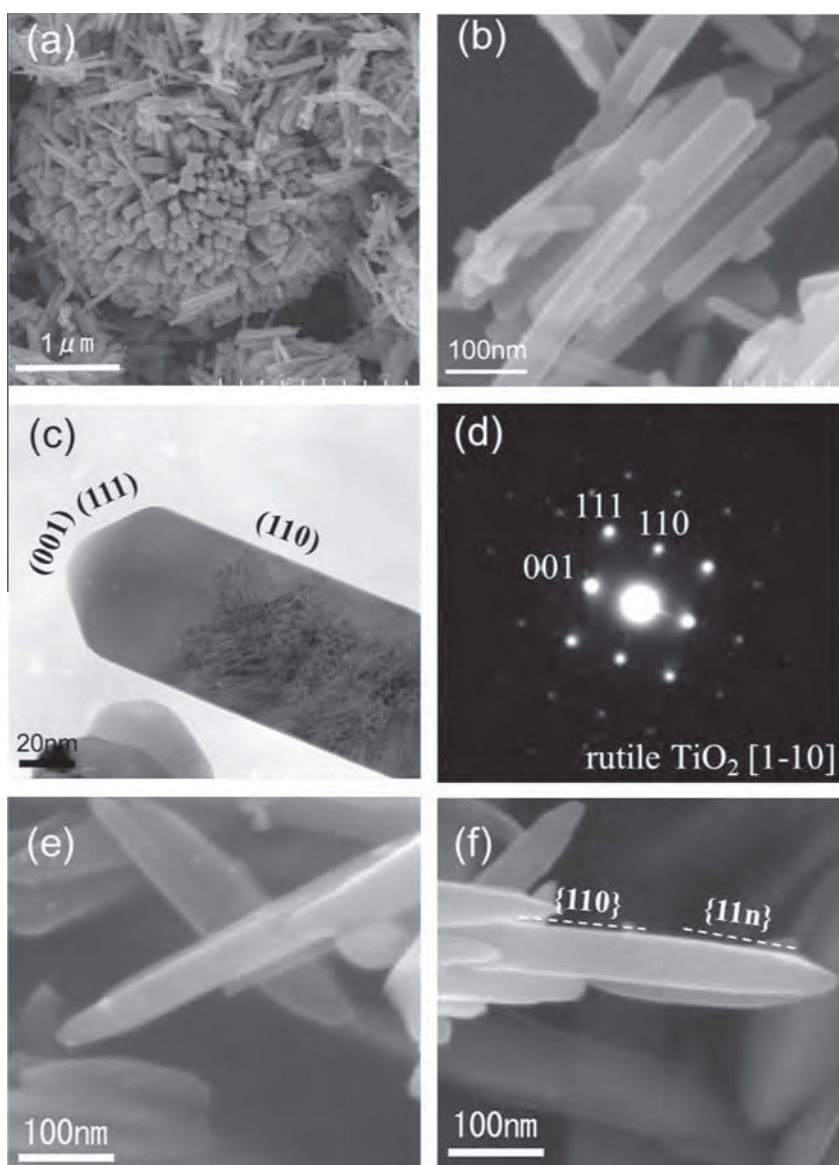


Fig. 2. SEM (a and b) and TEM (c) images and corresponding SAED (d) pattern for rutile TiO_2 -nanorods. SEM images for TiO_2 nanorods after H_2O_2 - NH_3 etching at 1 h (e) and at 4 h (f).

2.3. Reactivity evaluation of exposed crystal faces by photodeposition of Pt and lead(IV) oxide (PbO_2) on rutile TiO_2 nanorods

Photodeposition of Pt and PbO_2 was carried out to determine reduction and oxidation sites on the prepared TiO_2 nanorods, respectively. In order to determine reduction sites, photodeposition of Pt on exposed crystal surface of TiO_2 nanorods was performed. A 0.97 mM hexachloroplatinic acid ($\text{H}_2\text{PtCl}_6 \cdot 6\text{H}_2\text{O}$) solution (corresponding to 1 wt% Pt loading) was added to an aqueous rutile TiO_2 nanorod suspension (0.74 g L^{-1}) containing 4.6 M methanol and then the mixture was irradiated with a 300 W Xe-lamp (Perkin Elmer, PE300BF) for 3 h under full arc. The light intensity was determined by a spectroradiometer (USR-40D, Ushio) and set to be 0.1 mW/cm^2 . Ar gas was vigorously purged through the suspension during the irradiation. After irradiation, the color of the powder changed from white to silver, and the suspension was centrifuged and washed with Milli-Q water and then collected as powder after drying for 12 h at 70°C under reduced pressure.

Using this platinized TiO_2 nanorods, PbO_2 nanoparticles were deposited as a result of Pb^{2+} ion oxidation in order to identify

oxidation sites on the surface of rutile TiO_2 nanorods. This reaction was carried out in an aqueous rutile TiO_2 nanorod suspension (1 g L^{-1}) containing 1 M $\text{Pb}(\text{NO}_3)_2$ under an aerated condition. The pH of the solution for this reaction was adjusted to 1.0 by the addition of nitric acid according to the literature [20,23]. After photoreaction for 12 h using a 300 W Xe-lamp (Perkin Elmer, PE300BF) under full arc, the light intensity was 0.1 mW/cm^2 , and the color of the powder changed from white to brown, indicating that PbO_2 had been deposited on the surface. The resulting suspension was centrifuged and washed with Milli-Q water and then collected as powder after drying for 12 h at 70°C under reduced pressure. Pt and PbO_2 particles deposited on TiO_2 were observed with in a SEM and TEM.

2.4. Pt-Pb alloy NPs deposition as co-catalyst on rutile TiO_2

Site-selective deposited Pt-Pb NPs on TiO_2 were prepared by 2-step reduction in metal ions (2-step method). In the first, Pt was site-selectively deposited on the reduction site of rutile TiO_2 nanorods by photodeposition. The photodeposition of Pt on rutile

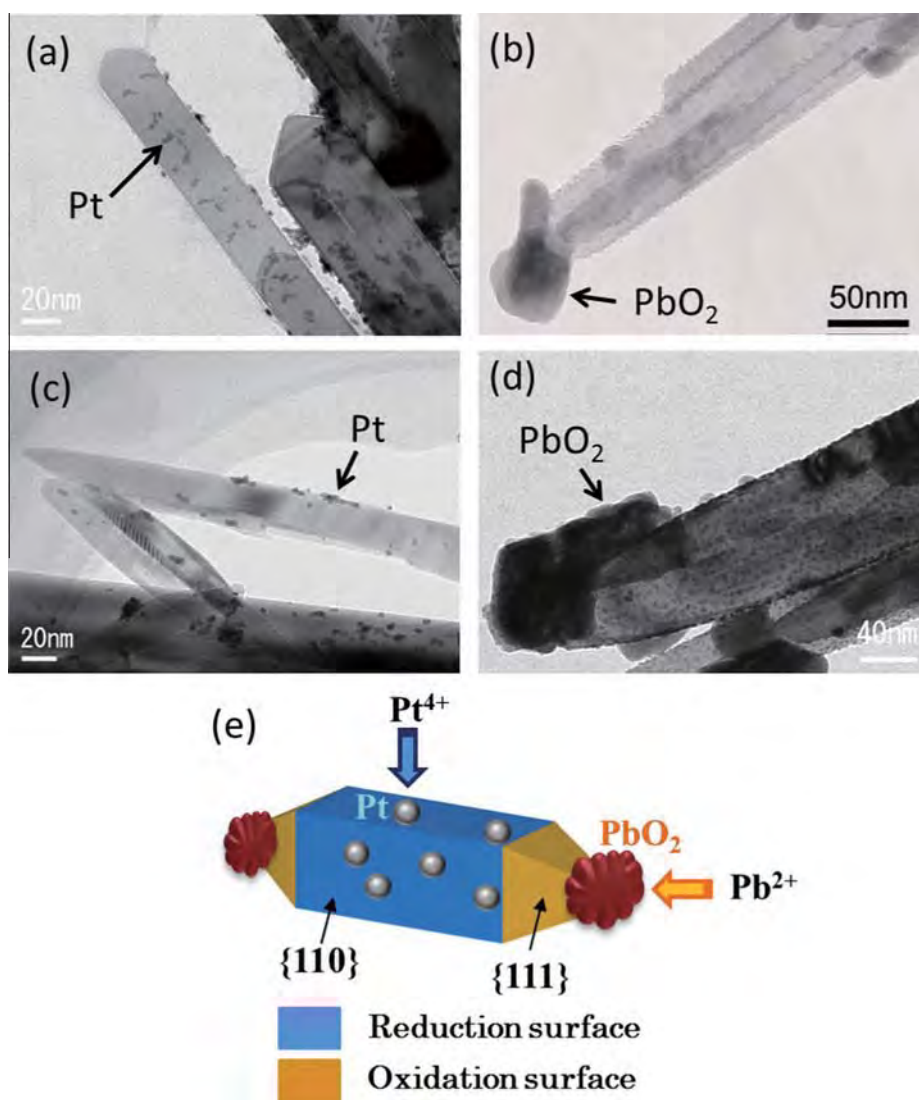


Fig. 3. TEM images for rutile TiO_2 nanorod after Pt-photodeposition (a) and PbO_2 -photodeposition (b), and etched TiO_2 nanorod after Pt-photodeposition (c) and PbO_2 -photodeposition (d). Schematic image of reactive surface for TiO_2 nanorods.

TiO_2 nanorods were carried out with the same procedure as noted in Section 2.3 (1 wt% Pt loading). In the second, Pb^{2+} ion was reduced and alloyed with the surface of Pt of the firstly prepared site-selectively platinized TiO_2 nanorod using microwave assisted polyol method. In the polyol method, the firstly prepared platinized rutile TiO_2 nanorods (200 mg) were dispersed in 50 mL ethylene glycol as reducing agent, and then 5.0 mg of lead acetate trihydrate ($\text{Pb}(\text{CH}_3\text{COO})_2 \cdot 3\text{H}_2\text{O}$) and 1 mg of potassium hydroxide were added to the suspension with vigorous stirring. The platinized rutile TiO_2 nanorod suspension contains lead precursor treated in the flask with a reflux set for 12 min under 300 W of a microwave (Focused microwave instrument, CEM). After cooling with water until to room temperature, the prepared Pt–Pb NPs deposited rutile TiO_2 nanorods were collected by centrifugation and washed with methanol and then collected as powder after drying for 12 h at 70 °C under reduced pressure. To make a comparative study for site selective deposition, random site deposited Pt–Pb NPs on TiO_2 were prepared by co-reduction of Pt and Pb ions with microwave assisted polyol method (1-step). A 200 mg TiO_2 power was dispersed in 50 mL ethylene glycol as reducing agent and then 3.8 mg of $\text{Pt}(\text{COD})\text{Cl}_2$, 5.0 mg of ($\text{Pb}(\text{CH}_3\text{COO})_2 \cdot 3\text{H}_2\text{O}$) and 1 mg of potassium hydroxide were added to the suspension

with vigorous stirring. The TiO_2 suspension was treated in the flask with a reflux set for 24 min under 300 W of a microwave (Focused microwave instrument, CEM). After cooling with water until to room temperature, washing and drying were conducted as the same procedure as 2-step.

2.5. Characterization of prepared samples

Phase identification was performed by means of X-ray diffraction (XRD) using $\text{Cu K}\alpha$ ($\lambda = 1.543 \text{ \AA}$) operation at 40 kV and 40 mA (Rigaku RINT-Ultima III). The surface morphology of the samples was observed by field emission scanning electron microscopy (FE-SEM) with a HITACHI SU-8010. Transmission electron microscopy (TEM) analysis was carried out with a JEOL 2100F microscope with an operating voltage of 200 kV. The composition of the prepared samples was analyzed by an EDS spectrometer, which was attached onto the TEM. Using a surface area analyzer (Micromeritics Tristar 3000), specific BET surface areas of the prepared TiO_2 nanorods were determined by their N_2 adsorption at $-196 \text{ }^\circ\text{C}$. UV–vis diffuse reflectance spectra (DRS) were obtained using a spectrometer (Shimadzu UV2600) by using BaSO_4 as an internal reference.

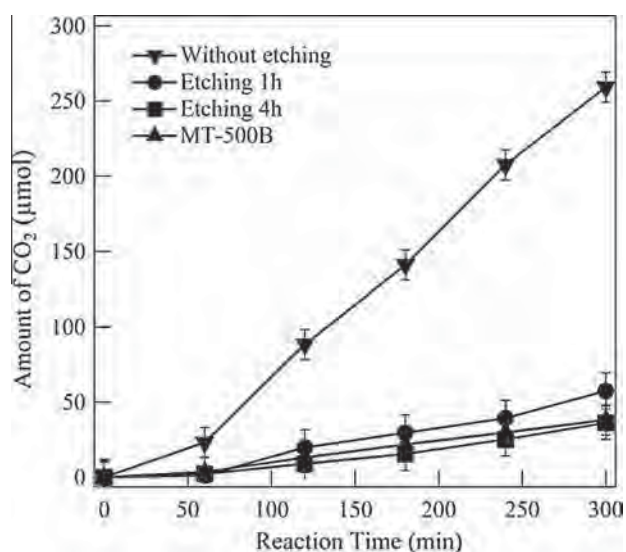


Fig. 4. Time course of CO₂ evolution for AcOH decomposition over rutile TiO₂ nanorod samples before and after etching with H₂O₂-NH₃ solution.

2.6. Photocatalytic decomposition of AcOH

The photocatalytic activities of the TiO₂ samples were evaluated by AcOH decomposition in an aqueous solution containing photocatalyst under oxygen (O₂) using a circulation system when irradiating by a Xe lamp (Perkin Elmer, PE300BF) under full arc. The light intensity was determined by a spectroradiometer (USR-40D, Ushio) and set to be 0.1 mW/cm². A powder sample (30 mg) and an aqueous solution of AcOH (5 vol%, 50 mL) were put into a quartz cell. After purging of air by vacuum, O₂ (30 kpa) was introduced to the circulation system with volume of 142.3 mL. The suspension was irradiated at 298 K using the 300 W Xe lamp and evolved CO₂ was measured as a function of irradiation time. Acetic acid is a stronger acid than carbonic acid, thus acetic acid keeps CO₂ away from the solution. So we assume that actual dissolved CO₂ in solution is negligibly small. During the reaction, the suspension was continuously stirred. Reference sample was selected to test the generality of our results (TEYCA, MT-500B as rutile spherical particle). The amount of evolved CO₂ amount as a result of decomposition of AcOH was measured by a gas chromatograph (Shimadzu, GC-8A).

3. Results and discussion

3.1. Characterization of TiO₂-nanorod

Fig. 1 shows powder XRD pattern for the prepared TiO₂-rod and after etching for 4 h. The crystal structure of prepared material was attributed to single phase for rutile TiO₂ (JCPDS21-1276) and the crystal structure was retained after the etching treatment. Fig. 2a and b shows SEM images of the TiO₂-rod. The prepared material was an aggregate of rods-shaped morphology with an approximate length of 300–400 nm and width of 20–50 nm. The specific surface area (*S*_{BET}) of the TiO₂-rod was 38 m²/g. Fig. 2c and d shows TEM image and its corresponding electron diffraction (SAED) pattern at the selected-area of TiO₂-rod. The TEM image shows the TiO₂ material was the rod like rectangular shape with a truncated square pyramid end. The sharp reflection spots in SAED pattern obtained from the TiO₂-rod, which corresponds to the $\langle 1-10 \rangle$ zone axis of rutile TiO₂, indicate that the individual rods were single-domain and of high crystallinity. Assignment of crystal planes for these exposed surfaces of the pre-

pared TiO₂-rod was confirmed by the TEM and the SAED pattern. Rutile TiO₂ is tetragonal, and exposed crystal faces of truncated square pyramid end were assigned to $\{111\}$, $\{100\}$ and large side surfaces were assigned to $\{110\}$, as pointed in the TEM image (Fig. 2c). Long axis of TiO₂-rod is equivalent to the $[001]$ direction. The exposed area of side faces (110) is larger than that of the other crystal faces, i.e. the side surfaces showed a higher ratio relative to the truncated pyramid end for the prepared TiO₂-rod. To control the ratio of side surface area to truncated pyramid end, chemical etching with H₂O₂-NH₃ solution was carried out according to the literature [21]. Fig. 2e and f shows SEM images for TiO₂-rod after etching with H₂O₂-NH₃ solution at 1 h and 4 h, respectively. Surfaces of TiO₂-rod were selectively etched from the square pyramid faces $\{111\}$ and neighboring side surface $\{110\}$ by H₂O₂-NH₃ etching, and the angle between square pyramid faces became sharper with increase in etching time. The newly exposed crystal faces on the TiO₂-rod after etching were assigned to $\{11n\}$ ($0 < n < 1$) faces and its close crystal faces as pointed in Fig. 2f. With an increase in etching time, the tip ends of the TiO₂-rod became sharper and flat side surface $\{110\}$ decreased.

3.2. Determination of reaction selectivity on crystal faces in TiO₂-rod

To determine reactive sites on the exposed crystal faces of the prepared TiO₂-rod, photodeposition of Pt and PbO₂ was carried out, which method is used to determine reactive sites for well-faceted TiO₂ material [19–21,23]. The colors of the prepared TiO₂ powder after UV-light irradiation in the presence of H₂PtCl₆ aqueous solutions changed to gray. This color change in rutile TiO₂-rod suggested that Pt particles were deposited on the TiO₂ surface. Under UV-light irradiation, the photogenerated electrons migrate to the TO₂ surfaces and can reduce Pt⁴⁺ to the metallic Pt while holes are consumed by hole scavenger (e.g., methanol), resulting in the formation of Pt NPs on the TiO₂ surfaces. The reductive site of photocatalyst material corresponds to the surface site where photogenerated electrons preferentially react with reactive substrate rather than other sites. Pt⁴⁺ is reduced by photogenerated electrons to metallic Pt in photodeposition of Pt; thus, the Pt site corresponds to the reductive site of TiO₂-rod. We can consider the Pt NPs deposition site as landmark covering the reductive site on TiO₂-rod surface. Fig. 3a shows TEM observations of the TiO₂-rod after photodeposition of Pt, where the deposited particles were analyzed by EDS analysis (see Fig. S1-a). Pt nanoparticles were mainly deposited on the side surfaces surrounded by $\{110\}$ faces of TiO₂-rod. This result indicates that the side surfaces exposed $\{110\}$ act as reductive face of TiO₂-rod providing dense surface reductive site of TiO₂-rod. According to literatures, rutile TiO₂ (110) surface is constructed by alternate arrangement of two different atomic rows, i.e., rows of 5-coordinated Ti atoms and of bridging oxygens [24]. There are number of surface exposed 5-coordinated Ti sites on (110) surface than those of other faces. The exposed lower 5-coordinated Ti site prefers to scavenge electron from bulk TiO₂ due to lower electron density than other sites. Therefore, (110) surface making many exposed 5-coordinated Ti sites are more likely to capture electron than other crystal faces and provide a number of the reductive sites of rutile TiO₂, while, after UV-light irradiation in the presence of Pb(NO₃)₂ under an aerated condition, the colors of the platinized TiO₂ powder changed to gray, indicating that PbO₂ particles were deposited on the TiO₂ surface. In photodeposition of PbO₂, Pb²⁺ was oxidized by hole in TiO₂ to produce PbO₂ nanoparticles while photogenerated electrons are consumed by electron scavengers (e.g., dissolved oxygen). Hence, the deposition site of PbO₂ is considered as landmark covering the photocatalytic oxidative site on TiO₂-rod surface. Fig. 3b shows TEM image of the TiO₂-rod after photodeposition of PbO₂ and corresponding EDS analysis is shown in Fig. S1-b. The compositional



Scheme 1. Preparation procedure for site-selective Pt–Pb deposition on the reduction site of rutile TiO₂ nanorod (2-step method). Photoreduction of Pt⁴⁺ on the reduction site of TiO₂ nanorod and followed by microwave assisted polyol reduction of Pb²⁺ and simultaneously alloying with Pt.

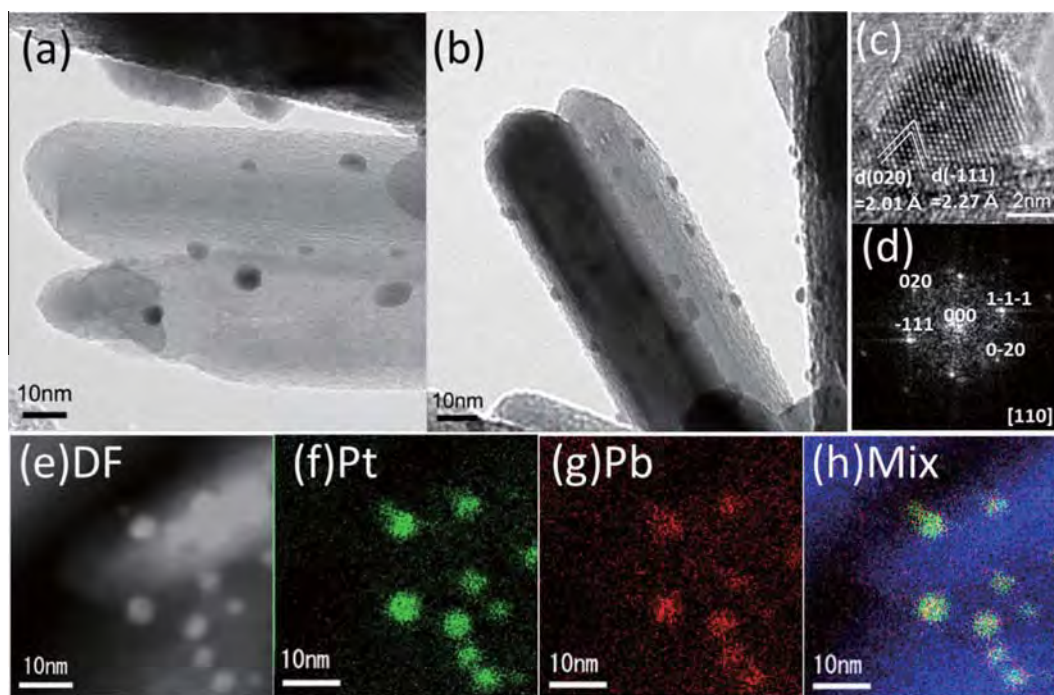


Fig. 5. TEM images (a and b), HRTEM image (c) and corresponding FFT pattern (d) for Pt–Pb NPs deposited TiO₂ nanorod prepared by 2-step method. STEM-DF image (e) and EDS elemental mapping of Pt (green) (f), Pb (red) (g), Ti (blue), composite image (h) for the Pt–Pb NPs.

analysis showed that the mole ratio was almost Pb/O = 1/2 ((Pb: O = 32.6:67.4 (at%)). Large PbO₂ particles with sizes of more than 100 nm were solely deposited on the square pyramid end surrounded by {001}, {111} faces as illustrated in Fig. 3e. These show that the rod ends exposed {001}, {111} act as oxidative face of TiO₂-rod providing dense surface oxidative site of TiO₂-rod. There are double rows of bridging oxygen alternating with single rows of exposed Ti atoms on (001) surface [24]. Since the exposed Ti atom position is shifted toward the direction of bulk with structure relaxation, bridging oxygen mostly covers the surface of (001) face. The bridging oxygen prefers to scavenge hole from bulk due to higher electron density than other atomic sites. Therefore (001) surface is more likely to capture hole at the bridging oxygen site and provides effective oxidative site. Moreover for (111), there is alternate arrangement of double rows of 2-coordinated oxygen

and single rows of Ti atoms [24]. The exposed Ti site of (111) surface is also shifted to the direction of bulk with structure relaxation; hence, the oxygen atomic sites are in rich on (111) surface, leading to prefer to scavenge hole at (111) surface. The exposed crystal faces and corresponding reactive faces of the prepared TiO₂-rod were consistent with the reported rutile TiO₂ nanorod [19]. Fig. 3c and d shows TEM images of H₂O₂–NH₃ chemical etched TiO₂-rod after the Pt and PbO₂ photodeposition under UV-irradiations, respectively. Pt nanoparticles were compactly deposited on the middle position of side surfaces, while it was rarely observed on newly exposed etched faces (Fig. 3c). These results indicate that the etched faces lose its function as reductive faces, while PbO₂ particles were deposited not only on rod ends but the newly exposed surfaces (Fig. 3d). Note that the newly exposed {111} faces with H₂O₂–NH₃ etching provide oxidative

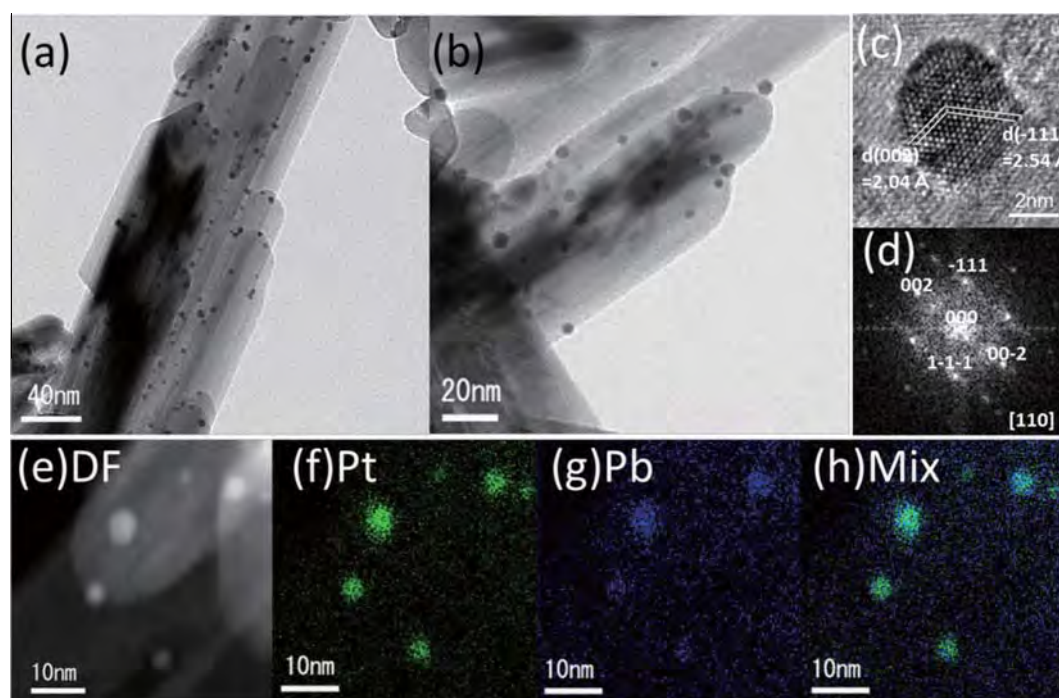


Fig. 6. TEM images (a and b), HRTEM image (c) and corresponding FFT pattern (d) for Pt–Pb NPs deposited TiO₂ nanorod prepared by 1-step method. STEM-DF image (e) and EDS elemental mapping of Pt (green) (f), Pb (blue) (g), and composite image (h) for the Pt–Pb NPs.

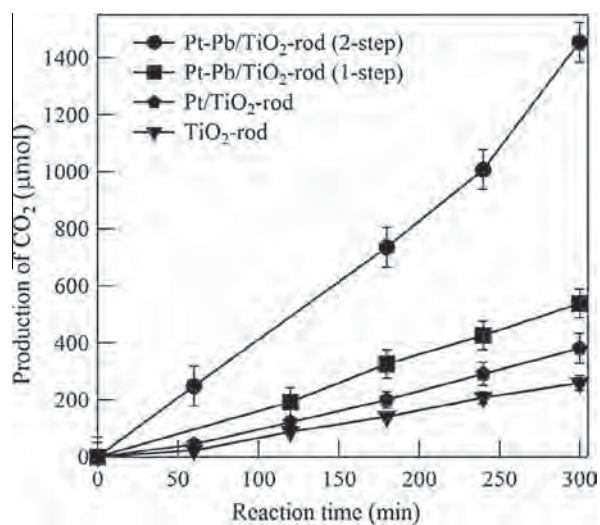


Fig. 7. Time course of CO₂ evolution for AcOH decomposition over Pt–Pb NPs deposited and Pt NPs deposited rutile TiO₂ nanorod samples.

faces. Fig. 4 shows the time course of CO₂ evolution for AcOH decomposition over TiO₂-rod before and after etching with H₂O₂–NH₃ solution. It is known that AcOH is completely oxidized to CO₂ in aerated solution ($\text{CH}_3\text{COOH} + 2\text{O}_2 \rightarrow 2\text{CO}_2 + \text{H}_2\text{O}$) [25]. In our experimental conditions, only CO₂ was produced and any by-product was not detected, indicating complete oxidation of AcOH. The prepared TiO₂-rod samples exhibited much higher photocatalytic activities than those of commercial spherical rutile TiO₂ particles (MT-500B). The specific BET surface area of the samples was not so different, 38 m²/g for TiO₂-rod and 35 m²/g for MT-500B. Thus photocatalytic activity in our experimental condition strongly depends on well-defined facet structure.

Using well-faced TiO₂-rod, the efficiency of charge separation will be enhanced as the result of the spatial separation between

oxidation site and reduction site on the surfaces. Because electrons and holes are preferentially captured at the reduction site and oxidation site, respectively, the electron–hole pairs could be spatially separated on the well-faced TiO₂ surfaces. Consequently, the recombination of photogenerated electron–hole pairs could be suppressed, leading to enhanced charge separation. The recombination of electron–hole pairs is more likely to occur in the case of poor faceted spherical particles because reduction and oxidation site cannot be sufficiently separated on the limited surface region.

When compared with chemical etched samples for the activity trend (Fig. 4), TiO₂-rod before etching showed the highest activity. The etched TiO₂-rod showed an appreciable decrease in photocatalytic activity. It has been reported that H₂O₂ treatment influences the absorption range due to the generation of surface peroxide species [26], but the difference in diffuse reflectance spectra was not observed among TiO₂-rod before and after etching as shown in Fig. S2 and a color change of samples was not observed after etching, indicating that the absorbed photon numbers in these TiO₂ samples are identical. Although the color of peroxide species on titanium ions is usually yellow [27,28], the influence of peroxide species was not the reason for decrease in photocatalytic activity. Also, surface areas of these samples are not so different, 38–41 m²/g for etched samples, and the photocatalytic reaction in the present condition proceeds under light limited condition. Based on these results, photocatalytic activity in our experimental condition strongly depends on exposed faces of TiO₂-rod. We suggest that modification of reactive surface by H₂O₂–NH₃ etching induced activity changes. Chemical etching affected the balance of reactive faces between reductive and oxidative face {110} side surface performing as reductive face was greatly decreased and alternatively newly exposed {11n} faces were increased with increasing the etching time. The activity test showed that higher ratio of reductive face induces to higher photocatalytic activity for AcOH decomposition. This suggests that reduction process has a predominant influence for photocatalytic activity of TiO₂-rod. Oxygen (O₂) reduction reaction is known as a counter process

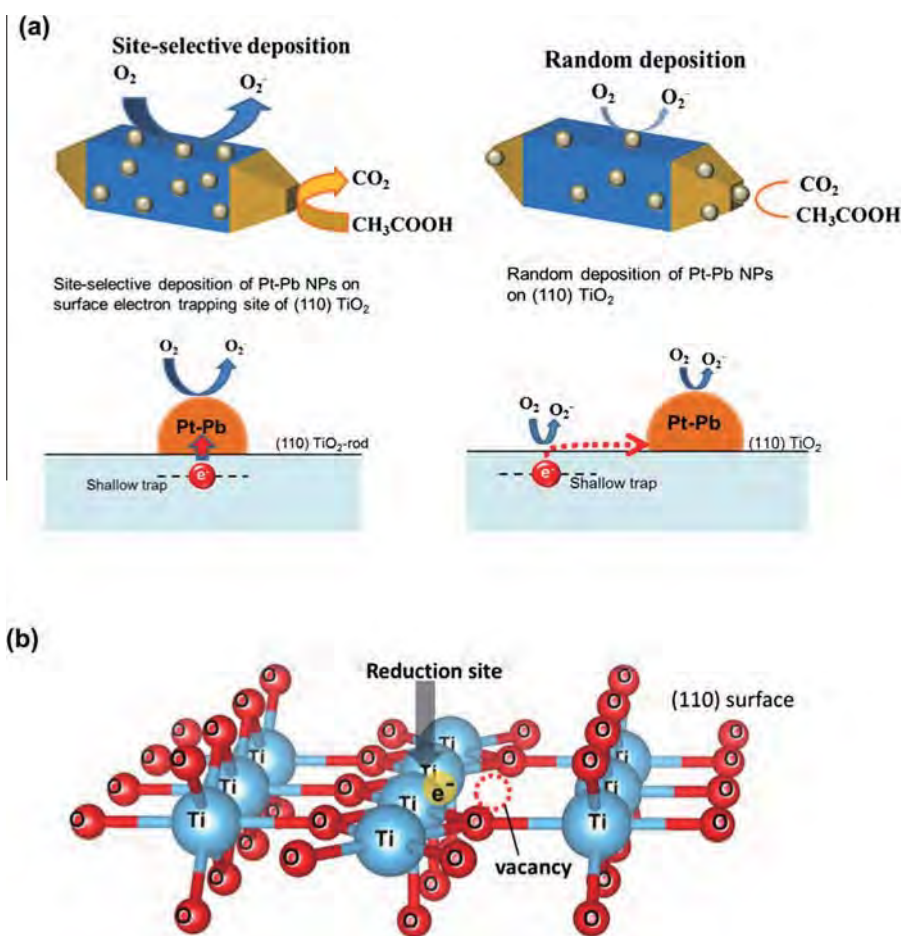


Fig. 8. Schematic images of interfacial electron transfer steps of Pt–Pb/TiO₂-rod (a) and reduction site of (110) TiO₂ surface (b).

of organic decomposition [29]. Since the degree of dissolved O₂ in aqueous solution is limited at much lower level, oxygen reduction reaction is, thus, most likely dominant process for AcOH decomposition under our experimental condition. Among exposed crystal faces on TiO₂-rod, oxygen reduction reaction will be preferentially promoted on {110} side surfaces assigned to reductive face. Since photogenerated-electrons were consumed by oxygen reduction reaction on the reductive face, holes remained at valence band could decompose AcOH efficiently, resulting in the high performance for the well-faceted TiO₂-rod without etching.

3.3. Site-selective Pt–Pb NPs deposition as cocatalyst on TiO₂ nanorod

Site-selectively deposited Pt–Pb NPs on TiO₂ was prepared by 2-step reduction of metal ions as illustrated in Scheme 1. In the first, Pt was site-selectively deposited on the reduction site of {110} face of TiO₂-rods by photodeposition method as evident from Fig. 3a. The site-selective photodeposition of Pt was carried out with the same procedure as noted in Section 2.3. In the second, Pb²⁺ ion was reduced and alloyed with the site-selectively deposited Pt to form Pt–Pb on the TiO₂ nanorod using microwave assisted polyol method. The prepared Pt–Pb alloy NPs thus site-selectively locate on the reduction site of TiO₂ nanorod as illustrated in Scheme 1. Fig. 5a and b shows TEM images for TiO₂ nanorod after loading of Pt–Pb NPs by successive reduction in metal ions (2-step method). The TEM observation confirmed that the prepared Pt–Pb were site-selectively deposited on {110} reductive face of TiO₂-rod (Fig. 5c). Rarely observed on the truncated pyramid end {001}, {111} oxidative faces. The average par-

ticle size of Pt–Pb NPs was 5.6 nm. HRTEM image (Fig. 5c) of Pt–Pb NPs and its corresponding FFT pattern (Fig. 5d) indicate that the Pt–Pb NPs formed FCC-type structure, showing the formation of solid solution phase in Pt–Pb alloy system. The elemental mapping with STEM–EDS over the Pt–Pb NPs is presented in Fig. 5e–h. Importantly, the distribution of Pt (green) and Pb (red) is uniform over the Pt–Pb NPs, as is evident from the composite image (Fig. 5h). The EDS spectra with point analysis confirmed that the Pt- to Pb atomic ratio in the Pt–Pb NPs is nearly 3:1 (Fig. S3). The molar ratio of metals in precursor solution was Pt/Pb ≈ 1/1.3. Excess Pb ion was fully removed under washing process as confirmed with ICP analysis of final catalyst (Table S1).

To make a comparative study for site selective deposition, Pt–Pb NPs were randomly deposited on TiO₂-rod by co-reduction method (1-step method). Pt⁴⁺ and Pb²⁺ are simultaneously reduced and alloyed to Pt–Pb NPs on TiO₂ surfaces by microwave assisted polyol reduction. Fig. 6a and b shows TEM images for TiO₂-rod after Pt–Pb NPs loading by 1-step method. The TEM observation shows that Pt–Pb NPs were randomly deposited on TiO₂-rod irrespective of exposed crystal faces. The HRTEM image and its corresponding FFT pattern indicate that Pt–Pb NPs prepared by 1-step formed FCC-type structure, solid solution phase as the same crystal structure as Pt–Pb NPs by 2-step. The average particle size was 3.7 nm, whose size was smaller than 2-step. The STEM–EDS analysis (Fig. 6e–h) confirmed that distribution of Pt (green) and Pb (blue) is uniform over the Pt–Pb NPs, as shown in the composite image (Fig. 6h). The Pt- to Pb atomic ratio is nearly 3:1 over Pt–Pb NPs (Fig. S3). The TEM observations of Pt–Pb/TiO₂ prepared by 1-step showed no major change of Pt–Pb particle size and

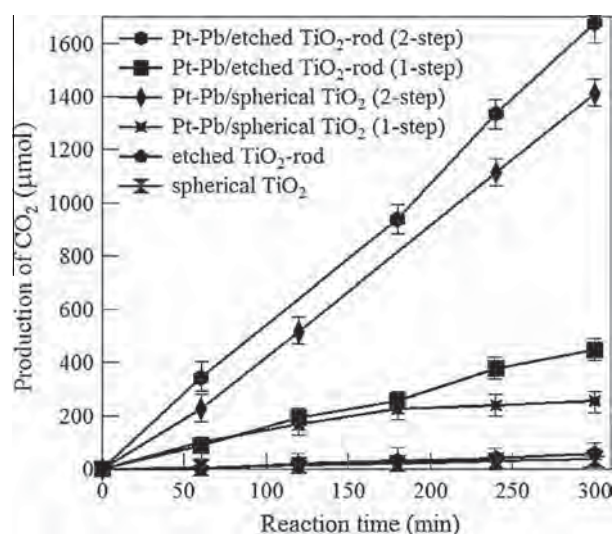


Fig. 9. Time course of CO₂ evolution for AcOH decomposition over Pt–Pb NPs deposited on etched TiO₂ nanorods (1 h etching) and on spherical TiO₂ (MT-500B).

particle dispersion among the three exposed TiO₂ faces (Fig. 6a and b). Thus, the difference of nucleation process between the three surfaces would be negligibly small. From these findings, we concluded that Pt–Pb alloy NPs prepared by polyol reduction (1-step) were randomly deposited on TiO₂-rod.

The activity of the Pt–Pb/TiO₂-rod materials toward the AcOH decomposition was tested (Fig. 7). The Pt–Pb loading enhanced significantly the activity of TiO₂-rod, and these activities were much higher than monometal Pt loading. The evolved CO₂ of Pt–Pb/TiO₂-rod prepared by 2-step was six times higher than that of bare TiO₂-rod and four times higher than Pt/TiO₂-rod. We calculated apparent quantum efficiency Φ_{app} to evaluate Pt–Pb/TiO₂ catalyst. Since the stoichiometry in this photocatalytic reaction system is known to be $\text{CH}_3\text{COOH} + 2\text{O}_2 = 2\text{CO}_2 + 2\text{H}_2\text{O}$, we assumed eight holes ($\text{CH}_3\text{COOH} + 2\text{H}_2\text{O} + 8\text{h}^+ \rightarrow 2\text{CO}_2 + 8\text{H}^+$) and electrons are required when Φ_{app} was calculated and ignored a possible radical chain mechanism (see Supplementary Information). Φ_{app} ($\lambda > 260$ nm) was calculated to 22.5% for site-selective Pt–Pb/TiO₂-rod. This efficiency is much higher than that of reported TiO₂ materials [30]. As discussed in Section 3.2, oxygen reduction reaction is predominant process for AcOH decomposition in our experimental condition. It is reported that Pt–Pb NPs exhibit excellent electrocatalytic activity for oxygen reduction reaction than Pt NPs [31]. This enhanced oxygen reduction activity of Pt–Pb NPs accounts for high photocatalytic performance of Pt–Pb/TiO₂-rod. Another factor contributing to catalytic performance of Pt–Pb NPs/TiO₂-rod might be stabilization of adsorbed O₂ on Pt–Pb NPs. The FTIR analysis in previous study [32] has shown that acetate species are preferentially coordinated on rutile TiO₂ surface when photocatalytic decomposition of AcOH solution indicates the difficulty of O₂ access on TiO₂ surface. According to thermodynamic data, the formation enthalpy of a stable Pb oxide (PbO₂) is large (-274.47 kJ/mol) [33], and thus it is predicted that Pb atom shows a strong oxygen affinity prefers to create a stable bonding to oxygen. We propose that dissolved O₂ would be stabilized on surface Pb atom on Pt–Pb NPs. The increase in adsorbed O₂ on TiO₂ surface leads to accelerate oxygen reduction reaction rate and may promote radical chain reaction process for AcOH oxidation, because the both reactions are enhanced by the presence of O₂ [29,34].

Compared with deposition method of Pt–Pb NPs, 2-step method was much effective to enhance the activity than 1-step (Fig. 7). The evolved CO₂ for 2-step was three times higher than that of 1-step despite larger particle was observed for 2-step than 1-step (Figs. 5

and 6). Chemical composition and elemental distribution of Pt–Pb NPs were almost the same level in the two samples as evident from the TEM observations. Diffuse reflectance spectra showed no obvious change among the two samples as shown in Fig. S2. From these results, the difference in physical property of Pt–Pb NPs was not reason for the activity variation for the Pt–Pb/TiO₂-rod. We assume that the deposition site of Pt–Pb NPs on TiO₂ greatly influences the activity.

Fig. 8a illustrates a schematic image of interfacial electron transfer steps of Pt–Pb/TiO₂-rod. 2-step method provides the site-selective deposition of Pt–Pb NPs just above the reduction sites on (110) reductive face of TiO₂-rod (see Fig. 5 and Scheme 1). Photogenerated electrons migrate from the bulk to the (110) surface and are captured at the reduction sites. If Pt–Pb NPs are selectively deposited on the reduction sites, the captured electrons at the reduction sites can be directly injected to co-catalyst Pt–Pb NPs through the Pt–Pb/TiO₂ interface. This direct injection of electrons through the interface will take the shortest route between the reduction site and co-catalyst Pt–Pb and this smooth electron injection leads to suppress recombination concerning at electron transfer from TiO₂ to co-catalyst, by contrast, when Pt–Pb NPs are randomly deposited on TiO₂ surfaces by 1-step method (Fig. 6). The trapped electrons at reduction sites need to depart from the reduction site and migrate to Pt–Pb NPs site due to the mismatch between the reduction site and co-catalyst deposition site (Fig. 8a). We expect that the extra migration of electron from the reduction site to Pt–Pb NPs site increases the probability of the recombination and may need more energy to migrate due to the de-trapping from the reduction site. This indirect electron injection from the reduction site to Pt–Pb NPs site will give rise to the low efficient activity for oxygen reduction reaction as the result of increase in recombination and a more difficult electron transfer. The well mating of the Pt–Pb NPs deposition site and the reduction sites by the site-selective deposition using 2-step method are very important for efficient charge transfer between co-catalyst Pt–Pb NPs and TiO₂. The efficient electron transfer and great oxygen reduction activity of Pt–Pb NPs doubly enhance oxygen reduction reaction on TiO₂ and suppress surface electron-hole recombination, giving rise to the high catalytic performance for the site-selectively deposited Pt–Pb NPs/TiO₂-rod.

The TEM and activity test results indicate that the reduction site on (110) surface is a key surface site for the enhancement of catalytic activity. Fig. 8b shows the schematic image of reduction site of (110) TiO₂ surface. As mentioned above, there are exposed 5-coordinated Ti atoms on (110) face. Among the exposed Ti atoms on (110) face, the Ti atoms located at surface defects such as step, kink, and neighboring oxygen vacancy will be expected to have a lower coordination numbers than those in terrace site, i.e., less than 5 coordination. The lower (<5) coordinated Ti atoms at surface defects will have lower electron density that is more benefit to scavenge photogenerated-electrons among the surface exposed Ti atoms. Therefore, these lower coordinated Ti atoms located at the surface defects are considered to be the reduction sites of (110) surface (Fig. 8b). In addition, the reduction sites involving surface defects will act as electron trapping sites for TiO₂. Di Valentin et al. reported that electrons populate surface trap sites due to the lattice relaxation associated with the trapping is more feasible at the surface site than in the bulk, and the surface trap energy levels are deeper with respect to the bulk levels, confirming that there is a driving force for electrons migrating from bulk to surface trapping site [35]. When considering energy level matching, electron transfer from the shallow trap electrons to Pt is preferable than from free electrons at conduction band. From these finding, we may expect that the surface defects of (110) surface will provide shallow trapping sites and act as reduction sites on TiO₂-rod.

In addition to promoting effect for reduction process in AcOH decomposition by Pt–Pb loading, the oxidation process would be affected by the difference in deposition method of Pt–Pb NPs. For oxidation reaction process, holes directly attack AcOH as first step in radical chain reaction process [29] and also produce OH radical by reacting with water, which radical has been often regarded to play an important role in the oxidation mechanism [36]. Since Pt–Pb NPs catalyze oxygen reduction reaction efficiently, it is probably that Pt–Pb NPs work as electron acceptor even though deposited on oxidative site. Hence, the presence of Pt–Pb NPs on oxidative face will promote recombination with trapped electron on Pt–Pb NPs and hole. The random site deposition using by 1-step method provided Pt–Pb NPs loading on the {001}, {111} oxidative faces (Fig. 6), and this would significantly reduce the catalytic efficiency for AcOH decomposition. On the other hand the site-selective deposition with 2-step avoided Pt–Pb NPs loading on the oxidative faces, leading to achieve full potential of strong oxidation power of holes for TiO₂.

3.4. Effect of TiO₂ morphology

In order to elucidate the general applicability of site-selective deposition for different shaped TiO₂ samples, the photocatalytic activity of the Pt–Pb NPs loaded on etched TiO₂-rod and spherical TiO₂ (MT-500B) toward AcOH decomposition was tested (Fig. 9). Similar to TiO₂-rod, Pt–Pb NPs loading significantly enhanced photocatalytic activity and higher activity was observed for 2-step than 1-step, indicating the site-selective deposition is extremely effective for several types of TiO₂ particles. Fig. 9 shows the enhancement effect by Pt–Pb co-catalyst loading as well as the effect of the shape of TiO₂. When Pt–Pb was randomly loaded on TiO₂ by 1-step, the catalytic activity strongly depended on the ratio of reductive face TiO₂ (110), where a higher ratio of reductive face (110) induces to higher photocatalytic activity, e.g., Pt–Pb/TiO₂-rod > Pt–Pb/TiO₂-etched rod > Pt–Pb/spherical TiO₂ (Fig. 7 and 9). The oxygen reduction reaction on TiO₂ will mainly occur at electron trapped site, i.e., reduction site, on TiO₂ (110) surface as illustrated in Fig. 8(a and b). However, if co-catalyst is loaded on TiO₂, the oxygen reduction reaction proceeds on co-catalyst site as well as the reduction site on TiO₂ (110) surface. Because of the mismatch between the reduction site and co-catalyst Pt–Pb site for randomly Pt–Pb deposited TiO₂ (1-step) samples, the oxygen reduction reaction will proceed simultaneously at the both sites, at the reduction site on TiO₂ (110) and at the Pt–Pb deposition site, as illustrated in Fig. 8(a). These suggest that the shape of TiO₂ largely influences catalytic activity in case of Pt–Pb/TiO₂ (1-step) samples because the oxygen reduction reaction on TiO₂ (110) surface significantly contributes to the catalytic activity.

On the other hand, the activities were not susceptible to TiO₂ morphology when Pt–Pb alloy was site-selectively loaded on the reduction site on TiO₂ (110) surface by 2-step. Similar activities were observed among the Pt–Pb/TiO₂ (2-step) samples (Figs. 7 and 9). This is because that the oxygen reduction reaction will preferentially proceed on the Pt–Pb surface instead of TiO₂ surface for Pt–Pb/TiO₂ (2-step) samples due to the well mating of the reduction site and Pt–Pb deposition site. When Pt–Pb NPs are selectively deposited on the reduction sites on TiO₂ (110) surface by 2-step, photogenerated-electrons in TiO₂ can be directly injected to co-catalyst Pt–Pb NPs through the Pt–Pb/TiO₂ interface and the oxygen reduction reaction are significantly accelerated on Pt–Pb surface as shown in Fig. 8(a). From these findings, the oxygen reduction reaction will preferentially occur on the Pt–Pb alloy surface rather than TiO₂ surface in case of Pt–Pb/TiO₂ (2-step) samples. The site-selective deposition (2-step) can get out full catalytic performance of Pt–Pb alloy. Since the site-selective Pt–Pb loading reduces a frequency of the oxygen reduction reaction on TiO₂ surface, it weak-

ens the morphology effect of TiO₂ for catalytic activity. Therefore, Pt–Pb/TiO₂ (2-step) samples showed essentially the same performance independently of the shape of TiO₂. Among the Pt–Pb/TiO₂ (2-step) samples, Pt–Pb/etched TiO₂-rod exhibited the best activity, which is higher than that of Pt–Pb/TiO₂-rod before etching (Fig. 7). Since the electron consumption with oxygen reduction reaction is significantly improved by the site-selective Pt–Pb deposition, it is suggested that the photocatalytic activity is affected by the difference of the oxidation power of TiO₂ after Pt–Pb loading by 2-step. The ratio of oxidative faces on TiO₂-rod was increased with the etching treatment as shown in Figs. 2f and 3d. The newly exposed {11n} faces by chemical etching will have a stronger oxidation power than those of originally exposed {110}, {111} as reported in previous paper [21]. Thus, the highest activity for etched TiO₂-rod after Pt–Pb loading by 2-step may result from the strong oxidation power of the newly exposed {11n} faces.

4. Conclusions

Site-selective Pt–Pb loaded TiO₂ nanorod was prepared. Pt–Pb NPs were selectively loaded on the reduction site of rutile TiO₂ by the successive 2-step reduction of metal ions, photo-reduction of Pt and followed by alloying with Pb by microwave assisted polyol reduction method. Photocatalytic activities for AcOH decomposition for site-selectively and randomly Pt–Pb loaded TiO₂ were carried out under UV-vis irradiation. The site-selectively Pt–Pb loaded TiO₂ exhibited a much higher activity than random deposited ones. This is attributed to the enhancement of oxygen reduction reaction due to the well mating of Pt–Pb loading site and reduction site of TiO₂. In addition, the site-selective deposition of Pt–Pb was effective for different shape of TiO₂ particles. We have demonstrated that the photocatalytic activities strongly depend on the deposition site of alloy NPs onto the specific crystal faces of rutile TiO₂. Control of deposition site of alloy NPs in the present study is a strategical way of enhancement on the photocatalytic activity of TiO₂. Site-selectively alloy loaded TiO₂ is promising photocatalyst material for organic decomposition.

Acknowledgment

A part of this work was supported by National Institute for Materials Science (NIMS) microstructural characterization platform as a program of “Nanotechnology Platform” of the Ministry of Education, Culture, Sports, Science and Technology (MEXT), Japan.

Appendix A. Supplementary material

Supplementary data associated with this article can be found, in the online version, at <http://dx.doi.org/10.1016/j.jcat.2016.05.027>.

References

- [1] A. Fujishima, T.N. Rao, D.A. Tryk, J. Photochem. Photobiol. C: Photochem. Rev. 1 (2000) 1–21.
- [2] J. Schneider, M. Matsuoka, M. Takeuchi, J. Zhang, Y. Horiuchi, M. Anpo, D.W. Bahnemann, Chem. Rev. 114 (19) (2015) 9919–9986.
- [3] A.L. Linsebigler, G. Lu, J.T. Yates Jr., Chem. Rev. 95 (3) (1995) 735–758.
- [4] Z.-Y. Zhao, J. Phys. Chem. C 118 (2014) 24591–24602.
- [5] X. Qiu, M. Miyauchi, K. Sunada, M. Minoshima, M. Liu, Y. Lu, D. Li, Y. Shimodaira, Y. Hosogi, Y. Kuroda, K. Hashimoto, ACS Nano 6 (2) (2012) 1609–1618.
- [6] K. Hashimoto, K. Sunada, M. Miyauchi, X.Q. Qiu, K. Yoshinobu, I. Hitoshi, N. Ryuichi, K. Jitsuo, Y.Y. Yao, PCT Patent Application, PCT/JP2010/073087.
- [7] X.Q. Qiu, M. Miyauchi, H.G. Yu, H. Irie, K. Hashimoto, J. Am. Chem. Soc. 132 (2010) 15259–15267.
- [8] Y. Shiraiishi, Y. Takeda, Y. Sugano, S. Ichikawa, S. Tanaka, T. Hirai, Chem. Commun. 47 (2011) 7863–7865.
- [9] H.B. Michaelson, J. Appl. Phys. 48 (1977) 4729.

- [10] N. Tokmoldin, N. Griffiths, D.D.C. Bradley, S.A. Haque, *Adv. Mater.* 21 (2009) 3475–3478.
- [11] Y. Shiraishi, H. Sakamoto, Y. Sugano, S. Ichikawa, T. Hirai, *ACS Nano* 7 (2014) 9287–9297.
- [12] D. Tsukamoto, A. Shiro, Y. Shiraisi, Y. Sugano, S. Ichikawa, S. Tanaka, T. Hirai, *ACS Catal.* 2 (2012) 599–603.
- [13] T. Gunji, G. Saravanan, T. Tanabe, T. Tsuda, M. Miyauchi, G. Kobayashi, H. Abe, F. Matsumoto, *Catal. Sci. Technol.* 4 (2014) 1436–1445.
- [14] T. Gunji, K. Sasaki, A.J. Jeevagan, T. Tanabe, S. Kaneko, F. Matsumoto, *ECS Trans.* 69 (39) (2015) 17–26.
- [15] T. Gunji, T. Tsuda, A.J. Jeevagan, M. Hashimoto, T. Tanabe, S. Kaneko, M. Miyauchi, G. Saravanan, H. Abe, F. Matsumoto, *Catal. Commun.* 56 (2014) 96–100.
- [16] T. Gunji, T. Tsuda, A.J. Jeevagan, M. Hashimoto, S. Kaneko, T. Tanabe, F. Matsumoto, *ECS Trans.* 61 (22) (2014) 55–59.
- [17] M. Hashimoto, T. Gunji, A.J. Jeevagan, T. Tanabe, T. Tsuda, S. Kaneko, M. Miyauchi, F. Matsumoto, *ECS Trans.* 61 (26) (2014) 17–22.
- [18] T. Gunji, A.J. Jeevagan, M. Hashimoto, T. Nozawa, T. Tanabe, S. Kaneko, M. Miyauchi, F. Matsumoto, *Appl. Catal. B* 181 (2016) 475–480.
- [19] E. Bae, N. Murakami, T. Ohno, *J. Mol. Catal. A: Chem.* 300 (2009) 72–79.
- [20] T. Ohno, K. Sarukawa, M. Matsumura, *New J. Chem.* 26 (2002) 11167–11170.
- [21] E. Bae, N. Murakami, M. Nakamura, T. Ohno, *Appl. Catal., A* 380 (2010) 45–54.
- [22] E. Bae, T. Ohno, *Appl. Catal. B* 91 (2009) 634–639.
- [23] Y. Matsumoto, M. Noguchi, T. Matsunaga, *J. Phys. Chem. B* 103 (1999) 7190–7194.
- [24] A. Fujishima, X. Zhang, D.A. Tryk, *Surf. Sci. Rep.* 63 (2008) 515–582.
- [25] H. Kominami, J. Kato, M. Kohno, Y. Kera, B. Ohtani, *Chem. Lett.* 12 (1996) 1051–1052.
- [26] T. Ohno, Y. Masaki, S. Hirayama, M. Matsumura, *J. Catal.* 204 (2001) 163–168.
- [27] B. Ohtani, Y. Azuma, D. Li, T. Ihara, R. Abe, *Trans. Mater. Res. Soc. Jpn.* 32 (2007) 401–404.
- [28] B. Ohtani, O.O. Prieto-Mahaney, D. Li, R. Abe, *J. Photochem. Photobiol. A: Chem.* 216 (2010) 179–182.
- [29] Y. Nosaka, M. Nishikawa, A.Y. Nosaka, *Molecules* 19 (2014) 18248–18267.
- [30] K. Nishijima, B. Ohtani, X. Yan, T. Kamai, T. Tsubota, N. Murakami, T. Ohno, *Chem. Phys.* 339 (2007) 64–72.
- [31] T. Gunji, G. Saravanan, T. Tanabe, T. Tsuda, M. Miyauchi, G. Kobayashi, H. Abe, F. Matsumoto, *Catal. Sci. Technol.* 4 (2014) 1436–1445.
- [32] A. Mattsson, L. Osterlund, *J. Phys. Chem. C* 114 (2010) 14121–14132.
- [33] M.W. Chase, *NIST-JANAF Thermochemical Tables, fourth Edition*, *J. Phys. Chem. Ref. Data, Monograph* 9, 1998.
- [34] B. Ohtani, Y. Nohara, R. Abe, *Electrochemistry* 76 (2008) 147–149.
- [35] C. Di Valentin, A. Selloni, *J. Phys. Chem. Lett.* 97 (2006) 166803.
- [36] Y. Kakuma, A.Y. Nosaka, Y. Nosaka, *Phys. Chem. Phys.* 17 (2015) 18691–18697.



Evaluation of Key Factors for Preparing High Brightness Surfaces of Aluminum Films Electrodeposited from AlCl_3 -1-Ethyl-3-Methylimidazolium Chloride-Organic Additive Baths



Kazuma Uehara^a, Keitaro Yamazaki^a, Takao Gunji^a, Shingo Kaneko^b, Toyokazu Tanabe^a, Takeo Ohsaka^b, Futoshi Matsumoto^{a,*}

^a Department of Material and Life Chemistry, Kanagawa University, 3-27-1 Rokkakubashi, Kanagawa-ku, Yokohama, Kanagawa 221-8686, Japan

^b Research Institute for Engineering, Kanagawa University, 3-27-1 Rokkakubashi, Kanagawa-ku, Yokohama-shi, Kanagawa 221-8686, Japan

ARTICLE INFO

Article history:

Received 18 June 2016

Received in revised form 2 August 2016

Accepted 24 August 2016

Available online 31 August 2016

Keywords:

Electrodeposition

Ionic Liquid

Aluminum

Additive

4-Pyridinecarboxylic Acid Hydrazide

ABSTRACT

The effects of additives, such as 4-pyridinecarboxylic acid hydrazide (4-PCAH) and its analogs, and organic solvents, such as toluene, benzene and xylene, on the brightness of aluminum (Al) prepared using constant-current deposition from an ionic liquid of ethyl-3-methylimidazolium chloride (EMIC)-aluminum chloride (AlCl_3) were investigated by light spectroscopy, scanning electron microscopy (SEM), reflectivity tests, X-ray diffraction (XRD), X-ray photoelectron spectroscopy (XPS) and electrochemical impedance spectroscopy. In order for the deposited Al films to exhibit high brightness, a combined use of 4-PCAH and toluene is effective. Moreover, the relationship between the brightness (*i.e.*, reflectance) of the prepared Al films and the molecular structure of a variety of additives was clarified. Both a pyridine ring and an acetyl hydrazine group are necessary for constituting an effective additive. The structural isomers of a given additive bring about different surface brightness, *e.g.*, for PCAHs the reflectance at 450 nm is in the order of *para*-isomer > *meta*-isomer > *ortho*-isomer. It was considered that in 4-PCAH electron-withdrawing acetyl hydrazine group is bounded to the pyridine ring, and consequently the electron density around the nitrogen atom in the pyridine ring is decreased, which is conducive to the adsorption of 4-PCAH on the cathode of deposited Al films. In addition, the reflectance was found to increase with decreasing the crystalline domain size of Al deposits and with increasing the reaction resistance for Al electrodeposition. The reaction mechanism of Al electrodeposition from the present ionic liquid media containing various additives is also discussed briefly.

© 2016 Elsevier Ltd. All rights reserved.

1. Introduction

Aluminum (Al) is the second most abundant metallic element in the Earth's crust. Al has been widely used as a coating material because Al has the ability to resist corrosion due to passivation and a high visible light reflectivity. Thin layers of Al are typically deposited onto a flat surface using physical vapor deposition [1], chemical vapor deposition [2] or hot-dip coating processes [3]. The electrochemical deposition of Al at ambient temperature in coating processes has been extensively investigated for many years, because this deposition process does not require expensive equipment and the size of the Al film deposited with a uniform thickness can be easily scaled-up or scaled-down and can be

prepared on surfaces with various shapes. Much attention has been devoted to the electrochemical deposition of Al using organic solvents [4–8] and ionic liquids [4,9–11] containing Al(III) ions to prevent a preferential hydrogen evolution in aqueous solutions. However, even in organic solvents and ionic liquids, the deposition of Al occurs with a low efficiency and the uniformness of the Al film deposited is still inadequate with poor smoothness and brightness [12]. Recently, the electrochemical deposition of smoother Al films composed of nanocrystalline deposits has been reported with several organic solvents [8] and ionic liquids [13,14], *i.e.*, they possess high reflectance values ranging from 70 to 80% in the visible light region [15–19]. If a high deposition efficiency and a smooth Al film formation can be achieved using electrochemical deposition, Al films would be applicable to a wide range of decorative coatings and optoelectronic materials. To form smooth surface with a high deposition efficiency, in many researches [16–25], additives such as organic and inorganic molecules have

* Corresponding author. Fax: +81 45 4139770.

E-mail address: fmatsumoto@kanagawa-u.ac.jp (F. Matsumoto).

been added to the electrodeposition bath, typically polyethylene amines [16] and dimethylammonium chloride [17] in dimethylsulfone- AlCl_3 baths, 1,10-phenanthroline and nicotinic acid in ionic liquids as well as mixtures of ionic liquids and organic solvents [20–22] and also organic solvents such as toluene are added to the baths [23]. In addition, more recently, systematic studies on the additives, which are selected in the viewpoint of electron-donating or –withdrawing properties in their molecules [24] and which are alkali metal chlorides, rare earth chlorides, small organic molecules, and surfactants [25] to clarify the key factors for fabricating Al films with bright surfaces, have been carried out.

In our recent studies, we have demonstrated that the addition of 4-pyridinecarboxylic acid hydrazide (4-PCAH) to an EMIC/ AlCl_3 /toluene mixture improves the brightness of the deposited Al film [26,27]. The prepared Al films possess surface characteristics of the degree that the characters reflected on the surfaces are readable. The reflectivity of the Al film prepared in EMIC/ AlCl_3 /toluene/4-PCAH was 84% at 450 nm. To the best of our knowledge, this reflectivity is the highest reported value. In the present study, to clarify how the addition of 4-PCAH to the EMIC/ AlCl_3 /toluene bath effectively improves the brightness of electrodeposited Al films, a systematic series of organic molecules were studied as molecular additives, and based on the SEM image, reflectance, XRD profile and reaction resistance data of the films obtained by adding the individual additives, the relationship between the brightness of the prepared Al films and the molecular structure of the additives was examined and based on the results obtained, the reaction mechanism of Al electrodeposition was discussed. In this paper, the additive is defined as the organic molecules added to the EMIC/ AlCl_3 ionic liquid, although, generally, the additive is defined as the molecules that are added to the solutions by small amount. The small molecules such as 4-PCAH and its analogues and solvents such as toluene and xylene are classified in the category of additives in this study. Generally ionic liquids are known as so-called green solvents and the EMIC/ AlCl_3 ionic liquid is also considered to be environmentally benign. The addition of organic solvent to the ionic liquids produces a negative effect in the viewpoint of environment. However, as mentioned below, the addition of organic solvent is required to achieve high brightness of electrodeposited aluminum surface.

2. Experimental

The electrolytic baths were prepared by the stepwise addition of anhydrous AlCl_3 grains (0.19 mol, Fluka, crystallized, 99%; used as received) into EMIC (9.5×10^{-2} mol, Wako Pure Chemicals Co. Ltd. (Wako), 99%; used as received) at 25 °C in an argon-filled glove box (MDB-1KXV, Miwa, Japan). After mixing AlCl_3 and EMIC (molar ratio EMIC: AlCl_3 = 1: 2) for 6 h at room temperature, toluene (0.87 mol, 99.0+%, Wako) was added to the pretreated EMIC/ AlCl_3 electrolyte bath prior to the final addition of each additive (1.8 mM) at 25 °C. The detailed procedure for preparation of the bath solutions for the Al electrodeposition is described in the Electronic Supplementary Information (ESI). The following organic molecules were used as additives without further purification: 4-pyridinecarboxylic acid hydrazide (4-PCAH, 98%), 3-pyridinecarboxylic acid hydrazide (3-PCAH) and 2-pyridinecarboxylic acid hydrazide (2-PCAH) (98%, Tokyo Chemical Industry (TCI)), 4-pyridinecarboxaldehyde (4-PCA, 98%, Alfa Aesar), 3-pyridinecarboxaldehyde (3-PCA) and 2-pyridinecarboxaldehyde (2-PCA) (98%, TCI), 4-methoxypyridine (4-MP), 3-methoxypyridine (3-MP) and 2-methoxypyridine (2-MP) (97%, Wako), 4-aminopyridine (4-AP, 98%, Kanto Chemicals Co. Ltd. (Kanto)), 3-aminopyridine (3-AP) and 2-aminopyridine (2-AP) (99%, Wako), benzoyl hydrazine (BH, 98%, TCI), pyridine-4-carboxamide (P-4-CA, 99%, Junsei Chemicals Co. Ltd.), pyridine-3-carboxamide (P-3-CA, 98%, Wako), pyridine-2-

carboxamide (P-2-CA, 95%, TCI), acetyl hydrazide (AH, 98%, Kanto), acetamide (AA) and 4-pyridyl hydrazide (4-PH) (98%, TCI), 4-(aminomethyl)pyridine (4-AP) and pyridine (PY) (99.5%, TCI).

The pretreated Cu plates were served as the working electrodes. Aluminum (99.999%, $5 \times 5 \text{ cm}^2$) sheets and Al wire (99.999%, 3 cm in length, 1 mm in diameter) were used as the counter and reference electrodes, respectively. The electrochemical deposition of Al was carried out with a constant-current mode of 8.0 mA cm^{-2} using an electrochemical analyzer (Hokuto Denko, HZ-5000). The method for pretreatment of Cu plates and the procedure for the electrochemical deposition of Al are explained in the ESI.

Field emission scanning electron microscopy (FE-SEM), X-ray diffraction (XRD), X-ray photoelectron spectroscopy (XPS) and electrochemical impedance spectroscopy (EIS) were used to characterize the prepared Al films (see the ESI for the FE-SEM, XRD, XPS and EIS procedures).

3. Results and discussion

3.1. Optimization of the bath composition

Fig. 1(A–F) show the micrographs of the Al film surfaces obtained by the electrodeposition of Al in the EMIC/ AlCl_3 /toluene bath containing different concentrations (0.45–3.6 mM) of the 4-PCAH additive. The EMIC/ AlCl_3 /toluene composition was fixed as mentioned in the Experimental section. A constant current density of 8.0 mA cm^{-2} and a deposition time of 2 h were used for all of the Al electrodeposition. To determine the brightness differences between the Al films, pictures were taken of the Al films on which the characters “KUKU UNIV” were reflected (upper part: Al film, lower part: printed-out characters). The visibility of the characters reflected on the Al films was considered as a measure indicating the surface brightness. As the concentration of 4-PCAH was increased, the “KUKU UNIV” characters became clearer (A–C), indicating an improvement in the surface brightness. At the concentration of 1.8 mM, the highest reflectance was observed (D). Then, the visibility decreased gradually due to the formation of yellow deposit. As can be readily seen from Fig. 1(G), the reflectance of visible light (450 nm) of the Al films indicates the similar 4-PCAH concentration dependence to that of the visibility, i.e., the reflectance increases from 69 to 78% with increasing the 4-PCAH concentration from 0.45 to 1.35 mM, and it attains its maximum (84%) at 1.8 mM and further increasing the concentration leads to a gradual decrease in the reflectance.

In Fig. 2, is shown the dependence of the reflectance of the Al films electrodeposited from EMIC/ AlCl_3 /4-PCAH bath upon the concentration of organic solvents added (i.e., toluene, benzene and xylene) in the concentration range of 4.96 to 10.79 M, in which the bath solutions containing benzene (or xylene) of 10.41 and 10.79 M could not be used as a uniform solution. Interestingly, we can see from Fig. 2 that the visibility of the characters reflected on the Al films largely depends on the organic solvent added, that is, among the solvents examined the addition of toluene brings about the significant improvement in the surface brightness and in addition, the visibility largely depends on the concentration of toluene and the highest visibility was obtained at 9.25 M. Fig. 2(E) demonstrates the dependence of the reflectance of visible light (450 nm) upon the toluene concentration. The maximum reflectance was obtained at 9.25 M. The reflectance maximum observed is considered to result from the dependence of the solution viscosity (η) and the concentration ($C(\text{Al}^{3+})$) of electroactive Al^{3+} species (Al_2Cl_7^- , mentioned below) in the bath solution on the amount of toluene added. The η and $C(\text{Al}^{3+})$ increases and decreases, respectively, with increasing the added amount of toluene. The low ion-conductivity due to the low viscosity of the bath solution induces the deposits of the Al films at high overpotential, leading to low

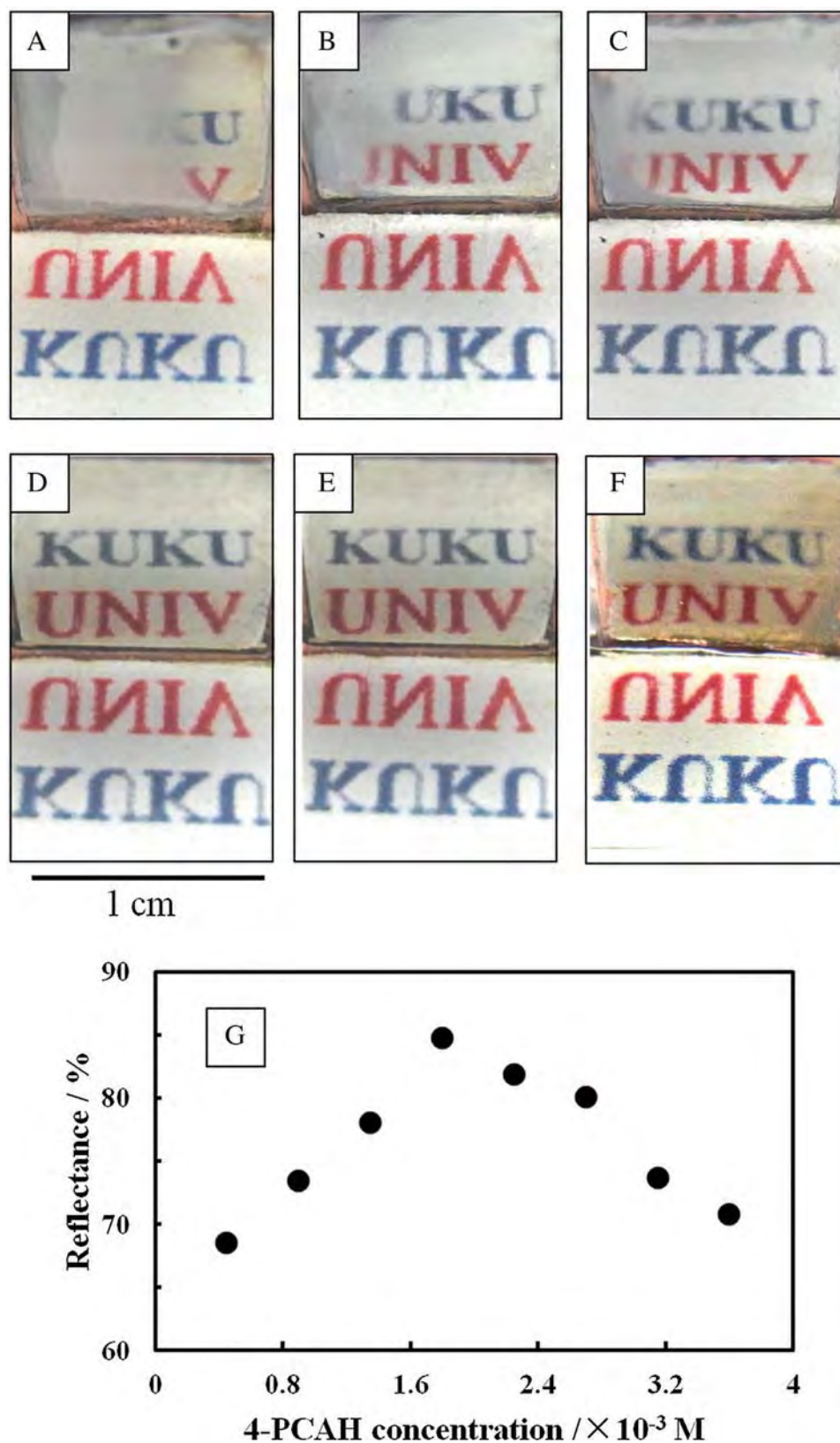
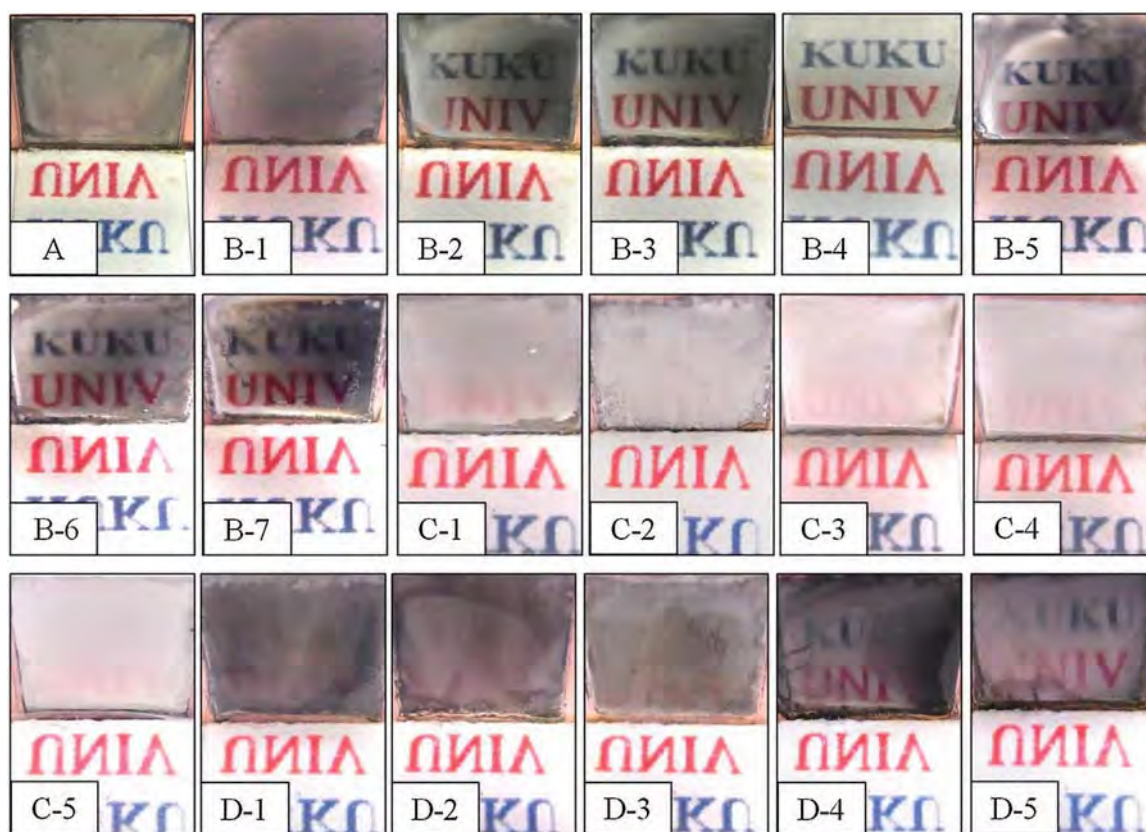


Fig. 1. Micrographs (A–F) of the Al film surfaces obtained by electrodeposition and dependence (G) of the reflectance of visible light (wavelength: 450 nm) on the 4-PCA concentration. The EMIC/ AlCl_3 /toluene composition was fixed at an EMIC- AlCl_3 molar ratio of 1:2 and 9.25 M toluene. The concentrations of 4-PCA were as follows: (A) 0.45, (B) 0.9, (C) 1.35, (D) 1.8, (E) 2.7 and (F) 3.6 mM. Deposition time: 2 h; constant current density: 8.0 mAcm^{-2} . The characters “KUKU UNIV” were reflected on the deposited Al (upper part: Al film, lower part: printed-out characters).



1 cm

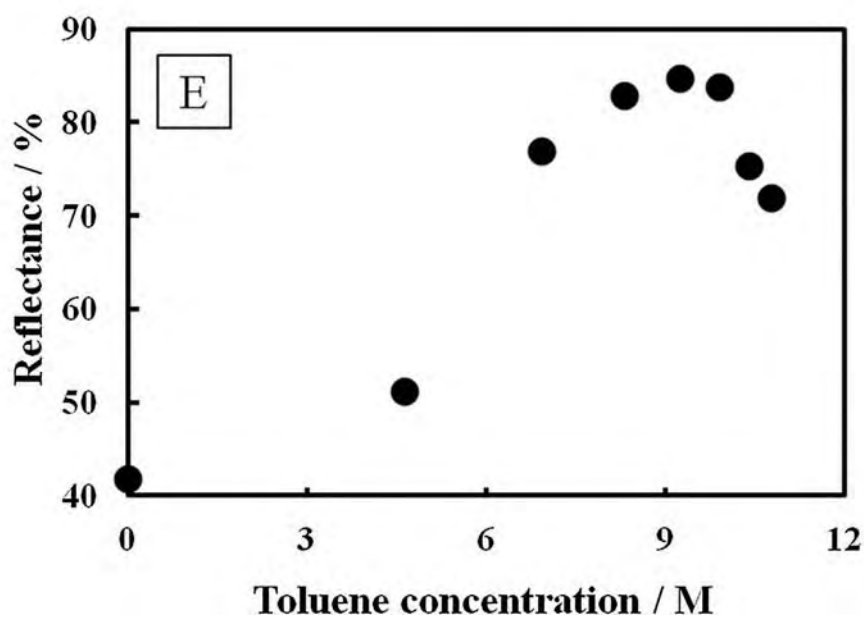


Fig. 2. Micrographs of the Al film surfaces obtained on Cu substrates by coulometric electrodeposition from (A) AlCl_3 -EMIC-4-PCAH, (B) AlCl_3 -EMIC-toluene-4-PCAH, (C) AlCl_3 -EMIC-benzen-4-PCAH and (D) AlCl_3 -EMIC-xylene-4-PCAH baths. Toluene, benzene and xylene concentrations in the individual baths: (1) 4.96, (2) 6.94, (3) 8.33, (4) 9.25, (5) 9.91, (6) 10.41 and (7) 10.79 M; deposition time: 2 h; and constant current: 8.0 mA cm^{-2} . The characters "KUKU UNIV" were reflected on the deposited Al (upper part: Al film, lower part: printed-out characters). (E): The plot of the reflectance of visible light (wavelength: 450 nm) against the concentration of toluene in the bath. The EMIC- AlCl_3 molar ratio (1:2) and the concentration of 4-PCAH (1.8 mM) were fixed for (A)-(E).

electro-efficiency due to undesirable electrochemical reactions and/or locally inhomogeneous deposition. The low concentration of electroactive Al_2Cl_7^- species in the bath also causes an inhomogeneous deposition of Al metal on local areas, resulting in non-uniform deposition of Al and then poor surface brightness. The appearance of the reflectance maximum is not surprising, but it should be noted that a proper quantity of toluene in the EMIC/ AlCl_3 /toluene/4-PCAH bath improves the surface brightness. In other words, toluene and other organic solvents should be recognized as effective additives to improve the surface brightness of the deposited Al and not as additives to decrease the viscosity of the bath solution, as reported previously [9,23,25].

Fig. 3 shows the surface SEM images of the Al films used in Fig. 2(A–D). The kind and concentration of organic solvents added to the bath solution are found to significantly influence the surface morphology of the Al films. It can be seen from the comparison of Figs. 2 and 3 that there is a strong relationship between the surface roughness and brightness of the deposited Al films. Therefore, obtaining a low surface roughness leads to a high brightness on the deposited Al surface. When the toluene concentration was 9.25 M,

the lowest surface roughness could be observed with the highest surface brightness. Thus, toluene is an effective additive for obtaining the electrodeposited Al film with a high surface brightness from the EMIC/ AlCl_3 /4-PCAH bath solution. In addition, the reflectance of the Al films as a function of the mol % of AlCl_3 to EMIC at the constant concentrations of toluene (9.25 M) and 4-PCAH (1.8 mM) was examined. The maximum reflectance was obtained at the EMIC: AlCl_3 molar ratio of 1:2 (see the ESI for the data (S1) and the discussion). Degradation of the EMIC/ AlCl_3 /toluene/4-PCAH bath solution with the number of usage for the electrodeposition of Al could not be seen (see the ESI for the data (S2)).

3.2. Characterization of Al films prepared with various additives

To elucidate the relationship between the molecular structures of additives and the surface brightness of the Al films prepared in their presence, the Al films were electrochemically deposited on a Cu electrode from AlCl_3 -EMIC (EMIC: AlCl_3 molar ratio = 1:2)-toluene (9.25 M) baths containing various additives (1.8 mM). Fig. 4

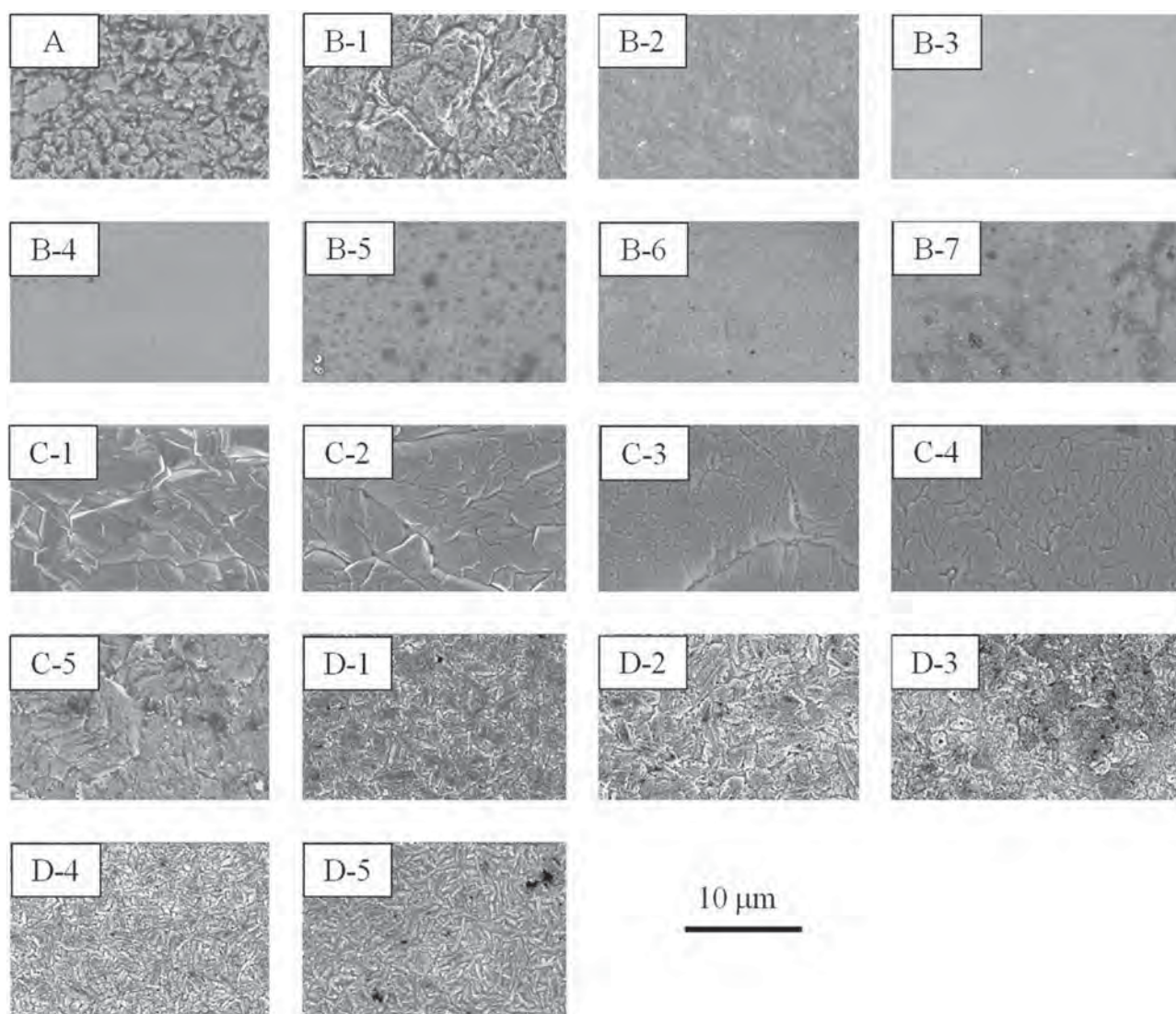


Fig. 3. Surface SEM images of the Al film surfaces obtained on Cu substrates by coulometric electrodeposition from (A) AlCl_3 -EMIC-4-PCAH, (B) AlCl_3 -EMIC-toluene-4-PCAH, (C) AlCl_3 -EMIC-benzen-4-PCAH and (D) AlCl_3 -EMIC-xylene-4-PCAH baths. Toluene, benzene and xylene concentrations in the individual baths: (1) 4.96, (2) 6.94, (3) 8.33, (4) 9.25, (5) 9.91 and (6) 10.41 M; deposition time: 2 h; constant current: 8.0 mA cm^{-2} ; and 4-PCAH additive concentration: 1.8 mM.



Fig. 4. Micrographs of the Al films obtained by the electrodeposition of Al from the EMIC/ AlCl_3 (EMIC: AlCl_3 = 1:2 (molar ratio))/toluene (9.25 M) baths containing (1) non-additive, (2) 4-PCAH, (3) 3-PCAH, (4) 2-PCAH, (5) 4-PCA, (6) 3-PCA, (7) 2-PCA, (8) 4-MP, (9) 3-MP, (10) 2-MP, (11) 4-AP, (12) 3-AP, (13) 2-AP, (14) BH, (15) P-4-CA, (16) P-3-CA, (17) P-2-CA, (18) AH, (19) AA, (20) 4-PH, (21) 4-AP and (22) PY. Deposition time: 2 h; constant current density: 8.0 mAcm^{-2} ; and additive concentration: 1.8 mM. The characters “KUKU UNIV” were reflected on the deposited Al films (upper part: Al film, lower part: printed-out characters).

shows the surface images of the Al films obtained from the EMIC/ AlCl_3 /toluene baths in the absence (1) and the presence of (2) 4-PCAH, (3) 3-PCAH, (4) 2-PCAH, (5) 4-PCA, (6) 3-PCA, (7) 2-PCA, (8) 4-MP, (9) 3-MP, (10) 2-MP, (11) 4-AP, (12) 3-AP, (13) 2-AP, (14) BH, (15) P-4-CA, (16) P-3-CA, (17) P-2-CA, (18) AH, (19) AA, (20) 4-PH, (21) 4-AP and (22) PY. A constant current of 8.0 mAcm^{-2} was used for all of the Al electrodeposition. In addition, to determine the differences in brightness of the Al films, as performed in Figs. 1 and 2, pictures of the Al films on which the characters “KUKU UNIV” were reflected (upper part: Al film, lower part: printed-out characters) were taken. The picture (1) was taken with the Al film prepared in the EMIC/ AlCl_3 bath (EMIC: AlCl_3 = 1: 2 (molar ratio))/toluene (9.25 M) without additives. The Al film obtained from the EMIC/ AlCl_3 /toluene/4-PCAH bath exhibited the highest brightness among all of the examined additives. As we reported previously [26], to the best of our knowledge, the Al film obtained in the presence of 4-PCAH (2) possessed the highest surface brightness among the Al films ever reported. Although the Al films obtained from the EMIC/ AlCl_3 /toluene/P-4-CA (15) and 4-AP (11) baths reflect the characters on their surfaces, these Al films have a

dull appearance. The films prepared from EMIC/ AlCl_3 /toluene/4-MP (8) and EMIC/ AlCl_3 /toluene/AH (18) barely reflect the characters, and only dull characters were observed in some areas. Depending on the molecular structure of the additives, the reflectance of the deposited Al films was dramatically changed. Additionally, from the surface SEM images of the deposited Al shown in Figs. 3 and 5 as well as the reflectance data shown in Fig. 4, it is obvious that the surface roughness is entirely related to the surface brightness. Clearly, minimizing the grain and/or crystalline sizes of the Al deposit leads to improvement in the surface brightness. The atomic force microscopy (AFM) images of the Al film prepared with 4-PCAH and its surface roughness analysis have been reported in our previous paper [26], in which the effect of 4-PCAH and 1,10-phenanthroline (PH) as an additive was compared from the viewpoints of the surface reflectance and the surface average roughness (R_a) evaluated with AFM for the surface area of $100 \mu\text{m} \times 100 \mu\text{m}$. The values of R_a of the Al films prepared with 4-PCAH and PH were 50 and 160 nm, respectively. In addition, the reflectivity of the Al film prepared with PH was 79% at 450 nm. As previously confirmed [26], the uniformity of the

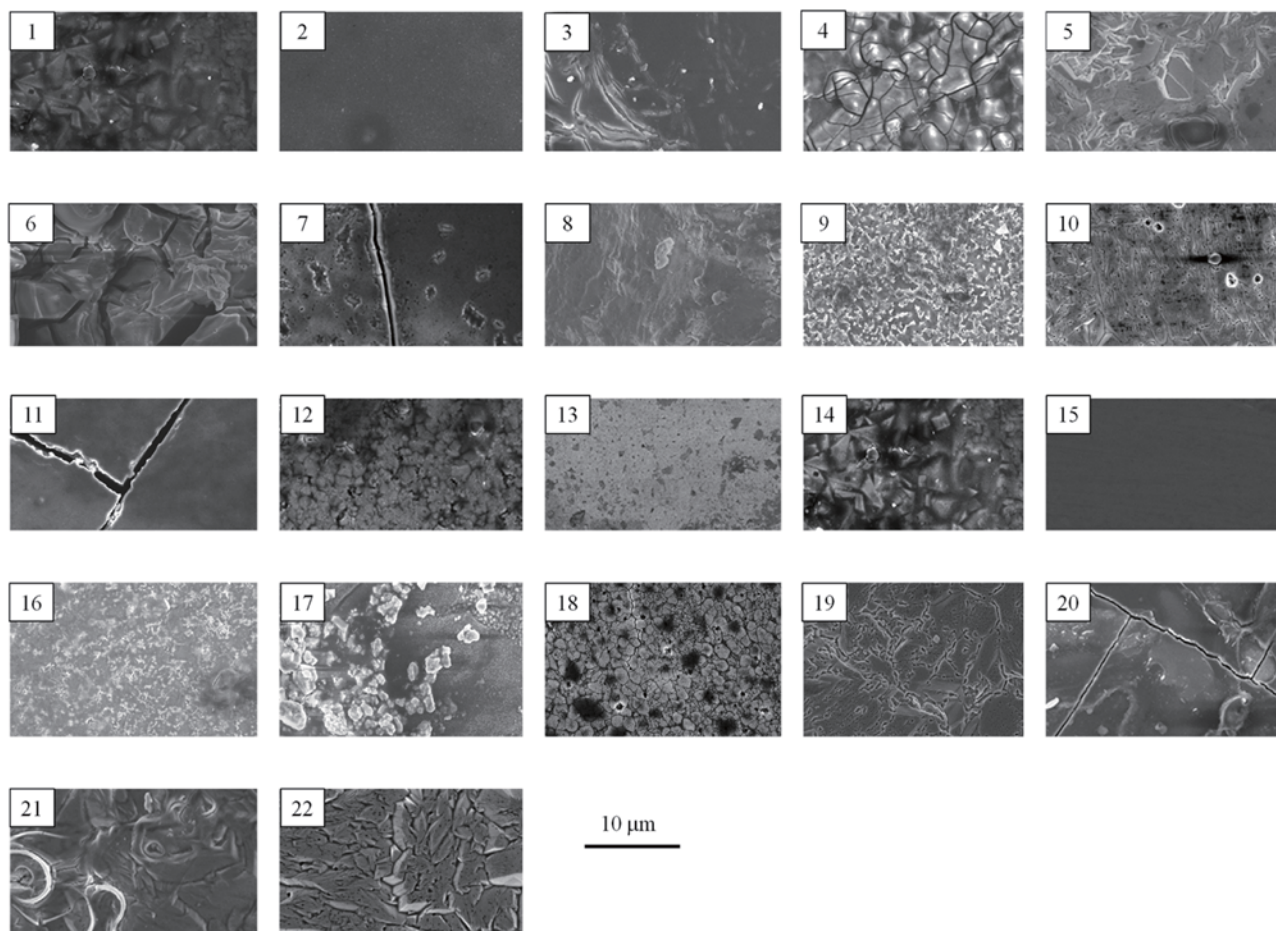


Fig. 5. SEM images of the surfaces of the Al films obtained by the electrodeposition of Al from the EMIC/ AlCl_3 (EMIC: $\text{AlCl}_3 = 1:2$ (molar ratio))/toluene (9.25 M) baths containing (1) non-additive, (2) 4-PCAH, (3) 3-PCAH, (4) 2-PCAH, (5) 4-PCA, (6) 3-PCA, (7) 2-PCA, (8) 4-MP, (9) 3-MP, (10) 2-MP, (11) 4-AP, (12) 3-AP, (13) 2-AP, (14) BH, (15) P-4-CA, (16) P-3-CA, (17) P-2-CA, (18) AH, (19) AA, (20) 4-PH, (21) 4-AP and (22) PY. Deposition time: 2 h; constant current density: 8.0 mAcm^{-2} ; and additive concentration: 1.8 mM.

deposited Al films in submicro-scale as well as micro-scale is required for a high surface brightness.

The Al films obtained using 4-PCAH (2) and P-4-CA (15) additives are smooth and composed of grains less than one micrometer in size. This grain size is significantly smaller than those of the Al films prepared using 4-MP (8) and AH (18). Although the Al film prepared with 4-AP (11) is characterized by a small grain size, as shown in its image, large and deep cracks are formed and spread throughout the deposited film. All of the Al films obtained in this study consisted of dense Al layers (see Ref. [26]). For all of the additives studied, the electro-efficiencies were close to 90–100% even for 12 h of electrodeposition (see the ESI for the data (S3)).

The XRD profiles of the Al films prepared from EMIC/ AlCl_3 /toluene bath in the absence and the presence of additives were measured. The crystalline domain sizes of the Al deposits on the Cu plate, which were calculated from the full width at half-maximum of the (200) peak in the XRD profiles using the Sherrer equation [28], was evaluated. The crystalline domain sizes of the Al deposits are strongly related to the surface brightness of the deposited Al films (Fig. 6), that is, as the crystalline domain size decreases, the surface brightness of the deposited film is improved. This result supports the relationship between the surface roughness presumed from the surface SEM images (Figs. 3 and 5) and the surface brightness (Figs. 2 and 4). Additionally, to further investigate the differences in the surface brightness of the Al films obtained using different additives, XPS measurements were carried out for several

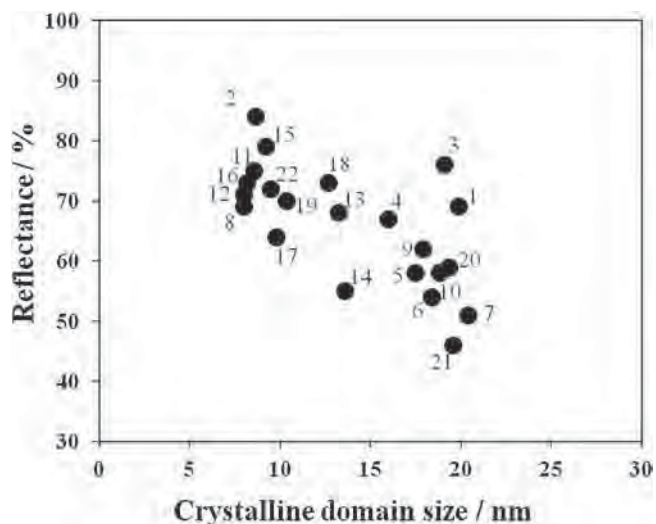


Fig. 6. Plot of the crystalline domain size vs. the reflectance of the Al films deposited from AlCl_3 -EMIC (EMIC: $\text{AlCl}_3 = 1:2$ (molar ratio))-toluene (9.25 M) baths containing (1) non-additive, (2) 4-PCAH, (3) 3-PCAH, (4) 2-PCAH, (5) 4-PCA, (6) 3-PCA, (7) 2-PCA, (8) 4-MP, (9) 3-MP, (10) 2-MP, (11) 4-AP, (12) 3-AP, (13) 2-AP, (14) BH, (15) P-4-CA, (16) P-3-CA, (17) P-2-CA, (18) AH, (19) AA, (20) 4-PH, (21) 4-AP and (22) PY. Deposition time: 2 h; constant current density: 8.0 mAcm^{-2} ; additive concentration: 1.8 mM.

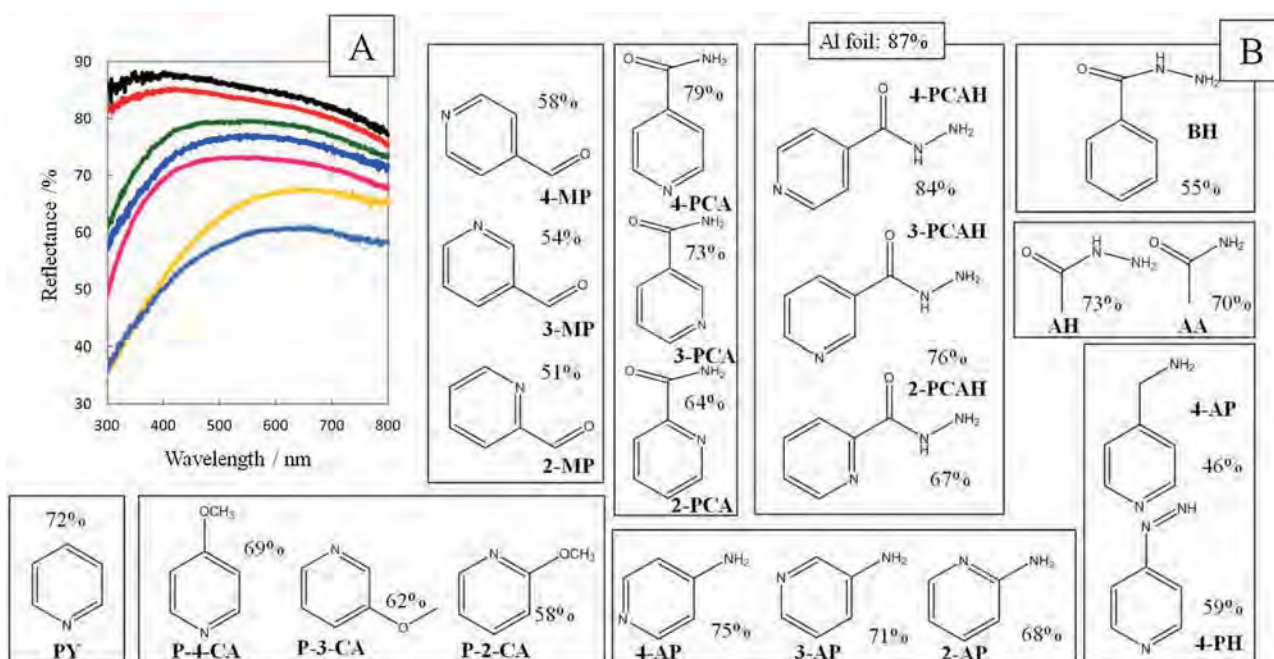


Fig. 7. (A) Reflectance spectra of Al films deposited from AlCl_3 -EMIC-toluene-additive. Additives: 4-PCAH (red line), 4-PCA (green line), 4-AP (blue line), P-4-CA (yellow line), BH (light blue line) and PY (pink line). The black line was obtained for a commercial Al foil. (B) Summary of the relationship between the reflectance of the prepared Al films at 450 nm and the molecular structure of the additives. Preparation conditions of the Al films: deposition time 2 h; constant current density 8.0 mAcm^{-2} ; bath composition: EMIC: $\text{AlCl}_3 = 1: 2$ (molar ratio); toluene concentration: 9.25 M; and additive concentration: 1.8 mM. (For interpretation of the references to colour in this figure legend, the reader is referred to the web version of this article.)

samples of the deposited Al films. The Al films with high brightness, prepared using (a) 4-PCAH and (b) P-4-CA, also show relatively high levels of Cl, N and C contamination. Therefore, the surface brightness of the Al film is not associated with the degree of its contamination (see the ESI for the data (S5)).

3.3. Relationship between the brightness of Al films and the molecular structure of additives

Fig. 7-(A) shows the reflectance spectra of Al films deposited from AlCl_3 -EMIC-toluene-additive baths in the wavelength range of 300 to 800 nm. The spectrum indicated in a black color was obtained with a commercial Al foil (A1N80H-H18, Mitsubishi Aluminum, Japan). The Al films were prepared using a deposition time of 2 h and a constant current density of 8.0 mAcm^{-2} . The reflectance spectrum observed for the Al film prepared with 4-PCAH is similar to that of the Al foil. The reflectance value measured for the Al films prepared with various additives is strongly dependent on the molecular structure of the additives.

As shown in Fig. 7-(B), the brightness (*i.e.*, the surface smoothness or grain size) of the Al films prepared in this study significantly differs depending on the structural isomers of the additives (*e.g.*, PCAH series: 4-PCAH, 3-PCAH and 2-PCAH or PCA series: 4-PCA, 3-PCA and 2-PCA). 4-PCAH, which has an N atom in the aromatic ring and an acetyl hydrazine group in the *para* position, produced the Al film with the highest reflectance among the isomers of PCAH. Similarly, the Al film prepared with 4-PCA had the highest reflectance among the films prepared with the individual PCA isomers. Additionally, for the structural isomer series examined in this study, *i.e.*, MPs, APs, PCAs, PCAHs and P-CAs, the reflectance is in the order of *para*-isomer > *meta*-isomer > *ortho*-isomer. The reflectance decreases in the order of 4-PCAH > 4-PCA > P-4-CA. As seen from the comparison of BH and PCAHs, a pyridine ring leads to a higher reflectance than a benzene ring. From the results obtained, it should be noted that pyridine compounds with acetyl hydrazine group are effective additives for

producing the Al films with a high surface brightness and in addition, the position of acetyl hydrazine group with respect to N atom in the pyridine ring significantly affects the surface roughness.

3.4. Relationship between the reaction resistance and the surface brightness of Al films

The reaction impedance for Al electrodeposition from the baths containing various types of additives and the solution resistance of the baths were measured with an electrochemical impedance spectroscopy (EIS). Although a constant current density of 8.0 mAcm^{-2} was used in the preparation of the Al films, in the EIS measurements, 1.0 mAcm^{-2} was used because the reproducible data could not be obtained with 8.0 mAcm^{-2} , probably due to the fact that the steady-state situation could not be reached actually at 8 mAcm^{-2} . The complex-plane impedance plots obtained during the Al deposition from the baths containing three typical additives and the non-additive bath are shown typically in Fig. S6.

From the diameters of the second circles (at lower frequencies) and the X-axis intercepts (at high frequencies) in Fig. S6, the reaction resistance at the working electrode ($R_{ct,w}$) and the solution resistance (R_u) were evaluated. In Fig. 8, the plots of the reaction resistance (A) or solution resistance (B) vs. the surface reflectance of the Al films are shown. There seems a linear relationship between the reaction resistance and the reflectance, indicating that the reaction resistance of the electroreduction of Al depends on the kind of additives and the electroreduction of Al with higher reaction resistance results in the Al film with higher brightness and reflectance. The reflectance seems not to be associated with the solution resistance (B).

3.5. Effects of toluene and other additives on the surface brightness

From the above-mentioned results, it is obvious that a decrease in the surface roughness and grain and/or crystalline size of the Al

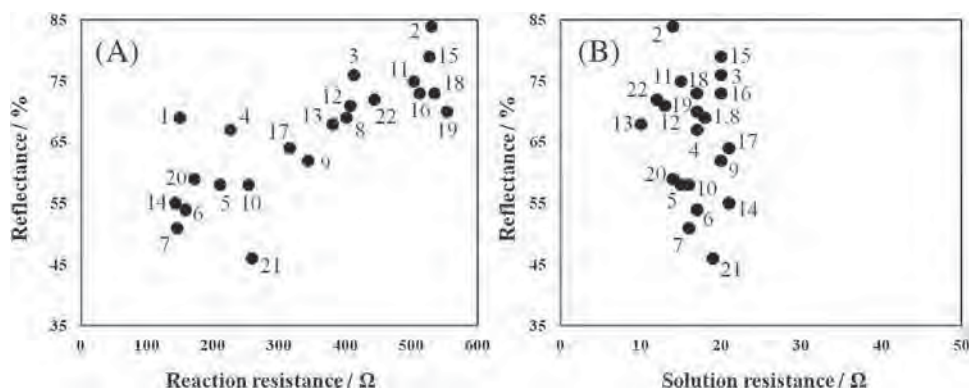


Fig. 8. Plots of (A) reaction resistance vs. reflectance and (B) solution resistance vs. reflectance of the deposited Al films. The Al films were prepared from the AlCl_3 -EMIC (EMIC: $\text{AlCl}_3 = 1:2$ (molar ratio))-toluene (9.25 M) baths containing additives: (1) non-additive, (2) 4-PCAH, (3) 3-PCAH, (4) 2-PCAH, (5) 4-PCA, (6) 3-PCA, (7) 2-PCA, (8) 4-MP, (9) 3-MP, (10) 2-MP, (11) 4-AP, (12) 3-AP, (13) 2-AP, (14) BH, (15) P-4-CA, (16) P-3-CA, (17) P-2-CA, (18) AH, (19) AA, (20) 4-PH, (21) 4-AP and (22) PY. Additive concentration: 1.8 mM.

films results in a high surface brightness. Among the organic solvents added to the bath, toluene is an effective additive that brings about a remarkable improvement in the surface smoothness. Liao et al. reported that the quality of the Al electrodeposit is greatly enhanced by the addition of benzene to EMIC- AlCl_3 baths and proposed the effect of a “cosolvent” on the grain size, lattice parameters and preferred crystallographic orientation of Al electrodeposits [29]. Koura et al. also reported that the addition of organic solvents such as toluene [9] and xylene [30] modifies the preferred crystallographic orientation of deposited Al films from EMIC- AlCl_3 baths. These results allow us to speculate the participation of cosolvents in the Al deposition reaction. Recently, Abbott et al. have suggested that charge transfer complexes are also formed between an Al containing species and the aromatic ring of toluene [8]. We also think that toluene and other additives have some interactions with the electroactive species of Al^{3+} (Al_2Cl_7^-) at the interface of the electrode/bath to improve the surface smoothness because the coexistence of toluene and other additives in the bath is essential for preparing Al films with high brightness, and, as mentioned below, the additive molecules that possess a high function as brighteners strongly adsorb on the surface of deposited Al films.

The EIS results indicate that the addition of additive showing higher reaction resistance to the bath causes higher brightness of the prepared Al film. From the viewpoint of high resistance, strong adsorption of additive molecule on the Al surface and uniform Al deposition (in other words, inhibition of local deposition inducing crystal growth) are considered to generate a smooth Al film surface, and actually a high brightness could be achieved with the EMIC/ AlCl_3 /toluene/4-PCAH bath. Further study on the interactions among (electroactive and electroinactive) Al^{3+} ion species, toluene and other additives on the deposited Al surface is under way to clarify why Al films with high surface brightness can be obtained by the electrodeposition of Al in non-aqueous solutions. Here, the reason why 4-PCAH as an additive in the EMIC- AlCl_3 -toluene bath could induce the highest brightness will be discussed briefly. As pointed out in many papers, pyridine derivatives have excellent effects as additives due to their stronger polarization ability and leveling action in both aqueous and ionic liquid baths [22,31,32]. Zhang et al. have examined the electrochemical deposition of Al from 1-butyl-3-methylimidazolium- AlCl_3 baths in the presence of three pyridine derivatives as additives; nicotinic acid, methyl nicotinate and 3-methylpyridine and have discussed the relationship between the negativity of the N atom in the pyridine ring of pyridine derivatives and the surface brightness of the Al films [24]. Nicotinic acid and methyl nicotinate, which have electron-withdrawing substituent groups on the pyridine ring,

strongly adsorb on the Al film surface compared with 3-methylpyridine, which has an electron-donating substituent group, because the adsorption of 3-methylpyridine is weakened due to the increase in the negativity of the active center (N atom in the pyridine ring). On the other hand, electron-withdrawing groups in nicotinic acid and methyl nicotinate are bonded to the pyridine ring and consequently the electron density around the nitrogen atoms is decreased, which is conducive to the adsorption of the additives onto the cathode.

Although the adsorption of organic molecules on metal surfaces occurs via not only an electrostatic interaction but also dipolar and hydrophobic interactions, the inductive and resonance effects of the N atom in the pyridine ring of pyridine derivatives as additive molecules upon the electron density and the degree of adsorption on the metal surfaces are also considered in comparing the electron density around the N atom in the pyridine ring among the additives. The following can be noted as the remarkable points compared to the results by Zhang et al. [24]. (1) Although the AP additives have a highly electron-donating amino group and the electron density around the N atom in the pyridine ring is very high, they exhibit relatively high brightness and reflectance values (for 4-AP, 75% at the wavelength of 450 nm). (2) The increase and decrease of the electron density by the inductive and resonance effects efficiently appears when substituents are at the *ortho* and *para* positions with respect to the N atom in the pyridine ring, for example, in the case of AP additives having an electron-donating amino group. According to the idea by Zhang et al. the degree of adsorption on the Al films should be 4-AP, 2-AP < 3-AP. However, the electrochemical impedance results indicate that 4-AP most strongly adsorbs on the Al surface, 3-AP is somewhat less active for adsorption, and 2-AP most weakly adsorbs. Such a difference between the results in this study and of Zhang et al. may suggest that the adsorption of additives on the Al film surface cannot be explained singly by electrostatic interaction, and the degree of adsorption is determined multiply by electrostatic, dipolar and hydrophobic interactions as well as steric effects. However, the fact that in the presence of PCAH, PCA and MP additives having electron-withdrawing groups the Al films with high brightness (or high reaction resistance) can be obtained might reflect the decrease in the electron density of the N atom in the parent pyridine ring in these additives. Through the results of this study, as a basic guidance for selecting additives with strong adsorption ability in the EMIC- AlCl_3 -toluene bath, the electron density of the N atom in the pyridine ring is considered to be one of the effective factors to determine the degree of adsorption of additives on the Al film. Thus, it can be concluded that a strong adsorption of additives on the Al film due to a decrease in the electron density around the

N atom in the pyridine ring leads to a smoother surface and smaller grain and/or crystalline domain size of Al deposits.

4. Conclusions

The effects of additives, *i.e.*, 4-PCAH and its analogues and organic solvents, *i.e.*, toluene, benzene and xylene on the surface brightness, crystallographic orientation, electrodeposition efficiency and chemical composition of prepared Al films were examined using SEM, XRD, visible light reflectance measurements and XPS. Furthermore, in order to correlate the obtained results with the reaction mechanism of the electrochemical deposition of Al from the EMIC- AlCl_3 bath, the reaction resistance was also measured with electrochemical impedance spectroscopy. The reaction resistances evaluated for the baths containing various additives showed a well-defined relationship with the surface brightness of the deposited Al films, suggesting that a strong adsorption of additives onto the surface of the growing Al nuclei hinders their further growth, producing very fine particles with sizes in the nanometer range and as a result the Al films with a high brightness. The strong adsorption (high reaction resistance) could be considered to come from the negativity of the N atom in the pyridine ring, typically demonstrated by PCAH and PCA additives, *i.e.*, a decrease in the electron density around the N atom in the pyridine ring is conducive to the adsorption of the additive onto the cathode surface, in accordance with the idea suggested by Zhang *et al.* [24]. Toluene molecules are effective for producing a bright and uniform Al film surface, probably due to the formation of charge transfer complexes with electroactive species of Al^{3+} ions [8] and their adsorption on the Al film.

Acknowledgement

This work was financially supported by the Strategic Research Base Development Program for Private Universities of the Ministry of Education, Culture, Sports, Science and Technology of Japan.

Appendix A. Supplementary data

Supplementary data associated with this article can be found, in the online version, at <http://dx.doi.org/10.1016/j.electacta.2016.08.125>.

References

- [1] HANDBOOK of Deposition Technologies for Films and Coatings, 2nd Edition, Noyes Publications, Park Ridge, New Jersey (1994).
- [2] T. Kobayashi, A. Sekiguchi, N. Akiyama, N. Hosokawa, T. Asamaki, Growth of Al films by gas-temperature-controlled chemical vapor deposition, *J. Vac. Sci. & Technol A* 10 (1992) 525–538.
- [3] S. Shawki, Z.A. Hamid, Effect of aluminium content on the coating structure and dross formation in the hot-dip galvanizing process, *Surf. Interface Anal* 35 (2003) 943–947.
- [4] Y. Zhao, T.J. VanderNoot, Electrodeposition of aluminium from nonaqueous organic electrolytic systems and room temperature molten salts, *Electrochim. Acta* 42 (1997) 3–13.
- [5] A. Okamoto, M. Morita, N. Yoshimoto, Preparation of aluminum foil by an electrodeposition method and its characterization, *J. Surf. Finish. Soc. Jpn.* 63 (2012) 641–645.
- [6] W. Simka, D. Puszczczyk, G. Nawrat, Electrodeposition of metals from non-aqueous solutions, *Electrochim. Acta* 54 (2009) 5307–5319.
- [7] M. Li, B. Gao, C. Liu, W. Chen, Z. Shi, X. Hu, Z. Wang, Electrodeposition of aluminum from AlCl_3 /acetamide eutectic solvent, *Electrochim. Acta* 180 (2015) 811–814.
- [8] A.P. Abbott, R.C. Harris, Y.T. Hsieh, K.S. Ryder, I.W. Sun, Aluminium electrodeposition under ambient conditions, *Phy. Chem. Chem.* 16 (2016) 14675–14681.
- [9] N. Koura, Y. Tashiro, M. Futamura, F. Matsumoto, Y. Idemoto, Electroplating of highly ordered aluminum from AlCl_3 -EMIC room temperature molten salt, *J. Surf. Finish. Soc. Jpn.* 52 (2001) 791–792.
- [10] W.H. Huang, M.L. Wang, H.W. Wang, N.H. Ma, The electrodeposition of aluminum on $\text{TiB}_2/\text{Al}_3\text{Si}_5$ composite from ionic liquid as protective coating, *Surf. Coat. Technol.* 213 (2012) 264–270.
- [11] Q. Zhang, Q. Wang, S. Zhang, X. Lu, X. Zhang, Electrodeposition in Ionic Liquids, *Chem. Phys. Chem.* 17 (2016) 335–357.
- [12] D. Pradhan, R.G. Reddy, Dendrite-Free Aluminum Electrodeposition from AlCl_3 -1-Ethyl-3-Methyl-Imidazolium Chloride Ionic Liquid Electrolytes, *Metall. Mater. Trans. B* 43 (2012) 519–531.
- [13] A. Bakker, V. Neubert, Electrodeposition and corrosion characterisation of micro- and nano-crystalline aluminium from AlCl_3 /1-ethyl-3-methylimidazolium chloride ionic liquid, *Electrochim. Acta* 103 (2013) 211–218.
- [14] S.Z.E. Abedin, P. Giridhar, P. Schwab, F. Endres, Electrodeposition of nanocrystalline aluminium from a chloroaluminate ionic liquid, *Electrochem. Commun.* 12 (2010) 1084–1086.
- [15] M. Miyake, Y. Kubo, T. Hirato, Electrodeposition of bright Al coatings from dimethylsulfone- AlCl_3 baths with the addition of tetraethylenepentamine, *J. Surf. Finish. Soc. Jpn.* 64 (2013) 364–367.
- [16] M. Miyake, Y. Kubo, T. Hirato, Hull cell tests for evaluating the effects of polyethylene amines as brighteners in the electrodeposition of aluminum from dimethylsulfone- AlCl_3 baths, *Electrochim. Acta* 120 (2014) 423–428.
- [17] H. Hoshi, A. Okamoto, S. Andoh, Properties of electroplated aluminum thin films, *Hitachi, Metals Technical Reviews* 27 (2011) 20–27.
- [18] Q. Wang, B. Chen, Q. Zhang, X. Lu, S. Zhang, Aluminum deposition from Lewis acidic 1-butyl-3-methylimidazolium chloroaluminate ionic liquid ($[\text{Bmim}]\text{Cl}/\text{AlCl}_3$) modified with methyl nicotinate, *ChemElectroChem* 2 (2015) 1794–1798.
- [19] S. Shiomi, M. Miyake, T. Hirato, Electrodeposition of bright Al-Zr alloy coatings from dimethylsulfone-based baths, *J. Electrochem. Soc.* 159 (2012) D225–D229.
- [20] A. Endo, M. Miyake, T. Hirato, *Electrochim. Acta* 137 (2014) 470–475.
- [21] L. Barchi, U. Bardi, S. Caporali, M. Fantini, A. Scrivani, A. Scrivani, Electroplated bright aluminium coatings for anticorrosion and decorative purposes, *Prog. Org. Coat.* 67 (2010) 146–151.
- [22] F. Endres, M. Bukowski, R. Hempelmann, H. Natter, Electrodeposition of nanocrystalline metals and alloys from ionic liquids, *Angew. Chem. Int. Ed.* 42 (2003) 3428–3430.
- [23] A.P. Abbott, F. Qiu, H.M.A. Abod, M.R. Ali, K.S. Ryder, Double layer, diluents and anode effects upon the electrodeposition of aluminum from chloroaluminate based ionic liquids, *Phys. Chem. Chem. Phys.* 12 (2010) 1862–1872.
- [24] Q. Wang, Q. Zhang, B. Chen, X. Lu, S. Zhang, Electrodeposition of bright Al coatings from 1-butyl-3-methylimidazolium chloroaluminate ionic liquids with specific additives, *J. Electrochem. Soc.* 162 (2015) D320–D324.
- [25] L. Liu, X. Lu, Y. Cai, Y. Zheng, S. Zhang, Influence of additives on the speciation morphology, and nanocrystallinity of aluminium electrodeposition, *Aust. J. Chem.* 65 (2012) 1523–1528.
- [26] X. Fang, K. Uehara, S. Kaneko, S. Sato, T. Tanabe, T. Gunji, F. Matsumoto, The effect of additives on the fabrication of electroplated bright aluminum films using AlCl_3 -1-ethyl-3-methylimidazolium chloride-toluene baths, *Electrochemistry* 84 (2016) 17–24.
- [27] K. Uehara, T. Gunji, T. Tanabe, S. Kaneko, F. Matsumoto, The effect of brighteners on the fabrication of electroplated bright aluminum films using an AlCl_3 -EMIC-toluene bath, *ECS Trans.* 69 (29) (2015) 7–13.
- [28] B.D. Cullity, *Elements of X-ray Diffraction*, Addison-Wesley Publishing Company, USA, 1956, pp. 62–269.
- [29] Q. Liao, W.R. Pitner, G. Stewart, C.L. Hussey, Electrodeposition of aluminum from the aluminum chloride-1-methyl-3-ethylimidazolium chloride room temperature molten salt + benzene, *J. Electrochem. Soc.* 144 (1997) 936–943.
- [30] K. Ui, T. Yatsushiro, M. Futamura, Y. Idemoto, N. Koura, Oriented electrodeposition of aluminum from the aluminum chloride-1-ethyl-3-methylimidazolium chloride ambient temperature molten salt – effects of xylene mixing to the orientation of Al deposit, *J. Surf. Finish. Soc. Jpn.* 55 (2004) 409–416.
- [31] Q. Zhang, Q. Wang, S. Zhang, Effect of nicotinamide on electrodeposition of Al from aluminium chloride (AlCl_3)-1-butyl-3-methylimidazolium chloride ($[\text{Bmim}]\text{Cl}$) ionic liquids, *J. Solid State Electrochem.* 18 (2014) 257–267.
- [32] J. Clayton, C. Roth, H. Leidheiser, The interaction of organic compounds with the surface during the electrodeposition of nickel, *J. Electrochem. Soc.* 100 (1953) 553–565.



Preparation of Water-Resistant Surface Coated High-Voltage $\text{LiNi}_{0.5}\text{Mn}_{1.5}\text{O}_4$ Cathode and Its Cathode Performance to Apply a Water-Based Hybrid Polymer Binder to Li-Ion Batteries

Toyokazu Tanabe^{a,b}, Takao Gunji^a, Youhei Honma^a, Koki Miyamoto^a, Takashi Tsuda^a, Yasumasa Mochizuki^b, Shingo Kaneko^c, Shinsaku Ugawa^d, Hojin Lee^d, Takeo Ohsaka^c, Futoshi Matsumoto^{a,b,*}

^a Faculty of Engineering, Kanagawa University, 3-27-1 Rokkakubashi, Kanagawa-ku, Yokohama, Kanagawa 221-8686, Japan

^b LIB Open-Lab., Kanagawa University, 3-27-1 Rokkakubashi, Kanagawa-ku, Yokohama, Kanagawa 221-8686, Japan

^c Research Institute for Engineering, Kanagawa University, 3-27-1 Rokkakubashi, Kanagawa-ku, Yokohama, Kanagawa 221-8686, Japan

^d JSR Corporation, 100 Kawajiri-cho, Yokkaichi, Mie 510-8552, Japan

ARTICLE INFO

Article history:

Received 15 October 2016

Received in revised form 9 December 2016

Accepted 9 December 2016

Available online 15 December 2016

Keywords:

Lithium ion battery

Water-based hybrid polymer binder

High-voltage cathode material

Surface Coating

Water-resistant property

ABSTRACT

Water-resistant $\text{LiNi}_{0.5}\text{Mn}_{1.5}\text{O}_2$ spinel cathode was prepared by surface coating with carbon, Al_2O_3 and Nb_2O_5 to use a water-based hybrid polymer (TRD202A, JSR, Japan) as a binder and to form the cathode film on an Al current collector. The surface composition and degree of the surface coverage of carbon, Al_2O_3 and Nb_2O_5 were characterized with field-emission scanning electron microscope (FE-SEM), transmission electron microscope (TEM), X-ray diffraction (XRD) and X-ray photoelectron spectroscopy (XPS). The coated $\text{LiNi}_{0.5}\text{Mn}_{1.5}\text{O}_2$ particles not only exhibited water-resistant property but also showed no decrease in discharge capacity and only a small degradation of discharge rate performance. In addition, the coated $\text{LiNi}_{0.5}\text{Mn}_{1.5}\text{O}_2$ particles, that were exposed to water-based binder solution for one week, exhibited the same charge/discharge cycle performance as observed for the cathode of the pristine $\text{LiNi}_{0.5}\text{Mn}_{1.5}\text{O}_4$ particles, suggesting that the coated particles are promising as cathode materials with a water-resistant property and therefore water can be used as solvent for preparing the cathode slurry solution in the place of e.g., carcinogenic N-methyl-2-pyrrolidone which is used actually.

© 2016 Elsevier Ltd. All rights reserved.

1. Introduction

Recently, water-soluble and aqueous polymers (water-based polymers) have attracted much attention as binders for lithium ion batteries (LIBs) because of the need for low-cost materials and environmentally compatible electrode fabrication processes [1–13]. N-methyl-2-pyrrolidone (NMP), which is listed as a carcinogenic chemical with reproductive toxicity [1,14,15], is often used as a solvent to prepare a binder slurry. The slurry is composed of cathode material particle, conducting carbon additive, conventional polyvinylidene difluoride (PVdF) binder and NMP solvent, and is casted on an aluminum current collector and finally is dried to evaporate the NMP. The NMP solvent should be recycled without releasing it to the atmospheric environment. A reduction in costs of

the LIBs is severely constrained because of facility investments for the process used currently. Therefore, shift of a nonaqueous solution-based fabrication process of LIBs to an aqueous solution-based one is widely investigated. For graphite anodes, styrene-butadiene rubber has already been employed as a water-based polymer binder in fabricating some commercially available Li-ion batteries [16,17]. Applying water-based polymer binders to the cathode is a next target to develop the low-cost and environmentally friendly fabrication process for LIBs. Some companies have produced prototype models using water-based polymer binders, and their battery test results have been reported to be comparable with those obtained with the conventional PVdF polymer binders [18,19]. We also have applied a water-based hybrid polymer binder composed of acrylic polymer and fluoropolymer, TRD202A (JSR, Japan) to high-voltage Li-rich solid-solution cathode, in which the water-based polymer binder slurry was used immediately after its preparation to prepare the cathode films [20]. Uniform cathode films were prepared with a Li-rich solid-solution ($\text{Li}[\text{Li}_{0.2}\text{Ni}_{0.18}\text{Co}_{0.03}\text{Mn}_{0.58}]\text{O}_2$) cathode material and water-based hybrid

* Corresponding author at: Faculty of Engineering, Kanagawa University, 3-27-1 Rokkakubashi, Kanagawa-ku, Yokohama, Kanagawa 221-8686, Japan.

E-mail address: fmatsumoto@kanagawa-u.ac.jp (F. Matsumoto).

polymer binder (TDR202A), carboxymethyl cellulose (CMC), and conducting carbon additive. The films exhibited stable charge/discharge cycle performances (average discharge capacity: 260 mAh g⁻¹) when cycled between 4.8 and 2.0 V for 80 cycles. The cathode film prepared with the water-based hybrid polymer binder showed longer-term reliability as well as higher electrochemical resistance when compared with that prepared using the conventional PVdF binder. Through our researches so far carried out concerning cathode/water-based hybrid polymer binders, we have understood that the water-based polymers binders cannot be applied to some cathode materials because of solubility of the cathode material surfaces in water (not shown in this paper). Many papers on the cathode materials/water-based polymers binders have been published [18–20], but in these cases, the water-based polymer binder slurries were used immediately after their preparation. In a practical production level, however, the cathode materials are put in water-based binder slurry solution at least for one week and therefore they are required to keep a “water-resistant” property for one week (“water-resistant” means slowing the penetration of water (but is not water-proof)).

In this study, we tried to modify the cathode surfaces with carbon material and water-stable metal oxides to isolate them from the aqueous solutions of the water-based slurry and to obtain stable charge/discharge cycle and rate performance even after the prepared cathode materials are exposed to the aqueous solutions of the cathode slurry for one week. The surface coating of the cathode material surfaces with carbon [21,22] and metal oxides [23,24] has been reported and the improvement of the charge/discharge cycle durability [24–26] and the rate performance [27,28] have been achieved with the aid of the surface coatings. The surface coating should not prevent the intercalation/deintercalation of Li⁺ ions to/from the cathode material layers although it is required to isolate the cathode material surface from the water-based polymer binder slurry during the cathode fabrication process. The surface coatings with a unique property, *i.e.*, they do pass Li⁺ ion, but not H₂O molecule, were investigated using carbon, aluminum oxide and niobium oxide. A LiNi_{0.5}Mn_{1.5}O₂ spinel cathode material was selected for the present surface coating. The LiNi_{0.5}Mn_{1.5}O₄ has attracted a lot of attention from many research groups in the field of energy storage, owing to its high specific energy of 658 Wh kg⁻¹ [29–31], which is much higher than commercially available cathode materials such as LiCoO₂ (518 Wh kg⁻¹), LiMn₂O₄ (400 Wh kg⁻¹), LiFePO₄ (495 Wh kg⁻¹), and LiCo_{1/3}Ni_{1/3}Mn_{1/3}O₂ (576 Wh kg⁻¹). In addition, the upper potential applicable for the charge/discharge reaction of LiNi_{0.5}Mn_{1.5}O₄ is around 4.7 V (*vs.* Li/Li⁺) and thus it is suitable to test the electrochemical oxidation resistance of the water-based polymer binders which are required to possess a high resistance to electrochemical oxidation. Furthermore, metal oxide cathodes containing a high percentage of Ni²⁺ ions such as LiNi_{0.5}Mn_{1.5}O₄ tend to suffer from chemical damage which is caused by the contact with water, *i.e.*, Ni³⁺ ion on the cathode material surface is reduced with H₂O to form Ni²⁺ ion. As a result of this reduction, lithium carbonate and lithium hydroxide are formed on the cathode material surface and dissolved into aqueous solutions. This leads to the corrosion of aluminum current collectors, especially in the case of water-based binders. Pieczonka et al. [32] reported self-Mn and Ni dissolution behaviors. The self-discharge reaction of LiNi_{0.5}Mn_{1.5}O₄ causes a decomposition of electrolyte, and the resulting HF can accelerate Mn and Ni dissolution from LiNi_{0.5}Mn_{1.5}O₄, and consequently various reaction products, such as LiF, MnF₂, NiF₂, and polymerized organic species, are found on the surface of LiNi_{0.5}Mn_{1.5}O₄ electrode. So, the cathode surface coating is important for inhibiting the degradation of cathode performance.

Therefore, the present study on the coating process to inhibit the chemical dissolution of the LiNi_{0.5}Mn_{1.5}O₄ containing a high percentage of Ni and Mn ions is considered to be suitable for realizing the degree of target achievement about the water-resistant property of cathode materials which could use a so-called water-based slurry binder solution in the practical fabrication process of LIBs.

2. Experimental

2.1. Preparation of carbon and metal oxide-coated cathode materials

A LiNi_{0.5}Mn_{1.5}O₄ particle sample was purchased from Hohsen Corp. (Japan). The particle was used as a cathode material without any purification. Surface coatings with carbon, AlO_x and NbO_x were conducted as mentioned below.

Carbon coating: Sucrose (Wako Pure Chemicals Co. Ltd. (Wako), Japan) as a source of carbon layer for coating was weighted with a proper amount to prepare 0.5, 1 and 10 wt% carbon-coated LiNi_{0.5}Mn_{1.5}O₄ particle samples (0.5 wt% carbon-coated LiNi_{0.5}Mn_{1.5}O₄ means that the sample was composed of 0.5 wt% of carbon and 99.5 wt% of LiNi_{0.5}Mn_{1.5}O₄). The sucrose and LiNi_{0.5}Mn_{1.5}O₄ particle weighted were mixed at first using agate mortar. Afterward, the mixed powder was further mixed using a wet planetary ball-milling machine with a Teflon jar (672 mL) containing Teflon balls (diameter 1.5 cm, 88 balls) and acetone (80 mL) at ambient temperature at a speed of 300 rpm for 1 h. After ball-milling, the mixture was dried up at 120 °C for 3 h. The dried mixture was then sintered at 600 °C for 3 h under argon atmosphere to form the carbon coating on the LiNi_{0.5}Mn_{1.5}O₄ particle surface.

AlO_x coating: 0.03 g of aluminum nitrate (Al(NO₃)₃, 98%, Wako) was dissolved in 20 mL of water. The precursor of AlO_x was precipitated by controlling the solution pH with ammonium aqueous solution. In this case, the solution pH was monitored with pH meter throughout the precipitation process. The precipitate was filtrated and dried. Afterward, the dried precursor of AlO_x was weighted to fix the coating weight percentage of AlO_x and was mixed with weighted LiNi_{0.5}Mn_{1.5}O₄ particle. After ball-milling at the same condition as the case of the carbon coating, the mixture was dried at 120 °C for 3 h. The dried mixture was then annealed at 450 °C for 6 h under air-atmosphere to form AlO_x coating on the LiNi_{0.5}Mn_{1.5}O₄ particle surface. 0.5, 1 and 2 wt% AlO_x-coated LiNi_{0.5}Mn_{1.5}O₄ samples were prepared by controlling the mixing ratio of AlO_x precursor and LiNi_{0.5}Mn_{1.5}O₄ particle before annealing.

NbO_x coating: 0.15 g of niobium (V) chloride (NbCl₅, Sigma-Aldrich, 99.9%) was dissolved in 20 ml of water. After that, in a similar manner as the formation of AlO_x coating on LiNi_{0.5}Mn_{1.5}O₄ particle surface, 0.5, 1 and 2 wt% NbO_x-coated LiNi_{0.5}Mn_{1.5}O₄ samples were prepared.

The weight percentage of carbon on the carbon-coated LiNi_{0.5}Mn_{1.5}O₄ particle was estimated with thermogravimetry (Thermo plus EVO TG8120, Rigaku) by calculating the difference of weight before and after annealing of the carbon-coated LiNi_{0.5}Mn_{1.5}O₄ sample under air-atmosphere. The weight percentages of AlO_x and NbO_x in the coated LiNi_{0.5}Mn_{1.5}O₄ particle samples were determined by ICP-MS using an Agilent, 7700x spectrometer after chemically dissolved in concentrated acids and diluted with water and by evaluating the concentrations of Al and Nb ions.

2.2. Characterization of synthesized cathode materials

The average sizes and shapes of the cathode particles were evaluated with a field-emission scanning electron microscope (FE-

SEM, S-4000, Hitachi). The detail of SEM-energy-dispersive X-ray spectroscopy (EDX) equipment and its experimental condition is mentioned in the Experimental 1.1 of ESI. A 200 kV transmission electron microscope (TEM and/or STEM, JEM-2100F, JEOL) equipped with two aberration correctors (CEOS GmbH) for the image- and probe-forming lens systems and an X-ray energy-dispersive spectrometer (JED-2300T, JEOL) were used for compositional analysis of the particle surfaces. Both aberration correctors were optimized to realize the point-to-point resolutions of TEM and scanning transmission electron microscopy (STEM) as 1.3 and 1.1 Å, respectively. A probe convergence angle of 29 mrad and a high-angle annular-dark-field (HAADF) detector with an inner angle greater than 100 mrad were used for HAADF-STEM observation. HAADF-STEM was used to perform microscopic observation of the morphologies and particle sizes of the samples. The samples for the HAADF-STEM analysis were prepared by dropping a methanol suspension of the sample powder onto a commercial TEM grid coated with a polymer film. The sample was thoroughly dried in a vacuum prior to observation. The chemical dissolution of Li, Ni and Mn ions from the pristine- and coated- $\text{LiNi}_{0.5}\text{Mn}_{1.5}\text{O}_4$ samples was evaluated by Cs-corrected STEM analysis (JEOL, JEM-ARM200F, 200 kV) with EELS (Gatan, GIF Quantum). In order to find out the distribution of Li, Mn, Ni and O atoms on the surfaces of the pristine- and coated- $\text{LiNi}_{0.5}\text{Mn}_{1.5}\text{O}_4$ samples, Li-K and Al-K edges were simultaneously obtained, and Mn-L, O-L, and Ni-L edges were also obtained at the same area (see the Experimental 1.2 in ESI and Fig. S1).

Powder X-ray diffractometry (pXRD) measurements were performed using $\text{CuK}\alpha$ radiation (Rigaku RINT-Ultima III; $\lambda = 0.1548$ nm) at an increment of 0.02 degrees at diffraction angles ranging from 20 to 80 degrees. An obliquely finished Si crystal (non-reflective Si plate) was used as the sample holder to minimize the background noise.

X-ray photoelectron spectroscopy (XPS) measurements (JEOL, JP-9010 MC) were performed to examine the chemical states (Al 2p,

Nb 3d and Mn 2p) of the cathode material. A Mg $\text{K}\alpha$ X-ray source with an anodic voltage (10 kV) at a current of (10 mA) was used for XPS measurements. All XPS spectra of the samples were obtained with a take-off angle of 45° with respect to the specimens by using the pass energies of 100 eV and 200 eV for narrow and survey scans, respectively.

2.3. Cell preparation and electrochemical tests

910 mg of accurately weighed $\text{LiNi}_{0.3}\text{Mn}_{1.5}\text{O}_4$ active material, 50 mg of acetylene black (AB, Denka Black, Denki Kagaku Gogyo, Japan), 10 mg of carboxymethyl cellulose (CMC, Polyscience Inc, cat.#6139) and 30 mg of water-based polymer binder (TRD202A, JSR, Japan) were mixed in Milli-Pore water (>18 M Ω) with planetary mixing equipment (Mazerustar, KK-250S, KURABO, Japan) until they formed a homogenous mixture; the mixture had a suitable viscosity for coating it as the cathode films while preserving the weight % of the cathode material:TRD202A:AB:CMC=91:3:5:1 in the prepared cathode films. The obtained mixture was coated using a doctor-blade (100 μm gap) coater on Al current collector. The mixture thin film-coated Al cathode was dried at 130 °C for 5 h in a vacuum drying oven. The loading of the cathode materials on the Al current collector was 3–4 mg cm^{-2} . For comparison, polyvinylidene difluoride (PVdF, KF9130, Kureha, Japan) was used as a binder as received without any further treatment. The weight % of the cathode films was kept as cathode material:PVdF:AB = 91:4:5. Electrochemical tests were performed using a CR2032 coin-type cell. The test cell was composed of a cathode and a lithium metal anode separated by a porous polypropylene film (Celgard 3401). The electrolyte used in the tests was a 1 M LiPF_6 -ethylene carbonate (EC)/dimethyl carbonate (DMC) (1/2 volume ratio) mixture (Ube Chemicals, Japan). The charge/discharge cycling was performed using a multi-channel battery tester (model BTS2004, Nagano Corp., Japan). All the tests were performed at room temperature. A constant-current/

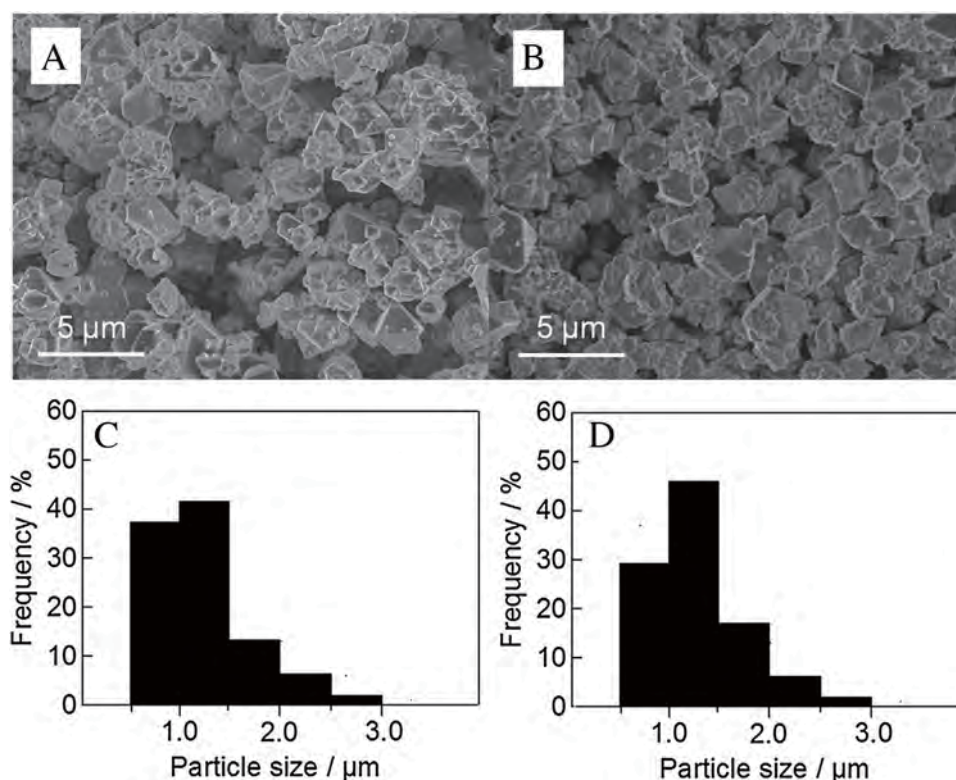


Fig. 1. (A, B) FE-SEM images and (C, D) histograms of particle size of (A, C) pristine and (B, D) AlO_x (1 wt%)-coated $\text{LiNi}_{0.5}\text{Mn}_{1.5}\text{O}_4$ samples.

constant-voltage (CC-CV) mode was used for the cycling tests. The charge/discharge cycling tests were performed at a charge/discharge current density of $0.07\text{--}0.09\text{ mA cm}^{-2}$ with a cutoff voltage of $2.0\text{--}4.8\text{ V}$ (vs. Li/Li^+). The charge/discharge capacities were calculated using the amount of $\text{LiNi}_{0.5}\text{Mn}_{1.5}\text{O}_4$ loaded on the current collector (*i.e.*, the amount of coating materials other than

the $\text{LiNi}_{0.5}\text{Mn}_{1.5}\text{O}_4$ was subtracted from the total amount of the coating loaded on the current collector to evaluate the coating amount of $\text{LiNi}_{0.5}\text{Mn}_{1.5}\text{O}_4$. The C rate was calculated based on the specific capacity of 125 mAhg^{-1} which was obtained for the non-treated $\text{LiNi}_{0.5}\text{Mn}_{1.5}\text{O}_4$ and PVdF binder at low constant current density 0.07 mA cm^{-2} for charge/discharge cycle tests.

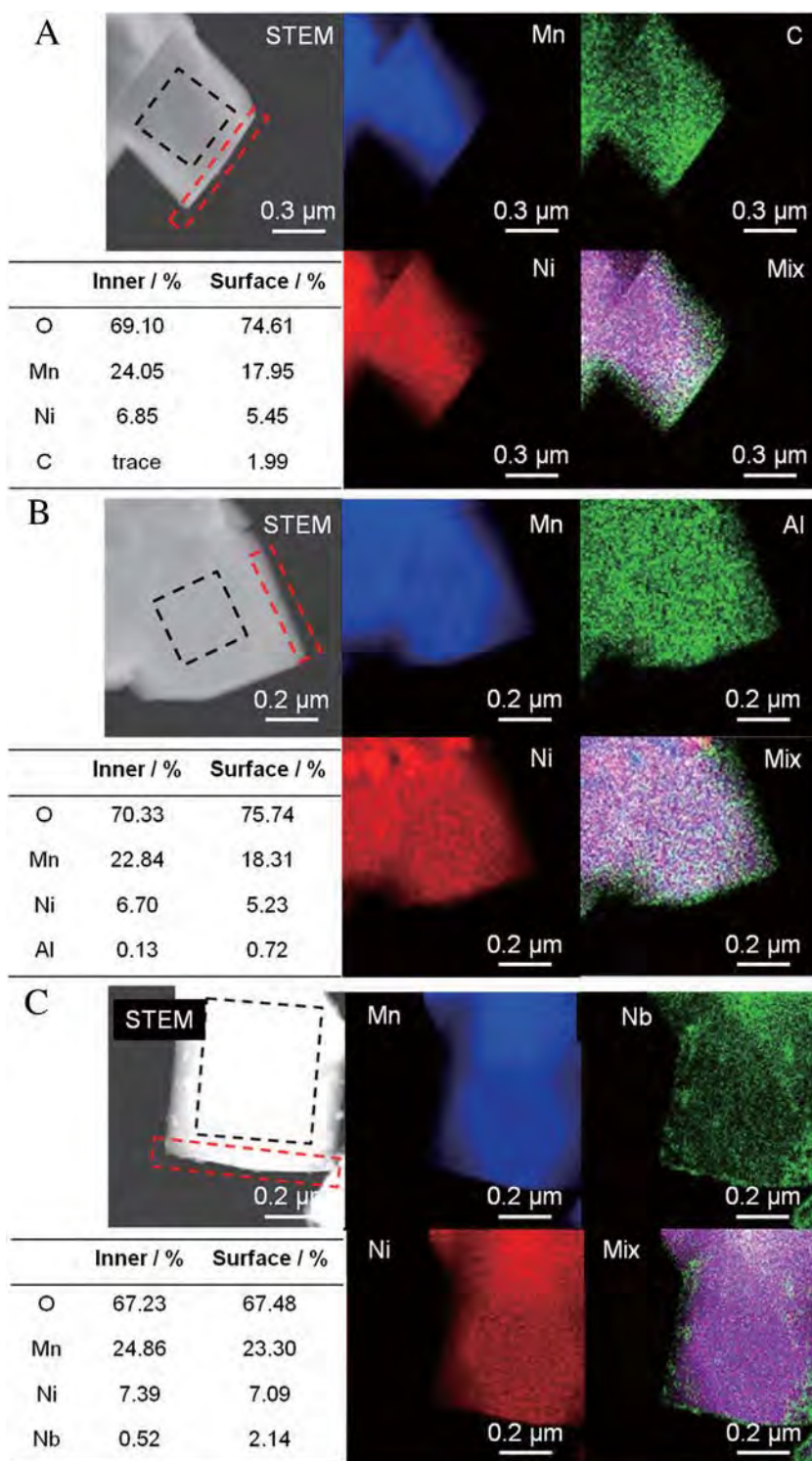


Fig. 2. TEM image, STEM-EDS element (Mn, Ni and C, Al or Ni) mapping profile images and summary of atomic % on the surface and inner part of (A) carbon-coated, (B) AlO_x -coated and (C) NbO_x -coated $\text{LiNi}_{0.5}\text{Mn}_{1.5}\text{O}_4$ samples. The red and black squares in the STEM images indicate the measured area for STEM-EDX mapping on the edge and inner parts of the samples, respectively. (For interpretation of the references to color in this figure legend, the reader is referred to the web version of this article.)

3. Results and discussion

3.1. Characterization of surface-coated cathode materials

Fig. 1 shows (A, B) SEM images and (C, D) histograms of particle size of (A, C) pristine and (B, D) AlO_x -coated $\text{LiNi}_{0.5}\text{Mn}_{1.5}\text{O}_4$ cathode particles. In both cases, $\text{LiNi}_{0.5}\text{Mn}_{1.5}\text{O}_4$ particles are of polyhedral shape and exhibit smooth surfaces with sharp edges. The distribution of size of the cathode particles was evaluated on the basis of approximately 100 particles in the SEM images. The average diameters of the pristine and AlO_x -coated $\text{LiNi}_{0.5}\text{Mn}_{1.5}\text{O}_4$ cathode particles were calculated as 1.23 ± 0.05 and 1.31 ± 0.05 μm , respectively. They exhibited narrow particle-size distributions. From the histograms in Fig. 1(C) and (D), it is obvious that the difference in the distribution of particle size between pristine and AlO_x -coated $\text{LiNi}_{0.5}\text{Mn}_{1.5}\text{O}_4$ cathode particles is very small, demonstrating that the particle size of $\text{LiNi}_{0.5}\text{Mn}_{1.5}\text{O}_4$ cathode is held even during the preparation process of AlO_x coating layer.

In order to confirm the distribution of Al element on the sample particle, the SEM-EDX mapping profile was measured with the AlO_x -coated $\text{LiNi}_{0.5}\text{Mn}_{1.5}\text{O}_4$ particle (Fig. S2). The even observation of small red dots indicates that Al elements are widely distributed over the whole surfaces of $\text{LiNi}_{0.5}\text{Mn}_{1.5}\text{O}_4$ particles although the large red dots suggesting the formation of AlO_x particle or AlO_x thick layer can be seen in some places of the image. The Al mapping (Fig. S2-(D)) is exactly the same in pattern as the SEM (A) image of the cathode material particle and the mapping of Mn (B) and Ni (C), indicating a uniform AlO_x coating of the cathode material surface.

The STEM and elemental mapping images of (A) carbon-coated (1 wt%), (B) AlO_x (1 wt%)-coated and (C) NbO_x (1 wt%)-coated $\text{LiNi}_{0.5}\text{Mn}_{1.5}\text{O}_4$ cathode materials were measured to confirm the thickness of these surface-coated layers and the atomic ratios of Mn, Ni and C (Al or Nb) on the surfaces (Fig. 2). In all the images, blue and red colors indicate the existence of Mn and Ni atoms, respectively, and green color corresponds to the C, Al or Nb atoms contained in the coated layer on the $\text{LiNi}_{0.5}\text{Mn}_{1.5}\text{O}_4$ cathode particles. In the image (A), a thin carbon-layer can be seen on the cathode particle surface. The signals of Mn, C and Ni overlap almost completely in the compositional mappings obtained for the carbon-coated $\text{LiNi}_{0.5}\text{Mn}_{1.5}\text{O}_4$ sample. The carbon signal can be seen nearly entirely throughout the cathode surface. Especially a

strong carbon signal (1.99 atomic %) is recognized around the edge of the surface, indicating the effective surface coating in the edge part. However, the carbon signal in the inner part is negligibly small (less than 0.1%). In the image (B), the Al signal can be seen entirely over the cathode surface and especially can be observed strongly at the edge side of the particle as seen in the case of the above-mentioned carbon-coating. The existence of Al atoms can be confirmed in the inner part as well as on the edge part. The atomic percentage of Al in the edge part is 0.72%, which is lower than that of the corresponding carbon. The difference in the atomic% of carbon and Al in the edge part is due to the different thicknesses of carbon layer and AlO_x layer coated on the cathode particle surfaces. In other words, the AlO_x layer formed on the surface is thinner and more uniform than the carbon layer. Also in the case (C) of Nb oxide coating, the element of Nb can be observed clearly on the particle edges in the EDX image. When compared with the EDX images of carbon- and AlO_x -coated particles, it can be seen that the Nb element is unevenly distributed on the particle surface. The atomic percentages of Nb on the surface and edge parts are 2.14 and 0.52%, respectively. NbO_x tends to be coated more preferentially on the edge when compared with the cases of carbon- and AlO_x -coating.

Fig. 3(A) shows the pXRD patterns observed for (a) pristine, (b) carbon-coated, (c) AlO_x -coated and (d) NbO_x -coated $\text{LiNi}_{0.5}\text{Mn}_{1.5}\text{O}_4$ cathode material powders along with simulated XRD profiles of $\text{LiNi}_{0.5}\text{Mn}_{1.5}\text{O}_4$ (ICDD #01-080-5507), graphite (#00-056-0159), Al_2O_3 (#00-042-1468), NbO_2 (#01-076-1095) and Nb_2O_5 (#01-071-0005). The patterns (a–d) are very similar and can be indexed as a cubic spinel structure with a space group of $Fd-3m$. No impurity phase of $\text{LiNi}_{0.5}\text{Mn}_{1.5}\text{O}_4$ was found. Even small peaks of graphite, Al_2O_3 , NbO_2 and Nb_2O_5 were not found in Fig. 3.

In addition, even in the Synchrotron X-ray diffraction pattern, the impurity peaks could not be seen in the obtained XRD patterns (see the Experimental 1.3 in ESI and Fig. S3). This may be due to the low content of surface coating materials and/or its amorphous state. Certainly, from the results of XRD, the crystalline structures of the surface coating materials on the $\text{LiNi}_{0.5}\text{Mn}_{1.5}\text{O}_4$ samples cannot be determined although it was confirmed from the SEM- and TEM-EDX results that the surface coating materials exist really on the $\text{LiNi}_{0.5}\text{Mn}_{1.5}\text{O}_4$ particle surface. The shift of the original peaks of the pristine $\text{LiNi}_{0.5}\text{Mn}_{1.5}\text{O}_4$ (a) due to the interaction between the surface coating layer and $\text{LiNi}_{0.5}\text{Mn}_{1.5}\text{O}_4$ surface can be observed in the XRD profiles of the surface coated

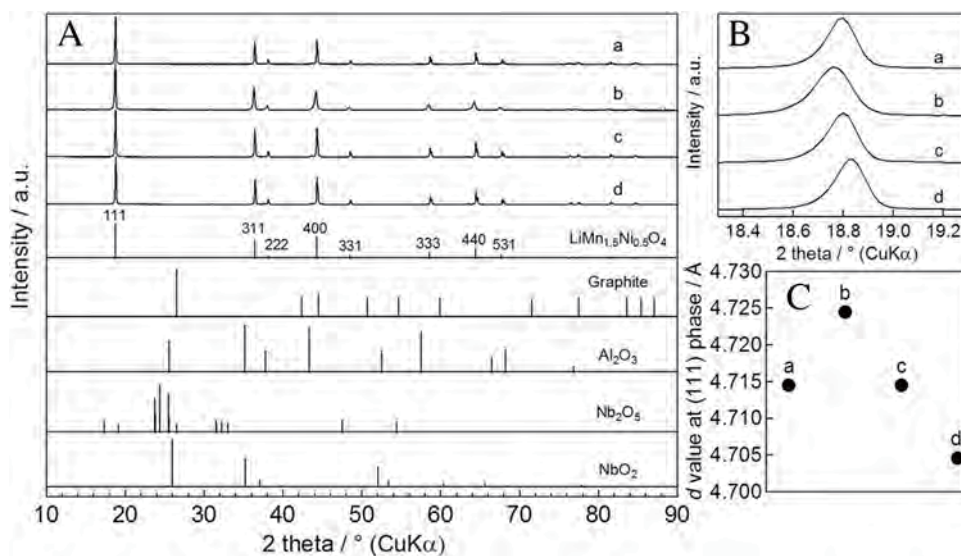


Fig. 3. X-ray diffraction (XRD) patterns of (a) $\text{LiNi}_{0.5}\text{Mn}_{1.5}\text{O}_4$, (b) carbon-, (c) AlO_x - and (d) NbO_x -coated $\text{LiNi}_{0.5}\text{Mn}_{1.5}\text{O}_4$. (B) Magnified presentation of typical (111) peaks. (C) d value of $\text{LiNi}_{0.5}\text{Mn}_{1.5}\text{O}_4$ at (111) phase for all the cathode materials.

LiNi_{0.5}Mn_{1.5}O₄ samples (a–c) (Fig. 3-(B)). The interlayer distance (*d*) values at (111) phase are summarized in Fig. 3-(C). The peak shift is due to the difference in annealing temperature to form the surface coating layer. The annealing temperature-dependent (relatively extensive) substitution of transition metal cations in tetrahedral 8*a* sites of the spinel-type structure has been reported [33]. Also in our surface-coated samples, the occupancy of the 8*a* tetrahedral lithium sites by transition metal cations in the LiNi_{0.5}Mn_{1.5}O₄ samples may occur to some extent. The Li:Ni:Mn elemental ratios of the surface-coated cathode samples were determined to be 1.0: 0.50–0.53: 1.5–1.52 using an ICP measurement. The elemental ratios in the AlO_x-coated and NbO_x-coated samples were not different from that of the pristine LiNi_{0.5}Mn_{1.5}O₄ sample. Thus, it is obvious confirmed that the constituent elements of LiNi_{0.5}Mn_{1.5}O₄ particle are not lost from the particle surface during the coating processes.

In order to determine the oxidation states of Al and Nb on the surface of the coated LiNi_{0.5}Mn_{1.5}O₄ particle and also to examine the electronic interaction between the surface coating layer and LiNi_{0.5}Mn_{1.5}O₄ particle surface, the XPS spectra for the Al 2*p* of the AlO_x-coated LiNi_{0.5}Mn_{1.5}O₄ particle, for the Nb 3*d* of the NbO_x-coated LiNi_{0.5}Mn_{1.5}O₄ particle and for the Mn 2*p* of the pristine, AlO_x- and NbO_x-coated LiNi_{0.5}Mn_{1.5}O₄ particles were measured. Fig. S4 shows the XPS spectra (black lines), fitting curves (red lines) and deconvoluted curves (blue lines). The XPS spectrum (A-1) for the Al 2*p* of AlO_x-coated LiNi_{0.5}Mn_{1.5}O₄ cathode confirms the formation of an Al₂O₃ layer on the cathode particles. In this case, the Al 2*p*_{3/2} peak was observed at 74.27 eV, which is by 1.27 eV higher than the corresponding peak of Al metal. The observed value of 74.27 eV is consistent with the reported value for Al₂O₃ [34], indicating that Al₂O₃ layer is formed on the cathode surface. The XPS spectrum in the Nb 3*d* region of the NbO_x-coated LiNi_{0.5}Mn_{1.5}O₄ is shown in Fig. S4-(A-2). The spectrum was curve-fitted for a doublet, *i.e.*, 209.86 (Nb 3*d*_{3/2}) and 207.13 (Nb 3*d*_{5/2}) eV. These values are consistent with the values (209.26 and 206.51 eV)

reported for Nb (V) [35]. It can be thus concluded that the surface of LiNi_{0.5}Mn_{1.5}O₄ was covered with Nb₂O₅.

The XPS spectra for Mn 2*p* of (1) pristine LiNi_{0.5}Mn_{1.5}O₄, (2) Al₂O₃- and (3) Nb₂O₅-coated LiNi_{0.5}Mn_{1.5}O₄ particles were measured to confirm the electronic states of the Mn atom in the LiNi_{0.5}Mn_{1.5}O₄ particles (Fig. S4-(B)). The Mn 2*p* peaks for the Al₂O₃- (642.93 eV) and Nb₂O₅-coated (642.87 eV) LiNi_{0.5}Mn_{1.5}O₄ were found to shift by 0.47 and 0.41 eV, respectively, to higher binding energies when compared with the corresponding peak (642.46 eV) for the pristine LiNi_{0.5}Mn_{1.5}O₄. These peaks seen around 642 eV can be assigned to Mn³⁺ ions in the Al₂O₃- and Nb₂O₅-coated LiNi_{0.5}Mn_{1.5}O₄ particles [36]. The shifts of binding energy in Mn 2*p* to higher binding energies indicate that the oxidation number of Mn ions in the LiNi_{0.5}Mn_{1.5}O₄ increases slightly. One of the key factors of LIBs degradation is Mn dissolution from the cathode materials. Substantial efforts have been made to understand Mn dissolution mechanisms in a spinel LiMn₂O₄ in operation and further to improve battery performance. Lee et al. have discussed the mechanism of Mn dissolution and proposed the method for preventing or minimizing Mn dissolution as follows [37]. The introduction of cations with low oxidation number by doping to the spinel LiMn₂O₄ increases the oxidation state of Mn ions. When the oxidation number of Mn ions in the spinel LiMn₂O₄ increases, the overall concentration of Mn³⁺ ions decreases. This phenomenon seems to prevent the Jahn-Teller distortion and disproportionation reactions of unstable Mn³⁺ ions by reducing the concentration of Mn³⁺ ions; this eventually reduces Mn dissolution. The similar idea may be also applied to explain the XPS data obtained for the Mn 2*p* in the present case in which the cathode particles are dipped into the water-based slurry solution: Slight increase in the oxidation state of Mn ions in the LiNi_{0.5}Mn_{1.5}O₄ samples may mitigate the dissolution of Mn ions from the surface of these samples in the water-based slurry. Also in the XPS spectra for Ni 2*p* peaks measured with the Al₂O₃- and Nb₂O₅-coated LiNi_{0.5}Mn_{1.5}O₄ (Fig. S5), the Ni 2*p* peaks for the

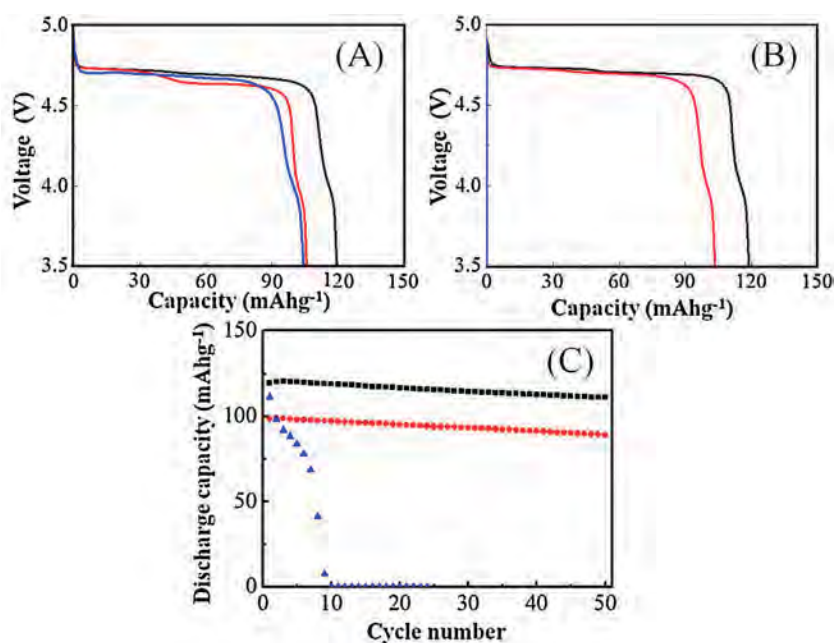


Fig. 4. Discharge voltage curves of LiNi_{0.5}Mn_{1.5}O₄ cathodes recorded at (A) 1st and (B) 10th cycle and (C) Cycle performance obtained with the LiNi_{0.5}Mn_{1.5}O₄ cathodes. The cathodes were prepared with (black lines and square) pristine LiNi_{0.5}Mn_{1.5}O₄ and PVDF binder, (red lines and circle) pristine LiNi_{0.5}Mn_{1.5}O₄ and water-based TRD202A binder, and (blue lines and triangle) “water-exposed” LiNi_{0.5}Mn_{1.5}O₄ and PVDF binder on Al current collectors. Note that the cathode prepared from the pristine LiNi_{0.5}Mn_{1.5}O₄ and water-based TRD202A binder was employed for the measurements immediately after its preparation, and “water-dispersed” means that the pristine LiNi_{0.5}Mn_{1.5}O₄ particle was dispersed in water for 12 h with magnetic stirrer. (For interpretation of the references to color in this figure legend, the reader is referred to the web version of this article.)

Al_2O_3 - (855.40 eV) and Nb_2O_5 -coated (855.28 eV) $\text{LiNi}_{0.5}\text{Mn}_{1.5}\text{O}_4$ are found to shift by 0.50 and 0.38 eV, respectively, to higher binding energies relative to the corresponding peak (854.90 eV) for the pristine $\text{LiNi}_{0.5}\text{Mn}_{1.5}\text{O}_4$. These peaks around 854 eV can be assigned to Ni^{2+} ions in the Al_2O_3 - and Nb_2O_5 -coated $\text{LiNi}_{0.5}\text{Mn}_{1.5}\text{O}_4$ samples [38]. The small increase in the oxidation state of Ni ions in the $\text{LiNi}_{0.5}\text{Mn}_{1.5}\text{O}_4$ samples also may contribute to preventing or minimizing the Ni dissolution as in the case of the above-mentioned Mn ions.

Thus, it can be concluded that the surface coating with Al_2O_3 and Nb_2O_5 induces the electronic protection against the dissolution of Mn and Ni atoms from the $\text{LiNi}_{0.5}\text{Mn}_{1.5}\text{O}_4$ surface to water.

3.2. Cycle performance and rate performance of surface-coated cathode materials

In order to check the water-resistant property of the pristine $\text{LiNi}_{0.5}\text{Mn}_{1.5}\text{O}_4$ particle, it was dispersed in water (i.e., “water-dispersed”) for 12 h with a magnetic stirrer, filtrated, and dried up at 100 °C and then the cathode film was prepared from the water-dispersed $\text{LiNi}_{0.5}\text{Mn}_{1.5}\text{O}_4$, PVDF binder and conducting carbon. The discharge voltage curves and cycle performance of the thus-prepared cathode are shown in Fig. 4 (blue line and circle). In addition, the cathode prepared from the water-based slurry composed of the pristine $\text{LiNi}_{0.5}\text{Mn}_{1.5}\text{O}_4$ particle, TRD202A binder and conductive carbon was also tested to confirm whether the surface of the pristine $\text{LiNi}_{0.5}\text{Mn}_{1.5}\text{O}_4$ particle has a water-resistant property (red line and circle) in the water-based slurry. The cathode prepared with the pristine $\text{LiNi}_{0.5}\text{Mn}_{1.5}\text{O}_4$ and PVDF binder as a reference sample (black line and circle) was also examined. At the 1st cycle, all the cathodes tested showed three discharge plateaus at around 4.7 and 4.0 V. The small plateau of ~4.0 V can reflect the amount of the residual Mn^{3+} in the $\text{LiNi}_{0.5}\text{Mn}_{1.5}\text{O}_4$ [39]. The amount of the residual Mn^{3+} is not dependent on the fabrication process of cathode films. The discharge capacity observed around 4.7 V for the cathode prepared with “water-exposed” $\text{LiNi}_{0.5}\text{Mn}_{1.5}\text{O}_4$ and PVDF binder is, although slightly, decreased. This may be due to the fact that Ni ions in the $\text{LiNi}_{0.5}\text{Mn}_{1.5}\text{O}_4$ particles are damaged by water contact, and as a result, the redox reaction of Ni ion ($\text{Ni}^{2+} \leftrightarrow \text{Ni}^{4+}$) taking place along with the Li^+ intercalation/deintercalation for discharging/charging processes do not occur on the surface of $\text{LiNi}_{0.5}\text{Mn}_{1.5}\text{O}_4$ particles [39]. At the 10th cycle, the $\text{LiNi}_{0.5}\text{Mn}_{1.5}\text{O}_4$ cathode prepared with the water-based slurry keeps the three-stage voltage plateau (red line). However, the cathode prepared with the “water-dispersed” $\text{LiNi}_{0.5}\text{Mn}_{1.5}\text{O}_4$ is entirely dead (blue line). When compared with the cycle performance of the cathode prepared with the pristine $\text{LiNi}_{0.5}\text{Mn}_{1.5}\text{O}_4$ and PVDF binder (as a reference), the cathode prepared from the pristine $\text{LiNi}_{0.5}\text{Mn}_{1.5}\text{O}_4$ and water-based TRD202A binder slurry exhibited a usual discharge capacity which can be observed for $\text{LiNi}_{0.5}\text{Mn}_{1.5}\text{O}_4$ [36,40], whereas the “water-dispersed” $\text{LiNi}_{0.5}\text{Mn}_{1.5}\text{O}_4$ cathode gave the large decrease in discharge capacity with charge/discharge cycling and the discharge capacity was zero actually after 10 cycles. The results indicate that the $\text{LiNi}_{0.5}\text{Mn}_{1.5}\text{O}_4$ particle is badly damaged in the contact with water and that the discharge performance of the $\text{LiNi}_{0.5}\text{Mn}_{1.5}\text{O}_4$ cathode prepared with the water-based TRD202A binder is, even when used immediately after its preparation, inferior to that obtained for the cathode prepared with the pristine $\text{LiNi}_{0.5}\text{Mn}_{1.5}\text{O}_4$ and PVDF binder.

Next, the charge/discharge cycle performance of the carbon-coated, Al_2O_3 -coated and Nb_2O_5 -coated $\text{LiNi}_{0.5}\text{Mn}_{1.5}\text{O}_4$ cathodes with various coating amounts was examined, in which the individual coated particles were exposed to the water-based binder slurry during preparing the water-based binder slurry and the cathode films were fabricated immediately after preparing the

water-based binder slurry. The typical results of such a charge/discharge cycling examination are shown in Fig. 5, in which the results obtained for the pristine $\text{LiNi}_{0.5}\text{Mn}_{1.5}\text{O}_4$ cathode prepared with PVDF/NMP slurry are also shown for comparison (black circle) and the charge/discharge voltage curves obtained are shown in Fig. S6. From Fig. S6, it can be seen that the $\text{LiNi}_{0.5}\text{Mn}_{1.5}\text{O}_4$ samples with and without the coating have similar charge–discharge profiles, exhibiting two charge plateaus and three discharge plateaus in the potential region from 3.5 to 4.8 V. Larger electrode impedance resulting from the surface coating cannot be almost implied from the charge/discharge curves of Fig. S6. When compared with the pristine $\text{LiNi}_{0.5}\text{Mn}_{1.5}\text{O}_4$ cathode, the carbon-,

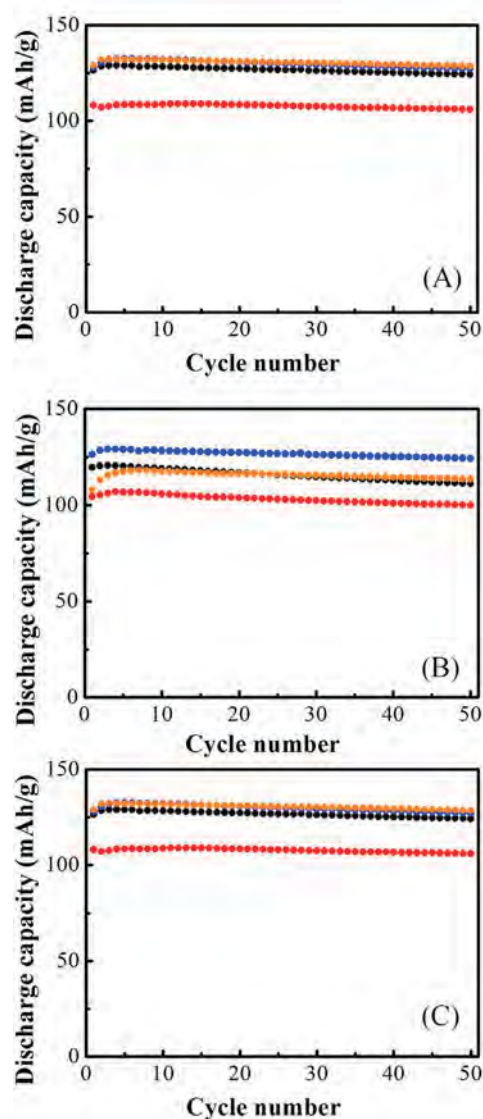


Fig. 5. Cycle performance obtained with (A) carbon-, (B) Al_2O_3 - and (C) Nb_2O_5 -coated $\text{LiNi}_{0.5}\text{Mn}_{1.5}\text{O}_4$ cathodes. Coating amounts of carbon, Al_2O_3 and Nb_2O_5 : (red circle) 0.5, (blue circle) 1.0 and (orange circle) 1.5 wt% (but 10 wt% in (A)). In every case, black circles correspond to the cathode prepared with pristine $\text{LiNi}_{0.5}\text{Mn}_{1.5}\text{O}_4$ and PVDF binder. Note that in the case of A and C the blue circles are overlapping almost with the orange ones. The carbon-, Al_2O_3 - and Nb_2O_5 -coated cathode particles were exposed to the water-based binder slurry (in the case of 1 wt% coating, it was composed of 910 mg cathode material, 50 mg AB, 10 mg CMC and 30 mg TRD202A in 10 mL H_2O) during preparing the water-based binder slurry and the cathode films were prepared immediately after preparing the water-based binder slurry. (For interpretation of the references to color in this figure legend, the reader is referred to the web version of this article.)

Al_2O_3 - and Nb_2O_5 -coated $\text{LiNi}_{0.5}\text{Mn}_{1.5}\text{O}_4$ cathodes exhibited lower discharge capacity because of the contact (and the subsequent dissolution of Mn and Ni) of the cathode surfaces with water during the exposure treatment in the water-based polymer binder solution, i.e., their imperfect surface coating.

The discharge capacity-cycle number performance obtained for the carbon-, Al_2O_3 - and Nb_2O_5 -coated (1 wt%) $\text{LiNi}_{0.5}\text{Mn}_{1.5}\text{O}_4$ cathodes was almost the same as that obtained for the cathode prepared with the pristine $\text{LiNi}_{0.5}\text{Mn}_{1.5}\text{O}_4$ and PVdF binder, indicating that these coated-cathode material particles were not damaged even in contact with water. However, increasing the coating amount of Al_2O_3 to 1.5 wt% led to the decrease in the discharge capacity probably because the intercalation/deintercalation of Li^+ to/from the cathode materials was inhibited accordingly. In contrary to the Al_2O_3 coating, carbon-coated (10 wt%) and Nb_2O_5 -coated (1.5 wt%) $\text{LiNi}_{0.5}\text{Mn}_{1.5}\text{O}_4$ cathodes did not show any degradation of discharge capacities. At the surface coating of more than 10 and 1.5 wt% with carbon and Nb_2O_5 , respectively, the decrease in the charge/discharge capacity due to the inhibition of the intercalation/deintercalation of Li^+ ions by thick coating could be observed from the first cycle (not shown here). The optimized coating amount of carbon, Al_2O_3 and Nb_2O_5 on the $\text{LiNi}_{0.5}\text{Mn}_{1.5}\text{O}_4$ cathode particles was found to be 1 wt% in this study.

Fig. 6 shows the discharge rate performance of the pristine, carbon-coated and metal oxide-coated $\text{LiNi}_{0.5}\text{Mn}_{1.5}\text{O}_4$ cathodes at room temperature. All the cells were charged at the same current with a 0.1C rate to ensure identical initial conditions for each discharge. The discharge current was changed as 0.1, 0.2, 0.5, 1, 2, 3 and 5C. It is clear from this figure that the discharge rate performance of carbon-coated and metal oxide-coated $\text{LiNi}_{0.5}\text{Mn}_{1.5}\text{O}_4$ cathodes is influenced by the surface coating for giving the cathode particle surface a water-resistant property. While the pristine sample has the capacity retention of 85% in 5C, the carbon-, Al_2O_3 - and Nb_2O_5 -coated $\text{LiNi}_{0.5}\text{Mn}_{1.5}\text{O}_4$ cathodes exhibit the capacity retention of 75, 74 and 82%, respectively, in 5C. The carbon-coated and metal oxide-coated $\text{LiNi}_{0.5}\text{Mn}_{1.5}\text{O}_4$ cathodes sacrifice the rate performance for giving the cathode particle surface a water-resistant property because of blocking the diffusion of Li^+ ions through the coating. However, the degradation of rate performance is not so much large. Among the surface coatings examined in this study, the carbon coating gave the worst discharge capacity characteristic. The Nb_2O_5 -coated $\text{LiNi}_{0.5}\text{Mn}_{1.5}\text{O}_4$ exhibited a relatively lower capacity retention probably due to the

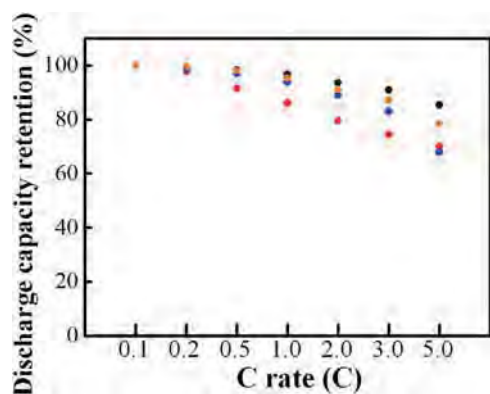


Fig. 6. The rate performance obtained with the cathodes prepared with (black circle) pristine $\text{LiNi}_{0.5}\text{Mn}_{1.5}\text{O}_4$, (red circle) carbon-coated (coating amount of carbon: 2 wt%), (blue circle) Al_2O_3 -coated (1 wt%), and (orange circle) Nb_2O_5 -coated (1 wt%) $\text{LiNi}_{0.5}\text{Mn}_{1.5}\text{O}_4$. The carbon-, Al_2O_3 - and Nb_2O_5 -coated particles were exposed to the water-based slurry during preparing the water-based binder slurry (see the caption of Fig. 5). (For interpretation of the references to color in this figure legend, the reader is referred to the web version of this article.)

ununiform distribution of Nb_2O_5 layer as shown in Fig. 2(C) and discussed above.

3.3. Durability of the water-based slurry containing surface-coated cathode materials

Shown in Fig. 7 the charge/discharge cycle performance of the pristine and carbon- and metal oxide-coated $\text{LiNi}_{0.5}\text{Mn}_{1.5}\text{O}_4$ cathode materials which were prepared from the corresponding cathode materials after exposing them to the water-based polymer binder slurry solution without a stirring for one week. As presumed from Fig. 4(C), the non-coated, pristine $\text{LiNi}_{0.5}\text{Mn}_{1.5}\text{O}_4$ cathode could not entirely hold the battery property observed for the cathode prepared with the pristine $\text{LiNi}_{0.5}\text{Mn}_{1.5}\text{O}_4$ and PVdF binder (Fig. 7, black circle). On the other hand, the carbon- and metal oxide-coated $\text{LiNi}_{0.5}\text{Mn}_{1.5}\text{O}_4$ cathodes exhibited a stable charge/discharge cycle performance. Thus, it was confirmed that the surface coating of $\text{LiNi}_{0.5}\text{Mn}_{1.5}\text{O}_4$ with carbon and metal oxides can provide a water-resistant property to the cathode particles. The difference in discharge capacity of three kinds of the coated cathodes might reflect the difference in the surface coverage of the individual coatings.

Fig. 8 shows STEM-EELS images of (a) pristine $\text{LiNi}_{0.5}\text{Mn}_{1.5}\text{O}_4$, (b) water-exposed $\text{LiNi}_{0.5}\text{Mn}_{1.5}\text{O}_4$ and (c) water-exposed, Al_2O_3 -coated $\text{LiNi}_{0.5}\text{Mn}_{1.5}\text{O}_4$ in which “water-exposed” means that $\text{LiNi}_{0.5}\text{Mn}_{1.5}\text{O}_4$ (b) and Al_2O_3 -coated $\text{LiNi}_{0.5}\text{Mn}_{1.5}\text{O}_4$ (c) particles were exposed in the water-based slurry for one week. The elemental distributions of the individual samples are largely different depending on the exposure to the water-based slurry and the surface coating.

As can be seen from Fig. S7, the surface of the pristine $\text{LiNi}_{0.5}\text{Mn}_{1.5}\text{O}_4$ exhibits a uniform distribution of Li, Mn and Ni atoms. On the other hand, in the surface of the water-exposed $\text{LiNi}_{0.5}\text{Mn}_{1.5}\text{O}_4$ (Fig. S8), Li atom (b) is dissolved in the thickness of over 10 nm, and the defect layer of Mn (c) is about 2–3 nm. Even Ni (d) is also leached out from the metal oxide layer in the thickness of less than 2 nm, by judging from the position (Fig. S8-(e)) of the edge of oxygen atom and STEM image (a). The comparison of two images ((a) and (b)) in Fig. 8 clearly indicates the difference in the distribution of the atoms contained in the surfaces of the pristine and water-exposed $\text{LiNi}_{0.5}\text{Mn}_{1.5}\text{O}_4$ samples. The Al_2O_3 -coated $\text{LiNi}_{0.5}\text{Mn}_{1.5}\text{O}_4$ (c) exhibits almost the same image as that observed for the pristine $\text{LiNi}_{0.5}\text{Mn}_{1.5}\text{O}_4$ (a). A uniform distribution of Li, Mn and Ni atoms over the water-exposed surface can be seen. That is, on the surface of the water-exposed Al_2O_3 -coated $\text{LiNi}_{0.5}\text{Mn}_{1.5}\text{O}_4$,

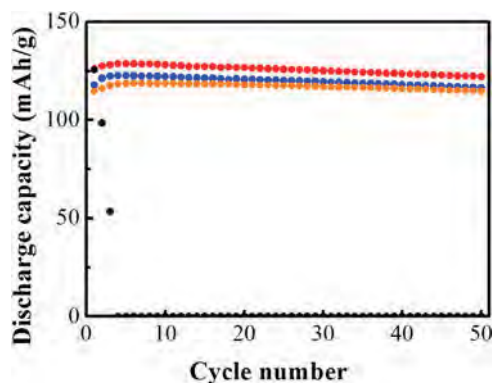


Fig. 7. Cycle performance obtained with the cathodes prepared with (black circle) pristine $\text{LiNi}_{0.5}\text{Mn}_{1.5}\text{O}_4$ and PVdF binder, (red circle) carbon-coated, (blue circle) Al_2O_3 -coated, and (orange circle) Nb_2O_5 -coated $\text{LiNi}_{0.5}\text{Mn}_{1.5}\text{O}_4$ (each coating amount: 1 wt%). All the cathode particles were exposed to the water-based slurry for one week. (For interpretation of the references to color in this figure legend, the reader is referred to the web version of this article.)

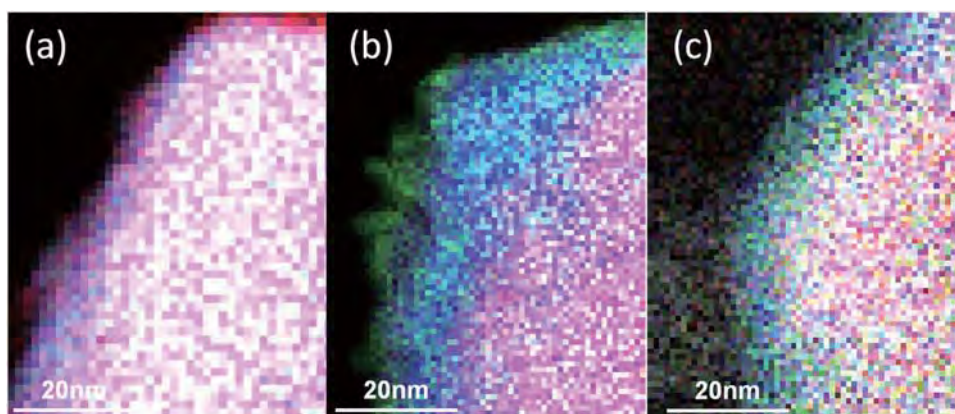


Fig. 8. STEM-EELS mapping of Li (red), Mn (blue), Ni (green), Al (light blue) and O (white) atoms on (a) pristine $\text{LiNi}_{0.5}\text{Mn}_{1.5}\text{O}_4$, (b) water-exposed $\text{LiNi}_{0.5}\text{Mn}_{1.5}\text{O}_4$ and (c) water-exposed, Al_2O_3 -coated $\text{LiNi}_{0.5}\text{Mn}_{1.5}\text{O}_4$ samples. “Water-exposed” means that the samples were exposed to the water-based slurry for one week. (For interpretation of the references to color in this figure legend, the reader is referred to the web version of this article.)

Li, Mn and Ni are uniformly distributed (Fig. S9) and, moreover, their dissolution is inhibited by Al_2O_3 coating. The surface coating by Al_2O_3 gave the particle surface a water-resistant property and thus significantly reduced the dissolution of Li, Mn and Ni atoms from the Al_2O_3 -coated $\text{LiNi}_{0.5}\text{Mn}_{1.5}\text{O}_4$ surface when it was exposed to the water-based binder slurry solution. From the above-mentioned SEM and TEM experiments, the “physically” perfect coating was not confirmed. Thus, the observed surface water-resistant property might be due to an electronic effect from the coating layer as well as keeping the particle surface in isolation from water by Al_2O_3 coating, as mentioned above based on the XPS results. In conclusion, we can say that the surface treatment with carbon and metal oxide coating to isolate the cathode particle surface from water and the change in electronic states of Mn and Ni atoms caused by the coating provide the observed water-resistant property. The shift of the STEM-EELS spectrum (Fig. S10) to the direction of higher energy loss for Li K-edge of the Al_2O_3 -coated $\text{LiNi}_{0.5}\text{Mn}_{1.5}\text{O}_4$ cathode (when compared with that of the pristine $\text{LiNi}_{0.5}\text{Mn}_{1.5}\text{O}_4$) may suggest that the dissolution of the Li atoms in the Al_2O_3 -coated $\text{LiNi}_{0.5}\text{Mn}_{1.5}\text{O}_4$ cathode from the surface becomes more retardant.

4. Conclusions

In this study, in order to establish the protocol to prepare water-resistant cathode materials of LIBs which can be used in the cathode preparation with water-based binders, carbon- and metal oxide-coated $\text{LiNi}_{0.5}\text{Mn}_{1.5}\text{O}_4$ cathode materials were prepared and the performance of the batteries prepared from these cathode materials with and without a water-resistant property was compared in the viewpoint of charge/discharge cycleability and discharge rate performance. The carbon and metal oxides (Al_2O_3 and Nb_2O_5) coating on the $\text{LiNi}_{0.5}\text{Mn}_{1.5}\text{O}_4$ cathode particles clearly suppressed the degradation in charge/discharge cycleability which is caused by contacting the particle surfaces with water. Namely, the carbon-, Al_2O_3 - and Nb_2O_5 -coated $\text{LiNi}_{0.5}\text{Mn}_{1.5}\text{O}_4$ cathode particles were found to possess a water-resistant property even when kept in the water-based TRD202A binder slurry for one week. These results indicate that the surface coating of the $\text{LiNi}_{0.5}\text{Mn}_{1.5}\text{O}_4$ cathode is effective to keep its battery performance even after contacting it with water. The observed water-resistant property may originate from an electronic effect from the coating as well as the isolation of the particle surface from water by the coating. However, pH increase of the water-based slurry with lengthening the storage time in it (e.g., after the storage of one week, the

solution pH reached around pH 10) due to dissolution of the cathode particle surface could not be entirely suppressed by the surface coating tried in this study. Further study on the surface coating materials with a higher water-resistant property is now in progress to develop the cathode materials which could not suffer from the chemical damage even in contact with water for a while (typically 30 days).

Acknowledgements

This work was financially supported by the Strategic Research Base Development Program for Private Universities of the Ministry of Education, Culture, Sports, Science and Technology (MEXT), Japan. The authors are grateful to Dr. Keiichi Osaka, JASRI, for his help in XRD measurements at BL19B2 of SPring-8 (Proposal No. 2015B1618, 2016A1560). We thanks K. Shinoda for his help in STEM measurements at National Institute for Materials Science (NIMS) Battery Research Platform.

Appendix A. Supplementary data

Supplementary data associated with this article can be found, in the online version, at <http://dx.doi.org/10.1016/j.electacta.2016.12.064>.

References

- [1] D.L. Wood III, J. Li, C. Daniel, Prospects for reducing the processing cost of lithium ion batteries, *J. Power Sources* 275 (2015) 234–242.
- [2] N. Yuca, H. Zhao, X. Song, M.F. Dogdu, W. Yuan, Y. Fu, V.S. Battaglia, X. Xiao, G. Liu, A Systematic Investigation of Polymer Binder Flexibility on the Electrode Performance of Lithium-Ion Batteries, *ACS Appl. Mater. Interfaces* 6 (2014) 17111–17118.
- [3] N. Yabuuchi, Y. Kinoshita, K. Misaki, T. Natsuyama, S. Komaba, Electrochemical Properties of LiCoO_2 Electrodes with Latex Binders on High-Voltage Exposure, *J. Electrochem. Soc.* 162 (2015) A538–A544.
- [4] M. He, L.X. Yuan, W.X. Zhang, X.L. Hu, Y.H. Huang, Enhanced Cyclability for Sulfur Cathode Achieved by a Water-Soluble Binder, *J. Phys. Chem. C* 115 (2011) 15703–15709.
- [5] M. Mancini, F. Nobili, R. Tossici, M.W. Mehrens, R. Marassi, High performance, environmentally friendly and low cost anodes for lithium-ion battery based on TiO_2 anatase and water soluble binder carboxymethyl cellulose, *J. Power Sources* 196 (2011) 9665–9671.
- [6] S. Komaba, N. Yabuuchi, T. Ozeki, Z.J. Han, K. Shimomura, H. Yui, Y. Katayama, T. Miura, Comparative Study of Sodium Polyacrylate and Poly(vinylidene fluoride) as Binders for High Capacity $\text{Si}/\text{Graphite}$ Composite Negative Electrodes in Li-Ion Batteries, *J. Phys. Chem. C* 116 (2012) 1380–1389.
- [7] M. Sun, H. Zhong, S. Jiao, H. Shao, L. Zhang, Investigation on Carboxymethyl Chitosan as New Water Soluble Binder for LiFePO_4 Cathode in Li-Ion Batteries, *Electrochim. Acta* 127 (2014) 239–244.

- [8] S. Klamor, M. Schröder, G. Brunklaus, P. Niehoff, F. Berkemeier, F.M. Schappacher, M. Winter, *Phys. Chem. Chem. Phys.* 175 (2015) 632–6641.
- [9] P.P. Prossini, C. Cento, M. Carewska, A. Masci, *Solid State Ionics* 274 (2015) 34–39.
- [10] K. Prasanna, T. Subburaj, Y.N. Jo, W.J. Lee, C.W. Lee, Environment-Friendly Cathodes Using Biopolymer Chitosan with Enhanced Electrochemical Behavior for Use in Lithium Ion Batteries, *ACS Appl Mater. Interfaces* 7 (2015) 7884–7890.
- [11] P.P. Prossini, M. Carewska, A. Masci, A high voltage cathode prepared by using polyvinyl acetate as a binder, *Solid State Ionics* 274 (2015) 88–93.
- [12] J. He, J. Wang, H. Zhong, J. Ding, L. Zhang, Cyanoethylated Carboxymethyl Chitosan as Water Soluble Binder with Enhanced Adhesion Capability and electrochemical performances for LiFePO₄ Cathode, *Electrochim Acta* 182 (2015) 900–907.
- [13] W.Y. Chou, Y.C. Jin, J.G. Duh, C.Z. Lu, S.C. Liao, A facile approach to derive binder protective film on high voltage spinel cathode materials against high temperature degradation, *Appl. Surf. Sci.* 355 (2015) 1272–1278.
- [14] G.M. Solomon, E.P. Morse, M.J. Garbo, D.K. Milton, Stillbirth after occupational exposure to N-methyl-2-pyrrolidone. A case report and review of the literature, *J. Occup. Environ. Med.* 38 (1996) 705–713.
- [15] T. Pinter, F. Hof, Just add tetrazole: 5-(2-Pyrrolo)tetrazoles are simple highly potent anion recognition elements, *Chem. Commun.* 47 (2011) 12688–12690.
- [16] H. Buqa, M. Holzapfel, F. Krumeich, C. Veit, P. Novák, Study of styrene butadiene rubber and sodium methyl cellulose as binder for negative electrodes in lithium-ion batteries, *J. Power Sources* 161 (2006) 617–622.
- [17] H.-H. Lee, S. Lee, U. Paik, Y.-M. Choi, Aqueous processing of natural graphite particulates for lithium-ion battery anodes and their electrochemical performance, *J. Power Sources* 147 (2005) 249–255.
- [18] Q. Wu, S. Ha, J. Prakash, D.W. Dees, W. Lu, Investigations on high energy lithium-ion batteries with aqueous binder, *Electrochim. Acta* 114 (2013) 1–6.
- [19] P.P. Prossini, M. Carewska, A. Masci, A high voltage cathode prepared by using polyvinyl acetate as a binder, *Solid State Ionics* 274 (2015) 88–93.
- [20] N. Notake, T. Gunji, S. Kosemura, Y. Mochizuki, T. Tanabe, S. Kaneko, S. Ugawa, H. Lee, F. Matsumoto, The application of a water-based hybrid polymer binder to a high-voltage and high-capacity Li-rich solid-solution cathode and its performance in Li-ion batteries, *J. Appl. Electrochem.* 46 (2016) 267–278.
- [21] H. Li, H. Zhou, Enhancing the performances of Li-ion batteries by carbon-coating: present and future, *Chem. Commun.* 48 (2012) 1201–1217.
- [22] J. Liu, Q. Wang, B.R. Jayan, A. Manthiram, Carbon-coated high capacity layered Li[Li_{0.2}Mn_{0.54}Ni_{0.13}Co_{0.13}]O₂ cathodes, *Electrochem. Commun.* 12 (2010) 750–753.
- [23] G. Kobayashi, Y. Irii, F. Matsumoto, A. Ito, Y. Ohsawa, S. Yamamoto, Y. Cui, J.-Y. Son, Y. Sato, Improving cycling performance of Li-rich layered cathode materials through combination of Al₂O₃-based surface modification and stepwise precycling, *J. Power Sources* 303 (2016) 250–256.
- [24] E. Zhao, X. Liu, H. Zhao, X. Xiao, Z. Hu, Ion conducting Li₂SiO₃-coated lithium-rich layered oxide exhibiting high rate capability and low polarization, *Chem. Commun.* 51 (2015) 9093–9096.
- [25] L. Shen, H. Li, E. Uchaker, X. Zhang, G. Cao, Environment-Friendly Cathodes Using Biopolymer Chitosan with Enhanced Electrochemical Behavior for Use in Lithium Ion Batteries, *Nano Lett.* 12 (2012) 5673–5678.
- [26] Y. Fan, J. Wang, Z. Tang, W. He, J. Zhang, Effects of the nanostructured SiO₂ coating on the performance of LiNi_{0.5}Mn_{1.5}O₄ cathode materials for high-voltage Li-ion batteries, *Electrochim Acta* 52 (2007) 3870–3875.
- [27] Q.Y. Wang, J. Liu, A.V. Murugan, A. Manthiram, High capacity double-layer surface modified Li[Li_{0.2}Mn_{0.54}Ni_{0.13}Co_{0.13}]O₂ cathode with improved rate capability, *J. Mater. Chem.* 19 (2009) 4965–4972.
- [28] Z. Chen, Y. Qin, K. Amine, Y.-K. Sun, Role of surface coating on cathode materials for lithium-ion batteries, *J. Mater. Chem.* 20 (2010) 7606–7612.
- [29] X.-W. Gao, C.-Q. Feng, S.-L. Chou, J.-Z. Wang, J.-Z. Sun, M. Forsyth, D.R. MacFarlane, H.K. Liu, LiNi_{0.5}Mn_{1.5}O₄ spinel cathode using room temperature ionic liquid as electrolyte, *Electrochim. Acta* 101 (2013) 151–157.
- [30] T. Ohzuku, S. Takeda, M. Iwanaga, Solid-state redox potentials for Li[Me_{1/2}Mn_{3/2}]O₄ (Me: 3d-transition metal) having spinel-framework structures: a series of 5 volt materials for advanced lithium-ion batteries, *J. Power Sources* 81 (1999) 90–94.
- [31] Q. Zhong, A. Bonakdarpour, M. Zhang, Y. Gao, J.R. Dahn, Advances in Stabilizing 'Layered-Layered' xLi₂MnO₃-(1-x)LiMO₂ (M = Mn, Ni Co) Electrodes with a Spinel Component, *J. Electrochem. Soc.* 144 (1997) 205–213.
- [32] N.P.W. Pieczonka, Z. Liu, P. Lu, K.L. Olson, J. Mootte, B.R. Powell, J.H. Kim, Understanding Transition-Metal Dissolution Behavior in LiNi_{0.5}Mn_{1.5}O₄ High-Voltage Spinel for Lithium Ion Batteries, *J. Phys. Chem. C* 117 (2013) 15947–15957.
- [33] H. Wang, H. Xia, M.O. Lai, L. Lu, *Electrochem. Commun.* 1 (2009) 1539–1542.
- [34] X. Zhang, I. Belharouak, L. Li, Y. Lei, J.W. Elam, A. Nie, X. Chen, R.S. Yassar, R.L. Axeibaum, Structural and Electrochemical Study of Al₂O₃ and TiO₂ Coated Li_{1.2}Ni_{0.13}Mn_{0.54}Co_{0.13}O₂ Cathode Material Using ALD, *Adv. Energy Mater.* 3 (2013) 1299–1307.
- [35] A.L. Viet, M.V. Reddy, R. Jose, B.V.R. Chowdari, S. Ramakrishna, General Strategy for Designing Core-Shell Nanostructured Materials for High-Power Lithium Ion Batteries, *J. Phys. Chem. C* 114 (2010) 664–671.
- [36] K. Raju, F.P. Nkosi, E. Viswanathan, M.K. Mathe, K. Damodaran, K.I. Ozoemena, Microwave-enhanced electrochemical cycling performance of the LiNi_{0.2}Mn_{1.8}O₄ spinel cathode material at elevated temperature, *Phys. Chem. Chem. Phys.* 18 (2016) 13074–13083.
- [37] Y.K. Lee, J. Park, W. Lu, Electronic and Bonding Properties of LiMn₂O₄ Spinel with Different Surface Orientations and Doping Elements and Their Effects on Manganese Dissolution, *J. Electrochem. Soc.* 163 (2016) A1359–A1368.
- [38] N.D. Rosedhi, N.H. Idris, M.M. Rahman, M.F.M. Din, J. Wang, Disordered spinel LiNi_{0.5}Mn_{1.5}O₄ cathode with improved rate performance for lithium-ion batteries, *Electrochim. Acta* 206 (2016) 374–380.
- [39] H. Liu, J. Wang, X. Zhang, D. Zhou, X. Qi, B. Qiu, J. Fang, R. Kloepsch, G. Schumacher, Z. Liu, J. Li, Morphological Evolution of High-Voltage Spinel LiNi_{0.5}Mn_{1.5}O₄ Cathode Materials for Lithium-Ion Batteries: The Critical Effects of Surface Orientations and Particle Size, *ACS Appl. Mater. Interfaces* 8 (2016) 4661–4675.
- [40] J. Mao, K. Dai, M. Xuan, G. Shao, R. Qiao, W. Yang, V.S. Battaglia, G. Liu, Effect of Chromium and Niobium Doping on the Morphology and Electrochemical Performance of High-Voltage Spinel LiNi_{0.5}Mn_{1.5}O₄ Cathode Material, *ACS Appl. Mater. Interfaces* 8 (2016) 9116–9124.

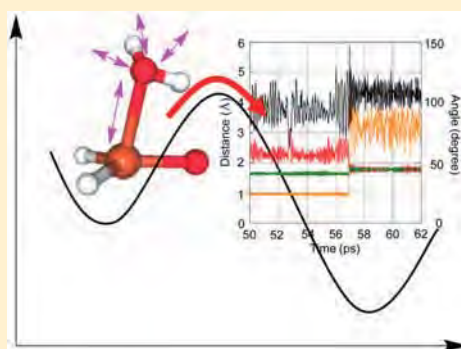
Theoretical Study of the Heterolytic σ Bond Cleavage on the Ge=O Bond of Germanone. An Insight into the Driving Force from Both Electronic and Dynamical Aspects

Toshiaki Matsubara*^{1b} and Tomoyoshi Ito

Department of Chemistry, Faculty of Science, Kanagawa University, 2946, Tsuchiya, Hiratsuka, Kanagawa 259-1293, Japan

Supporting Information

ABSTRACT: The mechanism of the σ bond cleavage of H₂O, NH₃, Me₂C=O, H₂, CH₄, BH₃, and SiH₄ on the Ge=O bond of germanone is examined by means of both quantum mechanical (QM) and molecular dynamics (MD) methods. The QM calculations show that the σ bonds of all the substrates are heterolytically broken on the very largely polarized Ge=O bond. Before the σ bond cleavage, the substrate at first approach the Ge=O germanium in the cases of H₂O, Me₂C=O, and NH₃, and in contrast, the Ge=O oxygen in the cases of H₂, CH₄, BH₃, and SiH₄. For the cases of H₂O, NH₃, and Me₂C=O, a cluster in which the substrate coordinates to the Ge exists before the σ bond cleavage, and this coordination of the substrate plays an important role on the heterolytic σ bond cleavage. The QM-MD simulations are also conducted for the case of H₂O, and they show that the kinetic energy of the H₂O-coordinated cluster especially concentrates on the coordinated H₂O oxygen to strongly oscillate the coordinate bond between the H₂O oxygen and the Ge. This oscillation further enlarges just before the O—H σ bond cleavage, and the kinetic energy of this oscillation would be transmitted to the normal mode of the O—H bond breaking. Thus, the coordination and the vibration of the H₂O oxygen was thought to be an important driving force of the heterolytic cleavage of the O—H σ bond in both electronic and dynamical aspects.



INTRODUCTION

When the carbonyl carbon of ketone R₂C=O is replaced by silicon or germanium, its stability is largely reduced, because the Si=O or the Ge=O double bond strongly polarizes and becomes highly reactive compared to the C=O double bond due to the greater difference in the electronegativities between the O and the Si or the Ge atoms and the less effective sp²-hybridization. Silanone and germanone R₂E=O (E = Si and Ge) indeed easily polymerize to form stable oligomeric or polymeric materials, although ketone exist as a monomer. Therefore, silanone and germanone have not been isolated until recently. On one hand, silanones had been only isolated in argon matrixes^{1–9} and in the gas phase,^{10,11} and first isolated by the electronic stabilization provided by transition-metal fragments.¹² On the other hand, germanone was also detected in a cryogenic matrix^{13,14} or in solution^{15–18} before the isolation.

It has been thought that these unstable silanone and germanone R₂E=O (E = Si and Ge) can be stabilized by an electron donor base or by an introduction of sterically bulky substituents on the E atom to protect the delicate E=O group. In fact, the various E=O double-bonded species have been isolated by the coordination of electron donor bases to the electron-deficient E atom.^{19–29} Tokitoh and co-workers have reported a monomeric germanone (Tbt) (Tip)Ge=O with the bulky substituents, Tbt = 2,4,6-tris[bis(trimethylsilyl)methyl]phenyl and Tip = 2,4,6-triisopropylphenyl, which is stable in

solution.¹⁵ Recently, Tamao and co-workers have succeeded in isolating the germanone (Eind)₂Ge=O by the incorporation of bulky substituents called Eind (1,1,3,3,5,5,7,7-octaethyl-*s*-hydrindacen-4-yl).³⁰ The computation at the B3LYP/6-31G(d,p) level of theory as well as the X-ray structure has shown that the isolated monomeric germanone has a planar tricoordinate structure. The computational results of the molecular orbital and the electrostatic potential revealed the large polarization of the Ge=O double bond. Some other groups have also conducted the theoretical calculations for germanone and its derivatives.^{31–37} Pandey has reported the optimized geometries of the germanones, (Eind)₂Ge=O, (Tbt) (Tip)-Ge=O, and R₂Ge=O (R = Ph and Me), by the density functional theory (DFT) calculations.³⁸

The isolated (Eind)₂Ge=O is really very reactive as experimentally reported by Tamao and co-workers. Reactions that do not proceed in the case of ketone easily proceed in the case of germanone. For example, the O—H bond of water adds to the Ge=O bond of germanone quickly at room temperature to form the germanediol. Acetone, phenylsilane, and CO₂ also react with the Ge=O to form the (hydroxyl)germyl enolate, the hydrosilylation product and the cyclic carbonate, respectively.

Received: December 12, 2016

Revised: January 30, 2017

Published: February 20, 2017

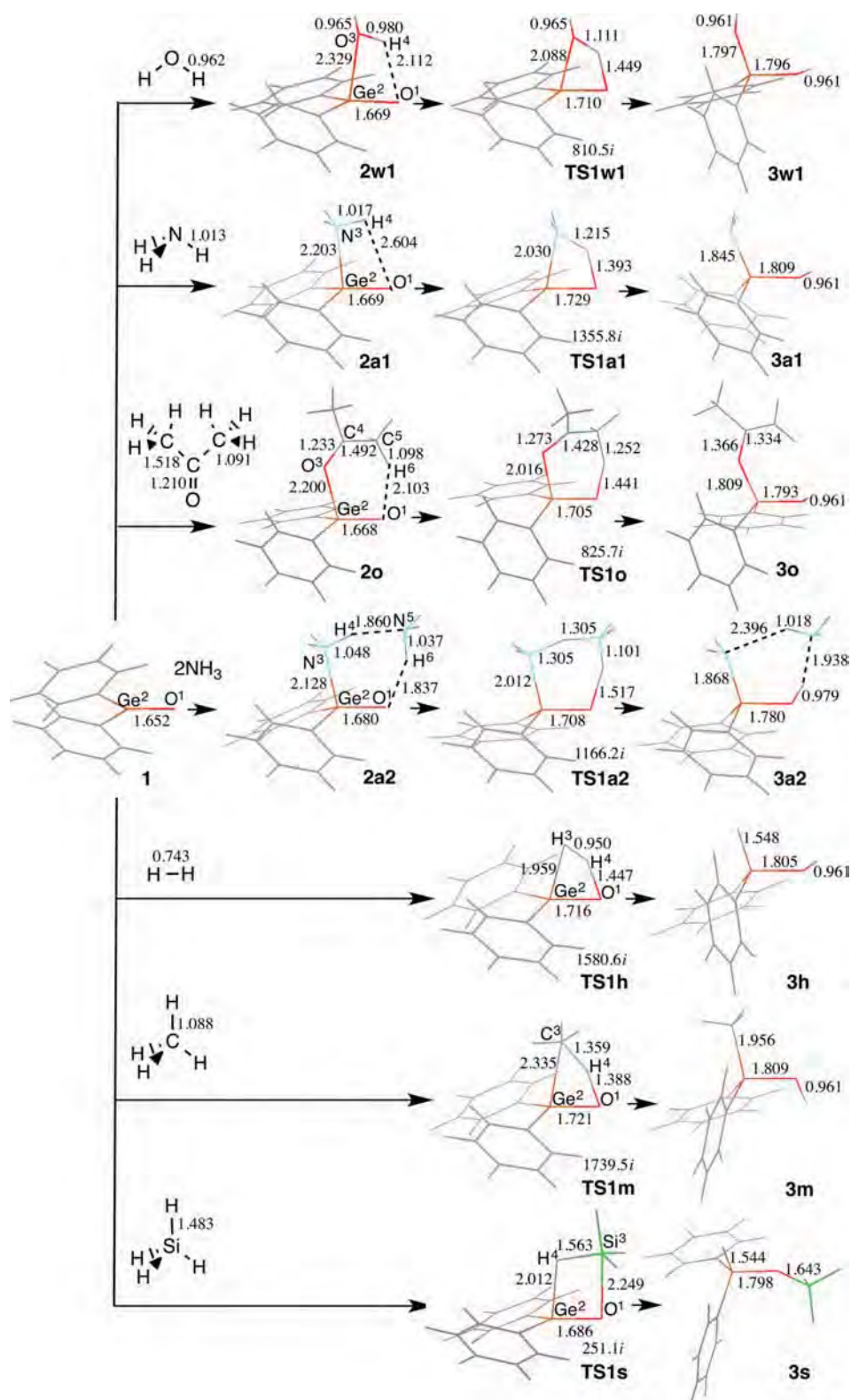


Figure 1. Optimized equilibrium and transition state structures (Å) of the reaction of $\text{Ph}_2\text{Ge}=\text{O}$ with H_2O , NH_3 , $(\text{CH}_3)_2\text{C}=\text{O}$, H_2 , CH_4 , and SiH_4 at the B3LYP/BSI level.

On the basis of the experimental results of the reactivity of germanone reported by Tamao and co-workers, Jissy and co-workers have investigated the nucleophilic addition of water

and CO_2 to germanones by the DFT method.³⁹ However, the detail of the reaction mechanism of the cleavage of the chemical bond on the $\text{Ge}=\text{O}$ double bond has not been clarified,

although the property and the reactivity of the germanon have been examined.

In this study, we therefore examine the mechanism of the σ bond cleavage on the Ge=O bond of germanone by means of both quantum mechanical (QM) and molecular dynamics (MD) methods. Here, we used H₂O, NH₃, Me₂C=O, H₂, CH₄, BH₃, and SiH₄ as a model substrate and Ph₂Ge=O and H₂Ge=O as a model germanone in addition to the real germanone (Eind)₂Ge=O. First, we analyze the reaction mechanism for all the substrate by the quantum mechanical (QM) method; second, we shed light on the dynamic factor that produces the driving force of the reaction taking account of the thermal motion of the molecule in the case of the substrate H₂O by means of the QM-molecular dynamics (MD) method. Following the explanation of the computational details, we will discuss these two things in turn. Conclusions are summarized in the final section.

■ COMPUTATIONAL DETAILS

We used model molecules, Ph₂Ge=O and H₂Ge=O, in addition to the real molecule (Eind)₂Ge=O as germanones, and H₂O, NH₃, Me₂C=O, H₂, CH₄, BH₃, and SiH₄ as substrates. We added w, a, o, h, m, and s as suffixes to the labels of the equilibrium and transition state structures to distinguish the substrates, H₂O, NH₃, Me₂C=O, H₂, CH₄, and SiH₄, respectively, and also added E to distinguish the Eind substituent from the Ph substituent, and C and Si to distinguish ketone and silanone from germanone, respectively. The numbers 1 and 2 attached to the letter w and a for the substrates H₂O and NH₃ means the number of molecules that participate in the reaction.

Quantum Mechanical (QM) Calculation. All the quantum mechanical (QM) calculations were performed using the GAUSSIAN09 program package.⁴⁰ For the system of Ph₂Ge=O with the substrate, the geometry optimizations and energy calculations were carried out by the density functional theory (DFT) at the B3LYP level, which consists of a hybrid Becke + Hartree–Fock exchange and Lee–Yang–Parr correlation functional with nonlocal corrections.^{41–43} For the basis set, we used aug-cc-pVTZ for the Ge=O of germanone, the Si=O of silanone, the C=O of ketone and the substrates, H₂O, NH₃, Me₂C=O, H₂, CH₄, BH₃, and SiH₄, and 6-31G(d) for the Ph substituent (BSI). The equilibrium and transition state structures were identified by the number of imaginary frequencies calculated from the analytical Hessian matrix. The reaction coordinates were followed from the transition state to the reactant and the product by the intrinsic reaction coordinate (IRC) technique.⁴⁴ The atomic charge was obtained by the natural bond orbital (NBO) analysis.⁴⁵ The basis set superposition error (BSSE) included in the interaction (INT) energies between the germanone and the substrate was corrected by the counterpoise method.^{46,47} We also confirmed that the geometries and the energetics of the reaction system of H₂Ge=O + H₂O at the HF/6-31G(d) level we adopted for the molecular dynamics simulation reproduce those of the reaction system of Ph₂Ge=O + H₂O at the B3LYP/BSI level very well (Figures S5 and S6).

QM-Molecular Dynamics (MD) Simulation. We further performed a molecular dynamics (MD) simulation for a model system of H₂Ge=O + H₂O to examine the mechanism of the σ bond cleavage on the Ge=O bond of germanone taking account of the thermal motion. For the molecular dynamics (MD) simulations, we used the QM-molecular dynamics (MD)

method⁴⁸ and the direct MD simulations were performed calculating the energy and its gradient by the QM method on the fly. The energy was calculated at the HF level of theory with the basis set 6-31G(d) for all the atoms, because the HF/6-31G(d) level was confirmed to be good enough to describe the geometries and the energetics of the reaction as mentioned above. For the development of the geometry during the molecular dynamics simulation, the force obtained from the potential energy surface is used. Because the shape of the potential energy surface is well reproduced by the HF level, the HF level is adequate in the MD simulations. The time evolution of the nuclei was performed using the Beeman algorithm⁴⁹ with a time step of 1 fs under the constant temperature through the use of Berendsen's velocity scaling algorithm.⁵⁰ The temperature was set to 300 K for the analysis of the H₂O-coordinated cluster **2w1**. However, we increased the temperature up to 1600 K for the simulation of the reaction. We have confirmed that the temperature of 1600 K is appropriate to give enough energy to the normal mode of the σ bond cleavage with a high possibility to cause the reaction. The optimized structure at the HF/6-31G(d) level is used as the initial geometry of the MD simulation and the potential energies relative to that of the optimized structure are presented.

■ RESULTS AND DISCUSSION

QM Calculations for H₂O, NH₃, and Me₂C=O. The optimized equilibrium and transition state structures of the reaction of Ph₂Ge=O with H₂O are presented in Figure 1. The cleavage of the O–H σ bond of the H₂O molecule occurs on the Ge=O bond of germanone. Before the breaking of the O–H σ bond, the intermediate **2w1** is formed. In **2w1**, the positively charged Ge (1.818 e) and the negatively charged O (−1.090 e) of the highly polarized Ge=O bond interact with the negatively charged O (−0.922 e) and the positively charged H (0.461 e) of the H₂O molecule, respectively. In fact, the H₂O oxygen, which has an interaction with the Ge with the O³–Ge² distance of 2.329 Å, coordinates to the Ge by the electron donation from the p-type nonbonding orbital of the H₂O oxygen to a s-character vacant orbital of the Ge, as shown by the molecular orbital ψ_{44} for **2w1** in Figure 2. The coefficient of the molecular orbital of ψ_{44} for **2w1** showed that the molecular orbital of the Ge has s-character rather than p-character. The binding energy between the coordinated H₂O and the Ph₂Ge=O in **2w1** was calculated to be 8.9 kcal/mol (Table 1). We have reported such a coordination of H₂O before the breaking of the O–H σ bond of H₂O for other cases.^{51,52} This coordination of the H₂O molecule does not occur when the Ge atom is replaced by the C atom because the vacant orbital of the C atom becomes higher in energy in addition to the small polarization of the C=O (C, 0.529 e; O, −0.553 e), although it similarly occurs in the case of Si (Figure S1). The electron donation from the H₂O oxygen to the Ge consequently causes an electron migration from the H⁺ to the O¹ through the O³ and the Ge², as shown by the changes in the charges of these atoms by the coordination of H₂O in Figure 3. The positive charge of the H⁺ increases to 0.523 e, and in contrast the negative charge of the O¹ increases to −1.190 e. Thereby, the H⁺–O¹ distance is shortened to 2.112 Å. In the transition state **TS1w1**, the distance H⁺–O¹ is further shortened to 1.449 Å, although the O³–H⁺ distance is still 1.111 Å. The molecular orbital ψ_{51} for **TS1w1** in Figure 2 indicates that the H⁺–O¹ bond is formed in some degree in **TS1w1**. The coordination of the H₂O oxygen to the Ge by the

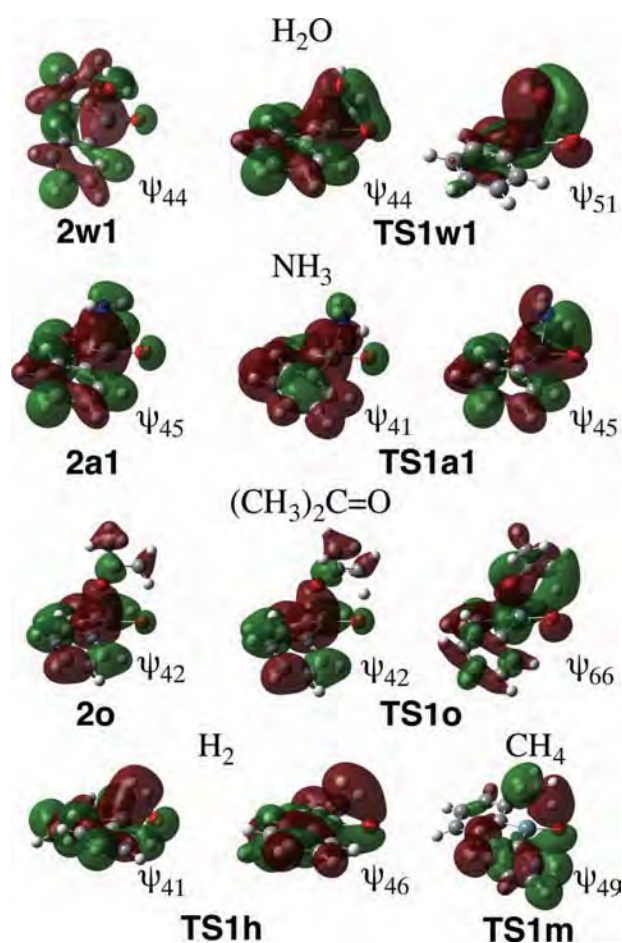


Figure 2. Selected molecular orbitals of the clusters and the transition states in the cases of H₂O, NH₃, (CH₃)₂C=O, H₂, and CH₄.

Table 1. Interaction (INT), Binding (BE), and Deformation (DEF) Energies^a (kcal/mol) between the Substrates H₂O, NH₃, and (CH₃)₂C=O and Fragment Ph₂Ge=O in the Clusters 2w1, 2a1, and 2o at the B3LYP/BSI Level

	INT	INT' ^b	BE	DEF
2w1	10.3	8.9	8.9	1.4
2a1	17.9	16.0	14.5	3.4
2o	16.8	13.9	14.0	2.8

^aINT = BE + DEF. ^bINT' is the BSSE corrected INT.

electron donation of the lone electron pair is still kept in TS1w1, as shown by the ψ_{44} for TS1w1. The approach of the proton-like H⁴ to the O¹ induces the electron migration from the Ge² to the O³ through the O¹ and H⁴ (Figure 3) and then the O³—H⁴ bond heterolytically splits. The produced OH⁻ and H⁺ form the covalent bonds with the Ge² and the O¹ in 3w1, respectively.

The potential energy profile of the reaction of Ph₂Ge=O with H₂O is presented in Figure 4. The intermediate 2w1 is more stable by 8.9 kcal/mol compared to the reactant 1 due to the coordination of the H₂O oxygen to the Ge of Ph₂Ge=O. Because this coordination is maintained even in the transition state TS1w1 as mentioned above, TS1w1 is more stabilized in energy than the reactant 1 and the energy barrier is reduced to 2.5 kcal/mol. This reaction of the O—H σ bond breaking of H₂O on the Ge=O bond was 51.9 kcal/mol exothermic. When

the Ge atom is replaced by the C atom, the energy profile drastically changes. In the case of C, the O—H σ bond breaking of H₂O occurs homolytically rather than heterolytically due to the small polarization of the C=O bond. The reaction proceeds without the coordination of H₂O oxygen to the C atom of the C=O and passes through the transition state TS1Cw1 (Figure S1). In TS1Cw1, one of the charge transfer interactions between the O—H and the C=O, i.e., the electron donation from the O—H σ orbital to the C=O π^* orbital, exists. This homolytic splitting of the O—H σ bond without the coordination of the H₂O oxygen makes the reaction so hard so that the energy barrier increases to 48.2 kcal/mol. However, in the case of Si, the reaction proceeds similarly to the case of Ge. The O—H σ bond breaking of H₂O occurs heterolytically with the coordination of the H₂O oxygen to the Si atom as shown by Figure S1. The energy profile is very smooth with the energy barrier of only 2 kcal/mol and the reaction is 60.1 kcal/mol exothermic. Even when we use the Eind groups instead of the Ph groups, the coordination of the H₂O oxygen to the Ge atom is kept in the intermediate before the O—H σ bond breaking (Figure S2). The interaction energy of 10.5 kcal/mol between the coordinated H₂O and the Ge atom in the case of the Eind group was almost the same as that of 10.3 kcal/mol in the case of the Ph group, although the binding energy was reduced from 8.9 to 1.4 kcal/mol due to the steric effect of the Eind groups.

We also calculated for the substrate NH₃ that has a lone electron pair. As expected, the NH₃ nitrogen coordinates to the Ge with the N³—Ge² distance of 2.203 Å in the intermediate 2a1 (Figure 1), which is similar to the case of H₂O. This coordination is ascribed to the electron donation from the lone electron pair of the NH₃ nitrogen to the vacant orbital of the Ge with a s-character as shown by the ψ_{45} for 2a1 in Figure 2. The binding energy of the NH₃ nitrogen with the Ge was calculated to be 14.5 kcal/mol (Table 1), which is larger than that for H₂O. Experimentally reported acetone also coordinates to the Ge with the O³—Ge² distance of 2.200 Å, as shown by 2o in Figure 2. The molecular orbital ψ_{42} for 2o in Figure 2 shows that the electron donation of the lone electron pair of acetone oxygen to the s-character vacant orbital of the Ge causes this coordination. The binding energy by this coordination was 14.0 kcal/mol (Table 1).

The coordination of both NH₃ and Me₂C=O to the Ge induces an electron migration as shown by the changes in the charge by the coordination presented in Figure 3, which is similar to the case of H₂O. In the case of NH₃, the electron migrates from the H⁴ to the O¹ thorough the N³ and the Ge² in 2a1, resulting in the increase in the positive charge of the H⁴ and the negative charge of the O¹. Likewise, in the case of Me₂C=O, the electron migration takes place from the H⁶ to the O¹ thorough the C⁵, C⁴, O³, and the Ge² to increase the positive charge of the H⁶ and the negative charge of the O¹. By these electron migrations, the H⁴—O¹ distance for NH₃ and the H⁶—O¹ distance for Me₂C=O are much shortened in the transition state, although the N³—H⁴ distance for NH₃ and the C⁵—H⁶ distance for Me₂C=O are not stretched so much (Figure 1). In each transition state for NH₃ and Me₂C=O, the other electron migration occurs to split each σ bond heterolytically, as mentioned above for H₂O. In TS1a1 for NH₃, the electron migrates from the Ge² to the N³ through the O¹ and the H⁴, whereas in TS1o for Me₂C=O, the electron migrates from the Ge² to the O³ through the O¹, H⁶, C⁵, and the C⁴.

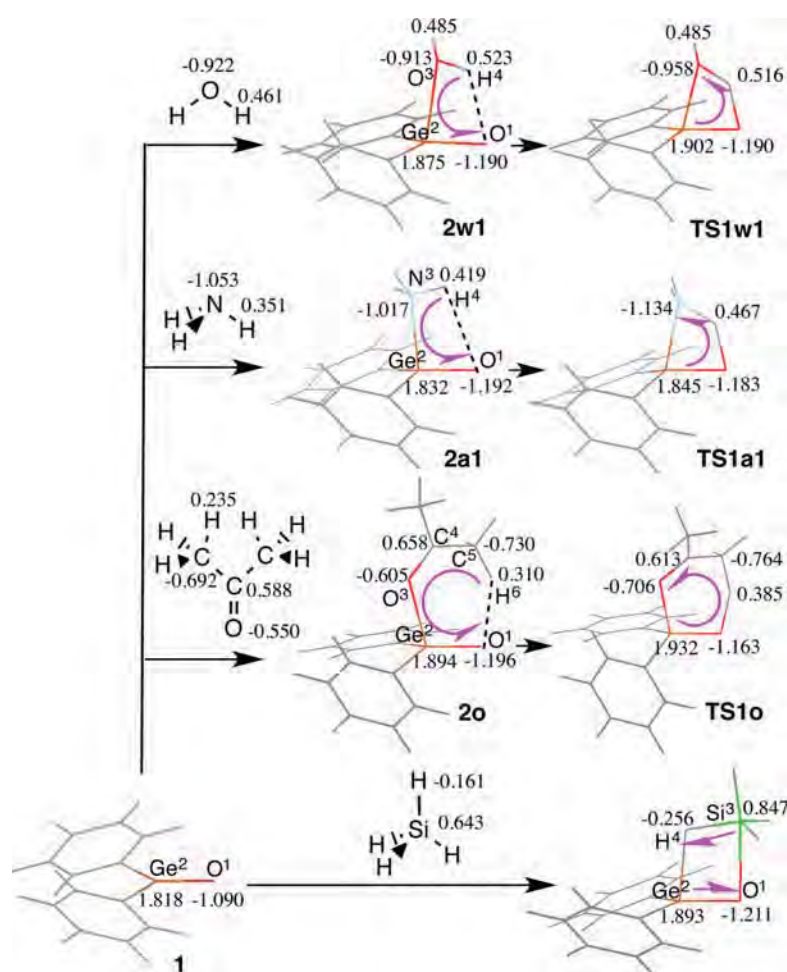


Figure 3. NBO charges (e) and flow of the electron (red arrow) during the reaction of $\text{Ph}_2\text{Ge}=\text{O}$ with H_2O , NH_3 , $(\text{CH}_3)_2\text{C}=\text{O}$, and SiH_4 at the B3LYP/BSI level.

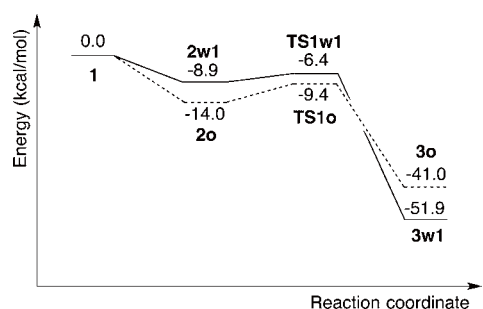


Figure 4. Potential energy profiles of the reaction of $\text{Ph}_2\text{Ge}=\text{O}$ with H_2O (normal line) and $(\text{CH}_3)_2\text{C}=\text{O}$ (dotted line) at the B3LYP/BSI level.

The potential energy profiles of the reaction of $\text{Ph}_2\text{Ge}=\text{O}$ with NH_3 and $\text{Me}_2\text{C}=\text{O}$ are presented in Figures 4 and 5. The energy barrier is larger for NH_3 and $\text{Me}_2\text{C}=\text{O}$ than for H_2O , because the intermediates **2a1** and **2o** for NH_3 and $\text{Me}_2\text{C}=\text{O}$ are more stabilized compared to the case of H_2O by the coordination of NH_3 and $\text{Me}_2\text{C}=\text{O}$. However, both reactions are largely exothermic, which is similar to the case of H_2O . The other functional of DFT method M06-2X also showed the same feature and tendency of the potential energy profile obtained by B3LYP, although the entire energy profile is

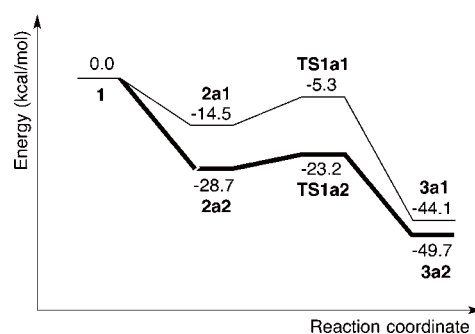


Figure 5. Potential energy profiles of the reaction of $\text{Ph}_2\text{Ge}=\text{O}$ with NH_3 (normal line) and 2NH_3 (bold line) at the B3LYP/BSI level.

stabilized as presented in Table S1. The consideration of the benzene solvent by the PCM approximation also did not change the potential energy profile so much. Although reactant **1** is stabilized by the entropy term, the potential energy profile is basically the same even when we take account of the thermochemical parameters.

In the cases of H_2O and NH_3 , we can consider the mediation of one additional molecule of the substrate in the migration of the split proton to the $\text{Ge}=\text{O}$ oxygen after the heterolytic cleavage of the $\text{O}-\text{H}$ and the $\text{N}-\text{H}$ σ bonds. This reaction

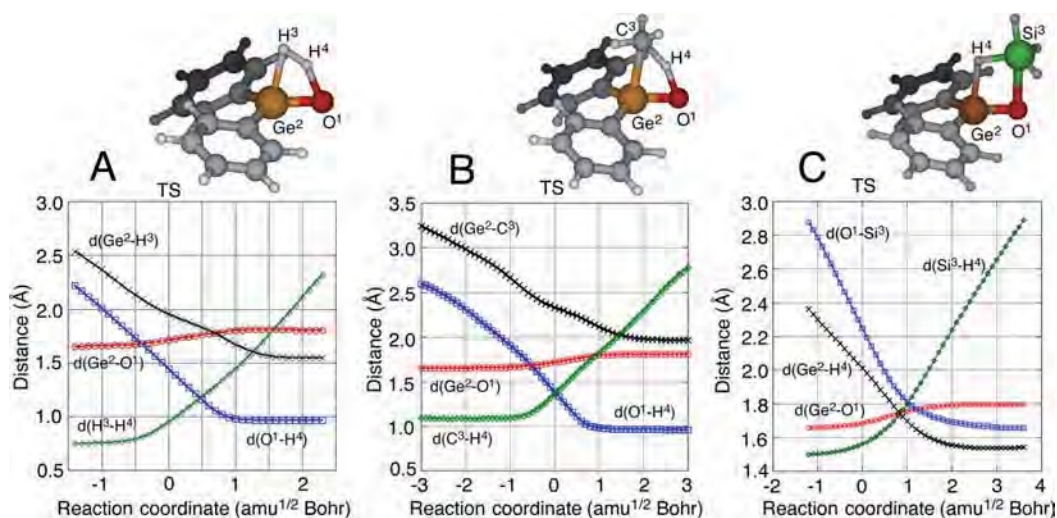


Figure 6. Changes in the geometric parameters during the reaction of $\text{Ph}_2\text{Ge}=\text{O}$ with H_2 (A), CH_4 (B), and SiH_4 (C).

mediated by one additional substrate for NH_3 is presented in Figure 1. After the formation of the intermediate **2a2**, the reaction $\text{2a2} \rightarrow \text{TS1a2} \rightarrow \text{3a2}$ proceeds by one step. In the transition state **TS1a2**, the H^4 migrates from the N^3 to the N^5 in some degree. However, the H^6 is still attached to the N^5 , although the distance O^1-H^6 is shortened to 1.517 Å. The potential energy profile of this reaction presented in Figure 5 shows that the energy barrier is reduced to about half compared to that without mediation of one additional substrate. This decrease in the energy barrier would be ascribed to the stabilization of the transition state **TS1a2** where the strain in the angles, $\angle \text{N}^3-\text{Ge}^2-\text{O}^1$ and $\angle \text{Ge}^2-\text{O}^1-\text{H}^6$, is largely relaxed. Thus, the reaction becomes more facile by the mediation of an additional substrate in the proton migration. By the same reason, the energy barrier disappears and then the reaction becomes downhill for H_2O (Figure S3).

QM Calculations for H_2 and CH_4 . The approach of the substrate to the $\text{Ge}=\text{O}$ of $\text{Ph}_2\text{Ge}=\text{O}$ in the σ bond cleavage drastically changes in the cases of H_2 and CH_4 (Figure 1). In both cases of H_2 and CH_4 , there is no intermediate with the coordination of the substrate to the Ge atom before the σ bond breaking. The plots of the geometric parameters along the reaction coordinate presented in Figure 6A for H_2 show that the H^4 rather than the H^3 first approach the O^1 and the H^3-H^4 bond breaking takes place after the O^1-H^4 and the Ge^2-H^3 bond formation. The H^3-H^4 bond distance of 0.950 Å in the transition state **TS1h** is not stretched so much compared to that of the free H_2 molecule and the H^3-H^4 bond is elongated and broken after passing through the transition state. The H^3-H^4 bond would be split heterolytically as shown by the charges of the H^3 (-0.209 e) and H^4 (0.259 e) in the transition state **TS1h**. The molecular orbitals, ψ_{41} and ψ_{46} , in **TS1h** displayed in Figure 2 show that the O^1-H^4 and the Ge^2-H^3 bonds are already formed in the transition state.

The similar approach of the substrate to the $\text{Ge}=\text{O}$ bond was found also for CH_4 . The H^4 of the C^3-H^4 σ bond first approach the O^1 of the $\text{Ge}=\text{O}$ as shown by the plots of the geometric parameters along the reaction coordinate for CH_4 (Figure 6B), because CH_4 without the lone electron pair cannot coordinate to the Ge^2 . The O^1-H^4 distance is shortened to 1.388 Å in **TS1m** (Figure 1) and the molecular orbital ψ_{49} in **TS1m** displayed in Figure 2 shows a bonding orbital of the

O^1-H^4 bond. The electron of the C^3-H^4 σ bond would be localized at the C^3 by this approach of the H^4 to the largely negatively charged O^1 . In fact, in **TS1m**, the negative charge of the C^3 increases from -0.818 e to -1.059 e, whereas the positive charge of the H^4 increases from 0.204 to 0.377 e. Figure 6B shows that the O^1-H^4 bond is nearly formed in the transition state. As a result, the C^3-H^4 σ bond of the CH_4 would be extremely polarized to form the CH_3^- anion and H^+ proton. After the transition state, the C^3-H^4 bond starts to lengthen and the consequently formed CH_3^- and proton are taken by the electron deficient Ge^2 and the electron sufficient O^1 , respectively. Thus, it is thought that the $\text{C}-\text{H}$ σ bond of CH_4 as well as the $\text{H}-\text{H}$ σ bond of H_2 is heterolytically split.

The potential energy profiles of the σ bond breaking on the $\text{Ge}=\text{O}$ bond for H_2 and CH_4 are presented in Figure 7.

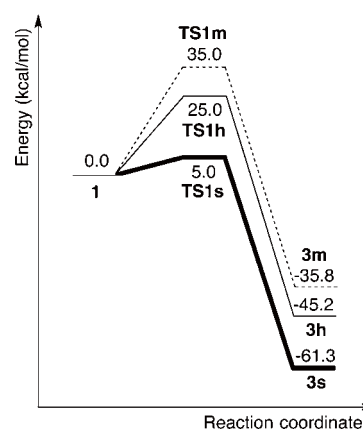


Figure 7. Potential energy profiles of the reaction of $\text{Ph}_2\text{Ge}=\text{O}$ with H_2 (normal line), SiH_4 (bold line), and CH_4 (dotted line) at the B3LYP/BSI level.

Both energy barriers for H_2 and CH_4 are very large, suggesting that the σ bond breaking is much harder for H_2 and CH_4 than for H_2O , NH_3 , and $\text{Me}_2\text{C}=\text{O}$, although the reaction is largely exothermic for both of them. These large energy barriers would be due to the absence of an intermediate with the coordination of the substrate that makes the heterolytic cleavage of the σ bond easy.

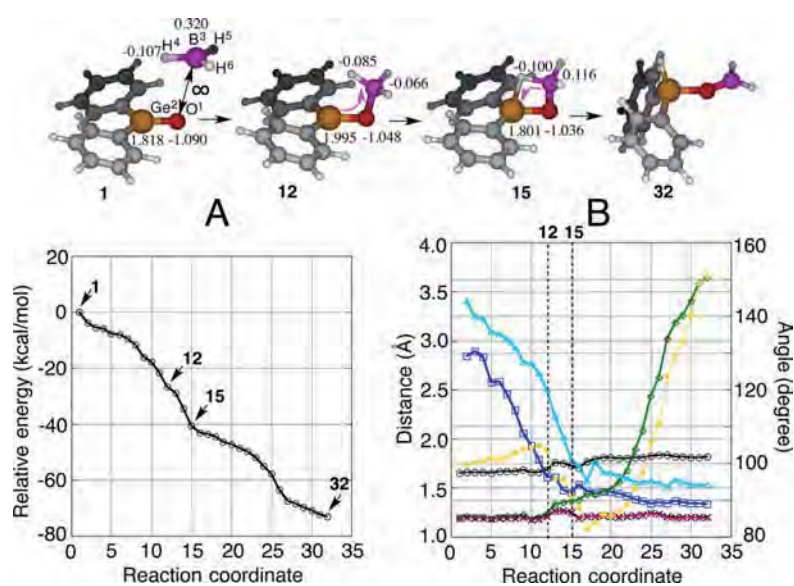


Figure 8. Potential energy profile (A) and changes in the geometric parameters (B) during the reaction of $\text{Ph}_2\text{Ge}=\text{O}$ with BH_3 at the B3LYP/BSI level together with the structures at the points, 1, 12, 15, and 32. 1 and 32 are the starting substance and the product, respectively. 12 and 15 are the arbitrary selected structures, which are close to a cluster and a transition state, respectively. The values of the NBO charges are also presented together with the structures, 1, 12, 15, and 32. The red arrows indicate the flow of the electron. In part B, the following markers apply: \circ , $d(\text{Ge}^2-\text{O}^1)$; \square , $d(\text{B}^3-\text{O}^1)$; \diamond , $d(\text{B}^3-\text{H}^4)$; \times , $d(\text{B}^3-\text{H}^5)$; $+$, $d(\text{B}^3-\text{H}^6)$; Δ , $d(\text{H}^4-\text{Ge}^2)$; \bullet , $\angle \text{B}^3-\text{O}^1-\text{Ge}^2$.

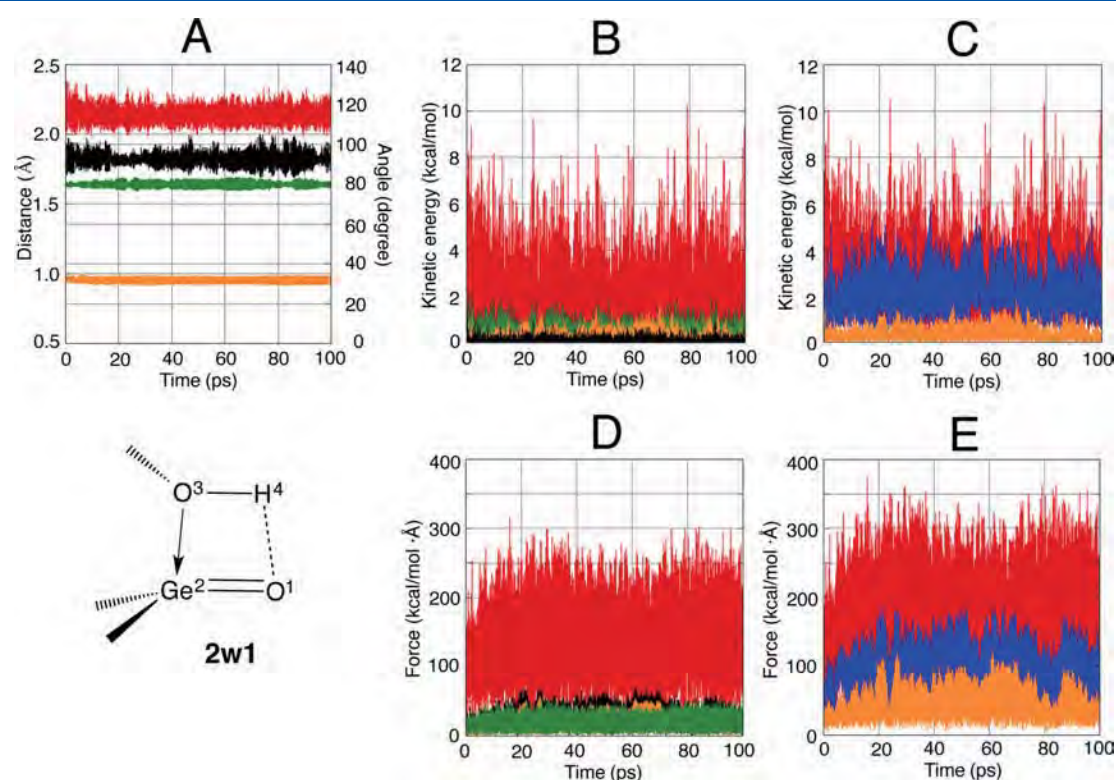


Figure 9. Changes in the geometric parameters (A), kinetic energies (B and C), and forces (D and E) of 2w1 during the QM-MD simulation at 300 K. In part A, the following colors apply: red, $d(\text{Ge}^2-\text{O}^3)$; green, $d(\text{Ge}^2-\text{O}^1)$; orange, $d(\text{O}^3-\text{H}^4)$; black, $\angle \text{O}^3-\text{Ge}^2-\text{O}^1$. In parts B and D, the following colors apply: red, O^3 ; green, H^4 ; orange, O^1 ; black, Ge^2 . In parts C and E, the following colors apply: red, H_2O ; blue, $\text{H}_2\text{Ge}=\text{O}$; orange, $\text{Ge}=\text{O}$.

QM Calculations for BH_3 and SiH_4 . The reaction of BH_3 with $\text{Ph}_2\text{Ge}=\text{O}$ was downhill, as presented in Figure 8A. The reactant 1 at the first point is $\text{Ph}_2\text{Ge}=\text{O} + \text{BH}_3$, and in the structure at the next point, the O^1-B^3 distance is set to be

3.0 Å, because the electron deficient B^3 at first attacks the electron sufficient O^1 before the $\text{B}-\text{H}$ bond breaking as shown by 12. In the first process before reaching 12, the O^1-B^3 distance is shortened, while the B^3-H^4 distance is almost constant,

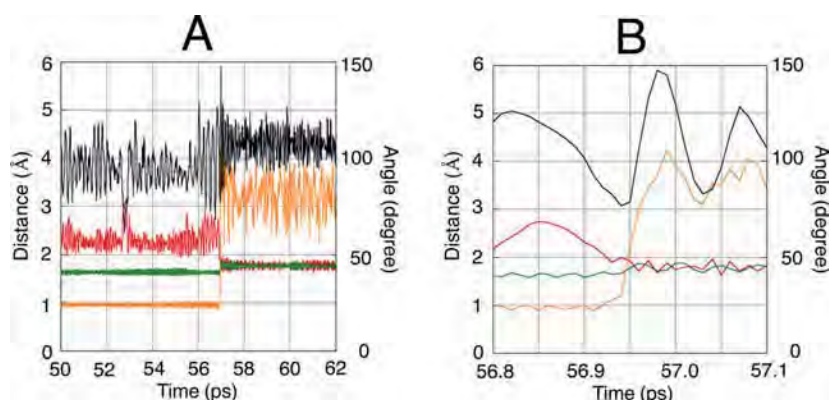


Figure 10. Changes in the geometric parameters in the reaction of $\text{H}_2\text{Ge}=\text{O}$ with H_2O during the QM-MD simulation at 1600 K. In parts A and B, the following colors apply: red, $d(\text{Ge}^2-\text{O}^3)$; green, $d(\text{Ge}^2-\text{O}^1)$; orange, $d(\text{O}^3-\text{H}^4)$; black, $\angle\text{O}^3-\text{Ge}^2-\text{O}^1$. (A) and (B) have different time scales.

as presented in Figure 8B. The binding of BH_3 by the electron donation from the O^1 to the B^3 , which is shown by the ψ_{58} of **12** in Figure S4, induces the electron migration from the Ge^2 to the B^3 in **12**. In the second process from **12** to **15**, the H^4-Ge^2 distance is shortened and the electron migrates from the B^3 to the Ge^2 through the H^4 forming the H^4-Ge^2 bond in addition to the O^1-B^3 bond as shown by the ψ_{42} and the ψ_{58} of **15** in Figure S4. In the third process after **15**, the positively charged B^3 and the negatively charged H^4 are heterolytically split.

Also in the case of SiH_4 , the Si atom attacks not the positively charged Ge^2 but the negatively charged O^1 of $\text{Ph}_2\text{Ge}=\text{O}$ as shown by the transition state **TS 1s** in Figure 1, because the Si atom of SiH_4 is positively charged due to its electronegativity that is smaller than that of the H atom. In **TS 1s**, the electron shifts from the Si^3 to the H^4 in the Si^3-H^4 σ bond and from the Ge^2 to the O^1 in the Ge^2-O^1 bond (Figure 3) by the approach of the Si^3-H^4 bond to the Ge^2-O^1 bond. The largely negatively charged H^4 is then abstracted as H^- by the Ge^2 . Thus, the $\text{Si}-\text{H}$ σ bond also heterolytically splits on the $\text{Ge}=\text{O}$ double bond.

As presented in Figure 7, the energy barrier of the σ bond cleavage is much smaller for the case of SiH_4 than for the cases of H_2 and CH_4 . This would be due to the interaction of the Si^3 with the O^1 before the $\text{Si}-\text{H}$ σ bond breaking, which increases the polarization of both the Si^3-H^4 and the Ge^2-O^1 bonds to promote a heterolytic split of the $\text{Si}-\text{H}$ σ bond. The plots of the geometric parameters against the reaction coordinate displayed in Figure 6C show that the O^1-Si^3 distance is considerably shortened before the Si^3-H^4 bond is lengthened. In fact, the interaction of the Si^3 with the O^1 was confirmed in the transition state **TS 1s** (see the ψ_{62} of **TS 1s** in Figure S4), which would be ascribed to the hypervalency of the Si^3 .

QM-MD Simulations for H_2O . We conducted the QM-MD simulations for the reaction with H_2O to examine a dynamic factor that produces the driving force of the reaction taking account of the thermal motion of the molecule. In the QM-MD simulations, we replaced the Ph group by the H atom in the germanone $\text{Ph}_2\text{Ge}=\text{O}$ and adopted the HF/6-31G(d) level for the quantum mechanical calculation to save the computational time, because we confirmed that the tendencies in the equilibrium and the transition state structures and the potential energy profile of the reaction at the B3LYP/BSI level for the $\text{Ph}_2\text{Ge}=\text{O} + \text{H}_2\text{O}$ system are well reproduced also at the HF/6-31G(d) level for the $\text{H}_2\text{Ge}=\text{O} + \text{H}_2\text{O}$ system, as presented

in Figure S5 and S6. The result of a QM-MD simulation in the gas phase at 300 K is displayed in Figure 9. The coordination of the H_2O oxygen to the Ge is maintained during the simulation with the O^3-Ge^2 distance of 2.1–2.2 Å, although O^3-Ge^2 more vigorously vibrates compared to Ge^2-O^1 and the O^3-H^4 , as shown in Figure 9A. The change in the kinetic energy of each atom with time presented in Figure 9B shows that the kinetic energy of the entire molecule always concentrates on the O^3 atom, suggesting that the motion of the O^3 atom plays an important role to produce a driving force of the reaction. We have made a similar discussion of a driving force for the $\text{S}_{\text{N}}2$ reaction of $\text{SiH}_3\text{Cl} + \text{Cl}^* \rightarrow [\text{Cl}^*\text{SiH}_3\text{Cl}]^- \rightarrow \text{SiH}_3\text{Cl}^* + \text{Cl}^-$.⁵³ Other atoms, H^4 , Ge^2 , and O^1 , which constitute the four-centered transition state of the $\text{O}-\text{H}$ σ bond cleavage of H_2O , have very small kinetic energies compared to that of O^3 . When we compare the total kinetic energy of the atoms between the substrate H_2O and the fragment $\text{H}_2\text{Ge}=\text{O}$, it is obvious that the kinetic energy of the entire molecule is localized on the substrate H_2O rather than the fragment $\text{H}_2\text{Ge}=\text{O}$ (Figure 9C). Especially, the $\text{Ge}=\text{O}$ of the fragment $\text{H}_2\text{Ge}=\text{O}$, which participates the reaction, has a very small kinetic energy. As for the force, the O^3 atom also always receives the largest force during the simulation and the larger force is added to the substrate H_2O rather than the fragment $\text{H}_2\text{Ge}=\text{O}$ (Figure 9D,E).

To simulate the cleavage of the $\text{O}-\text{H}$ σ bond of H_2O on the $\text{Ge}=\text{O}$ bond, we performed the QM-MD simulations at 1600 K. The interaction of the H_2O oxygen with the Ge is basically kept even at 1600 K, although the coordinated H_2O sometimes dissociates from the Ge. Figure 10 shows that the $\text{O}-\text{H}$ σ bond cleavage occurs at 56.95 ps. On the one hand, the oscillation of both the distance $d(\text{Ge}^2-\text{O}^3)$ and the angle $\angle\text{O}^3-\text{Ge}^2-\text{O}^1$ suddenly further enlarges just before the $\text{O}-\text{H}$ bond cleavage (Figure 10A), suggesting that the vibration of the Ge^2-O^3 produces a driving force of the $\text{O}-\text{H}$ σ bond cleavage as mentioned later. On the other hand, the oscillation of the distances $d(\text{Ge}^2-\text{O}^1)$ and $d(\text{O}^3-\text{H}^4)$ does not change. As shown by Figure 10B, when the $\text{O}-\text{H}$ bond is broken, the Ge^2-O^3 distance is shortened as much as possible, which would promote the electron migration for the heterolytic $\text{O}-\text{H}$ bond cleavage mentioned above.

The distribution of the kinetic energy of the entire molecule a little changes at 1600 K. The kinetic energy of the substrate H_2O is nearly the same as that of the fragment $\text{H}_2\text{Ge}=\text{O}$

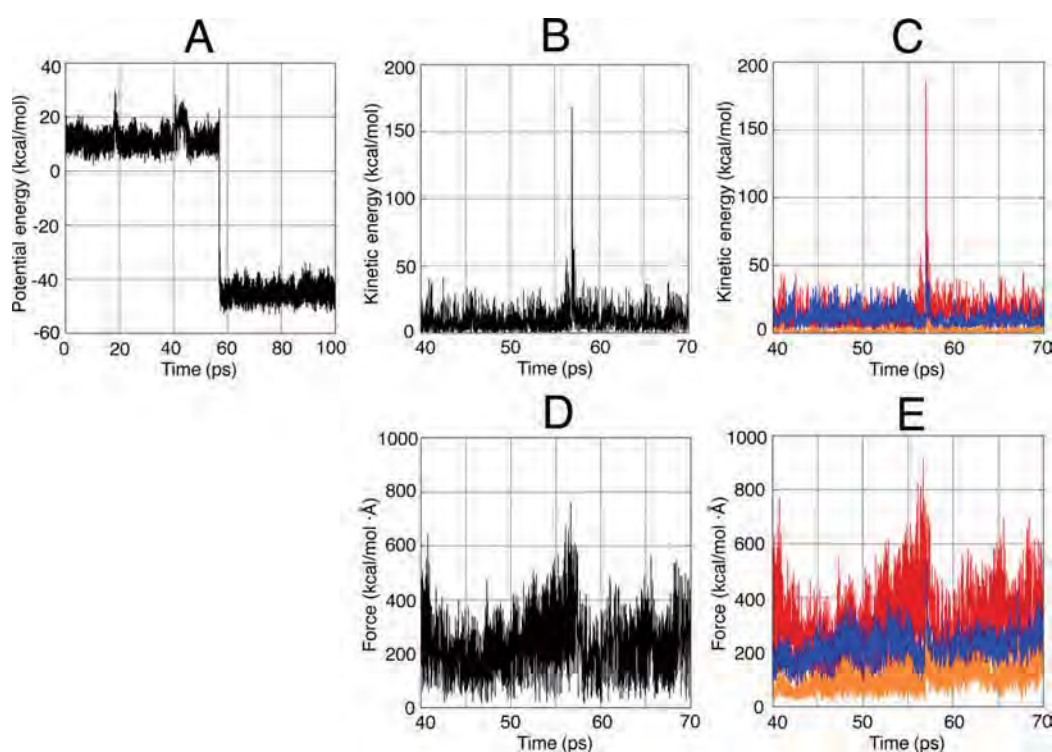


Figure 11. Changes in the potential energy of the entire molecule (A), kinetic energies (B and C), and forces (D and E) in the reaction of $\text{H}_2\text{Ge}=\text{O}$ with H_2O during the QM-MD simulation at 1600 K. In parts B, C, D, and E, the following colors apply: black, O^3 ; red, H_2O ; blue, $\text{H}_2\text{Ge}=\text{O}$; orange, $\text{Ge}=\text{O}$.

before the O—H bond cleavage, as shown by Figure 11C. However, this balance of the distribution of the kinetic energy is broken just before the O—H bond cleavage. The kinetic energy extremely localizes on the substrate H_2O and especially concentrates on the O^3 (Figure 11B,C), which is the reason why the vibration of the Ge^2-O^3 becomes vigorous just before the O—H bond cleavage as mentioned above. The forces added to the O^3 atom also increase just before the O—H bond cleavage as shown by Figure 11D. Thus, the Ge^2-O^3 interaction induces the heterolytic breaking of the O—H σ bond through the electron migration and the vibration of the Ge^2-O^3 becomes a driving force of the reaction. The kinetic energy concentrated on this Ge^2-O^3 vibration would be transmitted to the normal mode of the O—H bond breaking to advance the reaction. The heat of the reaction of about 55 kcal/mol that is released when the O—H bond is broken (Figure 11A) immediately dissipates via the O^3 atom as shown by Figure 11B,C.

CONCLUDING REMARKS

We examined the mechanism of the σ bond cleavage of H_2O , NH_3 , $\text{Me}_2\text{C}=\text{O}$, H_2 , CH_4 , BH_3 , and SiH_4 on the $\text{Ge}=\text{O}$ bond of germanone by means of both quantum mechanical (QM) and molecular dynamics (MD) methods. The QM calculations showed that the σ bond is heterolytically broken on the very largely polarized $\text{Ge}=\text{O}$ bond for all the cases of the substrates. In the cases of H_2O , NH_3 , and $\text{Me}_2\text{C}=\text{O}$ with the lone electron pair, the substrate coordinates to the Ge before the σ bond cleavage. An electron migration that promotes the heterolytic cleavage of the σ bond is induced by this coordination. As a result, the H of the σ bond is abstracted by the $\text{Ge}=\text{O}$ oxygen as a proton and the formed counterpart anion

switches the bond from the coordinate bond to the covalent bond with the Ge. In the cases of H_2 and CH_4 without the lone electron pair, the H of the σ bond at first approaches the $\text{Ge}=\text{O}$ oxygen, because the substrate cannot coordinate to the Ge. The σ bond, which is largely polarized by this approach of the H, is heterolytically broken. The energy barrier was much larger for the cases of H_2 and CH_4 without the coordination than for the cases of H_2O , NH_3 , and $\text{Me}_2\text{C}=\text{O}$ with the coordination. Meanwhile, in the case of BH_3 , the σ bond cleavage was energetically downhill. The B atom with the vacant p orbital at first coordinates to the $\text{Ge}=\text{O}$ oxygen in this case. After this coordination, the H atom is abstracted by the Ge as a H^- anion. Also in the case of SiH_4 , the electron deficient Si forms a bond not with the Ge but with the O of the $\text{Ge}=\text{O}$ before the σ bond cleavage. However, this reaction without the coordination of the Si has an energy barrier. Thus, it is thought that the coordination of the substrate plays an important role to induce a heterolytic cleavage and make the reaction facile.

We conducted the QM-MD simulations for the case of H_2O to examine a dynamic factor that produces the driving force of the reaction taking account of the thermal motion of the molecule. The coordination of the substrate H_2O to the Ge was maintained without the dissociation from the Ge even when we take account of the thermal motion. The kinetic energy of the entire molecule concentrates on the coordinated H_2O oxygen and the oscillation of the coordinate bond enlarges especially just before the O—H σ bond cleavage. The coordinate bond is shortened as much as possible when the O—H bond is broken to promote the electron migration for the heterolytic O—H bond cleavage. The kinetic energy concentrated on the coordinated H_2O oxygen would be transmitted to the normal mode of the O—H bond breaking. Thus, it is thought that the

vibration of the coordinate bond is an important driving force that overcomes the energy barrier of the reaction in both electronic and dynamical aspects.

■ ASSOCIATED CONTENT

Supporting Information

The Supporting Information is available free of charge on the ACS Publications website at DOI: 10.1021/acs.jpca.6b12478.

Additional figures and tables showing potential energy profiles with the optimized structures, a potential energy profile, molecular orbitals, optimized structures at the various levels, potential energy profiles at the various levels, and thermochemical parameters; and listings giving the optimized Cartesian coordinates of equilibrium structures and transition states at the B3LYP/BSI level (PDF)

■ AUTHOR INFORMATION

Corresponding Author

*T. Matsubara. Phone: +81-463-59-4111. E-mail: matsubara@kanagawa-u.ac.jp.

ORCID

Toshiaki Matsubara: 0000-0001-5416-0884

Notes

The authors declare no competing financial interest.

■ ACKNOWLEDGMENTS

A part of the computations was performed at the Research Center for Computational Science, Okazaki, Japan.

■ REFERENCES

- (1) Arrington, C. A.; West, R.; Michl, J. On the proposed thermal interconversion of matrix-isolated dimethylsilylene and 1-methylsilene: their reactions with oxygen atom donors. *J. Am. Chem. Soc.* **1983**, *105*, 6176–6177.
- (2) Withnall, R.; Andrews, L. Infrared spectroscopic evidence for silicon-oxygen double bonds: methyl- and dimethylsilanones in solid argon. *J. Am. Chem. Soc.* **1986**, *108*, 8118–8119.
- (3) Withnall, R.; Andrews, L. Matrix reactions of methylsilanes and oxygen atoms. *J. Phys. Chem.* **1988**, *92*, 594–602.
- (4) Khabashesku, V. N.; Kerzina, Z. A.; Baskir, E. G.; Maltsev, A. K.; Nefedov, O. M. Direct spectroscopic study of unstable molecules with silicon-oxygen multiple bonds: low temperature matrix stabilization of $(\text{CH}_3)_2\text{Si}=\text{O}$ and $(\text{CD}_3)_2\text{Si}=\text{O}$ in the gas phase. *J. Organomet. Chem.* **1988**, *347*, 277–293.
- (5) Khabashesku, V. N.; Kerzina, Z. A.; Kudin, K. N.; Nefedov, O. M. Matrix isolation infrared and density functional theoretical studies of organic silanones, $(\text{CH}_3\text{O})_2\text{Si}=\text{O}$ and $(\text{C}_6\text{H}_5)_2\text{Si}=\text{O}$. *J. Organomet. Chem.* **1998**, *566*, 45–59.
- (6) Schnöckle, H. Matrixreaktion von SiO mit F_2 . IR-spektroskopischer nachweis von molekularem OSiF_2 . *J. Mol. Struct.* **1980**, *65*, 115–123.
- (7) Schnöckel, H. Matrixreaktionen von SiO. IR-spektroskopischer nachweis der molekeln SiO_2 und OSiCl_2 . *Z. Anorg. Allg. Chem.* **1980**, *460*, 37–50.
- (8) Withnall, R.; Andrews, L. Infrared spectroscopic evidence for silicon-oxygen double bonds: silanone and the silanoic and silicic acid molecules. *J. Am. Chem. Soc.* **1985**, *107*, 2567–2568.
- (9) Patyk, A.; Sander, W.; Gauss, J.; Cremer, D. Dimethyldioxasilirane. *Angew. Chem., Int. Ed. Engl.* **1989**, *28*, 898–900.
- (10) Gliniski, R. J.; Gole, J. L.; Dixon, D. A. Oxidation processes in the gas-phase silane-ozone system. Chemiluminescent emission and the molecular structure of H_2SiO . *J. Am. Chem. Soc.* **1985**, *107*, 5891–5894.
- (11) Srinivas, R.; Böhme, D. K.; Sülzle, D.; Schwarz, H. Gas-phase generation and characterization of neutral and ionized HSiOH , H_2SiO , H_2SiOH , and H_3SiO by collisional-activation and neutralization-reionization mass spectrometry. *J. Phys. Chem.* **1991**, *95*, 9836–9841.
- (12) Filippou, A. C.; Baars, B.; Chernov, O.; Lebedev, Y. N.; Schnakenburg, G. Silicon–oxygen double bonds: A stable silanone with a trigonal-planar coordinated silicon center. *Angew. Chem., Int. Ed.* **2014**, *53*, 565–570.
- (13) Khabashesku, V. N.; Boganov, S. E.; Nefedov, O. M. The low-temperature matrix stabilization and IR spectrum of dimethylgermanone, $\text{Me}_2\text{Ge}=\text{O}$. *Bull. Acad. Sci. USSR, Div. Chem. Sci.* **1990**, *39*, 1079–1080.
- (14) Withnall, R.; Andrews, L. Matrix reactions of germane and oxygen atoms: infrared spectroscopic evidence of germylene-water complex, germanol, hydroxygermylene, and germanic acid. *J. Phys. Chem.* **1990**, *94*, 2351–2357.
- (15) Tokitoh, N.; Matsumoto, T.; Okazaki, R. Formation and reactions of the first diarylgermanone stable in solution. *Chem. Lett.* **1995**, *24*, 1087–1088.
- (16) Jutzi, P.; Schmidt, H.; Neumann, B.; Stammler, H.-G. Bis(2,4,6-tri-tertbutylphenyl)germylene reinvestigated: crystal structure, Lewis acid catalyzed C–H insertion, and oxidation to an unstable germanone. *Organometallics* **1996**, *15*, 741–746.
- (17) Matsumoto, T.; Tokitoh, N.; Okazaki, R. First oxazagermete: synthesis, structure and thermal cycloreversion into a germanone. *Chem. Commun.* **1997**, 1553–1554.
- (18) Wegner, G. L.; Berger, R. J. F.; Schier, A.; Schmidbaur, H. Ligand-protected strain-free diarylgermylenes. *Organometallics* **2001**, *20*, 418–423.
- (19) Xiong, Y.; Yao, S.; Driess, M. An isolable NHC-supported silanone. *J. Am. Chem. Soc.* **2009**, *131*, 7562–7563.
- (20) Yao, S.; Xiong, Y.; Driess, M. From NHC→germylenes to stable NHC→germanone complexes. *Chem. Commun.* **2009**, 6466–6468.
- (21) Xiong, Y.; Yao, S.; Müller, R.; Kaupp, M.; Driess, M. From silicon(II)-based dioxygen activation to adducts of elusive dioxasiliranes and sila-ureas stable at room temperature. *Nat. Chem.* **2010**, *2*, 577–580.
- (22) Yao, S.; Xiong, Y.; Wang, W.; Driess, M. Synthesis, structure, and reactivity of a pyridine-stabilized germanone. *Chem. - Eur. J.* **2011**, *17*, 4890–4895.
- (23) Zabula, A. V.; Pape, T.; Hepp, A.; Schappacher, F. M.; Rodewald, U.; Ch; Pöttgen, R.; Hahn, F. E. Trapping of tin(II) and lead(II) homologues of carbon monoxide by a benzannulated lutidine-bridged bisstannylene. *J. Am. Chem. Soc.* **2008**, *130*, 5648–5649.
- (24) Xiong, Y.; Yao, S.; Müller, R.; Kaupp, M.; Driess, M. Activation of ammonia by a Si=O double bond and formation of a unique pair of sila-hemiaminal and silanoic amide tautomers. *J. Am. Chem. Soc.* **2010**, *132*, 6912–6913.
- (25) Ghadwal, R. S.; Azhakar, R.; Roesky, H. W.; Pröpper, K.; Dittrich, B.; Klein, S.; Frenking, G. Donor–acceptor-stabilized silicon analogue of an acid anhydride. *J. Am. Chem. Soc.* **2011**, *133*, 17552–17555.
- (26) Muraoka, T.; Abe, K.; Haga, Y.; Nakamura, T.; Ueno, K. Synthesis of a base-stabilized silanone-coordinated complex by oxygenation of a (silyl) (silylene)tungsten complex. *J. Am. Chem. Soc.* **2011**, *133*, 15365–15367.
- (27) Xiong, Y.; Yao, S.; Driess, M. Chemical tricks to stabilize silanones and their heavier homologues with E=O bonds (E=Si–Pb): From elusive species to isolable building blocks. *Angew. Chem., Int. Ed.* **2013**, *52*, 4302–4311.
- (28) Rodriguez, R.; Troadec, T.; Gau, D.; Saffon-Merceron, N.; Hashizume, D.; Miqueu, K.; Sotiropoulos, J.-M.; Baceiredo, A.; Kato, T. Synthesis of a donor-stabilized silacyclopropan-1-one. *Angew. Chem., Int. Ed.* **2013**, *52*, 4426–4430.
- (29) Rodriguez, R.; Gau, D.; Troadec, T.; Saffon-Merceron, N.; Brandchadell, V.; Baceiredo, A.; Kato, T. A base-stabilized sila-β-lactone and a donor/acceptor-stabilized silanoic acid. *Angew. Chem., Int. Ed.* **2013**, *52*, 8980–8983.

- (30) Li, L.; Fukawa, T.; Matsuo, T.; Hashizume, D.; Fueno, H.; Tanaka, K.; Tamao, K. A stable germanone as the first isolated heavy ketone with a terminal oxygen atom. *Nat. Chem.* **2012**, *4*, 361–365.
- (31) Trinquier, G.; Barthelat, J. C.; Satge, J. Double bonds vs. carbene-like unsaturations in germanium intermediates. *J. Am. Chem. Soc.* **1982**, *104*, 5931–5936.
- (32) Trinquier, G.; Pelissier, M.; Saint-Roch, B.; Lavayssiere, H. Structure of germanone and germathione through ab initio calculations. *J. Organomet. Chem.* **1981**, *214*, 169–181.
- (33) So, S. P. Ab initio molecular orbital study of the hydroxygermylene potential energy surface. *J. Phys. Chem.* **1991**, *95*, 10658–10662.
- (34) So, S. P. Theoretical study of the potential energy surfaces of protonated germanone and germathione. *J. Phys. Chem.* **1994**, *98*, 11420–11423.
- (35) Lin, C.-L.; Su, M.-D.; Chu, S.-Y. Stabilization of a germanium-oxygen double bond: a theoretical study. *Chem. Commun.* **1999**, 2383–2384.
- (36) Jaufeerally, N. B.; Abdallah, H. H.; Ramasami, P.; Schaefer, H. F. Journey through the potential energy surfaces for the isomerization and decomposition reactions of the telluroformaldehyde analogues: $H_2A=Te$ and $HFA=Te$ ($A = C, Si, \text{ and } Ge$). *J. Phys. Chem. A* **2013**, *117*, 5567–5577.
- (37) Jaufeerally, N. B.; Abdallah, H. H.; Ramasami, P.; Schaefer, H. F., III. Novel germanetellones: $XYGe=Te$ ($X, Y = H, F, Cl, Br, I$ and CN) – structures and energetics. Comparison with the first synthetic successes. *Dalton Trans.* **2014**, *43*, 4151–4162.
- (38) Pandey, K. K. Structure and bonding analysis of germanones $[(Eind)_2Ge=O]$, $[(Tbt)(Tip)Ge=O]$ and $[R_2Ge=O]$ ($R = Me, Ph$): Significance of the dispersion interactions. *Comput. Theor. Chem.* **2015**, *1073*, 20–26.
- (39) Jissy, A. K.; Meena, S. K.; Datta, A. Reactivity of germanones: far removed from ketones – a computational study. *RSC Adv.* **2013**, *3*, 24321–24327.
- (40) Frisch, M. J.; Trucks, G. W.; Schlegel, H. B.; Scuseria, G. E.; Robb, M. A.; Cheeseman, J. R.; Scalmani, G.; Barone, V.; Mennucci, B.; Petersson, G. A.; et al. *Gaussian 09*, revision D.01; Gaussian, Inc.: Wallingford, CT, 2009.
- (41) Becke, A. D. Density-functional exchange-energy approximation with correct asymptotic behavior. *Phys. Rev. A: At, Mol, Opt. Phys.* **1988**, *38*, 3098–3100.
- (42) Lee, C.; Yang, W.; Parr, R. G. Development of the colle-salvetti correlation-energy formula into a functional of the electron density. *Phys. Rev. B: Condens. Matter Mater. Phys.* **1988**, *37*, 785–789.
- (43) Becke, D. Density-functional thermochemistry. III. The role of exact exchange. *J. Chem. Phys.* **1993**, *98*, 5648–5652.
- (44) Fukui, K.; Kato, S.; Fujimoto, H. Constituent analysis of the potential gradient along a reaction coordinate. Method and an application to methane + tritium reaction. *J. Am. Chem. Soc.* **1975**, *97*, 1–7.
- (45) Glendening, E. D.; Reed, A. E.; Carpenter, J. E.; Weinhold, F. *NBO*, Version 3.1.
- (46) Boys, S. F.; Bernardi, F. The calculation of small molecular interactions by the differences of separate total energies. Some procedures with reduced errors. *Mol. Phys.* **1970**, *19*, 553–566.
- (47) Simon, S.; Duran, M.; Dannenberg, J. J. How does basis set superposition error change the potential surfaces for hydrogen-bonded dimers? *J. Chem. Phys.* **1996**, *105*, 11024–11031.
- (48) Matsubara, T.; Dupuis, M.; Aida, M. The ONIOM molecular dynamics method for biochemical applications: Cytidine deaminase. *Chem. Phys. Lett.* **2007**, *437*, 138–142.
- (49) Beeman, D. Some multistep methods for use in molecular dynamics calculations. *J. Comput. Phys.* **1976**, *20*, 130–139.
- (50) Berendsen, H. J. C.; Postma, J. P. M.; van Gunsteren, W. F.; DiNola, A.; Haak, J. R. Molecular dynamics with coupling to an external bath. *J. Chem. Phys.* **1984**, *81*, 3684–3690.
- (51) Matsubara, T. Density functional study of the mechanism of $C\equiv C$, $O-H$, and $N-H$ bond activation at the $Pd=X$ ($X=Sn, Si, C$) bonds of the $(PH_3)_2Pd=XH_2$ complexes. *Organometallics* **2001**, *20*, 1462–1471.
- (52) Matsubara, T.; Hirao, K. Density functional study of the σ and π bond activation at the $Pd=X$ ($X = Sn, Si, C$) bonds of the $(H_2PC_2H_4PH_2)Pd=XH_2$ complexes. Is the bond cleavage homolytic or heterolytic? *J. Am. Chem. Soc.* **2002**, *124*, 679–689.
- (53) Matsubara, T.; Ito, T. Quantum mechanical and molecular dynamics studies of the reaction mechanism of the nucleophilic substitution at the Si atom. *J. Phys. Chem. A* **2016**, *120*, 2636–2646.



Hydrogen bonding network-assisted chemiluminescent thermal decomposition of 3-hydroxyphenyl-substituted dioxetanes in crystal



Nobuko Watanabe*, Hikaru Takatsuka, Hisako K. Ijuin, Ayu Wakatsuki, Masakatsu Matsumoto*

Department of Chemistry, Kanagawa University, Tsuchiya, Hiratsuka, Kanagawa 259-1293, Japan

ARTICLE INFO

Article history:

Received 19 March 2016

Revised 27 April 2016

Accepted 2 May 2016

Available online 3 May 2016

Keywords:

Dioxetane

Chemiluminescence

Hydrogen-bonding

Crystalline state

Thermolysis

ABSTRACT

Bicyclic dioxetane **1** bearing a 3-hydroxyphenyl group underwent thermal decomposition in solution (TD_{soln}) to form 3-oxopentyl 3-hydroxybenzoate **4** accompanied by the emission of light [$\lambda_{max}^{CL}(TD_{soln}) = 405$ nm] due to an excited 3-oxopentyl group in **4**. Dioxetane **1** also exclusively gave **4** by thermal decomposition in crystal (TD_{cryst}). However, in contrast to TD_{soln} , TD_{cryst} of **1** gave light [$\lambda_{max}^{CL}(TD_{cryst}) = 464$ nm] due to excited oxidobenzoate **3*** and/or its closely related species formed by CTID (charge-transfer induced decomposition) mechanism. The unique chemiluminescent TD_{cryst} of **1** was presumably the result of hydrogen bonding formed in the crystal between the phenolic proton of a dioxetane molecule and a peroxide oxygen of another dioxetane molecule. In this work, TD_{cryst} as well as TD_{soln} of bicyclic dioxetane analog bearing a 4-fluorenyl-3-hydroxyphenyl moiety **10** and of adamantylidene-dioxetane bearing a 3-hydroxyphenyl group **5b** were also investigated.

© 2016 Elsevier Ltd. All rights reserved.

Deprotonation of a 3-hydroxyphenyl-substituted bicyclic dioxetane **1** with a base produces unstable dioxetane **2** bearing a phenoxide anion, which decomposes by intramolecular charge-transfer-induced decomposition (CTID) mechanism to effectively give 3-oxopentyl 3-oxidobenzoate **3** with the emission of bright blue light (Base-Induced Decomposition: BID) (Scheme 1).^{1,2} On the other hand, when simply heated in a nonpolar solvent, dioxetane **1** decomposes to give 3-oxopentyl 3-hydroxybenzoate **4** accompanied by the emission of very weak light (Thermal Decomposition: TD). A similar tendency has been observed for an adamantylidene-substituted dioxetane **5a**, the BID of which effectively produces excited methyl 3-oxidobenzoate **6*** which emits blue light, while simple TD in solution gives light due to excited ketone moiety or an excited 3-hydroxybenzoate moiety in **4**.

When crystalline dioxetane **1** (mp 119.0 °C) was heated at 100 °C, the crystals of **1** emitted blue light, the spectrum of which had a maximum wavelength at $\lambda_{max}^{CL}(TD_{cryst}) = 464$ nm, as shown in Figure 1[(A)-(a)] and Table 1. On the other hand, TD_{soln} of **1** in hot *p*-xylene (110 °C) gave weak chemiluminescence with $\lambda_{max}^{CL}(TD_{soln}) = 405$ nm [Fig. 1(A)-(b), Table 1]. These results showed that the

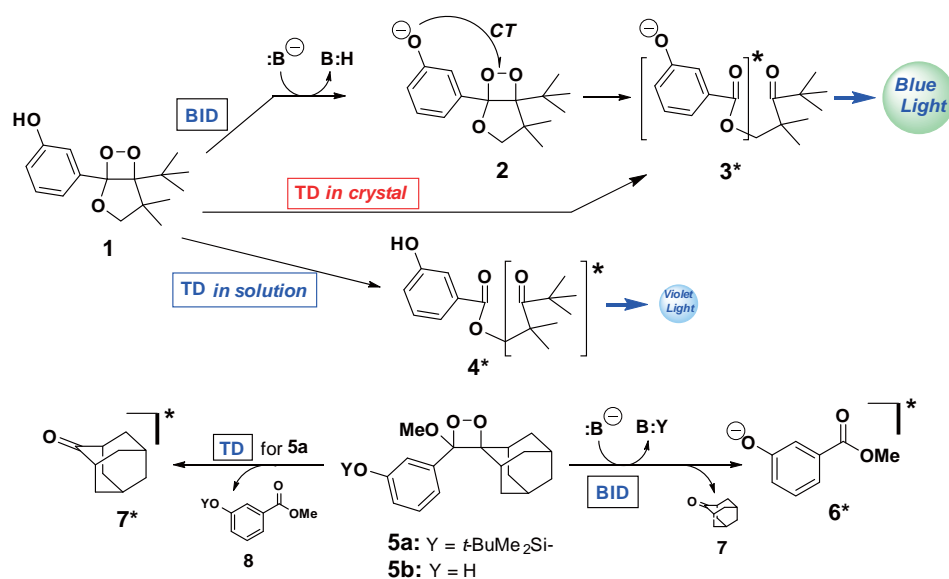
chemiluminescence for TD_{cryst} of **1** occurs via a mechanism different from that in the case of simple TD_{soln} in non-polar solvent (Scheme 1). Notably, ¹H NMR analysis showed that the spent crystalline mixture for TD_{cryst} exclusively gave keto ester **4** as in the case for TD_{soln} .

Thus, we measured the fluorescence of authentic keto ester **4** in crystal as well as in *p*-xylene solution. As shown in Figure 1[(B)-(a) and (b)] and Table 1, maximum wavelength of fluorescence, $\lambda_{max}^{fl}(soln)$, was observed at 360 nm in *p*-xylene, while $\lambda_{max}^{fl}(cryst)$ was observed at 346 nm in crystal. Next, we examined fluorescence of two model compounds in *p*-xylene. Methyl 3-hydroxybenzoate (**8**; Y = H) as a model of a 3-hydroxybenzoate moiety in **4** showed fluorescence with $\lambda_{max}^{fl}(soln) = 344$ nm, while di-*tert*-butyl ketone as a model of the ketone moiety in **4** showed fluorescence with $\lambda_{max}^{fl}(soln) = 407$ nm [Fig. 1(B)-(d) and (e)]. These results revealed that the chemiluminescence for TD_{soln} of **1** in *p*-xylene was undoubtedly due to an excited ketone moiety in **4**, while the chemiluminescence for TD_{cryst} of **1** could not be attributed to either the excited ketone moiety or the excited hydroxybenzoate moiety in **4**.

As has been reported for BID of **1**, intermediary oxidophenyl-substituted dioxetane **2** undergoes CTID to display chemiluminescence with $\lambda_{max}^{CL}(BID) = 466$ –470 nm.² Figure 1(A) shows the chemiluminescence spectrum for BID of **1** in TBAF (tetrabutylammonium fluoride)/acetonitrile as a representative together with those for TD_{soln} and TD_{cryst} of **1**. A comparison of these spectra shows that the chemiluminescence spectrum for TD_{cryst} overlapped

* Corresponding authors. Tel.: +81 463 59 4111; fax: +81 463 58 9684.

E-mail addresses: nwatanab@kanagawa-u.ac.jp (N. Watanabe), matsumo-chem@kanagawa-u.ac.jp (M. Matsumoto).



Scheme 1. Chemiluminescent decomposition of 3-oxophenyl-substituted dioxetanes **1** and **5**.

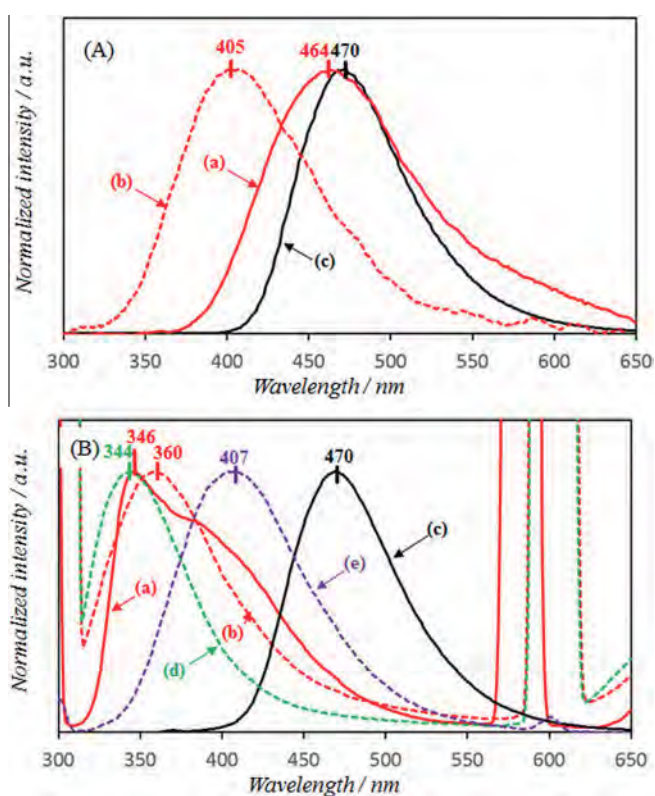


Figure 1. Chemiluminescence spectra of dioxetane **1** (A): (a) for TD_{cryst} , (b) for TD_{soln} in *p*-xylene and (c) for BID in TBAF/acetonitrile. Fluorescence spectra (B): for ketoester **4** (a) in crystal, (b) in *p*-xylene and (c) in TBAF/acetonitrile, and (d) for methyl 3-hydroxybenzoate **8** in *p*-xylene and (e) for di-*tert*-butyl ketone in *p*-xylene.

that for BID, though the former somewhat broadened, especially in the shorter wavelength region. Thus, the TD_{cryst} of **1** was presumed to proceed by a CTID mechanism as in the case of BID.

To better understand the significant difference in the chemiluminescence of **1** between TD_{soln} and TD_{cryst} , we performed an X-ray single crystallographic analysis of **1**.^{4,5} As shown in Figure 2,

Table 1
Maximum wavelength for chemiluminescence of dioxetanes **1**, **10** and **5b** and maximum wavelength for fluorescence of ketoesters **4** and **12**

	λ_{max}^{CL} for chemiluminescence of dioxetane/nm			λ_{max}^f for fluorescence of authentic emitter/nm		
	BID ^a	TD_{soln} ^b	TD_{cryst} ^c	Basic soln ^a	Neutral soln ^d	Crystal ^e
1	470	405	464	4	470	360, 407 ^f
10	500	377	398	12	500	381
5b	469	428	451	8^g	470	344, 430 ^h

^a 25 °C in TBAF/acetonitrile.

^b 110 °C in *p*-xylene.

^c 100 °C.

^d 25 °C in *p*-xylene.

^e 25 °C.

^f Di-*tert*-butyl ketone.

^g Y = H.

^h Adamantanone 7.

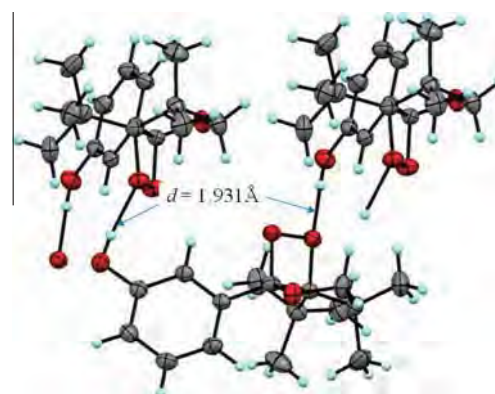


Figure 2. View of the intermolecular hydrogen bonding network for dioxetane **1** in crystal.

dioxetane **1** in crystal formed a network constructed by intermolecular hydrogen bonding between a phenolic OH of one molecule and a peroxide oxygen of another molecule (bond length $d = 1.931 \text{ \AA}$ and bond angle $\theta = 173.7^\circ$).⁶ Thus we can imagine that,

upon heating, a phenolic proton of dioxetane **1** in crystal is eventually transferred through the vibration of $O_{\text{phenol}}\text{---}H\text{---}O_{\text{peroxide}}$ to a peroxide oxygen to strongly induce a negative charge on O_{phenol} and to form a phenoxide anion as an extreme,⁷ which would spontaneously cause CTID of dioxetane to give blue light (Scheme 2).^{8,9} Note that the hydrogen bonding in crystalline **1** may also activate dioxetane O—O as an electron acceptor for CTID by inducing a positive charge on O_{peroxide} (vide infra).^{10–13} On the other hand, the results of ¹H NMR analysis suggested that **1** existed without any hydrogen bonding in *p*-xylene: the phenolic OH proton of **1** displayed a peak at δ_{H} 3.9 ppm in *p*-xylene-*d*₁₀.^{13–15} Thus, dioxetane **1** would thermally decompose without dissociation of the phenolic OH. Notably, the rate of decomposition for TD_{cryst} of **1** at 100 °C was ca. 40% faster than that for TD_{soln}: rate constant *k* for TD_{cryst} was $1.72 \times 10^{-5} \text{ s}^{-1}$, while *k* for TD_{soln} was $1.22 \times 10^{-5} \text{ s}^{-1}$.¹⁶

We next investigated the chemiluminescence for TD of dioxetanes **9** and **10** in crystal as well as in *p*-xylene. Dioxetane **9** is a 3-methoxyphenyl-analog of **1** that does not possess a phenolic proton capable of forming hydrogen bonds and, of course, hardly undergoes chemiluminescent CTID through an oxidophenyl-substituted dioxetane. Dioxetane **10** is an analog of **1** bearing a 3-hydroxyphenyl that is further substituted with a 9,9-dimethylfluoren-2-yl group at the 4-position, which would be expected to play an important role in the construction of a fluorophore of substituted 3-hydroxybenzoate when **10** decomposed.

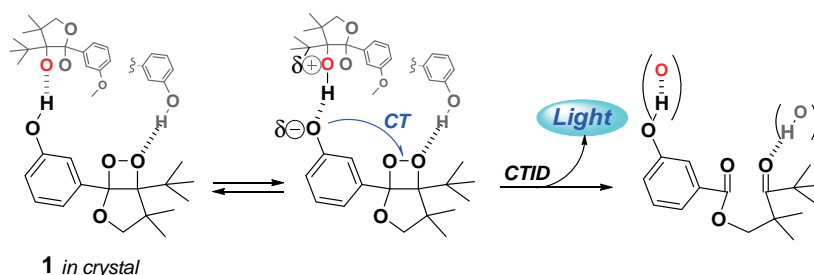
Upon heating at 80 °C, crystalline dioxetane **9** (mp 95 °C) hardly emitted light. Further heating at higher temperature (110 °C) caused crystalline **9** to melt and to give very weak chemiluminescence with $\lambda_{\text{max}}^{\text{CL}} = 422 \text{ nm}$. Dioxetane **9** underwent TD_{soln} in hot

p-xylene to afford weak light with $\lambda_{\text{max}}^{\text{CL}}(\text{TD}_{\text{soln}}) = 405 \text{ nm}$ (Scheme 3). The result showed that TD_{soln} of dioxetane **9** gave light from the excited ketone moiety but not from the excited 3-methoxybenzoate moiety of keto ester **11** similar to the case for TD_{soln} of **1**: methyl 3-methoxybenzoate as a model of the aromatic ester moiety in **11** gave fluorescence with $\lambda_{\text{max}}^{\text{fl}} = 350 \text{ nm}$.

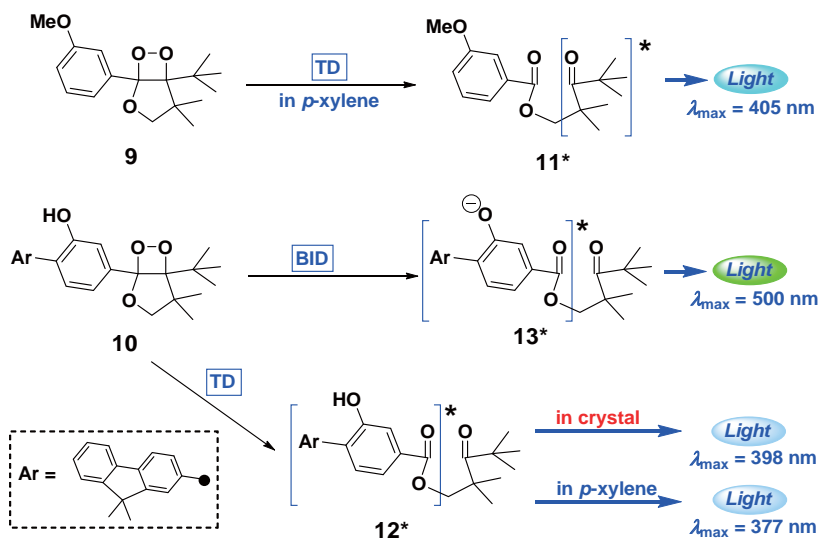
When dioxetane **10** was treated with TBAF in acetonitrile at 25 °C, BID took place accompanied by a flash of greenish blue light with $\lambda_{\text{max}}^{\text{CL}}(\text{BID}) = 500 \text{ nm}$ [Fig. 3(A)-(c), Table 1 and Scheme 3], the spectrum of which coincided with the fluorescence spectrum of 4-fluorenyl-3-oxidobenzoate **13** generated from keto ester **12** in TBAF/acetonitrile [Fig. 3(B)-(c) and Table 1].¹⁷ This result shows that the introduction of a 9,9-dimethyl-2-fluorenyl group at the 4-position of 3-hydroxyphenyl in dioxetane **1** was effective for promoting a red-shift of the chemiluminescence for BID of dioxetane **10**.

The effect of the introduction of a 2-fluorenyl group was also reflected in the TD_{soln} of **10**, which displayed chemiluminescence with $\lambda_{\text{max}}^{\text{CL}}(\text{TD}_{\text{soln}}) = 377 \text{ nm}$ in *p*-xylene [Fig. 3(A)-(b), Table 1]. Since free keto ester **12** showed fluorescence with $\lambda_{\text{max}}^{\text{fl}}(\text{soln}) = 381 \text{ nm}$ in *p*-xylene [Fig. 3(B)-(b), Table 1], we considered that the chemiluminescence for the TD_{soln} of **10** was due to an excited aromatic ester rather than to a ketone moiety of **12**, in contrast to the TD_{soln} of **1** and **9** (Scheme 3). However, emission from the excited ketone moiety of **12** should more or less take place for TD_{soln} of **10**: $\lambda_{\text{max}}^{\text{fl}}$ for di-*tert*-butyl ketone as a model of a ketone moiety of **12** was >20 nm longer than that for **12** (Table 1).¹⁸

Next, we investigated how dioxetane **10** displayed chemiluminescence with TD_{cryst}. When crystalline dioxetane **10**



Scheme 2. Thermal decomposition of dioxetane **1** assisted by intermolecular-hydrogen bonding in crystal.



Scheme 3. Chemiluminescent decomposition of dioxetanes **9** and **10**.

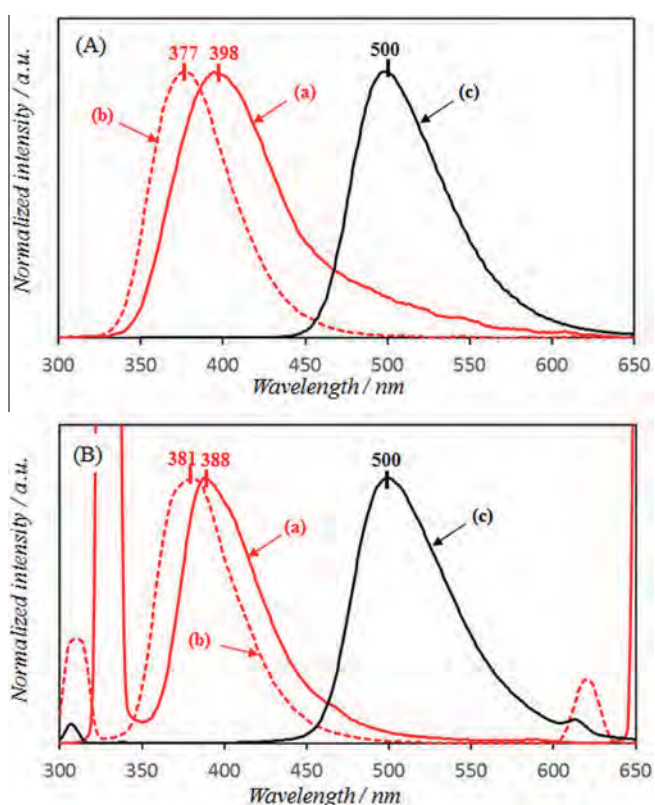


Figure 3. Chemiluminescence spectra of dioxetane **10** (A): (a) for TD_{cryst} , (b) for TD_{soln} in *p*-xylene and (c) for BID in TBAF/acetonitrile. Fluorescence spectra of ketoester **12** (B): (a) in crystal, (b) in *p*-xylene and (c) in TBAF/acetonitrile.

(mp 165.0 °C) was heated at 100 °C, the crystals emitted light with $\lambda_{max}^{CL}(TD_{cryst}) = 398$ nm [Fig. 3(A)-(a)]: crystalline keto ester **12** displayed fluorescence with $\lambda_{max}^{fl}(cryst) = 388$ nm [Fig. 3(B)-(a), Table 1]. As shown in Figure 3(A) and Table 1, $\lambda_{max}^{CL}(TD_{cryst})$ was much shorter than $\lambda_{max}^{CL}(BID)$ (500 nm), though rather longer than $\lambda_{max}^{CL}(TD_{soln})$ (377 nm) for **10**. These results showed that hydrogen bonding, if present, apparently did not cause CTID for TD_{cryst} of **10** as in the case of **1**.

The results of X-ray single crystallographic analysis were also suggestive.^{4,5} The phenolic proton of **10** in crystal was found to undergo two types of hydrogen bonding, *type A* (occupancy: 80%) and *type B* (occupancy: 20%). *Type A* was hydrogen bonding with a peroxide oxygen of another dioxetane, similar to the case of **1**, and in *type B*, the phenol ring lay on the opposite side to promote hydrogen bonding between the phenolic OH and an oxygen of the tetrahydrofuran ring in another dioxetane (Fig. 4). The bond distance of OH—O_{dioxetane} ($d = 2.024$ Å) for *type A* in **10** was longer and presumably weaker than that ($d = 1.931$ Å) for **1**. Therefore, even with heating at 100 °C, the peroxide oxygen could not attract the phenolic proton strongly enough to cause CTID of **10**. On the

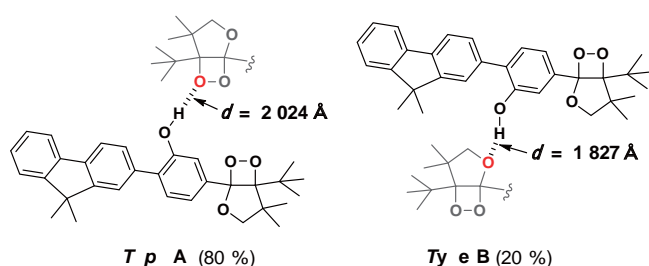


Figure 4. Hydrogen bondings for dioxetane **10** in crystal.

other hand, the hydrogen bond of *type B* ($d = 1.827$ Å) was shorter and presumably stronger than the hydrogen bond for **1**, so that it seemed to induce a negative charge on the phenolic oxygen in **10** that causes CTID to give long-wavelength light ($\lambda_{max}^{CL} \approx 500$ nm). However, such emission was hardly observed for TD_{cryst} of **10**, as shown in Figure 3(A)-(a). Although the low abundance of *type B* hydrogen bonds (only 20%) can explain why its effect was hardly reflected in the chemiluminescence spectrum of TD_{cryst} , the oxygen atom of the tetrahydrofuran ring in bicyclic dioxetane **10** acted as a strong proton acceptor but presumably could not well activate dioxetane O—O to cause CTID for *type B*.^{10–12}

Finally we investigated the chemiluminescent TD_{soln} and TD_{cryst} of dioxetane **5b** (mp 135 °C) which possessed a 3-hydroxyphenyl group, similar to **1**, although we were unable to perform X-ray single crystallographic analysis. TD_{soln} of **5b** in *p*-xylene at 110 °C gave light with $\lambda_{max}^{CL}(TD_{soln}) = 428$ nm due to **7***, while BID of **5b** in TBAF/acetonitrile showed chemiluminescence with $\lambda_{max}^{CL}(BID) = 469$ nm due to **6*** (Table 1, Scheme 1). On the other hand, crystalline **5b**, upon heating at 100 °C, emitted light with $\lambda_{max}^{CL}(TD_{cryst}) = 451$ nm (Table 1). Thus, TD_{cryst} of **5b** was presumed to proceed by CTID mechanism as in the case of crystalline **1**. However, as the $\lambda_{max}^{CL}(TD_{cryst})$ of **5b** was considerably shorter than the $\lambda_{max}^{CL}(BID)$, the hydrogen bonding for **5b** might be somewhat weaker than that for **1**, but stronger than that for **10**.

In conclusion, crystalline dioxetanes bearing a 3-hydroxyphenyl moiety **1** and **5b** were found to undergo thermal decomposition (TD_{cryst}) accompanied by the emission of light, the spectrum of which was quite different from that for thermal decomposition in a nonpolar solution (TD_{soln}). Hydrogen bonding between the phenolic proton of a dioxetane molecule and the peroxide oxygen of another dioxetane molecule was suggested to play an important role in TD_{cryst} . This suggestion led to the idea that the inclusion of an appropriate neutral hydrogen bonding donor/acceptor to a crystalline dioxetane bearing a phenol group should cause unique chemiluminescence in crystal. As an preliminary example, we showed that, when heated, a solid mixture of dioxetane **10** and *N,N'*-diphenylurea gave light with $\lambda_{max}^{CL}(TD_{cryst})$ at 488 nm.

Acknowledgment

The authors gratefully acknowledge financial assistance in the form of Grants-in-aid (Nos. 25350269, 25410056 and 25410057) or Scientific Research from the Ministry of Education, Culture, Sports, Science, and Technology, Japan.

Supplementary data

Supplementary data associated with this article can be found, in the online version, at <http://dx.doi.org/10.1016/j.tetlet.2016.05.004>.

References and notes

- (a) Beck, S.; Köster, H. *Anal. Chem.* **1990**, *62*, 2258–2270; (b) Adam, W.; Reihardt, D.; Saha-Möller, C. R. *Analyst* **1996**, *121*, 1527–1531; (c) Matsumoto, M. *J. Photochem. Photobiol., C* **2004**, *5*, 27–53; (d) Matsumoto, M.; Watanabe, N. *Bull. Chem. Soc. Jpn. Acc.* **2005**, *78*, 1899–1920; (e) Adam, W.; Trofimov, A. V. In *The Chemistry of Peroxides*; Rappoport, Z., Ed.; Wiley: New York, 2006; Vol. 2, p 1171.
- (a) Matsumoto, M.; Mizoguchi, Y.; Motoyama, T.; Watanabe, N. *Tetrahedron Lett.* **2001**, *42*, 8869–8872; (b) Watanabe, N.; Oguri, A.; Horikoshi, M.; Takatsuka, H.; Ijuin, H. K.; Matsumoto, M. *Tetrahedron Lett.* **2014**, *55*, 1644–1647.
- (a) Schaap, A. P.; Handley, R. S.; Giri, B. P. *Tetrahedron Lett.* **1987**, *28*, 935–938; (b) Schaap, A. P.; Chen, T. S.; Handley, R. S.; DeSilva, R.; Giri, B. P. *Tetrahedron Lett.* **1987**, *28*, 1155–1158; (c) Trofimov, A. V.; Vasil'ev, R. F.; Mielke, K.; Adam, W. *Photochem. Photobiol.* **1995**, *62*, 35–43; (d) Adam, W.; Matsumoto, M.; Trofimov, A. V. *J. Am. Chem. Soc.* **2000**, *122*, 8631–8634; (e) Wakasugi, T.; Fujimori, K.; Matsumoto, M. *Chem. Lett.* **2002**, *31*, 762–763.

- Collection of X-ray diffraction data and their analysis were shown in [Supplementary data](#). Crystallographic data for the structural analysis of **1** and **10** have been deposited at the Cambridge Crystallographic Data Center, CCDC-265174, CCDC-1458115. These data can be obtained free of charge via www.ccdc.cam.ac.uk/conts/retrieving.html (or from the Cambridge Crystallographic Data Center, 12 Union Road, Cambridge CB21EZ, UK; fax: (+44)1223-336-0333; or deposit@ccdc.cam.ac.uk).
- ORTEP views of **1** and **10** were shown in [Supplementary data](#).
- This hydrogen bonding is a typical 'moderate hydrogen bond', which is one of the three categories classified by Jeffrey Jeffrey, G. A. *An Introduction to Hydrogen Bonding*; Oxford University Press: Oxford, 1997.
- Pihko, P. In *Hydrogen Bonding in Organic Synthesis*; Pihko, P., Ed.; Wiley: Weinheim, 2009; pp 5–14.
- A related hydrogen bonding-assisted chemiluminescence from a phenolic dioxetane has been observed as SPD (Solvent-Promoted Decomposition) in an aprotic polar solvent.⁹
- Tanimura, M.; Watanabe, N.; Ijuin, H. K.; Matsumoto, M. *J. Org. Chem.* **2011**, *76*, 902–908.
- Catalysts with acidic sites, such as silica gel and alumina, have been reported to accelerate the rate of decomposition of dioxetane.¹¹
- Zaklika, K. A.; Burns, P. A.; Schaap, A. P. *J. Am. Chem. Soc.* **1978**, *100*, 318–320.
- It has been reported for the case of intramolecular hydrogen bonding of phenolic OH that a difference in the proton acceptor, i.e., oxygen of dioxetane O—O or of the tetrahydrofuran ring, significantly affects the thermal stability of dioxetanes: bicyclic dioxetane analogs bearing a hydroxynaphthyl, in which OH forms a hydrogen bond with oxygen of dioxetane O—O, decompose thermally ca. 10^5 times faster than analogs in which OH forms a hydrogen bond with oxygen of the tetrahydrofuran ring.¹³
- Hoshiya, N.; Watanabe, N.; Ijuin, H. K.; Matsumoto, M. *Chem. Lett.* **2007**, *36*, 516–517.
- It has been reported for oxyaryl-substituted dioxetanes that the aryl OH proton participating in hydrogen bonding (HB) displays a peak at δ_{H} 8–13 ppm in *p*-xylene-*d*₁₀ or CDCl₃, while the proton free from HB displays a peak at 4–6 ppm.¹⁵
- Tanimura, M.; Watanabe, N.; Ijuin, H. K.; Matsumoto, M. *J. Org. Chem.* **2010**, *75*, 3678–3684.
- Both TD_{soln} in *p*-xylene-*d*₁₀ and TD_{cryst} of **1** took place according to first-order kinetics to give **4**.
- Chemiluminescence properties for dioxetane **10** in TBAF/acetonitrile at 25 °C were as follows: chemiluminescence efficiency $\Phi^{\text{CL}} = 0.17$, efficiency of singlet chemiexcitation $\Phi_{\text{S}} = 0.71$, rate constant of CTID $k^{\text{CTID}} = 0.22 \text{ s}^{-1}$ at 25 °C.
- The emission from the ketone moiety might be hidden by the emission from the excited aromatic ester moiety of **12**: fluorescence efficiency Φ^{fl} in *p*-xylene was 0.53 for **12**, 6.7×10^{-3} for di-*tert*-butyl ketone and 4.0×10^{-2} for methyl 3-hydroxybenzoate.



Solvent- and temperature-controlled inversion of π -facial selectivity in the 1,2-cycloaddition of singlet oxygen to hydroxyphenyl-substituted cyclohexadihydrofurans



Nobuko Watanabe^{**}, Kiriko Hiragaki, Kunihiko Tsurumi, Hisako K. Ijuin, Masakatsu Matsumoto^{*}

Department of Chemistry, Kanagawa University, Tsuchiya, Hiratsuka, Kanagawa 259-1293, Japan

ARTICLE INFO

Article history:

Received 18 January 2017

Received in revised form

13 February 2017

Accepted 17 February 2017

Available online 20 February 2017

Keywords:

Singlet-oxygenation

1,2-Cycloaddition of singlet oxygen

Stereoselectivity

Solvent effect

Temperature effect

ABSTRACT

Singlet-oxygenation of 3-hydroxyphenyl-substituted dihydrofurans fused with a cyclohexane **1a–c** exclusively gave the corresponding *syn/anti*-stereoisomeric mixtures of dioxetanes **2a–c**. The *syn/anti*- π -facial selectivity in the 1,2-cycloaddition of singlet oxygen ($^1\text{O}_2$) was found to be remarkably sensitive to the solvent as well as the reaction temperature. In fact, the solvent effect was so conspicuous that inversion of the *syn/anti*- π -facial selectivity was observed in different solvents, such as chloroform and toluene. An LSER (linear solvation energy relationships) analysis suggested that the Lewis-acidity/basicity and HBD (hydrogen-bond donor)/HBA (hydrogen-bond acceptor) ability as well as dipolarity/polarizability of the solvent played an important role in this change in *syn/anti*- π -facial selectivity. An investigation of the temperature-dependency of the singlet-oxygenation suggested that the *syn/anti*- π -facial-selective 1,2-cycloaddition of $^1\text{O}_2$ to **1** was a conformationally-(entropy-) controlled process.

© 2017 Elsevier Ltd. All rights reserved.

1. Introduction

Experimental and theoretical studies have shown that singlet oxygen ($^1\text{O}_2$) attacks a carbon-carbon double bond *side-on* to give a perepoxide intermediate, which rearranges to a 1,2-dioxetane ([2 + 2] cycloaddition) or abstracts an allylic hydrogen atom, when present in a preferential conformation, to form an allylic hydroperoxide ('ene' reaction) (Scheme 1).^{1–8} Thus, for the singlet-oxygenation of olefins, the substituents sterically and/or electronically direct the incoming $^1\text{O}_2$ to the π -face and the side of the double bond (π -facial selectivity and side selectivity) to cause mode-,^{9–12} regio-,^{13–16} and/or stereo-selectivity.^{17–20} In addition to these effects in the chemical reactivity, it has recently been suggested that one stereochemical pathway is physically deactivated more rapidly through quenching of the incoming $^1\text{O}_2$ by C–H bond vibrations.^{19,20}

These selectivities are often strongly affected by solvent and

temperature.^{19,21–26} For instance, a change in solvent has been known to cause the inversion of mode-selectivity in 1,2-cycloaddition vs the 'ene' reaction²³ or 1,2-cycloaddition vs 1,4-cycloaddition²⁵ for the singlet-oxygenation of certain olefins (dienes). The solvent-dependent inversion of chemoselectivity (diastereoselectivity) has also been reported for the 1,2-cycloaddition of $^1\text{O}_2$ to a mixture of diastereoisomeric olefins.^{19,20} However, little is known about a solvent effect so strong that it can cause an inversion of the π -facial selectivity of $^1\text{O}_2$ for 1,2-cycloaddition to an olefin.

In the course of our study on high-performance dioxetane-based chemiluminescent compounds, we investigated the singlet-oxygenation of oxyphenyl-substituted dihydrofurans **1** fused with a cyclohexane ring [3,4-cyclohexa-2,3-dihydrofuran: 8-oxabicyclo [4.3.0]non-1 (9)-ene] which also had a substituent at the 3-position (Scheme 2). We unexpectedly found that inversion of the π -facial selectivity of $^1\text{O}_2$ occurred to preferentially give dioxetane *syn-2* or its stereoisomer *anti-2* depending on the type of solvent. We report here the features of this remarkable solvent effect on the *syn/anti*- π -facial selectivity in the 1,2-cycloaddition of $^1\text{O}_2$ to bicyclic dihydrofurans **1** together with the thermodynamic aspects of the present singlet-oxygenation.

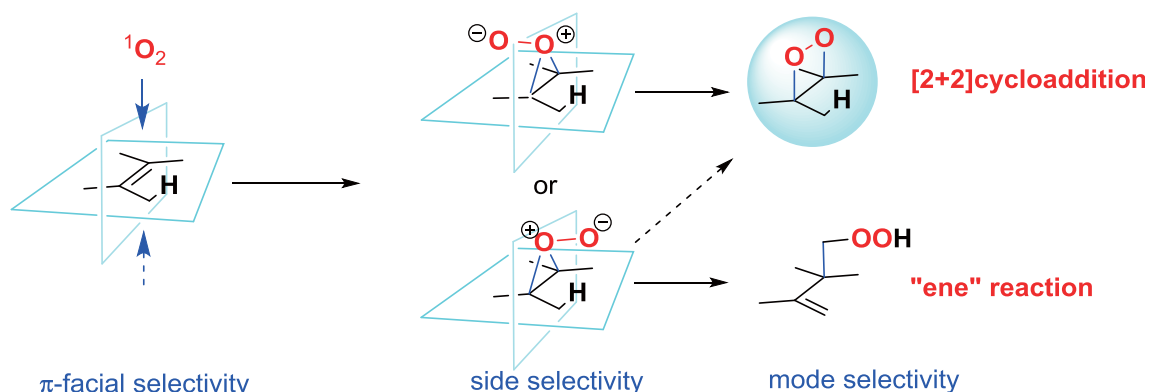
* Corresponding author.

** Corresponding author.

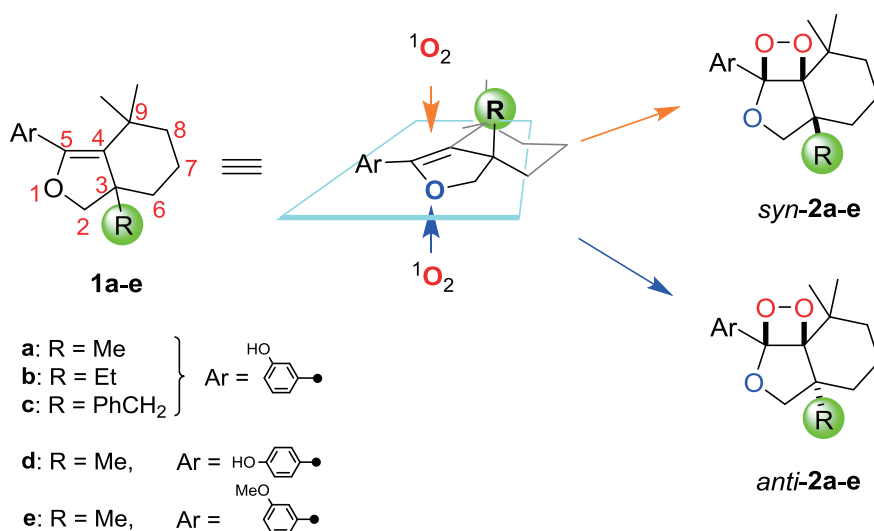
E-mail addresses: nwatanab@kanagawa-u.ac.jp (N. Watanabe), matsumo-chem@kanagawa-u.ac.jp (M. Matsumoto).

<http://dx.doi.org/10.1016/j.tet.2017.02.038>

0040-4020/© 2017 Elsevier Ltd. All rights reserved.



Scheme 1. Selectivities for the addition of singlet oxygen to an olefin.



Scheme 2. Stereoselective formation of *syn/anti*-dioxetanes **2** from 3,4-cyclohexa-2,3-dihydrofurans **1**.

2. Results and discussion

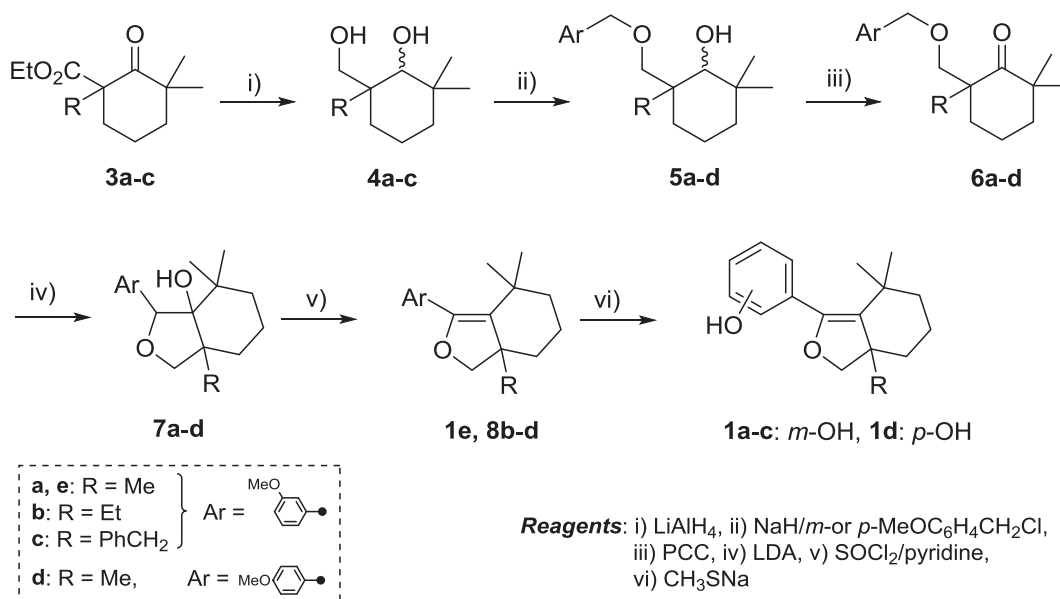
2.1. Synthesis of 5-(hydroxyphenyl)-3,4-cyclohexa-2,3-dihydrofurans

The dihydrofurans bearing a 5-(3-hydroxy)phenyl investigated here possessed further a substituent, Me (**1a**), Et (**1b**), or PhCH₂- (**1c**), at the 3-position (Scheme 2). 4-Hydroxyphenyl-isomer **1d** and 3-methoxyphenyl-analog **1e** were also investigated for comparison to **1a** in singlet-oxygenation. The bicyclic dihydrofurans **1** were synthesized through several steps starting from ethyl 3,3-dimethyl-2-oxocyclohexanecarboxylate **3** with a substituent (R) at the 1-position: R = Me for **3a**, Et for **3b** and PhCH₂- for **3c** (Scheme 3). These keto esters were reduced with LiAlH₄ to the corresponding diols **4a–4c**. Williamson ether synthesis using diol **4a** (R = Me) and 3-methoxybenzyl chloride selectively gave cyclohexylmethyl 3-methoxybenzyl ether **5a**. The remaining OH group of **5a** was in turn oxidized with pyridinium chlorochromate (PCC) to give 2-[(3-methoxy)benzyloxymethyl]cyclohexanone **6a** in high yield. Lithium diisopropylamide (LDA)-mediated cyclization²⁷ of **6a** effectively took place to give hydroxytetrahydrofuran fused with cyclohexane ring **7a**, which was successively dehydrated with SOCl₂/pyridine to give 3-methoxyphenyl-substituted bicyclic dihydrofuran **1e** in good yield. Finally, a methoxy group in **1e** was deprotected with CH₃SNa/DMF to give the bicyclic dihydrofuran **1a**.

As shown in Scheme 3, the bicyclic dihydrofurans **1b** and **1c** were similarly synthesized starting from **3b** and **3c**, respectively. By using *p*-methoxybenzyl chloride instead of its *m*-isomer, we prepared (4-methoxy)phenylmethyl ether **5d** via the Williamson synthesis from **4a**. Thus, 5-(4-methoxyphenyl)dihydrofuran **1d** was synthesized starting from **5d** through four steps **5d** → **6d** → **7d** → **8d** → **1d** (Scheme 3).

2.2. Solvent effect on the stereoselective 1,2-cycloaddition of singlet oxygen to 5-(oxyphenyl)-3,4-cyclohexa-2,3-dihydrofurans

For the singlet-oxygenation of dihydrofurans **1**, dioxetanes *syn*-**2** can be produced when ¹O₂ attacks the π-face where a substituent R lies, while stereoisomers *anti*-**2** can form when ¹O₂ attacks the opposite π-face (Scheme 2). When a solution of bicyclic dihydrofuran **1a** was irradiated together with a small amount of tetraphenylporphyrin (TPP) in toluene with a 940 W Na lamp under an oxygen atmosphere at 0 °C for 30 min, a mixture of dioxetane *syn*-**2a** and its isomer *anti*-**2a** (*syn/anti* = 79/21) was exclusively produced. Dioxetane *syn*-**2a** was isolated in pure form by recrystallization of the stereoisomeric mixture. On the other hand, the singlet-oxygenation of **1a** in chloroform at 0 °C gave a mixture mainly consisting of *anti*-**2a** (*syn/anti* = 13/87), which was also isolated in pure form by recrystallization. The structures of *syn*-**2a** and *anti*-**2a** were determined by ¹H NMR, ¹³C NMR, IR, Mass, and



Scheme 3. Synthetic pathway starting from 2-oxocyclohexanecarboxylates **3** to 3,4-cyclohexa-2,3-dihydrofurans **1**.

HRMass spectral analyses. In addition, X-ray single crystallographic analysis was successfully performed for both *syn*-**2a** and *anti*-**2a**: ORTEP views of these dioxetanes are shown in Fig. 1. These results indicate that inversion of the *syn/anti*- π -facial selectivity occurred between the use of chloroform and toluene for the 1,2-cycloaddition of $^1\text{O}_2$ to **1a**. Notably, the *syn/anti*-ratios of **2a** did not meaningfully change when CDCl_3 or toluene- d_8 was used instead of non-deuterated solvents, though the rates of the singlet-oxygenation appeared to be accelerated: the lifetime of $^1\text{O}_2$ is significantly prolonged in a deuterated solvent [lifetime of $^1\text{O}_2$ ($\times 10^{-6}$ s): 60–415 in CHCl_3 vs. 300–3600 in CDCl_3 , and 25–29 in toluene vs. 310–320 for toluene- d_8].²⁸

We were surprised to observe such a remarkable solvent effect on stereoselectivity in the 1,2-cycloaddition of $^1\text{O}_2$ to dihydrofuran **1a**, even though the *syn/anti*- π faces of **1a** differed from each other only sterically by a 3-methyl group on the bridgehead or a 6-methylene of a cyclohexane ring. We first considered that the change in *syn/anti*- π -facial selectivity was related to rotational isomerism of the 3-hydroxyphenyl group that accompanied a change in the dipole moment, which would be affected by the solvent polarity. Thus, we examined the singlet-oxygenation of

dihydrofuran **1d** bearing a 4-hydroxyphenyl that was symmetric around the bond axis, the rotation of which might cause only a slight change in the dipole moment. The singlet-oxygenation of dihydrofuran **1d** gave a 10/90 *syn/anti*-mixture of dioxetane **2d** in chloroform, and a 97/3 *syn/anti*-mixture of **2d** in toluene at 0 °C: *anti*-**2d** was isolated in pure form, though *syn*-**2d** was unstable and partly decomposed during purification (Scheme 2). This result showed that rotational isomerism of the aromatic ring did not meaningfully participate in the solvent-dependent change in *syn/anti*- π facial selectivity in the singlet-oxygenation of **1a**.

Next, to understand the steric interaction of $^1\text{O}_2$ with a 3-substituent (Me for **1a**), we investigated the singlet-oxygenation of dihydrofurans possessing an ethyl **1b** or benzyl **1c** at the 3-position, which are larger than a methyl group. Under singlet-oxygenation in chloroform or toluene at 0 °C, ethyl-analog **1b** and benzyl-analog **1c** exclusively gave the corresponding *syn/anti*-mixtures of dioxetane **2b** and **2c** (Scheme 2). The *syn/anti*-ratios for **2b** and **2c** are summarized together with those for **2a** in Table 1. As shown, toluene was rather preferable for *syn*- π -facial attack by $^1\text{O}_2$, while chloroform was preferable for *anti*- π -facial attack by $^1\text{O}_2$, regardless of the 3-substituent on **1**. However, we should note the

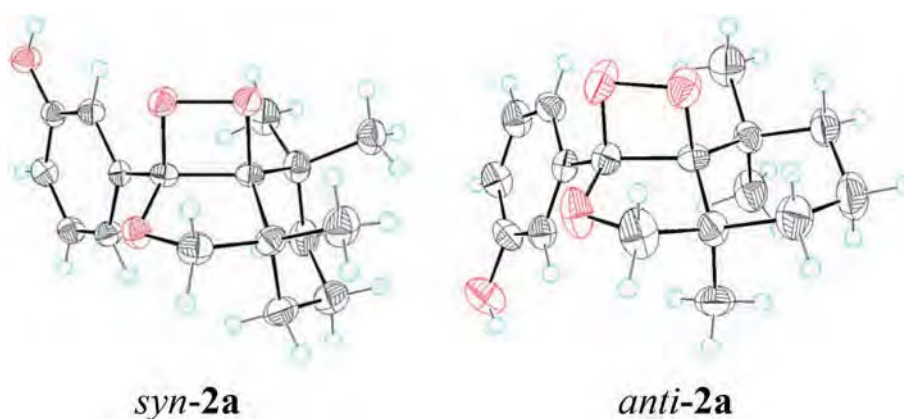


Fig. 1. ORTEP views of dioxetanes *syn*-**2a** and *anti*-**2a**.

Table 1
Solvent effect on selectivity of *syn/anti*-stereoisomeric dioxetanes **2** for the singlet-oxygenation of dihydrofurans **1**^a.

Solvent ^b	Ratio of <i>syn/anti</i> -dioxetane 2			
	2a	2b	2c	2e
chloroform	13/87	5/95	21/79	10/90
methanol ^c	21/79	3/97	26/74	30/70
dichloromethane	24/76	12/88	53/47	10/90
acetonitrile ^d	31/69	28/72	66/34	44/56
toluene	79/21	31/69	94/6	90/10
acetone	90/10	46/54	95/5	51/49

^a All reactions were carried out at 0 °C.

^b Unless otherwise stated, TPP was used as a sensitizer.

^c Rose Bengal was used as a sensitizer.

^d Methylene blue was used as a sensitizer.

following points with respect of the substituent effect. The ethyl group of **1b** apparently acted to suppress *syn*- π -facial attack by ¹O₂ more strongly than the methyl of **1a**. On the other hand, although **1c** had a benzyl group, which is far larger than an ethyl group, **1c** allowed *syn*- π -facial attack by ¹O₂ more favorably than **1b**. These results suggested that the usual steric interaction was not related to the substituent effect on the *syn/anti*- π facial selectivity of ¹O₂ for the singlet-oxygenation of **1** (vide infra).

To understand in more detail how the solvent influences the π -facial selectivity, we investigated the singlet-oxygenation of **1a–1c** in four different solvents, including dichloromethane, acetonitrile, acetone, and methanol, in addition to chloroform and toluene. In all of these solvents, *syn/anti*-isomeric mixtures of dioxetanes **2a–c** were selectively produced and their *syn/anti* ratios markedly changed depending on the solvent, as summarized in Table 1.

Table 1 shows several notable features in the solvent effect on the singlet-oxygenation of dihydrofurans **1**:

- Syn*- π -facial selectivity (*syn*-**2** selectivity) increased in the order chloroform \leq methanol $<$ dichloromethane $<$ acetonitrile $<$ toluene $<$ acetone.
- Syn*-**2**, especially *syn*-**2a** and *syn*-**2c**, showed high selectivity in polar acetone as well as in non-polar toluene.
- Acetonitrile had a much different effect on the *syn/anti*-stereoselectivity than acetone, even though these two solvents resemble each other in terms of measures of polarity, such as dielectric constant (ϵ), dipole moment (μ), polarity parameter (E^T), and nucleophilicity/electrophilicity parameter [DN (donor number)/AN (acceptor number)].²⁹
- Methanol favored the formation of *anti*-**2** while acetone favored the formation of *syn*-**2**, even though these two solvents have a similar DN/AN.

In conclusion, the solvent effect on *syn/anti*- π -facial selectivity for the singlet-oxygenation of **1** did not appear to simply correlate with any particular polarity index or parameter. Thus, we attempted to carry out an LSER (linear solvation energy relationships) analysis according to the following equation:³⁰

$$A = \ln(\text{syn-2}/\text{anti-2}) = s(\pi^* + d\delta) + a\alpha + b\beta + A_0 \quad (1)$$

where π^* is an index of solvent dipolarity/polarizability, α is a measure of the solvent hydrogen-bond donor (HBD) and Lewis-acidity, β is a measure of the solvent hydrogen-bond acceptor (HBA) and Lewis-basicity, and δ is a discontinuous polarization correction term (see SD).

A multivariate analysis of the data in Table 1 showed that the *syn/anti*- π -facial selectivity expressed as $\ln(\text{syn-2}/\text{anti-2})$ was well correlated with LSER, as shown in eqs. (2)–(4):

$$\ln(\text{syn-2a}/\text{anti-2a}) = -16.4(\pi^* + 0.4\delta) - 13.8\alpha + 11.4\beta + 14.5 \quad (R^2 = 0.992) \quad (2)$$

$$\ln(\text{syn-2b}/\text{anti-2b}) = -2.9(\pi^* - 0.1\delta) - 4.5\alpha + 4.2\beta - 0.2 \quad (R^2 = 0.964) \quad (3)$$

$$\ln(\text{syn-2c}/\text{anti-2c}) = -14.7(\pi^* + 0.3\delta) - 11.3\alpha + 8.9\beta + 12.9 \quad (R^2 = 0.950) \quad (4)$$

Equations (2)–(4) show negative coefficients for parameters π^* and α , and a positive coefficient for parameter β . Therefore, the LSER analysis suggested that *syn*- π -facial selectivity was disfavored in a solvent with large dipolarity/polarizability (π^* term) and/or HBD ability/Lewis-acidity (α term), and favored in a solvent with large HBA ability/Lewis-basicity (β term): a non-polar solvent favored *syn*- π -facial selectivity, since the A_0 term was positive especially for dihydrofurans **1a** and **1c**. Thus, the solvent effect on *syn/anti*- π -facial selectivity for the singlet-oxygenation of **1a** as an example can be explained as follows (see SD):

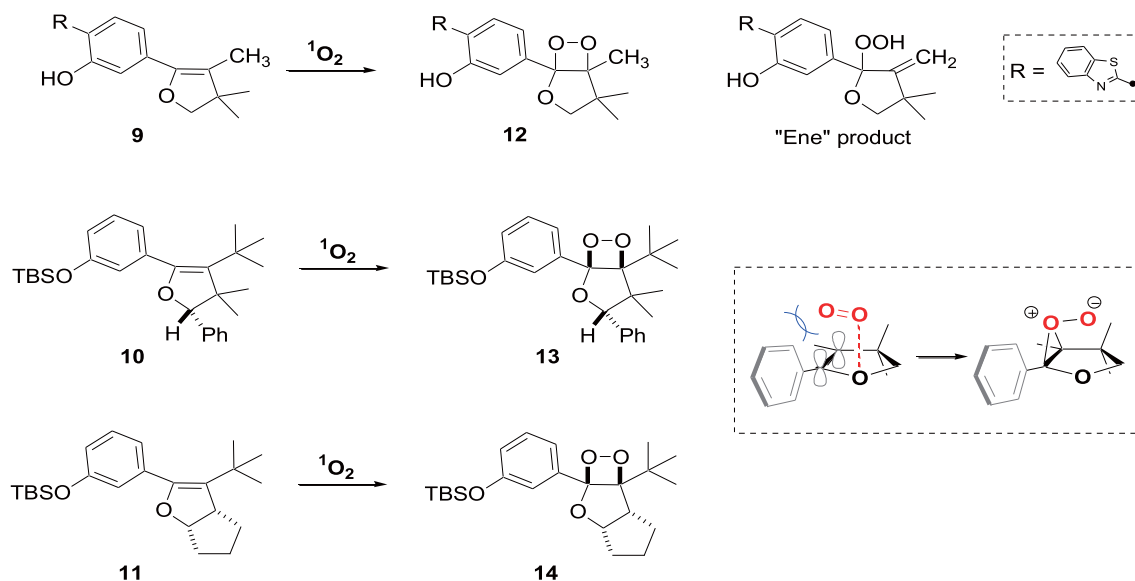
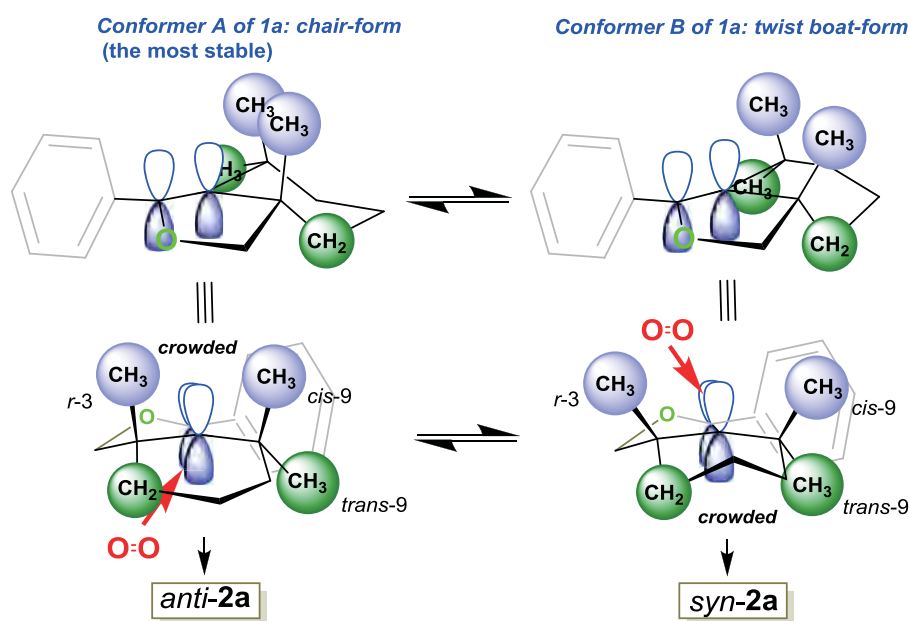
- High *anti*- π -facial selectivity may be mainly attributed to the solvent dipolarity/polarizability in the case of chloroform, and to the solvent HBD ability/Lewis-acidity in the case of methanol.
- The HBA ability/Lewis-basicity (β term) of acetone may play an important role in the high *syn*- π -facial selectivity.

According to suggestion b), a phenolic OH (a typical HBD/acid) of **1a** may participate in the expression of *syn*- π -facial selectivity in acetone (HBA/Lewis base). Thus, we investigated the solvent effect on the singlet-oxygenation of dihydrofuran **1e** bearing a 3-methoxyphenyl without phenolic OH, which exclusively gave a *syn/anti* mixture of dioxetane *syn*-**2e** and *anti*-**2e**. The results summarized in Table 1 showed that, as expected, the *syn/anti*- π -facial selectivity [ratio of *syn*-**2e**/*anti*-**2e**] in acetone was, in contrast to the case with **2a**, similar to that in acetonitrile, though high *syn*- and *anti*- π -facial selectivities were observed in toluene and chloroform, respectively. Notably, LSER analysis in the case of **1e** suggested that high *anti*- π -facial selectivity was mainly attributed to the solvent dipolarity/polarizability:

$$\ln(\text{syn-2e}/\text{anti-2e}) = -15.0(\pi^* - 0.2\delta) + 1.3\alpha - 0.4\beta + 7.1 \quad (R^2 = 0.981) \quad (5)$$

For the oxygenation of **1** with small and short-lived ¹O₂, the stereochemical (conformational) change in dihydrofurans **1** would be entirely responsible for the change in *syn/anti*- π -facial selectivity. To understand the present singlet-oxygenation, the known reactions of the related 5-aryl-2,3-dihydrofurans **9–11** were suggestive: dihydrofuran **9** selectively gave dioxetane **12**, though it possessed an 'ene'-active allylic methyl,³¹ and dihydrofurans **10** and **11** selectively gave the corresponding dioxetanes **13** and **14** with *anti*-stereochemistry (Scheme 4).^{32,33} These singlet-oxygenations suggested that the incoming ¹O₂ was guided to the side of the dihydrofuran ring, but not to the side of the 5-aryl group presumably by a "directing effect (*cis*-effect)"¹¹ of the dihydrofuran O atom and by a "large-group effect (*anti*-*cis*-effect)"³⁴ of the aryl group (Scheme 4). These effects on the side-selectivity could also play a role in the case of dihydrofurans **1a–1e**, for which the π -facial selectivity of the incoming ¹O₂ may be regulated by the steric environment around the dihydrofuran ring.

As illustrated in Scheme 5, the *syn*- π -face of dihydrofuran **1a** leading to *syn*-**2a** is surrounded by *r*-3-methyl, *cis*-9-methyl, and 5-(3-hydroxyl)phenyl groups, like a picket fence, while the opposite *anti*- π -face leading to *anti*-**2a** is surrounded by 6-methylene, *trans*-9-methyl, and 5-(3-hydroxyl)phenyl groups. Depending on the

Scheme 4. Stereoselective 1,2-cycloaddition of singlet oxygen to dihydrofurans **9–11**.Scheme 5. Steric regulation of the incoming singlet oxygen to the *syn/anti*- π -faces of conformers **A** and **B** of dihydrofuran **1a**.

conformational change in the cyclohexane ring of **1a**, these groups may change their relative stereochemistry such as the distances from the trigonal carbons of the 4,5-double bond, bond angles, and dihedral angles to open a picket fence or block a π -face for the incoming $^1\text{O}_2$. A theoretical study (conformational search: MMFF and HF/6-31G(d)) suggested that, in the most stable conformer **A** (chair form), the *anti*- π -face was less crowded, so that it was more favorable for the incoming $^1\text{O}_2$ than the *syn*- π -face, while the steric environment of the *syn/anti*- π -faces reversed for the next-stable conformer **B** with a twist-boat form (15–16 kJ mol⁻¹ less stable), as illustrated in Scheme 5 (SD). The equilibrium between conformers **A** and **B** would change with a change in the solvent and temperature, and, accordingly, the *syn/anti*- π -facial selectivity would also change.³⁵

In addition to steric control of the incoming $^1\text{O}_2$ through a

conformational change in the singlet-oxygenation of **1a–1c**, we should consider another factor to elucidate the substituent effect on the *syn/anti*- π -facial selectivity. As already mentioned, *anti*- π -facial selectivity increased in the order benzyl-analog **1c** < methyl-analog **1a** < ethyl-analog **1b** (Table 1). This order did not coincide with the order of the bulkiness of the 3-substituent, i.e., benzyl > ethyl > methyl. However, this discrepancy may be explained by considering the possible C–H bond-vibrational quenching of $^1\text{O}_2$.²⁰ If the 3-substituent acts to physically quench the incoming $^1\text{O}_2$, the effect should increase in the order benzyl < methyl < ethyl, and thus disfavor *syn*- π -facial selectivity in the same order: a larger number of C–H bonds to which *syn*- π -face of the double bond exposes may more effectively quench the incoming $^1\text{O}_2$.

2.3. Temperature effect on *syn/anti*- π -facial selectivity for the 1,2-cycloaddition of singlet oxygen to 3-hydroxyphenyl-substituted cyclohexadihydrofurans

The results in the previous section suggested that the *syn/anti*- π -facial selectivity of the 1,2-cycloaddition of $^1\text{O}_2$ was controlled by a conformational change in the cyclohexane ring in dihydrofurans **1**. The conformers of a cyclohexane are generally in a rapid equilibrium of chair \rightleftharpoons twist-boat \rightleftharpoons boat, which may be sensitively affected by temperature. Thus, we carried out the singlet-oxygenation of **1** at various temperatures ranging from 313 K to 215 K in CDCl_3 and toluene- d_8 , and the results are presented in Fig. 2. As shown, although the selectivity of *anti*-**2** tended to increase at lower temperature in both solvents, chloroform favored the *anti*-product regardless of the reaction temperature. Next, using the data obtained regarding the *syn/anti*-**2** ratios at various temperatures, we estimated the differential activation parameters ($\Delta\Delta H^\ddagger_{\text{syn-anti}}$ and $\Delta\Delta S^\ddagger_{\text{syn-anti}}$) between the formation of *syn*-**2** and *anti*-**2** by means of the following Eyring-relation.^{19,36}

$$\ln(k_{\text{syn}}/k_{\text{anti}}) = \ln(\text{syn-2}/\text{anti-2}) = \Delta\Delta S^\ddagger_{\text{syn-anti}}/R - \Delta\Delta H^\ddagger_{\text{syn-anti}}/RT \quad (6)$$

The results are summarized in Table 2, which shows that contribution of the differential activation entropy term $\Delta\Delta S^\ddagger_{\text{syn-anti}}$ is relatively high (30–67 J mol⁻¹ K⁻¹), while contribution of the differential activation enthalpy term $\Delta\Delta H^\ddagger_{\text{syn-anti}}$ is appreciable (7–20 kJ mol⁻¹) for a marked temperature dependence of the *syn/anti*-**2** selectivity. Thus, the *syn/anti*- π -facial-selective 1,2-cycloaddition of $^1\text{O}_2$ to **1** is based on a crucial balance of the enthalpy and the entropy terms, with the main contribution coming from the latter. The plots of $\ln(\text{syn-2}/\text{anti-2})$ vs $1/T$ according to

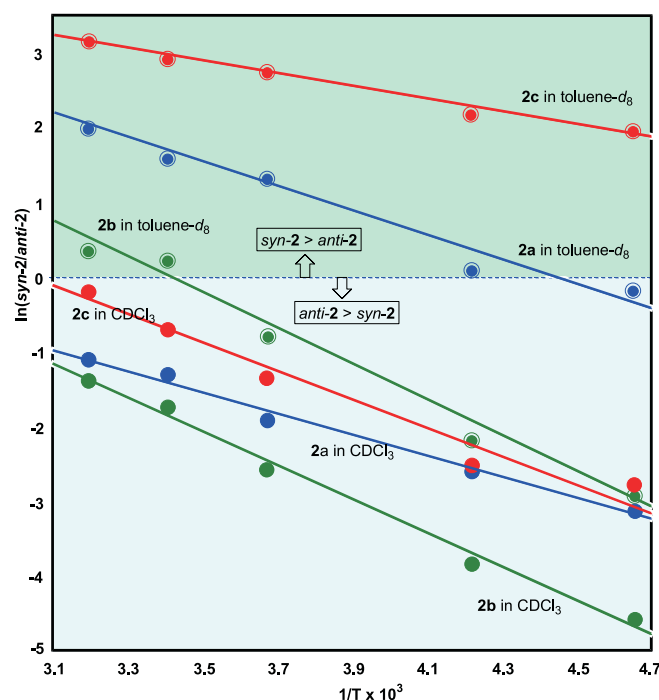


Fig. 3. Eyring plots of the ratios of *syn/anti*-stereoisomeric dioxetanes **2** produced for the singlet-oxygenation of dihydrofurans **1** in chloroform or toluene.

Eyring equation (eq. (6)) are shown in Fig. 3, from which we know that contribution of $\Delta\Delta S^\ddagger_{\text{syn-anti}}$ increases at higher temperature, while contribution of $\Delta\Delta H^\ddagger_{\text{syn-anti}}$ relatively increases at lower temperature and that the *syn/anti*-**2** selectivity may be reversed at a critical temperature even for **2c** in toluene, **2a** and **2b** in chloroform. The main contribution of the entropy term suggests that the ease of conformational motion of substrates **1**/transition states and their solvation are decisive in determining the preference for the *syn/anti*- π -face in the present reaction.

3. Conclusion

Singlet-oxygenation of oxyphenyl-substituted dihydrofurans fused with a cyclohexane **1a–1c** proceeded smoothly to exclusively give the corresponding dioxetanes **2a–2c** with *syn*- and *anti*-stereochemistry with respect to the substituent R at a bridgehead. The *syn/anti*- π -facial selectivity of dioxetane formation was remarkably affected by the solvent. Indeed, the solvent effect was so strong that inversion of the *syn/anti*- π -facial selectivity was observed in different solvents, such as chloroform and toluene. An LSER analysis suggested that the Lewis-acidity/basicity and HBD/HBA ability as well as dipolarity/polarizability of the solvent played an important role in the change in *syn/anti*- π -facial selectivity. The reaction temperature also sensitively affected the stereoselectivity of the 1,2-cycloaddition of $^1\text{O}_2$ to **1**, which was found to be an entropy-controlled process. A change in the conformation of a cyclohexane ring fused to a dihydrofuran ring was suggested to be responsible for the solvent- and temperature-sensitive change in the *syn/anti*- π -facial selectivity for the 1,2-cycloaddition of $^1\text{O}_2$ to dihydrofurans **1**.

4. Experimental

4.1. General

Melting points were uncorrected. IR spectra were taken on a FT/

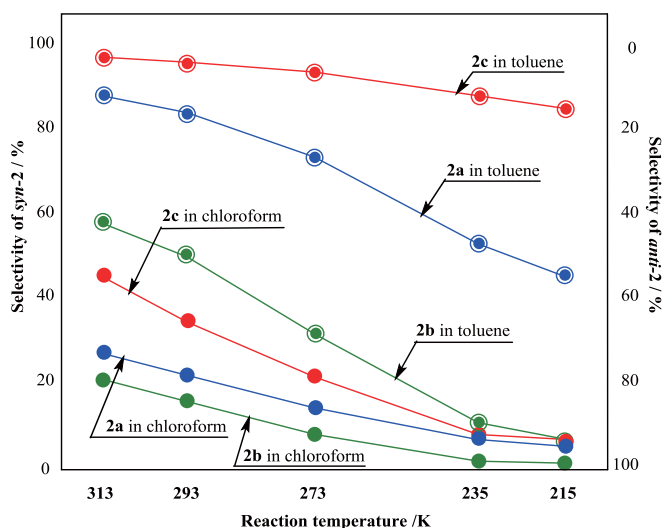


Fig. 2. Temperature effect on the selectivity of *syn/anti*-stereoisomeric dioxetanes **2** for the singlet-oxygenation of dihydrofurans **1** in chloroform or toluene.

Table 2
Differential activation parameters ($\Delta\Delta H^\ddagger_{\text{syn-anti}}$ and $\Delta\Delta S^\ddagger_{\text{syn-anti}}$) between the formation of dioxetanes *syn*-**2** and *anti*-**2** from dihydrofurans **1**.^{a)}

	Chloroform		Toluene	
	$\Delta\Delta H^\ddagger_{\text{syn-anti}}$ /kJ mol ⁻¹	$\Delta\Delta S^\ddagger_{\text{syn-anti}}$ /J mol ⁻¹ K ⁻¹	$\Delta\Delta H^\ddagger_{\text{syn-anti}}$ /kJ mol ⁻¹	$\Delta\Delta S^\ddagger_{\text{syn-anti}}$ /J mol ⁻¹ K ⁻¹
1a	12	30	13	58
1b	19	49	20	67
1c	15	46	6.9	48

IR infrared spectrometer. ^1H and ^{13}C NMR spectra were recorded on a 400 MHz, 500 MHz and 600 MHz spectrometers. Mass spectra were obtained using double-focusing mass spectrometers and an ESI-TOF mass spectrometer. Column chromatography was carried out using silica gel.

4.2. Data for compounds

4.2.1. 9-(3-Hydroxyphenyl)-2,2,6-trimethyl-8-oxabicyclo[4.3.0]non-1(9)-ene; 5-(3-hydroxyphenyl)-3,9,9-trimethyl-3,4-cyclohexa-2,3-dihydrofuran (**1a**); typical procedure

A solution of 9-(3-Methoxyphenyl)-2,2,6-trimethyl-8-oxabicyclo [4.3.0]non-1 (9)-ene (**1e**) (see SD) (8.87 g, 32.6 mmol) and sodium methanethiolate (95%, 4.62 g, 62.6 mmol, 1.92 eq.) in dry DMF (90 mL) was stirred under a N_2 atmosphere at 130 °C for 3 h. The reaction mixture was poured into sat. aq. NH_4Cl and extracted twice with AcOEt. The combined organic layer was washed five times with sat. aq. NaCl, dried over anhydrous MgSO_4 and concentrated *in vacuo*. The residue was chromatographed on silica gel and eluted with AcOEt–hexane (1:4) to give 9-(3-hydroxyphenyl)-2,2,6-trimethyl-8-oxabicyclo [4.3.0]non-1 (9)-ene (**1a**) as a colorless solid in 95% yield (7.99 g). 6-Ethyl-analog **1b**, 6-benzyl-analog **1c** and 9-(4-hydroxyphenyl)-analog **1d** were similarly synthesized.

1a: Colorless needles; mp 111.5–113.0 °C (from hexane–AcOEt). ^1H NMR (500 MHz, CDCl_3): δ_{H} 0.81 (s, 3H), 1.18–1.26 (m, 1H), 1.22 (s, 3H), 1.30 (s, 3H), 1.28–1.35 (m, 1H), 1.39–1.44 (m, 1H), 1.54–1.62 (m, 1H), 1.66–1.80 (m, 2H), 3.81 (d, $J = 7.8$ Hz, 1H), 4.06 (d, $J = 7.8$ Hz, 1H), 5.22 (broad s, 1H), 6.74 (ddd, $J = 8.0, 2.5$ and 0.9 Hz, 1H), 6.84 (s with fine coupling, 1H), 6.95 (d with fine coupling, $J = 7.6$ Hz, 1H), 7.16 (dd, $J = 8.0$ and 7.6 Hz, 1H) ppm. ^{13}C NMR (125 MHz, CDCl_3): δ_{C} 19.1, 25.8, 29.5, 31.5, 31.5, 37.7, 42.5, 46.0, 83.7, 115.7, 117.1, 122.5, 123.4, 128.8, 135.6, 146.9, 155.0 ppm. IR (KBr): $\tilde{\nu}$ 3348, 2924, 2860, 1595, 1205, 1045 cm^{-1} . Mass (m/z , %): 258 (M^+ , 25), 243 (100), 173 (8), 121 (36). HRMS (ESI) (m/z): 259.1692, calcd for $\text{C}_{17}\text{H}_{23}\text{O}_2$ [$\text{M} + \text{H}^+$] 259.1698.281.1511, calcd for $\text{C}_{17}\text{H}_{22}\text{O}_2\text{Na}$ [$\text{M} + \text{Na}^+$] 281.1517. Anal. Calcd for $\text{C}_{17}\text{H}_{22}\text{O}_2$: C, 79.03; H, 8.58. Found: C, 79.18; H, 8.79.

1b: 97% yield. Colorless needles; mp 97.5–100.0 °C (from hexane–AcOEt). ^1H NMR (400 MHz, CDCl_3): δ_{H} 0.81 (s, 3H), 0.99 (t, $J = 7.4$ Hz, 3H), 1.20 (s, 3H), 1.20–1.74 (m, 6H), 1.82–1.92 (m, 2H), 3.79 (d, $J = 8.3$ Hz, 1H), 4.20 (d, $J = 8.3$ Hz, 1H), 4.83 (broad s, 1H), 6.78 (dd, $J = 8.1$ and 2.7 Hz, 1H), 6.87 (s with fine coupling, 1H), 6.98 (d with fine coupling, $J = 7.6$ Hz, 1H), 7.18 (dd, $J = 8.1$ and 7.6 Hz, 1H) ppm. ^{13}C NMR (125 MHz, CDCl_3): δ_{C} 8.7, 19.3, 28.8, 31.0, 31.7, 31.9, 37.3, 43.0, 49.7, 81.2, 115.6, 117.2, 119.6, 122.8, 128.8, 136.0, 148.0, 155.0 ppm. IR (KBr): $\tilde{\nu}$ 3322, 2977, 2961, 2926, 2862, 1593, 1445, 1209, 1048 cm^{-1} . Mass (m/z , %): 272 (M^+ , 15), 257 (11), 244 (23), 243 (100), 173 (14), 139 (11), 121 (35). HRMS (ESI): 273.1882, calcd for $\text{C}_{18}\text{H}_{25}\text{O}_2$ [$\text{M} + \text{H}^+$] 273.1855.295.1683, calcd for $\text{C}_{18}\text{H}_{24}\text{O}_2\text{Na}$ [$\text{M} + \text{Na}^+$] 295.1674. Anal. Calcd for $\text{C}_{18}\text{H}_{24}\text{O}_2$: C, 79.37; H, 8.88. Found: C, 79.63; H, 9.25.

1c: 95% yield. Colorless needles; mp 161.0–162.0 °C (from AcOEt). ^1H NMR (500 MHz, CDCl_3): δ_{H} 0.86 (s, 3H), 1.04–1.12 (m, 1H), 1.26–1.35 (m, 1H), 1.36 (s, 3H), 1.49–1.54 (m, 1H), 1.60–1.66 (m, 1H), 1.85–1.97 (m, 2H), 2.76 (d, $J = 13.3$ Hz, 1H), 3.06 (d, $J = 13.3$ Hz, 1H), 3.45 (d, $J = 8.5$ Hz, 1H), 4.38 (d, $J = 8.5$ Hz, 1H), 5.42 (s, 1H), 6.74 (dd, $J = 8.2$ and 2.3 Hz, 1H), 6.86 (s, 1H), 6.97 (d, $J = 7.8$ Hz, 1H), 7.16 (dd, $J = 8.2$ and 7.8 Hz, 1H), 7.18–7.32 (m, 5H) ppm. ^{13}C NMR (125 MHz, CDCl_3): δ_{C} 18.8, 30.0, 31.6, 31.9, 33.6, 41.0, 42.7, 50.3, 78.5, 115.7, 117.0, 122.7, 123.1, 126.1, 128.0 (CH x 2), 128.9, 130.8 (CH x 2), 135.8, 138.4, 148.3, 155.0 ppm. IR (KBr): $\tilde{\nu}$ 3307, 2985, 2927, 2863, 1597, 1442, 1318, 1212, 1018 cm^{-1} . Mass (m/z , %): 334 (M^+ , trace), 244 (17), 243 (100), 173 (21), 121 (44), 115 (12), 107 (12), 93 (18), 91

(89), 69 (10), 65 (38), 55 (10). HRMS (ESI): 335.2096, calcd for $\text{C}_{23}\text{H}_{27}\text{O}_2$ [$\text{M} + \text{H}^+$] 335.2011. 357.1845, calcd for $\text{C}_{23}\text{H}_{26}\text{O}_2\text{Na}$ [$\text{M} + \text{Na}^+$] 357.1830. Anal. Calcd for $\text{C}_{23}\text{H}_{26}\text{O}_2$: C, 82.60; H, 7.84. Found: C, 82.75; H, 8.09.

1d: 92% yield. Colorless columns; mp 155.5–157.0 °C (from AcOEt). ^1H NMR (400 MHz, CDCl_3): δ_{H} 0.79 (s, 3H), 1.17–1.44 (m, 3H), 1.22 (s, 3H), 1.29 (s, 3H), 1.52–1.79 (m, 3H), 3.77 (d, $J = 7.8$ Hz, 1H), 4.03 (d, $J = 7.8$ Hz, 1H), 4.95 (broad s, 1H), 6.73–6.78 (m, 2H), 7.24–7.28 (m, 2H) ppm. ^{13}C NMR (125 MHz, CDCl_3): δ_{C} 19.2, 25.9, 29.6, 31.6, 31.6, 37.8, 42.6, 46.0, 83.5, 114.6 (x 2), 122.5, 126.9, 131.4 (x 2), 147.2, 155.9 ppm. IR (KBr): $\tilde{\nu}$ 3374, 2925, 1666, 1608, 1511, 1460, 1273, 1225 cm^{-1} . Mass (m/z , %): 258 (M^+ , 20), 244 (20), 243 (100), 173 (8), 121 (47), 107 (8), 93 (7). HRMS (ESI): 259.1688, calcd for $\text{C}_{17}\text{H}_{23}\text{O}_2$ [$\text{M} + \text{H}^+$] 259.1698.281.1511, calcd for $\text{C}_{17}\text{H}_{22}\text{O}_2\text{Na}$ [$\text{M} + \text{Na}^+$] 281.1517. Anal. Calcd for $\text{C}_{17}\text{H}_{22}\text{O}_2$: C, 79.03; H, 8.58. Found: C, 79.20; H, 8.97.

1e: Colorless plates; mp 52.5–55.0 °C (from hexane). ^1H NMR (600 MHz, CDCl_3): δ_{H} 0.81 (s, 3H), 1.20–1.26 (m, 1H), 1.24 (s, 3H), 1.30–1.36 (m, 1H), 1.31 (s, 3H), 1.40–1.45 (m, 1H), 1.55–1.60 (m, 1H), 1.67–1.80 (m, 2H), 3.81 (s, 3H), 3.81 (d, $J = 7.8$ Hz, 1H), 4.05 (d, $J = 7.8$ Hz, 1H), 6.86 (dd with fine coupling, $J = 8.3$, and 2.7, 1H), 6.93 (s with fine coupling, 1H), 6.98 (d with fine coupling, $J = 7.5$ Hz, 1H), 7.23 (dd, $J = 8.3$ and 7.5 Hz, 1H) ppm. ^{13}C NMR (150 MHz, CDCl_3): δ_{C} 19.2, 25.9, 29.6, 31.5, 31.6, 37.8, 42.6, 46.1, 55.2, 83.8, 114.4, 115.2, 122.7, 122.9, 128.6, 136.0, 147.5, 158.9 ppm. IR (KBr): $\tilde{\nu}$ 2962, 2927, 2862, 1593, 1462, 1429, 1317, 1269, 1269, 1232, 1182, 1043 cm^{-1} . Mass (m/z , %): 272 (M^+ , 25), 258 (20), 257 (100), 187 (7), 136 (8), 135 (23), 121 (9), 107 (8). HRMS (ESI): 295.1690, calcd for $\text{C}_{18}\text{H}_{24}\text{O}_2\text{Na}$ [$\text{M} + \text{Na}^+$] 295.1674. Anal. Calcd for $\text{C}_{18}\text{H}_{24}\text{O}_2$: C, 79.37; H, 8.88. Found: C, 79.46; H, 9.14.

4.3. Singlet-oxygenation of dihydrofurans 1

4.3.1. Isolation of 6-substituted 9-(3-hydroxyphenyl)-2,2-dimethyl-8,10,11-trioxatricyclo[5.4.0.0^{1,4}]undecane (**2**)

Although the singlet-oxygenation of dihydrofurans **1** was carried out at 0 °C in chloroform or in toluene in an initial experiment, the improved procedures to individually isolate *anti*- and *syn*-**2** are described here.

4.3.2. Isolation of *syn*-**2**; general procedure

A solution of **1** (ca 1.0 mmol) and TPP (ca 2.0 mg) in acetone (15 mL) was irradiated externally with 940W Na lamp under an O_2 atmosphere at 0 °C for 7.5 h. After concentration, the photolysate was chromatographed on silica gel (ether– CH_2Cl_2 , 1: 40) to exclusively give a mixture of *syn*-**2** (major) and *anti*-**2** (minor) as a pale yellow solid. Pure *syn*-**2** was isolated by recrystallization from hexane– CH_2Cl_2 .

syn-**2a**: Colorless plates; mp 145.0–148.0 °C (dec.) (from hexane– CH_2Cl_2). ^1H NMR (500 MHz, CDCl_3): δ_{H} 0.82 (s, 3H), 0.84 (s, 3H), 1.13 (s, 3H), 1.20–1.30 (m, 2H), 1.44–1.50 (m, 1H), 1.56–1.82 (m, 3H), 3.78 (d, $J = 8.2$ Hz, 1H), 4.44 (d, $J = 8.2$ Hz, 1H), 5.20 (broad s, 1H), 6.85 (d with fine coupling, $J = 8.2$ Hz, 1H), 6.94–7.30 (m, 2H), 7.26 (dd, $J = 8.2$ and 7.3 Hz, 1H) ppm. ^{13}C NMR (125 MHz, CDCl_3): δ_{C} 15.6, 17.4, 21.3, 26.9, 34.9, 35.6, 37.2, 44.0, 77.6, 103.0, 114.7 (broad CH), 116.3, 116.8, 120.1 (broad CH), 129.4, 138.1, 155.4 ppm. IR (KBr): $\tilde{\nu}$ 3448, 2977, 2917, 1604, 1218, 1034 cm^{-1} . Mass (m/z , %): 290 (M^+ , 4), 152 (28), 138 (22), 121 (100). HRMS (ESI): 313.1410, calcd for $\text{C}_{17}\text{H}_{22}\text{O}_4\text{Na}$ [$\text{M} + \text{Na}^+$] 313.1416. Anal. Calcd for $\text{C}_{17}\text{H}_{22}\text{O}_4$: C, 70.32; H, 7.64. Found: C, 70.40; H, 7.81.

syn-**2b**: Colorless columns; mp 142.5–145.0 °C (dec.) (from hexane– CH_2Cl_2). ^1H NMR (500 MHz, CDCl_3): δ_{H} 0.83 (s, 3H), 0.83 (s, 3H), 0.92 (t, $J = 7.6$ Hz, 3H), 1.19–1.31 (m, 2H), 1.42–1.69 (m, 4H), 1.75–1.84 (m, 1H), 1.93–1.99 (m, 1H), 3.83 (d, $J = 8.7$ Hz, 1H), 4.57 (d,

$J = 8.7$ Hz, 1H), 5.37 (broad s, 1H), 6.84 (dd, $J = 8.7$ and 2.3 Hz, 1H), 6.90–7.40 (m, 2H), 7.25 (dd, $J = 8.7$ and 6.9 Hz, 1H) ppm. ^{13}C NMR (125 MHz, CDCl_3): δ_{C} 8.9, 17.3, 21.4, 21.4, 27.2, 30.0, 35.6, 37.2, 48.0, 75.5, 103.8, 114.8 (broad CH), 116.3, 116.9, 120.0 (broad CH), 129.4, 138.1, 155.4 ppm. IR (KBr): $\tilde{\nu}$ 3440, 2973, 2938, 1604, 1450, 1307, 1218, 1050, 1018 cm^{-1} . Mass (m/z , %): 304 (M^+ , 4), 166 (31), 139 (12), 138 (36), 121 (100), 109 (11), 95 (20), 93 (14), 82 (33), 69 (17). HRMS (ESI): 327.1556, calcd for $\text{C}_{18}\text{H}_{24}\text{O}_4\text{Na}$ [$\text{M} + \text{Na}^+$] 327.1572. Anal. Calcd for $\text{C}_{18}\text{H}_{24}\text{O}_4$: C, 71.03; H, 7.95. Found: C, 71.18; H, 8.16.

syn-2c: Colorless needles; mp 140.0–142.5 °C (dec.) (from hexane– CH_2Cl_2). ^1H NMR (500 MHz, CDCl_3): δ_{H} 0.87 (s, 3H), 0.96 (s, 3H), 1.28–1.38 (m, 2H), 1.49–1.60 (m, 2H), 1.73–1.85 (m, 1H), 2.02–2.08 (m, 1H), 2.99 (q_{AB}, $J = 13.3$ Hz, 2H), 3.26 (d, $J = 8.9$ Hz, 1H), 4.68 (d, $J = 8.9$ Hz, 1H), 4.96 (broad s, 1H), 6.84 (dd, $J = 8.7$ and 2.3 Hz, 1H), 6.88–7.50 (m, 8H) ppm. ^{13}C NMR (125 MHz, CDCl_3): δ_{C} 17.2, 21.7, 27.5, 30.5, 34.4, 35.8, 37.3, 48.4, 75.6, 103.3, 114.7 (broad CH), 116.4, 116.8, 120.1 (broad CH), 126.6, 128.3 (CH x 2), 129.5, 130.3 (CH x 2), 137.6, 138.1, 155.4 ppm. IR (KBr): $\tilde{\nu}$ 3470, 2936, 1604, 1453, 1310, 1225, 1077, 1048, 1025 cm^{-1} . Mass (m/z , %): 229 (M^+ –137, 21), 228 (100), 213 (17), 144 (11), 131 (13), 129 (17), 121 (58), 109 (10), 93 (13), 91 (31), 69 (10). HRMS (ESI): 389.1701, calcd for $\text{C}_{23}\text{H}_{26}\text{O}_4\text{Na}$ [$\text{M} + \text{Na}^+$] 389.1729. Anal. Calcd for $\text{C}_{23}\text{H}_{26}\text{O}_4$: C, 75.38; H, 7.15. Found: C, 75.25; H, 7.25.

syn-2d: Pale yellow oil. ^1H NMR (600 MHz, CDCl_3): δ_{H} 0.82 (s, 3H), 0.84 (s, 3H), 1.12 (s, 3H), 1.14–1.24 (m, 2H), 1.42–1.49 (m, 1H), 1.56–1.65 (m, 1H), 1.67–1.80 (m, 2H), 3.76 (d, $J = 8.4$ Hz, 1H), 4.43 (d, $J = 8.4$ Hz, 1H), 5.24 (broad s, 1H), 6.82 (d with fine coupling, $J = 9.0$ Hz, 2H), 7.34–7.60 (m, 2H) ppm. ^{13}C NMR (150 MHz, CDCl_3): δ_{C} 15.7, 17.4, 21.4, 26.7, 34.9, 35.6, 37.2, 43.9, 77.2, 102.6, 114.9 (broad CH x 2), 117.2, 128.6, 129.4 (broad CH x 2), 156.5 ppm. IR (liquid film): $\tilde{\nu}$ 3379, 2933, 2871, 1608, 1693, 1517, 1514, 1460, 1275, 1165 cm^{-1} . Mass (m/z , %): 291 (M^+ +1, 6), 290 (M^+ , 15), 181 (26), 153 (23), 152 (29), 138 (15), 137 (31), 136 (23), 125 (10), 124 (19), 123 (14), 122 (13), 121 (100), 109 (13), 95 (17), 93 (10), 82 (13), 81 (24), 69 (35), 55 (11). HRMS (ESI): 313.1404, calcd for $\text{C}_{17}\text{H}_{22}\text{O}_4\text{Na}$ [$\text{M} + \text{Na}^+$] 313.1416.

syn-2e: Colorless oil. ^1H NMR (400 MHz, CDCl_3): δ_{H} 0.81 (s, 3H), 0.84 (s, 3H), 1.14 (s, 3H), 1.20–1.32 (m, 2H), 1.44–1.51 (m, 1H), 1.56–1.85 (m, 3H), 3.78 (d, $J = 8.4$ Hz, 1H), 3.82 (s, 3H), 4.45 (d, $J = 8.4$ Hz, 1H), 6.92 (dd, $J = 8.3$ and 2.5 Hz, 1H), 7.00–7.36 (m, 2H), 7.31 (dd, $J = 8.3$ and 7.5 Hz, 1H) ppm. ^{13}C NMR (150 MHz, CDCl_3): δ_{C} 15.6, 17.4, 21.3, 26.9, 34.9, 35.6, 37.2, 43.9, 55.3, 77.5, 102.8, 113.3, 114.9 (broad CH), 116.9, 120.0 (broad CH), 129.1, 137.9, 159.2 ppm. IR (liquid film): $\tilde{\nu}$ 2935, 2887, 1603, 1586 cm^{-1} . Mass (m/z , %): 304 (M^+ , 10), 152 (51), 135 (100), 124 (11), 107 (13). HRMS (ESI): 327.1545, calcd for $\text{C}_{18}\text{H}_{24}\text{O}_4\text{Na}$ [$\text{M} + \text{Na}^+$] 327.1572.

4.3.3. Isolation of anti-2; general procedure

A solution of **1** (ca 1.0 mmol) and TPP (ca 2.0 mg) in CH_2Cl_2 (15 mL) was irradiated externally with 940 W Na lamp under an O_2 atmosphere at -78 °C for 2.5 h. After concentration, the photolysate was chromatographed on silica gel (ether– CH_2Cl_2 , 1: 40) to exclusively give a mixture of *anti-2* (major) and *syn-2* (minor) as a pale yellow solid. Pure *anti-2* was isolated by recrystallization from hexane– CH_2Cl_2 .

anti-2a: Colorless column; mp 121.5–123.0 °C (dec.) (from hexane– CH_2Cl_2). ^1H NMR (500 MHz, CDCl_3): δ_{H} 0.76 (s, 3H), 1.10–1.16 (m, 1H), 1.26 (s, 3H), 1.35–1.50 (m, 3H), 1.38 (s, 3H), 1.54–1.64 (m, 2H), 3.97 (d, $J = 7.8$ Hz, 1H), 4.70 (d, $J = 7.8$ Hz, 1H), 5.11 (broad s, 1H), 6.86 (d with fine coupling, $J = 8.5$ Hz, 1H), 7.12 (s with fine coupling, 1H), 7.19 (d with fine coupling, $J = 7.8$ Hz, 1H), 7.27 (t, $J = 7.8$ Hz, 1H) ppm. ^{13}C NMR (125 MHz, CDCl_3): δ_{C} 17.9, 22.1, 22.5, 27.2, 27.3, 35.5, 36.2, 44.6, 81.1, 105.5, 114.0, 114.6, 116.5, 120.0, 129.6, 136.3, 155.4 ppm. IR (KBr): $\tilde{\nu}$ 3454, 2972, 2926, 1590, 1489,

1469, 1316, 1198 cm^{-1} . Mass (m/z , %): 290 (M^+ , 7), 203 (15), 153 (13), 152 (44), 138 (33), 121 (100), 109 (22), 93 (19), 82 (37), 81 (27), 65 (10), 55 (11). HRMS (ESI): 313.1426, calcd for $\text{C}_{17}\text{H}_{22}\text{O}_4\text{Na}$ [$\text{M} + \text{Na}^+$] 313.1416. Anal. Calcd for $\text{C}_{17}\text{H}_{22}\text{O}_4$: C, 70.32; H, 7.64. Found: C, 70.34; H, 7.81.

anti-2b: Colorless granules; mp 134.5–136.5 °C (dec.) (from hexane– CH_2Cl_2). ^1H NMR (500 MHz, CDCl_3): δ_{H} 0.78 (s, 3H), 1.00 (t, $J = 7.3$ Hz, 3H), 1.13–1.17 (m, 1H), 1.28 (s, 3H), 1.35–1.55 (m, 5H), 1.62–1.65 (m, 1H), 1.85–1.92 (m, 1H), 4.33 (d, $J = 7.8$ Hz, 1H), 4.50 (dd, $J = 7.8$ and 1.8 Hz, 1H), 5.36 (s, 1H), 6.84 (dd, $J = 7.8$ and 2.7 Hz, 1H), 7.09 (s with fine coupling, 1H), 7.16 (d, $J = 7.8$ Hz, 1H), 7.25 (t, $J = 7.8$ Hz, 1H) ppm. ^{13}C NMR (125 MHz, CDCl_3): δ_{C} 9.42, 17.7, 22.3, 22.6, 22.8, 27.9, 35.6, 36.1, 48.8, 74.1, 106.3, 113.7, 114.6, 116.5, 120.0, 129.5, 136.1, 155.5 ppm. IR (KBr): $\tilde{\nu}$ 3449, 2967, 2940, 1604, 1218 cm^{-1} . Mass (m/z , %): 304 (M^+ , 7), 217 (14), 166 (60), 138 (81), 121 (100), 109 (23). HRMS (ESI): 327.1560, calcd for $\text{C}_{18}\text{H}_{24}\text{O}_4\text{Na}$ [$\text{M} + \text{Na}^+$] 327.1572. Anal. Calcd for $\text{C}_{18}\text{H}_{24}\text{O}_4$: C, 71.03; H, 7.95. Found: C, 71.01; H, 8.15.

anti-2c: Colorless plates; mp 142.5–145.0 °C (dec.) (from hexane– CH_2Cl_2). ^1H NMR (500 MHz, CDCl_3): δ_{H} 0.88 (s, 3H), 1.22–1.27 (m, 1H), 1.34 (s, 3H), 1.36–1.58 (m, 3H), 1.72–1.77 (m, 1H), 1.82–1.92 (m, 1H), 2.69 (d, $J = 13.3$ Hz, 1H), 3.17 (d, $J = 13.3$ Hz, 1H), 4.22 (d, $J = 8.2$ Hz, 1H), 4.34 (d with fine coupling, $J = 8.2$ Hz, 1H), 5.20 (s, 1H), 6.86–6.91 (m, 1H), 7.22–7.38 (m, 8H) ppm. ^{13}C NMR (125 MHz, CDCl_3): δ_{C} 17.8, 22.5, 23.2, 27.9, 35.5, 35.6, 36.3, 49.2, 73.7, 106.0, 113.7, 114.7, 116.7, 120.1, 126.7, 128.4 (x 2), 129.7, 130.9 (x 2), 136.1, 137.9, 155.5 ppm. IR (KBr): $\tilde{\nu}$ 3428, 2939, 1604, 1220 cm^{-1} . Mass (m/z , %): 229 (M^+ –137, 21), 228 (100), 213 (17). HRMS (ESI): 389.1728, calcd for $\text{C}_{23}\text{H}_{26}\text{O}_4\text{Na}$ [$\text{M} + \text{Na}^+$] 389.1729. Anal. Calcd for $\text{C}_{23}\text{H}_{26}\text{O}_4$: C, 75.38; H, 7.15. Found: C, 75.18; H, 7.29.

anti-2d: Pale yellow amorphous solid. ^1H NMR (600 MHz, CDCl_3): δ_{H} 0.73 (s, 3H), 1.11–1.14 (m, 1H), 1.24 (s, 3H), 1.34–1.48 (m, 3H), 1.37 (s, 3H), 1.54–1.65 (m, 2H), 3.95 (d, $J = 7.5$ Hz, 1H), 4.68 (d with fine coupling, $J = 7.5$ Hz, 1H), 5.19 (s, 1H), 6.84 (d with fine coupling, $J = 8.8$ Hz, 2H), 7.50 (d with fine coupling, $J = 8.7$ Hz, 2H) ppm. ^{13}C NMR (150 MHz, CDCl_3): δ_{C} 18.0, 22.0, 22.5, 27.1, 27.2, 35.5, 36.1, 44.6, 80.8, 105.1, 114.3, 115.1 (CH x 2), 126.9, 129.2 (CH x 2), 156.6 ppm. IR (KBr): $\tilde{\nu}$ 3365, 2935, 1613, 1517, 1445, 1325, 1277, 1227, 1016, 983 cm^{-1} . Mass (m/z , %): 290 (M^+ , 2), 258 (10), 243 (15), 152 (26), 138 (15), 124 (15), 123 (10), 121 (100), 82 (10), 69 (11). HRMS (ESI): 313.1402, calcd for $\text{C}_{17}\text{H}_{22}\text{O}_4\text{Na}$ [$\text{M} + \text{Na}^+$] 313.1416.

anti-2e: Colorless columns; mp 110.0–112.0 °C (from hexane– CH_2Cl_2). ^1H NMR (600 MHz, CDCl_3): δ_{H} 0.75 (s, 3H), 1.10–1.15 (m, 1H), 1.26 (s, 3H), 1.36–1.50 (m, 3H), 1.39 (s, 3H), 1.56–1.65 (m, 2H), 3.83 (s, 3H), 3.98 (d, $J = 7.5$ Hz, 1H), 4.71 (d, $J = 7.5$ Hz, 1H), 6.93 (dd, $J = 8.2$ and 2.6 Hz, 1H), 7.18 (s with fine coupling, 1H), 7.21 (broad d with fine coupling, $J = 7.7$ Hz, 1H), 7.32 (dd, $J = 8.2$ and 7.7 Hz, 1H) ppm. ^{13}C NMR (150 MHz, CDCl_3): δ_{C} 17.9, 22.1, 22.5, 27.2, 27.3, 35.4, 36.1, 44.6, 55.3, 81.0, 105.4, 113.1, 114.1, 115.1, 119.9, 129.3, 136.1, 159.4 ppm. IR (KBr): $\tilde{\nu}$ 2965, 2920, 1610, 1582 cm^{-1} . Mass (m/z , %): 304 (M^+ , 7), 152 (49), 135 (100), 124 (11), 107 (14), 82 (12). HRMS (ESI): 327.1526, calcd for $\text{C}_{18}\text{H}_{24}\text{O}_4\text{Na}$ [$\text{M} + \text{Na}^+$] 327.1572.

4.3.4. Solvent dependency of syn/anti- π -facial selectivity for the singlet-oxygenation of dihydrofuran **1**; general procedure

A solution of dihydrofuran **1** (ca. 1×10^{-5} mol) and TPP (ca. 5×10^{-7} mol) in chloroform, dichloromethane, acetone, or toluene (2 mL) was irradiated with 940 W Na lamp under an oxygen atmosphere at 0 °C for 30 min. After concentration *in vacuo*, the photolysate was dissolved in CDCl_3 and the *syn/anti*-ratio of dioxetane **2** was measured by ^1H NMR. In methanol, Rose Bengal was used as a sensitizer, while, in acetonitrile, Methylene Blue was used as a sensitizer.

4.3.5. Temperature dependency of syn/anti- π -facial selectivity for the singlet-oxygenation of dihydrofuran **1**; general procedure

A solution of **1** (ca. 1×10^{-5} mol) and TPP (ca. 5×10^{-7} mol) in CDCl_3 or toluene- d_8 (2 mL) was irradiated with 940 W Na lamp under an oxygen atmosphere at 313, 293, 273, 235, or 215 K for 30–180 min. In the case of the reactions in toluene- d_8 , after concentration *in vacuo*, the photolysate was dissolved in CDCl_3 and the syn/anti-ratio of dioxetane **2** was measured by ^1H NMR.

4.4. X-ray single crystallographic analysis

X-ray diffraction data were collected on a Rigaku Mercury CCD diffractometer with graphite monochromated Mo K α ($\lambda = 0.71070$ Å) radiation. Data were processed using CrystalClear¹. The structures were solved by direct method (SIR2008)² and expanded using Fourier techniques. All non-hydrogen atoms were refined anisotropically. The hydrogen atoms were refined using the riding model. The final cycle of full-matrix least-squares refinement on F² was based on 3376 and 6407 observed reflections and 212 and 423 variable parameters respectively (for syn-**2a** and anti-**2a**). All calculations were performed using the CrystalStructure crystallographic software package^{3,4}.

Crystal data for syn-**2a**: $\text{C}_{17}\text{H}_{22}\text{O}_4$, ($M_r = 290.36$), colorless block, $0.20 \times 0.20 \times 0.10$ mm, orthorhombic, space group Pbc₁ (#61), $a = 8.59$ (6) Å, $b = 15.60$ (4) Å, $c = 22.12$ (7) Å, $V = 2964$ (25) Å³, $Z = 8$, $\rho_{\text{calcd}} = 1.301$ g cm⁻³, $T = 150$ K, $F(000) = 1248.00$, reflections collected/unique 27618/3376 ($R_{\text{int}} = 0.0915$), $\mu(\text{MoK}\alpha) = 0.914$ cm⁻¹. An empirical absorption correction was applied which resulted in transmission factors ranging from 0.765 to 0.991. The data were corrected for Lorentz and polarization effects. $R1 = 0.0690$ [$I > 2\sigma(I)$], $wR2 = 0.2014$ (all data), GOF on $F^2 = 1.006$, and residual electron density $0.69/-0.63$ e⁻Å⁻³.

Crystal data for anti-**2a**: $\text{C}_{17}\text{H}_{22}\text{O}_4$, ($M_r = 290.36$), colorless platelet, $0.10 \times 0.05 \times 0.05$ mm, triclinic, space group P-1 (#2), $a = 8.49$ (3) Å, $b = 13.60$ (5) Å, $c = 13.60$ (5) Å, $\alpha = 107.593^\circ$, $\beta = 90.0000^\circ$, $\gamma = 90.0000^\circ$, $V = 1496$ (9) Å³, $Z = 4$, $\rho_{\text{calcd}} = 1.289$ g cm⁻³, $T = 150$ K, $F(000) = 624.00$, reflections collected/unique 14956/6407 ($R_{\text{int}} = 0.0523$), $\mu(\text{MoK}\alpha) = 0.905$ cm⁻¹. An empirical absorption correction was applied which resulted in transmission factors ranging from 0.857 to 0.995. The data were corrected for Lorentz and polarization effects. $R1 = 0.0619$ [$I > 2\sigma(I)$], $wR2 = 0.0784$ (all data), GOF on $F^2 = 1.011$, and residual electron density $1.02/-0.59$ e⁻Å⁻³.

Crystallographic data for the structural analysis of compound syn-**2a** and anti-**2a** has been deposited at the Cambridge Crystallographic Data Center, CCDC-1520410 and 1520409. Free Copies of the data can be obtained, via <http://www.ccdc.cam.ac.uk/conts/retrieving.html> (or from the Cambridge Crystallographic Data Center, 12 Union Road, Cambridge CB2 1EZ, UK, (fax: +44-(0) 1223-336033 or e-mail: deposit@ccdc.cam.ac.uk).

Acknowledgements

The authors gratefully acknowledge financial assistance in the

form of Grants-in-aid (Nos. 25350269, 25410056, 25410057 and 16K05707) for Scientific Research from the Ministry of Education, Culture, Sports, Science, and Technology, Japan. The author (NW) further acknowledges financial support from the Strategic Research Base Development Program for Private Universities of the Ministry of Education, Culture, Sports, Science and Technology of Japan.

Appendix A. Supplementary data

Supplementary data related to this article can be found at <http://dx.doi.org/10.1016/j.tet.2017.02.038>.

References

- Kerns DR. *Chem Rev.* 1971;71:395.
- (a) Hasty NM, Kearns DR. *J Am Chem Soc.* 1973;95:3380; (b) Schaap AP, Faler GR. *J Am Chem Soc.* 1973;95:3381.
- McCapra F, Beheshti I. *Chem Commun.* 1977;517.
- Stephenson LM, Grdina MJ, Orfanopoulos M. *Acc Chem Res.* 1980;13:419.
- Frimer AA, Stephenson LM. The singlet oxygen ene reaction. In: Frimer AA, ed. *Singlet O₂*. vol. II. Florida: CRC; 1985:67–91.
- Stratakis M, Orfanopoulos M, Foote CS. *Tetrahedron Lett.* 1996;37:7159.
- (a) Yoshioka Y, Yamada S, Kawakami T, Nishino M, Yamaguchi K, Saito I. *Bull Chem Soc Jpn.* 1996;69:2683; (b) Singleton DA, Hang C, Szymanski MJ, et al. *J Am Chem Soc.* 2003;125:1319; (c) Leach AG, Houk KN, Foote CS. *J Org Chem.* 2008;73:8511.
- Adam W, Botke N, Krebs O. *Org Lett.* 2000;2:3293.
- Lerdal D, Foote CS. *Tetrahedron Lett.* 1978;19:3227.
- (a) Matsumoto M, Kobayashi H, Matsubara J, et al. *Tetrahedron Lett.* 1996;37:397; (b) Matsumoto M, Watanabe N, Kobayashi H, et al. *Tetrahedron Lett.* 1996;37:5939; (c) Matsumoto M, Kitano Y, Kobayashi H, Ikawa H. *Tetrahedron Lett.* 1996;37:8191.
- Nyilasa A. *Tetrahedron Lett.* 1997;38:2517.
- Adam W, Bosio SG, Turro NJ. *J Am Chem Soc.* 2002;124:14004.
- (a) Orfanopoulos M, Stratakis M, Elemes Y. *Tetrahedron Lett.* 1989;30:4875; (b) Orfanopoulos M, Stratakis M, Elemes Y. *J Am Chem Soc.* 1990;112:6417.
- (a) Adam W, Nestler B. *J Am Chem Soc.* 1992;114:6549; (b) Adam W, Nestler B. *J Am Chem Soc.* 1993;115:5041; (c) Adam W, Richter MJ. *Tetrahedron Lett.* 1993;34:8423.
- Adam W, Prein M. *J Am Chem Soc.* 1993;115:3766.
- (a) Adam W, Bruenker H-G. *J Am Chem Soc.* 1993;115:3008; (b) Bruenker H-G, Adam W. *J Am Chem Soc.* 1995;117:3976.
- Adam W, Peters K, Peters E-M, Schmbony SB. *J Am Chem Soc.* 2001;123:7228.
- Adam W, Bosio SG, Turro NJ. *J Am Chem Soc.* 2002;124:8814.
- Sivaguru J, Solomon MR, Saito H, et al. *Tetrahedron.* 2006;62:6707.
- Sivaguru J, Solomon MR, Poon T, et al. *Acc Chem Res.* 2008;41:387.
- Schaap AP, Zaklika KA. 1,2-Cycloaddition reactions of singlet oxygen. In: Wasserman HH, Murray RW, eds. *Singlet Oxygen*. NY: Academic; 1979: 174–243.
- Gollnick K, Kuhn HJ. In: Wasserman HH, Murray RW, eds. *Ene-reactions with Singlet Oxygen* in *Singlet Oxygen*. NY: Academic; 1979:284–429.
- Frimer AA, Bartlett PD, Boschung AF, Jewett JG. *J Am Chem Soc.* 1977;99:7977.
- Orfanopoulos M, Stratakis M. *Tetrahedron Lett.* 1991;32:7321.
- Greer A, Vassilikogiannakis G, Lee K-C, Koffas TS, Nahm K, Foote CS. *J Org Chem.* 2000;65:6876.
- Poon T, Sivaguru J, Franz R, et al. *J Am Chem Soc.* 2004;126:10498.
- Matsumoto M, Watanabe N, Ishikawa A, Murakami H. *Chem Commun.* 1997: 2395.
- Monroe BM. Singlet oxygen in solution: lifetimes and reaction rate constants. In: Frimer AA, ed. *Singlet O₂*. vol. I. Florida: CRC; 1985:177–224.
- Reichardt C. *Solvents and Solvent Effects in Organic Chemistry*. Weinheim: Wiley-VCH; 2003.
- Kamlet MJ, Abboud JLM, Taft RW. An examination of linear solvation energy relationships. In: Taft R, ed. *Progress in Physical Organic Chemistry*. vol. 13. New York: Wiley; 1981:485–630.
- Tanimura M, Watanabe N, Ijuin HK, Matsumoto M. *J Org Chem.* 2010;75:3678.
- Matsumoto M, Ito Y, Matsubara J, Sakauma T, Mizoguchi Y, Watanabe N. *Tetrahedron Lett.* 2001;42:2349.
- Watanabe N, Mizuno Y, Maeda Y, Ijuin HK, Matsumoto M. *Heterocycles*. 2016. [http://dx.doi.org/10.3987/COM-16-S\(5\)40](http://dx.doi.org/10.3987/COM-16-S(5)40).
- Stratakis M, Orfanopoulos M. *Tetrahedron Lett.* 1995;36:4291.
- A theoretical study suggested that the most unstable conformer **C** with boat-form possessed energy ca. 28 kJ mol⁻¹ higher than that for conformer **A** and that all three conformers **A-C** were individually in the equilibrium between two rotamers of a 3-hydroxyphenyl with practically same stability (± 0.07 kJ mol⁻¹) (see SD).
- Inoue Y. *Chem Rev.* 1992:741.

¹ CrystalClear: Data Collection and Processing Software, Rigaku Corporation (1998–2014). Tokyo 196–8666, Japan.

² SIR2008: Burla, M. C., Caliandro, R., Camalli, M., Carrozzini, B., Cascarano, G. L., De Caro, L., Giacovazzo, C., Polidori, G., Siliqi, D. and Spagna R. (2007). *J. Appl. Cryst.* 40, 609–613.

³ CrystalStructure 4.1: Crystal Structure Analysis Package, Rigaku and Rigaku/MS (2000–2003). 9009 New Trails Dr. The Woodlands TX 77381 USA.

⁴ CRYSTALS Issue 11: Carruthers, J.R., Rollett, J. S., Betteridge, P.-W., Kinna, D., Pearce, L., Larsen, A., and Gabe, E. Chemical Crystallography Laboratory, Oxford, UK. (1999).

SYNTHESIS OF TRICYCLIC DIOXETANES THAT EXHIBIT INTRAMOLECULAR CHARGE-TRANSFER-INDUCED DECOMPOSITION: RELATIONSHIP BETWEEN STRUCTURE AND CHEMILUMINESCENCE EFFICIENCY

Nobuko Watanabe,* Yuukou Mizuno, Yoshinori Maeda, Hisako K. Ijuin, and Masakatsu Matsumoto*

Department of Chemistry, Kanagawa University, Tsuchiya, Hiratsuka, Kanagawa 259-1293, Japan; E-mail address: nwatanab@kanagawa-u.ac.jp; matsumo-chem@kanagawa-u.ac.jp

Abstract – Tricyclic dioxetanes bearing a 3-oxyphenyl group **3–5** were stereoselectively synthesized in high yields by the singlet oxygenation of three types of 5-(3-oxyphenyl)-2,3-dihydrofurans fused with a cyclopentane ring **6b–8b**. Upon treatment with tetrabutylammonium fluoride (TBAF) in DMSO or acetonitrile at 25 °C, these dioxetanes underwent charge-transfer-induced decomposition (CTID) accompanied by the emission of bright blue light. Although all of these dioxetanes gave excited oxyanions of 3-hydroxybenzoate as an emitter, their chemiluminescence efficiencies were significantly different and depended on their structures.

INTRODUCTION

Intramolecular charge-transfer-induced decomposition (CTID) of a 1,2-dioxetane bearing an aromatic electron donor may lead to highly efficient chemiluminescence and is now believed to play a key role in the bioluminescence of various organisms such as the firefly.¹⁻³ Extensive research has been conducted to elucidate the chemiexcitation processes in both chemiluminescence and bioluminescence. CTID has also stimulated the development of high-performance dioxetane-based chemiluminescence systems that can be used in modern biological and clinical analysis, as represented by AMPPD[®] (**1**) and DIFURAT[®] (**2a**) (Figure 1).^{4,5}

In the course of our investigation to develop a high-performance chemiluminescence system, we attempted to modify the parent dioxetane **2b** to determine whether or not further stereochemical

regulation of the dioxetane skeleton fused to a dihydrofuran ring leads to an increase in chemiluminescence efficiency (Φ^{CL}). The thus-realized dioxetanes were 3-oxyphenyl-substituted tricyclic dioxetanes **3–5**, in which a tetrahydrofuran ring was further fused with a cyclopentane ring (Figure 1). We report here the synthesis of **3–5** and their CTID, for which the Φ^{CL} values differed from the value for **2b** depending on their structures, though they gave quite similar esters of 3-oxidobenzoic acid as an emitter.^{6,7}

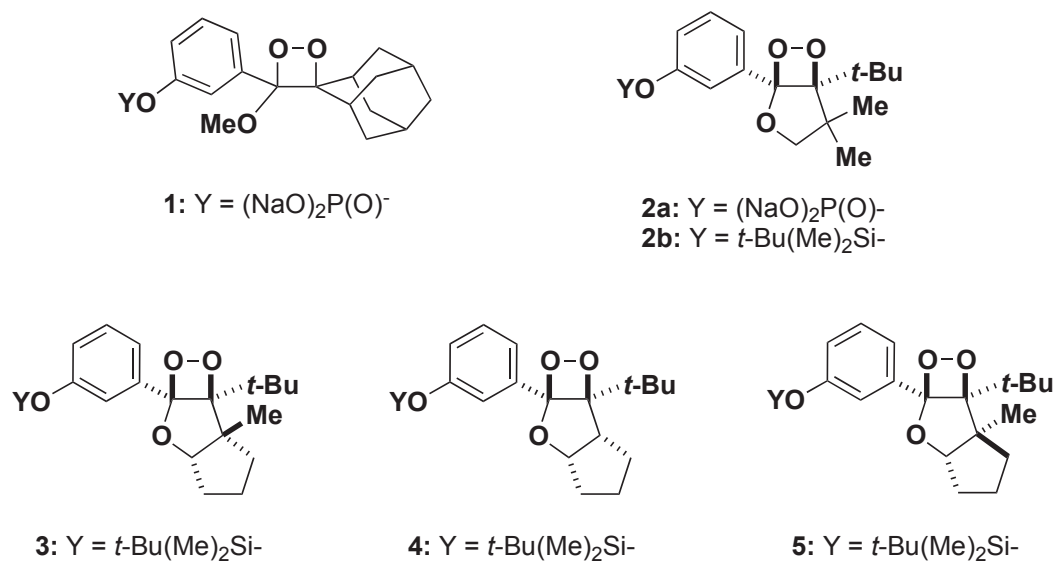


Figure 1. AMPPD[®] (**1**), DIFURAT[®] (**2a**) and tricyclic dioxetanes **3**, **4** and **5**

RESULTS AND DISCUSSION

Synthesis of tricyclic dioxetanes bearing a 3-(*tert*-butyldimethylsiloxy)phenyl group

Tricyclic dioxetanes bearing a 3-(*tert*-butyldimethylsiloxy)phenyl group **3**, **4** and **5** were prepared by singlet oxygenation of the corresponding 3-(*tert*-butyldimethylsiloxy)phenyl-substituted 2,3-dihydrofurans **6b**, **7b** and **8b** fused with a cyclopentane ring. These precursors were synthesized through several steps starting from *t*-2-methyl-*c*-2-(2,2-dimethyl-1-hydroxypropyl)cyclopentan-*r*-1-ol (*cis*-**9**), *c*-2-(2,2-dimethyl-1-hydroxypropyl)cyclopentan-*r*-1-ol (*cis*-**10**) and the *trans*-isomer (*trans*-**9**) of *cis*-**9**. These diols were prepared from pivaloylcyclopentanone **11** or **12** by reduction with LiAlH₄ or DIBAL. Williamson ether synthesis using diol *cis*-**9** and 3-methoxybenzyl chloride selectively gave cyclopentyl ether **13**, the remaining OH group of which was in turn oxidized with PCC to give benzyloxycyclopentyl *tert*-butyl ketone **14** in high yield. LDA-mediated cyclization⁸ of ketone **14** effectively took place to give hydroxytetrahydrofuran fused with a cyclopentane ring **15**, which was successively dehydrated with SOCl₂/pyridine to give 3-methoxyphenyl-substituted bicyclic dihydrofuran **16** in good yield. Finally, deprotection of the methoxy group in **16** with MeSNa/DMF followed by silylation with

When dihydrofuran fused with a *cis*-cyclopentane **6b** was irradiated in the presence of a small amount of tetraphenylporphin (TPP) with a 940 W Na lamp in CH₂Cl₂ under an O₂ atmosphere at 0 °C for 1.5 h, dioxetane **3** was the sole product.

A similar singlet oxygenation of dihydrofuran **7b** proceeded smoothly to exclusively give dioxetane **4**. The structures of **3** and **4** were determined by ¹H NMR, ¹³C NMR, IR, and HR Mass spectral analysis.

Thus, we know that singlet oxygenation proceeded with quite high π -face selectivity: both **3** and **4** were products due to the attack by ¹O₂ of the sterically less-congested π -face of dihydrofuran, which was opposite a fused cyclopentane ring. On the other hand, singlet oxygenation of dihydrofuran **8b** proceeded sluggishly even at 40 °C, albeit with high stereoselectivity: ¹O₂ attacked the π -face opposite the 3-methyl group to selectively give dioxetane **5**. The structure of **5** was determined by X-ray single crystallographic analysis in addition to ¹H NMR, ¹³C NMR, IR, and HR Mass spectral analysis: an ORTEP view is shown in Figure 2.

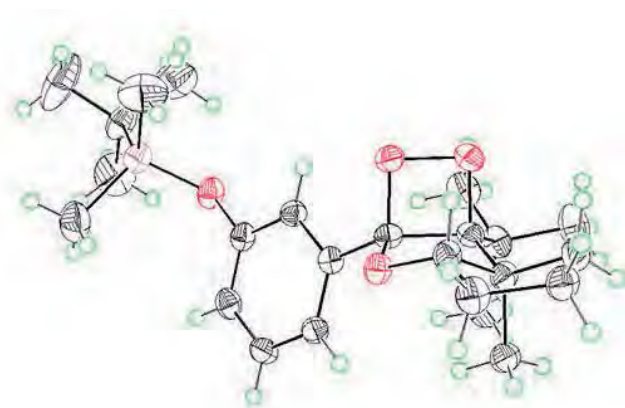
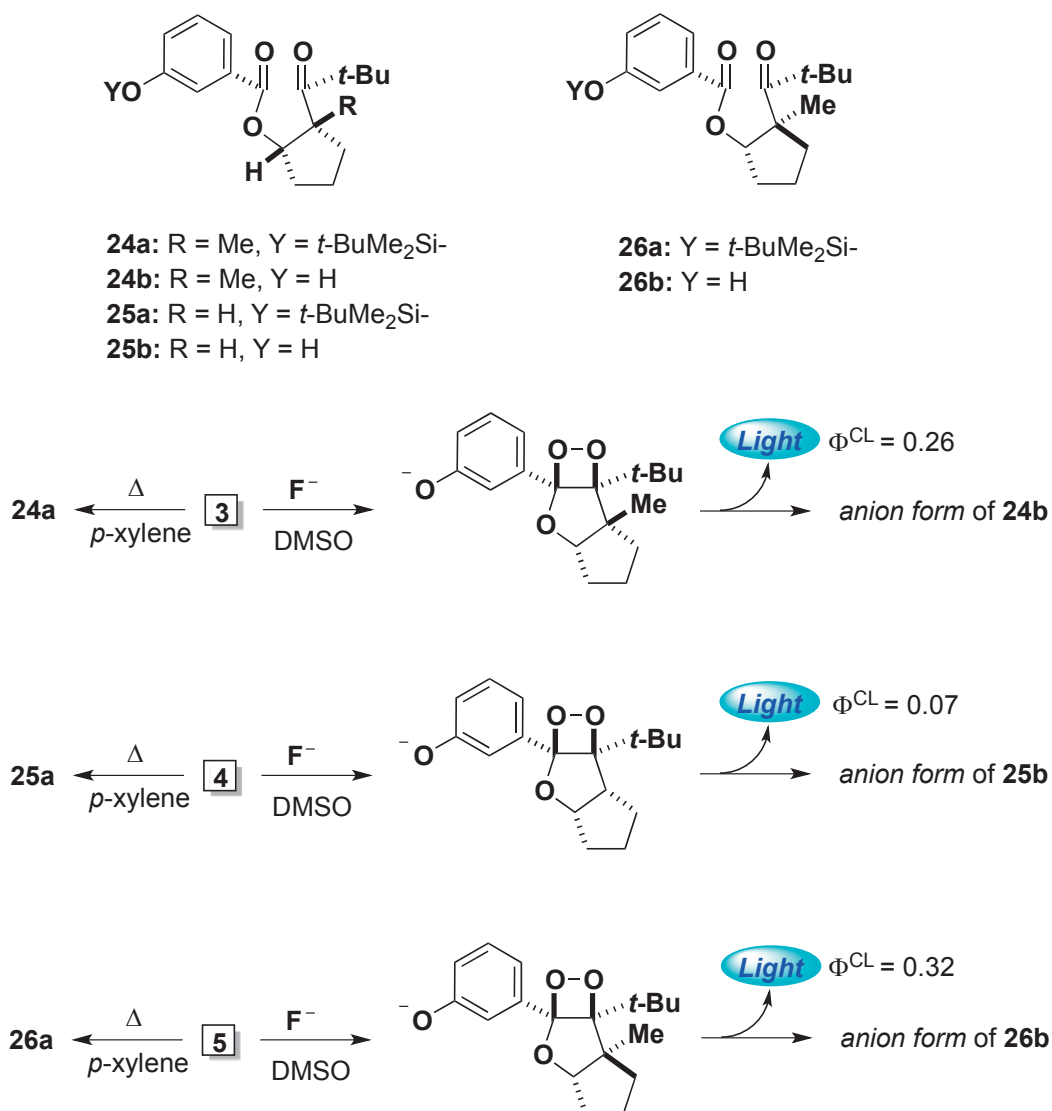


Figure 2. ORTEP view of dioxetane **5**

Chemiluminescent decomposition of tricyclic dioxetanes bearing a 3-(*tert*-butyldimethylsilyloxy)-phenyl group

Tricyclic dioxetanes **3**, **4** and **5** were thermally stable enough to permit handling at room temperature, though they decomposed exclusively into the corresponding ketoesters **24a**, **25a** and **26a** in refluxing *p*-xylene (Scheme 2). When dioxetane **3** was treated with a large excess of tetrabutylammonium fluoride (TBAF) in DMSO at 25 °C, **3** decomposed rapidly to emit intense blue light (maximum wavelength: $\lambda_{\max}^{\text{CL}} = 466$ nm, rate constant of CTID: $\text{CTID} = 0.039 \text{ s}^{-1}$, and half-life: $t_{1/2} = 18$ s) with chemiluminescence efficiency $\Phi^{\text{CL}} = 0.26$,^{9,10} the value of which was considerably higher than that for the parent dioxetane **2b** ($\Phi^{\text{CL}} = 0.20$)^{6a} as shown in Table 1 (Scheme 2). Dioxetanes **4** and **5** also decomposed in TBAF/DMSO to emit blue light ($\lambda_{\max}^{\text{CL}} = 466\text{--}467$ nm), though their Φ^{CL} values diverged from those for the parent **2b** and **3**. Thus, Φ^{CL} for **4** decreased to only 0.07 (relative Φ^{CL} was 2/5 of that for **2b** and 1/4 of that for **3**), whereas Φ^{CL} for **5** increased to 0.32, the value of which was the highest among the three dioxetanes presented here and 1.6 times higher than that for **2b** (Table 1, Scheme 2).



Scheme 2. Thermal- and base-induced decomposition of tricyclic dioxetanes

Table 1. Chemiluminescence properties of dioxetanes **3**, **4**, **5** and **2b** in a TBAF/DMSO system and in a TBAF/MeCN system

Dioxetane	TBAF/DMSO system ^{a)}				TBAF/MeCN system ^{a)}			
	$\lambda_{\text{max}}/\text{nm}$	Φ^{CL}	$\Phi_{\text{S}}^{\text{b)}$	$t_{1/2}/\text{s}$	$\lambda_{\text{max}}/\text{nm}$	Φ^{CL}	$\Phi_{\text{S}}^{\text{b)}$	$t_{1/2}/\text{s}$
3	466	0.26	0.79	18	470	0.13	0.54	64
4	466	0.07	0.21	7.7	470	0.035	0.15	33
5	467	0.32	0.97	0.56	470	0.19	0.79	2.1
2b	466 ^{c)}	0.20 ^{c)}	0.63 ^{c)}	4.6 ^{c)}	469 ^{d)}	0.10 ^{d)}	0.42 ^{d)}	19 ^{d)}

a) The reaction was carried out at 25 °C. b) $\Phi_{\text{S}} = \Phi^{\text{CL}} / \Phi^{\text{fl}}$, $\Phi^{\text{fl}} = 0.33$ for **3**, **4** and **5**, and 0.32 for **2b** in a TBAF/DMSO system; $\Phi^{\text{fl}} = 0.24$ for **3**, **4**, **5** and **2b** in a TBAF/MeCN system. c) ref. 6b. d) ref. 6a.

The spent reaction mixtures of **3**, **4** and **5** afforded the corresponding ketoesters **24b**, **25b** and **26b** after neutralization followed by the usual work-up.¹¹ The fluorescence spectra of oxido anions generated from authentic **24b**, **25b** and **26b** in TBAF/DMSO (MeCN) coincided with the chemiluminescence spectra for **3**, **4** and **5**, respectively. Thus, these oxido anions of ketoesters **24b–26b** were undoubtedly the emitters for the present CTID of dioxetanes **3–5**. The fluorescence efficiencies (Φ^{fl}) of the oxido anions of ketoesters **24b–26b** were all estimated to be 0.33, which was practically the same as the value for an emitter from **2b** ($\Phi^{\text{fl}} = 0.32$) in a TBAF/DMSO system.^{6a} Thus, the efficiencies of singlet-chemiexcitation ($\Phi_{\text{S}} = \Phi^{\text{CL}}/\Phi^{\text{fl}}$) in TBAF/DMSO were calculated to be 0.79 for **3**, 0.21 for **4** and 0.97 for **5**. These results showed that tricyclic dioxetanes **3** and **5** were excellent chemiluminescence compounds with singlet-chemiexcitation efficiency that was markedly high among oxyphenyl-substituted dioxetanes known to date.^{1,2,12,13}

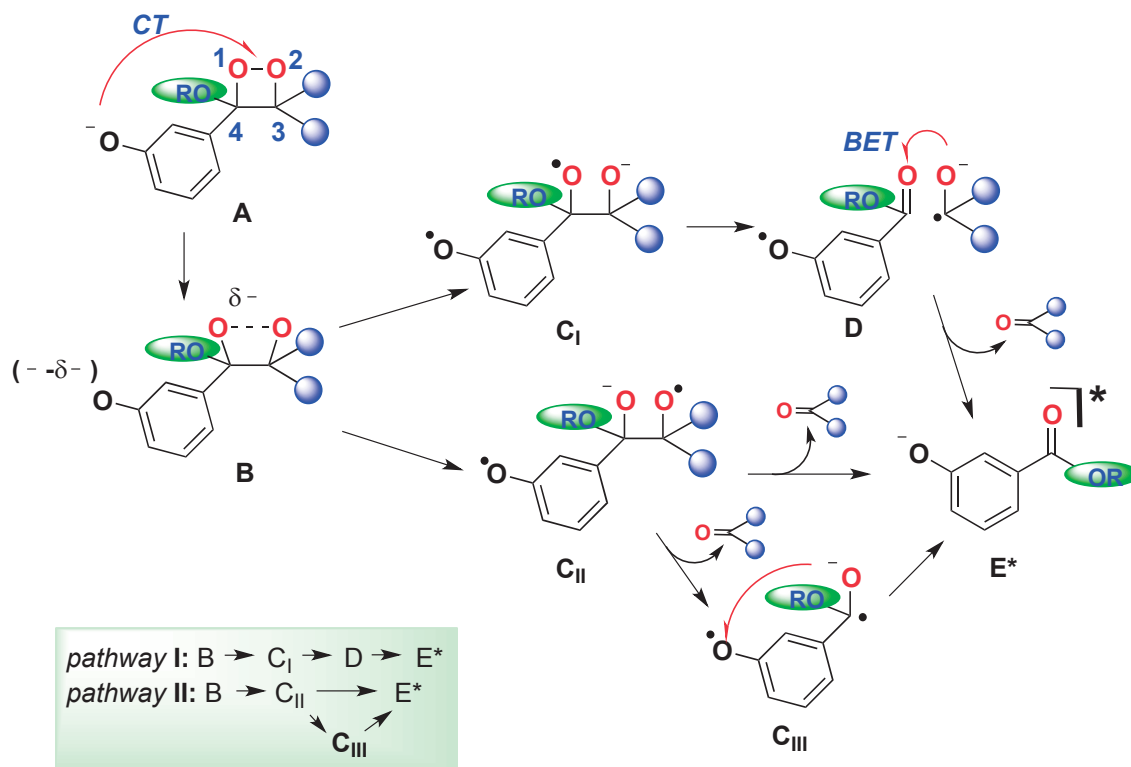
TBAF-induced chemiluminescent decomposition of these dioxetanes was also carried out in acetonitrile and the results are summarized in Table 1. When we compared the chemiluminescence properties of **3**, **4** and **5** in acetonitrile to those in DMSO, we found that $\lambda_{\text{max}}^{\text{CL}}$ was practically the same and $t_{1/2}$ was increased ca. 4-fold, while Φ^{CL} decreased to ca 1/2. However, the magnitude of Φ^{CL} was in the order of **5** > **3** > **2b** >> **4** both in DMSO and in MeCN. Thus, the efficiencies of singlet-chemiexcitation Φ_{S} were estimated similarly to the case of TBAF/DMSO and are summarized in Table 1.

As described above, both stereoisomeric tricyclic dioxetanes **3** and **5** fused with a cyclopentane ring showed effective singlet-chemiexcitation that was 25–50% (in DMSO) or 30–90% (in MeCN) higher than that for the parent dioxetane **2b**. However, singlet-chemiexcitation for dioxetane **4** was far less effective than in the case of **3**, though the structural features of **4** and **3** resembled each other except regarding the presence of a bridge-head methyl group. Thus, we will finally discuss how the chemiexcitation process was affected by the skeleton of the dioxetane bearing an oxidophenyl group.

Plausible mechanisms for singlet-chemiexcitation that have typically been proposed for CTID of oxidophenyl-substituted dioxetane **A** are illustrated in Scheme 3, where the reaction proceeds as follows:^{2,3,14,15}

- i) Intramolecular CT takes place from an oxidophenyl anion to O-O for dioxetane **A** to give **B**, which causes O-O bond cleavage to give two types of transient biradical anion, **C_I** and/or **C_{II}**, as an extreme structure.
- ii) Cleavage of the C-C bond in biradical anion **C_I** gives pair **D** of neutral radical/ketyl radical anion, which is annihilated by intermolecular backward electron transfer (BET) to form singlet-excited oxidobenzoate **E*** and neutral ketone (*pathway I*) [CIEEL¹⁶ (chemically initiated electron exchange luminescence) mechanism]. On the other hand, biradical anion **C_{II}** extrudes a neutral ketone

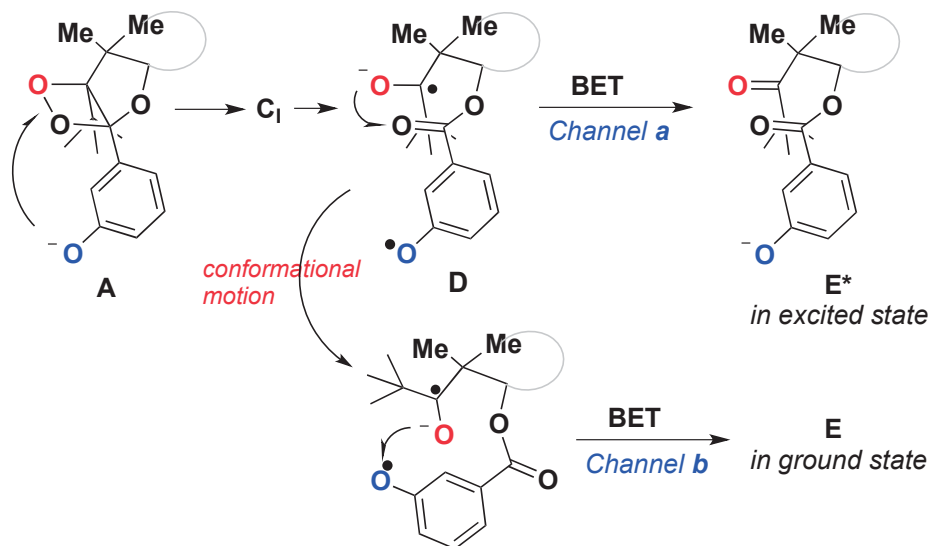
molecule in the ground state to give E^* directly or through intramolecular BET¹⁴ of diradical anion C_{III} (pathway II) [CT/direct mechanism].¹⁷



Scheme 3. Singlet-chemiexcitation mechanism for CTID of oxidophenyl-substituted dioxetane

If the CIEEL mechanism is operative, Φ_S of dioxetane **A** depends on the efficiency of BET (c **ann** *a*, i **in ra**) which occurs in a solvent cage. Therefore, diffusion of a ketyl radical anion would decisively decrease Φ_S for dioxetanes such as **1**.^{4c} On the other hand, this possibility can be excluded for bicyclic dioxetanes **2**, since a ketyl radical anion is tethered to an oxybenzoate radical by a $-\text{CH}_2\text{C}(\text{Me})_2-$ chain for **D**. However, another BET (c **ann** *b*) has been proposed to occur from ketyl radical anion to $\cdot\text{O-Ar}$ radical of a benzoate moiety with an accompanying conformational change to directly give a benzoate in the ground state (Scheme 4).¹⁸ According to this mechanism, the fact that Φ_S for tricyclic dioxetanes **3** and **5** were markedly higher than that for bicyclic dioxetane **2b** may be accounted for as follows. Since the conformational change of both the neutral radical of oxybenzoate and the ketyl radical anion is considerably regulated by the cyclopentane ring joining them for **D** produced from **3** or **5**, BET through c **ann** *b* becomes more difficult to occur than in the case of **2b**. If we consider that the structural features of **25** with a *cis*-*icina*-disubstitution pattern on a cyclopentane ring are the same as those of **24** except that the latter has a 3-methyl group, radical pair **D** for dioxetane **4** would have a steric environment similar to that for **3**. Therefore, while Φ_S for **4** was expected to be as high as that for **3**, it was only 1/4

of that for **3**. In conclusion, CIEEL (at a I) cannot well describe the relationship between structure and Φ_S for the chemiluminescent CTID of dioxetanes **2–5**.



Scheme 4. Two BET channels leading to **E*** or **E** for a bicyclic dioxetane

On the other hand, for the CT/direct mechanism (at a II), singlet-chemiexcitation occurs through **C_{II}**, which undergoes homolytic C-C bond cleavage to give excited ester **E*** either directly or through **C_{III}**. Thus, **C_{II}**, once produced, is presumed to effectively give **E***. Since a transient species **B** can give both **C_I** and **C_{II}**, effective singlet-chemiexcitation seems to depend on how **C_{II}** is preferentially produced for CTID of dioxetane **A**.¹⁹⁻²² This notion suggests that CTID of dioxetanes **2b** and **3–5** proceeded preferentially through **C_{II}** (at a II) in the order **5** > **3** > **2b** >> **4**. Note that this order apparently coincides with the order of steric congestion around the carbon at the 3-position of dioxetane **A**, i.e., **5** ≥ **3** > **2b** > **4**. These results suggest that the steric environment such as congestion around the carbon of dioxetane presumably affects singlet-chemiexcitation for oxyphenyl-substituted dioxetanes. Thus, we are now investigating chemiluminescent CTID of various oxyphenyl-substituted dioxetanes to determine how their singlet-chemiexcitation efficiencies relate to their structures mainly based on X-ray single crystallographic analysis.

CONCLUSION

Three types of 5-oxyphenyl-2,3-dihydrofurans fused with a cyclopentane ring **6b–8b** were oxygenated with ¹O₂ to stereoselectively give the corresponding tricyclic dioxetanes bearing an 3-oxyphenyl group **3–5** in high yields. TBAF induced CTID of **3–5** accompanied by the emission of a flash of blue light. Although all of these dioxetanes gave excited 3-oxidobenzoates as emitters with the very same

fluorescence efficiency, their chemiluminescence efficiencies diverged from that for the parent **2b** ($\Phi^{CL} = 0.20$) to within the range 0.07-0.32 depending on their structures. The results suggested that chemiluminescent CTID for these dioxetanes could not be well described by an intramolecular CIEEL mechanism through **at a I**. Alternatively, effective singlet-chemiexcitation was presumed to take place through **at a II** (CT/direct mechanism), where the preferred destination was affected by the steric conditions around the carbon of dioxetane.

EXPERIMENTAL

General Melting points were uncorrected. IR spectra were taken on a FT/IR infrared spectrometer. ^1H and ^{13}C NMR spectra were recorded on a 300 MHz, 400 MHz and 500 MHz spectrometers. Mass spectra were obtained using double-focusing mass spectrometers and an ESI-TOF mass spectrometer. Column chromatography was carried out using silica gel.

Synthesis of *r*-1-(3-methoxybenzyloxy)-*t*-2-methyl-*c*-2-(1-hydroxy-2,2-dimethylpropyl)cyclopentane (13**): typical procedure.** *t*-2-Methyl-*c*-2-(2,2-dimethyl-1-hydroxypropyl)cyclopentan-*r*-1-ol (**cis-9**) (2.10 g, 11.3 mmol) was added to a suspension of NaH (60% in oil, 510 mg, 12.8 mmol) in dry DMF (40 mL) under N_2 atmosphere at room temperature and stirred for 1 h. To the solution, 3-methoxybenzyl chloride (1.70 mL, 11.7 mmol) was added and stirred for overnight. The reaction mixture was poured into sat. aq. NH_4Cl and extracted twice with AcOEt. The organic layer was washed with sat. aq. NaCl, dried over anhydrous MgSO_4 , and concentrated **in vacuo**. The residue was chromatographed on silica gel with hexane–AcOEt (10:1) to give 3.068 g of **13**. The stereoisomer **17** of **13** was similarly synthesized.

13: 89% yield. colorless oil. ^1H -NMR (400 MHz, CDCl_3): δ_{H} 0.94 (s, 3H), 1.03 (s, 9H), 1.37-1.45 (m, 1H), 1.55-1.92 (m, 4H), 2.15-2.27 (m, 1H), 3.26 (d, $J = 3.2$ Hz, 1H), 3.59 (dd, $J = 4.6$ and 1.8 Hz, 1H), 3.67 (d, $J = 3.2$ Hz, 1H), 3.81 (s, 3H), 4.35 (d, $J = 12.0$ Hz, 1H), 4.56 (d, $J = 12.0$ Hz, 1H), 6.82 (dd, $J = 8.2$ and 2.4 Hz, 1H), 6.87-6.90 (m, 2H), 7.25 (dd, $J = 8.2$ and 7.9 Hz, 1H) ppm. ^{13}C -NMR (100 MHz, CDCl_3): δ_{C} 21.3, 23.3, 28.5, 29.4, 33.3, 36.7, 52.3, 55.1, 70.5, 80.6, 91.1, 112.4, 113.1, 119.4, 129.3, 140.0, 159.7 ppm. IR (liquid film): $\tilde{\nu}$ 3495, 2955, 2907, 2836, 1602 cm^{-1} . Mass (m/z , %): 306 (M^+ , 1), 185 (8), 138 (80), 121 (100). HRMS (ESI) (m/z): 329.2088, calcd for $\text{C}_{19}\text{H}_{30}\text{O}_3\text{Na}$ [$\text{M} + \text{Na}^+$] 329.2093.

17: 87% yield. colorless oil. ^1H -NMR (500 MHz, CDCl_3): δ_{H} 0.98 (s, 9H), 1.05 (s, 3H), 1.43-1.65 (m, 4H), 1.69-1.81 (m, 1H), 1.96-2.04 (m, 1H), 3.21 (s, 1H), 3.78 (t, $J = 8.7$ Hz, 1H), 3.81 (s, 3H), 4.28 (s, 1H), 4.45 (d, $J = 11.7$ Hz, 1H), 4.55 (d, $J = 11.7$ Hz, 1H), 6.82 (dd, $J = 8.3$ and 2.6 Hz, 1H), 6.87 (s with fine coupling, 1H), 6.89 (d, $J = 7.6$ Hz, 1H), 7.24 (dd, $J = 8.3$ and 7.6 Hz, 1H) ppm. ^{13}C -NMR (125 MHz, CDCl_3): δ_{C} 13.9, 19.0, 26.1, 28.3, 35.6, 37.0, 49.0, 55.2, 71.6, 88.7, 90.6, 113.0, 113.2, 119.8, 129.4,

139.4, 159.7 ppm. IR (liquid film): $\tilde{\nu}$ 3490, 2956, 2871, 1602 cm^{-1} . Mass (, %): 306 (M^+ , 11), 249 (8), 138 (62), 121 (100). HRMS (ESI) (): 329.2099, calcd for $\text{C}_{19}\text{H}_{30}\text{O}_3\text{Na}$ [$\text{M} + \text{Na}^+$] 329.2093.

Synthesis of *r*-1-(3-methoxybenzyloxy)-*t*-2-methyl-*c*-2-pivaloylcyclopentane (14): typical procedure.

Celite (10.4 g) and PCC (5.20 g, 24.1 mmol) was added to a solution of **13** (4.74 g, 15.5 mmol) in dry CH_2Cl_2 (50 mL) under N_2 atmosphere at room temperature and stirred overnight. To the reaction mixture, 2-propanol (5 mL) was added and stirred for 30 min, and then ether was added. The reaction mixture was filtered through celite and concentrated in **ac** . The residue was chromatographed on silica gel with hexane–AcOEt (10:1) to give of 4.46 g of **14**. The stereoisomer **18** of **14** was similarly synthesized from **17**.

14: 95% yield. colorless oil. $^1\text{H-NMR}$ (400 MHz, CDCl_3): δ_{H} 1.14 (s, 3H), 1.19 (s, 9H), 1.55-1.95 (m, 5H), 2.52-2.63 (m, 1H), 3.79 (s, 3H), 4.08 (d, $J = 3.8$ Hz, 1H), 4.31 (d, $J = 11.9$ Hz, 1H), 4.46 (d, $J = 11.9$ Hz, 1H), 6.75-6.84 (m, 3H), 7.20 (t, $J = 8.0$ Hz, 1H) ppm. $^{13}\text{C-NMR}$ (100 MHz, CDCl_3): δ_{C} 20.2, 22.6, 27.6, 28.1, 33.3, 45.0, 55.1, 62.1, 69.8, 87.4, 112.4, 112.9, 119.4, 129.0, 140.3, 159.5, 216.8 ppm. IR (liquid film): $\tilde{\nu}$ 2961, 2875, 1685, 1601 cm^{-1} . Mass (, %): 304 (M^+ , 8), 168 (13), 121 (100). HRMS (ESI) (/): 327.1934, calcd for $\text{C}_{19}\text{H}_{28}\text{O}_3\text{Na}$ [$\text{M} + \text{Na}^+$] 327.1936.

18: 86% yield. colorless oil. $^1\text{H-NMR}$ (400 MHz, CDCl_3): δ_{H} 1.25 (s, 9H), 1.39 (s, 3H), 1.46-1.79 (m, 4H), 1.83-2.03 (m, 2H), 3.81 (s, 3H), 4.41 (t, $J = 7.1$ Hz, 1H), 4.46 (d, $J = 12.7$ Hz, 1H), 4.52 (d, $J = 12.7$ Hz, 1H), 6.80 (d with fine coupling, $J = 8.1$ Hz, 1H), 6.89-6.93 (m, 2H), 7.23 (t, $J = 8.1$ Hz, 1H) ppm. $^{13}\text{C-NMR}$ (100 MHz, CDCl_3): δ_{C} 18.6, 20.4, 28.6, 29.4, 36.3, 45.4, 55.1, 58.8, 71.6, 83.6, 112.7, 112.8, 119.5, 129.1, 140.8, 159.5, 217.4 ppm. IR (liquid film): $\tilde{\nu}$ 2957, 2873, 1682, 1603 cm^{-1} . Mass (, %): 304 (M^+ , 14), 183 (8), 121 (100). HRMS (ESI) (/): 327.1941, calcd for $\text{C}_{19}\text{H}_{28}\text{O}_3\text{Na}$ [$\text{M} + \text{Na}^+$] 327.1936.

Synthesis of *cis*-2-(1-hydroxy-2,2-dimethylpropyl)cyclopentyl 3-methoxybenzoate (21).

3-Methoxybenzoyl chloride (2.23 mL, 15.9 mmol) was added to a solution of 2 *cis*-2-(2,2-dimethyl-1-hydroxypropyl)cyclopentan-1-ol (**cis-10**) (2.74 g, 15.9 mmol) and pyridine (3.2 mL, 39.6 mmol) in dry CH_2Cl_2 (30 mL) under argon atmosphere at 0 $^\circ\text{C}$ and stirred at room temperature for overnight. The reaction mixture poured into sat. aq. NaCl and extracted with AcOEt. The organic layer was washed with 1M HCl and then with sat. aq. NaCl, dried over anhydrous MgSO_4 and concentrated in **ac** . The residue was chromatographed on silica gel with hexane–AcOEt (10:1) to give 3.40 g of **21**.

21: 70% yield. colorless oil. $^1\text{H-NMR}$ (500 MHz, CDCl_3): δ_{H} 0.93 (s, 9H), 1.66-1.75 (m, 1H), 1.79-2.14 (m, 6H), 2.24-2.30 (m, 1H), 3.61-3.64 (m, 1H), 3.85 (s, 3H), 5.44-5.47 (m, 1H), 7.10 (dd, $J = 8.0$ and 2.8 Hz, 1H), 7.35 (t, $J = 8.0$ Hz, 1H), 7.53 (s with fine coupling, 1H), 7.56 (d, $J = 8.0$ Hz, 1H) ppm.

^{13}C -NMR (125 MHz, CDCl_3): δ_{C} 22.4, 22.4, 26.5, 32.7, 35.4, 44.8, 55.4, 77.6, 81.8, 114.1, 119.3, 121.6, 129.6, 131.9, 159.7, 165.9 ppm. IR (liquid film): $\tilde{\nu}$ 3551, 2957, 2871, 1714, 1602 cm^{-1} . Mass (, %): 306 (M^+ , 6), 249 (26), 153 (38), 135 (100). HRMS (ESI) (/): 329.1728, calcd for $\text{C}_{18}\text{H}_{26}\text{O}_4\text{Na}$ [$\text{M} + \text{Na}^+$] 329.1729.

***cis*-2-Pivaloylcyclopentyl 3-methoxybenzoate (22).** Similarly to the case of **13**, alcohol **21** was oxidized with PCC to give **22**.

22: 90% yield. colorless oil. ^1H -NMR (400 MHz, CDCl_3): δ_{H} 1.13 (s, 9H), 1.60-1.83 (m, 2H), 1.91-2.02 (m, 2H), 2.11-2.31 (m, 2H), 3.50 (ddd, $J = 8.9, 7.9$ and 6.2 Hz, 1H), 3.85 (s, 3H), 5.55-5.60 (m, 1H), 7.08 (ddd, $J = 8.3, 2.7$ and 1.0 Hz, 1H), 7.32 (dd, $J = 8.3$ and 7.7 Hz, 1H), 7.49 (s with fine coupling, 1H), 7.56 (d with fine coupling, $J = 7.7$ Hz, 1H) ppm. ^{13}C -NMR (100 MHz, CDCl_3): δ_{C} 22.6, 26.0, 28.2, 33.6, 44.7, 48.9, 55.3, 77.6, 113.7, 119.7, 122.0, 129.3, 131.4, 159.5, 165.6, 213.5 ppm. IR (liquid film): $\tilde{\nu}$ 2966, 2873, 1716, 1587 cm^{-1} . Mass (, %): 304 (M^+ , 7), 247 (26), 136 (11), 135 (100). HRMS (ESI) (/): 327.1574, calcd for $\text{C}_{18}\text{H}_{24}\text{O}_4\text{Na}$ [$\text{M} + \text{Na}^+$] 327.1572.

Synthesis of *cis*-4-*tert*-butyl-4-hydroxy-3-(3-methoxyphenyl)-5-methyl-2-oxabicyclo[3.3.0]octane (15): typical procedure. Butyllithium (1.6 M in hexane, 19.4 mL, 31.0 mmol) was added to a solution of diisopropylamine (4.44 mL, 33.9 mmol) in dry THF (50 mL) and stirred for 30 min under N_2 atmosphere at room temperature. To the solution, **14** (4.30 g, 14.1 mmol) in dry THF (10 mL) was added at -78 $^\circ\text{C}$ and stirred for 1 h and then at room temperature for 3 h. The reaction mixture was poured into sat. aq. NH_4Cl and extracted with AcOEt. The organic layer was washed with sat. aq. NaCl, dried over anhydrous MgSO_4 , and concentrated in vacuo. The residue was chromatographed on silica gel with hexane–AcOEt (5:1) to give 3.30 g of **15**.

15: 77% yield. colorless columns, mp 105.5–106.5 $^\circ\text{C}$ (from AcOEt–hexane). ^1H -NMR (400 MHz, CDCl_3): δ_{H} 0.92 (br-s, 9H), 1.34 (s, 3H), 1.30-1.38 (m, 1H), 1.70-1.91 (m, 3H), 2.03 (s, 1H), 2.00-2.10 (m, 1H), 2.53-2.62 (m, 1H), 3.80 (s, 3H), 4.46 (dd, $J = 5.7$ and 3.0 Hz, 1H), 5.05 (s, 1H), 6.79 (d with fine coupling, $J = 8.1$ Hz, 1H), 7.04-7.08 (m, 2H), 7.21 (dd, $J = 8.1$ and 7.5 Hz, 1H) ppm. ^{13}C -NMR (125 MHz, CDCl_3): δ_{C} 25.3, 25.7, 28.5, 35.1, 38.4, 38.6, 55.2, 58.6, 87.8, 90.1, 91.0, 112.7, 113.1, 120.0, 128.9, 142.7, 159.4 ppm. IR (KBr): $\tilde{\nu}$ 3556, 3017, 2963, 2881, 1604 cm^{-1} . Mass (m/z, %): 304 (M^+ , 20), 247 (9), 168 (33), 137 (19), 121 (61), 111 (100). HRMS (ESI) (/): 327.1938, calcd for $\text{C}_{19}\text{H}_{28}\text{O}_3\text{Na}$ [$\text{M} + \text{Na}^+$] 327.1936. Anal. Calcd for $\text{C}_{19}\text{H}_{28}\text{O}_3$: C, 74.96; H, 9.27. Found: C, 74.90; H, 9.34.

19: 21% yield. colorless columns, mp 128.0–128.5 $^\circ\text{C}$ (from hexane). ^1H -NMR (500 MHz, CDCl_3): δ_{H} 1.00-1.15 (m, 9H), 1.20-1.40 (m, 3H), 1.43 (ddd, $J = 12.0, 9.2$ and 1.9 Hz, 1H), 1.60-1.73 (m, 2H), 1.94-2.21 (m, 3H), 3.81 (s, 3H), 4.18 (dd, $J = 11.7$ and 7.3 Hz, 1H), 5.47 (s, 1H), 6.83 (d with fine coupling, $J = 8.1$ Hz, 1H), 7.08-7.12 (m, 2H), 7.29 (t, $J = 8.1$ Hz, 1H) ppm. ^{13}C -NMR (125 MHz,

CDCl₃): δ_C 17.4, 20.6, 24.9, 25.5, 27.4, 28.1, 29.0, 39.2, 55.2, 57.8, 83.7, 86.5, 92.1, 113.2, 114.2, 120.6, 129.4, 139.5, 159.6 ppm. IR (KBr): $\tilde{\nu}$ 3555, 2994, 2958, 2904, 2885, 1601, 1492, 1463 cm⁻¹. Mass (m/z, %): 304 (M⁺, 23), 247 (13), 183 (17), 168 (15), 137 (31), 121 (100). HRMS (ESI) (/): 327.1937, calcd for C₁₉H₂₈O₃Na [M + Na⁺] 327.1936.

Synthesis of *cis*-4-*tert*-butyl-3-(3-methoxyphenyl)-5-methyl-2-oxabicyclo[3.3.0]oct-3-ene (16): typical procedure. Thionyl chloride (1.00 mL, 13.7 mmol) was added to a solution of **15** (2.74 g, 8.99 mmol) and pyridine (7.0 mL) in dry THF (40 mL) at 0 °C and stirred for 1 h. The reaction mixture was poured into sat. aq. NaHCO₃ and then extracted with AcOEt. The organic layer was washed with sat. aq. NaCl, dried over anhydrous MgSO₄, and concentrated in vacuo. The residue was chromatographed on silica gel and eluted with hexane–AcOEt (10:1) to give 2.37 g of **16**.

16: 92% yield. colorless oil. ¹H-NMR (500 MHz, CDCl₃): δ_H 1.05 (s, 9H), 1.39 (s, 3H), 1.54-1.67 (m, 2H), 1.74-1.86 (m, 2H), 1.89-1.98 (m, 1H), 2.02-2.11 (m, 1H), 3.80 (s, 3H), 4.35 (dd, $J = 6.1$ and 3.1 Hz, 1H), 6.83-6.87 (m, 2H), 6.90 (d with fine coupling, $J = 7.6$ Hz, 1H), 7.24 (dd with fine coupling, $J = 8.0$ and 7.6 Hz, 1H) ppm. ¹³C-NMR (125 MHz, CDCl₃): δ_C 24.5, 28.4, 31.8, 32.5, 34.6, 41.5, 55.2, 58.2, 92.9, 113.8, 115.3, 122.4, 122.7, 128.9, 137.3, 149.5, 159.1 ppm. IR (liquid film): $\tilde{\nu}$ 2953, 2867, 1655, 1596 cm⁻¹. Mass (m/z, %): 286 (M⁺, 46), 271 (100), 257 (30), 135 (30). HRMS (ESI) (/): 309.1839, calcd for C₁₉H₂₆O₂Na [M + Na⁺] 309.1831.

20: 20% yield. colorless oil. ¹H-NMR (400 MHz, CDCl₃): δ_H 1.04 (s, 9H), 1.11 (s, 3H), 1.47-1.54 (m, 1H), 1.65-1.76 (m, 3H), 2.03-2.20 (m, 2H), 3.80 (s, 3H), 4.02 (dd, $J = 12.0$ and 7.8 Hz, 1H), 6.84-6.88 (m, 2H), 6.92 (d with fine coupling, $J = 7.6$ Hz, 1H), 7.23 (dd with fine coupling, $J = 8.9$ and 7.6 Hz, 1H) ppm. ¹³C-NMR (125 MHz, CDCl₃): δ_C 18.5, 19.6, 25.4, 29.1, 32.0, 32.3, 55.2, 56.4, 91.6, 114.1, 115.1, 122.4, 128.8, 133.4, 136.8, 155.3, 159.0 ppm. IR (liquid film): $\tilde{\nu}$ 2963, 2902, 2871, 1591 cm⁻¹. Mass (m/z, %): 286 (M⁺, 31), 271 (100), 215 (34), 135 (98). HRMS (ESI) (/): 309.1838, calcd for C₁₉H₂₆O₂Na [M + Na⁺] 309.1831.

Synthesis of *cis*-4-*tert*-butyl-3-(3-methoxyphenyl)-2-oxabicyclo[3.3.0]oct-3-ene (23).

TiCl₃ (5.19 g, 33.7 mmol) was suspended in dry THF (100 mL) under nitrogen atmosphere at room temperature and stirred for 30 min. To the solution, LiAlH₄ (729 mg, 19.2 mmol) was added at 0 °C and stirred at room temperature for 40 min, and then triethylamine (2.50 mL, 17.9 mmol) was added and refluxed for 1 h. To the solution, **22** (1.243 g, 4.08 mmol) in dry THF (20 mL) was added dropwise over 30 min at refluxing temperature and then stirred for 1.5 h. The reaction mixture was poured into chilled sat. aq. Na₂CO₃ and extracted with AcOEt. The organic layer was washed with sat. aq. NaCl, dried over anhydrous MgSO₄ and concentrated in vacuo. The residue (1.339 g) was dissolved together with pyridinium *p*-toluenesulfonate (PPTS) (101 mg, 0.402 mmol) in CH₂Cl₂ (15 mL) and stirred at refluxing

temperature for 4h. The reaction mixture was poured into sat. aq. NaHCO₃ and extracted with AcOEt. The organic layer was washed with sat. aq. NaCl, dried over anhydrous MgSO₄ and concentrated in vacuo. The residue was chromatographed on silica gel and eluted with hexane–AcOEt (20:1) to give of 751 mg of **23**.

23: 68% yield. colorless oil. ¹H-NMR (400 MHz, CDCl₃): δ_H 1.03 (s, 9H), 1.57-1.99 (m, 6H), 3.39-3.45 (m, 1H), 3.80 (s, 3H), 4.95 (ddd, $J = 8.6, 4.8$ and 2.0 Hz, 1H), 6.85 (ddd, $J = 8.2, 2.6$ and 0.9 Hz, 1H), 6.88 (s with fine coupling, 1H), 6.94 (d with fine coupling, $J = 7.5$ Hz, 1H), 7.23 (dd, $J = 8.2$ and 7.5 Hz, 1H) ppm. ¹³C-NMR (125 MHz, CDCl₃): δ_C 23.9, 30.8, 31.7, 34.4, 35.3, 51.0, 55.2, 85.2, 114.0, 115.1, 120.3, 122.3, 128.8, 136.2, 148.9, 159.1 ppm. IR (liquid film): $\tilde{\nu}$ 2956, 2865, 1664, 1601 cm⁻¹. Mass (m/z, %): 272 (M⁺, 27), 257 (100), 135 (37). HRMS (ESI) (m/z): 295.1681, calcd for C₁₈H₂₄O₂Na [M + Na⁺] 295.1674.

Synthesis of *cis*-4-*tert*-butyl-3-(3-hydroxyphenyl)-5-methyl-2-oxabicyclo[3.3.0]oct-3-ene (6a): typical procedure. 3-(3-Methoxyphenyl)-2-oxabicyclooct-3-ene **16** (2.12 g, 7.41 mmol) and sodium methanethiolate (95 %, 1.09 g, 14.8 mmol) in dry DMF (25 mL) was stirred under N₂ atmosphere at 140 °C for 4 h. The reaction mixture was poured into 1M HCl and extracted with AcOEt. The organic layer was washed with sat. aq. NaCl, dried over anhydrous MgSO₄ and concentrated in vacuo. The residue was chromatographed on silica gel with hexane–AcOEt (4:1) to give 1.872 g of **6a**.

6a: 93% yield. colorless needles, mp 113.0–114.0 °C (from AcOEt–hexane). ¹H-NMR (500 MHz, CDCl₃): δ_H 1.05 (s, 9H), 1.38 (s, 3H), 1.54-1.67 (m, 2H), 1.73-1.85 (m, 2H), 1.89-1.97 (m, 1H), 2.04-2.10 (m, 1H), 4.34 (dd, $J = 6.1$ and 3.1 Hz, 1H), 4.78 (s, 1H), 6.74-6.78 (m, 2H), 6.89 (d with fine coupling, $J = 7.6$ Hz, 1H), 7.19 (dd, $J = 7.8$ and 7.6 Hz, 1H) ppm. ¹³C-NMR (125 MHz, CDCl₃): δ_C 24.5, 28.4, 31.8, 32.5, 34.6, 41.5, 58.2, 92.9, 115.2, 117.0, 122.4, 123.0, 129.1, 137.1, 149.1, 155.2 ppm. IR (KBr): $\tilde{\nu}$ 3397, 2984, 2953, 2901, 1665, 1597 cm⁻¹. Mass (m/z, %): 272 (M⁺, 37), 257 (100), 243 (28), 121 (31). HRMS (ESI) (m/z): 295.1677, calcd for C₁₈H₂₄O₂Na [M + Na⁺] 295.1674. Anal. Calcd for C₁₈H₂₄O₂: C, 79.37; H, 8.88. Found: C, 79.39; H, 8.99.

7a: 78% yield. colorless columns, mp 146.5–147.0 °C (from AcOEt–hexane). ¹H-NMR (500 MHz, CDCl₃): δ_H 1.03 (s, 9H), 1.58-1.65 (m, 1H), 1.70-1.86 (m, 4H), 1.91-1.98 (m, 1H), 3.39-3.44 (m, 1H), 4.77 (s, 1H), 4.92-4.96 (m, 1H), 6.77 (dd, $J = 8.2$ and 2.6 Hz, 1H), 6.81 (s with fine coupling, 1H), 6.92 (d, $J = 7.6$ Hz, 1H), 7.18 (dd, $J = 8.2$ and 7.6 Hz, 1H) ppm. ¹³C-NMR (100 MHz, CDCl₃): δ_C 23.9, 30.8, 31.7, 34.3, 35.3, 50.9, 85.3, 115.4, 117.0, 120.7, 122.3, 129.0, 135.9, 148.4, 155.1 ppm. IR (KBr): $\tilde{\nu}$ 3355, 2953, 2903, 1680, 1599 cm⁻¹. Mass (m/z, %): 258 (M⁺, 27), 243 (100), 121 (37). HRMS (ESI) (m/z): 281.1515, calcd for C₁₇H₂₂O₂Na [M + Na⁺] 281.1518. Anal. Calcd for C₁₇H₂₂O₂: C, 79.03; H, 8.58. Found: C, 79.19; H, 8.73.

8a: 97% yield. Colorless needles melted at 95.0–96.0 °C (from CH₂Cl₂–hexane). ¹H-NMR (500 MHz, CDCl₃): δ_H 1.04 (s, 9H), 1.10 (br-s, 3H), 1.50 (ddd, $J = 11.6, 8.2$ and 2.4 Hz, 1H), 1.64–1.75 (m, 3H), 2.04–2.18 (m, 2H), 4.01 (dd, $J = 12.1$ and 7.8 Hz, 1H), 4.76–4.84 (m, 1H), 6.76–6.80 (m, 2H), 6.90 (d with fine coupling, $J = 7.6$ Hz, 1H), 7.19 (dd, $J = 8.0$ and 7.6 Hz, 1H) ppm. ¹³C-NMR (100 MHz, CDCl₃): δ_C 18.6, 19.6, 25.5, 29.1, 32.0, 32.3, 56.3, 91.6, 115.5, 116.9, 122.2, 128.9, 133.7, 136.4, 154.7, 155.0 ppm. IR (KBr): $\tilde{\nu}$ 3347, 2958, 1590 cm⁻¹. Mass (m/z , %): 272 (M⁺, 34), 257 (98), 201 (32), 121 (100). HRMS (ESI) (m/z): 295.1680, calcd for C₁₈H₂₄O₂Na [M + Na⁺] 295.1674. Anal. Calcd for C₁₈H₂₄O₂: C, 79.37; H, 8.88. Found: C, 79.31; H, 9.00.

Synthesis of *cis*-4-*tert*-butyl-3-[(3-*tert*-butyldimethylsiloxy)phenyl]-5-methyl-2-oxabicyclo[3.3.0]-oct-3-ene (6b): typical procedure. Phenol **6a** (869 mg, 3.19 mmol), imidazole (519 mg, 7.62 mmol) and *tert*-butyldimethylsilyl chloride (986 mg, 6.54 mmol) in dry DMF (10 mL) was stirred under nitrogen atmosphere at room temperature for 3 h. The reaction mixture was poured into sat. aq. NaCl and extracted with AcOEt. The organic layer was washed with sat. aq. NaCl, dried over anhydrous MgSO₄, and concentrated in vacuo. The residue was chromatographed on silica gel with hexane–AcOEt (20:1) to give 1.231 g of **6b**.

6b: quantitative yield. colorless oil. ¹H-NMR (500 MHz, CDCl₃): δ_H 0.18 (s, 6H), 0.98 (s, 9H), 1.04 (s, 9H), 1.38 (s, 3H), 1.53–1.66 (m, 2H), 1.73–1.85 (m, 2H), 1.89–1.97 (m, 1H), 2.04–2.10 (m, 1H), 4.34 (dd, $J = 6.0$ and 3.2 Hz, 1H), 6.76–6.80 (m, 2H), 6.89 (d with fine coupling, $J = 7.5$ Hz, 1H), 7.17 (dd with fine coupling, $J = 8.8$ and 7.5 Hz, 1H) ppm. ¹³C-NMR (125 MHz, CDCl₃): δ_C -4.4, 18.2, 24.5, 25.7, 28.4, 31.8, 32.5, 34.7, 41.6, 58.2, 92.8, 119.7, 121.7, 122.5, 123.0, 128.9, 137.3, 149.5, 155.2 ppm. IR (liquid film): $\tilde{\nu}$ 2954, 2930, 2860, 1654, 1596 cm⁻¹. Mass (m/z , %): 418 (M⁺, 0.2), 361 (33), 235 (100), 195 (28). Mass (m/z , %): 387 (M⁺+1, 18), 386 (M⁺, 53), 372 (34), 371 (100), 357 (14), 329 (12), 235 (15). HRMS (ESI) (m/z): 409.2531, calcd for C₂₄H₃₈O₂SiNa [M + Na⁺] 409.2539.

7b: 90% yield. colorless oil. ¹H-NMR (400 MHz, CDCl₃): δ_H 0.18 (s, 6H), 0.98 (s, 9H), 1.02 (s, 9H), 1.52–1.99 (m, 6H), 3.38–3.45 (m, 1H), 4.94 (ddd, $J = 8.6, 4.7$ and 2.2 Hz, 1H), 6.78 (ddd, $J = 8.1, 2.4$ and 1.1 Hz, 1H), 6.81 (s with fine coupling, 1H), 6.93 (ddd, $J = 7.6, 1.5$ and 1.1 Hz, 1H), 7.17 (dd with fine coupling, $J = 8.1$ and 7.6 Hz, 1H) ppm. ¹³C-NMR (100 MHz, CDCl₃): δ_C -4.4, 18.1, 23.9, 25.7, 30.8, 31.7, 34.3, 35.3, 50.9, 85.1, 119.9, 120.1, 121.6, 122.9, 128.8, 136.3, 148.9, 155.1 ppm. IR (liquid film): $\tilde{\nu}$ 2956, 2901, 2861, 1663, 1598 cm⁻¹. Mass (m/z , %): 372 (M⁺, 25), 358 (31), 357 (100), 249 (7), 235 (20). HRMS (ESI) (m/z): 395.2379, calcd for C₂₃H₃₆O₂SiNa [M + Na⁺] 395.2382.

8b: 98% yield. colorless oil. ¹H-NMR (400 MHz, CDCl₃): δ_H 0.18 (s, 6H), 0.98 (s, 9H), 1.03 (s, 9H), 1.10 (s, 3H), 1.46–1.57 (m, 1H), 1.65–1.75 (m, 3H), 2.02–2.19 (m, 2H), 4.01 (dd, $J = 12.0$ and 8.1 Hz, 1H), 6.77–6.79 (m, 2H), 6.91 (d with fine coupling, $J = 7.6$ Hz, 1H), 7.17 (dd with fine coupling, $J = 8.8$ and

7.6 Hz 1H) ppm. ^{13}C -NMR (100 MHz, CDCl_3): δ_{C} -4.3, 18.2, 18.6, 19.7, 25.5, 25.7, 29.2, 32.0, 32.3, 56.4, 91.6, 119.9, 121.6, 123.0, 128.7, 133.2, 136.8, 155.0, 155.2 ppm. IR (liquid film): $\tilde{\nu}$ 2958, 2930, 2898, 2859, 1588 cm^{-1} . Mass (, %): 386 (M^+ , 24), 371 (100), 315 (26), 235 (65). HRMS (ESI) (/): 409.2535, calcd for $\text{C}_{24}\text{H}_{38}\text{O}_2\text{SiNa}$ [$\text{M} + \text{Na}^+$] 409.2539.

Synthesis of *cis-1-transoid-1,3-cis-3-(6-tert-butyl)-7-methyl-3-[3-(tert-butyldimethylsiloxy)phenyl]-2,4,5-trioxatricyclo[5.3.0.0^{3,6}]*decane (3): typical procedure. A solution of **6b** (350 mg, 0.905 mmol) and TPP (1.2 mg) in CH_2Cl_2 (25 mL) was irradiated with Na lamp (940W) under O_2 atmosphere at 0 °C for 1.5 h. The photolysate was concentrated and chromatographed on silica gel with hexane– Et_2O (20:1) to give 367 mg of **3**.

3: 97% yield. colorless granules, mp 67.5–68.5 °C (from MeOH). ^1H -NMR (500 MHz, CDCl_3): δ_{H} 0.18 (s, 6H), 0.97 (s, 9H), 0.98 (s, 9H), 1.12 (s, 3H), 1.53-1.64 (m, 1H), 1.90-2.18 (m, 5H), 4.91 (d, $J = 5.4$ Hz, 1H), 6.85 (ddd, $J = 8.0, 2.4$ and 1.0 Hz, 1H), 7.06 (s with fine coupling, 1H), 7.13 (br-d, $J = 7.8$ Hz, 1H), 7.23 (dd, $J = 8.0$ and 7.8 Hz, 1H) ppm. ^{13}C -NMR (125 MHz, CDCl_3): δ_{C} -4.4, 16.2, 18.2, 24.7, 25.7, 26.9, 27.1, 34.0, 36.9, 57.6, 90.6, 106.0, 115.6, 119.8, 121.0, 121.1, 128.9, 137.5, 155.4 ppm. IR (KBr): $\tilde{\nu}$ 2956, 2931, 2860, 1603, 1585 cm^{-1} . Mass (, %): 418 (M^+ , 3), 386 ($\text{M}^+ - 32$, 0.4), 361 (17), 235 (100). HRMS (ESI) (/): 441.2432, calcd for $\text{C}_{24}\text{H}_{38}\text{O}_4\text{SiNa}$ [$\text{M} + \text{Na}^+$] 441.2437. Anal. Calcd for $\text{C}_{24}\text{H}_{38}\text{O}_4\text{Si}$: C, 68.86; H, 9.15. Found: C, 68.59; H, 9.35.

4: 80% yield. pale yellow oil. ^1H -NMR (500 MHz, CDCl_3): δ_{H} 0.18 (s, 3H), 0.18 (s, 3H), 0.95 (s, 9H), 0.98 (s, 9H), 1.67-1.87 (m, 3H), 1.94-2.03 (m, 1H), 2.07-2.22 (m, 2H), 2.64-2.70 (m, 1H), 5.42-5.45 (m, 1H), 6.85 (ddd, $J = 8.0, 2.5$ and 0.9 Hz, 1H), 7.07 (s with fine coupling, 1H), 7.13 (d with fine coupling, $J = 7.8$ Hz, 1H), 7.24 (dd, $J = 8.0$ and 7.8 Hz, 1H) ppm. ^{13}C -NMR (125 MHz, CDCl_3): δ_{C} -4.4, 18.2, 25.7, 25.8, 27.6, 29.7, 35.4, 53.9, 85.7, 106.5, 115.2, 119.7, 121.0, 121.1, 129.0, 136.8, 155.4 ppm. IR (liquid film): $\tilde{\nu}$ 2958, 2934, 2860, 1604, 1586 cm^{-1} . Mass (, %): 404 (M^+ , 17), 372 ($\text{M}^+ - 32$, 0.8), 347 (67), 235 (100). HRMS (ESI) (/): 427.2273, calcd for $\text{C}_{23}\text{H}_{36}\text{O}_4\text{SiNa}$ [$\text{M} + \text{Na}^+$] 427.2281.

5: 93% yield. pale yellow granules, mp 95.0–96.0 °C (from hexane– CH_2Cl_2). ^1H -NMR (500 MHz, CDCl_3): δ_{H} 0.18 (s, 3H), 0.19 (s, 3H), 0.97 (s, 9H), 0.98 (s, 9H), 1.10 (s, 3H), 1.19-1.25 (m, 1H), 1.68-1.84 (m, 2H), 1.90-1.98 (m, 1H), 2.16-2.23 (m, 2H), 5.32 (dd, $J = 12.8$ and 7.1 Hz, 1H), 6.84-6.89 (m, 1H), 7.17 (s with fine coupling, 1H), 7.23-7.28 (m, 2H) ppm. ^{13}C -NMR (125 MHz, CDCl_3): δ_{C} -4.4, -4.4, 16.1, 18.2, 19.4, 24.1, 24.3, 25.7, 26.8, 36.3, 54.8, 85.6, 104.2, 119.6, 120.9, 121.4, 122.3, 129.1, 136.9, 155.5 ppm. IR (KBr): $\tilde{\nu}$ 2957, 2932, 2897, 2861, 1604, 1586 cm^{-1} . Mass (m/z, %): 418 (M^+ , 0.9), 386 ($\text{M}^+ - 32$, 0.2), 361 (38), 235 (100). HRMS (ESI) (): 441.2440, calcd for $\text{C}_{24}\text{H}_{38}\text{O}_4\text{SiNa}$ [$\text{M} + \text{Na}^+$] 441.2437. Anal. Calcd for $\text{C}_{24}\text{H}_{38}\text{O}_4\text{Si}$: C, 68.86; H, 9.15. Found: C, 68.84; H, 9.34.

Thermolysis of tricyclic dioxetanes: typical procedure. Dioxetane **3** (53 mg) was stirred in *p*-xylene (2 mL) under N₂ atmosphere at 140 °C for 2 h. The reaction mixture was concentrated *in vacuo*. ¹H NMR spectral analysis showed that the residue included the desired keto ester exclusively. The residue was chromatographed on silica gel with hexane–AcOEt (10:1) to give 47.5 mg of *t*-methyl-*c*-2-pivaloylcyclopentyl *r*-3-(*t*-butyldimethylsiloxy)benzoate (**24a**).

24a: 89% yield. colorless oil. ¹H-NMR (500 MHz, CDCl₃): δ_H 0.21 (s, 3H), 0.21 (s, 3H), 0.98 (s, 9H), 1.19 (s, 9H), 1.27 (s, 3H), 1.67-1.92 (m, 4H), 2.19-2.28 (m, 1H), 2.59-2.68 (m, 1H), 5.51 (d, *J* = 4.8 Hz, 1H), 7.01 (ddd, *J* = 8.0, 2.5 and 0.9 Hz, 1H), 7.26 (dd, *J* = 8.0 and 7.8 Hz, 1H), 7.39 (s with fine coupling, 1H), 7.52 (d with fine coupling, *J* = 7.8 Hz, 1H) ppm. ¹³C-NMR (125 MHz, CDCl₃): δ_C -4.5, -4.5, 18.1, 19.6, 21.6, 25.6, 28.4, 30.8, 33.9, 45.1, 60.9, 82.6, 120.8, 122.5, 124.9, 129.4, 131.5, 155.7, 165.2, 215.6 cm⁻¹. IR (liquid. film): $\tilde{\nu}$ 2957, 2931, 2859, 1720, 1688, 1600 cm⁻¹. Mass (m/z, %): 418 (M⁺, 3), 361 (16), 279 (6), 235 (100). HRMS (ESI) (m/z): 441.2432, calcd for C₂₄H₃₈O₄SiNa [M + Na⁺] 441.2437.

25a: 90% yield. colorless oil. ¹H-NMR (500 MHz, CDCl₃): δ_H 0.22 (s, 3H), 0.23 (s, 3H), 0.99 (s, 9H), 1.12 (s, 9H), 1.60-1.69 (m, 1H), 1.74-1.81 (m, 1H), 1.91-2.00 (m, 2H), 2.11-2.29 (m, 2H), 3.48 (ddd, *J* = 9.0, 7.9 and 6.3 Hz, 1H), 5.57 (ddd, *J* = 6.3, 5.7 and 3.0 Hz, 1H), 7.01 (ddd, *J* = 8.0, 2.5 and 0.9 Hz, 1H), 7.27 (dd, *J* = 8.0 and 7.8 Hz, 1H), 7.42 (s with fine coupling, 1H), 7.55 (d with fine coupling, *J* = 7.8 Hz, 1H) ppm. ¹³C-NMR (125 MHz, CDCl₃): δ_C -4.5, -4.5, 18.2, 22.6, 25.6, 26.1, 28.2, 33.6, 44.7, 48.9, 77.5, 120.9, 122.6, 124.9, 129.4, 131.5, 155.6, 165.6, 213.3 ppm. IR (liquid film): $\tilde{\nu}$ 2957, 2931, 2860, 1719, 1601 cm⁻¹. Mass (m/z, %): 404 (M⁺, 17), 347 (62), 235 (100). HRMS (ESI) (m/z): 427.2276, calcd for C₂₃H₃₆O₄SiNa [M + Na⁺] 427.2281.

26a: quantitative yield. colorless oil. ¹H-NMR (500 MHz, CDCl₃): δ_H 0.21 (s, 6H), 0.99 (s, 9H), 1.27 (s, 9H), 1.45 (s, 3H), 1.60-1.90 (m, 4H), 2.12-2.24 (m, 2H), 5.78 (t, *J* = 6.3 Hz, 1H), 7.02 (ddd, *J* = 8.0, 2.5 and 0.9 Hz, 1H), 7.28 (dd, *J* = 8.0 and 7.8 Hz, 1H), 7.48 (s with fine coupling, 1H), 7.61 (d with fine coupling, *J* = 7.8 Hz, 1H) ppm. ¹³C-NMR (125 MHz, CDCl₃): δ_C -4.5, -4.4, 18.2, 19.0, 20.8, 25.6, 28.6, 30.1, 35.7, 45.4, 58.9, 79.0, 120.9, 122.5, 124.7, 129.3, 131.9, 155.7, 165.6, 216.0 ppm. IR (liquid film): $\tilde{\nu}$ 2957, 2931, 2859, 1721, 1685, 1601, 1585 cm⁻¹. Mass (m/z, %): 418 (M⁺, 1), 362 (14), 361 (50), 279 (13), 235 (100). HRMS (ESI) (m/z): 441.2428, calcd for C₂₄H₃₈O₄SiNa [M + Na⁺] 441.2437.

Isolation of ketoester of 3-hydroxybenzoic acid from the spent reaction mixture after chemiluminescent decomposition of dioxetane 3: typical procedure. A solution of TBAF (1 M in THF, 0.70 mL) in dry DMSO (2.0 mL) was added to a solution of dioxetane **3** (56.0 mg, 0.134 mmol) in dry THF–DMSO (1:10, 3.3 mL) and stirred for 1 h at room temperature under N₂ atmosphere. The reaction mixture was poured into sat. aq. NH₄Cl and extracted with AcOEt. The organic layer was washed with sat. aq. NaCl, dried over MgSO₄, and concentrated *in vacuo*. The residue was purified by

column chromatography on silica gel with hexane–AcOEt (4:1) to give 40.5 mg of **t-2-methyl-c-2-pivaloylcyclopentyl r-3-hydroxybenzoate (24b)**.

24b: quantitative yield. colorless columns melted at 116.5–117.0 °C (from AcOEt–hexane). ¹H-NMR (400 MHz, CDCl₃): δ_H 1.19 (s, 9H), 1.29 (s, 3H), 1.65-1.94 (m, 4H), 2.20-2.31 (m, 1H), 2.58-2.72 (m, 1H), 5.51 (d, $J = 5.0$ Hz, 1H), 6.16 (s, 1H), 7.05 (ddd, $J = 8.1, 2.6$ and 0.9 Hz, 1H), 7.28 (dd, $J = 8.1$ and 7.7 Hz, 1H), 7.41 (s with fine coupling, 1H), 7.49 (d with fine coupling, $J = 7.7$ Hz, 1H) ppm. ¹³C-NMR (125 MHz, CDCl₃): δ_C 19.5, 21.3, 28.4, 30.9, 33.9, 45.3, 61.0, 82.8, 116.2, 120.6, 121.5, 129.7, 131.1, 156.3, 165.6, 217.5 ppm. IR (KBr): $\tilde{\nu}$ 3456, 3081, 2988, 2968, 2882, 1694, 1602, 1481, 1457. Mass (m/z, %): 304 (M⁺, 0.1), 247 (33), 122 (9), 121 (100), 57 (9). HRMS (ESI) (/): 327.1571, calcd for C₁₈H₂₄O₄Na [M + Na⁺] 327.1572. Anal. Calcd for C₁₈H₂₄O₄: C, 71.03; H, 7.95. Found: C, 70.89; H, 7.91.

25b: 86% yield. pale yellow granules, mp 94.5–96.0 °C (from AcOEt–hexane). ¹H-NMR (500 MHz, CDCl₃): δ_H 1.14 (s, 9H), 1.61-1.70 (m, 1H), 1.74-1.82 (m, 1H), 1.91-2.01 (m, 2H), 2.11-2.32 (m, 2H), 3.51 (ddd, $J = 9.3, 7.9$ and 6.2 Hz, 1H), 5.54-5.58 (m, 1H), 6.73 (s, 1H), 7.04 (ddd, $J = 8.2, 2.6$ and 1.0 Hz, 1H), 7.27 (dd, $J = 8.2$ and 7.6 Hz, 1H), 7.42 (dd, $J = 2.6$ and 1.6 Hz, 1H), 7.52 (d with fine coupling, $J = 7.6$ Hz, 1H) ppm. ¹³C-NMR (125 MHz, CDCl₃): δ_C 22.7, 26.0, 28.2, 33.7, 44.9, 49.2, 77.7, 116.2, 120.4, 121.5, 129.6, 131.1, 156.2, 165.8, 215.4 ppm. IR (KBr): $\tilde{\nu}$ 3183, 2971, 2873, 1699, 1587 cm⁻¹. Mass (, %): 290 (M⁺, 2), 233 (31), 138 (6), 121 (100). HRMS (ESI) (/): 313.1419, calcd for C₁₇H₂₂O₄Na [M + Na⁺] 313.1416.

26b: quantitative yield. colorless oil, ¹H-NMR (500 MHz, CDCl₃): δ_H 1.26 (s, 9H), 1.44 (s, 3H), 1.62-1.90 (m, 4H), 2.12-2.24 (m, 2H), 5.78 (t, $J = 6.5$ Hz, 1H), 5.93 (br-s, 1H), 7.05 (ddd, $J = 8.1, 2.6$ and 0.9 Hz, 1H), 7.29 (dd, $J = 8.1$ and 7.7 Hz, 1H), 7.52 (s with fine coupling, 1H), 7.56 (d with fine coupling, $J = 7.7$ Hz, 1H) ppm. ¹³C-NMR (125 MHz, CDCl₃): δ_C 19.1, 20.8, 28.6, 30.0, 35.6, 45.4, 58.9, 79.2, 116.3, 120.1, 121.8, 129.6, 131.9, 155.8, 165.8, 216.4 ppm. IR (KBr): $\tilde{\nu}$ 3408, 2971, 2877, 1717, 1686, 1601 cm⁻¹. Mass (, %): 304 (M⁺, trace), 247 (41), 121 (100). HRMS (ESI) (/): 327.1584, calcd for C₁₈H₂₄O₄Na [M + Na⁺] 327.1572.

Chemiluminescence measurement: general procedure. Chemiluminescence was measured by using a JASCO FP-750, FP-6500 spectrometer and/or Hamamatsu Photonics PMA-11 multi-channel detector. Freshly prepared solution (2 mL) of TBAF (1.0 x 10⁻² mol dm⁻³) in DMSO (or MeCN) was transferred to a quartz cell (10 x 10 x 50 mm) and the latter placed in the spectrometer, which was thermostated with stirring at 25 °C. After 3-5 min, a solution (1 mL) of the dioxetane (1.0 x 10⁻⁵ mol dm⁻³ or 1.0 x 10⁻⁶ mol dm⁻³) in DMSO (or MeCN), which was thermostated at the same temperature as that of the above TBAF solution, was added with a syringe with immediate starting of measurement. The intensity of the

light emission time-course was recorded and processed according to first-order kinetics. The total light emission was estimated by comparing it with that of adamantylidene dioxetane **1b**, whose chemiluminescent efficiency Φ^{CL} has been reported to be 0.29 and was used here as a standard.¹⁰

X-Ray Single Crystallographic Analysis. X-Ray diffraction data were collected on a Rigaku Mercury CCD diffractometer with graphite monochromated Mo K α ($\lambda = 0.71070 \text{ \AA}$) radiation. Data were processed using CrystalClear.*¹ The structures were solved by direct method (SIR92)*² and expanded using Fourier techniques. The non-hydrogen atoms were refined anisotropically. Hydrogen atoms were refined using the riding model. The final cycle of full-matrix least-squares refinement on σ was based on 5379 observed reflections and 300 variable parameters (for **compound 5**). All calculations were performed using the CrystalStructure crystallographic software package.*^{3,4}

Crystal data for **5**: C₂₄H₃₈O₄Si, ($V_r = 418.65$), colorless platelet, 0.50 x 0.50 x 0.20 mm, triclinic, space group $P\bar{1}$ (#2), $a = 10.000(9) \text{ \AA}$, $b = 11.334(5) \text{ \AA}$, $c = 12.6982(4) \text{ \AA}$, $\alpha = 64.46(12)^\circ$, $\beta = 69.80(13)^\circ$, $\gamma = 78.20(2)^\circ$, $V = 1216.0(12) \text{ \AA}^3$, $Z = 2$, $\rho_{\text{calcd}} = 1.143 \text{ g cm}^{-3}$, $T = 173 \text{ K}$, $d(000) = 456.00$, reflections collected/unique 25846 / 5380 ($R_{\text{int}} = 0.024$), $\mu(\text{MoK}\alpha) = 1.215 \text{ cm}^{-1}$. An empirical absorption correction was applied which resulted in transmission factors ranging from 0.859 - 0.976. The data were corrected for Lorentz and polarization effects. $wR = 0.0673$ [$>2\sigma(F_o)$], $R = 0.1806$ (all data), GOF on $F^2 = 1.792$, and residual electron density 0.76 / -0.34 e \AA^{-3} . Crystallographic data for the structural analysis of compound **5** has been deposited at the Cambridge Crystallographic Data Center, CCDC-265173. Free Copies of the data can be obtained, via <http://www.ccdc.cam.ac.uk/conts/retrieving.html> (or from the Cambridge Crystallographic Data Center, 12 Union Road, Cambridge CB2 1EZ, UK, (fax: +44-(0)1223-336033 or e-mail: deposit@ccdc.cam.ac.uk).

*1; CrystalClear: Data Collection and Processing Software, Rigaku Corporation (1998-2014). Tokyo 196-8666, Japan. *2; SIR92: Altomare, A., Cascarano, G., Giacovazzo, C., and Guagliardi, A. (1993). *J. Appl. Cryst.* 26, 343-350. *4; CrystalStructure 4.1: Crystal Structure Analysis Package, Rigaku and Rigaku/MSO(2000-2003). 9009 New Trails Dr. The Woodlands TX 77381 USA. *5; CRYSTALS Issue 11: Carruthers, J. R., Rollett, J. S., Betteridge, P. W., Kinna, D., Pearce, L., Larsen, A., and Gabe, E. *Chemical Crystallography Laboratory, Oxford, UK.* (1999).

ACKNOWLEDGEMENTS

The authors gratefully acknowledge financial assistance in the form of Grants-in-aid (Nos. 25350269, 25410056 and 25410057) for Scientific Research from the Ministry of Education, Culture, Sports, Science, and Technology, Japan. The author (NW) further acknowledges financial support from the

Strategic Research Base Development Program for Private Universities of the Ministry of Education, Culture, Sports, Science and Technology of Japan.

REFERENCES AND NOTES

- (a) S. Beck and H. Köster, *Journal of Organic Chemistry*, 1990, **62**, 2258; (b) W. Adam, D. Reihardt, and C. R. Saha-Möller, *Journal of Organic Chemistry*, 1996, **121**, 1527; (c) M. Matsumoto, *Journal of Organic Chemistry*, 2004, **5**, 27; (d) M. Matsumoto and N. Watanabe, *Journal of Organic Chemistry*, 2005, **78**, 1899.
- (a) W. Adam and A. V. Trofimov, In *Organic Chemistry*, ed. by Z. Rappoport, Wiley: New York, 2006, Vol. 2, pp. 1171–1209; (b) W. J. Baader, C. V. Stevani, and E. L. Bastos, In *Organic Chemistry*, ed. by Z. Rappoport, Wiley: New York, 2006, Vol. 2, pp. 1211–1278.
- (a) I. Navizet, Y. Liu, N. Ferré, D. Roca-Sanjuán, and R. Lindh, *Journal of Organic Chemistry*, 2011, **12**, 3064; (b) L. Yue, Y. Liu, and W. Fang, *Journal of Organic Chemistry*, 2012, **134**, 11632; (c) B. R. Branchini, C. E. Behney, T. L. Southworth, D. M. Fontaine, A. M. Gulick, D. J. Vinyard, and G. W. Brudvig, *Journal of Organic Chemistry*, 2015, **137**, 7592. See also refs. therein.
- (a) A. V. Trofimov, R. F. Vasil'ev, K. Mielke, and W. Adam, *Journal of Organic Chemistry*, 1995, **62**, 35; (b) W. Adam, I. Bronstein, B. Edwards, T. Engel, D. Reinhardt, F. W. Schneider, A. V. Trofimov, and R. F. Vasil'ev, *Journal of Organic Chemistry*, 1996, **118**, 10400; (c) W. Adam, I. Bronstein, A. V. Trofimov, and R. F. Vasil'ev, *Journal of Organic Chemistry*, 1999, **121**, 958.
- M. Yamada, K. Kitaoka, M. Matsumoto, and N. Watanabe, In *Organic Chemistry*, ed. by A. Tsuji, M. Matsumoto, M. Maeda, L. J. Kricka, and P. E. Stanley, World Scientific: Singapore, 2004, pp. 487–490.
- (a) M. Matsumoto, Y. Itoh, J. Matsubara, T. Sakuma, Y. Mizoguchi, and N. Watanabe, *Journal of Organic Chemistry*, 2001, **42**, 2349; (b) M. Matsumoto, N. Watanabe, N. C. Kasuga, and F. Hamada, *Journal of Organic Chemistry*, 1997, **38**, 2863.
- Part of this work was presented as an unpublished result in a review (ref. 1d).
- M. Matsumoto, N. Watanabe, N. C. Kasuga, F. Hamada, and K. Tadokoro, *Journal of Organic Chemistry*, 1997, **38**, 2863.
- Chemiluminescence yields (Φ^{CL}) were based on the reported value for 3,3-adamantylidene-4-(*t*-butyldimethylsiloxyphenyl)-4-methoxy-1,2-dioxetane: $\Phi^{CL} = 0.29$ in TBAF/DMSO.¹⁰
- A. V. Trofimov, K. Mielke, R. F. Vasil'ev, and W. Adam, *Journal of Organic Chemistry*, 1996, **63**, 463.
- Ketoesters **25a** and **25b** were rather unstable under the strong base conditions and underwent retro-Michael addition into pivaloylcyclopentene and a 3-hydroxybenzoic acid fragment.
- CTID of a 3-oxyphenyl-substituted dioxetane has been reported to give 3-oxidobenzaldehyde with 100% of Φ_S ($\Phi^{CL} = 0.037$).¹³

13. (a) A. L. P. Nery, S. Röpke, L. H. Catalani, and W. J. Baader, *Chemical Communications*, 1999, **40**, 2443; (b) A. L. P. Nery, D. Weiss, L. H. Catalani, and W. J. Baader, *Chemical Communications*, 2000, **56**, 5317.
14. L. Francisco, M. L. Ciscato, F. H. Bartoloni, D. Weiss, R. Beckert, and W. J. Baader, *Chemical Communications*, 2010, **75**, 6574.
15. M. Matsumoto, H. Suzuki, N. Watanabe, H. K. Ijuin, J. Tanaka, and C. Tanaka, *Chemical Communications*, 2011, **76**, 5006.
16. G. B. Schuster, *Chemical Communications*, 1979, **12**, 366.
17. The pathway through **C_{III}** be considered an extreme feature of the CT/direct mechanism.
18. (a) W. Adam, M. Matsumoto, and A. V. Trofimov, *Chemical Communications*, 2000, **65**, 2078; (b) W. Adam, M. Matsumoto, and A. V. Trofimov, *Chemical Communications*, 2000, **122**, 8631.
19. An alternative mechanism has very recently been reported on the basis of experimental results for the viscosity-dependence of Φ^{CL} . According to this mechanism, O-O bond cleavage of **A** gives **C_I** or **C_{II}**, for which intramolecular BET and C-C bond cleavage occur in concert to give **E***, and the syn/anti conformational change for **C_I** or **C_{II}** affects Φ_S (see Scheme 3).²⁰ However, this mechanism does not apparently well describe the marked difference in Φ_S between dioxetanes **3** and **4**.
20. E. L. Bastos, S. M. da Silva, and W. J. Baader, *Chemical Communications*, 2013, **78**, 4432.
21. Although various theoretical studies on the chemiluminescent CTID of dioxetanes have been reported, none have clearly explained the relationship between Φ_S and the stereochemistry of dioxetanes.²²
22. (a) Y. Takano, T. Tsunesada, H. Isobe, Y. Yoshioka, K. Yamaguchi, and I. Saito, *Chemical Communications*, 1999, **72**, 213; (b) H. Isobe, Y. Takano, M. Okumura, S. Kuramitsu, and K. Yamaguchi, *Chemical Communications*, 2005, **127**, 8667; (c) H. Isobe, S. Yamanaka, M. Okumura, and K. Yamaguchi, *Chemical Communications*, 2009, **113**, 15171; (d) F. Liu, Y.-J. Liu, L. D. Vico, and R. Lindh, *Chemical Communications*, 2009, **131**, 6181; (e) J. Tanaka, C. Tanaka, and M. Matsumoto, *Chemical Communications*, 2011, **13**, 16005; (f) L. Yue, Y.-J. Liu, and W.-H. Fang, *Chemical Communications*, 2012, **134**, 11632; (g) L. Yue, D. Roca-Sanjuán, R. Lindh, N. Ferré, and Y.-J. Liu, *Chemical Communications*, 2012, **8**, 4359; (h) L. Yue and Y.-J. Jiu, *Chemical Communications*, 2013, **9**, 2300.

Journal of Renewable Energy
Electrochemistry for Environment

Arockiam John Jeevagan¹, Takao Gunji¹, Toyokazu Tanabe¹,
Shingo Kaneko², Futoshi Matsumoto¹

¹Department of Materials and Life Chemistry, Kanagawa University, 3-27-1,
Rokkakubashi, Kanagawa-ku, Yokohama, Kanagawa 221-8686, Japan

²Research Institute for Engineering, Kanagawa University,
3-27-1, Rokkakubashi, Kanagawa-ku, Yokohama, Kanagawa 221-8686, Japan

Abstract

In this paper, we demonstrate a one-pot synthesis of a reduced graphene oxide (RGO)-supported freely assembled binary alloy catalyst (PtAu/RGO) under alkaline conditions. The synthesized PtAu/RGO catalyst was characterized by powder X-ray diffraction (XRD), transmission electron microscopy (TEM), energy dispersive X-ray spectroscopy (EDX) and X-ray photoelectron spectroscopy (XPS). It was found that graphene oxide (GO) was successfully reduced to RGO. The PtAu nanoparticles exhibited an alloyed structure with an average diameter of approximately 3.60 ± 0.20 nm and were uniformly distributed across the RGO surface. Furthermore, the electrocatalytic activity of the catalyst for formic acid (FA) oxidation was examined, and it exhibited better catalytic activity for the FA oxidation reaction.

Introduction

Noble metal (Pt, Pd and Au)-based bimetallic alloyed nanoparticles (NPs) supported on carbon black have been widely used as electrocatalysts. In particular, highly dispersed Pt-based NPs on Vulcan carbon (VC), carbon nanotubes (CNTs) and carbon fibers (CF) exhibit enhanced electrocatalytic activities in electrocatalytic reactions such as oxygen reduction, as well as formic acid (FA), methanol and ethanol oxidations. However, pure Pt is poisoned by the reaction intermediates, mainly CO, which strongly adsorbs on the Pt active sites, resulting in slow reaction kinetics.¹ Therefore, alloying Pt with a second metal and modifying the Pt electronic structure are expected to improve the catalytic performance. It has been reported that when Au exists as ultrafine particles, it exhibits an enhanced activity for the CO and FA oxidation reactions.² Thus, the incorporation of Au into Pt structures can be expected to significantly enhance the catalytic activity of the system.

To further maximize the electrocatalytic activity of PtAu NPs, a suitable carbon support is required to disperse these NPs. Recently, graphene has been studied extensively as a functional nanomaterial because of a host of fascinating properties such as high surface area, electrical conductivity and specific thermal/chemical stability.^{3,4} Because of its large surface area and high conducting nature, graphene is being actively explored for use in applications ranging from electrocatalysis, photocatalysis and nanoelectronics to supercapacitors.^{5,6} Graphene exhibits a unique structure of two-dimensional sp^2 -bonded carbon atoms with single-atom thickness and possesses a large surface area and higher electrical conductivity than CNTs. Additionally, it has been reported that chemically reduced exfoliated graphene oxide (GO) can act as an effective catalyst support because of the oxygen-containing functional groups on its surface, which

act as binding sites for Pt NPs.⁷ However, the efficient immobilization of Pt NPs on a graphene surface remains a substantial challenge. Several methods have been used to prepare graphene-supported electrocatalysts. Among these methods, the chemical reduction of GO is effective for the production of graphene. In the chemical reduction method, the graphene-supported electrocatalyst is synthesized in the presence of a stabilizing agent. Recently, it has been reported that the stabilizers can passivate the surface of metal NPs, thus decreasing the activity of the catalysts.⁸ Hence, a new strategy is needed to improve the synthesis of reduced graphene oxide (RGO) nanocomposites and to suppress the undesirable effects of the stabilizers. Herewith, we report on the synthesis of RGO-supported PtAu NPs under alkaline conditions and our examination of their catalytic activity toward FA oxidation.

Experiment

Materials

Graphite powder was purchased from Alfa Aesar and was used as received. Metal precursors, $\text{H}_2\text{PtCl}_6 \cdot 6\text{H}_2\text{O}$ and $\text{HAuCl}_4 \cdot 3\text{H}_2\text{O}$, were purchased from Sigma Aldrich and were used as received. NaNO_3 , H_2SO_4 , KMnO_4 , H_2O_2 , $\text{CH}_3\text{CH}_2\text{OH}$, KOH and FA were all analytical grade reagents purchased from Wako (Japan) and were used without further purification. Millipore water was used for all of the experiments. VC-supported Pt (20 wt% Pt/CB) was obtained from E-TEK.

Synthesis of GO

GO was synthesized using Hummers' method with a slight modification.⁹ Conc. H_2SO_4 (12 mL) was added to graphite flakes (0.5 g) and NaNO_3 (0.25 g), and the mixture was cooled to 0°C. Thereafter, KMnO_4 was slowly added to the mixture while the temperature was maintained at 20°C. The reaction mixture temperature was slightly increased to 35°C, and the mixture was stirred for 30 min. After that, 23 mL of water was added. The temperature was maintained at 98°C by overall heating for 15 min. The reaction was terminated by the addition of water and 0.5 mL of 30% H_2O_2 . Finally, the reaction mixture was cooled, washed with 0.1 M HCl and water to remove the metal ions and then dried.

Synthesis of Pt/RGO

The synthesized GO was used to synthesize PtAu/RGO by the reported method with a slight modification.¹⁰ The as-synthesized GO (12 mg) was dispersed in 40 mL of Millipore water, and the mixture was sonicated for 2 h to form an exfoliated GO suspension. Then, the exfoliated GO suspension was mixed with the Pt precursor (8 mg) and the Au precursor (5.2 mg). Subsequently, 40 mL of EtOH was added to the mixture. The pH of the mixture was adjusted to 9-10 with the addition of a 1.0 M KOH aqueous solution. Thereafter, the mixture was refluxed in an oil bath at 80°C for 2 h with constant stirring to ensure the complete reduction of GO and the metal salts. The RGO (without precursors) and Pt/RGO were also prepared under identical conditions.

Characterization

The surface morphology, solid phases and electronic structure of the synthesized catalysts were characterized by powder X-ray diffraction (XRD), transmission electron microscopy (TEM)/scanning TEM (STEM) and X-ray photoelectron spectroscopy (XPS).

XRD was performed using $\text{Cu } \alpha$ radiation (Panalytical X'Pert PRO; $\lambda = 0.1548 \text{ nm}$) with an increment of 0.02 degrees over a range of diffraction angles from 20 to 80 degrees. An obliquely finished Si crystal (non-reflection Si plate) was used as a sample holder to minimize the background. XPS measurements were used to examine the

chemical states of the catalyst, and the spectra were collected using a JPS-9010 (JEOL, Japan) instrument with a monochromatic Mg K_{α} source.

electrochemical measurement

Prior to the modification of the glassy carbon (GC) disk electrode, the GC electrode was mirror polished with a 0.05 μm alumina slurry for 10 min, sonicated for 5 min to remove any adsorbed impurities and dried under Ar. The NP catalysts were coated on the GC disk electrode (diameter = 5 mm) using a suspension prepared by the ultrasonic mixing of RGO, Pt/RGO, PtAu/RGO or the commercial Pt/CB (1 mg) and Milli-Q water (995 μL), isopropanol (250 μL) and Nafion solutions (5 μL) for 30 min. A total of 6 μL of the catalyst suspension was dropped on the cleaned GC electrode and dried under vacuum. The electrochemical measurements were performed in a standard three-electrode system with a catalyst-coated GC electrode as the working electrode, a platinum wire as the auxiliary electrode and NaCl (3 M) Ag/AgCl as the reference electrode. The electrochemical measurements were carried out on a Bio-Logic SAS workstation (Model, VMP3). The working electrode was first activated with cyclic voltammograms in a N_2 -purged 0.1 M H_2SO_4 aqueous solution over the potential range of -0.2–1.2 V. To measure the FA electro-oxidation current, a solution of 0.1 M H_2SO_4 + 0.5 M FA was purged with N_2 before the measurements. During electrochemical measurements, the catalyst-coated electrode was rotated at 2000 rpm using an electrode rotator (Hokuto Denko, Japan, HR-30) to remove bubbles that formed on the NP surfaces.

Resonance

The crystalline structures of the Pt NPs and PtAu NPs on the RGO supports were confirmed by XRD measurements. Fig. 1 shows the XRD patterns of GO (a), RGO (b), Pt/RGO (c) and PtAu/RGO (d) catalysts. A sharp peak at $\sim 11^\circ$ was detected in the XRD pattern shown in (a). The peak was assigned to the GO (002) plane. This peak was absent from the XRD patterns of RGO (b) and the RGO supported catalysts (c, d), indicating that GO was completely converted to RGO. The diffraction peaks observed in the XRD pattern of Pt/RGO (c) are characteristic of the (111), (200) and (220) planes of the face centered cubic crystalline phase of Pt. It should be noted that in the XRD pattern of the PtAu/RGO catalyst (d), the 2θ diffraction peaks of the binary catalyst were shifted to low diffraction angles compared with the Pt/RGO catalyst, which suggest that Au was alloyed with Pt.

The morphology, particle size and dispersion of the catalysts on the RGO surface were examined by TEM. Figure 2 presents a typical TEM image of the Pt/RGO (A) and PtAu/RGO (B) catalysts. As shown in Fig. 2-(A) and -(B), the Pt and PtAu binary alloy NPs were well distributed over the RGO support without any agglomerations. The average particle size (1.8 nm) and distribution of the PtAu NPs on the RGO surface were similar to those of Pt/RGO (2.1 nm). The XRD and TEM/STEM results indicate that the formation of PtAu alloy NPs on the RGO surface occurred.

Figure 3-(A) shows the full XPS spectrum of Pt/RGO. The peaks located at binding energies of 71.40 eV and 75.00 eV were assigned to Pt $4f_{7/2}$ and Pt $4f_{5/2}$, respectively, indicating the presence of Pt on the RGO surface. Figure 4-(B) shows the full XPS spectrum of the PtAu/RGO catalyst. As shown in the Fig. 3-(B) inset, the two main peaks located at 72.4 and 76.0 eV were assigned to Pt $4f_{7/2}$ and Pt $4f_{5/2}$, respectively. For the Au region, the doublet consisting of Au $4f_{7/2}$ and Au $4f_{5/2}$ at 85.10 eV and 88.80 eV corresponds to Au metal. The binding energies of the Pt peaks in PtAu/RGO were shifted from those of the corresponding metallic Pt regions, as shown in the inset of (B).

The doublet peaks of the Pt 4f region for PtAu/RGO were observed at 72.6 and 76.4 eV. The variation in the binding energy values between PtAu/RGO and Pt/RGO might be attributed to a charge transfer between Au and Pt, which indicates that Au exists as an alloy with Pt.

The electrocatalytic activity of PtAu/RGO (Pt mass loading on RGO: 20%, as estimated by ICP-MS) was examined with a solution of 0.1 M H₂SO₄ + 0.5 M FA. The catalytic activity of PtAu/RGO was compared with that of Pt/RGO (Pt mass loading on RGO: 20%) and that of the commercially available Pt/VC (Pt mass loading on VC: 20%). Figure 4 shows the linear sweep voltammograms obtained with Pt/RGO (a), PtAu/RGO (b) and Pt/VC (c) in the 0.1 M H₂SO₄ aqueous solution containing 0.5 M FA. As seen in Fig. 4, two separate oxidation peaks (I and II) were clearly observed in the three voltammogram curves. Peak I was assigned to the direct oxidation of FA to CO₂, whereas peak II corresponded to the oxidation of the CO_{ads} generated from the dissociative adsorption step of the FA oxidation reaction.^{11,12} The current densities of peak I followed the order PtAu/RGO > Pt/RGO > commercial Pt/VC. This result indicates that RGO can effectively enhance the activities of the PtAu and Pt catalysts, which may be due to the strong interaction between the NPs and the RGO surface. In contrast, the current densities of peak II followed the order PtAu/RGO < Pt/RGO < commercial Pt/VC. This indicates that the presence of RGO in Pt/RGO and PtAu/RGO restricted the formation of the poisoning intermediate CO_{ads} during the FA oxidation reaction and that the alloying of Pt with Au further prevented the poisoning of the surface by CO_{ads}. Based on the present and previously reported results,^{13,14} the uniform distribution of NPs and the electronic interactions between Pt and Au, in addition to the interactions between the PtAu NPs and RGO, enhance the system's catalytic activity for FA oxidation.

on ion

In summary, freely assembled PtAu/RGO nanocomposites were synthesized under alkaline conditions. On the basis of XRD, TEM and XPS measurements, the GO was converted to RGO, and the PtAu NPs were uniformly distributed across the RGO surface. The PtAu/RGO catalyst exhibited high catalytic activity for the FA oxidation reaction compared with the other catalysts—Pt/RGO and the commercial Pt/VC. This work provides a simple and fast approach to synthesize a novel RGO-based catalyst having high electrocatalytic activity for FA oxidation.

Referen e

1. A.S. Arico, S. Srinivasan and V. Antonucci, *Fuel Cell*, , 133 (2001).
2. N. Kristian, Y.S. Yan and X. Wang, *Chem. Commun.* (2008).
3. A.H.C Neto, F. Guineo, N.M.R. Peres, K.S. Novoselov and A.K. Geim, *Rev. Mod. Phys.*, , 109 (2009).
4. R.H. Baughman, A.A. Zakhidov and W.A. de Heer, *Science*, , 787 (2002).
5. S. J. Guo, S.J. Dong and E.K. Wang, *ACS Nano*, , 547 (2010).
6. M.D. Stoller, S. Park, Y. Zhu, J. An and R.S. Rouff, *Nano Lett.*, , 3498 (2008).
7. B. Seger and P.V. Kamat, *J. Phys. Chem. C*, , 7990 (2009).

8. J. Yang, C.G. Tian, L. Wang and H. Fu, *J. Mater. Chem.* , 3384 (2011).
9. N.I. Kovryukhova, P.J. Ollivier, B.R. Maritn, T.E. Mallook, S.A. Chizik, E.V. Buzanera and A.D. Gorchinguiy, *Chem. Mater.* , 771 (1999).
10. F. Ren, C. Wang, C. Zhai, F. Jiang, R. Yue, Y. Du, P. Yang and J. Xu, *J. Mater. Chem. A* , 7255 (2013).
11. S. Zhang, Y.Y. Shao, G.P. Yin and Y.H. Lin, *Angew. Chem.,Int. Ed.* , 8175 (2010).
12. X.C. Zhou, W. Wing, C.P. Liu and T.H. Lu, *Electrochem. Commun.* , 1469, (2007).
13. S. Zhang, Y. Shao, H-gang Liao, M.H. Engelhard, G. Yin and Y. Lin, *ACS Nano* , 1785 (2011).
14. S. Zhang, Y. Shao, H-gang Liao, J. Liu, I.A. Aksay, G. Yin and Y. Lin, *Chem. Mater.* , 1079 (2011).

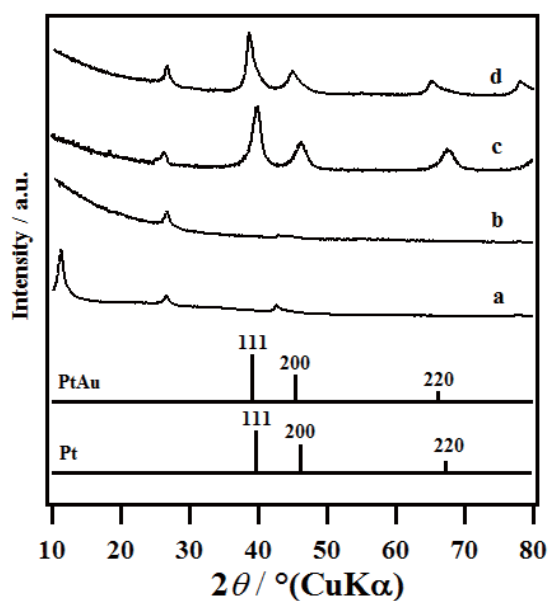


Figure 1 shows the XRD patterns of GO (a), RGO (b), Pt/RGO (c) and PtAu/RGO (d) catalysts. The solid bars at the bottom are the simulated XRD peaks for Pt and the binary alloyed phase of PtAu.

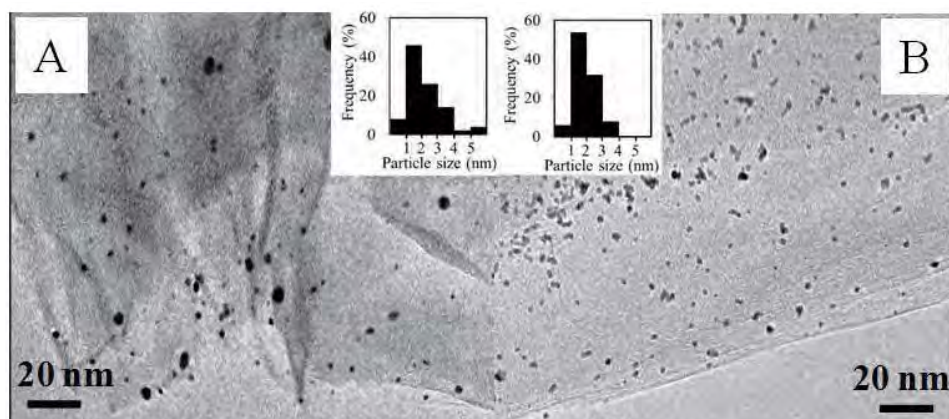


Figure 1. TEM images of Pt/RGO (A) and PtAu/RGO (B) catalysts. Inset: particle size distribution of Pt (A) and PtAu (B) NPs.

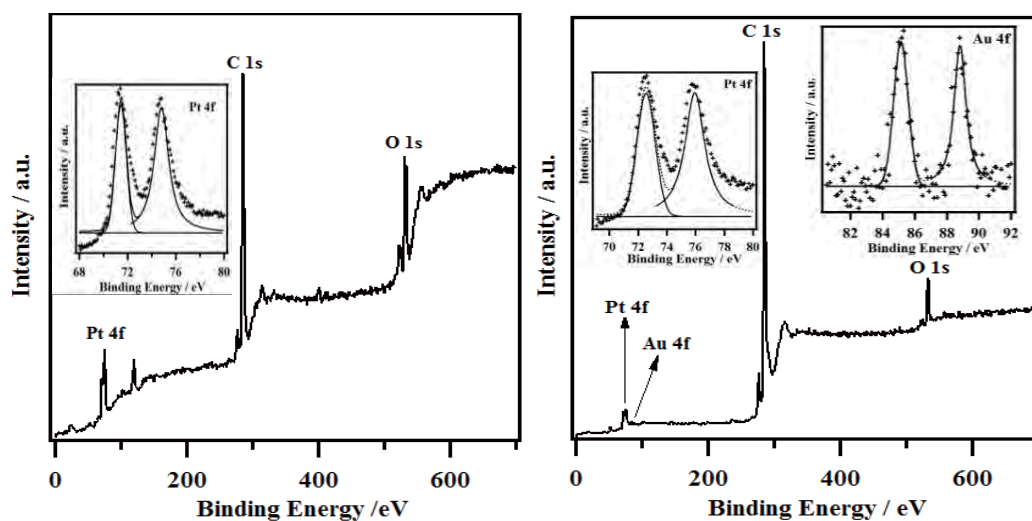


Figure 2. Full XPS spectra for (A) Pt/RGO and (B) PtAu/RGO. The insets in (A) and (B) represent the XPS profiles of the Pt 4f and Au 4f regions.

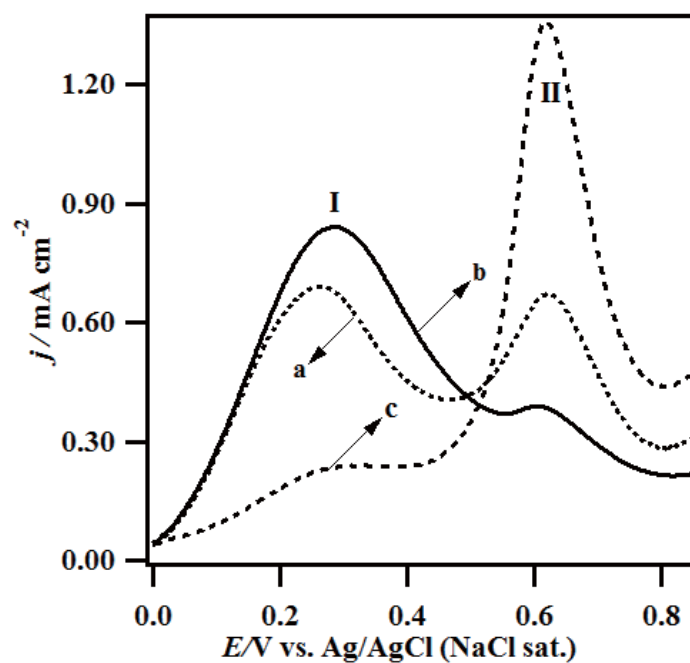


Figure 1. Linear sweep voltammograms obtained with (a) Pt/RGO, (b) PtAu/RGO and (c) Pt/CB in an Ar-saturated 0.1 M H₂SO₄ aqueous solution containing 0.5 M HCOOH at an electrode rotation rate of 2000 rpm and at a potential scan rate of 10 mVs⁻¹.

enhancement of the oxygen reduction reaction (ORR) on the titanium oxide
intercalated carbon nanotube (ICNT) electrode in alkaline solution

Fuma Ando¹, Takao Gunji¹, Toyokazu Tanabe¹,
Shingo Kaneko², Tsuyoshi Takeda³, Takeo Ohsaka², Futoshi Matsumoto¹

¹ Department of Materials and Life Chemistry, Kanagawa University, 3-27-1,
Rokkakubashi, Kanagawa-ku, Yokohama, Kanagawa 221-8686, Japan

² Research Institute for Engineering, Kanagawa University,

3-27-1, Rokkakubashi, Kanagawa-ku, Yokohama, Kanagawa 221-8686, Japan

³ Sankei Giken Kogyo Co., Ltd., 2-5-1 Akabane Minami Kita-ku, Tokyo 115-8588, Japan

Abstract

PtPb ordered intermetallic nanoparticles (NPs) deposited on titanium oxide (TiO₂)/cup-stacked carbon nanotubes (CSCNT), PtPb NPs/TiO₂/CSCNT, were prepared by synthesis of TiO₂ with Ti-alkoxide under Ar atmosphere, by photodeposition of Pt NPs on the TiO₂ surface of TiO₂/CSCNT and by selective deposition of Pb atoms to Pt NPs with polyol method. The PtPb NPs/TiO₂/CSCNT is, at the first potential cycle, inferior to bench-marked Pt NPs/carbon black (Pt/CB) in the oxygen reduction reaction (ORR) in acidic aqueous solution, whereas after 100 potential cycles between 0.3 and 1.1 V (vs RHE), the ORR was accelerated largely when compared with the Pt/CB. The ORR activity of PtPb NPs/CB degraded with potential cycle due to the dissolution of Pb from the surface of PtPb NPs. On the other hand, the dissolution of Pb was suppressed to a lesser degree on the PtPb NPs deposited on TiO₂ by the interaction between PtPb and TiO₂. The dealloyed NP surface composed of the Pt atoms and the residual Pb atoms is considered to bring about the enhancement of ORR.

Introduction

For polymer electrolyte membrane fuel cells (PEMFCs) to become widespread in our daily life for practical uses, it is urgent to develop a low-cost electrocatalyst with highly improved kinetics toward the oxygen reduction reaction (ORR) (1). To achieve this purpose, several methods have been developed, such as using nanostructures to increase the surface-to-volume ratio (2), using an alloying technique to incorporate non-precious metals into the nanostructures, and replacing core atoms in Pt nanoparticles (NPs) with a non-precious metal (3). These approaches have not achieved the performance to satisfy the requirements of customers. Recently, strong metal-support interactions (SMSI) have attracted great attention because they can lead to excellent catalytic activity (4). For example, Cheng et al. have synthesized a robust Pt-on-ZrC nanocomposite catalyst by taking advantage of atomic layer deposition (ALD) to improve the strong metal-support interactions at the atomic level; their results show that the ORR activity of ALD-Pt/ZrC nanocomposites is approximately 5- and 3-fold more stable than those of commercial Pt/C and Pt/ZrC which was synthesized by a conventional chemical reduction method, respectively (5). Additionally, in our previous studies (6-8), we reported that the ordered intermetallic NPs of PtPb deposited on titanium oxide (TiO₂) support an enhanced ORR in acidic aqueous solutions. However, the reason for the ORR enhancement on the PtPb/TiO₂ catalyst has not been examined in detail. In addition, very recently, we have

found that PtPb/carbon black (CB) exhibits a gradual decrease in the ORR activity with increasing the number of potential cycle, while the ORR activity of PtPb/TiO₂/cup-stacked carbon nanotube (CSCNT), PtPb NPs/TiO₂/CSCNT, increases with the number of potential cycle until 100 cycles (8). The enhancement of the ORR activity on the PtPb NPs/TiO₂/CSCNT is considered to be related to a change of the surface structures of PtPb NPs. Therefore, in this study, the effects of the support materials on ORR activity were examined by comparing the electronic states and surface atomic ratios of Pb to Pt atoms of the PtPb NPs on TiO₂/CSCNT and CB supports before and after potential cycling as well as considering the electronic interactions between PtPb NPs and TiO₂ support. CSCNTs were used as a conductive material, which makes up for the lower conductivity of TiO₂. The CSCNTs, which are tubular carbon nanostructures with a stacked-cup arrangement of grapheme layers, were used as a conductive material which makes up for the lower conductivity of TiO₂. The edges of the graphene layers are greatly exposed to the surface of the CSCNT and can be used as scaffolds to completely cover the CSCNT surface with TiO₂ layers.

Experiment

Preparation of PtPb NPs/TiO₂/CSCNT

The preparation of PtPb NPs/TiO₂/CSCNT and PtPb NPs/CB (Vulcan carbon, XC-72, E-TEK) was previously described (6-8). Briefly, the preparation method will be described below. A commercially available CSCNT (50 nm ϕ , Sankei Giken Kogyo Co., Ltd., Japan) was treated with an acidic solution of H₂SO₄ (6 M) and HNO₃ (6 M) at 90 °C for 6 h to introduce carboxylic acid functional groups on the CSCNT surfaces; the surfaces were then washed with water, followed by drying overnight at 110 °C. The purchased CSCNTs had the following characteristics: average length of 2.0 μ m; BET surface area of 99 m²g⁻¹; volume resistivity of 0.05 Ω ·cm (30 MPa); and G/D Raman peak ratio of 0.85. A Ti precursor solution was prepared by dissolving titanium (IV) isopropoxide (TTIP, 0.2 g, 95.0%, Wako, Japan) in isopropanol (100 mL, 99.7%, Wako, Japan). The functionalized CSCNT was added to the solution under vigorous stirring. De-ionized water (1.0 mL) was used to accelerate the reaction of TTIP. After further stirring for 6 h, the resulting mixture was collected and dried overnight under a vacuum, followed by heat treatment at 450 °C for 1 h under an Ar atmosphere to yield CSCNT-supported TiO₂ (TiO₂/CSCNT, 30 wt%-TiO₂). Pt NPs were photochemically deposited onto TiO₂/CSCNT. Next, 3 mmol of H₂PtCl₆, which was used as the Pt source, and 10 mg of TiO₂/CSCNT were dissolved in a 50 vol% aqueous methanol solution (20 mL). This solution was stirred for 12 h under irradiation with a UV lamp (Xe lamp, 300 W). The PtPb NPs/TiO₂/CSCNTs were prepared using the polyol method: The Pt NPs/TiO₂/CSCNTs (0.030 g) and Pb(CH₃COO)₂·3H₂O (0.022 mmol) were dissolved in 50 mL of ethylene glycol. The mixture was sonicated and then treated in the flask under reflux for 1 min with 300-W microwave radiation. The mixture in the flask was cooled to room temperature with water. The mixture was again treated with microwave radiation (focused microwave instrument, CEM) at 300 W for 9 min. After the mixture cooled, PtPb NPs/TiO₂/CSCNT was collected by centrifugation, washed sequentially with methanol and dried under vacuum. The loading of Pt onto the TiO₂/CSCNT support was determined to be 10.0 wt%. For the preparation of PtPb NPs/CB, similar to the preparation of the PtPb NPs/TiO₂/CSCNT sample (25 wt%-Pt), the polyol method with commercially available Pt/CB (20 wt%-Pt, E-TEK) and Pb(CH₃COO)₂·3H₂O was applied to generate the ordered intermetallic NPs of PtPb on CB.

Characterization

The powder X-ray diffractometry (XRD) experiments were performed using Cu α radiation (Rigaku RINT- Ultima III; $\lambda = 0.1548$ nm) at increments of 0.02 degrees from 20 to 80 degrees. An obliquely finished Si crystal (non-reflection Si plate) was used as a sample holder to minimize the background. X-ray photoelectron spectroscopy (XPS) measurements (JEOL, JP-9010 MC) were performed to examine the chemical states (Pt 4 f and Pb 4 f) of the samples. MgK α was used as the X-ray source with an anodic voltage of 10 kV and a current of 10 mA. All of the XPS spectra for the samples were obtained with a take-off angle of 45° relative to the specimens, and pass energies of 100 eV and 200 eV for the narrow and survey scans, respectively, were used. The binding energy of the photoelectrons was referenced to the peak position of C (1s), which was a contaminant in the samples. As the reference sample, TiO₂ (anatase) powder, which was purchased from Wako (Japan), was used without any treatment. A 200-kV transmission electron microscope (TEM and/or STEM, JEM-2100F, JEOL) equipped with two aberration correctors (CEOS GmbH) for the image- and probe-forming lens systems and an X-ray energy-dispersive spectrometer (JED-2300T, JEOL) for the compositional analysis was used. Both of the aberration corrections were optimized to realize point-to-point resolutions of 1.3 and 1.1 Å for the TEM and scanning transmission electron microscopy (STEM) images, respectively. A probe convergence angle of 29 mrad and a high-angle annular-dark-field (HAADF) detector with an inner angle greater than 100 mrad were used during the HAADF-STEM observations. An ultra-high-vacuum STEM (UHV-STEM; TECNAI G²) was used to observe the morphology. The samples for the UHV-STEM experiments were prepared by depositing a methanol suspension of the sample powder onto a commercial TEM grid coated with a polymer film. The sample was dried thoroughly under vacuum before the observations. The chemical composition of the samples and loading weight of Pt/Pb on CB or TiO₂/CSCNT were determined using inductively coupled plasma-mass spectrometry (ICP-MS, Agilent, 7700x). The loading weight of TiO₂ on the TiO₂/CSCNT was estimated by thermogravimetry (Thermo plus EVO TG8120, Rigaku) under air.

Electrochemical Measurement

An aliquot of 1 mg Pt/Pb NPs/TiO₂/CSCNT or Pt/Pb NPs/CB was suspended in a solution of 995 μ L of distilled water and 250 μ L of isopropyl alcohol. Additionally, 5 μ L of a 5% w/w Nafion[®] solution (EW: 1,100, Aldrich) in alcohol was added to this suspension. The resulting suspension was sonicated for 1 h. The suspension was used to coat a 5-mm-diameter GC electrode. The ORR activities of Pt/Pb NPs/TiO₂/CSCNT and Pt/Pb NPs/CB were subsequently examined in O₂-saturated 0.1 M HClO₄ using a three-electrode cell with an Ag/AgCl (3 M NaCl) reference electrode and a salt bridge of NaClO₄. The electrochemical tests were performed at room temperature (23 \pm 1°C) at a sweep rate of 10 mVs⁻¹ and a rotation speed of 2000 rpm. The geometric area of the GC electrode was used to calculate the current density of the ORR. The electrode potential measured using the Ag/AgCl reference electrode was converted to the value referred to the reversible hydrogen electrode (RHE) in the voltammograms shown in this paper.

Results and Discussion

Figure 1 shows the XRD profiles for () CSCNT, () TiO₂/CSCNT, () Pt NPs/TiO₂/CSCNT, () Pt/Pb NPs/CB and () Pt/Pb NPs/TiO₂/CSCNT. The simulated

XRD peak patterns for () TiO₂ (anatase), () Pt and () an ordered intermetallic phase of PtPb are shown to confirm the crystal structures of the individual products. All of the XRD profiles in Fig. 1 exhibit four very small peaks at 26.1°, 43.5°, 54.3° and 77.8° that correspond to the diffraction from CSCNT ().

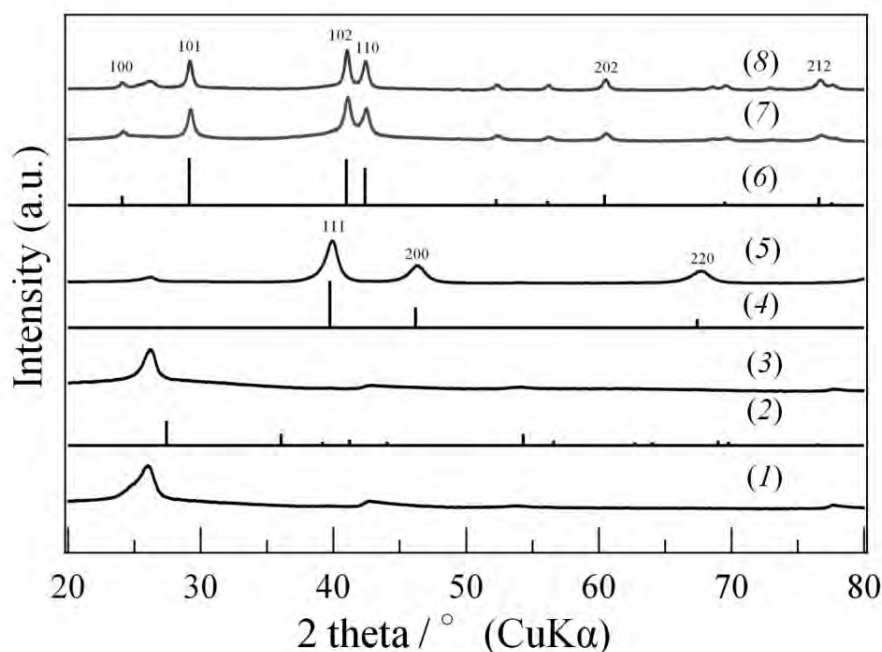


Figure 1 shows the XRD patterns of () CSCNT, () TiO₂/CSCNT, () Pt NPs/TiO₂/CSCNT, () PtPb NPs/CB and () PtPb NPs/TiO₂/CSCNT catalysts. The solid bars of (), () and () are the simulated XRD peak patterns for TiO₂ (anatase), Pt and an ordered intermetallic phase of PtPb, respectively.

The sample (), that was prepared by forming TiO₂ on CSCNT as described in the Experimental section, did not show any diffraction peaks for TiO₂ () but showed the diffraction peaks that arise from CSCNT (). The formation of the TiO₂ deposit on CSCNT could not be confirmed from the XRD measurements. The XRD profile () for the sample that was obtained by photochemically depositing Pt NPs onto TiO₂/CSCNT showed the characteristic reflection peaks at 39.8°, 46.2° and 67.5°, which are assigned to (111), (200) and (220) reflection planes, respectively, (FCC-type structure, $a = 0.3922$ nm, JCPDS 04-0802) and correspond to Pt (). The XRD profile () for the product prepared from the Pt/TiO₂/CSCNT and Pb precursors showed the characteristic reflection peaks at 24.1°, 29.1°, 41.0°, 42.2°, 52.3°, 56.1°, 60.4°, 68.5°, 72.7°, 76.4°, and 83.8°, which are assigned to (100), (101), (102), (110), (201), (103), (202), (004), (203) and (212) reflection peaks, respectively, (NiAs-type structure, $P6_3/mmc$, $a = 0.4259$ nm; $c = 0.5267$ nm) () (9). The observed reflection planes clearly revealed the formation of an intermetallic phase between Pt and Pb. The PtPb NPs/CB prepared from the Pb precursor and Pt NPs/CB also showed a characteristic reflection profile similar to the simulated PtPb peak patterns. These results indicate that the intermetallic phase between Pt and Pb can be formed on TiO₂ or CB supports through a wet-chemical synthesis route at ambient temperature. The average particle sizes of the PtPb NPs on the TiO₂ of the TiO₂/CSCNT and the CB support were calculated to be 10.3 and 8.2 nm, respectively, from the reflection peak of (102) for PtPb using the Scherrer formula. Because the

formation of TiO_2 on the CSCNT support could not be confirmed with the XRD experiment, XPS profiles for the Ti 2p region were measured for the () PtPb NPs/ TiO_2 /CSCNT, () Pt NPs/ TiO_2 /CSCNT, () TiO_2 /CSCNT and () TiO_2 catalysts as shown in Fig. 2. The XPS profile () was measured using the reference sample of TiO_2 . The peaks () for Ti 2p_{3/2} can be observed at approximately 458.5 eV. The peak positions match that of Ti 2p_{3/2} () observed for the TiO_2 reference sample. Therefore, it can be concluded that the TiO_2 moiety was deposited on the CSCNT support in the above-mentioned formation process of TiO_2 . In addition, because the XPS peak positions in the profiles () are the same as that the profile (), no change occurs in the oxidation state of TiO_2 on the CSCNT, even after the polyol process was performed to form PtPb NPs.

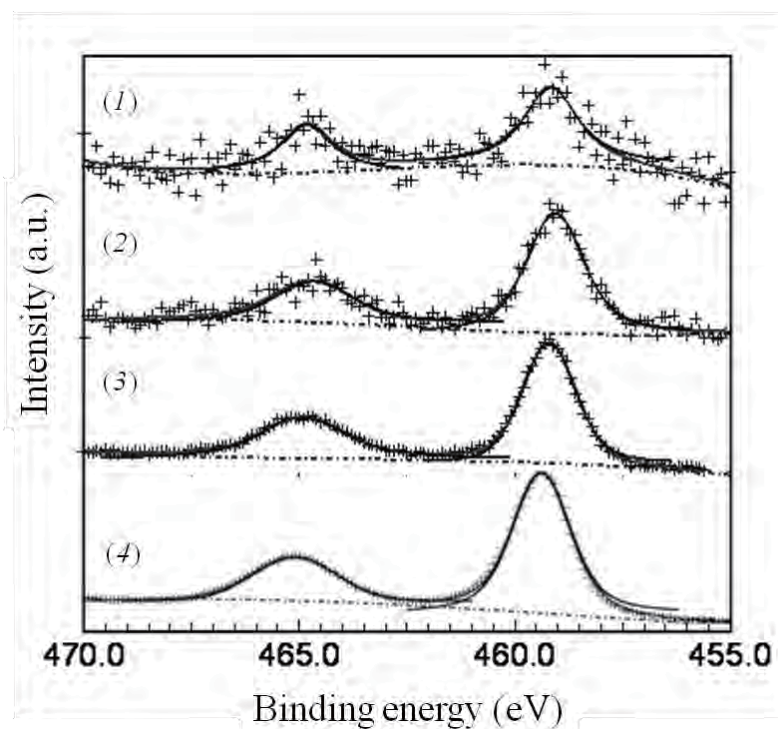


Figure 2 shows the XPS spectral profiles in the Ti 2p region of () PtPb NPs/ TiO_2 /CSCNT, () Pt NPs/ TiO_2 /CSCNT, () TiO_2 /CSCNT and () TiO_2 .

The compositional maps based on the STEM images were obtained to reveal the distribution of the Pt and Pb atoms in the PtPb NPs. STEM (A)-EDS mapping profile (B-F) images of PtPb/ TiO_2 /CSCNT ((B) C, (C) Ti, (D) Pt, (E) Pb, and (F) the overlay of B-E) are shown in Fig. 3. Although some of the PtPb NPs seem to sit outside the TiO_2 islands, it is evident from the EDS mapping that the majority of PtPb NPs sit on the TiO_2 . The average particle size of the PtPb NPs (11.0 nm) on TiO_2 which is evaluated from the STEM image (A), is consistent with those estimated from the XRD results using the Scherrer formula. Figure 3-G presents the profile of the EDS line scan along with a STEM image of NPs that shows the position of the line used for the line scan (inset). Although a Pt-rich core in the PtPb NPs can be clearly recognized in the region surrounded by the dotted lines in Fig. 3-G (Pt: Pb = 54.5: 45.5 (atomic%)), the surface atomic% of the PtPb NPs is almost 1:1. These XRD, XPS and TEM/STEM results suggest the formation of PtPb intermetallic compound NPs on the TiO_2 deposited on the CSCNT support. The formation of PtPb intermetallic compound NPs on the CB was also

confirmed by the similar measurement (average particle size from a TEM image: 7.6 nm, although the results are not shown in this paper).

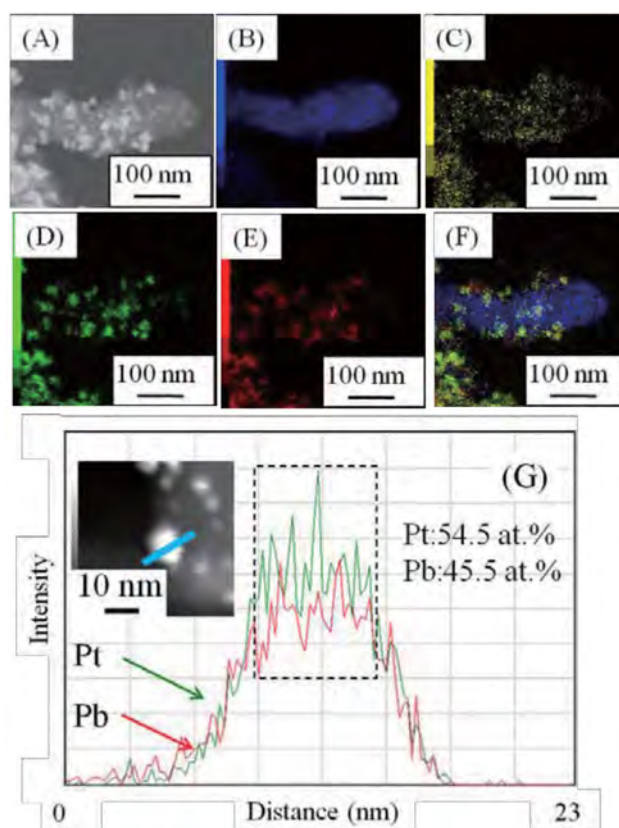


Figure 7 shows the STEM (A)-EDS mapping profile (B–F) images of PtPb NPs/TiO₂/CSCNT. (B) C, (C) Ti, (D) Pt, (E) Pb, and (F) their overlay. (G) EDS Pt (green line) and Pb (red line) line profiles of PtPb NPs/TiO₂/CSCNT along with a STEM image showing the position of the scan line used (inset).

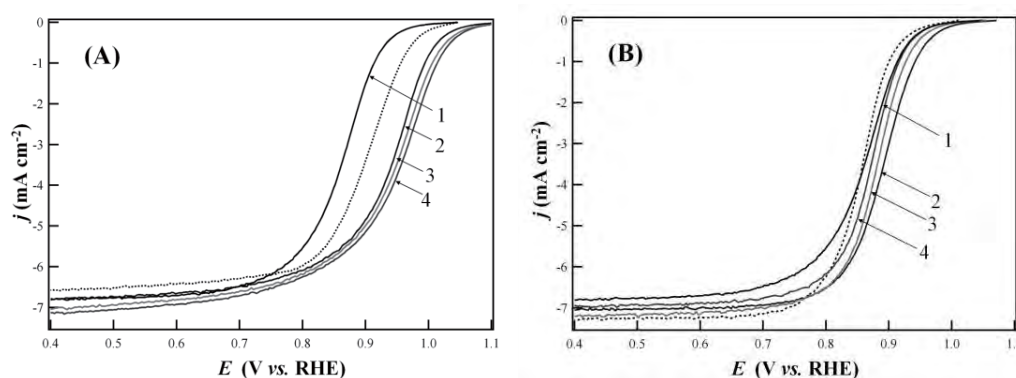


Figure 8 shows cyclic voltammograms obtained for the ORR using (A) PtPb NPs/TiO₂/CSCNT and (B) PtPb NPs/CB in O₂-saturated 0.1 M HClO₄ aqueous solution at an electrode rotation rate of 2000 rpm and potential scan rate of 10 mVs⁻¹ at the () 1st, () 25th, () 50th and () 100th cycle. The dotted lines were obtained using Pt NPs/CB at the 1st cycle.

Figures 4-A and -B show cyclic voltammograms (CVs) for the ORR on the (A) PtPb NPs/TiO₂/CSCNT and (B) PtPb NPs/CB at a potential scan rate of 10 mVs⁻¹ in O₂-saturated 0.1 M HClO₄ aqueous solution. In these figures, the CVs measured at the () 1st, () 25th, () 50th and () 100th cycle are shown along with those (dotted lines in (A) and (B)) obtained with the Pt/CB at the 1st cycle under the same conditions. Both (A) PtPb NPs/TiO₂/CSCNT and (B) PtPb NPs/CB show an increase in the ORR activity with the number of potential cycle in the early stage of multiple potential cycles between 0.4 and 1.1 V as can be seen from the shift of the voltammograms to the positive direction of potential with increasing the potential cycle number. In the case of the PtPb NPs/CB, the ORR activity exhibits a maximum at the 25th potential cycle (Fig. 4-(B)-()). After further potential cycle, the ORR activity decreases with the number of potential cycle. On the other hand, for the PtPb NPs/TiO₂/CSCNT, the ORR activity increases until the 100th cycle (Fig. 4-(A)-()). The current densities at 0.9 V are summarized in Table 1 to compare the ORR activities at the PtPb NPs/TiO₂/CSCNT and PtPb NPs/CB catalysts. The PtPb NPs/TiO₂/CSCNT catalysts exhibits a current density of -5.2 mAcm⁻² at the 100th potential cycle, which is much higher than the maximum current density of -3.0 mAcm⁻² at the 25th potential cycle that was obtained for the PtPb NPs/CB catalysts. The ORR activity decreased gradually with the potential cycling after 100 cycles. The potential cycling for ORR in acidic aqueous solutions might result in dealloying of Pb atoms from the PtPb NP surface. The optimum surface structure and/or chemical state that accelerate the ORR on the NP surface appear when half of the Pb atoms have been dealloyed from the PtPb NP surface. Because the PtPb NPs/TiO₂/CSCNT exhibits a much higher ORR activity than the PtPb NPs/CB, it is thought that the ORR activity is dominated by not only the surface composition of the Pt and Pb atoms, but also the electronic interactions among Pt, Pb and TiO₂.

e Summary of the current density at 0.9 V (s RHE) for the ORR using PtPb NPs/TiO₂/CSCNT, PtPb NPs/CB and Pt NPs/CB in an O₂-saturated 0.1 M HClO₄ aqueous solution at an electrode rotation rate of 2000 rpm and potential scan rate of 10 mVs⁻¹

Sample	Current density at 0.9 V (mAcm ⁻²)			
	1 st cycle	25 th cycle	50 th cycle	100 th cycle
PtPb/TiO ₂ /CSCNT	-3.4	-4.9	-5.0	-5.2
PtPb/CB	-1.0	-3.0	-2.3	-1.7
Pt/CB	-1.5			

To investigate the surface electronic states of the Pt and Pb atoms after the potential cycling, the XPS profiles for Pt 4_f and Pb 4_f before and after the potential cycling of the PtPb NPs/TiO₂/CSCNT and PtPb NPs/CB catalysts were measured. The peak areas and positions obtained for the PtPb NPs deposited on the CB and TiO₂ supports were compared before and after the 100 potential cycles. Figure 5 shows the XPS profiles (Pt

4 and Pb 4) obtained for the PtPb NPs/TiO₂/CSCNT and PtPb NPs/CB. In the XPS profiles, a linear background approximation was used to subtract the background signal from the data. The cross points are the measured data points. The curve fitting was performed assuming Gaussian-Lorentzian peak shapes. Several deconvoluted curves for Pt and Pb 4 doublet paired peaks and a convoluted curve that shows a good fit with the data points can be observed in the XPS results for the PtPb NPs/TiO₂/CSCNT and PtPb NPs/CB catalysts treated with and without multiple potential cycling. Based on the curve fitting results in Fig. 5, the chemical states of the Pt and Pb atoms and the atomic ratios of Pb to Pt atoms on the NP surfaces were evaluated using the chemical shift of the peak position for the deconvoluted 4_{7/2} signal and the relative sensitivity factors of the Pt and Pb atoms (15.86 and 12.83 for 4_{7/2} signal, respectively). The values of the peak positions and atomic % are summarized in Table 2. It is clear from the data that the peak positions of the 4_{7/2} signal of the Pt and Pb atoms for the PtPb NPs/TiO₂/CSCNT are different from those of the PtPb NPs/CB. The deposition of PtPb on the TiO₂ caused a shift in the peak positions to lower binding energies (peak shift: 0.08 eV for Pt, 0.17 for Pb).

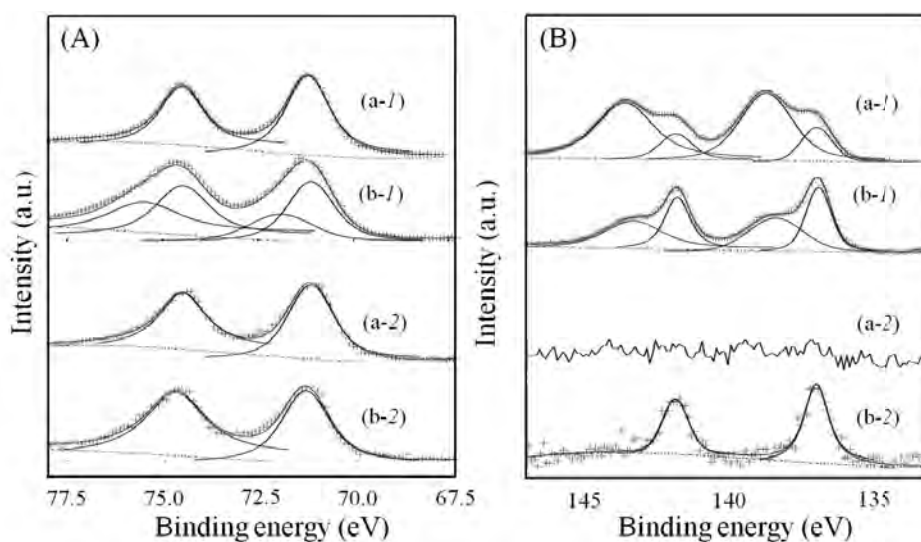


Figure 5. XPS spectral profiles in the (A) Pt 4f and (B) Pb 4f regions of (a) PtPb NPs/CB and (b) PtPb NPs/TiO₂/CSCNT measured (—) before the potential cycles and (---) after 100 potential cycles.

The observed shift suggests that the TiO₂ supports donate electrons to the PtPb NPs. As mentioned above, the peak shifts of the Ti 2p signals could not be detected for the Pt and PtPb NPs deposited on the TiO₂ supports (Fig. 2). This absence of the peak shift might be due to the difference in volume between Pt (or Pb) NPs and TiO₂ moiety. The chemical state in the larger volume of the TiO₂ support is not affected by the electron-donation to the small volume of PtPb NPs. A drastic difference can be observed in the atomic ratios of Pt to Pb atoms on the NP surfaces before and after the potential cycling of the PtPb NPs/TiO₂/CSCNT and PtPb NPs/CB catalysts. Both PtPb NPs/TiO₂/CSCNT and PtPb NPs/CB catalysts were dealloyed by multiple potential cycling, which actually decreased the atom% of Pb on the NP surfaces. In particular, after 100 potential cycles between 0.3 and 1.1 V (vs RHE), the XPS signal of the Pb atoms could not be detected on the PtPb NPs/CB. On the other hand, the remaining Pb atoms could be confirmed with the 100 potential cycle-treated PtPb NPs/TiO₂/CSCNT. The electron donation from TiO₂ to PtPb NPs is considered to prevent the electrochemical dissolution of the Pb atoms on

the PtPb NPs. In addition, it is also considered that the electronic state of the Pt atoms on the PtPb NP surface is related to the ORR activity and is affected by the Pb atoms in the PtPb NP and the TiO₂ support. From our previous study, when the ordered intermetallic phase of PtPb is formed, the 4_{7/2} peak of Pt shifts by 0.2–0.25 eV to the higher binding energy, compared with the 4_{7/2} peak of the pure Pt NPs. The electronic state of the Pt atoms in the PtPb NPs/TiO₂/CSCNT is in a more electron-rich state than that of the bench-marked Pt NPs/CB. The relationship between the electronic state of Pt and ORR activity is usually discussed in terms of the d band center of the Pt atoms on the NP surfaces, and it has been reported that a shift of the d band center of the Pt atoms of approximately -0.2 eV exhibits the maximum ORR activity (10, 11). In the present case, it is likely that the 4_{7/2} orbital in the Pt atoms might be affected by the electronic interactions between the Pt atoms and the Pb atoms as well as between the Pt atoms and the TiO₂ supports and consequently a more electron-rich state in the Pt atoms compared with those in pure Pt is formed on the PtPb NPs/TiO₂/CSCNT catalyst, resulting in the enhancement of the ORR.

e Summary of the XPS results to evaluate the atomic % on the PtPb NP surfaces before and after 100 potential cycles using the PtPb NPs/CB and PtPb NPs/TiO₂/CSCNT samples.

Entry	Pt4f _{7/2} position / eV	Pb4f _{7/2} position / eV	Atom% / Pt : Pb
PtPb/CB as-prepared	70.61	136.42	41.3 : 58.7
PtPb/CB after 100 cycles	70.39	trace	94.6 : 5.4
PtPb/TiO ₂ /CSCNT as-prepared	70.53	136.25	48.6 : 51.4
PtPb/TiO ₂ /CSCNT after 100cycles	70.50	136.30	76.0 : 24.0

on ion

TiO₂/CSCNT-supported PtPb NPs exhibits an increased ORR activity with the potential cycling in the potential range between 0.3 and 1.1 V; its activity is higher than that of PtPb NPs/CB after 25 potential cycles and increases with the potential cycling and the maximum activity is obtained at 100 cycles and further potential cycling causes a gradual decrease in the ORR activity. On the other hand, the PtPb NPs/CB is inferior in the ORR activity to the PtPb NPs/TiO₂/CSCNT and its activity decreases gradually with increasing the potential scan number from 25 to 100 times. Thus, the dealloyed surface of the PtPb NPs on the TiO₂/CSCNT, which is formed by the electrochemical dissolution of Pb atoms from the PtPb NPs, can be considered to have specific catalytic properties for the ORR. From the comparison of the XPS results obtained before and after the potential cycling, the remaining Pb atoms were clearly detected for the PtPb NPs/TiO₂/CSCNT catalyst after a100 cycles, while the signal of the Pb atoms could not be detected for the PtPb NPs/CB catalyst, suggesting that the extent of the dealloying of the Pb atoms from the NP surface is decreased by the electronic interaction between PtPb and TiO₂. This

electronic interaction could be observed in the shift of the $4_{7/2}$ peak of Pt. Specific surface structures or electronic states of the dealloyed PtPb NPs composed of Pt atoms and the remaining Pb atoms in which both the Pt atoms and the Pb atoms have electronic interactions with the TiO_2 support, are closely associated with the enhancement of the ORR on the PtPb NPs/ TiO_2 /CSCNT catalyst. Further study regarding the surface structure and electronic state of the dealloyed PtPb NPs (deposited on the TiO_2 /CSCNT support) with the maximum ORR activity is currently under way along with the purpose of retaining the high ORR activity.

no e e ment

This work was financially supported by the Strategic Research Base Development Program for Private Universities of the Ministry of Education, Culture, Sports, Science and Technology of Japan.

Referen e

1. R.F. Zhou, M. Jaroniec, S.Z. Qiao, *Chem Cat Chem.*, , 3808 (2015).
2. S. Polarz, *Adv. Funct. Mater.*, , 3214 (2011).
3. J.S. Lee, G.S. Park, H.I. Lee, S.T. Kim, R.G. Cao, M.L.Liu, J. Cho, *Nano Lett.*, , 5362 (2011).
4. Y. Ning, M. Wei, L. Yu, F. Yang, R. Chang, Z. Liu, Q. Fu, X. Bao, *J. Phys. Chem. C*, , 27556 (2015).
5. N. Cheng, M.N. Banis, J. Liu, A. Riese, S. Mu, R. Li, T.-K. Sham, X. Sun, *Energy Environ. Sci.*, , 1450 (2015).
6. T. Gunji, G. Saravanan, T. Tanabe, T. Tsuda, M. Miyauchi, G. Kobayashi, H. Abe, F. Matsumoto, *Cat. Sci. Technol.*, , 1436 (2014).
7. T. Gunji, K. Sakai, Y. Suzuki, S. Kaneko, T. Tanabe, F. Matsumoto, *Catalysis Communications*, , 1 (2015).
8. F. Ando, T. Gunji, H. Fujima, T. Takeda, T. Tanabe, S. Kaneko, F. Matsumoto, *Chem Lett.*, , 1741 (2015).
9. *Pearson's Handbook of Crystallographic Data for Intermetallic Phases*, Vol. 3; Villars, P. L., Calvert, L. D., Eds.; American Society for Metals: Metals Park, OH, USA pp. 3044, 3058, 3059 (1985).
10. J. Zhang, M.B. Vukmirovic, Y. Xu, M. Mavrikakis, R.R. Adzic, *Angew. Chem. Int. Ed.*, , 2132 (2005).
11. V. Stamenkovic, B.S. Mun, K.J. J. Mayrhofer, P.N. Ross, N.M. Markovic, J. Rossmeisl, J. Greeley, J.K. Norskov, *Angew. Chem. Int. Ed.*, , 2897 (2006).

■原 著■ 2015 年度神奈川大学総合理学研究所共同研究助成論文

Al³⁺ および Ga³⁺ イオンを開口部に導入した Open-Dawson 型ポリ酸塩の合成と構造解析

松永 諭^{1,2} 井上雄介¹ 長田宏紀¹ 大滝卓也¹ 三原航平¹
力石紀子^{1,2} 野宮健司^{1,2,3}

Syntheses and Characterization of Open-Dawson Polyoxometalates Containing Al³⁺ and Ga³⁺ Ions

Satoshi Matsunaga^{1,2}, Yusuke Inoue¹, Hironori Osada¹, Takuya Otaki¹,
Kohei Mihara¹, Noriko Chikaraishi Kasuga^{1,2} and Kenji Nomiya^{1,2,3}

¹ Department of Chemistry, Faculty of Science, Kanagawa University, Hiratsuka City, Kanagawa 259-1293, Japan

² Research Institute for Integrated Science, Kanagawa University, Hiratsuka City, Kanagawa 259-1293, Japan

³ To whom correspondence should be addressed. E-mail: nomiya@kanagawa-u.ac.jp

Abstract: Open-Dawson polyoxometalates (POMs) containing tetra-aluminum(III) and tetra-gallium(III) clusters, i.e., K₁₀[{Al₄(μ-OH)₆}{α,α-Si₂W₁₈O₆₆}]·28.5H₂O (potassium salt of Al₄-open) and K₁₀[{Ga₄(μ-OH)₆}{α,α-Si₂W₁₈O₆₆}]·25H₂O (potassium salt of Ga₄-open), were synthesized by the reactions of [A-α-SiW₉O₃₄]¹⁰⁻ with Al(NO₃)₃·9H₂O or Ga(NO₃)₃·nH₂O, and characterized by X-ray crystallography, FTIR, elemental analysis, and TG/DTA. X-ray crystallography revealed that the {M₄(μ-OH)₆}⁶⁺ (M = Al, Ga) clusters were accommodated in an open pocket of the open-Dawson polyanion, [α,α-Si₂W₁₈O₆₆]¹⁶⁻, which was constituted by the fusion of two trilacunary Keggin POMs via two W-O-W bonds. These two open-Dawson POMs showed a clear difference in the bite angles depending on the size of ionic radii. The solution ²⁹Si and ¹⁸³W NMR spectra in D₂O showed only one signal and five signals, respectively. These spectra were consistent with the molecular structures of Al₄- and Ga₄-open, suggesting that these polyoxoanions were obtained as single species and that they maintained their molecular structures in solution.

Keywords: polyoxometalates, open-Dawson structural POM, aluminum, gallium

序論

分子性の酸化物クラスターであるポリ酸塩は、強酸性、耐酸性、豊富な酸化還元特性などの極めて多彩な性質を有しているため、触媒、表面化学、材料科学、医薬など様々な観点から広く研究がなされている¹⁾。様々な構造のポリ酸塩が知られているが、近年 open-Dawson 型ポリ酸塩が新しいタイプのポリ酸塩として注目されている²⁾。古くからよく知られる Dawson 型ポリ酸塩は、2つの Keggin 型ポリ酸塩三欠損種が6本の W-O-W 結合により縮合した構造を有している(図1)。しかし、負電荷の大きいゲストアニオン XO₄⁴⁻ (X = Si, Ge) を内包する Keggin 型三欠損種は、静電反発により通常の Dawson 型

構造にはなりづらく、電荷反発を避けるように2本の W-O-W 結合のみで連結した open-Dawson 型ポリ酸塩を形成する(図1)。つまり、open-Dawson 型ポリ酸塩は、従来の Dawson 型ポリ酸塩が中央で口を開いた様な構造を有している。その開口部には、様々な金属イオンを最大6個まで導入することが可能であり、これまでに様々な金属イオンを導入した open-Dawson 型ポリ酸塩が報告されている²⁻⁴⁾。特に、多核金属中心による共同的な触媒反応や基底高スピンを有する単分子磁石などのプラットフォームとして期待でき、実際に5個の Ni イオンを開口部に含む open-Dawson 型ポリ酸塩が水の酸化分解触媒とし

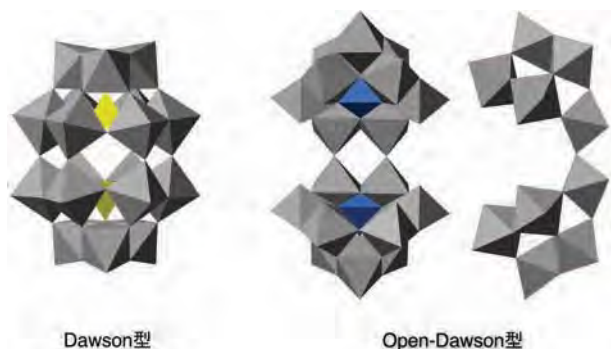


図1. 通常の Dawson 型ポリ酸塩と open-Dawson 型ポリ酸塩の構造。

て効果的に機能することが報告されている³⁾。しかし、これまで報告されている open-Dawson 型ポリ酸塩は、偶然合成されることがほとんどであり合成法の確立が急務である。

一方で、第13属元素である Al や Ga は、水中で非常に複雑な多核ヒドロキシクラスターを形成しており、その構造や溶液中での挙動に興味を持たれている⁵⁾。Al や Ga を含むポリ酸塩は、これら多核ヒドロキシクラスター化学種の安定な分子モデルと見なすことができ、この様なポリ酸塩を合成し構造を明らかにする事は、有用な知見を与えられ考えられる。これまでもポリ酸塩骨格の W 原子を Al および Ga で置換した化合物は報告されているが、結晶構造を明らかにした例はあまり多くない。特に Ga 置換ポリ酸塩の構造解析例は Patzke らの報告のみである⁶⁾。

今回我々は、Al³⁺ および Ga³⁺ イオンを開口部に導入した open-Dawson 型ポリ酸塩、K₁₀[Al₄(μ-OH)₆{α,α-Si₂W₁₈O₆₆}]・28.5H₂O (Al₄-open カリウム塩) および K₁₀{[Ga₄(μ-OH)₆]{α,α-Si₂W₁₈O₆₆}]・25H₂O (Ga₄-open カリウム塩)、の合成に成功し、構造を明らかにしたので報告する。

材料と方法

材料

硝酸アルミニウム九水和物、硝酸ガリウム n 水和物 (n = 7 ~ 9)、塩酸、水酸化カリウム、塩化カリウム (和光純薬) 重水 (関東化学) は、精製せずに購入したものをそのまま用いた。Keggin 型ポリ酸塩三欠損種ナトリウム塩およびカリウム塩は既報^{7,8)}に従い合成した。

合成法

K₁₀{[Al₄(μ-OH)₆]{α,α-Si₂W₁₈O₆₆}]・28.5H₂O (Al₄-open カリウム塩) の合成

Keggin 型ポリ酸塩三欠損種 Na⁺ 塩 Na₁₀[A-α-SiW₉O₃₄]

・18H₂O (6.0 g, 2.16 mmol) を純水 120 mL に懸濁させた。0.1 M HCl_{aq} を用いて pH 7.5 に調整した。この溶液に Al(NO₃)₃・9H₂O (1.62 g, 4.32 mmol) を加え 80°C で 30 分間攪拌した。この段階での pH は 2.00 であった。その溶液を 1 M KOH_{aq} を用いて pH 6.5 に調整し、飽和 KCl 水溶液を 6 mL 加えた。一日後、不純物を含む粗結晶が析出するため濾過により除去した。ろ液に飽和 KCl 水溶液を 6 mL 加え、さらに一日間室温にて放置することにより、無色針状結晶が析出した。析出した結晶をメンブランフィルター (JG 0.2 μm) を使ってろ取り、冷水にて洗浄し、減圧乾燥を二時間おこなうことで、Al₄-open カリウム塩 0.818 g (0.148 mmol) を得た (収率 13.7%)。

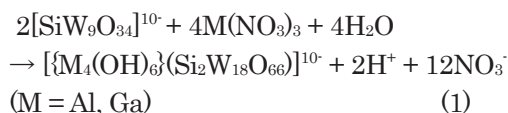
K₁₀{[Ga₄(μ-OH)₆]{α,α-Si₂W₁₈O₆₆}]・25H₂O (Ga₄-open カリウム塩) の合成

Keggin 型ポリ酸塩三欠損種 K⁺ 塩、K₁₀[A-α-SiW₉O₃₄]・10H₂O (3.0 g, 1.07 mmol) を純水 60 mL に懸濁させた。0.1 M HCl_{aq} を用いて pH 7.5 に調整した。この溶液に Ga(NO₃)₃・nH₂O (0.86 g, 2.14 mmol, n=8 で計算) を加え 80°C で 30 分間攪拌した。この段階での pH は 1.78 であった。その溶液を 1 M KOH_{aq} を用いて pH 6.5 に調整し、飽和 KCl 水溶液を 1.8 mL 加えた。一日後、無色針状結晶が析出した。析出した結晶をメンブランフィルター (JG 0.2 μm) を使ってろ取り、減圧乾燥を二時間おこなうことで、Ga₄-open カリウム塩 0.79 g (0.140 mmol) を得た (収率 26.2%)。

結果と討論

合成と同定

Al₄-open カリウム塩 K₁₀{[Al₄(μ-OH)₆]{α,α-Si₂W₁₈O₆₆}]・28.5H₂O は、Keggin 型ポリ酸塩三欠損種ナトリウム塩 Na₁₀[A-α-SiW₉O₃₄]・18H₂O と Al(NO₃)₃・9H₂O をモル比 1 : 2 で反応させた後、飽和 KCl 水溶液を加えることで、結晶として得た。Ga₄-open カリウム塩 K₁₀{[Ga₄(μ-OH)₆]{α,α-Si₂W₁₈O₆₆}]・25H₂O もほぼ同様の条件で合成したが、前駆体として Keggin 型ポリ酸塩三欠損種カリウム塩 K₁₀[A-α-SiW₉O₃₄]・10H₂O を用いている点で異なっている。収率はそれぞれ 13.7% (Al₄-open カリウム塩)、26.2% (Ga₄-open カリウム塩) であった。Al₄-open および Ga₄-open の反応式を以下に示す。



Al₄-open カリウム塩における結晶化の初期段階では、目的物の結晶以外にも副生成物として Al³⁺ 16 核

クラスターで連結された Keggin 型ポリ酸塩四量体 $[\{\alpha\text{-Al}_3\text{SiW}_9\text{O}_{34}(\mu\text{-OH})_6\}_4\{\text{Al}_4(\mu\text{-OH})_6\}]^{22-}$ の結晶も析出した⁹⁾。そのため、副生成物を含む粗結晶をろ過により除去し、ろ液に飽和 KCl 水溶液を追加し結晶化することで、Al₄-open カリウム塩のみを単離することができた。Ga₄-open カリウム塩の場合も、Ga イオン 3 つが置換した Keggin 型ポリ酸塩二量体⁶⁾が副生成物として稀に生成した。この場合も、副生成物を含む粗結晶を除去し、ろ液に飽和 KCl 水溶液を加えて結晶化することで純粋な Ga₄-open カリウム塩を得ることができた。また、副生成物を含むサンプルを熱再結晶することでも精製が可能であった。

Al₄-open カリウム塩および Ga₄-open カリウム塩の合成において、大過剰の K⁺ イオンの添加が不可欠である。既報の open-Dawson 型ポリ酸塩の大部分はカリウム塩として単離されている。これは、対イオンに Na⁺ を用いると、open-Dawson 型ではなく多核金属イオンクラスターを 2 つの Keggin 型三欠損種で挟み込んだ、所謂サンドイッチ型ポリ酸塩の生成が支配的となるためである。後述の X 線構造解析から、open-Dawson 型ポリアニオンの酸素原子と対イオンである K⁺ イオンとの間に明確な相互作用が存在し、open-Dawson 型ポリ酸塩を安定化していることが示唆された。このことから、大過剰の KCl を加えることが、open-Dawson 型ポリ酸塩の合成において重要であることが明らかとなった。

Al₄-open カリウム塩および Ga₄-open カリウム塩の FTIR の結果、1000 cm⁻¹ 付近に $\nu_{\text{as}}(\text{Si-O})$ 、960 cm⁻¹ 付近に $\nu_{\text{as}}(\text{W-O})$ に基づく振動バンドが観測された。また、900-600 cm⁻¹ の領域においても W-O の振動および変角に基づく特徴的な吸収が観測された。これらの IR スペクトルは、既報の open-Dawson 型ポリ酸塩のスペクトル形状とよく似ており、open-Dawson 型ポリアニオン骨格に特徴的な吸収である事が確認できた。

結晶構造

Al₄-open カリウム塩の単結晶 X 線構造解析の結果を図 2 左上に示す。2 つの Keggin 型ポリ酸塩三欠損種が二本の W-O-W 結合で連結した open-Dawson 型骨格 $[\alpha, \alpha\text{-Si}_2\text{W}_{18}\text{O}_{66}]^{16-}$ を形成しており、その開口部に Al³⁺ 4 核ヒドロキシクラスター $\{\text{Al}_4(\mu\text{-OH})_6\}^{6+}$ が導入された構造 $[\{\text{Al}_4(\mu\text{-OH})_6\}\{\alpha, \alpha\text{-Si}_2\text{W}_{18}\text{O}_{66}\}]^{10-}$ であった。開口部内の 4 つの Al³⁺ イオンは長方形型に配列していた。隣接している Al³⁺ イオン同士は稜共有型 (O67, O68, O69, O70) および頂点共有型酸素原子 (O71, O72) で連結されており、全ての Al³⁺ は六配位八面体構造であった。BVS 計算¹⁰⁾の結果から、Al³⁺ イオ

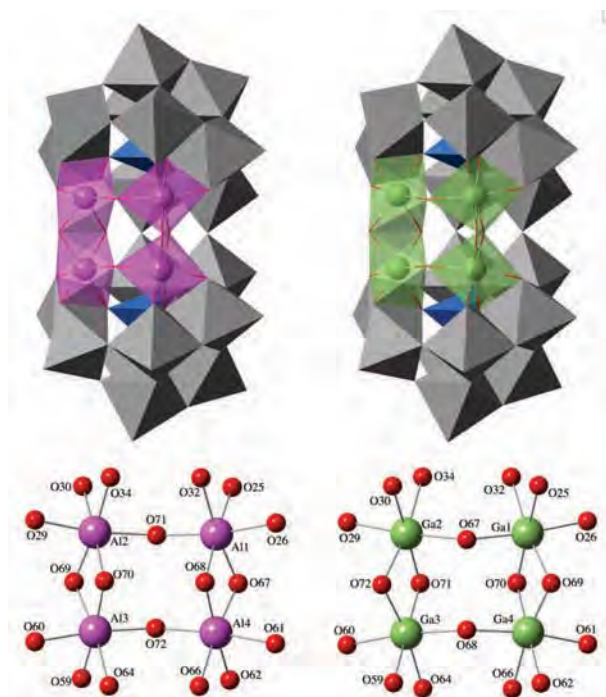


図 2. Al₄-open のアニオン部位の構造 (左上) と開口角内の Al クラスターの部分構造 (左下), および Ga₄-open の構造 (右上) と Ga クラスターの部分構造 (右下). 灰色, 水色, ピンク色, および緑色の多面体はそれぞれ $\{\text{WO}_6\}$, $\{\text{SiO}_6\}$, $\{\text{AlO}_6\}$, $\{\text{GaO}_6\}$ を示している。

ンを架橋する酸素原子はすべて OH⁻ である事が示唆された (BVS 値 ; O67, 0.992; O68, 0.945; O69, 0.965; O70, 0.974; O71, 0.958; O72, 0.984)。

Ga₄-open カリウム塩の構造は、Al₄-open カリウム塩と同構造であった (図 2 右上)。この様な 4 つの金属イオンが長方形型に配列した open-Dawson 型ポリ酸塩は、Fe を導入した $\text{K}_2\text{Na}_8[\{\text{Fe}_4(\text{OH})_6\}\{\alpha, \alpha\text{-Si}_2\text{W}_{18}\text{O}_{66}\}] \cdot 44\text{H}_2\text{O}$ のみが知られている⁴⁾。

Open-Dawson 型ポリ酸塩は、開口部の開き具合を開口角として定義することができ、導入された金属クラスターに依存して開口角が変化する。今回の化合物の開口角は Al₄-open が 54.277°, Ga₄-open が 56.118° であり、Ga₄-open の方が約 2° 大きいことがわかった (図 3 上)。両者は同構造である事から、この開口角の違いは導入金属のイオン半径に由来すると考えられる。Al と Ga のイオン半径はそれぞれ 0.53Å, 0.76Å であり、Ga の方が僅かに大きいため、開口角が大きくなったと考えられる。

両化合物ともに、ポリ酸塩の酸素原子と対イオンの K⁺ イオンとの間に多くの相互作用が存在していた。特に open-Dawson 型ポリ酸塩のチョウツガイ部分に相当する $\{\text{WO}_6\}$ の酸素原子 (O16, O21, O49, O55) と K イオン (Al₄-open の K1, K4, Ga₄-open の K1, K3) の相互作用 (図 3 下) は、既報の open-Dawson 型ポリ酸塩でも観測されている。この相互

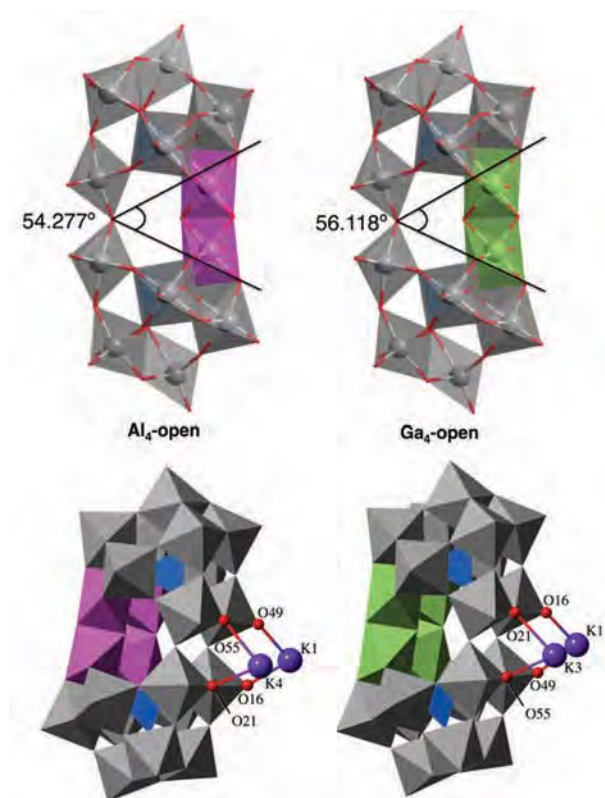


図 3. $\text{Al}_4\text{-open}$ と $\text{Ga}_4\text{-open}$ の開口角の比較 (上) とポリ酸塩と K イオンとの相互作用 (下).

作用が open-Dawson 型骨格を安定化している重要な要因であると我々は考えており、合成時に大過剰の KCl の添加が不可欠であることと対応している。この相互作用以外にも、ポリ酸骨格の酸素原子、結晶水、 K^+ イオンとの間で多くの相互作用が存在し、結晶構造中で三次元ネットワーク構造を構成している。

^{29}Si および ^{183}W NMR スペクトル

D_2O 中での $\text{Al}_4\text{-open}$ および $\text{Ga}_4\text{-open}$ の ^{29}Si NMR の結果、 -82.55 ($\text{Al}_4\text{-open}$) および -82.31 ($\text{Ga}_4\text{-open}$) ppm に一本線ピークが観測された。また、 ^{183}W NMR では両者ともに open-Dawson 構造から予想される 5 本線ピークが積分比 2 : 2 : 2 : 1 : 2 で観測された (-79.67 , -83.33 , -149.84 , -175.17 , -197.67 ppm for $\text{Al}_4\text{-open}$; -64.31 , -72.52 , -151.79 , -167.10 , -194.70 ppm for $\text{Ga}_4\text{-open}$)。このことから、溶液中でも open-Dawson 構造を維持していることが明らかとなった。また、結晶化の初期段階で生成する副生成物のピークも観測されず、純度良く合成できていることがわかった。

まとめと展望

我々は、open-Dawson 型ポリ酸塩の開口部に Al, Ga を導入した $\text{Al}_4\text{-open}$ および $\text{Ga}_4\text{-open}$ カリウム塩の合成法を確立し、構造を決定することに成功

した。今回第 13 属元素である Al と Ga を導入したが、同族でイオン半径の大きな In (0.94 \AA) を導入した open-Dawson 型ポリ酸塩を合成することができれば、同族元素で構造の比較が可能であり、イオン半径が open-Dawson 型ポリ酸塩の構造に与える影響を系統的に評価することができる。第 5 および第 6 周期の元素には多彩な触媒活性を有するものが数多く存在するが、これらを導入した open-Dawson 型ポリ酸塩の例はこれまでに報告されていない。複数の金属イオンを密に配列することができる open-Dawson 型ポリ酸塩に第 5 および第 6 周期元素を導入することができれば、多核金属中心による共同的な触媒活性を発現しうるのではないかと考えている。そのためにも、上記のような同族元素による系統的な評価は、今後の分子設計を考える上で重要であり、現在さらなる研究を進めているところである。

謝辞

本研究は、研究課題「様々な金属を導入した新規 open-Dawson 型ポリオキソメタレート合成」に対する 2015 年度総合理学研究所共同研究の研究助成 (RIIS201505) を受けて行いました。厚く御礼申し上げます。

文献

- Hill CL, Ed. (1998) Polyoxometalates. *Chem. Rev.* 98: 1-390.
- Laronze N, Marrot J and Hervé G (2003) Synthesis, molecular structure and chemical properties of a new tungstosilicate with an open Wells-Dawson structure, $\alpha\text{-}[\text{Si}_2\text{W}_{18}\text{O}_{66}]^{16-}$. *Chem. Commun.*: 2360-2361.
- Zhu G, Glass EN, Zhao C, Lv H, Vickers JW, Geletii YV, Musaev DG, Song J and Hill CL (2012) A nickel containing polyoxometalate water oxidation catalyst. *Dalton Trans.* 41: 13043-13049.
- Leclerc-Laronze N, Marrot J and Hervé G (2006) Dinuclear vanadium and tetranuclear iron complexes obtained with the open Wells-Dawson $[\text{Si}_2\text{W}_{18}\text{O}_{66}]^{16-}$ tungstosilicate. *C. R. Chimie* 9: 1467-1471.
- Mensingher ZL, Wang W, Keszler DA and Johnson DW (2012) Oligomeric group 13 hydroxide compounds—a rare but varied class of molecules. *Chem. Soc. Rev.* 41: 1019-1030.
- Allmen K, Car PE, Blacque O, Fox T, Müller R and Patzke GR (2014) Structure and properties of new gallium-containing polyoxotungstates with hexanuclear and tetranuclear cores. *Z. Anorg. Allg. Chem.* 640: 781-789.
- Tézé A and Hervé G (1990) α -, β -, and γ -Dodecatungstosilicic acids: isomers and related lacunary compounds. *Inorg. Synth.* 27: 85-96.
- Laronze N, Marrot J and Hervé G (2003) Cation-directed synthesis of tungstosilicates. 1. Syntheses

- and structures of $K_{10}A-\alpha-[SiW_9O_{34}]\cdot 24H_2O$, of the sandwich-type complex $K_{10.75}[Co(H_2O)_6]_{0.5}[Co(H_2O)_4Cl]_{0.25}A-\alpha-[K_2\{Co(H_2O)_2\}_3(SiW_9O_{34})_2]\cdot 32H_2O$ and of $Cs_{15}[K(SiW_{11}O_{39})_2]\cdot 39H_2O$. *Inorg. Chem.* **42**: 5857–5862.
- 9) Inoue Y, Matsunaga S and Nomiya K (2015) Al_{16} -hydroxide cluster-containing tetrameric polyoxo-metalate, $[\{\alpha-Al_3SiW_9O_{34}(\mu-OH)_6\}_4\{Al_4(\mu-OH)_6\}]^{22-}$. *Chem. Lett.* **44**: 1649–1651.
- 10) Brown ID and Altermatt D (1985) Bond-valence parameters obtained from a systematic analysis of the Inorganic Crystal Structure Database. *Acta Crystallogr.* **B41**: 244–247.